
**EIGHTH INTERNATIONAL SYMPOSIUM ON
APPLICATIONS OF LASER TECHNIQUES TO FLUID MECHANICS**

VOLUME II

DISTRIBUTION STATEMENT A

Approved for public release
Distribution Unlimited

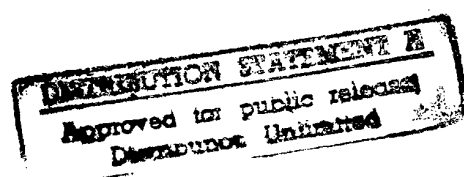
19970516 053

July 8th to 11th 1996
Lisbon, Portugal

DTIC QUALITY INSPECTED

**EIGHTH INTERNATIONAL SYMPOSIUM ON
APPLICATIONS OF LASER TECHNIQUES TO
FLUID MECHANICS**

VOLUME II



**July 8 - 11, 1996
Lisbon, Portugal**

PREFACE

The proceedings volumes I and II comprised the papers that were accepted for presentation at the *Eighth International Symposium on Applications of Laser Techniques to Fluids Mechanics*, which was held at The Calouste Gulbenkian in Lisbon, during the period of July 8 to 11, 1996. The prime objective of this Eighth Symposium is to provide a forum for the presentation of the most advanced research on laser techniques for flow measurements, and reveal significant results to fluid mechanics. The applications of laser techniques to scientific and engineering fluid flow research is emphasised, but contributions to the theory and practice of laser methods are also considered where they facilitate new improved fluid mechanic research. Attention is focused on laser-Doppler anemometry, particle sizing and other methods for the measurement of velocity and scalars, such as particle image velocimetry and laser induced fluorescence.

The papers comprising the formal record of the meeting were selected following high standard reviews, by members of the Advisory Committee, from approximately 300 extended abstracts submitted for presentation at this meeting.

Volume I comprises the papers to be presented during the first and second Days of the Symposium, namely July 8 and 9, while Volume II includes the papers of the following days, Wednesday, July 10, and Thursday, July 11.

We would like to take this opportunity to thank those who assisted us. The assistance provided by the Advisory Committee is highly appreciated. We are highly indebted for the financial support provided by the Sponsoring Organisations that made this Symposium possible. Many thanks are also due to the Secretariat of the Symposium, Graça Pereira, Carlos Carvalho, Anabela Almeida, Luisa Martins and Ana Nunes.

THE ORGANIZING COMMITTEE

ORGANIZING COMMITTEE

- **Ronald J. Adrian**
Department of Theoretical and Applied Mechanics
University of Illinois at Urbana - Champaign
Urbana, Illinois 61801
USA
- **Diamantino F. G. Durão**
Department of Mechanical Engineering
Instituto Superior Técnico
Av. Rovisco Pais
1096 Lisboa Codex
PORTUGAL
- **Franz Durst**
Lehrstuhl für Strömungsmechanik
Erlangen Universität - Nuremberg
Egerlandstraße 13
D-8520 Erlangen
GERMANY
- **Manuel V. Heitor**
Department of Mechanical Engineering
Instituto Superior Técnico
Av. Rovisco Pais
1096 Lisboa Codex
PORTUGAL
- **Masanobu Maeda**
Department of Mechanical Engineering
Keio University
1-14-1 Hioshi, Kohuku
Yokohama 223
JAPAN
- **James H. Whitelaw**
Imperial College of Science, Technology and Medicine
Department of Mechanical Engineering
Exhibition Road
London SW7 2BX
England, United Kingdom

ADVISORY COMMITTEE

R. A. Antonia	W. Merzkirch
C. Arcoumanis	J. F. Meyers
W. D. Bachalo	R. H. Miles
A. Boutier	E. A. Müller
C. H. CAspersen	T. Nakajima
A. Coghe	N. Nakatani
W. J. A. Dahm	A. Naqwi
D. Dopheide	K. Ohba
H. Eickhoff	T. Obokata
M. Escudier	J. C. Pereira
A. F. Falcão	H. J. Pfeifer
L. Fingerson	F. Pinho
M. Gharib	M. L. Riethmüller
G. Gouesbet	D. Rockwell
I. Grant	X. Shen
J. A. C. Humphrey	R. L. Simpson
D. A. Jackson	R. N. Syred
R. Karlsson	A. M. K. P. Taylor
K. Ishida	E. P. Tomasini
J. Kompenhans	C. Tropea
L. Lading	J. T. Turner
B. Lehmann	J. E. S. Venart
A. Leipertz	P. O. Witze
A. Melling	G. Wigley
	M. Yanneskis

SPONSORING ORGANISATIONS

- Caixa Geral de Depósitos
- DHL
- Direcção Geral de Turismo
- European Commission
- European Research Office:
United States Army,
Navy and Air Force Departments
- Calouste Gulbenkian Foundation
- FLAD, Portuguese-American Foundation for the Development
- IST - Instituto Superior Técnico
- ITEC/CRAPS
Centro de Robótica, Automação e Processamento de Sinal
- JNICT - Junta Nacional de Investigação Científica e Tecnológica
(Portuguese Research Council)
- TAP, Air Portugal

LOCAL SECRETARIAT

Graça Pereira

Carlos Carvalho

Anabela Almeida

Luisa Martins

Ana Paula Nunes

Instituto Superior Técnico

Departamento de Engenharia Mecânica

Pavilhão de Mestrados

Av. Rovisco Pais, 1096 Lisboa Codex

Portugal

Telephone: (351 1) 841 73 79

Fax: (351 1) 849 61 56

EMail: mheitor@tercomb.ist.utl.pt

LIST OF CONTENTS

VOLUME I (SESSION 1-20)

SESSION 1. PLENARY SESSION

- 1.1. Effects of Centrebody Rotation on Laminar Flow Through an Eccentric Annulus
M.P. Escudier and I. W. Gouldson
- 1.2. Molecular Tagging Diagnostics for the Study of Kinematics and Mixing in Liquid Phase Flows
M. M. Koochesfahani, R.K. Cohn, C.P. Gendrich and D.G. Nocera
- 1.3. Two-dimensional Laser Diagnostics For Sooting Flames
S. Schrami, S. Will, D. Hofmann, K.-U. Münch and A. Leipertz

SESSION 2. 2 PHASE FLOWS INSTRUMENTATION I

- 2.1. A Device For Phase Shift Measurement in an Advanced Phase Doppler Velocimeter
J. Evenstad, A. Naqwi and R. Menon
- 2.2. Optimization of the Shape of Receiving Aperture in a Phase Doppler System
A. Naqwi
- 2.3. A Novel Architecture for Real-Time Phase Measurement
K.M. Ibrahim and W.D. Bachalo
- 2.4. The Influence of Flame on Phase Doppler Anemometry
S. Tsushima, F. Akamatsu, M. Katsuki, Y. Mizutani and Y.-D. Cho
- 2.5. Determination of Effective Measurement Area in a Conventional Phase-Doppler Anemometry
T. Maeda, H. Morikita, K. Hishida and M. Maeda
- 2.6. Measurement Uncertainties of Phase Doppler Technique Due To Effect of Slit Location, Control Volume Size and Flame Front Presence (in Application for Combusting Spray)
Y. Ikeda, T. Hirohata and T. Nakajima

SESSION 3. COMBUSTION I

- 3.1. Investigations of Turbulent Jet Diffusion Flames by Spontaneous Raman Scattering and Laser-Induced Fluorescence
W. Meier, A. Vyrodov, V. Bergmann, U. Meier and W. Stricker
- 3.2. Quantitative LIF and Rayleigh Measurements of Temperature and Absolute Concentration of OH Radical in Strained Diffusion Flames
T. Croonenbroek, Th. Daguse, N. Darabiha and J.C. Rolon
- 3.3. Application of PIV to Turbulent Reacting Flows
L. Muñiz, R.E. Martinez and M.G. Mungal
- 3.4. Velocity Measurements in Highly Turbulent Premixed Flames by a PIV Measurement System
N. Paone, G.M. Revel and E. Nino
- 3.5. Flame Surface Density Measurements in Turbulent Premixed Combustion
C. Martel, J. Piana, V. Liard, N. Darabiha and D. Veynante
- 3.6. Whole-Field Measurements on an Excited Premixed Flame Using On-Line PIV
H. Shen, L. Lourenco, A. Krothapalli and P. Strykowski

SESSION 4. 3D-IMAGING VELOCIMETRY

- 4.1. Dual-Plane Correlation for Three-Dimensional Particle Image Velocimetry on Planar Domains
M. Raffel, C. Willert, A. Derville, O. Ronneberger and J. Kompenhans
- 4.2. Spatial Correlation Analysis for 3-D Scanning PIV: Simulation and Application of Dual-Color Light-Sheet Scanning
Ch. Brücker
- 4.3. Three Dimensional Velocity Measurements using Hybrid HPIV
J. Zhang, B. Tao and J. Katz
- 4.4. Improvements of Holographic Particle Image Velocimetry (HPIV) by Light-in-Flight Holography
M. Böhmer, H. Hinrichs, K.D. Hinsch and J. Kickstein
- 4.5. Scalar Imaging Velocimetry Measurements of the Velocity Gradient Tensor Field in Turbulent Flows
L.S. Su and W.J. Dahm **CANCELLED**
- 4.6. Some Statistical Results from Concentration and Velocity Field Measurements using Laser Induced Fluorescence Tomography
G. J. Merkel, P. Rys, F.S. Rys and T.A. Dracos

SESSION 5. MANUFACTURER'S TECHNICAL PRESENTATION

SESSION 6. 2-PHASE FLOWS INSTRUMENTATION II

- 6.1. Characteristics of a Miniaturized Probe Employing the Pulse Displacement Technique
C. F. Hess
- 6.2. Determination of Submicronic Particles Size by Analysis of Light Scattered By a Gas Stream
L. Azizi, P. Herve and A. Kleitz
- 6.3. Advantages of UV Lasers in Laser and Phase Doppler Anemometers for Submicrometer Particles
F. Durst, A. Melling and P. Volkholz
- 6.4. On Particle Flux and Concentration Measurement by Shadow Doppler Velocimetry
M. Maeda, H. Morikita, I. Prassas, A.M.K.P. Taylor and J.H. Whitelaw
- 6.5. Scattering of a Gaussian Beam by an Infinite Cylinder: Numerical Results in GLMT-Framework
K.F. Ren, G. Gouesbet and G. Gréhan
- 6.6. Time Domain Single Tone Analysis using Quadrature Algorithm
V. Strunck, H. Müller and D. Dopheide

SESSION 7. COMBUSTION II

- 7.1. Turbulent Propagation Velocity and Mean Reaction Rates of Premixed Turbulent Flames in Stagnation Flows
E. Bourguignon, Y. Michou and I. Gökalp
- 7.2. Combustion-Turbulence Interaction in Stagnation Flows
F.I.E. Doolaar and T.H. van der Meer
- 7.3. On the Use of Laser Rayleigh Scattering to Study the Aerothermochemistry of Recirculating Premixed Flames
F. Caldas, D. Duarte, P.C. Ferrão, M. V. Heitor and C. Poppe
- 7.4. A PIV Investigation in an Axisymmetric non Premixed Bluff Body Burner Flame
A. Susset, M. Perrin, D. Jaffre, C. Gray and J.B. Richon
- 7.5. Methane Concentration by MIE Scattering Imaging Technique in Axisymmetric Non-Premixed Bluff Body Flames
K. Mokaddem, J.C. Rolon, D. Jaffre and M. Perrin
- 7.6. Non-Intrusive Spectroscopic Measurements with a Tunable Excimer Laser in an Atmospheric Combustor with Premixing and Prevaporization
R. Lachner, D. Theisen, H. Kettl, D. Rist, G. Kappler and A. Schmid

SESSION 8. AERODYNAMIC FLOWS AND ROTATING MACHINES I

- 8.1. LDA-Investigations on Turbulent Shear Stress in full Scale Centrifugal Pump
M. Lutz, V. Denk and A. Delgado
- 8.2. Velocity Measurement in the Impeller and in the Volute of a Centrifugal Pump by Particle Image Displacement Velocimetry
M. Oldenburg and E. Pap
- 8.3. Mean and Turbulent Flow Characteristics of Single Hyperboloid Impeller Stirred Vessels
F.M. Piqueiro, M.F. Proença, F.T. Pinho and A.M. Santos
- 8.4. Detailed LDV-Measurements for Visualisation of the Flow Field Within a Rushton-Turbine
M. Höfken, M. Schäfer and F. Durst
- 8.5. The Decay of the Trailing Vortices from Impeller Blades
N.J. Fentiman, N. A. Borrett, K.C. Lee and M. Yianneskis
- 8.6. Particle Tracking Velocimetry Measurements in a Radial Pump with Particle Pair Detection using the HOUGH Transform
C. Rothlübbers, T. Scheffler, R. Orglmeister and H. Siekamann

SESSION 9. 2-PHASE FLOWS INSTRUMENTATION III

- 9.1. A Single-Beam Velocimeter based on Rainbow-Interferometry
J.P.A.J. van Beeck and M.L. Riethmuller
- 9.2. Size Insensitive Rainbow Refractometry: Theoretical Aspects
N. Roth, K. Anders and A. Frohn
- 9.3. An Advanced Rainbow Signal Processor for Improved Accuracy in Droplet Temperature Measurements
S.V. Sankar, D.M. Robart and W.D. Bachalo
- 9.4. Investigations on Accuracy and Resolution of Refractive Index Measurements with an Extended Phase-Doppler Anemometer
G. Brenn, C. Tropea, and T. -H. Xu
- 9.5. Phase Doppler Particle Sizing with Off-Axis Angles in Alexander's Darkband - A Promising Approach for Complex Technical Spray Systems
M. Willmann, A. Glahn and S. Wittig

SESSION 10. COMBUSTION III

- 10.1. The Development of Spark Ignited Turbulent Flames
R. A. Hicks, M. Lawes, C. G. W. Sheppard and R. Woolley
- 10.2. Aerodynamic Flow Characterisation of a Swirl Burner
B. Poireault, J.-M. Most and J. Imbach

- 10.3. Mixing Processes and Combustion of a Gas Jet Flame Surrounded by a Shroud of Combustion Air
P.X. Tran, M.P. Mathur and J.M. Ekmann
- 10.4. Visualisation of Coherent Structures in a Highly Turbulent Swirling Flame
W. Fick, A. J. Griffiths and T. O'Doherty
- 10.5. Size-Classified Droplet Dynamics of Combusting Spray in 0.1 MW Oil Furnace
N. Kawahara, Y. Ikeda, T. Hirohata and T. Nakajima

SESSION 11. DOPPLER GLOBAL VELOCIMETRY AND INTERFEROMETRY

- 11.1. Evolution of Doppler Global Velocimetry Data Processing
J. Meyers
- 11.2. Doppler Global Velocimetry in the Flow of a Swirler
I. Röehle and R. Schodl
- 11.3. Development of Doppler Global Velocimetry for Turbomachinery Applications
H. D. Ford and R.P. Tatam
- 11.4. An Improvement in Doppler Global Velocimetry: The Use of a CW Dye Laser
B. Leporcq, J. F. Le Roy, B. Pinchemel and C. Dufour
- 11.5. Combined Techniques of Holographic Interferometry and Particle Track Laser Sheet to Study Flame Spread Over Liquids
G. Tashtoush, A. Narumi, A. Ito, K. Saito and C. Cremers

SESSION 12. 2-PHASE FLOWS INSTRUMENTATION IV

- 12.1. Usage of the Spatial Filter Method for Measurements of Local Particle Velocities in Circulating Fluidized Beds
O. Fiedler, N. Labahn, J. Kumpart, K. Christofori
- 12.2. Frequency Response of Solid Particles in Oscillating Flows
G. Tedeschi and R.K. Menon
- 12.3. Size and Velocity Measurements in a Two-Phase Flow using Stereoscopic Particle Image Velocimetry
V. Palero and P. Arroyo
- 12.4. Comparison Between Velocity Measurements by LDV Techniques and Double Fiber Optic Sensors in Two Phase Jets
M. Gasparetti, G.L. Rossi, A. Campi and R. Onori
- 12.5. The Locus of Centres Method for LDA and PDA Measurements
Th. Panidis and M. Sommerfeld
- 12.6. A Fourier Optics Method for the Simulation of Measurement-Volume-Effect by the Slit Constraint
H. -H. Qiu and C.T. Hsu

SESSION 13. ENGINES I

- 13.1. Spray Characteristics in the Manifold , Port and Cylinder of a Four-Valve Spark-Ignition Engine
B. Cousyn, F. Neveu, M. Posylkin, D. S. Whitelaw and J.H. Whitelaw
- 13.2. Turbulent Flow Field Characteristics in a Reciprocating Engine: Appropriate Cut-off Frequencies for Cycle-resolved Turbulence, an Analysis of Co-incident 3D LDV Data Based on Combustion-related Dimensional-arguments
P. Dimopoulos, K. Boulouchos and G. Valentino
- 13.3. LIF Visualization of Liquid Fuel in the Cylinder of a Spark Ignition Engine
P. O. Witze and R. M. Green
- 13.4. Investigation of the Structure of Injection Sprays in Diesel Engines by Means of a Light-Scattering Technique
K. Prescher, A. Astachow, G. Krüger, J. Henße and D. Potz
- 13.5. Characterization of Spray Flows under High Fuel Temperature using Phase Doppler Anemometer
T. Obokata, T. Ishima, T. Koyama, K. Uehara, K. Kobayashi and M. Tukagoshi
- 13.6. Spray Formation and Dispersion of Size-Classified Fuel Droplet of Air-Assist Injector
Y. Ikeda, T. Nakajima and N. Kurihara

SESSION 14. AERODYNAMIC FLOWS AND ROTATING MACHINES II

- 14.1. Near Wake L.V. Investigation on Hovering Rotor Blades
J. Ramos, M. Mba, D. Favier and E. Berton
- 14.2. The Application of Laser Anemometry to Eddy Capture in a Propeller Inflow
J.M. Harden and M.V. Lawson
- 14.3. Measurement of Vortical Structures on a Helicopter Rotor Model in a Wind Tunnel by LDV and PIV
M. Raffel, U. Seelhorst and K.A. Bütetfisch
- 14.4. Three Component LDA Study of the Flow Field Surrounding the Helicopter Landing Pad of a Frigate
C. Swales, J. Rickards, M. Crompton, N. Terry and G. Breeze
- 14.5. Vortex Investigation on a Retreating Helicopter Blade with 3D Laser Velocimetry in DNW
A. Boutier, J. Lefevre and F. Micheli
- 14.6. Secondary Flow in Axial Flow Fans of Non-Free Vortex Operation
J. Vad and F. Bencze

SESSION 15. PARTICLES & MARKERS

- 15.1. Seeding for Laser Velocimetry in Confined Supersonic Flows with Shocks
J. Lepicovsky and R.J. Bruckner
- 15.2. A Repeatable Laser-Generated Localized Perturbation for Application to Fluid Mechanics
J. D. Schmisser, S. P. Schneider, T.R. Salyer and S.H. Collicot
- 15.3. Observations of Fluid Flow Produced in a Closed Cylinder by a Rotating Lid using the PHANTOMM (Photo-Activated Non Intrusive Tracking of Molecular Motion) Flow Tagging Technique
S. R. Harris, R.B. Miles and W.R. Lempert
- 15.4. Quantitative Velocity Measurements in Turbulent Taylor-Couette Flow by PHANTOMM Flow Tagging
M. Biage, S.R. Harris, W.R. Lempert and A.J. Smits
- 15.5. Measurements of Velocity and Temperature In Turbulent Flow using Laser Photothermal Effect with the New Interferometers
N. Nakatani, Oshio and T. Sakabe

SESSION 16. ENGINES II

- 16.1. Evaluation of Time and Spatial Turbulence Scales in a D.I. Diesel Engine
M. Auriemma, F.E. Corcione, R. Macchioni and G. Valentino
- 16.2. Characteristics of Steady Flows through the Inlet Ports of Multi-Valve Engines
Z. Mahmood and M. Yianneskis
- 16.3. Steady Flow Characteristics through the Intake Valves of a FORD Four-Valve Cylinder Head
C. Arcoumanis, B. French and J.M. Nouri
- 16.4. Laser Doppler Measurements of the Instantaneous Volume Flow Rate in Periodically Operating Systems
D. Trimis, M. Weclas and F. Durst

SESSION 17. WALL FLOWS I

- 17.1. A Study of Streaky Structures in a Turbulent Channel Flow With Particle Image Velocimetry
Z. -C. Liu, R. Adrian and T.J. Hanratty
- 17.2. Spanwise Vorticity Measurements in a Turbulent Boundary Layer using LDV
C.L. Gan, L. Djenidi and R.A. Antonia
- 17.3. An LDA Study of Longitudinal Vortices Embedded in a Turbulent Boundary Layer
H.-L-Zhang, X. Zhang and D.W. Hurst

- 17.4. The Differential Speckle Strophometry - A Light Scattering Technique for the Measurement of Velocity Gradients in Turbulent Fluid Flow
R. Schulz and W. Staude

SESSION 18. 2 D PIV AND PTV

- 18.1. High-Speed Digital Video Camera Systems and Related Software for Application of PIV in Wind Tunnel Flows
C. Willert, B. Stasicki, M. Raffel and J. Kompenhans
- 18.2. High Resolution Digital Two-Color PIV (D2CPIV) and its Application to High Free Stream Turbulent Flows
S. P. Gogineni, D.D. Trump, L. P. Goss, R.B. Rivir and D.J. Pestian
- 18.3. Visualization of Structure in a Turbulent Boundary Layer using Stereoscopic Particle Image Velocimetry
W.T. Lai, R.J. Adrian, C.D. Meinhart and Z.-C. Liu
- 18.4. Fibre Optic PIV Studies in an Industrial Combustor
D. J. Anderson, C.A. Greated, J.D.C. Jones, G. Nimmo and S. Wiseall
- 18.5. Measurement of Vortical Flows in a Low Speed Wind Tunnel using Particle Image Velocimetry
J.N. Stewart, Q. Wang, R.P. Moseley, P. W. Bearman and J.K. Harvey
- 18.6. PIV, LDA and CTA: Common Features and Differences
D.R. McCluskey, F.E. Jorgensen and P. Gjelstrup

SESSION 19. FLOWS WITH ROTATION

- 19.1. Combined Application of Particle Image Velocimetry (PIV) and Laser Doppler Anemometry (LDA) to Swirling Flows under Compression
J. Volkert, C. Tropea, R. Domann, W. Hübner and I. Lengyel
- 19.2. A Laser-Doppler Analysis of Cooling and Mixing in a Research Combustor
P. Anacleto, M.V. Heitor and A.L.N. Moreira
- 19.3. Interaction of Swirling Flows from Two Adjacent Coal Burners
A. Aroussi, S. Tarr and S.J. Pickering
- 19.4. The Turbulent 3D Flow Field in a Rotating Annular Flume
V. Spork, A. Cüppers and J. Köngeter
- 19.5. A Study of the Flows in a TORE® Slurry Transportation Unit
M.G. Faram, N. Syred, and T.O'Doherty
- 19.6. LDA Measurements of Axial and Tangential Velocity Components in a DMS Cylindrical Cyclone
B. Chiné, F. Concha and G. Ferrara

SESSION 20. SPRAYS

- 20.1. Comparative Mass Flux Measurements in Sprays using Patternator and Phase Doppler Anemometers
K. Dullenkopf, M. Willmann, S. Wittig, F. Schöne, M. Stieglmeier, C. Tropea and Chr. Mundo
- 20.2. Spray Visualization and Phase Doppler Anemometry Measurements of Charged Hydrocarbon Sprays
J.S. Shrimpton, A.J. Yule and A.P. Watkins
- 20.3. Characterization of a Pulsed Fuel Injector
E. Haile, F. Lacas, D. Veynante and D. Durox
- 20.4. Application of Extended Phase-Doppler Anemometry in Liquid-Gas Atomization
J. Domnick, J. Raimann and G. Wolf
- 20.5. Control of Droplet Atomisation in an 'Air-Assist' Atomizer
A.K. Gupta, R. Aftel, C. Cook and C. Presser
- 20.6. Dual-Mode PDA Measurements in Large Twin-Fluid Atomizers
J. Domnick, F. Durst, S. Gerstner and U. Weiss

VOLUME II (SESSION 21-40)

SESSION 21. PIV AND PTV SIGNAL PROCESSING I

- 21.1. Sparse Array Image Correlation
D. P. Hart
- 21.2. Young's Fringes Analysis by Neural Networks
F. Carosone and A. Cenedese
- 21.3. Double Image Two-Phase Flow PIV
J.I. Garcia-Palacin and M.G. Mungal
- 21.4. Quantitative Flow Visualization of Velocity Distributions by Parallel Image Processing using PPH (Photo-Conductor Plastic Hologram)
P.M.F. Kato, I. Shimizu, Y. Shibata, T. Isago and H. Taki
- 21.5. Simultaneous Multiple Pixel Processing Algorithms for PTV and PIV
T. Uemura, M. Yoshimoto and M. Tatumi

SESSION 22. ENGINES III

- 22.1. LDA-Measurements of the Coolant Flow of a Highly Complex Reciprocating Engine
J. Reuber and E. Blümcke

- 22.2. Measurement of Axial Flow Velocity in a Cylinder of an S.I. Engine by a Single-Incidence-Beam Reference-Mode LDA
C. Takeda, Y. Ohta, T. Ishima, K. Ishii and T. Obokata
- 22.3. PIV Measurements and Characterisation of In-Cylinder Flows in Combustion Engines
M.R. Heikal, M. Faure and N.S. Jackson
- 22.4. A Novel Diode PTV System for the Investigation of Intake Flows in I.C. Engines
C. Freek, A. Wüste and W. Hentschel
- 22.5. A Study on the Speed Dependence of the Intake Flow of a Motored Four - Stroke Engine, using Laser - Doppler Velocimetry
M. Socoliuc and M. Brun

SESSION 23. STRATIFIED FLOWS

- 23.1. Investigation of Turbulent Penetrative Convection
V. Troy and R. Adrian
- 23.2. PIV-Measurements in a Separated Flow Bounded by a Free Surface
G. Janke and L.P. Bernal **CANCELLED**
- 23.3. Application of DPIV to the Experimental Investigation of a Spilling Water Wave
D. Dabiri and M. Gharib **CANCELLED**
- 23.4. LDV-Measurements on Thermal Convective Instabilities in Spherical Gap Flow
C. Egbers, W. Beyer and H. Rath
- 23.5. Mixing in Gravity Current Heads Flowing over Rough Surfaces
W.D. Peters, J.E.S. Venart and S.R. Cogswell

SESSION 24. SCALAR MEASUREMENTS

- 24.1. Single-Shot Spectrally Resolved UV Rayleigh Scattering Measurements in High Speed Flow
R. G. Seasholtz
- 24.2. Measurement of the Transient Three-Dimensional Density Distribution using Photoconductor-Plastic
K. Ikeda, K. Okamoto, F. Kato and I. Shimizu
- 24.3. LIF Investigation of the Flow Pressure Chemical Vapor Deposition (LPCVD) Using Cul as Precursor
R. Kall, A. Möller, V. Till, G. Wortberg, G. Adomeit
- 24.4. Degenerate Four-Wave Mixing Investigations of Boundary Layer Chemistry in a Thermal Plasma CVD System
T. Owano, E. H. Wahl, and C. Kruger

- 24.5. UV Laser Diagnostics of Compressible Flows
M. Rodenburg, N. Dam, P.M. Huisman-Kleinherenbrink and J.J. ter Meulen
- 24.6. Temperature Measurement of 3-D Thermal Flow Fields using Color Image Processing
I. Kimura and M. Ozawa

SESSION 25. LIQUID FILMS

- 25.1. Droplet Concentration and Velocity Fields in Spark-Ignition Engines
C. Arcoumanis, D.S. Whitelaw and J.H. Whitelaw
- 25.2. Velocity Profiles in Shear-Driven Liquid Films: LDV-Measurements
S. Wittig, A. Elsässer, W. Samenfink, J. Ebner and K. Dullenkopf
- 25.3. Internal Transport Mechanisms of Shear-Driven Liquid Films
J. Ebner, W. Samenfink, A. Elsässer, S. Wittig, and K. Dullenkopf
- 25.4. Microscopic Super Laminar Flow Measurements in a Journal Bearing using a 2D Solid-State LDA
E.B. Li, A.K. Tieu and M.R. MacKenzie
- 25.5. Applications of Low Coherence Interferometry to Dynamic Oil Film Thickness Measurement
S. R. Taplin, A. Gh. Podoleanu, D. J. Webb, D. A. Jackson and S. R. Natrass
- 25.6. Experimental Analysis by Laser Extinction of the Evolution of the Liquid Crown Produced by the Splash of a Drop on Thin Liquid Film
A. Coghe and G.E. Cossali

SESSION 26. COMPLEX FLOWS I

- 26.1. Phase-Shifted Two-Camera DPIV For the Study of Flow Past Artificial Heart Valves
Ch. Brücker
- 26.2. LDV Measurement in a Full Scale Passenger-Car-Cabin
P. Castellini, M. Gasparetti and N. Paone
- 26.3. A Comparison Between LDA Measurements and Numerical Simulations for a Flow in a Tridimensional Cavity
E. Ovalle and A. Barrientos
- 26.4. LDV Measurements of the Flow Around a Fence in a Three-Dimensionally Stretched Channel
J.M.M. Sousa, N. Garcia and J.C.F. Pereira
- 26.5. Velocity Field Characteristics of Multiple Jets Impinging on a Flat Plate
A. Bernard and J.L. Bousgarbiès
- 26.6. Three-Component Laser-Doppler Measurements of the Confined Model Flow behind a Swirl Nozzle
B. Lehmann, C. Hassa and J. Helbig

SESSION 27. PIV & PTV SIGNAL PROCESSING II

- 27.1. Temporal Mapping of the Spring Model for Particle Image Velocimetry
K. Okamoto, M. Koiumi, H. Madarame and Y. A. Hassan
- 27.2. Subpixel Interpolation and Filters for PIV
A. Host-Madsen, A.H. Nielsen and M. R. Schmidt **CANCELLED**
- 27.3. Error Detection in the Analysis of PTV Images using Proper Orthogonal
Decomposition
A. Cenedese, M. Miozzi and G.P. Romano
- 27.4. Tackling the Problem of Trajectory Occlusion in Multi-Frame PIV (PTV) Using a
Neural Network Method
X. Pan and I. Grant

SESSION 28. AERODYNAMIC FLOWS AND ROTATING MACHINES III

- 28.1. Experimental Aspects of PIV Measurements of Transonic Flow Fields at a Trailing
Edge Model of a Turbine Blade
M. Raffel, F. Kost, C. Willert and J. Kompenhans
- 28.2. 3D Fibre Optic Laser Doppler Velocimetry
S.W. James, R.A. Lockey, D.A. Egan, R.P. Tatam and R.L. Elder
- 28.3. LDV Investigation of the Rotor-Stator Aerodynamic Interaction in a Centrifugal
Turbomachine
M. Ubaldi, P. Zunino, A. Ghiglione and G. Barigozzi
- 28.4. Aeroacoustic Measurements on an Aerofoil
C. Swales, E.C. Nash, and M.V. Lowson

SESSION 29. WALL FLOWS II

- 29.1. A Check of Taylor's Hypothesis using Two-Point LDV Measurements in a Turbulent
Boundary Layer
R. Elavarasan, L. Djenidi and R.A. Antonia
- 29.2. LDA Measurements of Laminar-Turbulent Transition in a Flat-Plate Boundary Layer
M. Kruse and S. Wagner
- 29.3. Measurement of Temporal and Spatial Evolution of Transitional Pipe Flow with PIV
A.A. Draad and J. Westerweel
- 29.4. Turbulent Transport Mechanism in a Drag Reducing Flow with Surfactant Additive
Investigated by Two Component LDV
Y. Kawaguchi, Y. Tawaraya, A. Yabe, K. Hishida and M. Maeda

SESSION 30. FREE FLOWS I

- 30.1. On the Relationship Between the Formation Number and Passive Scalar Pinch-Off in Starting Jets
H. Johari, D. Dabiri, A. Weigand and M. Gharib
- 30.2. Planar Doppler Velocimetry in Supersonic Jets
J.-H. Kim, P. Clancy and M. Samimy **CANCELLED**
- 30.3. Large Scale Vortical Structures in a Turbulent Coaxial Jet
A. Talamelli, G. Buresti, A. Mordacci and G. Tanzini
- 30.4. Simultaneous Velocity and Concentration Measurements in Confined Coaxial Jets
M.M.C.L. Lima, J.M.L.M. Palma and N.A. Silva
- 30.5. Coupled Multiple-Jets Excitation
U. Vandsburger and S. D. LePera

SESSION 31. LDV SIGNAL PROCESSING

- 31.1. Development of a PC-Based Miniature Signal Processor for LDA and PDA Measurements
M. Zhongming and X. Shen
- 31.2. Velocity Doppler Measurements in a High Speed Water Flow using a Fabry-Perot Interferometer
B. Leporcq, J. F. Le Roy, B. Pinchemel, C. Dufour and G. Houssaye
- 31.3. New Processing Methods for LDA Signals
A. Host-Madsen and P. Gjelstrup
- 31.4. Application of the Wavelet Transform to Laser-Doppler Signal Processors
H.R.E. van Maanen and F. J. Nijenboer
- 31.5. Development of a Velocity Profile Monitor in an Unsteady Flow by Using Semiconductor Laser Velocimeter with FFT-based Multi-Channel Signal Processing
T. Hachiga, N. Furuichi, J. Mimatsu, K. Hishida and M. Kumada

SESSION 32. 2-PHASE FLOWS I

- 32.1. Particle Dispersion in an Acoustically Excited Round Jet
M. V. Heitor, A.L. N. Moreira and R. Hoffmann
- 32.2. Influence of Cavitation on the Water Flow in a Pipe with a sudden Expansion
G. Wigley, R. Klasinc, R.H. Logar and T. Dum
- 32.3. Eddy Diffusivity of Liquid Droplets in a Vertical Flow of Vapor Produced at Boiling Liquid Surface
K. Ohtake, T. Miyata and F. Ogino

- 32.4. Experimental Study of Turbulent Flow with Bubble Injection at the Wall
T. Tjiptahasdja, C. Gabillet, C. Colin, J. Borée and J. Fabre
- 32.5. Experiments on Particulate Turbulent Jets
J.A. Garcia, L.M. Cerecedo, J.I. Garcia-Palacin and L. A. Aisa

SESSION 33. FLOWS WITH UNSTEADINESS

- 33.1. Measurements of Unsteady Velocity and Heat Transfer for Cylinders in Cross Flow
J. W. Scholten, D.B. Murray and J.A. Fitzpatrick
- 33.2. Measurements of Flow around Two-Dimensional Circular Cylinder Bundles with LDV
K. Tsunoda, S. Okamoto, N. Abe, M. Kijima and S. Higashi
- 33.3. Turbulence Scales and Spectra in Staggered Tube Bundle Flows
S. Balabhani and M. Yianneskis
- 33.4. Simultaneous Flow Velocity and Boundary Pressure Measurement for the Investigation of Flow-Induced Multiple-Mode Gate Vibrations
P. Billeter and M. Benesch **CANCELLED**
- 33.5. Pulsatile Flow Behaviour Near Cardiac Prostheses:
Application and Limitation of Laser and MRI Techniques
**F. Hirt, K. Eisele, Z. Zhang, E. Jud, R. Botnar, P. Bösiger, J. Kepner
And T. Baldwin**

SESSION 34. OPTICS 1

- 34.1. Power and Sensitivity Improvement of LDA-Systems by Fiber Amplifiers
H. Többen, H. Müller, D. Dopheide
- 34.2. Two-Component Directional Laser Doppler Anemometer based on a Frequency Modulated Nd:YAG Ring Laser and Fiber Delay Lines
J.W. Czarske and H. Müller
- 34.3. Fibre Optical Multicomponent LDA-System using the Optical Frequency Difference of Powerful DBR-Laser Diodes
H. Müller, H. Wang and D. Dopheide
- 34.4. Integrated Laser Doppler Anemometer Made By Ion-Exchange in Glass Substrate
P.L. Auger, A. Cartellier, P. Benech and I. S. Dupont
- 34.5. Laser Resonance Anemometer Optics
N. Kurihara and M. Takamoto

SESSION 35. FREE FLOWS II

- 35.1. Two-Scale Grid Turbulence Mixing
M. Gottero, G. Iuso and M. Onorato
- 35.2. The Effect of a Single Bubble on Turbulence Structure in Grid Turbulence Flow by Combined Shadow-Image and PIV Technique
A. Tokuhira, M. Maekawa, K. Lizuka, K. Hishida and M. Maeda

- 35.3. The Separation of Large-Scale and Small-Scale Turbulence in a Shallow Mixing Layer
J. Tukker and R. Booij
- 35.4. Damping of a Vortex Ring in a Stratified Fluid
T. S. Laursen, J.J. Rasmussen, B. Stenum and D.R. McCluskey
- 35.5. Flow of Shear-Thinning Fluids around a Cylinder: Vortex Shedding and Drag Characteristics
P.M. Coelho, F.T. Pinho and A.H. Rodrigues
- 35.6. Turbulent Natural Convection around a Heated Vertical Slender Cylinder
J. Persson and R.I. Karlsson

SESSION 36. LDV DATA PROCESSING

- 36.1. Uncertainty Estimates for any Turbulence Statistic
L.H. Benedict and R.D. Gould
- 36.2. Refined Reconstruction Techniques for LDA Data Analysis
H. Nobach, E. Müller and C. Tropea
- 36.3. Analysis of Randomly Sampled Data using Fuzzy and Non-Linear Techniques
A. Porporato and I. Ridolfi
- 36.4. Estimation of the Auto Correlation Function of Turbulent Velocity Fluctuations using the Slotting Technique with Local Normalisation
H.R.E. van Maanen and M. Tummers
- 36.5. Minimizing Errors for Cross Spectral Analysis using Laser Doppler Anemometry Measurements
J. Scholten, S. Dawson, J.A. Fitzpatrick and L. Simon
- 36.6. Understanding Biases in the Near-Field Region of Two-Point Correlation Measurements using LDA
L.H. Benedict and R.D. Gould

SESSION 37. COMPLEX FLOWS II

- 37.1. Use of the Complementary PIV and LDV Techniques to Study Industrial Complex Flows
C. Cahen, J. Bénard, M. Barcouda and F. Hofmann
- 37.2. LDA-Study For Modelling Flows through Screens
U. Ullum, J.P. Frederiksen, E. Akoh, N.F. Nielsen and P.S. Larsen
- 37.3. Filtration of Dirty Gases by Ceramic Candle Filters
A. Aroussi, K. Simmons and S.J. Pickering
- 37.4. The Holographic Determination of the Particle Dynamics in an Electro-Hydrodynamic Flow-Field
H.-J. Schmid and H. Umhauer

- 37.5. LDA Experiments on a Multiple Split Flow at 90°
G. Bäumer, V.A. Campos and J.C.F. Teixeira
- 37.6. Pulsatile Flow Through Tapered U-Bends as Simulated Aortic Arch (Velocity Field Measurements by Laser-Induced Fluorescence Method)
K. Ohba, A. Sakurai, S. Ikedo, T. Urabe and K. Sawa

SESSION 38. 2-PHASE FLOWS II

- 38.1. Application of Laser-Doppler Anemometry to Flows in Liquid/Liquid and Solid/Liquid-Extraction Columns
G. Wigley, C. Weiss and R. Marr
- 38.2. Insights into Grain Entrainment Using Particle Image Velocimetry
M.W. Gallagher and I.K. McEwan
- 38.3. Flow and Particle Aerodynamic Properties in Aerial Dispersion of Pathogen Spores
A. Rambert, P. Gougat and L. Huber
- 38.4. An Experimental Study of the Aerodynamic Break-Up of Liquid Drops using Laser Diffraction Technique
S. H. Zaidi and B. J. Azzopardi
- 38.5. Experimental Investigation and Visualisation of Particle Motion in a Model of a Beater Wheel Mill Model
M. Founti, Th. Achimastos and D.A. Dimopoulos

SESSION 39. OSCILLATING FLOWS AND FLAMES

- 39.1. Velocity, Temperature and Pressure Characteristics of Pulsed Premixed Flame
E.C. Fernandes and M V. Heitor
- 39.2. Measurement of the Periodic Flow Instability during a Self Excited Combustion Oscillation by LDV
P. Zangl, J. Hermann, A. Orthmann and D. Vortmeyer
- 39.3. Characteristics of Oscillating Control Spray for the Suppression of Low Frequency Combustion Instabilities
E. Lubarsky and Y. Levy
- 39.4. Acoustic Velocity Measurements by Means of Laser Doppler Velocimetry
Ph. Herzog, J.C. Valière, V. Valeau and G. Tournois

SESSION 40. OPTICS II

- 40.1. Evaluation of the Gaussian Beam Model for the Prediction of LDV Fringe Fields
P.C. Miles and P.O. Witze
- 40.2. Miniaturizing and Ruggedising Laser Anemometers
L. Lading, L.R. Lindvold, S.G. Hanson, H. Imam and B. Rose

- 40.3. Effects of Particle Size on Reference LDA Scanning Probe for Profile Measurements
V. Strunck and D. Dopheide
- 40.4. Development of Fiber Optic Laser Doppler Velocimeter Sensor for Measurement of
Local Blood Velocity
K. Ohba and K. Korenaga
- 40.5. Velocity Distribution using a Transmission Grating
T. Nakajima and Y. Ikeda

AUTHORS' INDEX

SESSION 21

PIV and PTV Signal Processing I

SPARSE ARRAY IMAGE CORRELATION

by
Douglas P. Hart

Massachusetts Institute of Technology
Department of Mechanical Engineering, Room 3-246
Cambridge, MA 02139-4307

ABSTRACT

A new algorithm has been developed for correlating PIV images at high-speeds. This algorithm is based on the sparse array format of image data - a format characteristic of variable-length image compression. Because PIV images are, in general, highly sparse, this algorithm typically results in much higher correlation speeds and lower memory requirements than spectral and statistical correlation techniques. Accurate software processing at speeds greater than 500 vectors/sec on a Pentium PC are typical using 64x64 pixel correlation windows and 8 bit pixel values with seeding densities of ten particle pairs per window.

This paper describes the methodology of sparse array image correlation as well as the speed, accuracy, and limitations of this unique image correlation technique.

NOMENCLATURE

Φ	Correlation function
Δ	Correlation search length [pixels]
γ	Fraction of interrogation image above threshold value
I	Pixel intensity
I'	Run-length-encoded pixel intensity
i,j	Image coordinates [pixels]
m,n	Data array indices
l	Run-length encoded data entry length [pixels]
M, N	Interrogation image diameter [pixels]
x,y	Pixel image coordinates
$\Delta i, \Delta j$	Distance between pixels

1. INTRODUCTION

Until recently, Particle Image Velocimetry, PIV, has been limited to applications in which two-dimensional, instantaneous velocity measurements are of interest. Most flows, however, are unsteady and three-dimensional in nature and thus, there has been a growing effort to develop three-dimensional velocity measurement techniques and techniques to quantitatively resolve unsteady flows. This effort has resulted in the development of Holographic Particle Image Velocimetry (HPIV) and PIV cinematography. Both these techniques are highly computationally intensive often requiring the determination of millions even tens of millions of vectors. With present software processing speeds, a single

experimental run using HPIV or PIV cinematography can take several hours of computer time to obtain results. Because of this, dedicated coprocessors are often utilized in these application. These costly coprocessors, although significantly faster than present PC software processing, are still slower than desired. Ideally, one would like to process PIV images at a rate faster than they can be acquired. This negates the need to store the images requiring only that the results be stored. It also allows an investigator to observe the results in near real-time for system setup.

At present, electronic imaging systems operate with pixel transfer rates on the order of 10 million pixels per second. At 8 bits per pixel, this is roughly twice the speed at which most PC's can stream uncompressed data to a harddisk. Even compressed by a factor of ten, more than one megabyte of storage is needed for each second of video signal. A typical statistical correlation with 64x64 pixel windows and 50% overlap requires more than 75 million multiplications and 225 million memory calls per second to process data at this rate - far faster than the capabilities of present PC technology. Fourier correlation techniques require significantly fewer operations but due to multiple memory calls and floating-point calculations, their processing requirements are still well beyond present PC capabilities for "real-time" PIV. Thus, if real-time PIV processing is to be achieved without the need for a dedicated coprocessor, an algorithm must be developed that significantly reduces the number of memory calls and arithmetic operations. This paper introduces one such algorithm, sparse array image correlation.

2. METHODOLOGY

Sparse array image correlation is based on storing and correlating a compressed data set which retains the particle displacement information from the original PIV image. By reducing coding and interpixel redundancy, far fewer memory calls and calculations must be made to correlate the image. PIV images typically contain significant data redundancy. Compression ratios of 30:1 or greater are normal. Thus, since the time required to correlate an image is proportional to the square of the number of data entries, significant gains in processing speed are possible.

Background

The simplest form of data reduction that can be made to a PIV image is to eliminate the low intensity pixels from the image file. Since the low intensity pixels contribute little to no information about particle displacement, their elimination has very little effect on the accuracy of the image correlation. Several high-speed algorithms have been developed based on this type of data reduction. The most recent of these algorithms is the one by Hatem and Aroussi (1995) in which a probability histogram of possible particle displacements is used to determine the velocity vector. Unlike Hatem and Aroussi's algorithm, sparse array image correlation relies on a true correlation of the image—it is not a particle tracking type algorithm and it does not rely on the binary (0,1) representation of particles. The relative intensity difference between pixels is maintained despite the utilization of an image compression scheme. A more pertinent algorithm to the present algorithm is the one by Adrian (1986) in which the low intensity pixels are eliminated from the data before it is correlated. Like the present algorithm, Adrian's algorithm processes the data in a sparse format. This is the basic scheme by which the present algorithm correlates images. Unlike Adrian's algorithm, however, both coding redundancy and interpixel redundancy are reduced during image preprocessing. Further speed is gained by encoding the remaining data specifically for 32-bit processing and utilizing an error correlation function to eliminate multiplication and division operations.

As with all correlation schemes that require preprocessing of images, a tradeoff is made between the time required to reduce the data set and the time required to correlate the reduced data set. The original intent of the sparse array image correlation algorithm was to process PIV images at video rates. Therefore, the algorithm presented here uses a relatively simple data compression scheme to facilitate the processing of a video signal as it is being downloaded from a camera. This allows a data set from a previous frame to be analyzed at the same time the video data from a camera is being compressed. It is desired to perform both preprocessing and correlation of the images at roughly the same rate, 1/30 of a second. The result is an image compression algorithm that is not necessarily optimized for data reduction but allows pipelining of the original image data set to reduce image preprocessing time and data transfer latency.

Sparse Image Array Generation

The first step in sparse array image correlation is to generate a data array which contains enough information to determine the displacement of particles in a PIV image or between two images in the case of cross-correlation. In order to facilitate processing, it is desired to retain the minimum amount of data to obtain a specified resolution in the final results. Unfortunately, it is difficult to determine *a priori* the exact information that is needed to achieve this. It is, however, clear from the statistical correlation function that pixels with low intensities do not contribute significantly to the overall correlation of the image relative to the pixels of higher intensity which depict the tracer particles;

$$\Phi_{\Delta i, \Delta j} = \frac{\sum_{m=1}^{M-|\Delta i|} \sum_{n=1}^{N-|\Delta j|} [I_{m+|\Delta i|, n+|\Delta j|} \cdot I_{m,n}]}{\sqrt{\sum_{m=1}^{M-|\Delta i|} \sum_{n=1}^{N-|\Delta j|} I_{m,n}^2} \cdot \sqrt{\sum_{m=|\Delta i|+1}^M \sum_{n=|\Delta j|+1}^N I_{m,n}^2}}$$

Therefore, as with many PIV data reduction algorithms, the first step in sparse array image preprocessing is to eliminate the low intensity pixels from the image. This preprocessing, in addition to compressing the data set by almost 10:1, has been found to significantly improve the correlation signal to noise ratio by reducing correlated electronic pixel noise in the images.

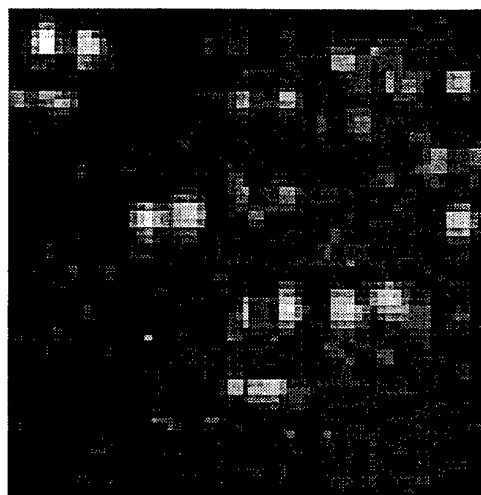


Figure 1. - Typical 64x64 pixel region of a PIV image.

Data Redundancy

PIV images are typically bimodal, composed of light particle images on a dark background. It is, therefore, relatively easy to eliminate the low intensity pixels from the data. A threshold level is set and all pixels with intensities above the threshold are retained. A common technique for setting the threshold level is to perform a histogram concavity analysis [Rosenfield and De La Torre, 1982]. A simpler and somewhat faster technique is to generate an intensity distribution curve which indicates the number of pixels with intensities above a specified level. Since the curve is an accumulation of pixel numbers, it is smooth and thus, it is a simple matter to select a threshold level which corresponds to a specific slope on the curve. This technique is not as robust or accurate as the histogram concavity analysis but, because the pixel intensities in PIV images are so strongly bimodal, the precise threshold level is not critical. In the case of PIV cinematography where multiple images are processed, it is often necessary to perform a threshold analysis only once to set a threshold level for all subsequent image analysis. The speed of the technique for determining the correct threshold level, in this case, is not particularly critical. There are cases, however, such as with rotating

machinery in which there are large variations in intensity from one image to the next. In these cases, it is necessary to perform a threshold analysis on each individual image. Thus, the speed of the thresholding technique can be significant.

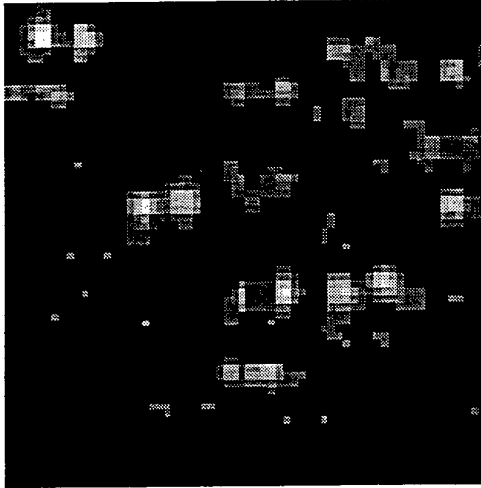


Figure 2. - Reconstructed image of Figure 1. after the elimination of the low intensity background pixels and local intensity equalization is performed. This preprocessing of the image typically results in a compression ratio of 10:1.

In practice, the pixel intensity and distribution often varies significantly, not only between images, but from one region to the next within the same image. It is, therefore, advantageous to perform an intensity analysis which accounts for these variations. The simplest technique to accomplish this is to break the image into non-overlapping subregions and locally threshold and equalize each subregion independently of the others. This technique, however, leads to an effect known as checkerboarding in which one region has a different mean intensity than an adjacent region. Checkerboarding can be eliminated by using a local threshold and equalization scheme based on a subregion around each individual pixel. The added computational intensity of this type of processing scheme is not as severe as it may first appear since information from the previous pixel computation can be carried to the next. Thresholding and equalization of each new pixel requires calculation of only an additional row or column of the subregion surrounding the pixel. Although a detailed analysis of the effects of checkerboarding on image correlation has not been made, it does not appear to warrant the use of a more computationally intensive equalization scheme.

Variable-Length Encoding

Further data reduction is achieved by variable-length encoding the image before storing it. This is done by combining adjacent pixels that have the same most significant bit (MSB) values into a single pixel value with length l and an intensity I' equal to the intensity value of the combined pixels. Variable-length encoding typically results in a data compression of around 2.5:1 with most PIV images.

Thus, it increases processing speed by a factor of about 6. Some data is lost by combining pixels in this manner. Variable-length encoding, however, is done after local thresholding and intensity equalization is performed. The pixel intensity distribution of the particle images is expanded exaggerating the differences between adjacent pixel intensities. The areas in a PIV image where most of the compression takes place, therefore, are near the outside edge and near the center of the particle images. These are areas where there is a low gradient in the particle intensity profile. Compressing these regions steepens the profile of the correlation peak. It does not significantly effect the location of the correlation peak itself and thus, has little effect on the accuracy of the algorithm. Regions with low intensity gradients, in general, do not significantly effect the location of the correlation peak. It has been found that pixel combinations with lengths greater than about three can be eliminated from the data set with no significant effects. This reduces the size of most PIV data set by a factor of only about 1.2 resulting in an image compression ratio of roughly 3:1 *after* the background pixels have already been eliminated. The net result of the entire sparse array correlation preprocessing algorithm is to reduce the image data set by a factor of about thirty.

When correlating an image compressed in variable-length format, the length of the pixel combinations as well as the intensity variation must be accounted for. The actual location of a pixel set in the i th direction is $[i+(l-1)/2]$. The correlation value $I_1 \cdot I_2$, therefore, becomes $0.5 \cdot [l_1 + l_2 - l_1 - l_2] \cdot I'_1 \cdot I'_2$ when processed in variable-length format. The value, $0.5 \cdot [l_1 + l_2 - l_1 - l_2]$, is always an integer and equal to the shortest length. In practice, it is faster to simply compare the lengths l_1 to l_2 and multiply by the shortest.

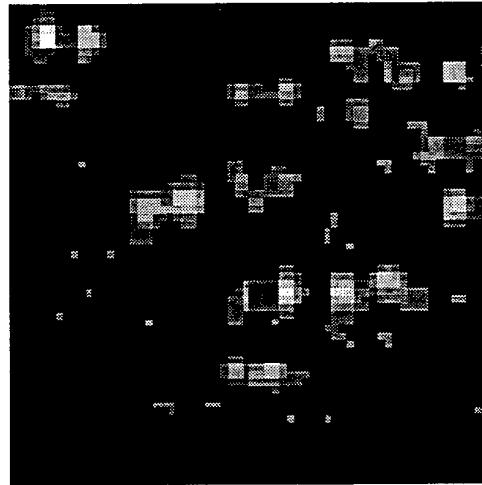


Figure 3. - Reconstructed image of Figure 2. after variable-length encoding. Variable-length encoding has very little effect on the appearance of the image despite a reduction in the data set by a compression ratio of 3:1. The data set representing this image is 1/30 the size of the data set shown in Figure 1.

Data Encryption

The sparse image array is stored with each pixel indices and intensity combined into a single 32 bit word. This reduces the number of memory calls that must be made when correlating. For example, $i=2, j=2, I=254$ is stored as 000000000010000000000101111110 binary = 2,097,918. By masking the bits, the values of i, j , and I can be extracted from this single entry in a few clock cycles of most processors.

Along with the sparse image array, an indices table is generated which contains the location in the sparse image array of the first entry representing a pixel combination in the next line of a PIV image. This line index array is used to jump to the next value of j in the sparse image array when a specified pixel separation is exceeded in the i th direction. When correlating large images, this index array significantly speeds processing.

Window Sorting

The reduction in the number of data entries in the PIV image data array by the elimination of the dark pixels and the variable-length encoding of the remaining pixels greatly improves the speed at which correlation windows can be sorted from the data set. In addition, the line index array reduces the number of multiple entries into the sparse image array that must be made to extract the pixels located in a given correlation subwindow. Despite this, window sorting is a slow memory intensive task that requires considerable processing time. The present algorithm requires almost as much time to sort the correlation subwindows from the image data as it does to correlate the subwindows once they have been sorted.

Correlation window sorting in sparse array format is considerably more difficult than it is in an uncompressed format since the spacing of the data entries is image dependent. A simple block transfer as is commonly done in an uncompressed format cannot be done in the sparse array format. A solution to this is to generate the sparse array at the same time that the correlation windows are being extracted from the image. This technique works well as long as there is no significant overlap of the correlation windows. If there is significant overlap, the number of redundant calls to memory greatly slows processing. The fastest technique is to presort all of the correlation windows as the sparse array is generated. This technique, unfortunately, requires a significant increase in memory storage depending on the overlap in the correlation windows. A 50% overlap results in a four times increase in memory storage. The 32-bit sparse array data encryption scheme, itself, requires four times the number of bits per pixel. Therefore, there is an increase in memory storage requirement by a factor of sixteen. Image compression, however, sufficiently reduces the number of data entries such that there is a net reduction in data storage by roughly a factor of four compared with storing the entire image in memory at one time. In addition, presorting the windows in this manner moves the processing time for window sorting from the basic correlation algorithm into the image preprocessing algorithm. This allows more time for

image correlation within the 1/30 of a second video framing speed.

Search Length Selection

We can further increase processing speed while, at the same time, reducing the odds of obtaining spurious correlation values by limiting our search for the maximum correlation. This is done by allowing the user to specify a maximum change in Δi and Δj based on knowledge of the image being correlated. An adaptive scheme can be used to narrow the correlation search - a scheme which predicts the range of correlation values to calculate based on previous calculations from subwindows of the same image. This procedure, however, is not particularly robust and can result in spurious errors in obtaining the maximum correlation. Because the sparse array correlation process is inherently very fast, adaptive schemes generally do not gain enough processing speed to warrant their use. It is sufficient to set a single value for the in correlation range for an entire image.

Subwindow Correlation

By using the error correlation function rather than a statistical correlation function, image correlation can be carried out using integer addition and subtraction only. Integer addition and subtraction is a very fast operation for most microprocessors requiring only a few clock cycles. It is far faster to perform these calculations than to use a 'look-up table' scheme to avoid 8-bit or 4-bit pixel multiplication. The use of the error correlation function, therefore, significantly improves processing speed over the more commonly used statistical correlation function. A detailed analysis of the error correlation function in comparison to the statistical correlation function is presented in a paper by Roth, Hart, and Katz (1995). It was shown that the error correlation function produces essentially the same results as the more computationally intensive statistical correlation function.

The error correlation function can be expressed as,

$$\Phi_{\Delta i, \Delta j} = \frac{\sum_{m=1}^{M-\Delta i} \sum_{n=1}^{N-\Delta j} [I_{m,n} + I_{m+\Delta i, n+\Delta j} - |I_{m,n} - I_{m+\Delta i, n+\Delta j}|]}{\sum_{m=1}^{M-\Delta i} \sum_{n=1}^{N-\Delta j} [I_{m,n} + I_{m+\Delta i, n+\Delta j}]}$$

such that,

$$\Phi_{\Delta i, \Delta j} = 1 - \frac{\sum_{m=1}^{M-\Delta i} \sum_{n=1}^{N-\Delta j} [I_{m,n} - I_{m+\Delta i, n+\Delta j}]}{\sum_{m=1}^{M-\Delta i} \sum_{n=1}^{N-\Delta j} [I_{m,n} + I_{m+\Delta i, n+\Delta j}]}$$

The value of this correlation function ranges from 1 when the images are perfectly correlated to 0 when there is no correlation between the images. This function, aside from being faster to calculate than the statistical correlation function, has the added benefit of being significantly easier to

implement in hardware without the need for a microprocessor. Unlike the more common statistical correlation function, the error correlation function used in sparse array image correlation is not computed one entry at a time. The entire correlation table is constructed by summing entries as they are found while iterating through the sparse image array. In this way, a PIV image can be correlated in compressed form. It is difficult, however, to obtain the denominator in the correlation expression this way. Fortunately, the denominator can be approximated as twice the sum of the pixel intensities in the image divided by the image area in pixels times the correlation window size,

$$\sum_{m=1}^{M-|\Delta i|} \sum_{n=1}^{N-|\Delta j|} [I_{m,n} + I_{m+|\Delta i|,n+|\Delta j|}] \cong 2 \frac{(M-|\Delta i|)(N-|\Delta j|)}{M \cdot N} \sum_{m=1}^M \sum_{n=1}^N I_{m,n}$$

This provides an easily calculated normalization value without the need to sum all of the pixels in the correlation window overlap for each entry. It is accurate as long as the images being correlated are large compared with the correlation distance and the pixel intensities in the image are fairly evenly distributed. The correlation value of interest, however, usually presents itself as a strong local maxima in the correlation table and the exact normalization of the correlation function has little effect on the final results. Because of this, normalization of the correlation function is usually unnecessary and correct results are obtained by assuming the denominator has a value of 1.

When autocorrelating subwindows, each entry in the sparse image array is compared with the entries below it and a correlation approximation between the entries is added into the correct location in the correlation table based on the difference in i and j between the array entries. If the location is out of range of the specified search length in the i th direction, the entry is ignored and processing continues with the next entry specified in the line index array. If the location is out of range in the j th direction, the entry is ignored and a new series of iterations are made starting with the next sparse image array entry. Because the sparse array is correlated from the top down, only the half of the correlation table representing the positive j direction is calculated. The autocorrelation of an image is symmetrical and thus, it is pointless to calculate both halves.

Cross-correlation is calculated by generating two sparse image arrays representing the two images being correlated. The entries of one array are then compared to *all* of the entries of the other array that are within the search length. Because the difference in array indices can be both positive and negative in both the i and j directions, the entire non-symmetrical correlation table is calculated.

Once the correlation table is complete, the table is searched for the maximum correlation value. A simple bilinear interpolation scheme is then used to determine the correlation maximum within subpixel resolution. Bilinear interpolation is ideal in this application since reducing the data set by image preprocessing and using the error correlation function results in a very steep, nearly linear, correlation peak.

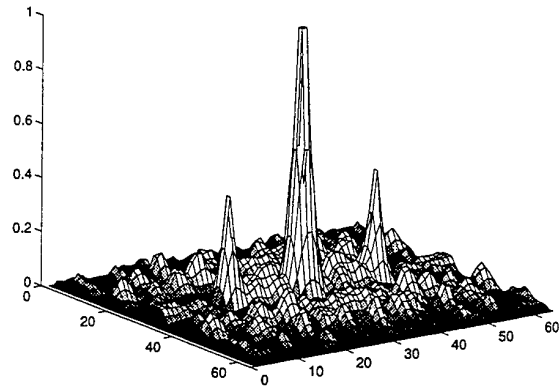


Figure 4. - Correlation table resulting from sparse array error correlation of the image in Figure 3. In practice, the sparse array image data set is correlated from the top down so that only half of the correlation table is calculated. Both halves of the symmetrical correlation table are shown here for clarity. Note the extremely steep correlation peaks. These sharp peaks improve subpixel interpolation accuracy.

3. PROCESSING SPEED

The computational intensity of sparse array image correlation is comparable to the better known statistical correlation technique except that the image data set is compressed in preprocessing. If the data set is reduced to a fraction, γ , of the original image data set, then the number of data comparisons that must be made is, $\frac{1}{2} \gamma \Delta^2 (\gamma N^2 - 1) + \gamma N^2$ for sparse array autocorrelation and $\gamma^2 \Delta^2 N^2$ for cross-correlation. For PIV images where the particle seeding densities are high such that, $\gamma N^2 \gg 1$ and $\gamma \Delta^2 \gg 1$ then $\frac{1}{2} \gamma \Delta^2 (\gamma N^2 - 1) + \gamma N^2$ is approximately equal to, $\frac{1}{2} \gamma^2 \Delta^2 N^2$. A typical PIV data set can be reduced by a factor of 30 such that $\gamma=0.3$. Thus, a typical 64×64 pixel correlation subwindow requires a little less than one-thousand data comparisons to complete an autocorrelation with a search window of 20×20 pixels. During each comparison, three memory calls are made, one to retrieve a data entry to be compared with the data entry already in the processors register, one to retrieve the value of the correlation table entry, and one to place the comparison result in memory. Memory calls require significantly more processing time than integer addition and subtraction so that the time for each data entry comparison is essentially the time it takes to make these memory calls. PCI based systems can transfer over 60Mbytes of data per second or about two-million 32-bit data entries per second over the bus. By ordering data entries sequentially when extracting the correlation subwindows from the image data set, bus transfer rates of this speed can be achieved by block memory transfers. Thus, correlation speeds of 2,000 vec./sec. are theoretically possible. In practice, it is difficult to write an algorithm that can maintain optimal use of the data bus. Very little effort has been made to optimize the present code for

fast data transfer. The fastest speeds obtained so far for images that compress by a factor of 30 have been on the order of 500 vec./sec. on a Pentium 160MHz computer.

4. ACCURACY AND ROBUSTNESS

The accuracy and robustness of the sparse array image correlation algorithm was tested empirically by comparing results obtained by correlating synthesized and experimental PIV images with spectral correlation results. Although it is impossible to account for every factor that may effect the results in this type of an analysis, the sparse array correlation algorithm consistently gave results within 0.2 pixels of the spectral results. In many cases, the sparse array correlation algorithm appeared to perform better than the spectral correlation. This is believed to be due to the elimination of correlated background noise in the images by the sparse array algorithm and to improved subpixel interpolation resulting from the steeper correlation peak generated by the sparse array algorithm.

Synthesized Image Comparison

Comparisons were made between spectral correlation and sparse array correlation using 200 synthetic PIV images. The PIV images were 64x64 pixels with an average of 10 particle pairs per image. An example image is shown in Figure 5. The images were generated with Gaussian particle profiles and had particle displacements ranging from 0 to 32 pixels in both the i and j directions.

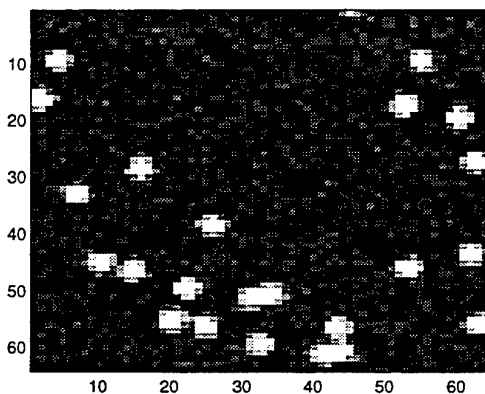


Figure 5. - Typical synthetic 64x64 pixel PIV image used to estimate the relative accuracy of the sparse array correlation algorithm. The images are created using Gaussian pixel intensity profiles representing particle pairs that have been randomly placed in the image. Each particle pair represents a 15.5 pixel displacement.

The difference between the particle displacements in the synthetic images and the correlation results obtained from the spectral and sparse array algorithms were plotted for each of the 200 images on two scatter plots shown in Figures 6. and 7. Bilinear interpolation was used to determine subpixel resolution in both the spectral analysis and the sparse array

correlation analysis. From these plots, sparse array correlation appears to be considerably more accurate than the spectral analysis. This is, however, deceiving since bilinear interpolation is better suited for sparse array analysis than it is for spectral analysis. It is assumed that the spectral analysis produces exact results and the variation between the two plots is primarily due to the subpixel interpolation scheme. Regardless, the plots indicate that sparse array correlation is accurate to within the expected correlated variation of the synthetic images.

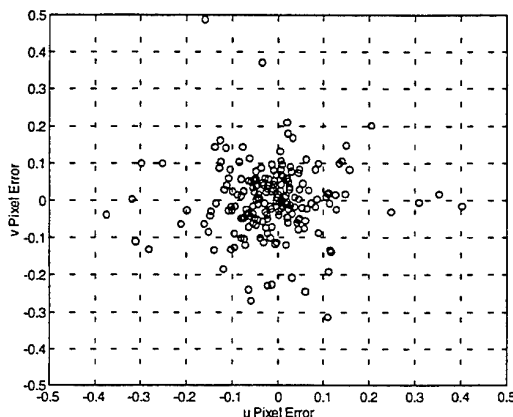


Figure 6. - Scatter plot showing the difference between the expected correlation of 200 synthetic generated images and the correlation obtained by spectral analysis. Most of the deviation from zero is assumed to be due to errors associated with the bilinear subpixel interpolation scheme.

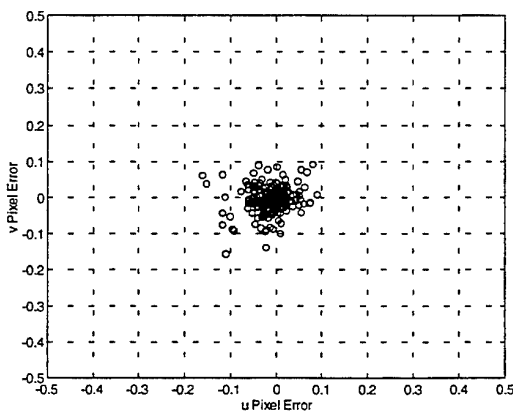


Figure 7. - Scatter plot showing the difference between the expected correlation of 200 synthetic generated images and the correlation obtained by sparse array analysis. The deviation from the expected correlation is significantly less than the deviation shown in Figure 6. The difference is due to the accuracy of the bilinear subpixel interpolation used in determining the maximum correlation of the steep correlation peak generated by the sparse array correlation algorithm.

Experimental Data Comparison

Experimental PIV images are never as clear as synthetic images. Variations in particle image intensity and size, correlated background noise, poor contrast, insufficient illumination and optical aberrations are only a few of the many factors which effect the quality of experimental images. For a correlation algorithm to be useful, it must be robust enough to generate accurate results from less than ideal data.

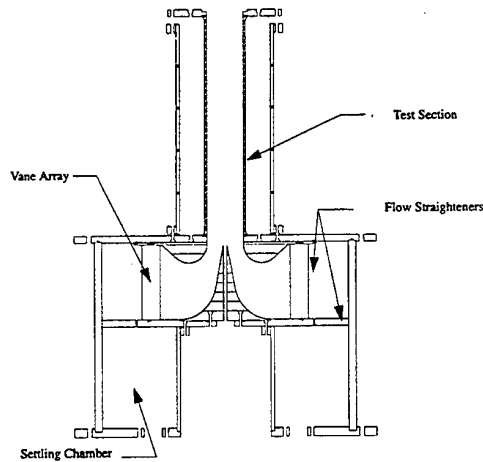


Figure 8. - Setup of swirling flow experiment. PIV images of swirling flow through a 10cm diameter glass pipe are recorded on film by a camera facing along the pipe axis. A two pulsed frequency doubled Nd:YAG laser is used to illuminate fluorescent 50 μ m particles in the flow.

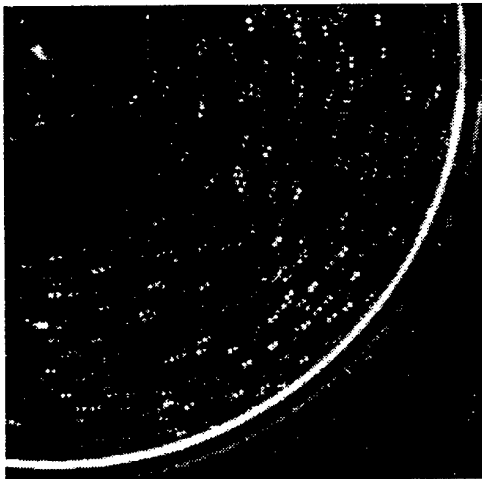


Figure 9. - Typical PIV image recorded from the experimental setup shown in Figure 8. The light intensity in the image varies significantly due to the distortion caused by the curvature of the pipe.

The sparse array algorithm was tested using PIV images taken of a swirling coaxial flow using the experimental setup shown in Figure 8. A frequency doubled Nd:YAG laser was used to illuminate a 10cm diameter section of glass pipe containing a 1m/s axial flow at a swirl number of 0.8. The flow was seeded with 50 μ m florescent particles. Images were taken parallel to the flow axis and recorded on 35mm 400ISO Kodak film. A typical image is shown in Figure 9. The bright region shown in the image is the reflection of the pipe where it intersects the laser sheet. Because of the curvature of the pipe, all of the images exhibit significant variations in light intensity. No attempt was made to adjust the exposure quality of the images before processing them.

The experimental images were processed using the sparse array correlation algorithm with 64x64 pixel subwindows that overlapped by 50% in both the X and Y directions. A maximum correlation search length was set at 20 pixels. The sparse array algorithm processed these images at 868 vec./sec. on a Pentium 160Mhz computer with 16Mbytes of memory. An example of the output is shown in Figure 10. The vectors shown on the right hand side of the graph are the result of particle reflections on the pipe wall. Blanks in the vector map are due to poor illumination and/or low seeding density in these regions. The magnitude and direction of the vectors calculated by the sparse array correlation algorithm appear to be correct but it is difficult to tell the accuracy of the calculation since the precise characteristics of the flow are not unknown. The algorithm, however, does appear to handle large local variations in image intensity without significantly slowing processing or producing spurious vectors.

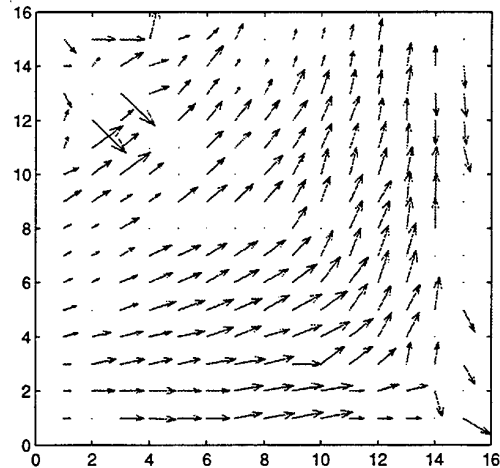


Figure 10. - Vector map obtained from sparse array autocorrelation of the image in Figure 9. The blank spaces in the vector map are due to poor illumination and/or low particle seeding densities. The vectors located in the lower right corner are due to reflections of particle images on the glass pipe wall.

5. SUMMARY AND CONCLUSIONS

Sparse array image correlation is a technique by which PIV images can be accurately processed at high-speeds. It is based on a compression algorithm in which the number of data set entries containing tracer particle displacement information is reduced. Very high correlation speeds are obtained by encrypting the reduced data set into 32-bit integers and correlating the data entries using an error correlation function to eliminate multiplication and division operations.

The data compression algorithm used to preprocess the images in sparse array correlation is designed for video rate compression of images as they are received from a CCD camera. PIV correlation speeds including data compression of 500 vec./sec. are typical with speeds greater than 1,000 vec./sec. being recorded for images with low seeding densities.

The maximum correlation value associated with sparse array image correlation is characterized by a very steep peak which improves subpixel interpolation. Synthetic images processed using both sparse array correlation and spectral correlation indicate that inaccuracies in the sparse array technique are typically smaller than other sources of errors associated with PIV analysis. Experimental images processed using sparse array correlation demonstrate that this technique is capable of correlating images with large local variations in intensity without significantly slowing processing or generating spurious vectors. Although it is impossible to test for all conditions that may be encountered, sparse array image correlation appears to be fast, accurate, and robust.

REFERENCES

- Adrian, R. J. (1986b) "Multi-point optical measurement of simultaneous vectors in unsteady flow—a review." *Int. J. Heat and Fluid Flow*, pp. 127-145.
- Adrian, R. J. (1991) "Particle imaging techniques for experimental fluid mechanics." *Annual Review of Fluid Mechanics* 23, pp. 261-304.
- Hatem, A.B., Aroussi, A., 1995, "Processing of PIV Images." SAME/JSME and Laser Anemometry Conference and Exhibition, August 13-18, Hilton Head, South Carolina, FED-Vol. 229, pp.101-108.
- Hennessy, J.L., Patterson, D.A., 1990, "Computer Architecture - A Quantitative Approach." Morgan Kaufmann Pub., San Mateo, CA.
- Rosenfeld, A., De La Torre, P., 1983, "Histogram concavity analysis as an aid in threshold selection." *IEEE Transactions on Systems, Man, and Cybernetics*, Vol. 13(3), pp. 231-235.
- Roth, Hart, and Katz, (1995) "Feasibility of Using the L64720 Video Motion Estimation Processor (MEP) to increase Efficiency of Velocity Map Generation for Particle Image Velocimetry (PIV)." ASME/JSME Fluids Engineering and Laser Anemometry Conference, Hilton Head, South Carolina, pp. 387-393.

YOUNG'S FRINGES ANALYSIS BY NEURAL NETWORKS

F. Carosone, A. Cenedese.

University of Rome "La Sapienza"
V. Eudossiana 18, Roma 00184
Department of Hydraulics, Transport and Roads
Tel. + 39 / 6 / 44585218; Fax: + 39 / 6 / 44585217
e-mail: carosone@cenedese1.ing.uniroma1.it

ABSTRACT

A system of artificial neural networks is proposed for automatic analysis of Young's fringe images from high density P.I.V. images. The basic idea is that images are first compressed, and analysis is carried on the compressed files. The reduced size of these is responsible for a higher speed of analysis. The approach seems interesting because hardware exists for a real-time image compression, and the computational complexity of the neural analysis is orders of magnitude lower than a well-established technique of fringe analysis, that is the inverse two-dimensional FFT calculation. The method was tested on over one thousand simulated P.I.V. images, where the mean digitized particle displacement varied from 12 to 32 pixels, and with orientation angular step of approximately 2.8 degrees in the range 0° - 180° . The accuracy of the measurements performed by the neural system, relative to the tolerance intervals $\pm 1.4^{\circ}$ for orientation and ± 0.5 pxls for the estimation of particle mean displacements from fringe spacing, is 96.3% for orientation, 93.6% for spacing.

1. A NEURAL APPROACH TO YOUNG'S FRINGES

Adrian (1991) focused his attention on Young's fringes as a fast way for processing high density P.I.V. images. To this aim, he investigated the possibilities offered by ad-hoc firmware, like array processors. Adrian's paper assessed the primacy of the inverse FFT method, primarily because very fast digital processor board are available for the 2-D FFT computations. This method has become a standard. A Young's fringe pattern in flow visualization comes from optical or digital Fourier transform on an *interrogation area* of a P.I.V. image. Inverse FFT of the power spectrum yields the autocorrelation function of the source P.I.V. image via the Wiener-Khinchine theorem. Although the

FFT can be fastened on an array processor, the computational cost of the method must include the search for the autocorrelation tallest peaks, whose complexity is of the same order as the FFT, and can be poorly vectorized. To make an idea, a 256×256 fringe image needs about 5 Mflop (fair estimation), and the time spent for the peak search is about half the time spent for the FFT. A good indicator of the computational complexity of analysis methods is the number of floating point operations (*flop*). Since the hardware is generally characterized by the number of floating point operations per seconds (FLOPS), the time spent for the analysis is easily known by their quotient. For instance Meinhardt et al. (1992) improved the analysis speed by using ad hoc processors each capable of 80 MFLOPS, maintaining the same algorithmic complexity.

The relation between the inverse FFT method and the development of array processors is somewhat similar to what is happening in general to the field of image recognition, where artificial neural network play an important role mainly because analog/digital processor "neural" boards are becoming available, onto which neural networks are physically or digitally cabled and act as a programmable circuitry. The development of neural software, running on personal computers or workstations, leads to the optimal configuration of the board. The 'configuration parameters' are then downloaded to the board. In such a way, neural boards have shown tremendous speed-ups towards more classical methods in the field of image analysis, being able of 10 MFLOPS to 2 GFLOPS directly attached to video cameras [Treleaven (1989), Rückert (1993)]. Hence, in a way, a neural board is, for neural networks, what an array processor is for an FFT. A big difference in the next future for fringe analysis might be that neural networks can produce orientation and spacing at the output of the board, without further processing as required by the FFT approach with the peaks'

search. With this concept in mind, the research on the capabilities of neural networks for fringe image analysis gets worthy to be investigated.

This paper presents a software simulation of a system of neural networks whose input is a digital fringe image and whose output is the orientation and the spacing of the fringe pattern. Both accuracy and computational complexity are reported. Section 2 introduces the networks used in the project, while Section 3, 4 and 5 deal respectively with the image formation, compression and analysis and give results.

2. THE NEURAL NETWORKS IN THIS PROJECT

From a topological viewpoint, neural networks consist of a big number of processing elements (called *neurons*) densely interconnected, each performing rather simple operations (Hecht-Nielsen, 1990): typically, a neuron sums its inputs and passes the summation to a non-linear transfer function, then sends its output to other neurons (Haykin, 1992). Usual transfer functions are the sigmoid or the step function. Linear functions are also used. Neural networks are arranged in layers: input data feed an input layer of sensors, then signals are propagated to subsequent (*hidden*) layers through modifiable connections. The last layer has a number of neurons, whose outputs are taken as the network output.

The optimal configuration of a network is achieved through a *training* process in which the strength of the connections are modified. After training, the operational phase of a neural network follows, at fixed connections. Training may be *supervised* or *unsupervised*. In a supervised training, the aim is vector association: a set of input vectors is proposed to the network, each with a corresponding desired output vector. The whole set of pairs is called "training set". A *training algorithm* drives the changes in the net connections so to accomplish the desired input-output matches. This often requires the training set to be repeated to the network a number of times called *epochs*. In an unsupervised training, the goal is vector classification: only input vectors are presented at the network input sensors, and the training algorithm again modifies the net connections so to activate specific neurons as a response to clusters of input vectors. In all cases, the training algorithm is controlled by one parameter, the *learning rate*, which has an influence on the speed of the training phase and on its stability.

Two very popular neural networks were used in this project: the Frequency Sensitive Competitive Learning (FSCL) network, and a Back-Propagation network. The FSCL (Desieno, 1988) was derived by the Kohonen (1984) network and it is an unsupervised network. It "learns" to

group a population of vectors into a rather small number of clusters, each represented by a prototype vector, and assigned to a neuron in the network. The FSCL training algorithm makes the network develop a set of *equiprobable* prototypes (Kohonen, 1990), which means that each cluster is assigned the same number of inputs of the training set. This statistical property is achieved through layers of neurons where a competition occurs that controls the formation of clusters within the network. Since one of the ways to code a multivariate probability density function (pdf) of the input vectors is the subdivision of the input space in equiprobable domains, the equiprobable distribution of the prototype neurons in the FSCL network synthesizes the pdf. This consideration is useful for many purposes in signal processing, among which image compression.

The BP is a supervised multi layer network, proposed by Rumelhart and McClelland (1986) and improved in the last years (Nguyen and Widrow, 1990). It is a non-linear interpolator of sets of multivariable continuous functions (interpolation is meant in the least squares' sense). The BP is often applied to data modelling, i.e. when experimental data are to be fitted to an analytical model that depends on adjustable parameters. While brilliant techniques are available for linear interpolation (orthogonal decomposition, SVD), for non-linear interpolation one must resolve to iterative methods: in these cases, the BP network is often convenient. Even in the linear field, the BP network is also useful for its property of developing suitable basis functions. As all supervised networks it can be used for pattern association, once a pattern has been transformed into a vector.

3. IMAGE FORMATION

A set of 1280 digital fringe patterns were used to develop and test the algorithms. All fringe patterns were obtained by Fourier transforming simulated P.I.V. images. The main advantage of simulated over real images is that the particle displacement is a priori known precisely and can be used as a test for the developed software. Simulation also allows a wide generality of examples to be achieved easily, which is fundamental for training neural networks that can only learn by experience.

A 2-D Langevin equation, modified in order to obtain a spatial correlation among neighbouring trajectories (Cenedese et al., 1993), produced 20 displacement fields defined in terms of mean velocity, turbulence intensity and velocity correlations. All fields had the same direction but different displacement magnitudes. These data were utilized to form 20 synthetic P.I.V. images, with a 512×512 pixel size and a 8-bit resolution (i.e. 256 grey-levels).

The particle image mean displacement modulus ranged from 12 to 31 pixels. The P.I.V. images simulated a triple exposure of 1000 seeding particles.

Then every image was 2-D Fourier transformed and the power spectrum was computed to obtain a Young's fringe pattern. Each of the 20 base images was finally rotated digitally 64 times to cover uniformly the range 0° - 180° (corresponding to a step angle of $\approx 2.8^\circ$).

All fringe images were attached a label, indicating the corresponding particle mean displacement d and flow direction θ of the source P.I.V. image. We remember that the fringe spacing is inversely proportional to d and that fringe orientation is orthogonal to θ . As an example, a fringe image is shown in fig. 1, with fringes rotated at 30° over the right horizontal axis: it corresponds to a flow whose direction is 120° over the same axis and the mean image displacement is 22 pixels.

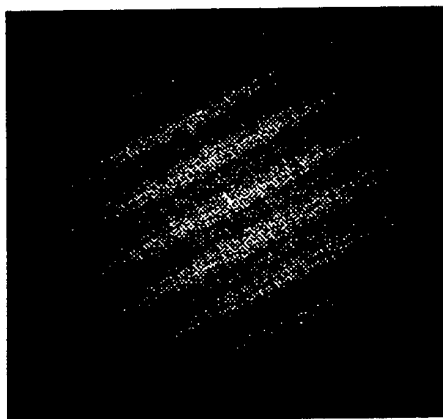


Fig. 1. Young's fringe pattern from a P.I.V. image.

The neural system was trained to match each image of this database and the corresponding labels d and θ . It is to be noted that, in such a way, the neural system showed to be capable of analyzing fringe patterns and give information directly on the source P.I.V. image flow. In other words, an attempt was done to perform a direct calibration of the focusing optical set-up.

4. IMAGE COMPRESSION

The huge fringe image database, as a whole occupying 320 MB of computer memory, was compressed to approximately 1.5 MB. Such an impressive compression was obtained by adopting a two-level hierarchical neural network. In fact, the FSCL network is currently used for image compression (Lancini and Tubaro, 1995) at constant compression ratio (ratio between original and compressed

size). The advantage of using neural networks for image compression lies in that they learn a specific set of images and, optimized on that set and only, can produce superior results over well-known compression techniques (i.e. JPEG) of general purpose.

Compression methods for images are different from those for data/program storage in that a small degradation in the image quality after retrieval is generally tolerated for a higher compression ratio to be achieved [Rabbani and Jones (1991)]. A retrieved image, after compression and decompression, is reported in fig. 2.

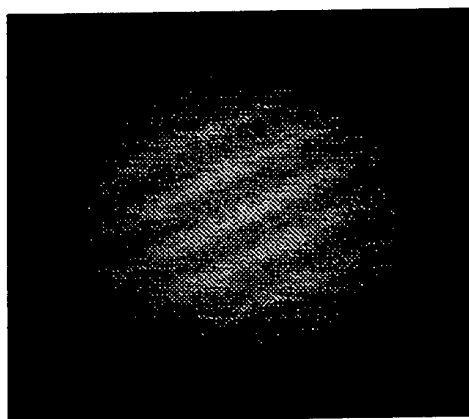


Fig. 2. Fringe image of fig. 1 after compression and decompression.

The "by eye" impression about it, compared to the original in fig. 1, is that image quality is poor. Compression has destructive effects in the grey-level histogram, smoothes boundaries and dumps the fringe brightness. Nevertheless, it preserves orientation and spacing, which is all that is needed for fringe analysis.

The FSCL network actuates the principles of *Vector Quantization* (Linde et al., 1980). The name stems from the image partition into vectors. Hierarchical Vector Quantization was proved to outperform JPEG in recent tests (Ghafourian and Huang, 1995).

In this research, a tree of neural FSCL networks, performing Hierarchical Vector Quantization, was used to compress the fringe pattern images. 160 images (1/8 of the whole database) were used to train the network. Due to Nyquist, the 256×256 central zone of the fringe pattern was considered. Each row of an image was a 256-component image vector, therefore the input layer of the network had 256 neurons. The network is sketched in fig. 3. Signals are propagated to a first competitive layer of 64 neurons and distributed to only 64 out of 4096 neurons in the second layer, in a tree fashion. Altering the number of neurons enabled different compression ratio to be

investigated. We remark that the statistical properties (equiprobability) of the FSCL algorithm make the neural network achieve *optimal* Vector Quantization, i.e.

minimizing distortion error at a given algorithmic complexity.

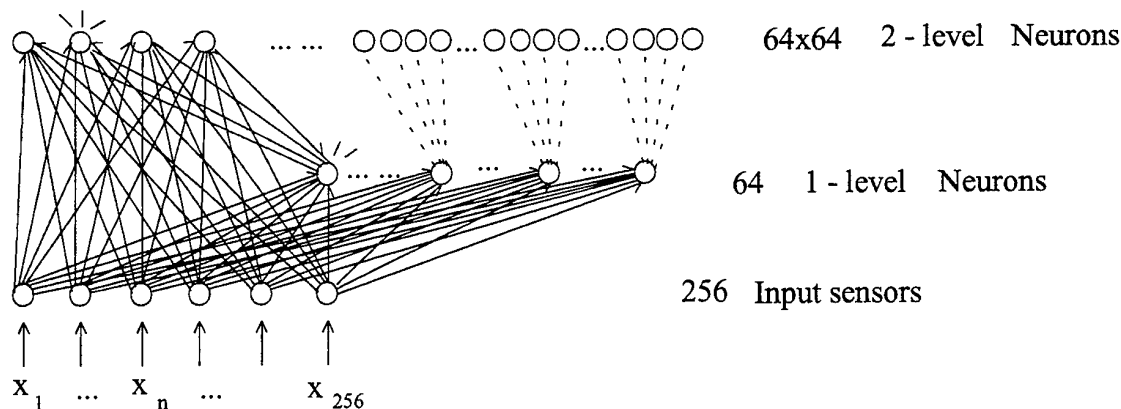


Fig. 3. Sketch of neural network for compression.

After training, the network is ready to compress. When an image is to be compressed, its rows are sent one by one to the input layer. The 256 input sensors sketched in fig. 3 receive the grey-level values of an image row in parallel, and activate one neuron in the last layer. Each of these 4096 output neurons represents a prototype row, which is most similar to the row being processed. Since every image has 256 rows, the compressed file is a list of 256 words of length 12 bit ($4096 = 2^{12}$), indicating the sequence of the activated neurons. The 256×256 image is then compressed at compression ratio $r \approx 170$. The computational complexity of the neural compressor is equal to:

$$C = \text{rows} \cdot (\text{columns} + 1) \cdot L \cdot N$$

where L is the number of tree levels ($L=2$) and N is the neurons of a branch ($N=64$).

In our case, $C \approx 128$ flop per input pixel (much less than JPEG). Predominant operations are multiples and adds, with rather few compares required.

The decompressor is a look-up table that needs the information stored in the network and retrieves it selectively on the basis of the indices contained in the compressed file. Hence Vector Quantization is instantaneous in the decompression phase. However, in the fringe analysis, the decompressor is not used. As a result of the compression, every fringe image in the database was reduced to a 256-word string, ready for further analysis.

5. RECOGNITION OF FRINGE ORIENTATION AND SPACING

The main topic of this paper regards the rather surprising capability that neural networks showed for recovering information from compressed image files. It is clear that a compressed image file retains almost all the relevant information about the source image, but it is also apparent that information is coded into an encrypted form that wouldn't be intelligible to any human. Despite of that, a Back-Propagation network with two hidden layers was successfully trained to extract the correct orientation and the fringe spacing from the compressed files of the 1280 images of the available database.

A sigmoid function was used in the first layer, a step function was used in the second layer, and a linear function was used in the third layer as the neuron transfer function. The network was initialized with Nguyen-Widrow conditions and trained by the Back-Propagation algorithm with a learning rate $\eta = 0.3$. It employed 256 neurons in the input layer (that received the 256 words of the compressed image file in parallel), 96 neurons in the first layer, 11 in the second and 2 in the output layer. The network was taught to produce orientation (in degrees) and spacing (in pixels) at its two output neurons. Please note that orientation and spacing are measured simultaneously at the network output. The network is sketched in fig. 4.

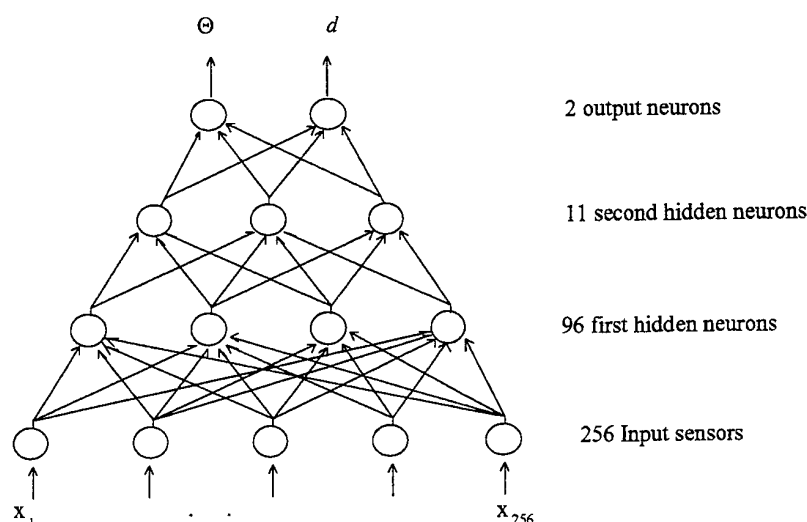


Fig. 4. BP network for recognition of fringe orientation and spacing

The training progressed for about 2500 epochs and took about one hour on a IBM RISC 6000 workstation.

After the training, the performance of the measurements was tested on the whole database of fringe images. Fringe orientation was recognized by the neural network within a $\pm 1.4^\circ$ accuracy in 96.3 % of the images, while fringe spacing was selected correctly (± 0.5 pixels) in 93.6 % of the images. The images not included in the correct behaviour percentages are mistakes rather than errors: this means that they can be easily detected and clipped in a subsequent procedure on the basis of consistency with neighbouring measurements in the flow field.

The execution time of every neural network is very different in the training phase and in the working phase. This concept is especially crucial for feed-forward networks, since BP network is extremely fast at work. Our experience is that it analyzes over 300 compressed fringes per second on a IBM RISC 6000 workstation, while the inverse FFT could process only 1-2 fringes per second on the same workstation. The brilliant performance in speed is mainly due to the reduced size of the compressed files. The computational complexity for the neural network may be approximately estimated from:

$$C \approx (n_0 \cdot n_1) + (n_1 \cdot n_2) + (n_2 \cdot n_3)$$

where n_0 , n_1 , n_2 , and n_3 are the number of neurons, respectively, in the input layer and in the subsequent layers of the network. In our case, the first term of the sum is predominant and $C \approx 25000$ flop. Compared to the 5 Mflop complexity of the inverse FFT, the execution time reported before shows to be justified.

CONCLUSIONS AND DEVELOPMENTS

Young's fringe patterns from high density P.I.V. images were directly processed by a totally neural system that has the main advantage of speeding up the analysis of orders of magnitude over a classical approach, the inverse FFT method. Two popular neural networks were used, the Kohonen FSCL and the BP network (no original ad-hoc network was developed). A complexity analysis shows that the BP neural network is about 200 times lighter than the inverse FFT method when run on the same hardware. Moreover, neural networks are so far simulated on a workstation, but the possibility of implementing them on neural processor boards must be taken into account.

The accuracy of measurements was tested on over one thousand simulated fringe patterns. The network recognized 96.3 % orientations and 93.6 % spacings correctly. Tolerance are respectively $\pm 1.4^\circ$ for angles and ± 0.5 pxl for displacements. In fact, the neural network output was directly calibrated to mean particle image displacement. This paper has reported a work that is still in progress: further tests are needed on more critical images, i.e. noisy or with velocity gradients that create more confused fringe patterns. A performance comparison with current techniques is also planned for the next future, along with the application to interrogation areas with reduced size (i.e. 128×128 pixels) to make the technique more suitable for digital P.I.V. In particular, the size reduction of the interrogation area is expected to further increase the number of vectors per second that the method is able to yield.

REFERENCES

- Adrian, R.J. 1991, Particle-Imaging Techniques for Experimental Fluid Dynamics, Ann. Rev. Fluid Mechanics, vol. 21, pp. 261-304.
- Cenedese A., Monti P. and Sallusti 1993, PIV: a numerical simulation, Laser Anemometry- Advances and Applications, Washington, USA, 2052, pp. 493-500.
- Desieno D. 1988, Adding a conscience to competitive learning, Proc. Int. Conf. on Neural Networks, vol.1, pp. 117-124.
- Ghahfourian M.A. and Huang C.M. 1995, Comparison between Several Adaptive Search Vector Quantization Schemes and JPEG Standard for Image Compression, IEEE Trans. on Communications, vol. 43, n. 2/3/4, February, March, April, pp. 1308-1312.
- Haykin 1992, Neural networks, a Comprehensive Foundation, MacMillan NY;
- Hecht-Nielsen R. 1990, Neurocomputing, Addison-Wesley;
- Kohonen T. 1984, Self-Organization and Associative Memory, Springer-Verlag;
- Kohonen T. 1990, The Self-Organizing Map, Proc. IEEE, Vol. 78, 9, September.
- Lancini R. and Tubaro S. 1995, Adaptive Vector Quantization for Picture Coding using Neural Networks, IEEE Trans. on Communications, vol. 43, n. 2/3/4, February, March, April, pp.534-544.
- Linde Y., Buzo A. and Gray R. 1980, An Algorithm for Vector Quantizer Design, IEEE Trans. on Communications, Vol. 28, n.1, January, pp. 84-95.
- Meinhart C.D., Prasad A.K. and Adrian R.J. 1992, Parallel Digital Processor System for Particle Image Velocimetry, Proc. 6th Int Symp on Appl of Laser Techniques to Fluid Mechanics, pp 30.1.1-6.
- Nguyen and Widrow 1990, Improving the learning speed of 2-layer neural networks by choosing initial values of the adaptive weights, Proc. Int.Joint Conf. of Neural Networks, vol. 3, pp. 21-26.
- Rabbani M. and Jones P.W. 1991, Digital Image Compression Techniques, SPIE Press.
- Rückert U 1993, Microelectronic Implementation of Neural Networks, in Workshop on Neural Networks at RWTH Aachen, eds. Huning, Neuhauser, Raus and Ritschel,, pp. 77-86.
- Rumelhart and McClelland 1986, Parallel Distributed Processing, MIT Press.
- Treleaven P.C. 1989, Neurocomputers, Int Journal of Neurocomputing, vol 1, pp 4-31.

QUANTITATIVE FLOW VISUALIZATION OF VELOCITY
DISTRIBUTIONS BY PARALLEL IMAGE PROCESSING USING PPH
(PHOTO-CONDUCTOR PLASTIC HOLOGRAM)

*Fumitake KATO, Isao SHIMIZU, Yuichi SHIBATA,
Takashi ISAGO and Hiroyuki TAKI

Dept. of Mechanical Engineering, Ibaraki College of Technology

ABSTRACT

Authors have developed a new technique which can quantitatively determine the velocities and orientation of particle displacement in flow. The sizes and orientations of loci of particle image displacement taken by double exposure photography can be discriminated instantaneously and simultaneously by the technique using a Multiplexed Matched Spatial Filter (MMSF). The location of particles loci in each size and orientation can be displayed simultaneously and instantaneously. And a new system automatically and rapidly making hologram which consisted of Photo-conductor Plastic processed by solvent vapour has been developed by authors. In order to making a MMSF, the hologram can be processed at the setting place on the optical system loading the Photo-conductor Plastic Hologram (PPH) system. Easy and precise discrimination can be realized by the system with a MMSF.

1. INTRODUCTION

At present, quantitative visualizations for the velocity distributions of flow by Particle Image Velocimetry (PIV) technique are based on digital correlation method which is using two images of displacement of seeded particles in flow. The technique has difficulty about the

determination of the orientation of flow and the process taking huge time for calculations of auto-correlation.

In order to settle these problems, a new technique has been developed by authors. To determine the orientation of flow, special double exposure has been used ¹⁾. The image gives orientation and magnitude of the velocity of the particle displacement in flow. The MMSF technique has been used to discriminate the location of loci in each length and orientation. This holographic filtering technique can discriminate the all of location of loci in each length and orientation instantaneously and simultaneously.

Former techniques had shortcoming to take long time processing the holographic plate. And it was very sensitive about vibrations. To resolve these problems, PPH system has been developed by authors ²⁾. The system which is processed by solvent vapour can make a hologram easily and rapidly at initial setting place. And the optical parts are aligned on an optical rail base to avoid the vibration, therefore the system can make hologram without vibration isolation table.

2. FLOW VISUALIZATION BY THE PARTICLES IMAGE DISPLACEMENT METHOD WITH DOUBLE EXPOSURE

Schematic diagram of flow visualization of particles displacement by double exposure is shown in fig.1. Sheet light laser(Ar^+) illuminates flow and the scattered image of the particle displacement is taken photograph by a camera. The double exposure has first short exposure for the particle position and second long exposure for the particle displacement. The image gives the orientation and the velocity of the particle displacement in flow.

3. INSTANTANEOUS AND SIMULTANEOUS DISCRIMINATION OF LOCATION OF LOCI OF PARTICLES BY A MMSF

The optical system discriminating loci of particles displacement by a MMSF is shown in fig.2. At first, the distribution of the double exposed images of particle loci are taken by photograph. The diffraction patterns generated from the image at the frontal focal plane of the convex lens L_1 in the parallel coherent laser beam are superimposed at the back focal plane P_2 of the lens and the images of particle loci are filtered by a MMSF. The groups of auto-correlation peaks which discriminated the each locus appear in each measuring field skew-symmetrically to the position of the loci at P_3 . The distributions of loci in each velocity could be measured simultaneously and instantaneously using the technique.

4. PHOTO-CONDUCTOR PLASTIC HOLOGRAM SYSTEM

The optical system discriminating loci of particles displacement by a MMSF constructed of PPH is shown in fig.3. Equipment making photoconductor-plastic hologram processed with solvent vapour as shown in fig.4. At first, softening layer of plastic with solvent vapour. And adding high voltage about 5 kV on the surface of the plastic from the outside with laser

beam exposure. The frost deformation are generated on the surface of plastic of which parts are illuminated by laser light, and the interference pattern corresponding to the intensity of light is recorded on the surface of plastic. The optical system is composed under aligning the optical parts and the cell in which photo-conductor plastic plate is processed with solvent vapour, on a rail base. Hologram can be made automatically under processing hologram plate at the initial setting place. One hologram plate can be used about 10 times to renew the hologram. The minimum power of the beam on the hologram plate is about $5 \mu \text{W}/\text{cm}^2$, and the time making hologram only needs about 2 minutes. The efficiency for the 1st order diffraction pattern is about 27 % under the condition 1000 line/mm of resolution.

Traditional holographic optical system had been arranged on the heavy base supported by air suspension to intercept the influence of the vibration. In this experimental research, to intercept the vibration and to intend to compact the optical setup, the optical system making hologram (MMSF) is aligned simply on a optical rail base. It is possible to make hologram even on a wooden table taking no countermeasure to cope with the vibration. The new optical system making hologram became compact in comparison with traditional optical system.

5. EXPERIMENTAL RESULT

The experimental result for discrimination of the each velocity of particle in flow is shown in fig 5. In fig.5, figure (a) shows the reference pattern, (b) shows the loci of particles in flow and (c) shows the distributions of discriminated signals(auto-correlation peaks) by a MMSF. Fig.5 (c) indicates that double exposed image of particles loci and locations are discriminated with each velocity distribution in the flow simultaneously and instantaneously. The experimental result shows that the orientation and magnitude of velocity in flow can be

discriminated instantaneously and simultaneously by this technique.

6. CONCLUSION

(1) In order to discriminate the particle velocity distributions simultaneously and instantaneously, a new technique has been developed by using a MMSF. Images of loci and its location can be discriminated with a double exposure photograph.

(2) This technique can discriminate orientation and magnitude of velocity in flow simultaneously and instantaneously.

(3) A new technique which the photoconductor-plastic is processed with solvent vapour to make hologram easily and rapidly, has been developed by authors. And the equipment can make hologram at the initial setting place. In order to intercept the vibration and to intend to compact the optical setup, a new optical system making MMSF is aligned simply on a rail base.

REFERENCE

- 1) I.Shimizu, K.Suzuki and et al. (1994), [Quantitative visualization of velocity distributions in flow], Proc. of 7th International Symposium on Application of Laser Techniques to Fluid Mechanics (1994-7) Vol. II 22.4.1-8
- 2) I.Shimizu, F.Kato and et al. (1996), [Developmental research on simultaneous discrimination of shapes by a photoconductor-plastic hologram automatically processed by solvent vapour], Proc. International Symposium on Optical Systems Design and Production II (1996-5)

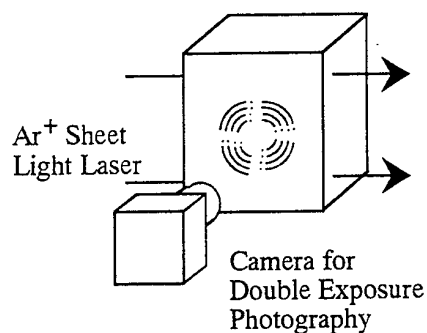


fig.1 Schematic diagram of flow visualization of particles displacement by double exposure

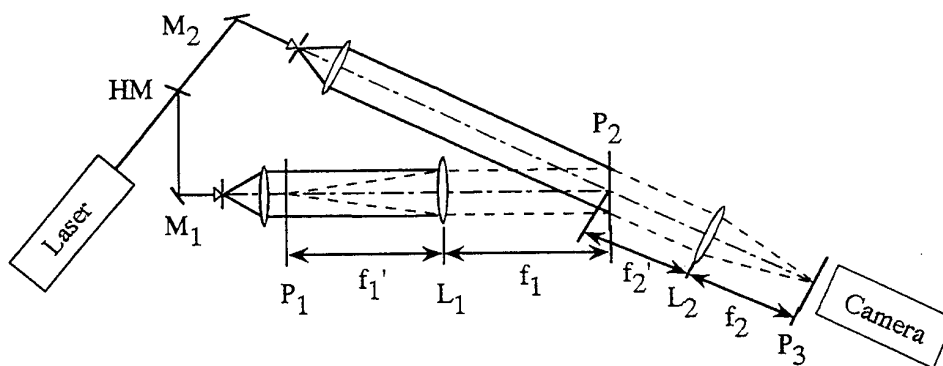


fig.2 Optical system discriminating loci of particles displacement by a MMSF

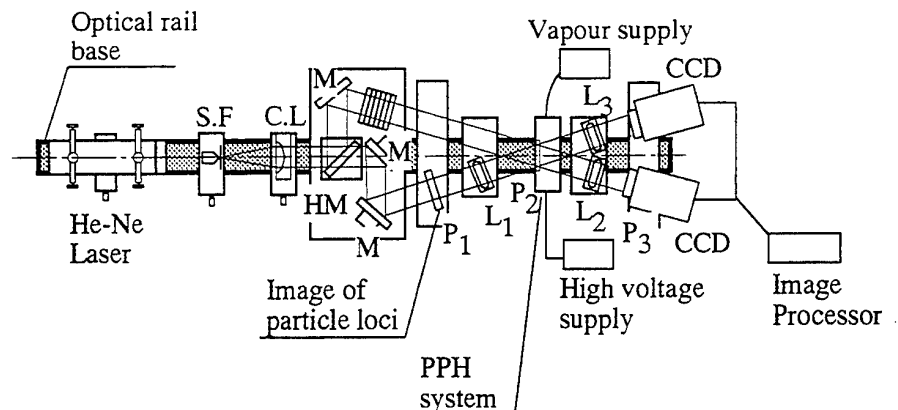


fig.3 Optical system discriminating shape and size of objects by a MMSF composed of PPH

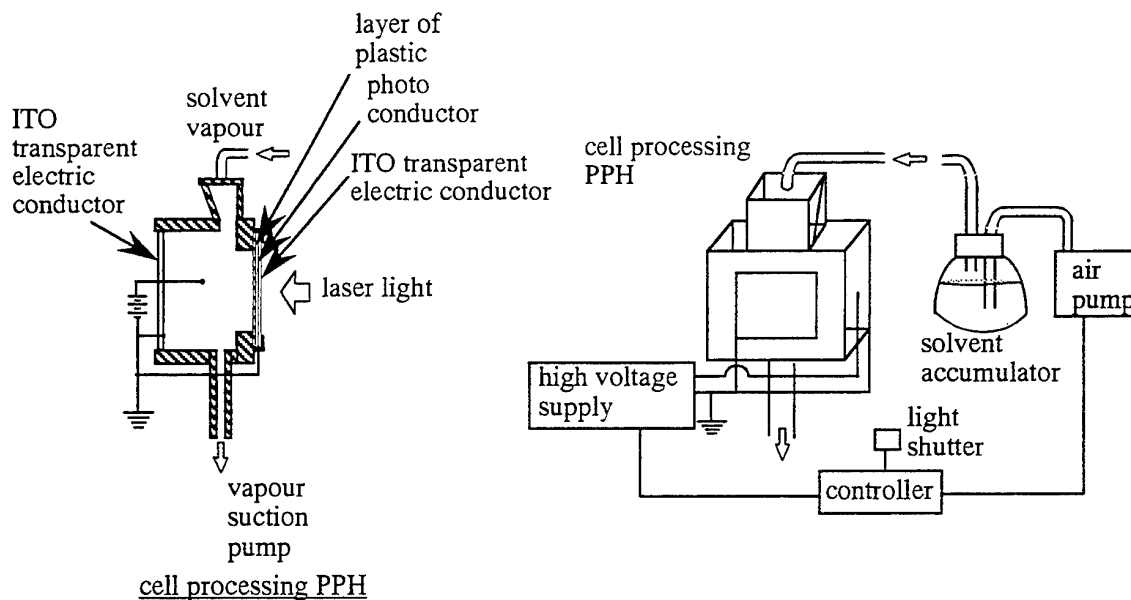


fig.4 Equipment making photoconductor-plastic hologram processed with solvent vapour

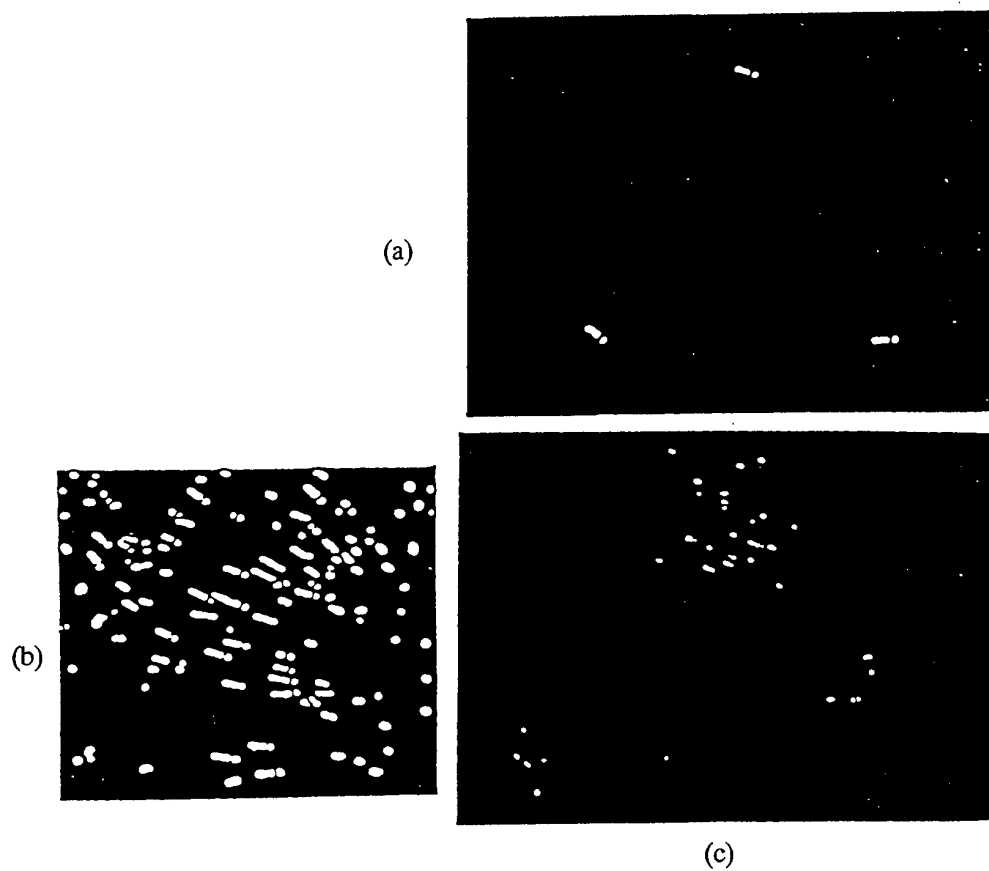


fig.5 Discrimination of direction and velocity of flow
(a) Position of reference loci of particles double exposed
(b) Distribution of measured loci of particles in the flow
(c) Output signals of auto-correlation peaks

SESSION 22

Engines III

LDA-MEASUREMENTS OF THE COOLANT FLOW OF A HIGHLY COMPLEX RECIPROCATING ENGINE

J. Reuber¹ and E. Blümcke²

¹ Institute of Hydraulic Engineering and Water Resources Management, Aachen University of Technology, Germany

² Audi AG, Dept. I/EK-92, Ingolstadt, Germany

ABSTRACT

In the present investigation the flow field inside the water jacket of a highly complex reciprocating engine was measured using a one-component LDA-device. Simultaneously the three-dimensional, isothermal flow field was calculated using the CFD-code STAR-CD (COMP. DYNAMICS, 1995). Although CFD-codes are more applied in the industry in order to support design decisions (see HAAG, BRASNER 1989; HOLLINGWORTH 1989; DANCKERT, WERSCHING 1990; JENNINGS, MOREL 1991) there remains the task to develop a detailed validation procedure for every complex application like the coolant flow analysis. This investigation aimed to contribute to that goal.

The critical evaluation of the measured velocities inside the water jacket of the gasoline engine showed a very satisfactory accuracy of the applied CFD-code

STAR-CD. This can also be seen from the good agreement between the measured and the calculated volume flux distribution over the cylinder head gasket as well as from the reproduction of the flow field structures in the water jacket of the cylinder head. Some discrepancies observed are mainly due to differences between the modelled geometry (based on technical drawings) and the actual geometry of the engine which is not obviously the same.

Based on the numerical results, the arrangement of the holes of the cylinder head gasket was changed resulting in a higher coolant efficiency which could be proved by temperature measurements: A reduction of the material temperatures of 15 K was achieved.

1. INTRODUCTION

For the calculation of the flow field inside the water jacket of a highly complex reciprocating engine a

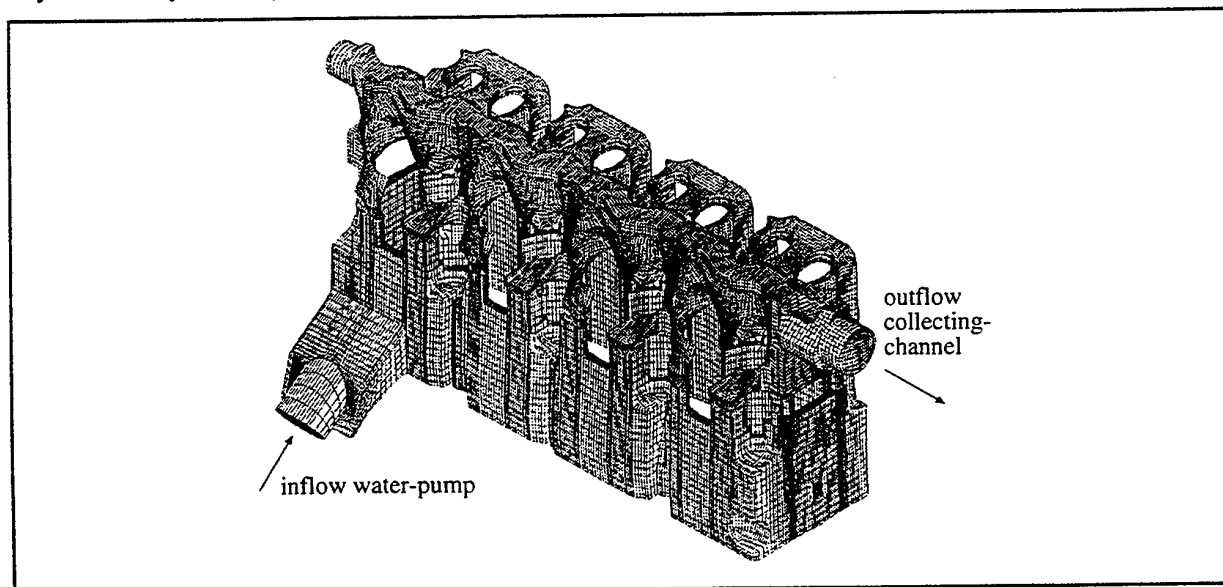


Fig. 1 Geometry of the engine and computational mesh of the water jacket of an Audi 1.8l 4-cylinder 5-valve

three-dimensional simulation model is used, which is based on the finite volume method. The aim of the numerical simulation is to increase the efficiency of the cooling system in internal combustion engines. To validate the numerical simulations it was necessary to carry out physical investigations.

Therefore flow velocities in 10 selected sections in the engine block and 13 sections in the cylinder head had been recorded as well as the velocity profile at the outlet of the water pump. Fig. 1 shows the complex geometry of the engine and the computational mesh of the water jacket of an Audi 1.8l 4-cylinder 5-valve engine consisting of 400000 computational cells.

2. EXPERIMENTAL PREPARATIONS

Before starting the measurements the 4-cylinder 5-valve engine had to be prepared to give optical access not even to the block but also to some measurement positions in the cylinder head of the engine. Material was milled away on the side of the block and the cylinder head as well as on the outlet of the water-pump and was replaced by transparent plexiglas. Fig. 2 and Fig. 3 show the whole engine and a part of the head with the prepared sections.

The whole engine was fixed to 2 steel plates, which were connected with bolts, allowing an easy ad-

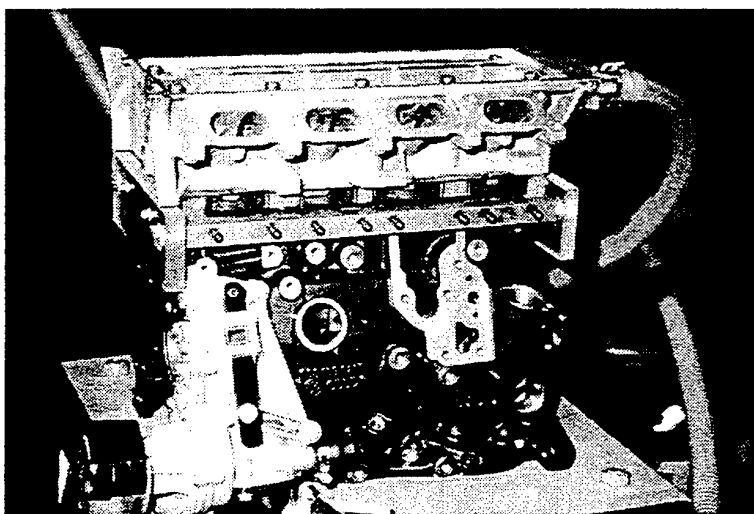


Fig. 2 Side-view of prepared engine

Position of cross-section

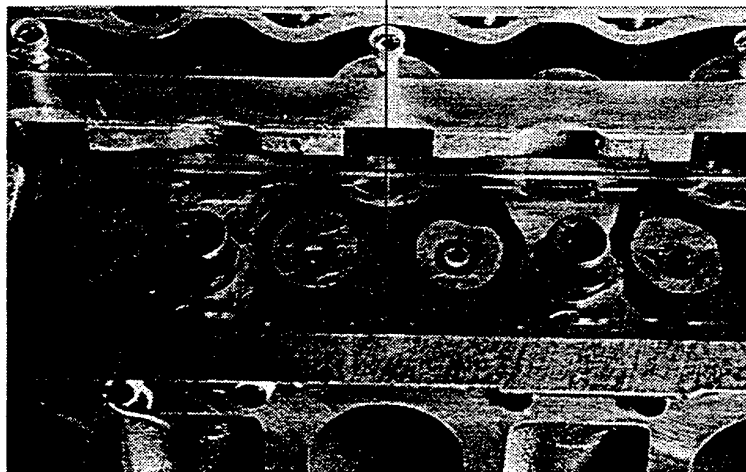


Fig. 3 Detailed view of the head during measurement (profile 13)

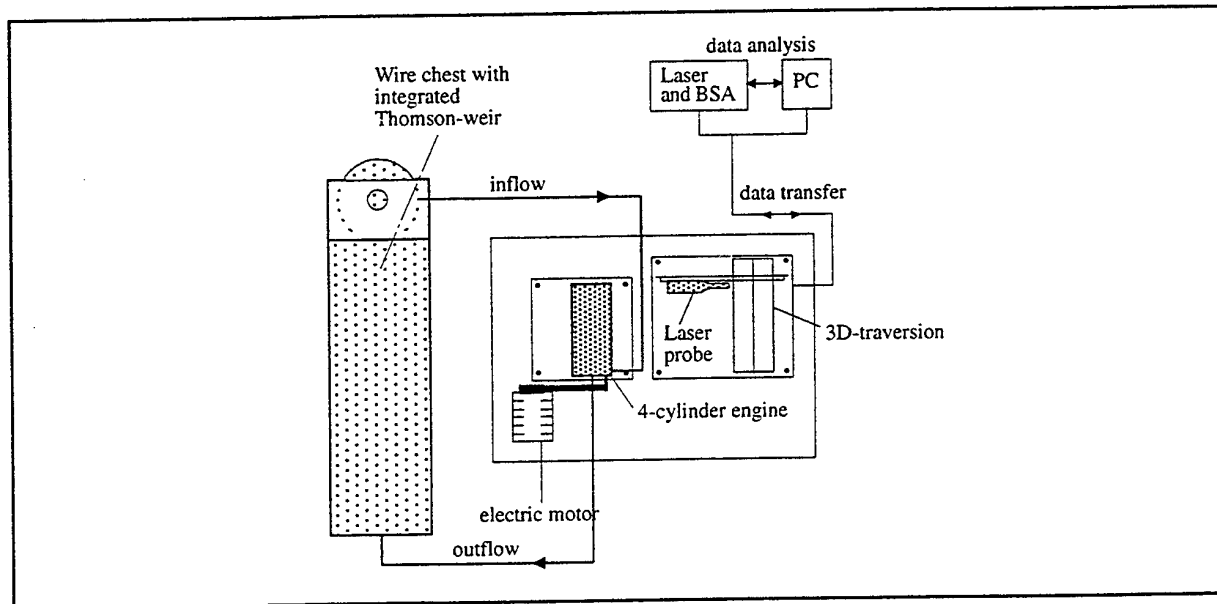


Fig. 4 Sketch of the model setup

justment and rotation of the engine. The lower steel plate was fixed to a concrete column to avoid vibrations, due to the propulsion of the water pump by an electric motor with a speed of 5250 rpm.

The traversion for the LDA-probe was placed on a second concrete column to allow an exact alignment of the probe in 3 dimensions. The coolant was running in a closed circuit. 3 % of a colourless anti-freezing agent was added to avoid corrosion inside the engine. Fig. 4 shows a sketch of the model setup.

3. MEASURING TECHNIQUE AND INVESTIGATION PROGRAM

For the measurement of flow-velocities inside the water-jacket of the engine a one-dimensional DANTEC Laser-Doppler-Velocimeter with 10 mW power has been used (see DANTEC, 1993). The Laser is working in backscatter-modus. The recieved signals were evaluated by a burst spectrum analyser (BSA), based on a Fast Fourier Transformation. To analyse the data the evaluated signals were transmitted to a conventional PC.

Mean- and cross-components of velocity were measured in 1217 points in the engine block and 2237 points in the engine head. An overview of the measurement positions in the head is given in Fig. 5. At the outlet of the water-pump mean- and cross-components in 2 profiles parallel to the measuring-section in 573 points were received.

10000 bursts were collected for every measuring point by a maximum duration of 45 seconds. Due to

the relatively high flow velocities and the anti-freezing agent added to the water it was not necessary to use any kind of seeding.

The Laser-probe was adjusted by a computer controlled traversion with a step-width accuracy of 0.03 mm and a repetiton accuracy of 0.007 mm. The distance between the measuring points was 2 mm, which allowed an exact determination of flow velocities in the highly complex engine-geometry.

4. NUMERICAL MODEL

As already mentioned, the three-dimensional, isothermal flow field was calculated using the CFD-code STAR-CD. It is based on the well-known finite volume technique. The standard k- ϵ -turbulence model in conjunction with the logarithmic law of the wall and the time averaged Navier-Stokes equations are used in order to close the set of equations. Although more sophisticated differencing schemes are available the use of the Upwind Differencing Scheme (UDS) is sufficient to produce reasonable results. Starting with the preprocessing, every process was handled on workstations. On a two processor SGI Challenger R 4000 the solution on a mesh of roughly 400000 computational cells takes about 25 hours CPU time.

The computational mesh of the engine was built up using technical drawings and a model of the water jacket. Based on the Reynolds analogy a heat transfer coefficient is calculated. This parameter is used to judge the local coolant efficiency. A more detailed

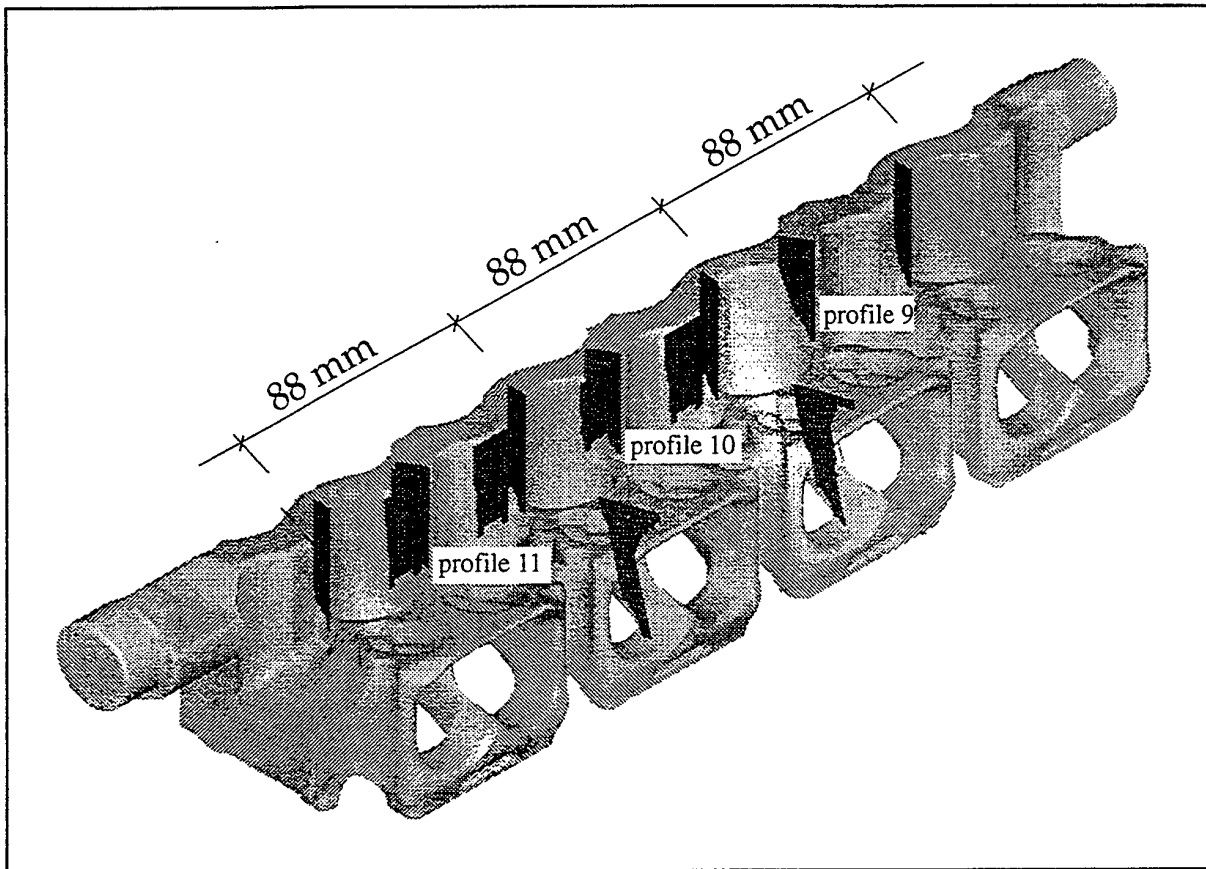


Fig. 5 Position of LDA-measurement planes in the head

analysis of the numerical results will be given in BLÜMCKE, STENZEL (1996).

5. MEASURING RESULTS AND COMPARISON WITH NUMERICAL SIMULATIONS

To visualize the results of the LDA measurements within the typological background of the engine the 3D software package Advanced Visual System (AVS) was used. The flow velocities were represented by vector plots. Optional it was possible to visualize the primary moments by colors.

As an example Fig. 6 shows the measured velocities in profiles 9 to 11 in the head. The length of the single vector in the right upper corner represents a velocity of 1.0 m/s. Fig. 7 shows the measured velocities in 4 profiles in the block of the engine consisting of two components.

As it appeared the quality of measurements was very good in spite of the difficult geometry and the high resolution.

The critical evaluation of the measured velocities inside the water jacket of the gasoline engine showed a reasonable accuracy of the applied CFD-code STAR-

CD. This can be seen from the good agreement between the measured and the calculated volume flux distribution over the cylinder head gasket. This is documented in Fig. 8. The upper value represents the flux as a result of the integration over the measured flow velocities. The lower value is the volume flux calculated by the numerical simulation described above. The values are in % of the whole volume flux. The differences between the measured and the calculated values range up to a maximum of 15 %.

The observed discrepancies are mainly due to differences between the modelled geometry (based on technical drawings) and the actual geometry engine, which is obviously not the same.

Further reasons are the difficulties to measure the velocities close to the walls. The numerical model is able to calculate velocities in these areas exactly, which could be verified with some detailed measurements.

Based on the numerical results, the arrangement of the holes in the cylinder head gasket was changed resulting in a higher coolant efficiency which could be proved by temperature measurements. A reduction of the material temperatures of 15K was achieved.

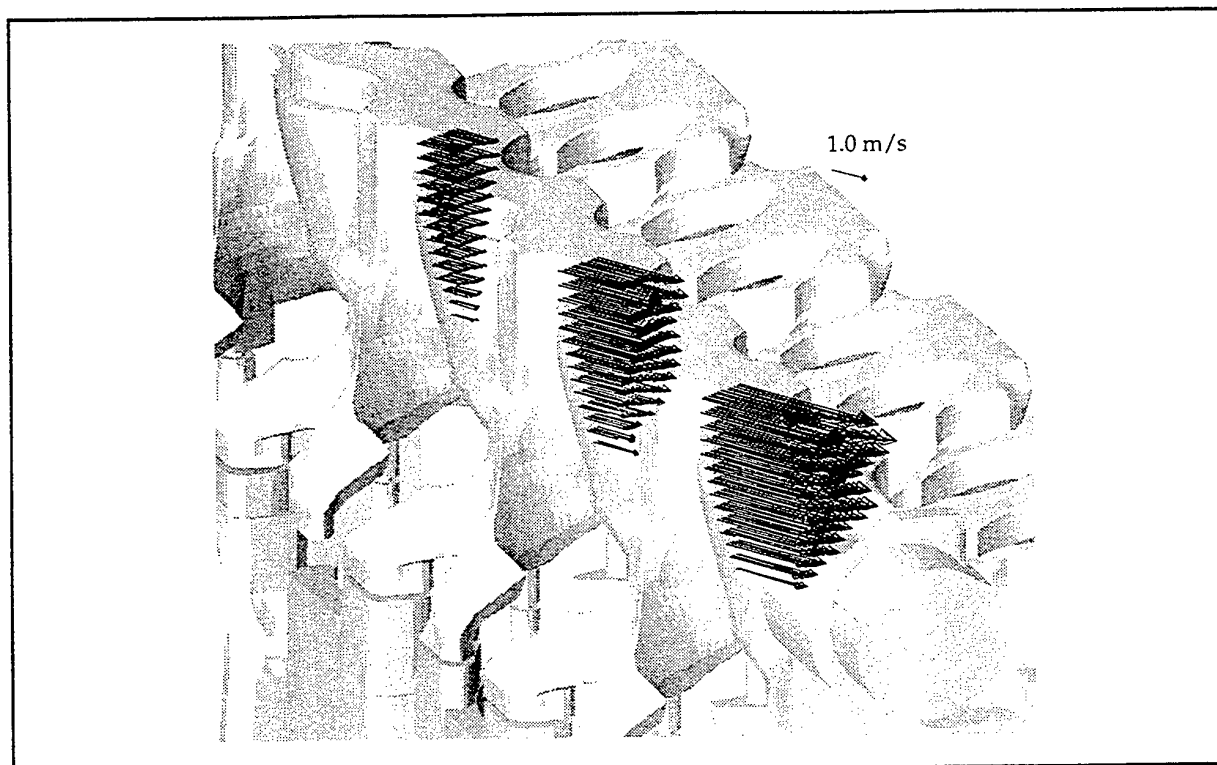


Fig. 6 Measured velocities in profiles 9 to 11 in the engine head

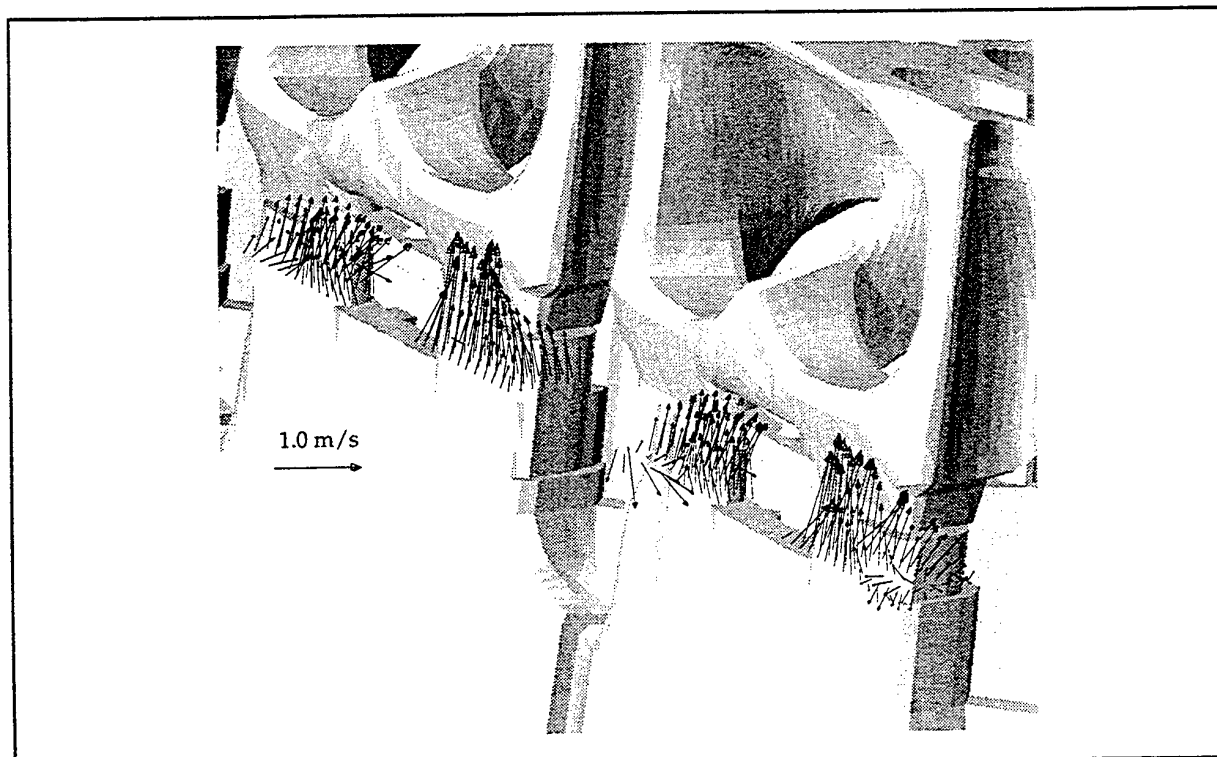


Fig. 7 Measured velocities in 4 profiles in the engine block

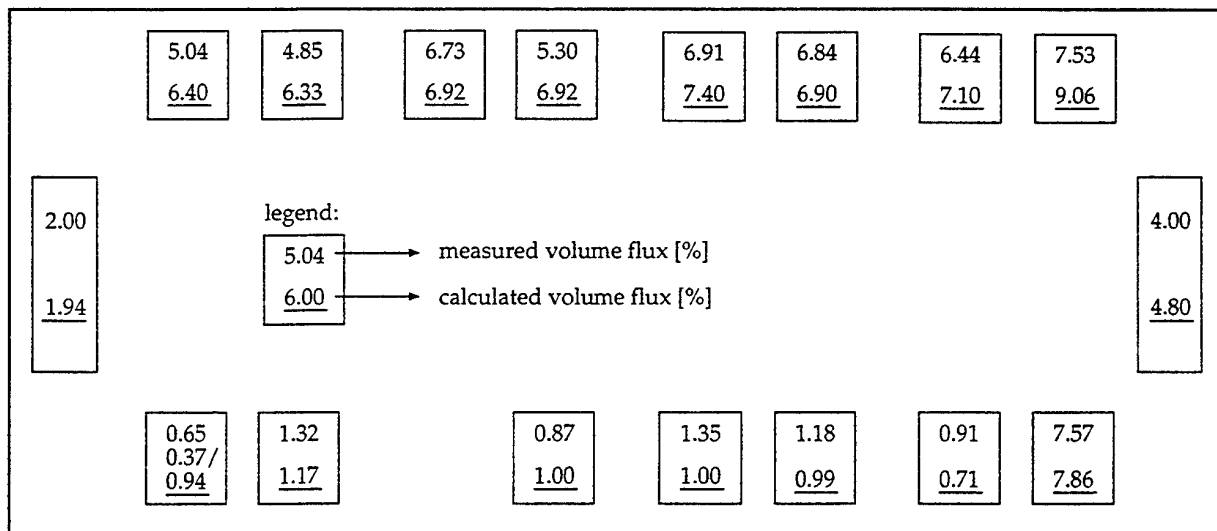


Fig. 8 Comparison of measured and calculated volume flux distribution in the cylinder head gasket

The calculation method presented in the actual paper is embedded in a procedure aimed to improve the overall performance of the engine cooling management (see BLÜMCKE, E.; NEFISCHER, P. 1995). The analysis of the coolant flow inside the engine closes the gap between the design of the water pump and that of the radiator.

6. REFERENCES

- BLÜMCKE, E.; STENZEL, M. (1996) "Validierung und Einsatz eines Verfahrens zur Berechnung der isothermen Strömung im Kühlwasserkreislauf von Fahrzeugmotoren", 8th Int. VDI-Berechnungstagung, Würzburg 1996 (in german)
- BLÜMCKE, E.; NEFISCHER, P. (1995) "Improved Engine Cooling Systems using Calculation Methods", 2nd VTMS Conference, London 1995
- COMPUTATIONAL DYNAMICS (1995) "STAR-CD Manual Version 2.2", London 1995
- DANCKERT, H.; WERSCHING, R.; SCHÖCKLE, S. (1990) "3-dimensionale Berechnung der Wasserströmung in einem Zylinderkopf", Automobil-Industrie 35, Heft 5, 1990 (in german)
- DANTEC (1993) "Burstware-Installation and users guide", Manual
- DANTEC (1993) "FLOWLITE- Installation and users guide", Manual
- HAAG, K.L.; BRASNER, S. (1989) "The use of flow visualization and CFD in cylinder head cooling jacket development", SAE 891897, 1989
- HOLLINGWORTH, P. (1989) "The design of an engine coolant circuit using computer simulation", High-Tech-new engine, ImechE 399/25
- JENNINGS, M.J.; MOREL, T. (1991) "Computational Study of Wall Temperature Effects in Engine Heat Transfer", SAE 910459, 1991

MEASUREMENT OF AXIAL FLOW VELOCITY IN A CYLINDER OF AN S. I. ENGINE BY A SINGLE-INCIDENCE-BEAM REFERENCE-MODE LDA

Chikashi TAKEDA^{*1}, Yuji OHTA^{*1}, Tsuneaki ISHIMA^{*1},
Kiyoshi ISHII^{*2} and Tomio OBOKATA^{*1}

^{*1} Dept. of Mechanical System Engineering, Gunma University.

^{*2} Honda R&D Co., Ltd. Wako R&D Center.

ABSTRACT

At practical use engine, in order to measure the swirl and radial velocities in the cylinder by means of a laser Doppler anemometer (LDA) through a small measuring window on the cylinder head, a back-scattering fringe mode LDA was easily used. It, however, could not measure the velocity component in the axial direction of the cylinder. Therefore, a single incidence-beam reference-mode LDA is developed to measure the velocity component along the optical axis of the LDA and used to measure the fluctuating flow velocity in the axial direction of the cylinder. Ensemble-averaged mean velocity and fluctuation intensity of the velocities measured by the LDA show good agreement with those measured by the conventional fringe mode LDA. Based on these results, it can be concluded that the reference-mode LDA is applicable to measure the flow velocity in the axial direction of the cylinder through the small window on the cylinder head.

1. INTRODUCTION

More improvement of the combustion has been required to have better efficiency and lower pollution in internal combustion engines. To improve the combustion, it is important to understand the relationship between gas flow and combustion and control the gas flow in the cylinder. Recently, numerical simulations have shown the gas flow in the engines. It can get much information by means of the computer simulation, but the models used in the calculation must be verified by experimental data. It is also possible now to measure directly the gas flow velocity in the engines by LDA. There are many reports measuring the flow in a two-cycle engine on firing [1] and examining relation between the gas flow and the combustion in the cylinder of a four-cycle engine [2-3]. These measurements have made the flow in engines clear gradually. The flow in the cylinder is always three

dimensional and has the distribution in the space, however the velocities were usually measured by one or two-dimensional LDAs. Dimopoulos et al. [4] only carried out the three-dimensional measurement of the flow in a cylinder on motored operation. It needs multiple wide windows and the application is restricted to a model engine, because their fringe mode LDA has three incident beam pairs from different two directions. But, it is difficult to create multiple windows on the practical use engine. So, it is advisable to make it possible to do the three-dimensional measurement of the velocity in the combustion chamber through a small measuring window on the cylinder head. In this case, if a back-scattering fringe mode LDA is used, it could be easy to measure the radial (r) and tangential (θ) velocities, but it is difficult to measure the axial (z) velocity. A single incidence-beam reference-mode LDA (Axial-LDA: ALDA) is proposed here as a basis of three-dimensional LDA to measure the axial velocity through a small measuring window [5]. In this experiment, we use ALDA for measurement of the axial velocity in the engine and examine the applicability.

2. PRINCIPLE AND COMPOSITION OF THE ALDA

2.1 Principle of measurement

The reference-mode LDA [6] has been often used for velocity measurement especially for a vibration measurement of solid wall [7]. When it measures a particle velocity of incidence-beam direction, the principle of measurement of the reference-mode LDA is shown in Fig. 1. We consider a case where a laser beam of wavelength λ_i is incident at an angle of θ to z -axis from I -direction. The particle with velocity V_p passes measurement point at an angle of α to z -axis. If the velocity of light is c , a velocity component of I -direction for the particle P is V_{Pi} , and a component velocity of S -direction is V_{Ps} , the scattered light wavelength λ_s has

shifted by Doppler effect shown as below:

$$\lambda_s = \frac{c + V_{pz}}{c - V_{pi}} \lambda_i, \quad (1)$$

where

$$V_{pz} = V_p \cos(\theta - \alpha)$$

$$V_{pi} = V_p \cos(\theta + \alpha)$$

Thus,

$$\lambda_s = \frac{c + V_p \cos(\theta - \alpha)}{c - V_p \cos(\theta + \alpha)} \lambda_i. \quad (2)$$

If it superimposes the reference light of the same wavelength as the incident beam from another light path and the frequency difference between incidence beam frequency ν_i and the frequency ν_s of scattering light S is denoted the Doppler frequency ν_D , ν_D is:

$$\begin{aligned} \nu_D = \nu_s - \nu_i &= \frac{c}{\lambda_s} - \frac{c}{\lambda_i} \\ &= \frac{c}{\lambda_i} \left\{ \frac{c - V_p \cos(\theta + \alpha)}{c + V_p \cos(\theta - \alpha)} - 1 \right\} \end{aligned} \quad (3)$$

and expanded by using $V_p \ll c$ as follows:

$$V_{pz} = -\frac{\lambda_i \nu_D}{2 \cos \theta}, \quad (4)$$

where the negative sign indicates that the increase of the frequency corresponds to the opposite direction velocity increase in the figure. From this equation the incident angle θ is required to restrict a measurement point. However it affects directly the values of the velocity. So, it causes an error in V_{pz} measurement. But for practical applications it is possible to consider the particle velocity of z-axis direction, because the difference between $\theta=7.1$ deg. and $\theta=0$ deg. is only about 0.8%.

2.2 Composition of the optical system

Fig. 2 shows a component of a single incidence-beam reference-mode LDA (ALDA) made as a trial and Table 1 shows the specifications of it. The laser source is Ar-ion gas laser (Spectra-Physics Stabilite 2016, total power 4W). An output laser beam is separated into two beams by beam splitter. And the beams are given each frequency shift of 85MHz and 75MHz (or 80MHz in measurement of jet flow and the fluctuating flow). Then beams are guided to the probe by optical fibers. The 85MHz shifted beam is incident at an angle of 7.1deg. (θ) to a measurement point by a lens (L1). After made to be parallel and restricted by an aperture (A), the scattering light from a particle passing the measurement point is condensed by a lens (L2). And it is guided to a photomultiplier through a half mirror (HM) and a 100 μ m pinhole (PH). Another 75MHz shifted beam is used as the reference light. The beam passes through a right angle

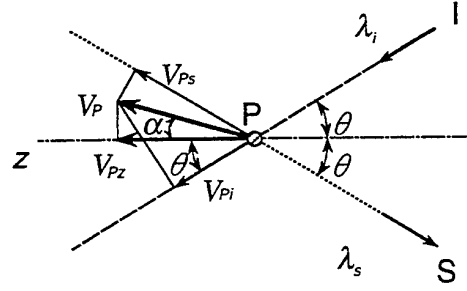


Figure 1 Measuring principle of the reference-mode LDA

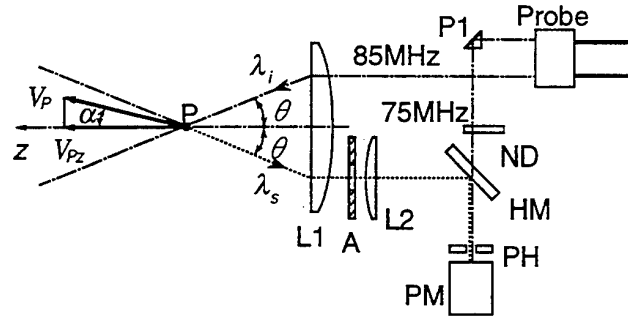


Figure 2 Component of ALDA

Table 1 Specifications of ALDA

Wave length	514.5nm
Laser power (Fiber output power)	35mW~50mW
Focal length of front lens	200mm
Incidence angle θ	7.1 deg.
Calibration factor	0.259 m/s / MHz
Diameter of measuring volume	0.11mm
Length of measuring volume	0.95mm

prism (P1), a neutral-density filter (ND), the half mirror and is superimposed to the scattering light. Doppler signal obtained at the photomultiplier is processed by a frequency analyzing processor (Dantec 57N20: BSA).

3. EXPERIMENTAL EQUIPMENT AND METHOD

The ALDA made as trial in this study was used to measure the air jet flow from a pipe, the fluctuation flow made by cylinder-piston system, and the velocity in the combustion chamber of the clear-acrylic-made two-cycle engine. The velocity of jet flow was measured at the same time by means of ALDA and a fringe mode LDA. At the measurement of the fluctuation flow, measured velocity by ALDA was compared with that obtained by a fringe mode LDA.

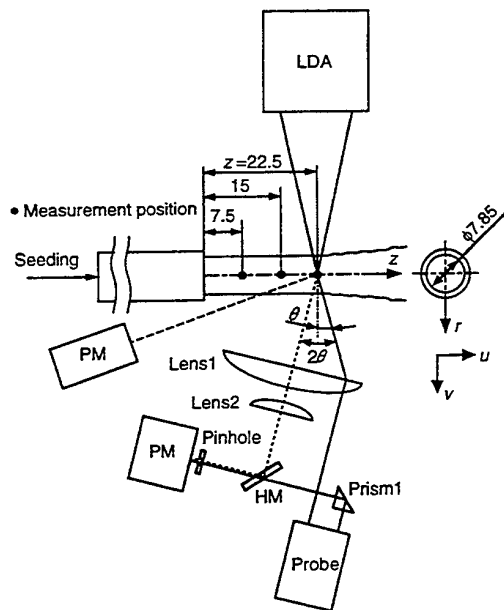


Figure 3 Arrangement of measuring the air jet flow

3.1 Measurement of the air jet flow

Fig. 3 shows the arrangement of measuring the air jet flow as preliminary test and Table 2 shows the setting values of BSA in this test. The water droplets (Mean particle diameter is about $7\mu\text{m}$), made by an ultrasonic humidifier, were added to the jet as the scattering particles. And it also supplied around the jet. The inner diameter of the pipe is 7.85mm and Reynolds number of jet flow is about 1420.

3.2 Measurement of the fluctuation flow

Fig. 4 shows the arrangement of measuring the fluctuation flow as preliminary test and Table 2 shows the setting values of BSA in this measurement. The fluctuating flow is made by cylinder-piston system however there is no cylinder wall around the measurement points. The flow fluctuating in the radial direction of the cylinder is measured at two points shown in Fig. 4. The measured velocity is the fluctuating flow at the space that was made between the engine cylinder and the cylinder head. Water droplets were used as the scattering particles.

3.3 Measurement of the velocity in the combustion chamber

We modified a two-cycle engine as a test engine for measuring the velocity in the disk type combustion chamber. The specifications of the test engine are shown in Table 3, the arrangement of measuring the flow in the combustion chamber is shown in Fig. 5, the measurement points are shown in Fig. 6, the setting values of BSA are

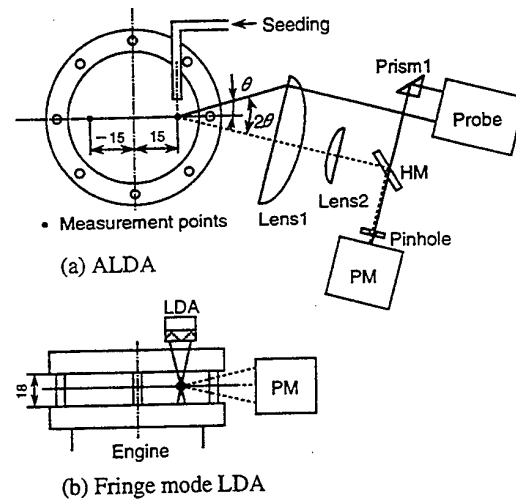


Figure 4 Arrangement of measuring the fluctuation flow

Table 2 Setting values of BSA

	Measurement of jet flow	Measurement of fluctuation flow	Measurement of flow in cylinder
Frequency span	8MHz	8MHz	16MHz
Center frequency	5MHz	5MHz	10MHz
FFT record length	64 samples	64 samples	64 samples

Table 3 Specifications of a test engine

Engine type	2 cycle single cylinder		
Base engine	HONDA MD24E		
Bore×Stroke	66mm×72mm		
Effective compression ratio	2.4		
Combustion chamber	Disk		
Scavenging method	External Blower		
Port timing	Exhaust	Open: EPO	95° BBDC
		Close: EPC	94° ABDC
	Scavenging	Open: SPO	58° BBDC
		Close: SPC	57° ABDC

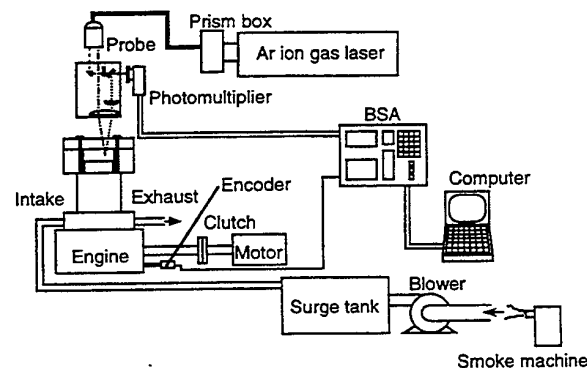


Figure 5 Arrangement of measuring the flow in the combustion chamber

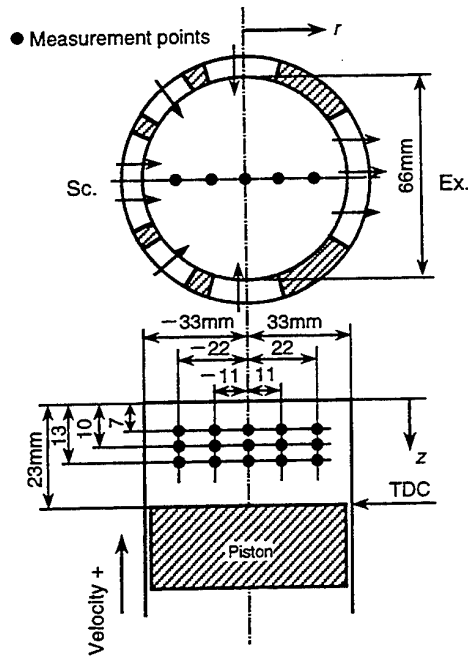


Figure 6 Measurement points in the combustion chamber

shown in Table 2. The mist of light oil (mean particle diameter is about $5\mu\text{m}$), made by a smoke generator (Invent), was used as the scattering particle. The test engine was operated at 300rpm.

4. RESULTS AND DISCUSSION

4.1 Jet flow

Fig. 7 shows time series of axial (u) and radial (v) velocities at $z=15\text{mm}$ and $r=4\text{mm}$. In the figure, axial velocity (u) measured by a fringe mode LDA is rather large fluctuation. But relative turbulence intensity is about 4%. This result maybe have some error in the present condition, because it can be considered that the air flow was affected by the water drops gathered in the pipe. Radial velocity (v) measured by ALDA is small mean velocity, but it has fluctuation. Fig. 8 shows time series of turbulent velocity at $z=15\text{mm}$ $r=4\text{mm}$. The turbulent velocities u' and v' were nondimensionalized by each mean turbulent velocities $u'_{r.m.s.}$ and $v'_{r.m.s.}$. The cross-correlating of u' and v' in Fig. 8 is shown in Fig. 9. The figure shows a tendency for u' and v' with same phase and the frequency is about 10Hz.

Fig. 10 shows nondimensional plot of axial velocity. The axial velocity (u) was nondimensionalized by the maximum velocity at jet center and the measurement point of radial direction was nondimensionalized by the distance corresponding to half value width of u_{max} . The distribution of dimensionless

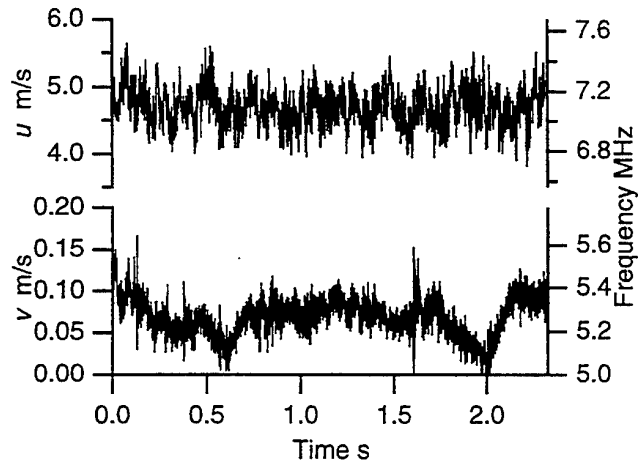


Figure 7 Time series of jet flow velocities

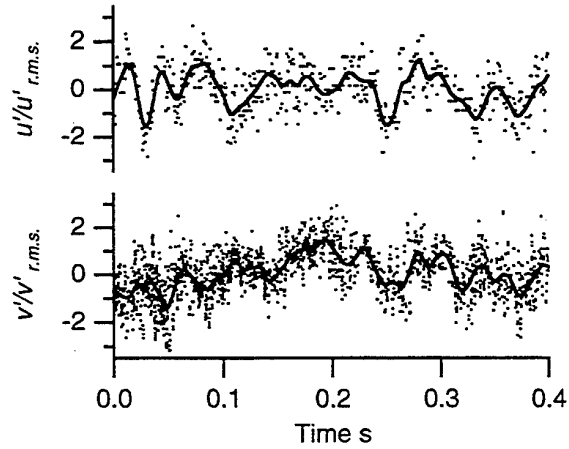


Figure 8 Time series of nondimensionalized turbulent velocities

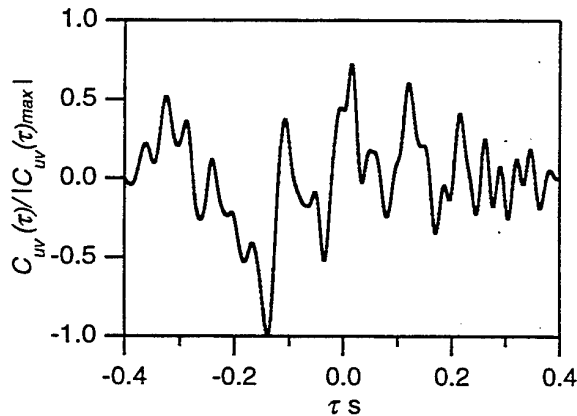


Figure 9 Cross correlation of u' and v'

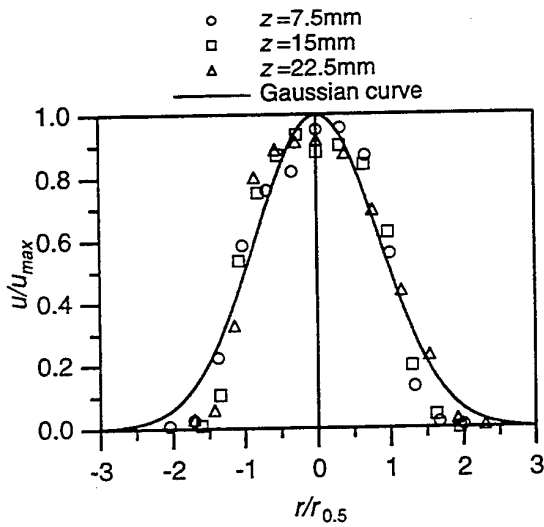


Figure 10 Nondimensionalized velocity of axial direction

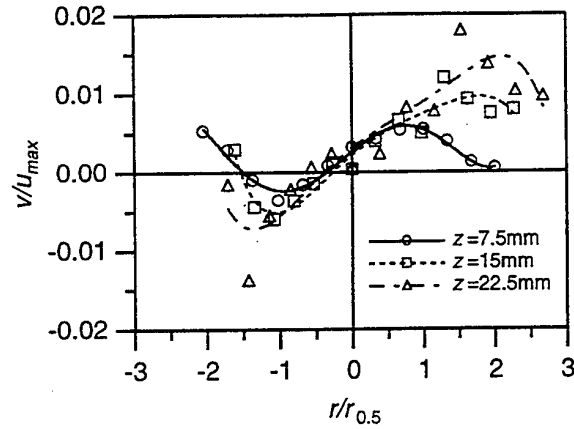


Figure 11 Nondimensionalized velocity of radial direction

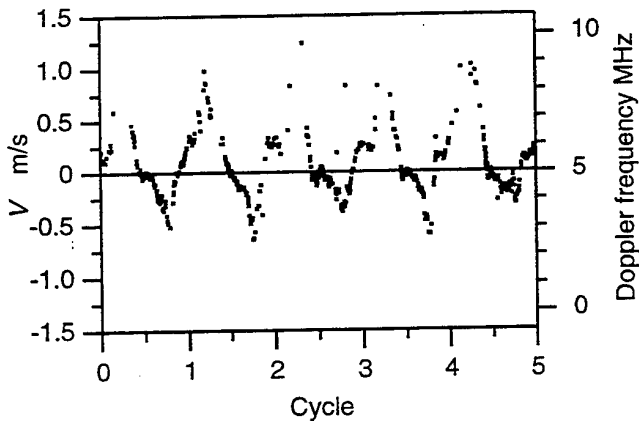


Figure 12 Time series of fluctuation ($r=15\text{mm}$)

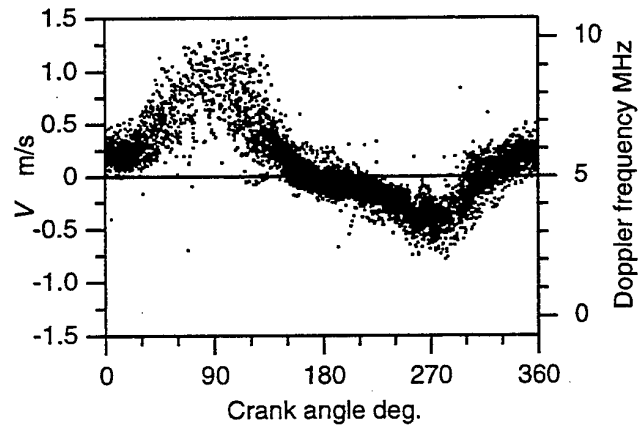


Figure 13 Crank angle distribution of velocity ($r=15\text{mm}$)

velocity agrees with the gaussian curve except the jet edge. Fig. 11 shows nondimensional plot of radial velocity. The radial velocities is little shifted to left side in the figure, but similar velocity distributions are observed in both sides increasing with z direction.

4.2 Measurement of the fluctuation flow velocity

Fig. 12 shows time series of radial velocity (V) at point $r=15\text{mm}$ from cylinder center, $z=9\text{mm}$ from ceiling of the cylinder as shown in Fig. 4. Periodical change of the flow velocity expresses the cyclic fluctuation. Fig. 13 and Fig. 14 show phase matched plots of 80 cycles fluctuating velocity. Both fluctuating air flows made by the piston movement are almost coincidence in symmetry. Mean velocity (\bar{V}) of ensemble-averaged by a step of 3.6° and its fluctuation intensities ($V'_{r.m.s.}$) at two

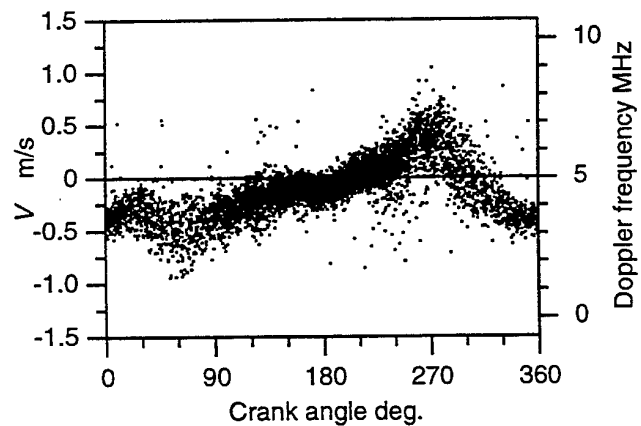


Figure 14 Crank angle distribution of velocity ($r=-15\text{mm}$)

measurement points by ALDA and at point $r=15\text{mm}$ by LDA (Fig. 4(b)) are shown in Fig. 15. At $r=15\text{mm}$, flow velocity (solid line) by ALDA is almost the same as measured (dashed line) by LDA in every crank angle and flow velocity (dot line) by ALDA at point $r=-15\text{mm}$ is symmetric to the velocity of that at point $r=15\text{mm}$. At both crank angles of 90° and 270° of high piston speed, velocity fluctuation intensities are also high. The values of simple-averaged mean velocity and fluctuation intensities for all cycles are showed in Table 4. Measured values of mean velocity and fluctuation intensity by ALDA are higher, 8% at \bar{V} and 27% at $V'_{r.m.s.}$, than that of LDA. These differences are not small but allowable in the present situation of the experiment. From the above results, the developed ALDA can measure flow velocity about the same as LDA, and ALDA has been proved to have potential for practical application. But the conversion factor of velocity to Doppler frequency is small, i.e., about $0.259(\text{m/s})/\text{MHz}$. Application of ALDA for fluctuating velocity of small amplitude is no problem. But in the flow with large fluctuating velocity, there will be some problems due to the dynamic frequency range limitation of signal processor.

4.3 Measurement of the velocity in the engine

Fig. 16 shows time series of axial flow velocity in the cylinder measured through the acrylic cylinder head at point $r=-11\text{mm}$ from center of the cylinder and $z=13\text{mm}$ from cylinder head as shown in Fig. 6. Though there are scattered velocities, periodic flow are observed. Fig. 17 shows phase matched plot of flow velocities (V) and 0 degree means top dead center (TDC). There are a number of data and scattering of velocities is small from the end of compression stroke to the half way of expansion stroke. Referring to the open and close ports timings in the figure, data rate decrease rapidly at exhaust port open (EPO), flow velocity fluctuation is very hard from scavenging cycle to the first half of compression stroke. Because this experiment was made under motored operation, it seems that the air with a little scattering particles flowed from exhaust pipe to the cylinder when exhaust port opened. Scattering of measured velocity is also caused by the apparent fluctuation due to the velocity gradient at the measuring volume. On the other hand, the flows of exhaust and scavenging did not affect the flow at around the TDC. Fig. 18 shows the ensemble-averaged mean velocity (\bar{V}) and the fluctuation intensity ($V'_{r.m.s.}$) averaged at every 1 degree crank angle. At the point $z=13\text{mm}$, dashed line shows the estimated velocity (V_{P2}) in proportion to the piston velocity. Comparing V_{P2} with measuring velocity at $r=-11\text{mm}$ (solid line), between bottom dead center (-180°) and -30° , there is a difference

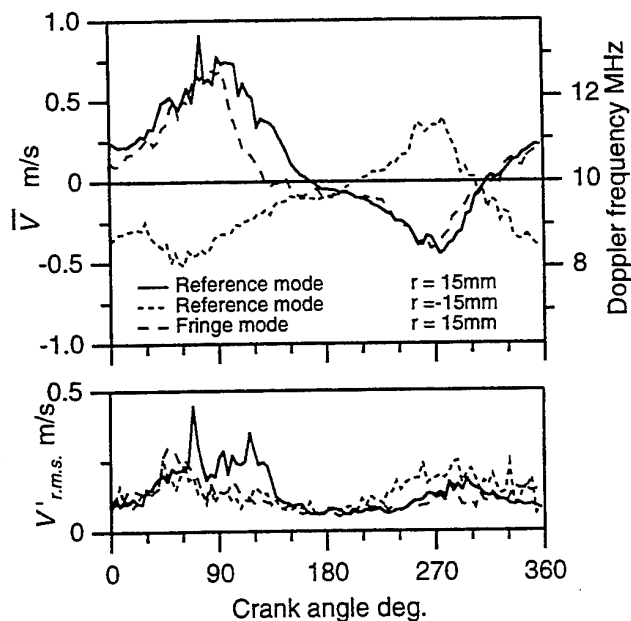


Figure 15 Ensemble averaged velocity and fluctuation intensity ALDA ($r=\pm 15\text{mm}$) and fringe mode LDA

Table 4 Mean velocity and fluctuation intensity

	\bar{V} m/s	$V'_{r.m.s.}$ m/s
$r=15\text{mm}$	0.131	0.141
$r=-15\text{mm}$	-0.137	0.137
Fringe mode	0.123	0.102

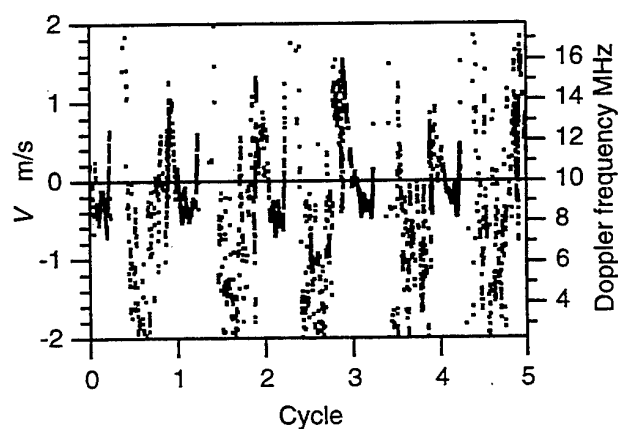


Figure 16 Time series of measurement in the combustion chamber ($z=13\text{mm}$ $r=-11\text{mm}$)

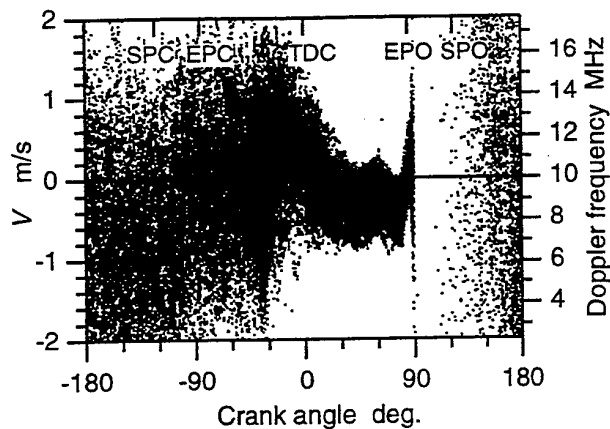


Figure 17 Clank angle distribution of velocity ($z=13\text{mm}$ $r=-11\text{mm}$)

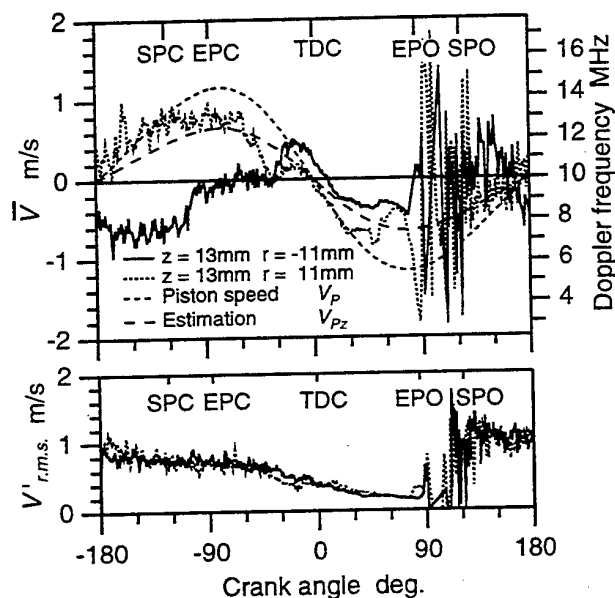
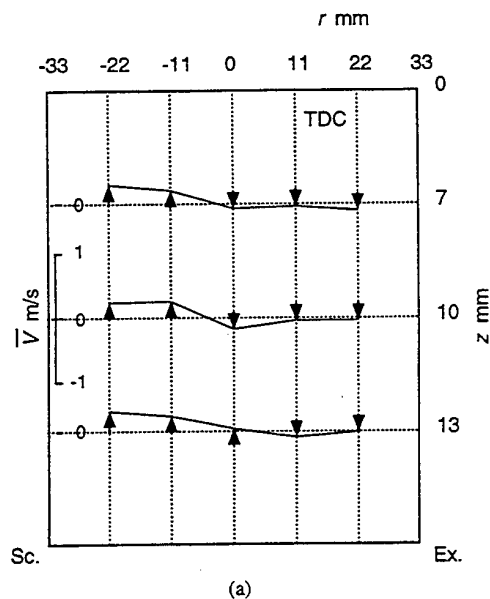


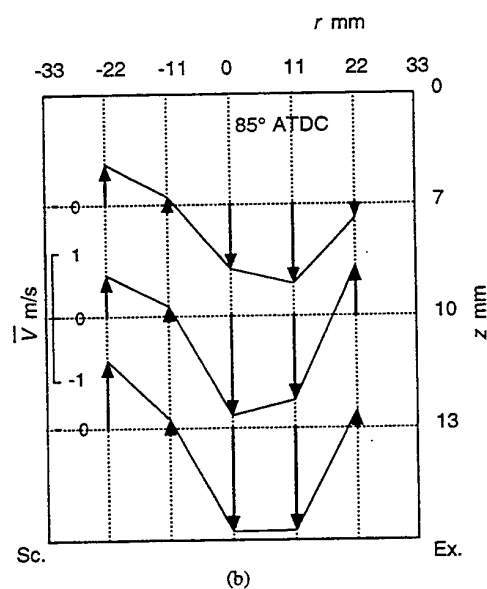
Figure 18 Phase averaged velocity and fluctuation intensity ($z=13\text{mm}$ $r=\pm 11\text{mm}$)

of flow velocity between V_{pz} and measuring velocity, and subsequent flows are corresponded each other. Flow velocity (dot line) at point $r=11\text{mm}$ is good agreement with V_{pz} between BDC and around 90° . It seems that the swirl flow in a longitudinal section has an effect on a difference between two velocities. And the fluctuation intensity is as same as both measurement points.

Fig. 19 shows velocity distributions measured in the whole combustion chamber at TDC and after TDC (ATDC) 85° . Fig. 20 shows radial distribution of axial velocity from BTDC 60° to ATDC 85° at measurement point of $z=13\text{mm}$. In Fig. 19(a), swirl flow was observed



(a)



(b)

Figure 19 Distribution of axial direction velocity in combustion chamber

in a longitudinal section at TDC, upward flow was observed at scavenging port (Sc.) and rear side of the engine and downward flow observed at exhaust port (Ex.) side of engine. And at points $z=7\text{mm}$, 10mm and 13mm the velocity distribution are almost the same. Fig. 19(b) shows the highest downward speed at around the center of the cylinder, and at the point $z=\pm 22\text{mm}$ near the cylinder wall, upward flow to the cylinder head was observed against piston downward motion. So we can image that a donut type big vortex was made in the cylinder. In Fig. 20,

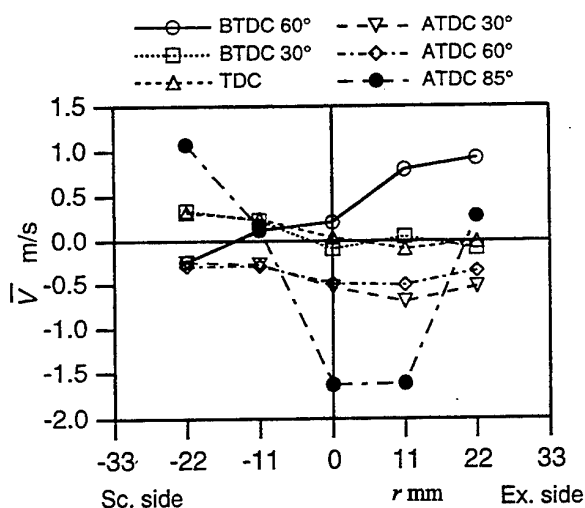


Figure 20 Crank angle variation of the velocity ($z=13\text{mm}$)

high upward velocities were observed at BTDC 60° depending on the upward piston motion. But the flow velocities decreased with piston closing to TDC. Subsequently, in expansion stroke, the flow direction was changed to downward, and the velocities increased with piston motion. At ATDC 85° , downward velocities are observed at around the center of the cylinder and the upward velocities were observed at near the cylinder wall as shown in Fig. 19(b).

5. CONCLUSIONS

The laminar jet flow, the fluctuation flow made by cylinder-piston system and the axial direction fluctuating flow in the cylinder were measured by the single incidence-beam reference-mode LDA which was developed to measure the velocity component along the optical axis of the LDA. The results obtained from the experiment are summarized as follows:

- (1) From the measurement of jet flow, it was suggested that proposed axial-LDA can be used to measure the axial flow velocity like a conventional LDA.
- (2) The mean velocity and the fluctuation intensity in the fluctuating flow measured by ALDA are just a little larger than that by the conventional fringe mode LDA. But we have confirmed the applicability

of this ALDA under the present conditions.

- (3) In the experiment of axial velocity measurement in the cylinder, if seeding is enough, ALDA can be used to measure the fluctuating velocity in real time. Since the conversion factor of velocity to Doppler frequency is small in this ALDA, a signal processor with a wide dynamic range is needed.
- (4) The measurement of axial fluctuation flow velocity in the two-cycle engine cylinder shows that the crank angle variation of the flow pattern presents clearly, thus the advantage of the ALDA was demonstrated.

In the future, it is expected that the ALDA combined with 2 dimensional conventional LDA could measure the three-dimensional velocity in the combustion chamber of a practical engine through a small measuring window on the cylinder head.

ACKNOWLEDGMENTS

The authors appreciate Prof. Zhengbai Lui and Dr. Xiaofeng Yang for their advice to clarify the article. This research has been carried out at the Center for Cooperative Research, Gunma University.

REFERENCES

- [1] Obokata, T. et al., 1988, Laser Doppler Anemometer Measurement of Gas Flow in the Wedge Type Combustion Chamber of a Two-Cycle Spark Ignition Engine, *Proc. of the Institution of Mechanical Engineers*, paper No. C 48/88, pp. 213-223.
- [2] Witze, P. O. & Foster, D. E., 1987, Velocity Measurements in the Wall Boundary Layer of a Spark-Ignited Research Engine, *SAE Paper*, No. 872015.
- [3] Obokata, T. et al., 1992, LDA Characterization of Gas Flow in a Combustion Chamber of a Four-Stroke S. I. Engine, *SAE Paper*, 920519.
- [4] Dimopoulos, P. and Boulouchos, K., 1995, Reynolds Stress Components in the Flow Field of a Motored Reciprocating Engine, *SAE Paper*, 950725.
- [5] Takeda, C. et al., 1995, *Trans. of JSME*, (in Japanese), 61-592, B, pp. 4498-4503.
- [6] Durst, F. et al., 1981, *Principles and Practice of Laser-Doppler Anemometry*, 2nd Edition, pp. 87, Academic Press.
- [7] Buchhave, P., 1975, Laser Doppler Vibration Measurements Using Vibration Frequency Shift, *DISA Information*, No. 18, pp. 15.

PIV MEASUREMENTS AND CHARACTERISATION OF IN-CYLINDER FLOWS IN COMBUSTION ENGINES

M. Faure, M.R. Heikal ⁽¹⁾
N. Jackson ⁽²⁾

(1) University of Brighton, UK
(2) Ricardo Consulting Engineers, UK

ABSTRACT

This article presents the results of an experimental study of the flow characteristics in a four-valve pent-roof engine. The tests were carried out on the Ricardo/Brighton dynamic water-analogue rig and Particle Image Velocimetry was used to obtain velocity maps at the bottom dead centre of the induction stroke. Different flow characterisation parameters were derived and used for the post-processing of the PIV maps. Values for some of these parameters are presented for two different cylinder heads with different inlet port configurations. Finally, initial examination of the correlation between some of these parameters and the combustion behaviour of the head is discussed.

1. INTRODUCTION

Particle Image Velocimetry techniques have been used in internal combustion engines in recent years either in water-analogue rigs [1, 2, 3, 4 and 5] or in motored engines [7 and 8]. The use of a water-analogue rig limits the study to the induction stroke and relies on the assumption that the flow behaviour is preserved when matching the Reynolds number [1]. Nevertheless, such rigs enable good optical access to the flow and thus are ideal for visualisation and PIV. Although the conditions at the end of the compression stroke influence the combustion behaviour, it is believed that all the information needed is contained at the bottom dead centre of the induction stroke. Furthermore, if a good correlation can be found between the flow topology at BDC and the combustion characteristics of the head, it is more convenient to study the induction stroke when investigating the influence of port geometry and valve profiles. Although the velocity vector maps obtained with PIV give good visual understanding of the flow topology at bottom dead centre, post-processing is needed to extract more information in order to examine correlations with the combustion characteristics of the engine. Traditional post-processing such as vorticity and tumble ratio (or swirl ratio) have been widely used [2, 4, 5, 6 and 8] but are not sufficient to describe complex in-cylinder flows. It is therefore necessary to introduce other parameters to characterise different

features of the flow at BDC and ultimately to examine the correlation with the combustion behaviour of the engine.

2. DYNAMIC FLOW RIG

A water analogue rig was developed as a joint project between the University of Brighton and Ricardo Consulting Engineers [2 and 3] to investigate intake generated flow topology in internal combustion engines. The experimental set-up consists of an actual cylinder head with a glass cylinder fitted directly onto it. Computer controlled stepper motors are used to activate the valves and the transparent piston. This allows maximum flexibility as different engines can quickly be configured in the software. The optical distortion caused by the differences in refractive indices is corrected by mounting a glass box filled with water around the glass cylinder. The rig can be run at different equivalent crank angle speeds and engine bores up to 115 mm and strokes up to 150. The illumination system is composed of a continuous argon ion laser with a multimode fibre optic and a set of lenses. Visualisation videos of the flow can be recorded with a colour sVHS camera or a high speed cross-correlation camera can be used to save successive particle images at any crank angle position. The laser can be pulsed using an electro-optical shutter synchronised with the video output of the camera. The PIV processing is performed with the VISIFLOW™ general PIV package and the results are imported into MATLAB™ for post-processing.

3. EXPERIMENTAL CONDITIONS

Two different cylinder heads were considered for this study (figure 1). The first (Head A) was a port-generated tumble head obtained by physically blocking the top sections of the inlet ports forcing the intake flow to exit only from the bottom part of the port and thus generating a very high tumble pattern. The second (Head B) was a masked valve head; the top sections of the inlet valves had a 2 mm shroud allowing the flow to exit from the top part of the port only at high valve lift. The different tumble patterns are then obtained by changing the valve lift profile.

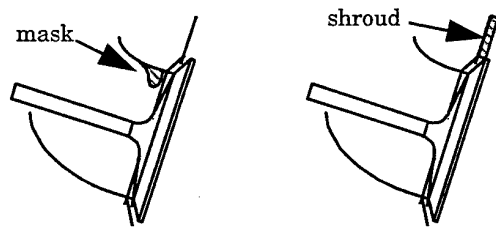


Figure 1: Port configuration

Both heads were tested at a rig speed of 0.85 rad/s for a bore of 83 mm and a stroke of 90 mm. Head B was studied with different cam profiles (figure 2) to obtain different tumble patterns: A high valve lift cam profile (8.45 mm at 122° ATDC) has been used to generate low tumble and a low valve lift profile (5.95 mm at 102° ATDC) to get a high tumble. A third profile, similar to the low valve lift but with high advance (5.95 mm at 84° ATDC) has also been investigated. Head A was only studied with the high valve lift cam profile.

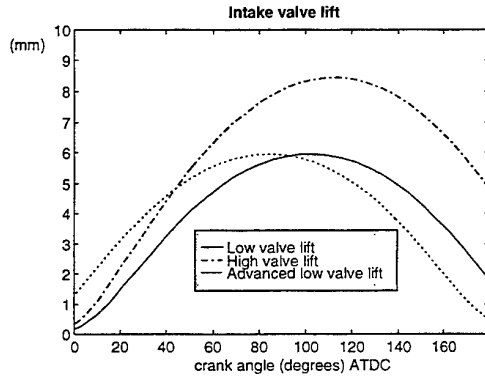


Figure 2: Cam profiles for the test heads

For each configuration, the laser sheet was positioned at 4 different parallel tumble planes (planes perpendicular to a line joining the two inlet valves). The first was the mid-cylinder plane (plane of symmetry) and the other three positioned at 9 mm, 18 mm and 27 mm respectively from mid cylinder. The 18 mm plane corresponds to the mid-valve plane. For the PIV analysis, cross-correlation was performed between two images of the flow at BDC. The images were 640 x 480 pixels and were grabbed with the svhs camera. The interrogation spot size for cross-correlation was 64 x 64 pixels and each final map contained 990 vectors.

4. FLOW CHARACTERISATION PARAMETERS

In order to examine possible correlation between the in-cylinder flow characteristics and the combustion performance of the engine, several flow characterisation parameters were derived.

Time averaging

Time averaged maps of different strokes at the same experimental conditions were obtained. For each velocity vector of the averaged map, a standard deviation was computed for magnitude and angle, giving a good spatial representation of stroke to stroke variation. The mean values

of these standard deviations for the complete map were saved and used to calculate a quantitative measurement of the repeatability.

$$SD_{mag} = \frac{1}{n} \sum_{i=1}^n \left(\sqrt{\frac{1}{m} \sum_{j=1}^m (\bar{V}_i - V_{ij})^2} \right) \quad (1)$$

$$SD_{ang} = \frac{1}{n} \sum_{i=1}^n \left(\sqrt{\frac{1}{m} \sum_{j=1}^m (\bar{\alpha}_i - \alpha_{ij})^2} \right) \quad (2)$$

It can be argued that PIV is an instantaneous measurement technique and therefore time averaging should not be used, especially with a small number of single maps. In the present study, only the large scale structure of the flow was of interest and the turbulence was not investigated. As far as the number of maps that should be used for the average is concerned, figure 3.a shows the mean flow velocity and the mean standard deviation for different sample sizes. Figure 3.b is a plot of the main two tumble ratios (equations 7 and 8) against the number of samples used for the average. It can clearly be seen from the two figures that at least 10 single maps should be used for the averaging.

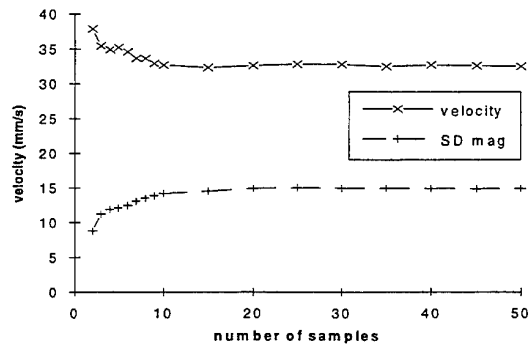


Figure 3.a: Effect of averaging on velocity magnitude

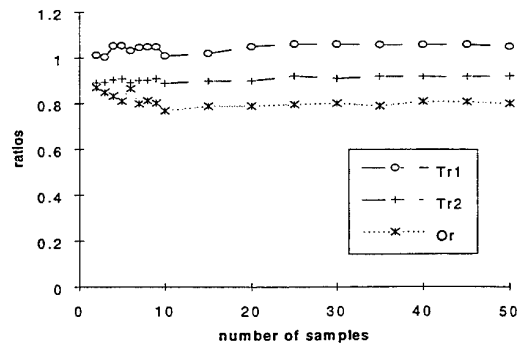


figure 3.b: Effect of averaging on tumble ratios

Velocity V and vorticity ζ

For each vector map the minimum, maximum and mean values of velocity and vorticity magnitudes as well as their

standard deviations are given. Vorticity is defined by the curl of velocity:

$$\zeta = \frac{\partial v}{\partial x} - \frac{\partial u}{\partial y} \quad (3)$$

Velocity ratio V_r

$$V_r = \frac{\text{mean flow velocity}}{\text{mean piston velocity}} = \frac{\pi \bar{V}}{\omega S} \quad (4)$$

As the values for flow velocity depend directly on the piston velocity, the velocity ratio, V_r can be used to compare the mean flow velocity of different heads. V_r also gives an indication of the actual size of the ports and valves relative to the piston size.

Location of the main vortex centre

To locate the position of the main eddy centre automatically, the vorticity of the normalised vector field is first calculated:

$$\zeta \left(\frac{\bar{V}}{V} \right) = \frac{\delta(v/V)}{\delta x} - \frac{\delta(u/V)}{\delta y} = \frac{\delta \sin \alpha}{\delta x} - \frac{\delta \cos \alpha}{\delta y} \quad (5)$$

The value of this parameter is zero in the case of parallel vectors of different magnitudes but easily locates the change in vector direction as in the case of an eddy. As the vortex centre corresponds to a local minima of velocity and a local maxima of vorticity, a map of the vorticity divided by the velocity magnitude can also be used to identify the main eddy centre (figure 4). The position of the positive peaks indicate the centres of vortices rotating in the positive direction. It is then possible to choose the peak with the best signal to noise ratio which indicates the eddy centre and can be used as a frame of reference.

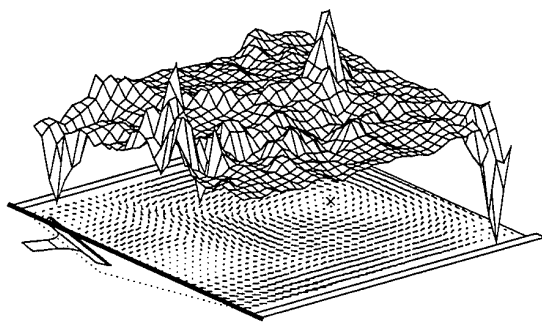


Figure 4: Location of the eddy centre

Eddy size

An algorithm to find the main eddy boundary was developed based on a comparison with a pure solid body rotation model and using the angles and the magnitudes of the vectors. Once

the centre of the eddy had been located, an equivalent angular velocity was then calculated as follows:

$$\omega_{equ} = \frac{1}{n} \sum_{i=1}^n (V t_i / r_i) \quad (6)$$

Next, radial lines were drawn from the eddy centre with an angular increment of 1 degree and profiles for the velocity magnitude and angle constructed from the eddy centre along each line (figure 5.a and 5.b). At any radius on the profile, the magnitude and angle of the flow velocity was then compared with the theoretical values of a solid body motion of angular velocity ω_{equ} . The point at which the difference, either in magnitude or in direction, exceeds a set limit is taken as the eddy boundary on this radial line. An example is shown in figures 5.a, 5.b and 6 for a radial line at 160 degrees. For each radial line, the distance from the edge to the eddy centre was stored and the eddy boundary was obtained by joining all the boundary radii (figure 6).

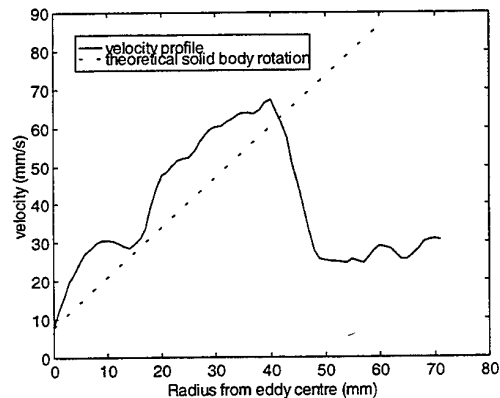


Figure 5.a: Velocity magnitude profile

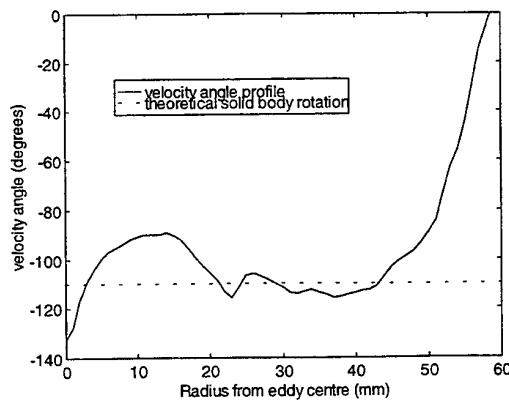


Figure 5.b: Velocity angle profile

This technique has the advantage of being very robust but, unfortunately, does not give a continuous eddy boundary. Other algorithms are currently being tested. The eddy area and boundary are parameters of great importance when

characterising the flow pattern and essential for calculating the tumble ratio of the flow inside the main eddy only.

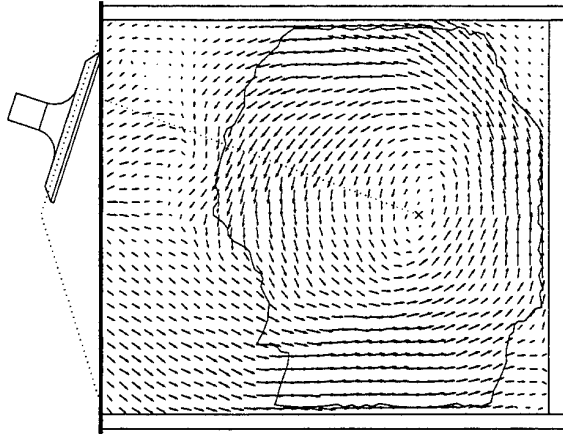


Figure 6: Example of eddy boundary

Tumble ratio based on angular momentum Tr_1

This tumble ratio was calculated about a centre-point which could be either the centre of the cylinder or the centre of the main eddy in the flow [2].

$$Tr1 = \frac{8 \sum_{i=1}^n (v_i \cdot x_i - u_i \cdot y_i)}{n \omega B^2} \quad (7)$$

Tumble ratio $Tr1$ is derived from the angular momentum equation and as calculated from equation 7 about the centre of the cylinder should give values close to those measured on a traditional steady flow rig. The disadvantage of using $Tr1$ is that it is dependent on the position of a centre-point in the flow (either mid-cylinder or eddy centre) and its value is sensitive to flow vectors far from the centre-point. These limitations can produce misleading interpretation of the flow characteristics.

Tumble ratio based on vorticity Tr_2

$$Tr2 = \frac{\sum_{i=1}^n \zeta_i}{2n\omega} \quad (8)$$

Tumble ratio $Tr2$ was based on the mean value of vorticity. It represents the amount of large and small scale rotation in the flow. For a rotating solid body, vorticity has a constant value equal to twice the angular velocity. $Tr2$ can therefore be translated as the ratio of the mean angular velocity of the eddy divided by the crank angle velocity. As can be seen from equation 8, the value of $Tr2$ is not relative to a particular position in the cylinder.

Tangential and radial velocities V_t, V_n

As for the velocities and vorticity, the mean, maximum and minimum values of tangential and radial velocities as well as their standard deviations were also calculated. Radial and tangential velocities were computed around the centre of the eddy by resolving each velocity vector into its two components.

Tangential velocity ratios Tvr, Tvr_2, Tvr_3, Tvr_4

$$Tvr = \frac{1}{n} \sum_{i=1}^n \frac{V_{t_i}}{V_i} \quad (9)$$

$$Tvr2 = \frac{\sum_{i=1}^n V_i^2}{n(\omega S/2)^2} \quad (10)$$

$$Tvr3 = \frac{\sum_{i=1}^n V_{t_i}^2}{n(\omega S/2)^2} \quad (11)$$

$$Tvr4 = \frac{\sum_{i=1}^n (r_i V_{t_i}^2)}{n S/2 (\omega S/2)^2} = \frac{8 \sum_{i=1}^n (r_i V_{t_i}^2)}{n \omega^2 S^3} \quad (12)$$

The tangential velocity ratio Tvr is a means of measuring the closeness of the flow to a pure solid body motion. This ratio is based on the use of the angle between the flow vector and its projection onto the tangential direction. Any vector in the clockwise direction is considered as having a negative tangential velocity and can have a dramatic influence on Tvr . The ratios $Tvr2$ and $Tvr3$ are measures of the amount of kinetic energy stored in the flow, either globally ($Tvr2$) or in rotation ($Tvr3$). Finally, $Tvr4$ is equal to the integral of a kinetic energy term multiplied by the radius from the centre and can be understood as the torque applied to an imaginary torque meter placed in the flow.

These four ratios are of course very sensitive to the position of the eddy centre and do not apply in the case of flows without a main well formed rotating structure.

Angular velocity ratio Ωr

This ratio is again calculated around the centre of the eddy.

$$\Omega r = \frac{\sum_{i=1}^n (V_{t_i} / r_i)}{n\omega} \quad (13)$$

The angular velocity ratio Ωr is the average of the angular velocity of the entire flow field. It is calculated by dividing the tangential component of each vector by the radius from the centre-point. For solid body motion, this ratio is equal to $Tr2$ (equation 8).

Spatial averaging

In order to obtain values equivalent to a three-dimensional tumble ratio from a 3D vector map [4 and 10], an average value, weighted by the area of the 4 positions (mid-cylinder, 9mm, 18mm, and 27mm from mid-cylinder) was used:

$$Tr_{av} = \frac{1}{\sum_{k=1}^4 n_k} \sum_{k=1}^4 (Tr_k n_k) \quad (14)$$

With n_k being the number of vectors for the averaged maps of each position since the vector grid separation is the same for all maps.

5. RESULTS AND DISCUSSION

The 4 configurations were first tested on the Ricardo steady flow rig to obtain 4 steady flow tumble ratios [3]. The fixed tumble ratio for Head A was 1.5. The same value (1.5) was obtained for the variable tumble ratio head at low valve

lift for both standard and advanced profiles. At high valve lift, the tumble ratio for Head B was 0.6. Figure 8.a shows the different flow ratios which are independent of the position of the main eddy for the 4 different configurations while figure 8.b shows the ratios which are a function of the position of the eddy centre. The averaged velocity vector maps are shown in figures 7.a to 7.d for the different configurations at mid-cylinder and mid-valve planes.

The velocity vector maps clearly show visual differences between each configuration. It is particularly interesting to note that although the tumble motions measured by the steady flow rig gave the same value for Heads A and Head B at low valve lift, the flow vector maps show significant differences in the flow patterns as can be seen in figure 7.a, 7.b and 7.c.

The fixed high tumble head (Head A) produces a very powerful and well formed single eddy structure about the centre of the cylinder. The eddy almost occupied the complete volume. The same structure can also be seen in the mid-valve plane which indicates good uniformity of the structure in 3D.

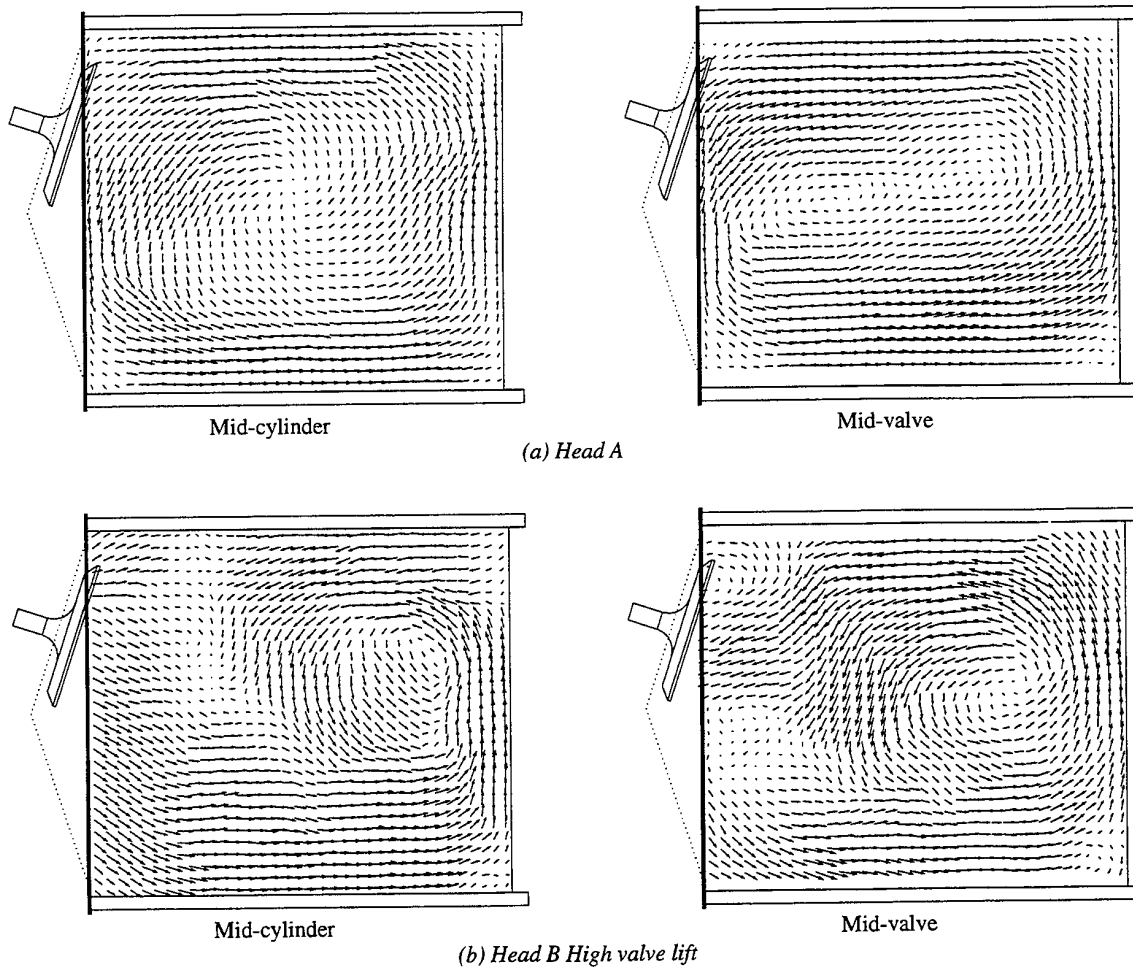


Figure 7: Averaged velocity vector maps

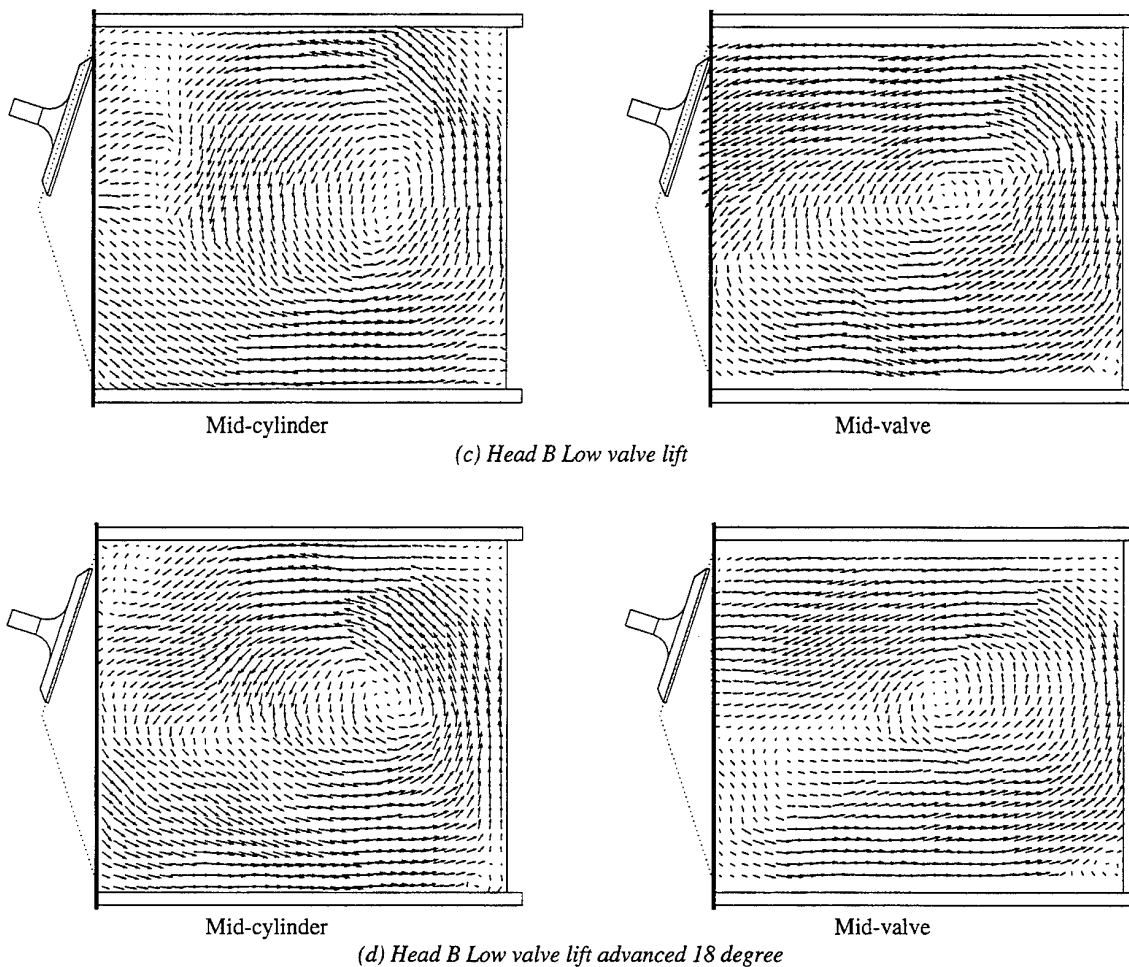


Figure 7: Averaged velocity vector maps

The masked valve head, however, exhibited a more complex flow structure (figure 7.b, 7.c and 7.d). The patterns for the high lift configuration showed the evolution of the flow with the valve displacement. During the early part of the stroke, when the valve lift was low, the flow was forced towards the exhaust valves, as little or no fluid flowed from the masked upper part of the port. This resulted in the onset of tumble motion. As the valve lift increased, exceeding the mask, fluid emerged from the upper part of the valve. This in turn produced a vortex rotating in the opposite direction to that generated earlier, and can easily be detected using equation 5 (figure 4). This counter rotating vortex had two main effects on the flow structure. Firstly, it reduced the size of the main eddy and forced it to the top right hand corner, producing lower tumble ratios and a less uniform energy distribution over the section. The second effect was the increased energy losses leading to reduced mean flow velocities, which can be seen from the values of the velocity ratio V_r in figure 8.a.

With the low valve lift cam profile, a fairly high tumble was generated away from the mid-cylinder plane. However, the counter rotating eddy near the valve limited the size of the main vortex in the mid-cylinder plane (figures 7.c). This type of 3 dimensional non-uniformity could lead to an uneven distribution of turbulence intensity, which in turn may have an adverse effect on combustion behaviour. Advancing the opening of the inlet valve increased the initial vortex generation part of the valve lift, thus increasing the size of the main vortex as well as the values of the tumble ratios and the energy uniformity over the section. This can be seen from the velocity vector maps (figures 7.d). In fact the flow pattern moved toward that of the flow generated by head A but with a much lower value for the velocity ratio V_r (figure 8.a). The high valve lift configuration generated a low tumble pattern, with low velocities and a small main vortex. It is in this configuration that the second vortex appears to be the more significant (Figure 7.b).

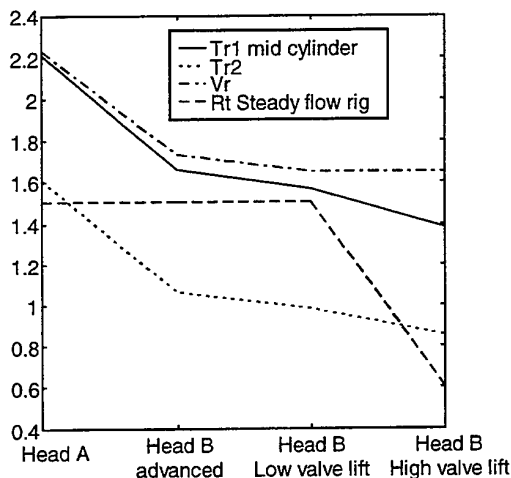


Figure 8.a: Flow ratios for the different configurations

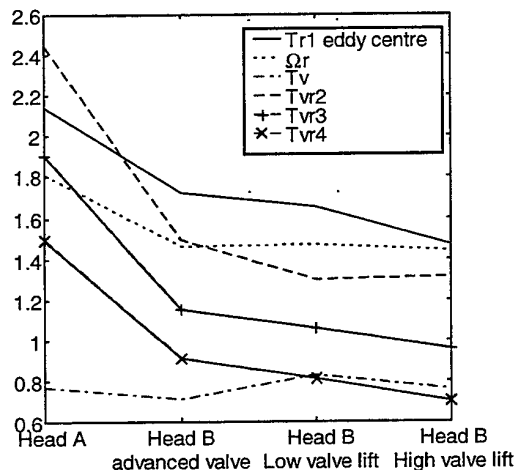


Figure 8.b: Flow ratios for the different configurations

The various flow characterisation parameters, described earlier, are shown in figure 8.a and 8.b for the four geometries. It is clear that all the parameters rate the four geometries in the same ranking order. The modified port geometry (Head A) clearly produced much superior performance than all the other three masked port geometries (Head B) in terms of tumble ratios, kinetic energy, eddy size and uniformity. Not surprisingly the second highest values of the parameters were produced by the low valve lift with advance since its flow pattern was the closest to that of Head A. The lowest values of the flow parameters were those of the high valve lift Head B.

The four configurations were also tested for combustion performances at full load. Figure 9 shows the ignition timing, delay angle (ignition to 10 %), and 10 to 90 % burn angle. In all the tests, Head A was outstanding with fast flame propagation and good overall combustion characteristics. Head B with high valve lift cam profile showed a long delay angle and had to be highly advanced compared to the other three configurations. Head B with low

valve lift (standard and advanced cam profiles) were limited by knock limit in terms of advance, resulting in a total burn period up to 30 degrees ATDC.

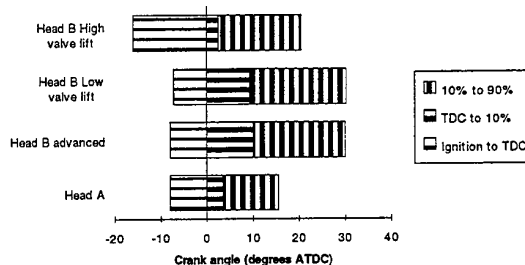


Figure 9: Combustion data for the 4 configurations

From figures 9 and 8, it can be seen that, although the four configurations produced considerably different combustion behaviour, the steady flow rig measurements were unable to differentiate between three of them giving a tumble ratio of 1.5. On the other hand, the flow characterisation parameters described earlier and shown in figure 8 clearly ranked the head in a manner which is consistent with their combustion performances.

CONCLUSION

The dynamic water analogue test rig results showed clear differences between cylinder heads which produced the same bulk characteristics from conventional steady flow tests. The flow characterisation parameters presented in this study offer much higher levels of discrimination for combustion correlation. More work is required to establish the complete link between these flow parameters and the combustion data, but the work so far is already proving to be a cost-effective guide to engine performances and to be fully compatible with engine development.

ACKNOWLEDGEMENTS

The authors would like to thank L Beristain, K Breitenbach, R Laborie and L Platret for the work they have done on this project as well as JH Downie, CR Hogg, SG Cox, SM Begg and FMJ Mc Cluskey for their help and support.

Nomenclature

nnumber of vectors
mnumber of single maps used for averaging
x, ycartesian coordinates of velocity vector (mm)
u, vX and Y components of velocity vector (mm/s)
V, αmagnitude and angle of velocity vector (mm/s)
r, θpolar coordinates of a velocity vector
V_t, V_nnormal and tangential components of velocity vector relative to the centre-point
ζvorticity (s^{-1})
Bcylinder bore (mm)
Sstroke (mm)
ωcrank angle speed (rad/s)
\bar{V}mean flow velocity (mm/s)
O_i, X, Ylocal orthogonal axis set

All coordinates are defined in the local set of axes with its origin at the centre of the eddy, X axis parallel to the cylinder axis and Y axis parallel to a line joining the inlet and the exhaust valves.

REFERENCES

- (1) T. Ma, M. Davies, N. Collings. Ford Motor Comp., Cambridge university. *Low speed dynamic similarity modelling in internal combustion engines*. SAE 860239. 1986.
- (2) N.S Jackson, J. Stokes, Ricardo Consulting Engineers, M.R. Heikal, J.H. Downie, University of Brighton. *A dynamic flow visualisation rig for automotive combustion system development*. International Congress and exposition, Detroit, USA. SAE 950728, Feb-Mar 1995.
- (3) N.S. Jackson, J. Stokes, T.H. Lake, S.M. Sapsford, M.R. Heikal, I. Denbratt. Ricardo Consulting Engineers, University of Brighton and Volvo Car Corp. *Understanding the CCVS stratified EGR combustion system*. International Congress and exposition, Detroit, USA. SAE 960837, Feb 1996.
- (4) N. Trigui, J.C. Kent, Y. Guezennec and W.C. Choi. Ford Motor Company. *Characterization of intake generated fluid flow fields in IC engines using 3-D Particle Tracking Velocimetry (3-D PTV)*. International Congress and exposition, Detroit, USA. SAE 940279, Feb-Mar 1994.
- (5) B. Khalighi, S.H. Tahry, D.C. Haworth, M.S. Huebler. *Computation and measurements of flow and combustion in a four-valve engine with intake variations*. GM R&D Center. International congress and exposition, Michigan. 1995.
- (6) J. Chapman, M.W. Garrett, A. Warburton. *Barrel swirl the new standard*. Proceedings of the second British/Italian workshop on heat engines. Bath, UK, Mar 1991.
- (7) M. Reeves, C.P. Garner, J.C. Dent, and N.A. Halliwell. Loughborough University of technology. *Study of barrel swirl in a four-valve optical IC engine using Particle Image Velocimetry*. International Symposium COMODIA 94, Yokohama, Japan. Jul 1994.
- (8) M. Rönnbäck, W.X. Le, J.R. Linna. Volvo Car Corp. and Chalmers University. *Study of induction tumble by Particle Tracking Velocimetry in a 4-valve Engine*. International Fuels and Lubricants Meeting and Exposition, Toronto, Canada. SAE 912376. Oct 1991.
- (9) P. Jones, J.S. Junday. *Full cycle computational fluid dynamics calculations in a motored four valve pent roof combustion chamber and comparison with experiment*. International congress and exposition, Detroit, Michigan, 1995.
- (10) M.A. Faure, M.R. Heikal, N.S. Jackson. University of Brighton and Ricardo Consulting Engineers. *3-Dimensional in-cylinder flow maps using 2D PIV system*. I Mech-E, Optical Methods and Data Processing in Heat and Fluid Flow. City University, London, UK. Apr. 1996.

A STUDY ON THE SPEED DEPENDENCE OF THE INTAKE FLOW OF A MOTORED FOUR - STROKE ENGINE, USING LASER - DOPPLER VELOCIMETRY

M. Socoliuc and M. Brun

Laboratoire de Machines Thermiques, Ecole Centrale de Lyon
36, Av. Guy de Collongue, B.P. 163, 69131 Ecully Cedex, France

ABSTRACT

To develop a better understanding of the in-cylinder flow, an accurate knowledge of intake flow is absolutely necessary at present. Air flow in the intake pipe of a four-stroke single-cylinder research engine was examined by the Laser Doppler Velocimetry (LDV) technique. Measurements of axial and tangential components of the velocity were made at five points located on a diameter of the intake pipe, 10 mm upstream of the cylinder head, to provide accurate initial conditions for numerical simulation codes. The mean motion and turbulence intensity was computed using a filtering procedure on the LDV data. This allowed us to identify three characteristic phases and to follow the evolution of profiles of velocity during the intake process. Here we present some experimental results which show that the intake flow behaviour depends on phase distribution and operating conditions and we review possible future developments.

INTRODUCTION

The accuracy of combustion modelling of an internal combustion engine depends strongly on the calculation of intake and compression processes. This, in its turn, is fundamentally influenced by the chosen initial inlet conditions which can be more or less close to real conditions.

There exist at present several approaches for the calculation of admission and compression phases based on calculation codes, but whichever code we select (KIVA 2, STAR - CD etc.), it is necessary to validate the numerical prediction with experimental data. In this case the initial and boundary conditions provided to the code are very important.

Trigui et al., [12], use an hydraulic analogy to obtain the experimental data by measuring three-components of the velocity by 3-D Particle Tracking Velocimetry (3D PTV). Nevertheless their calculations were made in a simplified case called "no moving valves", where the ports were set either fully open or fully closed during the intake and compression stroke, respectively.

To take the valve admission lift into account Argueyrolles et al., [1], represent this valve as an infinitely thin disc that penetrates into the combustion chamber. In this case the area of calculation is limited by the plane of the valve. The major drawback of this method is the necessity to know the distribution of axial, radial and tangential velocity in the plane situated at the level of the valve of admission through the whole of the admission phase. These profiles of admission valve velocities can be determined by combining the profiles of velocities measured in a steady state flow bench for different positions of the admission valve with the instantaneous mass flow measured on the engine, [2].

To avoid these difficulties the real geometry of the valve is nowadays taken into account and the calculation area is expanded to the entry of the admission pipe.

The purpose of our experimental study is to characterize the inlet flow at the entrance of the cylinder head of a four stroke internal combustion engine and to provide initial kinematic conditions for a numerical simulation code.

EXPERIMENTAL SET-UP

Test engine

The test engine used in this study was a four-stroke single-cylinder research engine, [11]. The valve gear consists of typical overhead valves. The timing diagram insures a null valve overlap in order to eliminate all interference between the inlet and exhaust processes. The intake pipe was modified to allow LDV measurement just at the entry of the cylinder head. The optical access is obtained by means of a cylindrical transparent pipe with the same diameter as the duct of the cylinder head. The engine characteristics are given in Table 1. A cross-section view of the cylinder head, in the new configuration, is shown in Figure 1. The engine allows us also to obtain different filling conditions by restricting the intake cross sectional area with a throttle plate placed in the intake pipe.

Table 1 : Engine Characteristics

Bore [mm]	100
Stroke [mm]	90
Displacement [dm ³]	0.7
Compression ratio	1 : 7.5
Connecting rod length [mm]	163
Intake valve opening (IVO) [deg]	0 TDC
Intake valve closing (IVC) [deg]	85 ABTC
Exhaust valve opening (EVO) [deg]	75 BBTC
Exhaust valve closing (EVC) [deg]	6 BTDC
Speed range (motored) [rpm]	500 - 2000

Furthermore it presents a large optical access to the combustion chamber which allows the measurement of the in chamber gas velocity.

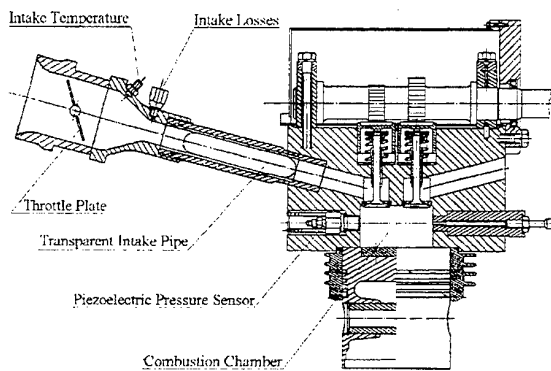


Figure 1 : Cross-section drawing of cylinder head of engine

Laser - Doppler Velocimeter system

For the set of measurements described here the Laser - Doppler Velocimeter (LDV) is a one-component system operating in forward-scatter configuration, (Figure 2). This disposition of the optical elements offers here the best signal-noise ratio, [3].

An argon - ion laser (514.5 nm) (1) was connected to the emission optics by an optical fiber (2). The power of laser was set at 125 mW. A single-mode polarisation optical fiber was used and the factor of transmission was higher than 60%.

The receiving optics (7) were placed opposite the emission optics (3) on the other side of the transparent intake pipe (5) of the engine (4).

The emission and receiving optics were each mounted on an extruded aluminium optical rail which was supported on three micrometers. This allowed accurate and repeatable positioning of measurement volume in the transparent intake pipe.

The flow was seeded using incense which was burnt in a smoke generator (6). The Doppler signal was processed by a

Burst Spectrum Analyser (BSA) (8) that performs a spectrum analysis in order to extract the Doppler frequencies. The validated data were transmitted to a computer (9). Besides the stocking of the data this allows, with the assistance of software, the choice of various measurement parameters.

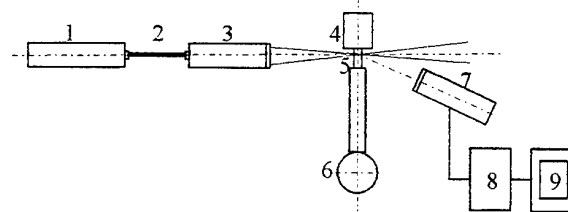


Figure 2: Schematic diagram of experimental set up

A shaft encoder, connected to the camshaft, drives a gating circuit which enables the BSA for the measurements. It opens the input gate during expansion stroke of the engine cycle in order to give the best position for the whole intake process during the acquisition of data.

MEASUREMENT LOCATION and RUNNING CONDITIONS

The axial and tangential (radial) components of the velocity were measured in five locations. All of them were at the same horizontal diameter of the intake pipe, 10 mm upstream of the cylinder head, (Figure 3).

This distance has been chosen after preliminary tests which showed that it gives a compromise between increasing the parasite reflections by the wall of the cylinder head and increasing the number of cells of computation grid.

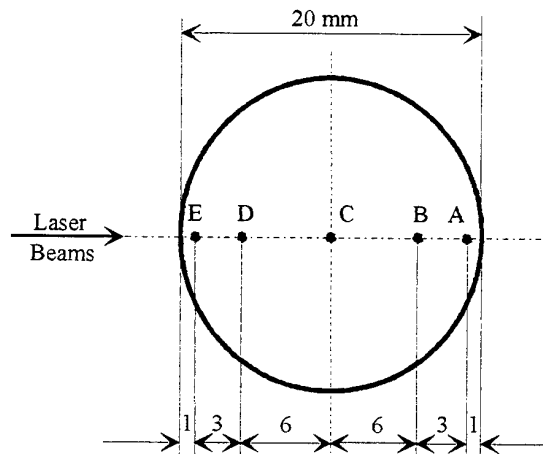


Figure 3 : Measurement locations in the intake pipe

Furthermore, as this diameter is chosen in an "horizontal" plane H, the two laser beams had the same optical path length through the transparent wall of the pipe.

This condition would not be satisfied in the case of a "vertical" diameter as it appears on the Figure 4.

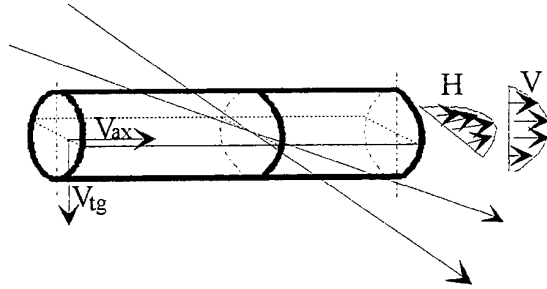


Figure 4 : Path beams in the intake pipe

Running conditions of an internal combustion engine are well defined by the rotation speed, the load and the coolant temperature. In the actual configuration of the test bench and for motored conditions, the speeds may vary from 250 at 2000 rpm with openings of the throttle plate between 100% and 0% and the temperature of cooling fluid was set at a constant value 358 K. Nevertheless all of the results presented later in this report have been obtained with a full opening of the throttle plate.

DATA REDUCTION : CYCLE-RESOLVED VELOCITY

Whatever the location in the intake flow, for a particular cycle i and an angular position θ of the engine crankshaft and using the Reynolds's decomposition, the local instantaneous velocity can be written for an unsteady turbulent flow :

$$U(\theta, i) = \bar{U}(\theta) + u(\theta, i) \quad (1)$$

where the average value $\bar{U}(\theta, i)$ represents here the mean evolution of the velocity $U(\theta, i)$ during the cycle i considered, and $u(\theta, i)$ the turbulent fluctuation of velocity about this average, [6], [7], [8].

The present study is conducted under assumption of quasi-periodic flows in the engine.

During a following cycle j , a random modification of conditions can lead to an average value which is slightly different. Because of these cycle to cycle fluctuations a new averaged velocity valid over N_c cycles, the ensemble averaged mean velocity, is defined as

$$\bar{U}(\theta) = \frac{1}{N_c} \sum_{i=1}^{N_c} U(\theta, i) \quad (2)$$

This velocity is a function of crank angle only since cyclic variation has been averaged out.

The difference between the mean velocity in a particular cycle and ensemble averaged mean velocity over many cycles is defined as the cycle to cycle variation in mean velocity :

$$\tilde{U}(\theta, i) = \bar{U}(\theta, i) - \bar{U}(\theta) \quad (3)$$

Finally the instantaneous velocity can be split into three components, the ensemble averaged mean velocity, the cycle to cycle variation in mean velocity and the turbulent fluctuation :

$$U(\theta, i) = \bar{U}(\theta) + \tilde{U}(\theta, i) + u(\theta, i) \quad (4)$$

For the present study, the engine was motored such that the cycle to cycle variations of the rotation speed were minimized and $\tilde{U}(\theta, i) \approx 0$. This assumption was used also by Lee for an experimental study of in-cylinder air flow, [8].

In this case the ensemble averaged turbulence intensity $u'(\theta)$ is provided by the root mean square (rms) of the velocity fluctuations about the ensemble averaged mean velocity :

$$u'(\theta) = \sqrt{\frac{\sum_{i=1}^{N_c} [u(\theta, i)]^2}{N_c}} = \sqrt{\frac{\sum_{i=1}^{N_c} [U(\theta, i) - \bar{U}(\theta)]^2}{N_c}} \quad (5)$$

However it is important to note that $u'(\theta)$ includes all fluctuations about the ensemble averaged mean velocity.

In order to obtain the profiles of velocities along the measurement diameter, at a given instant of the cycle, data files of the measured values at the five locations should be synchronized and should have the same time resolution. This condition is not fulfilled in the case of the LDV system, where acquisitions are made randomly, that is, at the time when a particle arrives in the measurement volume and velocity is validated.

In order to remedy this difficulty we conceived a new form of data treatment to interpolate the experimental data and restore a smoothed time evolution of the velocity discretized at regular intervals $\Delta\theta$.

Ensemble averaged mean velocity $\bar{U}(\theta)$ is then evaluated by means of a moving window, F_m degree wide, which provides a low pass numerical filtering. More precisely $\bar{U}(\theta)$ is calculated as the arithmetical mean of the N_v values of the instantaneous velocities contained inside this window, symmetrically about θ . The width of the moving window is chosen according to the selected cut off frequency, f_c , that is the frequency which is considered as separating the low frequencies phenomena, the in cycle mean evolution, and the high frequencies phenomena due to turbulence. This width F_m is given by the spectral response of the numerical filter :

$$f_c = \frac{6N}{F_m} \quad (6)$$

with $F_m = (N_v - 1)\Delta\theta$

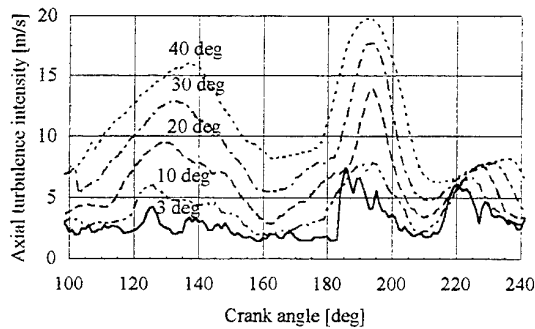


Figure 5 : Influence of the width of the moving window

The axial turbulence intensity is then given by the relationship (5). Rask [10] showed that this intensity depends on the choice of f_c and Figure 5 reports $u'(\theta)$ calculated near the BDC at location B (4 mm from the intake pipe wall) for $N = 750$ rpm and F_m varying from 3° to 40° CA.

Finally it seemed to us that a reasonable compromise can be set up with initial smoothing over five successive raw acquisitions, an interpolation of the results and then low pass filtering with a 10° CA wide moving window. Indeed the cut off frequency which corresponds to this window is 600 Hz at 1000 rpm and agrees well with that of Hall and Bracco [5] or Liou et al. [9].

EXPERIMENTAL RESULTS

Axial velocity

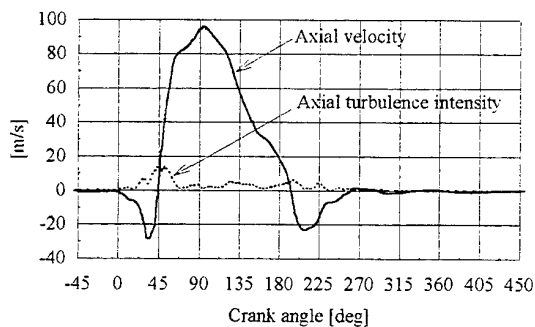


Figure 6: Ensemble averaged mean axial velocity and the axial turbulence intensity at 750 rpm

Figure 6 plots the evolution versus crank angle of the ensemble averaged mean axial velocity and the axial turbulence intensity at the location B (4 mm from the intake pipe wall) and for an engine speed of 750 rpm. The mean feature of the first phase is a backflow which begins at the intake valve opening due to non overlapping of the valves that induces high pressure in the combustion chamber at TDC, Figure 7.

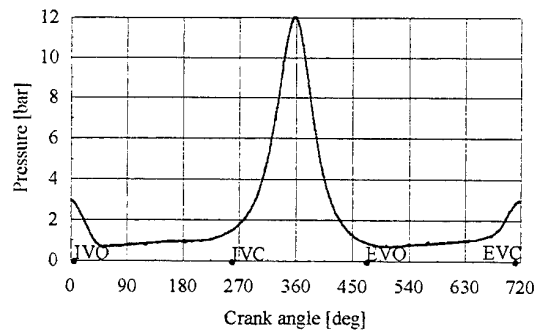


Figure 7 : Pressure record at 750 rpm and full opening of the throttle plate

The second phase is a direct flow from intake pipe to combustion chamber. We can observe a rapid increase of the velocity which reaches its maximum value near 90° ATDC and then decreases progressively.

During a third phase the piston moves up and induces a second backflow which begins near the BDC. After the intake valve close, the mean velocity vanishes but a small damped oscillation of the air column may be observed.

Elsewhere the axial turbulent intensity increases significantly near the first change of the flow sense and then maintains values which vary from 1 to 5 m/s. The Figure 8 reports the ensemble averaged mean axial velocity at the five measurement locations for $N = 1000$ rpm and with wide open throttle plate again.

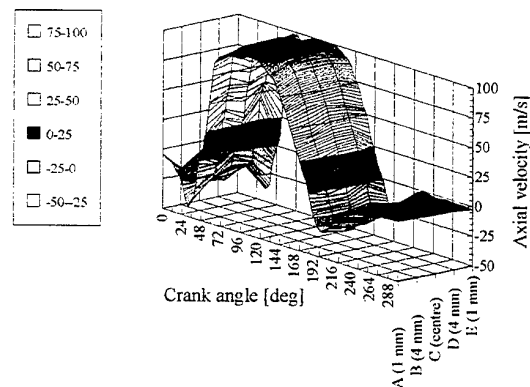


Fig 8 : Spatial and temporal variation of ensemble averaged mean axial velocity at 1000 rpm

During the direct flow, from 80° to 170° ATDC, i.e. when the intake valve is wide open it appears clearly that near the pipe wall, at the locations A and E, the mean velocities are smaller than that measured at the locations B, C and D, as detailed on Figure 9, whereas during the backflow the velocity profiles are quite different.

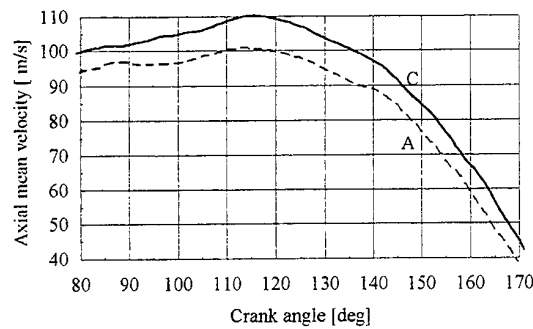


Fig 9 : Detail of evolution of ensemble averaged mean axial velocity during the direct flow at 1000 rpm

Tangential velocity

The ensemble averaged mean tangential velocities at the five measurement locations are plotted on Figure 10 for $N = 1000$ rpm and with wide open throttle plate. Although their evolution seems not to be easy to understand we notice a smoother evolution during the direct flow with values generally much weaker than the axial ones as they do not exceed ± 15 m/s, but of the same order of magnitude during the backflows.

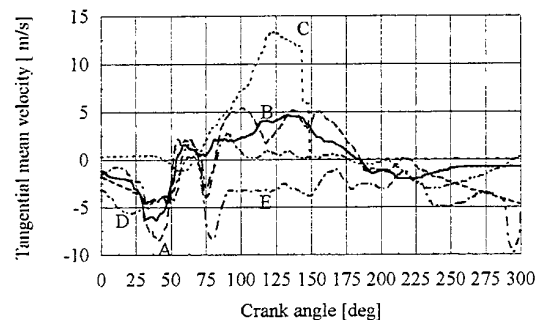


Figure 10 : Ensemble averaged tangential mean velocities at 1000 rpm

Velocity profiles

For $N = 1000$ rpm with the throttle plate wide open and assuming zero velocities at the wall of the pipe, the axial velocity profiles are plotted for various crank angles.

During the first backflow, Figure 11, the maximum velocities are always observed at the locations near the wall rather than in the center of the pipe. This phenomenon may be explained by the diagram given in Figure 12 which shows high velocities on the periphery of the valve when it is nearly closed.

The same observation was made for the tangential velocity, Figure 13.

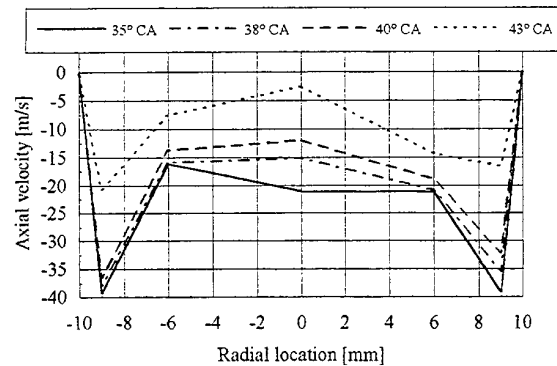


Fig 11 : Profile of axial velocity during the first backflow

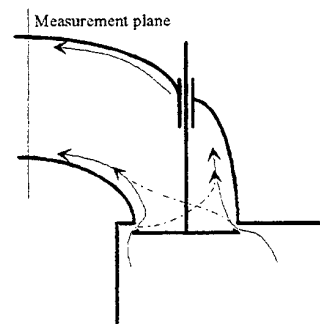


Fig 12 : Representation of the backflow

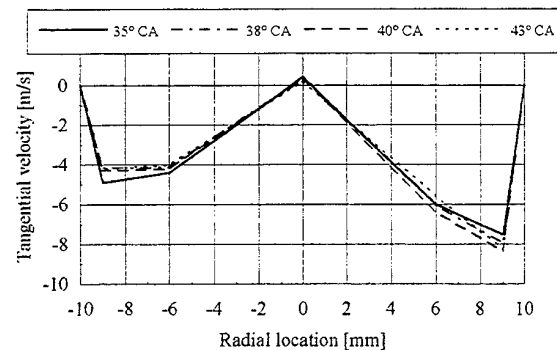


Fig 13 : Profile of tangential velocity during the first backflow

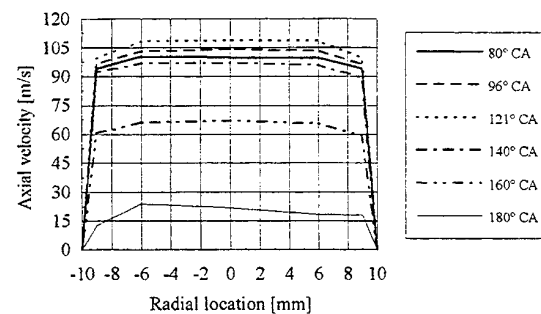


Figure 14 : Profile of axial velocity during the direct flow

For the direct flow, Figure 14, the velocity profiles are quite flat up to 4 mm from the wall. Near the BDC they become asymmetric due to a swirl which appears clearly on the tangential velocity profiles, Figure 15.

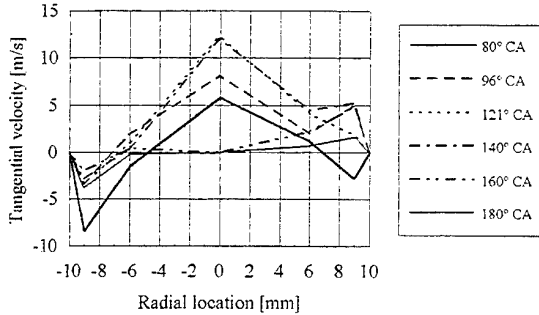


Figure 15 : Profile of tangential velocity during the direct flow

Figure 16 and 17 allow detailed comparison of the axial and tangential turbulence intensity profiles for 4 angular positions during the direct flow, between the maximal left of intake valve and the BDC.

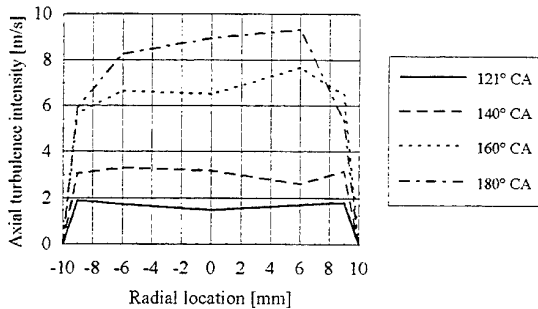


Figure 16 : Profile of axial turbulence intensity during the direct flow

The maximum axial turbulence intensity increases by a factor of 5 during this period. It is always higher than the tangential turbulence intensity which does not reach 1 m/s.

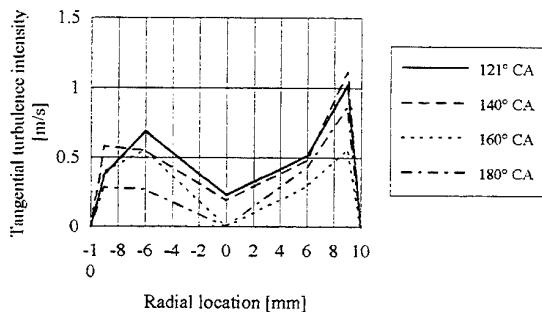


Figure 17 : Profile of tangential turbulence intensity during the direct flow

Influence of the engine speed

The influence of the engine speed on the axial mean velocity measured on the pipe axis is shown on Figure 18. We observe that during the first backflow and the direct flow the velocities increase with engine speed. In contrast, during the second backflow the velocities begin to increase slightly when engine speed grows to 1000 rpm and then decrease. Simultaneously the direct flow duration increases while the second backflow duration decrease. These observations highlight the air column inertia which progressively causes the second backflow to disappear at the higher speeds. This phenomenon then limits the decrease in volumetric efficiency.

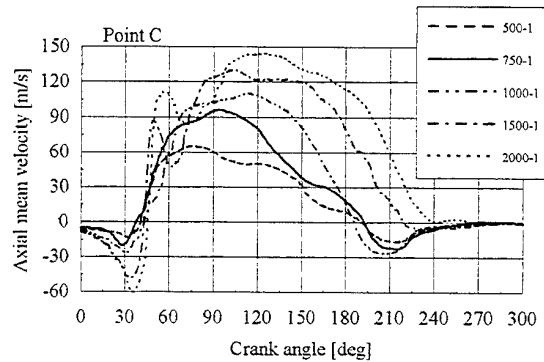


Figure 18 : Axial mean velocity for several crankshaft rotation speeds and complete opening of throttle plate

Figure 19 plots the axial velocity measured for a wide opening of the intake valve versus the engine speed. As observed by Catania and Spessa [4] in the chamber, a general trend of this velocity to increase with the engine speed is clear but with a less than proportional dependence.

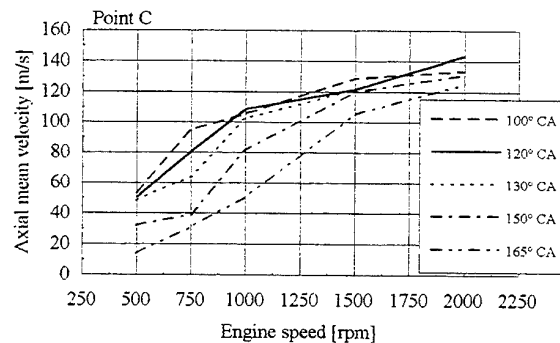


Figure 19 : Dependence of axial mean velocity on speed of engine

The logarithmic representation shown on Figure 20, of the axial velocity measured on the pipe axis when the intake valve is wide open ($\theta = 130^\circ \text{ATC}$) gives a value of 0,81 for

the exponent in $V_{ax} = b \cdot N^a$. In the same conditions but at the location A, at 1 mm from the wall of the pipe, the value of a reaches 0,96. This can be explained by the fact that this location is in the boundary layer at the slower speed whereas at the higher speed this layer gets thinner. The location A is thus no longer within this layer and hence velocity increases faster with N than in location C.

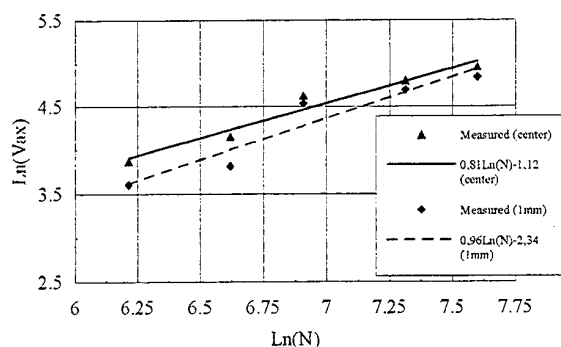


Figure 20 : Logarithmic representation of dependence of axial mean velocity of speed of engine

The time evolution of the axial turbulence intensity is shown in Figure 21 for various engine speed. A marked increase of turbulence is particularly evident at the first reversal of the flow for the higher speeds. The turbulence then decreases to a minimum when the valve is wide open. Subsequently, this turbulence increases during the second backflow phase, especially at the higher engine speeds.

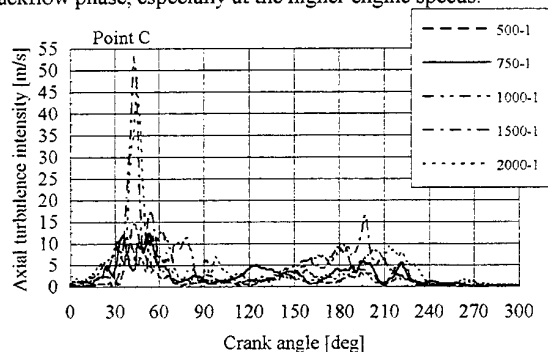


Figure 21 : Evolution of the axial turbulence intensity for several engine speeds and complete opening of throttle plate

CONCLUSIONS

- (1) The method of measurement developed allows the characterization of the intake flow in the pipe of an internal combustion engine.
- (2) We have thus a base of experimental data that can be utilised for initial conditions of numerical simulation

code. In the future it will allow also the study of the intake flow not only according to the running conditions of the engine but also by taking account of the pipe configuration.

- (3) LDV measurement of the axial component of velocity shows three characteristic phases of the intake process, a direct flow towards the cylinder who is framed by two backflow.
- (4) The maximum velocities were observed near the intake pipe wall during the backflow phases and at the center of the pipe during the direct flow phase.
- (5) The axial turbulence intensity is minimum during the maximum opening of the valve. It increases by a factor of 5 between wide opening of intake valve and BDC.
- (6) The evolution of the tangential velocity fact emerge the existence of a swirl in the intake pipe which appears more clearly close to the BDC.
- (7) The axial velocity increases with engine speed, but with a less than proportional dependence. The maximum value of this velocity also approaches then the BDC. At the same time, the effect of the inertia of the intake air column increases with engine speed and this phenomenon is highlighted by the diminution and even the disappearance of the backflow after the BDC.
- (8) These remarks can be useful for the future study of interactions between the fuel spray and the intake flow.

ACKNOWLEDGEMENTS

Support for this work was provided by the ADEME and Renault S.A.

REFERENCES

- 1 ARGUEYROLLES B., BAILLY O., BUCHOU C., GLAZIN F., MANTEL T., *Développements Récents du Calcul en Aérodynamique et Combustion sur Moteur à Allumage Commandé à l'aide du Code KIVA2*, Congrès SIA, Palaiseau, 1993.
- 2 BEFRUI B.A., BRANDSTATTER W., HOFER T., PITCHER G., WIGLEY G., *Dreidimensionales Simulationsmodell zur Berechnung der turbulenten Luftbewegung in Zylindern*, Motortechnische Zeitschrift (MTZ), N°3, 1993.
- 3 BOUTIER A., *Principe et applications aérodynamiques de la vélocimétrie laser*, Mesures-Régulation-Automatismes, Avril 1978.
- 4 CATANIA, A.E., SPESSA, E., *Speed Dependence of Turbulence Properties in a High-Squish Automotive Engine Combustion System*, SAE Paper 960268, 1996
- 5 HALL, M.J., BRACCO, F.V., *Cycle-resolved velocity and turbulence measurements near the cylinder wall of a firing S.I. engine*, SAE Paper 861530, 1986

- 6 HEYWOOD, J.B., *Internal combustion engine fundamentals*, McGraw-Hill, 1988
- 7 HINZE, J.O., *Turbulence*, Second edition, McGraw Hill, New York, 1975
- 8 LEE, K. et col., *An Experimental Study of In-Cylinder Air Flow in a 3.5L Four-Valve SI Engine by High Speed Flow Visualization and Two-Component LDV Measurement*, SAE Paper 930478, 1993
- 9 LIOU T.M., HALL, M., SANTAVICCA D.A., BRACCO, F.V., *Laser Doppler Velocimetry Measurements in Valved and Ported Engine*, SAE Paper 840375, 1984
- 10 RASK R.B., *Comparison of Window, Smoothed-Ensemble, and Cycle-by-Cycle Data Reduction Techniques for Laser Doppler Anemometer Measurements of in-Cylinder Velocity*, Fluid Mechanics of Combustion Systems, ASME, 1981
- 11 SOCOLIUC, M., BRUN, M., POINT, R., LAURENT, P., *Caractérisation de l'écoulement dans le conduit d'admission d'un moteur à combustion interne*, Fuel Economy, Safety, Reliability of Motor Vehicles - ESFA'95, Bucharest, Romania, 1995.
- 12 TRIGUI N., AFFES H., KENT J.C., *Use of Experimentally Measured In-Cylinder Flow Field Data at IVC as Initial Conditions to CFD Simulations of Compression Stroke in I.C. Engines - A Feasibility Study*, SAE Paper 940280, 1994

NOMENCLATURE

- CA Crank angle in degree
 f Frequency
 F_m Moving window of low pass numerical filtering
 U Mean velocity
 u' Turbulence intensity
 θ Crank angle
 Subscript
 c corresponds to cut-off frequency

SESSION 23

Stratified Flows and Waves

INVESTIGATION OF TURBULENT PENETRATIVE CONVECTION

V. Troy and R. Adrian

Department of Theoretical and Applied Mechanics
Department of Mechanical and Industrial Engineering
University of Illinois at Urbana-Champaign, USA

ABSTRACT

Turbulent thermal convection in a layer of water heated from below and capped on top by a stably stratified layer has been studied using stereo particle image velocimetry. All three velocity vector components were simultaneously measured at more than 17000 points in a vertical plane. Two different inversion layer (Figure 1) temperature gradients, $\Gamma = 0.29^\circ\text{C/cm}$ and 0.55°C/cm were studied. This convection system is a good model of the convection that occurs in the atmospheric under an inversion layer, and interest in it centers on the interaction between the turbulence and waves in the stable layer and the effects of the upper boundary on the structure of the mixed layer. The experiments were conducted in a wide horizontal layer with homogeneous upper and lower boundary conditions. As a consequence, the turbulent flow field was statistically homogeneous in horizontal planes, and statistically symmetric about the vertical direction.

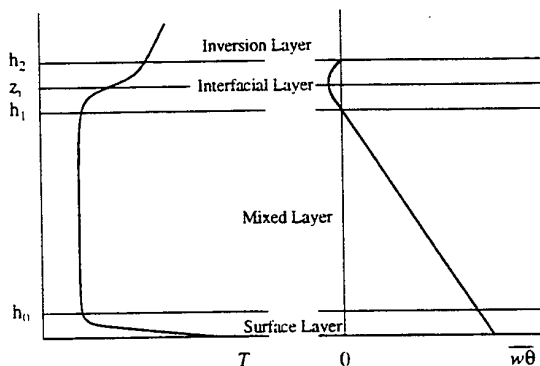


Figure 1 Left: Profile of the Mean Temperature, Right: Profile of the Temperature Flux.

Coherent structures in the form of mushroom-like plumes and sheet-like down-drafts were clearly observed in the velocity fields. The plumes had strong positive and negative out-of-plane motion in adjacent bands which suggests that they spiral as they move upwards. Sheet-like down-drafts were observed in the velocity fields.

First, second, and third-order moments were calculated and compared with atmospheric, laboratory, and computational measurements. Dissipation was computed by explicitly calculating seven out of the nine terms. The other two terms were calculated by assuming the flow to be axisymmetric. The dissipation profiles compare very well with measurements made in the atmosphere where the flow was assumed to be isotropic. Probability density functions of velocity, vorticity, and dissipation were measured at several heights, as was the two-point in-plane spatial correlation tensor.

1. INTRODUCTION

1.1 Motivation

The atmospheric boundary layer (ABL) is the lowest portion of the atmosphere. It is produced by large-scale air currents in combination with turbulent friction, Coriolis force and density stratification of air. The ABL is approximately the lower 1 km region of the approximate 11 km atmosphere.

The ABL goes through a daily cycle. In the night time, radiative cooling sets up a stably stratified air layer above the cool ground. During the daylight hours the ground increases in temperature and when the critical Rayleigh number is exceeded turbulent convection begins: positively buoyant, mushroom-like plumes ascend into the stable layer, also known as the inversion layer. The plumes *penetrate* a short distance into the inversion layer due to their inertia, causing warmer air from the inversion layer to entrain into the convective mixed layer. This mechanism of entrainment throughout the daylight hours erodes the inversion layer and increases the height of the mixed layer with time.

There are large coherent structures in the ABL composed of buoyant up-drafts of warm air rising in narrow columns surrounded by larger areas of slowly sinking down-drafts. The up-drafts are composed of two main coherent structures: thermals and plumes. Plumes span the depth of the ABL from the surface to the capping inversion and are quasi-steady, while thermals are finite, buoyant fluid elements rising in the ABL which grow in size due to lateral entrainment (Schmidt and Schumann 1989). Thermals rising from the surface either merge together into plumes or are destroyed in the lower part of the ABL (Deardorff 1972, Schmidt and Schumann 1989). Once the plumes reach the inversion base, the air spreads out laterally and produces dome-like depressions at the interface (Deardorff *et al.* 1969, Willis and Deardorff 1979). On occasion plumes appear to be in a state of rotation, giving the appearance of a dust devil (Willis and Deardorff 1979).

Over the last 25 years, numerous researchers have studied the ABL in field, laboratory, and computational experiments. From these studies a fairly complete knowledge of the vertical profiles of second and third order moments of turbulent fluctuations, horizontal spectra and probability distributions of vertical velocity, vertical profiles of temperature fluctuation and skewness has been obtained (Ferreira 1978, Smidt and Schumann 1989). A vast majority of the previous velocity measurements performed in the field or in tank experiments have been one-point measurements. In the past two decades Large Eddy Simulation (LES) has given researchers a tool for obtaining full-field information about the ABL. A great need for experimental multi-point velocity measurement data has arisen. This data can be used as a bench mark against which LES can be tested. It will also serve as a way to visualize the role of coherent structures in turbulent thermal convection.

If the flow is assumed to be axisymmetric about the gravity vector, λ_i , and inhomogeneous in the z -direction, then the two-point spatial correlation function which is a function of three-component separation vectors can be reduced to a simple form given by Chandrasekhar (1950)

$$R_{ij}(\mathbf{r}, z) = Ar_i r_j + B\lambda_i \lambda_j + C\delta_{ij} + Dr_i \lambda_j + Er_j \lambda_i,$$

where r_i is a separation vector between the first and second velocity positions. The scalar functions A, B, C, D , and E are arbitrary functions of $r^2, r_i \lambda_i$, and z . From the correlation tensor we can measure important length scales of the flow, such as Taylor's micro-scale and the integral length scale without having to resort to Taylor's hypothesis. Certain quantities, such as dissipation can be calculated more accurately, because 7 of the 9 terms in the equation can be explicitly calculated and the remaining two terms can be calculated by assuming rotational symmetry.

Table 1 Approximate Experimental Parameter Ranges

Parameter	From	To
z , (mm)	110	150
w , (mm/s)	3.00	3.80
Re ,	350	650
Q_0 ($^{\circ}\text{C mm/s}$)	0.100	0.150

In the present experiments the flow is assumed to be horizontally homogeneous, i.e., mean quantities are functions of only the vertical (z) direction (y is the horizontal in-plane direction and x is the horizontal out-of-plane direction). We also assume that there is no mean flow in the mixed and entrainment layers.

1.3 Scaling

The present experimental data was non-dimensionalized by Deardorff (1970) convective scaling. Away from the boundaries energy is primarily transported by convective motion whose length scale is of the order of the layer depth, therefore, thermal diffusivity is no longer important except in the small scales (Adrian 1975). Deardorff (1970) suggested that the governing parameters for turbulence in the mixed layer are $\beta g Q_0$ and z_i , where z_i is the mean height of the interfacial layer (Figure 1), β is the volumetric coefficient of thermal expansion, and Q_0 is the kinematic heat flux at the lower boundary. The statistics are hypothesized to be universal functions of z/z_i when length, velocity, and temperature, are non-dimensionalized by z , w , and θ , respectively, where

$$\begin{aligned} z &= z_i, \\ w &= (\beta g Q_0 z_i)^{1/3}, \\ \theta &= Q_0 / w. \end{aligned}$$

The Reynolds number can be defined as $Re = w z_i / \nu$. The experiments were performed while the mixed layer depth grew from approximately 110 mm to 150 mm. The values of the experimental parameter ranges is shown Table 1. The values of β and ν were calculated based on the mixed layer's temperature for each velocity field. The lengths and velocities were scaled by z and w , respectively, for each velocity field. The scaling parameters for each velocity field were calculated based on the height of the inversion layer, the heat flux, and the mixed layer's temperature at the time the data was taken. Numerous researchers have successfully collapsed data obtained in field, tank, or computational experiments using convective scaling. They include; Willis and Deardorff (1974), Caughey and Palmer (1979), Lenschow *et al.* (1980), Deardorff and Willis (1985), Adrian *et al.* (1986), Kumar and Adrian (1986), Schmidt and Schumann (1989), and Troy (1994).

2. EXPERIMENTAL APPARATUS

2.1 Test Section

The experiments were performed in a square 800 mm \times 800 mm test section as shown in Figure 2. The walls of the test section consisted of 12.7 mm thick Plexiglas. Plate glass windows with thickness 9.5 mm were mounted in the Plexiglas in regions where optical access was necessary. These regions included the sides of the test section through which the illuminating laser sheets passed through, and the side through which photographic recording took place. The lower boundary of the test section consisted of a 25.4 mm thick aluminum plate. The plate's surface was treated with a combination of nitriding and Teflon impregnation to minimize corrosion. The side walls of the test section were insulated with 25 mm thick foam rubber surrounded by 50 mm thick Styrofoam.

The lower boundary was heated electrically by means of a heater wire bonded to the underside of the aluminum plate. The heat flux was chosen to closely match with that of Kumar (1983). Thirteen thermistor probes were embedded in the aluminum plate 10 mm from its upper surface to monitor its temperature during the experiments (Figure 2). The test section's upper boundary consists of a double-pane Plexiglas box, which allowed visual access from above during the experiment. During the experiment compressed heated air was circulated in the cavity of the box to maintain a constant temperature upper boundary.

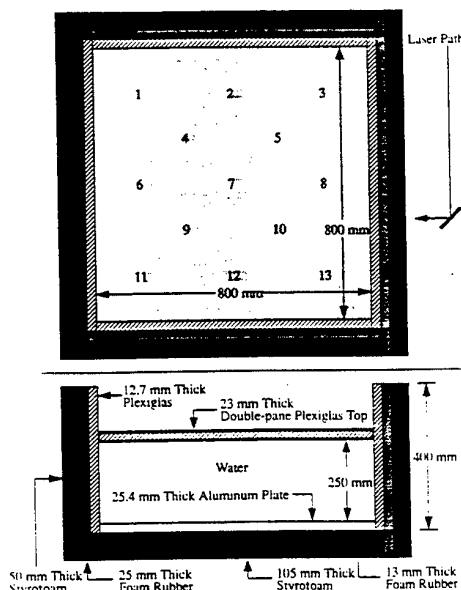


Figure 2 Schematic of Thermal Convection Test Section. Top Diagram: Plan View, Numbers Indicated Positions of Thermistor Probes. Bottom Diagram: Side View.

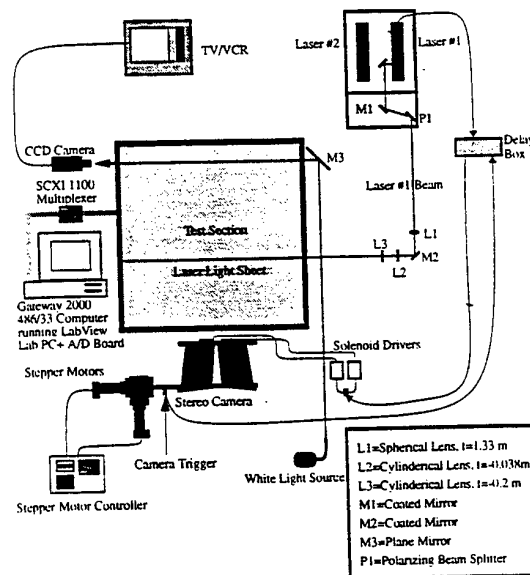


Figure 3 Experimental Set Up

2.2 Illumination and Optics

The flow tracing particles were illuminated by a Continuum Lasers, Inc., frequency-doubled Nd-YAG laser emitting at a wavelength, $\lambda = 532$ nm with a pulse frequency of approximately 10 Hz. The laser could deliver up to 350 mJ/pulse with a 6 ns pulse duration. Typically, only 250 mJ/pulse was used for the experiments. The optics formed the light sheet as shown in Figure 3. The thickness of the light sheet was measured to be approximately 1.1 mm in the middle of the object plane.

The particles were imaged three times with pulse separation, $\Delta t = 96.3$ ms. Only one laser was used to illuminate the particles to ensure the consecutive laser sheets were perfectly registered and had the same intensity.

Kodak TMAX-400 100 mm \times 125 mm film was used to record the particle images. This film was chosen because of its high resolution and good sensitivity at $\lambda = 532$ nm.

The tracer particles used in the experiments were hollow glass spheres. The particles had a nominal diameter of 8 μ m and a specific gravity of 1.1. Their settling velocity of approximately 10^{-3} mm/s is much smaller than the flow velocity.

2.3 Stereo Camera

The stereo camera used in these experiments has been described previously in Prasad and Adrian (1993). The stereoscopic configuration has been referred to as the lateral decentering system or the translational method. In

this configuration, the two camera-lens axes are parallel to each other and perpendicular to the illumination plane. The lenses are simply *translated* relative to one another. The depth of field, δx , required for the translational configuration is the same as for conventional PIV.

Two identical Nikkor ED 120 mm F5.6 (Nikon Inc.) lenses with a design magnification of unity were mounted in the camera's front plate parallel to each other and separated by 140.0 mm. All the experiments were performed with the f-number set at $f/11$ and shutter speed set at $1/4$ s. The depth of field equation is (Adrian 1991),

$$\delta x = 4(1 + M^{-1})^2 f \#^2 \lambda,$$

where M is the camera magnification. In the present case, the nominal magnification was approximately 0.5, yielding a depth of field for the present experiments of approximately 2.3 mm. Therefore, the entire depth of the laser sheet was in focus. Using even a larger f-number would have been beneficial, because it would have reduced the effects of astigmatic aberrations, but in the present situation increasing the f-number any further would have attenuated the image intensity too much. The back plate consisted of two 100 mm \times 125 mm format film holders separated by 260.0 mm. Bellows were used to connect the front and back plates.

In the present experiments the particles were imaged through a large liquid layer followed by a liquid-air interface. Also the particles were imaged at large off-axis angles leading to astigmatic aberrations. Due to the aberrations the surface of least confusion was no longer planar but curved. The particle images were also no longer spherical but smeared out in the radial direction away from the lens axis resulting in elliptical images, even on the plane of least confusion. To minimize the distortion and aberration affects, the film planes were tilted at 3.7° from the back plate. This angle was obtained by tilting the film plane until the particles appeared to have the least aberrations. This caused the magnification to vary over the entire field and to depend on the off-axis angle. The physical distances used for the stereoscopic PIV recording system for all the experiments were: $d_{\text{liquid layer}} = 310.06$ mm, $d_{\text{air layer}} = 128.2$ mm, and $d_{\text{image distance}} = 180.3$ mm.

An aluminum beam connected the camera's back plate to an XY-stepper motor stage. The stepper motor enabled the film plane to be translated at a constant velocity in the y-direction during PIV recording to provide a simple method of image shifting to resolve directional ambiguity. The image shift velocity used for all the experiments equaled 4.202 mm/s.

The camera triggering mechanism layout is shown in Figure 3. During the PIV recording process the camera's film plane translated from left to right at a constant ve-

locity. The solenoid drivers activated the solenoids after a predetermined time delay to open both lens shutters simultaneously.

2.4 Interface Layer Height Measurement

The shadowgraph technique has been previously applied by Heidt (1977) to investigate the interfacial layer. Index of refraction variations due to the variation in the water temperature are greatest near the plate surface and in the interfacial layer. The strong variation of index of refraction at the interface made possible the measurement of the interface location as a function of time.

A white light source was used for the illumination. The light source was placed as far away from the test section as possible to minimize errors caused by non-parallel light rays. The light was reflected 90° by a plane mirror into the test section as shown in Figure 3, and the shadowgraph image was projected on draftsman paper. The images on the paper were then recorded by a video camera. The interface could be seen clearly from the shadowgraph and the mean height of the interface region was defined by averaging in the y-direction. The error in measuring the interface height was estimated to be approximately 2 mm.

2.5 Interrogation and Stereo Combination

The PIV negatives were interrogated using the interrogation system described in Meinhardt *et al.* (1993). The system used eight Intel i860 array processors running in parallel to perform the FFTs (Fast Fourier Transforms) for calculating the cross-correlation. The system used an adaptive windowing technique to optimize its performance. In this technique the relative offset of the second correlation window is adapted based on neighboring vectors to maximize the signal to noise ratio and to minimize in-plane velocity bias caused by loss of in-plane image pairs. In the present situation the flow field had two velocity scales, one for the mixed layer and the other for the inversion layer. Due to the large dynamic range it was critical to have a system which could continually vary the relative window offset during the interrogation for good signal-to-noise ratio.

A computer program was then used to remove bad vectors and replace the missing and removed vectors with either the choice 2 or 3 vectors. Choice 2 and 3 vectors were calculated from the second and third highest correlation peaks, respectively. Typically, no more than 5% of the velocity vectors were permanently removed, and roughly 1 to 2% of the vectors were choice 2 or 3.

The two velocity fields were combined using the stereo program described in Prasad and Adrian (1993). This program uses a raytracing scheme to measure all three velocity vector components from the two measured in-plane velocity fields. The combining algorithm removed the affects of the distortions caused by the liquid-air interface. The present experimental data was not smoothed.

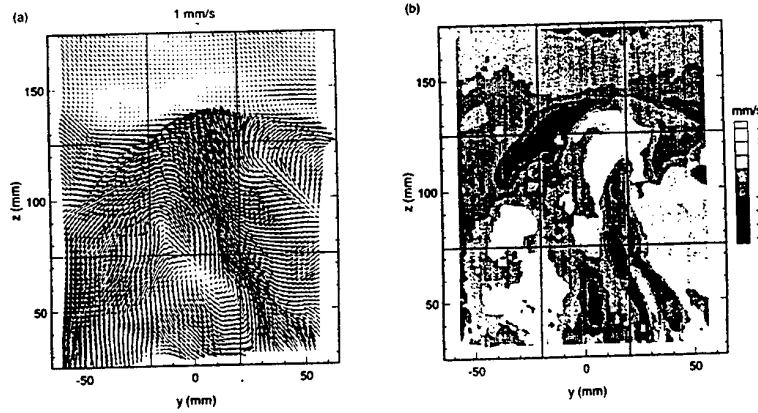


Figure 4 Velocity Field for $\Gamma = 0.29$ °C/cm : (a) In-Plane Velocities (Only Every Other Vector Shown),
(b) Contours of Out-Of-Plane Velocities. $z = 134$ mm, $w = 3.49$ mm/s, $Re = 526$, $Q_0 = 0.127$ °C mm/s.

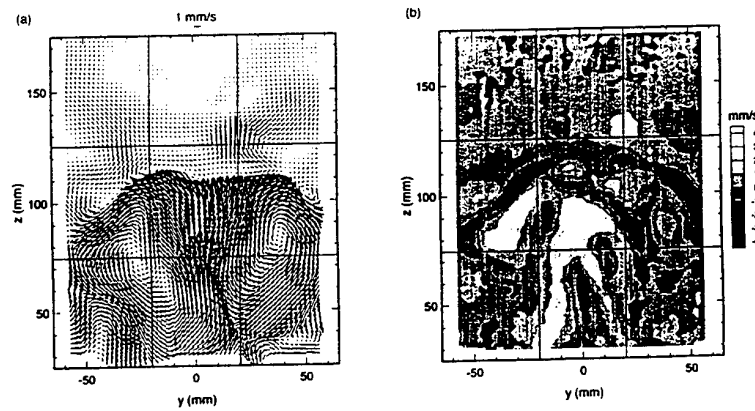


Figure 5 Velocity Field for $\Gamma = 0.55$ °C/cm : (a) In-Plane Velocities (Only Every Other Vector Shown),
(b) Contours of Out-Of-Plane Velocities. $z = 110$ mm, $w = 3.03$ mm/s, $Re = 361$, $Q_0 = 0.107$ °C mm/s.

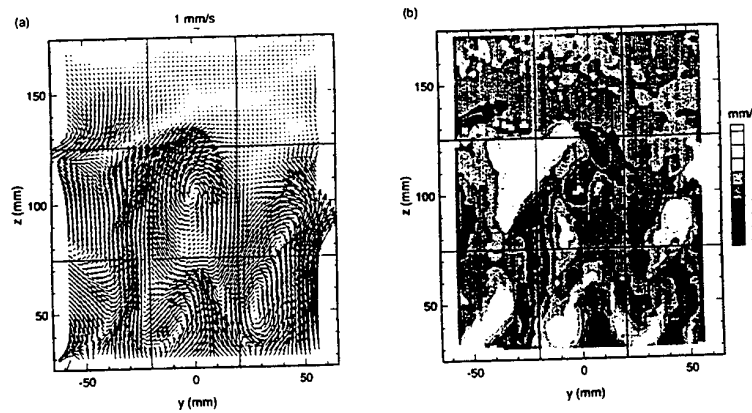


Figure 6 Velocity Field for $\Gamma = 0.55$ °C/cm ; (a) In-Plane Velocities (Only Every Other Vector Shown),
(b) Contours of Out-Of-Plane Velocities, $z = 131$ mm, $w = 3.41$ mm/s, $Re = 483$, $Q_0 = 0.128$ °C mm/s.

3. Results

3.1 Velocity Fields

Figures 4, 5, and 6 show three examples of velocity fields measured in the experiments. From the various velocity fields measured certain characteristics were observed:

- Two coherent structures were observed, upward moving mushroom-like plumes, and downward moving sheet-like down-drafts.
- The plumes spanned the height of the mixed layer.
- The plumes grew in width as they ascended upwards due to lateral entrainment.
- The plumes spread out latterly at the inversion.
- The plumes have large out-of-plane motion and appear to be three-dimensional.
- The flow in the inversion layer seems to be approximately two-dimensional.
- Vortices seem to form near plumes.
- Down-drafts occupy a much larger area than plumes.
- Down-drafts span the entire height of the layer.
- The plumes penetrate further for the $\Gamma = 0.29^\circ\text{C/cm}$ than for $\Gamma = 0.55^\circ\text{C/cm}$ case.

All the plumes measured exhibited adjacent bands of strong positive and negative out-of-plane motion around the core and head of the plume, indicating that they spiral as they move upwards.

3.2 RMS Velocity Profiles

All the vertical profiles were calculated by first normalizing the velocities by w , and then ensemble averaging along constant z/z_i . Figures 7 and 8 show the measured horizontal and vertical rms velocity profiles for the present experiments along with other laboratory, atmospheric, and numerical results. The profiles are the ensemble average of the two interface layer temperature gradient cases. The trend of the present results seem to behave the same as the comparitors, except the present results are consistently lower in value. The present results are believed to be lower, because the Reynolds number of the present flow is lower than in other cases. The results of Kumar (1983) compare well with the current results, and the Reynolds numbers are similar for both cases.

The difference between the measured σ_u and σ_v is partly due to the error in measuring the out-plane velocity component (u), which is approximately three times larger than for the in-plane component (v) (Prasad and Adrian 1993). The added error would simply have the effect of shifting the rms profile to the right, which is clearly seen in Figure 7.

The rms profiles were checked for statistical convergence by examining how the rms values approached an asymptotic value with increased number of averaged velocity fields. It was concluded that the profiles are statis-

tically converged for z/z_i between approximately 0.3 to 1.25.

3.3 Dissipation Profiles

The measured dissipation profile is compared with dissipation measured in the atmosphere, other tank experiments, or obtained computationally in Figure 9. The dissipation for the present results was calculated by explicitly measuring 7 of the 9 dissipation terms, and the remaining two terms were calculated by assuming the flow to be axisymmetric. The measured dissipation compares well with those measured in the atmosphere, but it is almost twice as much as the dissipation obtained from LES or the other tank experiment of Deardorff and Willis (1985). They assumed the flow was isotropic when they calculated the dissipation. This assumption is incorrect, because the Reynolds number of their flow is too small. On the other hand, the Reynolds number in the atmosphere is five orders of magnitude higher than in tank experiments, and assuming isotropy is valid. The dissipation acts on the sub-grid scale, which is modeled in the LES. The models used in both of the LES seem to underestimate the dissipation.

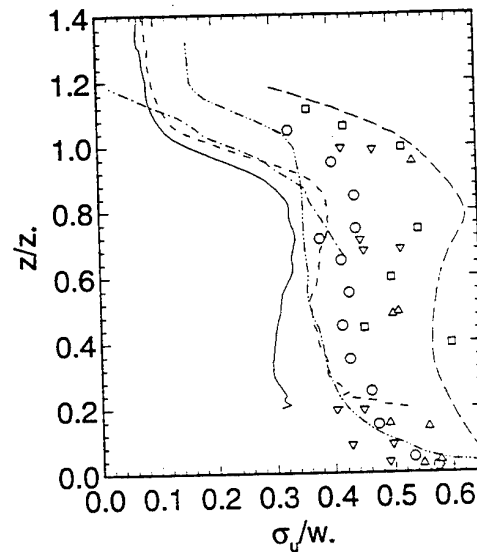


Figure 7 Comparison of Horizontal RMS Velocity Profiles. Solid Line = Present Data (σ_v), Dashed Line = Present Data (σ_u), Dash-Dot Line = Kumar (1983), Dotted Line = Schmidt and Shumann (1989), Long Dash = Caughey and Palmer (1979), Dash-Dot-Dot Line = Deardorff (1980), Open Circles = Willis and Deardorff (1974) Case S1, Open Squares = Deardorff and Willis (1985), Open Triangles = Lenschow *et al.* (1980) Feb. 24, Open Upside Down Triangles = Lenschow *et al.* (1980) Feb. 16.

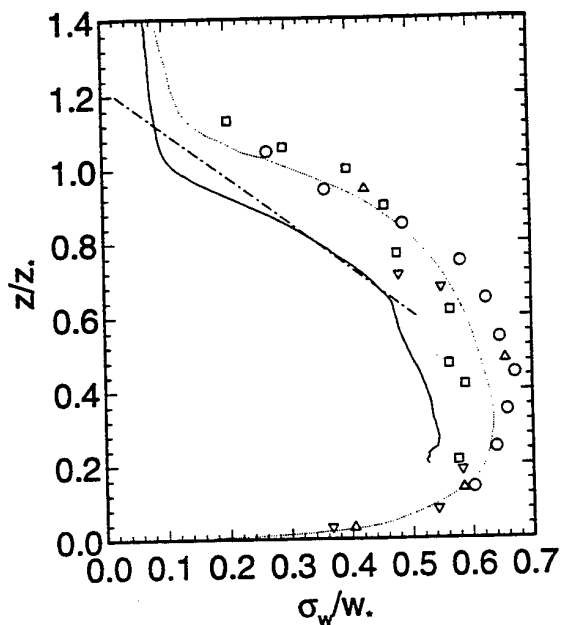


Figure 8 Comparison of Vertical RMS Velocity Profiles. Solid Line = Present Data. Other Symbols are Same as in Figure 7.

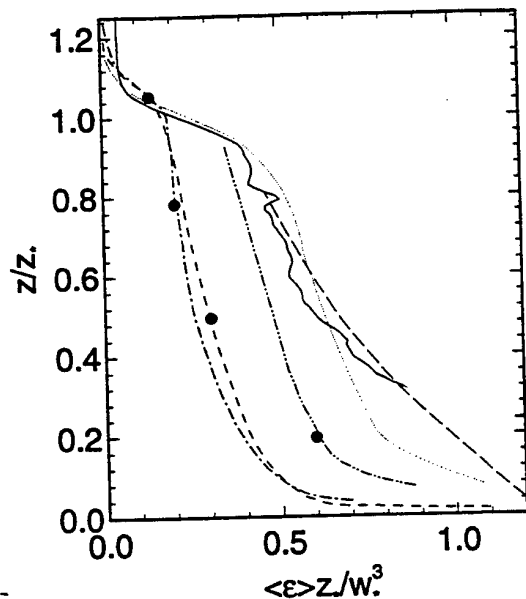


Figure 9 Comparison of Dissipation Profiles. Solid Line = Present Data. Dashed Line = Schmidt and Shumann (1989). Dotted Line = Caughey and Palmer (1979). Dash-Dot Line = Deardorff (1974). Long Dash Line = Druihet *et al.* (1983). Dash-Dot-Dot Line = Lenschow *et al.* (1980). Closed Circles = Deardorff and Willis (1985).

3.4 Two-Point Spatial Correlation Function

The two-point in-plane spatial correlation function was computed at 5 heights. A full three-dimensional axisymmetric two-point spatial correlation function database now exists. An example of the two-point in-plane correlation function is shown in Figure 10. The non-dimensional displacement vector in the y-direction between the first and second velocity positions is denoted by r_y/z .

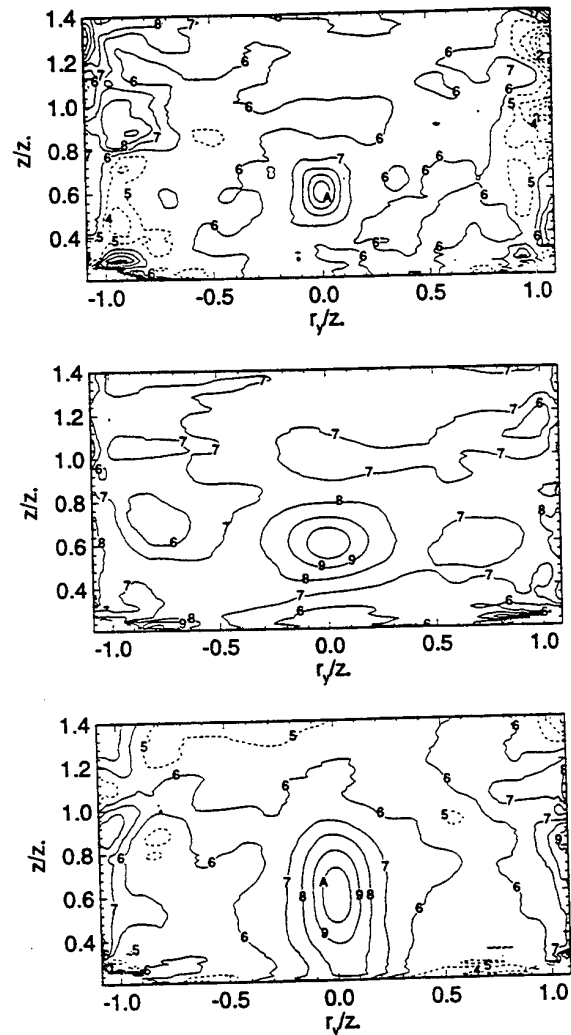


Figure 10 Two-Point In-Plane Spatial Correlation Function, $\Gamma = 0.29^\circ\text{C/cm}$, Stationary Point $z/z_0 = 0.6$, R_{xx} (Top Diagram), R_{yy} (Middle Diagram), R_{zz} (Bottom Diagram). Contour Marker = Contour Value: 6 = 0.0, 7 = 0.2, 8 = 0.4, 9 = 0.6, A = 0.8, B = 1.0.

REFERENCES

- Adrian, R.J. 1975, Turbulent Convection in Water Over Ice, J. Fluid Mechanics, vol. 69, pp. 753-781.
- Adrian, R.J. 1991, Particle-Imaging Techniques for Experimental Fluid Mechanics, Annual Rev. Fluid Mech., vol. 23, pp. 261-304.
- Caughey, S.J. & Palmer, S.G. 1979, Some Aspects of Turbulence Structure Through the Depth of the Convective Boundary Layer, Quarterly J. Royal Meteorological Soc., vol. 105, pp. 811-827.
- Chandrasekhar, S. 1950, The Theory of Axisymmetric Turbulence, Philosophical Transactions A, vol. 242, pp. 557-577.
- Deardorff, J.W. 1970, Convective Temperature and Velocity Scales for the Unstable Planetary Layer and for Rayleigh Convection, J. Atmospheric Sci., vol. 36, pp. 1211-1213.
- Deardorff, J.W. 1972, Numerical Investigation of Neutral and Unstable Planetary Boundary Layers, J. Atmospheric Sci., vol. 29, pp. 91-115.
- Deardorff, J.W. 1974, Three-Dimensional Numerical Study of Turbulence in an Entraining Mixed Layer, Boundary-Layer Meteorology, vol. 7, pp. 199-226.
- Deardorff, J.W. & Willis, G.E. 1985, Further Results Form a Laboratory Model of the Convective Planetary Boundary Layer, Boundary-Layer Meteorology, vol. 32, pp. 205-236.
- Deardorff, J.W., Willis, G.E. & Lilly, D.K. 1969, Laboratory Investigation of Non-Steady Penetrative Convection, J. Fluid Mechanics, vol. 35, pp. 7-31.
- Druilhet, A., Frangi, J.P., Guedalia, D., & Fontan, J. 1983, Experimental Studies of the Turbulence Structure Parameters of the Convective Boundary Layer, J. Clim. Appl. Met., vol. 22, pp. 594-608.
- Ferreira, R.T.D.S 1978, Unsteady Turbulent Thermal Convection, Ph.D. Thesis, University of Illinois, Urbana, Illinois.
- Heidt, F.D. 1977, The Growth of the Mixed Layer in a Stratified Fluid Due to Penetrative Convection, Boundary-Layer Meteorology, vol. 12, pp. 439-461.
- Kumar, R. 1983, Studies in Unsteady Penetrative Thermal Convection, Ph.D. Thesis, University of Illinois, Urbana, Illinois.
- Kumar, R. & Adrian, R.J. 1986, Higher Order Moments in the Entrainment Zone of Turbulent Penetrative Thermal Convection, J. Heat Transfer, vol. 108, pp. 323-329.
- Lenschow, D.H., Wyngaard, J.C. & Pennel, W.T. 1980, Mean-Field and Second-Moment Budgets in a Baroclinic Convective Boundary Layer, J. Atmospheric Sci., vol. 37, pp. 1313-1326.
- Meinhart, C.D., Prasad, A.K. & Adrian, R.J. 1993, A Parallel Digital Processor System For Particle Image Velocimetry, Measurement Sci. Tech., vol. 4, pp. 619-626.
- Prasad, A.K. & Adrian, R.J. 1993, Stereoscopic Particle Image Velocimetry Applied to Liquid Flows, Experiments in Fluids, vol. 15, pp. 49-60.
- Schmidt, H. & Schumann, U. 1989, Coherent Structure of the Convective Boundary Layer Derived From Large-Eddy Simulations, J. Fluid Mechanics, vol. 200, pp. 511-562.
- Troy, V. 1994, A Study of Turbulent Penetrative Thermal Convection Using Stereoscopic Particle Image Velocimetry, M.S. Thesis, University of Illinois, Urbana, Illinois.
- Willis, G.E. & Deardorff, J.W. 1974, A Laboratory Model of the Unstable Planetary Boundary Layer, J. Fluid Mechanics, vol. 31, pp. 1297-1307.
- Willis, G.E. & Deardorff, J.W. 1979, Laboratory Observation of Turbulent Penetrative Convection Planforms, J. Geophysical Research, vol. 84, pp. 295-302.

ACKNOWLEDGMENT

This research was supported by a grant NSF ATM 89-20605.

LDV-MEASUREMENTS ON THERMAL CONVECTIVE INSTABILITIES IN SPHERICAL GAP FLOW

Christoph Egbers, Wolfgang Beyer and Hans J. Rath

Center of Applied Space Technology and Microgravity (ZARM)
University of Bremen, 28359 Bremen, F.R.G.

ABSTRACT

The hydrodynamic instabilities of a viscous incompressible fluid flow in the gap between two concentric spheres are investigated for the case, that under axial gravitation the inner sphere is heated and the outer one remains at a lower temperature. New flow visualization studies and laser-Doppler measurements are presented for a wide range of Rayleigh numbers ($Ra \leq 3 \cdot 10^6$) and aspect ratios ($0.08 \leq \beta \leq 0.5$). It was found, that the laminar convective basic flow loses its stability in different ways. The instabilities occurring depend strongly on the aspect ratio and on the Rayleigh number. Steady and fully three-dimensional banana-type cells as well as time dependent ring vortices and polygonal structures are obtained.

1 INTRODUCTION

Thermal convection in the gap between two concentric spherical shells under a central force field represents an important model for astro- and geophysics. In contrast, natural convection in an axially stratified spherical fluid shell — considered here — is of practical interest in various engineering applications such as heat exchangers, thermal storage systems and solar energy collectors. Furthermore, investigations on thermal instabilities occurring in the spherical gap flow are of basic importance especially for the understanding of symmetry-breaking bifurcations during the transition to turbulence. Most of previous experimental investigations were restricted to the case of heat transfer measurements at two isothermal concentric spheres (Bishop et al, 1966; Powe et al., 1980; Scanlan et al, 1970). Figure 1 shows the basic motion inbetween two concentric spheres due to a radial temperature gradient in an axial gravitational field (Bühler, 1993). Depending on the aspect ratio and the temperature gradient, three other distinct types of flow were observed. These are the "crescent-eddy" type for all gap widths, the "kidney-shaped-eddy" type arising in wide gaps and the "falling-vortices" type occurring in narrow gaps.

The crescent-eddy and kidney-eddy types of flow are steady and axisymmetric, whereas the falling-vortices type is unsteady and highly three-dimensional. The highly three-dimensional character of the first instability could be improved in other experiments in narrow and medium gaps (Nakagawa et al., 1992; Egbers, 1994). The superposition of rotation and thermal convection in the spherical gap yields to equatorially asymmetric Taylor vortices (Bühler, 1993; Dallmann et al, 1980).

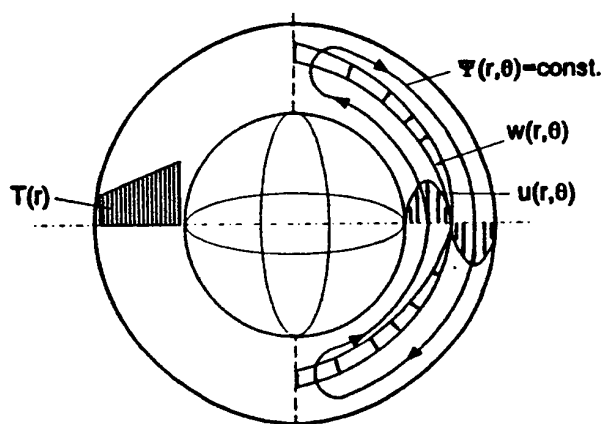


Fig.1: Geometry of the spherical gap, temperature profile and basic convective motion (Bühler, 1993)

In this work, we concentrate only on thermal convective instabilities without rotation. The convective motions are characterized by three control parameters, i.e. the aspect ratio $\beta = (R_o - R_i)/R_i$, the Rayleigh number $Ra = (\alpha \cdot g \cdot \Delta T \cdot d^3) / (\chi \cdot \nu)$ and the Prandtl number $Pr = \nu / \chi$, where R_i and R_o are the inner and outer radii, d is the gap width, α the expansion coefficient, g axial gravitation, ΔT the temperature difference between the inner and outer sphere ($T_i > T_o$), ν is the kinematic viscosity and χ the thermal diffusivity.

2 EXPERIMENTAL METHODS

2.1 Experimental configuration

For the experimental investigations reported here, the spherical Couette flow apparatus and the laser-Doppler measuring system were used as in our previous work on isothermal Taylor-vortex flow and wide gap instabilities (Egbers & Rath, 1996). The outer sphere ($R_o = 40.00 \pm 0.02$ mm) is composed of two transparent acrylic plastic hemispheres. The upper hemisphere has a spherical outer surface of about $0 \leq \theta \leq 110^\circ$ to investigate whether the occurring flow patterns are symmetric with respect to the equatorial plane or not. The four inner spherical shells with aspect ratios $\beta = 0.08$, $\beta = 0.18$, $\beta = 0.33$ and $\beta = 0.5$ are made out of aluminium. For heating the inner spheres uniformly, a heating facility was mounted into the inner spherical shells. A temperature accuracy of $\pm 0.1^\circ\text{C}$ was achieved for all six temperature sensors (PT 1000) used in our experiments: For controlling the Rayleigh number, three temperature sensors are installed just below the outer surface of the inner sphere at latitudes $\theta_{11} = 10^\circ$, $\theta_{12} = 80^\circ$ and $\theta_{13} = 160^\circ$. Three other temperature sensors are installed at the inner surface of the outer sphere at latitudes $\theta_{o1} = 0^\circ$, $\theta_{o2} = 45^\circ$ and $\theta_{o3} = 90^\circ$. A constant temperature gradient, i.e. Rayleigh number is obtained using a special PID-control.

2.2 Flow visualization

The thermal driven fluid flow inbetween the spherical gap was made visible using small aluminium flakes as tracer particles. The concentration by weight was 0.05%. The viscosities of the working fluids with tracer particles were measured with a VOR-rheometer (BOHLIN-Reologi AB, Sweden). An effect on the viscosity was not detected. The meridional direction of the flow was obtained by light sheet illumination, while for the azimuthal and polar regions a global illumination was used as described in the work of Egbers (1994).

2.3 Laser-Doppler-velocimeter measuring system

For the application of laser-Doppler-velocimetry (LDV) on the spherical Couette flow experiment, a special traversing system has been constructed to mount the optic probe on the spherical Couette flow experiment as depicted in figure 2 (a), while the laser and the transmitter are mounted apart from the experiment on a mounting bench. The traversing system consists of a high-precision bow with a traversing sledge and a traversing table. The traversing sledge is capable of moving the optic probe in meridional direction ($0 \leq \theta \leq 110^\circ$) and the traversing table is capable of moving in radial direction over a range of 60 mm in order to determine the meridional dependence of the

velocity and to obtain velocity profiles. The laser-Doppler-velocimeter system used in our experiments, consists of a 100 mW Ar-laser, a transmitter unit and a 1-D fiber-flow optic-probe (DANTEC-Electronics, Denmark). A frequency shift is added by the Bragg-cell-unit to one of the beam pair to allow for measurements of reversing flows. The optic probe with a fibre optic cable is connected to the transmitter via manipulators. The optical part of the laser-Doppler-system, which uses the dual beam backscatter geometry, is shown schematically in figure 2(b). The backscattered light is focussed on a photomultiplier tube. All LDV measurements were made with the traversing system mentioned above. Data records of each measurement in the radial direction of the gap consisted of 12000 validated Doppler bursts accumulated in the buffer interface. A principle sketch of the data processing technique with the laser-Doppler signal-processor, which is based on FFT-technique, is shown in figure 2(c). Parameters characterizing the laser-Doppler-velocimeter and traversing data are listed in table 1. For all LDV-measurements small titanium dioxide particles ($0.5 \mu\text{m}$) are suspended in the working fluid (M3-oil, $\text{Pr} = 37.5$).

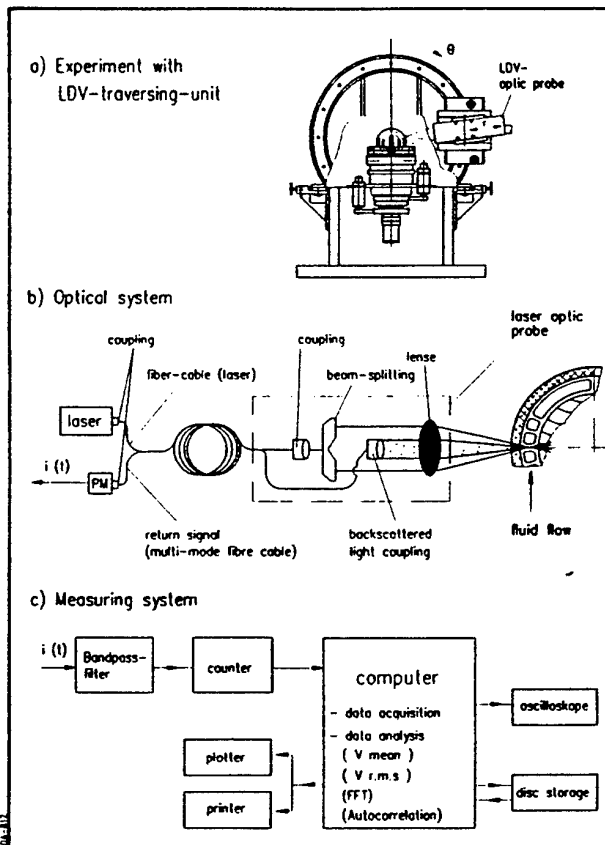


Fig. 2: Schematic diagram of the applied laser-Doppler-velocimeter (LDV) system:

- (a): Traversing system for the LDV optic probe
- (b): Optical system
- (c): Measuring system

Table 1: Instrumentation data of the laser-Doppler velocimeter and the traversing system

Ar-laser	100	[mW]
focal length	160	[mm]
wavelength	514.5	[nm]
beam spacing	38	[mm]
beam diameter	2.2	[mm]
number of fringes	22	[-]
probe volume: length	0.4	[mm]
diameter	0.05	[mm]
fringe spacing	2.18	[μ m]
Bragg-cell frequency	40	[MHz]
meridional traversing angle	$0 \leq \theta \leq 110^\circ$	
radial traversing distance	$0 \leq r \leq 60$ mm	

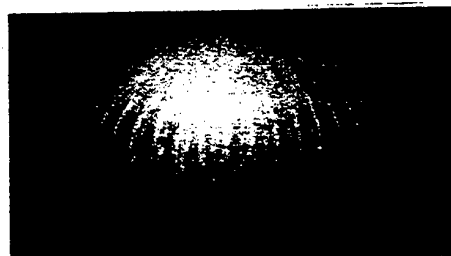
The application of the LDV-technique on the spherical Couette flow experiment requires an optical correction for the accurate determinations of the probe volume locations and for the interference fringe spacing due to refraction effects of the spherical outer surface. Because the probe is adjusted in radial direction, the optical axis of the front lense of the probe passes perpendicular through the spherical outer surface. Thus, the correction for the two laser beams, which are in the same plane, could be calculated for a cylindrical surface. However, the fact, that a small probing volume is needed to produce sufficient spatial resolution, which could be obtained only by a large intersection angle, the small-angle approximation cannot be used in this case. The correction method used in this work for the case of large intersection angles has been applied earlier by Egbers (1994). The ray tracing begins at the front lense of the LDV optics. The equations describing the beam propagation follow immediately from Snells law and from geometric considerations. For further details, the reader might be referred to our previous works (Egbers, 1994; Egbers & Rath, 1996).

3 RESULTS

3.1 Visual observations of thermal convective flows

Some characteristic photographs of thermal convective instabilities between concentric spheres as a function of aspect ratio and Rayleigh numbers are illustrated in figure 3(a)-(d): For small and medium aspect ratios ($0.08 \leq \beta \leq 0.18$), the first instability manifests itself as a transition from laminar basic convective to a fully three-dimensional flow in the form of steady, non-axisymmetric and non-equatorially symmetric banana cell type, oriented in north-south direction and concentrated in the northern hemisphere (figure 3(a),(b)). The corresponding critical Rayleigh numbers are $Ra_c = 7 \cdot 10^3$ ($\beta=0.08$) and $Ra_c = 1.2 \cdot 10^4$ ($\beta=0.18$) for the transition from

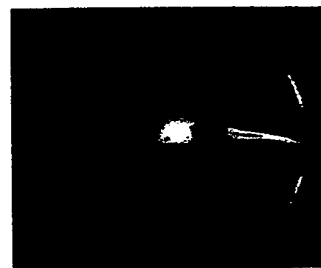
axisymmetric laminar basic flow to fully three-dimensional banana-type vortex flow. The results of critical Rayleigh numbers and the number of banana-type cells are in a very good agreement with a fully three-dimensional numerical simulation of the problem calculated by Liu et al. (1995).



(a): $\beta = 0.08$, $Ra = 1.57 \cdot 10^4$



(b): $\beta = 0.18$, $Ra = 4.24 \cdot 10^4$



(c): $\beta = 0.33$, $Ra = 1.4 \cdot 10^5$



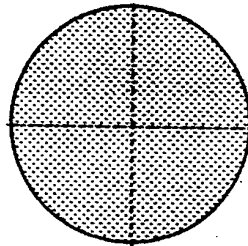
(d): $\beta = 0.50$, $Ra = 1.0 \cdot 10^6$

Fig. 3: Thermal convective instabilities between concentric spheres as a function of aspect ratio and Rayleigh numbers:

- (a)-(b): steady "banana-cell" type instability
- (c)-(d): polygonal structures and time-dependent "ring-vortices"

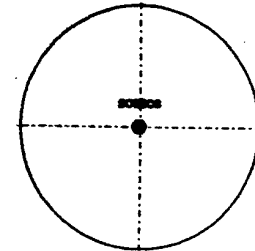
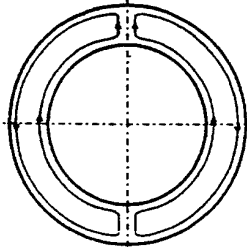
1: basic state ($v = 0$)

perspective of
meridional plane

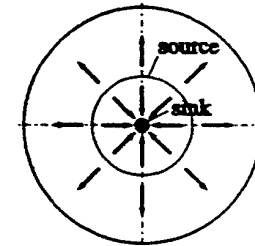
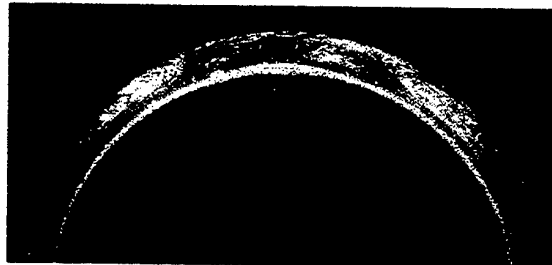
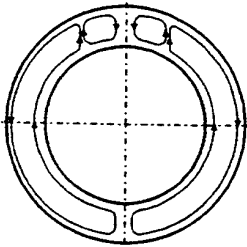


perspective of outer
sphere (northpole)

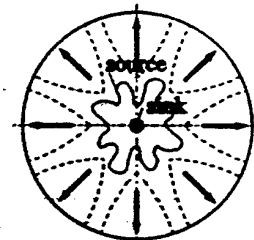
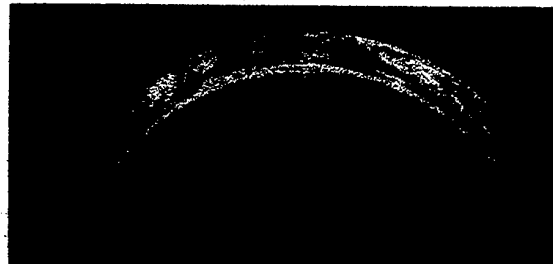
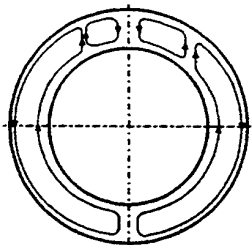
2: basic flow



3: axisymmetric



4: non-axisymmetric



5: banana type cell instability

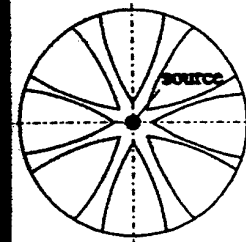
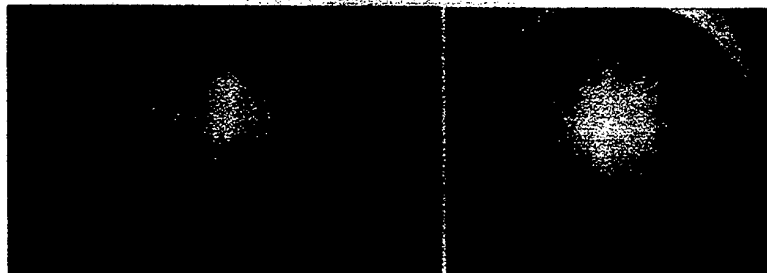
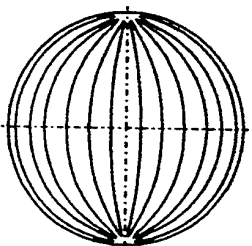


Fig. 4: Principle sketch of the development of thermal rolls in small and medium gap widths ($\beta \leq 0.18$):
Perspective of the meridional plane (left) and of the northpole (right)

Figure 4 shows the principle sketch of the development of the steady banana cell type instability (thermal rolls). Based on the conducting state ($v = 0$), the flow starts in the form of a basic motion due to buoyancy effects along the inner sphere up to the north pole, moves to the top and then along the outer sphere down to the south pole (closed motion in meridional direction). This basic flow remains rotational-symmetric until the Rayleigh number reaches the critical value. Just above Ra_C , a small vortex pair appears near the north pole, which becomes non-axisymmetric and spreads to the south pole. The whole gap is filled with spreading vortices in the form of non-axisymmetric banana cells. The corresponding perspective of the outer sphere from the northern pole describes the same development in the form of sources and sinks.

For wide gap width $\beta \geq 0.33$, however, banana-type cells could not be detected. The first instability manifests itself as a direct transition to time dependent motions with unsteady ring-vortices. These ring-vortices tend to change into a polygonal structure (figure 3(c)) with increasing time as was also reported by Nakagawa et al. (1992). For $\beta = 0.5$, we only find a direct transition from laminar basic flow into a time dependent ring vortex flow as illustrated in figure 3 (d). This flow can be described as illustrated schematically in figure 5. Due to increasing buoyancy with increasing the Rayleigh number, the meridional velocity along the inner sphere also increases and different vortices occur at the north pole, which move along the outer sphere down to the equatorial region. The frequencies of these time dependent ring vortices spreading from the pole to the equator were measured by optical tracking. The results are illustrated in figure 6 as a function of the Rayleigh number and two different Prandtl numbers. With increasing the Rayleigh number, the ring vortex frequency also increases. This type of flow remains unsteady until the flow becomes fully turbulent.

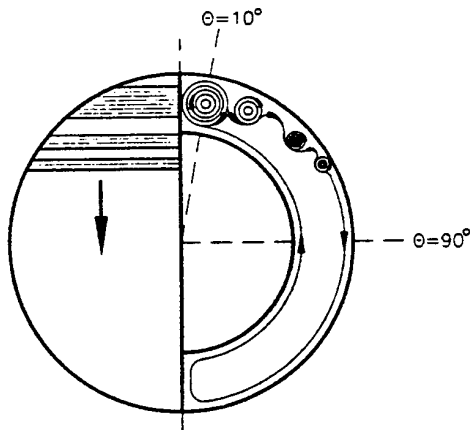


Fig. 5: Principle sketch of the development of unsteady ring vortex flow in wide gap width ($\beta = 0.5$): global side view (left); meridional plane (right)

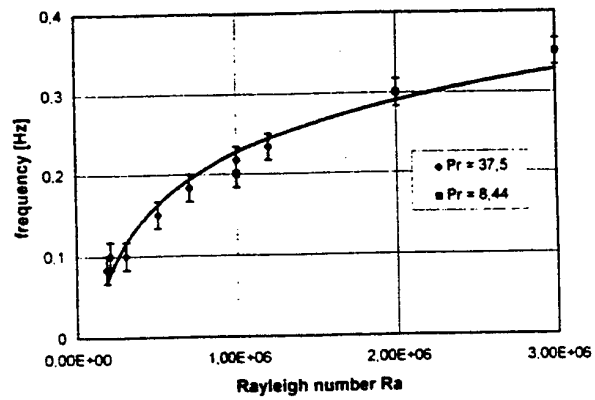


Fig. 6: The dependence of thermal ring vortex frequency as a function of the Rayleigh number

3.2 LDV-measurements on thermal ring vortices

The LDV-measurements were undertaken to describe the time dependent behaviour and the generation of the thermal convective instability in wide gaps in the form of ring vortices falling down from the pole to the equator. The meridional velocity profiles as a function of different Rayleigh numbers and of the radial coordinate ($0 \leq r^* \leq 1$) were measured. Characteristic results are illustrated in figure 7(a) for $Ra = 1.5 \cdot 10^5$ and in figure 7(b) for $Ra = 1.0 \cdot 10^6$ ($Ra_C = 1.8 \cdot 10^5$). The measurements were made at the equator ($\theta = 90^\circ$).

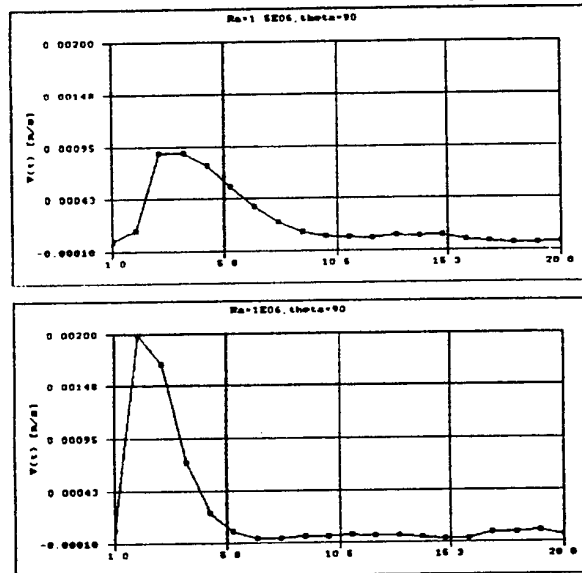


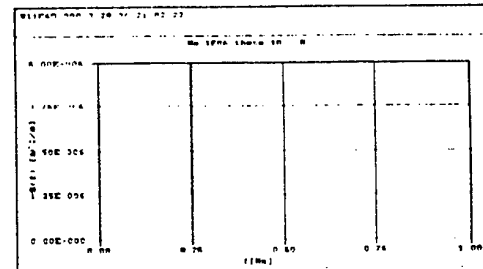
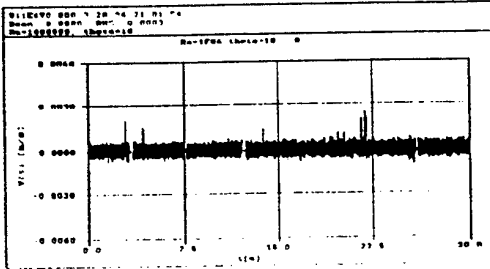
Fig. 7: The meridional velocity profile $u(r, \theta)$ as a function of the radial coordinate ($0 \leq r^* \leq 1$) for $\beta = 0.5$, $\theta = 90^\circ$: (a) $Ra = 1.5 \cdot 10^5$, (b) $Ra = 1.0 \cdot 10^6$

Figure 8 shows the velocity/time plots, the frequencies and autocorrelation functions of the meridional velocity as a function of the radial coordinate ($0 \leq r^* \leq 1$).

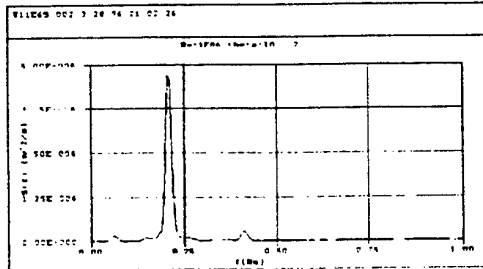
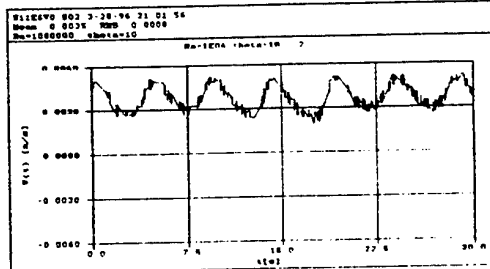
velocity/time plots

Fourier spectra

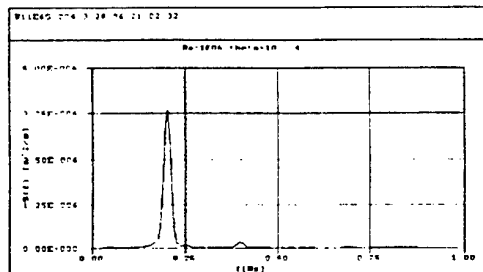
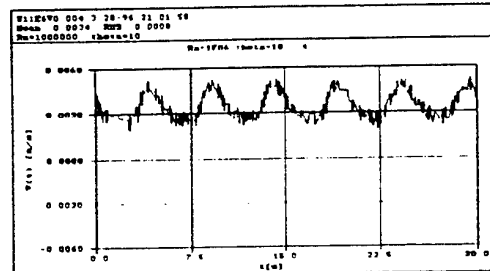
$r^* = 0.0$



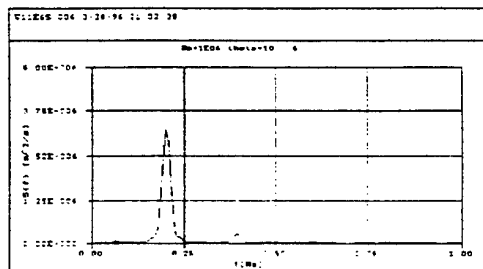
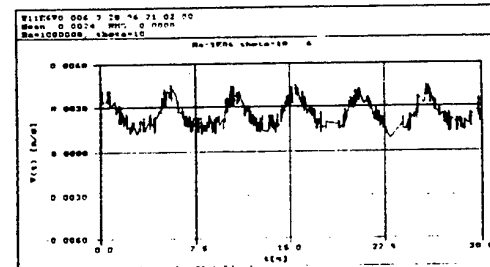
$r^* = 0.1$



$r^* = 0.2$



$r^* = 0.3$



$r^* = 0.4$

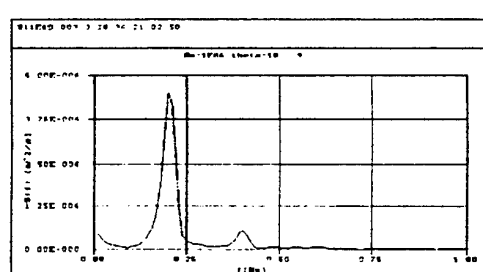
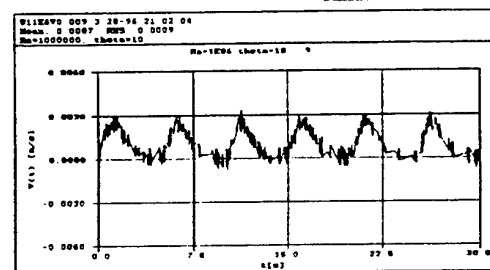
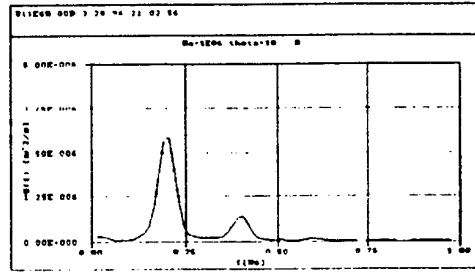
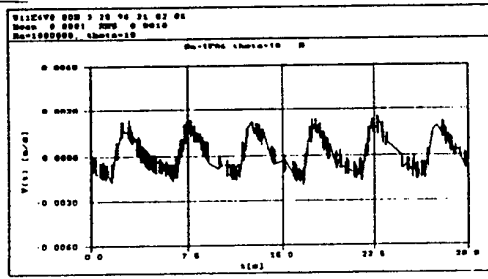


Fig. 8: The temporal dependences (left) and the calculated Fourier spectra (right) of the meridional velocity component for the time-dependent ring vortex flow as a function of the radial coordinate ($0 \leq r^* \leq 1$) for $Ra = 1.0 \cdot 10^6$, $\beta = 0.5$, $\Theta = 10^\circ$

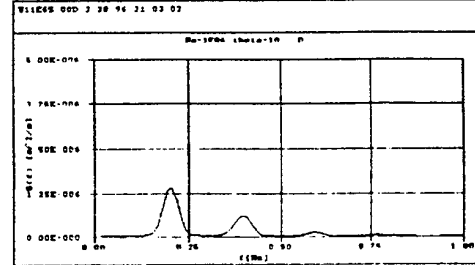
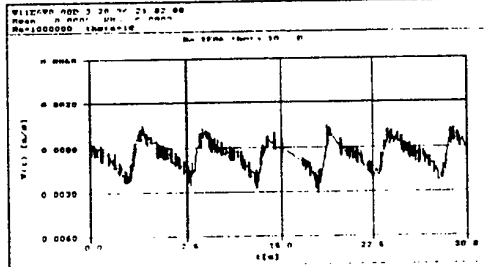
velocity/time plots

Fourier spectra

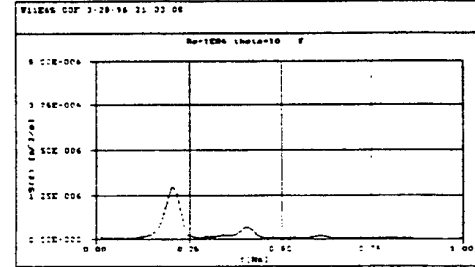
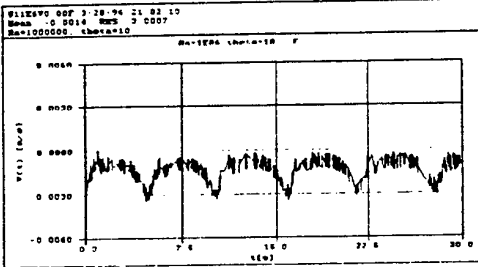
$r^* = 0.5$



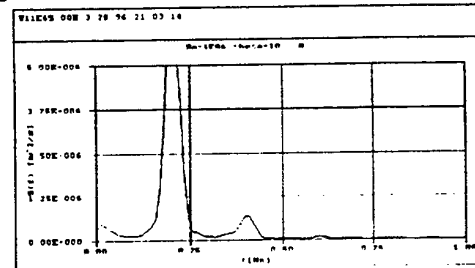
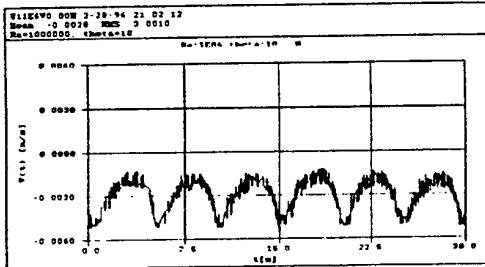
$r^* = 0.6$



$r^* = 0.7$



$r^* = 0.8$



$r^* = 1.0$

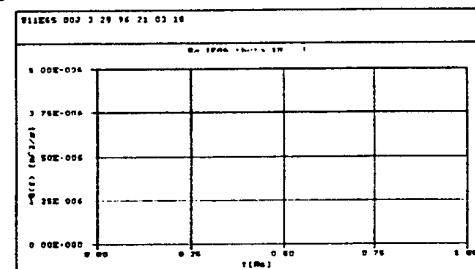
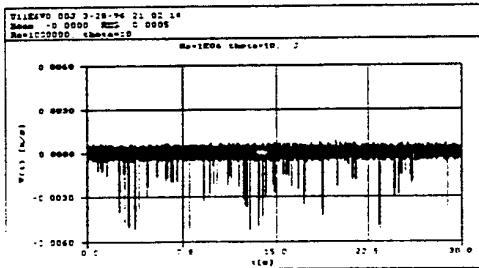


Fig. 8: The temporal dependences (left) and the calculated Fourier spectra (right) of the meridional velocity component for the time-dependent ring vortex flow as a function of the radial coordinate ($0 \leq r^* \leq 1$) for $Ra = 1.0 \cdot 10^6$, $\beta = 0.5$, $\theta = 10^\circ$

These measurements were carried out near the polar region ($\Theta = 10^\circ$), where the ring vortices begin to oscillate. The corresponding autocorrelation functions and the power spectra show the conservation of this periodicity.

4 CONCLUSION

In the present paper it has been shown that the laminar basic convective flow in between two concentric spherical shells heated from within bifurcates in different ways depending on the aspect ratio. For small and medium gap widths ($\beta \leq 0.18$), the first instability manifests itself in the form of steady thermal rolls ("banana cell instability"), while for larger gap widths a time dependent motion in the form of unsteady ring vortices occur. The frequencies of this ring vortex flow spreading from the north pole to the equator were obtained by LDV-measurements of the meridional velocity component. The results are in a good quantitative agreement with the frequencies obtained by optical tracking and flow visualization studies.

ACKNOWLEDGEMENTS

This work is supported by the Deutsche Agentur für Raumfahrtangelegenheiten (DARA) under grant number 50 WM 9443. The authors thank Prof. Bühler and Prof. Busse for fruitful discussions and the students Mr. Fischer and Mr. Linek for their help during this work.

REFERENCES

- Bishop, E.H., Mack, L.R. & Scanlan, J.A. (1966): Heat transfer by natural convection between concentric spheres. Int. J. Heat Mass Transfer **9**, 649-662
- Bühler, K. (1993): Taylor vortex flow with heat transfer in spherical gap flows. Proceedings of 8th Couette-Taylor Meeting, Nice, France, March 29-31
- Dallmann, R.J. & Douglass, R.W. (1980): Convection in a rotating spherical annulus with a uniform axial gravitational field. Int. J. Heat Mass Transfer **23**, 1303-1312
- Egbers, C. (1994): Zur Stabilität der Strömung im konzentrischen Kugelspalt. Dissertation, Univ. Bremen
- Egbers, C. & Rath, H.J. (1995): The existence of Taylor vortices and wide-gap instabilities in spherical Couette flow. Acta Mech., **111**, 3-4, 125-140
- Egbers, C. & Rath, H.J. (1996): LDV-measurements on wide gap instabilities in spherical Couette flow. Developments in Laser Techniques and Applications to Fluid Mechanics. Proc. 7th Int. Symp., Lisbon, Port., eds.: R.J. Adrian, D.F.G. Durao, F. Durst, M.V. Heitor, M. Maeda & J. Whitelaw, 45-66, Springer
- Linek, M. (1994): Experimentelle Untersuchungen zur thermischen Konvektion im konzentrischen Kugelspalt. Internal report, ZARM, Universität Bremen
- Liu, M., Egbers, C. & Rath, H.J. (1995): Three-dimensional natural convection in a narrow spherical shell. submitted to J. Fluid Mech.
- Nakagawa, T., Zierep, J., Bühler, K., Wimmer, M. and Kircharz, K.R. (1992): Thermal Convection between two concentric spheres. Proceedings of the 2nd JSME-KSME thermal engineering conference, Oct. 19-21
- Powe, R.E., Warrington, R.O. & Scanlan, J.A. (1980): Natural convective flow between a body and its spherical enclosure. Int. J. Heat Mass Transfer **23**, 1337-1350
- Scanlan, J.A., Bishop, E.H. & Powe, R.E. (1970): Natural convection heat transfer between concentric spheres. Int. J. Heat Mass Transfer **13**, 1857-1872
- Yin, S.H., Bishop, E.H., Scanlan, J.A. & Powe, R.E. (1970): Natural convective flow patterns in spherical annuli. Int. J. Heat Mass Transfer **16**, 1785-1795

MIXING IN GRAVITY CURRENT HEADS FLOWING OVER ROUGH SURFACES

W.D. Peters¹, J.E.S. Venart² and S.R. Cogswell³

¹ Department of Engineering, University of Prince Edward Island, Charlottetown, Prince Edward Island, Canada

² Fire Science Centre, University of New Brunswick, Fredericton, New Brunswick, Canada

³ EMR Microwave Technology Corporation, Fredericton, New Brunswick, Canada

ABSTRACT

A two-dimensional full-field quantitative visualization technique is used to assess the mixing that occurs in gravity current heads flowing over rough surfaces. This technique combines small-scale saltwater modelling, laser-induced dye fluorescence and video image enhancement to provide information about the mixing behaviour and associated concentration fields that exist in this density-differentiated fluid mixing system. The effects of surface roughness and initial fluid density difference on flow dynamics and head dilution are examined with potential contributions in the area of heavier-than-air gas (HTAG) dispersion.

1. INTRODUCTION

Gravity currents belong to a class of fluid flows in which buoyant forces, generated by density variations, produce motions predominantly in a direction normal to the gravity vector. This flow can be created, for instance, when a heavier fluid is introduced into a reservoir of less dense fluid after which it slumps to the bottom and spreads horizontally as a gravity current. Since the fluids forming this flow system are generally miscible, mixing plays an important role in the flow dynamics.

The dominant feature of this fluid structure is a well defined raised head at the leading edge of a shallower flowing layer. The leading point, or nose, is slightly elevated, allowing less dense ambient fluid to be overrun by the head. As the system advances, fluid settles into the area behind the head and above the upstream current layer.

Two basic gravity current mixing mechanisms have been defined by the large amount of research performed on the subject. Firstly, Kelvin-Helmholtz instabilities, initiated by velocity and density gradients at the intruding head/ambient fluid interface, lead to mixing in this region. Secondly, mixing internal to the head region arises as a layer of lighter ambient fluid is overrun by the advancing head. The velocity shear between this overrun fluid and the current head causes further Kelvin-Helmholtz instabilities at this level; additionally, Taylor instabilities, due to

packets of lighter fluid rising through the structure, further contribute to, and perhaps, even dominate, the internal dilution process.

2. REVIEW OF PAST WORK

Many fluid flow problems exist in which laser-induced fluorescence can provide valuable information about the interior fluid regions not possible with conventional dye techniques. Mapping of species concentration, density or temperature in a planar field, or along a line, is the most frequently cited use of this technique.

Research by Hesselink (1988), Nash et al. (1995) and Cruyningen et al. (1990), for instance, adds to the credibility of this widely accepted visualization method. As the success of this technique is closely linked to the fluorescent dye that is used, it is necessary to completely understand its behaviour. Walker (1987) provides a very thorough and extensive quantitative examination of one of the more popular fluorescent dyes, fluorescein sodium.

Salt water modelling has been shown to be very useful in the study of gravity current flows (Peters et al., 1996). Researchers such as Chen (1980), Chobotov et al. (1986), Zukoski and Kubota (1988), Simpson (1987), Simpson and Britter (1979) and Winant and Bratkovich (1977) have used this technique extensively to examine the same class of flows yielding a valuable resource of information. However, none of this work has used laser-induced fluorescence as the visualization technique.

One conclusion of the Simpson and Britter work, for instance, was that the shear between the gravity current head and ambient fluid was the main mixing process at the front. Consequently, they stated that the overrun less dense fluid may be neglected in terms of the overall mixing.

Winant and Bratkovich, however, observed large density fluctuations in the head region. They concluded that these variations seemed to be a result of the gravitational instability between discrete parcels of unmixed lighter fluid entrained at the leading edge of the structure, rather than any active turbulent fluctuations.

Of particular importance to this work is the research concerned with the influence of surface roughness on gravity current propagation and mixing. The amount of salt water modelling in this area is, unfortunately, small and, unlike the present study, generally limited to flows over single obstacles (Chobotov et al., 1986, Simpson, 1987, Lane-Serff et al., 1995).

In terms of heavier-than-air gas dispersions, the effects of surface roughness are generally considered through wind tunnel studies. Petersen and Ratcliff (1989) and Roberts et al. (1990) used wind-tunnel simulations to consider flows over a variety of roughness arrays. They reported that cloud concentrations in a dispersion over a roughness scale typical of an urban area were reduced by as much as 25 times over those found for a similar advance over a grassy plain.

3. FLOW PARAMETERS AND SCALING LAWS

The gravity current flow parameters for the salt-water modelling used here are defined in Figure 1. The ambient fluid depth, h_1 , and initial fluid densities, ρ_A and ρ_B , are controlled and set prior to the experiment. The controlled upstream source condition is quantified by the current flowrate per unit channel width, Q , and the initial fluid density difference, $\Delta\rho/\rho_A$.

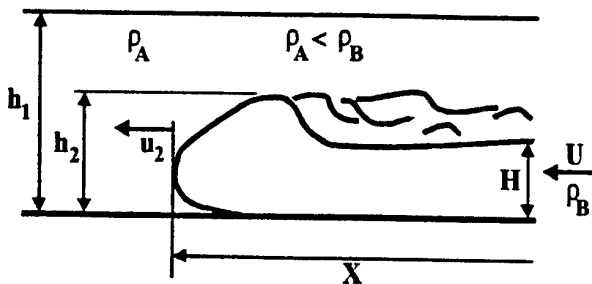


Figure 1. Definition of the experimentally controlled and observed gravity current flow parameters.

Based on continuity, Q is the product of the feeding current layer depth, H , and the feeding current layer velocity, U . At any downstream channel position, the feeding current layer velocity, U , can be derived with good approximation based on the observed feeding current layer depth, H , where $U = (Q/H)$. Other observed parameters are the current head height, h_2 , the current head frontal velocity, u_2 , and the current nose position, X .

When investigating full-scale heavier-than-air gas dispersion, for instance, much of the scaling difficulty arises when near-source modelling is attempted; in far-field modelling many of these scaling concerns are eliminated. The flow is now stabilized as a negatively buoyant layer and propagates away from the source solely under the influence of buoyancy.

Under these conditions, the primary dimensionless groups characterizing the flow are the Reynolds and Froude numbers, as well as, the initial fluid density difference. Dilution of the dense gas cloud at this point has typically reduced its density sufficiently such that the Boussinesq approximation may be used.

When modelling large-scale flows, however, equality of both the full-scale Reynolds and Froude numbers is generally not possible for small-scale lab experiments. When a choice has to be made, however, Froude number scaling is more important (Hoot and Meroney, 1974).

Fortunately, the requirement of exact Reynolds number equality can be relaxed as long as highly turbulent characteristics are exhibited in the flows. It has been shown that these characteristics exist in gravity current flows with Reynolds numbers, based on the current head height and velocity, as low as 1000 (Keulegan, 1957, Simpson, 1987, Chobotov et al., 1986).

Some confusion seems to exist in the literature over the definition to be used for the gravity current Reynolds number. It has been defined in terms of: (1) the dense feeding current layer depth, H , and the current head frontal velocity, u_2 , (Simpson and Britter, 1979) and, (2) the dense feeding current layer depth, H , and velocity, U (Zukoski and Kubota, 1988).

Fundamentally, the second of these definitions seems to be more appropriate as it is based on the controlled source condition for the current flowrate. Consequently, a Reynolds number based on the source flowrate, $Q = (UH)$, is used here. This definition is also independent of the shape of the gravity current head. These same variables are used to define the Froude number.

A balance between buoyant and inertial forces for an inviscid gravity current produces characteristic scales that can be used to normalize lengths, times and velocities. The scales used by Chen (1980) and Chobotov et al. (1986) are adopted, i.e.,

$$d_{\text{REF}} = (Q^2/g')^{1/3}$$

$$t_{\text{REF}} = (Q/g'^2)^{1/3}$$

$$u_{\text{REF}} = (g'Q)^{1/3}$$

The term g' is the reduced gravity term resulting from the Boussinesq approximation.

4. EXPERIMENTAL FACILITY

Figure 2 illustrates the water channel apparatus and circulation system used to create small-scale gravity current flows. The facility consists of an open plexiglass channel, 2.4 m long and 0.2 m wide with a maximum possible ambient fluid depth of 0.3 m. It is filled with the less dense ambient fluid prior to an experiment and allowed to become quiescent.

The saline fluid that is injected to form the gravity current flow enters the channel through an entry box section

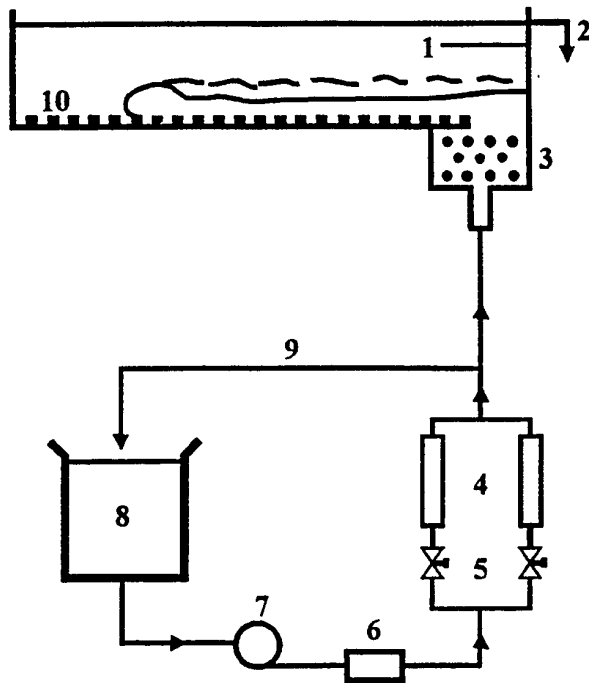


Figure 2. Schematic diagram of the water channel apparatus and circulation system used to generate small-scale gravity current flows.

- | | |
|------------------------|-----------------------------|
| 1) splitter plate | 6) filter |
| 2) overflow weir | 7) circulating pump |
| 3) inlet entry box | 8) saline storage reservoir |
| 4) flowmeters | 9) recirculation line |
| 5) flow control valves | 10) roughness array |

located on the channel bottom at the upstream end. This box is filled with porous plugs that provide a uniform flow entry condition. The source injection flowrate is controlled by a pair of variable area flowmeters. The depth of the less dense ambient fluid in the channel is controlled by means of an adjustable overflow weir located at the upstream end of the channel.

Surface roughness is created using two-dimensional arrays of square cross-section elements positioned on the channel floor perpendicular to the direction of flow. The elements span the full channel width over the entire channel length. The first is positioned flush with the inlet edge.

Four sizes of roughness elements were used with nominal dimensions of 6, 13, 19 and 25 mm on a side. Elements were positioned with a spacing equal to the side dimension. Including the smooth floor, five surface conditions can, thus, be examined.

The flow visualization system is represented schematically in Figure 3. Fluorescein sodium dye is added to the gravity current fluid at a known concentration such that its emitted fluorescent intensity is linearly proportional to its concentration in the fluid (Walker, 1987). It is then possible to map concentration fields based on sampled intensity fields. From Walker's conclusions, the ambient and

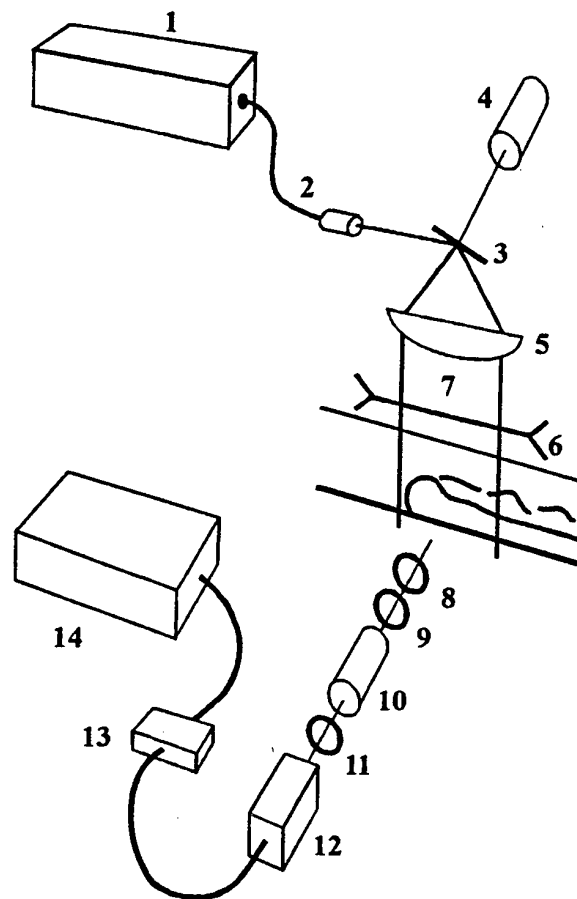


Figure 3. Schematic diagram of the gravity current flow visualization system.

- | | |
|------------------------|----------------------------|
| 1) argon ion laser | 8) high-pass colour filter |
| 2) fiber optics | 9) 25 mm lens |
| 3) scanning mirror | 10) image intensifier |
| 4) drive motor | 11) 18 mm lens |
| 5) collimating lens | 12) video camera |
| 6) slit assembly | 13) time signal encoder |
| 7) visualization sheet | 14) video recorder |

gravity current fluids are buffered to a pH above 8 to maximize dye efficiency.

The 488 nm blue-line of a four W argon ion laser is used to excite the dye. The laser beam is reflected off a high speed rotating front-surface mirror scanning at a frequency of 500 Hz. It is then passed through a plano-cylindrical lens and slit mask to generate a collimated laser sheet approximately 20 cm wide and 1.5 mm thick. Finally, the sheet is passed through the longitudinal vertical mid-plane of the water channel to illuminate the flow.

The laser sheet generating and video recording systems are mounted on a computer controlled, stepper motor driven traversing carriage that can track the gravity current head as it progresses down the channel. With this system, accurate control over the tracking parameters can be

maintained while feedback on carriage position and velocity is provided.

The illuminated flows are sampled at a fixed rate of 30 images/second using a standard B/W CCD video camera (Panasonic WV BD-400) with an 18 mm lens. The camera is coupled to a low light level image intensifier (Astrolight 9100) equipped with a 25 mm lens and sharp cut-off high-pass Schott colour filter (Ealing OG-515). A S-VHS video cassette recorder (Panasonic AG-6720) is used to record images for future processing and analysis. A time signal encoder (For-A VTG-22) is used to superimpose a reference time signal on the video record.

Real-time video images are analyzed using a PC-based image processing system equipped with a Matrox MVP-AT/NP frame grabber board. The board acquires images with a resolution of 512 x 480 pixels yielding a spatial resolution of approximately 0.5 mm x 0.5 mm for the field of view utilized. This system, along with custom and commercial software packages for image processing, allows single snapshots and/or time-averaged segments to be grabbed and analyzed.

5. EXPERIMENTAL MATRIX

Three series of tests were performed with fluid density differences, $\Delta\rho/\rho_A$, of 0.010, 0.030 and 0.050. Injection flowrates, Q , of 10.3, 10.6 and 10.8 cm³/s, corresponding to the above density differences, were used to maintain a Reynolds number, $Re = Q/\nu$, of 1000. When the Reynolds number is based on head height and velocity, a value much greater than 1000 was achieved, ensuring that the flow exhibited a turbulent nature. The depth of the ambient fluid, h_1 , was set to 30.0 cm for each test. Five surface roughness conditions were examined for each of the three test series giving a total of fifteen tests.

6. ANALYSIS AND DISCUSSION OF RESULTS

In general, gravity current advance rates can be classified into two flow regimes. The first is where viscous forces are negligible compared to the inertial and buoyant forces; under these conditions, the current advances with a constant velocity. The second is one in which viscous forces dominate inertial forces, producing a deceleration due to increasing floor shear forces with downstream position.

Chen (1980) suggested that the transition from a constant velocity to a decelerating flow regime occurs at a downstream position given by

$$X_t = 0.1 \frac{Q^2}{u_{REF} \nu}$$

When normalized with d_{REF} , this transition length becomes $X_t^* = 0.1Re$ so that the normalized transition length is a function only of the injection rate and the fluid viscosity. In this form, there is no dependence on the initial fluid density difference.

Figure 4 shows the normalized nose position versus normalized time for the fifteen tests performed. The slopes of these curves represent the normalized frontal velocities, u_2^* . The linear line shown reflects the constant velocity advance in the observed inertially dominated region of the smooth surface flows for each fluid density difference.

Examination of these smooth surface cases shows that the slope of the line is independent of $\Delta\rho/\rho_A$ and has a value of 0.89. If the data for each fluid density difference with a constant surface roughness is considered, it can be further concluded that u_2^* is independent of the fluid density difference over the range of surface roughness used.

Based on Chen's work, the experimental data points for the smooth surface flow cases should deviate from this straight line at the transition length, $X_t^* = 100$. This appears to be supported by the data. It should be noted, however, that flow deceleration can, in part, be attributed to end wall effects. (Chobotov et al., 1986).

As Chen's work was developed for smooth surface flows, there is no indication of how the transition from a constant velocity to a decelerating flow regime is affected by surface roughness. It is reasonable to assume, however, that the transition length would decrease with increased roughness. Surface roughness should act, in addition to viscosity, to intensify the floor shear forces so that the advance rates exhibit greater deceleration for increasing surface roughness.

The experimental data for the rough surface cases strongly supports this hypothesis. As roughness increases, further deviation from the smooth surface data is apparent. It is evident, then, that increased boundary shear forces, induced by the roughness, significantly influence the advance. The inertially dominated, constant velocity regime is not evident indicating that the transition length can be considered to have been reduced to zero.

In addition to the gravity current advance rates, the variation in head concentration with downstream position was also examined. Here, concentration refers to saline content and, thus, fluid density. Data extracted from one second (30 frame) time-averaged images was used to produce maps of the normalized head density at various positions down the channel. This information was collected for each experiment at nominal downstream positions of 25, 60, 100, 135, 175 and 210 cm.

Figure 5 illustrates the normalized concentrations obtained for three channel positions for a flow with a fluid density difference, $\Delta\rho/\rho_A$, of 0.010 and a surface roughness scale, h_R^* , of 0.63. Contours are shown for 20% intervals and represent the local fluid density difference as a fraction of the maximum fluid density difference, $(\Delta\rho/\rho_A)_{MAX}$.

In this example, the height of the roughness element array was approximately 2 cm. Visually, the gravity current is seen to flow above it, interacting with the fluid in the spaces between the roughness elements as it progresses down the channel. Individual roughness elements are not apparent in these views as the maps are time-averaged.

As the current advances down the channel, the normalized density within the head reduces significantly due to mixing with the ambient fluid. Surprisingly, though,

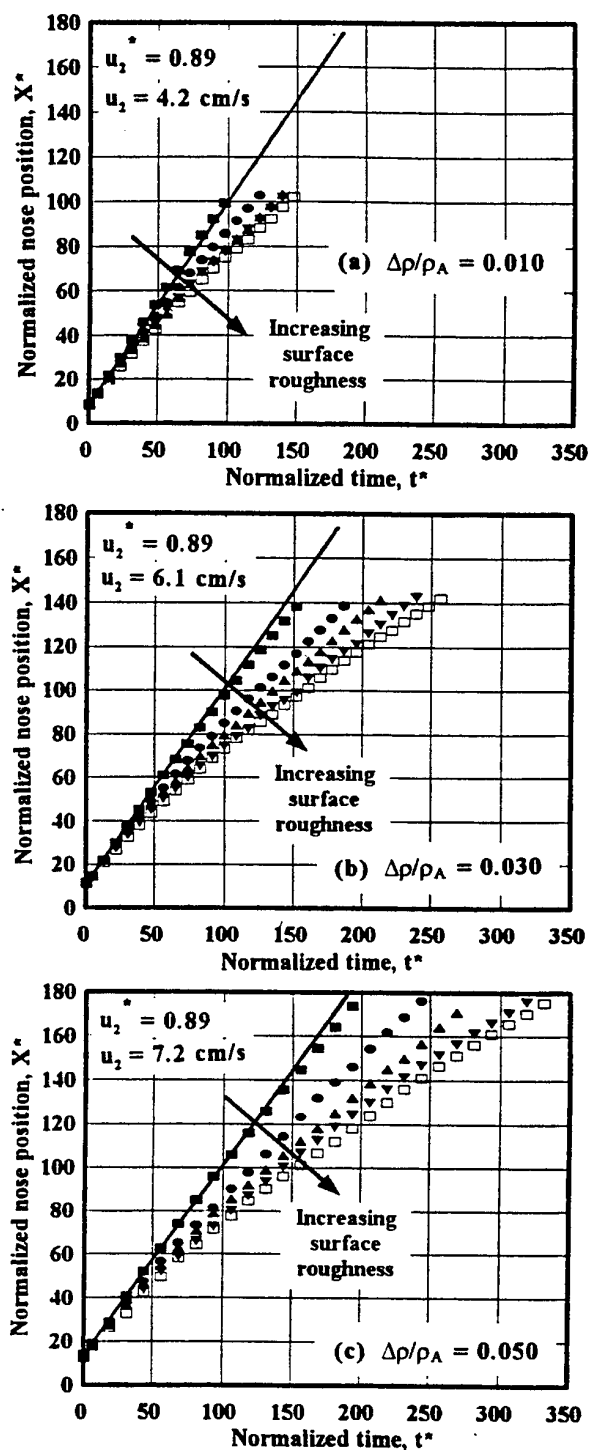


Figure 4. Normalized nose position versus normalized time.
 (a) $\Delta\rho/\rho_A = 0.010$, $h_R^* = 0.00 \blacksquare 0.20 \bullet 0.43 \blacktriangle 0.63 \blacktriangledown 0.83 \square$
 (b) $\Delta\rho/\rho_A = 0.030$, $h_R^* = 0.00 \blacksquare 0.27 \bullet 0.58 \blacktriangle 0.84 \blacktriangledown 1.11 \square$
 (c) $\Delta\rho/\rho_A = 0.050$, $h_R^* = 0.00 \blacksquare 0.32 \bullet 0.68 \blacktriangle 1.00 \blacktriangledown 1.32 \square$

the head remains intact even for fluid density differences of 10% of the maximum. This represents a density within the head of only 0.1% greater than ambient.

Mean head density differences can be estimated from the concentration maps. This is done by first calculating the volume under the density profile surface using discretized sampling with a spatial resolution of approximately $0.5 \text{ cm} \times 0.5 \text{ cm}$. The mean head fluid density difference is, then, determined by dividing this volume by the area of the current head that is projected onto the base plane of the concentration map.

The variations of normalized mean head fluid density difference with normalized downstream channel position are given in Figure 6. Again, the normalized mean fluid density difference is presented as a fraction of the maximum fluid density difference, $(\Delta\rho/\rho_A)_{\text{MAX}}$.

The stable smooth surface flows have nearly constant dilution rates over the channel length. This is indicative of the fact that these flows are primarily inertially dominated with constant rates of advance.

The immediate conclusion, however, is that dilution rates increase significantly with roughness scale; the normalized mean head density decreases asymptotically to zero with channel position. For the test described in Figure 5, the normalized mean head concentration near the end of the channel is 80-90% lower than that for the corresponding smooth surface flow.

On examination of the data and the video records, it is concluded that, for a particular roughness array, the lightest gravity current flows are seen to ride up and over the roughness arrays without significant mixing with the fluid in the array spaces. Heavier flows, however, will more vigorously interact and mix with the less dense ambient fluid trapped in the regions between the roughness elements. This results in significantly greater dilution rates.

This increase in dilution rate can be seen particularly between the tests with $\Delta\rho/\rho_A = 0.010$ and 0.030 . It is not so evident when examining the heaviest gravity current cases. This result strengthens our premise that the contribution of packets of overrun less dense ambient fluid to the total head dilution is much more significant than presented by other authors such as Simpson and Britter (1979). In addition, this observation is in agreement with the conclusions of Winant and Bratkovich (1977).

7. CONCLUSIONS

For the smooth surface flows considered in this work, both the inertial and viscous flow regimes were evident. The observed locations for the transition from inertially dominated to viscous dominated flows were in good agreement with Chen's work.

It is not possible, however, to extend his conclusions to rough surface flows due to the significantly increased floor shear forces. The roughness scale range used in these tests tends to reduce the transition length to zero such that a

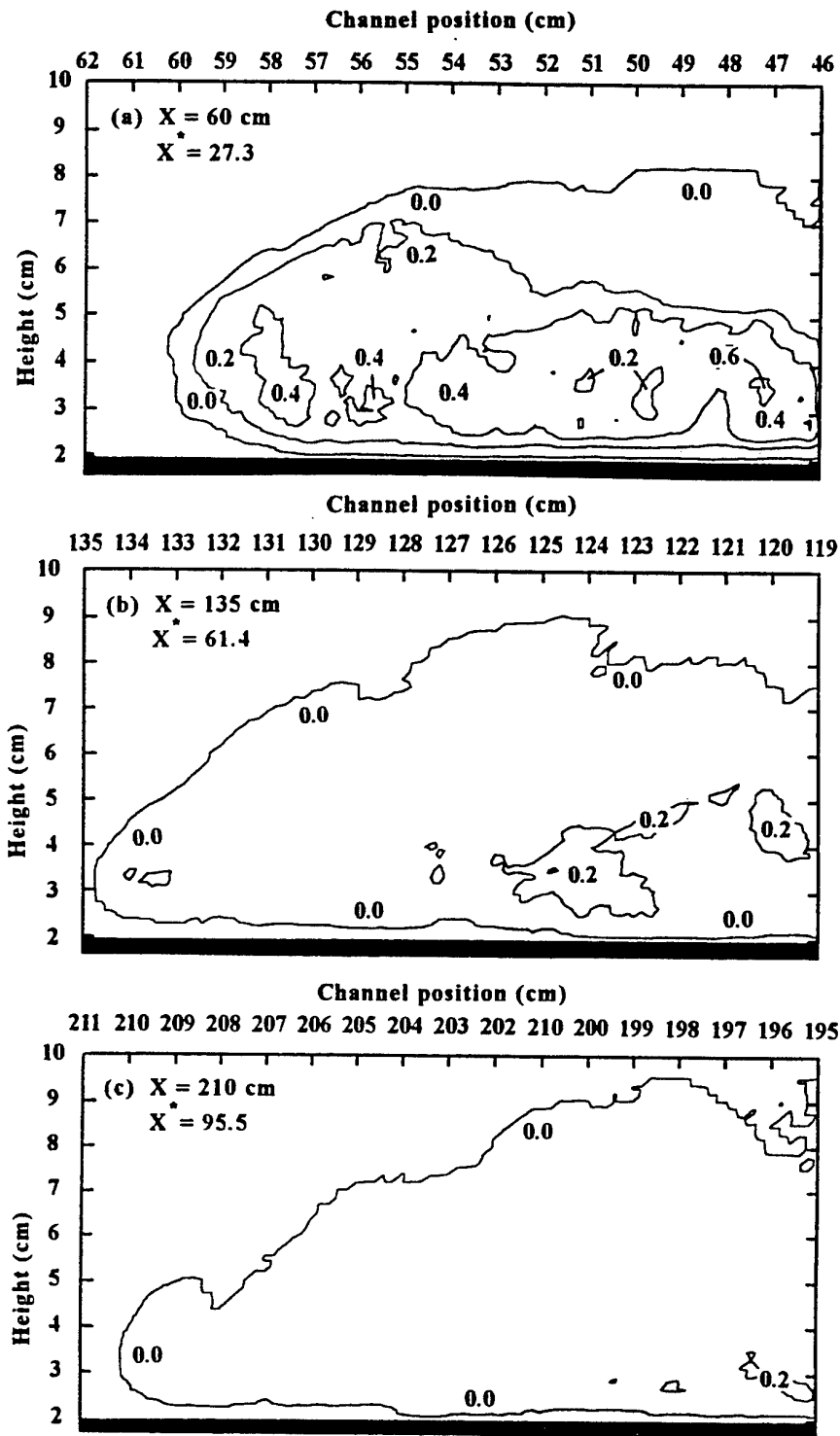


Figure 5. Concentration maps showing normalized head fluid density difference profiles for $\Delta p/\rho_A = 0.010$ and $h_R^* = 0.63$ at downstream channel positions of (a) $X^* = 27.3$ (b) $X^* = 61.4$ (c) $X^* = 95.5$.

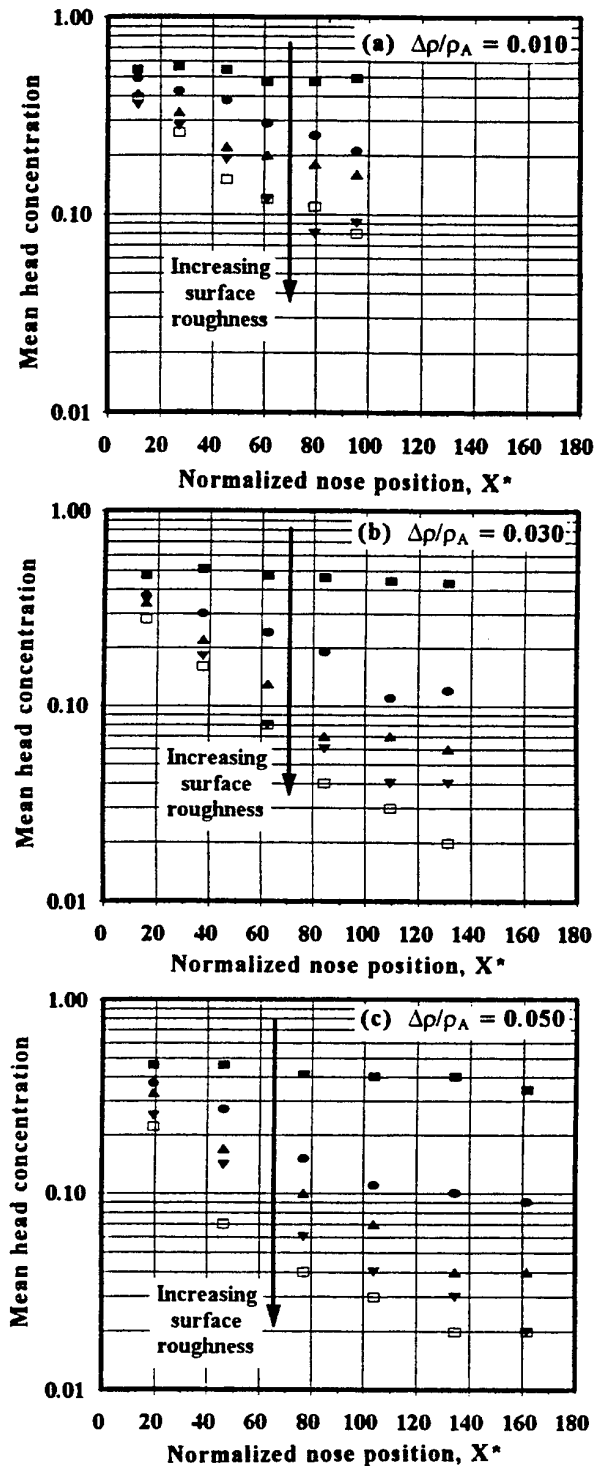


Figure 6. Normalized mean head concentration versus normalized nose position.

- (a) $\Delta\rho/\rho_A = 0.010$, $h_r^* = 0.00 \blacksquare 0.20 \bullet 0.43 \blacktriangle 0.63 \blacktriangledown 0.83 \square$
 (b) $\Delta\rho/\rho_A = 0.030$, $h_r^* = 0.00 \blacksquare 0.27 \bullet 0.58 \blacktriangle 0.84 \blacktriangledown 1.11 \square$
 (c) $\Delta\rho/\rho_A = 0.050$, $h_r^* = 0.00 \blacksquare 0.32 \bullet 0.68 \blacktriangle 1.00 \blacktriangledown 1.32 \square$

decelerating flow regime exists for the full channel length. As a result, the normalized frontal velocities experience a much greater deceleration over rougher surfaces. When normalized, the frontal advance velocity appears to be independent of the fluid density difference.

Closely connected to the frontal advance rate is the dilution rate of the gravity current head as it travels down the channel. Significantly increased dilution rates are observed in connection with flow deceleration and increased surface roughness. Near the channel end, normalized mean head concentrations in rough surface flows are observed to be at least 20 times less than those of comparable smooth surface flows.

The head dilution rate does not appear to be independent of the fluid density difference. Increased interaction and mixing with the less dense ambient fluid trapped in the spaces between roughness elements is observed for heavier gravity current flows. This is a significant conclusion as the role of the overrun less dense ambient fluid in the total head dilution process has been given little attention in the past.

NOMENCLATURE

d_{REF}	characteristic length scale
g'	reduced gravity due to Boussinesq approximation
H	feeding current layer depth
h_R	roughness element height
h_1	ambient fluid depth
h_2	current head height
Q	source injection flowrate per unit channel width
Re	gravity current Reynolds number
t_{REF}	characteristic time scale
U	feeding current layer velocity
u_{REF}	characteristic velocity scale
u_2	current head frontal velocity
X	current nose position
ρ_A	ambient fluid density
ρ_B	current fluid density
$\Delta\rho/\rho_A$	fluid density difference
ν	kinematic viscosity
*	indicates normalized data

ACKNOWLEDGEMENTS

Support for this work was received from Emergency Preparedness Canada, the Natural Sciences and Engineering Research Council of Canada and the Society of Fire Protection Engineers.

REFERENCES

- Chen, J.C., 1980, Studies on Gravitational Spreading Currents, Rept. No. KH-R-40, W.M. Keck Laboratory of Hydraulics and Water Resources, California Institute of Technology, Pasadena, CA.

Chobotov, M.V., Zukoski, E.E. and Kubota, T., 1986, Gravity Currents with Heat Transfer Effects, Center for Fire Research, National Bureau of Standards, Gaithersburg, MD, Rept. No. NBS-GCR-87-522, 158 p.

Cruyningen, I. van, Lozano, A. and Hanson, R.K., 1990, Quantitative Imaging of Concentration by Planar Laser-Induced Fluorescence, Experiments in Fluids, Vol. 10, pp. 41-49.

Hesselink, L., 1988, Digital Image Processing Flow Visualization, Annual Review of Fluid Mechanics, Vol. 20, pp. 421-485.

Hoot, T.G. and Meroney, R.N., 1974, The Behaviour of Negatively Buoyant Stack Gases, Proc. 67th Annual Meeting of APCA, Denver, CO, Paper 74-210, 20 p.

Keulegan, G.H. 1957, An Experimental Study of the Motion of Saline Water from Locks into Fresh Water Channels, National Bureau of Standards, Washington, D.C., Report No. 5168.

Lane-Serff, G.F., Beal, L.M. and Hadfield, T.D., 1995, Gravity Current Flows Over Obstacles, Journal of Fluid Mechanics, Vol. 292, pp. 39-53.

Nash, J.D., Jirka, G.H. and Chen, D., 1995, Large Scale Planar Laser Induced Fluorescence in Turbulent Density-Stratified Flows, Experiments in Fluids, Vol. 19, pp. 297-304.

Peters, W.D., Cogswell, S.R. and Venart, J.E.S., 1996, Dense Gas Simulation Flows Over Rough Surfaces, Journal of Hazardous Materials, Vol. 46, pp. 215-223.

Petersen, R.L., and Ratcliff, M.A., 1989, Effect of Homogeneous and Heterogeneous Surface Roughness on Heavier-Than-Air Gas Dispersion, American Petroleum Institute, Washington, D.C., API Pub. No. 4491, 354 p.

Roberts, P.T., Puttock, J.S. and Blewitt, D.N., 1990, Gravity Spreading and Surface Roughness Effects in the Dispersion of Dense Gas Plumes, Proc. AIChE 1990 Health and Safety Symposium, Session IIB: Modelling of Aerosol Clouds, Orlando, FL, Mar. 18-22, 1990.

Simpson, J.E., 1987, Gravity Currents: In the Environment and the Laboratory, Ellis Horwood Limited, West Sussex, U.K., 244 p.

Simpson, J.E., and Britter, R.E., 1979, The Dynamics of the Head of a Gravity Current Advancing Over a Horizontal Surface, Journal of Fluid Mechanics, Vol. 94, Part 3, pp. 477-495.

Walker, D.A., 1987, A Fluorescence Technique for Measurement of Concentration in Mixing Fluids, Journal of Physics, E, Scientific Instruments, Vol. 20, pp. 217-224.

Winant, C.D., and Bratkovich, A., 1977, Structure and Mixing Within the Frontal Region of a Density Current, Proc. 6th Australasian Hydraulics and Fluid Mechanics Conference, Adelaide, Australia, Dec., 1977.

Zukoski, E.E. and Kubota, T., 1988, Experimental Study of Environment and Heat Transfer in a Room Fire, Center for Fire Research, National Institute of Standards and Technology, Gaithersburg, MD, Rept. No. NIST-GCR-88-554, 26 p.

SESSION 24

Scalar Measurements

SINGLE-SHOT SPECTRALLY RESOLVED UV RAYLEIGH SCATTERING MEASUREMENTS IN HIGH SPEED FLOW

Richard G. Seasholtz

NASA Lewis Research Center
Cleveland, OH 44135, U.S.A.

ABSTRACT

A single-shot UV molecular Rayleigh scattering technique to measure velocity in high speed flow is described. The beam from an injection-seeded, frequency quadrupled Nd:YAG laser (266 nm) is focused to a line in a free air jet with velocities up to Mach 1.3. Rayleigh scattered light is imaged through a planar mirror Fabry-Perot interferometer onto a CCD array detector. Some laser light is also simultaneously imaged through the Fabry-Perot to provide a frequency reference. Two velocity measurements are obtained from each image. Multiple-pulse data are also given. The Rayleigh scattering velocity data show good agreement with velocities calculated from isentropic flow relations.

1. INTRODUCTION

Rayleigh scattering offers a means to measure gas flow parameters including density, temperature, and velocity. Since Rayleigh scattering is a molecular scattering process, no seeding of the flow is necessary. The Rayleigh scattered power is proportional to the gas density, the spectral width is related to the gas temperature, and the shift in the frequency of the spectral peak is proportional to one component of the bulk velocity. We have used this technique in a variety of aerospace applications including rocket exhaust plumes [Seasholtz *et al* (1991)] and wind tunnels [Kourous and Seasholtz (1993), Seasholtz *et al* (1995)]. This previous work used visible laser light, either the 488 or 514 nm lines of an argon-ion laser, or the 532 nm second harmonic of a Nd:YAG laser. There is considerable interest in using shorter wavelengths for two reasons. First, the Rayleigh scattering cross section varies as the inverse fourth power of wavelength. Thus the number of Rayleigh scattered photons will be higher by a factor of eight for a given laser power if the wavelength is halved. (Where the effect of the photon energy has been taken into account.) The second reason for

using short wavelengths is that the reflectivity of metallic surfaces is generally less than it is at longer wavelengths.

This is of particular interest in confined flow situations, such as small wind tunnels and aircraft engine components, where the stray laser light scattered from windows and internal surfaces in the test facility is a limiting factor in the application of Rayleigh scattering diagnostics. The previous study by Seasholtz *et al* (1995) used an iodine absorption cell [the filtered Rayleigh scattering technique developed by Miles *et al* (1991)] to block stray laser light. This approach, however, is more complex in that it requires that the laser frequency be tuned to a specific frequency in an iodine absorption line.

In this paper, we present the results of an initial study to use molecular Rayleigh scattering of the 266 nm fourth harmonic of a pulsed Nd:YAG laser for measuring velocity in a high speed air flow. The frequency of the Rayleigh scattered light is analyzed with a planar mirror Fabry-Perot interferometer used in a static imaging mode, with the images recorded on a cooled, high quantum efficiency CCD. The image consists of concentric interference fringes, where the fringe radii are Doppler-shifted by the bulk velocity of the fluid and are broadened by the thermal motion of the molecules. In addition, some unshifted light from the same laser pulse is also imaged through the interferometer to generate a reference fringe pattern, which is used to obtain the interferometer phase and finesse for the incident light. Any pulse-to-pulse variation in the laser frequency is accounted for since the Rayleigh and reference images are obtained from the same laser pulse. Small subregions located on the interference fringes of the Rayleigh scattered light are then analyzed using a least squares fit to the model function. Data are shown for measurements obtained with single laser pulses in a free jet with velocities up to Mach 1.3. Multiple laser pulse data are also given. In addition, data are presented for measured reflectivity of stainless steel and aluminum at 266 nm and 532 nm.

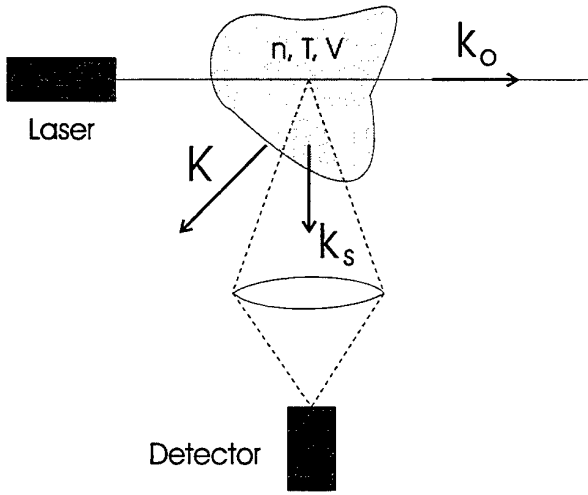


Fig. 1 - Light scattering experiment; k_o and k_s are wavevectors of incident beam and scattered beams; scattering wave vector $K = k_s - k_o$.

2. THEORY

2.1 Rayleigh scattering

Rayleigh scattering [Young (1982)] is a result of the interaction of an electric field with an atom or molecule. Because the wavelength is much larger than the size of a molecule, a dipole moment is induced that oscillates and radiates at the frequency of the incident field. This is an elastic scattering process, where the internal energy of the molecule is not changed, so the frequency of the scattered light is equal to the frequency of the incident light altered only by the Doppler effect due to the motion of the molecules. Because of the random spatial distribution of the molecules in a gas, the total intensity of the scattered light from a volume of gas is the sum of the intensities of the light scattered from the individual molecules. At low gas densities, molecular interactions are rare and the Rayleigh scattering spectrum is determined only by the molecular velocity distribution; for the usual Maxwellian velocity distribution, the spectrum is thus a simple Gaussian. However, at higher gas density, the molecular motions become correlated and the character of the spectrum changes. The spectrum can be analyzed either by considering the scattering from the individual molecules with proper accounting of the collective effects or by considering the scattering as being caused by fluctuations in the gas density.

The number of detected photoelectrons collected by an optical system with solid collection angle Ω (fig. 1)

$$N_R = \frac{\epsilon E_o n L_x \lambda \Omega}{hc} \left(\frac{d\sigma}{d\Omega} \right) \sin^2 \chi \quad (1)$$

where λ is the laser wavelength, E_o is the laser energy, n is the gas number density, L_x is the length along the beam of

the scattering volume, $d\sigma/d\Omega$ the differential scattering cross section, χ is the angle between the electric field vector of the (linearly polarized) incident light and the direction of the scattered light, ϵ is the overall collection efficiency (including the detector quantum efficiency), h is Planck's constant, and c is the velocity of light. The Rayleigh differential scattering cross section is related to the index of refraction μ of the gas by

$$\left(\frac{d\sigma}{d\Omega} \right) = \frac{4\pi^2}{\lambda^4 n^2} (\mu - 1)^2 \quad (2)$$

Since the refractive index of most gases is only weakly dependent on the wavelength, we see that the scattering cross section varies as the inverse fourth power of the wavelength. This strong dependence on wavelength is illustrated by the blue color of the sky, where shorter wavelength blue light is more strongly scattered than the longer wavelengths in the solar spectrum. For flow diagnostics, use of short wavelength ultraviolet lasers has obvious benefits. In addition to the much stronger scattering intensities, operating in the UV should reduce the problem of stray laser light because the reflectivity of metals tends to be less than at shorter wavelengths. This advantage, however, is offset by the reduction of available laser power in the UV. For example, in our Nd:YAG laser the pulse energy is reduced from about 800 mJ at 532 nm to about 80 mJ at 266 nm. In addition, the quantum efficiency of detectors is also less in the UV. Our back-illuminated CCD has a quantum efficiency of 70 % at 532 nm, but is only about 25 % at 266 nm. Another consideration is the availability of high quality imaging optics for UV operation. For the work reported here, we used the ubiquitous 105 mm focal length, $f/4.5$ 35-mm camera lens. Taking all these factors in consideration leads to the conclusion that, considering only the Rayleigh scattering signal, one is better off using the longer wavelength. This would be the case for open flows, such as free jets and larger wind tunnels, where one can easily control stray laser light. On the other hand, in confined flow experiments, control of stray laser light is much more difficult because of the close proximity of the measurement region to windows and metallic surfaces. In this case, the lower Rayleigh scattering signal level is more than offset by the increase in the ratio of Rayleigh scattering signal to stray laser light.

The shape of the Rayleigh scattering spectrum is determined by the gas density and scattering angle. We define, as is customary, a non-dimensional collision frequency $y = p/\eta Ka$ where p is the gas pressure, η is the shear viscosity, $K = (4\pi/\lambda)\sin(\theta_s/2)$ is the magnitude of the interaction wave vector $K = k_s - k_o$ (with k_o and k_s being the wave vectors of the incident and scattered light), θ_s is the scattering angle, and $a = (2\kappa T/m)^{1/2}$ is the most probable molecular speed (with κ being Boltzmann's constant, m the molecular mass, and T the gas temperature). Thus y is the optical frequency shift and collision frequency ($\sim p/\eta$) normalized with respect to Ka , which is on the order of the frequency of a sound wave in the gas with wavelength $\Lambda_s = 2\pi/K$. (Note that $a = c_s(2/\gamma)^{1/2}$, where c_s is the speed of

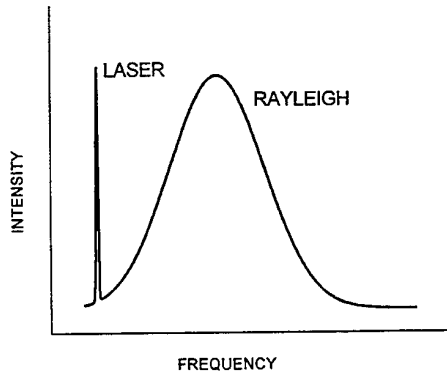


Fig. 2 - Rayleigh scattering spectrum showing thermal broadening and shift caused by bulk velocity.

sound and γ is the ratio of specific heats.) Alternatively, γ can be interpreted as the ratio of the acoustic wavelength Λ_s to the molecular mean free path.

For a single-component, low density gas, where $\gamma \ll 1$, the normalized spectrum of the Rayleigh scattered light is given by the Gaussian (fig. 2)

$$S(f - f_o) df = \frac{1}{\sqrt{\pi} aK} \exp \left\{ - \left[\frac{2\pi (f - f_o) - \mathbf{K} \cdot \mathbf{u}}{aK} \right]^2 \right\} df \quad (3)$$

where f_o is the laser frequency and \mathbf{u} is the mean gas velocity. As shown in figure 2, the spectral peak is shifted by a frequency proportional to the component of the bulk velocity in the \mathbf{K} direction. The spectral width is proportional to the square root of the gas temperature.

Note that in this limiting case for low density gases, the spectral shape is not a function of the γ parameter. However, for higher density gases (where $\gamma \sim 1$), the spectrum is no longer Gaussian and is a function of the γ parameter. For $\gamma \gg 1$ (high density gases), the scattering spectrum is strongly influenced by collective effects and is characterized by a central peak and two sidebands. The sidebands can be thought of as being caused by scattering from thermally excited random acoustic waves and is referred to as the Brillouin-Mandelstam doublet [Young (1982)]. A continuum theory, such as given by Clark (1975) can be used to model the spectrum here. The spectral shape in this regime is only a function of the γ parameter. However, the spectrum in the transition regime, where $\gamma \sim 1$, requires a more detailed kinetic theory. We used the S6 model developed by Tenti *et al* (1974) for our work. This model requires the shear viscosity, the thermal conductivity, the internal specific heat, and the bulk viscosity of the gas. In all cases, the Rayleigh scattering spectral shape is a function of the gas thermodynamic properties, which forms the basis for a diagnostic to measure gas density, temperature, and velocity.

The Rayleigh scattered light collected from one vantage point contains sufficient information to determine the gas density, temperature, and one component of the bulk

velocity. (Spectra measured at other \mathbf{K} vectors would give other velocity components.) Density is proportional to the total Rayleigh scattering as given by equation 1. This, however, generally requires calibration to determine the proportionality constant. (Although it is also possible to determine the density from the spectral shape for a limited range of γ parameters values, as shown by Lock *et al* (1992)).

2.2 Measurement of Rayleigh Scattering Spectrum

Because the Rayleigh linewidth is on the order of one GHz, a very high spectral resolution instrument is required. Conventional grating spectrometers generally do not have adequate resolution. A Fabry-Perot interferometer, either confocal or planar mirror type, can provide the needed resolution and is the most common instrument used for Rayleigh scattering studies. Both scanning techniques and imaging techniques have been used. In the scanning mode the passband of the interferometer is scanned across the Rayleigh spectrum by varying either the mirror spacing or the pressure of the gas in the Fabry-Perot cavity. This method is limited to time average measurements, usually at a single point in the flow. With the imaging technique, a region of the fluid illuminated by a laser beam is imaged through the interferometer onto an array detector, usually a CCD camera. As discussed below, the intensity of the recorded image is a function of the Rayleigh spectrum and the interferometer transmission function. Two features of this technique compared to scanning measurements are (1) a single image can give measurements at a number of locations in the flow and (2) these measurements can be made with a single laser pulse, giving instantaneous measurements. One problem with the Fabry-Perot used in a single pass mode is its limited selectivity, which means that it is unable to measure a weak signal in the presence of a strong interfering signal. This, unfortunately, is the situation encountered when using Rayleigh scattering diagnostics in small enclosed flows, where a large amount of stray light exists due to scattering from windows and solid surfaces.

2.3 Fabry-Perot interferometer

The Fabry-Perot interferometer (fig. 3) consists of two partially transmitting planar mirrors, which act as a multiple beam interference device. Multiple reflections between the mirrors result in a transmission function (defined as the fraction of light transmitted by Fabry-Perot for a monochromatic source) [Vaughan (1989)].

$$I_{FP}(\psi) = \left[1 + F \sin^2 \left(\frac{\psi}{2} \right) \right]^{-1} \quad (4)$$

where ψ is the phase change (neglecting any phase change on reflection) of the light between successive reflections given by

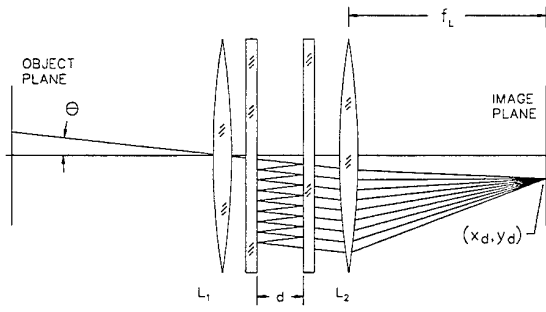


Fig. 3 - Fabry-Perot interferometer; single ray from point on object plane is imaged to single point on image plane; L_1 is collimating lens and L_2 is fringe forming lens.

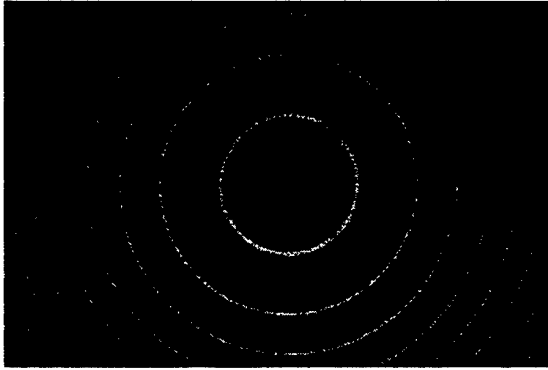


Fig. 4 - Fabry-Perot interference pattern of single frequency light from extended source.

$$\Psi(f, \theta_r) = \frac{4\pi f \mu d \cos \theta_r}{c} \quad (5)$$

Here, $f=c/\lambda_o$ is the optical frequency, μ is the refractive index of the medium in the Fabry-Perot cavity, d is the Fabry-Perot mirror spacing, θ_r is the angle between the ray and the optic axis, and $F = 1/(\sin^2(\pi/2N_E))$ where N_E is the effective finesse. The image of a monochromatic extended source located in the object plane consists of a series of unequally spaced concentric rings, such as shown in figure 4. With the innermost fringe located on the optical axis (i.e., having zero radius), the other fringe radii are given $r_n = f_L(n\lambda_o/d)^{1/2}$ for $n=1,2,3,\dots$, where f_L is the focal length of the fringe forming lens. Note that although the fringes are unequally spaced, their frequency separations are all equal to the free spectral range $FSR=c/2d$.

The Fabry-Perot interferometer can be used in the static, imaging mode, which takes advantage of the angular sensitivity of the transmission to achieve frequency resolution (see eq. 5). In this method a region of the flow

illuminated with laser light is imaged through the Fabry-Perot onto an array detector. The fringe location is radially shifted and broadened by an amount related to the frequency shift and spectral shape of the scattered light (the fringes move outward as the frequency increases). The spectrum can only be measured over a spatial region that includes part of an interference fringe. (Note that there is a one-to-one correspondence between an object point in the flow and an image point in the fringe plane.) This results in a measurement that is spatially averaged over that region. However, with several fringes in the field of view, measurements can be obtained at a large number of locations. This imaging method is the basis for the technique described in this paper.

2.4 Model of Rayleigh spectral measurements using Fabry-Perot interferometer

Small subregions located on the interference fringes of the Rayleigh scattered light are then analyzed using a least squares fit to the model function

$$\langle N_{Dq} \rangle = \int \int \int_{\Omega, \Delta, -\infty}^{\infty} [A_R S_R(f, \Omega) + A_W \delta(f - f_o)] I_{FP}(f, \theta_r) d\Omega d\Delta dB_q \quad (6)$$

where $\langle N_{Dq} \rangle$ is the expected number of detected photons for the q^{th} pixel, A_R is the total amount of Rayleigh scattering that would be detected by the q^{th} pixel if the Fabry-Perot interferometer were not present, and θ_r is the angle of the light ray with the optical axis. A_W represents the unshifted laser light scattered from windows and walls at the laser frequency $f_o=c/\lambda_o$. The spectrum of the Rayleigh scattered light is $S_R(f, \Omega)$ and $I_{FP}(f, \theta_r)$ is the Fabry-Perot instrument function. Broadband background light, detector dark current, and readout noise are represented by B_q . The integration over the solid angle is necessary to account for the range of \mathbf{K} vectors over the light collection aperture. The $S6$ model developed by Tenti *et al* (1974) is used for the spectrum.

3. EXPERIMENT

3.1 Optical setup

The optical setup is shown in figures 5 and 6. The beam from an injection-seeded, frequency-quadrupled, Nd:YAG laser with 70 mJ pulse energy and 10 Hz pulse rate was focused with a 200 mm focal length lens. To avoid air breakdown, the lens was intentionally misaligned to introduce some aberrations. The beam crossed the nozzle axis at 45° , and the beam size at the measurement location was approximately $150 \mu\text{m}$. This Rayleigh scattered light was collected at a 90° scattering angle and collimated with a 250 mm focal length lens. The light was then passed through a 3.2 mm thick uncoated fused silica beamsplitter and the Fabry-Perot interferometer. A commercially available Fabry-Perot interferometer was used. The mirrors (70 mm diameter, $\lambda/200$ flatness, and 90% reflectivity at 266 nm) were set at a 7.50 mm spacing for the measurements reported

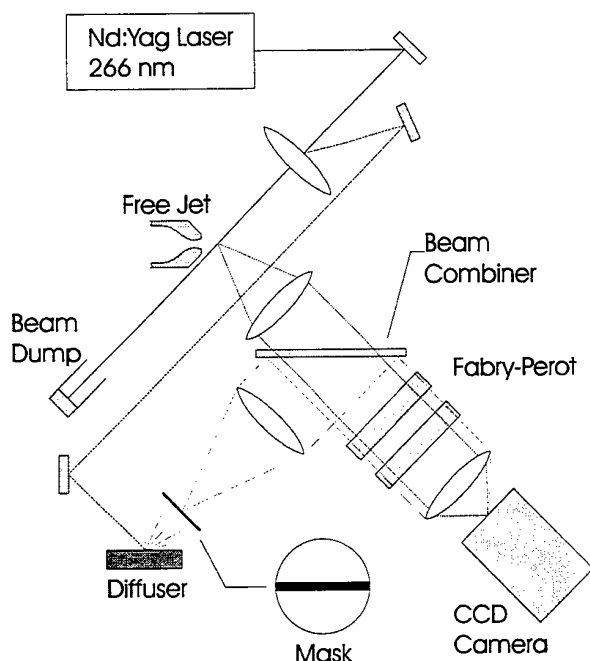


Fig. 5 - Optical layout of Rayleigh scattering experiment; see figure 6 for details.

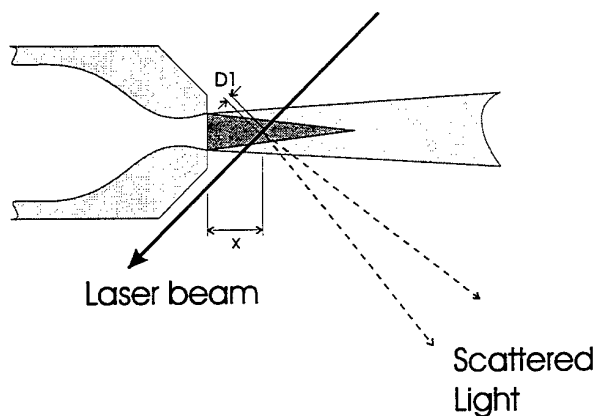


Fig. 6 - Detail view of Rayleigh scattering measurement region; x is the distance from the nozzle exit plane to the measurement region; D_1 is the separation between the two measurement obtained from each image.

here, which corresponded to free spectral range (FSR) of about 20 GHz. The light emerging from the Fabry-Perot was focused onto the detector (liquid nitrogen cooled, back illuminated, CCD array with 1752×532 $15 \mu\text{m}$ square pixels, 25% quantum efficiency at 266 nm) by a 105 mm focal length, $f/4.5$, 35 mm UV camera lens. Note that use of this relatively slow lens with an aperture of only 23 mm means that the full 70 mm aperture of the Fabry-Perot is not used. To reduce data storage requirements, only a 200×200 pixel region of the CCD was used, which gave a field of

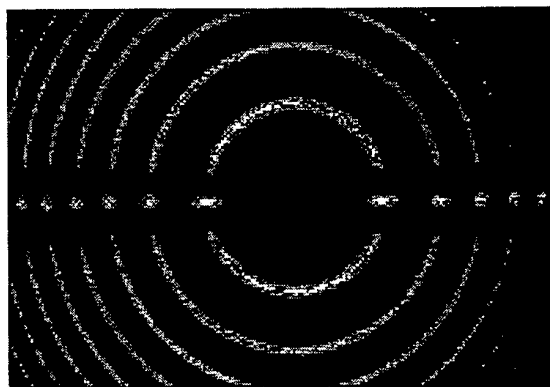


Fig. 7 - Image of light imaged through Fabry-Perot interferometer showing reference light (upper and lower) and Rayleigh scattering light (center).

view in the flow of 7.1×7.1 mm.. The images were digitized with a 14 bit A/D converter and transferred to a laboratory computer for storage and analysis.

To include the effects of laser shot-to-shot frequency variation and drift of the Fabry-Perot interferometer, reference data was simultaneously recorded along with the Rayleigh scattering data. Any pulse-to-pulse variation in the laser frequency thus is accounted for since the Rayleigh and reference images are obtained from the same laser pulse. This was accomplished by directing some of the unshifted laser light onto a diffusely scattering aluminum surface. A 100 mm focal length lens collimated the light from the diffuser, which was directed into the Fabry-Perot via the beamsplitter. A 0.30 mm diameter wire was placed in the focal plane of the 100 mm lens. This served to block unshifted Nd:YAG light in the reference path from a horizontal strip in the CCD image; the blocked area comprised about 12 % of the total number of rows of pixels. For single-shot data, the camera was operated with a shutter speed of 0.1 sec. A 1 sec exposure was used for the multiple-shot data (giving a 10 pulse average). The test cell lights were turned off to limit ambient background light. Figure 7 shows a typical image with the Rayleigh scattered light along the center line and the Nd:YAG reference light in the upper and lower parts of the image. The reference fringes are only broadened by the instrument response function of the interferometer, while the Rayleigh scattering fringes are also Doppler-shifted by the bulk velocity of the fluid and are broadened by the thermal motion of the molecules.

3.2 Test nozzle

The Mach 1.3 supersonic nozzle had an exit diameter of 9.3 mm. The air supply was filtered with a $0.2 \mu\text{m}$ filter to remove particles. Data were obtained at subsonic velocities and at Mach 1.3. The plenum pressure was measured with an electronic pressure meter and the isentropic flow equations were used to calculate the exit velocity.

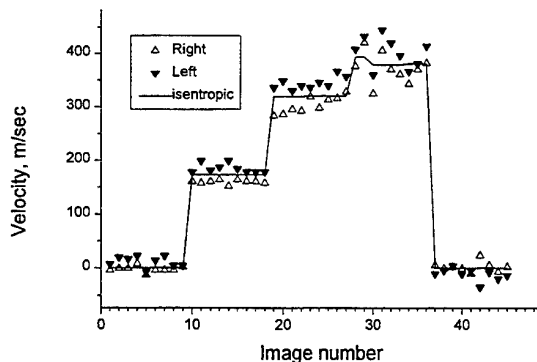


Fig. 8 - Single-shot velocity measurements in free jet; nine images taken at each of 3 flow conditions (with zero velocity condition at beginning and end); distance from nozzle exit $x = 15$ mm; two measurements/image with separation $D_1 = 1.8$ mm; velocity calculated for isentropic flow also shown. (note that flow was not constant during each condition).

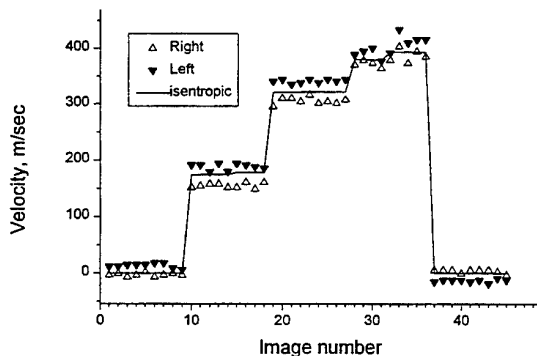


Fig. 9 - Ten-shot average velocity measurements in free jet $x=15$ mm from exit plane; two measurements/image with separation $D_1 = 1.8$ mm; velocity calculated for isentropic flow also shown.

3.3 Data processing

The data reduction procedure was as follows. The first step was to analyze the upper and lower regions to determine both the Fabry-Perot interferometer phase and finesse. (The measured finesse includes the effect of the finite linewidth of the Nd:YAG laser.) This was done by using a least-squares fit of the image to a model function for the Nd:YAG reference fringes (eq. 6 with $A_R = 0$). This fit gives the

Table 1 - Comparison of velocity measured by Rayleigh scattering and velocity calculated from isentropic flow relation; mean velocity and standard deviation in m/sec.

Single-shot data (see fig. 8)

Right	Left	Right+Left	Isentropic
159 (4)	184 (14)	172 (14)	173
304 (16)	344 (11)	323 (25)	320
373 (29)	403 (29)	388 (32)	383

Ten-shot data (see fig. 9)

Right	Left	Right+Left	Isentropic
155 (4)	188 (6)	172 (17)	176
306 (6)	341 (3)	323 (19)	321
380 (12)	403 (17)	392 (19)	387

coordinates of the center of the fringe pattern. Four 15×15 pixel subregions (equal to about a 0.54 mm square region in the flow) on the inner fringe (just outside the central band) are then analyzed to obtain reference values for the phase on the left and right sides of the central fringe (given by the mean of the upper and lower phases of the reference light). The Rayleigh scattering image is likewise analyzed to determine its phase at two locations on the inner fringe. The shift in the peak of the Rayleigh scattering fringe is related to the axial velocity component. The model function (eq. 6) was evaluated at 9 points in each pixel for the numerical integration over the area of each pixel. The flow direction was assumed to be along the tunnel axis for the purpose of converting the measured velocity component (which is along K) to the velocity magnitude. The y parameter was about 0.5 , so the Tenti S6 model for the Rayleigh spectrum was used.

4. RESULTS

4.1 Rayleigh scattering velocity measurements

Examples of Rayleigh scattering velocity measurements are shown in figures 8 and 9. The axial velocity component was measured near the jet center line for two subsonic velocities and for Mach 1.3 supersonic flow. Nine images were obtained at each flow condition, with a set of images at zero flow being taken at the beginning and the end of the experiment. Two velocities (separated by the inner fringe diameter $D_i \approx 2$ mm, as shown in fig. 6) were obtained from each image. Figure 8 shows data obtained with a single laser pulse. Figure 9 shows similar data obtained with 10 laser pulses. Also shown are velocities calculated from the ambient and plenum pressures and the total temperature using the isentropic flow relations [Ames Research Staff (1953)]. Note that the velocity was not necessarily constant at each flow condition because of variation in the air supply pressure. The statistical properties of the measured velocities are shown in Table 1. The two

Table 2 - Measured Reflectance of stainless steel and aluminum

316 Stainless Steel		
incidence angle	266 nm	532 nm
4°	32%	58%
45°	44%	66%
Aluminum		
incidence angle	266 nm	532 nm
4°	89%	93%
45°	94%	87%

velocities (labeled Right and Left) appear to have a systematic error that results in the two measurements being displaced in opposite directions from the isentropic velocity. The source of this error is not known at the present time. However, as shown in Table 1, the mean of the two measurements shows very good agreement with the isentropic velocity. It should be noted that no calibration was used. (The only measured parameters were the Fabry-Perot mirror spacing and the scattering angle.)

The standard deviation in the single-shot data (Right or Left) was about 15 m/sec for the two lower velocities and about 30 m/sec for the Mach 1.3 flow. One cause of the larger standard deviation in the Mach 1.3 flow is velocity variations caused by fluctuations in the air supply pressure. The high acoustic noise level, which can affect the stability of the Fabry-Perot (no acoustic shielding was used), could also contribute to the larger standard deviation. This larger variance is also evident in the ten-shot data.

4.2 Reflectance measurements of stainless steel and aluminum

The factor limiting Rayleigh scattering diagnostics in enclosed flows is frequently the amount of stray laser light resulting from scattering from surfaces in the test rig. We measured the reflectance of two materials commonly found in test facilities (316 stainless steel and aluminum) at 266 nm and 532 nm to determine if this scattering would less in the UV. The stainless steel was polished using a 1 μ m diamond polishing compound, but showed some residual surface pits. The aluminum sample was evaporated onto a glass plate. The estimated thickness of the aluminum was 150 nm. The measurements were made by measuring the incident and reflected power with a thermal type power meter. Two angles of incidence were measured (45° and near normal). The results of these measurements are shown in Table 2. Note that the stainless steel reflectance is substantially lower at 266 nm compared to 532 nm. However, the aluminum did not show this reduction.

5. CONCLUDING REMARKS

The feasibility of using a UV laser for Rayleigh scattering velocity measurements was demonstrated. Signal levels were high enough to allow measurements with a single laser pulse. The use of the Fabry-Perot interferometer used in the static, imaging mode allows measurements to be made simultaneously at multiple locations in the flow. Although only two measurements per image were obtained here, it is possible to obtain many more. This capability could be used to measure spatial velocity correlations. Although the system described here measured a single velocity component, it could be extended in a straightforward manner to simultaneously measure two or three components. This could be done by adding one or two additional sets of collection optics at other scattering angles.

One difficulty in working in the UV is the small selection of imaging-quality optics. In this work, the collection optics solid angle was only $f/11$. The Fabry-Perot interferometer used here has 70 mm diameter mirrors. Use of the full Fabry-Perot aperture would increase the collection angle to $f/3.6$, which would increase the collected Rayleigh scattered light by an order of magnitude. Another consideration is the focal length of the fringe forming lens. A longer focal length results in a higher spatial resolution, which means the Rayleigh scattering spectrum can be more accurately measured.

One precaution that should be used with this technique in high acoustic noise environments is to provide sufficient acoustic shielding of the Fabry-Perot interferometer and the laser. Another highly desirable addition would be automatic control of the Fabry-Perot alignment. The present procedure involves manual adjustment of the Fabry-Perot to maintain alignment, which takes time during the test and requires a skilled operator.

6. ACKNOWLEDGMENTS

We would like to acknowledge the diligent efforts of Mr. W. Trevor John who was responsible for setting up and aligning the optical system. Also, we thank Prof. G. Tenti for providing us with the computer code for his 6 moment Rayleigh scattering model.

7. REFERENCES

- Ames Research Staff, 1953, Equations, Tables, and Charts for Compressible Flow, NACA Report 1135.
- Clark, N.A. 1975, Inelastic Light Scattering from Density Fluctuations in Dilute Gases. The kinetic hydrodynamic transition in monatomic gas, *Phys. Rev.* A12, pp. 232-244.
- Kourous, H.E. & Seasholtz, R.G. 1994, Fabry-Perot Interferometer Measurement of Static Temperature and Velocity for ASTOVL Model Tests, *FED-Vol. 1, Laser Anemometry - 1994: Advances and Applications*. ASME.

Lock, J.A., Seasholtz, R.G., & John, W.T. 1992, Rayleigh-Brillouin Scattering to Determine One-Dimensional Temperature and Number Density Profiles of a Gas Flow Jet, Appl. Opt., vol. 31, no. 15, pp. 2839-2848.

Miles, R.B., Lempert, W.R. & Forkey, J. 1991, Instantaneous Velocity Fields and Background Suppression by Filtered Rayleigh Scattering, AIAA 29th Aerospace Sciences Meeting, Reno, AIAA paper 91-0357.

Seasholtz, R.G., Buggele, A.E., & Reeder, M.F. 1995, Instantaneous Flow Measurements in a Supersonic Wind Tunnel Using Spectrally Resolved Rayleigh Scattering, SPIE International Symposium on Optical Science, Engineering, and Instrumentation, San Diego, July 9-14.

Seasholtz, R.G., Zupanc, F.J., & Schneider, S.J. 1992, Spectrally Resolved Rayleigh Scattering Diagnostic for Hydrogen-Oxygen Rocket Plume Studies, J. Propulsion and Power, vol. 8, no.5, pp. 935-942.

Tenti, G., Boley, C.D., & Desai, R.C. 1974, On the Kinetic Model Description of Rayleigh Brillouin Scattering from Molecular Gases, Can. J. Phys. Vol. 52, pp. 285-290.

Vaughan, J.M. 1989, The Fabry Perot Interferometer. History, Theory, Practice and Applications, pp. 89-112, Adam Hilger, Bristol.

Young, A.T. 1982, Rayleigh Scattering, Physics Today, January (1982) pp. 42-48.

MEASUREMENT OF THE TRANSIENT THREE-DIMENSIONAL DENSITY DISTRIBUTION USING PHOTOCONDUCTOR-PLASTIC

Koh IKEDA and Koji OKAMOTO
Nuclear Engineering Research Laboratory
University of Tokyo
Tokai-mura, Ibaraki, 319-11, JAPAN

Fumitake KATO and Isao SHIMIZU
Ibaraki College of Technology,
Hiachinaka-shi, Ibaraki, 312, JAPAN

ABSTRACT

The time sequential measurement technique for three-dimensional density distributions in a channel was evaluated. Using the holographic interferometer, information of the density distributions are visualized as fringes. The holographic interferometer is a method that interferes the waves modulated by the field before and after the disturbance.

In the real time method, the wave before disturbance is recorded on a hologram, then the hologram is developed at the initial set position. When the hologram is reconstructed, the fringes are caused by the interference between reconstructed wave of the undisturbed field and wave through the disturbed field. These fringe pattern represent only the optical phase changes between two images. In this method, it is very difficult to develop because the hologram should not move or shrink. If the position of the hologram has been moved, it is impossible to re-locate the position where the interference occurred, for it needed sub-micron order alignment.

Hologram made by photoconductor-plastic processed by solvent vapor is developed without any movement or shrinkage. Developing of the hologram needs only about two minutes. Using the photoconductor-plastic, it is easy to construct the real time holographic interferometer.

In this study, the buoyancy driven exchange flow of air and helium gas was measured. The density distribution in the channel was visualized, showing the effectiveness of the real time holographic technique using photoconductor-plastic. The high resolution and high light sensitivity of the photoconductor-plastic was confirmed.

1. INTRODUCTION

The High Temperature Gas-cooled Reactor (HTGR) is an advanced type nuclear power plant, which can generate high temperature gas, e.g., 1000°C. The core of the HTGR is cooled by the high pressurized helium (4MPa). For the accidental analysis of the HTGR, the study on the buoyancy driven gas exchange flow is very important. In the stand pipe rupture accident, the heavy air outside the reactor flow into the reactor vessel inversely with exchanging with light helium, i.e., buoyancy-driven exchange flow. The exchange flow rate of air should be evaluated because the air may corrode the carbon moderator in the core. However, there are a few studies on the characteristics of the exchange flow field, since it is very difficult to measure the transient three-dimensional flow field. Okamoto and Fumizawa (1993) measured the transient two-dimensional density field of the exchange flow for the specific case.

In the buoyancy driven helium-air exchange flow through multiple opening channels, the exchange flow rate depended on the interaction between the upward helium and downward air flow (Kang et al., 1992). However, the interaction was too complex to predict the exchange flow rate. The flow pattern outside the opening channel was measured by the Mach-Zehnder Interferometer (Tsuru et al., 1993), showing the unstable flow. However, the density distribution inside the opening channel had not been measured.

Using the computer tomography technique with interferogram image, the 3D density distributions can be reconstructed (Merzkirch, 1974). Therefore, when the interferogram images are obtained, the three-dimensional density distributions can be measured. However, it is very difficult to visualize the flow inside the opening channel, because of the refraction at the channel surface. The transient density

distribution and velocity distribution inside the openings are very important to predict the exchange flow rate.

There are several techniques to measure the flow inside the channel, i.e., double pulsed holographic interferometer and real time holographic interferometer. In the double pulsed holographic interferometer, the interferogram images are obtained using double pulse, i.e., without and with flow inside the channel. The refraction on the channel surface can be neglected using the double pulse, since the both pulses pass the same path lines except the flow inside the channel. However, with this method, only the spontaneous image can be taken.

On the other hand, using the real time holographic interferometer, the transient interferogram images can be obtained. Initially, the hologram is taken without the flow inside the channel. Then, the hologram is developed and re-positioned. However, the holographic plate should be re-positioned at the exactly same position before developing the plate. Finally the transient interferogram with the flow inside the channel can be obtained. However, because of its sensitivity of repositioning of the hologram, it is very difficult to apply the technique to general purpose.

In this study, with using the two photoconductor-plastic as holographic plates, transient density distributions inside the channel of the buoyancy driven exchange flow were measured. To verify the effectiveness of the real time hologram, the helium jet was also visualized through curved wall.

2. METHOD

In order to measure the transient density variation, two lay interferometer technique, e.g., Mach-Zehnder interferometer, is usually used, since it is easy to operate and to obtain high resolution images. However density distribution in a channel is not measured by the two lay interferogram technique. Because the coherent plane wave passes through the flow field in a channel, the modulated wave includes the effects of not only flow field density variation but also the refraction on the channel surface. Therefore, if the effect of channel surface refraction is not negligible, the two lay interferometer technique can not be used.

Using the one lay technique, e.g., double pulse holographic interferometer, the refraction on the channel surface can be taken into account. The holographic interferometer is a method that interferes the waves modulated by the field before and after the disturbance. When coherent plane wave passes through the flow field in a channel without the density variation, the plane wave is modulated only by the variation of the refractive indices of the channel. The modulated plane wave is,

$$O_{p1}(x, y) = A \exp \left\{ j \left(\frac{2\pi}{\lambda} (\ell + \int_{\ell} n_c d\ell) + \omega t \right) \right\}, \quad (1)$$

where A is amplitude of wave, j is the imaginary unit, λ is spatial wave length of light, ℓ denotes the distance along the lay, and n_c is the variation of refractive index of the

channel. The second term denotes the modulation by the refraction of the channel.

While, coherent plane wave passes through the flow field with the density variation, the plane wave is modulated by the variation of the refractive indices of the fluid and the channel. The modulated plane wave is,

$$O_{p2}(x, y) = O_{p1} \exp \left\{ j \left(\frac{2\pi}{\lambda} \int_{\ell} \Delta n_f d\ell \right) \right\}, \quad (2)$$

where Δn_f is variation of the refractive index of the fluid.

In the double pulse method, O_{p1} and O_{p2} are recorded on a single hologram plate by the first and second pulse, respectively. When the hologram is reconstructed by the reference beam, the interference fringes are reconstructed. The fringes are caused by the interference between the O_{p1} and O_{p2} , i.e., the difference between the O_{p1} and O_{p2} . Then the density distribution of the fluid are measured as the fringes.

In the real time method, initially O_{p1} are recorded on a hologram. Then the hologram is developed at the initially set position. The hologram contains the effects of the channel. When the hologram is reconstructed the original O_{p1} is reconstructed. The interference fringes are caused by the interference between the reconstructed wave, O_{p1} , and the wave through the disturbed field, $O_{p2}(t)$. Then the fringes indicate the density distribution of the fluid. Since the modulated wave, $O_{p2}(t)$, varies with time, the transient distribution is measured as transient fringes. However, the hologram should be settled at the same place before and after the development to reconstruct the original O_{p1} , correctly.

In order to measure the three-dimensional flow field, the interferogram fringes are usually obtained with a double pulse method. Since the fringes are the projection data of three-dimensional field, the 3D field is reconstructed by the computer tomographic technique. However, with this method, only spontaneous projection can be measured, resulting in the spontaneous 3D distribution. In the real time method, the transient distributions can be measured. However, it is very difficult to develop without movement or shrinkage.

Recently, the photoconductor-plastic had been proposed. Using the photoconductor-plastic processed by solvent vapor, it is able to develop without movement or shrinkage. It is not affected by the thermal strain such as like thermoplastic. The system of photoconductor-plastic with solvent vapor, hologram can be easily constructed. The system contains two steps, i.e., solution and freeze.

- The photoconductor-plastic is melt by solvent vapor.
- The plastic is corona electrified.
- the frost are generated as a function of the light intensity.

The hologram can be developed without movement or shrinkage. Therefore, the real time hologram can be easily constructed using the photoconductor-plastic.

With this method, the obtained fringes are expressed as follows.

$$\begin{aligned} I(x, y) &= O_{p2}(x, y)O_{p1}^* + \delta \\ &= A \exp \left\{ j \left(\frac{2\pi}{\lambda} \int_l \Delta n_f(x, y, z) dl \right) \right\} \\ &\quad + \delta(x, y) \end{aligned} \quad (3)$$

Where I is intensity of the fringe. $\delta(x, y)$ is back ground intensity. Then the fringes denote only the effects of the density distributions in the fluid.

Extraction of Fringe Data

The fringe data are recorded on the CCD camera directly. Then the black and white fringe images are analyzed by computer. In general, with increasing the intensity, the the noise level also increases, including the laser speckle. Thus in order to determine the fringe pattern, the location of fringe minima rather than maxima are used. It is also difficult to measure the data between minima and maxima. The position of the minima is expressed as follows, (figure 1 (b))

$$\int_l \Delta n_f dl = \left(m + \frac{1}{2}\right) \lambda \quad (4)$$

Where m is fringe shift at the point. Between the minima, the integration are interpolated linearly.

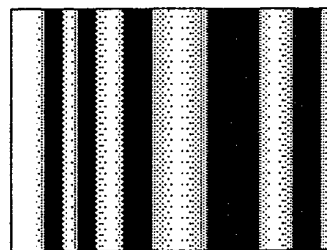
With analyzing the fringe minima on the images, the distributions of fringe shift, m , are obtained. The fringe shift is expressed as the integration of the variation of refraction indexes in the fluid. The projection data, i.e., fringe shift distribution, should be obtained from two or more different angles. In this study, the projection data from two different angles were measured using two photoconductor-plastics.

The reconstruction of cross sectional density distributions from projection data is carried out using the Computer Tomography (CT) technique. Usually the CT needs several hundreds of projection data, to reconstruct the cross section correctly. Verhoeven (1993) reviewed the CT technique from the limited number of projection data. However, the number of projection data is not enough for the reconstruction in this study, i.e., only two, resulting in the relatively noisy distributions. To get more accurate distributions, several directional images are needed.

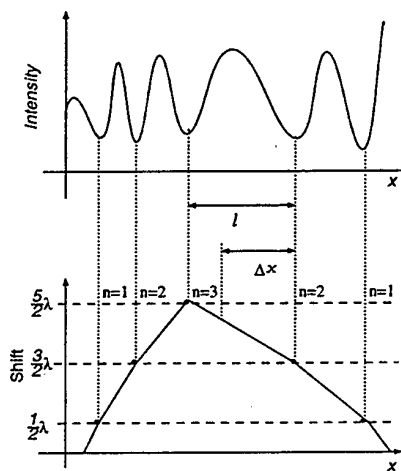
3. RESULTS AND DISCUSSION

Visualization of exchange flow inside a rectangular opening

In the HTGR safety analysis, the buoyancy driven exchange flow of helium and air through a breach should be precisely evaluated. In order to evaluate the basic characteristics of the buoyancy driven exchange flow, simple experiment with small scale model was carried out. Figure 2 shows the schematic of the test section. The test section consisted of two sections, i.e., bottom tank and opening channel. The volume of the bottom tank was about 0.8ℓ.



(a)



(b)

Figure 1: Evaluation of fringe pattern

At the top of the tank, the rectangular opening was settled. The top of the opening was covered by rubber stopper. Although the actual opening in HTGR was cylinder, the rectangular opening was used for the simplicity. The cross-section of the opening was 10mm×10mm square. The height of the opening was 100mm. Since the aspect ratio of the height to equivalent diameter was 10, the exchange flow pattern was classified into the Turbulent Diffusion Region (Epstein 1988).

Initially, the bottom tank and the opening were filled with helium. With removing the rubber stopper at the top of the opening, the light helium inside the tank and the heavy air outside the tank began to exchange through the opening. Then the buoyancy driven exchange flow was formed inside the opening. In this study, the transient density distributions inside the opening channel were measured using the photoconductor-plastics.

Figure 3 shows the schematic of the optical setup for the experiment. As an illumination, 50mW CW diode excited Nd:YAG Laser ($\lambda = 532\text{nm}$) was used. The expanded laser beam was separated into object beam and reference beam by the half mirror (A). To generate the two directional views, the beams were separated by the half mirror (B)

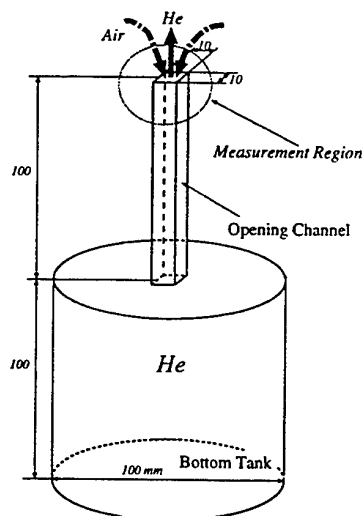


Figure 2: Test section for the exchange flow experiment

and (C), respectively. Then the hologram were recorded in two directions as shown in Fig. 3. The opening was settled at the cross region of the two object beam. Since the size of the laser beam was about 40mm diameter, top of the opening was illuminated as shown in Fig. 2.

On the recording of the hologram, the initial condition of the opening with pure helium was recorded, when the opening was covered by the rubber stopper. The refraction variation of the openings and helium gas were recorded into the hologram of photoconductor-plastics. With reconstructing the hologram, the top cover of the opening was removed to initiate the buoyancy driven exchange flow. The observed interferogram were recorded onto the video tape using the CCD camera. With the fringes of the interferogram images, transient three-dimensional density distribution could be reconstructed using the computer tomography technique.

Figure 4 shows the example of the interferogram images inside the opening. The fringe pattern was clearly shown inside the rectangular opening. In this image, the horizontal fringes were artificially shown with varying the mirror angle slightly. Therefore, the fringe shift was calculated from the variation of the horizontal fringe. With exchanging the helium with air, the fringe pattern shifted slowly, which indicated the helium mole fraction inside the opening decreased slowly.

Unfortunately, the fluctuation inside the opening was too small to visualize the fluctuation of fringe pattern. The flow inside the opening was mainly determined by the diffusion, since the flow pattern was classified into turbulent diffusion. Also, the variation of the mole fraction inside the opening was too small to detect the fringe movement. Further experiment will be carried out to visualize the buoyancy driven exchange flow inside the channel.

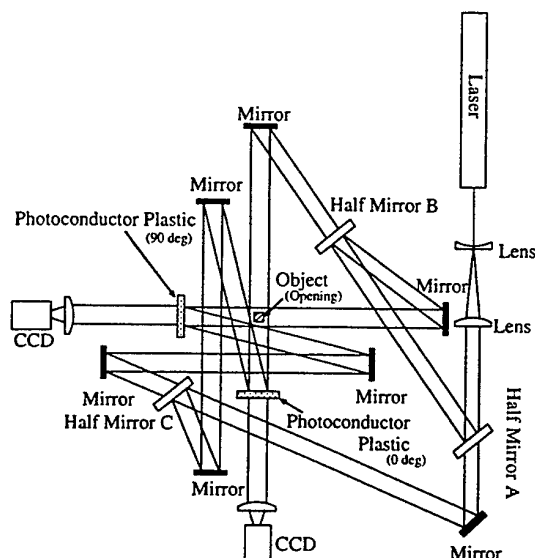


Figure 3: Experimental setup for the real time hologram

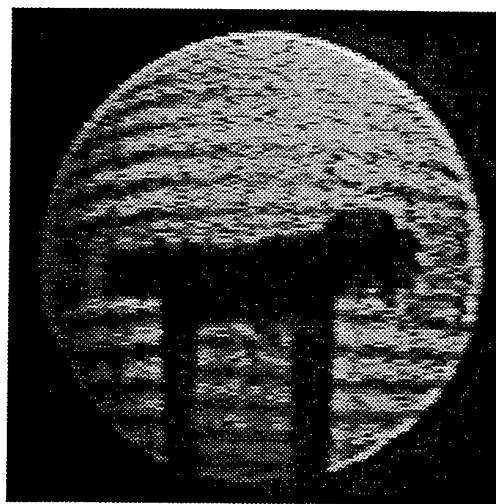


Figure 4: Example of interferogram image inside the opening

The experimental results just show the fringe pattern inside the rectangular channel was measurable. However, with using the photoconductor-plastic as a hologram, visualization of the density inside the opening could be easily carried out, showing the effectiveness of the technique. With analyzing the results, the flow inside the channel could be qualitatively investigated.

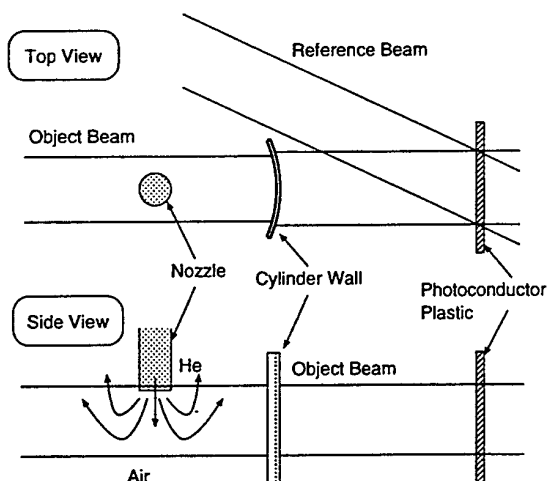


Figure 5: Experimental setup of the cylindrical wall

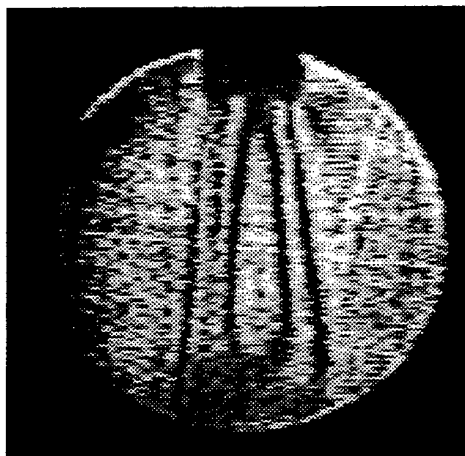


Figure 6: Example of the image through cylindrical wall

Helium jet visualization through a curved wall

In the above experiment, the relatively flat wall was used, therefore, the effects of refraction at the wall was not so large. In this section, to verify the effectiveness of the real time hologram technique with photoconductor-plastic, the helium jet inside the cylindrical wall was visualized.

Figure 5 shows the experimental setup. The part of the acrylic cylinder was set in front of the hologram. The diameter and the thickness of the cylinder were 200mm and 1mm, respectively. Because of the refraction at the wall surface, the laser light was expanded as shown in Fig. 5. Since the effects of the expansion was not so large, the laser light was assumed to be parallel. The hologram on the

photoconductor-plastic contained the information of cylindrical surface refraction. The part of the cylinder was set between the downward helium jet and hologram.

Figure 6 shows the interferogram image of the downward helium jet. The fringe pattern caused by the helium was clearly visualized. In the reconstruction of the image, the expansion effects of the laser were geometrically solved. The results indicated that the effects of curved wall refraction can be easily removed with using the photoconductor-plastic.

The final target of this study is the visualization of the density distribution inside the cylindrical channel. Further experiment will be carried out.

4. CONCLUSION

Using the photoconductor-plastic processed by solvent vapor, hologram is easily developed without any movement or shrinkage. Its high resolution and its high light sensitivity had been confirmed. With this hologram, it is easy to construct real time holographic interferometer.

The helium-air exchange flow inside a small opening was visualized using the photoconductor-plastic. The helium jet was also visualized through a curved wall. The effectiveness of the photoconductor-plastic were demonstrated.

REFERENCES

- Epstein, M., 1988, "Buoyancy-driven exchange flow through small openings in horizontal partitions," *J. Heat Trans.*, Vol.100, pp.885-.
- Kang, T.I., Okamoto, K., Madarame, H. and Fumizawa, M., 1992, "Helium-air exchange flow through a partitioned vertical opening," *Proc. of 5th Int. Topical Meeting on Nucl. Reactor Thermal Hydr.*, vol.II, pp.541-456.
- Merzkirch, M., 1974, *Flow Visualization*, Academic Press.
- Okamoto, K. and Fumizawa M., 1994, "Measurement of Transient Density Distribution Using Mach-Zehnder Interferogram Image," *JSME International J.*, Ser. B, Vol.37, No.3, pp.503-508.
- Tsuru, D., Sato, Y., Madarame, H., Okamoto, K., Fumizawa, M. and Hishida, M., 1995, "Buoyancy-driven exchange flow through an opening with a partition," *J. Visualization Soc. Japan*, Vol. 15, No. S-1, pp.245-248, (in Japanese).
- Verhoeven, D., 1993, "Limited-data computed tomography algorithms for the physical sciences," *Appl. Opt.*, Vol.32, pp. 3736-3754.

TEMPERATURE MEASUREMENT OF 3-D THERMAL FLOW FIELDS USING COLOR IMAGE PROCESSING

Ichiro Kimura * and Mamoru Ozawa **

*Department of Electro-Mechanics
Osaka Electro-Communication University, JAPAN

**Department of Mechanical Engineering
Kansai University, JAPAN

ABSTRACT

It is an important challenge to analyze a three-dimensional thermal flow field in engineering, science, and agriculture. For such an analysis, it is essential to measure physical quantities over the entire thermal flow field.

This paper presents a measurement system based on color image processing for temperature distributions in a three-dimensional thermal flow field. Flow visualization is accomplished by the use of thermo-sensitive liquid crystal tracers. Its color gives temperature information.

An algorithm for the color-to-temperature transformation using a multi-layer feedforward neural network is applied to a three-dimensional natural convection in a rotating circular cell. Two-dimensional temperature distributions on a slit plane are obtained by using the algorithm. A three-dimensional temperature distribution is consequently constructed by interpolating the two-dimensional distributions using the B-spline function.

1. INTRODUCTION

It is essential to measure a temperature and a velocity distribution in order to experimentally analyze such thermal flow fields as a natural convection. For the measurement, the acquisition of velocity and temperature information is needed. A most appropriate method for flow visualization is a thermo-sensitive liquid crystal suspension method. The movement of a liquid crystal tracer pattern during a constant time interval gives a velocity vector and its color indicates a temperature. Recently, Kimura *et al.* (1989) and Ozawa *et al.* (1992) have reported such a two-dimensional measurement system based on color image processing.

The system can obtain simultaneously both two-dimensional velocity and temperature fields in thermal flow fields.

For analyzing a more highly complex field, it is essential to measure three-dimensional quantitative information over the entire flow field. The purpose of this study is to expand the temperature measurement to a three-dimensional thermal flow field. A rotating natural convection in a cylindrical cell is visualized by using a thermo-sensitive liquid-crystal tracer. The three-dimensional temperature distribution is obtained from the visualized color images by using the algorithm for color-to-temperature calibration using artificial neural networks reported by Kimura *et al.* (1993) and the B-spline interpolation.

2. FLOW VISUALIZATION AND IMAGE PROCESSING SYSTEM

Figure 1 shows a side view of the experimental setup for flow visualization. The test volume (1) is a cylindrical cell 50 mm in radius and 50 mm in height. The top and the bottom walls of the enclosure (2 and 3) are composed of an acrylic resin plate 2 mm in thickness and a copper plate 25 mm in thickness, respectively. Above and below the plates, water jackets (4 and 5) are attached. Constant-temperature water circulates in the water jackets for heating or cooling the test fluid.

A thermo-sensitive liquid crystal suspension method is adopted for flow visualization. A silicon oil is used as the operating fluid because a combination of silicon oil and the cholesteric liquid crystals gives a very vivid color. Microencapsulated cholesteric liquid crystals about 20 μ m in diameter are used as tracer particles and the concentration of the liquid crystals is about 0.1 weight percent. The thermo-sensitive tracers turn from colorless to red and pass through green and

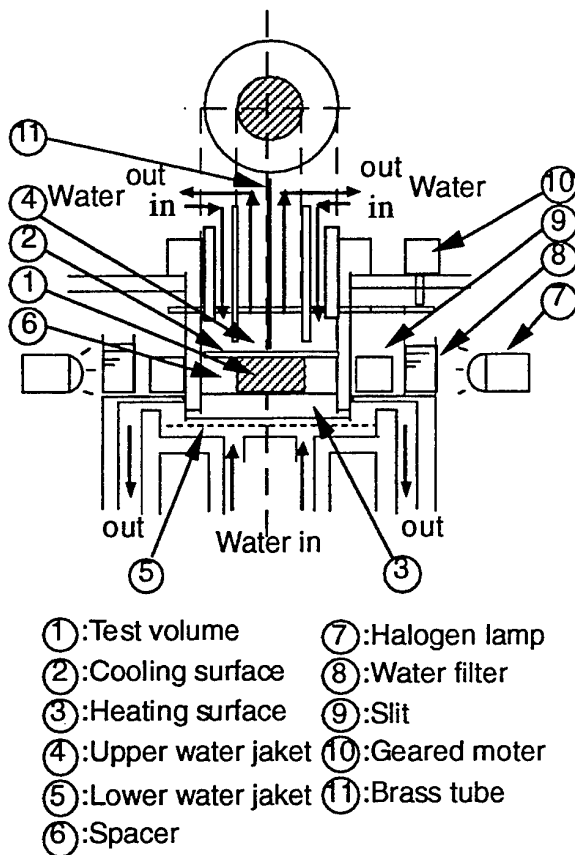


Fig.1 Experimental setup for flow visualization

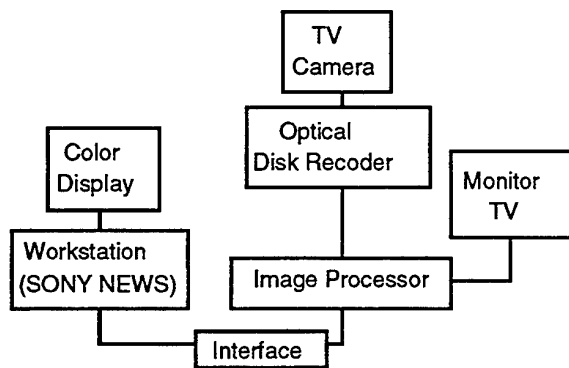


Fig.2 Schematic diagram of image processing

blue before turning colorless again with an increase in the temperature.

The thermo-sensitive tracers are illuminated through slits (9) 7 mm in slit width by halogen lamps (7).

A water filter (8) is placed in front of each lamp to prevent excessive radiant heat transfer from the lamp to the test fluid. The reflected light is observed by a TV camera installed at right angles to the illuminated sheet. Since the cell is cylindrical, it distorts and deforms the views because of the difference of refractive index between liquid and air. The images are reconstructed in a simple way as follows. A graph paper is placed at the slit plane. The images are geometrically transformed using a simple formula obtained from known point coordinates of the graph paper on both the image and slit planes.

The calibration of color to temperature for the thermo-sensitive liquid crystals is undertaken as follows. First, a thermal stratification is formed in the test volume by heating the upper heating surface (18.3 °C) and cooling the lower one (14.7°C) for a few hours. Next, the temperature in the test volume is measured with a Chromel-Alumel thermocouple led through a brass tube (11). The thermocouple is traversed vertically from the top to the bottom in the thermal stratification. The position of the thermocouple and the color of the liquid crystals are recorded by an optical disk recorder.

The experiment is carried out in the following manner. First, the temperatures of the upper and lower walls of the test volume, which is rotating at 10.1 r.p.m. with a geared motor (10), are kept respectively at lower and higher temperatures (15.6°C and 17.9°C). After several hours, a steady natural convection is formed in the test section. In this case, the Rayleigh number is 2.55×10^5 .

Figure 2 shows a schematic diagram of the image processing. Each color image obtained by a TV camera is separated into R, G, and B (red, green, and blue) images and stored in an image processor. The image data are sent to a workstation for color image processing. Finally, the results are displayed on a graphic display.

3. TRANSFORMATION OF COLOR TO TEMPERATURE USING NEURAL NETWORKS.

Figure 3 shows the normalized r(red), g(green), and b(blue) values versus the temperature T_m , which is obtained by the calibration of color to temperature. The temperature T_m is the values measured by the thermocouple. The normalized r,g,b values are calculated by

$$r = \frac{R}{R+G+B}, \quad g = \frac{G}{R+G+B}, \quad b = \frac{B}{R+G+B} \quad (1)$$

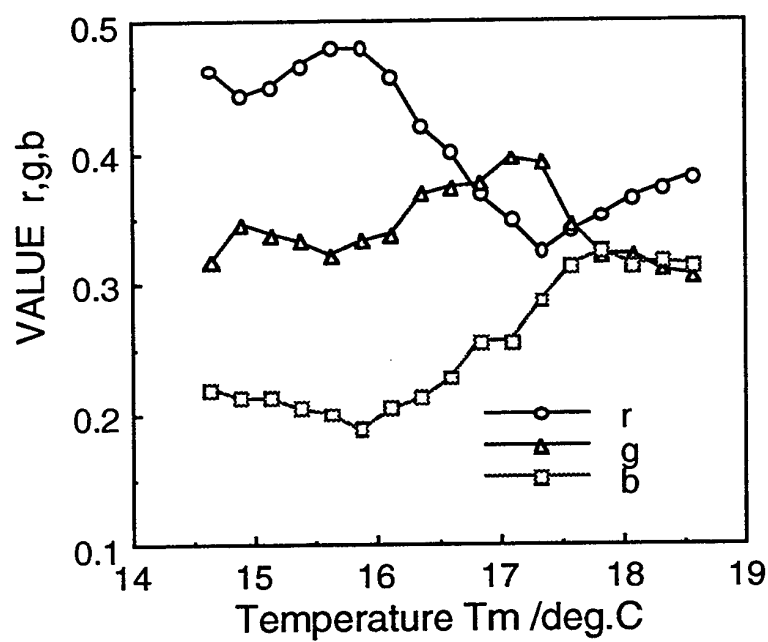


Fig. 3 Relationship between r,g,b and temperature T_m

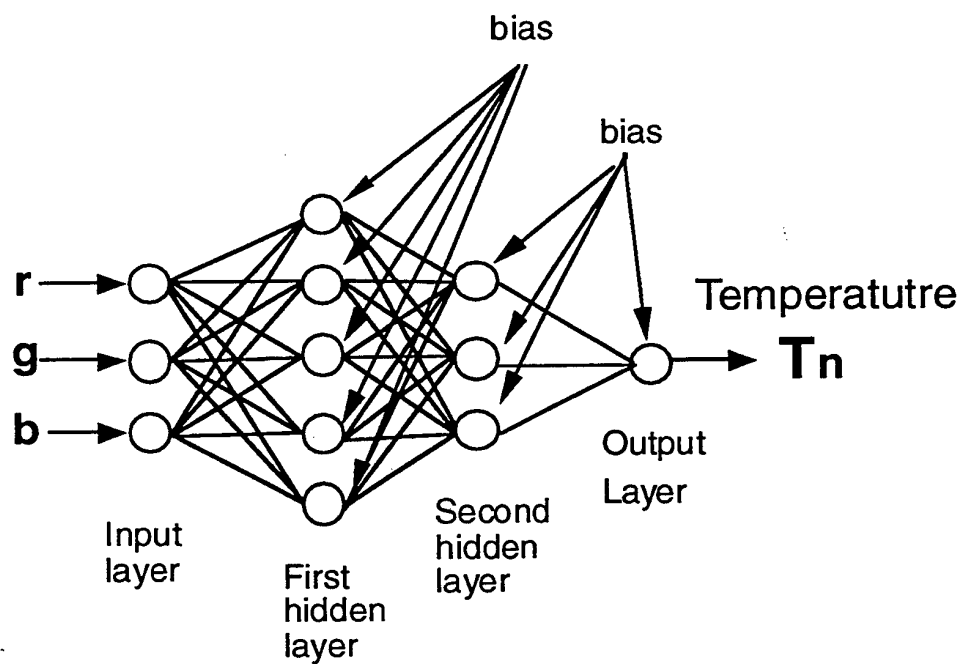


Fig.4 Neural network structure

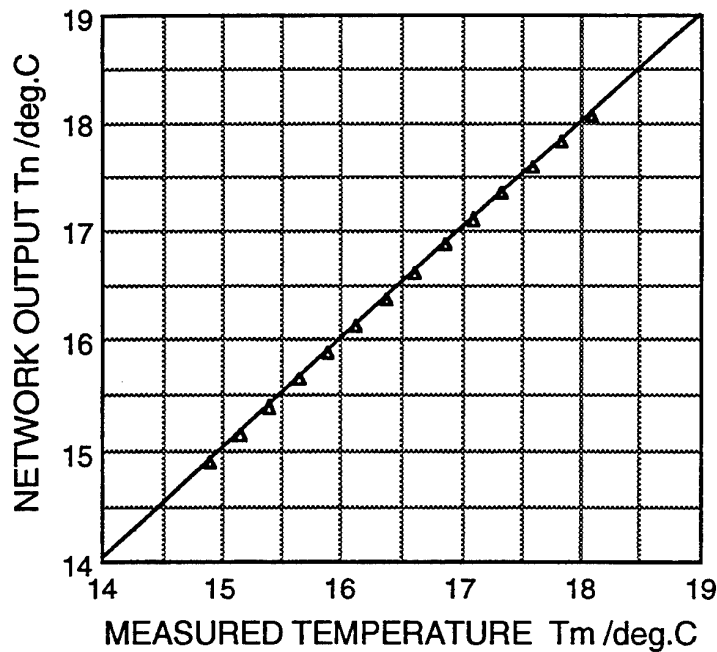


Fig.5 Relationship between measured temperature T_m and network output T_n

Formularizing the color-to-temperature relationship has emerged as an important problem because of its strong nonlinearity. To solve the problem, we adopt a four-layer feedforward neural network shown in Fig. 4. The inputs of the network are r , g , and b values. The output is the temperature T_n . The network consists of four layers, namely, an input, a first hidden, a second hidden, and an output layer. The five units in the first hidden layer, three units in the second hidden layer, and one unit in the output layer are neurons. The three units in the input layer are linear devices. The parameters in the network are determined so that the output T_n corresponding to the inputs of r , g , b patterns agrees well with the T_m measured by the thermocouple. We use the Back-propagation algorithm reported by Rumelhart *et al.* (1986) for learning. The input data are 14 patterns of r , g , b corresponding to the temperature T_m at every 0.25 K in the range of 14.7-18.3 °C and the teaching data are the corresponding measured temperature T_m . The number of times for learning is 5,000.

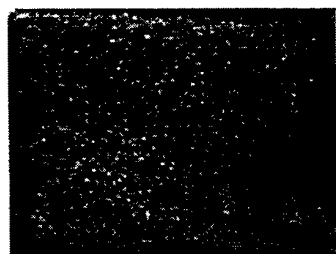
Figure 5 shows the relationship between the measured temperature T_m and the network output T_n after learning. The T_n agrees well with T_m almost over the entire measurement range. By using the neural

network, the color at each pixel in the images can be transformed into temperature. Applying the transformation to all the pixels on a visualized image gives a two-dimensional temperature distribution over the entire field. Some image noises, however, exist in the distribution. In order to eliminate the noises, the Median filter is used.

4. APPLICATION TO A ROTATING NATURAL CONVECTION

Figure 6 shows an example of the visualized images of the rotating steady natural convection at a slit section and its temperature distribution, which is expressed by using pseudo colors, obtained by the image processing. Since the test volume rotates, 178 such temperature distributions per one rotation are obtained.

From the distributions, such a horizontally sectional view as shown in Fig. 7 is reconstructed. It must be the temperature distribution in a horizontal cross section at the distance $Z=25$ mm from the top of the test volume. The distribution, however, lacks



(a) Visualized image



(b) Image processing output

Fig.6 Visualized image and its temperature distribution at a slit section

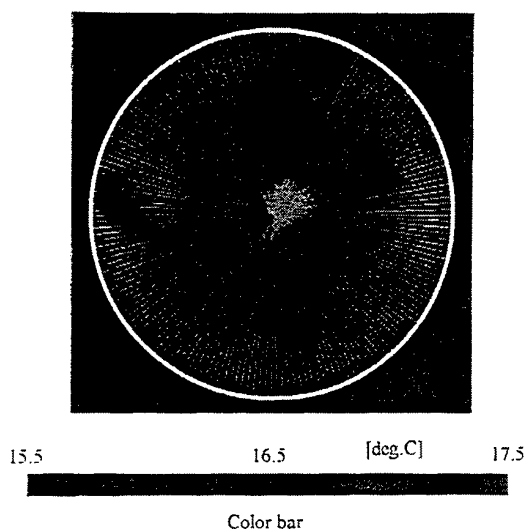


Fig.7 Horizontal view reconstructed from temperature distributions at a slit section

temperature information in the area between a measured vertical cross section and the next. It must be interpolated accordingly.

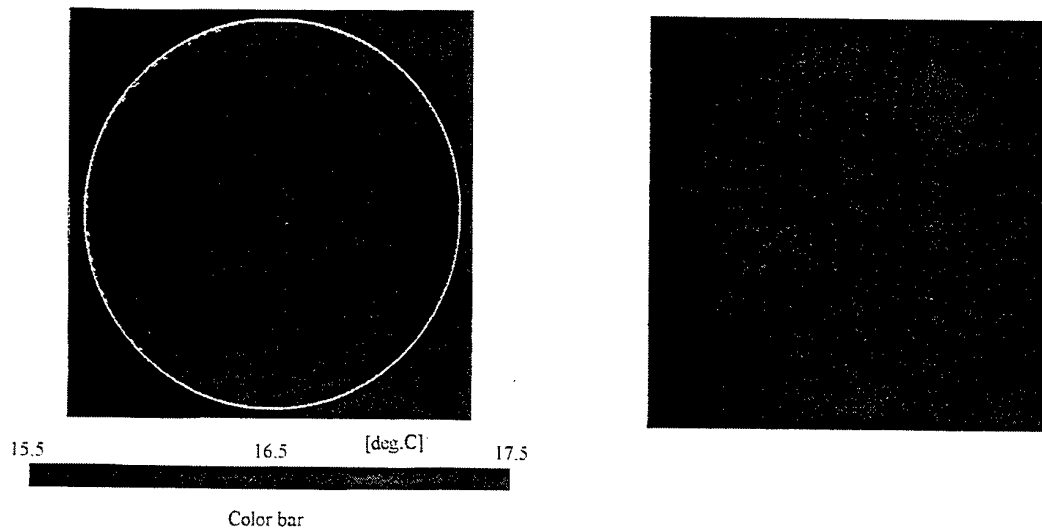
Figure 8 (a) shows the temperature distribution obtained by interpolating unmeasured temperatures using the B-spline function from the 178 temperature

distributions. The distribution agrees well comparatively with the visualized image in almost the same horizontal cross section ($Z=25$ mm) shown in the figure (b). The fluid in the middle of the test volume has a higher temperature, while in the vicinity of the outer wall the fluid has a lower temperature and partly shows a higher temperature.

Figure 9 shows a set of temperature distributions at six horizontal cross sections, which must be the three-dimensional representation of the rotating natural convection. From this figure, the following phenomenon can be derived. The fluid at a higher temperature moves upwards from the bottom to the top in the middle of the test volume. On the other hand, the fluid at a lower temperature moves downwards from the top to the bottom along the side wall. Furthermore, it is assumed that six secondary rolling convections exist in the vicinity of the bottom.

5. CONCLUSION

We carried out to measure a three-dimensional temperature distribution in a rotating natural convection by applying the color image processing to the images visualized by thermo-sensitive liquid crystal tracers. Consequently, it was confirmed that the measurement system is very useful for experimentally analyzing three-dimensional thermal flow phenomena. A three-dimensional velocity distribution, however, will be needed for more detailed analysis and be able to be measured using the spatio-temporal correlation method



(a) Temperature distribution

(b) Visualized image

Fig.8 Comparison of the measured result with visualized image

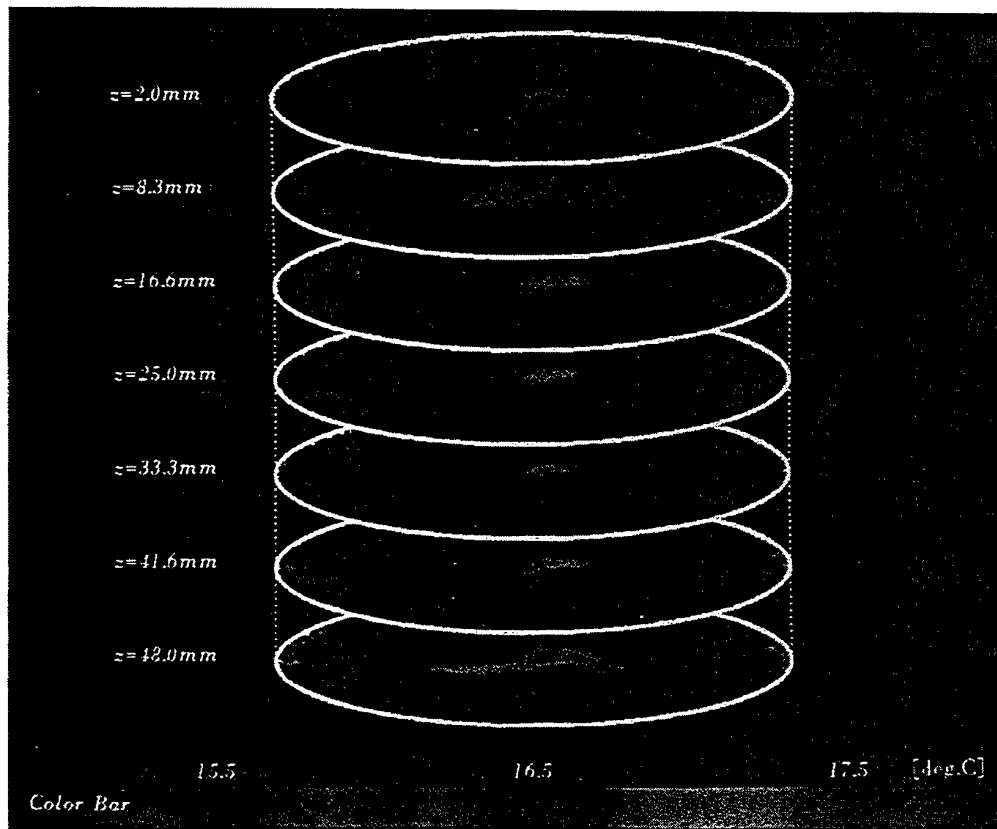


Fig.9 Three-dimensional representation of temperature distributions

developed by Kimura *et al.* (1991,1993). We will have been measuring simultaneous velocity and temperature fields for the three-dimensional rotating natural convection.

ACKNOWLEDGMENT

The authors would like to thank Messrs. T.Hyodo and M.Shinoki for their help with experiments and computer programming.

REFERENCES

Kimura,I., Takamori,T.,Ozawa, M., Takenaka,N. & Manabe,Y. 1989, Quantitative Thermal Flow Visualization Using Color Image Processing (Application to a Natural Convection Visualized by Liquid Crystals), ASME, FED-vol.85, pp.69-76 .

Kimura,I., Kohno, Y. & Takamori,T., 1991, Measurement of Three-Dimensional Velocity Vectors in a Flow Field Based on Spatio-Temporal Image Correlation, Proc. 3rd Int. Symp. on Fluid Control, Measurement, and Visualization, San Francisco, pp.609-615.

Kimura,I., Bando, R., & Kuroe,Y., 1993, Measurement of 3-D Velocity Vectors Based on Spatio-Temporal Image Correlation (Processing of Erroneous Vectors Using Neural Network), ASME FED-vol.172, pp.121-126.

Kimura,I., Kuroe,Y., & Ozawa, M., 1993, Application of Neural Networks to Quantative Flow Visualization, J. Flow Visualization and Image Processing, vol.1, pp.261-269.

Ozawa, M., Muller,U., Kimura,I.,& Takamori,T., 1992, Flow and Temperature Measurement of Natural Convection in a Hele-Shaw Cell Using a Thermo-Sensitive Liquid Crystal, Experiments in Fluid no.12, pp. 213-222.

Rumelhart,D.E., Hinton,G.E. & Williams,R.J. 1986, Learning Representations by Back-Propagating Errors, Nature, no.323, pp.533-53

SESSION 25

Liquid Films

DROPLET CONCENTRATION AND VELOCITY FIELDS IN SPARK-IGNITION ENGINES

C. Arcoumanis D S Whitelaw and J H Whitelaw
Thermofluids Section, Department of Mechanical Engineering
Imperial College of Science, Technology and Medicine
London SW7 2BX

1. ABSTRACT

High speed photographs obtained with a Cu-vapour laser synchronised to a cine camera, and phase Doppler measurements at various positions were used to characterise the spray development from an inclined gasoline injector mounted on an idealised port simulating the spray/wall interaction in the intake system of spark-ignition engines. Tests were performed at two air flowrates resulting in dry wall and wet wall conditions at the time of the spray impingement. With the lower air velocity, the fuel wall film survived from one injection to the next and became thicker with the result that a region of large droplets was identified downstream of the location of injection and immediately above the film. The higher air velocity, on the other hand, was able to convect downstream a much wider droplet size range thus leading to a nearly dry wall at the time of the subsequent fuel injection. It is expected, however, that longer times between injection will favour dry wall conditions and shorter times a wet wall. Larger angles of spray injection are expected to lead to thickening of the wall film and to results similar to those with small times between injection and low air velocities. On the other hand, a hot surface will tend to evaporate the liquid on the wall so that the film will decrease in thickness with associated reduction in the secondary atomisation induced at the Weber numbers of the present spray.

2. INTRODUCTION

The impingement of sprays on walls has been examined in previous papers including, for example, those of Naber and Farrell (1993) and Chandra and Avedisian (1991) who examined single drops of n-heptane, Hardalupas et al (1993) with a gasoline injector and Arcoumanis and Chang (1993, 1994), Arcoumanis and Cutter (1995), Arcoumanis, Cutter and Whitelaw (1995) with Diesel injectors. In addition, there have been several investigations of droplets of gasoline within the cylinders of engines, including those of Hardalupas et al (1995a) and Cousyn et al (1995). Also Hardalupas et al (1991) reported detailed measurements of a gasoline spray in ambient air. The measurements of Hardalupas et al (1993) and Hardalupas et al (1995b) are particularly relevant to the present investigation in that

they reported measurements of the droplet characteristics in the vicinity of a gasoline spray which impinged on a flat surface and on a rod, respectively. In the former investigation, a gasoline spray was directed at a disk 40 mm from the injector, with the angles between the axis of the spray and the surface of 0, 20, and 45 degrees, and the results showed that the size range of the droplets generated by secondary atomisation depended on the angle between the incident spray and the inclination of the disk and was largest for the 20 degree angle. Hardalupas et al (1995b) reported measurements of drop velocity, diameter and volume flux in the vicinity of a 7 mm diameter rod located 40 mm from a gasoline injector to demonstrate that approximately half of the gasoline formed a film on the rod; also, about half of the liquid flux impinging on the rod was subject to secondary atomisation so that smaller droplets were observed to move away from the rod for a short distance. It can be expected that liquid films and secondary atomisation will form an important part of the present investigation.

3. FLOW CONFIGURATION AND INSTRUMENTATION

3.1 Flow configuration

The flow configuration is shown on figure 1 and comprised a small wind tunnel with a working section of 32 mm x 172 mm cross-section and free-stream air velocities of 5 and 15 m/s. An injector could be fixed to the top surface of the channel and arranged to project its spray towards the lower surface. The results described in the following section were obtained with an injector (Bosch 280 150 701) arranged on the centre line of the tunnel, at 20 degrees angle from vertical, operating with iso-octane (type 2,2,4-Trimethylpentane with density 692 kg/m³) with the fuel line pressure set to 3 bar and the injector energised for 10 ms every 100 ms and, therefore, representative of a high load in an operating spark-ignition engine. This last specification ensured that a film remained on the surface after the first injection with the low air velocity and less so with the high air velocity which was sufficient to sweep away most of the surface liquid between injections.

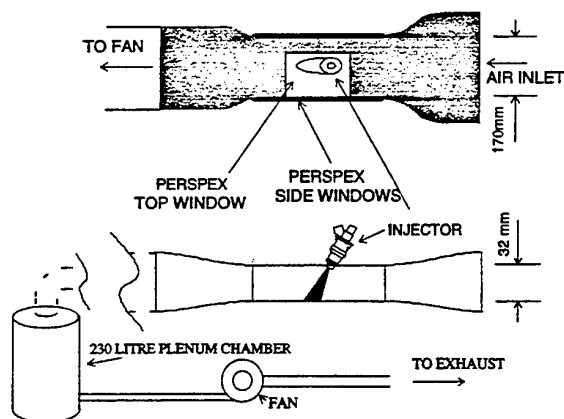


Figure 1 Flow configuration of flat channel which is shown in third angle projection.

The air flow in the tunnel was investigated first in the absence of the injected fluid and it was shown that for both the cross-stream velocities the boundary layer existed within only 5 mm of the channel wall and the remainder of the velocity profile across the channel was uniform. Measurements away from the axis of the flow confirmed that the flow was essentially two-dimensional apart from the boundary layer on the side wall which did not interfere with the results presented below.

The monojet injector comprised a body, a needle and a solenoid armature. With no current in the solenoid winding, the needle was forced against its seat at the valve outlet side by a helical spring and, when current flowed, the solenoid winding was excited and the needle rose approximately 0.1 mm from its seat, allowing fuel to pass through the precision ring opening.

3.2 Instrumentation

The instrumentation included a phase-Doppler velocimeter and photographic components as described below. The air flow measurements were obtained with the phase-Doppler velocimeter operating as a laser-Doppler velocimeter, the air flow seeded by particles generated in a smoke generator (Danichi PS 1001), and all information of droplets with a combination of fast photography and phase-Doppler velocimetry.

The phase-Doppler velocimeter was similar to that used by Arcoumanis et al (1995) to investigate the impingement of Diesel sprays on surfaces and comprised of a Spectra Physics argon-ion laser set to wavelength 514.5 nm and operating at a power of 200 mW, the beam from which was focused onto a circular diffraction grating within a custom made transmitting optical unit. The diffraction grating acted as a beam splitter and was rotated to provide a frequency shift of 0.5 MHz between the two beams. After collimation the beams were refocused to form the control volume at their point of intersection using a 600 mm lens and the light scattered from particles passing through this control volume was collected using a receiver unit (Aerometrics RCV-2100) oriented at 30 degrees to the forward axis. The signals were processed (Aerometrics PDP-3100) and

analysed with the help of a microcomputer. The optics were aligned to record droplet velocity and diameter parallel to the channel surface and side walls. Figure 2 provides a photograph of the phase-Doppler velocimeter arranged around the flat channel.

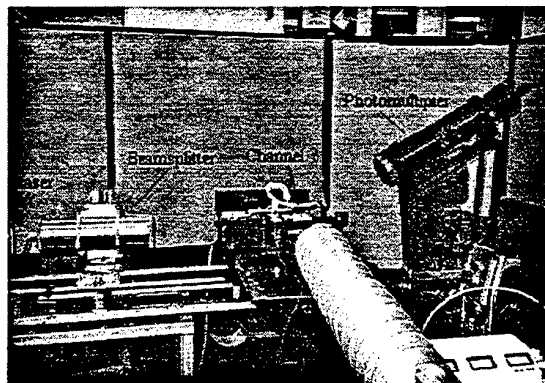


Figure 2 View of the phase doppler instrumentation arranged around the flat channel.

The photographic investigation involved positioning a high speed cine camera (Hadland Photec 16 mm) perpendicular to the direction of the air flow to photograph the injector spray through the side window of the channel. A series of extension rings were used in conjunction with a Mamiya 80 mm lens to provide the magnification enabling close up pictures of the spray hitting the wall to be taken, as well as photographs of the entire spray. The camera was equipped with a half-sized rotating prism providing twice the standard camera frame rate at 20000 frames / s at the expense of half height frames. Illumination of the droplets was provided by a copper-vapour pulsed laser (Oxford Lasers Cu 15). An optical fibre was used to direct the light into the camera with a semi-transparent plastic sheet as a diffuser, thus back lighting the droplet or directed to provide front lighting of the droplets, with the back of the channel blacked off to prevent reflection. The copper vapour laser offered the benefits of freezing the droplet motion due to the 10-40 ns pulse length of the laser light, increasing light energy with pulse frequency compensating for the decreasing exposure time, and the facility to synchronise the laser pulse rate to the frame rate of the camera. The camera was triggered by passing a low power He-Ne laser beam across the top of the nozzle exit, which was directed into a photodiode whose associated circuitry triggered the camera on interruption of the light beam. High speed film (Kodak 7250 16 mm) provided a clear image up to 10 mm downstream from the nozzle up to a frame rate of 14,000 frames / s. The arrangement is shown on figure 3.

The following section presents measurements made with the injector spraying into atmospheric air, followed by the consequences of impingement upon the wall of the flat channel.

4. RESULTS AND DISCUSSION

Measurements of droplet characteristics in the free spray were obtained at a distance of 80 mm from the nozzle which is a typical distance to the back of the inlet valve at which the spray is usually targeted in intake ports. The spacing between the measurement locations was between 2 and 4 mm with small intervals around the locations of large droplets flux. Mean droplet characteristics represent an ensemble-average over 1500 droplets and the temporal characteristics are shown for times after the beginning of injection. Liquid fluxes are presented in arbitrary units.

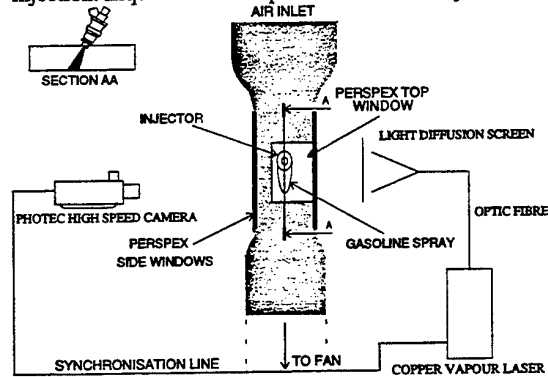


Figure 3 Diagram of photographic arrangement in relation to the flat channel

Figure 4 indicates the patterning of the spray and that the flow rate of the fuel increased linearly with the duration of injection pulse in the range 2.5 - 10 ms which is typical for automotive SI engine applications. The spray was of a hollow cone shape with the flux peak opening of around 10 degrees and with some 20 degrees opening of the base area of the cone. The Sauter mean diameter of the droplets ranged from 90 to 160 μm and the mean axial velocity of the droplets reached 18 m/s as indicated in figure 5. The first droplets arrived at the measuring location about 6.5 ms after the start of injection and had sizes and velocities of around 150 μm and 15 m/s, respectively. The droplet velocity reached a maximum of around 27 m/s at the middle of the injection period and decreased afterwards suggesting that the injector did not reach a steady phase over the pulse. The velocities of the large droplets were highest and this is to be expected due to their longer relaxation times. There were no large droplets at the trailing edge of the spray and associated with the closure of the pintle.

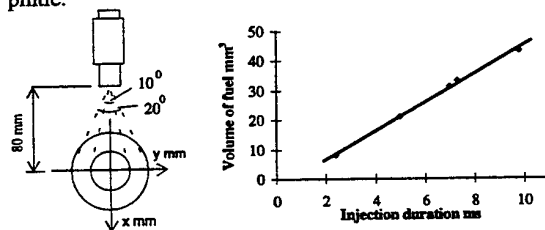


Figure 4 Spray patterning diagram and fuel volume plotted against duration.

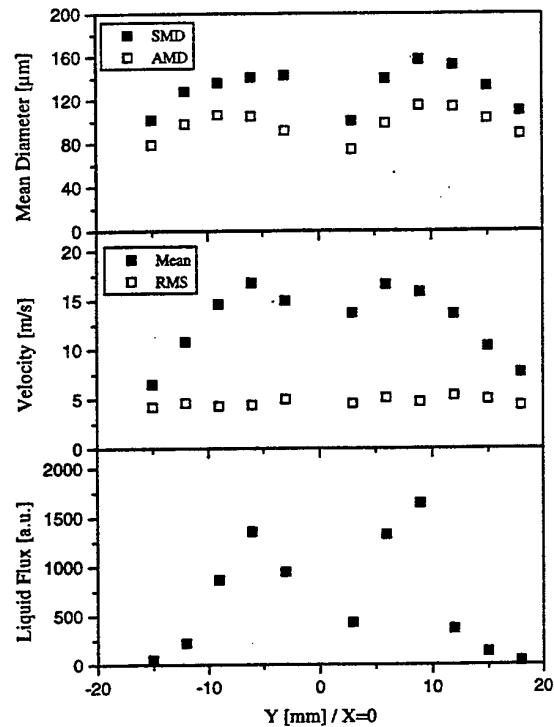


Figure 5 Centreline profiles of mean diameter, velocity and liquid flux for the Bosch injector.

The contour plots of figure 6 are based on about 70 measurement locations within the two-dimensional plane of the cone normal to the surface and through the axis, and calculated in terms of a weighted average and a smoothing algorithm. As expected, they show that the largest diameters, velocities and fluxes were associated with the same location which was close to the centre of the cone. The spatially-averaged Sauter mean diameters, weighted with the data rate at each location, were around 130 μm .

The same injector was assembled on the top surface of the flat wall wind tunnel and the droplets were observed photographically as, for example, in the film sequences of figure 7 which correspond to an air flow velocity of 15 m/s and a time interval of 0.5 ms from the initiation of the spray. The greater deflection with the higher velocity is apparent, although the effect is small, together with the larger number of droplets in the wake of the spray. The angle of the impinging spray is of the same order as that of the free spray referred to above, namely 10 degrees, and the locations of impingement of the bisector of this angle were 9 and 16 mm from the plane of the injector

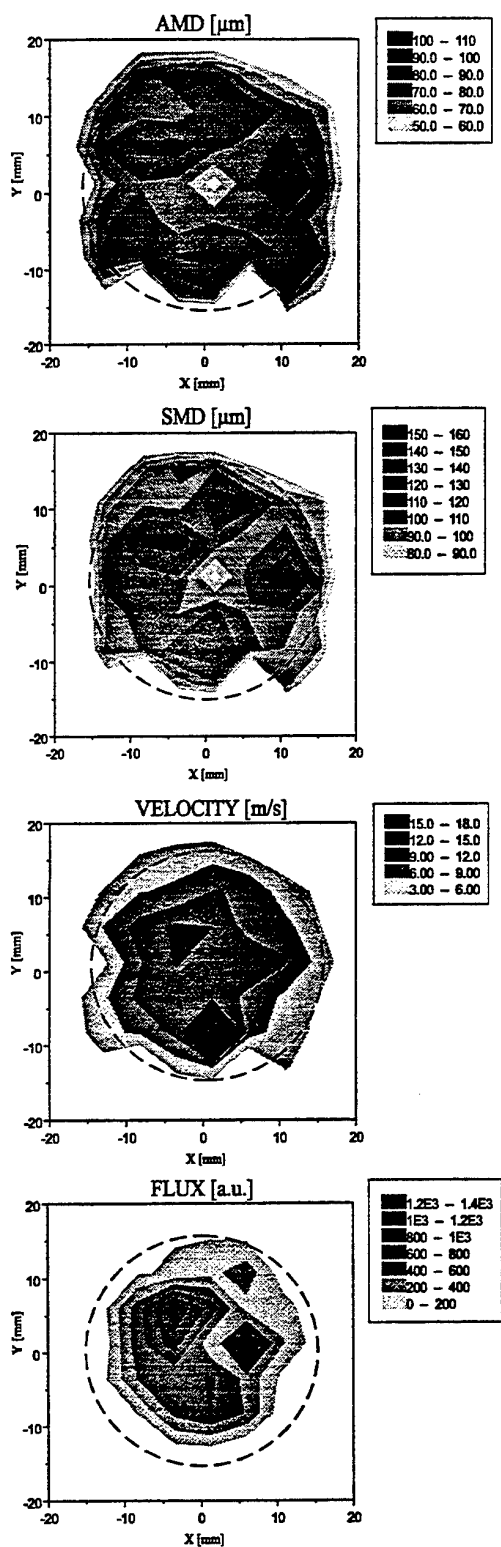


Figure 6 Contour plots of mean diameter velocity and volume flux for the Bosch injector.

Close inspection of figure 7 reveals that the tip of the unconfined spray spread outwards on leaving the injector with a cone angle which increased to around 20 degrees as it descended towards the plate. With a period of 100 ms between injections, which implies an almost dry surface between injections with the higher air velocity, the large leading droplets impinged on the surface to form a number of individual films which, with the arrival of later droplets, joined to form a single film.

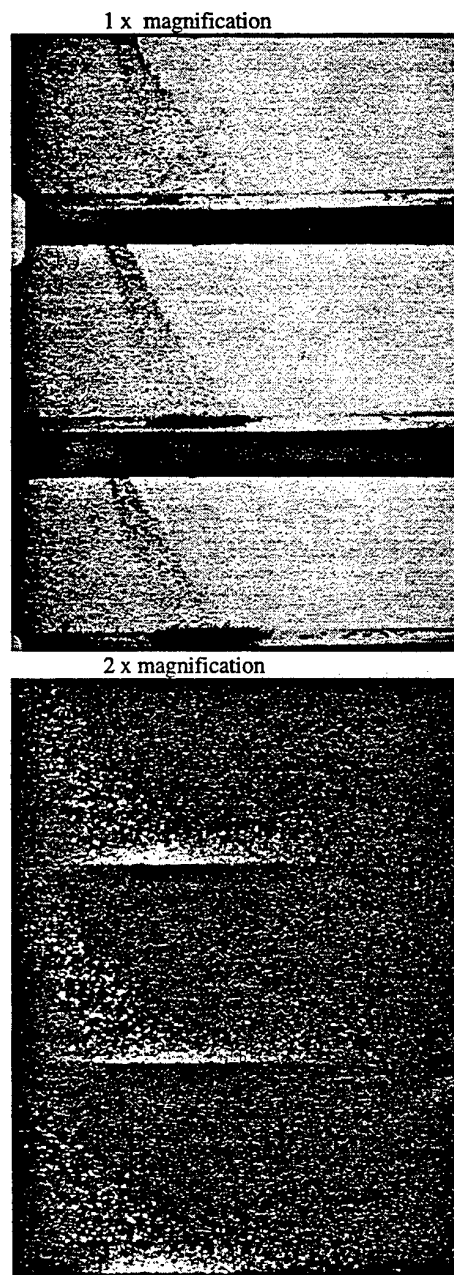


Figure 7 High speed photographic sequences of spray impinging on the bottom surface of the flat channel, filmed at approximate 13000 frames / s.

It has been shown by Ozdemir and Whitelaw (1993) that secondary atomisation occurs when a diesel spray impacts upon a plate coated with a film of diesel oil generated from previous injections and implied that, the thicker the liquid film, the larger the droplets formed from secondary atomisation. In the present case it would thus be expected that the droplets formed from secondary atomisation with the higher air flow would be smaller than those produced with the lower air flow due to the thinner film. The photographs support this idea as a fine mist tended to develop above the plate and in the region of impingement so that observation rapidly became difficult. This mist was probably associated with droplets striking the film as it reached its maximum thickness and it can be expected that it decreased in density with the lower air velocity with which the film was not swept away between injections. The close-up pictures of figure 7, obtained with back-scattered light, show the larger droplets with higher clarity, and demonstrate that there are larger droplets within the mist and resulting from the secondary atomisation. These droplets had a low trajectory and impacted on the plate further downstream. It is this process that wetted the plate downstream of the spray, at the start of injection, and before the film was moved downstream by the action of the air and the flow induced by the impinging spray. Small droplets achieved higher trajectories, and those in the wake of the spray were transported downstream by the air flow and more so with the higher air velocity. With the lower velocity, the liquid film encompassed a region upstream of the impingement region as well as downstream and the less dense mist was confirmed.

Sauter Mean Diameters were measured parallel to the plate with air velocities of 5 and 15 m/s and the results plotted in figure 8. With the lower air-flow velocity, there was a region of large droplets greater than 167 μm in diameter extending from 25 mm downstream and up to 2 mm above the plate. The droplet diameters decreased at larger values of y except within the incoming spray. This region of high SMDs close to the plate is probably due to the impaction of the spray on the liquid film left from the previous injection and was of the order of 0.5 mm thick. With the higher air-flow velocity, the range of SMDs was smaller, up to a maximum of 167 μm , in accordance with the idea that the secondary atomisation from the thinner film produced smaller droplets. The region of impingement of the injected spray, up to 20 mm downstream, shows an area of smaller droplet sizes for both air-flow velocities. This is due to the large number of smaller droplets formed from the secondary atomisation, whilst the larger droplets with larger momentum moved downstream on a trajectory almost parallel to the plate. The air velocity close to the film is probably too low to strip droplets from the film.

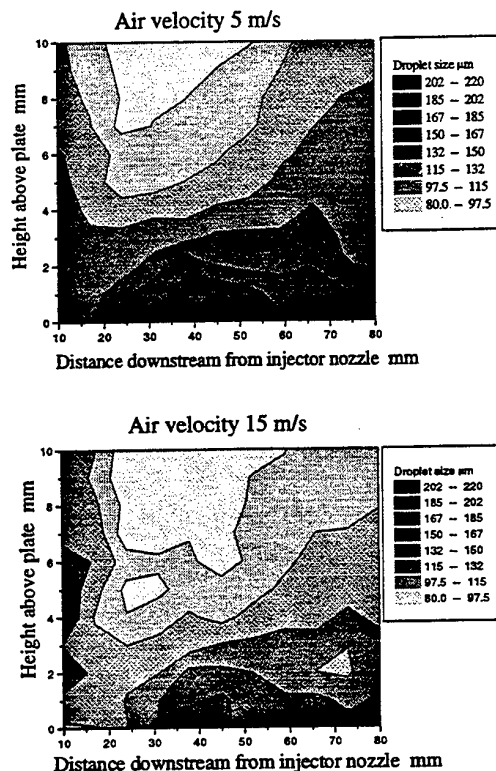


Figure 8 Contour plots of Sauter mean diameter

Ensemble averages of the velocity components measured parallel to the plate with air velocities of 5 and 15 m/s are presented in the form of contour plots, figure 9, and confirm that the lowest velocities occurred at the stagnation point and increased in all directions. The maximum velocities in the region of measurements were 8 and 12 m/s for the two air velocities and may be compared with a maximum droplet velocity of around 15 m/s at 80 mm from the exit of the injector. It should be remembered that these velocities are more representative of smaller droplets than of large ones since there are more of the former in the ensemble averages. It can be seen that the velocity of the spray declined rapidly as it approached the plate and particularly so very close to the plate since the measurements include droplets which travelled against the spray as a consequence of impingement and the formation of the mist of small droplets.

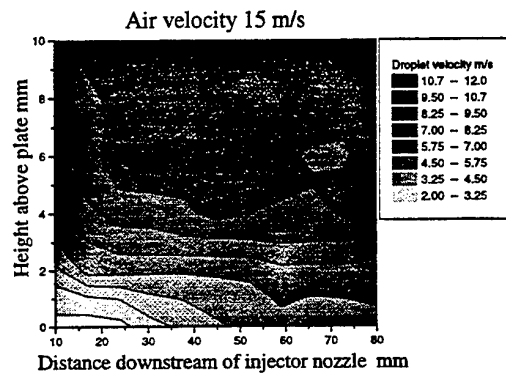
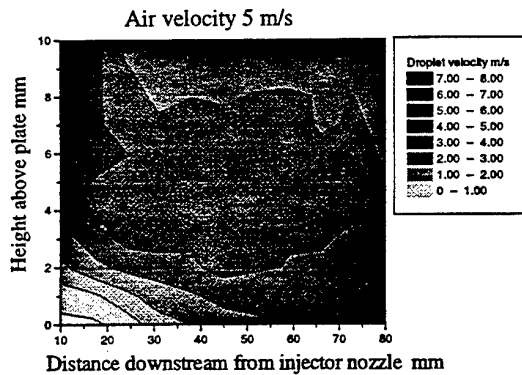


Figure 9 Contour plots of droplet velocity measured parallel to the base plate of the channel.

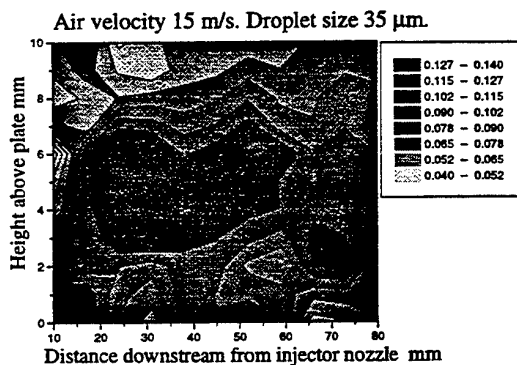
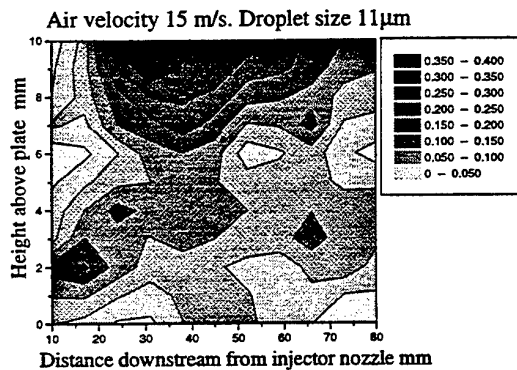


Figure 10 Contour plots of normalised population density.

This is consistent with the results of Hardalupas et al (1993) and is confirmed by the low SMDs in the stagnation region of figure 8. Higher droplet velocities are evident in a region immediately downstream of the injected spray, where the population density of droplets, plotted for droplet sizes 11 and 35 μm for high air velocity and referred to in terms of their normalised median values and shown in figure 10, was largest for sizes between 11 and 35 μm . For the high air velocity case, this is due to acceleration of the small droplets from the outer region of the spray and, with the smaller air velocity, to the horizontal component of velocity of the spray from the injector of around 7 m/s, being higher than the 5 m/s cross flow velocity, and the smaller droplets being forced from the side of the spray by the larger droplets and the entrained air, as observed also by Hardalupas et al (1993).

5. CONCLUDING REMARKS

It is clear from the above, that the gasoline spray impinged on a surface which became wet as the spray continued so that small diameter droplets formed a mist above the plate and downstream of the location of impingement. With the lower cross-stream air velocity, the film survived from one injection to the next and became thicker with the result that a region of large droplets existed downstream of the location of injection and immediately above the film. It was expected that longer times between injection would emphasise the first result and shorter times between injection the latter. Larger injection angles can be expected to lead to thickening of the film and to results similar to those with short times between injections and low air velocities while a hot surface will tend to evaporate the liquid so that the film will decrease in thickness, again with reduction in secondary atomisation with the Weber numbers of the present injector.

The implications for droplets injected into an intake port are that a film is likely to form on the valve stem from any part of the spray which strikes it, consistent with that of Hardalupas et al (1995b), and on the port wall and valve. Since the air flow will initially be only that induced by the spray, if the valves are closed, films are likely to form with some splash atomisation to provide a region of small droplets in the vicinity of impingement and larger droplets close to the surfaces away from impingement. Evaporation will occur, with magnitude dependent upon the surface temperature and residence time and valve opening will lead to an air flow which will rapidly sweep out the vapour and droplets and subsequently atomise any film but more slowly and with large droplets. With injection against an open valve, the air velocities will be large and the surfaces will tend to remain dry so that droplets should be smaller than those of the spray, as in the present experiment with the higher velocity but more so.

It is known from results such as those of Cousyn et al (1995) and Hardalupas et al (1995a) that the number and size of droplets which emerge from the inlet valves and enter the cylinder will depend on the timing of injection so that early injection with the valves closed leads to small

concentrations of droplets in the cylinder whereas injection with the valves open can lead to most of the fuel entering the cylinder in the form of droplets. In both cases, but with vastly different numbers of droplets, the flow from the inlet valve is mainly across the head towards the exhaust valve with high probability of impingement on the liner and with droplet velocities similar to those investigated here. The air velocities are less certain but likely to be rather less than the droplet velocities so that the present experiment is a reasonable model except in respect of the wall temperature. Thus the arguments of droplets transported by the tumble flow with injection during valve opening seem plausible and the corresponding assumption of rapid evaporation of the film is also likely since it will tend to evaporate very shortly after formation.

6. ACKNOWLEDGEMENTS

We are grateful to Messrs M Migl and M Posylkin for many discussions, assistance with the injectors and the use of some of their free-spray results. The flow rig was designed by Mlle S Capinaux of PSA to whom we are also grateful for collaboration and the provision of the injectors and associated equipment. It was assembled and modified by Mr P Bruni. Continuing discussions with Mr B Cousyn of PSA and Dr T Baritaud of IFP are gratefully acknowledged.

7. REFERENCES

- Arcoumanis, C. & Chang, J.-C. 1993, Heat transfer between a heated plate and an impinging transient Diesel spray, Experiments in Fluids, vol 16, pp. 105-119.
- Arcoumanis, C. & Chang, J.-C. 1994, Flow and heat transfer characteristics of impinging transient Diesel sprays, SAE Paper, 940678.
- Arcoumanis, C. & Cutter, P.A. 1995, Flow and heat transfer characteristics of impinging Diesel sprays under cross-flow conditions, SAE Paper, 950448.
- Arcoumanis, C., Cutter, P.A. & Whitelaw, D.S. 1995, Heat transfer of impinging transient Diesel sprays, Proc. 4th I. Mech. E. U.K. National Conference on Heat Transfer, pp. 25 - 29.
- Chandra, S. & Avedisian, C.T. 1991, On the collision of a droplet with a solid surface, Proc. R. Soc. Lond., vol. A432, pp. 13-41.
- Cousyn, B. Posylkin, M., Vannobel, F. & Whitelaw, J. H. 1995, Droplet characteristics in two cylinders of a firing spark-ignition engine, SAE Paper, 952466.
- Dementhon, J. B. & Vannobel, F. 1991, Phase Doppler anemometry in gasoline sprays: in atmosphere and in steady flow rig. Proceedings of International Conference on Sprays and Aerosols, Balachandran W. (Ed), pp. 48 -53.
- Hardalupas, Y., Taylor, A.M.K.P. & Whitelaw, J.H. 1991, Unsteady sprays by a pintle injector, Proc Japanese Soc Mech Eng, vol. 33, pp. 117.
- Hardalupas, Y., Okamoto, S., Taylor, A.M.K.P. & Whitelaw, J.H. 1993, Application of phase-Doppler anemometer to a spray impinging on a disk, Applications of Laser Techniques to Fluid Mechanics, vol. 6, pp. 490-506.
- Y Hardalupas, A M K P Taylor, L Ponyaev & Whitelaw, J.H. 1995b, Secondary atomisation of a petrol spray impinging on a rod, Imperial College, Mechanical Engineering Department Report TF/95/19.
- Hardalupas, Y., Taylor, A.M.K.P., Whitelaw, J.H., Miyano, H., Ishii, K. & Urata, Y. 1995a, Influence of injection timing on in-cylinder liquid and vapour fuel distribution in a Honda VTEC-E engine, SAE Paper, 950507.
- Migl, M., Posylkin, M. & Whitelaw, J.H. 1995, Effect of injection timing and fuel spray atomisation on combustion performance during cold start and warm-up, Imperial College, Mechanical Engineering Department. Report TF/95/22.
- Migl, M. 1995, Effects of equivalence ratio, injection timing and fuel spray characteristics on combustion performance and hydrocarbon emissions during cold start and warm up phases of a four-valve SI engine. Diplomarbeit, Friedrich-Alexander-Universitat Erlangen-Nurnberg.
- Nader, J.D. & Farrell, P.V. 1993, Hydrodynamics of droplet impingement on a heated surface, SAE Paper, 930919.
- Ozdemir, I.B. & Whitelaw, J.H. 1993, Impingement of an unsteady two-phase jet on unheated and heated flat plates, J Fluid Mech, vol. 252, pp. 499-523.

VELOCITY PROFILES IN SHEAR-DRIVEN LIQUID FILMS: LDV-MEASUREMENTS

S. Wittig, A. Elsäßer, W. Samenfink, J. Ebner, K. Dullenkopf

Lehrstuhl und Institut für Thermische Strömungsmaschinen
Universität Karlsruhe (TH)
D-76128 Karlsruhe, Germany

ABSTRACT

In design and layout of fuel preparation systems for SI-engines or gas turbines as well as other technical systems working with shear-driven liquid films accurate information on the velocity distribution within the film as a function of film height is necessary for numerical modeling. To meet this requirements an improved LDV system was built which allows for the first time accurate velocity measurements in thin and wavy liquid films down to an average thickness of about $100\ \mu\text{m}$. Layout and the optical arrangement of the new system is presented in details together with some exemplary applications.

1. INTRODUCTION

The prediction of internal fuel films plays an important role in the design of combustion engines. Typical examples are prefilming airblast atomizers (Wittig et al. (1992)), prevaporating combustors in gas turbines (Pfeiffer (1992)), oil films in aero engine bearing chambers (Glahn et al. (1995)), or intake manifolds of sparc ignition engines (Elsäßer et al. (1994)). Especially in sparc ignition engines liquid fuel stored in wall films introduces a characteristic delay time to engine reaction, also causing high pollutant emissions during load changes or in cold start conditions.

A major problem in numerical modeling of the film flow is the lack of information about the velocity distribution as a function of the film height.

For an accurate prediction of the film transport and evaporation characteristic the knowledge of the precise velocity profile is required. If the assumed profile is incorrect, the liquid film thickness and as a consequence the interaction with the air flow cannot be calculated adequately. This leads to a poor prediction of the heat and mass transfer at the phase boundary.

In the literature different theories for the internal film velocity profile are proposed. Some investigators assume that the film is of turbulent nature, others suppose laminar conditions. However, most of the authors were not able to verify the velocity profiles in shear-driven films directly, due to the small average layer thickness of $50 \leq \bar{h}_F \leq 200\ \mu\text{m}$ of typical films for example in intake manifold flows.

2. VELOCITY MEASUREMENTS IN LIQUID LAYERS

To our knowledge none of the instruments available is suitable to perform velocity profile measurements within thin shear-driven films. Due to the thin layer an optical, non intrusive technique has to be applied. Especially using a the Laser-Doppler-Velocimeter (LDV) has some potential in this case. Some investigators have already applied the LDV technique to perform velocity profile measurements inside thicker liquid films or microscopic flows within small gaps. Some of the methods are discussed in the following, especially with respect to the applicability to thin and wavy films under the influence of high air velocities.

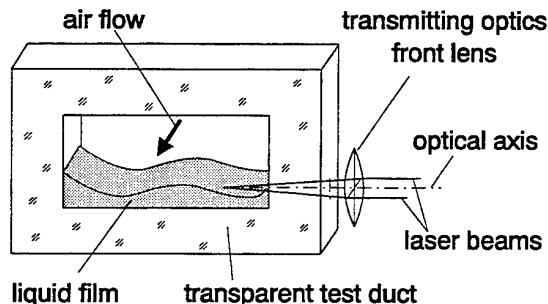


Fig. 1: Transmitted optics located horizontally at the side wall of the test duct

The methods described in the literature differ primarily in the orientation of the probe volume with respect to the film surface. Mudawar and Houpt (1993) used a transparent film splitter to cut a slice from a vertical falling film. This method allows lateral access to the film by focusing the beams of a LDV system in a certain film height, as shown in Fig. 1. The transmitting and receiving optics were aligned in the optical axis of a forward scattering setup. The probe volume had a length of $150\ \mu\text{m}$ and a diameter of $29\ \mu\text{m}$. The main problem using this method in shear-driven films was, that measurements were possible only when the surface waves are two-dimensional line shaped. This is due to the fact that the convergent beams of the transmitting optics, the probe volume itself, and the path of the scattered light to the photomultiplier might not be disturbed by the air/liquid interface and therefore have to be completely inside the film. However, shear-driven liquid films in contrast to falling films have a distinct three-dimensional wavy structure. They contain large regions with a typical thickness of only $20 - 30\ \mu\text{m}$ embedded in wave fronts with maximum heights of $150 - 500\ \mu\text{m}$, depending on the liquid volume flux and the shear force conditions. Due to this conditions the path of the light will be interrupted most of the time and therefore a different optical arrangement is required.

Another method to arrange the LDV optics with respect to the film is shown in Fig. 2, where the transmitting optics is applied vertically to the bottom wall. This method is used by some investigators to determine velocity profiles in thin liquid layers. Tieu et al. (1995) measured the single-phase flow profile in a small gap using a diode-laser LDV system in 180° backscattering mode. By means of a extremely short focal length in the transmitting optics the resulting probe volume length was $10\ \mu\text{m}$

and the diameter $5\ \mu\text{m}$. This very small probe volume size offered an excellent spatial resolution in the liquid layer. The major drawback of this arrangement to study shear-driven films results from the wavy surface, as outlined in Fig. 2. If measurements are performed near the wavy boundary for a wide range of surface angles strong reflections are directed towards the detector. In shear driven films these conditions may be present quite often, therefore the applicability of this method for the films under investigation in this study is questionable.

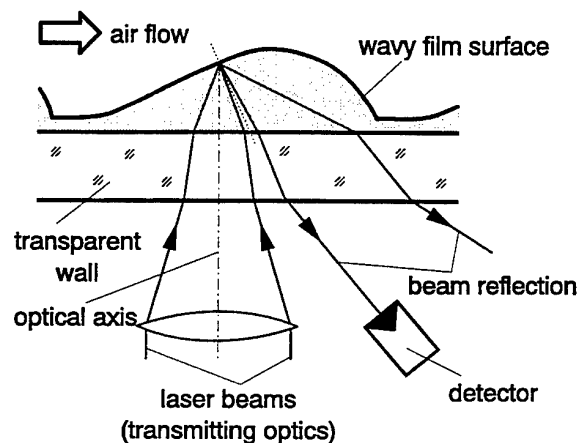


Fig. 2: Transmitted optics arrangement and beam reflections at the wavy film surface

A similar method was used by Paras and Karabelas (1992) to analyze annular shear-driven liquid layers. In their case a probe volume of $121\ \mu\text{m}$ length and $23\ \mu\text{m}$ in diameter was utilized. The air flow velocities had been low for their study, and only films with a thickness in the range of $3.4 \leq \bar{h}_F \leq 7.6\ \text{mm}$ had been investigated. Due to these thick films the resolution along the optical axis was sufficiently high. However, in their measurements the effect of beam reflections at the air/liquid interface could clearly be detected by the photomultipliers. If these reflections were treated as Doppler signals they would lead to wrong results. Furthermore Paras and Karabelas (1992) set a limit for measurements with their system to $1 - 2\ \text{mm}$ below the film surface. Measurements closer to the surface had not been possible.

Plimon (1991) used a similar arrangement of the transmitting optics. It was located vertically below a transparent horizontal bottom wall of a rectangular

duct also. The difference to the methods described previously was the position of the receiving optics above the film surface at an off-axis angle of 45° to reach an optimum between the signal to noise ratio and scattering efficiency. The resolution along the optical axis was about $25\ \mu\text{m}$ by using a short focal length in the transmitting optics. In his paper Plimon presented a velocity profile determined at low air velocity ($20\ \text{m/s}$) and high liquid volume flux. These conditions were ideal for the detection of the scattered light through the air/liquid interface. At higher air velocities it can be assumed that the signal quality would become significantly worse due to the strongly wavy film surface.

Because of their distinct shortcomings, none of the previously described systems was applicable in our study. Therefore a different setup had to be developed especially adapted to the conditions of thin wavy liquid films.

3. NEW APPROACH FOR FILM PROFILE MEASUREMENTS

3.1 Test Rig

The basic item of the test rig used for the experiments is a transparent duct with a cross section of $30 \times 196\ \text{mm}$ and a length of $1000\ \text{mm}$. It is connected with the suction side of a blower. To vary the free-stream turbulence intensity turbulence grids can be inserted in the inflow.

The test liquid (demineralized water) is seeded with MgCa-particles and supplied to the channel floor wall through a row of small holes and forms a continuous film. Free stream and film conditions including temperature, pressure and volume flux are controlled continuously.

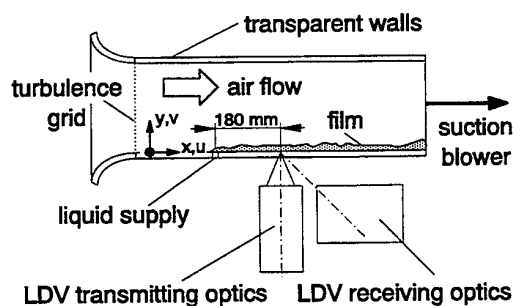


Fig. 3: Test section

3.2 Transmitting Optics

The newly designed setup consists of a transmitting optics looking vertically up through a transparent bottom wall of the horizontal test section. This provides good optical access to the film flow. The probe volume can be exactly located without any disturbances due to the wavy film surface, see Fig. 2. As basic system a two-component fiber optic LDV system was used. The LDV system includes a $4\ \text{W}$ Argon-ion Laser in multi mode operation, a standard optics with $40\ \text{MHz}$ Bragg-cell, color and beam separators and a 2D-fiber probe. To achieve the resolution suitable for film flow under investigation a beam expander and a short focal length front lens ($f = 80\ \text{mm}$) have been used in the transmitter. They reduce the probe volume size to a length of $\Delta y_F \approx 200\ \mu\text{m}$ and a diameter of $\Delta x_F \approx \Delta z_F \approx 25\ \mu\text{m}$.

However, the size Δy_F is still larger than the desired spatial resolution of about $30\ \mu\text{m}$ in the direction of the optical axis. Therefore, the probe volume has to be reduced further by the receiver design.

3.3 Receiving Optics

As shown already mentioned the 180° backscattering mode is unfavorable for detailed film profile measurements. Firstly, the sensible area of the detector is still too large, and secondly the reflections at the film surface cause serious problems considering the signal to noise ratio in a wide range of surface angles. To solve these problems the detector was shifted to an off-axis angle with respect to optical axis of the transmitter, thus cutting a narrow section of the probe volume as shown in Fig. 4 for one component. Simultaneously, this helps to solve the reflection problem at the film interface. An angle of 45° to the optical axis was chosen, because previous investigations have shown that reflections in this range occurs relatively seldom for conditions used in the tests. To observe only a defined section of the probe volume in the y -axis direction a slit aperture is positioned in front of the color splitter in the receiver. The signals have been detected by a two-component photomultiplier setup in combination with counter processors and a self developed software for data acquisition and analysis.

As demonstrated in Fig. 5, the receiving optics is located below the test section in line with the transmitting optics. Its optical axis would cross the bot-

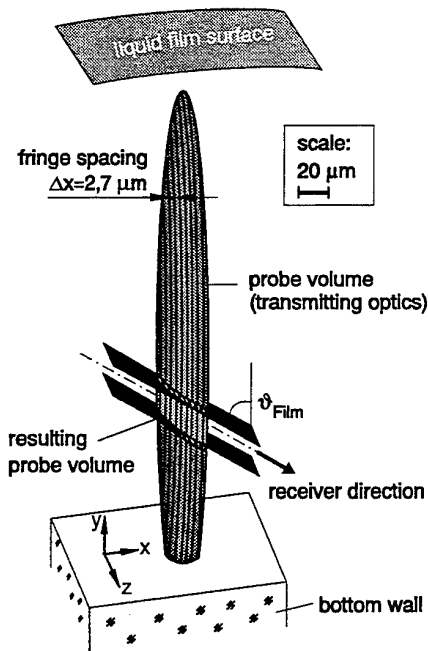


Fig. 4: Reduction of the resulting probe volume length by off-axis location of the receiver aperture

tom wall under 45° in air. However, the arrangement with a simple flat bottom wall is unfavorable due to multiple refraction at the air/glass and glass/liquid interfaces, as pointed out in the top part of Fig. 5. In this case the beams have already different angles $\vartheta_{Li1,Glass} \neq \vartheta_{Li2,Glass}$ when passing the bottom wall and consequently a strong distortion of the focus occurs. This distortion may be reduced by using thin walls, but this is not possible in our case. Therefore, as shown in Fig. 5b a prism is fixed perpendicular to the optical axis in order to obtain equal refraction conditions for both beams at the air/glass interface. Different angles of incidence appear only at the glass/liquid interface. This interface has a small variation in the index of refraction and the optical paths are short (about $500 \mu m$) to the intersection point $P_{Measure}$. By means of this measure a minimal aberration for all beams parallel to the optical axis and intersecting in $P_{Measure}$ can be achieved.

In Fig. 6 a sketch of the optical receiver arrangement is given. Two lenses with equal focal length give a 1:1 projection of the probe volume onto the slit aperture. To determine the exact value of the section height caused by different beam path and

the distortion of the focus a numerical analysis of the beam trajectories is provided. The analysis indicates that due to the different angles of incidence at the glass/liquid interface the focal points of all parallel beams are not located at an identical position inside the film. The results of the calculation are plotted in Fig. 7. It shows the computed 1:1 projection of the slit aperture focus inside the liquid film. The coordinates of the film internal foci are calculated for the envelope in the drawing plane (\parallel -mode) and the plane perpendicular to this (\perp -mode). In the figure the locations of the minimum focus size in both directions as envelopes of the whole beam are plotted. The symbols characterize the points achieved by a receiving optics traverse of $\Delta y = 50 \mu m$ and $\Delta x = 0 \mu m$. The corresponding points for discrete positions of the receiving optics are connected with lines in the figure. These lines are very close to the optical axis which is inclined under $\vartheta_{SF} = 53.9^\circ$ in

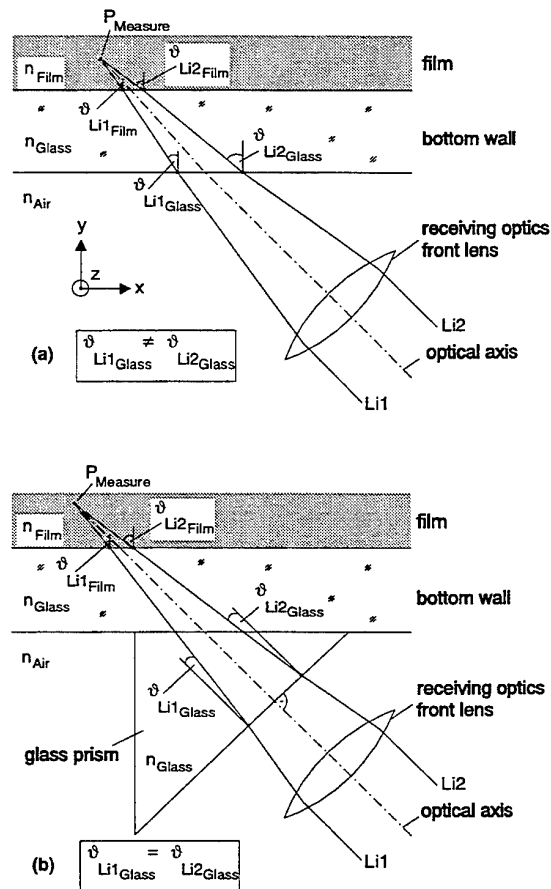


Fig. 5: Improvement of projection quality by a prism perpendicular to the optical axis

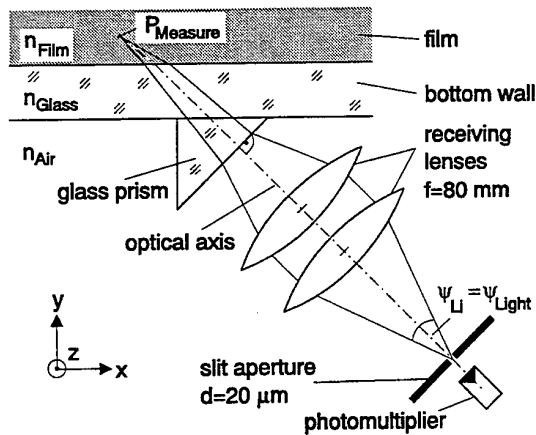


Fig. 6: Sketch of the receiving optics realization including the glass prism

the fluid. To illustrate this effect, a schematic of the focus shape in the film is given in Fig. 7 also. Between the two modes the distance of the foci is very short, so a useful projection is achieved. The difference between the focus location of both modes increases with larger height in the liquid layer. For a detailed construction of the optics the mode parallel to the drawing plane is of special interest, because it determines directly the size in the film height direction. The focus dimension of the perpendicular mode can be neglected when using a slit aperture. Beams with this orientation pass the slit along its long expansion and therefore will be detected anyway.

Additionally the maximum collection angle is varied in the calculation in the range of $2^\circ \leq \Psi_L \leq 5^\circ$. An angle of $\Psi_L = 5^\circ$ is the maximum value in the realized optics, limited by an iris aperture. For the design it is important to keep in mind that the slit is projected nearly at the same position for different values of Ψ_L . The angle dependent deviation is therefore negligible. However, as mentioned above, between the foci of the ||-mode and the ⊥-mode a noticeable difference appears.

Furthermore, the focus point of the ||-mode moves not only vertical by a y -motion of the collecting optics. Therefore, the receiving optics has to be traversed in both, y -axis and x -axis direction, to obtain a sole vertical movement of the probe volume. The corresponding ratio between Δx and Δy for an exclusive vertical movement can be derived by this calculation, too.

Finally the solution of the reflection problem at

the film surface will be discussed. Because it is necessary to protect the photomultipliers from reflected light to avoid overload and erroneous Doppler signals, the laser beams are switched off by a Bragg-cell for reflecting conditions. An additional laser beam of different wavelength ($\lambda_{Pilot} = 633 \text{ nm}$) is used as a indicator for reflecting conditions. The pilot beam is coupled into the receiving fiber of the standard fiber probe, thus forming a focus by the front lens, too. The time span necessary for the electronic and the Bragg-cell to switch off the main beams is gained by the specific optical arrangement in the receiver. The front lens of the receiver collects scattered light in an angle range of $\Psi_L = 20^\circ$ and this complete field is used in the red light detection for the switch-off device. The angular range of the green and the blue photomultipliers is reduced by an iris aperture to 5° . Therefore, light is reflected into the pilot beam detector first and the main beams can be switched off prior to full illumination of the photomultipliers by reflection.

The layout of the newly designed optics is shown in Fig. 8. The complete system is mounted on a high precision 3D-traversing device. The indepen-

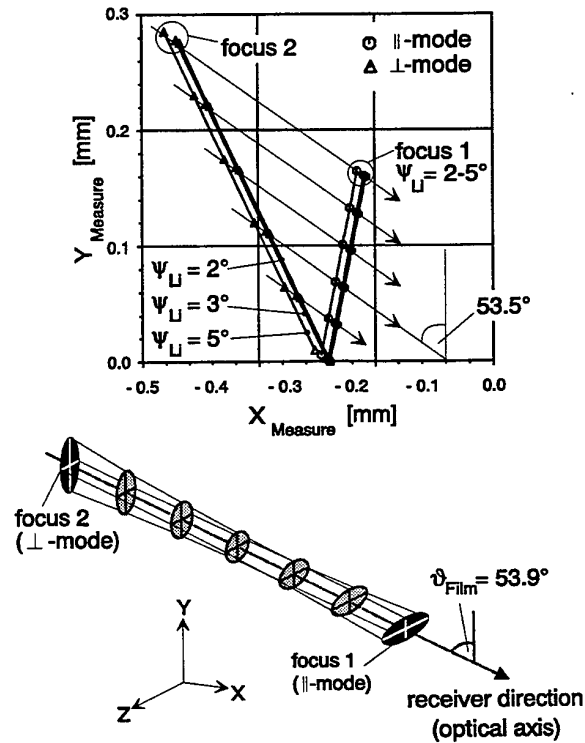


Fig. 7: Computed optical conditions in the focal point

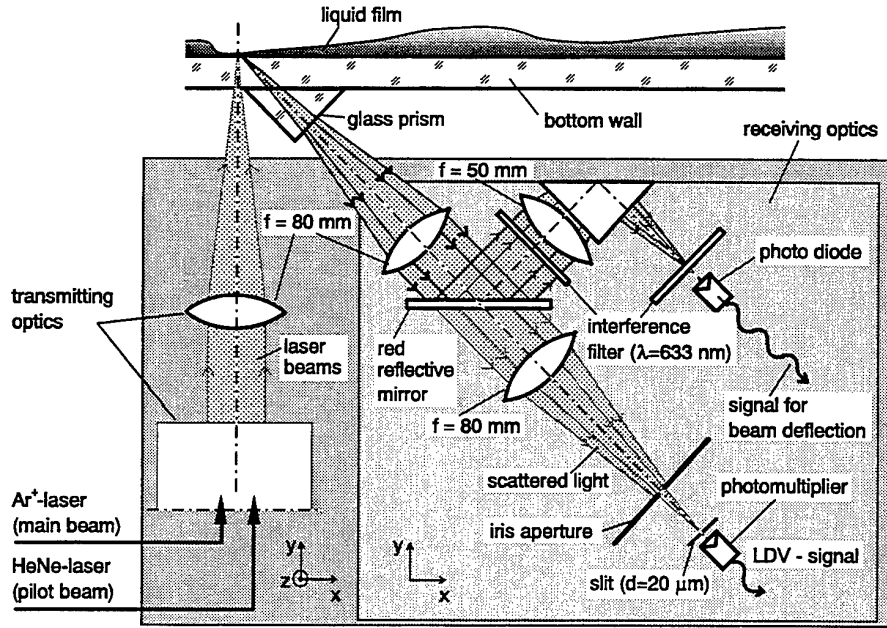


Fig. 8: Setup of the LDV system for velocity profile measurements in thin and wavy liquid films

dant spatial movement of the receiving optics relative to the transmitting optics is achieved by a second extremely accurate 2D-traverse unit.

4. RESULTS

4.1 Measurements in a Typical Shear-driven Water Film

An exemplary result of the time mean velocity profile in main stream direction is shown in **Fig. 9** for an air velocity of 30 m/s and the liquid volume flux of $\dot{V}/b = 0.434 \text{ cm}^3/\text{cm s}$. This condition leads to a shear stress of $\tau = 3.9 \text{ N/m}^2$ at the air/liquid in-

terface. The time mean film thickness for this layer is $\bar{h}_F = 177 \mu\text{m}$. To determine the film thickness value a novel optical measurement system developed at the Institut für Thermische Strömungsmaschinen at Karlsruhe University and described by Samenfink et al. (1996) was used.

The step width of the profile measurement in y -direction was $\Delta y = 15 \mu\text{m}$. In addition to the time mean velocity distribution the velocity fluctuations are given too, centered around the mean value for different film heights and marked by the dotted lines. On the right of **Fig. 9** three probability density charts are given for three specific film heights. The histograms show, as expected, that the veloc-

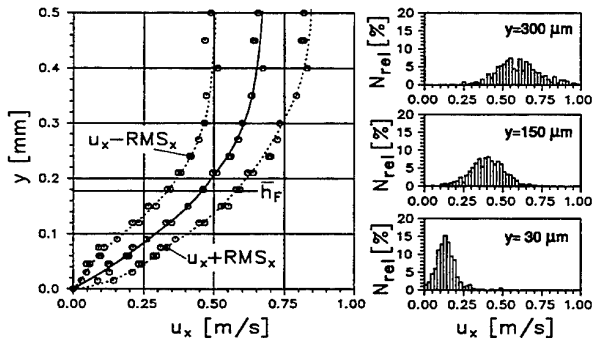


Fig. 9: Mean stream velocity measurements, $u_{Air} = 30 \text{ m/s}$, $T_F = 20^\circ \text{C}$

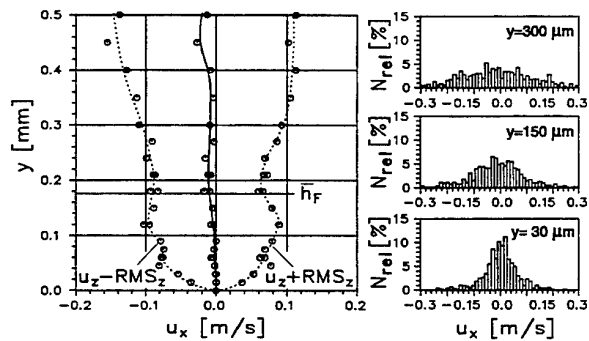


Fig. 10: Cross stream direction velocities, $u_{Air} = 30 \text{ m/s}$, $T_F = 20^\circ \text{C}$

ity fluctuations are weaker near the wall than in the wave crest region.

As expected by the two dimensional character of the flow the time mean velocity in the cross-flow direction is close to zero for all heights, as plotted in Fig. 10. The RMS value shows increasing values with increasing wall distance, too. This is also present in the histogram charts of the velocity distribution in different y -positions inside the film.

4.2 Influence of Volume Flux on the Film Velocity Profiles

To determine the effect of liquid volume flux on the profile shape within shear-driven films additional investigations have been performed. In Fig. 11 the results of a volume flux variation in the range of $0.175 \leq \dot{V}/b \leq 0.868 \text{ cm}^3/\text{cm s}$ are shown. The time mean thickness of the film was $108 \leq \bar{h}_F \leq 245 \mu\text{m}$ for the conditions plotted in the figure. By varying the volume flux of the liquid the shear-stress induced on the film is changed too, because of different wave structure and roughness effects. Fig. 11 indicates that the velocity profiles are nearly identical from the bottom wall up to a film height of about $150 \mu\text{m}$. Above this height the profiles split in the individual

curves corresponding to the volume flux. This also points out, that the film differ only in the wave region under constant air flow conditions. The profiles have a nonlinear shape in height and therefore a turbulent character. This confirms the trend in the results of Plimon (1991) where the parabolic shape of the film velocity profile is shown for a thicker shear-driven film. First comparisons with profile assumptions given by Deissler (1954) show a good agreement for water films, too.

In Fig. 12 the RMS values of the measurements described earlier are presented. The RMS values deviate much earlier than the mean velocities. Considering the velocity fluctuations the distributions start to diverge significantly at a height of about $40 \mu\text{m}$. For a detailed explanation of this effect corresponding film thickness measurements are necessary. The height of $40 \mu\text{m}$ is approximately the minimum film height being present for all investigated volume fluxes. This minimum film thickness represents a thin sublayer on top of which waves of different heights, depending on the volume flux, move driven by shear forces.

For an accurate prediction of liquid film flows the knowledge of the different transport mechanisms is crucial. More detailed information about these complex phenomena can only be obtained by simulta-

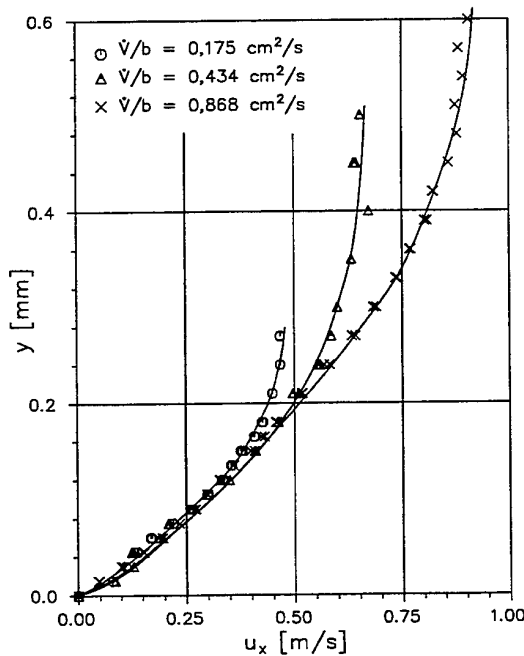


Fig. 11: Mean velocity profiles in water films,
 $u_{Air} = 30 \text{ m/s}$, $T_F = 20^\circ \text{ C}$

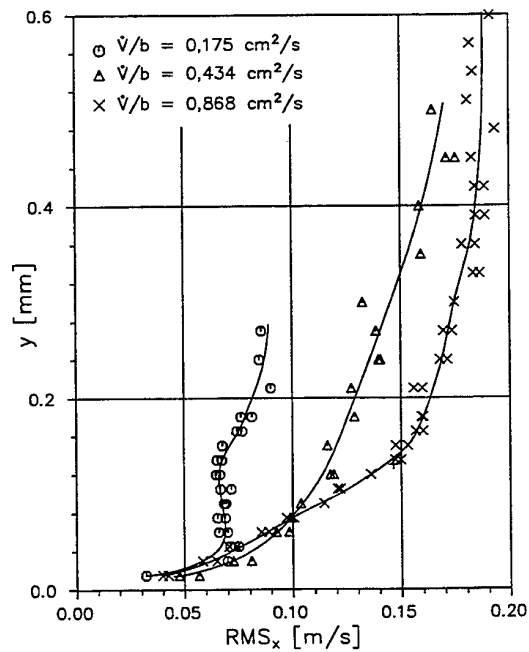


Fig. 12: RMS values in water films,
 $u_{Air} = 30 \text{ m/s}$, $T_F = 20^\circ \text{ C}$

neous measurements of film thickness and film velocity. Comprehensive efforts have been directed at the Institut für Thermische Strömungsmaschinen at Karlsruhe University to combine the two measurement systems previously mentioned, and some first results will be given in Samenfink et al. (1996). By the simultaneous use of both systems a detailed characterization of mass transport profiles in wavy shear-driven films will be possible.

5. CONCLUSIONS

To improve the knowledge of the transport mechanisms in wavy shear-driven liquid films important in many technical applications a novel LDV system was designed and presented. For the first time it allows accurate velocity profile measurements in thin and wavy films with average thickness of about $100\text{ }\mu\text{m}$ from the bottom up to the wave crest region. The instrument combines a active small probe volume and an acousto-optical switching device to protect the photomultiplier-tubes from the intensive reflections from the film surface.

The results presented in the paper show that the time mean velocity profiles inside the film have a parabolic shape and are non-linear with the height. These first results can already be used to validate film velocity assumptions required to improve the prediction of mass and heat transfer in shear force driven film flows.

REFERENCES

- [1] Deissler, R.G.: Heat Transfer and Fluid Friction for Fully Developed Turbulent Flow of Air and Supercritical Water with Variable Fluid Properties. ASME-Journal of Fluids Engineering, 76, pp. 73 – 85, 1954.
- [2] Elsäßer, A., Samenfink, W., Hallmann, M. and Wittig, S.: Mixing Phenomena of Fuel Sprays in Intake Manifolds. In: Proceedings on the Sixth International Conference on Liquid Atomization and Spray Systems (*iclass94*), Rouen, France, Paper VII-10, 1994.
- [3] Glahn, A. and Wittig, S.: Two-Phase Air/Oil Flow in Aero Engine Bearing Chambers - Characterization of Oil Film Flows. ASME-Paper 95-GT-114, 1995.
- [4] Mudawar, I. and Houpt, R.: Measurement of Mass and Momentum Transport in Wavy-Laminar Falling Liquid Films. International Journal of Heat and Mass Transfer, 36, No. 17, pp. 4151 – 4162, 1993.
- [5] Paras, S.V. and Karabelas, A.J.: Measurements of Local Velocities Inside Thin Liquid Films in Horizontal Two-Phase Flow. Experiments in Fluids, 13, pp. 190 – 198, 1992.
- [6] Pfeiffer, A.: Entwicklung einer keramischen Kleingasturbinen-Brennkammer: Neue Möglichkeiten zur schadstoffarmen Verbrennungsführung. Dissertation, Institut für Thermische Strömungsmaschinen, Universität Karlsruhe (T.H.), 1992.
- [7] Plimon, A.: Velocity Profiles in Shear Force Driven Wall Films. Experiments in Fluids, 11, pp. 339 – 340, 1991.
- [8] Samenfink, W., Elsäßer, A., Wittig, S. and Dulenkopf, K.: Internal Transport Mechanisms of Shear-driven Liquid Films. Eighth International Symposium on Applications of Laser Techniques to Fluid Mechanics, Lisbon, Portugal, 8-11 July, 1996.
- [9] Tieu, A.K., Mackenzie, M.R. and Li, E.B.: Measurement in Microscopic Flow With a Solid-State LDA. Experiments in Fluids, 19, pp. 293 – 294, 1995.
- [10] Wittig, S., Himmelsbach, J., Noll, B., Feld, H.J. and Samenfink, W.: Motion and Evaporation of Shear-Driven Liquid Films in Turbulent Gases. ASME-Journal of Engineering for Gas Turbines and Power, 114, pp. 395 – 400, 1992.

INTERNAL TRANSPORT MECHANISMS OF SHEAR-DRIVEN LIQUID FILMS

W. Samenfink, A. Elsäßer, S. Wittig, K. Dullenkopf
Lehrstuhl und Institut für Thermische Strömungsmaschinen
Universität Karlsruhe (TH)
D-76128 Karlsruhe, Germany

ABSTRACT

To study the motion and structure of wavy liquid films driven by shear stress an experimental study has been performed applying a novel optical diagnostic tool developed at the Institut für Thermische Strömungsmaschinen at Karlsruhe University. The instrument is capable to determine accurately the thickness and the wave structure of thin liquid films. Applied in combination with the modified LDV system described by Wittig et al. (1996) the system can be used for simultaneous measurements of the film thickness, wave structure, and velocity.

1. INTRODUCTION

In the design process of modern combustion engines towards reduced fuel consumption and low emissions it is essential to understand the behavior of fuel films within the engine. Considering the fuel preparation in oil fired gas turbines typical those types of flows are present in the internal film transport of airblast atomizers or in the motion and evaporation of the fuel in combustion chambers with prevaporization (Wittig et al. (1992)). Another area where films play an important role is the intake manifold of spark ignition engines, where droplets of the injected spray interact the wall and form a liquid layer (Elsäßer et al. (1994)). Especially in intake manifolds, the mixing process is strongly affected by the presence of a

fuel film, storing a large amount of fuel. Due to its inertia, the fuel in the film introduces a characteristic time delay to the mixing process resulting in a unsuitable fuel to air ratio in the cylinder. This phenomenon leads to high pollutant emissions at cold start conditions and during changes of engine load.

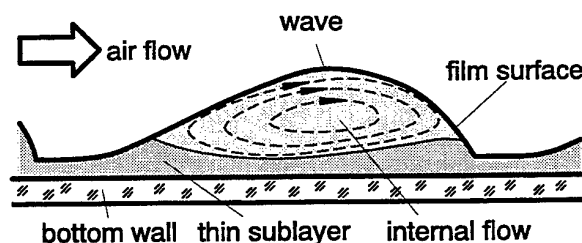


Fig. 1: Model of the internal flow structure in a wavy film

For an accurate prediction of the film transport and evaporation process, precise information about the time-averaged liquid layer thickness as well as maximum and minimum values of the film height are crucial. Furthermore, the knowledge of the internal hydrodynamical transport mechanism within the film is essential. In the literature the theory of rolling waves is well known (Wurz (1979)). The waves typically move on a thin liquid layer near the wall, which is present even between the wave fronts, cf. Fig. 1. In contrast to sea wave conditions, at shear-driven films the major part of the liquid mass

is carried within the waves. However, considering this type of flow, all models in literature are based on assumptions simplified, which may cause severe errors in prediction.

2. FILM THICKNESS AND FILM SURFACE STRUCTURE MEASUREMENT SYSTEMS

To achieve a comprehensive insight in the physics of liquid transport phenomena, detailed information of the time dependend film height, wave shape and velocity profiles within the film are required. In the literature different methods to determine these values have been discussed. For the thin and wavy liquid layers under investigation in the present study only a nonintrusive technique is applicable.

In order to study liquid films some authors used short time sparc photography techniques lateral to the film flow direction (Wurz (1979), Hall and Taylor (1963), Hewitt (1978)). The individual waves have been projected as dark areas in front of a bright illuminated background. So the general wave shape, maximum film heights, or by using a multiple exposure technique the velocity of the actual wave front can be determined. However, the surface of a typical shear driven films has a three-dimensional wave structure and therefore, the flow has to be transformed into a two-dimensional structure using an extremely narrow duct to prevent wave interaction. Furthermore, the conditions for photographic techniques are rather difficult due to the large wavelength to film thickness ratios of $1/10 \leq \lambda_F/h_{F,max} \leq 1/30$ (cf. Fig. 7), as being typical for thin fuel films inside intake manifolds. Among others the major problem using this technique is the enormous time necessary for a statistical analysis or comprehensive parameter variation, because only one wave front can be recorded on each exposure.

If only film thickness and no surface structure information is required, different electrical and optical approaches have been applied for flow analysis from numerous authors. The layer thickness can be determined using capacitive or inductive sensors, or detecting the electrical resistance. Many investigators used these methods in the past, for example Dukler (1960), Hewitt (1978) or Simon (1990). However, the spatial resolution of these methods is often limited by sensor dimensions of about 3 to 5 mm in diameter, so individual waves usually could not be

detected.

The various optical systems described in the literature differ in the physical effect employed to determine the film thickness. A number of investigators used the flourescence of additives in the film fluid like Johnen and Haug (1995) or Driscoll et al. (1992). A similar approach applied by (Hanratty (1957), Sill (1982)) is based on the absorption of light passing a dyed liquid layer. However, this methods are unfavorable to study evaporating films, because the dye has different evaporating conditions and is therefore concentrated in the remaining liquid layer and consequently leading to wrong results. An approach avoiding this problem was presented for the first time by Wittig et al. in 1992. The paper describes an advanced absorption technique without dyes applicable in water or alcohols, using the effect of absorption in the near infrared in combination with a quite good correction function for intensity losses by reflections or fiber coupling. However, as mentioned earlier, all these methods decribed do not give direct information on the spatial surface structure, but the film thickness can be recorded as a function of time.

A major step in the understanding of the internal flow and the transport mechanisms inside the film can be achieved when using time resolved thickness data in combination with the velocity measurements in the film, published by Wittig et al. (1996). For the combined measurements additionally information on the film structure is required in the moment when a particle pass the probe volume. Therefore, a measurement technique with a high spatial and temporal resolution is necessary. The realization a newly develloped film thickness measurement system fulfilling these requirements is described in the following section.

3. ADVANCED TECHNIQUE FOR FILM THICKNESS AND FILM SURFACE DETERMINATION

3.1 Test Rig

The test section shown in Fig. 2, has a rectangular shape and a cross section of 30 x 196 mm. The complete section is built of acrylic glas and therefore allows excellent optical access to study the two-phase flow. The channel is connected with the suction pipe of a blower. Behind the bell mouth intake turbulence grids can be installed to generate different turbulence levels in the free stream. The liquid

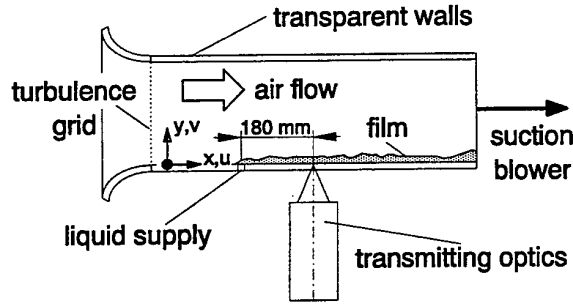


Fig. 2: Test rig

film is introduced to the channel floor wall through a row of small holes, its temperature and volume flux is controlled continuously. The measurement location is $\Delta x = 180 \text{ mm}$ downstream of the film supply.

3.2 Film Thickness

The technique used in the advanced instrument is based on absorption and deflection of laser light. A focussed laser beam passes the film perpendicular to the wall. Using an infrared wavelength the intensity of the laserlight is reduced inside the film, due to absorption. The absorption coefficient k' depends on the liquid and the wavelength of the light used. For fundamental investigations pure liquids like water, methanol or ethanol are used often. For these species the absorption coefficient increases significantly for infrared wavelength, as seen in Fig. 3. However, wavelength of 1400 nm or more have to be used to obtain a significant absorption in thin liquid films of less than $100 \mu\text{m}$, typical in technical applications. Using light in this wavelength range measurements can be performed without coloring the liquid to obtain the matching absorption coefficient.

Using the ratio of the transmitted and the incident intensity I/I_0 the film thickness h_F can be computed by the well-known Lambert-Beer law.

$$\frac{I}{I_0} = \exp(-k' \cdot h_F) \quad (1)$$

Using two Laser beams with different wavelength is the most significant feature in this novel system. The first Laser with $\lambda_1 = 1480 \text{ nm}$ is utilized for film thickness measurements by absorption whereas the second Laser with $\lambda_2 = 830 \text{ nm}$ is used for a correction scheme. The second wavelength, of almost not absorbed in the liquid, is used to detect losses

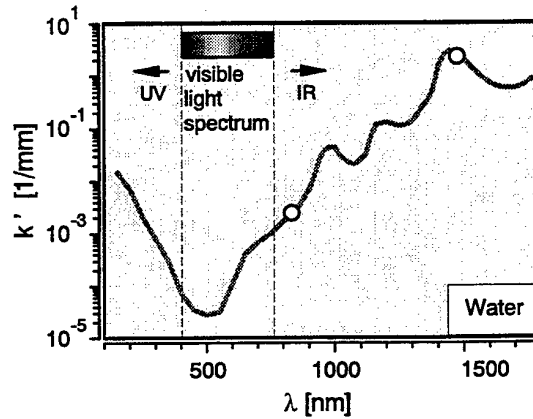


Fig. 3: Spectral absorption coefficient k' of water

by reflections at the wavy film surface. Additionally, the intensity losses at the fiber coupling can be eliminated successfully, as confirmed by Wittig et al. (1992).

3.3 Film Structure

In general shear-driven fuel films occurring in combustion engines show a three-dimensional pattern of the surface waves, which looks like tears or the scale structure of fish. These waves affect the internal flow in the film. Therefore, it is necessary, to record the surface structure and the film thickness simultaneously. The surface structure is represented by the wave angle α . It can be calculated from the deflection of the transmitted Laser beam which is focussed perpendicular to the bottom wall.

In Fig. 4 the trajectory of a transmitted beam is shown. The ray is refracted at the interface between various material with different refractive indices. After passing bottom wall and liquid film the beam enter the air with an angle δ . If the exit angle δ can be determined experimentally, α can be calculated by means of law of Snellius.

$$\alpha = \arcsin\left(\frac{n_2}{n_1} \sin \delta\right) \quad (2)$$

However, the main problem remaining is that with a simple setup only the displacement Δx with respect to the optical axis can be detected in the experiments. As a consequence the major source of errors is the variation in the height of point P on the film surface caused by the wavy film directly affecting the beam displacement Δx . Therefore a more

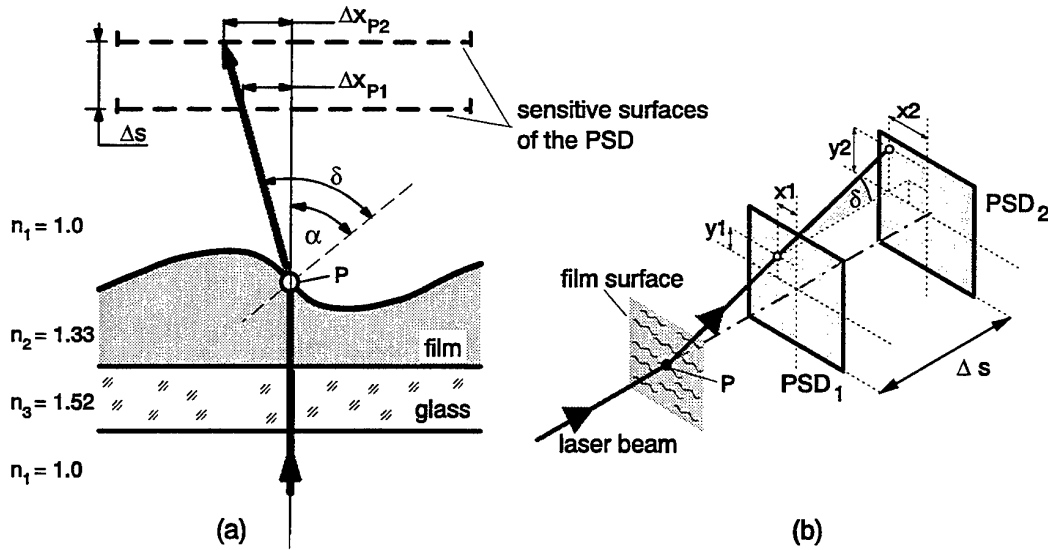


Fig. 4: Principle of surface angle measurement

sophisticated technique to determine the exit angle δ had to be applied. As pointed out in Fig. 3a and Eqn. 3 two independent displacement detectors (Δx_1 and Δx_2) separated by the known distance Δs are necessary. Because real waves are three-dimensional in general, beam deflection occurs in cross stream direction also. The determination of the exit angle δ is therefore based on a two-dimensional measurement to detect the components δx and δy in main and cross stream direction respectively.

$$\begin{aligned}\delta_x &= \arctan\left(\frac{x_2 - x_1}{\Delta s}\right) \\ \delta_y &= \arctan\left(\frac{y_2 - y_1}{\Delta s}\right)\end{aligned}\quad (3)$$

Combining the measured distances the angle δ can be calculated.

$$\delta = \arctan\left(\frac{\sqrt{(x_2 - x_1)^2 + (y_2 - y_1)^2}}{\Delta s}\right)\quad (4)$$

3.4 Optical Arrangement

In Fig. 5 the optical set-up of the combined film thickness and film surface structure measurement system is presented. It is organized in three functional units: the laser diode drive and controlling

unit, the transmitting optics, and the receiver optics.

In the laser diode drive and controlling unit containing the electronic management is located capable to drive three temperature controlled laser diodes of different wavelength. The wavelength of the lasers are employed $\lambda_1 = 680 \text{ nm}$, $\lambda_2 = 830 \text{ nm}$ and $\lambda_3 = 1480 \text{ nm}$ respectively. The fiber coupler combines the three wavelength and delivers the light to the transmitter via a single optical fiber.

The transmitter optics directs the focused light on the film. To avoid errors caused by intensity changes due to variations in the coupling losses a reference intensity detector is included in the transmitter as shown in Fig. 5. When performing simultaneous film height and velocity measurements the transmitter of the LDV described in details by Wittig et al. (1996) is used to direct the beams to the liquid film. The three wavelength are coupled into the fiber probe receiver fiber and focused together with the four LDV transmitter beams in the film.

On the opposite side of the film the receiver optics is located to detect the light intensity I and the deflection angle δ . Intensity and position signals are transferred through the controller unit to a personal computer including an ADC-board for data acquisition and processing.

The receiving unit allows simultaneous measurement of beam deflection and intensity, using two beam splitters located outside of the test duct, as presented in Fig. 6. Behind the beam splitter the

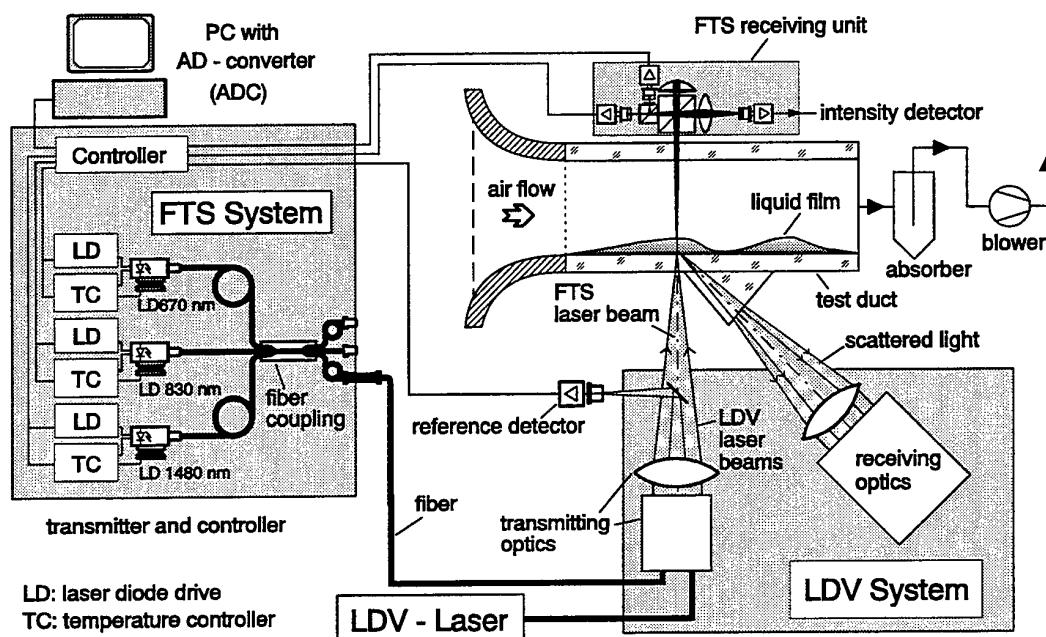


Fig. 5: Combined film thickness and film surface structure measurement system

reflected part is focussed on the intensity detector thus yielding the intensity losses due to absorption. For the alignment of the optics and the surface angle detection unit the transmitted beam is used. After reflection at a concave mirror the beam is divided again in the beam splitter. The transmitted part of the beam is used as an adjustment measure. By positioning the concave mirror exactly in the optical axis of the transmitting optics the focuses of incoming and reflected beam are located on top of each

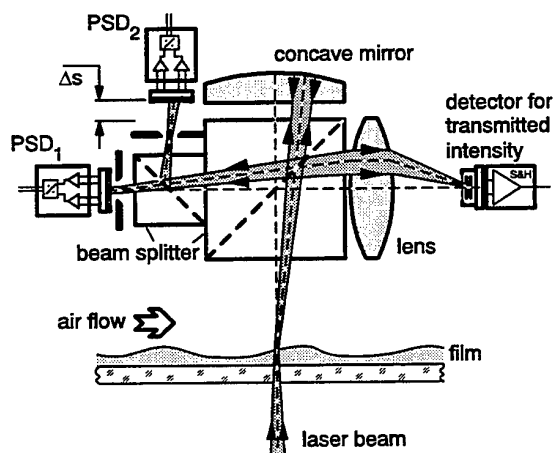


Fig. 6: Receiving unit of the measurement system

other. This procedure minimize errors in the angle detection.

The position measurement is carried out using the beam passing the second beam splitter. Each beam leaving the second beam splitter is focused on an aperture in front of the position detectors avoiding exposure from reflected and scattered light. The detectors are located in a way that the difference in the distances to the beam splitter is equal to Δs . The output of the position detectors PSD1 and PSD2 are proportional to the location of the incident beams. According to the equations previously described the surface angle α can be calculated in the computer.

3.5 Data Acquisition

In order to simplify the setup both wavelength are detected with the same device silicium/germanium sandwich detectors. Fast timing is crucial for these kind of measurements, because all signals have to be recorded at the same instant of time. Therefore, an ADC board with sample and hold amplifiers is used for data acquisition allowing a sampling rate of 2000 Hz which corresponds to air velocities up to $u_{Air} = 70 \text{ m/s}$.

As mentioned previously film height and struc-

ture together with detailed velocity information can be collected simultaneously using the modified LDV system (see Wittig et al. (1996)) and the above described instrument. In contrast to the thickness measurement system which runs continuously on a certain internal clock rate, the LDV samples randomly according to the particles crossing the probe volume. To synchronize the data acquisition of both systems the data ready signal of the LDV is used as a trigger event for the continuously sampling thickness system. In order to collect a comprehensive data a certain amount of pre and post data points are recorded too. With this information the wave structure can be determined and from this the exact position of the LDV measurement in the wave is known.

4. RESULTS

4.1 Measurements in a Characteristic Shear-driven Water Film

A typical result of the film thickness measurement as a function of time is presented in Fig. 7. The selected point of operation with an air velocity of $u_A = 30 \text{ m/s}$ and a volume flux of $\dot{V}/b = 0.434 \text{ cm}^3/\text{cm s}$ is representative for fuel films occurring in combustion engines. A significant feature for shear-driven films is the continuous liquid layer near the wall with thickness of about $50 \mu\text{m}$ in this case. On top of this thin sublayer the waves of different size are transported by shear stress. Under the conditions given above the time mean layer thickness was $\bar{h}_F = 177 \mu\text{m}$ and the dominating wave frequency calculated using standard *FFT* routines is about 50 Hz.

A closer look on the thickness trace shows an asymmetrical shape of the wave. As expected the

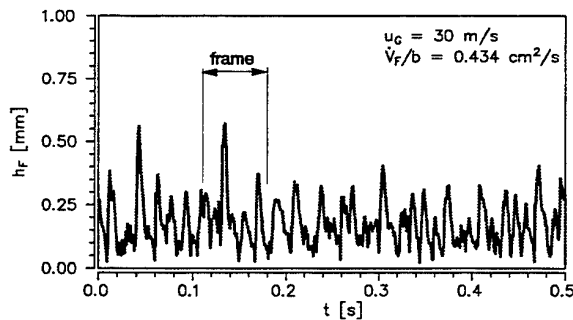


Fig. 7: Time-dependent film thickness signal

rise of the wave front is faster than the decline. This is demonstrated in Fig. 8 presenting the marked frame of Fig. 7 in an extended manner. It shows the time trace of film thickness as well as the corresponding surface angle α . Negative values of α represent the wave front and positive values the part of the wave surface exposed to the air flow. Changes of film thickness correspond to changes of α and the range of α is determined to be within $-10^\circ \leq \alpha \leq 20^\circ$.

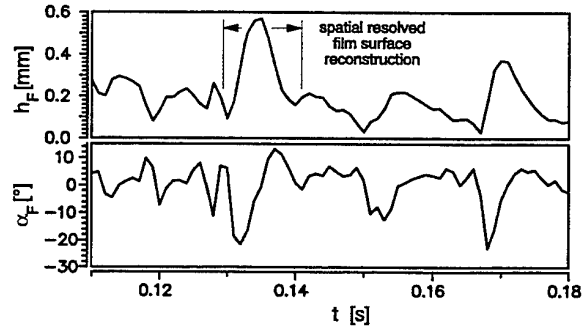


Fig. 8: Simultaneous measurement of film thickness and surface angle

The reconstruction of the wave structure can be done by combining film thickness and surface angle signals. Calculating the derivative of the time-dependent film thickness the variation of film thickness as a function of time is obtained. This function $h'_F(t)$ can be splitted in a time dependent and a spatial dependent term.

$$h'_F(t) = \frac{dy}{dt} = \frac{dy}{dx} \cdot \frac{dx}{dt} \quad (5)$$

The spatial term represents the surface angle variation and can be expressed as a function of $\alpha_F(t)$.

$$\tan \alpha_F(t) = \frac{dy}{dx} \quad (6)$$

Assuming that the transport velocity of the waves $c_W = dx/dt$ is constant the value of c_W can be determined by comparing the film thickness and the surface angle measurements using of a least square fit.

The relation between local and time dependant information is obtained by this procedure. The constant factor c_W allows to express the film thickness as a function of a local coordinate with high spatial resolution as plotted in Fig. 9. Visualizations of the film flow support the assumption of a

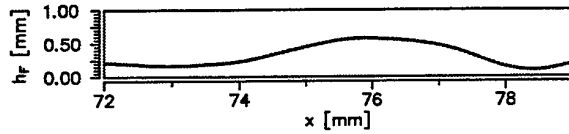


Fig. 9: Spatial resolved film surface reconstruction

constant c_w indicating that the wave mean velocities varies marginally between large and small sized waves. Therefore, the obtained surface structure represents the real wave shape passing the probe volume with a high level of accuracy.

4.2 Film Height Dependant Volume Flux

The comprehensive data derived by the simultaneous use of both measurement techniques allows for the first time the calculation of the volume flux as a function of film height in thin shear-driven liquid films. To determine this height dependent volume flux a sector volume flux $\dot{V}_{L,i}$ in a certain section element Δy_i is defined. It is normalized by the width of the film b .

$$\dot{V}_{L,i} = \frac{p(\Delta y_i) \cdot u_x(\Delta y_i) \cdot \Delta y_i}{b} \quad (7)$$

The film thickness and velocity data have to be adjusted to the grid choosen. Therefore, Fig. 10 shows the probability function of film thickness in each layer as well as the discretized velocities determined in the paper of Wittig et al. (1996). The height of the internal layer elements is $\Delta y = 10 \mu\text{m}$.

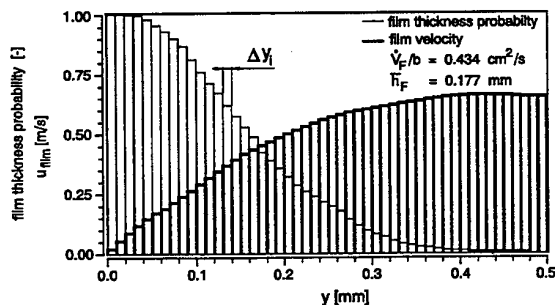


Fig. 10: Discretized film thickness probability density and film velocity distributions

In Fig. 11 the function of $\dot{V}_{L,i}$ in relation to the total volume flux versus the film height is shown. The conditions for this plot have been the same as

previously shown, an air velocity of $u_{Air} = 30 \text{ m/s}$ and a total flow rate of $\dot{V}/b = 0.434 \text{ cm}^3/\text{cm s}$.

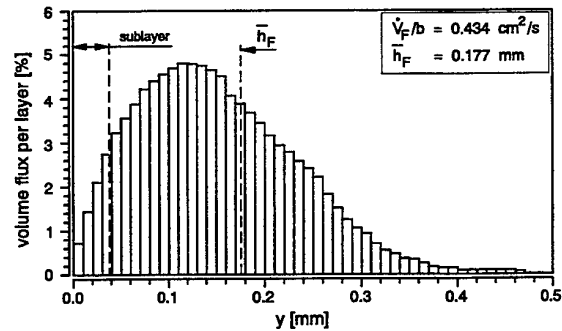


Fig. 11: Layer volume flux $\dot{V}_{L,i}$ versus film height

As demonstrated in Fig. 11 the volume flux distribution increases up to a maximum value, which is located below the average film thickness \bar{h}_F . Above \bar{h}_F the value of $\dot{V}_{L,i}$ decreases until the maximum wave height is reached. The layer volume flux depends on the film velocity $u_x(\Delta y_i)$ and on the probability $p(\Delta y_i)$ of the film in each discrete element Δy_i . The elements near the wall contribute less to the total mass flux. Their probability density is almost 100 %. However, the velocities u_x are very small in this region. With larger distance to the wall the film velocity increases, but $p(\Delta y_i)$ decreases only slowly. Due to this fact $\dot{V}_{L,i}$ increases fast up to its maximum value. Above this height the values of $p(\Delta y_i)$ slowly drop down to zero in the wave surface region, cf. Fig. 10. On the other hand the film velocities $u_x(\Delta y_i)$ almost stay constant in this area. Due to this fact the contribution of the layers near the wave surface to mass transport is less compared to the region below the average film thickness \bar{h}_F . Here about 70 % of the total volume flux takes place. Despite of the large velocity in the wave crests these areas are not relevant for mass transportation in the film due to their low probability.

The accuracy of the volume flux determination can be checked by comparing the integrated layer volume fluxes to the amount of liquid introduced into the test duct. The difference between these values is generally small and about 5 % for the conditions shown previously.

5. CONCLUSIONS

The design of modern combustion engines towards reduced fuel consumption and low emissions requires

an understanding of fuel film behavior within the engine. To study the motion and structure of wavy shear-driven films an experimental work has been carried out using a newly developed optical diagnostic tool. This instrument is capable to determine the thickness and the wave structure simultaneously with high level of accuracy by using the latest generation of optical components. This system in combination with the modified LDV system described by Wittig et al. (1996) also allows simultaneous measurements of the film thickness, the wave structure, and the velocity distribution inside the film.

Based on the results of the film thickness and surface angle measurement system the spatial wave structure can be reconstructed. Furthermore, in combination with film velocity data, the mass flux distribution versus the film height is determined for a wavy shear-driven liquid film. With these instruments powerful tools for internal film analysis have been developed and presented for the first time.

REFERENCES

- [1] Driscoll, D.J., Schmitt, R.L. and Stevenson, W.H.: Thin Flowing Liquid Film Thickness Measurement by Laser Induced Fluorescence. JFE, 114, pp. 107 – 112, 1992.
- [2] Dukler, A.E.: Fluid mechanics and heat transfer in vertical falling-film systems. Chem. Eng. Progress Symposium Series, 56, No. 30, pp. 1–10, 1960.
- [3] Elsässer, A., Samenfink, W., Hallmann, M. and Wittig, S.: Physical Phenomena in the Mixing Process Resulting from Fuel Spray in Intake Manifolds. July 1994. 6th International Conference on Liquid Atomisation and Spray Systems, Rouen, France.
- [4] Hall Taylor, N.H., Hewitt, G.F. and Lacey, P.M.: The motion and frequency of large disturbance waves in annular two-phase flow of air-water mixtures. Chem. Eng. Sci., 18, pp. 537 – 552, 1963.
- [5] Hanratty, T.J. and Engen, J.M.: Interaction between a turbulent air stream and a moving water surface. AIChE-J, 3, 1957.
- [6] Hewitt, G.F.: Measurement of two phase flow parameters. Academic Press, London, 1978.
- [7] Johnen, T. and Haug, M.: Spray Formation Observation and Fuel Film Development Measurements in the Intake of a Spark Ignition Engine. SAE - International Congress, Detroit, USA, 950511, pp. 1 – 12, 1995.
- [8] Sill, K. H.: Wärme- und Stoffübergang in turbulenten Strömungsgrenzschichten längs verdunstender welliger Flüssigkeitsfilme. Dissertation, Institut für Thermische Strömungsmaschinen, Universität Karlsruhe (T.H.), 1982.
- [9] Simon, N.: Kraftstoffwandfilmuntersuchungen im Saugrohr des Ottomotors mit Zentraleinspritzung. VDI-Fortschrittsberichte, Reihe 12: Verkehrstechnik/Fahrzeugtechnik, No. 141, 1990.
- [10] Wittig, S., Elsässer, A., Samenfink, W., Ebner, J. and Dullenkopf, K.: Velocity Profiles in Shear-driven Liquid Films. Proceedings of the Eight International Symposium on Applications of Laser Techniques to Fluid Mechanics, Lisbon, Portugal, 8, 1996.
- [11] Wittig, S., Himmelsbach, J., Noll, B., Feld, H. J. and Samenfink, W.: Motion and Evaporation of Shear-Driven Liquid Films in Turbulent Gases. ASME-Journal of Engineering for Gas Turbines and Power, 114, pp. 395 – 400, 1992.
- [12] Wittig, S., Müller, H., Hallmann, M., Bellmann, Elsässer, A. and Samenfink, W.: Sprühstrahl- und Wandfilmverhalten in Saugrohren von Ottomotoren (submitted for publication). MTZ – Motortechnische Zeitschrift, 1996.
- [13] Wurz, D.: Wellengeschwindigkeit und Wellenstruktur an der Oberfläche schubspannungsgetriebener Flüssigkeitsstrahlen. In: Festschrift zum 70. Geburtstag von Prof. Dr.-Ing. Rudolph Friedrich, Institut für Thermische Strömungsmaschinen, Universität Karlsruhe (T.H.), 1979.

Microscopic Superlaminar Flow Measurements in a Journal Bearing Using a 2D Solid-State LDA

A K Tieu, E B Li, J Y Peng and M R Mackenzie

Department of Mechanical Engineering, University of Wollongong,
Wollongong, NSW 2522, Australia

1 INTRODUCTION

This study is part of the continuing research into turbulent fluid film lubrication which began in the late fifties to early sixties. Most notable are those by Constantinescu (1959), Ng and Pan (1965), Elrod and Ng (1967), and Hirs (1973). Their studies were confined only to study the resulting bearing performance characteristics. Very little work has been reported on the experimental velocity characteristics in the lubrication fluid films. In bearings the fluid velocity is usually a result of combined Couette and Poiseuille flows. However the mechanism of their interaction in the turbulent regime is still unknown.

Tieu et al (1995) developed solid state laser Doppler anemometers (LDA) specifically designed to investigate this interaction. The following work describes the application of a recently developed two-dimensional LDA (Li et al, 1996) to a journal bearing test rig.

2 EXPERIMENTAL FACILITY

The bearing is based on that presented by Tieu et al in 1994 however a number of significant improvements have been made which warrant its description. Figure 1 shows the journal bearing test rig. The shaft is supported onto the base, 1, by precision ball bearings, 2, to minimise the radial motion of the shaft. To obtain high Reynolds numbers the working fluid is water. However this introduces serious corrosion problems of the ball bearings which were only solved by mounting the ball bearings separate from the journal and by using a series of seals, 3 & 4. Chrome plating the shaft, 6, to a mirror surface proved to be effective in obtaining measurements close to the shaft which would not otherwise have been possible. Signals corresponding to the shaft surface appeared only when the measuring volume was very close to or reaching the shaft surface. In this case, the flow velocity and shaft speed could be separated from each other during data processing.

The journal is formed by the perspex housing, 5. The eccentricity is adjustable by loosening the screws, 7, and sliding the housing until the desired

gap size is obtained. The bearing length and diameter are 70mm and the clearance between the journal and housing is 1.2mm.

A 3 phase induction motor (0.75 kW) with a maximum speed of 2800 rpm operates a belt drive system with a step up ratio of two. The gearing allows greater speeds to be obtained producing transitional through into fully turbulent flow.

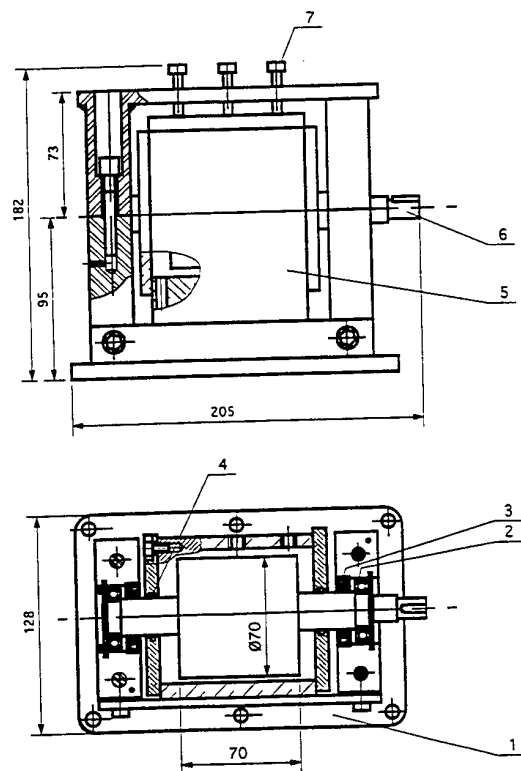


Fig. 1 Journal bearing test rig. (1) base, (2) precision ball bearing, (3) and (4) seals, (5) perspex housing, (6) shaft, (7) fastening screws

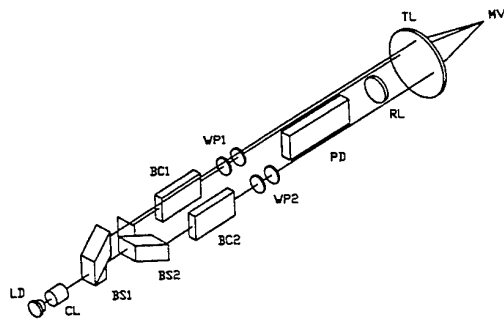


Fig. 2 Optical layout of the 2D solid-state LDA; LD=laser diode, CL=collimating lens, BS1=beamsplitter 1, BS2=beamsplitter 2, BC1=bragg cell 1, BC2=bragg cell 2, WP1=wedge prism 1, WP2=wedge prism 2, PD=photodiode, RL=receiving lens, TL=transmitting lens, MV=measuring volume.

The LDA system consists of all solid-state components. The reason for using solid-state components in this work is that they allow a very compact system to be designed which offers a great advantage in the measurement of microscopic flows since it provides for easy and precise positioning of the LDA. Economy of these components was also considered important. The particular laser diode chosen (Toshiba TOLD 9150) has a wavelength of 685nm which is visible to the human eye thus greatly simplifying alignment.

Briefly the principle of the two-dimensional LDA system is as follows. To provide two dimensional velocity measurements two orthogonal sets of fringes were produced. The fringes were labelled using two different optical frequency shifts. This allows the Doppler signals from each set of fringes to be separated.

Figure 2 shows the optical layout of the LDA system. The visible laser diode (LD) was first collimated by a gradient index rod lens, CL, and then split into three parallel beams by two beam-splitters, BS1 and BS2. All the beams are of nearly equal intensity. Two Bragg cells, BC1 and BC2, were used to introduce frequency shifts of 60 MHz and 70 MHz respectively to the lower two beams. Optical wedge pairs, WP1 and WP2, were positioned after the Bragg cells to adjust the direction of the beams from the cells to be parallel to the top beam. The three incident beams, BM1 (60 MHz shifted), BM2 (70 MHz shifted) and BM3 (unshifted) were focused by a transmitting lens, TL. The backscattering light from particles in the measuring volume was focused by the receiving lens, RL, onto an APD with a pre-amplifier (Mackenzie et al, 1992).

The measurement volume is about 40 μm long. (For measurement in bearings in which the minimum gap is usually less than 0.5 mm, the dimensions of the measuring volume, especially the length, should be small compared to the gap). To minimise the fringe gradients in the measuring volume special attention was paid in alignment of the LDA optics. The collimating lens was carefully adjusted to ensure that the waists of the incident beams were located at the

measuring volume. The probe has been tested for laminar flow and the result compared very well with the theoretical parabolic flow profile (Li et al, 1996).

3 EXPERIMENTAL RESULTS

Along the axial direction of the shaft, four positions spaced at intervals of 5mm were selected for measurements. The eccentricity of the shaft was set so that at the place of measurement the gap size was 0.45mm. Measurements were made at a rotating speed of 2350rpm which resulted in a Reynolds number of 3900. The velocities in the circumferential, u , and axial direction, v , are shown in Figures 3 and 4 respectively and their turbulent intensities in Figures 5 and 6.

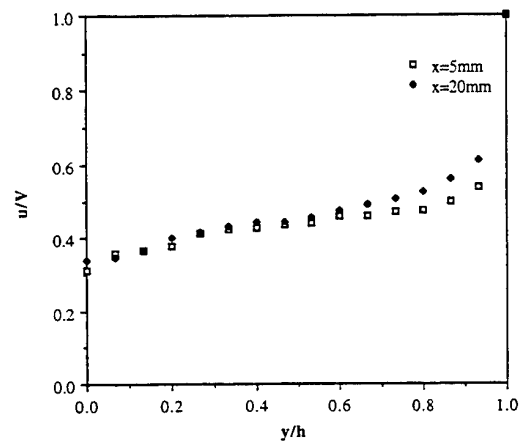


Fig. 3 Circumferential velocity component, u , at $x=5\text{mm}$ and $x=20\text{mm}$ from shaft centre; y =radial coordinate, h =gap size (0.45mm), V =shaft speed.

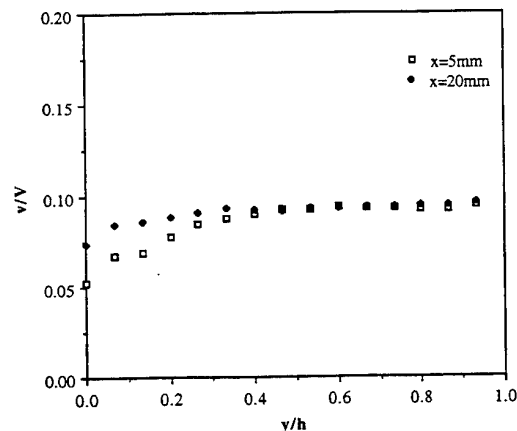


Fig. 4 Axial velocity component, v , at $x=5\text{mm}$ and $x=20\text{mm}$ from shaft centre; y =radial coordinate, h =gap size (0.45mm), V =shaft speed.

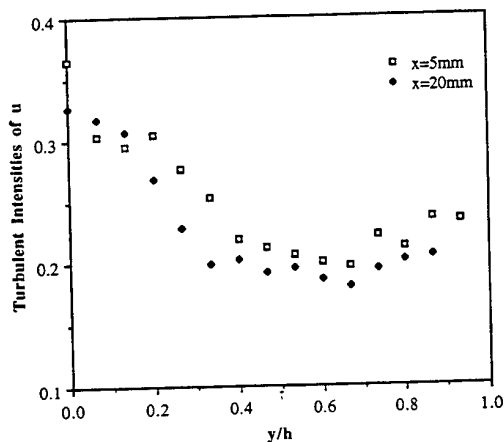


Fig. 5 Turbulent intensities of circumferential velocity, u , at $x=5\text{mm}$ and $x=20\text{mm}$ from shaft centre.

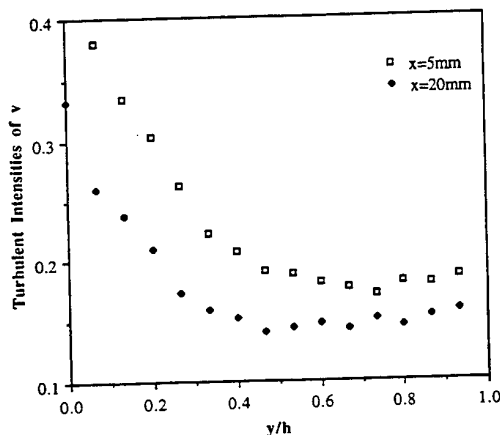


Fig. 6 Turbulent intensities of axial velocity, v , at $x=5\text{mm}$ and $x=20\text{mm}$ from shaft centre.

From Figure 3 (for u/V) the measurements close to the stationary wall are difficult to obtain. Apart from the surface finish it was found that optical alignment can also affect the close-to-wall measurement. In these figures, the results correspond to the axial locations $x=5\text{mm}$ and $x=20\text{mm}$ from the shaft centre. The circumferential velocities close to the shaft surface for $x=20\text{mm}$ are higher than those at $x=5\text{mm}$, whereas for the axial direction, the velocities close to the stationary surface at $x=20\text{mm}$ are higher than those at $x=5\text{mm}$. This is attributed to the different pressure gradients at these locations. The turbulent intensities in both directions are higher in the case of $x=5\text{mm}$. The turbulent intensities increase to higher values when moved closer to the stationary wall. This increase was also observed by Kjaer and Enni (1987). The flow field is summarised in Figure 7.

The measurement results qualitatively agree with the velocity profiles predicted by the theoretical model (Tieu et al, 1994). This transitional turbulent flow theory is based on an empirical formula describing the mixing length first proposed by Granville (1989). Granville modified the well known

van-Driest formula (1956) to account for flows with a pressure gradient. This mixing length formula for pressure gradients is given by

$$l = \kappa y^+ \sqrt{\tau^+} \left(1 - e^{-y^+/\lambda} \right)$$

where λ is a function of the shear stress gradient, $\partial\tau^+/\partial y^+$ such that

$$\left(\frac{A}{\lambda} \right)^2 = 1 + B \frac{\partial\tau^+}{\partial y^+}$$

where A and B be are constants. Tieu and Kosasih (1992) showed experimentally using LDA measurements on flow in a narrow channel that the appropriate values of the constants A and B for bearing type flow are 26 and 55 respectively.

4 CONCLUSION

Two-dimensional measurements of microscopic superlaminar flow in a laboratory journal bearing have been presented. The velocity profiles in a 0.45 mm gap have been measured at a number of positions along the axial direction under different Reynolds numbers. Improvements in the resolution of the LDA probe are needed to permit measurements in smaller gaps.

ACKNOWLEDGMENTS

The financial support from the Australian Research Council (ARC) is gratefully acknowledged.

REFERENCES

- Constantinescu, V.N., 1959, On the Turbulent Lubricant, *Proc. Inst. Mech. Eng.*, vol. 173, pp. 881-900.
- Elrod, H.G., & Ng, C.W., 1967, A Theory for Turbulent Fluid Films and its Application to Bearings, *ASME Journal of Lubrication Technology*, vol. 89, pp. 381-391.
- Granville, P.S., 1989, A Modified Van Driest Formula for the Mixing Length of Turbulent Boundary Layers in Pressure Gradients, *ASME Journal of Fluids Engineering*, vol. 111, pp. 94-97.
- Hirs, G.G., 1973, A Bulk Flow Theory for Turbulence in Lubricant Films, *ASME Journal of Lubrication Technology*, vol. 95, pp. 137-146.
- Kjaer, J., & Enni, B., 1987, LDA Measurements in Thin Channels, *Dantec Information*, vol. 4.

Li, E.B., Tieu, A.K., & Mackenzie, M.R., 1996, Development of a 2D Solid State LDA for Velocity Measurements in Turbulent Bearing Flow, accepted for publication in Measurement Science Technology.

Mackenzie, M.R., Tieu, A.K., Binh, L.N., & Kosasih, P.B., 1992, A Sensitive Optical Receiver with Application to a Visible Laser Diode Anemometer, Meas. Sci. Technol., vol. 3, pp. 685-686.

Ng, C.W., & Pan, C.H.T., 1965, A Linearized Turbulent Lubrication Theory, ASME Journal of Lubrication Technology, vol. 87, pp. 675-688.

Tieu, A.K., & Kosasih, P.B., 1992, An Expression of Reynolds Stress in Turbulent Lubrication Theory, ASME Journal of Tribology, vol. 114, pp. 57-60.

Tieu, A.K., Kosasih, P.B., & Mackenzie, M.R., 1994, A Study of Fluid Velocities in Tribological Fluid Film, ASME Journal of Tribology, vol. 116, pp. 133-138.

Tieu, A.K., Mackenzie, M.R., & Li, E.B., 1995, Measurements in Microscopic Flow with a Solid-State LDA, Exp. Fluids, vol. 19, pp. 293-294.

van Driest, E.R., 1956, On Turbulent Flow Near a Wall, Journal of Aeronautical Sciences, vol. 23, pp. 1007-1011, 1036.

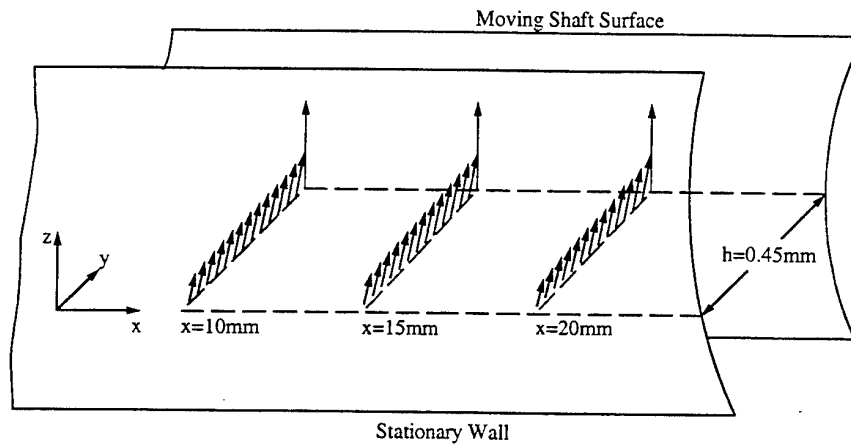


Fig.7 Velocity vectors in journal bearing.

APPLICATIONS OF LOW COHERENCE INTERFEROMETRY TO DYNAMIC OIL FILM THICKNESS MEASUREMENT

S. R. Taplin, A. Gh. Podoleanu, D. J. Webb, D. A. Jackson and S. R. Nattrass*

Physics Department, University of Kent at Canterbury, UK

ABSTRACT

A technique for measuring the thickness of dynamic thin oil films in a bearing simulator rig is presented. The resolution achieved is $\sim 0.1\mu\text{m}$ over a $500\mu\text{m}$ range. An argument for the benefits of this technique over existing methods of measurement is given along with suggestions for the future direction of this work. Novel probe design and details of the signal processing procedure are discussed and results for a fixed set of running conditions of the bearing simulator rig are shown with independent validation of the system's performance.

1. INTRODUCTION

Oil film thickness in lubricated contacts of moving machinery is important to both lubricant and equipment manufacturers. In the interests of energy efficiency, it is desirable to reduce oil viscosity whilst ensuring that an adequate oil film is still maintained under all machinery operating conditions. The capability to measure dynamic oil film thickness directly in running machinery is therefore very important to the lubricant formulator. Clearly, any measurement technique providing this capability must withstand the harsh environment of working machinery whilst permitting minimally invasive access to the region of interest.

A number of techniques are already in use for such 'in-situ' measurements. There are electrical techniques utilising miniature probes which rely for their operation on the properties of inductance,

resistance or, more commonly, capacitance. There are also optical techniques, of which the most common is fibre-optic laser induced fluorescence (LIF) as described for example by Brown et al. (1993).

Whilst these techniques have served well, they each have deficiencies which either limit their effectiveness or complicate their implementation. For example, with capacitance, it can be difficult to isolate contributions from the desired measurement zone. With LIF, great care is required in the transfer of an off-line light-intensity calibration to the harsh in-situ environment. For such reasons, new techniques are constantly being sought.

The film thickness technique described here uses white light interferometry incorporating the channelled spectrum technique, which exhibits an accuracy of $\sim 0.1\mu\text{m}$ and allows absolute distance measurements to be made over approximately 5mm working range previously described by Taplin et al. (1993). In order to overcome the zero offset characteristic of white light interferometers, a novel probe design is described that utilises a Titanium Dioxide (Ti-O_2) coating to improve the reflectance of the fibre-end.

The technique offers a number of potential advantages. It is essentially an optical FM technique and therefore offers high immunity to intensity noise which is so often associated with the application of optics to in-situ measurement. It is implemented with single mode fibre and so is ideally suited to delivering minimally-invasive measurements of high spatial resolution and in comparatively inaccessible locations.

The potential of the technique is illustrated in its application to a bearing simulator rig described by

* S.R. Nattrass is with Shell Research Ltd., SRTCT, PO Box 1, Chester, CH1 3SH, England

Bates et al. (1993). Results are presented showing the distribution of oil film thickness for a given speed of a rotating shaft.

2. EXPERIMENTAL ARRANGEMENT

The experimental arrangement for this application is depicted in Fig. 1. Light from a broad band super-luminescent diode (SLD) is transferred to the sensing region by a pigtailed fibre. A Fabry-Perot interferometer is formed between a Ti-O_2 coated fibre surface and the metal surface of the rotating shaft (described in more detail in section 5). The returned light is collimated and projected on the diffraction grating and the dispersed light is monitored with a linear CCD array.

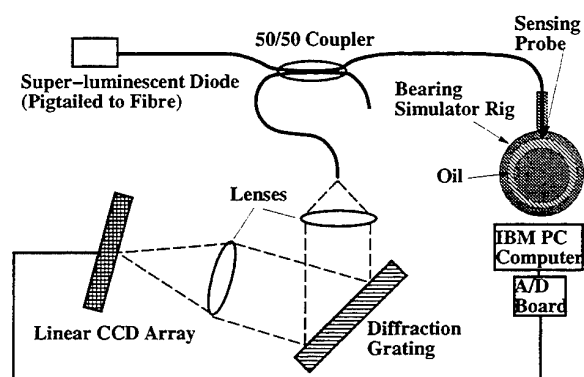


Fig. 1 Experimental Arrangement for Measurement of Oil Thickness by White Light Technique.

3. PROBE DESIGN AND BEARING TEST RIG

In order to use white light processing, the optical path difference (OPD) of the sensing cavity must exceed the coherence length of the source. If this condition is not met the light is coherent and interference only occurs at a discrete wavelength instead of over a range of wavelengths as is required for white light processing. In the present application the coherence length is of the order of $\sim 20\mu\text{m}$ and so to measure the film thickness in the region of close contact ($\sim 0\mu\text{m}$) it is necessary that the probe is offset from zero. This can be achieved by simply pulling the fibre away from the face of the bearing. The problem with this approach is that the void will be filled with

oil, which will be subject to the pressure fluctuations in the bearing but will not be identical to that of the actual oil film of interest. To overcome this problem a special probe was built with an integral offset as shown in Fig. 2(b).

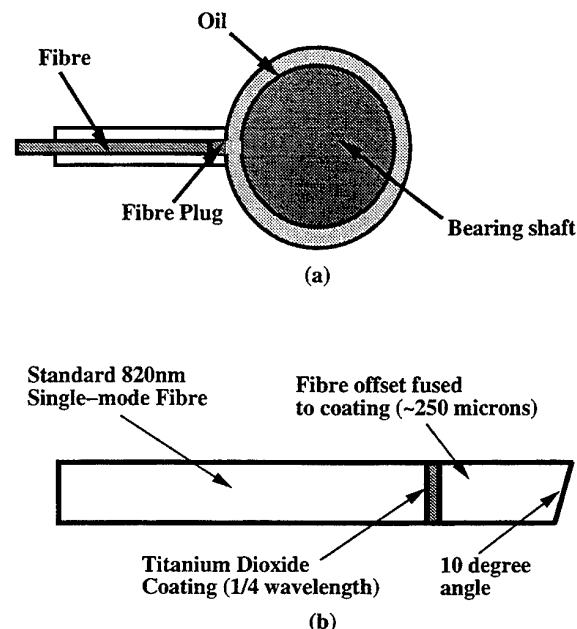


Fig. 2 (a) Access Port to Bearing, (b) Probe Design for Application Technique.

The refractive index of the oil is comparable to that of the fibre (approximately 1.4 at RTP) so there is a low reflectance at the fibre-oil interface. To overcome this problem, a Ti-O_2 coating is applied to the fibre end-face using electron beam deposition. The compound has a refractive index of approximately 2.6 so a good level of reflectance is achieved at the new interface. The void left by the fibre is removed by fusing a further piece of fibre onto the coating to fill the recess up to the bearing surface using a technique outlined by Inci (1992). It is brought flush to the surface through successive polishing with lapping film to form a plug approximately $250\mu\text{m}$ in size.

The cavity is created between the metal shaft and the recessed Ti-O_2 coating (shown in Fig. 2a). Any concern over an additional cavity being formed between the coating and the fibre end-face at the bearing wall is addressed by introducing a ten degree

angled polish to limit reflections on both sides of the fibre end-face as detailed by Ulrich (1980). Despite the reduced reflections at this surface, the angle still permits coupling of light into the fibre. The high power of the SLD device removes the concern of any coupling losses.

4. PROCESSING OF THE CHANNELLED SPECTRUM

Once the light is returned from the sensor, through the system, it is collimated onto a diffraction grating (1800 lines/mm) and the dispersed light focused by a lens onto a linear CCD array. The signal read out from the linear CCD array is a voltage representation of the channelled spectrum (Fig. 3). The non-linearity of the spectrum over the wavelength range observed is small and therefore, does not require any correction. The physical wavelength of light recorded by the CCD is converted to a time scale as it is read from the device. The frequency of the peaks within the time-encoded spectrum is depends linearly with the OPD between successive interfering reflections within the Fabry-Perot cavity (as described by eqn. 1).

$$I(\lambda, \delta) = C \cdot e^{-\frac{(\lambda - \lambda_0)^2}{\Delta\lambda^2}} \cdot \left(1 - \frac{F \cdot \sin^2\left(\frac{2\pi n d}{\lambda}\right)}{1 + F \cdot \sin^2\left(\frac{2\pi n d}{\lambda}\right)} \right)$$

Eqn. 1. Airy Formula for a Parallel Fabry-Perot Cavity (where λ is wavelength, λ_0 is the peak wavelength of the source of amplitude C , $\Delta\lambda$ is the linewidth of the source at the 1/e point, F is a function of finesse of the Fabry-Perot, n is the refractive index of the gap and d is the cavity width.)

We deduce this frequency by taking the Fourier Transform using a software Fast Fourier Transform (FFT) algorithm to determine the signal's frequency. A least squares fit of the data to a gaussian model is performed (Fig. 4) to ascertain more precisely, the position of the peak maximum allowing interpolation between data points for greater accuracy. Since the cavity, in practice, has a low finesse, eqn.1 approaches the form of a gaussian multiplied by a

sinusoid. After the Fourier transformation, the result is simply a gaussian whose position is determined by the frequency of the sinusoid thus validating the use of a gaussian model. This procedure is described in more detail by Taplin et al. (1994).

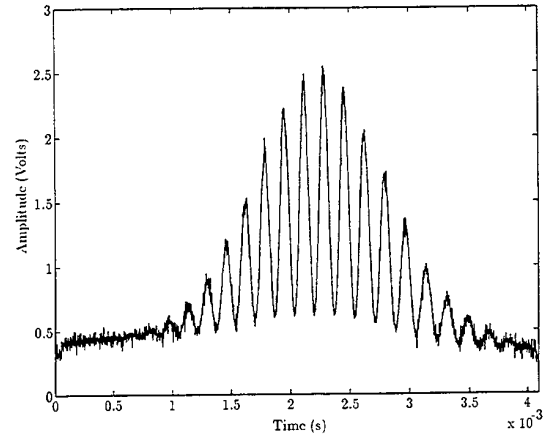


Fig. 3 Channelled Spectrum Output from Linear CCD Array.

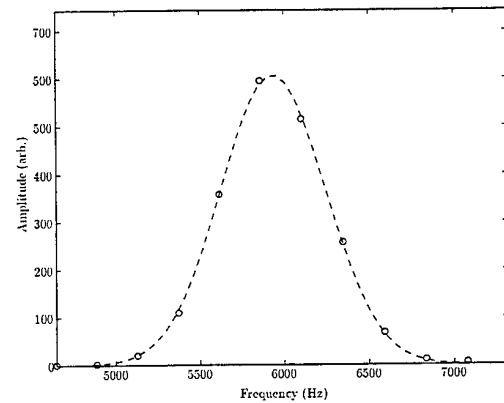


Fig. 4 Gaussian Fit performed on FFT of Channelled Spectrum.

Calibration is achieved beforehand by running a capacitive feedback loop piezo-electric transducer with a resolution of 2nm to model cavities over a given range. An air cavity is formed between the fibre end-face of the coupler's spare output and a mirror

attached to the PZT. The resolution achieved over the region of interest, $0\mu\text{m}$ - $500\mu\text{m}$ ($56\mu\text{m}$ - $556\mu\text{m}$ including the offset of $56\mu\text{m}$), is approximately $0.1\mu\text{m}$ (RMS deviation from linearity) as seen in Fig 5.

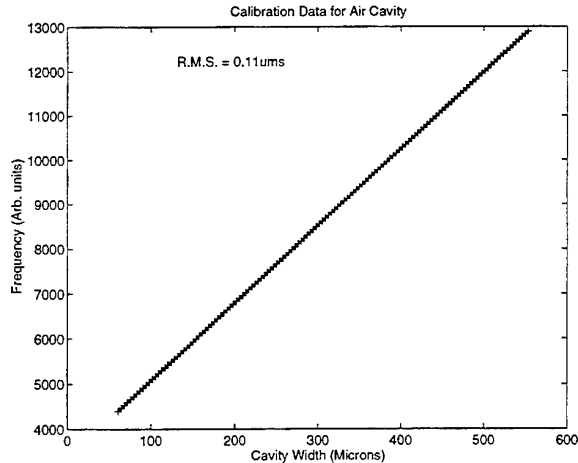


Fig. 5. Calibration Line for Air Cavity.

Processing of the data takes approximately one second per OPD determination and so is, currently, not suited to real time processing in its current form. Post processing is therefore applied to the data after enough samples have been taken from the sensor for a fixed set of conditions. The measurement bandwidth is limited by the speed at which information is read from the CCD device (currently 1ms). If the fringes are seen to move during the exposure time of the CCD, the fringes will blur, reducing contrast. Therefore, the bandwidth has to be sufficiently high to 'freeze' the fringes in motion and hence the contrast is dependent on the rate of change of the oil film thickness. In this experiment, the rate of change of the fringes is small enough to not cause problems with the bandwidth limit. Logging the data taken by the A-to-D board takes ~ 2 seconds. It is envisaged that the use of a transient recorder or some other large memory device will permit measurements up to the 1kHz read-out rate of the CCD array.

5. RESULTS FOR THE BEARING RIG

The probe enters the bearing wall at the 10 degree angle described above. The bearing wall (or

stator) surrounds a shaft (or rotor) which is driven by a motor. Both are encapsulated in a chamber devised to keep the bearing flooded in oil.

The measurements are not synchronised (although this could be possible for a fixed point on the bearing by triggering the CCD capture) but instead, are taken randomly in time over the period required to acquire sufficient samples for a statistical study of the oil-film behaviour in the sensing region. Slow data logging rates prevent a continuous trace of the bearing profile. Possibilities exist to vary the film thickness, and hence the bearing load, by varying the positioning of the rotor with respect to the stator. Coupled with the variation of the speed of the shaft, a number of running conditions can be achieved.

To demonstrate the sensor's application, a histogram representing the spread of oil film thickness for over 300 samples taken at a fixed set of running conditions (6.4 rpm) is seen in Fig. 6. The rotor position is adjustable within the bearing rig and, for this data, was moved $100\mu\text{m}$ from concentricity away from the sensor as monitored by an LVDT (Linearly Variable Displacement Transformer). The rotor, previously measured with a moving stylus profilometer (Talysurf, Rank Taylor Hobson), was found to have an eccentricity of $\sim 14\mu\text{m}$ due to factors such as a slight elliptical profile and a non-concentric centre position. This is seen in the results where the thickness is contained within a range of $\sim 14\mu\text{m}$. The figure shows more readings at the edges of the data, in the extremal regions since this demonstrates the turning points of the rotor's sinusoidal motion, to and from the sensor affecting the optical path length. Theoretically, the extremal bins at the edges of the histogram (set at $1/3\mu\text{m}$) should be the largest values in the graph but resolution limitations reveal themselves with a final, lower valued histogram bin in each case containing the error in effective path length.

Spatial resolution is close to the core diameter of the fibre ($\sim 5.5\mu\text{m}$) for a static gap but clearly, for the dynamic case, the exposure time of the CCD coupled by the passage of the rotor (dependent on the speed and diameter of the rotor), will limit the spatial resolution of the probe.

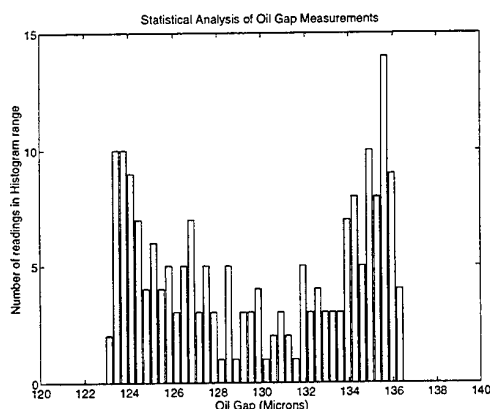


Fig. 6 Oil Film Distribution for Rotor Speed 6.4 rpm.

6. CONCLUSIONS

Careful design of the sensing probe has enabled the demonstration of the application of a white light system to the determination of oil film thickness. The bearing simulator chosen for the demonstration presented most of the engineering challenges that would be faced in implementing the measurement in a true bearing. At the same time, it allowed sufficient control over the oil film regime for independent verification of the white light system performance. In this respect, the measurement of the dynamic oil-filled cavity achieved a sub-micron resolution comparable to that of a static air filled cavity.

Future work will address the two key areas of acquisition speed and the accommodation of refractive index variation in the oil as a function of temperature and oil degradation. The first of these will be tackled by the use of higher speed CCD's and/or the adoption of a rotation synchronised snapshot procedure. This will then allow much greater, more realistic, rotational speeds to be employed.

The refractive-index issue presents a greater challenge. Whilst the temperature dependence alone can be handled by temperature measurement, the effects of lubricant degradation are probably best tackled by an in-situ reference. This would entail simultaneous measurement of a fixed film thickness of the same oil. A potentially more powerful solution,

however, would be to determine oil index directly from the dependence of fringe visibility on the relative indices of oil and probe. The feasibility of the latter approach remains to be tested.

7. ACKNOWLEDGEMENTS

S. R. Taplin acknowledges the support of Shell Research Ltd.. A. Gh. Podoleanu participated in this work with the support of the TEMPUS scheme. Special thanks are extended to S. R. Kidd et al. at Heriot-Watt university for the supply of the Ti-O₂ coated fibres used in this work and to N. Horswill of Shell Research for assistance in the bearing simulator application.

8. REFERENCES

- Brown, M.A. et al. 1993, Characterisation of the Oil Film Behaviour between the Linear and Piston of a Heavy-duty Diesel Engine, *SAE*, No. 932784, pp.135-150.
- Taplin, S.R. et al. 1993, Displacement Sensor using Channelled Spectrum Dispersed on a Linear CCD Array, *Electron. Lett.*, vol. 29, pp. 896-897.
- Inci, M.N. et al. 1992, Fabrication of Single Mode Fibre Optic Fabry-Perot Interferometers using Fusion Spliced Titanium Dioxide Optical Coatings, *Meas. Sci. Technol.*, vol. 3, pp. 678-684.
- Taplin, S.R. et al. 1994, White-light Displacement Sensor incorporating Signal Analysis of Channelled Spectra, *SPIE (Fibre Optic & Laser Sensors XII)*, vol. 2292, pp. 94-100.
- Bates, T.W. et al. 1993, Assessment of Lubricant Load Bearing Capacity Using a Journal Bearing Simulator Bench Test, *Fourth CEC International Symposium*.

EXPERIMENTAL ANALYSIS BY LASER EXTINCTION OF THE EVOLUTION OF THE LIQUID CROWN PRODUCED BY THE SPLASH OF A DROP ON THIN LIQUID FILM

A. Coghe[°] and G.E. Cossali^{°°}

[°] Dipartimento di Energetica, Politecnico di Milano - Milano- Italy

^{°°} Facoltà di Ingegneria, Università di Bergamo - Bergamo- Italy

ABSTRACT

The cylindrical sheet of liquid produced by the drop impact (hereinafter called "crown") is responsible of the possible formation of liquid jets, protruding from its upper rim, that may break-up into smaller drops (secondary atomisation). The paper presents measurements of the crown radius evolution by a laser obscuration technique used in conjunction with a photodiode array. Experiments were designed to span over a relatively large range of conditions in terms of drop Weber number ($370 \div 880$), Ohnesorge number ($0.002 \div 0.028$) and nondimensional film thickness ($0.6 \div 1.5$). The results were interpreted following the available theoretical models and qualitative agreement was found relatively to the crown evolution law, although the theory appears to overestimate the effect of the film thickness on the crown expansion velocity. A correlation of the measured data with nondimensional film thickness, Weber number and Ohnesorge number is also reported.

INTRODUCTION

Splash of a liquid drop on solid dry or wetted surfaces is a phenomenon which was recognised to be of capital importance in many applied fields; internal combustion engine (impact of fuel spray droplets on the combustion chamber walls or intake manifolds), spray painting, water spray cooling, erosion of soil, are some of those fields where a deeper knowledge of the drop-wall interaction phenomena can be usefully applied.

The impact of a drop on a thin liquid film (i.e. a film whose thickness is comparable or

smaller than the drop diameter) produces a cylindrical liquid sheet that expands in radius and height; under certain circumstances, it may generate a number of liquid jets protruding from its upper rim which then break-up into smaller droplets (secondary atomisation); if no secondary droplets are produced, the phenomenon is often referred as deposition.

The phenomenon was experimentally studied by many researchers since the first important work of Worthington (1896) mainly by photographic means and with different purposes. Recently, some effort was spent on defining the so called splashing/deposition limit (i.e. the threshold between splashing with secondary atomisation and deposition).

Stow and Hadfield (1981) and later Mundo et al. (1995) proposed a correlation for the definition of the splashing threshold for impact on dry surfaces, based on the characteristics of the impinging drops that can be summarised in nondimensional form by the values of the Weber number ($We = \rho V_o^2 D / \sigma$ where: D =drop diameter, V_o = drop velocity, ρ =density, σ = surface tension) and the Ohnesorge number ($Oh = \mu / (D\sigma\rho)^{1/2}$; where μ =viscosity). The relevance of gravitational effects on the phenomenon is usually established by the value of the Froude number ($Fr = V_o^2 D / g$).

A correlation for the splashing limit was proposed by Walzel 1980, Coghe et al. (1995) and Cossali et al. (1996) for the splash on a thin liquid film. In this case also the value of the nondimensional film thickness ($\delta = h/D$, where h is the film thickness) influences the threshold.

When additional features are considered, like for example the surface roughness, the impact angle and the impact frequency, other non-dimensional numbers must be considered, like the non-dimensional roughness R_{nd}

($R_{nd}=R_a/D$) and the non-dimensional impact frequency f_{nd} ($f_{nd} = f/f^*$, where f^* is, for example, equal to V_0/D).

Yarin and Weiss (1995) analysed theoretically and experimentally the general problem of the impact of a train of drops over an initially dry surface. The theory proposed is based on the appearance of a kinematic discontinuity: assuming an initial form of the velocity distribution in the liquid film, they were able to describe the evolution of the

discontinuity wave (the crown) and the time law of the crown radius was found to take the form $R_c/D=A(\tau-\tau_0)^{1/2}$, where τ is the non-dimensional time ($\tau = tD/V$) and A is a parameter that contains (for single drop impact) only the film thickness. Indeed, the effects of surface tension and viscosity were neglected in Yarin and Weiss analysis, so that the only nondimensional parameter that can affect the crown radius time law is the nondimensional film thickness.

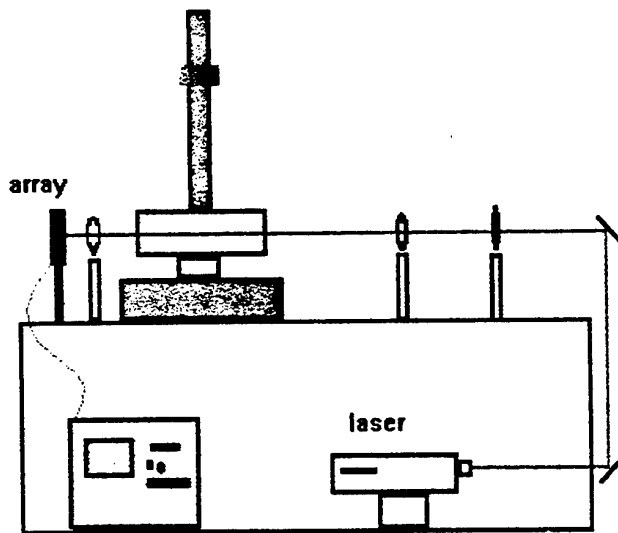


Fig 1 Schematic representation of the experimental set-up

The validity of that time law for the radius crown was checked on a limited set of experimental results and found to be consistent. The crown radius together with the crown thickness are expected to determine the size of the drops produced by the splash and experimental evidence exists that the size of secondary droplets produced by the impact of a drop on a solid wall covered by a thin liquid film varies with time (Coghe et al., 1994).

The present paper reports direct measurements of the time evolution of the crown produced by a liquid drop impacting on a thin film ($\delta=0.6\div1.5$) under different impact condition ($We = 370\div885$) and different liquid characteristics ($Oh=0.00212\div0.028$).

EXPERIMENTAL SET-UP

The experimental set-up comprised a single drop generator producing drops of about 3 mm

diameter; the drops were let to fall on a wetted surface by gravity and the splash velocity was varied by varying the drop generator height. The liquid film was generated by submerging into a small tank an aluminum disk whose position, relative to the free liquid surface, could be varied with a 10 μm precision (Coghe et al., 1994). In the present experiment a laser source was used to produce a continuous light sheet imaged onto a linear photodiode array in a way similar to that applied for studying the flame propagation in an engine (Witze, 1985). The method relies on the obscuration of the laser sheet produced by the liquid crown and due to the light reflection and refraction at the liquid-air interfaces.

The light sheet was produced by a low power (1 mW) He-Ne laser through a combination of spherical and cylindrical lenses (Diemunsch and Prenel, 1987), and was aligned parallel to the impact surface at a distance of about 1 mm (see fig.1). The selection of the

distance was critical; in fact, the necessity of the shortest possible distance for better sensitivity at the early stage of the crown formation contrasted with the need of avoiding false triggering from noise due to the perturbation of the liquid film, induced by drop impingement. The laser sheet was imaged onto a Reticon linear photodiode array made of 1024 elements, each one 13 μm wide, and thus about 13.3 mm long. The highest possible scan rate was 12 MHz per photodiode but a lower value (4 MHz) was used, equivalent to 3.9 kHz per scan of the array, allowing a time resolution of 256 μs . For a typical experiment on the crown propagation after drop impact, this scan rate resulted in at least 50 measurements of the radial dimension. The array detects the extension of the shadow produced by the liquid structure crossing the laser sheet as an area of reduced signal intensity.

Because the array was only 13.3 mm long, its first element was positioned in such a way to be very close to the location corresponding to the drop impact point. In this way it was possible to utilise the entire array length to record the radial dimension of the growing crown. The crown radius as a function of time, can be deduced accurately from the number of obscured photodiodes by a calibration made with a reference cylindrical object and accuracy of 0.01 mm.

noise ratio resulted very good and the two main phenomena, drop impact and liquid crown propagation, were clearly distinguishable and measurable. This technique allowed high speed acquisition reducing the quantity of stored data, without loss of information. The most important feature of the measuring instrument is the ability to record the linear motion of relatively fast events with a very high spatial resolution, due to the large number of closely-spaced detectors. Moreover, the technique is non perturbing and relatively simple to apply.

To verify the accuracy and reliability of the present technique, a photographic method was also implemented, using a flash lamp (10 μs duration) and a CCD camera with microsecond time exposure resolution. A delay unit, triggered by the obscuration of a laser beam, imaged onto a photodiode, caused by the passage of the falling drop, allowed to select the time delay of each image and thus to obtain a record of the whole phenomenon by a discrete number of digitised images. This procedure requires more time and a very large number of images to obtain a comparable space resolution and statistical accuracy, but it was used to compare the results obtained by means of the linear array with those deduced by the analysis of the video images. The comparison revealed a reasonable agreement.

Exp. N.	Liquid	Oh	We	δ
W1	Water	0.00212	372, 558, 744	0.6÷1.5
W2	Water	0.00212	372, 558, 744	0.6÷1.5
W3	Water	0.00212	372, 558, 744	0.6÷1.5
G1	H ₂ O-glycerine 50%	0.010	441, 661, 882	0.6÷1.5
G2	H ₂ O-glycerine 50%	0.010	441, 661, 882	0.6÷1.5
G3	H ₂ O-glycerine 50%	0.010	441, 661, 882	0.6÷1.5
H1	H ₂ O-glycerine 65%	0.0277	442, 663, 884	0.6÷1.5
H2	H ₂ O-glycerine 65%	0.0277	442, 663, 884	0.6÷1.5
H3	H ₂ O-glycerine 65%	0.0277	442, 663, 884	0.6÷1.5

Table 1 - Ranges of Experimental conditions

Each element of the detector was configured as an optical switch converting the signal to single bit digital form; the output signal switches on/off as the incident light intensity crosses a threshold, thereby monitoring the presence of a liquid structure on the light path. The laser light intensity was adjusted in order to avoid photodiode saturation and to produce a signal output slightly higher than the on/off threshold in order to get the largest sensitivity. Threshold setting of the voltage comparators was found not very critical to the accuracy of the measurements: above a certain level the signal to

With the linear array the overall accuracy in defining the origin of the time axis was estimated to be about 0.3 ms; the uncertainty in defining the position of the drop centre at the impact was estimated to be better than 0.02 mm. Those uncertainties are of the order of the time and space resolution of the technique.

RESULTS AND DISCUSSION

Ranges of experimental conditions are reported, in nondimensional form, in table 1.

Figure 2 shows an example of the raw data yielded by the instrumentation; the first peak (A)

is due to the passage of the drop that produces partial obscuration of the photodiodes.

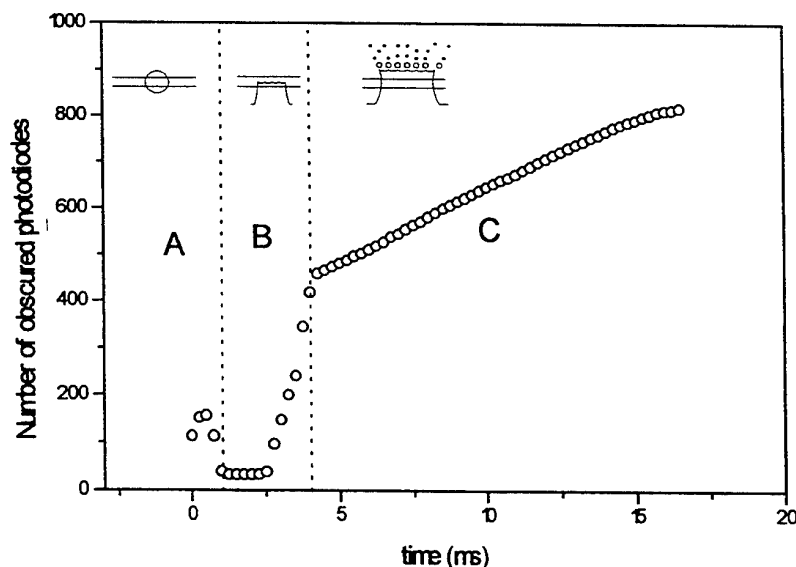


Fig 2 Example of raw data yielded by the instrumentation

The amplitude of the peak carries information about the exact drop impact position; in fact, when drops are let falling from more than few centimetres from the impactor, the final impact position may change slightly from drop to drop, due to many causes like the appearance of tangential component on the aerodynamic action on a slightly deforming drop, or a possible horizontal component of the initial velocity when drop detach from the drop generator, etc.

The knowledge of the number of photodiodes obscured by the drop and that of the drop diameter allows to define the position of the drop centre at a given instant. The part of the curve (B) just after the first peak shows a rapid obscuration of an increasing number of photodiodes, and it is caused by the rising of the crown from the liquid film, which covers almost at once a large number of photodiodes. Finally, part (C) of the curve contains information about the evolution of the crown radius.

Curves obtained from different drops impacting under the same conditions (We, Oh, δ) were first shifted in time setting $t=0$ at the drop peak location; then, each curve was shifted in the y direction to overlap the drop peak in order to have a common spatial location at the same time. The number of obscured photodiodes was then translated into a physical length by means of the calibration parameter K (which gives the number

of obscured photodiodes when a solid cylinder, 1mm diameter, is placed across the laser sheet) and at the drop peak amplitude was assigned the value of the drop radius, so that $x=0$ is the location where the drop centre hits the wetted surface. At this point all the information contained in the part A of the curve (figure 2) was used and part A and B were eliminated, whereas parts C of every drop impact were ensemble averaged.

Following Yarin and Weiss (1995), the crown radius evolution is expected to follow the time law: $R_c/R_0 = B(\tau - \tau_0)^{0.5}$ where R_0 is the drop radius ($=D/2$), $\tau = tV_0/D$ and B is a nondimensional parameter; thus the crown radius time derivative ($dR_c/dt \equiv V_{cr}$) will depend on time as: $V_{cr}/V_0 = B/4 (\tau - \tau_0)^{-0.5}$ and that means that: $R_c V_{cr} = \beta V_0^2$; where $\beta = B^2/4$.

Figure 3 shows the parameter β plotted vs time for some experimental conditions; in partial agreement with the above mentioned theoretical result, the product remains almost constant (data scattering is partially due to the numerical derivation involved in calculating V_{cr}). From the experimental data the average value of $(R_c V_{cr})/(V_0^2) = \beta$ over a time interval spanning from 5 to 15 ms (the actual width of the time interval was slightly different for different conditions) was evaluated for each experimental condition.

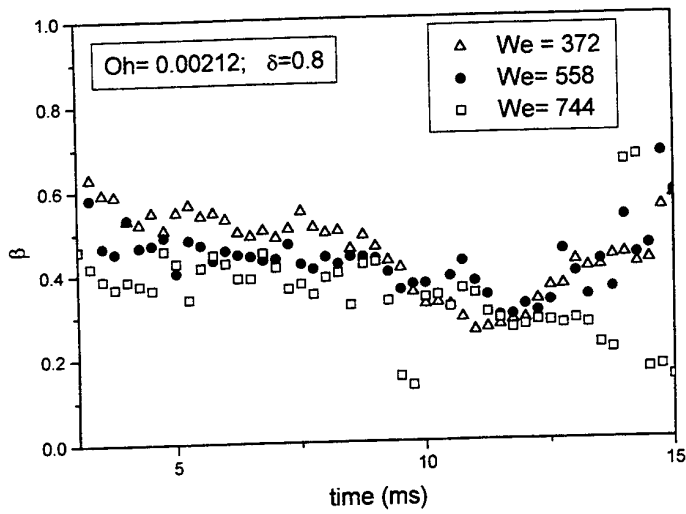


Fig. 3 Parameter β plotted vs time for some experimental conditions

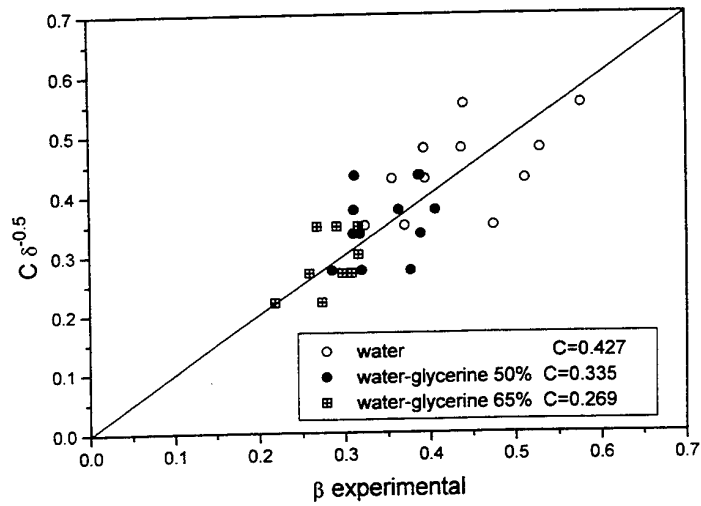


Fig 4 Comparison of Yarin and Weiss correlation with present experimental data

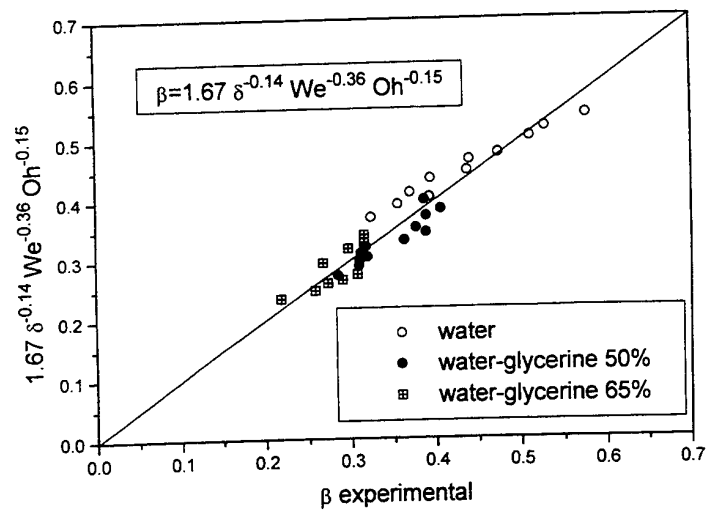


Fig 5 Comparison of the proposed empirical correlation with present experimental data

Yarin and Weiss (1995) model predicts a value of β equal to $(2/3)^{0.5} \delta^{-0.5}$ (independent of We and Oh) but it is easily seen that such values overestimate the experimental data. An attempt was made to fit the experimental values of β following the above mentioned model, i.e. in the form: $\beta = C \delta^{-0.5}$, using three different values of C , one for each fluid, and the results are reported in figure 4. The dispersion is large, and the calculated values of the constant C are much lower than the predicted one.

A more accurate correlation was found allowing for an arbitrary value of the exponent of δ and taking into account the influence of We and Oh . The best fit was obtained with:

$$\beta = 1.67 \delta^{-0.14} We^{-0.36} Oh^{-0.15}$$

and figure 5 shows the comparison with the experimental data.

It is interesting to consider the effect of the above mentioned constancy of the product $R_c V_{cr}$ on the total liquid mass contained in the crown.

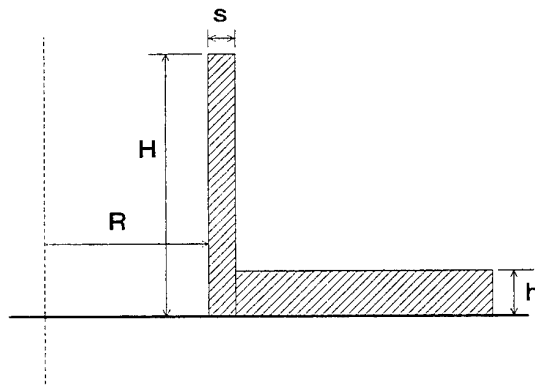


Fig. 6 Schematic representation of the crown following Macklin and Metaxas (1980)

If the Macklin and Metaxas model (1980) is accepted (see fig. 6 for the schematic representation), then the total mass contained into the crown is equal to:

$$M_T = \rho \pi R_c^2 h + M_0$$

(where $M_0 = \rho \pi 4R_0^3/3$ is the drop mass) and:

$$\begin{aligned} dM_T/dt &= \rho \pi 2 R_c dR_c/dt h = \\ &= \rho \pi 2 R_c V_{cr} h = \rho \pi 2 \beta V_0 R_0 h \end{aligned}$$

so that :

$$M_T - M_0 = \rho \pi 2 \beta V_0 R_0 h (t - t_0)$$

and the increases of the crown mass with time can be written as:

$$M_T/M_0 = 1 + 6 \delta \beta (\tau - \tau_0)$$

The total mass increases linearly with time at a rate which increases with the film thickness (as $\delta^{0.86}$) and decreases with drop velocity (as $V_0^{-0.72}$).

CONCLUSIONS

The time evolution of the cylindrical sheet of liquid produced by the drop impact on a wetted surface was measured by a laser obscuration technique, using a laser light sheet and a linear photodiode array.

The technique was validated by comparison with still camera images obtained by illuminating with a flash lamp at variable delay.

The investigation was extended to a wide range of experimental conditions in terms of Weber and Ohnesorge numbers and nondimensional film thickness, to allow a reliable comparison with the existing theoretical model of Yarin and Weiss (1995).

The measured crown evolution partially confirms the theoretical prediction: the product $R_c V_{cr}$ remains almost constant over a relatively large time interval, thus corroborating the square-root time law

The average value of $\beta = R_c V_{cr}/R_0 V_0$ evaluated over a time interval spanning from about 5 to 15 ms after drop impact was found to depend on We , Oh and δ and an empirical correlation was given.

ACKNOWLEDGEMENT

This work was performed at CNPM-CNR Laboratories. The authors would like to acknowledge Mr. T. Ferrari for the design and fabrication of the electronics used with the detector and Mr. G. Brunello for the assistance in the experimental work.

REFERENCES

- Coghe A., Cossali, G.E., Marengo, M. (1995) "A first study about Single Drop Impingement on thin liquid film in a low Laplace number range", *Proceeding PARTEC '95*, Nürnberg.
- Cossali G.E., Coghe A., Marengo M., "The impact of a single drop on a wetted solid surface" Submitted to: *Experiment in Fluids*.
- Diemunsch, G. and Prenel, J.P.: (1987) *Optics and Laser Technology*, vol.19, No.3, 141.

- Emmerson G.S., Snoek C.W. (1978): "The effect of pressure on the Leidenfrost point of discrete drops of water and Freon on a brass surface", Int. J. Heat & Mass Transfer, 21
- Engel O.G. (1967): "Initial pressure, Initial flow velocity and the time dependence of crater depth in fluid impact", J. of Appl. Phys., 38, 3935
- Hobbs P.V., Osheroff T. (1967): "Splashing of drops on shallow liquid", Science, 158, 1184
- Macklin W.C., Metaxas G.J. (1976): "Splashing of drops on liquid layers", J. of Appl. Phys., 47, 3963
- Mundo Chr., Sommerfeld M., Tropea C. (1995): "Droplet-Wall Collisions: Experimental Studies of the Deformation and Breakup Process", Int. J. Multiphase Flow, 21, 151
- Naber J.D., Farrel P.V. (1993) "Hydrodynamics of droplet impingement on a heated surface", SAE paper n. 930919
- Stow C.D., Hadfield M.G. (1981): "An experimental investigation of fluid flow resulting from the impact of a water drop with an unyielding dry surface", Proc.R.Soc.London, 373, 419
- Walzel P. (1980): "Zerteilgrenze beim Tropfenprall", Chem.-Ing.-Tech., 52, 338
- Witze, P.O.: (1985) Expts. in Fluids, 3, 174
- Worthington A.M., Cole R.S. (1896): "Impact with a Liquid Surface studied by the Aid of Instantaneous Photography", Proc. R. Soc. London, 137-148
- Yarin A.L., Weiss D.A. (1995): "Impact of drops on solid surfaces: self-similar capillary waves, and splashing as a new type of kinematic discontinuity", J.Fluid Mech., 283, 141

SESSION 26

Complex Flows I

PHASE-SHIFTED TWO-CAMERA DPIV FOR THE STUDY OF FLOW PAST ARTIFICIAL HEART VALVES

Ch. Brücker

Aerodynamic Institute, RWTH Aachen, Templergraben 55, 52062 Aachen, Germany

ABSTRACT

A video-based Digital-Particle-Image-Velocimetry (DPIV) system with a time-shifted two-camera video recording was build up for investigation of the unsteady flow structure in a pulsatile flow behind artificial heart valves. The time-shift is adjustable by the phase synchronization of the consumer video-cameras and allows a cheap and easy adaptation of video-based cross-correlation DPIV to high velocities like that in heart valve flows. A calibration procedure was done to match the image acquisition system with regard to translation and small rotation of both cameras. With a framing rate of 50 Hz and long time recording the flow development can be captured in detail as demonstrated by a sequence that shows the generation and swept down of starting vortices behind the leaflets for the Björk-Shiley-Monostrut (BSM) and Sorin-Bicarbon (SB) heart valves during the opening phase. Continuous recording with the video system over several hundreds of beating cycles also allows statistical investigation of cycle-resolved fluctuation and evaluation of shear stresses. In general, this system is well suitable for video-based DPIV at higher velocities where a pulsed and synchronized illumination is not available or difficult to implement.

1. INTRODUCTION

Qualitative visualization of biomedical flows using the recordings of particle traces has a long history, see Lighthill (1972), which has its origin in the first drawings of Leonardo da Vinci. The reason for particle imaging techniques being well suited in biomedical flow visualization is the illustrative fieldwise presentation of flow features in the often highly unsteady and three-dimensional flows. Streakline techniques are within these flow conditions and the often naturally complex geometry in many cases unsuccessful. One subject of special interest is the flow field past artificial heart valves because of the received knowledge of the link between the detailed flow dynamics and thrombosis, clot formation and eventually malfunction of the valve with dramatic consequences for the patient. Nowadays it is known that the

damage of blood depends on the local stress load (Wurzinger, 1988) while thromboembolism and clot formation are promoted by the interplay of stressed blood cells and stasis. The replacement of natural heart valves by artificial mechanical valves induces such critical flow conditions which mainly depends on the design of the valves. For optimisation and comparison of the available valves, full field measurements or numerical simulation of the time-dependent flow field are very necessary. These however are extremely difficult because of the highly unsteady and three-dimensional flow conditions in the human aortic region due to the complex geometry, the flow function, elastic walls, moving bodies (e.g. the valve occluder) etc. In view of the today still low spatial and temporal resolution of in-vivo measurement techniques like Magnetic resonance imaging (MRI), the only chance for measuring the flow field in detail is within in-vitro flow circuits where the valves are tested under near physiological conditions. In most of the quantitative in-vitro flow studies, classical pointwise techniques like hot wire anemometry or laser doppler velocimetry (LDV) were used which did not provide cycle-resolved full field velocity information (for a review, see Lim et al. 1994).

With the upcoming of computer assist image processing, Particle-Image-Velocimetry (PIV) became a well-suited non-invasive measuring technique that provides the instantaneous two-dimensional velocity field throughout a planwise illumination and offers the calculation of derived quantities as the vorticity or shear rate. First detailed velocity field measurements of the flow past artificial heart valves using PIV were carried out by Affeld et al. (1989) in a 10:1 upscaled model of a Björk-Shiley-Monostrut (BSM) valve and even enlarged model of the ventricle and aorta. The reason using an enlarged model was to get a deeper view into flow details and, in combination with water as the model-fluid, to enlarge the time-scales when fulfilling the similarity laws. Hence, they were able to study the flow development in detailed regions with conventional video-technique and frame-by-frame correlation. One major disadvantage, however is, that those studies are not well applicable for existing valves because the manufacturing of the enlarged models is both costly and very difficult. The more recent PIV studies of the flow in artificial

in naturally flow visualization. Here, the time-shifted two-camera DPIV-system is well applicable when high velocities are under investigation. Besides, the two-camera set-up is in operation very similar to the systems which are used for digital 3-D PTV with two or more synchronized video cameras. Thus, the equipment, if present, the procedure and algorithms for calibration of the camera system, which is important for getting accurate results, can be easily adapted to the present method or even the same set-up can be used.

2.2 Calibration of the image acquisition system

For precise and accurate results of DPIV-measurements with the time-shifted two-camera system, the positions of the image planes of both cameras have to be corrected for translation and slight rotation in relation to the object plane after carefully arranging the cameras for viewing the same field. The high resolution grey level cameras (Philips, VCM 3250/50) were of the same type and supplied with equal optical lens systems with an invariable focal length (this ensures the same magnification). For calibration, a precision grid, which consisted of 35×26 equally spaced nodes with a spacing of $h=1\text{mm}$, was recorded in the region of interest (this field represents also the mesh system on which the velocity field is evaluated by subimage correlation). The grid could be placed during channel operation from far downstream of the valve into the region of interest past the valves. The calibration was done before every run of the experiment. On both video image planes, the grid nodes positions were determined with subpixel accuracy by cross-correlating small subimages (16×16 pixels) with a synthetic „cross“-template. Then, we were able to formulate the image-to-object relation of both cameras with 2-D polynomial transformation equations of second order between the grid nodes position of the master and slave camera with respect to the original positions similar as done usually in stereoscopic 3-D PIV for calibration of the cameras, see (Brücker 1995). The coefficients can be obtained from a Means-Nelder minimization algorithm with least means square condition. To take into account the image transformation for accurate results of the velocity measurements, one possibility is to transform the slave and master image pixel by pixel using the transformation functions so that the images of both cameras match each other. However, the necessary application of pixel-interpolation reduces the accuracy of the correlation results twice because of addition of the pixel-interpolation-error in both images plus the error of both transformation functions itself. On the other hand, one can cross-correlate subregions of the calibration images containing the grid nodes (of which locations were estimated before) and subtract the resulting displacement field from the correlation results of the particle images later on. The translation and slight rotation of the images do not influence the accuracy of the correlation results significantly. A slight rotation can be tolerated because it has the only effect of decreasing the signal to noise ratio of the correlation. In comparison, this method has only one additional error source which is the accuracy with which the shift between the grid nodes can be obtained by the

correlation technique (assuming that the local grid displacement vector is considerably lower than the fluid displacement). In general, this is of order of the subpixel accuracy.

To check the accuracy of the time-shifted two-camera DPIV system, we recorded a rotating disc marked with randomly distributed particle pointers. Figure 2 shows the disc used and the calibration grid as recorded by the camera.

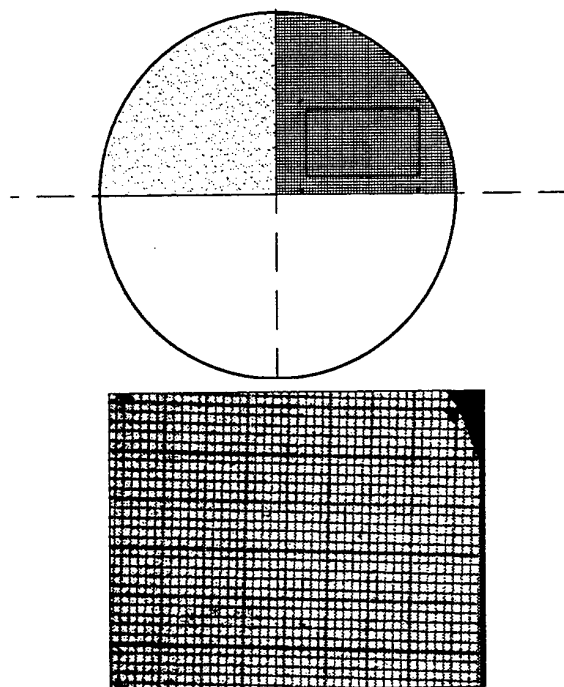


Figure 2: Sketch of the rotating disc with the particle markers and the recorded calibration grid.

The internal shutter of both cameras was adjusted to an exposure of $1/10000$ sec to avoid blurring of the particle images at maximum velocities of 10m/s in the experiment. One test was made at a rotation rate of $\approx 71/\text{s}$ where a minimum velocity of 1.42 m/s at $r=20\text{mm}$ and a maximum velocity of 3.55 m/s at $r=50\text{ mm}$ are expected, which are in the range of the maximum velocities in the heart valve flow studies (the time-shift was 0.3 ms). Then, the node positions of the recorded grid (therefore the disc was held stationary) were evaluated and, at these positions, the displacement field of the markers was obtained by cross-correlation when they came into the field of view during disc rotation. Figure 3 shows on the left the obtained displacement field of the recorded grid-nodes (the maximum displacement is of order of 4 pixel) to demonstrate the relation between both image-planes.

Overall, the displacement field shows both a slight mutual rotation and translation of the image planes. On the right side in figure 3, the unprocessed result of the rotating disc velocity field is shown. The rms-error of the measurements amounted to 4% in comparison to the actual velocity values at the grid

node positions. The maximum velocity is approximately 3.6 m/s.

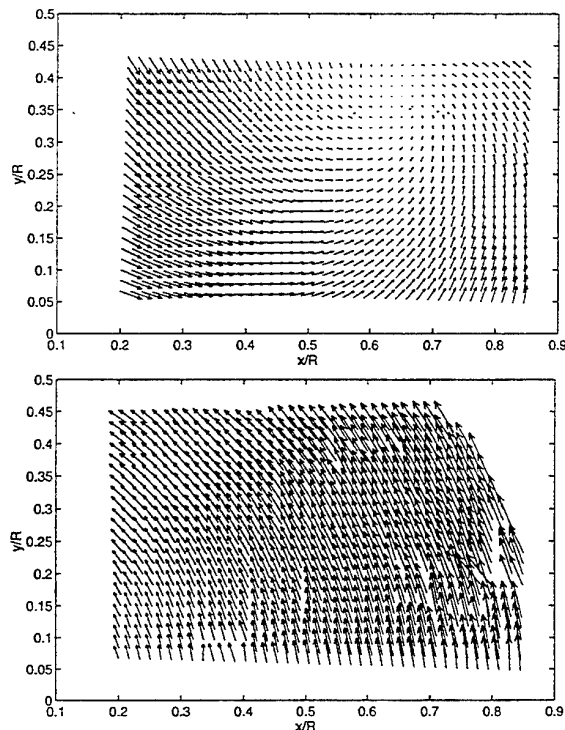


Figure 3: Top: Displacement field of grid nodes between master and slave image (maximum displacement is of order of 4 pixel); bottom: original results of measured rotating disc velocity field

3. EXPERIMENTAL METHOD

3.1 Artificial heart valve prostheses and pulsatile flow circuit

Figure 4 shows the two investigated mechanical heart valve prostheses, on the left a single-leaflet valve, the Björk-Shiley Monostrut (BSM), and on the right a bileaflet ones, the Sorin-Bicarbon (SB), both designed for an annulus diameter of 25 mm.

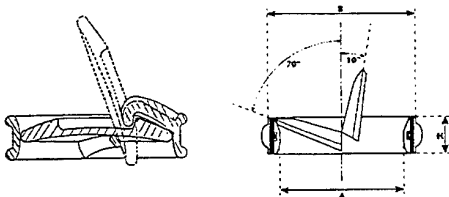


Figure 4: Schematic sketch of the tested mechanical prostheses in closed and opened condition; left: Björk-Shiley Monostrut valve (BSM, $d_A=25\text{mm}$); right: Sorin-Bicarbon (SB, $d_A=25\text{mm}$)

The occluder of the BSM valve has no bearings but is limited in its angular operation in the valve housing by two

struts which are fixed on the valve ring. The downstream strut acts as a hook which reaches in a circular mill-out of the occluder. In contrast, both occluder of the SB are fixed in the valve ring by a pin-like bearing. In a rough view, the shape of its occluder resembles that of a shovel. The mock circuit in which the heart valves were investigated is shown in Figure 5. The circuit consists of a rigid perspex model of the human aorta with a quick-valve-exchanger that contains the aortic valve prostheses. A windkessel is applied in the aorta to simulate the damping of the flow profile due to the elasticity of the natural aorta. Using the rigid model, a near-valve influence of the flexible walls is ignored which however has no important influence on the flow behaviour as shown by Bellhouse and Talbot (1969).

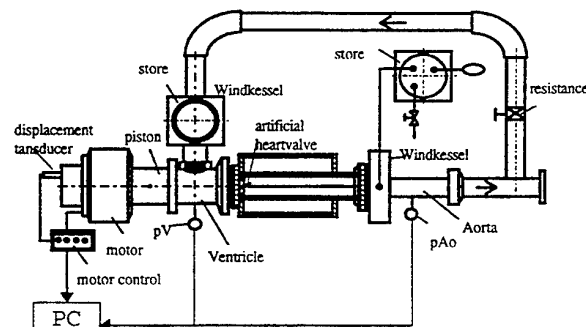


Figure 5: Pulsatile mock circuit for simulation of aortic flow function

The fluid returns via reflux tubing to the model ventricle which consists of an axisymmetric flow channel with a feedback controlled electromagnetic driven piston. A second valve is placed in the entrance of the ventricle to conduct the flow in one way. The arterial pressure is regulated by a resistance placed in the reflux tubing.

The test stand used does not lay claim to simulate exact comparable flow conditions as in the human aorta since the sinus bulbs (valsalva), the curvature of the aorta and the elasticity are not modelled. The main purpose of such a test stand however is, that it allows to test and compare different valves in terms of their hydrodynamic properties while having reproducible and even conditions (Köhler et al. 1990). To avoid widely gravitational influence on the occluder cinematic, the valves were carefully positioned with vertical pivot axes. Because of the complications using mammalian blood in experimental in-vitro studies, we used an aqueous glycerine-water solution (37% Glycerine) as working fluid with the same viscosity of blood but with a Newtonian behaviour. As also noted by Hirt et al. (1994) in their PIV study the non-Newtonian influence of human blood only becomes important if the vessel diameter is comparable to the blood cell size (which is not the case in the aortic flow).

The motion of the piston (50 mm in diameter), which caused the flow into the aorta, was controlled by a PC and a microcomputer-based AD-DA board. In the present study, physiological rest conditions with a heart beat frequency of

70/min and a stroke volume of 70ml were simulated. Figure 6 displays the measured profiles of aortic and ventricular pressure and the time derivative of the piston displacement representing the flow into the aorta for one cycle of duration $T = 850\text{ms}$. The wall pressure taps were located at the ventricle and three aortic diameter downstream of the valve in the model aorta. By adjusting the resistance and the air-volume in the windkessel, the endsystolic and enddiastolic pressure values could be adapted to the physiological values of ca. 120 mmHg and 80 mmHg for healthy conditions. Due to the modification of the set-up for DPIV-measurements and the need of leakage of the piston to avoid clotting of the particles in the sealing, the enddiastolic pressure could not exactly match 80 mmHg for every run of the experiment (depending on the heat-up of the fluid, process time of the set-up etc.). However, for the study of flow development past the valves, accurate physiological pressure values are of less importance unless the valve function is changed significantly.

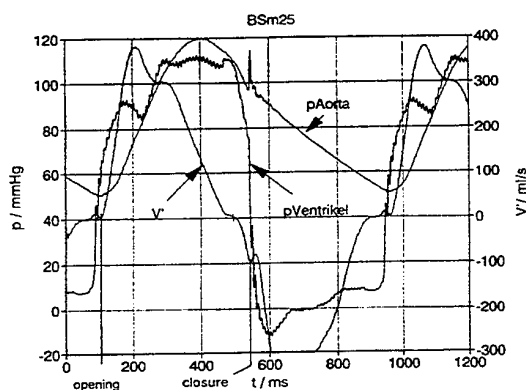


Figure 6. Profiles of aortic and ventricular pressure and flow function for a stroke cycle (the implanted valve was the BSM)

At $t \approx 100\text{ms}$ the intersection of the aortic and ventricular pressure profiles marks the start of the ejection phase. Valve closure happens at $t \approx 540\text{ms}$ characterized by the strong closure peak in the aortic pressure. The nearly identical profiles of the pressure in the 1st and 2nd cycle (the 2nd cycle initiates at $t \approx 950\text{ms}$) point out the good reproducibility of the cycles in this mock circuit.

3.2 DPIV procedure

For DPIV, the working fluid was seeded with particles with a mean diameter of $\varnothing = 50\mu\text{m}$ (Vestosint, Hüls GmbH, $\rho \approx 1.01\text{g/cm}^3$) in a concentration of 0.6g/liter. Before running the piston, the arranged camera system was calibrated. Therefore the grid, which was mounted on a rod, was placed directly downstream of the closed valve. Then the grid was removed to a position far downstream and the pulsating mock circuit was started. The flow was illuminated in the horizontal midplane of the aorta in a light-sheet of 1 mm thickness perpendicular to the pivot axis of the occluder of the valve.

Simultaneously to the flow recordings, measurements were carried out of the aortic and ventricular pressure values p_{Aorta} and p_v , the flow function and the corresponding time-signal and stored on a PC. This allowed the DPIV results to be correlated to the pressure signal and flow function. For the study of the BSM, we used a time-shift of the cameras of $\Delta t = 0.2\text{ms}$ and for the SB a time-shift of $\Delta t = 0.3\text{ms}$. Both cameras operated with a shutter speed of 1/4000 seconds. After the experiments, the video tapes were digitized (Frame grabber VFG 100, Imaging Technology Inc. Texas, 768x512 pixel) frame by frame using the time-code information on the audio track. The corresponding images from the master and slave video were cross-correlated in subregions at locations of the grid nodes on the image plane. The evaluated area has a size of $34 \times 25\text{ mm}^2$ with 35×26 node points with a spacing of 1 mm which equals approximately 16 pixel units. We used a 32×32 pixel correlation window size and a gaussian subpixel analysis for determination of the correlation peak position. With the maximum attainable displacement of approximately 12 pixel units (1/3 of the window size), the range of velocities which could be measured is between 0.06m/s up to $\approx 7.5\text{ m/s}$. A realistic estimate of the error of DPIV gives an accuracy of 0.1 pixel units (see Westerweel et al. 1993). The uncertainty of the measurements is however of order of 0.2 pixel units due to the twofold addition of errors of once the correlation and secondly the calibration of the two-camera system.

4. RESULTS

The profiles shown in Figure 6 belong to the flow cycle for which the DPIV results of the BSM are shown in the following. The start of the ejection phase and opening of the valve is approximately at $t \approx 100\text{ms}$. The velocity field past the BSM valve in the plane of symmetry during this cycle is shown in Figure 7 by means of the 2D vector field (overlaid with short sectional streamlines to show the flow structure) and isolines of the amount of vorticity (only the out-of-plane component of the complete vorticity vector and only regions of concentrated vorticity were displayed using an offset value*). The absolute maxima are given in the title of the graphs. The occluder is signed in the diagrams by the black filled region without taking into account the struts or extensions of the valve ring. The time interval between the adjacent velocity fields of 20ms is that of the difference between the video frames. One remarkable result of the velocity and vorticity field is to see the generation and swept down of a starting vortex at the trailing edge of the occluder, which could be obtained by the DPIV-system used. Similar qualitative observations were made using the hydrogen bubble technique in an 3:1 upscaled model, see Knoch et al. (1991).

* Due to the large change of volume flux in the opening cycle, a constant offset and increment of the isolines is not useful but it has to be adapted to each situation. Also, illustrating the flow structure is therefore not easy with use of velocity vectors why we also included the streamline patterns, which were overlaid on the vector plot

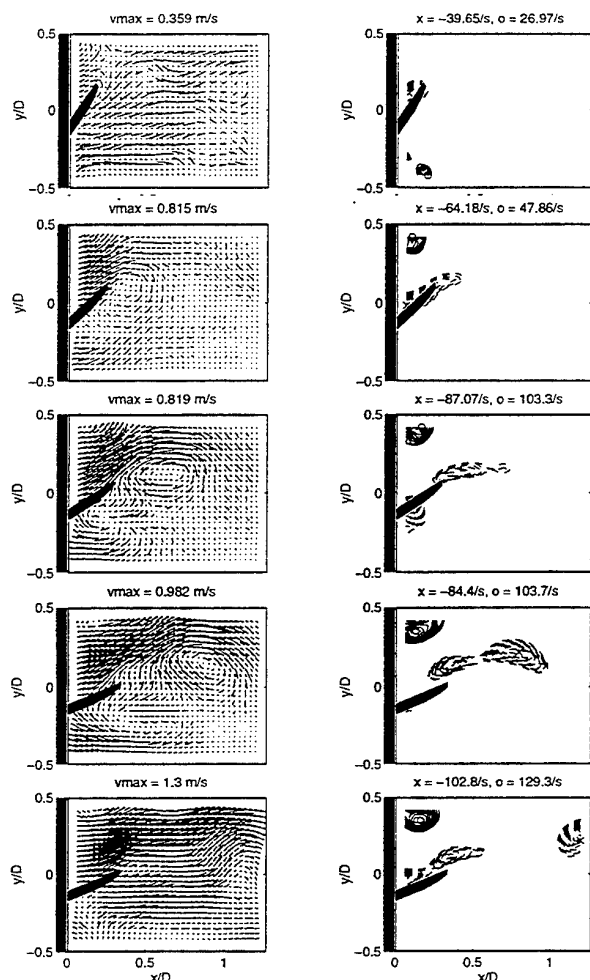


Figure 7: Sequence of the velocity field and regions of concentrated vorticity past the BSM valve during the opening phase ($\Delta t=20$ ms, left: sectional streamline pattern and in-plane velocity distribution; right: isolines of ω/ω_{\max} between 0.66 and 1 in ten steps for negative (--) and positive values (-))

While in the early phase of valve opening the fluid behind the occluder in the upper part moves with the opening occluder and around the sharp trailing edge within the aorta, the upstream moving leading edge of the occluder induces backflow into the ventricle. This region of backflow persists until the complete opening of the valve and is then washed down. For later moments (not shown here), one can see the large velocity defect in the wake behind the strut. Also it was found, that the flow in the phase of peak flow (peak systole) still is affected by the previous time-history of the flow in the opening phase. Hence, comparisons with studies in steady flow circuits even at the same Reynolds-number are questionable. Along the upper side of the occluder, an elongated region of concentrated vorticity and high shear rate has been build up. This is also the case in the wake of the valve ring, which is well seen in the upper left corner of the graphs. Because the flow in the lower half has not yet fully

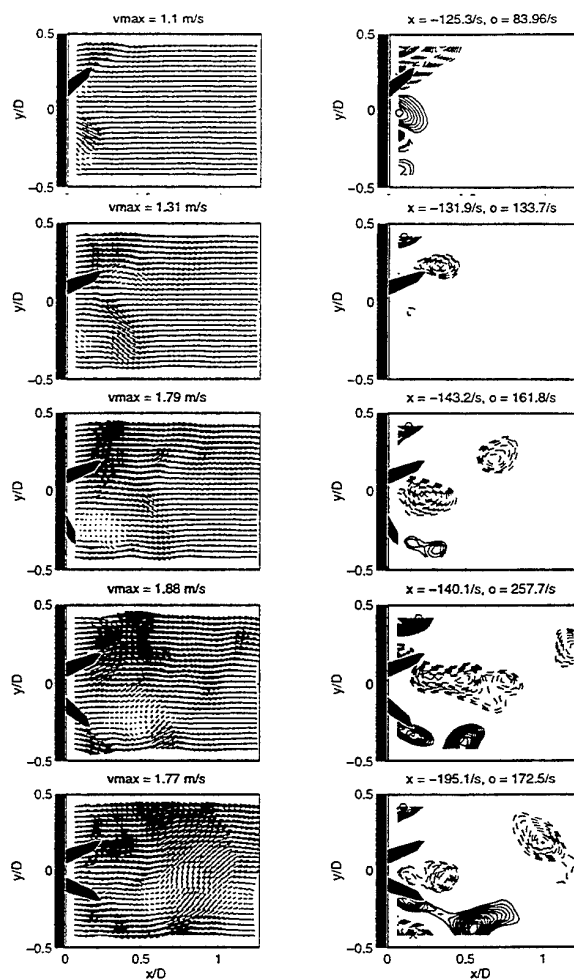


Figure 8: Sequence of the velocity field and regions of concentrated vorticity past the SB valve during the opening phase ($\Delta t=20$ ms, left: in-plane velocity distribution; right: isolines of ω/ω_{\max} between 0.5 and 1 in ten steps for negative (--) and positive values (-))

developed, these regions there are still of low vorticity.

In comparison to single-leaflet valves, the SB prosthesis with two occluder divides the flow in three jets. Flow visualization showed, that the freestream between both occluder is mostly separated on one side. Which side depends on the history of flow development in the opening phase as found in our results, see below. This also influences the cinematic behaviour of the occluder in the closing phase according to the observation, that the suction effect (Coanda effect) of the jet streaming along one of the occluder delays this from initiation of closing (see Brücker and Köhler 1994). Then, proportional to the delay between the closing of the occluder, the impact velocity of the latest one increases which may promote the tendency of cavitation (cavitation is a further one important influencing factor in hemolysis). Additionally, bileaflet valves have a higher tendency for occluder sticking which was observed both in in-vitro pulsatile tests and also in implanted situation (Köhler and Wirtz 1991). When sticking

occurs, the flow situation is much more complex and significant increase of the maximum shear rate (and hence a higher blood damage rate) and larger stagnant regions can be expected. One example of the flow development past the SB valve with a partly sticking occluder is shown in figure 8 (note, that this only represents one cycle). The sticking happened several times spontaneously with no preferring of one of the occluder and therefore we could exclude mechanical influence of our valve housing which was carefully designed to avoid any deformation of the ring. Here, the long-term recording property of consumer video enabled to capture such a spontaneous situation, see figure 8. Again, the occluder are signed by a blackfilled region in the graphs. One can see the different opening behaviour. Note, that the lower occluder remains not sticking inside the valve ring but is ejected rapidly when the other occluder already has reached its maximum angle position. In the beginning of the valve opening, the flow field again shows the swept down of a starting vortex which is generated at the trailing edge of the upper occluder. In the region near the axial centerline, the fluid enters the aorta oblique to the bottom (in the graph) through the gap between the open and still closed occluder. Behind the closed one, a large separation region with high vorticity has developed, which is being swept down when the sticking occluder starts moving. Also at the trailing edge of the late opening occluder a starting vortex can be observed. Similar to the BSM results, the wake region of the valve ring is during valve opening a permanent region of high vorticity (and shear rate) combined with stagnant behaviour at the lateral flow boundaries.

5. CONCLUSION

The present study showed the well applicability of PIV to quantitative flow studies of the flow past artificial heart valves within in-vitro tests. Using a time-shifted two-camera video system, we were able to capture once the high dynamic range of the pulsating heart valve flow by the enabled application of cross-correlation methods and also to gain high velocities in the flow region up to 10m/s over sufficient large areas with conventional video-technique. The maximum velocity in this study is only because of the use of a continuous light source instead of a synchronized pulsed laser, however for the profit of a cheap and easy implementation. The property of multi-frame and long-term recording of video-technique allowed to study the development of the velocity field when individual or stochastic flow phenomena occurred in the flow past the heart valve prostheses which has not been able before. Future studies will concentrate on the comparison of the flow dynamics and occluder cinematic past different available valve prostheses in the aortic and the mitral position as well.

6. REFERENCES

- Affeld, K., Walker, P.; Schichl, K. 1989, The use of image processing in the investigation of artificial heart valve flow, Trans. Am. Soc. Artif. Intern. Organs, XXXV, pp. 294-298
- Brücker, Ch. & Köhler, J. 1994, In vitro-study of occluder cinematics of the SJM aortic heart valve prostheses in pulsatile flow, in Proc. 3rd Int. Symp. Biofluid Mechanics, ed. D. Liepsch, pp. 295-306, Springer Verlag, New York, Berlin
- Brücker, Ch. & Köhler, J. 1995, Velocity field measurements of unsteady flow downstream of artificial heart valves using Digital-Particle-Image-Velocimetry (DPIV), Int. Journal of Artificial Organs 18 (8), pp. 441
- Brücker, Ch. 1995, 3-D PIV using a scanning light-sheet and stereoscopy: Study of flow development around a spherical cap, FED-Vol. 229, Laser Anemometry ASME, pp. 497-503
- Dabiri, D. & Gharib, M. 1991, Digital Particle Image Thermometry: The method and implementation, Exp. Fluids 11, pp. 77-96
- Hind, A. K. & Christy, J. R. E. 1993, Digital PIV applied to flows around artificial heart valves: analysis by autocorrelation, in Flow Visualization and Image Analysis, ed. F.T.M. Nieuwstadt, pp. 259-271, Kluwer Academic Publ.
- Hirt, F., Jud, E., Zhang, Z. 1994, Investigation of the local flow topology in the vicinity of a prosthetic heart valve using Particle-Image-Velocimetry, Proc. 7th Int. Symp. Appl. Laser Tech., Lisbon, pp. 37.3.1 - 37.3.7
- Köhler, J., Küpper, H., Wirtz, R. 1990, In-vitro simulation of cardiovascular flow, Proc. 7th Meeting Europ. Soc. Biomech., July 8-11, Aarhus, Denmark
- Köhler, J. & Wirtz, R. 1991, Cinematics and sticking of heart valves in pulsatile flow test, Int. Journal Artificial Organs 14, no. 5, pp. 290-294
- Knoch, M., Reul, H., Rau, G. 1989, Model studies at mechanical aortic heart valve prostheses in steady and physiological pulsatile flow, in Proc. 2nd Int. Symp. Biofluid Mechanics, ed. D. Liepsch, pp. 75-89, Springer Verlag, New York, Berlin
- Lecordier, B., Mouqallid, M., Vottier, S., Rouland, E., Allano D, Trinite, M. 1994, CCD recording method for cross-correlation PIV development in unstationary high speed flow, Exp. Fluids 17, pp. 205-208
- Lighthill, J. 1972, Physiological fluid mechanics, Springer-Verlag, New York, Berlin
- Lim, W. L., Chev, Y. T., Chew, T. C., Low, H. T. 1994, Particle-Image-Velocimetry in the investigation of flow past artificial heart valves, Ann. Biomed. Eng. 22, pp. 307-318
- Wurzinger, L. J. 1988, Thrombogenese und Hämodynamik, Hämostasiologie 8, pp. 173-182

LDV MEASUREMENT IN A FULL SCALE PASSENGER-CAR-CABIN

P. Castellini, M. Gasparetti, N. Paone

Dip. di Meccanica, Univ. degli Studi di Ancona
Via Brecce Bianche, 60131 Ancona - Italy

ABSTRACT

The paper describes the development of a test bench in which the LDA measurement of the air velocity inside the cabin of a full size passenger car is carried on. Measurements are performed in case of forced convection, with the purpose of assessment of passenger climatic comfort in vehicles. Preliminary experiments have been performed on a 1:2 scale model of car cabin in order to define the measurement procedure.

1. INTRODUCTION

The knowledge of the flow field inside the cabin of a car (Klemp et al., 1991) cannot be disregarded in order to improve the climatic comfort of the passengers, important especially for the performance of the driver and therefore for safety. The thermic sensation is in fact mostly due to four contributions:

- temperature,
- humidity,
- air velocity,
- local turbulence,

with the last two quantities mainly involved in the heat exchange of the human body.

A precise settlement of the fluid flow properties in a passenger car cabin is also necessary to validate numerical codes, to optimise the position of the inlet and outlet air openings, to improve the functionality of air conditioning systems, to evaluate fundamental parameters of qualitative standards like the equivalent temperature (Olesen, 1993), to better understand the modalities of the heat exchange between the cabin and the outside.

This work addresses the problem by way of an experimental investigation of the internal fluid flow made by a non intrusive velocity measurement system. The paper reports briefly the tests on a 1:2 scale model of car cabin and then focuses on the measurements on the real full size passenger car. All the described experimental results are obtained in steady state conditions. Attention is put on the measurement procedure.

2. EXPERIMENTAL SET-UP AND MEASUREMENT METHODOLOGY

The experimental study consists in two sequential phases.

Preliminary experiments have been performed on a 1:2 scale model of the cabin of a passenger car in order to define the measurement rig and the seeding of the flow. This model, made in wood, presents several perspex windows to allow the optical access for the laser measurements. All internal components, as front and rear seats and other normal equipment, are in 1:2 scale. In the model a dashboard is mounted with a heating and ventilation system of a real car, which have undergone a series of interventions to allow the respect of the scale factor for these components too.

In the final experiments it has been used an Alfa Romeo 164 Super, a medium class vehicle. The car body is without the engine but with the luggage-van, concerned in the fluid-dynamic field. The car shape is modified for optical access, but with attention to reduce any modification to the internal volume. Main modifications are the substitution of the four doors with transparent slabs made in perspex and the cutting of the roof and its substitution with a transparent one. The car therefore offers optical access from all sides; the front wind-screen and the rear-window, all four lateral doors and moreover from the top of the roof. The internal geometry is not modified significantly; inside the car all the seats and the normal equipment are left unmodified. Figure 1 shows one of the transparent surfaces, in a door of the car body, used as optical access.

Each transparent slab has a thickness of 3 mm, and is made in perspex. Slab curvature is always negligible, so that no lens effect appears evident and no distortion of LDV probe volume is present.

For the control of the behaviour of the experimental system and of the external conditions some sensors are installed on the model and, then, on the real car. In fact when the velocity magnitude of the air is very low, as in condition of natural convection but also, as in this case, in condition of forced convection, small changes in external conditions can have large effects on velocity distribution inside the cabin or his model. In particular the temperature of the inlet air and the speed of the propeller in the ventilation system are monitored. Air humidity and pressure, which have a slow variation, are not checked during the test.

In both cases of model and real car the measurement system is based on a 2-D fiber optic Dantec laser Doppler velocimeter. This is composed by a 4W ion-Argon laser, a fiber optic device for remote measurement and two Burst Spectrum Analysers, a positioning system automatically controlled.

The main problems related to measurements in the flow inside the car are related to the very low velocities, the presence of large recirculating regions and of extremely

varied time scales of vortical motions, the very large scale of the flow field (more than 2 m from front to rear window and the same order of magnitude in width and height).

For the first problem the choice of seeding particles must satisfy the requirement of long settling time and long survival time. Tests have been performed with several aerosols; they are injected outside the car body close to the air suction and then transferred inside the car body by the air ventilation system, through a small fan and a series of tubings and valves. Particles therefore enter the car body from the air inlet openings located in the front of the car.

The seeding of the inlet air is obtained by an atomiser, operating with a solution of water with 5% of sugar, so that the particles can survive longer. The presence, in the inlet duct, of a centrifugal fan, determines a selection of only the smallest droplets and allows to have a quite uniform dimension of the obtained particles of about 1 mm. The velocity conditions force to acquire data for very long time in order to have statistically meaningful results; this causes problems of long time requirement to perform the experiment and a large amount of data is needed. Major issue in the measurement procedure is the setting of the data rate and of the length of the time window over which data are collected. In fact, in order to measure velocities in regions of slowly moving vortices, it is necessary a very long time to acquire statistically meaningful data, because data acquisition must be one order of magnitude longer than typical time scale.

For the measurement of the flow velocity, focal lengths of 600 mm, for the symmetry planes of the driver and of the front passenger, and of 1200 mm, for the symmetry plane of the car, allow to reach all the points of the cabin. The ensuing probe volume dimensions are respectively 0.146x2.37 mm and 0.292x9.56 mm.

The large examined volume imposes some problems in the choice of the spatial resolution: in fact to allow the analysis of small scale eddies a fine grid of measured points is requested. In this case the total time necessary for the measurement in the whole cabin may be very long. To reduce the amount of time for the whole analysed field is necessary to use a different time in each zone, where the fluid-dynamic behaviour is constant.

The appropriate acquisition time for any point and the spatial resolution have been set locally according to the following procedure. The car body is divided in different regions, which prove to have different kind of flow after a visualisation (smoke and laser light sheets). In the central point of each region is calculated the mean velocity v_f after a 1000 seconds long acquisition with an average data rate of 0.1 kHz. The mean velocity is evaluated again after different observation time windows, that is as a function of the acquisition time:

$$v_m(t) = \frac{1}{t - t_0} \int_{t_0}^t v(\tau) d\tau$$

In figure 2 the mean velocity, computed with an increasing number of instantaneous data point, is plotted versus time; initially it appears fluctuating, then the oscillations dump out and the average value converges to a single and stable number. The time after which v_m differs less than 5 % from the final value v_f is recorded and all data acquisitions in that region are performed for a time 30% longer than that, so that confidence in statistics is reasonably good.

The data rate has been set according to the need to acquire a number of data not too large to cause memory problems in the PC used for data acquisition; generally about 50000 data per point are acquired.

Table 1 shows the acquisition time in different zones of the cabin. It should be observed that times larger than 800 s per point are sometime necessary, and that times of about 500 s per point are usual. For grid having more than 100 points, total measurement time is therefore very long. This causes several problems, the most serious being that of stationarity of the flow for so long time, which is difficult to control, as well as thermal stability. To this purpose during all measurements temperature and inlet flow rate are monitored, and measurements at a fixed location are repeated, to monitor eventual long term unsteadiness of the phenomena.

Another solution to reduce the acquisition time to a value compatible with industrial requirements is the use of a not regular grid, due to the differences in geometry of the regions and to the dimensions of the vortical structures expected after the flow visualisation. In fact where the structure of the eddies is large it is possible to save time with a coarse grid; where the vortex dimension is small, the grid must be finer.

In this last zone the time consumption is anyway reduced because this local velocity distribution allows a sufficiently fast convergence of mean value, and then a short acquisition time.

3. RESULTS AND DISCUSSION

The experimental study is in progress and, at the moment, measurements have been taken over three longitudinal planes and one transversal plane in the model and over one longitudinal plane inside the real car cabin. The planes are chosen to observe the structure of the flow field in correspondence to the sections of the air inlets, of the driver seat and of the front passenger seat. To better understand the characteristics of the fluid flow between the front and the rear seats, also the velocity over a transversal plane in that region has been investigated in the cabin model.

In each point of the grids the two velocity components lying in the analysed planes are measured and mean velocities and rms fluctuations are calculated. The third component can be monitored through the transparent car roof.

In all the cases the air has been introduced only by the central ventilation openings in the dashboard. The fluid flow gets out from the cabin through holes in the rear-board: in the real car they lead to the luggage-van. The air openings have been positioned to direct horizontally the entering flow. The maximum velocity of the air supplied by the inlet openings was about 1.5 m/s.

In figure 3 the flow fields in the symmetry plane of the driver are described. A 3d view in the case of the real car is shown in figure 4. The resulting turbulence level, not reported here, reaches values up to 1000 %, mainly owing to the very low velocities that can be found in certain points of the field, while falls below 50% in the regions where the flow is better directed.

In the cabin the fluid stream coming from the inlet apertures, passes between the seats, arrives to the rear part of

the car and, after it has been diverted by the rear-window, comes back towards the front mostly through the side and the upper parts of the cabin. This back flow, meeting with obstacles constituted by the seats, produces big eddies that concern the areas occupied by the passengers. The differences between the flow fields in the simulated and in the real cabin are due to the different internal geometries, which in the model is rather far from the reality because of the requirements for a comparison with the results computed by a numerical code. It is remarkable that in the real car, above the driver seat, a stream from the rear to the front with velocity not too low is generated, even if this situation may change in the presence of the passengers, condition that could be reproduced by some manikins.

ACKNOWLEDGEMENTS

The authors would like to acknowledge Ing. Roberto Marconi, Centro Ricerche FIAT and Alfa Romeo R&D, for information and availability of the used test car.

REFERENCES

Klemp K., Herwig H., Kiel R. and Wickern G. 1991 LDA Measurements in a model of a passenger-car-cabin, Dantec Information n. 10, pp. 2-4.

Olesen W. 1993 Standards for Design and Evaluation of the Indoor Thermal Environment, *ASHRAE Journal*, n. 8, pp. 20-25.



Figure 1. One of the transparent surfaces used as optical access.

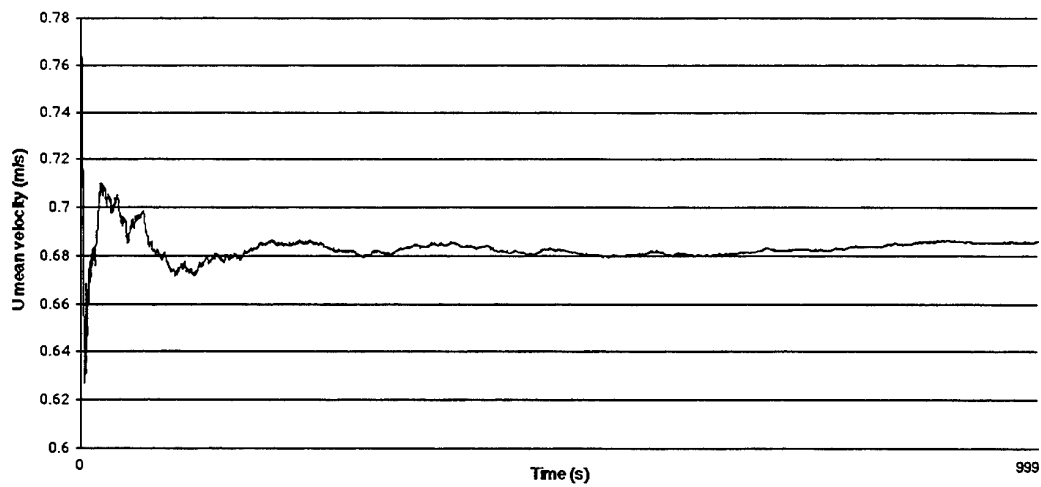
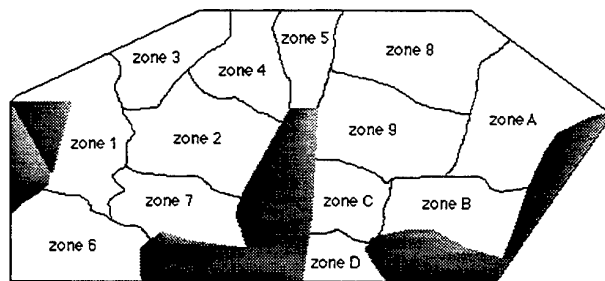
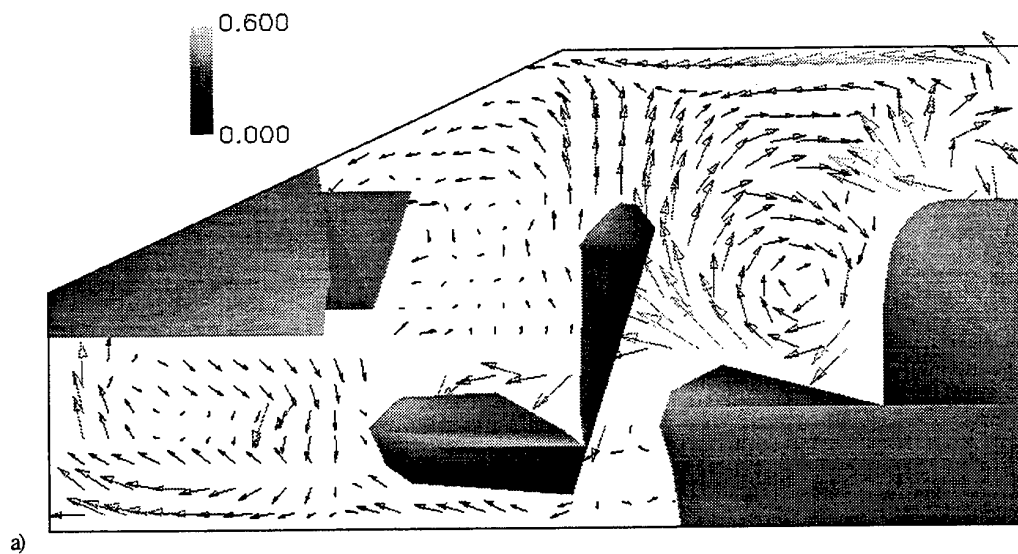


Figure 2. One of the graphs used to determine the time of acquisition.

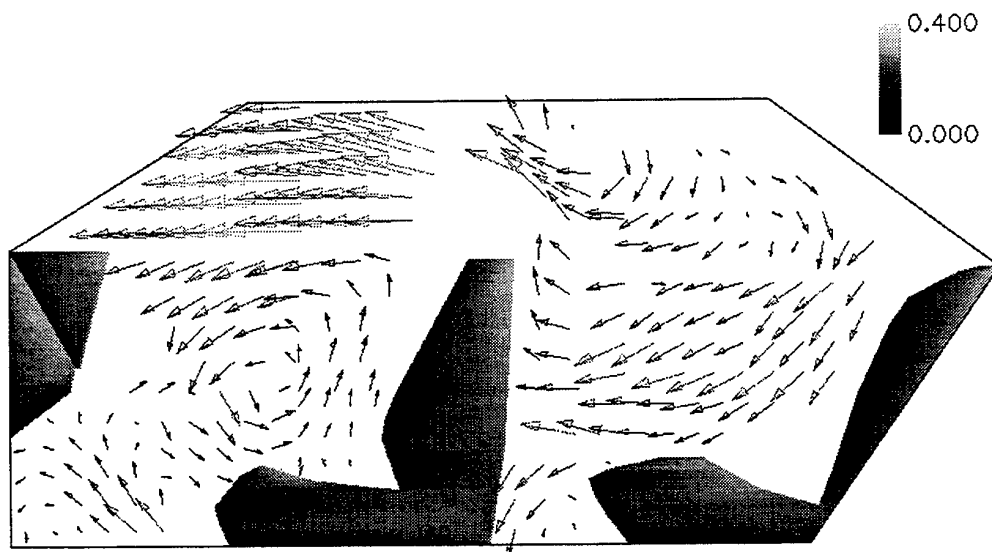


Zone and velocity component	Mean velocity (m/s)	Δv 5% (m/s)	Time (s)
1 u	-0.21817	0.011	120
1 v	-0.05363	0.0027	390
2 u	-0.03938	0.0020	700
2 v	0.0814	0.0041	600
3 u	-0.24375	0.012	145
3 v	-0.02443	0.0012	420
4 u	-0.2915	0.0146	40
4 v	0.024133	0.0012	800
5 u	-0.302	0.015	40
5 v	0.107	0.0054	340
6 u	-0.05982	0.003	700
6 v	0.06349	0.0032	600
7 u	0.0237	0.0012	850
7 v	0.0527	0.0026	800
8 u	-0.00811	0.0004	800
8 v	-0.1818	0.0091	180
9 u	-0.1315	0.0066	320
9 v	0.0778	0.0039	600
A u	-0.02	0.001	650
A v	-0.215	0.011	230
B u	-0.1138	0.0057	570
B v	-0.248	0.012	320
C u	-0.138	0.007	250
C v	0.0625	0.0031	500
D u	-0.0415	0.0021	450
D v	-0.118	0.006	420

Table 1. Velocity and acquisition time in different zones of the cabin.



a)



b)

Figure 3. Velocity field (m/s) in the symmetry plane of the driver : a) 1:2 scale model; b) real car.

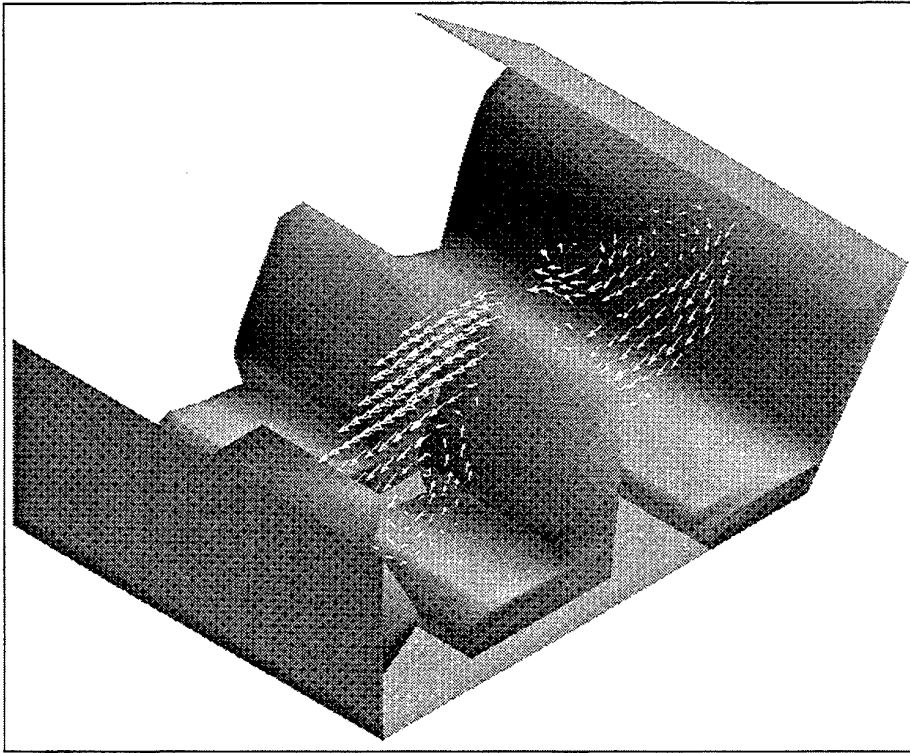


Figure 4. 3d view of the measured flow field in the car cabin.

A COMPARISON BETWEEN LDA MEASUREMENTS AND NUMERICAL SIMULATIONS FOR A FLOW IN A TRIDIMENSIONAL CAVITY.

E. Ovalle, A. Barrientos

Departamento de Ingenieria Metalúrgica,
Universidad de Concepción, Casilla 53-C, Correo 3, Concepción, Chile
Fax number: +56-41-243418, +56-41-230759
E-Mail: eovalle@buho.dpi.udec.cl
abarrie@euler.met.udec.cl

ABSTRACT

The internal flow in a built perspex model of a tridimensional cavity ($20 \times 10 \times 15 \text{ cm}^3$) is experimentally studied with the aim of doing a comparison between experimental and numerical simulation.

The modeling work involves predicting velocities and turbulent intensities. The model equations are: the continuity equation for the mean flow, the three-dimensional Reynolds equations of motion for the mean flow, and the closure equations relating the fluctuations with the mean flow.

The better agreement between measurements and calculations for velocity field was obtained utilizing the second order closure model DSM (Differential Stress Model) for turbulence. Good agreements were also obtained between numerical calculations and the experimental determination of turbulent kinetic energy.

1. INTRODUCTION

Sedimentation is a basic and widely used process in both water and waste-water treatment. Despite the importance and longevity of this process, sedimentation tanks or sedimentation basins display poor performance as a result of basic design problems.

On the other hand, it is a very known fact that a subject of great importance in mineral processing is the classification operation of particulate mineral in water, by size and/or density, for obtaining an appropriate product for the following operations, in a conventional plant of metallurgical processes. One of these devices are the so-called transversal flux classifiers, similar than sedimentation basins or sedimentation tanks. They use the gravitational sedimentation as the mechanism for classification. One of the aims of this work is to provide an experimental support for the validation of the numerical modeling of this phenomenon.

In literature, the modeling of these devices is restricted to one-dimensional models, such as Hazen (1904) and Concha and Almendra (1978); both of them assume that the particles follow the fluid in the horizontal direction and they have the terminal velocity in vertical direction, and the flow is laminar. However, Camp (1946) and Schubert and Neesse (1973) assume, based on experimentation, that the flow in the tanks is turbulent, so that the turbulent dispersion plays a decisive role in the separation efficiency and the capacity of treatment. Schubert and Neesse (1973) show that the critical Reynolds number (laminar-turbulent transition) is about 10^3 ; for industrial basins the Reynolds number is about 10^4 , so that we have turbulent flow in applications.

In general, the industrial sedimentation tanks often display poor performance as a result of basic design problems, such as the flow distribution, inadequate dissipation of inlet energy, and creation of short-circuiting within the basin.

In spite of its importance, no detailed models (tridimensional) were found in literature. The optimization of the design of sedimentation basins has only approaches on the experimental, Kawamura (1981). The present work appears as a first approach for obtaining a very complete picture of the flow inside a sedimentation tank, giving lines for tackling the important problem of theoretical optimization of these type of equipment.

2. EXPERIMENTAL

2.1 Test facility

The experiments were performed in a perspex model of a tridimensional cavity ($20 \times 10 \times 15 \text{ cm}^3$) (Fig. 1) Measurements were made through a lateral face, in 4 vertical planes parallel to the direction of flow in transversal coordinates $y=5, 25, 45$ and 65 mm . ($y=0.03, 0.16, 0.30$ and 0.43 in normalized coordinates). In each plane, 19×10 points were measured and 500 to 1000

samples were obtained. Frequency shift was used for all measurements in order to avoid directional bias.

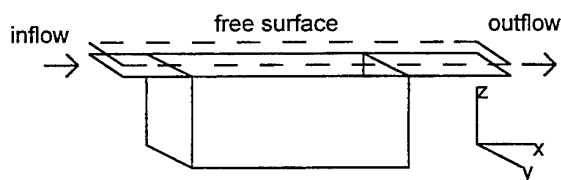


Figure 1. General view of the cavity flow

The fluid feed at the inlet was made through several obstacles to produce a flow with a reasonably uniform mean velocity. A screen was placed also at the beginning of the inflow region. The maximum of stream wise velocity in the free surface was about 0.2 m/s.

Due to the flow was slow, was necessary to use latex particles as seeding particles.

2.2 Measurement techniques

The velocity profiles were measured with a DANTEC laser Doppler two component of 300 mW of power; see Figure 2 showing the experimental rig. The coherent light was an Argon laser of Ion Laser Technology, model 5500A with 750 mW of maximum power.

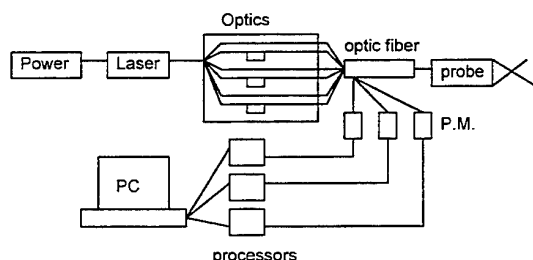


Figure 2. The processing system.

The measurements in the perspex model were made with a 55X optical mode and using two colors light (514.5 nm. and 488 nm.), using a shifter for a beam of each component. The four beams were directed into the probe of lens of 60 mm. and 160 mm. of focal length. The measurements were made in continuous mode and using a back scattering configuration. The measurement volume of the system was about of 0.64 mm. of length.

For the positioning of the probe, was used a traverse system with a range of 540x540x540 mm., and a repeatability of 40 μm. The traverse system was controlled by a Personal Computer.

The Doppler signals were processed in two Burst Spectrum Analyzers (BSA), 57N20 for the green component and 57N35 model S for the blue.

All the operations, as collection of data, movement of the traverse, process and presentation of the data was made using the BurstWare 2.0 software.

This work was performed in the laboratories of the Department of Metallurgical Engineering of University of Concepción (Chile).

3. MATHEMATICAL MODELING

We consider the isothermal motion of water in a sedimentation tank. The flow is assumed to be steady in the mean and incompressible. So, the Reynolds motion equations govern the mean flow:

$$\text{div} \bar{\mathbf{v}} = 0 \quad (3.1)$$

$$(\nabla \bar{\mathbf{v}}) \bar{\mathbf{v}} = -\frac{1}{\rho_0} \nabla \bar{p} + \nu \Delta \bar{\mathbf{v}} + \frac{1}{\rho_0} \text{div} \mathbf{T}^{(t)} + \hat{\mathbf{F}}$$

where $\bar{\mathbf{v}}$ is the mean velocity field, \bar{p} is the mean pressure field, $\mathbf{T}^{(t)} = -\rho_0 \overline{\mathbf{v}' \mathbf{v}'}$ is the Reynolds or Turbulent Stress tensor, \mathbf{v}' is the fluctuation velocity field, $\hat{\mathbf{F}}$ the specific field force, ρ_0 the constant density of the fluid, ν the kinematic viscosity of the fluid, and ∇ , div and Δ are the gradient, divergence and Laplacian operators.

The mathematical model is closed using the DSM (Differential Stress Model) for the transport of the Reynolds Stresses; see Deissler (1984) or Launder (1989).

The boundary conditions were: a mass boundary condition in the cross section in the feed (0.112 Kg/s); a gauge pressure boundary condition at the outlet (0 Pa.) and a free boundary condition at the free surface. At the solid boundaries a non-slip condition was used

4. RESULTS

The solution of the equations of the model was approximated using the commercial Flow-d package from AEA Technology Company, which uses the finite volume technique; see Patankar (1980).

The computing domain was discretized in 30300 elements in total, where 27600 correspond to the cavity properly and the others to the inflow and outflow sections. The final residuals for mass were about 10^{-8} to 10^{-5} .

A typical stream wise velocity in the bulk of the cavity was 0.05 m/s, producing a Reynolds number between 10^3 and 10^4 . In this conditions the flow was turbulent. Although in regions of low velocity the experimental data contains noise, it is possible to observe that, in general, the agreement between measurements and calculations was good. This good agreement was only possible when we used the DSM model.

Horizontal and vertical experimental and simulated velocity profiles, at seven different positions, are illustrated in Figure 3. It is observed that the computations predict the general tendency.

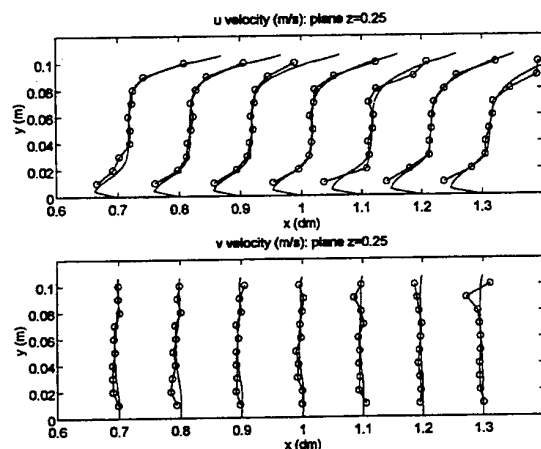


Figure 3. Measured and predicted stream wise or horizontal velocity (u) and cross or vertical velocity (v) for a central section of the cavity (second plane from the wall)

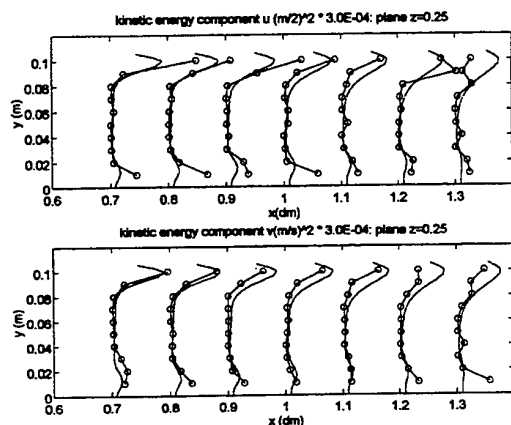


Figure 4. Measured and predicted stream wise or horizontal and cross or vertical turbulent kinetic energy for a central section of the cavity (second plane from the wall)

For a comparison of the predicted and experimental turbulent kinetic energy in the cavity, were compared the

component of turbulent kinetic energy of the u component $(1/2)(u'_{rms})^2$ with a third of the turbulent kinetic energy obtained by computation. The same was made with vertical component v. Experimental and simulated kinetic energy, at seven different positions, are illustrated in Figure 4. It is also observed that the computations predict the general tendency.

5. CONCLUSIONS

A first step to the tridimensional modeling of sedimentation tanks is presented.

The overall agreement between computed and experimental results was found to be reasonable. Considering the complexity of the flow, the results were encouraging.

It is hoped that the procedure described in the present work should prove useful in evaluating performance as well as design modifications of sedimentation basins.

ACKNOWLEDGMENTS

This work was partially supported by Fondef Project MI-08 and University of Concepción IIT Project O.T. 94-259-1.

REFERENCES

1. Camp T.R., 1946, *Sedimentation and the design of settling tanks*, Trans ASCE, 895-958.
2. Concha F. and Almendra E.R., 1978, *Modeling of Cross-Flow Classifiers, Part 1, A study of the Hazen Model of Settling Tanks*, Internal Report; Metallurgical and Material Engineering Department COPPE, Universidade Federal do Rio de Janeiro, Brasil.
3. Hazen A., 1904, *On Sedimentation*, Transactions of American Society of Civil Engineers, Paper N°980, 45-88.
4. Kawamura S., 1981, *Hydraulic scale-model simulation of the sedimentation process*, Journal of the American Water Works Association, 372-379.
5. Schubert H. and Neesse T., 1973, *The role of turbulence in wet classification*, IMPC, London, paper 29
6. Deissler R.G., 1984, *Turbulent Solutions of the Equations of Fluid Motion*, Reviews of Modern Physics 56, N°2, Part 1, 223-254.

7. Launder B.E., 1989, *Second-Moment Closure: Present ... and Future?*, Int.J.Heat and Fluid Flow 10, N°4, 282-300.

8. Patankar S.V., 1980, *Numerical Heat Transfer and Fluid Flow*. Series in Computational Methods in Mechanics and Thermal Sciences. W.J.Minkowycz and E.M. Sparrow, editors. Mc Graw-Hill, London.

EXPERIMENTAL STUDIES OF LIQUID-SOLID FLOW THROUGH A PIPE EXPANSION WITH A CENTER BODY

J.C.F. Pereira, Chr. Mundo* and J. Raposo

Instituto Superior Técnico
Mech. Eng. Dept./LASEF
Av. Rovisco Pais, Lisbon Portugal

ABSTRACT

Measurements of particle mean and rms velocity were obtained by PDA in the descending water flow with 0.13% volumetric diluted concentration of 81.2 μm mean diameter spherical glass particles $\rho_p/\rho_w=2.9$, the flow enters a sudden pipe expansion of 1:5 and impinges on a cylindrical body hemispherical head. Firstly the flow at $Re \approx 0.0$ is considered by closing the water circuit allowing only particles to fall by gravity into the stagnant water in the test section. The results show that the nonlinear two-way coupling process between the ambient turbulent field originated by the particles, and the particles themselves, triggers an instability on the "particle organised wakes", similar to a free jet instability. Secondly, the two-phase flow impinging on a center body at $Re=4 \times 10^4$ is investigated. For this case detailed characteristics of the particulated phase are reported, from the inlet pipe expansion to the gap between the pipe and center body.

INTRODUCTION

Particle laden flows are of general engineering interest and advances in our understanding of these flows are limited by the inherent difficulties of the non linear coupling between the particles motion and the turbulence, see e.g. Al-Taweel and Landau (1977), Shuen et al (1985) and Gore and Crowe (1989). Many experimental studies using LDA/PDA extensions to particulate flows, see Durst (1982), and numerical direct simulation of homogeneous flows, see e.g. Stock (1996), have been performed to investigate turbulence modulation by the particles and also changes in the energy spectra. Among other coupled effects, the dissipation of turbulent kinetic energy from an eddy to accelerate a particle, yields turbulence reduction, but turbulence intensity may also increase, see e.g. Lee and Durst (1982) and Tsuji et al (1984), by shedding of vortices or the

presence of wakes behind the particles, that are dependent on a critical particle Reynolds number. More precisely, a particle size/turbulence scale ratio, should be used, see e.g. Gore and Crowe (1989), Yarin and Hetsroni (1994) and Sato and Hishida (1995), to be able to distinguish the increase of dissipation due to the presence of particles and their counteraction by disturbances due to growing particle wakes which supplements turbulence generation, particularly when the relative velocities of the particles are large. In addition for complex two-phase flows particles may acquire turbulence also by "fan spreading" phenomenon due to the interaction between particle radial turbulence fluctuation and cross-stream spatial gradients in particle mean velocity, see Hardalupas et al (1989).

The aim of this work is concentrated on two limiting influences of turbulence modulation as follows: i) For lightly loaded flows the turbulence of the continuum phase is not affected by the particles and ii) for a quasi stationary homogeneous flow caused by particles falling in a stagnant water bath, where all turbulence properties are due to effects of turbulence modulation. For the first case the descending water-solid mixture entering a sudden pipe expansion and impinging on a center body was considered. Extensive studies in vertical liquid-solid pipe flows, with or without baffles have been reported by Nouri et al (1987) up to 14% volumetric concentrations. Fluctuating particle velocities decrease with increase in concentration and the recirculation region of the flow of particles downstream of the baffle was shorter than in single phase. Experiments conducted in liquid-solid pipe expansion by Founti and Papaioannides (1994) supported the same conclusions. Other experiments in liquid-solid flows have been reported mainly for jets, see e.g. to Parthasarathy and Faeth (1987) and Hishida et al (1989). For the other limiting influence to turbulent modulation, we consider the flow case originated by particles falling by gravity in a nearly stagnant water bath. The experiment was conducted in the same test section, but the water valve was closed, so a "particle like jet"

* LSTM, Erlangen

enters the pipe sudden expansion. Experiments in particles moving in their self-generated homogenous turbulent field have been reported, e.g. by Parthasarathy and Faeth (1990a; 1990b) concluding that turbulence modulation in dilute particle-laden flows, will require a better understanding of particle wake properties undergoing turbulent dispersion.

The experimental study is described in the next section. This is followed by the presentation of the results divided into two sets of results obtained in the same test section facility, corresponding to $Re \approx 0.0$ and $Re=4 \times 10^4$.

FLOW CONFIGURATION AND EXPERIMENTAL TECHNIQUE

Figure 1 shows the setup of the test rig used in the experiments. Water is discharged by gravity from a top plenum

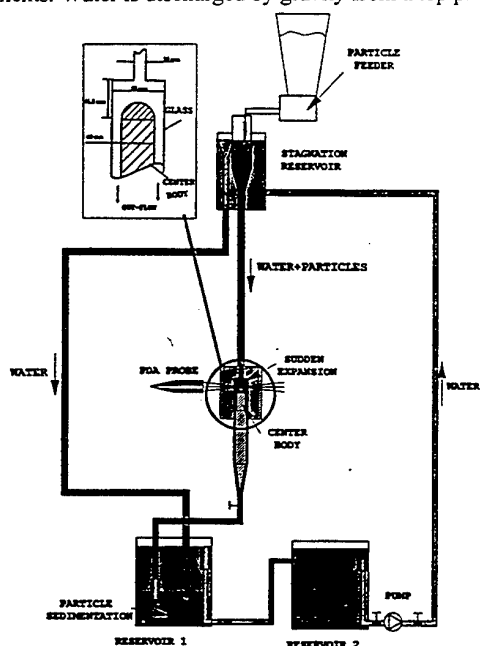


Fig.1: Experimental setup and details of the test section

chamber where glass spheres with density to water, $\rho_p/\rho_w=2.9$, were mixed. The mixture is fed into the test section located 1.5m above the plenum chamber by a vertical glass pipe of 10 mm diameter. The particle feeder and the design of the plenum chamber ensure a constant mass flux of particles without particles walls deposition on the plenum chamber. The test section consists of a sudden pipe expansion, 1:5, with a inner concentric body located 21.5 mm from the pipe expansion, see Figure 1. The body has cylindrical shape with 40 mm diameter and interchangeable head. Results for a flat head have been reported by Chen et al (1996) and an hemispherical head is presently considered. To minimise the displacement of the measuring volume inside the test section due to the curvature of the pipe walls, the test section was enclosed by a square glass box filled with water as stretched in Figure1. The water-particle mixture is discharged leaving the test section by gravity in a plenum tank to allow sedimentation of the glass particles. The

water level was kept constant, in the particle sedimentation tank, by connecting it to another tank where the water was filtered and pumped back to the top plenum tank.

A two-component Dantec fiber optics phase-Doppler anemometer with a multiline Argon-Ion Laser of 800 mW was used. The receiving optics were mounted, 73° off-axis from the scattering direction and both transmitting and receiving optics were mounted in a 3D computer controlled transversing table and the test section was stationary. Mean and rms particle velocities and mean diameter were calculated from 10 000 individual samples. Error sources using the same optical configuration have been discussed see e.g. Xu and Tropea (1994) and were estimated to be up to 3% in the mean and 5% in the rms velocities and particle mean diameter.

RESULTS FOR $Re \approx 0.0$

Prior to PDA measurements, an extensive flow visualisation study was recorded to understand qualitatively the flow field driven by particles entering the sudden expansion only under gravity action. Figure 2a) shows the jet like motion corresponding to a constant mass flux of particles ≈ 15

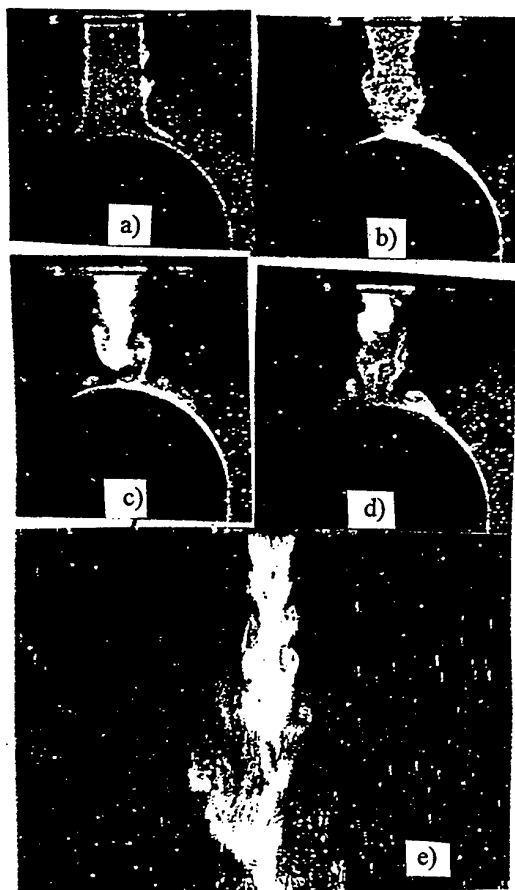


Fig.2: Flow visualisation at $Re \approx 0.0$; a),b),c),d) particles free fall impinging on centerbody, case I e) large stagnation plenum chamber, case II

seconds after start of the experiment. The particle motion is similar to a jet with a clear and stable cylindrical shape without any disruption on the surface. Figure 2 b) shows the starting of a organised motion on the particles wake approximately 2 minutes after start. Figure 2 c) and d) were taken 3 and 4 minutes after start.

The interesting feature of this experiment was the effect of the non-linear interaction between turbulent dispersion of particles in the turbulent field that they create and also the non-linear interaction of the effect of the turbulent field (generated by the particles) on the properties of the wakes. Figure 2 c) was obtained removing the center body and the outer pipe and keeping only the outer glass box of dimensions 0.29x0.14x0.18 m to allow a stagnant bath of larger volume. For this case experiments will be referenced as test case II, while for the case of sudden pipe expansion with center body as test case I. Table I shows the particle size distribution characteristics

Table 1: Characteristics of the glass beads

Test section:	
Test case I	
Size	Diameter 50mm x 40mm
Test case II	
Size	290 x 140 x 180mm
Particles:	
Diameter d_{10}	81.2 μm
Diameter d_{20}	158.4 μm
Diameter d_{30}	202.7 μm
Density ratio ρ_p/ρ_l	2.9
Volumetric flow rate	0.0326 ml/s

A two phase flow is commonly characterised by its governing time-scales. In flow fields where the interaction of the particles with the turbulence structure of the fluid and the particle-particle interaction are in focus of interest, the particle relaxation time τ_t and the inverse particle-particle collision frequency $\tau_c = 1/f_c$ are appropriate time-scales. Therefore the comparison of the two time-scales might be used as characteristic criterium, for dilute two phase flows $\tau_t/\tau_c \ll 1$ and for dense two phase flows, $\tau_t/\tau_c \gg 1$. Under the assumption that there are only collisions between two particles and that the diameter and velocities of the particles are not correlated the collision frequency might be estimated, see Sommerfeld (1995), as follows.

Assuming a Gaussian distribution of the fluctuation velocities with the standard deviation velocities $\sqrt{\sigma_u^2}$ and $\sqrt{\sigma_v^2}$ the average time between the collisions of the two particles with the diameter d_1 and d_2 is,

$$\tau_c = \frac{1}{2^{2/3} \pi^{1/2} N_2} \frac{V}{\pi(d_1 + d_2)^2 \sqrt{\sigma_u^2 + \sigma_v^2}}$$

where V/N_2 gives the number of particles of the second size class per volume.

The volume and mass concentration are defined with

$$c_v = \frac{\pi}{6V} \sum_i d_i^3$$

and $c_m = c_v \cdot \rho_p$. For a mono dispersed particle size distribution the following volume concentration, is obtained to distinguish between dispersed and dense two phase flows:

$$c_v = \frac{3}{\sqrt{32}} \sqrt{\pi} \frac{\mu_l}{d_p \rho_p \sqrt{\sigma_u^2 + \sigma_v^2}}$$

and the mass concentration is given by $c_m = c_v \cdot \rho_p$

Due to the small density ratio $\rho_l/\rho_p \approx 2.9$ all the forces in the particle momentum equation (Drag+Pressure gradient+Virtual mass+Basser+Gravity) have a significant influence on the particle motion. Due to the fluid being at rest with zero velocity at the beginning of the experiments, the motion of the fluid must be created by the movement of the particles. This velocity field of the fluid must therefore influences the motion of the particles. It is essential to estimate

the particle response time τ_t or the particle response length scale l_t on a velocity jump function of the fluid. Due to simplicity the particle momentum equation was integrated only considering the drag forces due to relative velocity between the water and a single glass sphere. Table 2 shows the results. For the 100 μm glass spheres the length of the relaxation way is 47.4 μm , which is even much smaller than the extension of the largest turbulent eddies. These are comparable in size with the radius of the test section $r = 25$ mm or the width of the test section of 70 mm in test case II, respectively. Furthermore, the terminal velocity of a single glass sphere was calculated, accounting only for drag and gravity forces. Table 2 shows the result of the integration

Table 2: Particle relaxation time and length scales and the terminal velocity under gravity, τ_{St} : Stokes time-scale, l_{St} : relaxation length scale for a velocity jump function of $\Delta v = 0.1$ m/s, v_{term} : terminal velocity

	Diameter					
	10	50	100	150	200	μm
τ_{St}	16.1	40.27	1611	3625	6444	$\times 10^{-6}$ s
l_{St}	0.635	13.4	47.4	96.8	158.8	$\times 10^{-6}$ m
v_{term}	0.102	2.477	9.0	17.2	27.6	$\times 10^{-3}$ m/s

Due to their higher Re number, the larger spheres of $d=200$ μm have a higher terminal velocity of $v=2.7 \times 10^{-2}$ m/s than the small spheres with $d=20$ μm , whose terminal velocity is $v=1.02 \times 10^{-4}$. Figure 2 a) shows clearly that in the beginning of the experiment the particles forms a stable, round jet without any disruptions on the surface. But with increasing time, the outer mantle becomes more and more unstable and disrupted. Due to the fact that the average velocity of the fluid field must be zero, this disruption of the jet must be caused by the motion

of the particles and the interference with the liquid. Therefore it is valuable to compare the flowfield structure with the structure of a free jet injected into a stagnant fluid reservoir, see e.g. Bejan (1984). Were the shear layer increases in thickness with increasing distance to the nozzle. The shear layer is governed by turbulent eddies which are generated inside the shear layer due to viscous forces between the injected liquid and the fluid in the reservoir at rest. Near the nozzle, the interface wavelength, scales with the local shear layer thickness, and when this scale reaches the size of the jet, the local diameter of the jet scales with the shear layer thickness. The maximum length scale is given with the actual distance from the outlet and it makes the relation $D \sim L$. Therefore, integrating the momentum equation and neglecting viscous forces we find

$$\int_{-\infty}^{+\infty} u^2 r dr = \text{const.}, \text{ or } \frac{\bar{u}_1}{u_2} = \frac{R_1}{R_2}$$

which gives the maximum average velocity of the free jet in the streamwise direction (viscous forces were neglected).

Now in the experiment presented here, the flow situation is comparable. Due to the motion of the particles which are moving under gravity forces, fluid is accelerated and therefore viscous forces are acting at the outer edge of the particle jet. The acceleration of the fluid by the particles can be seen clearly by the reduction of the drag forces, which will be shown later. Now the motion of the fluid inside the jet leads to a secondary, recirculating flow field outside the jet in the container, because the average flow velocity of the water has to be zero, and to viscous drag forces acting on the outer edge, which lead to the formation of a shear layer.

The general difference between the actual flow situation and a free jet is the mean velocity in streamwise direction, which is decreasing in a free jet and kept constant in the 'particle free jet' because the gravity forces acting on the particles lead to a constant velocity of the glass spheres. Now to clearly identify that both fluid structures are comparable, we will first have a look at the local velocity profiles of the particles at different distances from the outlet, and furthermore we will estimate the size of the largest eddies which has to increase in the streamwise direction.

Figure 3 shows the mean particle diameter profiles, for the two test cases presented here. The diameter distribution, in radial

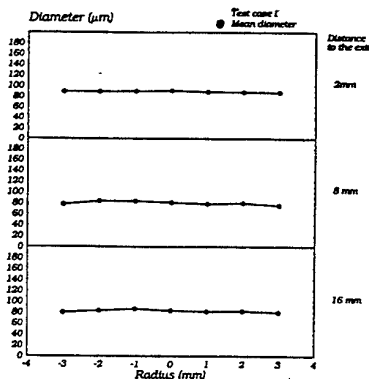


Fig. 3 Diameter profiles at different distances to the outlet, $Re \approx 0.0$.

and axial direction is nearly constant, therefore there is no redistribution of glass spheres due to fluidmechanic effects, as we would expect it for instance in air/spray flows. The reason is the small density ratio 2.9, which leads to a very short particle response time. Now, in the local velocity profiles the differences between the two test cases can be observed: see Fig 4a) in the Test case I, near to the outlet of the tube into the container the average velocity of the glass spheres is about $v = 0.023$ m/s, which corresponds to the terminal velocity in the vertical tube. The numerical prediction of the terminal velocity gives ~ 0.009 m/s for glass spheres with $d = 100 \mu\text{m}$. This difference results from the high concentration of the particle flow: taking the mean fluctuation velocity of $u' = v' = 0.02$ m/s, and calculating C_v for a mean diameter of $d_{10} = 80 \mu\text{m}$, we obtain a critical volume

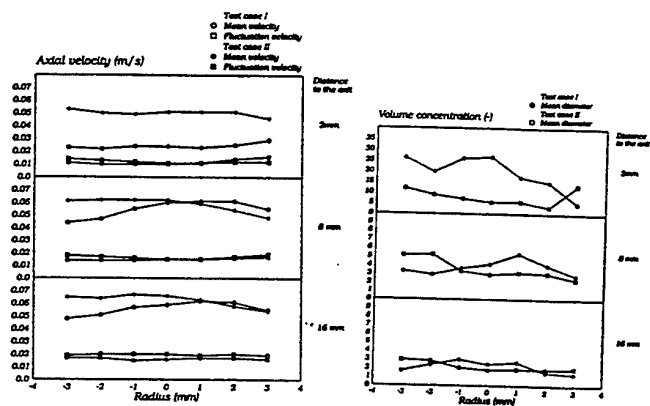


Fig.4a): Axial velocity profiles at different distances to the outlet, b) Volume concentration profiles at different distances to the outlet

concentration of $c_v = 0.143 \text{ m}^3/\text{m}^3$. The measured volume concentration (see Fig 4b) gives about $c_v = 10$ to $30 \text{ m}^3/\text{m}^3$. Therefore the particles motion is mainly governed by particle-particle collisions, and not by fluidmechanic forces. Nevertheless, due to error sources in concentration measurements it has to be regarded as a first and fairly rough estimation. In Test case I the higher axial velocity results from the high concentration of particles, which leads to a reduction of the individual drag coefficient and to decrease of the relative velocity between the fluid and the particles due to an acceleration of the water. Further downstream, the acceleration of the water in the streamwise direction increases, due to the formation of a recirculation zone. In case of the Test case II, which was performed at 5 times higher volume flux of glass spheres than in Test case I, the terminal velocity is even higher. Due to this high concentration, the acceleration of the water is even stronger, leading to an increase of the terminal velocity. As it was shown the instability of the particle jet results from the increasing shear layer thickness downstream the outlet of the vertical tube. This might be proved by an estimation of the

length scale of the turbulent eddy structure, which influences the motion of the particles. Therefore the auto correlation function $R_{u''}(\Delta t)$ of the axial velocity component was calculated Fig.5a) shows an example of the autocorrelation function of the axial fluctuation velocity. Integrating this function with respect to Δt and multiplying it with the average

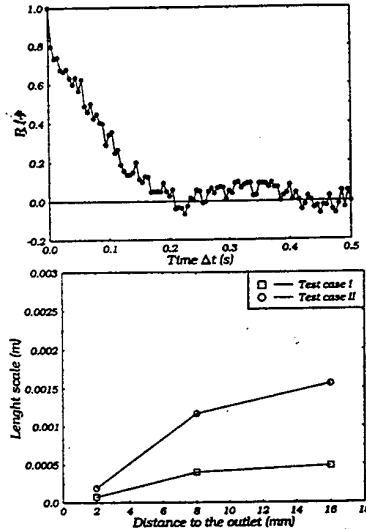


Fig 5a) Autocorrelation function of the streamwise velocity component, 5b) Characteristic length scale on the centreline of the flow

fluctuation velocity $\overline{u'^2}$ gives the local turbulent length scale. The results are shown in Fig 7. For both test cases the turbulent length scale increases significantly, leading to maximum value of 500 μm or 1.7 mm, respectively.

RESULTS FOR $Re=4 \times 10^4$

PDA measurements of water-glass beads mixture under diluted, 0.13% volumetric concentration have been obtained in a sudden pipe expansion with a center body, Figure 6 a) show the mean particles velocity vectors and the corresponding mean axial and radial particle velocities, at different axial stations, are shown in Figures 6 b) and 6 c) respectively. Founti and Papaioannides (1994) have investigated single and two-phase, (liquid-solid), flow for several pipe expansions up to 2.7% volumetric particle concentrations using refractive index matching. From these experiments and the present results shown in Figure 6 a) to c) one can conclude that the main effect of the centerbody is to deflect the flow towards the pipe wall causing early reattachment ($X_R/H=1.82$), than in free sudden expansion flow ($X_R/H=9$), with H being equal to $(D_2-D_1)/2=20$ mm. The inlet jet flow show similar velocities profiles with small radial velocities in the shear layer. The sudden expansion originates a separated flow region that accelerates the flow promoting a decrease in pressure as the flow accelerates into the gap between the centerbody and the wall. However due to the flow deflection towards the wall the flow separates on the center body surface

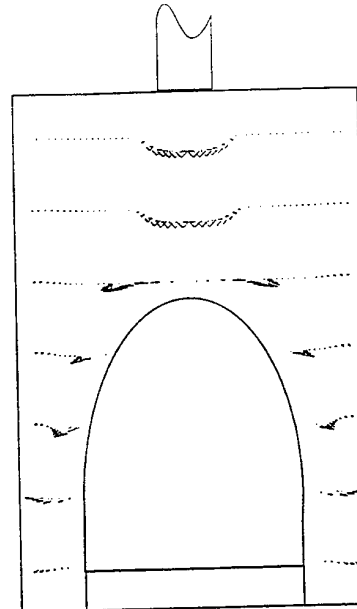


Figure 6 Mean particle velocities for $Re=4 \times 10^4$, a) mean particle velocity patterns

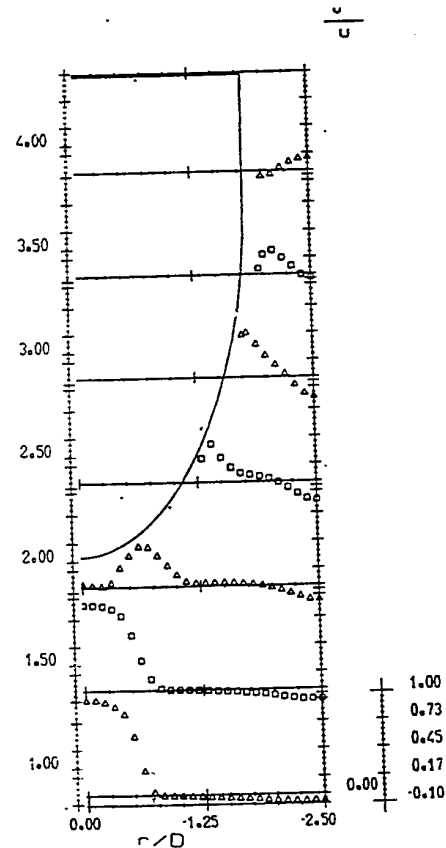


Figure 6 Mean particle velocities for $Re=4 \times 10^4$, b) mean axial particle velocity

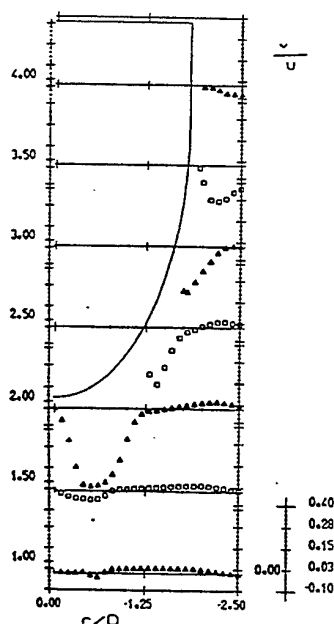


Figure 6 Mean particle velocities for $Re=4 \times 10^4$, c) mean radial particle velocity

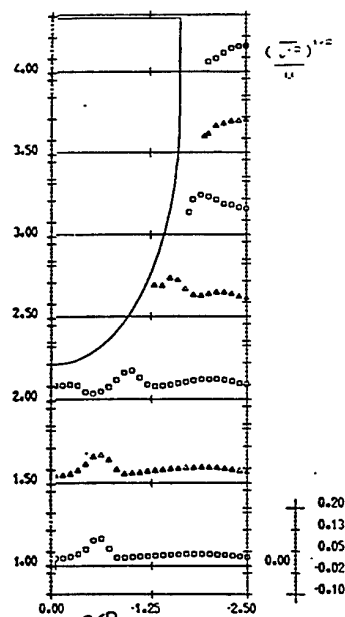


Figure 7 Particle velocity rms fluctuations, b) rms radial fluctuating velocity

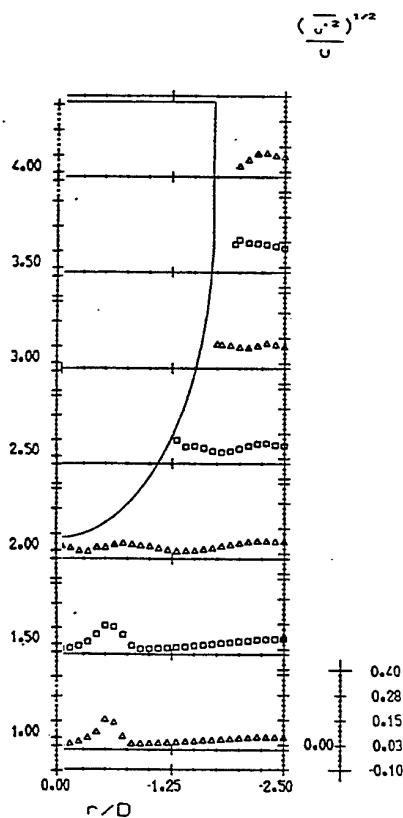


Figure 7 Particle velocity rms fluctuations, a) rms axial fluctuating velocity

immediately after the hemispherical head ($X/D=0.83$) and reattaches at ($X/D=0.92$). Both values of detachment and reattachment on the center body as well as the value of $X_R/H=1.82$ on the outer pipe wall are based in mean particle axial velocity. The highest negative axial velocities are present very close to the pipe wall. The rms axial and radial fluctuating velocities shown in figure 7a) and b) also show an increase towards the wall, particularly the radial particle fluctuations, denoting the importance of particle wall interaction, specially inside the recirculation region. In the jet shear layer, the values of axial fluctuating particle velocity are almost twice the value of radial particle rms velocities. These values decrease in the accelerating flow region and become almost isotropic, denoting the effect of the flow curvature around the center body to stabilise turbulence.

CONCLUSIONS

In this investigation, experiments were performed to reveal the strong coupling of the particle and the fluid phase in a dense particle jet of small glass spheres, injected into a water reservoir at rest. It was shown, that the instability of the particle jet is comparable to the instability of a liquid free jet injected into a stagnant reservoir. The liquid motion due to particle wakes is accelerated in streamwise direction and therefore leads to a growing shear layer, where the turbulent length scale increases with distance from the sudden pipe expansion inlet. The main difference between a particle jet and pure fluid jet is the gravity acting as a constant force on the particles in the particles free jet. Therefore, decrease of the mean velocity due to the

broadening and the loss of momentum is compensated, and the particles velocity are independent of the axial distance to the outlet. From the present experiment it may be derived the conclusion that non-linear interaction between turbulent dispersion of particles in the turbulent field that they create may yield locally to an organised particle wake motion with very different turbulent properties from the surrounding field. This may be further investigated in dense two-phase flows.

For $Re=4 \times 10^4$ the particle mean field shows a very short sudden pipe expansion separated flow region due to the center body influence that deviates and accelerates the flow towards the wall. This flow deflection yields separation on the center body after the hemispherical head on the cylinder. The particle axial velocity fluctuations do not exhibit any increase very close the stagnation point on the impingement of the flow with the center body, denoting that the particle wall interaction is negligible for the present diluted liquid-solid flow on the contrary they are relevant on the wall covered by the separated flow region. The present result for $Re=4 \times 10^4$ may be useful to test particle dispersion models (one-way coupling between the phases) under geometrical complex flows.

ACKNOWLEDGEMENTS

The work was supported by CE-Human Capital and Mobility Network, CHRX-CT93-0389 and the mobility research grant to Dr. Chr. Mundo is gratefully acknowledged.

References

- Al-Taweel, A.M. and Landau, J. 1977, Turbulence modulation in two-phase jet. Int. J. Multiphase Flow Vol.3, pp 341-351
- Bejan, A. 1984 Convection Heat Transfer, J Wiley & Sons, New York
- Chen, X.Q., Freck, C. and Pereira J.C.F., 1996 Experiments and calculations of diluted water-solid mixture on a sudden expansion with a centerbody. To be submitted for publication
- Devenport W., J. and Sutton, E.P. 1993 An Experimental study of two-phase flows through an axisymmetrical sudden expansion, Experiments in Fluids, Vol.14, pp 423-432
- Durst, F. 1982 Review- Combined Measurements of Particle velocities, size Distribution and Concentration, ASME Journal of Fluid Engineering, Vol. 104, pp 284-296
- Founti, M. and Papaioannides, G. 1994 Influence of Expansion ratio on the size of recirculation zone in two-phase sudden Expansion flows, Proc. Seven. Int. Symp. on Appl. of Laser Techniques to Fluid Mechanics, Lisbon, pp 33.1.2 to 33.1.6.
- Gore, R. and Crowe, C.T. 1989, Effect of particles size on modulating turbulent intensity, Int. J. Multiphase Flow Vol.15, pp 279-285
- Hardalupas, Y., Taylor, A.; M; K; P and Whitelaw, J.H. 1989 Velocity and Particle-flux characteristics of turbulent particle-laden jets. Trans. Royal Soc. London, A 246, pp 31-78
- Hishida, K., Nakano, H. and Maeda M., 1989 Turbulent Flow characteristics of liquid-solid particle confined jet. Proc. Int. Conf. on Mechanics of two-phase flows, Taiwan, pp 209-214.
- Lee, S.L. and Durst, F. 1982 On the motion of particles in turbulent duct flow. Int. J. Multiphase Flow, Vol. 8, pp 125-146
- Nouri, J. M., Whitelaw, J. H. and Yianneskis, M. 1987 Particle Motion and Turbulence in Dense Two-Phase Flows, Int. J. Multiphase Flow, Vol.13, N.6, pp 729-739.
- Parthasarathy. R.; N., and Faeth, G. M. 1990a Turbulence modulation in homogeneous dilute particle-laden flows, J. of Fluid Mech., Vol.220, pp 485-514.
- Parthasarathy. R.; N., and Faeth, G. M. 1990b Turbulent dispersion of particles in self generated homogeneous turbulence, J. of Fluid Mech., Vol.220, pp 515-537.
- Sato, Y. and Hishida, K. 1995 Transport Process of Turbulence energy in particle-laden turbulent flow, Proceedings 10th Symposium on turbulent shear flows, pp 25-13 to 25-18
- Sommerfeld, M. 1985, Modellierung und numerische Berechnung von partikelbeladenen, turbulenten Strömungen mit Hilfe des Euler/Lagrange Verfahrens, Habilitationsschrift, LSTM Univ. Erlangen-Nürnberg Germany.
- Stock, D.E. 1996 Particle Dispersion in Flowing gases -1984 Freeman scholar lecture, Asme Journal of Fluids Engineering, Vol.118, pp 4-17
- Tsuji, Y., Morikawa, Y. and Shiomi, H. 1984 LDV-measurements of air-solid two-phase flow in a vertical pipe, J. Fluid Mech., Vol. 139, pp 417-437
- Yarin, L.P. and Hetsroni, G. 1994 Turbulence Intensity in dilute two-phase flows-3, Int.J. of Multiphase Flow, Vol. 20, pp 27-44.

VELOCITY FIELD CHARACTERISTICS OF MULTIPLE JETS IMPINGING ON A FLAT PLATE

A. Bernard and J.L. Bousgarbiès

Laboratoire d'Etudes Aérodynamiques
Bât. H, 40 avenue du recteur Pineau, 86022 Poitiers Cedex, FRANCE

ABSTRACT

The aim of this study was to describe the flow field when an array of fifteen round jets impinge on a flat wall of a rectangular duct. Unlike the majority of previous works which often were interested in thermal sight, the present work concerns the aerodynamic field. A global exploration of this one was first conducted with the help of flow visualizations. The spreading over method allowed to apprehend the flow aspect near the injection wall while visualizations by LASER sheets revealed us the complex vortical structure of impinging jets. This qualitative study was completed by measurements of velocity vector components with LASER Doppler Anemometry. The profiles analysis of RMS and mean values as well as those of skewness and flatness allowed to improve the comprehension of this flow not very studied until now. The examination of instantaneous velocity histograms, rebuilt from stored data, confirms the very big complexity of the flow and its strong unsteady nature.

1. INTRODUCTION

The manufacturers are confronted for a long time with cooling problems of walls in contact with overheated gas. The aeronautics which is particularly concerned requires the film cooling technology for protecting walls of combustion chambers and turbines blades, from important thermal aggressions under which they were put. In the more critical case, the protection can be performed by the presence of an array of impinging jets on the other side of the wall to be cooled. Many works were already realized with this configuration type, but in the multiple impingement case, they principally concern the heat transfer coefficient on the impinged wall surface. However the value of this parameter strongly depends on the dynamic field near this wall and the improvement of the heat transfer process requires a good understanding of the velocity field in the concerned region. It is to achieve this end that the present study was undertaken.

Results were recently published in the case of one impinging jet. The article of Cooper *et al.* (1993) concerns detailed measurements of velocity profiles in axisymmetrical case. Barata *et al.* (1993) made visualizations and velocity measurements for an impinging

jet with a cross flow. The presence of this last one generates a swirling rolling up which surrounds the impingement zone. Rolling up of similar type were observed when we consider the impingement of an array of round jets (Bousgarbiès *et al.*, 1996).

In the work presented here they are the result of the interaction between impingement zones of fifteen cylindrical jets without an initial cross flow. The first aim was the description of the flow aspect created by a such system. For this, we first realized two visualization types. The first concerned the flow at close proximity of the wall owing to the spreading over method. The second were interested in the flow between the injection wall and the impinged surface with local LASER sheet visualizations. These first results were completed by a quantitative study enclosing velocity measurements by LASER anemometry.

2. EXPERIMENTAL FACILITY

The test apparatus used is a right-angled parallelepiped ($240 \times 120 \times 20$ mm) closed on three of its lateral sides.

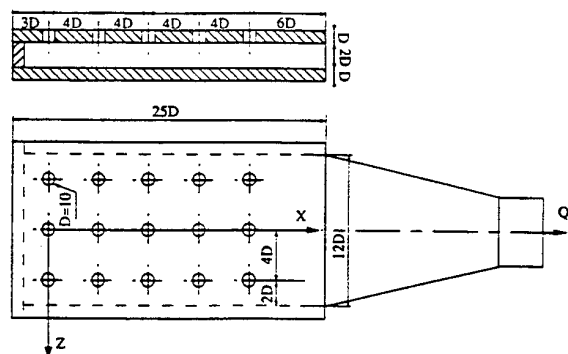


Figure 1: Test section.

The fourth is unrestrained and connected to a depression engine through a metallic convergent system. A flow rate apparatus is inserted between the convergent system exit and

the depression engine to measure the global flow rate Q_v . All the walls of the channel (thickness of 10 mm) are transparent for allowing to make visualizations and measurements by LASER anemometry. The upper wall is drilled by fifteen holes (diameter $D = 10$ mm) distributed in five rows of three orifices (r_1 , r_2 , r_3 , r_4 and r_5). Each hole was separated from its neighbours by a $4D$ distance. The lower wall which is the impinged plate is $2D$ apart from the injection wall (figure 1). The injection Reynolds number which characterizes the flow is defined from the global flow rate Q_v imposed to the convergent system and from the holes diameter ($Re = 4Q_v/15\pi Dv$ with v the kinematic air viscosity).

The wall visualizations were realized with the spreading over method. After the mixing drying made up of particles of calcium carbonate in suspension in oil, the impingement plate was dismantled and then photographed.

For the LASER sheet visualizations, the flow was enlightened by a light sheet obtained from an Argon LASER (7 W maximum power). The use of an optical fibre with an embedded optical system at its end, allows to obtain relatively fine planes (≈ 1 mm). The surrounding air is just sowed at the upstream of some injection holes by an aerosol made with water and glycerine. It's a delicate operation because for obtaining some well contrasted pictures the tracer may be only injected at the upstream of injection orifices corresponding to enlightened jets. More, the sediment of the aerosol droplets on the test chamber walls imposes some very frequent cleanings.

The exploration of the velocities field was made with the Doppler Signal Analyser system (AEROMETRICS). The light source was the same as the one used by LASER sheet visualizations and the surrounding air is sowed before the injection holes by an vegetable oil aerosol. The measurements are made in backward-scatter mode. The emission/reception probe, connected to the analysis and processing system (DSA analyser, oscilloscope and computer) transmit at the time of two components measurements, four LASER beams (one green, one shifted green, one blue and one shifted blue). These four beams make a square base pyramid which the angle at its top is 0.199 rad. This beams disposition and the weak thickness of the test section ($2D$) complicate the measurements. For putting the measurements volume in the median region, it was in fact necessary to incline the emission/reception optics in order to be in position to approach successively the upper and lower walls. The choice of one declination angle respect to the optical axis of the probe (0.105 rad) allowed to come closer the wall at a two tenth millimetres distance in favourable conditions (without very speed dirtying of the walls by vegetable oil sediments). The instantaneous raw data provided by the DSA system were stored for being them used to restore the velocity histograms and to deduce the mean values and RMS profiles as well as those of skewness and flatness.

3. RESULTS AND DISCUSSIONS

3.1 Visualizations

The visualizations of wall streamlines by the spreading over method allowed to observe that the flow generated by

the impingement of fifteen jets get organised according to a cellular structure (Bousgarbies *et al.* 1995). An example corresponding to the impingement zone of the median jet of the fourth row is presented figure 2. Each impingement zone is bounded by an accumulation line of coat that can be easily seen in front of and on sides of the zone and which indicates a detachment presence. Between the two accumulation lines relative to neighbouring impingements, we note the existence of an "ear" shape structure, typical of a three-dimensional reattachment phenomenon. This configuration with an "ear" shape can be noted at the upper and lower parts of the figure 2.

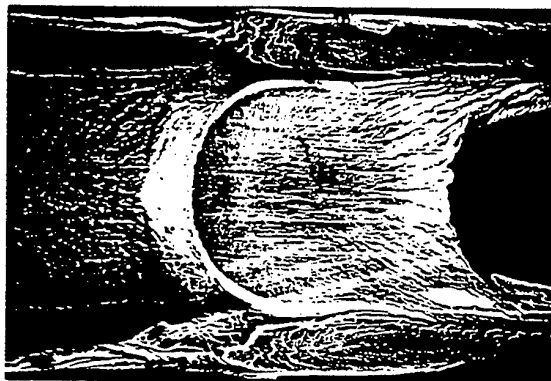


Figure 2: Wall streamlines on impinged surface: Central jet of the fourth row ($x = 12D$, $z = 0$, $Re = 12580$).

The LASER sheet visualizations confirm the previous results and bring some new precisions. The figure 3 is a longitudinal section of the central jet of the fourth row realized by putting the light sheet along the symmetry plane of jet (vertical scale drawn, multiplied by two). We can first notice that under the cross flow effect resulting from the upstream jets presence, the jet bends. The impingement zone centre is like this shifted to downstream respect to the injection orifice axis corresponding. At the time of its meeting with the impingement wall, the fluid radially spreads out, in majority to the downstream while a less important quantity is deviated to upstream (black mark on figure 3) before going away from the wall. This rising which is due to the meeting with the fluid coming from the upstream (central jet of the third row) induces the rolling up formation well visible on figure 3. The same phenomenon is the result of the interaction between the jets of the fourth and the fifth rows but it is less easily seen on the digitised picture (white arrow).

A similar interaction between impingements of median jets of rows r_4 (sowed) and r_5 (not sowed) can be also distinguished on the lateral sections of the flow like the one presented figure 4. This digitised picture was extracted from a video sequence recorded when the light plane go through injection orifices axes of the fourth row ($x = 12D$). For this experiment, the median jet (to the left on the figure 4) and its right neighbour are sowed. The interaction between the two jets after their impingement on the lower wall is easy to watch like before on the side view, the fluid coming from

each impingement is inclined to move apart from the wall as and when it goes closer the plane $z = 2D$ equidistant from two lines. This deviation induces the formation of two counter rotative vortices, which axes are parallel to the mean flow direction in the test section. Under these two rolling up, we can notice the presence of a region not sowed by fluid

coming from either two considered jets. This zone location (clear on the figure 4) correspond to this one where visualizations with coat revealed a structure of wall "ear" shape streamlines, characteristic of a reattachment phenomenon.



Figure 3: LASER sheet visualization: Side view of an impinging jet ($z = 0$, $Re = 12580$).

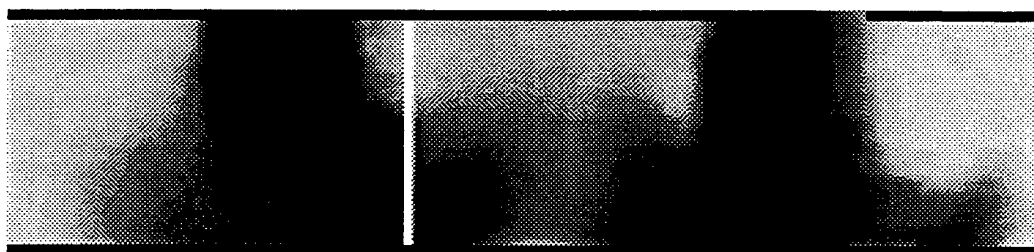


Figure 4: LASER sheet visualization: Cross view of two impinging jets ($x = 12D$, $Re = 12580$).

These observations lead to a schema of flow presented figure 5. Two secondary rolling up with a thickness too small for them to be visible on LASER sheet visualizations, are located under the pair of principal counter rotative vortices. The reattachment line R (perpendicular to the plane

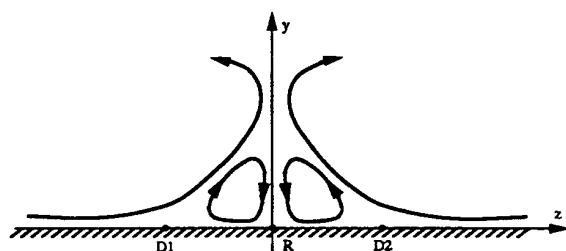


Figure 5: Counter rotative vortices schema.

of the figure 5) is located in the $z = 2D$ plane while the two detachment lines D_1 and D_2 , symmetrical respect to this same plane, correspond to the accumulation lines of coat. The same schema may be considered on the whole border separating one impingement zone from its neighbours that leads to a flow structure relatively complicated, constituted with juxtaposed cells. To this complexity, a character strongly fluctuating with time is added as well as the video recording analysis shows it.

3.2 Velocity measurements

The velocity measurements have been realized at a limited number of positions corresponding to characteristic zones of flow defined after an analysis of visualization experiments. The presented results concern two crossings of the flow made along the normal to the impingement wall. The first was located along the central injection hole axis of

the fourth row ($x = 12D$, $z = 0$, figure 3). The profiles of mean and RMS values as well as skewness and flatness profiles relative to the three components of velocity vector are presented figure 6a to figure 6f. Histograms of instantaneous values of each component at three different distances from the experiment wall are equally given. The figures 7a to 7f rally the profiles and the histograms of the same quantities deduced from measurements made along the normal to the point with $x = 12D$ and $z = D$ coordinates (figure 4).

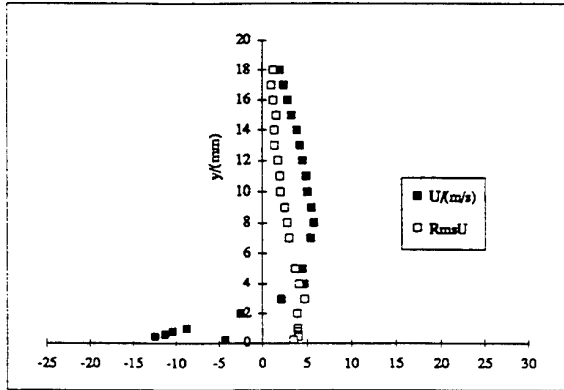


Figure 6a: Mean velocity and RMS profiles of u component ($x = 12D$, $z = 0$, $Re = 12580$).

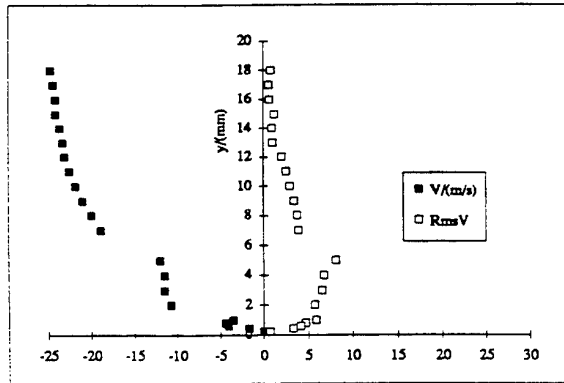


Figure 6b: Mean velocity and RMS profiles of v component ($x = 12D$, $z = 0$, $Re = 12580$).

In the course of the first traverse, the displacement of the sampling volume of the LASER anemometer is made in the side view plane obtained before by LASER sheet visualizations. The way followed is indicated by a white line on the digitised picture given figure 3. Going from the injection wall to the impingement one (y decreasing) we can observe that the mean longitudinal velocity u increases regularly (figure 6a), goes through a maximum for y bordering on 8 mm, and then diminishes. U goes closer zero for $y = 2.5$ mm, becomes then clearly negative and goes through a minimum in the vicinity of the measurement

before last station ($y = 0.2$ mm) before coming back to zero on the impingement surface. Along the same way, the normal velocity decreases from 25 m/s at the vicinity of the injection hole exit ($y = 18$ mm) to zero on the impingement wall ($y = 0$), but we note (figure 6b) that the v profile presents a brutal change of slope for $y \approx 5$ mm. This position coincide with the one of the upper part of the vortex located at the upstream of the impingement zone at the time of visualizations, like the white line on the side view shows it (figure 3). At this point the v RMS values profile presents a maximum (figure 6b).

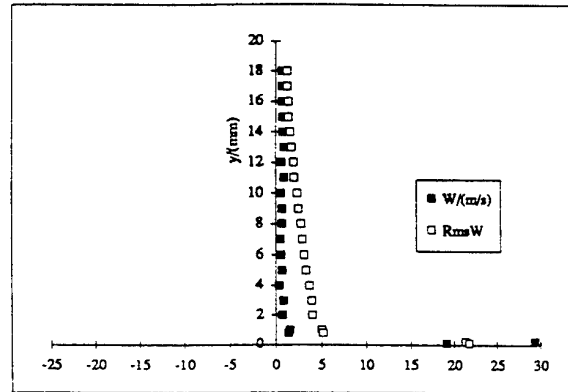


Figure 6c: Mean velocity and RMS profiles of w component ($x = 12D$, $z = 0$, $Re = 12580$).

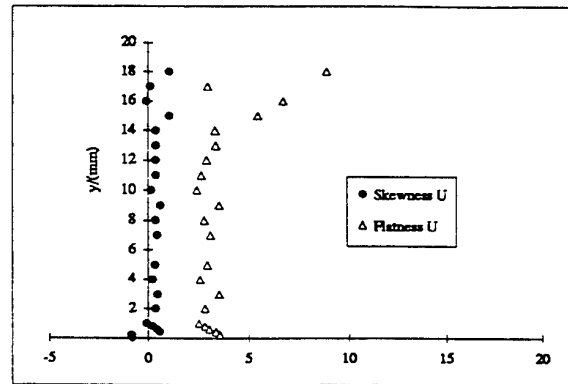


Figure 6d: Skewness and flatness profiles of u component ($x = 12D$, $z = 0$, $Re = 12580$).

The w mean cross component is approximately zero for practically all the crossing of the channel (figure 6c), that is normal because this traverse is made in principle in the symmetry plane of jet. The results of measurements at the nearest four last positions from the impingement wall still show that there is a small distance between the sampling point way and the symmetry plane. Effectively we notice the presence of strong values of w which goes through a maximum for $y = 0.2$ mm before decreasing and coming to zero. The RMS value profile of w , drawn on the same figure

shows a regular growth of the fluctuations level as and when the impingement wall is approached, except for the immediate proximity of this one where strong values are recorded.

Generally we observe that the impingement wall vicinity is characterised by the presence of strong fluctuations of the three velocity components, result in harmony with the observations made in the course of the flow visualizations. The instantaneous values distributions show strong flatness like we can observe it on profiles of figure 6d to figure 6f.

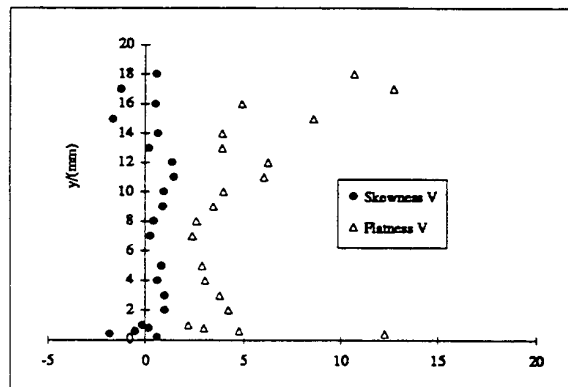


Figure 6e: Skewness and flatness profiles of v component ($x = 12D$, $z = 0$, $Re = 12580$).

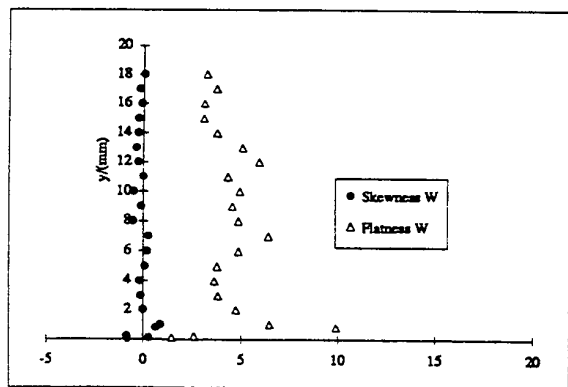


Figure 6f: Skewness and flatness profiles of w component ($x = 12D$, $z = 0$, $Re = 12580$).

The examination of v and w histograms, rebuilt from measurements made at $y = 0.8$ mm from the impingement wall are presented figure 6g and figure 6h. We can notice that for these two examples, most of the values are concentrated around the principal mode but that the others, in reduced number, are very applied on both sides of this mode. The lateral component w (figure 6h) in particular, which value is the most time included between -7 m/s and 10 m/s can sometime reach ± 24 m/s. This result is the consequence of the flapping which is observed in particular

in z direction at the time of experiments by LASER sheet visualizations. This phenomenon which corresponds to a intermittent movement of the impingement region centre also finds expression in important fluctuations of the v normal component between -19 m/s and 9 m/s (figure 6g). This histogram presents a light dissymmetry to the right, property which is found on the most distributions of u and v obtained at the time of the crossing (figure 6d and figure 6e). For the w component, there is practically no dissymmetry (figure 6f) except near the impingement wall and in particular at the position $y = 0.8$ mm considered previously (figure 6h).

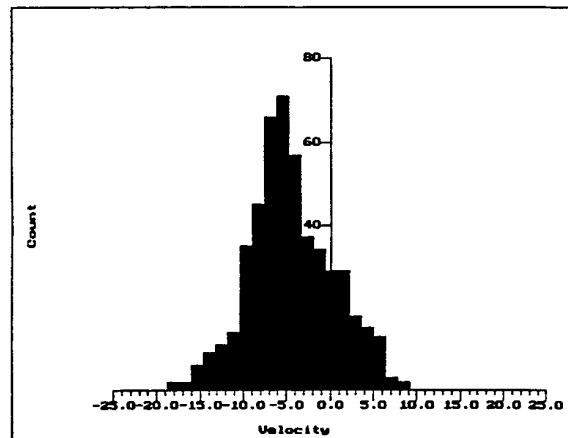


Figure 6g: Histogram of v ($x = 12D$, $y = 0.08D$, $z = 0$).

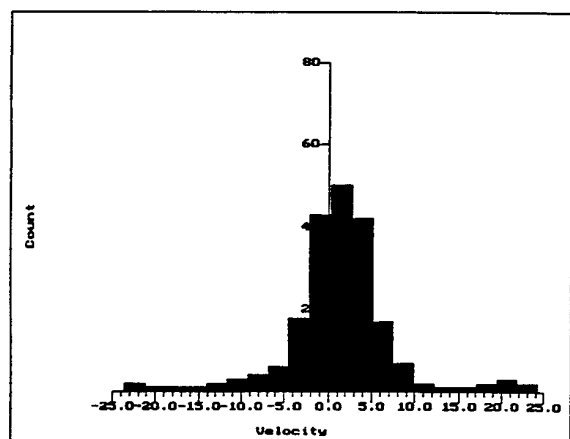


Figure 6h: Histogram of w ($x = 12D$, $y = 0.08D$, $z = 0$).

The position of the second crossing is indicated figure 4 (white line). It is located in the same transversal plane than the first ($x = 12D$) but it is deviated laterally respect to the injection hole axis from a distance equal to D . The longitudinal velocity profile (figure 7a) shows that u is negative near the impingement wall which indicates that in this region the fluid moves towards the upstream in an about 2 mm thickness. In the same time, this fluid goes away from the wall because v is positive (figure 7b) and from the

impingement centre (strongly positive values of w on the figure 7c profile). This result confirms the presence of a jet fluid rising at the periphery of the impingement zone which is traduced by the birth of the swirling rolling up observed on the LASER sheet visualizations. It is in fact necessary to

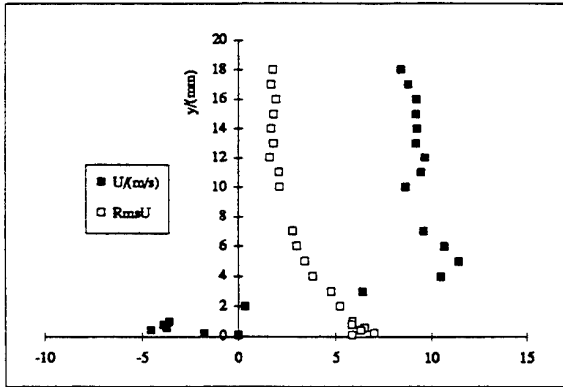


Figure 7a: Mean velocity and RMS profiles of u component ($x = 12D, z = D, Re = 12580$).

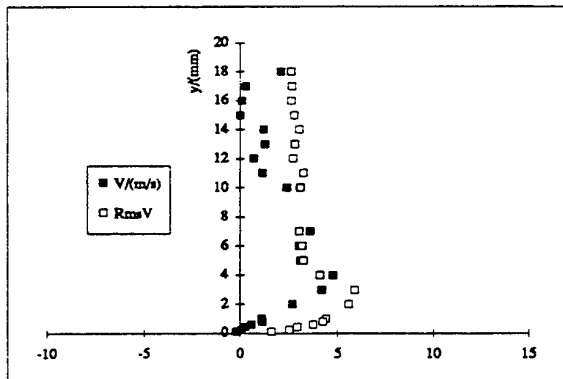


Figure 7b: Mean velocity and RMS profiles of v component ($x = 12D, z = D, Re = 12580$).

notice that the profiles of figure 7a to figure 7c are the result of a crossing made straight up from a point of the coat accumulation line (figure 2). The presence of the detachment phenomenon confirmed by LASER sheet visualizations explains the v values clearly positive observed on the profile of the figure 7b. On this last curve, we also note that at the nearest measurement position from the wall ($y = 0.1$ mm), v changes of sign and takes a negative value (-0.2 m/s). The fact that the fluid then moves towards the wall seems to indicate that this measurement point is located in the upper part of the secondary counter rotative vortex schematised figure 5.

In this peripheral region of the impingement where the detachment phenomenon has been displayed the lateral velocity w is high (figure 7c). The maximum value is recorded at $y = 0.4$ mm where the flow rises from the

impingement wall (v positive). On the contrary near the injection wall, w becomes negative that denotes the presence of a recirculating motion in this upper part of the channel like the transversal view lets presage it (figure 4). In this same zone the velocity fluctuations are bigger than those measured at the first position, along the injection axis. In the other part of the field $0 \leq y \leq 12$ mm, we find again the RMS values approximately neighbouring in the two cases. We still note that the maximum position of the normal component fluctuation approaches to the wall when we go away from the impingement centre ($y = 5$ mm on figure 6b and $y = 3$ mm on figure 7b).

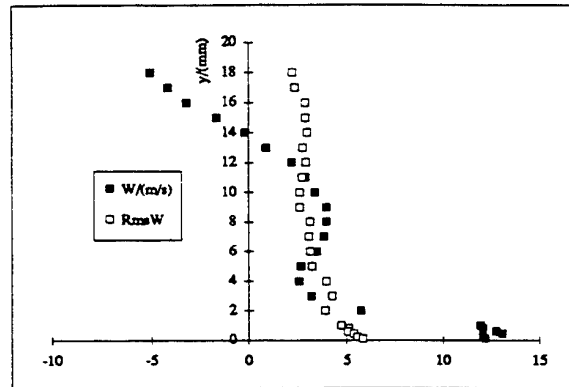


Figure 7c: Mean velocity and RMS profiles of w component ($x = 12D, z = D, Re = 12580$).

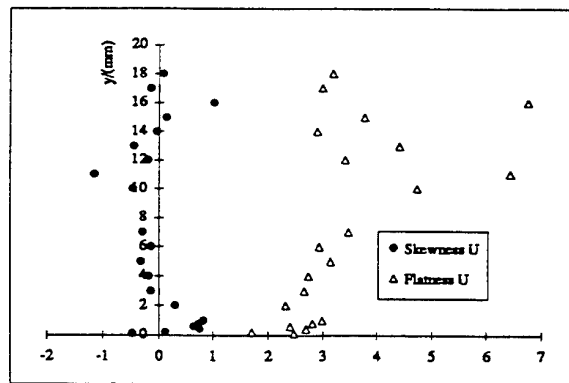


Figure 7d: Skewness and flatness profiles of u component ($x = 12D, z = D, Re = 12580$).

The y evolution of the third-rate and of the fourth-rate moments of the velocity components fluctuations shows the unsteady nature of the flow. The u distribution presents a clearly positive skew near the walls (injection one and impingement one) and a negative skew on the crossing remainder (figure 7d). Near the impingement wall, the flatness is bordering on 3 while it is superior to 3 in the channel upper half. This last result generally indicates the presence of a intermittent phenomenon like Townsend

(1949) for wakes and Wignanski and Fiedler (1970) for mixing layers could show it.

The v distribution is quasi gaussian in the channel upper half (*skewness* = 0 and *kurtosis* \approx 3, figure 7e). On the contrary in the lower region, the distributions are dissymmetrical particularly in the region where the maxima of the v fluctuations profiles is observed (figure 7b). In this point, we record moreover a bimodal histogram (figure 7g) with an aspect which can be connected to the observations made on the transversal views like this presented figure 4.

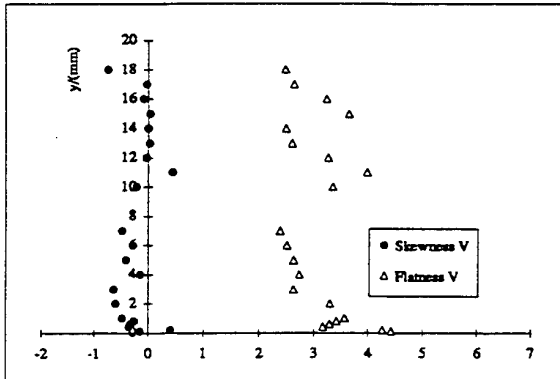


Figure 7e: Skewness and flatness profiles of v component ($x = 12D$, $z = D$ $Re = 12580$).

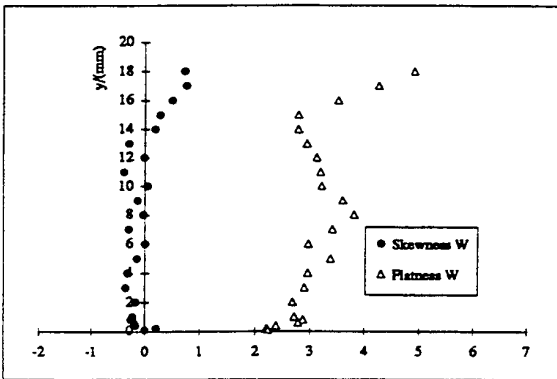


Figure 7f: Skewness and flatness profiles of w component ($x = 12D$, $z = D$, $Re = 12580$).

The examination of the recorded video sequence reveals in fact that the rolling up centre moves on both sides of the $z = D$ plane so creating a very sharp transition from normal positive velocity to a negative value with a important modulus. This variation with the time of the rolling up axis position generates a flapping phenomenon which is also seen on the flatness and skewness profiles of the lateral velocity distributions (figure 7f). The first presents strong values in the middle of the channel and near the injection wall that corresponds to histograms with relatively pointed shape like the example of the figure 7h shows it. These last

results reveal the intermittent nature of the flow in the corresponding regions and agree with observations made previously.

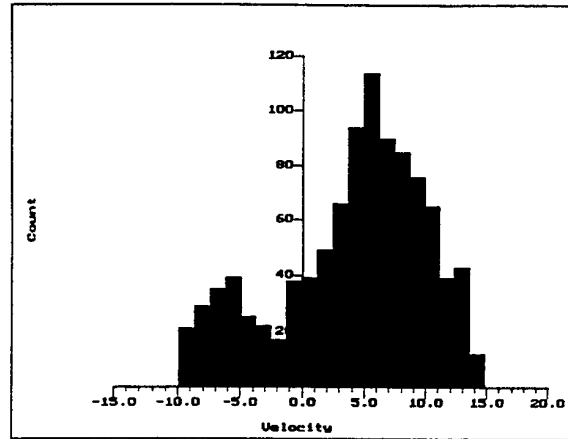


Figure 7g: Histogram of v ($x = 12D$, $y = 0.3D$, $z = D$).

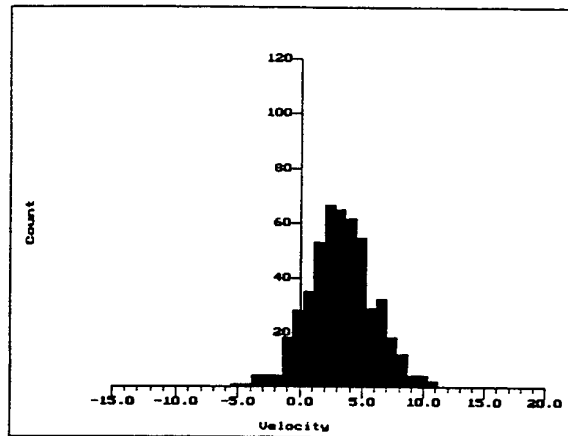


Figure 7h: Histogram of w ($x = 12D$, $y = D$, $z = D$).

4. CONCLUSION

Two visualizations techniques allowed to best apprehend the flow aspect due to the impingement on a plane wall of fifteen distributed jets. The spreading over method showed the flow cellular sight. The LASER sheet visualizations revealed the swirling rolling up presence created by the opposed movements resulting from the impingement of two neighbouring jets. Because of the confinement effect, the fluid coming from the two impingements brutally goes away from the wall and gives birth to a counter rotative vortices pair which holds an important part of the space between the impingement wall and the injection one. Their presence is traduced by the network existence of reattachment and detachment lines at the impingement wall surface. More it gives to the flow a strongly three dimensional sight and a high unsteady nature. The flapping phenomenon presence has been shown by the

LASER sheet visualizations and has been confirmed by the local velocity measurements. This intermittent motion which makes the considered flow study more delicate, is on the contrary a very favourable element for the improvement of the heat transfer between the jets fluid and the impingement wall.

This work was supported by the Direction des Recherches, Etudes et Techniques.

Barata, J.M.M., Durao, D.F.G., Heitor, M.V. & McGuirk, J.J. 1993, On the Analysis of an Impinging Jet on Ground Effects, Exp. in Fluids, vol. 15, pp. 117-129.

Bousgarbies, J.L., Bernard, A., Brizzi, L.E., Dorignac, E. & Vullierme, J.J. 1996, Flow Field Near a Plane Surface Impinged by Multiple Jets; Application to Wall Cooling, R.F.M., n°2 (to be published).

Bousgarbies, J.L., Deniboire, P., Bernard, A. & Foucault, E. 1995, Visualisations de la Structure de l'Ecoulement dû à un Ensemble de Jets Impactant une Paroi Plane, 6th Col. Natl. de Visu. et de Trait. d'Images en Mec. des Fluid., St Etienne. Cooper, D., Jackson, D.C., Launder, B.E. & Liao, G.X. 1993, Impinging Jet Studies for Turbulence Model Assessment-I. Flows Field Experiments, Int. J. Heat Mass Transfer, vol. 36, n°10, pp. 2675-2684.

Townsend, A.A. 1949, Proc. Roy. Soc. A., vol. 197, p.124.

Wynanski, I. & Fiedler, H.E. 1970, The Two-Dimensional Mixing Region, J. Fluid. Mech., vol.41, part 2, pp. 327-361.

THREE-COMPONENT LASER-DOPPLER MEASUREMENTS OF THE CONFINED MODEL FLOW BEHIND A SWIRL NOZZLE

Lehmann, B., Hassa, C., Helbig, J.

Deutsche Forschungsanstalt für Luft- und Raumfahrt (DLR) e. V.
Institut für Antriebstechnik
Abt. Turbulenzforschung, Berlin
Germany

ABSTRACT

Results are reported of three-component laser-Doppler measurements in the highly complex flow field behind a model nozzle as used for the atomization of liquid fuel in gas turbines. The flow field consists of two concentric air streams leaving a concentric dual nozzle system both with slightly different but equally directed swirls. The outer ring flow forms a 1 mm thick ring film which interacts strongly with the inner flow and the surrounding flow field.

Mean and rms velocities were measured as well as double and triple cross-correlations of the three velocity components. Frequency analysis exhibited a strong coherent fluctuation of the radial velocity component near the nozzle exit. The measured data are needed to improve atomization and combustion effectiveness and for numerical modelling of the flow.

1. INTRODUCTION

For aeroengine combustors the method of fuel preparation is of importance for all performance aspects related to mixing and flow homogeneity in the combustor primary zone: combustion efficiency, the required pressure loss of the combustor, smoke production and gaseous emissions of unburnt hydrocarbons, carbon monoxide and nitrogen oxides. Since the installation of international emission regulations in 1981, the use of airblast atomizers, which were particularly successful in limiting smoke production, became customary throughout the industry. In these devices, the pressure difference between the customer casing and flametube is used to produce a swirling air

flow. It forms in some extent the recirculation zone for the aerodynamic flame stabilisation, but also disrupts the low velocity fuel film due to the shearing forces between liquid and air and subsequently atomises and disperses the liquid.

To obtain mathematical models of airblast atomizers which can be used for design purposes, physical submodels for the turbulent swirling air flow, the atomization and the turbulent dispersion of the polydisperse spray have to be found and validated. Then their interaction can be investigated in a practical combustor. For that purpose, an airblast atomizer nozzle was built (Blümcke, E., Eickhoff, H. and Hassa, Ch. 1989) to provide good experimental conditions. Axial symmetry of the swirling flow, optical access to the atomizer lip and the swirl channels had to be realised whereas the essential features of practical nozzles had to be retained. Such features were a good atomization and mixing, a wide range of flow and combustion stability and low emissions. Investigations of the cold two-phase flow (Hassa, C., Blümcke, E., Brandt, M. and Eickhoff, H. 1992) with low and high liquid loading (Brandt, M., Hassa, C. and Eickhoff, H. 1992) and with combustion (Hassa, C., Deick, A. and Eickhoff, H. 1993) have already been made. Finally Hassa (1994) gave a detailed analysis of the production and the dynamics of liquid fuel spray behind a combustion nozzle.

This contribution reports on the use of a 3-D laser-Doppler measuring system for the detailed investigation of the aerodynamics, especially near the nozzle exit. As it is well known, such flows exhibit anisotropic turbulence and often diverge from ideal axisymmetry near the geometric centerline. Therefore one- or two-component laser Doppler measurements are problematic to be applied for the meas-

urement of the three velocity and six Reynolds-stress components by means of subsequently rotate the sytems.

2. EXPERIMENTAL FACILITY

2.1 NOZZLE AND FLOW CHAMBER

The experimental facility consisted of the nozzle device blowing into a cylindrical plexiglass flow chamber with 128 mm inner diameter and a length of 300 mm. The air was taken from a high-pressure relief system and expanded to almost the ambient pressure before entering the nozzle. At the end of the nozzle chamber, a circular end plate left open a 30 mm wide slit between the plate and the cylinder body so that the air flow could leave it in a preferably radial direction. The pressure drop in the nozzle structure was about 3 percent of the flows' total pressure. Two partial flows were introduced into the nozzle structure by means of two hoses each.

The two air supply hoses for each partial air stream led to the nozzle plenums and were coupled together and connected with two separate rotameter measurement devices. In between they were connected to the common exit of a seeder device which served to introduce solid tracer particles into the nozzle flows. The seeder air flow rate was kept low enough to be neglected compared with the main nozzle flow rates.

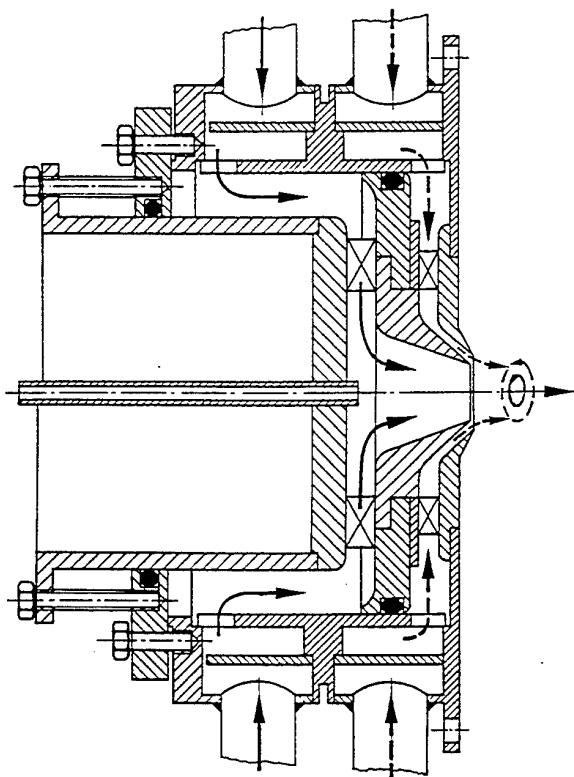


Fig. 1: Plane view into the co-swirling dual-flow atomization nozzle

The nozzle structure is shown schematically in Fig. 1. It consisted of an inner convergent nozzle mouth with a diameter of 17 mm being concentrically enclosed with a ring-film nozzle the air film flow of which was nearly one mm thick. The thickness of the concentric wall separating the two different jets reduced at knife-edge dimensions at the nozzle exit plane.

Both jets obtained a uniquely directed swirl introduced by means of two separately arranged swirl vanes being passed by the two partial air streams in the radial direction. The flow volume rates were different. Nearly 34 m³/h passed through the central nozzle and the ring-film flow was controlled to be 20 m³/h. This resulted in nearly 75 m/s maximum axial and circumferential velocities forming a swirl number of nearly $s=1$ for the different jets.

2.2 OPTICAL DEVICES AND SIGNAL PROCESSING

A three-component laser-Doppler measurement facility was built up of a DISA 55X dual-colour dual-component anemometer with a common 40 MHz Bragg cell for the two components. An additional single-component system consisting of the very first generation DISA 55L „flow direction adapter“ was rectangularly directed onto the common measurement volumes of the dual system. Only one of the two Bragg cells of this adapter system was exited for a frequency shift.

For the dual-component system the green and blue light colours of a water-cooled 5 Watt Argon laser were applied. They served to measure the axial w and the circumferential v velocity components (Fig. 2). The radial u component was measured with the green light of an air-cooled 300 mW Argon laser. Signal separation of the two green component devices could be easily attained by means of working in forward-scatter modes for all three components.

The light-beam separation angles were adjusted between about 4.5 and 7.5 degrees and the focus lengths of the emission optics were 500 mm. The signal-receiving photomultipliers were positioned at about 300 mm away from the measurement volumes. All emitting and receiving optical systems for the three velocity components were fixed on a common support which could be vertically shifted together with the big Argon laser by means of a computer control. The light for the third component was led from the stationary small laser to the 55L system by means of an optical glass fiber device. Adjustment devices enabled the probe volumes to be sensitively adjusted for maximum effective intersection as required for the correlation measurements.

Most of the discussed data have been collected and analysed by means of three BSA enhanced FFT processors for Doppler signals. They were controlled for coincidence conditions under the exactly working hardware-coincidence mode in most of the discussed cases. Some data had been acquired and analysed by means of a self-developed FFT-processor the possibility of which to run the FFT with up to 2048 data-points was helpful in certain cases.

2.3 OPTICAL ACCESS TO THE FLOW CHAMBER

The flow chamber was fixed vertically on a horizontal two-coordinate traversing device. Together with the vertical traverse of the optics, the total space of interest could be covered.

An undisturbed optical access for the light beams of the two-component device and for scatter light reception was achieved by means of two 250 mm long and about 25 mm wide glass windows pasted in opposite positions on the slitted cylinder wall. In this way the inner wall contour of the chamber exhibited only small deviation from circular shape.

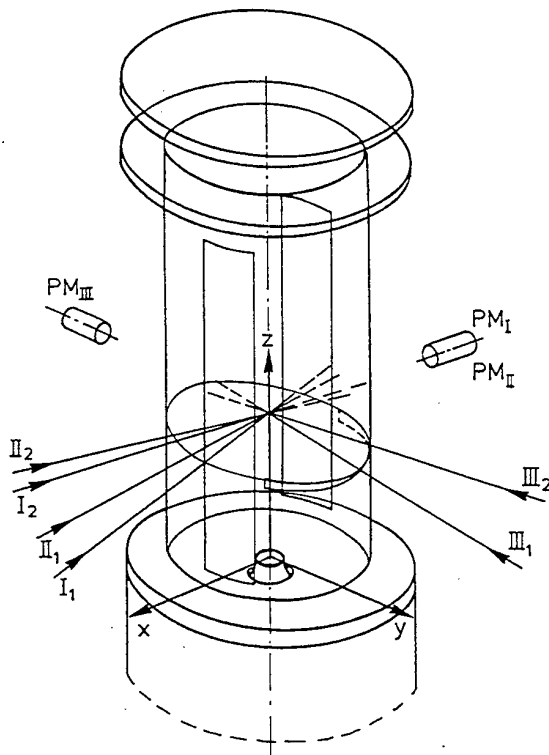


Fig. 2: Nozzle and flow chamber with optical arrangements and coordinates

Thus, the two-component optics could be traversed in a parallel direction with the chamber axis and with the windows as well as rectangularly to them in parallel with a chamber diameter. The necessity of also traversing the radial u component device in parallel with a chamber diameter would imply severe optical de-adjustments due to the 3 mm thick plexiglass wall of the flow chamber.

This problem could be overcome by replacing the chamber wall by a piece of overhead-projector foil in those regions where the optics had to be traversed. Because of its low thickness, the foil exerted only small disturbances to the measurement volume even if the light beams passed it under rather oblique orientation.

In order to keep the mechanical stability of the wall's contour, the chamber wall was provided with cir-

cumferential slits in the regions where the light beams had to penetrate the wall, and the slits were covered by the foil pasted on the inner wall of the chamber. The signal scatter light, however, was received under the forward direction through the original wall thickness and needed only small re-adjustments of the receiving optics in the course of traversal.

2.4 SEEDING TECHNIQUE

Different seeding materials had been tested for the discussed application. These materials ranged from liquid glycerine particles to solid particle powders of SiC, TiO₂ and SiO₂. In all cases, the most numerous particle diameters were below 1 micrometer, and the maximum diameter was about 2 micrometers. The most suitable choice was the use of the SiO₂ particles. This product, named „monospher 800“ of the German Merck company is a nearly monodisperse powder around the particle diameter of 800 nm \pm 20 % and the particle shape is nearly spherical. Similar powders with other particle diameters are available. It may be supposed that the monodispersity would be the main reason of suitability.

This material was dispersed into a low volume-rate air flow with a self-developed seeder. The seeder enables small portions of the powder to be separated almost continuously from a supply vessel and its dispersion by means of a high-velocity air jet from a 0.6 mm diameter wide air nozzle. The primarily seeded air was introduced into the two main air streams of the experimental nozzle through two pressure apertures whose diameters were adapted to the different flow rates of the main streams. In this way an optimum continuity of seeding concentration for the two nozzle air streams should be attained.

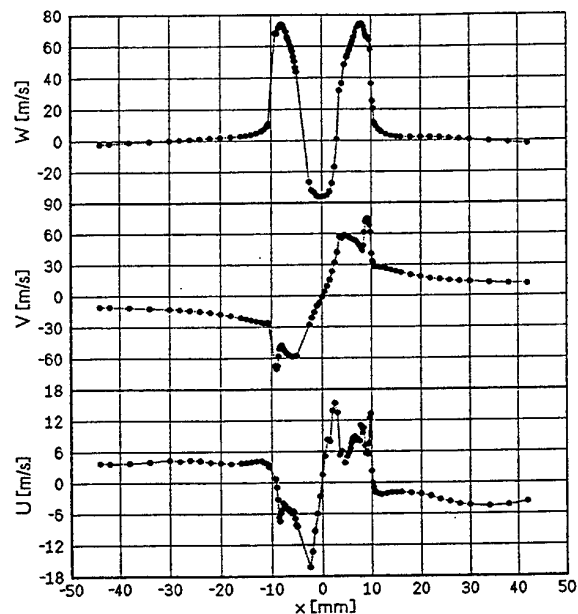


Fig. 3: Mean velocity profiles at $z=2$ mm behind nozzle exit

3. MEASUREMENT RESULTS

3.1 RESULTS FROM THE NOZZLE EXIT PLANE

3.1.1 MEAN VELOCITIES

Though no fuel atomization took place in the present case, the velocity field near the nozzle was of primary interest. Therefore, and also as the initial flow condition for numerical flow-field modelling, the velocity profiles in close proximity to the nozzle had been measured. This was at about 2 mm downstream of the nozzle exit.

In Fig. 3 the measured mean exit velocity profiles are plotted. The mean axial component W shows maximum velocities of about 75 m/s and in the center a back-flow region with nearly 40 m/s maximum negative velocity. This backflow is caused by the swirl which forms a low-pressure region along the nozzle axis. It is demanded for flame stabilisation.

The mean tangential (circumferential) velocity V exhibits a quite characteristic difference between the kernel and the ring-film flow. The ring flow has a higher swirl than the kernel flow, whereas the mean axial w -component of the film flow is obviously somewhat smaller than for the central flow. Thus we can estimate from the W and V velocities (Fig. 3) that the swirl number is about $s=1.15$ for the film flow and $s=0.75$ for the inner flow. The mean radial velocity U is almost an order of magnitude lower than V and W .

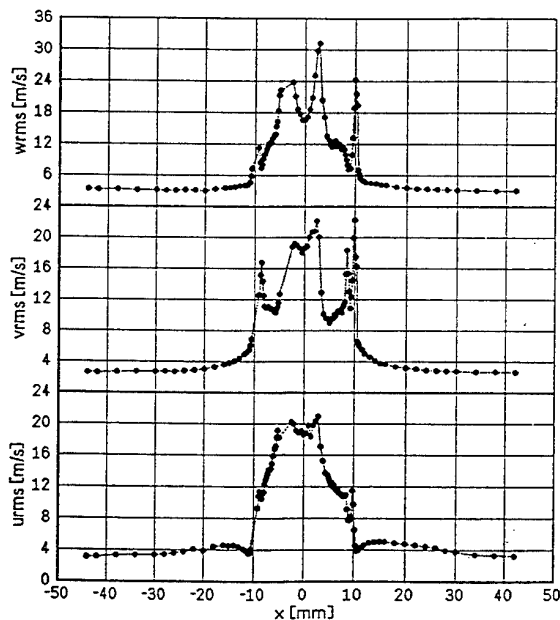


Fig. 4: Turbulence intensities at $z=2$ mm

It must be mentioned that there is a lack of velocity data around the positions $x=-10$ mm and $x=4$ mm. Due to a 1 mm thick pin which supported the slitted chamber wall, the measuring light beams were blocked, and under coincidence conditions no data were collected for the three components. Therefore, at $z=2$ mm, the profiles are more

complete and more detailed for the positive x -coordinate being, therefore, the subject of further discussion.

The linear slope of the U -profile across the nozzle axis and the slight non-linear slope of the V -profile point out a deviation of the flow field from solid-body rotation behaviour. For increasing radial displacement, the flow field is more and more influenced by the shear layer along the inner nozzle wall. An intermediate maximum of the U -profile accompanied by a minimum of the V -profile are due to the wake of the knife-edged wall that separates the inner and the ring-film air streams.

A more detailed and finer structured shape can be recognised in the U profile compared with the V and W profiles in the region near $x=10$ mm where the film flow interacts with the center flow. This might be due to the orientation of the optical probe volumes with regard to the film-flow's contour and dimensions. In the course of the optical traverse, the u -component measurement volume passed the film flow contour under tangential orientation.

The common optical probe volume of the v - and w -system with the length of more than 1.5 mm penetrated the film under rectangular orientation and thus could suffer from an integration effect along its own length. One might deduce therefore that the spatial resolution of the u -component in respect to the film thickness must be better than for the v and w components.

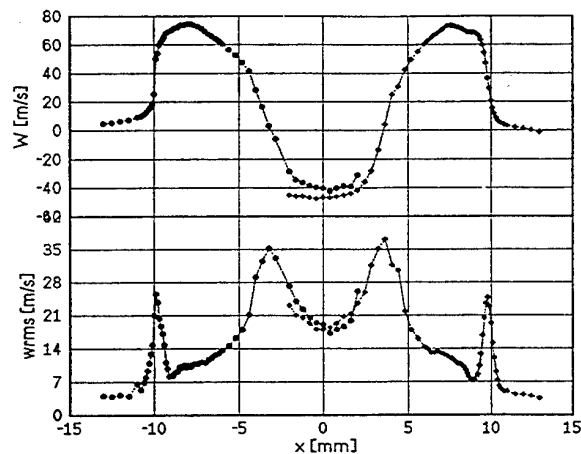


Fig. 5: Test of optical resolution under differently outlined measurement volume at $z=1.5$ mm. Half-profiles at left hand side: probe volume penetrates the film flow perpendicularly, at right hand side: probe volume tangential to the film

This interpretation contradicts the plots in Fig. 4 where the $vrms$ and the $wrms$ profiles seem to have at least the same spatial resolution as the $urms$ profile. The sharp double peaks of the $vrms$ plot exhibit a much higher spatial resolution than the length of the probe volumes would allow.

The only explanation for this is the fact that the discussed measurements have been collected under triple-coincidence conditions for the three components. The discrimination effect of coincidence condition is a reduction

of the probe volumes to the location and the dimensions of the common intersection area. That means that the effective probe volume has the dimensions of the optical probe volumes' diameters, which were of the order of 0.15 mm.

Fig. 5 shows the result of a check concerning the orientation of the probe volume in respect to the circular film flow. Due to the geometric conditions of the experimental devices, it was only possible to carry it out for the axial w component. This component was measured at $z=1.5$ mm for the tangential (right-side half profile) and for rectangular (left-side half profile) orientation of the probe volume with respect to the flow film. No coincidence condition was applied. The half profiles of the mean velocities as well as of the wrms values do not show any characteristic difference concerning the spatial resolution of the measurement.

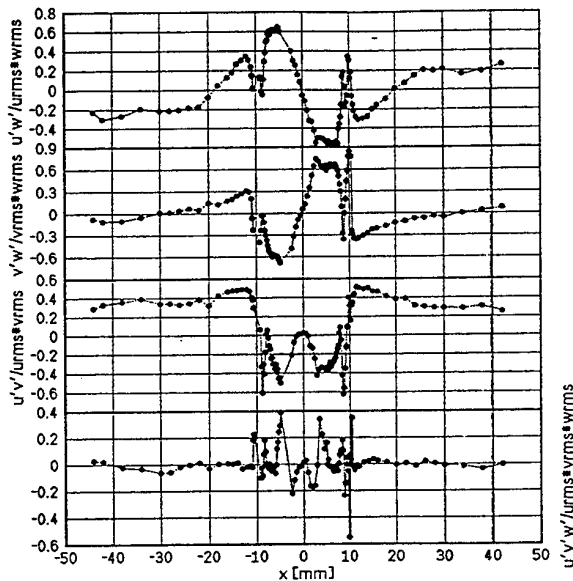


Fig. 6: Cross-correlation profiles at $z=2$ mm

3.1.2 CORRELATION RESULTS

Cross-correlation coefficients were measured and calculated of the velocity fluctuations u' , v' , w' and named e.g. $u'v'$, meaning the time average of the product $u'v'$.

In Fig. 6 the three normalised double cross-correlation coefficients of the velocity components and the triple correlation coefficients are plotted. All the evaluated correlation coefficients are zero in the center of the nozzle. Maximum $u'v'$ correlation is attained just at the outer edge of the ring-film flow at $x=10$ mm. All double correlation coefficients attain maximum variation in the region of the inner nozzle flow and near the film flow. Correlation values are obtained of 0.9 maximum and frequently are of the order of ± 0.6 . The $v'w'$ correlation has a positive maximum at the outer edge of the film flow and a

negative peak at its inner edge where also the $u'v'$ values peak to considerable correlation.

Antisymmetry can be stated for the normalised $u'w'$ - and $v'w'$ -correlations, whereas the $u'v'$ correlation coefficient has a symmetrical profile referred to the $x=0$ position. Far off the nozzle area the normalised $u'w'$ and $u'v'$ tend to absolute values between 0.2 and 0.4, since the $v'w'$ correlation coefficient tends to zero.

The normalised triple correlation $u'v'w'$ slopes are more complicated and more variable. A certain symmetry of the variations with respect to the $x=0$ position can be recognised.

3.2 FURTHER DEVELOPMENT OF THE FLOW FIELD

Additional flow-field data have been measured in the chamber cross-sections $z=15$ mm and $z=100$ mm downstream of the nozzle. Fig. 7 and Fig. 8 show the plots of the mean velocities at the two axial positions. The velocity values reduce by a factor of 10 up to the $z=100$ mm position. The backflow region exists even at that position along a diameter of 80 mm. The tangential velocity V basically keeps its shape and spreads its maxima for increasing z .

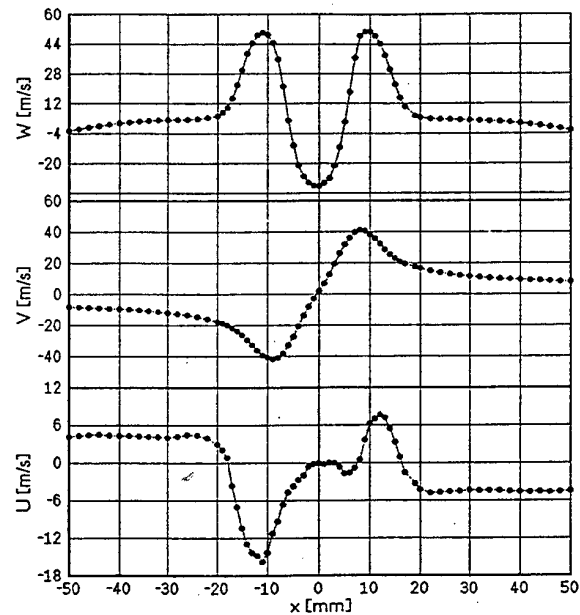


Fig. 7: Mean velocities at $z=15$ mm

In the near-nozzle region up to $z=15$ mm, a divergence angle of the flow can be estimated from the maxima of the U and W profiles of Fig. 3 and Fig. 7. It is about 22 degree if taken from the W profiles but the V profiles make no divergence to be recognised.

The U -profiles in Fig. 7 and Fig. 8 show a considerable deviation from having the expected antisymmetrical slope. It is caused by a small deviation of the mean flow's rotation center from the origin of the x - y -coordinate system which is bent to the flow chamber.

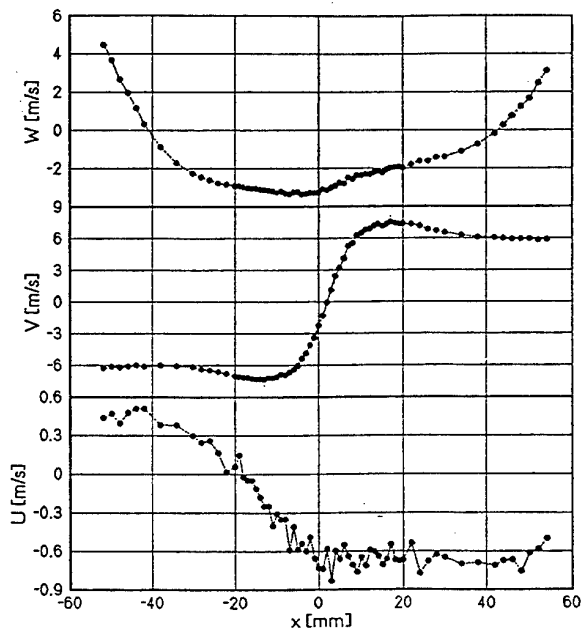


Fig. 8: Mean velocities at $z=100$ mm

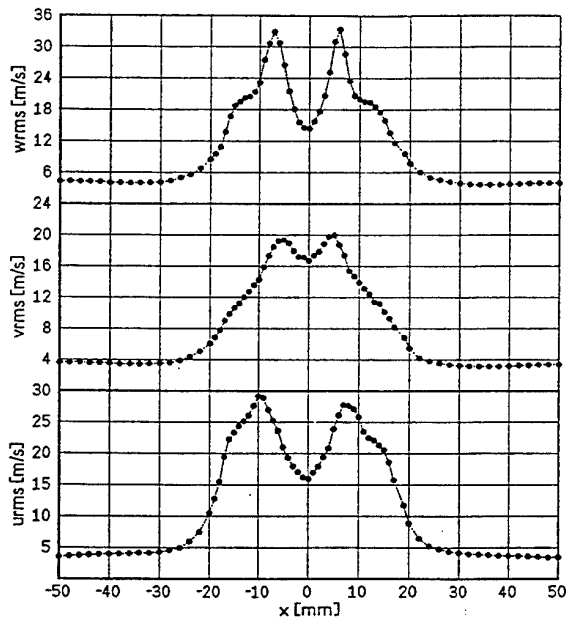


Fig. 9: Turbulence intensities at $z=15$ mm

The estimated delay of both centers was less than 1mm in the $z=100$ mm plane, which is obviously enough for the relatively large shift and deformation of the U-velocity profile. If this 1mm value is interpolated to the $z=15$ mm plane, only the order of 0.15 mm of center deviation seems to be responsible for the strong deformation of the U-profile near $x=0$ mm of Fig. 7.

Further experiments showed that it was almost impossible, to adapt the traverse for a reproducible check of the flow rotation center. It is assumed that the observed unstable behaviour of the data is caused by the length of the measurement probe volume together with the low u velocity to be measured.

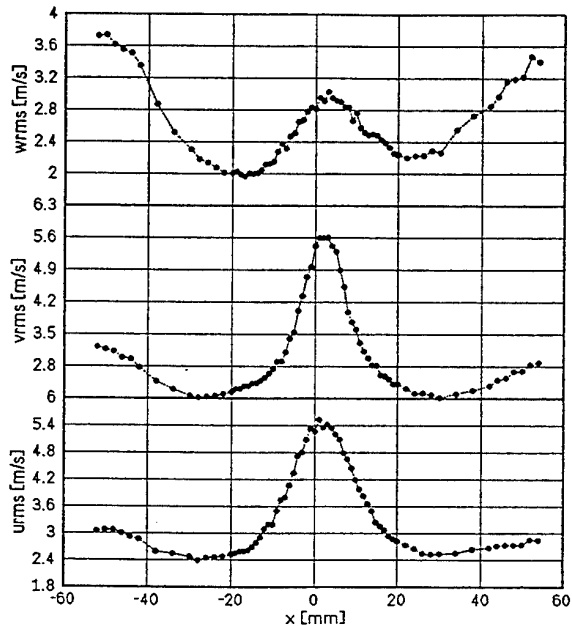


Fig. 10: Turbulence intensities at $z=100$ mm

Fig. 9 and Fig. 10 exhibit the fluctuation rms-values of the velocity components. At the $z=15$ mm position the w_{rms} and the u_{rms} values dominate the v velocity component but are adapted to it or reduced to relatively lower values at $z=100$ mm.

This differently intensive exchange of turbulent energy between the components is also expressed by the correlation coefficients in Fig. 11 and Fig. 12. The $u'w'$ -correlations are higher than the other ones which expresses a stronger interaction between these two components than between the others.

The structure of the triple correlation profiles seems to be still influenced by the mixing process of the different jets at $z=15$ mm but considerably equalised at $z=100$ mm. In spite of the low triple correlation values at $z=100$ mm, its profile's shape scales with the chamber diameter and shows that the flow field has attained a structure at this position which is dominated by the chamber dimensions and no longer by the features of the nozzle.

Due to the considerable deviations of the U profiles from antisymmetry (Fig. 7 and Fig. 8), a check was to be made in order to consider the influence of the flow center delay to the correlation profiles. The result is also shown in Fig. 12. At $z=100$ mm only small deviations were exerted to all four correlation profiles in the region near $x=0$ if the traverse was delayed by 2mm away from the geometrical center. The correlation data far off the flow rotation center were practically not influenced.

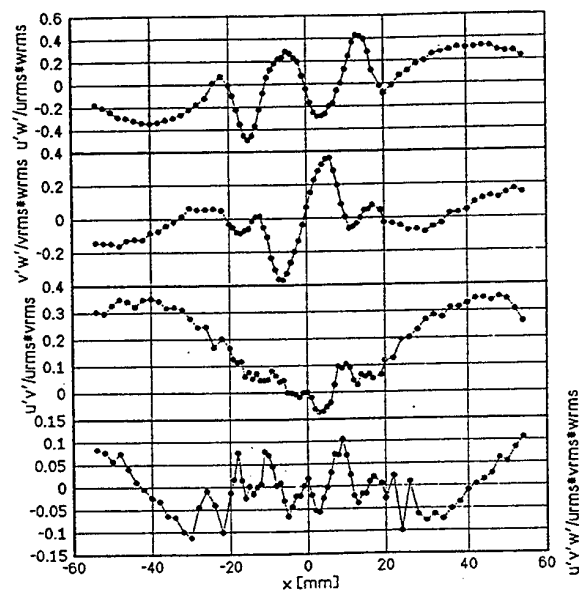


Fig. 11: Cross-correlation profiles at $z=15\text{mm}$

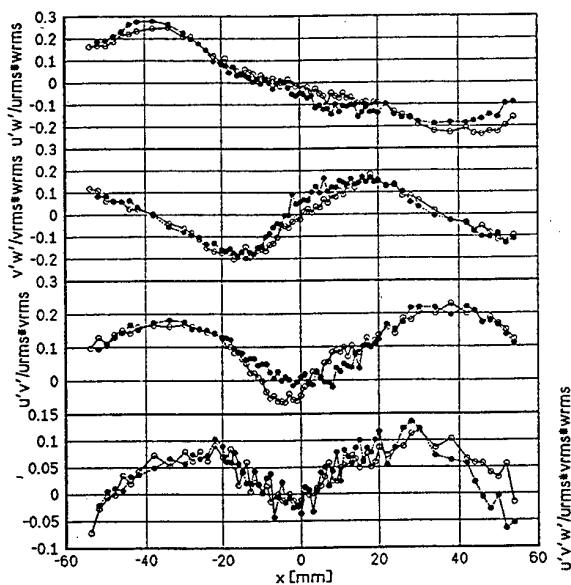


Fig. 12: Cross-correlation profiles at $z=100\text{ mm}$. Traverses of closed and open symbols' profiles differ with about 2 mm of flow-rotation center distance, closed symbols profile nearly passing the center

3.3 DETECTION OF INSTABILITY EFFECTS

An inspection for flow-field instabilities was done in the course of the measurements by means of frequency

analysis of the velocity fluctuations. In fact, there were found very distinct fluctuation frequencies of the spectra in the vicinity of the nozzle.

Fig. 13 shows the superimposed plots of ten linear frequency spectra of the u -component as could be measured at the $z=15\text{ mm}$ and $x=10\text{ mm}$ position. The strong and reproducible frequency peak describes a strong fluctuation of only the u -component, whereas similar results for the v - and the w -components could not be obtained. If a frequency peak could be observed at all for these components, it was highly smeared and diffuse in the spectrum.

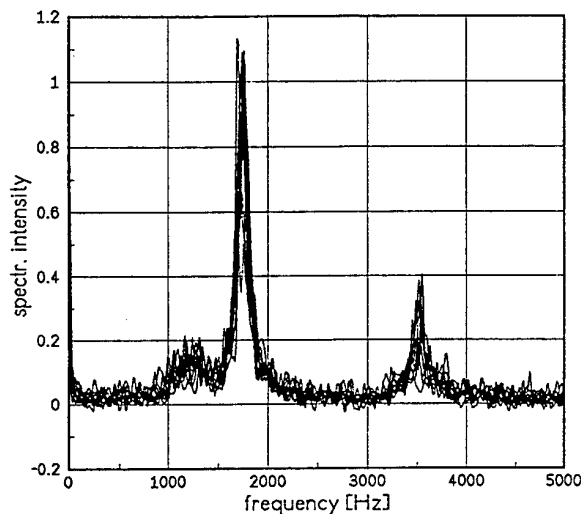


Fig. 13: Frequency spectra of the radial u fluctuations, measured at $z=15\text{ mm}$ and $x=10\text{ mm}$, 10 spectra superimposed

A similar frequency spectrum was measured without the flow chamber and with the nozzle flows blowing as free flows. This check was done in order to investigate whether the fluctuation coherence would possibly be a resonance effect of the chamber. Compared with the chamber conditions and for the same volume flow rates, the frequency peaks were shifted to somewhat higher frequencies. In addition the experiment showed clearly that the second frequency peak is not a higher harmonic of the first and most intensive one.

In the course of further experiments the partial volume flows were varied for frequency analysis in the freely blowing nozzle flow and at the same position as chosen for Fig. 13. If the inner partial flow was reduced and the outer ring flow volume was kept constant, both frequency peaks are shifted to lower frequencies. At the same time the higher frequency peak reduced its intensity and vanished totally at 50% inner flow-volume rate whereas the lower frequency peak reduced its bandwidth and became very sharp.

No remarkable effect was exerted to the frequency spectrum if the inner volume flow rate was kept constant and the one of the ring film was reduced. If both partial

flows were reduced by the same amount, both frequency peaks reduced their frequencies in proportion to the volume flow rates.

It must be concluded from the experiments, that the inner partial flow of the nozzle dominates the fluctuation behaviour especially of the radial velocity component. The lower frequency peak seems to be caused by a primary instability of the inner flow, whereas the interaction with the outer ring-film flow produces obviously the higher frequency peak.

Frequency spectra were also measured at $z=100$ mm away from the nozzle. At this position, no residual KHz frequencies were detected but low frequency peaks were found near 20 Hz.

4. CONCLUSIONS

The three-component laser-Doppler measurements of the flow field behind the atomization nozzle with two concentric, separately swirled air streams with equal swirl directions enable us to conclude that

- in spite of relatively large optical probe volumes with more than 1.5 mm of length and working in forward-scatter mode, measurements with high resolution were possible to be made also in the shear region of a not much more than 1 mm thick film flow area,
- it is not quite clear whether such a high resolution could only be attained due to the applied triple-coincidence technique, which causes a reduction of the effective probe-volume dimensions since the coincidence check would meet exclusively the same tracer particle for all three velocity-component events,
- the radial mean U profile is very sensitive to a small deviation of the traverse from the actual rotational flow center,
- the double and triple cross-correlation coefficients of the three velocity components' fluctuations are widely insensitive in respect to the afore-mentioned deviation,
- a very coherent instability existed with a frequency of about 1.7 KHz measured from the radial u-velocity component at $z=15$ mm behind the nozzle exit, whereas a similarly strong fluctuation behaviour of the v- and the w-velocity components could not be detected. At $z=100$ mm only low frequencies on the order of 20 Hz. were analysed.

The measurement results are of interest for the development of more effective atomization nozzles and for numerical modelling of the flow.

5. REFERENCES

- Blümcke, E., Eickhoff, H., Hassa, Ch. 1989, Untersuchungen zur turbulenten Partikeldispersion an einer Luftstromzerstäuberdüse, VDI-Berichte Nr 765, pp. 635-644.
- Brandt, M., Hassa, C., Eickhoff, H. 1992, An Experimental Study of Spray-Gasphase Interaction for a Co-Swirling Airblast Atomizer, Proc. Eighth Annual European Conference on Liquid Atomization and Spray Systems. Sept./Oct. 1992, Amsterdam, The Netherlands.
- Hassa, C., Blümcke, E., Brandt, M., Eickhoff, H. 1992, Experimental and Theoretical Investigation of a Research Atomizer/Combustion Chamber Configuration, Proc. International Gas Turbine and Aeroengine Congress and Exposition, June 1992, Cologne, Germany.
- Hassa, C., Deick, A., Eickhoff, H. 1993, Investigation of the Two-Phase Flow in a Research Combustor under Reacting and Non-Reacting Conditions, AGARD Conference Proc. 536 on 'Fuels and Combustion Technology for Advanced Aircraft Engines, May 1993, pp. 41-1 to 41-12, Firenze, Italy.
- Hassa, C., 1994, Experimentelle Untersuchung der turbulenten Partikeldispersion in Drallströmungen, thesis, research report no. 94-20, Deutsche Forschungsanstalt für Luft- und Raumfahrt, Institut für Antriebstechnik, Cologne

SESSION 27

PIV and PTV Signal Processing II

TEMPORAL MAPPING OF THE SPRING MODEL FOR PARTICLE IMAGE VELOCIMETRY

Koji OKAMOTO, Masaki KOIZUMI and Haruki MADARAME
Nuclear Engineering Research Laboratory
University of Tokyo
Tokai-mura, Ibaraki, 319-11, JAPAN

Yassin A. HASSAN
Department of Nuclear Engineering
Texas A&M University
College Station, TX, 77843

ABSTRACT

The cross correlation tracking technique is widely used to analyze image data, in Particle Image Velocimetry (PIV). The technique assumes that the fluid motion, within small regions of the flow field, is parallel over short time intervals. However, actual flow fields may have some distorted motion. If the distortion of the flow field is great enough the fluid motion can not be tracked well using the cross correlation technique. The Spring Model technique is applicable to the flow field which exhibit characteristics such as rotation, shear and expansion.

In this study, in order to improve the accuracy of the Spring Model technique, the temporal information were analyzed. Using the improved Spring Model technique, the velocity vectors could be reconstructed from noisy and/or large displacement images.

1. INTRODUCTION

Particle Image Velocimetry (PIV) is a superior measurement technique for studying fluid flows. It offers many advantages over other conventional velocimetrys, such as laser doppler anemometry and hot-wire anemometry. The primary advantage is the ability to capture spatial velocity distributions simultaneously and noninvasively.

The fluid flow is visualized by seeding it with small particle tracers. Then the flow visualization images are analyzed to obtain the velocity distribution of the flow. Many algorithms for analyzing the images have been proposed. These include the cross correlation technique(Adrian 1991, Hassan et al., 1992, Uemura et al., 1990) and the particle tracking technique(Nishino et al., 1989).

In the cross correlation techniques, the motion of the particles is implicitly assumed to be parallel. However, in

a real flow field, there are other kinds of motion. These include rotation, shear and expansion. If the other motions are not negligible between the images, the cross correlation technique can not track the flow.

Okamoto et al. (1995a) proposed a Spring Model technique for particle tracking based on a pattern matching technique which can accept rotation, shear and expansion. A highly accurate velocity distribution can be reconstructed in a short calculation time. This technique can be extended readily for three-dimensional measurements.

The Spring Model technique can be applied to the condition in which the particle displacement between two images are relatively large. It can also be superior to tracking in the noisy images. That is, the correct velocity field could be reconstructed even from noisy images.

However, the Spring Model technique still had some erroneous vectors, when the displacements of the particle were too large and/or when the image had too many noises. In

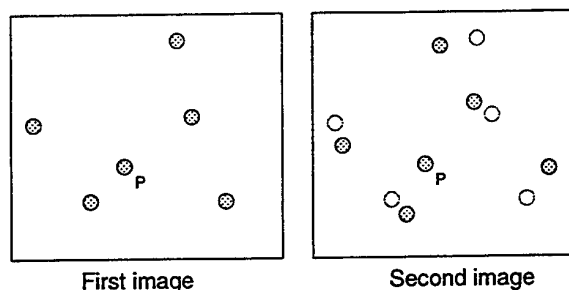


Figure 1: Schematic of particle displacement in two images

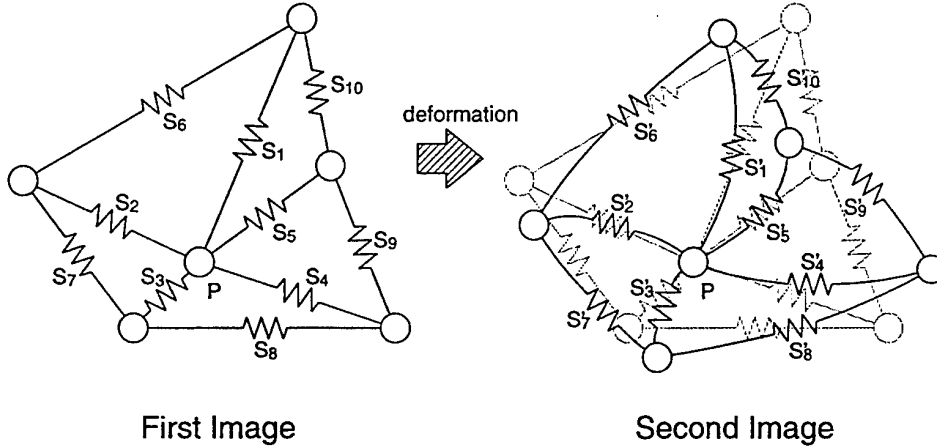


Figure 2: Spring model

the experiment, several images were serially taken usually. Therefore, in this study, the several serial images were analyzed, in order to improve the applicability of the Spring Model technique to the highly noisy images and/or the larger displacement images.

2. ALGORITHM

2.1 Spring Model

In the Spring Model technique (Okamoto et al., 1995a), the individual particle was tracked with using the information of particle cluster. The particle clusters were matched in consecutive images using the information of spring forces.

Typical patterns, for a particle cluster in two consecutive images, are illustrated in Figure 1. In the second image, the pattern changes with a small rotation and shear. In this case, the cross correlation factor between the two images is very small, since there is no overlapping of the particles between the images, except for the center particle. Therefore, using conventional cross correlation techniques, the correct result can not be obtained.

In the Spring Model, the particles are assumed to be connected by invisible elastic springs as shown in Figure 2. The evaluated particle P is called the target. Each particle around the target P is connected by a spring from P . These particles are also connected to their neighbors. In the first image, all the springs are in the base condition (i.e., springs have no force).

In the second image, the cluster of particles is shifted by rotation and shear. According to the changes of shape, every invisible spring holds some force:

$$E_i = \frac{|\vec{s}'_i - \vec{s}_i|}{|\vec{s}_i|} \quad (1)$$

where \vec{s} and \vec{s}' are the relative vectors of the springs in the first and second image, respectively. The average force for the invisible springs is:

$$E = \frac{1}{N} \sum_i^N E_i \quad (2)$$

where N is a number of springs in the particle cluster.

When there is no rotation, shear or expansion, the average force is zero (i.e., $\vec{s}'_i = \vec{s}_i$). When there is a small rotation, shear or expansion, the average force has a small value, because of the small deformations of the springs. If the target particle position in the first and second image do not correspond, the average force will be very large, since the particle cluster shape will probably be very different. Therefore, pattern matching can be conducted by considering the spring force.

For the target particle in the first image, the average spring force for every possible target particle in the second image can be calculated. In this case, the particle cluster with the smallest force corresponds to the target particle cluster in the first image.

In the Spring Model, even when rotation, shear and expansion are applied to the flow, the particles can be tracked correctly. For example, in Figure 1, the invisible spring force is not zero, but it is very small, since the deformation caused by rotation and shear is not very large, thus allowing the particle cluster to be tracked correctly between the images.

In this model, noise in the image may result in erroneous particle positions which lead to larger spring forces. To reduce noise effects, the maximum force, E_i , is limited to 1. Particles appearing in the second image but not the first (or the reverse) result from image noise and the movement of particles in and out of the illuminated area. The effects of these particles on particle tracking were taken into

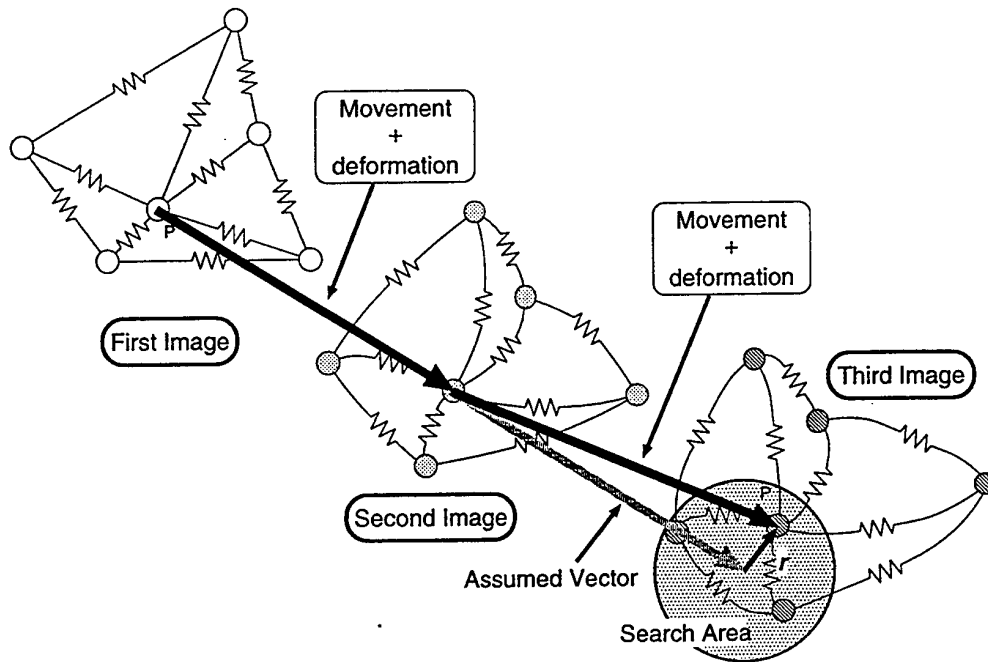


Figure 3: Concept of the temporal mapping

account using the penalty parameter. Appearing and/or disappearing particles are considered to be a generated or broken springs in this model. The generated or broken spring is assumed to cost a force of 0.3. The value of 0.3 was determined empirically. With the concept of the penalty parameter for the appearing and/or disappearing particles, the Spring Model technique could track the particles correctly even from the noisy images.

If three-dimensional particle positions are known, the same procedure can be applied to obtain the three-dimensional velocity field. The invisible spring force is calculated using the information already obtained about particle positions. Then, the three-dimensional velocity distributions can be calculated with the Spring Model technique.

2.2 Improved Spring Model

In order to improve the accuracy of the particle tracking by the Spring Model, the concept of the temporal mapping is introduced. In this technique, the several serial images are analyzed to track the particle cluster.

Figures 3 and 4 show the schematic view of the temporal mapping and the flow chart of the improved technique, respectively. Initially, using the first and second images, the particle tracking is carried out using the original Spring Model technique (Fig.4(a)). When the images have many noise particles, the results still have several erroneous vectors.

Then using the vector between the first and second images, the particle position in third image is assumed

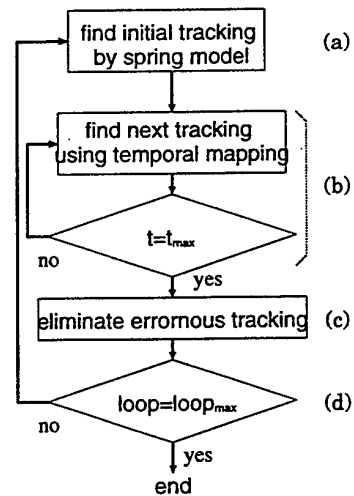


Figure 4: Flowchart of the improved Spring Model

as shown in Fig.3. The candidate particle clusters are searched around the assumed particle position. In this study, the weight factor f for the Spring Force E is introduced to consider the assumed particle position. The weight factor f is expressed with the parameter of the distance, $|\vec{r}|$, from the assumed position.

$$f = \text{MAX}(0.8, \frac{2.4}{R_{\max}} |\vec{r}| - 0.4) \quad (3)$$

When the distance, $|\vec{r}|$, is less than $R_{\max}/2$, the factor is constant, $f = 0.8$. With increasing the distance, $|\vec{r}|$, the factor also increases monotonously. In the cluster matching, the weighted Spring Forces, (fE) , are used as a matching factor (Fig.4(b)). Since the smaller Spring Force gives correct vector, the vector with large distance from the assumed point has large penalty value.

Now, the pattern matching of the particle clusters are carried out using the weighted Spring Forces, resulting in the velocity vectors. Even though the improved Spring Model technique, the erroneous vectors are still included in the velocity vectors. In this stage, the erroneous vectors are removed using the information of velocities. That is, the 1st vectors from the 1st-2nd images and the 2nd vectors from the 2nd-3rd images are compared. When the 1st vector has large discrepancies from the 2nd vector, the vectors are assumed to be erroneous vectors. The criteria of the erroneous vector are the velocity amplitude and direction (Fig. 4(c)).

Then, the correct vectors are obtained using the improved Spring Model technique. The above procedures (search and remove) are repeated several times using the information of the particles in the images to get the correct vectors (Fig. 4(d)).

Using the improved Spring Model, the velocity distributions can be measured even from highly noisy or larger displacement images.

3. VERIFICATION

In order to verify the improved Spring Model technique velocity distributions were reconstructed from synthetic particle data and actual visualized images.

3.1 Simulation

The effectiveness of the Spring Model technique were already investigated in the previous studies (Okamoto et al., 1995a, Okamoto et al., 1995b). In these studies, the results by the Spring Model were compared with that by the cross correlation technique (Hassan et al., 1992), showing the higher yield and higher accuracy.

In this study, the effects of noise and displacement on the tracking technique were systematically evaluated. The noise ratio, R_n , was defined as the ratio of noise particles to the simulated particles, i.e., $R_n = N_{\text{noise}}/N_{\text{simulation}}$. The average displacement between the sequential images, $|\vec{v}|$, was calculated from the particle movement without noise. In the simulation, the noise ratio, R_n , and the average displacement, $|\vec{v}|$, were varied from 0 to 40% and from 10 to 50 pixel/interval, respectively.

The simulated flow were Couette Flow, Poiseuille Flow and Vortex Flow. In these flow, 500 particles were inserted into the image of 200×200 pixels. Since the velocity distributions of the simulated flow were known, the particle location were numerically calculated. To add the artificial

noise, the noise particle were randomly generated in the images. Using the original Spring Model and improved Spring Model, the yield and the correct ratio were calculated with varying the noise ratio and average displacement.

The yield was defined as the ratio of number of obtained vectors to number of simulated particles(500). The correct ratio was calculated as the number of correct vectors divided by the number of obtained vectors.

Figures 5 and 6 show the relationship between the yield and noise ratio, and that between the correct ratio and average displacement, respectively. The results indicate that the improved Spring Model was better than the original Spring Model. When the noise ratio exceeded 30%, the yield for the original Spring Model decreased rapidly. While, using the improved Spring Model, more than 50% vectors could be reconstructed. The original Spring Model was superior to the noise effects (Okamoto et al., 1995a). The improved Spring Model was found to be more effective to the noise.

When the particle displacement was small, the correct ratio for both techniques were high. With increasing the displacement, the erroneous vectors also increased. However, using the improved Spring Model, the correct vectors could be measured even from the larger displacement vectors, i.e., more than 30 pixels between images. With increasing the displacement, the rotational motion and/or shear motion could not be neglected. Therefore, the improved Spring Model technique had advantages in tracking the larger displacement movement.

3.2 Experimental Application

The Spring model technique was applied to a two dimensional flow field near free surface. Figure 7 shows the schematic of the test section. The measurement system was the same as that of Okamoto et al. (1995c). The jet was injected from the horizontal nozzle beneath the free surface. The interaction between the jet and free surface caused the turbulent free surface condition. The free surface was visualized by a laser light sheet. The seeds, 0.05 mm in diameter, were injected into the liquid phase. The Froude number and Reynolds number were about 1.0 and 3000, respectively. The flow field is illuminated by the pulse Nd:YAG Laser with 10 nsec band width. The visualized image was digitized into a 640×480 pixel image every 53.8 msec.

Figures 8 and 9 show the velocity distributions reconstructed by the cross correlation and the original Spring Model technique, respectively. In this condition, the average velocity was about 50 pixel/interval. Therefore, in the cross correlation technique, the interrogation region and search area were 16×16 pixels and $128 \times 128 (\pm 64)$ pixels, respectively. Since the displacement between the two images were too large to track the particle correctly, in this case. So both cross correlation technique and original Spring Model technique could not reconstruct the flow field correctly.

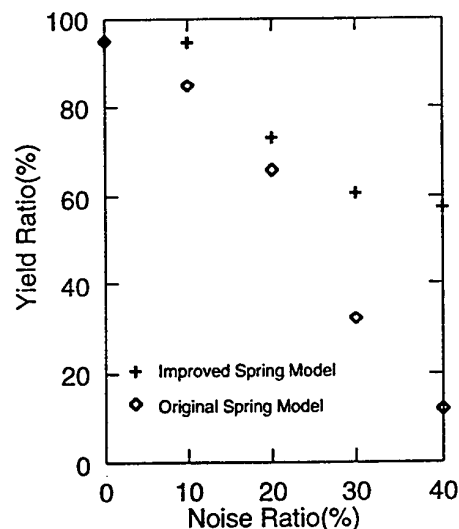


Figure 5: Comparison between Original and Improved Spring Model using computer simulation (noise effects)

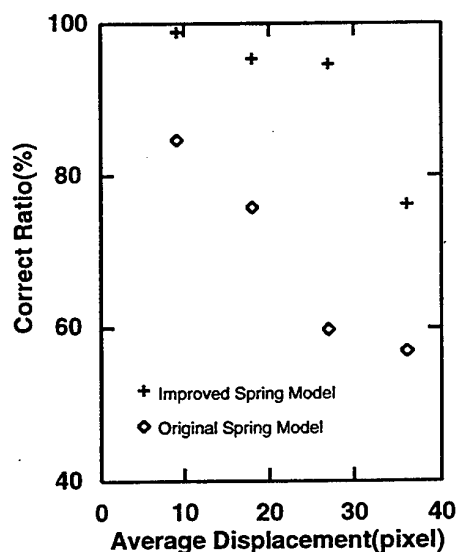


Figure 6: Comparison between Original and Improved Spring Model using computer simulation (displacement)

Figures 10 and 11 show the velocity distributions reconstructed by the present improved Spring Model technique from three and four serial images, respectively. With applying the improved technique, the flow field could be reconstructed more clearly. From three serial images (Fig.10), there still were several erroneous vectors. With increasing the images to four (Fig.11), the erroneous vectors were

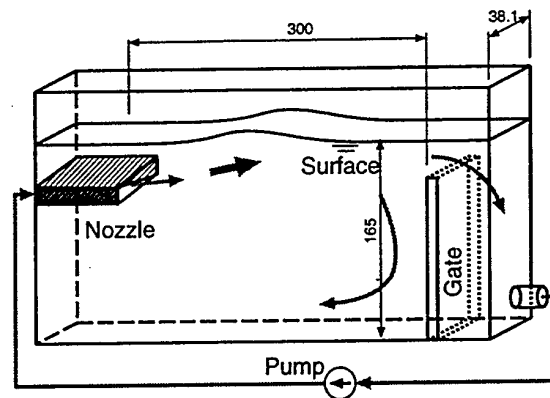


Figure 7: Schematic of Surface Experiment

reduced. However, the number of the vectors decreased rapidly. Since the illumination was two-dimensional and the flow was three-dimensional, several particles were lost in the third or fourth images, which causes the noise ratio to increase.

The improved Spring Model could reconstruct the velocity field even from the noisy images and large displacement, with large shear and/or rotation. However, the results still contained some errors. So additional improvement of the Spring Model technique is still needed.

4. CONCLUSION

The Spring Model tracking algorithm for Particle Image Velocimetry has been improved, which can be applied to a flow field with rotation, shear and expansion. Corresponding patterns of particle clusters in the first and second image are composed. In the first image, the particles of the particle cluster are assumed to be connected by invisible elastic springs. In the second image, according to the pattern changes of the particle cluster, the invisible springs have some forces. The smallest force pattern in the second image corresponds to the original pattern in first image. Using this information, the particle movement can be tracked.

Using the temporal information, the improved Spring Model had been proposed, in order to improve the accuracy of the technique. In the technique, several serial images were analyzed. The effectiveness of the improved technique was verified with synthetic data and experimental data. The results showed a high degree of effectiveness, even from the noisy and large displacement images.

REFERENCES

- Adrian R. J., 1991, "Particle-imaging techniques for experimental fluid mechanics," *Ann. Rev. Fluid Mech.*, Vol.23, pp.261.

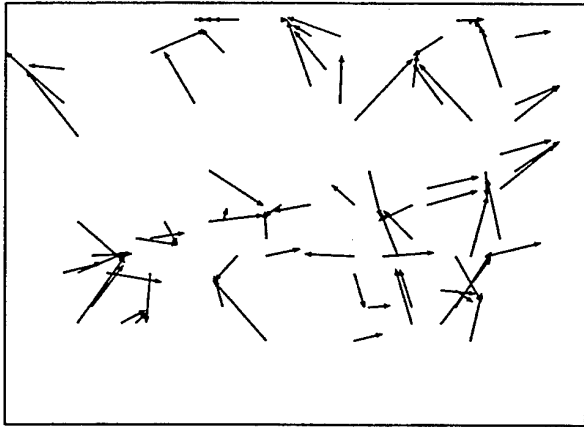


Figure 8: Results using Cross Correlation technique

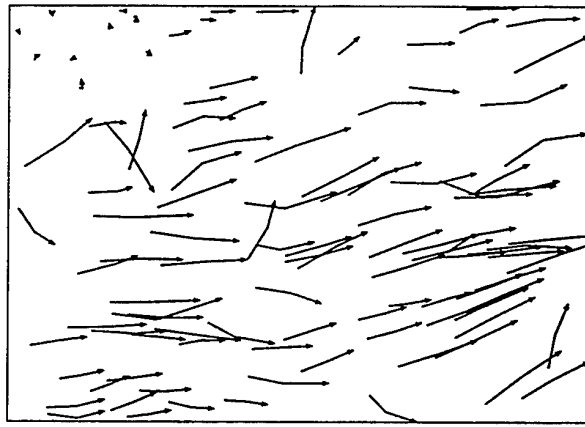


Figure 10: Results using Improved Spring Model with 3 images

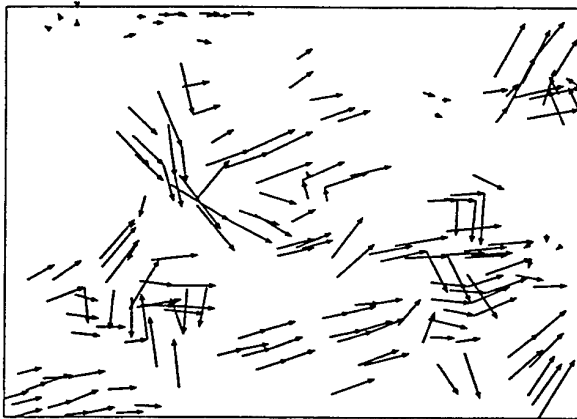


Figure 9: Results using Original Spring Model

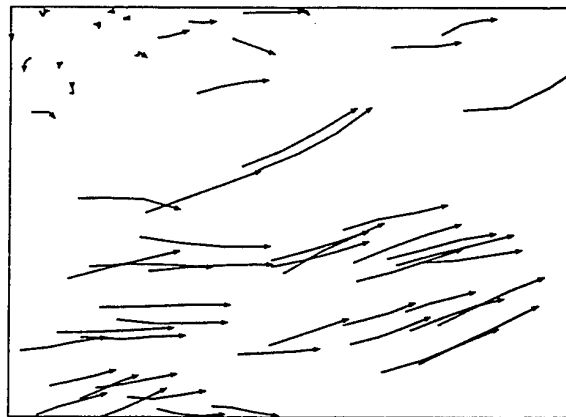


Figure 11: Results using Improved Spring Model with 4 images

Hassan Y. A., Blanchat, T. K., Seeley Jr., C. H. and Canaan, R. E., 1992 "Simultaneous velocity measurements of both components of a two-phase flow using particle image velocimetry," *Int. J. Multiphase Flow*, Vol.18, No.3, pp.371.

Nishino, K., Kasagi, N. and Hirata, M., 1989, "Three-dimensional particle tracking velocimetry based on automated digital image processing," *Trans. ASME, J. Fluid Eng.*, Vol.111, pp.384.

Okamoto, K., Hassan Y.A. and Schmidl, W.D., 1995a, "New Tracking Algorithm for Particle Image Velocimetry," *Experiment in Fluids*, Vol.19, No.5, 342-347.

Okamoto, K., Schmidl, W.D. and Hassan, Y.A., 1995b, "Spring model tracking algorithm for three-dimensional particle image velocimetry," *ASME FED*, Vol.209, 91-97.

Okamoto, K., Philip, O.G. and Hassan, Y.A., 1995c, "Measurement of the Interaction Between the Flow and the

Free Surface of a Liquid," *Proc. NURETH-7*, NUREG/CP-0142, Vol.1, 497-507.

Uemura T., Yamamoto, F. and Koukawa, M., 1990, "A High Speed Algorithm of Image for Particle Tracking Velocimetry Using Binary Picture Correlation," *J. Visualization Soc. Japan*, Vol.10, No.38, pp.196.

ERROR DETECTION IN THE ANALYSIS OF PTV IMAGES USING PROPER ORTHOGONAL DECOMPOSITION

A. Cenedese*, M. Miozzi*, G. P. Romano**

University of Rome "La Sapienza"

Via Eudossiana 18, 00184, Rome

*Dept. of Hydraulics, **Dept. of Mechanics and Aeronautics

Tel: + 39 / 6 / 44585218; Fax: + 39 / 6 / 44585217

Email: max@cenedese1.ing.uniroma1.it

ABSTRACT

The detection of errors associated with the use of PTV (Particle Tracking Velocimetry) techniques in the measurement of velocity fields in a convective flow are analysed using POD (Proper Orthogonal Decomposition). The error source is the digitisation process, leading to the acquisition of false particles and quite false images. Sensibility of POD results to false data is shown; a method to correct the velocity fields is proposed.

1. INTRODUCTION

The investigation of 2-D velocity fields in a convective flow is performed using Particle Tracking Velocimetry (PTV): it is a very useful, non invasive tool to detect large scale motion in fluid flows. Those large structures are frequently hidden into background random turbulent fields, and a wide variety of methods have been recently proposed for the eduction of simple patterns (modes) from apparently complicated flow fields: VITA (Blackwelder, R.G., 1983), Quadrant Analysis (Lu S.S., 1973), Linear Stochastic Estimation (Adrian, R.J., 1988), Wavelet Analysis (Farge M., 1992) to cite only the main ones. The POD (Karhunen-Loève decomposition) is proved to be, among the various tools, optimal in an energetic sense: POD has the maximum convergence rate and the maximum amount of energy in each element of the base. Many authors in literature have shown POD applications to numerical and experimental data: here after an application of POD decomposition to the detection of PTV measurement errors on a very long time history (about 30 minutes) is proposed: results are obtained by looking at the behaviour of fundamental modes, each one modulated with a time amplitude, and associated with a time averaged energy level.

Convective flows have been extensively studied in the past: typical subjects are Rayleigh-Bénard convection and simulations of the atmospheric boundary layer. In this

work, however, the interest is focused on a particular geometric configuration: a rectangular vessel, with adiabatic side walls and isothermal top and bottom surfaces, heated from below by a linear element. Similar configurations have been analysed in literature, both numerically (Desrayaud, G. et al., 1993) and experimentally (Moses et al., 1993, Merzkirch et al., 1994): the main pattern of the flow consists on two counter rotating vortices originating from the heating element and filling the whole tank. With the imposed boundary conditions and control parameters, this configuration starts to oscillate on a vertical plane (quasi-bidimensional flow), in an almost regular fashion. If the control parameters are increased, the flow shows a chaotic behaviour. Power spectra of some measured quantities (i.e. horizontal or vertical component of the velocity in a point) give distinct peaks with characteristic frequencies.

In spite of the efforts performed to optimise the experimental set-up, several phenomena can take place along the measurement chain leading to erroneous measurements. In this paper two different kinds of errors are investigated: the grabbing of wrong images and the reflection of light inside the tank. The domain of influence of those errors is different from each one: the former affects the whole spatial field at time t at which the error occurs, the latter has an action on a single spatial position but it persists for all time t of the acquisition.

If no correction occurs, type-1 error leads to isolated wrong values in the time history of the velocity components in all the points of the measured field: the effect is important if the evaluation of some quantity related to the instantaneous amount of energy in the system is required. The type-1 error has no characteristic periodicity, so it doesn't affect Fourier analysis.

Type-2 error gives values for the velocity components in a single point that are completely false, appearing as a random series of data. Reflections on the perimeter of the vessel are easily cutted off, and the resulting velocity field has new boundaries embedded into the old ones; this

problem will not be treated here. Reflections inside the tank gives faulty time histories of the velocity in the point where the reflection occurs. The spatial localisation of the error restricts its action inside a neighbour of the reflection point: type-2 error will affect temporal statistics and Fourier analysis of the velocity histories. It can induce other errors on the evaluation of vorticity fields.

The eduction of those errors is achieved using POD results: modal behaviour clearly shows the time instant in which measure anomalies appears (type-1 errors) and spatial position where bad particles were recorded (type-2 errors). Manipulation of the modal coefficients suggests a way to correct PTV errors.

Unrepaired velocity fields obtained from raw data of PTV remains a good measure of the fluid behaviour: type-1 and type-2 errors has a very little global influence on the whole data.

POD sensibility to those soft presences and its capability to detect their characters are the emphasised points we are interested.

In section 2 the experimental set-up for the quasi-bidimensional convection and for PTV measurements is described. A short review on POD is presented in section 3. The detection and correction of errors in PTV is given in section 4.

2. THE EXPERIMENTAL SET-UP AND THE VELOCITY MEASUREMENT

The convective motion starts in a prismatic vessel, $D = 12$ cm (width) \times $H = 6$ cm (height) \times 10.4 cm (depth), filled

with a mixture of water and glycerol (7.5% in glycerol). Side walls (1 cm in thickness) are made of perspex (adiabatic), whereas horizontal surfaces (1 cm in thickness) are made of aluminium, and are kept at constant temperature by means of two heat exchangers (consisting of a channel system in which water at controlled temperature flows).

Convection is generated by a cylindrical element (0.8 cm in diameter), heated by an internal electrical resistance connected to a power supply: the heating element is placed at 0.3 cm from the lower surface (fig. 1). For given dimensions of the vessel, two control parameters can be defined: the Prandtl and the Rayleigh numbers. They are defined as :

$$Pr = \frac{\nu}{\kappa} \quad Ra = \frac{\beta g q H^3}{\nu \kappa \lambda}$$

where β is the thermal expansion coefficient, g is the gravity acceleration, q is the heat flux per unit length of the heating element, H is the vessel height, ν is the cinematic viscosity, κ is the thermal diffusivity and λ is the thermal conductivity. In this work the Prandtl number is $Pr=10$ and the Rayleigh number is $Ra=1.6 \cdot 10^9$. The heat flux over the whole element is $Q=24$ W (so the flux for unit length is $q=2.3$ W/cm) and the sampling time is about half an hour.

The PTV is a well known measuring technique characterised by the capability to provide the time evolution of the velocity field over the whole tested volume. It is based on the tracking of non buoyant particles (conifer pollen, 80-120 μ m in diameter), seeding the fluid (a mixture of water and glycerine) on a measurement plane.

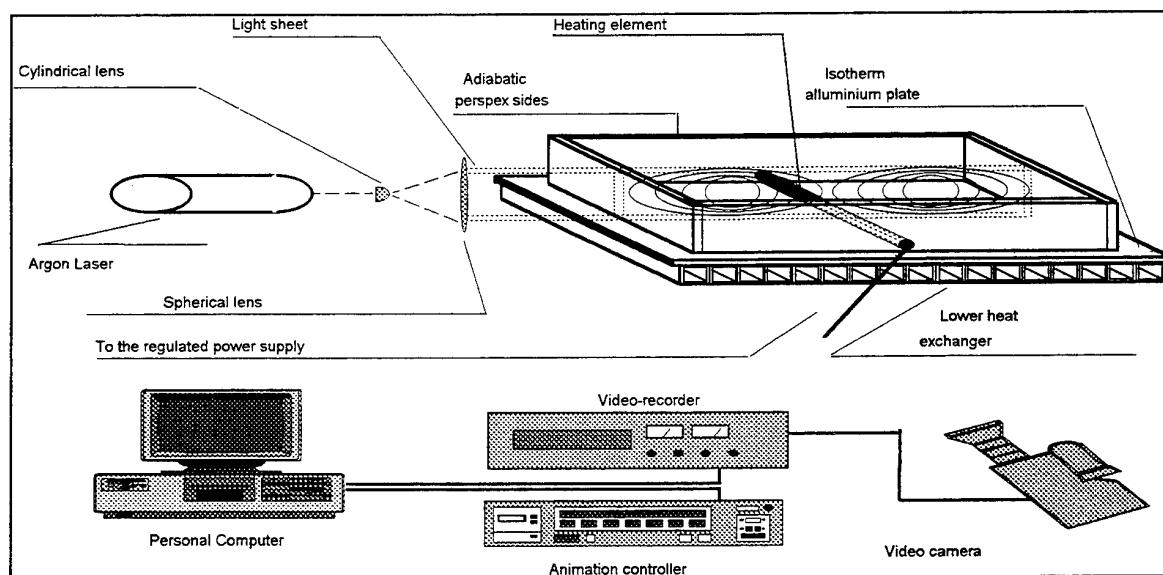


Fig. 1: The experimental set-up

This plane is obtained using a light sheet by an argon laser and it is placed on the middle of the vessel, orthogonal to the heating element. Images of the particles are recorded by a CCD video camera on a S-VHS tape with a sampling frequency of 25 Hz. During the recording, an animation controller insert a code on each frame, so each frame can be individually reached during the off-line analysis. One out of every three frames is digitised, using a frame grabber with 512x512x8 bit resolution, so that the resulting sampling rate is 8.33 Hz. Images of seeding particles are recognised on each frame and centroid locations are computed and stored together with the frame code were they have been found. Using centroid locations, trajectories of seeding particles are obtained, under the conditions that the predefined maximum distance between two successive locations and the maximum difference between two successive displacements are not exceeded

(this correspond to the assumption of a maximum velocity and maximum acceleration in the investigated field). The Lagrangian description of velocity samples is used to obtain an Eulerian description of the field: the samples are interpolated and reduced to a 10 x 21 regular grid, obtained superimposing 7 successive instantaneous fields.

The final result is a series of velocity fields, given on a 210 points, at a rate of 1.19 HZ. This frequency is much greater than those involved in the convection phenomena.

In fig. 2 the mean velocity field is reported. It consists of two counter rotating vortices: the flow rises above the heat source ($x/D=0.5$, $y/D \approx 0.1$) and moves downward along the side walls. At the selected values of Prandtl and Rayleigh numbers the plume oscillates in a plane orthogonal to the line element in a quasi-two dimensional motion, as shown in figure 3 and 4.

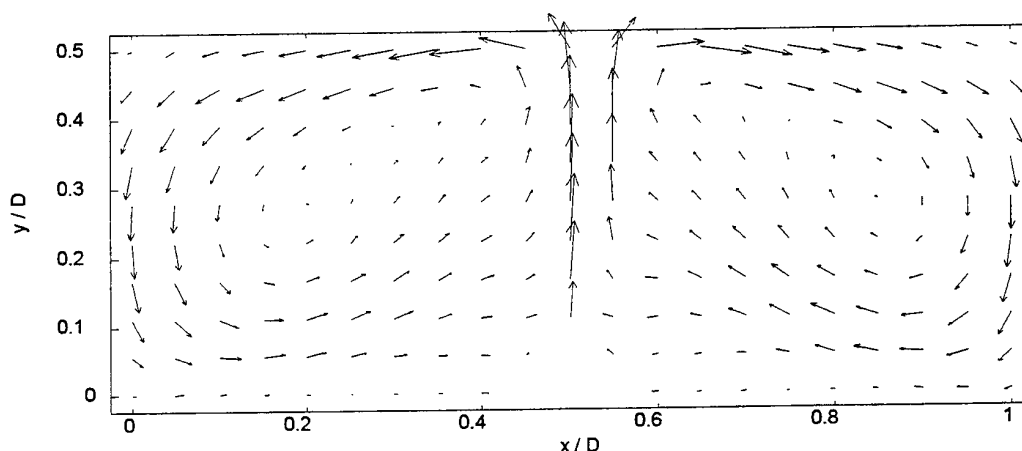


Fig. 2: Averaged velocity field.

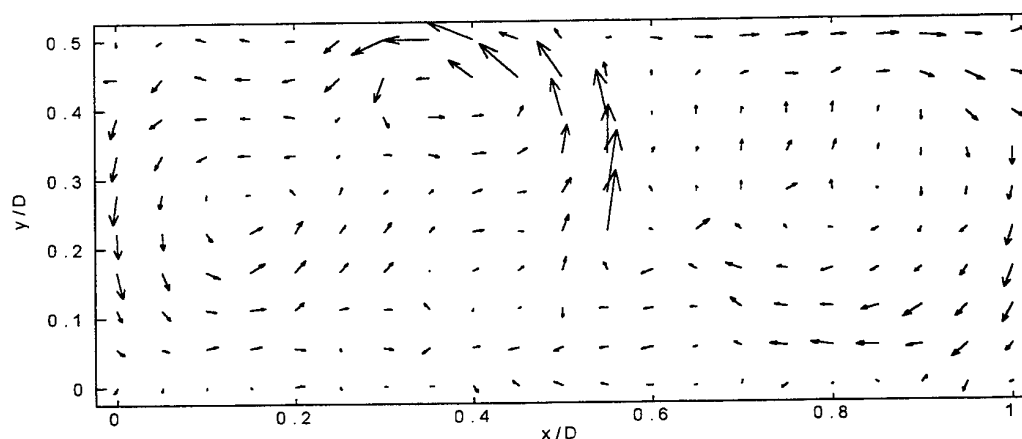


Fig. 3: Instantaneous velocity field: left swaying of the buoyant plume

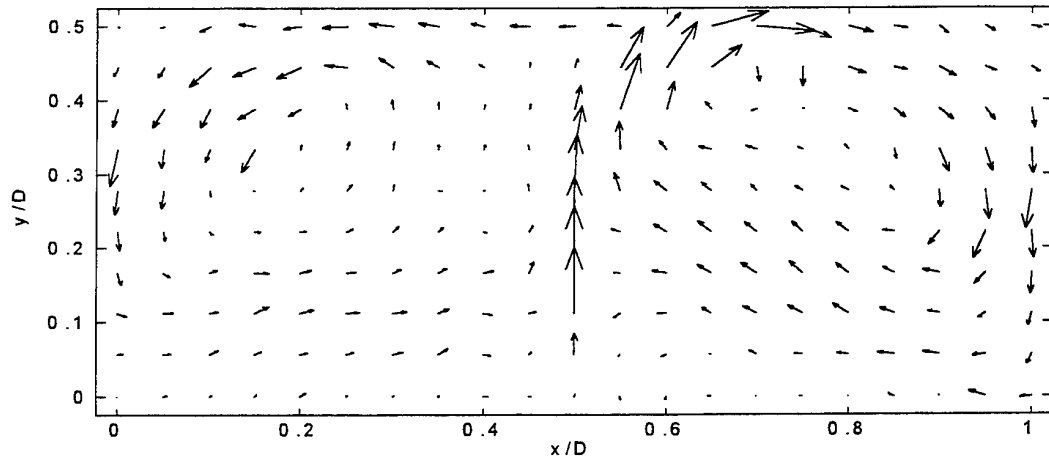


Fig. 4: Instantaneous velocity field: right swaying of the buoyant plume.

3. PROPER ORTHOGONAL DECOMPOSITION

By mean of Proper Orthogonal Decomposition (Lumley, J. L. (1967), (1981); Berkooz, G., Holmes P. and Lumley J. (1993); Sirovich, L. (1987, I, II, III); Sirovich, L., Maxey, M. and Tarman, H. (1989)) a complete set of orthonormal

functions (modes) $\{\Phi^{(n)}(\underline{X})\}$ is evaluated, together with

the corresponding set of modal amplitudes time evolution $\{a^{(n)}(t)\}$ (Miozzi, M., Querzoli, G., 1995). The POD modes are the "best correlated" functions, in an energetic sense, with the whole velocity field. They are the

eigenfunctions $\{\Phi^{(n)}(\underline{X})\}$ of the two point correlation matrix of the velocity.

From a practical point of view POD analysis is applied to PTV data on a regular grid of $n_r = 10$ rows and $n_c = 21$ columns for two velocity components ($N = 420$ degrees of freedom), by solving the Fredholm integral equation of the first kind whose symmetric kernel is the two point correlation matrix: in this way the magnitude of the projection of the eigenfunctions over the velocity fields is maximised in a mean square sense. Each eigenvalue, λ_n , can be interpreted as a measure of the mean energy of the projected flow energy onto the corresponding eigenspace (Deane, A. E. and Sirovich, L., 1991). The original velocity field, $\underline{u}(\underline{X}, t)$, can be rebuilt at each instant, using modes and modal amplitudes, i.e.

$$\underline{u}(\underline{X}, t) = \sum_n a^{(n)}(t) \Phi^{(n)}(\underline{X}) \quad (1)$$

The first few modes retain the greater amount of energy (Berkooz, G., Holmes P. and Lumley J., 1993), i.e. the first 35 modes (on 420 eigenvectors) retain about 90% of the total energy. The first mode is, in this experience, very close to the mean field. This character will be useful in the eduction of type-1 error.

The POD tool is in a practical sense without approximations and can be applied to a wide variety of turbulent flows of current interest (Sirovich, L. 1987).

4. DETECTING ERRORS IN PTV

In this work two sources of errors, rising from the PTV measurement technique, are investigated: the grabbing of wrong images and the reflection of laser light inside the tank.

The former error gives, in each single frame, false particles positions. Trajectories by PTV deteriorate in number and in quality at that time: this is due to the fact that the grabbing of the single frame is obtained by the videotape: the tape has to be stretched in the right way, so the selected frame (labelled by the animation controller) can be acquired because it is placed in front of the magnetic heads. An example of centroid evaluation on a correctly digitised frame is shown in figure 5. During present measurements, it was observed (four times on ten thousands) that the tape stopped when the magnetic heads were positioned between two frames and a wrong image was grabbed (see figure 6).

Reflections give wrong values of the velocity on corresponding points. As a matter on fact, reflections in a point are detected as the presence of a particle in that position: the tracking algorithm finds wrong values of the

velocity in that point. Time series of velocity in those points look like random values.

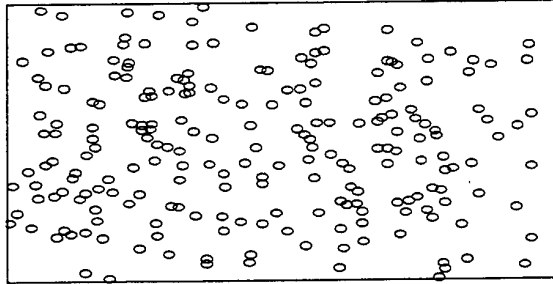


Fig. 5: an example of right digitised frame. Centroid locations are shown.

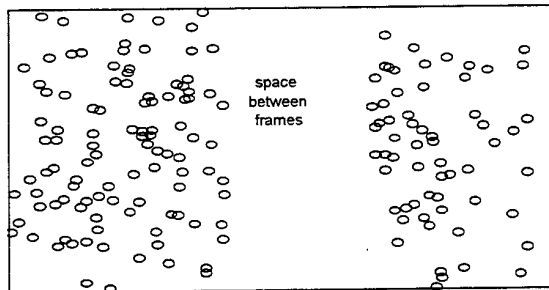


Fig. 6: An example of wrong digitised frame. Digitised image shows the space between two frames at the center.

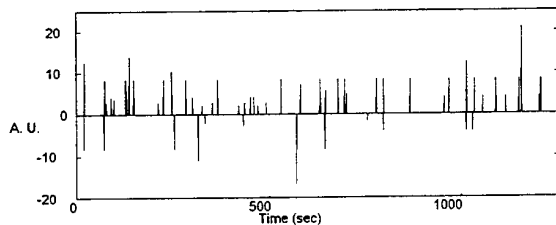


Fig. 7: Time history of the horizontal velocity near the heating element.

In the present measurements reflections on horizontal and lateral walls are removed by cutting off small strips of the original images near the boundaries of the vessel (about five pixels in width). On the other hand, reflections on the heat source (placed inside the measurement field), remain on the image, and give bad velocity values (see figure 7).

4.1 Correction of wrong digitised frames

The errors due to the acquisition of false images can be detected by means of statistics of modal amplitudes and visual observation of orthonormal functions. The time

instant at which error occurs can be established looking at the values of:

$$E(t) = \sum_n \left[a^{(n)}(t) \right]^2$$

$E(t)$ can be assumed to be the energy of the system at time t , whereas the energy retained, in a mean sense, in the single mode is (Deane, A. E. and Sirovich, L., 1991):

$$\langle a^{(i)}(t) \cdot a^{(j)}(t) \rangle = \delta_{ij} \lambda_i$$

(brackets are for time averaging).

Fig. 8(a) shows the function $E(t)$ with values between 2 and $4 \cdot 10^4$ (Y axis values are divided by 10^5), with several anomalous peaks after $t=1100$ sec. Errors in digitising images occurs only after this time, may be because the long time the videotape was working continuously.

A more readable result is obtained by looking at the mode that at time t retains the maximum amount of energy:

$$n(t) = \{ n : (a^{(n)}(t) \cdot a^{(n)}(t)) = \max (a^{(i)}(t) \cdot a^{(i)}(t)), i = 1, N \}$$

where N is the number of POD modes. Fig. 8(c) shows a zoom of $n(t)$ between $t=1100$ sec and $t=1256$ sec. The peaks of fig. 8(a) are clearly detected in fig. 8(c) as the positions at which the dominant mode in an average sense ($\lambda_1 > \lambda_i$) is not the dominant mode in instantaneous sense ($a^{(1)}(t) \cdot a^{(1)}(t) < a^{(n(t))}(t) \cdot a^{(n(t))}(t)$)

The nature of flow, which is organised in very large structures, makes the POD first mode able to retain about 70% of the total energy, except when the errors occur.

Function $E(t)$ has been evaluated also for a test function consisting of the measured velocity series in which three random fields are introduced at $t=100$, $t=200$ and $t=300$ sec, to simulate the presence of false images. The presence of those uncorrelated events is clearly depicted in fig. 8(b).

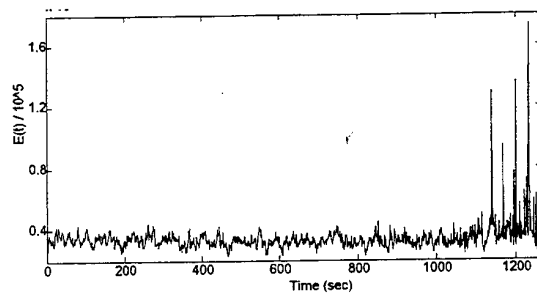


Fig. 8(a): Time history of $E(t)$

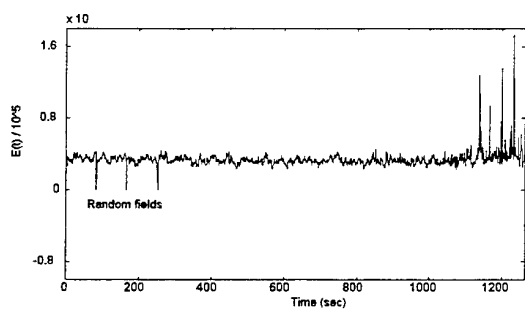


Fig. 8(b): Time history of $E(t)$ on modified data (test function). Random fields are clearly depicted. Y-values are divided by 10^5

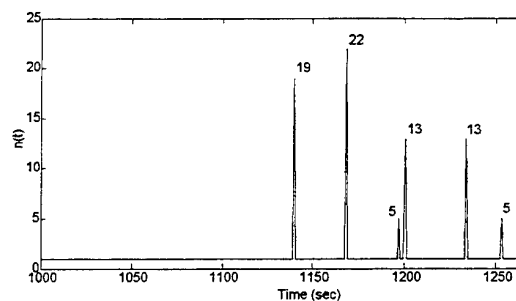


Fig. 8(c): Time history of $n(t)$ (zoom of the interesting zone)

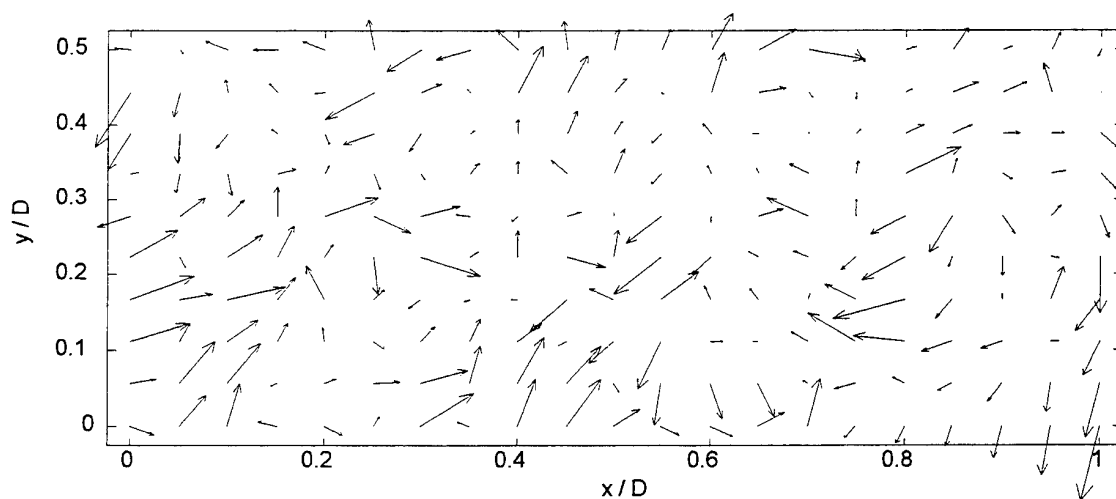


Fig 9(a): The original corrupted velocity field, obtained using false images.

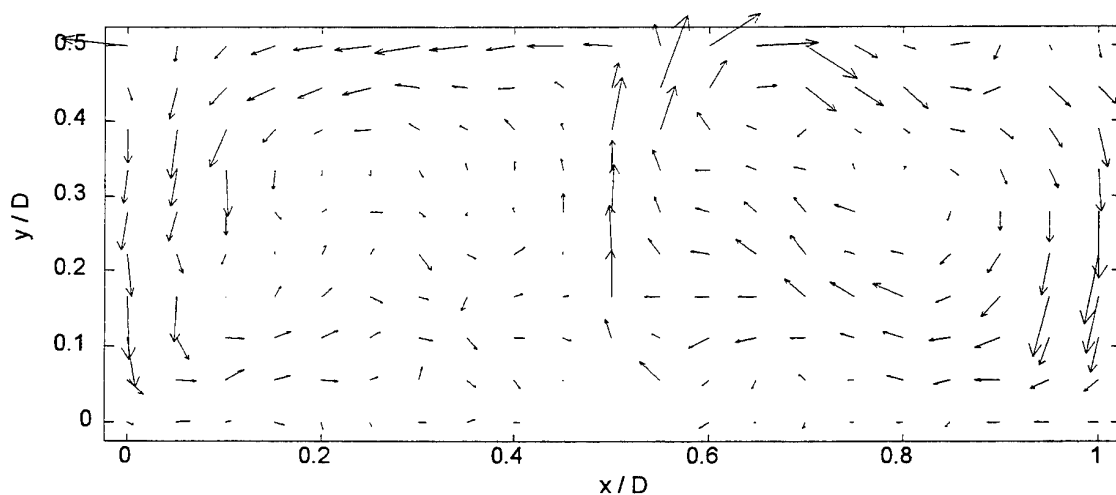


Fig. 9(b): the velocity field after correction, obtained using evaluated eigenfunctions and interpolated modal amplitudes.

On detection, a correction of errors is performed, and velocity fields are improved. In fig 9(a) a frame is plotted where the first error is present, together with the corrected one (fig. 9(b)). Correction is obtained simply by substituting to the modal amplitudes $a^{(n)}(t)$ at the instant at which a bad frame was acquired, the mean value of the modal amplitudes in the previous and successive instants. The correction is performed with an interpolation over monodimensional data: a completely new (bidimensional) velocity field is obtained taking POD modes and interpolated amplitudes. It is to notice that the eigenfunctions used to obtain this new velocity field have been found using series of data that contains false images: the correction is applied only on modal amplitudes $a^{(n)}(t)$ (see equation 1).

4.2 Correction of reflections

The detection of the errors due to reflections inside the vessel is obtained by looking at the spatial pattern of the eigenfunctions. First running of POD, applied to the raw series of data, furnish a set of modes some of them with anomalous properties. The first mode, i.e. the eigenfunction that retains the maximum amount of energy, in a mean sense, is always close to the mean field. But the second mode shows, on a weakly background field, only a 'non fluid-dynamic' vector, placed on the heating element. The same behaviour is observed for the third mode. The fourth one look like a fluid-dynamic eigenvector, but not the fifth (see figure 10(a,b)).

To solve this problem, once detected vectors in locations near the heating element are imposed to be zero, for the whole time series. Modes with isolated vectors disappear, as shown in figure 12. A test is made to clarify POD sensibility to time series of random data in a point of the velocity field.

First, the raw field is modified, near the heating element, as shown before. Then, time series of horizontal and vertical velocity in the centre of the right half of the vessel are substituted with the same random series, of zero mean and standard deviation five times higher than that of the velocity field. All the eigenfunctions obtained using POD are not modified, but a new mode, with a single vector placed in the modified position appears; the mode is classified at the second energy level (see figure 11).

The behaviour of POD in presence of random data (i.e. reflection in a point of the measure field and false centroid velocities) can be thought as the capability to retain

phenomena that are correlated with themselves, but unrelated to all the others. The high value of standard deviation of the random series used in the test makes those results more readable, because of the high value of energy retained in the corresponding mode.

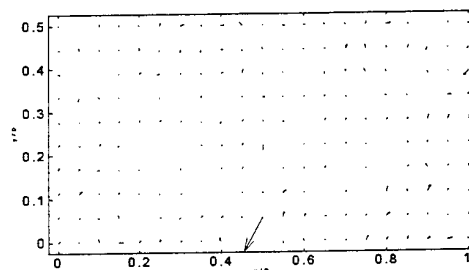


Fig. 10(a): Reflections:non fluid-dynamic POD mode. Second mode.

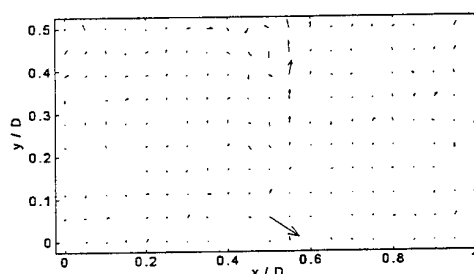


Fig. 10(b): Reflections:non fluid-dynamic POD mode. Third mode.

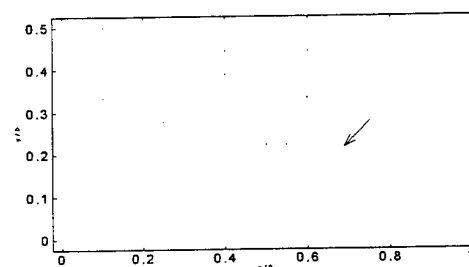


Fig. 11: the presence of the same random series for horizontal and vertical velocity in a point is retained completely in the second mode.

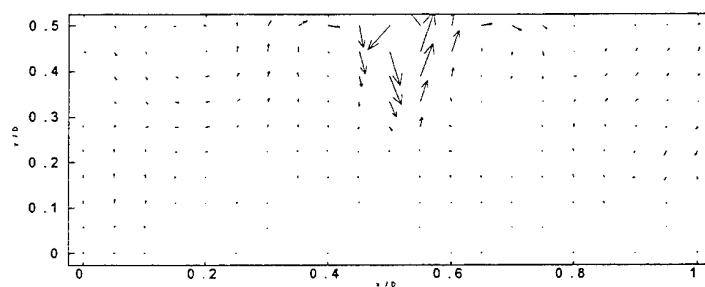


Fig. 12(a): the second mode evaluated with modified time series of velocity near the heating element.

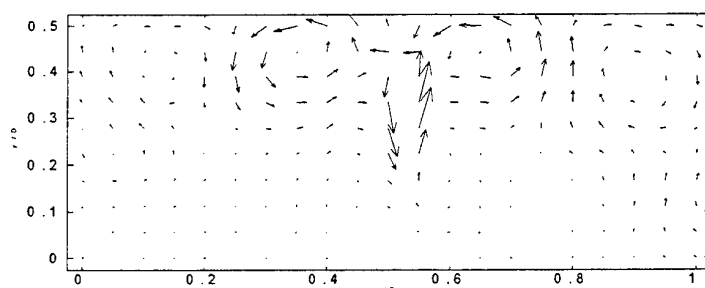


Fig. 12(b): the third mode, with the modified time series near the heating element.

Bibliography

- Adrian, R. J. (1988): Linking correlations and structure: stochastic estimation and conditional averaging. In: Near Wall Turbulence-Zoran Zaric Memorial Conf. pp. 420-436, Hemisphere Publishing Corporation.
- Berkooz, G., Holmes P. and Lumley J.(1993): The proper orthogonal decomposition in the analysis of turbulent flows. Annual reviews in Fluid Mechanics, vol. 25, pp. 539-575.
- Blackwelder, R. J. and Haritodinis, J. H. (1983): Scaling of the bursting frequency in turbulent boundary layer. Jour. Fluid Mech, vol. 132, p.87.
- Deane, A. E. and Sirovich, L. (1991): A computational study of Rayleigh Benard convection. Part 1. Rayleigh number scaling. Jour. Fluid Mech, vol. 222, pp. 231-250.
- Desrayaud, G. and Lauriat, G. (1993): Unsteady confined buoyant plumes. Journ. Fluid Mech, vol. 252, pp. 617-646.
- Farge, M. (1992): Wavelet transform and their applications to turbulence. Annu. Rev. Fluid Mech., vol. 24, pp. 395-457.
- Lu, S. S. and Willmarth, W. W. (1973): Measurements of the structure of the Reynolds stress in a turbulent boundary layer. Jour. Fluid Mech, vol. 60, p. 481.
- Lumley, J. L. (1967): The structure in inhomogeneous turbulence. In: A. M. Yaglom and V. I. Tatarski (ed.), Atmospheric turbulence and wave propagation. Moscow: Nauka, pp. 166-178.
- Lumley, J. L. (1981): . Coherent structures in turbulence. In: R. E. Mayer (ed.) Transition and turbulence New York: Academic, pp. 215-242.
- Merzkirch W., Mrosewski T., Wintrich H. (1994): Digital particle image velocimetry applied to a natural convective flow. Acta Mechanica, vol. 4.
- Miozzi, M., Querzoli, G. (1995): PTV and POD analysis of the instabilities in a quasi two dimensional convective flow. Submitted to Applied Scientific Research.
- Moses E., Zocchi, G., Libchaber, A. (1993): An experimental study of laminary plumes. Journ. Fluid Mech, vol. 251,
- Sirovich, L. (1987): . Turbulence and the dynamics of coherent structures. Part I: Coherent structures. Quarterly of applied mathematics, vol. XLV, 3, pp.561-571
- Sirovich, L. (1987): . Turbulence and the dynamics of coherent structures. Part II: Symmetries and transformations. Quarterly of applied mathematics, vol. XLV, 3, pp.573-582.
- Sirovich, L. (1987): Turbulence and the dynamics of coherent structures. Part III: Dynamics and scaling. Quarterly of applied mathematics, vol. XLV, 3, pp.583-590.
- Sirovich, L., Maxey, M. and Tarman, H. (1989): An eigenfunction analysis of turbulent thermal convection. In: Turbulent shear flow 6. Springer-Verlag Berlin Heidelberg, pp.68-77.

SESSION 28

Aerodynamics and Rotating Machines III

Experimental aspects of PIV measurements of transonic flow fields at a trailing edge model of a turbine blade

M. Raffel, H. Höfer, F. Kost, C. Willert, J. Kompenhans

Institut für Strömungsmechanik
Deutsche Forschungsanstalt für Luft- und Raumfahrt (DLR)
Bunsenstraße 10, D-37073 Göttingen, Germany

ABSTRACT

PIV measurements have been performed in order to achieve quantitative information of the interaction between the transonic flow field at the trailing edge model of a turbine blade and the mass flow of cooling air ejected out of the trailing edge. The structure of the wake and of the trailing edge shock system have been determined for various mass flow rates at two different outlet Mach-numbers. The PIV technique offers special advantages for the investigation of transonic flow fields, but also yields to special experimental difficulties.

1 INTRODUCTION

Reduction of fuel consumption and carbon dioxide emission are two main objectives in gas turbine research. These goals can be achieved by further increasing operating temperatures. However, higher gas temperatures require new materials and/or internal cooling of turbine blades. Due to high mechanical loads in high pressure stages of gas turbines, trailing edges of turbine blades can not be built as thin as desired for reduction of viscous losses. The design of thin turbine blades is additionally complicated if integration of cooling flow is required. The wake of thick trailing edges causes significant losses especially in transonic flows.

In Figure 1 a schlieren image is shown in which a trailing edge (left hand side), a neighbouring blade surface (lower edge), and typical features of the flow without air ejection are shown. The expansion fans, the subsequent oblique compression shocks, the reflection of one of the shocks by a shock boundary layer interaction at the surface of the neighbouring blade, and the formation of a vortex street can be seen.



Figure 1: Schlieren photography of the trailing edge wake of a transonic turbine blade at $Ma_2 = 1.25$.

Such flow phenomena were investigated during many different experiments and numerical simulations (Meyer 1972, Dietrichs et al. 1987, Sieverding et al. 1980, Kiock et al. 1986). However, an ejection of cooling air at the trailing edges is

expected to cause significant changes of the flow. Knowledge of the interaction between the mass flow rate of the ejection of cooling air and the flow field around the trailing edge is therefore of great importance. The goals of our investigations were: quantitative determination of the structure of the wake and of the trailing edge shock system at various mass flow rates of the ejected cooling air. Additionally, the experimental results are supposed to yield comprehensive information for optimization and validation of numerical codes for two-dimensional numerical simulations, which shall serve as a tool for blade design in future. Therefore, two-dimensional velocity data were required in a plane on the center line of a turbine blade trailing edge model. The use of pressure or hot-wire probes for velocity or pressure measurements was unsuited as they cause disturbances of the flow field to be investigated, especially in transonic flows. This can be avoided by using non-intrusive optical methods like Laser Doppler Velocimetry (LDV). In case of unsteady flows, or if the measurements have to be done in short time, LDV measurements are difficult since they have to be performed pointwise. Therefore, the measurements described here have been performed by means of Particle Image Velocimetry (PIV). This technique was found to be well suited, as the investigations had to be carried out for several Mach-numbers and mass flow rates of the cooling air within very short time intervals. The instantaneous recording of the flow velocity fields does not only save tunnel operating time and costs, but also enables to study instationary effects. However, the PIV technique does not only offer special advantages, but also yields to special experimental difficulties. Both will be described in this article.

2 EXPERIMENTAL FACILITY

Wind tunnels usually used for the study of plane turbine cascades allow only small models (e.g. EGG of DLR in Göttingen: chord $c_t = 60$ mm, spanwidth $s = 125$ mm). Since thick trailing edges were needed for adequate instrumentation with pressure probes, our experiments have been conducted in a larger facility. The configuration used was similar to the one described by Sieverding et al. (1980). Systematic measurements in straight cascades of the afore mentioned authors have shown a strong correlation between the pressure at the base of the trailing edge and the outlet pressure. They have demonstrated that such a simulation of the trailing edge flow without cooling air ejection yields realistic results. Schlieren images and pressure measurements of a symmetric flow field at an enlarged trailing edge model with cooling air ejection have been performed by Motallebi and Norbury (1981), in order to investigate the relationship between the vortex formation and the base pressure. Their schlieren images show the flow phenomena at the trailing edge in great detail. It has been shown, that a Karman vortex street can only be observed for low mass flow of cooling air.

The turbine blade trailing edge model was set up in the high-speed blow-down wind tunnel (HKG) of DLR in Göttingen. Transonic flow velocities were obtained by sucking air from an atmospheric intake into a big vacuum tank. A quick-acting valve, located downstream of the test section, is quickly opened to start the flow. Ambient air, which is dried before entering the test chamber, flows for max. 20 seconds through a test section with 725 mm spanwise extension. Grids in the settling chamber and a high contraction ratio of more than 20:1 lead to a low turbulence level in the test section.

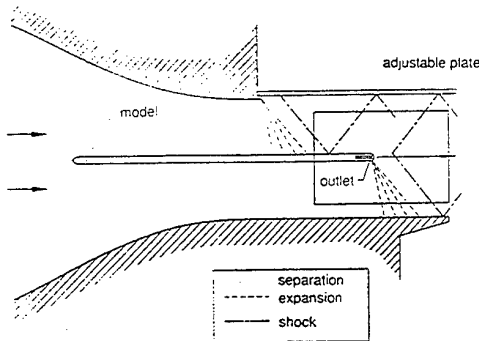


Figure 2: Diagram of model and wind tunnel geometry.

Figure 2 shows the trailing edge model in the wind tunnel. Due to specially adapted wind tunnel walls above and below the model, and an adjustable tailboard above the model, the flow field with structures as described in the following could be obtained. On the lower side of the model the flow accelerates continuously down to the trailing edge. On the upper side the Mach number distribution has positive and negative gradients. Downstream of the smallest cross section Mach number values between $Ma = 0.9$ and $Ma = 1.8$ can be observed depending on the prior defined angle of the tailboard. The expected flow phenomena are shown in Figure 2.

The step between the contour of the upper wall of the nozzle and the tailboard simulates the trailing edge of the neighbouring cascade blade. The step generates an expansion fan and the subsequent oblique compression shock. The tailboard can be adjusted to a predefined angle, which defines the outlet flow direction and therefore also the outlet Mach-number downstream of the model trailing edge. The tailboard angle also determines the maximum Mach-number and the strength of the shock impinging on the upper surface of the model. The upper side of the blade therefore simulates the suction side of the turbine blade downstream the smallest cross-section, whereas the lower side represents the pressure side. The planar section of the lower nozzle contour is to simulate the suction side of the next blade of the cascade.

3 MEASUREMENT TECHNIQUE

Our experimental set up of a PIV system for application in aerodynamics consists of several subsystems. First of all *tracer particles*, generated by an aerosol generator, have to be added to the flow. These particles have to be *illuminated* in a plane of the flow two times within a short time interval. The light scattered by the particles has to be *recorded*. The displacement of the particle images between the two light pulses has to be determined at the *evaluation* of the PIV recordings. In order to

be able to handle the great amount of data, which are collected by employing the PIV technique, a sophisticated *post processing* system is required. A summary of the theoretical and experimental aspects of the PIV technique is given by Adrian (1991).

3.1 TRACER PARTICLES

First applications of PIV have already shown that difficulties appear to provide high quality seeding in high speed air flows compared to applications in water flows or in low speed air flows (Höcker & Kompenhans 1991, Towers et al. 1991, Humphreys et al. 1993, and Molezzi & Dutton 1993). High speed air flows require small tracer particles in order to minimize the velocity lag. This problem is discussed in literature intensively (Hunter & Nichols 1985, Melling 1986, and Meyers 1991). However, by decreasing the particle size the light scattered by the particles will be reduced considerably. Thus, a modern high power pulse laser is necessary for recording of tracer particles with a diameter of one micron or less. A much larger volume has to be seeded for PIV than for LDA as the flow velocity is not only measured at a single point but in a whole plane. Moreover, at PIV there should be no gaps in the seeding, as this would lead to data dropout in the instantaneous velocity field. It is known from simulations of the PIV evaluation process, that typically 15 particles per interrogation volume are essential for a high quality evaluation (Keane & Adrian 1990). In order to keep constant the number of particles per PIV recording, more particles have to be added to the flow with increasing flow velocity. Thus, a powerful aerosol generator is required for transonic flows. For our experiments we have utilized several Laskin nozzles in parallel. This proved to be sufficient to seed a large stream tube surrounding the model and the observation area. Finally we could attain a high density of tracer particles of the order of up to 4 particles/ mm^3 (this corresponds to ≈ 30 particles per interrogation volume) during the experiments. The aerodynamic diameter of the olive oil particles was about $1 \mu\text{m}$ (Schäfer 1995). It is well known from LDA measurements in large wind tunnels and in high speed flows, that the size and the distribution of the tracer particles may change during the travel from the aerosol generator to the seeding device in the settling chamber of the wind tunnel and, finally, to the test section, where the measurements take place. It is therefore advisable, to provide information about the particles and especially about the velocity lag directly from the observation area. This has been done during prior tests in a transonic flow field around a bluff cylinder in the same wind tunnel (Kompenhans & Raffel 1993). This test showed that it does not make much sense to utilize tracer particles with a diameter much smaller than $1 \mu\text{m}$ for such experiments, because the spatial resolution of the velocity measurement is not limited by the response of a particle to a velocity gradient, but due to the fact that during the evaluation of a PIV recording the velocities are averaged within each interrogation spot (width of a shock \approx a few micrometers, width of an interrogation volume \approx a few millimeters). Smaller tracer particles would be necessary only, if e.g. a higher spatial resolution in the vicinity of the shock would be required.

In contrast to prior high speed PIV applications, the measurements described here were additionally complicated by the fact that the air ejected from the trailing edge had also to be seeded. Therefore, tracer particles had to be generated against a

pressure level of 4 bar. The seeded air passed a distributor system that contained tiny nozzles inside the model where supersonic flow conditions were obtained. Therefore, some particles have been precipitated inside the model and have left the outlet from time to time in form of larger droplets. Recordings on which those droplets have been observed have not been evaluated. Figure 3 shows a part of a PIV recording obtained at $Ma_2 = 1.27$ and a mass flow rate of 1.4%. On the left hand side parts of the contour of the trailing edge model can be seen twice due to image shifting applied between both exposures. The recording further illustrates some of the above mentioned problems: Varying intensity of the particle images due to droplet formation inside the ejected air stream and a reduced seeding density directly above and below the model due to the influence of the boundary layers along the plate.



Figure 3: A part of a PIV recording at $Ma_2 = 1.27$ with the model contour on the left hand side.

3.2 Illumination system

A double oscillator Nd:YAG pulse laser was used for illumination. The output energy was approximately 2×40 mJ during these measurements. This energy was sufficient to illuminate a sheet with a height of 20 cm, when recording the light scattered by the $1 \mu\text{m}$ particles on a highly sensitive photographic film. The time delays Δt between the two laser pulses was set to $4 \mu\text{s}$ for these experiments. The optical access to the test section was complicated by the fact that the test chamber of the wind tunnel is generally on a pressure level below the atmospheric pressure during the tunnel run. Therefore, the laser was located outside the tunnel, whereas the light sheet optic was mounted onto the floor of the test chamber. The light was directed into the tunnel through a small orifice in the wall. The optical path between laser and observation area had a length of more than 5m. The last mirror was located 1.5 m downstream of the model and close to the shear flow of the open test section. The size of the observation area was approximately $100 \times 150 \text{ mm}^2$. The light sheet thickness was adjusted to $\sim 0.5 \text{ mm}$. The sheet was oriented normal to span direction in mid span.

3.3 Recording

A PIV system for application in wind tunnels also requires some special developments, which are not commercially available. One major problem is associated with the limited amount of light scattered by the small tracer particles. Typically, the depth of focus at recording is of the order of 1 mm in our experiments, which means that the intensity of the light as scattered by out-of-focus particles is not high enough to expose the photographic material sufficiently.

Focusing

Already first PIV experiments in large wind tunnels have shown that a high quality and reliable fast focusing device is absolutely necessary, in order to save time at the alignment of the system. For this purpose our photographic 35 mm camera is equipped with a device for fast focusing (Kompensans & Raffel 1993). A CCD sensor with high spatial resolution was mounted in the viewfinder of a SLR camera, yielding an image of a small part in the center of the observation area. The position of the CCD sensor is carefully aligned in such a way that the distance between lens and sensor via the mirror is exactly the same as from the lens to the film plane. The distance between light sheet and film plane can be changed by moving the complete camera system by means of a traversing table, thereby observing for minimum diameter of the particle images on a TV monitor.

Diffraction limits, spherical aberration, and depth of field

This section provides a description of diffraction limited imaging, which is an problem of practical significance in the study of optical instrumentation, and of particular interest for PIV recording in aerodynamics. The image of a distant point source (e.g. a small scattering particle inside the light sheet), is never a point. It is a diffraction pattern even if it is formed by a perfectly aberration-free lens (Hecht & Zajac 1974). The small tracer particles used in aerodynamic investigations scatter only little light resulting in low exposures of the photographic film in form of circular particle image patterns, which are known as the Airy disks.

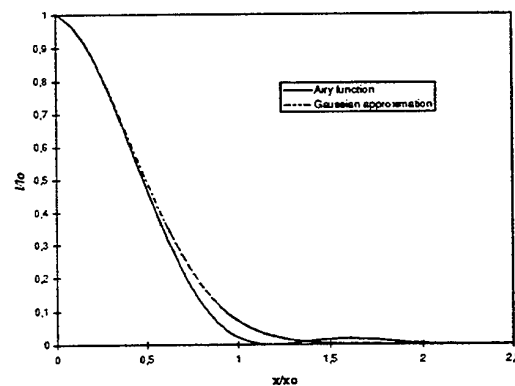


Figure 4: Normalized intensity distribution of an Airy pattern and its approximation by a Gaussian bell curve.

The solid line in Figure 4 represents the normalized circular symmetric intensity distribution of an Airy pattern. This function represents the impulse response of an aberration-free lens, the so called point spread function. As can be seen the central disk is surrounded by a dark ring, which can be used to define the extent of the Airy disk. This ring corresponds to the first zero of the first order Bessel function.

In Figure 4 the value of the radius of the ring and therefore of the Airy disc can be found.

$$(I/I_0 = 0) \Rightarrow \frac{d_i}{2x_0} = 1.22 \quad (3.3.1)$$

$$\text{wherein } x_0 = \lambda \cdot A / Da$$

The focus criterion ($A = f(M+1)$) yields the minimum diameter of an image:

$$d_i = 2.44 \cdot f_{\#}(M+1) \cdot \lambda, \quad (3.3.2)$$

where M is the magnification and $f_{\#}$ the focal length f divided by the aperture diameter Da (for details see Goodman 1968).

In practice the point spread function is often approximated by a normalized Gaussian curve also shown in Figure 4 and defined by:

$$\frac{I}{I_0} = e^{-\frac{x^2}{2\sigma^2}}, \quad (3.3.3)$$

wherein the parameter must be set to $\sigma = f_{\#}(1+M)\lambda\sqrt{2}/\pi$, in order to approximate diffraction limited imaging without spherical aberration (for details see, e.g. Westerweel 1993). This approximation is particularly useful because it allows a considerable simplification of the mathematics encountered in the derivation of modulation transfer functions, which also includes other kinds of aberrations as will be described later.

In PIV, the minimum image diameter d_i will be obtained only, when recording small particles at small magnifications. For larger particles and/or larger magnifications the influence of geometric imaging becomes more and more important. The image of a finite-diameter particle is given by the convolution integral of the point spread function with the geometric image of the particle. Approximating both functions leads to the following formula for the image diameter (Adrian & Yao 1985):

$$d_{pi} = \sqrt{d_g^2 + d_i^2}, \quad (3.3.4)$$

wherein $d_g = M d_p$ if the lens is well focused. The following formula can be used to estimate the enlargement of the geometric image diameter Δd_g of an image point as a function of the difference between object distance employed and object distance needed for sharp imaging ΔB .

$$\Delta d_g = \frac{M^2 \Delta B}{f_{\#}(M+1)} \quad (\text{after Solf 1975}) \quad (3.3.5)$$

The following formula can be used to estimate the depth of field, if assuming that an enlargement of the geometric image diameter Δd_g smaller than the minimum diameter due to diffraction limited imaging d_i can be tolerated:

$$\delta_z = 2 f_{\#} d_i (M+1)/M^2 \quad (3.3.6)$$

Table 1: Values for diffraction limited imaging
($\lambda = 532 \text{ nm}$, $M = 1/4$, $d_p = 1 \mu\text{m}$).

$f_{\#}=f/D_a [1]$	$d_{pi} [\mu\text{m}]$	$\delta_z [\text{mm}]$
2.8	4.7	0.5
4.0	6.6	1.1
5.6	9.1	2.0

Some typical values for the diffraction limited imaging of small particles ($d_p \approx 1 \mu\text{m}$) are shown in Table 1 (calculated with a wavelength of $\lambda = 532 \text{ nm}$, a magnification of $M = 1/4$). It can

be seen in Table 1, that a large aperture diameter is needed to get enough light from each individual particle within the light sheet, and to get sharp particle images, because the size of the diffraction pattern can be decreased by increasing the aperture diameter. Unfortunately a big aperture diameter yields a small focal depth which is a significant problem when imaging small tracer particles.

In practice there are two good reasons for minimizing the particle image diameter:

First, a detailed analysis of PIV evaluation shows, that the error in velocity measurement δ_u underlies a type of *uncertainty principle*, i.e.:

$$\delta_u \Delta x_{max} = c u_{max} d_{pi}, \quad (\text{Adrian 1986a}) \quad (3.3.7)$$

wherein $\Delta x_{max} = c u_{max} \Delta t$ is the spatial uncertainty in the location of the velocity measurement, fixed by the maximum velocity range spanned by the instrument. For a given maximum velocity u_{max} , the uncertainty is minimized by minimizing both the image diameter d_{pi} and the uncertainty in locating its centroid, represented by c .

Second, sharp and small particle images are particularly essential in order to obtain a high particle image intensity I , since the light energy per unit area increases with decreasing image areas ($I \sim 1/d_{pi}^2$). If the light energy contained in a single particle image is spread over a large area it might not expose the sensor or film sufficiently.

Since lens aberrations have a great influence on the recording of small objects, high quality lenses are essential for PIV. A useful parameter in evaluating the performance of a lens system is the contrast or image modulation defined by the following equation:

$$Mod = \frac{I_{max} - I_{min}}{I_{max} + I_{min}}. \quad (3.3.8)$$

The measurement of the ratio of image modulation *Mod* for varying spatial frequencies yields the modulation transfer function (MTF). The modulation transfer function has become a widely used means of specifying the performance of lens systems and films (Hecht & Zajac 1974) and can be used to analyse the influence of lens aberrations on the PIV recording.

In practice an approximation of the MTF can be obtained by an inverse Fourier transformation of the point spread function. Using the Gaussian approximation given by Eq. (3.3.1) and shown in figure 4 greatly simplifies this transformation. In the following the equations will be given in one-dimensional representation in order to simplify their derivation. The Fourier transformation of a one-dimensional Gaussian function is given by:

$$\sigma \sqrt{2\pi} e^{-2\pi^2 \sigma^2 r^2} \xleftrightarrow{F} \frac{1}{\sigma \sqrt{2\pi}} e^{-\frac{x^2}{2\sigma^2}}, \quad (3.3.9)$$

wherein r is the spatial frequency in line pairs per millimeter.

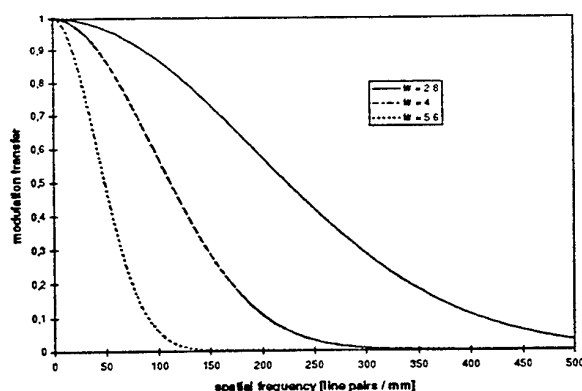


Figure 5a: Image modulation versus spatial frequency for three hypothetical lens systems without spherical aberrations (Gaussian approximations).

Figure 5a shows a plot of image modulation versus spatial frequency for three apertures of a hypothetical lens system without lens aberrations as obtained by the inverse transformation of the Gaussian approximation. Although the shape of such curves only roughly approximates the shape of the real functions the qualitative behaviour can clearly be seen.

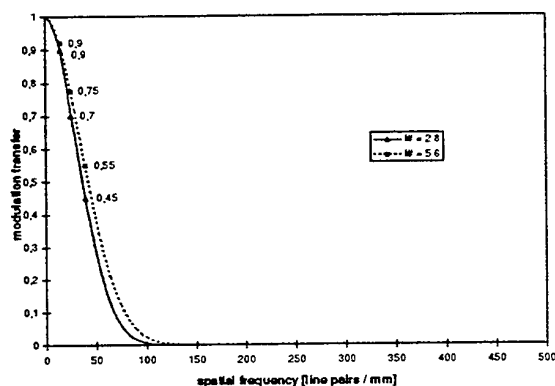


Figure 5b: Measured values of image modulation versus spatial frequency for a high quality 100 mm lens together with a Gaussian fit.

However, considering lens aberrations yields a complete change of the modulation transfer functions especially when using small f-numbers. This can be seen in Figure 5b where measured values of the lens used for these PIV measurements (ZEISS Makro-Planar T* 100mm f/2.8) are shown together with a Gaussian curve through the value measured at the highest frequency. Such values of the modulation transfer are often given in the data sheets of a lens system for different f-numbers and magnifications or can easily be estimated when studying diagrams of the modulation versus the image height. From our experience those values can be used for a rough estimation of the image diameters to be expected, regardless of the fact that they were originally measured using white light and therefore also consider chromatic aberrations. If, we assume that the MTF can be described by the inverse Fourier transform of the Gaussian approximation of the normalized image intensity distribution I/I_0 , it can be written in normalized form as:

$$\tilde{M}_{TF} = e^{-2\pi^2 \sigma^2 r'^2} \quad (3.3.10)$$

The modulation transfer value of the highest spatial frequency has been taken to determine σ and therefore a function through a point in the MTF (e.g. $\tilde{M}_{TF}(r') = 0.55$ at $r' = 40$ lp/mm):

$$\sigma = \sqrt{\frac{-\ln(\tilde{M}_{TF}(r'))}{2\pi^2 r'^2}} \quad (3.3.11)$$

Now, Eq. (3.3.3) can be used to approximate the normalized intensity distribution of an image of a small object. In contrast to the Bessel function the Gaussian approximation has no zero-crossings (Fig. 4). An image diameter can therefore not be determined by taking the x-value of the first zero. This requires to define some kind of threshold level for further theoretical analysis. In photographic PIV this threshold level represents the start of the nonlinear behaviour of the film materials used for recording and contact copy. As described by Pickering and Halliwell (1984), a contact copy is normally used to reduce the effects of the film fog and other background noise for subsequent optical evaluation. In digital PIV a certain threshold is normally used because of electronic background noise. In practice every particle image has a different intensity due to different particle sizes, observation angles, and a locally varying illumination intensity. Therefore, a constant threshold level will clip each particle image at a different level of the normalized intensity I/I_0 . This explains varying particle image diameters in spite of identical imaging conditions of very small particles. However, in order to estimate the mean particle image diameter we assume that the lower 20% of the intensity of an image will not be used for evaluation. This assumption and Eq.(3.3.3) yield the following formula for half the width of an image respectively the radius of a particle image:

$$x' = \sqrt{-2\sigma^2 \ln(0.2)} \quad (3.3.12)$$

In order to obtain an approximation of the half image width for a line with the width of $\frac{1}{2r'}$ we substitute Eq. (3.3.11):

$$x' = 0.8 \sqrt{\frac{-\ln(\tilde{M}_{TF}(r'))}{r'^2}} \quad (3.3.13)$$

For the estimation of objects which are small compared to the line width $\frac{1}{2r'}$ Eq. (3.3.4) can be used to obtain:

$$d_i \approx \sqrt{0.64 \frac{-\ln(\tilde{M}_{TF}(r'))}{r'^2} - \left(\frac{M}{2r'}\right)^2} \quad (3.3.14)$$

The definition of a MTF is a practical approach to describe optical processes, which in reality are much more complex. The description would be more complete when considering also the commensurate relative phase shift over varying frequencies in form of the phase transfer function PTF. However, phase shifts in optical systems occur only off axis and therefore for most problems the PTF is of less interest than the MTF (Hecht & Zajac 1974).

For many practical applications the overall MTF of an optical system can be assumed to be simply the product of the MTF's

of the individual components. Therefore, the value of the film MTF at r' can be multiplied with lens MTF value for the same spatial frequency and Eq. (3.3.14) can be used to estimate the image diameter for a given recording condition. Practical experience has shown that the resolution of a film with high sensitivity (3200 ASA) and a modulation transfer of $\approx 80\%$ at 40 line pairs / mm can be used to perform high quality PIV measurements even in case of difficult recording conditions (Kompenhans & Raffel 1993). The image diameter estimated by formula (3.3.14) is $\approx 20\mu\text{m}$ ($M = 1/4$, $f_s = 2.8$) and is in good correspondence with image diameters found during the experiments.

However, inspecting the PIV recordings of this experiment under the microscope has shown that sharp particle images can not be found in the vicinity of the oblique shocks and close to the trailing edge. In a very small area where the oblique shocks are imaged no particle images could be observed at all. This area did not lead to a significant data drop out, since its width was small with respect to the width of the interrogation window. More severe problems occur in the area directly behind the trailing edge. Only few and and large particle images were found here (see Fig. 3). From schlieren images (see Fig. 1) and pressure measurements it is known that very high density gradients appear there.

In order to estimate the influence of the density variations in the flow field onto imaging we determine the variation of the refractive index Δn using the Gladstone-Dale equation:

$$n - 1 = G(\lambda) \cdot \rho \quad (3.3.15)$$

wherein $G(\lambda)$ represents the Gladstone-Dale-number and ρ the density of the fluid. $G(\lambda)$ for our laser light ($\lambda = 532\text{nm}$) has been estimated by formula :

$$G(\lambda) = 2.2244 \cdot 10^{-4} \frac{\text{m}^3}{\text{kg}} \left(1 + \left(\frac{6.7132 \cdot 10^{-8} \text{m}}{\lambda} \right)^2 \right) \quad (3.3.16)$$

The following estimation of the density effects is based on assumptions which are not valid in general, but allow to model the imaging of the base region, which was located close to the center of the observation area and therefore in the vicinity of the optical axis of the lens. We assume a particle located in the object plane at position X and a density step due to a compression shock at position X_s (see Fig. 6). For X_s larger than half the aperture diameter the rays through the upper and the lower edge of the aperture will be deflected in the same direction. This can result in a slight displacement of particle images, but this effect is expected to reduce the sharpness of the images in only a minor way. For X_s smaller than half the aperture diameter (as shown in Fig. 6) we can estimate the geometric particle image diameter by tracing two rays which are forming the image and determining their displacement in the image plane: $\Delta d_g = x_2 - x_1$. When tracing the ray of scattered

light propagating parallel to the optical axis, density variations can be neglected and standard imaging condition are valid resulting in $x_1 = MX$ where M is the magnification factor. The ray incident on a compression shock - considered as a plane interface of two media of refractive indices n_1 and n_2 - under a small angle γ will be deflected towards the medium with higher density under an angle of $(\gamma + \epsilon)$ with respect to the interface

(Fig. 6). For small variations of the diffraction index the following equation can be obtained as a solution of Snell's law of refraction:

$$\epsilon = \sqrt{2(\Delta n / n_1) + \gamma^2} - \gamma \quad (\text{Oertel \& Oertel (1989)}) \quad (3.3.17)$$

Eq. (3.3.17) shows that ϵ increases with decreasing γ and for $\lim_{\gamma \rightarrow 0} \epsilon$ converges to $\sqrt{2(\Delta n / n_1)}$. From Figure 6 it can be

seen that $x_2 = f \cdot \tan(\gamma + \epsilon)$. The displacement of two rays in the image plane in worst case ($X = X_s = (b-f-s/2)\tan(\epsilon)$). Therefore, the enlargement of the geometric particle image can be approximated by:

$$\Delta d_g = (f - M \cdot (b - f - s/2)) \cdot \tan(\sqrt{2(\Delta n / n_1)}) \quad (3.3.18)$$

Using Eqs. (3.3.15) and (3.3.16) and assuming $P_1/P_2 \approx 0.5$ which corresponds to values found during the experiments yields: $n_2 = 2 \cdot 10^{-4}$ and $n_1 = 1 \cdot 10^{-4}$. Using $M = 0.2$, $f = 100 \text{ mm}$, $s/2 = 362.5 \text{ mm}$ and the lens equations $1/f = 1/a + 1/b$ and $M = a/b$ results in:

$$\Delta d_g = 1025 \mu\text{m}.$$

It has to be mentioned that the determination of Δd_g based on the assumption of a step in the refractive index of the flow medium might be too pessimistic. Although the extent of strong compression shocks is much smaller than the scale of other flow structures it can be a few times larger than the wavelength of the laser light. This fact could be taken into account by a quantitative estimation of diffraction effects, which would enable to consider also density gradients due to vortex formation in the base region. However, our aim was to motivate, that the variation of refractive index in transonic flow fields can result in unsharp imaging if the optical path is parallel to shock waves (e.g. in the center of the observation area). This fact limits the quality of PIV recording in 2d-flow facilities because there the observation angle can not be changed easily due the size and location of the schlieren windows which give the optical access to the flow.

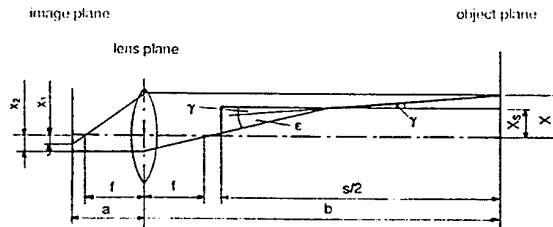


Figure 6: Diagram of imaging (shock wave and particle position close to the optical axis).

Image shifting

Another problem becomes obvious from the description of the recording process as given above, i.e. the direction of the motion of the particles within each interrogation spot can not be determined if employing the 'dual illumination - single frame' recording technique since there is no way to decide which image is due to the first and which is due to the second exposure of a particle. Although, for many applications the sign of the velocity vector can be derived from a priori knowledge of

the flow, in reverse flows, for example in areas of detached flow and in wakes behind models, steps have to be taken to determine the sign of the displacement and hence the velocity vector correctly. The great interest in PIV measurements in many different fields of research requires a flexible technique for ambiguity removal which can be applied to a variety of experimental situations. Especially for aerodynamic investigations it is very important to be able to apply this technique at high speed flows, i.e. with short time intervals of a few microseconds between both illuminations. The most straightforward approach is the recording of both exposures separately, e.g. on two video frames as described by Cho (1989) and their subsequent analysis by means of cross-correlation (Willert & Gharib 1991). However, in order to apply this 'single illumination - dual frame' recording technique high speed video cameras are needed, which do not yet offer the spatial resolution needed for larger observation areas (Rouland et al. 1994, Raffel et al. 1995). A different method for ambiguity removal has to be used for photographic PIV. Such a method is the image shifting technique as described by Adrian (1986b), which enforces a constant additional displacement, which must be greater than the maximum displacement due to the reverse flow, on the images of all tracer particles at the time of their second illumination. Only minor modifications of the evaluation technique by means of correlation methods are required when applying the image shifting method for recording at PIV. It offers also the advantage that zero flow velocity can be measured. At present the most widely used experimental technique for image shifting is to utilize a rotating mirror system. The observation area in the flow is imaged onto the recording area in the camera via the mirror. The magnitude of the additional displacement of the images of the tracer particles depends on the number of revolutions of the mirror per time, the distance between light sheet plane and mirror, the magnification of the imaging system and the time delay between the two illuminations, see Landreth et al. (1988). Another scheme by which the directional ambiguity problem may be resolved has been presented by Wormell & Sopchak (1993) and involves a CCD camera in which the charge associated with the first illumination is electronically moved by a known distance within the sensor during the time period between the first and the second laser pulse. In their arrangement a minimum pulse separation of $\approx 40 \mu\text{s}$ can be used. In order to achieve very high shift velocities electro-optical methods employing differently polarized light for illumination have been proposed and applied by Landreth & Adrian (1988) and Lourenço (1993). The constant shift of the particle images is obtained e.g. by means of birefringent crystals of appropriate thickness. Molezzi & Dutton (1993) have successfully applied this technique in the separated wake region behind a two-dimensional base model in a Mach 0.4 flow, revealing features of the von Kármán vortex street wake and underlying small-scale structures in great detail. However, at DLR a high speed rotating mirror system has been developed in order to be able to carry out measurements also in transonic flows. The frequency of rotation ranges from 1 Hz to 100 Hz, thus covering a range of shift velocities from 5 m/s to 500 m/s. A detailed analysis of the errors involved with image shifting by means of a rotating mirror has also been given by Raffel & Kompenhans (1995). The rotational speed of the mirror was set to 2,400 rev/min during the experiments, resulting in a virtual shift velocity of 279 m/s.

3.4 Evaluation and post processing

Each PIV recording ($24 \times 36 \text{ mm}^2$ format) was interrogated in small sub areas (92×56 interrogation areas with a step size yielding an overlap of 50% along the x and y-axis). The local displacement vector for the images of the tracer particles has been determined for each interrogation area by means of statistical methods. It has been assumed that all particles within one interrogation area have moved homogeneously between the two illuminations. The projection of the vector of the flow velocity into the plane of the light sheet (2d velocity vector) was computed taking into account the time delay between the two illuminations and the magnification at imaging. Due to difficult recording conditions further improvements of the evaluation algorithms were required. Unlike the autocorrelation methods used in conventional evaluation systems, our improved digital evaluation system uses a cross-correlation between image interrogation areas, which are displaced with respect to each other. This method, first described by Keane and Adrian (1992), has been implemented into a fully digital evaluation system of photographic PIV recordings (Willert 1996). After evaluation, a certain number of obviously incorrectly determined velocity vectors can usually be found by visual inspection of the raw data. In order to reject these incorrect data the raw flow field data have to be validated. For this purpose automatically working algorithms have been developed (Raffel et al. 1993). These algorithms ensure with high level of confidence that no questionable data are stored in the PIV data set. Questionable data were rejected, if it can not be decided by application of the validation algorithm whether data are valid or not.

Vector operators have been applied to analyse the two-dimensional vector data as obtained by the evaluation process in more detail. It has to be emphasized that all velocity vectors have been recorded simultaneously. Those parts of fluid mechanical equations that describe temporal fluctuations have therefore not to be taken into account when analysing local variations within a single recording. The equations used for estimation of divergence and out-of-plane (z-) component of the vorticity are shortly described in the following.

The 2d-divergence operator is defined as:

$$\text{div}_{2D}(\vec{u}) = \frac{\partial u}{\partial x} + \frac{\partial v}{\partial y} \quad (3.4.1)$$

The equation of continuity in 3d-form is of fundamental importance for the interpretation of the divergence operator:

$$\frac{\partial \rho}{\partial t} + \text{div}(\rho \vec{u}) = 0 \quad \Leftrightarrow \quad (3.4.2)$$

$$\frac{\partial u}{\partial x} + \frac{\partial v}{\partial y} + \frac{\partial w}{\partial z} = -\frac{1}{\rho} \left(\frac{\partial \rho}{\partial t} + u \frac{\partial \rho}{\partial x} + v \frac{\partial \rho}{\partial y} + w \frac{\partial \rho}{\partial z} \right)$$

Density variations due to temporal gradients can be neglected when comparing different locations within the observation area, since all vectors were recorded at the same short time interval:

$$\frac{\partial \rho}{\partial t} \approx 0$$

Due to the experimental arrangement, the observed flow fields can be assumed to have sufficiently small out-of-plane component so that: $w = 0 \Rightarrow \frac{\partial w}{\partial z} = 0$. This yields:

$$\frac{\partial u}{\partial x} + \frac{\partial v}{\partial y} = \text{div}_{2D}(\vec{u}) = -\frac{1}{\rho} \left(u \frac{\partial \rho}{\partial x} + v \frac{\partial \rho}{\partial y} \right) \quad (3.4.3)$$

As has been demonstrated by Höcker & Kompenhans (1991), the location of oblique and normal compression shocks can therefore be found by analysing the maximum values of the divergence distributions of PIV recordings. The operator has been implemented in discrete form:

$$\text{div}(i, j) = \frac{\Delta u(i, j)}{\Delta x} + \frac{\Delta v(i, j)}{\Delta y} \quad (3.4.4)$$

wherein $i \in \{1, 2, 3, \dots, 92\}$, $j \in \{1, 2, 3, \dots, 56\}$, Δx and Δy are the displacements of the interrogation areas backprojected into the observation area ($\Delta x = \Delta y \approx 3 \text{ mm}$), and $\Delta u(i, j)$ and $\Delta v(i, j)$ are the differences of neighbouring velocity components. The divergence operator was used for localization of the shock waves and their characterization.

Depending on flow parameters and trailing edge geometry the wake flow of transonic turbine cascade blades appears to consist of vortex streets. Shedding frequencies and corresponding Strouhal-numbers have been investigated for different blade geometries by Heinemann et al. (1975) by means of an electro-optical device. As described in the following, the Strouhal-numbers can also be extracted by analysing the vorticity distribution computed from the PIV data. The following operator yields the out-of-plane component of the vorticity:

$$\text{rot}_z(\vec{u}) = \frac{\partial u}{\partial y} - \frac{\partial v}{\partial x} \quad (3.4.5)$$

The operator has been implemented in discrete form:

$$\text{rot}_z(i, j) = \frac{\Delta u(i, j)}{\Delta y} - \frac{\Delta v(i, j)}{\Delta x} \quad (3.4.6)$$

wherein $i \in \{1, 2, 3, \dots, 92\}$, $j \in \{1, 2, 3, \dots, 56\}$, Δx and Δy are the displacements of the interrogation areas backprojected into the observation area, and $\Delta u(i, j)$ and $\Delta v(i, j)$ are the differences of neighbouring velocity components. The vorticity operator was used for localization of the distinct vortices and their average displacement Δx_{vort} . The flow velocity at the centers of the vortices has been used to estimate their convection speed U_{conv} . The Strouhal-number is defined as:

$$\text{Str} = \frac{f_{\text{shed}} \cdot d}{U_2} \quad (3.4.7)$$

wherein f_{shed} is the frequency of vortex shedding, d is the trailing edge thickness of the blade, and U_2 the downstream velocity. The shedding frequency has been estimated by:

$$f_{\text{shed}} = \frac{U_{\text{conv}}}{\Delta x_{\text{vort}}} \quad (3.4.8)$$

One statement should be made concerning the accuracy of the PIV technique. The absolute over-all accuracy of the PIV

system depends on many different parameters and has to be checked separately for each experiment. It is no simple means available to check the accuracy of PIV against another measuring technique. Thus, usually it is tried to determine the accuracy of each individual component of the PIV system to derive a statement about the over-all accuracy. It has to be distinguished between three different error sources: the first one influences all velocity vectors of a PIV recording in the same manner (e.g. the magnification factor at imaging, scale factor of the evaluation system), the second one influences each velocity vector in a different, but steady way (e.g. velocity lag of tracer particles, optical distortion of the lens system, out-of-plane velocity component, errors due to image shifting) - however, neighbouring vectors are affected in a similar way (Sinha 1988, Raffel & Kompenhans 1994), and the third one would be random errors associated with e.g. the evaluation process (see e.g. Keane & Adrian 1990 and Willert 1996). The first two error sources would affect the evaluation of spatial structures in the flow field only in a minor way. The random errors associated with e.g. the evaluation process can be reduced to a minimum when having imaged the particles sharply and using advanced evaluation systems. We can demonstrate the relative accuracy of our system by successfully resolving very weak spatial structures in flow fields with turbulence levels below 0.5%.

4 RESULTS AND DISCUSSION

Measurements of the flow field have been taken at two different cascade outlet Mach-numbers ($Ma_2 = 1.17$ und $Ma_2 = 1.27$) and at four different mass flow rates (0%, 0.8%, 1.4, 2.5%). The mass flow rate is defined as the ratio between the mass flow of the cooling air and the mass flow between two blades. In the following results of $Ma_2 = 1.27$ will be shown and described briefly:

Outlet Mach-number $Ma_2 = 1.17$; mass flow rate 0%

Results for $Ma_2 = 1.17$ are shown in Figures 7, 8, and 9. Figure 7a shows the instantaneous flow velocity field at the trailing edge without cooling air ejection. Expansion waves and terminating shocks can easily be seen. The distribution of velocity divergence in the observation area (Fig. 7b) allows an easy detection of the shock waves, due to the strong velocity gradients. The point of intersection of both main shock waves was located 10 mm behind the trailing edge of the model. A shock reflected from the tailboard above the observation field can be seen on the upper right hand side. The wake is characterized by a vortex street (see Fig. 7c). A Strouhal-number of $\text{Str} \approx 0.38$ was determined by the procedure described above. This value indicates the unsteady behaviour of the wake flow, and agrees well with Strouhal-numbers measured by Heinemann et al. (1975).

Outlet Mach-number $Ma_2 = 1.27$; Mass flow rate 0.8%

The following changes in the velocity field can be observed for a cooling air mass flow rate of 0.8% (see Fig. 8). The strength of the shock wave is significantly reduced. The negative velocity gradients, which follow the expansion waves below and above the trailing edge, cover relatively large areas. On the upper side two expansion and compression waves can be observed. The wake flow is separated by two shear layers from the main flow in which some distinct vortices can be observed.

ACKNOWLEDGEMENT

The authors would like to thank the team of WT-WK-HKG Göttingen for their help during the wind tunnel tests. This research project was supported by the German Ministry of Education, Science, Research, and Technology (BMBF) by the grant 'Nr.: 0326800F'. The authors are responsible for the content of this publication.

REFERENCES

- Adrian R J, Yao C-S 1985: Pulsed laser technique application to liquid and gaseous flows and the scattering power of seed materials. *Appl. Optics* 24, pp. 44-52.
- Adrian R J 1986a: Multi-point optical measurements of simultaneous vectors in unsteady flow - a review. *Int. Journal of Heat and Fluid Flow* 7, pp. 127-145.
- Adrian R J 1986b: Image shifting technique to resolve directional ambiguity in double-pulsed velocimetry. *Appl. Optics* 25, pp. 3855-3858.
- Adrian R J 1991: Particle-Imaging techniques for Experimental Fluid Mechanics. *Ann. Rev. Fluid Mech* 23, pp. 261-304.
- Cho Y-C 1989: Digital image velocimetry. *Appl. Optics* Vol. 28, 740-748.
- Dietrichs H-J, Hourmouziadis J, Malzacher, F, Bräunling W 1987: Flow phenomena in transonic turbine cascades - Detailed experimental and numerical investigation. *Proc. 8th Int. Symp. on Air Breathing Machines (ISABE)*, pp. 360-368.
- Goodman J W, 1968: Introduction to Fourier optics. McGraw-Hill Book Company, San Francisco.
- Hecht E, Zajac A 1974: Optics. Addison-Wesley Pub. Company Inc., Massachusetts.
- Heinemann H-J, Lawacek O, Bütetisch K A 1975: V. Káman vortices and their frequency determination in the wake of profiles in the sub- and transonic regimes. *Symposium Transsonicum II*, ed. K. Oswatitsch and D. Rues, Springer Verlag, Berlin, Heidelberg, New York.
- Höcker R, Kompenhans J 1991: Application of particle image velocimetry to transonic flows. *Appl. of Laser Techniques to Fluid Mechanics*, ed. R.J. Adrian et al., Springer Verlag, Berlin, Heidelberg, Tokio, pp. 415-434.
- Humphreys W M, Bartram S M, Blackshire J L 1993: A Survey of Particle Image Velocimetry Applications in Langley Aerospace Facilities. *Proc. 31st Aerospace Sciences Meeting, Reno, AIAA paper 93/041*.
- Hunter W W, Nichols C E (eds.) 1985: Wind Tunnel Seeding Systems for Laser Velocimeters. NASA Conference Publication 2393, NASA Langley.
- Keane R D, Adrian R J 1990: Optimization of particle image velocimeters. Part I: Double pulsed systems. *Meas. Sci. Technol.* 1, pp. 1202-1215.
- Keane R D, Adrian R J 1992: Theory of cross-correlation analysis of PIV images. *Appl. Sci. Res.* 49, pp 191-215.
- Kiock R, Lehthaus F, Baines N C, Sieverding C 1986: The transonic flow through a plane turbine cascade as measured in four european wind tunnels. *ASME Journal of Engi. for Gas Turbines and Power*, Vol. 108, 285-292.
- Kompenhans J, Raffel M 1993: Application of PIV technique to transonic flows in a blow-down wind tunnel. *Int. Symp. on Optical diagnostics in fluid and thermal flows*, SPIE Proc. Vol. 2005, 425 - 436.
- Landreth C C, Adrian R J, Yao C S 1988: Double pulsed particle image velocimeter with directional resolution for complex flows. *Exp. Fluids* 6, pp. 119-128.
- Landreth C C, Adrian R J 1988: Electrooptical image shifting for particle image velocimetry. *Appl. Optics* 27, pp. 4216-4220.
- Lourenço L M 1993: Velocity bias technique for particle image velocimetry measurements of high speed flows. *Appl. Optics* 32, 2159-2162.
- Meyers J F 1991: Generation of Particles and Seeding. Von Káman Institute for Fluid Dynamics, Lecture Series 1991-05, Brussels.
- Melling A 1986: Seeding Gas Flows for Laser Anemometry. *Conf. on Advanced Instrumentation for Aero Engine Components*, AGARD-CP 399, paper 8.
- Molezzi M J, Dutton J C 1993: Application of particle image velocimetry in high-speed separated flows. *AIAA Journal*, Vol. 31, No. 3, pp. 438-446.
- Motallebi F, Norbury J F 1981 The effect of base bleed on vortex shedding and base pressure in compressible flow. *Journal of Fluid Mech.* 110, pp. 273-293.
- Meyer J B 1972: Theoretical and experimental investigations of flow downstream of two-dimensional transonic turbine cascades. *ASME paper* 72-GT-43.
- Oertel H (sen.), Oertel H (jun.) 1989: *Optische Strömungsmeßtechnik*. G. Braun Karlsruhe.
- Pickering C J D, Halliwell N A, 1984: Speckle photography in fluid flows: signal recovery with two-step processing. *Appl. Optics* 23, pp. 1128-1129.
- Raffel M, Leiti B, Kompenhans J 1993: Data Validation for Particle Image Velocimetry. *Appl. of Laser Techniques to Fluid Mechanics*, ed. R.J. Adrian et al., Springer Verlag, Berlin, Heidelberg, Tokio, pp.210-226.
- Raffel M, Kompenhans J 1994: Error analysis for PIV recording utilizing image shifting. *7. Int. Symp. on Appl. of Laser Techniques to Fluid Mech.*, Lisbon, Portugal, paper 35-5.
- Raffel M, Kompenhans J, Stasicki B, Bretthauer B, Meier G E A 1995: Velocity measurement of compressible air flows utilizing a high-speed video camera. *Exp. in Fluids* Vol. 17, pp. 204-206.
- Raffel M, Kompenhans J 1995: Theoretical and Experimental Aspects of Image Shifting by Means of a Rotating Mirror System for Particle Image Velocimetry. *Measurement, Science and Technology* Vol. 6, pp. 795-808.
- Rouland E, Vottier S, Lecordier B, Trinité M 1994: Cross-correlation PIV development for high speed flows with a standard CCD camera. *2nd Int. Seminar on Opt. Methods & Data Processing in Heat and Fluid Flow*, 9-20.
- Schäfer H J 1995: private communication, ISL, St. Louis, France.
- Sieverding C H, Stanislas M, Snoeck J 1980: The base pressure problem in transonic turbine cascades. *Journal of Eng. for Power* Vol. 102, 711-718.
- Sinha S K 1988: Improving the accuracy and resolution of particle image or laser speckle velocimetry. *Exp. in Fluids* Vol. 6, pp. 67-68.
- Solf K.D 1975: *Fotografie: Grundlagen, Technik, Praxis*. Fischer-Verlag.
- Towers C E, Bryanston-Cross P J, Judge T R 1991: Application of particle image velocimetry to large-scale transonic wind tunnels. *Optics & Laser Technology* Vol. 23, No 5, pp. 289-295.
- Westerweel J 1993: Digital particle image velocimetry - Theory and application. Delft University Press.
- Willert C E, Gharib M 1991: Digital particle image velocimetry. *Exp. Fluids* Vol. 10, pp. 181-193.
- Willert C E, 1996: The fully digital evaluation of photographic PIV recordings. Accepted for publication in *Applied Scientific Research*, November 1995.
- Womell D C, Sopchak J 1993: Particle image velocimetry system using a high-resolution CCD camera. in *Optical Diagnostics in Fluid and Thermal Flow*, ed. S. S. Cha, J. D. Trolinger, *Proc. SPIE* 2005, pp. 648-654.

Outlet Mach-number $Ma_2 = 1.27$; Mass flow rate 1.4%

For a further increased mass flow rate of 1.4% the shock intensity was relatively strong. Furthermore, on the upper right hand side of the observation area two further shock waves can be detected (see Fig. 9). The oblique shock has been reflected at the tailboard above the observation field. This shock wave was again reflected at the wake of the model. This yields the vertical line of maximum divergence values at the right hand edge of the observation field. Varying positions of the shock reflected at the wake can be seen when comparing different PIV measurements taken at the same tunnel run and for the same parameters.

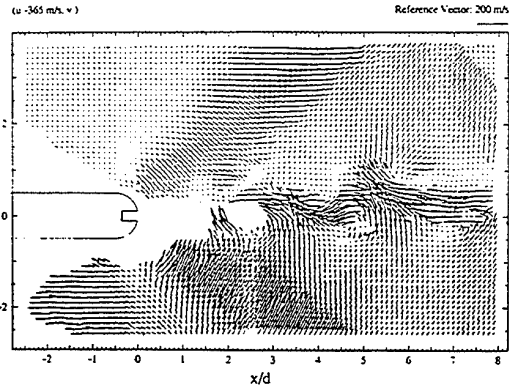


Figure 8: Velocity field at $Ma_2 = 1.27$ and 0.8% mass flow.

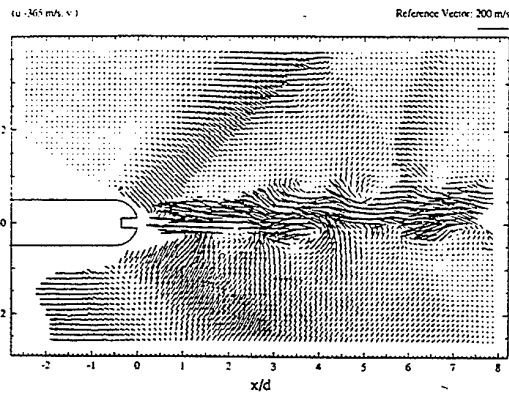


Figure 9: Velocity field at $Ma_2 = 1.27$ and 1.4% mass flow.

5 CONCLUSIONS

The short-time measurement of flow velocity fields behind the trailing edge of a turbine blade model and the subsequent computer aided evaluation and analysis yield detailed information on the features of such flow fields. In spite of difficult recording conditions the obtained velocity data is well suited for future comparison with data obtained by numerical simulations. Limits of imaging have been presented based on practical experiences and theoretical analysis. The following relations between the flow phenomena around the trailing edge and the mass flow rate of cooling air in the case of trailing edge ejection could be demonstrated and quantified by PIV:

- A vortex street exists even in case of transonic cascade exit Mach-numbers.
- This vortex street can be suppressed by trailing edge cooling air ejection at low mass flow rates.
- The strength of the shock waves can be reduced by ejecting a low cooling air mass flow out of the trailing edge. For higher mass flow rates the strength of the shock waves increases again. That indicates the existence of a optimum mass flow rate with respect to the efficiency of the process.

Figure 7: Velocity, divergence, and vorticity field at $Ma_2 = 1.27$ and 0% mass flow.

3D FIBRE OPTIC LASER DOPPLER VELOCIMETRY

Stephen W. James⁺, R.A. Lockey⁺, David Egan⁺ Ralph P. Tatam⁺ and R.L. Elder^{*}

⁺Optical Sensors Group, Centre for Photonics and Optical Engineering,

^{*}Turbomachinery Research Group, School of Mechanical Engineering,

Cranfield University, Cranfield, Bedford MK43 0AL, U.K.

ABSTRACT

Conventional single headed 3D Laser Doppler Velocimetry (LDV) geometries rely upon the use of 3 Doppler difference channels, inclined at differing angles with respect to the mechanical axes of the probe. The transformation between the non-orthogonal measurement co-ordinate system and the Cartesian system can result in large errors in the calculated velocities. These considerations have lead to the development of a single headed LDV probe based around the use of two Doppler difference channels to directly measure the transverse velocity channels, and a reference beam channel to measure the on axis velocity component. The probe may be operated in two regimes, using cw radiation and wavelength division multiplexing to distinguish the three channels, or using a pulsed source and time division multiplexing.

1. INTRODUCTION

Full characterisation of the complex, time varying 3 dimensional flows encountered in engineering systems such as turbomachinery has long been the goal of research in flow measurement instrumentation. Laser Doppler velocimetry (LDV) is capable of producing high quality, high spatial resolution data from a wide range of flow systems. The demands for improved fuel efficiency, reduced emissions, and the requirement for high quality data to allow validation of increasingly complex computational fluid dynamic codes is driving the development of new, simultaneous 3D LDV configurations.

3D flow characterisation requires the presence of 3 LDV channels in the flow, distinguished using wavelength, time or frequency bias. Ideally the channels directly measure the three orthogonal velocity components. In general, however, the optical access to the flow is limited, such that the measurements have to be made with the 3 channels being inclined at an angle with respect to the Cartesian co-ordinate

system. The transformation between the non-orthogonal measurement system and the Cartesian system is sensitive to uncertainties in the angular configuration of the channels, resulting in large errors in the calculated velocity components.

A number of 3D LDV configurations using Doppler difference channels have been demonstrated, all of which show significant limitations when considered in the context of the limited optical access available in turbomachinery applications. In this paper the development of a single headed, fibre optic based, 3D laser Doppler velocimeter is discussed. The probe uses two Doppler difference channels to measure the transverse velocity components, and a reference beam channel to measure the on axis velocity component. The operation of the device using time-division-multiplexing and wavelength-division-multiplexing is discussed.

2. 3D LASER DOPPLER VELOCIMETRY

The potential of LDV to allow 3D characterisation of flow fields was realised soon after the first demonstration of the technique. A system based around the use of three reference beam channels, using a single illuminating beam and three sets of receiving optics was reported by Huffacker (1970). The optical configuration spatially multiplexed the channels and provided three angularly separated measurements to allow calculation of the orthogonal velocity components. Since then a number of schemes have been proposed and demonstrated, (see for example reviews by Dancey (1987) and Meyers (1985)) While the reference beam technique formed the basis of the first 3D LDA configuration, it suffered from a number of practical limitations which complicated its practical implementation. These limitations included the dependence of the measured frequency shift upon the viewing direction, poor signal to noise characteristics due to mismatch in the ratio of signal to reference beam powers, stringent alignment conditions for

efficient heterodyning which require alignment of signal and reference beams to better than a few minutes of arc, and a limited collection aperture due to coherence considerations. The development of the Doppler difference method, in which the frequency shift is independent of viewing direction and is dependent only upon the geometry of the illuminating beams, lead to reference beam systems being largely abandoned. The Doppler difference method allowed large apertures to be used to collect scattered light, and alignment and beam ratio requirements to be relaxed, being transferred to the illumination section of the system, where they could be more easily satisfied. As a result the 3D LDV schemes rely upon the use of three inclined Doppler difference channels (Ahmed (1990) (1992)), formed using 5 (Stauter 1993) or 6 beams (Yanta 1979). In flow systems with limited optical access the orientation of the channels results in each measuring only a small component of the on-axis velocity, with the result that the co-ordinate transformation amplifies small geometrical uncertainties, requiring stringent alignment procedures to obtain meaningful measurements of the on-axis velocity component. This has been shown in a number of analyses of 3D LDV geometries, for example Orloff (1982), Snyder (1984) and Morrison (1991). For direct measurement of the three orthogonal velocity components using a single headed probe a hybrid configuration, employing Doppler difference channels to measure transverse velocity components and a reference beam channel to measure the on axis component has to be employed. This has been proposed by a number of authors, see Orloff (1980), Schwiesow (1977) and Seasholtz (1986). While a number of 2D LDV configurations using a single Doppler difference channel and a reference beam channels have been reported, and the extension to simultaneous 3D measurement discussed, to date there has been no report of the operation of such a simultaneous 3D LDV instrument, which may be related to the practical difficulties encountered when implementing bulk optic based reference beam anemometers.

3. PROBE DESIGN

The use of optical fibres is central to the operation of the probe, easing the limitations associated with bulk optic reference beam configurations, allowing the direct measurement of the on axis velocity component. Constraining the signal and reference beams to propagate through the same fibre automatically satisfies the stringent alignment conditions required to achieve optimum heterodyning conditions. The fibres spatially filter the collected scattered radiation, producing high quality wavefronts. We have recently demonstrated an optical configuration which allows optimisation of the signal to reference beam ratios while making optimum use of available light, a significant consideration when using infra-red radiation (James 1995). Optical fibres also allow the sensitive semiconductor laser diodes and detectors to be kept remote from the flow region.

A schematic diagram of the beam geometry is shown in figure 1. Five beams illuminate the flow, the two Doppler difference channels directly measuring the transverse components, while the slightly off axis illumination direction of the reference beam channel results in the measurement predominantly containing the axial component with a small

contribution from the transverse components. The use of off axis illumination is aimed at reducing the effects of flare from solid surfaces, allowing the performance of near wall measurements, and reducing the length of the measurement volume.

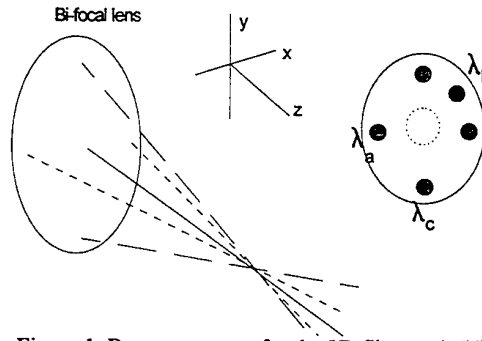


Figure 1. Beam geometry for the 3D fibre optic LDV

Figure 2 shows a cross section of the probe head. Light is delivered to the head by polarisation maintaining (pm) optical fibre, to ensure matching of polarisation states and optimum fringe visibility. The fibre ends are terminated with GRIN lens collimators, and the beams focused into the flow by the front lens. The outer portion of this lens collimates backscattered light, and the second lens launches this into the multi-mode fibre. The central portion of the bi-focal lens launches scattered light into the pm fibre mode fibre to act as the signal for the reference beam channel.

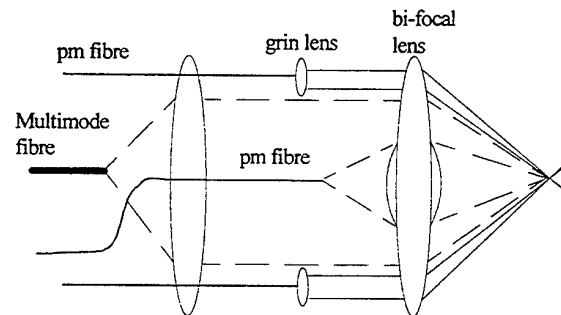


Figure 2. Cross section of the probe head

Probe Specifications

working distance	200 mm
lens focal lengths	200 mm, 40 mm
input beam waist	0.5 mm
wavelength	800 nm
beam spacing	40 mm
half angle	5.7°
fringe spacing	4 μm
measurement volume size (Doppler diff. channels)	50 μm x 50 μm x 500 μm
measurement volume size (reference beam channel)	24 μm x 24 μm x 500 μm

4. CHANNEL SEPARATION

Two demultiplexing techniques for separating the channels have been investigated: wavelength-division-

multiplexing and time-division-multiplexing. The following section outlines the different optical configurations required for the two different schemes.

4.1 WAVELENGTH DIVISION MULTIPLEXING

Wavelength division multiplexing is being implemented using three semiconductor laser diodes, operating around 800 nm with output power 150 mW, to illuminate the three measurement channels. The diodes operate at slightly differing wavelengths.

Figure 3 shows a schematic of the lay-out of the of the launch/receive unit. The output from the laser diodes are launched into polarisation maintaining fibre. The two Doppler difference channels incorporate fibre pigtailed 40 MHz Bragg cell frequency shifters which act as 50/50 beamsplitters and allow direction discrimination. The reference beam channel is launched into a variable split ratio polarisation preserving directional coupler, with 95 % travelling to the probe head, and the remaining 5% used as the reference beam. This ratio can be adjusted to optimise the signal to noise ratio.

The scattered light is returned via the multi-mode fibre and a polarisation preserving fibre. The output from the multimode fibre is incident upon a diffraction grating to demultiplex the wavelengths. The two Doppler difference signals are monitored on avalanche photodiodes. The signal for the on axis measurement is derived from the polarisation maintaining return fibre, and mixed with a frequency shifted reference beam. The signals are analysed on Dantec Burst Spectrum Analysers.

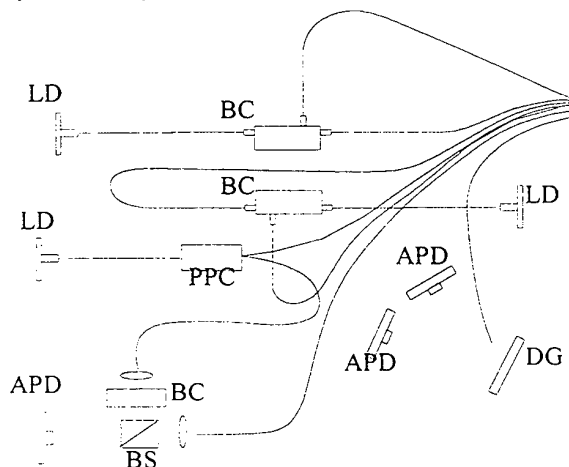


Figure 3. Schematic of launch/receive section. LD, laser diode; DG, diffraction grating; APD, avalanche photodiode; BG, fibre pigtailed Bragg Cell; PPC, variable split ratio polarisation preserving coupler

4.2 TIME DIVISION MULTIPLEXING

Time-division multiplexed 3D LDV is performed by sequentially pulsing the illumination for the three measurement channels. A particle passing through the measurement volume scatters light from each fringe pattern. The collected light is monitored on a single detector, yielding a train of pulses in which the pulses from each channels are interleaved. The channels are then separated by taking every third pulse from the pulse train.

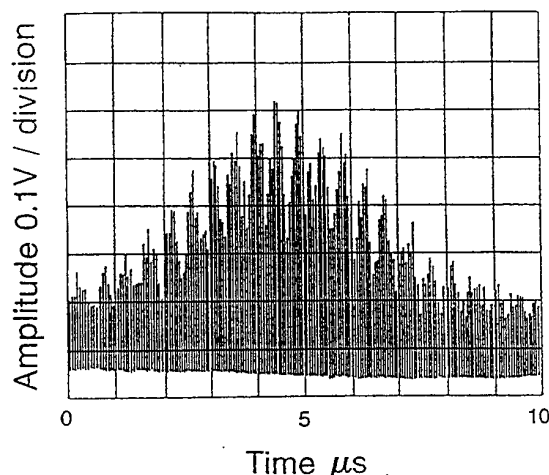


Figure 4. Pulsed LDV signal

The envelope of the pulse amplitudes is then a cosinusoidal oscillation at the Doppler frequency, inside a gaussian envelope and superimposed on a gaussian pedestal. Figure 4 shows an single channel pulse train obtained from the experimental configuration described in section 4.1. The channels are not simultaneously present in the measurement volume, with the result that there is no cross talk. Since the technique presents a sampled Doppler envelope to the signal processing system, the pulse frequency must be at least twice the maximum expected Doppler frequency to satisfy the Nyquist limit.

A previous TDM scheme reported by Carbonaro (1984), using an Argon-ion laser and a mechanically chopped configuration in which each channel was masked in turn, was limited to low Doppler frequencies. Semiconductor laser diodes are ideally suited to this application, since they offer the capability for high frequency modulation. The practical implementation of TDM LDV may be achieved by the sequential pulsing of three separate laser diode sources, as reported by Dopheide (1993). This technique requires the use of a separate laser diode, power supply, temperature controller and pulse generator for each channel, and the channels have to be electronically synchronised.

The use of optical fibres allows the construction of an elegant LDV configuration which uses a single optical source and a single detector to monitor all three channels (Lockey 1994). A schematic diagram of a three component TDM LDV configuration is shown in figure 5.

The sequential pulsing of the channels is achieved by incorporating optical delay lines into the fibre web. A single pulsed laser diode is launched into the fibre network. A 66/33 directional coupler sends one third of the power into the first channel, while a 50/50 directional coupler splits the remaining power between the other two channels. The delay line lengths are selected such that the pulses emerge from each channel in turn, and that they are regularly spaced. The division of the output from a single source between the three channel clearly imposes a penalty in terms of power per channel. However, pulsed operation enables the laser diode to be driven at much higher peak powers (Yoo 1991). A multi-mode optical fibre is used to collect the scattered light and deliver it to an avalanche photodiode. The pulse train is stored on a digital oscilloscope, which acts as a transient recorder, and is downloaded to a personal computer for processing.

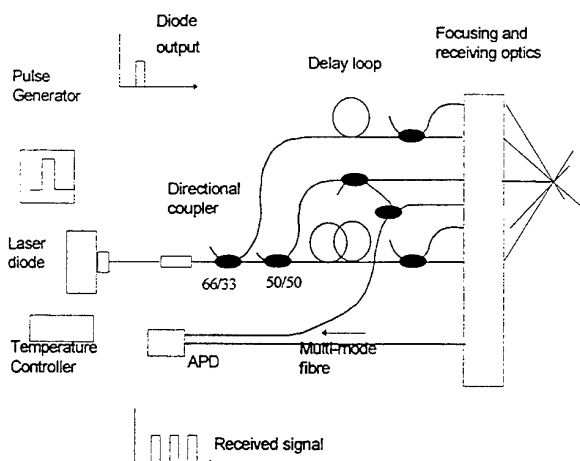


Figure 5. Time-Division Multiplexed multi-component LDV configuration utilising fibre optic delay lines

4.2.1 EXPERIMENTAL CONFIGURATION

The operation of the multi-component fibre optic TDM LDV has been demonstrated using a 2D system incorporating two Doppler difference channels. The fibre web was constructed using mono-mode optical fibres, and incorporated polarisation state controllers to enable the output beams' polarisation states to be matched and ensure optimum fringe visibility. A Sharp LTO24 single-mode laser diode, operating at 780 nm, was biased at threshold and driven with square pulses at 33 MHz with duty cycle of 20%. The light was launched into a 50/50 coupler to distribute the light between the channels. A 2.2m delay line is incorporated in one of the channels, giving a 10ns separation between the projected pulses.

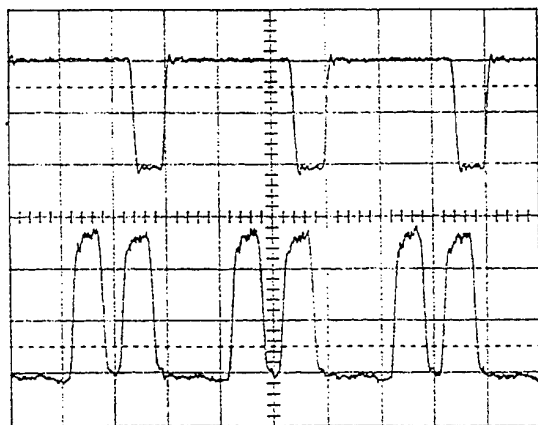


Figure 6. Pulse separation using fibre delay lines. The upper trace shows the pulses, inverted, applied to the laser diode drive current. The lower trace shows the pulse pairs separated by 9.8 ns.

The separated pulses are shown in figure 6. The fringes in the measurement volume had a spacing of $4.9\mu\text{m}$, which with the 33 MHz modulation frequency provides a measurable velocity limit of 80 ms^{-1} . Scattered light is collected using multi-mode fibre, and the pulses detected

using a Hamamatsu C5658 avalanche photodiode, bandwidth 1.5 GHz, and captured on a digital oscilloscope in single shot mode. The data is then downloaded to a PC, the pulse amplitudes separated into their respective channels, and a fast Fourier transform performed on each set

4.2.2 RESULTS

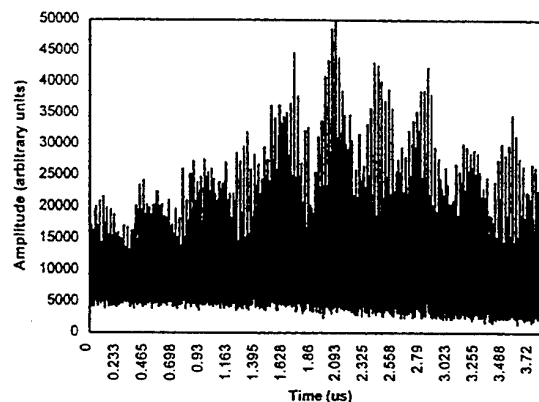


Figure 7(a)

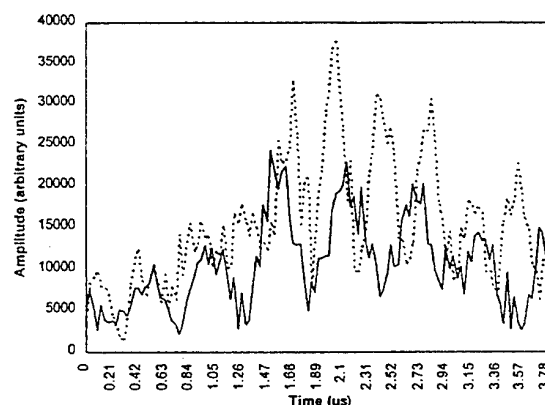


figure 7(b)

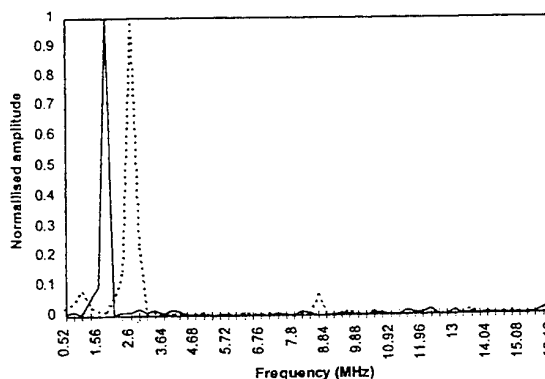


figure 7(c)

Figure 7. Processing of a Doppler transit. (a) the captured burst (b) the extracted Doppler signals for each channel (c) the Doppler frequency spectra.

The measurement channels illuminated the flow from a water seeded air jet. A typical particle transit is illustrated in figure 7(a), and the extracted pulse envelopes in figure 7(b). The cosinusoidal amplitude modulation is clearly visible on each

channel. The results of a fast Fourier transform performed on this data is shown in figure 7(c), where the Doppler frequencies are 2.6 MHz and 1.82 MHz, for the two channels respectively yielding velocity components of 12.7ms^{-1} and 8.9ms^{-1} respectively. The mean x and y velocity components across the jet, 5mm from the nozzle, are shown in figure 8, with the jet inclined at 30° to the x component.

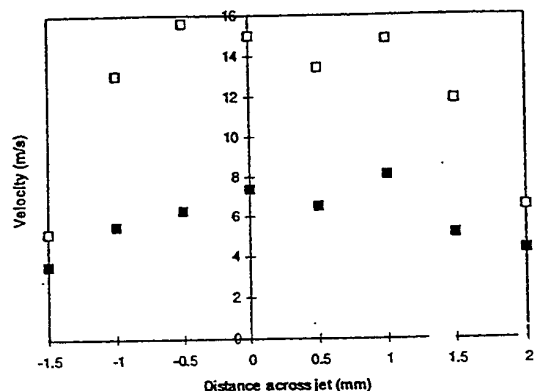


Figure 8. Mean transverse velocity component measured across a water seeded air jet

We have recently demonstrated a pulsed reference beam LDV configuration, and thus the TDM LDV could be readily extended to permit 3D flow characterisation. (James 1995).

4.3 DIRECTIONAL DISCRIMINATION

To provide information on the direction of the flow, the system has been modified to incorporate a Bragg Cell. The experimental configuration is illustrated in figure 9. The output from the pulsed laser diode is passed through an 80 MHz Bragg Cell which acts as a 50/50 beamsplitter. A second Bragg Cell is used to allow control over the exact frequency shift, and to bring it within the Nyquist limit. The fibre configuration then splits the shifted and unshifted beams to form the two measurement channels by incorporating the appropriate delay lines in each arm.

4.4 DISCUSSION

Semiconductor laser diodes and optical fibres are versatile components for application in laser Doppler velocimetry instrumentation, allowing the construction of WDM and TDM based systems. The practical implementation of these two demultiplexing techniques produce configurations with differing optical and electronic complexities. WDM systems require the use of three sources and three detectors, with a Bragg Cell frequency shifter for each channel. The signal processing may be achieved using conventional, off the shelf units. The TDM system contains less complex optics, requiring a single source and detector and in principle requires only a single Bragg Cell to allow direction discrimination for all three channels. However, the technique requires a complex high bandwidth electronic system for pulsing the source, separating the pulse train into the appropriate channels, and to perform the FFT to determine the Doppler frequency. The choice of multiplexing scheme will be determined by the requirements of the application,

and by the levels of electronic and optical complexity that may be tolerated.

5. SUMMARY

The development of a single headed 3D LDV configuration has been discussed, in which two Doppler difference channels directly measure the transverse velocity components, and a reference beam channel measures the on axis velocity component. The operation of the instrument in wavelength and time division multiplexed configurations has been outlined.

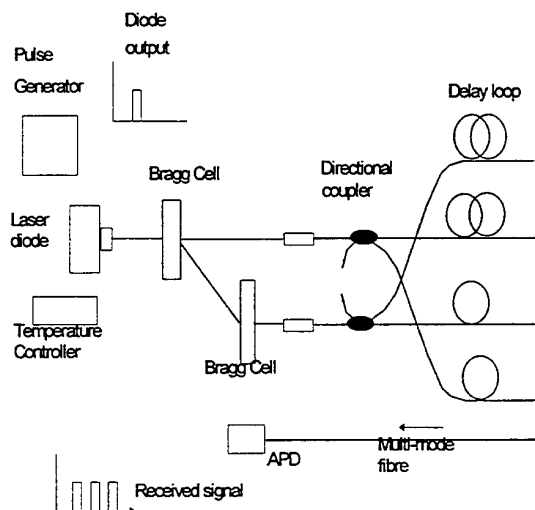


Figure 9. Schematic of multi component TDM LDV with directional discrimination

REFERENCES

- Ahmed et al. 1990 Miniature Laser Anemometer for 3D Measurements, *Measurement Science and Technology* vol pp 272.
- Ahmed et al. 1992 Fibre Optic Laser Anemometry for Turbomachinery Applications, *Optics and Lasers in Engineering* vol 16 pp 193-205
- Carbonaro, M. 1984, Conception and Design of a new type of Three Component Laser Doppler Velocimeter, Von Karman Institute Technical Memorandum, October.
- Dancey CL, 1987, A Review of Three Component Laser Doppler Anemometry, *Journal of Optical Sensors* vol. 2 pp 437-469.
- Dopheide D et al, 1993 High Frequency Pulsed Laser Diode Application in Multi-Component Laser Doppler Anemometry, *Optics and Lasers in Engineering*, vol 18, pp 135-143.

Huffacker RM 1970, Doppler Detection Systems for Gas Velocity Measurements, Applied Optics Vol. 9, pp1026-1028.

James SW et al 1995, Fibre Optic Reference Beam Laser Doppler Velocimetry Optics Communications, Vol 119, pp 460-.

Lockey RA & Tatam RP 1994 High Frequency Pulsed-Diode Laser Anemometry Proc SPIE vol 2341 pp 102.

Meyers JF 1985 The Elusive Third Component, International Symposium on Laser Anemometry, ASME Florida pp 247.

Morrison GL et al 1991 Advantages of Orthogonal and Non-Orthogonal Three Dimensional Anemometer Systems Flow Measurement Instrumentation vol 2 pp 89

Orloff KL & Logan SE 1973 Confocal Backscatter Laser Velocimeter with On-Axis Sensitivity Applied Optics vol 12 pp2477.

Orloff KL & Snyder PK 1982 Laser Doppler Anemometer Measurements using Non-Orthogonal Velocity Components: Error Estimates Applied Optics vol 21 pp39

Schwiesow RL et al 1977 Coherent Differential Doppler Measurements of Transverse Velocity at a Remote Point Applied Optics vol 16 pp 1145.

Seasholtz RG & Goldman LJ 1986 Combined Fringe and Fabry-Perot Laser Anemometer for Three Component velocity Measurements in a Turbine Stator NASA TM 87322.

Snyder PK et al, 1984 Reduction of Flow Measurement Uncertainties in Laser Velocimeters with Non-Orthogonal Channels AIAA Journal vol 8. pp1115

Stauter RC 1993 Measurement of the Three Dimensional Tip Region Flow Field in an Axial Compressor Journal of Turbomachinery vol 115 pp 469.

Yanta WJ 1979 A Three Dimensional Laser Doppler Velocimeter for use in Wind Tunnels ICIASF record pp294.

Yoo JS et al. 1991 On the Surface Recombination Velocity and Output Intensity Limit of Pulsed Semiconductor Lasers, IEEE Photonics Technology Letters Vol 7. pp594.

LDV INVESTIGATION OF THE ROTOR-STATOR AERODYNAMIC INTERACTION IN A CENTRIFUGAL TURBOMACHINE

Marina Ubaldi, Pietro Zunino, Giovanna Barigozzi, Andrea Ghiglione

Istituto di Macchine e Sistemi Energetici
Università di Genova, Italy

ABSTRACT

Rotor-stator aerodynamic interaction in a centrifugal stage has been experimentally investigated by means of a four-beam two-colour laser Doppler velocimeter.

Potential flow and wake generated interaction mechanisms have been studied surveying the flow on two cross-circumferential measuring stations located immediately upstream of the rotor blade trailing edge and the diffuser vane leading edge, respectively. Use of appropriate data processing techniques helped to highlight the distinctive features of the two different interaction mechanisms.

1. INTRODUCTION

Flow unsteadiness generated by rotor-stator aerodynamic interaction affects aerodynamic, structural and acoustic performance of turbomachinery components through two distinct mechanisms: wake and potential flow effects.

The wake effect originates from the periodic impingement and convection of the wakes shed from the preceding row through the successive blade row in relative motion. The potential flow effect is induced by the interaction of the inviscid flow fields generated by the adjacent blade rows in relative motion.

Due to the challenging aspects and the engineering relevance of the phenomenon, several research projects have been reported in the technical literature. Restricting the field only to the experimental investigations in centrifugal turbomachines, pioneering works are those of Krain (1981) and Inoue and Cumpsty (1984) on centrifugal compressors. More recently detailed investigations of the rotor-stator interaction in pumps have been presented (e. g. Arndt et al., 1990, and Casey et al., 1995).

Ubaldi et al. (1994, 1996) have investigated the upstream effect of the vaned diffuser on the impeller outflow in the radial gap of a turbomachine model representative of a low specific speed centrifugal pump. Their results have been adopted as a test case for numerical code validations by a working group of S.H.F. (Société Hydraulique de France).

The present paper reports new data which build up those previous investigations. Both potential and wake generated interactions have been analysed using a four-beams two-colour laser Doppler velocimeter. Data processing techniques appropriate to show up the two different interaction mechanisms have been employed.

2. EXPERIMENTAL FACILITY AND MEASURING TECHNIQUES

2.1 Test Model

The experiment was carried out on a centrifugal stage which consists of an unshrouded centrifugal impeller and a vaned diffuser. The stage is shown in Fig. 1.

The rotor has an outlet diameter of 420 mm and seven single curvature backward blades. The diffuser is equipped with twelve vanes and the vaneless radial gap is about 6 per cent of the impeller outlet radius, a value which is typical of modern centrifugal turbomachines. The vanes are fixed on a steel ring, which is allowed to rotate on a bearing plane for modifying the relative position of the diffuser vanes with respect to the instrumented casing.

The geometrical characteristics of the impeller and diffuser passages determine geometrical diffusion ratios respectively of 1.42 and 2.03, setting the diffusion channels of the two components near the line which separates the regions of non appreciable stall and corner stall in the chart of performance of two-dimensional diffusers with rotation (Rothe and Johnston, 1976).

The axial width of impeller and diffuser is constant and equal to 40 mm, while the tip clearance between blades and casing is 0.4 mm.

The casing is constituted by a thick Plexiglas ring, instrumented with flush mounted pressure transducers, hot wire probe holders and a rectangular glass window, which provides the optical access to large part of the impeller and diffuser internal passages for LDV measurements.

The air enters the model at the atmospheric conditions through an inlet pipe equipped with honeycomb and filtering sections and a throttling valve for varying the operating point. The flow is discharged through the diffuser directly into the atmosphere.

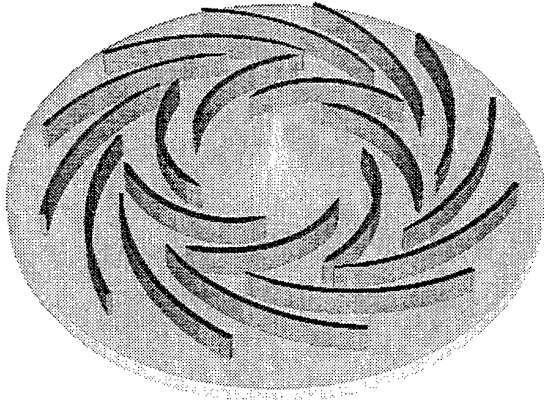


Fig. 1 Centrifugal impeller and vaned diffuser

The experiment was conducted at the constant rotational speed of 2000 rpm at the nominal operating point.

Model geometry and nominal operating conditions are summarized in Table 1. Coordinates of the impeller blade and diffuser vane profiles are given by Ubaldi et al. (1996).

2.2 Instrumentation and Measuring Procedure

A four-beam two-colour fibre optic LDV system with back scatter collection optics (Dantec Fiber Flow) has been used in the present investigation. The light source is a 300 mW argon ion laser operating at 488 nm (blue) and 514.5 nm (green).

The probe consists of an optical transducer head of 60 mm diameter connected to the emitting optics and to the photomultipliers by means of optic fibres. A front lens of 160 mm focal length with a beam separation of 38 mm provides a probe volume of 0.08 mm diameter and 0.64 mm length. The probe volume contains two sets of blue and green fringes (with spacing of 2.1 μm and 2.2 μm respectively), which allow the contemporaneous measurement of two velocity components in the plane perpendicular to the probe optical axis. A Bragg cell is used to apply a frequency shift (40 MHz) to one of each pair of beams, providing directional sensitivity and reducing angle bias for all velocity measurements.

The probe, oriented with the axis along the blade spanwise direction, was traversed using a three-axis computer controlled probe traversing system. The circumferential investigation of the flow was performed by rotating the ring carrying the diffuser vanes with the probe volume maintained at a fixed position.

The flow was seeded with a 0.5-2 μm atomised spray of mineral oil upstream of the inlet pipe in order to minimise flow disturbances.

The signals from the photomultipliers were processed by two Burst Spectrum Analysers operating in encoder enabled mode.

An one per revolution signal obtained from the rotor shaft by means of an optical probe was used to trigger the processors during the measurements. In this way a complete set of information for each channel, including instantaneous velocity, transit time, arrival time and reference time, is acquired and transferred to the computer. This procedure

Table 1. Geometric data and operating conditions

Impeller		
inlet blade diameter	D_1	= 240 mm
outlet diameter	D_2	= 420 mm
blade span	b	= 40 mm
number of blades	z_i	= 7
inlet blade angle	β_1'	= -65 deg
outlet blade angle	β_2'	= -70 deg
Diffuser		
inlet vane diameter	D_3	= 444 mm
outlet vane diameter	D_4	= 664 mm
vane span	b	= 40 mm
number of vanes	z_d	= 12
inlet vane angle	α_3'	= -74 deg
outlet vane angle	α_4'	= -68 deg
Operating conditions		
rotational speed	n	= 2000 rpm
flow rate coefficient	ϕ	= 0.048
total pressure coefficient	ψ	= 0.65
Reynolds number	$Re = U_2 l / \nu$	= $6.5 \cdot 10^5$
Inlet air reference conditions		
temperature	T	= 298 K
air density	ρ	= 1.2 Kg/m ³

allows free running of the laser velocimeter and contemporaneous acquisition of a position information useful to assign each instantaneous velocity measurement to the proper circumferential location relative to the impeller blade. An ensemble average procedure was applied to the data in order to separate the signal periodic component at the rotor frequency from the random component due to turbulence, vortex shedding and all the flow fluctuations not correlated with the rotor speed. For each measuring point, defined by the radial (r), axial (z), and circumferential (θ) coordinates, the data are sorted into 420 separate groups each representing a particular shaft position. Omitting for simplicity the indices of the radial and axial coordinates, the equations defining the ensemble averaged velocity and the ensemble averaged random unsteady velocity are as follows:

$$\bar{c}(j, k) = \frac{1}{N} \sum_{n=1}^N c(j, n, k) \quad (1)$$

$$\sqrt{\bar{c'^2}(j, k)} = \sqrt{\frac{1}{N} \sum_{n=1}^N [c(j, n, k) - \bar{c}(j, k)]^2} \quad (2)$$

where $c(j, n, k)$ is the instantaneous velocity measured for the particular rotor window j , at the revolution n , for the relative probe-diffuser vane position k . N is the total number

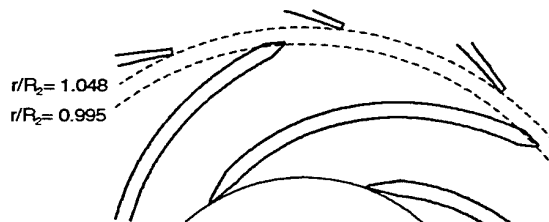


Fig. 2 Measurement locations

of measurements in the measuring window j .

At each measuring point 200000 velocity data for each velocity component were acquired, giving an average of 480 data for each of the 420 circumferential points.

Sources of errors associated with LDV velocity measurements have been widely discussed in literature (e. g. Boutier, 1991). A review for turbomachinery applications with guide lines for error evaluation is provided by Strazisar (1986). A specific error analysis for frequency domain processors is given by Modarress et al. (1988).

According to the above mentioned references, uncertainties of 2 and 6 per cent have been evaluated for the mean and rms velocities respectively. However, in the wake region, where the turbulence intensity is large and the lowering of data rate causes a reduction of the number of samples to be used for averaging, uncertainties increase to 4 and 10 per cent respectively.

2.3 Data Processing for the Investigation of Rotor-Stator Interaction

The flow was surveyed over two cross-circumferential surfaces shown in Fig. 2: one just upstream of the rotor outlet, at $r/R_2=0.995$, and one just upstream of the diffuser vane leading edge, at $r/R_2=1.048$ ($R_3/R_2=1.057$). Each circumferential surface is described by 17 measuring points in the axial direction and the measurements were repeated for 24 different circumferential relative positions (k) between the probe volume and the diffuser vane.

Therefore, at the rotor outlet, the circumferential grid is defined by 420 points (60 for each impeller passage), corresponding to the measuring windows (j), but the flow field depends also on the 24 circumferential positions (k) between the probe and the diffuser vane.

For the stator, on the contrary, the flow quantities over one diffuser circumferential pitch are defined at the 24 circumferential measuring positions (k), while the evolution in time is described by the 420 different time instants (j) in one revolution period of the impeller.

To highlight the rotor-stator interaction effects, the two sets of data have been analysed according to the following data processing procedures.

Effect of the vaned diffuser on the rotor flow.

According to Ubaldi et al. (1996), the ensemble averaged velocity at the rotor outlet $\bar{c}(j,k)$, can be split into two components: a circumferential ensemble averaged

component $\bar{c}(j)$ and a circumferential distributed fluctuating component $\tilde{c}'(j,k)$. The former, obtained by averaging the K distributions of the ensemble averaged velocity, is representative of the impeller flow regardless of the diffuser vane position:

$$\bar{c}(j) = \sum_{k=1}^K (\bar{c}(j,k) \Delta\theta_k) / \sum_{k=1}^K \Delta\theta_k \quad (3)$$

The fluctuating component $\tilde{c}'(j,k)$ is due to the upstream effect of the vaned diffuser on the rotor relative flow. The root of the circumferentially averaged square values of this quantity represents the stator generated unsteadiness on the impeller flow:

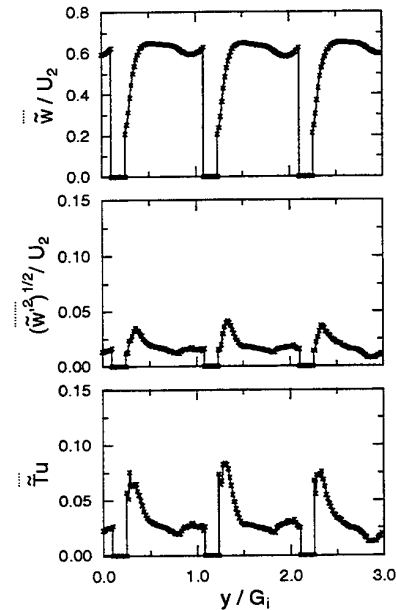


Fig. 3 Circumferential ensemble averaged relative velocity, stator generated and unresolved unsteadiness at the impeller outlet, midspan position.

$$\sqrt{\tilde{c}'^2(j)} = \sqrt{\sum_{k=1}^K [\bar{c}(j,k) - \bar{c}(j)]^2 \Delta\theta_k / \sum_{k=1}^K \Delta\theta_k} \quad (4)$$

The circumferential ensemble averaged relative velocity and the stator generated unsteadiness at midspan are shown as an example in Fig. 3.

An alternative description of the periodically unsteady rotor flow can be achieved by correlating the data in both time and space, in such a way to obtain instantaneous flow pictures corresponding to different relative positions between impeller blades and diffuser vanes, as shown for instance by Inoue and Cumpsty (1984). A detailed description of the adopted procedure is given by Ubaldi et al. (1996).

Instantaneous distributions of the impeller outflow perturbed by the diffuser vanes in relative motion, obtained according to the above mentioned procedure, are shown in Figs. 4-6.

Effect of the non uniform rotor flow on the vaned diffuser. By time averaging, the ensemble averaged velocity $\bar{c}(j,k)$ at the vaned diffuser inlet can be divided into a steady state velocity $\bar{c}(k)$, which does not depend on the relative rotor-stator position, and a rotor generated fluctuating component $\tilde{c}'(j,k)$ (e. g. Inoue and Cumpsty, 1984, Suder et al., 1987, Casey et al., 1995).

$$\bar{c}(k) = \sum_{j=1}^J \bar{c}(j,k) / J \quad (5)$$

The root of the time averaged square values of the fluctuating component is the rotor generated unsteadiness:

$$\sqrt{\tilde{c}'^2(k)} = \sqrt{\sum_{j=1}^J [\bar{c}(j,k) - \bar{c}(k)]^2 / J} \quad (6)$$

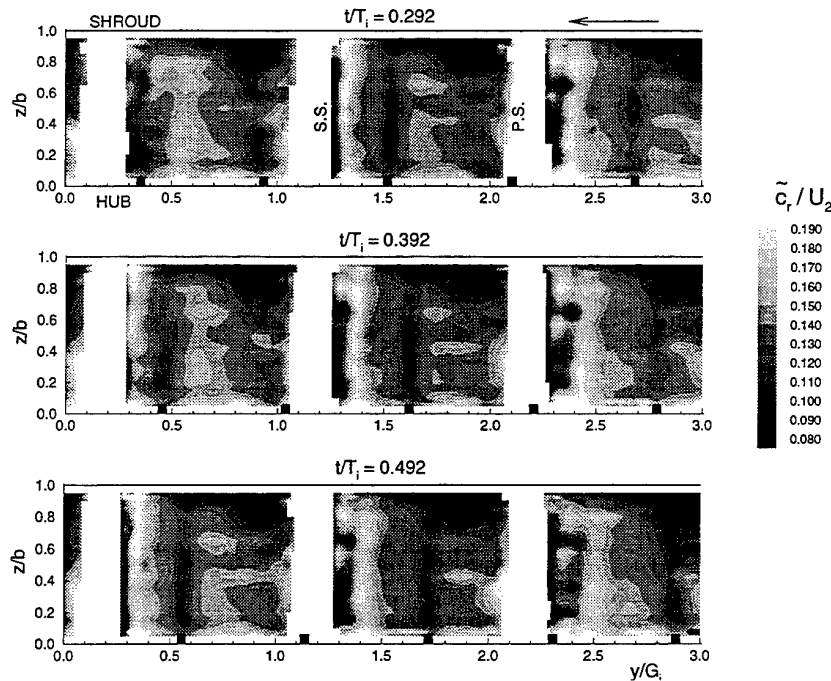


Fig. 4 Instantaneous pictures of the ensemble averaged radial velocity at the impeller outlet.

The steady state absolute velocity and the rotor generated unsteadiness at midspan of the diffuser vane inlet are shown as an example in Fig. 7.

The data at the diffuser vane inlet have also been interpolated at constant time instants to obtain pictures of the absolute flow for different relative positions between impeller and diffuser blades. Results are shown in Figs. 8-10.

3. RESULTS AND DISCUSSION

The results are given in terms of instantaneous pictures of ensemble averaged velocity components as well as stator and rotor generated unsteadiness distributions.

All the kinematic quantities are normalized with the rotor tip speed U_2 . The circumferential coordinate y is made non dimensional by means of the rotor circumferential pitch $G_i = 2\pi r / z_i$. The axial coordinate z is normalized by the blade span b . The time t is divided by the rotor blade passing period $T_i = 2\pi / \omega z_i$.

3.1 Flow at the Impeller Outlet

Figure 3 shows results obtained at midspan: on the top of figure there is the circumferential ensemble averaged relative velocity. The same figure also reports the comparison between the stator generated unsteadiness and the circumferentially averaged unresolved unsteadiness. The stator generated unsteadiness is rather weak but not negligible, being lower but still comparable with the

circumferentially averaged random unsteadiness $\tilde{T}u$. The largest values (4 per cent of the rotor tip speed U_2) can be observed at the suction side of the impeller passage, near

the beginning of the region of large relative velocity gradients due to the blade suction side separating boundary layer.

Figure 4 shows the instantaneous distributions of the ensemble averaged radial velocity for three different diffuser-impeller relative positions. The radial velocity at the rotor outlet is rather uniformly distributed on the impeller passage except for the presence of a through flow wake located in the pressure side/shroud corner, typical of unshrouded centrifugal impellers (e.g. Hathaway et al., 1993). The absence of a jet and wake structure, which is characteristic of highly loaded centrifugal impellers, depends on the above mentioned low geometrical diffusion ratio of the impeller channels associated with the strongly backward blade inclination.

The periodic upstream potential flow effect generated by the vaned diffuser is represented by the narrow vertical bands of low radial velocity, which correspond to the diffuser vane circumferential locations marked with small black squares in the figure. The diffuser blockage effect is accompanied by a flow acceleration on the left side appearing as a lighter vertical band.

The two vertical bands move against the impeller rotation at different circumferential velocities. The blockage effect rotates at the impeller speed, while the accelerated flow rather tends to extend toward mid-passage, when the diffuser vane moves from the suction side of the rotor blade toward the pressure side (see for instance the time evolution of the impeller central passage in the figure).

However, the stator vanes induce large periodic circumferential variations of the radial velocity. In the present case concerning lightly loaded impeller blades, at the normal operating conditions, the stator effect is not strong enough to cause flow recirculation at the impeller outlet, but in case of higher aerodynamic loads periodic

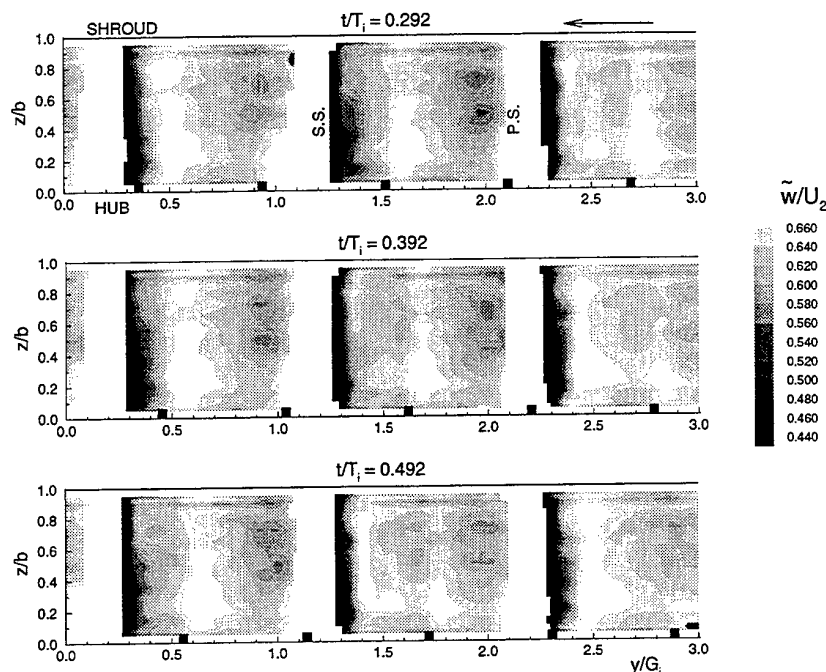


Fig. 5 Instantaneous pictures of the ensemble averaged relative velocity at the impeller outlet

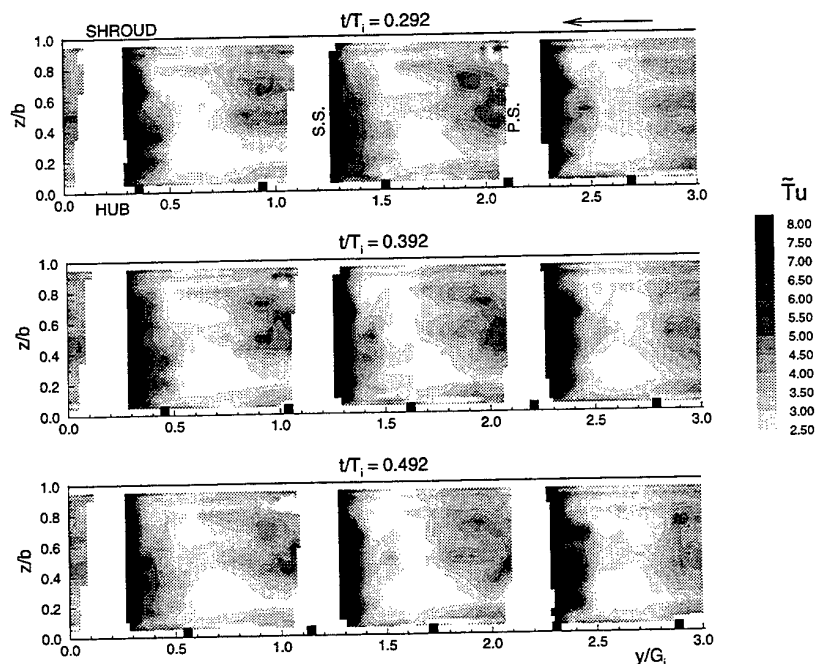


Fig. 6 Instantaneous pictures of the random unsteadiness at the impeller outlet.

separation of the impeller blade boundary layer is expected to occur.

The upstream effect of the diffuser vanes on the relative velocity (Fig. 5) appears as an increase of the velocity in correspondence of the pressure side of the vane and a decrease on the opposite side, resulting from the deflection of the relative streamlines. This perturbation can

modify the extent of the low momentum fluid in the suction side trailing edge region and the through flow wake near the pressure side/shroud corner.

The instantaneous distributions of the random unsteadiness at the impeller outlet are shown in Fig. 6. The random unsteadiness is low in the centre of the passage, it increases in the region near the pressure side occupied by

the through flow wake previously identified in the velocity distributions and becomes very intense in the boundary layer separating from the blade trailing edge suction side. The upstream potential flow effect on the random unsteadiness seems negligible with only a weak influence on the extension of the above mentioned regions of high turbulence intensity.

3.2 Flow at the Vaned Diffuser Inlet

Figure 7 shows results obtained at midspan: on the top of figure there is the ensemble and time averaged absolute velocity. The same figure also reports the comparison between the rotor generated unsteadiness and the time averaged unresolved unsteadiness.

The ensemble and time averaged absolute velocity decreases slightly from the suction to the pressure side of the diffuser passage. The steeper decrease on the left of each passage is due to the stagnation effect of the vane leading edge.

The rotor generated unsteadiness and the time averaged random unsteadiness are comparable and both are about 5 per cent, that is a rather large value, considering that these quantities are made nondimensional by the peripheral velocity U_2 . In practice the first distribution represents the rms of the absolute velocity periodic fluctuations, while the latter results as a mean of the random velocity fluctuations, which are high in the impeller blade wake and low in the impeller passage center.

Figure 8 shows the distributions of the radial velocity at the vaned diffuser inlet for three different time instants. The impeller blade positions are marked by small triangles. It is clear that the flow variations induced by the blade passing are larger than the potential flow gradients generated by the diffuser vanes. The perturbation generated

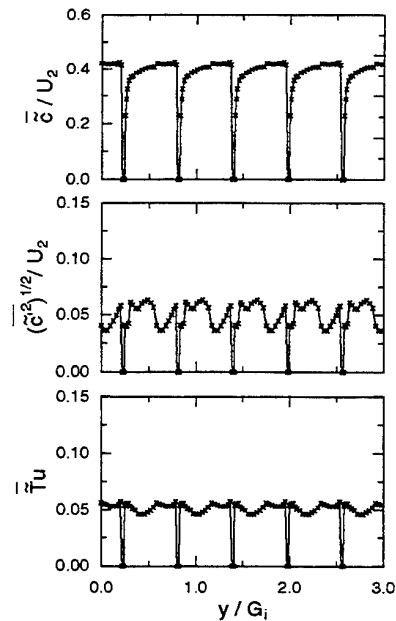


Fig. 7 Ensemble and time averaged absolute velocity, rotor generated and unresolved unsteadiness at the diffuser inlet, midspan position.

by the impeller blade passing is constituted by two regions of low radial velocity: one is associated with the blade wake, the second one, more extended and deep, located on the left of the triangle marking the impeller blade, is caused by the flow deviation near the pressure side of the blade trailing edge. The resulting effect is that conditions of low and large flow rate alternate in adjacent diffuser passages.

The effect of the non uniform rotor flow at the diffuser

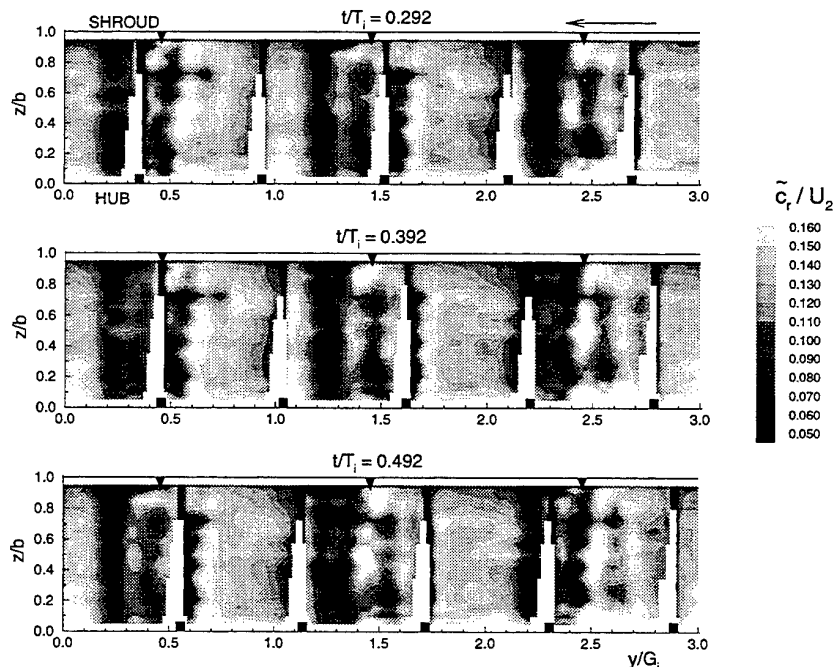


Fig. 8 Instantaneous pictures of the ensemble averaged radial velocity at the diffuser inlet.

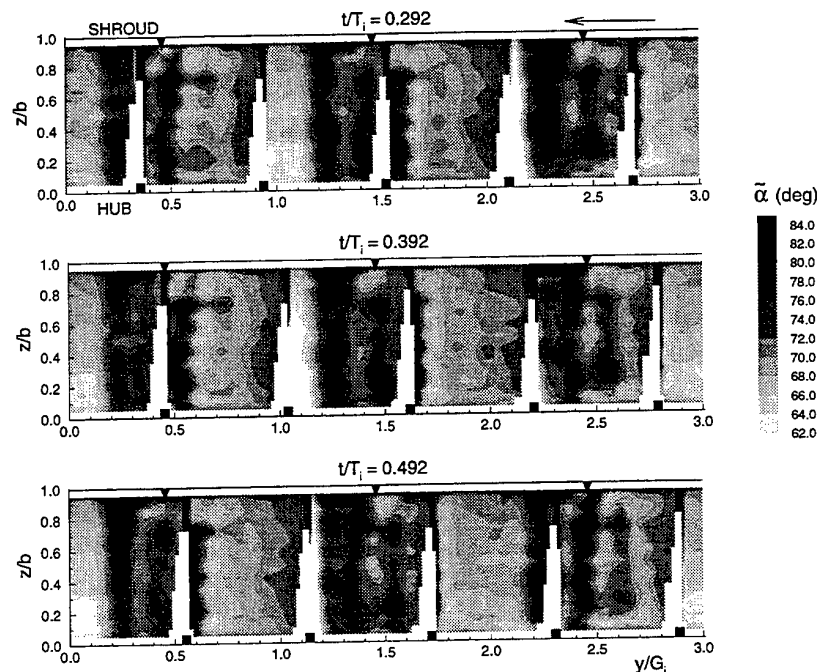


Fig. 9 Instantaneous pictures of the ensemble averaged absolute flow angle at the diffuser inlet.

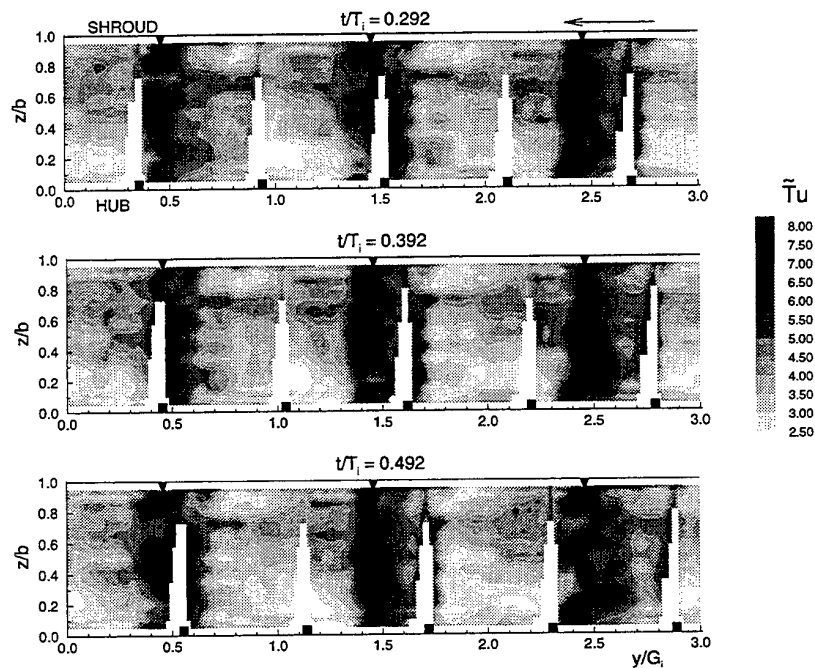


Fig. 10 Instantaneous pictures of the random unsteadiness at the diffuser inlet.

inlet is even more evident for the absolute flow angle (Fig. 9). The diffuser vanes undergo cyclic incidence angle variations as large as 20 deg, which are expected to influence severely the viscous flow development in the diffuser passages.

In Fig. 10 the instantaneous distribution of the random unsteadiness depends only on the periodic rotor outflow.

The blade wakes are clearly marked by concentrations of random unsteadiness which stand out against the non turbulent through flow. The global effect is the generation of a periodic flow pattern with adjacent passages operating alternatively on turbulent and non turbulent flow. The rotor wakes are chopped by the diffuser vanes, generating wake segments which enter into the diffuser passages affecting the

vane boundary layer development and influencing the pressure recovery process.

4. CONCLUSIONS

A LDV investigation of the rotor-stator aerodynamic interaction in a centrifugal turbomachine has been performed. Use of appropriate data processing techniques has allowed to detect both upstream potential flow diffuser effects and rotor blade wake passing perturbations.

The main upstream effect on the impeller outflow is the periodic blockage induced by the diffuser vanes, which can produce local periodic flow separation on the impeller blade suction side.

The rotor blade wake perturbation on the diffuser is more relevant. The highly distorted impeller flow does not appear to mix out before arriving at the vane leading edge. Cyclic incidence angle variations as large as 20 deg occur in the diffuser vane entry zone. Highly turbulent and non turbulent flow conditions alternate in adjacent diffuser passages, being the circumferential wake extension comparable with the vaned diffuser pitch.

Further detailed flow investigations within the diffuser are planned to evaluate the effect of the unsteady flow features observed at the diffuser entry zone on the vane boundary layer development and the diffusing process.

NOMENCLATURE

b	impeller blade span
c	absolute velocity
G_i	local impeller blade circumferential pitch
l	impeller blade chord length
p_t	total pressure
Q	flow rate
r	radial coordinate
R_2	impeller outlet radius
t	time
T_i	impeller blade passing period
Tu	turbulence intensity $= \left[\left(\frac{\tilde{c}_r^2 + \tilde{c}_\theta^2}{2} \right)^{1/2} / U_2 \right] \cdot 100$
U_2	peripheral velocity at the impeller outlet
w	relative velocity
y	circumferential coordinate
z	axial coordinate
z_i	number of impeller blades
α	absolute flow angle with the radial direction
β'	impeller blade angle with the radial direction
ν	kinematic viscosity
ρ	fluid density
ϕ	flow rate coefficient $= Q / (U_2 \pi R_2^2)$
ψ	total pressure rise coefficient $= 2(p_{t4} - p_{t0}) / (\rho U_2^2)$
ω	angular velocity

Subscripts

r	in the radial direction
θ	in the circumferential direction

0	in the suction pipe
2	at the impeller outlet
3	at the diffuser vane inlet
4	at the diffuser outlet

Superscripts

'	unsteady quantity
\sim	ensemble average
—	time average
\dots	circumferential average

REFERENCES

- Arndt, N., Acosta, A. J., Brennen, C. E. & Caughey, T. K., 1990, Experimental Investigation of Rotor-Stator Interaction in a Centrifugal Pump With Several Vaned Diffusers, *ASME Journal of Turbomachinery*, vol. 112, pp. 98-108.
- Boutier, A., 1991, Accuracy of Laser Velocimetry, Lecture Series 1991-05, VKI, Brussels.
- Casey, M. V., Eisele, K., Zhang, Z., Gülich, J. & Schachenmann, 1995, Flow Analysis in a Pump, Part 1: LDA and PTV Measurements of the Unsteady Flow, in *Laser Anemometry*, ASME FED-vol. 229, pp. 89-100.
- Hathaway, M. D., Chriss, R. M., Wood, J. R., & Strazisar, 1993, A. J., Experimental and Computational Investigation of the NASA Low-Speed Centrifugal Compressor Flow Field, *ASME Journal of Turbomachinery*, vol. 115, pp. 527-542.
- Krain, H., A Study on Centrifugal Impeller and Diffuser Flow, 1981, *ASME Journal of Engineering for Power*, Vol. 103, pp. 689-697.
- Inoue, M. & Cumpsty, N. A., 1984, Experimental Study of Centrifugal Impeller Discharge Flow in Vaneless and Vaned Diffusers, *ASME Journal of Engineering for Gas Turbine and Power*, vol. 106, pp. 455-467.
- Modarress, D., Tan, H. & Nakayama, A., 1988, Evaluation of Signal Processing Techniques in Laser Anemometry, *Proc. Fourth International Symposium on Application of Laser Anemometry to Fluid Dynamics*, Lisbon, paper 1.20.
- Rothe, P. H. & Johnston J. P., 1976, Effects of System Rotation on the Performance of Two-Dimensional Diffusers, *ASME Journal of Fluids Engineering*, vol. 98, pp. 422-430.
- Strazisar, T., 1986, Laser Anemometry in Compressors and Turbines, ASME Lecture on Fluid Dynamics of Turbomachinery.
- Suder, K. L., Hathaway, M. D., Okiishi, T. H., Strazisar, A. J. & Adamczyk, J. J., 1987, Measurements of the Unsteady Flow Field Within the Stator Row of a Transonic Axial-Flow Fan I -Measurement and Analysis Technique, ASME Paper no. 87-GT-226.
- Ubaldi, M., Zunino, P., Barigozzi, G. & Ghiglione A., 1994, Non-Intrusive Measurements of the Unsteady Flow in the Radial Gap Between Centrifugal Impeller and Vaned Diffuser, *Proc. 12th Symposium on Measuring Techniques for Transonic and Supersonic Flow in Cascades and Turbomachines*, Prague, paper 27.
- Ubaldi, M., Zunino, P., Barigozzi, G. & Cattanei, A., 1996, An Experimental Investigation of Stator Induced Unsteadiness on Centrifugal Impeller Outflow, *ASME Journal of Turbomachinery*, vol. 118, pp. 41-54.

AERO-ACOUSTIC MEASUREMENTS ON AN AEROFOIL

C.Swales, E.C.Nash, M.V.Lowson

Department of Aerospace Engineering
University of Bristol
Bristol, England

ABSTRACT

A fundamental study has been undertaken on the self noise generated by aerofoils, an issue crucial to the design of propellers, helicopters and wind turbines. There is still little understanding of the fluid mechanisms involved, and consequently few suggestions for noise reduction. In this study use has been made of a low turbulence, closed working section, wind tunnel modified to quasi-anechoic conditions and a Dantec 3 component laser Doppler anemometer (LDA). Analysis of the results, presented in the form of time series, spectral analyses, and velocity profiles, have provided important insights into the mechanisms involved. For these studies the LDA has again proved to be a uniquely capable tool.

1. INTRODUCTION

Aerofoil noise radiation is an important issue for helicopter, propeller, and wind turbine designs. Excessive noise has for example emerged as a crucial issue in obtaining consents for the installation of wind turbines in rural areas. However, prior to being able to design a new generation of, in this case, "quiet" wind turbines, the fluid mechanisms involved on even the simplest static wing need to be better understood. The present study is therefore part of a fundamental study on aerofoil noise generation being undertaken at the University of Bristol and involves detailed measurements on two different aerofoils - a NACA 0012 and an FX79 - mounted within the department's low turbulence wind tunnel. The investigation involves extensive use of a 3-component Dantec laser Doppler anemometer (LDA).

It is well established that there are four principal sources of self-noise on an aerofoil, and these are shown schematically in Fig. 1. It is turbulent boundary layer trailing edge noise, Fig. 1a, (see Ffowcs Williams and Hall (1970)) and laminar boundary layer vortex shedding noise, Fig. 1d, (see Brooks et al. (1989)) which are of particular interest in this study. The former produces broadband noise, while the latter produces discrete tones, the frequency of which for wind turbines lies between 1000 and 5000Hz, ie. in the range of maximum response

of the human ear, and at sound levels more than 20dB above background noise. Despite a number of recent studies on noise, and the mechanisms involved, there are few suggestions as to methods for noise reduction. The engineer therefore has little information on which to base design judgements for quieter blades.

This lack of quality data can partly be attributed to difficulties in establishing suitable test conditions. The majority of previous studies have been conducted in open-jet, anechoic facilities, thereby ensuring that there is no spurious acoustic feedback involving reflections from nearby solid surfaces such as would be caused by the solid floor and ceilings of a closed section wind tunnel. However, there are several problems associated with employing an open-jet wind tunnel which might make measurements within closed section wind tunnels more desirable. These include strict limits on the chord length and angles of attack that can be used, large corrections which need to be applied to the measurement of the angle of attack, and the higher levels of background noise encountered. The solution employed at Bristol University is therefore to combine the best features of these two distinct approaches by introducing an anechoic lining to the working section of a closed working section, closed loop wind tunnel. The acoustic lining was in the form of large hollow boxes filled with acoustic foam fitted above and below the working section, and flush with the wind tunnel floor and ceiling (Fig. 2). As shown by Nash and Lowson (1995) this has been found to successfully remove the dominant resonant frequencies.

A number of techniques are available which, potentially, can be used for boundary layer studies. However, in practice it has been shown that noise generation is extremely sensitive to the state of the boundary layer. For this reason the best results are obtained by those techniques which in no way affect either the surface or the boundary layer itself. Flow visualisation techniques such as china-clay and oil-streaks have been shown to produce different results to the LDA, and later in this paper it will be shown how the hot-wire locally affected the flow. For this reason the LDA was used for the majority of the program and it is essentially results from the LDA which have provided insights into the key

mechanisms involved in the noise generation. This paper will briefly describe the tests and will identify and draw conclusions on some of the principal issues as regards the LDA and not the fluid dynamics.

2. LDA SYSTEM

The LDA employed was a full 3 component Dantec Fibre-Flow system, the principal components of which are shown in Fig. 3. The light source is a 5 Watt Spectra-Physics 2016 Stabilite Argon-ion laser. Ten-metre long fibre optic cables enable the three dominant wavelengths to be transmitted to two independently mounted 1600mm focal length optic heads - green (514.5nm) and blue (488nm) beams are emitted from one optic head (referred to as the 2D head), violet beams from a second (1D) optic head. The substantial gimbal mounts within which the optic heads are mounted can be dipped and swept to provide the required optical configuration. Both gimbal mounts are affixed to an optic bench, and in turn to a high precision 3 axis Dantec traverse. The traverse enables a 600mm by 600mm by 600mm grid to be considered with a step size accurate to 0.005mm.

Collection of the scattered light can be achieved by both optic heads, and hence two distinct modes of operation are possible. In the backscatter mode the light scattered by the seeding particles passing through the measurement volume created by the intersection of the beams from one optic head is collected by the same optic head; cross-coupled the light is collected, off-axis, by the other optic head. In both cases the collected light passes back down the fibre-optic cable to three "filtered" photomultipliers. The resulting signal from each photomultiplier is then fed to an Enhanced Burst Spectrum Analyser - one for each wavelength. The method of accurately determining the frequency/velocity calibration factor is described in Swales et al. (1996). A 133MHz Pentium provided the computer hardware to control both the data acquisition and the traverse movement.

The experimental requirement was for three component, non-intrusive, and directionally unambiguous velocity data. These criteria were successfully met by the above system. The further important requirement of ensuring good spatial resolution was only satisfied by collecting light off-axis, achievable only after the development of a quantitative alignment technique described by Swales et al. (1993) and Swales (1994).

3. EXPERIMENTAL SET UP

Each aerofoil was mounted horizontally across the low turbulence wind tunnel, spanning the test section (Fig. 2). One end of the wing slotted through the side of the wind tunnel wall, clamped in a rotating circular collar enabling the incidence to be changed through ± 20 degrees. The other end of the wing was pin mounted to the window to ensure good access for the laser beams.

The LDA traverse was mounted on a rigid base external to the wind tunnel working section with the optic heads arranged in such a way that the measurement volume created by the intersecting beams could access all regions of interest. The reference, (0, 0, 0), position was defined as being mid-span, at the trailing edge, and at the surface. The surface position was found by traversing the measurement volume towards the wing surface and noting the photomultiplier anode current output until a maximum value was reached - this corresponded to the surface of the wing (see Boutier (1991)). In most cases the measurements presented are for the green beams aligned with a small dip and with negligible sweep relative to the wind tunnel, thereby measuring a velocity component aligned with the freestream direction.

The requirement was for high quality velocity measurements within the boundary layer with which to relate the structure of the flow with the noise generating mechanism. This might not at first appear to warrant the use of an LDA, and indeed previous studies have employed hot-wire anemometers with supposed success. However, results by Nash and Lowson (1995) showed that for certain cases, whereas the LDA was indicating a region of separated flow the hot-wire results showed the flow to be attached and laminar. Fig. 4 shows the LDA measurement volume and a standard Dantec Type 55P11 hot-wire probe located alongside, 5mm upstream from the trailing edge, mid-span, and 1mm from the surface. A series of velocity profiles through the boundary layer (Fig. 5) shows that with the LDA measurement volume 5mm alongside the hot-wire the two instruments provide very similar results. From these and similar results it can be concluded that both instruments must be providing a correct measure of the velocity, but that the hot-wire, the probe holder or the mount must be adversely affecting the flow. Subsequent tests have shown the principal source of disturbance to be the two prongs of the hot-wire; in addition the type of hot-wire probe (55A22, 55P11, 55P14 were all employed) made little difference to the results. As boundary layer velocity measurements play such a crucial part in the study it is therefore evident that only an LDA can provide a representative measure of the velocity, and a number of previous studies must be regarded with caution.

4. TYPES OF LDA MEASUREMENT

4.1 Boundary Layer Velocity Profiles

The boundary layer velocity profiles given in Fig. 6 show a clear progression with angle of attack for the NACA 0012 aerofoil. These boundary layer velocity profiles, acquired at the trailing edge with the aerofoil from 1 to 13 degrees incidence, are for the suction surface. From these velocity profiles, in this case non-dimensionalised relative to height, the key boundary layer parameters, such as displacement and momentum thickness, can be determined. These boundary layer parameters provide the input for a noise prediction routine

defined by Lowson (1995) which describes how for broadband turbulent boundary layer trailing edge noise the source of the noise moves away from the surface with increase in angle of incidence (Fig. 7).

With the LDA employed in the off-axis mode of light collection velocity measurements can routinely be acquired to within 0.05mm of the surface though in many cases this detail is unnecessary. In the case of determining the displacement thickness, δ^* , however values near the surface have the greatest effect on the final result and therefore for this case accurate measurement of the velocity very near to the surface is imperative and it is in this respect that the LDA excels. The backscatter mode could only be employed in the outer reaches of the boundary layer and consequently this mode was never employed. In effect the level of alignment was also such that the backscatter mode never needed to be used.

4.2 Velocity Histograms and Time Series

In themselves the boundary layer velocity profiles reveal certain important issues regarding the fluid mechanisms involved. Equally important, in certain situations, are the generation of probability density function (pdfs) showing the distribution of velocities measured at a given station within the boundary layer, and time series showing the variation of velocity with time.

Fig. 8 shows a sample boundary layer velocity profile (in this case of root mean square (RMS) velocity) which reveals three, as opposed to the more conventional one, local maxima (labelled a, b, and c). Corresponding velocity pdfs and time series are shown for these three maxima and also for a station near the top of the boundary layer. For station "d" the pdf reveals a narrow distribution (from 37.7 to 39.6 m/s) and consequently the amplitude in the time series is small - in addition there is no structure. Both distributions are typical of the outer extremities of a boundary layer. For station "c" the pdf distribution is wider, indicating a more turbulent flow (the amplitude of the velocities in the time series is also correspondingly higher) but there is also evidence that there are two distinct peaks. The time series explains the phenomenon by showing the flow to be cyclical. For this station a time series is arguably more informative than a velocity histogram.

At station "b", which corresponds to the maximum value of rms, the two distributions are again very different with no structure in the time series. Finally at station "a" the data rate is too low (200Hz) to reveal any structure in the time series (see below). As opposed to station "c" it is the histogram which in this case is more informative. Twin peaks are again evident, and although the measured velocities range from -8.26 to +8.32 m/s the mean velocity is approximately zero. For this case even if the hot-wire had been able to measure the velocity without adversely affecting the flow, which as has been described above is not the case, the measured velocity would have been approximately 3 m/s.

4.3 Spectral Analysis

A Brüel & Kjær microphone was placed 0.15m above the wing trailing edge and at a mid-span position. The microphone signal was fed directly to a Brüel & Kjær (B&K) frequency analyser. A microphone, unlike an LDA or a hot-wire, cannot however provide a local measure of the frequency content within the flow. The hot-wire was dismissed due to its intrusive nature.

Historically frequency trackers have been used to supply an analogue output of the unsteady content of the flow (d'Emilia and Tomasini (1987)). For this study a Dantec analogue tracker (Type 55N21) was used in conjunction with a Dantec frequency shifter (Type 55N11), together with the LDA components described above, to provide an analogue output. The tracker had to have a quasi-continuous burst signal, which required extreme levels of seeding which in many cases such as near the surface simply could not be maintained.

Direct analogue outputs are now available for BSAs, and this feature has in these, and other tests (see Harden (1996)), proved invaluable. The signal can be fed directly to a frequency analyser, such as the B&K Type 2144/7651, to provide an on-line frequency output. Fig. 9 shows a series of frequency spectra from the B&K microphone, the tracker and the analogue output from the BSAs. It can be seen that although the frequency at which the tone occurs is the same for all three devices the amplitude of this disturbance varies. For the discrete tone at approximately 1050 Hz the microphone and the analogue output from the BSA both show the tone to be 30dB above background noise; however the tracker shows it to be only 15dB above background, and yet for the tracker a data rate of 40KHz rather than 25 KHz is required. A lesser peak could therefore be "missed" by the tracker. Finally the signal from the analogue output can be analysed whilst acquiring other velocity information. In the case of the tracker the seeding level required is so high that all other tasks have to be stopped.

For all frequency spectra measurements by laser anemometry it is accepted that the data rate must be a certain factor higher than the frequency to be measured, though the value quoted for this factor varies considerably, eg. from 5 (Host-Madsen and Caspersen (1994)) to 20 (Adrian and Yao (1987)). Experimental evidence at Bristol suggests that the factor is approximately 10. This value was determined by acquiring measurements "on-line" and then switching off the seeding input to the wind tunnel. The data rate then decreases in line with the seeding level, as does the measured frequency *amplitude*. Fig. 10 shows the correlation of measured frequency amplitude with data rate for three different flow conditions each with a different dominant frequency. Though not shown, the actual frequency measured remains unaffected by data rate.

The settings on the frequency analyser had no effect on either the frequencies measured or their amplitudes; the settings on the BSAs did have, but only in so far as different settings caused different data rates which in turn

affected the frequency amplitudes. This relationship was established by having a constant seeding level and by simply increasing either the processor gain or photomultiplier high voltage. If these results are combined with those for the 1288Hz results shown in Fig. 10 then the two sets of data clearly collapse to a single curve (Fig. 11), indicating that the effect of increasing the signal amplitude manifests itself only in terms of a variation in the data rate. However the effect of doubling the bandwidth of the BSA is to halve the amplitude of the measured peak, which corresponds to the 6dB drop shown.

Finally the random data acquired can also be resampled to produce pseudo-equi-time spaced data which can then be transformed using Fast Fourier Transforms (FFTs). For this study the post-processing was carried out within "Burstware" and a number of different parameters could be set. Again the answers agree well with those from other methods, and a sample result is shown in Fig. 12. It is clear from the time series that the data rate is such that the cyclic behaviour of the flow is fully captured, with around a dozen individual velocity realisations defining each cycle. The 20+ cycles which can be observed over the 20ms window corresponds to the measured frequency of just over 1000Hz, as shown in the frequency distribution. The "smoothness" of the pdfs and the sharp "cut-off" at the two extremities is proof of the quality of the velocity measurements - a noisier signal would have resulted in spurious velocity readings.

In conclusion therefore this study has employed three methods of obtaining local frequency spectra. The tracker, because of the extreme levels of seeding which are required, proves the least valuable. It is the analogue output which, with the signal being fed to an external frequency analyser producing an on-line measure of the frequency, is the most powerful. Provided that the data rate is maintained at a reasonable level, and most importantly the bandwidth is not varied, it can be used to gain an idea, not only of the frequencies of oscillations present within a flow, but also of the amplitude of the oscillations. Hence for the first time the distribution of noise around an object can be mapped with ease.

5. CONCLUSIONS

The laser anemometer has revealed itself to be an excellent tool for aero-acoustic studies, in this case providing important results on an aerofoil mounted within a closed section wind tunnel, modified to provide quasi-anechoic conditions. Results have been presented in the form of velocity histograms, time series and velocity profiles. It is however use of the LDA to provide spectral information on the flow which reveals the most important information on the fluid mechanisms present. A direct analogue output of the velocity signal has also been shown to be potentially invaluable.

REFERENCES

- Adrian, R.J. and Yao, C.S. 1987 Power Spectra of Fluid Velocities Measured by Laser Doppler Velocimetry, Experiments in Fluids, No. 5.
- Boutier, A. 1991 Advanced Systems: Multicomponent LDV, VKI Lecture Series 1991-05, Laser Velocimetry.
- Brooks, T.F., Pope, D.S., and Marcolini, M.A. 1989 Airfoil Self Noise and Prediction, NASA RP 1218.
- D'Emilia, G. and Tomasini, E.P. 1987 Experimental Verification by LDA of Rectangular Orifice Flow Coefficient, Second International Conference on Laser Anemometry Advances and Applications, Strathclyde.
- Ffowcs Williams, J.E. and Hall, L.H. 1970 Aerodynamic Sound Generation by Turbulent Flow in the Vicinity of a Scattering Half Plane, Journal of Fluid Mechanics, Vol. 40, Part 4.
- Harden, J.M. and Lowson, M.V. 1996 The Application of Laser Anemometry to Eddy Capture in a Propeller Inflow, 8th International Symposium on Applications of Laser Techniques to Fluid Mechanics, Lisbon, Portugal.
- Host-Madsen, A. and Caspersen, C. 1994 The Limitations in High Frequency Turbulence Frequency Estimation, Eighth International Symposium on Applications of Laser Techniques to Fluid Mechanics, Lisbon, Portugal.
- Lowson, M.V. 1995 Aerofoil Noise Radiation Models, AIAA Aeroacoustics Meeting, Munich.
- Nash, E.C. and Lowson, M.V. 1995 Noise due to Boundary Layer Instabilities, First Joint Aero-acoustics Conference AIAA/CEAS, Munich.
- Swales, C., Rickards, J., Brake, C.J., and Barrett, R.V. 1993 Development of a Pin-hole Meter for Aligning Three Dimensional Laser Doppler Anemometers, Dantec Information, Vol. 12.
- Swales, C. 1994 Advanced LDA Techniques for Measurement of 3D Boundary Layer Velocity Profiles on a Helicopter Rotor, PhD Thesis, University of Bristol, Department of Aerospace Engineering.
- Swales, C., Rickards, J., Crompton, M., Terry, N., and Breeze, G. 1996 Three Component LDA Study of the Flow Field Surrounding the Helicopter Landing Pad of a Frigate, Eighth International Symposium on Applications of Laser Techniques to Fluid Mechanics, Lisbon.

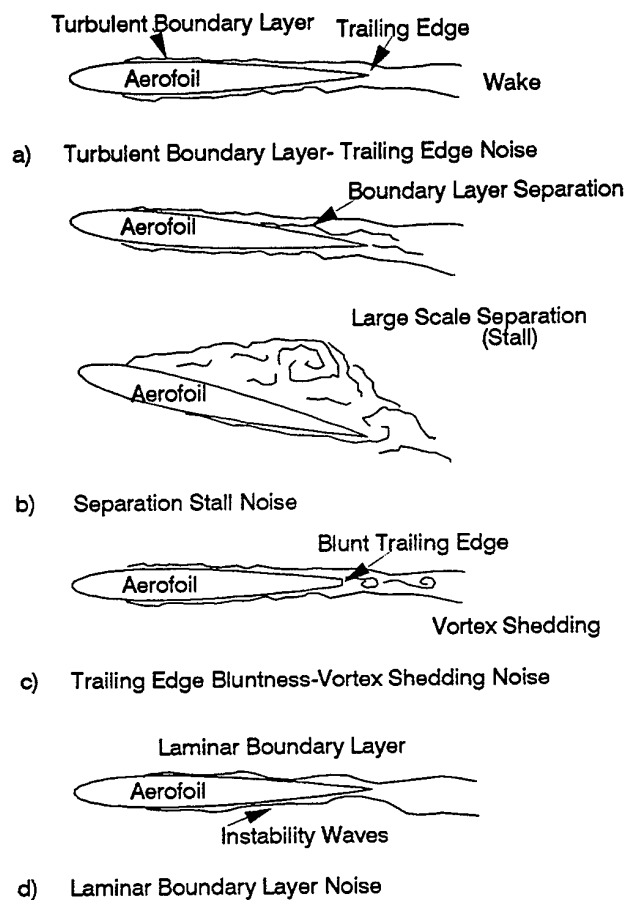


Fig. 1 Four Sources of Aerofoil Self-Noise (Brooks, Pope and Marcolini)

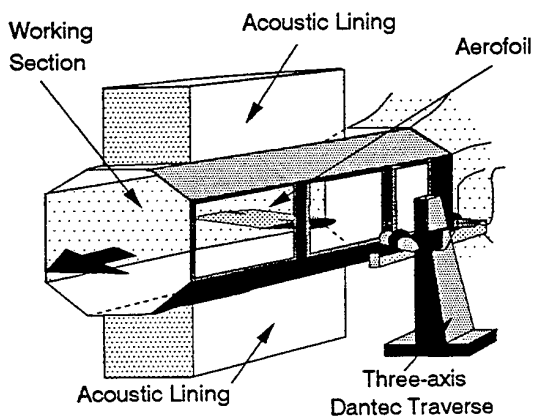


Fig. 2 Schematic Showing Experimental Setup

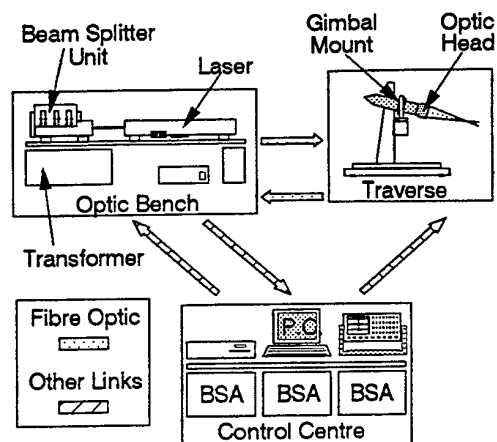


Fig. 3 Schematic of LDA Components

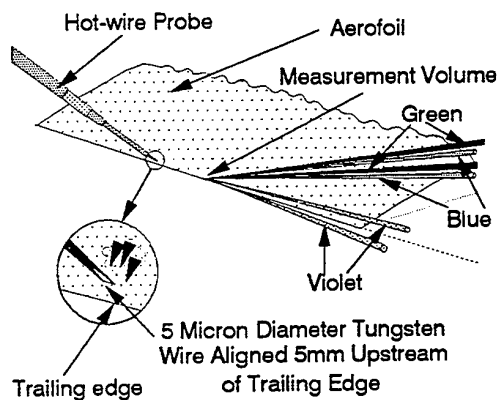


Fig. 4 LDA and Hot Wire Configuration

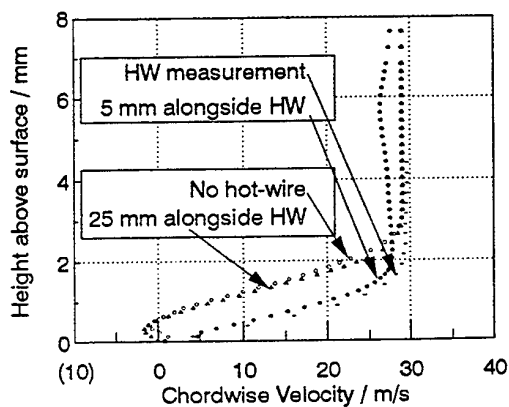


Fig. 5 Hot-wire Versus LDA Velocity Profiles

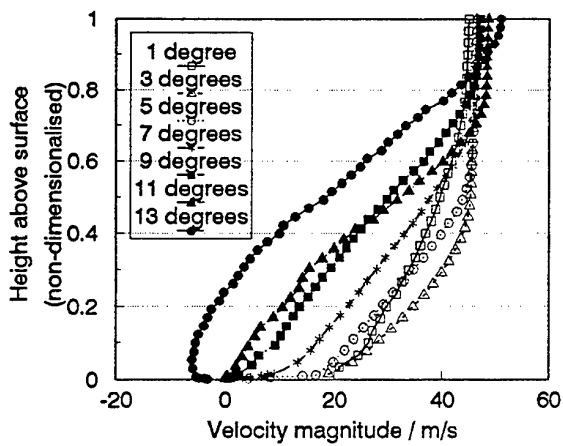


Fig. 6 Mean Velocity Profiles for NACA0012

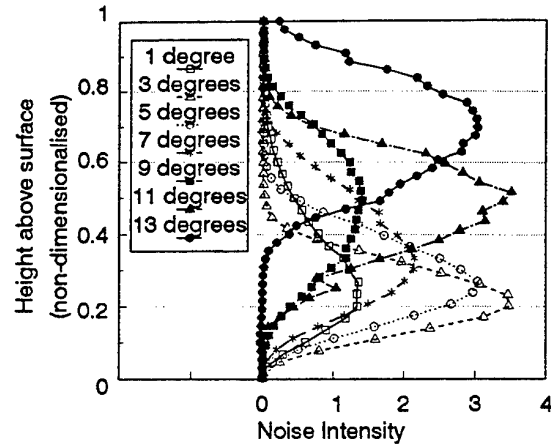


Fig. 7 Noise Intensity Profiles for NACA0012

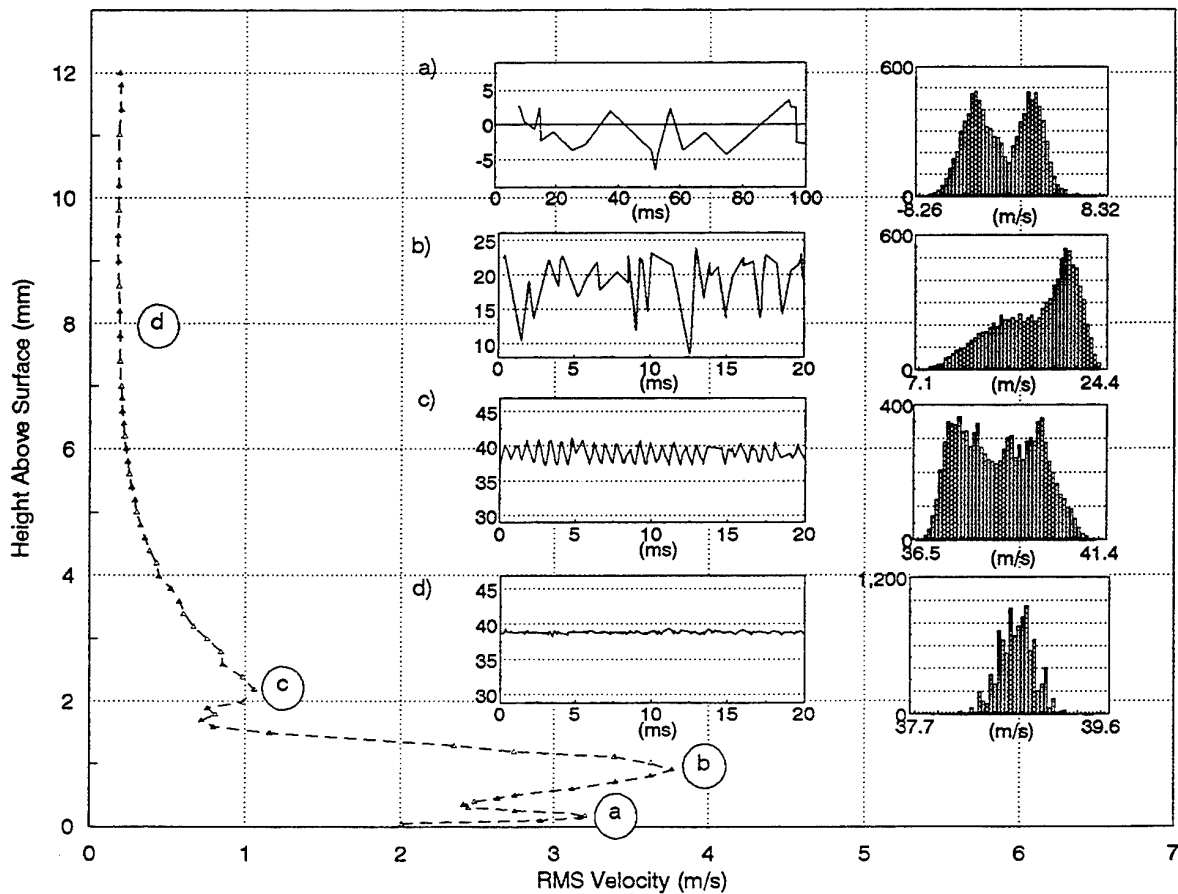


Fig. 8 Boundary Layer Velocity Profile, Time Series, and Velocity Histograms for FX 79 Aerofoil at 30m/s, 3 Degrees Incidence

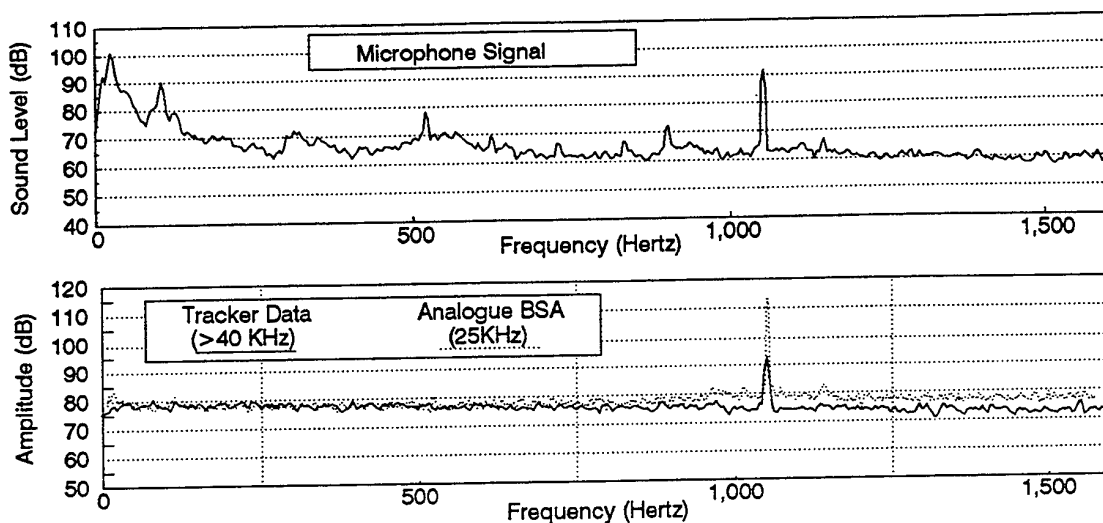


Fig 9 Frequency Spectra from Microphone, Tracker, and Analogue BSA Outputs

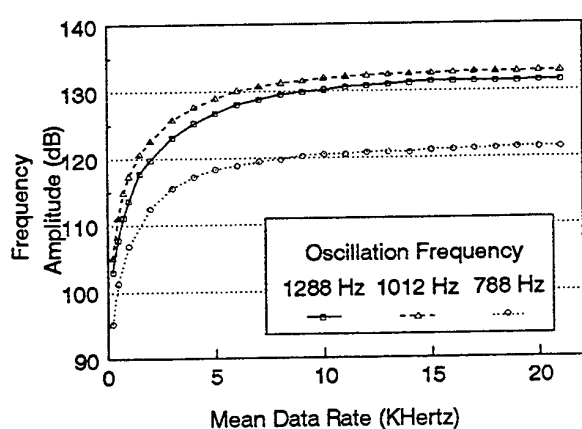


Fig. 10 Required Data Rate for Different Flows

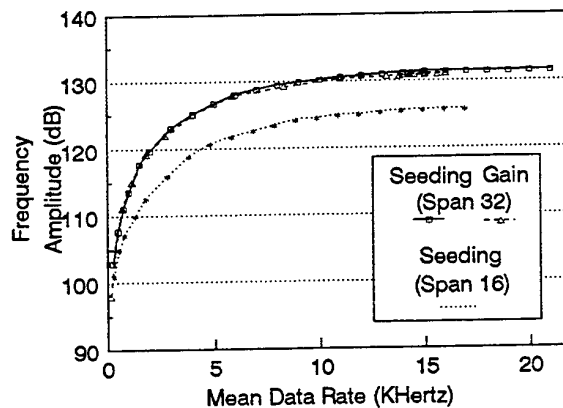


Fig. 11 Effect of Settings on Amplitude

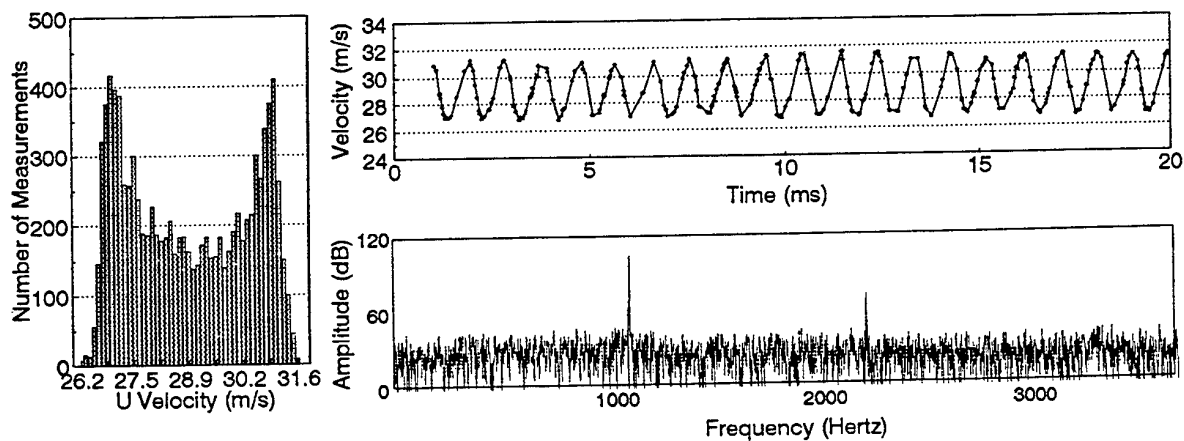


Fig 12 Velocity Histogram, Time Series, and Frequency Spectra (2.84mm above surface)

SESSION 29

Wall Flows II

A CHECK OF TAYLOR'S HYPOTHESIS USING TWO-POINT LDV MEASUREMENTS IN A TURBULENT BOUNDARY LAYER

R. Elavarasan, L. Djenidi and R. A. Antonia
Department of Mechanical Engineering
University of Newcastle, N.S.W. 2308 Australia

ABSTRACT

Two-point velocity correlation measurements are used to evaluate Taylor's hypothesis in the near-wall region of a turbulent boundary layer. The results indicate that the hypothesis is not a good approximation in the region $y^+ < 15$. The convection velocity deduced from the space-time correlations follows the local mean velocity for $y^+ > 30$, but it is about 35% higher in the region $y^+ < 15$.

1. INTRODUCTION

Taylor's hypothesis allows the spatial derivative to be inferred from the temporal derivative, viz,

$$\frac{\partial()}{\partial t} = -U_c \frac{\partial()}{\partial x} \quad (1)$$

where U_c is the convection velocity and x, y, z are the longitudinal, wall-normal and transverse directions respectively. Eq. (1) is extensively used in experimental work on turbulence. Yet, very few experimental checks have been made on Taylor's hypothesis in the near-wall region ($y^+ \leq 40$) of a turbulent boundary layer (Nakagawa and Nezu, 1981 and Krogstad et al., 1995). The procedure generally requires the measurement of the velocity correlation between two points separated in the streamwise direction [if Eq. (1) is to be tested for velocity]. While hot-wires can provide reliable measurements when the separation Δx is relatively large, they become less reliable when Δx is small due to the possible interference from the thermal wake of the upstream wire. Possible ways of overcoming this difficulty consist in laterally separating the wires or introducing a wake correction factor when calculating the correlation (Champagne et al., 1970).

Regardless of the separation between the two measuring volumes, the non-intrusive Laser Doppler Velocimeter (LDV) offers, in principle, the possibilities of estimating two-point velocity correlations more reliably than with the use of thermal anemometry. Various LDV configurations have been used in the past for such measurements. For example, Morton and Clark (1971) used two separate LDVs to measure the spatial correlation coefficients along lateral and longitudinal directions in a pipe flow. Fraser et al. (1986) used a dual beam configuration, consisting of only one elongated measuring volume and two optical fibre detectors, for their length scale measurements in reacting and non-reacting turbulent flows. Cenedese and Romano (1991) used an optical configuration in which a split lens was used to form two measuring volumes. They conducted their experiments in a channel flow with high turbulence intensity ($u'/U = 20\%$, U and u' are the mean and rms of the longitudinal velocity respectively) and verified the Taylor's hypothesis on the centre line of the channel.

The main aim of the present study is to check Taylor's hypothesis in the near-wall region of a turbulent boundary layer, a flow region for which hot-wires have limitations. The paper reports LDV measurements of longitudinal and temporal correlations of the streamwise velocity fluctuations.

2. EXPERIMENTAL SET UP

The experiments were performed in a closed circuit constant head vertical water tunnel and the details are given in Ching et al. (1995). The vertical 2 m high working section (250 mm square cross section) is made of 20 mm thick clear perspex. A roughness strip was recessed into a cavity

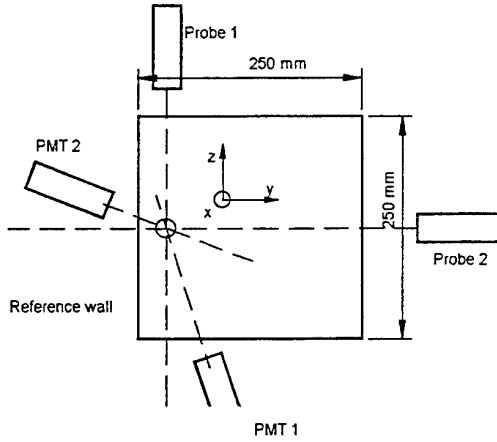


Figure 1: LDV configuration

100 mm downstream from the exit of the contraction and used to trip the boundary layer. The measurements were made 0.95m from the trip. The Reynolds number based on the momentum thickness (θ) was $Re_\theta = 700$, corresponding to a freestream velocity U_1 of 0.23 ms^{-1} . The freestream turbulence intensity was about 1% and the pressure gradient was negligible (Ching et al., 1995).

A three component fibre optic LDV system (Dantec, 5W Ar-ion) was used in a forward scattering mode. For correlation measurements, two pairs of light beams, green and blue, respectively, were transmitted in two separate probes and placed in orthogonal directions so that both probes allowed the measurement of u -component of the velocity (Fig. 1). The dimensions of the measuring volumes were $(0.047 \times 0.047 \times 0.4 \text{ mm})$ and $(0.044 \times 0.044 \times 0.4 \text{ mm})$ for green and blue beams, respectively. Enhanced Burst Spectrum Analyzers (BSA) were used for processing the Doppler signals. The data collection was made in coincidence mode. In this mode, the BSAs process the signals only when two signals are within the set coincidence interval of 0.16ms. The maximum data rate was about 500 Hz at $y^+ = 30$. At each measuring point, 40000 samples were collected. The flow was seeded with iriodin silver particles (about 2 mm in size). Standard Dantec software (BURSTware) was used to process the signals from the photo multipliers.

The spatial correlation coefficient of u -component of the velocity fluctuation is defined

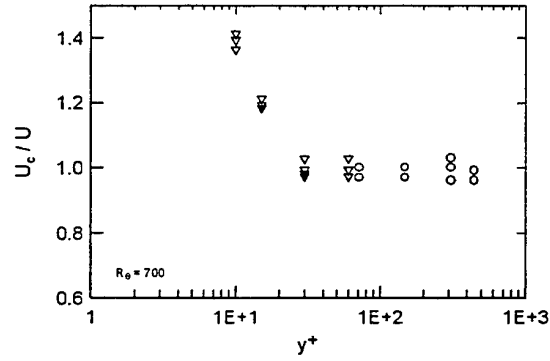


Figure 2: Variation of convection velocity across the boundary layer. O, Krogstad et al. (1995). ∇ , present measurement.

as

$$\rho_{\Delta x} = \frac{\overline{u(x_0, t)u(x_0 + \Delta x, t + \tau)}}{\overline{u(x_0)'u(x_0 + \Delta x)'}} \quad (2)$$

where x_0 is the longitudinal location of the reference measuring volume (Fig. 1), Δx is the separation between the probes and τ is the time lag. Since the verification of Taylor's hypothesis requires the velocity data to occur at regular intervals, a linear interpolation scheme was used prior to computing the correlation.

3. RESULTS

Taylor's hypothesis is often used to estimate the streamwise spatial correlation coefficients via the temporal correlation coefficient ρ_τ viz.

$$\rho_\tau = -U_c \rho_{\Delta x} \quad (3)$$

In a turbulent boundary layer, u'/U can be as large as 40-50% in the near-wall region making Taylor's hypothesis questionable in that region. Previous studies have indicated that the convection velocity may be approximated by the local mean velocity in the region $y^+ > 30$ (Lumley, 1965; Champagne et al., 1970; Poimelli et al., 1989). However, this approximation can be found inaccurate in the region of $y^+ < 30$ (Zaman and Hussain, 1981; Hussain and Clark, 1981). Studies of coherent motions in the boundary layer have revealed that the convection velocity might indeed depend on the scale of the motion considered (Perry and Abell, 1977; Kim and Hussain 1992; Krogstad et al., 1995). Favre et al. (1967) measured the convection velocity in boundary layers and found it to be greater than the local mean

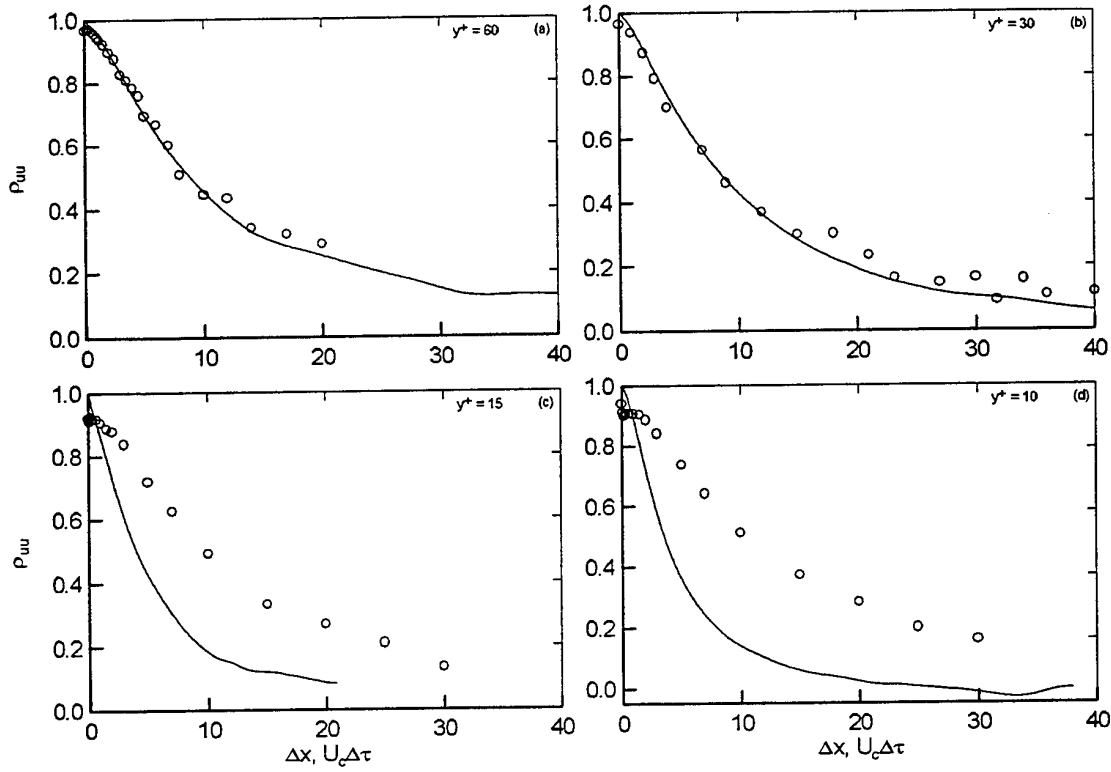


Figure 3: Verification of Taylor's hypothesis. —, calculated with Taylor's hypothesis; O, obtained from two point velocity measurements.

velocity by 12-15% near the wall (approximately equal to the local mean at around $y/\delta = 0.25$) and slightly smaller than the local velocity in the intermittent region. To avoid this ambiguity in the present experiment, the convection velocity was inferred from the space-time correlation data. There are several ways of determining the convection velocity using space-time correlations (e.g. Hussain and Clark, 1981; Spina et al., 1991). In this present work, the time delay corresponding to the peak of the correlations and the separation distance between the two control volumes were used to compute the convection velocity:

$$U_c = \frac{\Delta x}{\Delta \tau_{max}} \quad (4)$$

Figure 2 shows the measured distribution of the convection velocity normalised by the local mean velocity at various y^+ locations. Hot wire data obtained in a turbulent boundary layer by Krogstad et al. (1995) are also shown. It can be seen that the convection velocity is almost equal to the local mean velocity in the region $y^+ > 30$ which is consistent with the findings of Krogstad et al.

(1995) and those (not shown here) of Piomelli et al. (1989). However, the convection velocity is considerably higher than the local mean velocity in the region $y^+ < 20$, indicating that fluctuations in that region are travelling faster than the local mean velocity by about 30%. DNS data of a fully developed turbulent channel flow (Kim and Hussain, 1992) showed that the convection velocity is virtually constant and is 60% of the local velocity in the region $y^+ < 20$. Antonia et al. (1988) also observed an increase in the convection velocity in the buffer region of the boundary layer. In the present experiment U_c is about 35% higher than the local mean velocity at $y^+ = 10$.

To test Taylor's hypothesis, values of $\rho_{\Delta x}$ and ρ_τ were measured at $y^+ = 60, 30, 15$ and 10 (in the region $y^+ < 30$ the flow is strongly non-homogeneous and $u'/U \geq 0.2$). Figures 3a-d show distributions of the calculated [using Eq. (3)] and measured spatial correlation coefficients at various y^+ locations. It should be mentioned that, at zero separation, the measured value $\rho_{\Delta x}$ is 3-4% smaller than the theoretical value of 1. Ideally, when the two control volumes are at the same

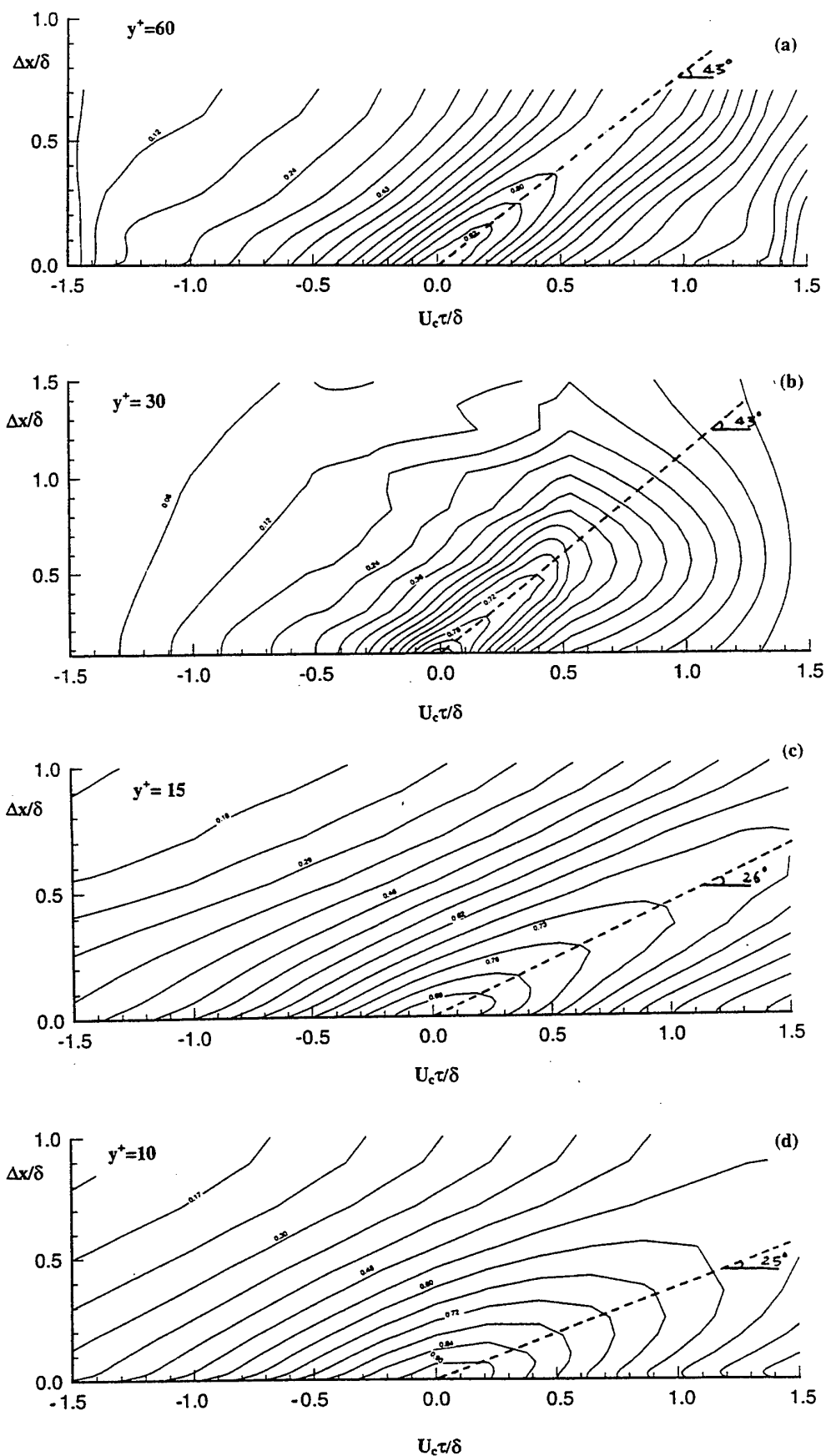


Figure 4. Space-time iso-contours along the streamwise direction.

measuring point, one would expect that the corresponding signals should be identical and $\rho_{\Delta x}$ should be equal to one. In practice, this is difficult to achieve because the two signals collected by the PMTs are not emitted from the same particle (Eriksson and Karlsson, 1995). Alternately, the measuring volumes may be detecting the same particle with a time delay.

Figures 3a and 3b show close agreement between measurement and calculation in support of the hypothesis in the region $y^+ \geq 30$. However, it is clear that the hypothesis is violated in the region $y^+ < 15$ (Figs. 3c and 3d).

The hypothesis can also be checked through space-time correlations. The measured space-time iso-correlation contour of $\rho_{\Delta x}$ are shown in Figs. 4a-4d. The time axis is normalised with the convection velocity and the boundary layer thickness δ . At $y^+ = 30$ and 60 (Figs. 4a and 4b) the 43° inclination of the contours indicates that Taylor's hypothesis is a good approximation. Perfect agreement with Eq. (3) would have required the inclination to be 45° . The iso-contours at $y^+ = 15$ and 10 (Figs. 4c and 4d) exhibit much smaller angle of inclination (about 25°) reflecting the inadequacy of the hypothesis.

4. CONCLUSION

The present experiment conducted in the near-wall region of a smooth wall turbulent boundary layer using the non-intrusive LDV technique indicates that Taylor's hypothesis is inadequate in the region $y^+ < 15$. This result is in agreement with the previously obtained using DNS data. In this region, the convection velocity is higher than the local mean velocity by nearly 35%.

ACKNOWLEDGMENT

The support of the Australian Research Council is acknowledged.

REFERENCES

- Antonia, R. A., Fulachier, L., Krishnamoorthy, L. V., Benabid, T. and Anselmet, F. (1988). Influence of Wall Suction on the Organised Motion in a Turbulent Boundary Layer. *J. Fluid Mech.*, **190**, 217-240.
- Cenedese, A. and Romano, G. P. (1991). Experimental Testing of Taylor's Hypothesis by LDA in Highly Turbulent Flow. *Expts. in Fluids*, **11**, 351-358.
- Champagne, F. H., Harris, G. and Corrsin, S. (1970). Experiments on Nearly Homogeneous Turbulent Shear Flow. *J. Fluid Mech.*, **41**, 81.
- Ching, C. Y., Djenidi, L. and Antonia, R. A. (1995). Low-Reynolds Number Effects on the Inner Region of a Turbulent Boundary Layer. *Expts. in Fluids*, **19**, 61-68.
- Eriksson, J. G. and Karlsson, R. I. (1995) An Investigation of the Spatial Resolution Requirements for Two-Point Correlation Measurements Using LDV. *Expts. in Fluids*, **18**, 393-396.
- Favre, A., Gaviglio, J. and Dumas, R. (1967). Structure of Velocity Space-Time Correlations in a Boundary Layer. *Phys. Fluids Suppl.*, S138-S145.
- Fraser, R., Pack, C. J. and Santavicca, D. A. (1986). An LDV System for Turbulence Length Scale Measurements. *Expts. in Fluids*, **4**, 150-152.
- Hussain, A. K. M. F. and Clark, A. R. (1981) Measurements of Wavenumber-Celerity Spectrum in Plane and Axisymmetric Jets. *AIAA Jnl.*, **19**, 51-55.
- Kim, J. and Hussain, A. K. M. F. (1992). Propagation Velocity and Space-Time Correlation of Perturbations in Turbulent Channel Flow. *Report TM-103932*, NASA-Ames.
- Krogstad, P. Å., Kaspersen, J. H. and Rimestad, S. (1995). A Study of the Taylor Hypothesis using Wavelet Analysis. *Proc. Twelfth Australasian Fluid Mechanics Conference*, Sydney, 379-382.
- Lumley, J. L. (1965). Interpretation of Time Spectra Measured in High Intensity Shear Flows. *Phys. Fluids*, **8**, 1056.
- Morton, J. B. and Clark, W. H. (1971). Measurements of Two-Point Velocity Correlations in a Pipe Flow Using Laser Anemometers. *J. Phy. E, Sci. Instrum.*, **4**, 809-814.
- Nakagawa, H. and Nezu, I. (1981). Structure of Space-Time Correlations of Bursting Phenomena in an Open-Channel Flow. *J. Fluid Mech.*, **104**, 1.

- Perry, A. E. and Abell, C. J. (1977). Asymptotic Similarity of Turbulence Structures in Smooth and Rough Walled Pipes. *J. Fluid Mech.*, **79**, 785-799.
- Piomelli, U., Balint, J-L. and Wallace, J. M. (1989). On the Validity of Taylor's Hypothesis for Wall Bounded Flows. *Phys. Fluids A*, **1**, 609-611.
- Spina, E. F., Donovan, J. F. and Smits, A. J. (1991). Convection Velocity in Supersonic Turbulent Boundary Layers. *Phys. Fluids A*, **3**, 3124-3126.
- Zaman, K. B. M. Q. and Hussain, A. K. M. F. (1981). Taylor Hypothesis and Large-Scale Coherent Structures. *J. Fluid Mech.*, **112**, 379.

LDA MEASUREMENTS OF LAMINAR-TURBULENT TRANSITION IN A FLAT-PLATE BOUNDARY LAYER

M. Kruse, S. Wagner

Institut für Aero- und Gasdynamik (IAG), Universität Stuttgart, Stuttgart, FRG

ABSTRACT

Laser-Doppler anemometer measurements on controlled laminar-turbulent transition in a Blasius boundary layer are presented. An oscillating wire used in combination with spacers triggers fundamental-type laminar-turbulent transition with regularly appearing aligned Λ -vortices. Detailed measurements describe the initial disturbances as well as phase-locking mechanisms of the evolving 2-D/3-D waves leading to high amplification rates and strong spanwise modulation. Finally the Λ -vortices with their synchronized waves were confirmed by measurement and visualizations using a hydrogen bubble technique.

INTRODUCTION

Small-amplitude oscillations in laminar boundary layers are damped or amplified depending on Reynolds number and frequency. Amplification is a prerequisite for the laminar-turbulent breakdown. In controlled experiments noise, vibrations, and free-stream turbulence have to be kept at the lowest possible level so that the downstream development of a well defined oscillation or spectrum of disturbances can be investigated. Introducing a 2-D wave into an unstable boundary layer by means of a line source will either trigger subharmonic-type transition with staggered Λ -vortices or fundamental-type transition with aligned Λ -vortices (see Fig. 1). If the initial 2-D wave is sufficiently large and amplified immediately, the fundamental type, with its so-called peak and valley structure, will be generated (Kachanov & Levchenko (1984)). Several landmark experiments (e.g. Klebanoff et al. (1962), Kachanov et al. (1989)) and also Direct Numerical Simulations (DNS, e.g. Rist & Fasel (1995), Kloker & Fasel (1995)) have been conducted on fundamental-type laminar-turbulent transition. Nevertheless, there is still a lack in understanding

the complete transitional process. Measurements of all three velocity components were presented by Kovasznay et al. (1962), Williams et al. (1984), and by Cork et al. (1989) (subharmonic breakdown).

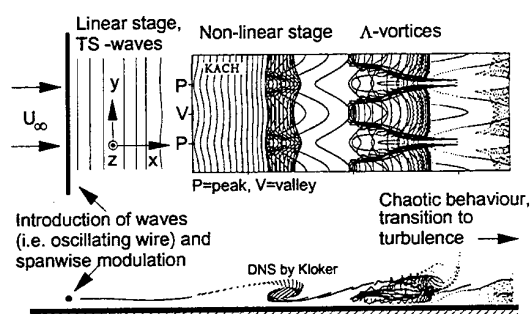


Figure 1: Sketch of fundamental-type transition, time-lines from DNS (see also Kloker & Fasel (1995))

The laminar water channel at the IAG (see Strunz & Speth (1987)) has been used for transition experiments for a long time. Wortmann (1977) started with visualizations of transitional processes downstream of the Tollmien-Schlichting stage. Because of the large scales in water, the channel is highly suitable for visualization techniques (Kruse & Wagner (1995b), Strunz & Speth (1987), Wortmann (1977)). Using hot-film anemometry, Wiegand et al. (1995) investigated boundary-layer transition initiated by a point source. They also confirmed the high quality of the channel flow by turbulence measurements identifying oncoming fluctuations of less than 0.05 % (0.1 to 10 Hz). In another experiment, Kruse & Wagner (1995a) introduced Tollmien-Schlichting waves into the boundary layer and investigated their streamwise development by LDA. Amplification rates according to Linear Stability Theory (LST) could be measured despite low data rates and a signal-to-noise ratio that is inferior to hot-film anemometry.

Presently, fundamental-type transition (also called Klebanoff-type or K-type, Fig. 1) excited by a line source is being investigated in detail by LDA and a Fourier analysis procedure especially adapted to LDA properties. Both the u - and the w -component of the velocity vector were recorded, and, in addition, appearing structures were visualized using hydrogen bubbles illuminated by a laser light sheet (Kruse & Wagner (1995b)).

EXPERIMENTAL SET-UP

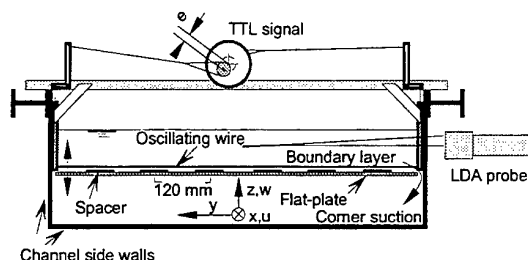


Figure 2: Cross-section of channel and set-up of disturbance input (sketch)

A flat-plate with an elliptical nose (ratio 10:1) is mounted in the laminar water channel (the set-up is shown in Figs. 2 and 4). A pressure difference between the upper and the lower side of the plate sucks the unstable corner boundary layer at the side walls under the plate and therefore extends the range of laminarity on the plate. At a free-stream velocity of $U_e = 12.8$ cm/s, this set-up leads to Blasius conditions with a shape factor H_{12} of 2.6 ± 1 %. Two-dimensional Tollmien-Schlichting waves are generated by an oscillating wire placed 1100 mm behind the nose of the flat-plate ($x=0$). The wire is 0.3 mm thick, hinged 4 mm above the plate, and oscillates with an amplitude of 0.35 mm at a frequency $f \approx 0.267$ Hz. In order to fix the appearing vortices in span, spacers, 1 mm thick, 60 mm wide, had to be placed regularly underneath the wire setting the fundamental spanwise wavelength λ_y to 120 mm (Fig. 2). Wire amplitude and frequency, free-stream velocity, and spacer height were chosen to match the following criteria: regular and symmetrical appearance of the Λ -vortices in time and space, high amplification according to LST (Arnal (1984)), and, where possible, comparability to existing experiments (e.g. ratio of stream- and spanwise wavelengths in Kachanov et al. (1989)). It should be noted that the channel flow has immanent spanwise variations in the boundary layer

that force the use of quite thick spacers. Fig. 3 shows the measurement path in the stability diagram over Reynolds number based on boundary-layer displacement thickness δ_1 .

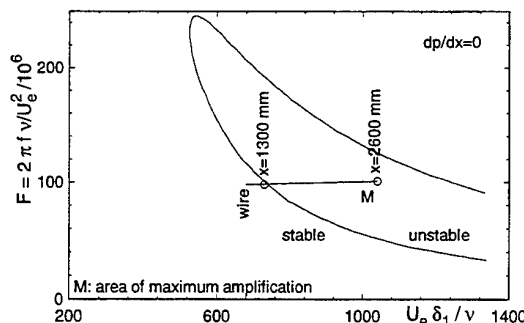


Figure 3: Location of experiment in the stability diagram for the Blasius boundary layer

The hinges for the wire obstruct the flow at the side walls and generate a disturbance wedge. Even without such distortions a finite line source will produce 3-D effects within a wedge of 16° as calculated by Mack (1984). The presented data is recorded far away from these distorted areas (Fig. 4).

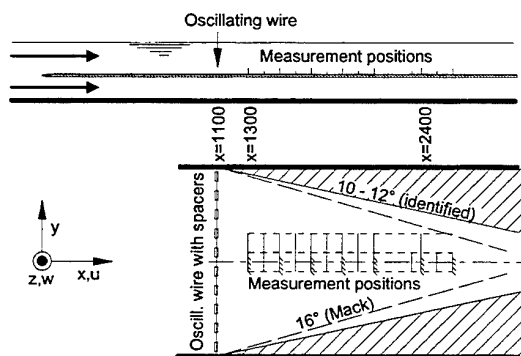


Figure 4: Measurement area

In all measurements, the wire oscillation generates a TTL trigger signal which is taken as time reference so that the phases of the waves and therefore wavelengths and phase velocities can be determined.

The LDA works in backward scatter mode and can measure two velocity components. The system features a measurement volume of $70 \mu\text{m}$ in diameter and uses two Burst Spectrum Analyzers for burst evaluation. The TTL signal of the oscillating wire is connected to the Sync1-input of the BSAs and recorded together with the bursts. In the data

files, the TTL events are stored with negative arrival time. In order to set the probe almost perpendicular to the glass side walls of the channel, the lower beam can be shifted into the centre of the optics. This also halves the beam intersection angle for the vertical velocity w causing a longer measurement volume and a higher noise level compared to the streamwise component. The lowest turbulence level measurable with the applied LDA is 0.8 % for the u -velocity.

The free-stream data rate was about 40 to 120 Hz depending on the penetration depth of the laser beams into the water. At a few streamwise positions the rate was much less, which is due to a local quality drop of the channel side walls. The record length was 16 to 21 wire cycle times depending on the stage of the transition process. In general the achieved repeatability was very good.

Two traverse schemes were used. One to obtain the boundary layer profiles and eigenfunctions at four positions per spanwise wavelength λ_y ($y = -60$ (valley), -30 ; 0 (peak) and 30 mm) and the other to obtain a high resolution cut in span at fixed wall distance with 16 or 32 points per λ_y .

DATA ANALYSIS

After positioning the measurement volume by sight – using the photo multiplier anode current as an indicator for wall reflections – and taking the measurements, the wall distance is calculated by linear extrapolation of the boundary-layer profile for the u -component. Consecutive measurements gave a repeatability of about ± 1 % for the shape factor H_{12} and the displacement thickness δ_1 .

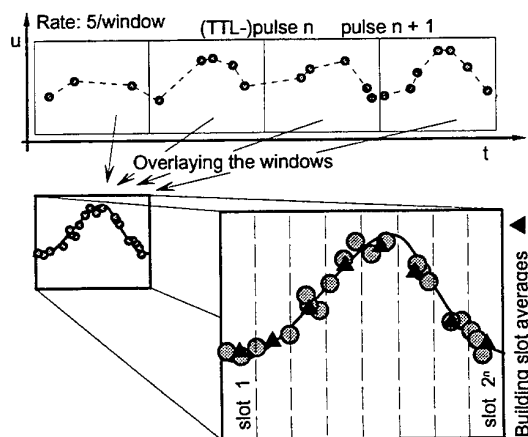


Figure 5: Sketch of phase-averaging Fourier analysis

In order to measure the flow oscillations, a Fourier analysis had to be adapted to LDA properties (Kruse & Wagner (1995a)). Currently two techniques are used: linear interpolation of the data and subsequent Fast-Fourier analysis (FFT) for judgement of the entire spectrum, and a phase-averaging technique (SFT) using slots in time for exact determination of amplitude and phase of the oscillations in the flow (Fig. 5). The second method is superior when data rates are low. Both procedures evaluate time signals that are cut to multiples of the wire cycle time and calculate the phases with respect to the oscillating wire. The programs also support the file format of the commercial measurement software so that the data can be analyzed from position A to B all at once.

Fourier transformation in time followed by a transformation in span leads to the amplitudes $a_{h,k}$ and phases $\phi_{h,k}$ according to the following ansatz:

$$u'(x, y, z, t) = \sum_{h=1}^H \sum_{k=-K}^K a_{h,k}(x, z) \sin(h2\pi ft - k2\pi/\lambda_y y + \phi_{h,k}(x, z)).$$

The indices h and k denote wave-number coefficients in time and span, respectively, and specify the various (h, k) -modes of the double Fourier transformation. As the triggered process is symmetrical the amplitudes and phases for $-k$ should be the same as for $+k$. By using a resolution of 16 to 32 points per λ_y aliasing was avoided. If the data is recorded over two wavelengths in span, vanishing subharmonics $k \pm 0.5$ reflect good parallel appearance of structures of equal strength.

RESULTS

Boundary-Layer Mean Flow

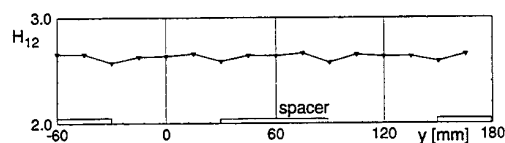


Figure 6: Impact of spacers on boundary layer shape factor H_{12} at $x=1300$ mm

The impact of the spacers on the boundary layer with the oscillating wire switched off (base flow) is presented in Fig. 6. At the spacer edges, the shape factor H_{12} is locally decreased. A Fourier analysis

of the base flow indicates (0,-2)- and (0,-4)-modes rather than a dominant (0,-1)-mode.

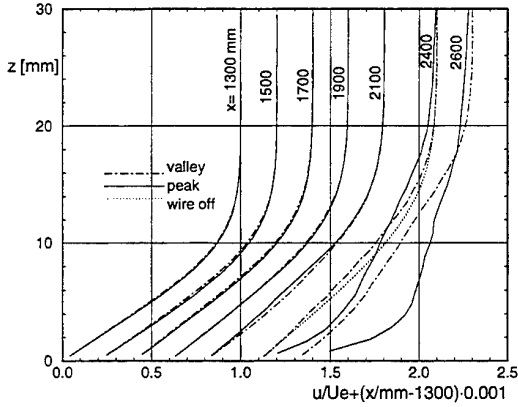


Figure 7: Development of boundary layer profiles for valley ($y=-60$ mm) and peak ($y=0$)

Figure 7 shows the boundary-layer profiles $u/U_e(z)$ at various downstream positions for peak and valley with the wire switched on. Starting at $x=2100$ mm, the profiles for the peak-position are distorted by the transition process. The corresponding shape factors H_{12} are presented in Fig. 8 together with the free-stream velocity U_e . For $x=2400$ mm wire-off data is also presented.

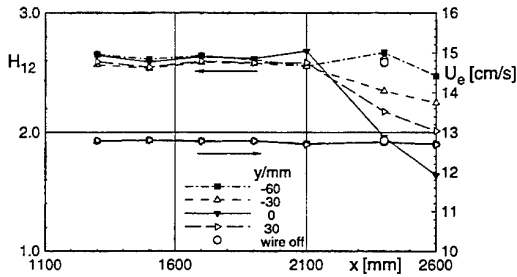


Figure 8: Shape factor and free-stream velocity

Initial Disturbance

For $x=1300$ mm and $y=-60$ mm (valley), Fig. 9 demonstrates a typical spectrum obtained by FFT. The spectrum has a very discrete character with good SNR detecting waves for $k=1,2$ and 3. Low frequencies contribute little to the spectrum.

The initial (h,k) -modes, recorded 200 mm behind the wire at $z=4$ mm near the maximum of the boundary layer oscillation, are presented in Fig. 10. Additional to 2-D waves ($k=0$), two significant

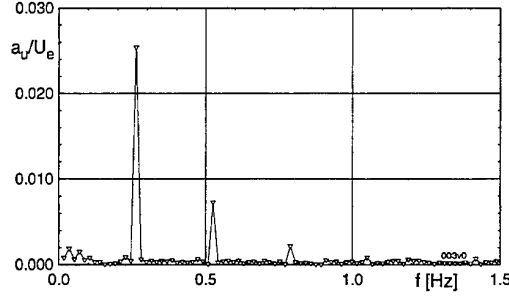


Figure 9: Amplitudes for u at $x=1300$ mm, $y=-60$ mm and $z \approx 3.4$ mm

symmetrical pairs of 3-D waves can be measured. It is not clear whether these waves have been generated behind the wire by interaction of the 2-D wave with the underlying variations in the base flow, or directly at the wire by wire-spacer interaction. Fig. 10 also illustrates that all the subharmonics in span are close to zero. The amplitude of the (1,0)-mode is about 60 % compared to the experiment by Kachanov et al. (1989).

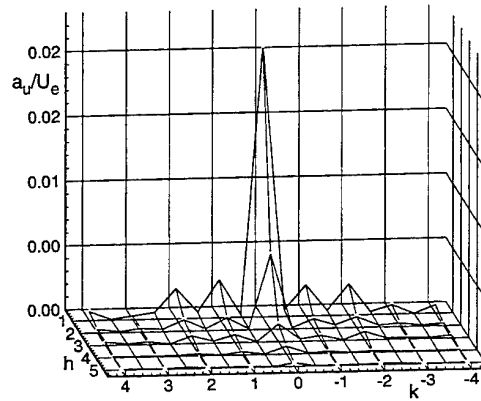


Figure 10: Amplitudes of (h,k) -modes for u at $x=1300$ mm and $z=4$ mm

At $x=1500$ mm, the measured u -profiles are compared with a Falkner-Skan profile having the average H_{12} and δ_1 of the boundary layer (Fig. 11). For the Falkner-Skan profile, the theoretical eigenfunction was calculated according to LST and plotted together with the LDA results for the 2-D wave (1,0). Both the amplitudes and the phases fit excellently the theory and demonstrate the proper introduction of Tollmien-Schlichting waves into the boundary layer.

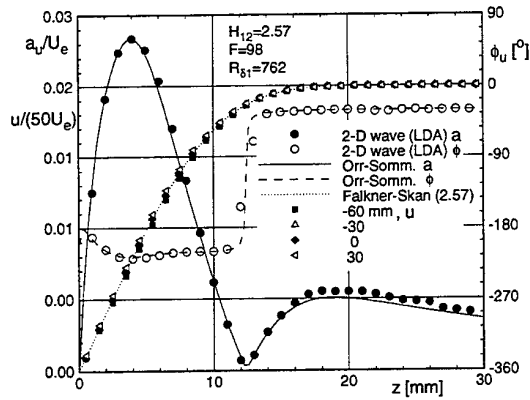


Figure 11: Comparison of measured 2-D wave with LST at $x=1500$ mm

Phase Locking

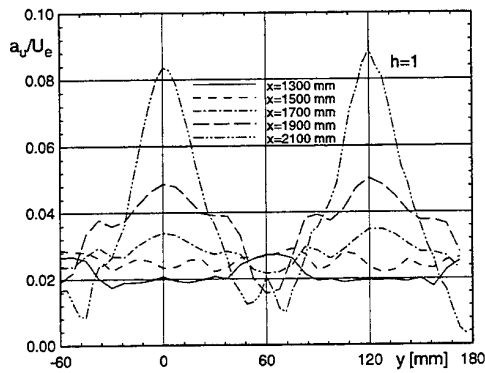


Figure 12: Development of u -amplitudes ($h=1$), $z=4$ mm

Although LDA data taken right behind the wire at $x=1300$ mm exhibit stronger oscillations at $y=-60$ mm than at $y=0$, further downstream the higher amplitudes occur at peak position $y=0$ (Fig. 12). This behaviour is in contrast to the experiments presented in Klebanoff et al. (1962) and Kachanov et al. (1989) where the oscillations have their maxima at peak-position from the start and where the amplitudes grow faster. So some rearranging of the waves must take place and hinder a rapid amplification of the oscillations. This can be shown by displaying the amplitudes and phases of the $(1,k)$ -modes as a function of streamwise position (Fig. 13, upper plot). Between $x=1300$ and 1800 mm, the phases of the $(1,\pm 1)$ -modes and the $(1,0)$ -mode have different values and slopes, which

means that the waves are not synchronized at $y=0$ (peak) and that they have different speeds. From $x=1800$ mm on, they synchronize and travel together. As a result, the $(1,\pm 1)$ -modes start growing rapidly. Calculating the wavelength λ_x for the $(1,0)$ -mode results in 174 mm which differs only slightly from the theoretical value of 170 mm given by LST.

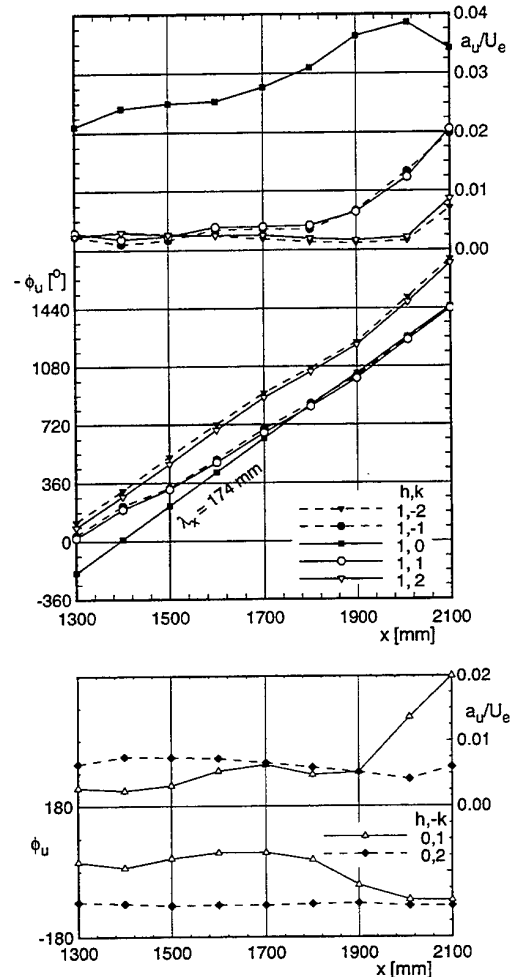


Figure 13: Amplitudes of $(1,k)$ -modes and phase locking ($k = 0, \pm 1, \pm 2$), $z=4$ mm (upper); corresponding amplitudes and phases of $(0,k)$ -modes (lower)

The modulation of the mean flow is described by the $(0,-k)$ -modes. Figure 13 (lower plot) demonstrates that the $(0,-1)$ -mode is also amplified shortly after the $(1,\pm 1)$ -modes. Coinciding with this amplification is a spanwise phase shift of the $(0,-1)$ -mode towards the $(0,-2)$ -mode at -90° which leads to a decrease of the u -velocity at peak position. This decrease is known for the early stages

of Λ -vortex formation. However, it was a held believe that the $(0, -1)$ -mode generates the $(1, \pm 1)$ -modes and not vice versa.

As soon as the waves are phase-locked and synchronizing at peak position, the base-flow becomes significantly modulated, the maxima of the oscillations move away from the wall and Λ -vortices will be generated. In addition, the 2-D wave will get a different shape compared to LST as the wave development will be dominated by non-linear effects.

Λ -Vortices

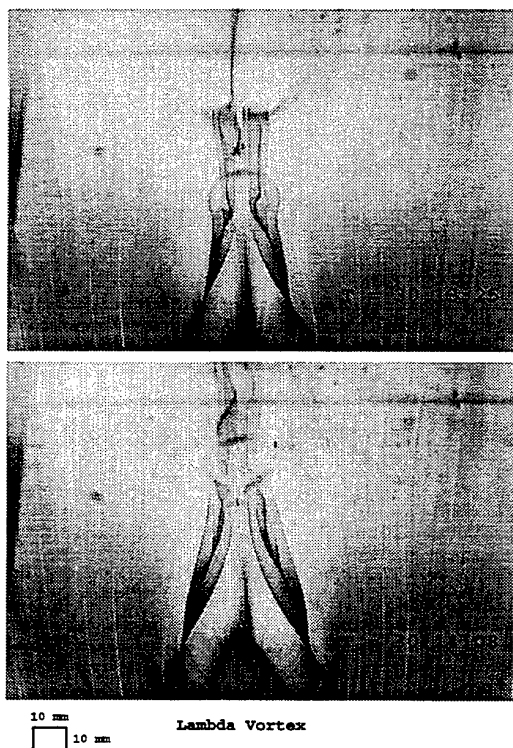


Figure 14: Λ -vortex (from Kruse & Wagner (1995b))

At about $x=2300$ – 2400 mm, visualizations using a laser sheet confirmed that with this set-up a fundamental breakdown with regularly appearing, aligned Λ -vortices is triggered (see Fig. 14, excerpt from Kruse & Wagner (1995b)).

Using measurement data, these vortices can be displayed by plotting the contours of the velocity in the span-time plane. Although a time reference is given by the disturbance input, it is difficult to generate such a plot directly with the time signals as the LDA data is not equi-spaced. Therefore, new data was synthesized with the results of the double

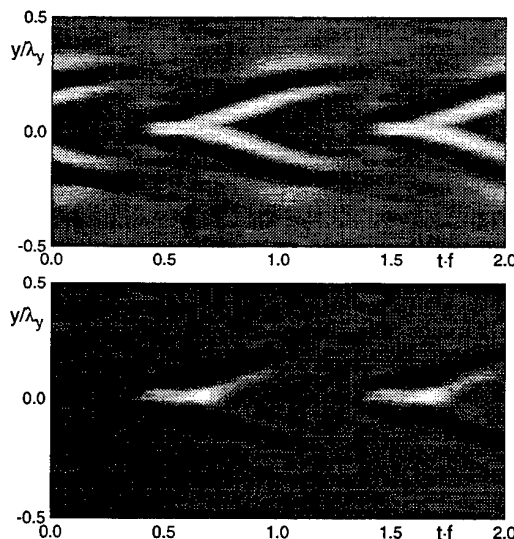


Figure 15: Contours of w -velocity over two periods at $x=2340$ mm, $z=4$ mm (upper) and $z=8$ mm (lower) (light grey indicates high values)

Fourier transformation for $h=1$ to 6 and $k=-12$ to 12 and the significant mean flow modulation. The results for $x=2340$ mm, $z=4$ mm and $z=8$ mm are plotted in Fig. 15 featuring nicely the Λ -shapes.

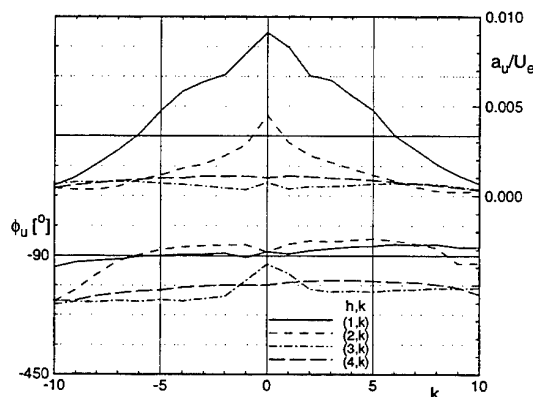


Figure 16: Amplitudes $a_{h,k}/U_e$ and phases $\phi_{h,k}$ for u at $x=2400$ mm and $z=18$ mm

At the edge of the boundary layer in the region where these vortices occur, the oscillations are confined to the peak position where fluid is ejected into the free stream. At this place, the double Fourier transformation results in a broad symmetrical disturbance spectrum (Fig. 16) with most of the waves being synchronized for fixed h . Such a synchronization produces the large ampli-

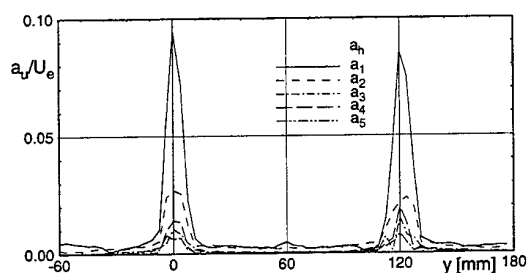


Figure 17: Amplitudes a_u/U_e at $x=2400$ mm and $z=18$ mm versus y ($h = 1, \dots, 5$)

tudes at peak-position and a wave cancellation in the valley (Kachanov (1987)). This is demonstrated in Fig. 17, where the corresponding amplitudes are plotted over y .

CONCLUDING REMARKS

Fundamental-type transition (K-breakdown) in a flat-plate boundary layer was investigated by LDA. Tollmien-Schlichting waves and pairs of 3-D waves were generated using an oscillating wire device and spacers. Adjusting the transition process with the help of flow visualization led to a configuration that produced symmetrical and regular events.

Compared to Kachanov & Levchenko (1984), differences occurred in the development of the waves. They might be due to base-flow or spacer shape variations, or just a different initial disturbance spectrum. Nevertheless, the different initial wave development with its phase-locking mechanisms could be well described by the LDA measurements. It was shown, that the synchronization of the $(1, \pm 1)$ -modes with the $(1, 0)$ -mode leads to high amplifications followed by a lift of the $(0, -1)$ -mode. Finally, Λ -vortices with their typical spectrum could be confirmed.

In order to conduct the presented experiment, a Fourier analysis technique had to be adapted to LDA properties also allowing for the large amount of data that was recorded.

It could be shown that the LDA is suitable to investigate a transitional process.

REFERENCES

Arnal D. 1984, *Description and Prediction of Transition in Two-Dimensional Incompressible Flow*; AGARD-R-709

Cork, T.C., Mangano, R.A. 1989, *Resonant Growth of Three-Dimensional Modes in Transitioning Blasius Boundary Layers*; J. Fluid Mech. 209, pp. 93-150

Kachanov Y.S., Levchenko, V.Y. 1984, *The resonant interaction of disturbances at laminar-turbulent transition in a boundary layer*; J. Fluid Mech. 138, pp. 209-247

Kachanov Y.S. 1987, *On the resonant nature of the breakdown of a laminar boundary layer*; J. Fluid Mech. 184, pp. 43-74

Kachanov Y.S., Kozlov, V.V., Levchenko, V.Y., Ramazanov, M.P. 1989, *The nature of K-breakdown of laminar boundary layer*; Izv. SO AN SSSR, Ser. Tekh. Nauk 2, pp. 128-158, (in Russian)

Klebanoff P.S., Tidstrom K.D., Sargent L.M. 1962, *The three-dimensional nature of boundary layer instability*; J. Fluid Mech. 12, pp. 1-41

Kloker M., Fasel H. 1995, *Direct Numerical Simulation of Boundary Layer Transition with Strong Adverse Pressure Gradient*; in *Laminar-Turbulent Transition*, 4. IUTAM Symposium, Sendai, Japan 1994, ed. Kobayashi, pp. 481-488, Springer

Kovaznay L.S.G., Komoda H., Vasudeva B.R. 1962, *Detailed Flow Field in Transition*; Proc. 1962 Heat Transfer & Fluid Mech. Inst., Stanford Univ. Press, pp. 1-26

Kruse M., Wagner S. 1995a, *Messung von Schwingungen in transitionellen Grenzschichten*; Lasermethoden in der Strömungsmesstechnik, 4. Fachtagung der GALA, 12.-14. Sep., Rostock, FRG

Kruse M., Wagner S. 1995b, *Λ -vortices in a flat-plate boundary layer*; video presented at the APS/DFD Meeting, Gallery of Fluid Motion, 19.-21. Nov., Irvine CA, USA

Mack, L.M. 1984, *Line Sources of Instability Waves in a Blasius Boundary Layer*; AIAA 84-0168, Reno, USA

Rist U., Fasel H. 1995, *Direct Numerical Simulation of Controlled Transition in a Flat-Plate Boundary Layer*; J. Fluid Mech. 298, pp. 211-248

Strunz M., Speth J.F. 1987, *A new laminar water tunnel to study the transition process in a Blasius boundary layer and in a separation bubble and a new tool for industrial aerodynamics and hydrodynamic research*; AGARD CP-413, pp. 25-1-25-5

Wiegand Th., Bestek H., Wagner S., Fasel H. 1995, *Experiments on a wave train emanating from a point source in a laminar boundary layer*; AIAA 95-2255

Wortmann F.X. 1977, *The Incompressible Fluid Motion Downstream of Twodimensional Tollmien Schlichting Waves*; Laminar-Turbulent Transition, AGARD-CP-224, Kopenhagen, DK

Williams, D.R., Fasel, H., Hama, F.R. 1984, *Experimental Determination of the Three-Dimensional Vorticity Field in the Boundary-Layer Transition Process*; J. Fluid Mech. 149, pp. 179-203

Measurement of Temporal and Spatial Evolution of Transitional Pipe Flow with PIV

A.A. Draad and J. Westerweel*

Laboratory for Aero & Hydrodynamics

Delft University of Technology

Rotterdamseweg 145, 2628 AL Delft, the Netherlands

Abstract

Turbulent 'slugs' were generated by injection of small amounts of fluids into a fully-developed laminar pipe flow at a Reynolds number of 5,800. Digital particle image velocimetry (PIV) was applied to measure the instantaneous flow field at different locations at different downstream locations with respect to the point of injection. At each location the passage of the turbulent slug could be recorded in a sequence of images. The results show the development in space and time of the turbulent slug as it progresses inside the pipe. The present results indicate that the slug has begun to re-laminarize at 40 pipe-diameters away from the point of injection. For one location the consecutive PIV results were compiled into a single data set that represents a (quasi-instantaneous) cross section of the turbulent slug. From this data set it is possible to identify the flow structures that occur in the leading, central and trailing parts of the turbulent slug.

1 Introduction

The transition to turbulence in pipe flows is still far from being understood. Up to now, measurements of transitional flow structures has been performed mainly with single-point measurement techniques in combination with conditional averaging. It is anticipated that the measurement of the temporal and spatial development of the transitional flow field may shed more light on understanding the mechanisms involved in transition to turbulence and re-laminarization (Darbyshire & Mullin 1995).

We used particle image velocimetry (PIV) to study the laminar-turbulent transition process in a pipe flow. For these experiments we used a digital image acquisition system that was designed especially for the purpose of digital PIV measurements in turbulent flows; in a previous measurement of a fully-developed turbulent pipe flow it was demonstrated that the accuracy and spatial resolution of this system are comparable to those of a photographic-based system (Westerweel *et al.* 1996). The experiments presented in this paper are a continuation of earlier (preliminary) digital PIV measurements in transitional pipe flow (Westerweel *et al.* 1994; Draad *et al.* 1995).

In Section 2 we describe the experimental facility that was used for these measurements, and in Section 3 we give

a detailed description of the measurements. The results are presented in Section 4, and Section 5 summarizes the main conclusions from this study.

2 Flow facility

The pipe flow facility that was used for this experiment was designed especially for the purpose of studying transitional flows. In this section we give a brief description of this flow facility; further details can be found in the thesis of Draad (1996).

The main flow line of the facility consists of a smooth pipe with an inner diameter of 40 mm, and a total length of 34 m. A sketch of the pipe flow facility is given in Figure 1. The flow in this facility remains laminar over the full length of the pipe for Reynolds numbers up to 60,000 (for Newtonian fluids). During the experiments the flow rate was kept at a constant value, which is monitored directly with a magnetic-inductive flow meter. The flow rate during the measurements was 609 ± 3 liters per hour (l/h), which corresponds to a Reynolds number of about 5,800 (based on the pipe diameter and the bulk velocity).

A transition to a turbulent flow state is induced by injection of fluid at a distance of 29 m from the pipe inlet (this long distance is to ensure that the laminar flow has been completely developed, and that the transition to turbulence is induced by the injection of the fluid alone). The fluid is injected through a 1.0 mm hole in the pipe wall and the duration of the injection is 0.5 s. The jet is fed by a small container placed above the pipe and the injection speed can be manipulated using a regulator. When the injection is stopped, the flow returns to the laminar state, and we can observe the development of a turbulent 'slug' along the downstream section of the pipe.

3 Measurements

In this section we describe the measurements and experimental conditions. An overview is shown in Table 1.

To facilitate measurements with PIV, the flow was seeded with small tracer particles (with a nominal diameter of $30 \mu\text{m}$) and illuminated with a scanning-beam light sheet (using an argon-ion cw-laser and a rotating polygon

*correspondence to: J. Westerweel

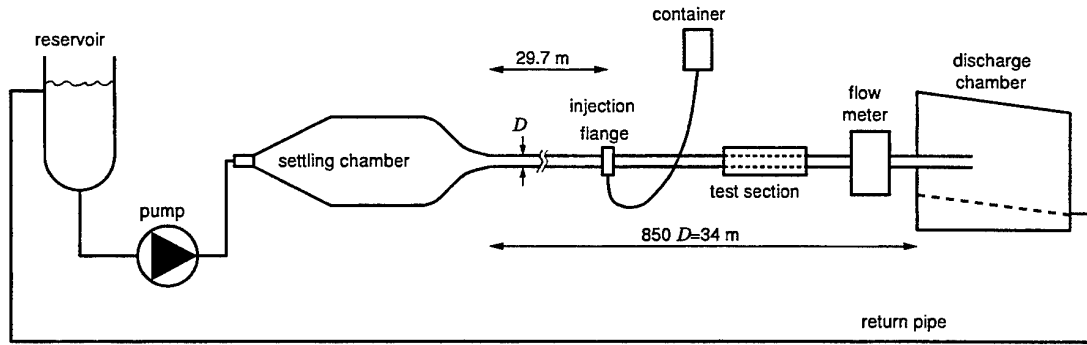


Figure 1: Schematic of the pipe flow facility (not to scale).

Table 1: An overview of relevant experimental conditions.

<i>Pipe:</i>		
diameter	40.0	mm
length	34	m
wall thickness	0.19	mm
<i>Flow:</i>		
fluid	water	
kinematic viscosity	0.9327	mm ² /s
bulk flow rate	609	l/h
bulk velocity	135	mm/s
Reynolds number	5,790	
<i>Seeding:</i>		
type	Optimage	
nominal diameter	30	μm
<i>Light sheet:</i>		
type	scanning beam	
source	cw Ar ⁺ laser	
power	0.5	W
thickness	0.5	mm
exposure time delay	1.725	ms
number of exposures	8	
<i>Recording:</i>		
type	electronic (CCD)	
resolution	1000×1016	pixels
lens focal length	50	mm
numerical aperture	2.8	
image magnification	0.305	
viewing area	39.4×40.0	mm ²
<i>Interrogation:</i>		
resolution	32×32	px
area	1.26×1.26	mm ²
<i>Data set:</i>		
vectors/image	3,481	
images/data set	131	
number of data sets	45	

mirror). The width of the light sheet is approximately 0.5 mm, and the plane of light sheet coincides with the centerline of the pipe. The light-sheet scan time is 1.725 ms, and each image is exposed 8 times. We could thus achieve a high image density, while keeping the volume fraction and number density of the tracer particles at a minimum.

The measurements are carried out for different injection conditions at four downstream locations in the pipe, i.e.: 365, 655, 870 and 1660 mm downstream the point of injection. At the measurement location the pipe is enclosed in a rectangular box filled with water. The pipe wall inside this box was replaced by a thin sheet (with a thickness 0.19 mm) with a refractive index that is very close to that of water. We could thus record images with minimum distortion due to the curvature of the pipe wall and differences in refractive index of water and air.

The PIV images are recorded with a CCD camera that has a spatial resolution of 1000×1016 pixels. The field-of-view of the camera is exactly one pipe diameter (in the radial direction). The camera is connected to an acquisition system that captures sequences of 131 images at a rate of 10 images per second. The recording of the first image of each sequence coincides with the end of the injection. Further details regarding this acquisition system are given by Westerweel *et al.* (1996).

We interrogate the digital images in 32×32-pixel sub-images with a spacing of 16 pixels (i.e., a 50% overlap). The pattern of interrogation locations is symmetric with respect to the centerline of the pipe. Each image yields a total of (59×59=) 3,481 velocity vectors, and each measurement—consisting of 131 images—yields a total of 456,011 velocity measurements.

All velocity fields are tested for spurious velocity measurements. Most of the spurious vectors occur near the pipe wall, where the velocity gradient is very large and where there is a high probability that subsequent particle images overlap. The number of spurious vectors at the upper wall is higher in comparison to that at the lower wall. In a turbulent flow the tracer particles are mixed continuously by the flow, so that a homogeneous distribution of

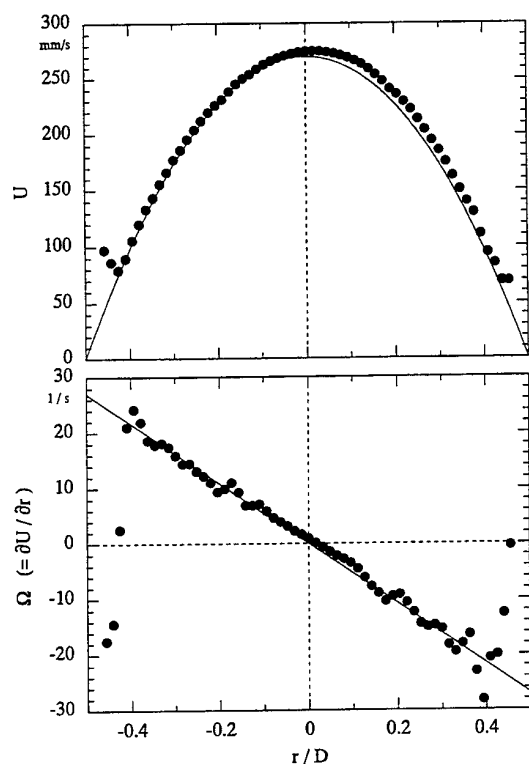


Figure 2: Profiles of the axial velocity (U) and the vorticity (Ω) as a function of the distance (r) from the centerline with respect to the pipe diameter (D). The solid lines represent the Poiseuille profiles for a water flow rate of 609 l/h.

the particles is maintained. This mixing process is absent in a laminar flow, so particles that do not exactly match the density of the ambient fluid will settle. In this particular experiment the flow is laminar between the inlet of the pipe and the injection location (i.e., 29 m), and it takes (on average) about 200 seconds for a tracer particle carried by the flow to travel this distance. As a result the concentration of tracer particles near the upper wall is lower in comparison with that near the lower wall, and explains the higher occurrence of spurious vectors near the upper wall.

4 Results

In total 45 image sequences (with a total volume of 6 Giga-byte) were recorded (which include measurements at different downstream locations and for each location for four different circumferential injection positions). Presently, only a small fraction of the data have been processed, and we will present here the results that were obtained from a set of four image sequences that were recorded at the four measurement locations under equal injection conditions.

4.1 Poiseuille flow

In the fully-developed laminar flow state the velocity field only depends on the radial coordinate. We could therefore

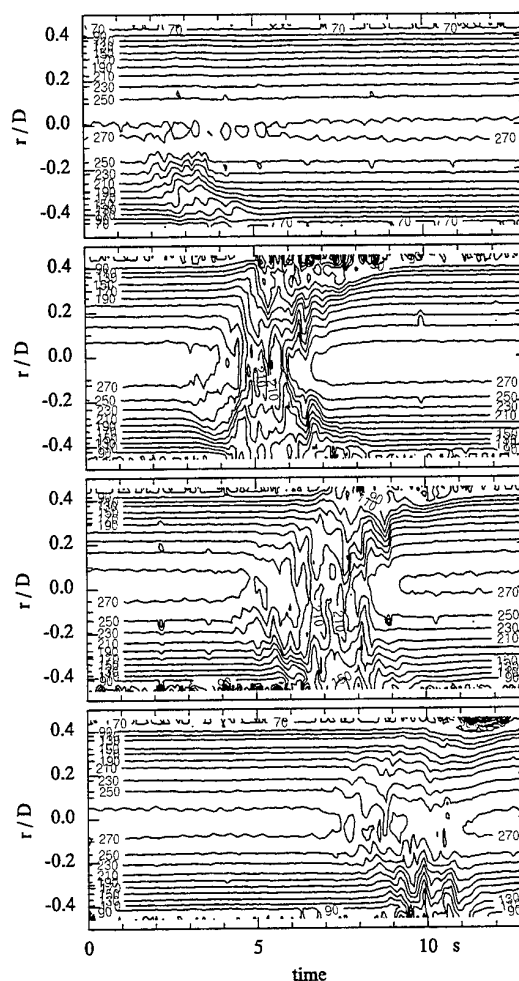


Figure 3: The temporal evolution of the locally-averaged axial velocity profiles for at four measurement locations behind the injection point (from top to bottom: 365, 655, 870 and 1660 mm).

determine the laminar velocity profile by averaging the velocity data over each row, and then ensemble averaging the data over all images for which the flow was in the laminar flow state.

Fig. 2 shows the results for the radial profiles of the axial velocity and the shear rate (viz., vorticity); the solid lines represent the corresponding profiles for a Poiseuille flow with a flow rate of 609 liters per hour. The differences between the experimental results and the Poiseuille profiles are small. However, the experimental results for the laminar velocity profile is not exactly symmetric. The skew appears to be caused by the Earth's rotation, and it has not been reported in experiments by others. This may be partly due to the fact that most facilities used by others contain air flows in which the effect smaller due to the larger kinematic viscosity of air with respect to that of water. This aspect is discussed in further detail by Draad (1996).

The measured shear rate coincides with the expected

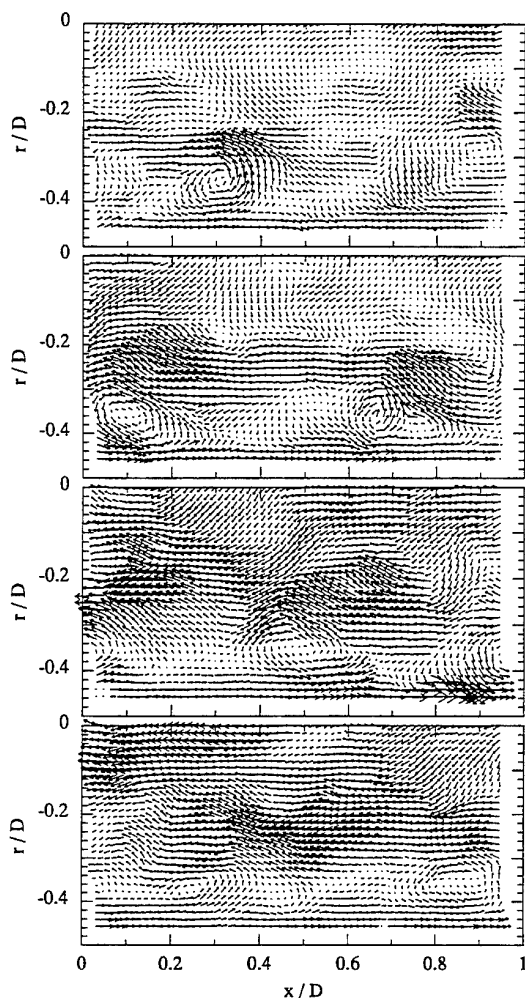


Figure 4: The instantaneous velocity relative to the mean velocity of the laminar flow state for four consecutive PIV measurements (from top to bottom: 4.5, 4.6, 4.7 and 4.8 s after the end of the injection) at a distance of 655 mm behind the injection location.

shear rate over almost the full pipe diameter ($|r| < 0.4D$). The deviations of the data points close to the pipe wall is directly related to the presence of spurious measurements that remained undetected.

4.2 Transitional flow

To visualize both the spatial and temporal development of the disturbance, we determine for each PIV measurement the axial velocity profile over the each individual image, i.e.:

$$U_i(r) = \frac{1}{L} \sum_j \tilde{u}_i(r, x_j) \Delta x_j \quad (1)$$

where the index i denotes the number of the frame, \tilde{u} is the instantaneous velocity, L the width of the image, and where r and x are the radial and axial coordinates respectively. In this particular situation we have: $L \approx D$. In Fig. 3 are plotted the combined results for $U_i(r)$ for all

frames at the four measurement locations. Note that the disturbances near the centerline of the pipe arrive earlier at the first measurement station than the disturbances close to the wall. When the disturbance arrives at the second measurement location, it fills the complete cross-section of the pipe, and it remains turbulent also at the third measurement station. However, at the final station the disturbance appears to be less prominent. This might be an indication that the disturbance does not maintain itself, and eventually may re-laminarize.

The digital PIV measurements allow us to investigate the detailed structure of the disturbance. Fig. 4 shows the velocity maps of the lower halves of four consecutive recordings. At $Re=5,800$ the bulk velocity is about 135 mm/s; hence, the expected mean displacement of structures between two consecutive recordings is roughly 0.3 pipe diameters. With this knowledge we can identify coherent structures in the subsequent maps in Fig. 4.

In particular, note a vortical flow pattern close to the lower pipe wall in Fig. 4; by overlaying identical flow patterns in subsequent vector maps it is possible to compile a quasi-instantaneous picture of the full turbulent slug in the pipe. The problem that arises is that flow structures near the pipe wall advect at a smaller rate than flow structures close to the centerline. Ideally, one would like to use a pattern matching algorithm that takes into account the advection velocity of every individual flow structure. However, such an algorithm could not be developed at this moment; instead we matched the patterns by eye. To eliminate any discontinuities related to the edges of individual PIV data fields, the overlapping data were merged using a weight value for each data point which decreases linearly as a function of the distance from the middle of the image.

The result in Fig. 5 is a compilation of 60 PIV results, covering an elapsed time of 6 seconds, recorded at a distance of 655 mm behind the injection position. The remaining data set contains 59×1392 data points.

The total length of the slug appears to be more than 20 times the pipe diameter. At the top we plotted the axial velocity at centerline; this would compare to the time trace of a passing slug as measured by a single-point probe (e.g., a laser-Doppler anemometer). Initially the velocity at the centerline is equal to two times the bulk velocity (i.e., $2 \times 135 = 270$ mm/s). One can observe how instabilities grow in size and amplitude, until they cover the full width of the pipe. The velocity at the centerline drops and fluctuates around the dash-dotted line which represents the mean centerline velocity for a fully-developed turbulent pipe flow (i.e., $1.3 \times 135 = 176$ mm/s; the constant of 1.3 is only valid for fully-developed turbulent pipe flow at low Re , see Eggels *et al.* 1994). At the trailing interface the flow returns to a laminar flow state. Note that the re-laminarization starts by the centerline velocity becoming equal to the value for a laminar flow for a very brief instant; this event is perhaps related to a so-called 'incursion' (Darbyshire & Mullin 1995).

The compiled data of the slug as shown in Fig. 5 allow us to study the flow structures that appear in the front,

middle and rear sections of the slug. In Figure 6 we show the vector maps at different locations. Note that the instantaneous velocity fields still contain some spurious data (in particular near the upper pipe wall); this is due to the effect described in Section 3.

Before discussing the results shown in Figs. 5 and 6 we would like to emphasize that so far we have only been able to carry out such a compilation for a single image sequence; evidently, observations from these data may not be generally valid, and require validation with results from other measurements.

In Fig. 5 the position $x = 0$ denotes the first image in which a deviation from the average laminar velocity profile appears, which occurs 3.1 s after the end of the injection. We use negative x -positions to indicate that this part of the slug can be envisaged to be located upstream of the beginning of the disturbance. From $x = 0$ to $x \approx -300$ the disturbance increases in strength gradually. Initially, the disturbance seems to display some periodic behavior with a period in x of approximately 60. The vortices shown in Figs. 4 and 6a correspond to the white spots in the radial velocity around $x = -286$ and $x = -310$. A little further upstream, i.e. $x \approx -325$, the centerline velocity quickly approaches the turbulent value and the flow becomes turbulent over the entire cross section of the pipe. The fluctuations in the centerline velocity are much larger than in a fully developed turbulent flow. Re-laminarization sets in at $x \approx -520$ and seems to occur in phases. The centerline velocity profiles shows an almost step-wise increase towards the laminar value separated by sudden decreases. Again, some periodicity appears to be present, now with a spacing of roughly 100 mm. Clearly, the turbulence decays very slowly near the wall. Note that the sharp peak in the centerline velocity at $x = -436$ is possibly an artifact related to an undetected spurious vector.

Again, we would like to emphasize that we need to investigate the remaining image sequences in order to confirm the findings described above.

5 Conclusions

A transition of the laminar flow into a turbulent flow state was induced by injection of small amounts of fluid into the pipe, and the development of the transition along the pipe was investigated with digital PIV.

The present results demonstrate that digital PIV is a useful tool for the investigation of transient flow phenomena. It is possible to study a large variety of flow conditions with high accuracy and detail within a relatively short time (provided one has access to a high-capacity storage facility).

At the Reynolds number studied here, a turbulent slug should grow in length (Wyganski & Champagne 1973). Flow visualization experiments using dye in the same facility (Draad 1996) suggest a transition to turbulence under the same flow and disturbance conditions. However, Fig. 3 shows that the disturbance may perhaps not be stable, and appears to re-laminarize. We need the other data in order to conclude whether re-laminarization occurs

generally. Also, it might be possible that—due to the skewed laminar profile—the development and stability of the slug depends on the direction of the injection.

We believe that the most prominent result in this paper is the compiled data set shown in Fig. 5. This data set allows us to observe the instantaneous transitional flow structure as a whole (which covers more than 20 pipe diameters in the flow direction). The compilation procedure is now done partly by hand, and needs to be optimized. At this moment we have only compiled one image sequence out of the total of 45; we anticipate that the image sets that remain to be investigated will provide additional information. So far, with only one of these data sets it is impossible to make any definite conclusions, although we feel that the present data set reveals a number of potentially significant structures.

The PIV recordings for the other injection conditions are currently being analyzed; the results will be presented in a forthcoming paper.

Acknowledgments

The research of dr.ir. J. Westerweel has been made possible by a fellowship of the Royal Netherlands Academy of Arts and Sciences. Dr.ir. A.A. Draad received financial support from Shell Research.

References

- DARBYSHIRE, A.G., & MULLIN, T. 1995. Transition to turbulence in constant-mass-flux pipe flow. *J. Fluid Mech.*, **289**, 83–114.
- DRAAD, A.A. 1996. *Laminar-turbulent transition in pipe flow for Newtonian and non-Newtonian fluids*. Ph.D. thesis, Delft University of Technology.
- DRAAD, A.A., KUIKEN, G.D.C., & NIEUWSTADT, F.T.M. 1995. Transition to turbulence in pipe flow. *Pages 103–110 of: et al., R. KOBAYASHI (ed), Proc. IUTAM Symp. "Laminar-Turbulent Transition"*.
- EGGELS, J.G.M., UNGER, F., WEISS, M.H., WESTERWEEL, J., ADRIAN, R.J., FRIEDRICH, R., & NIEUWSTADT, F.T.M. 1994. Fully developed turbulent pipe flow: a comparison between direct numerical simulation and experiment. *J. Fluid Mech.*, **268**, 175–209.
- WESTERWEEL, J., DRAAD, A.A., VAN DER HOEVEN, J.G.TH., & VAN OORD, J. 1994. A fast data acquisition system for digital PIV: application to fully-developed and transitional turbulent pipe flow. *In: Proc. 7th Int. Symp. on Applications of Laser Techniques to Fluid Mechanics*.
- WESTERWEEL, J., DRAAD, A.A., VAN DER HOEVEN, J.G.TH., & VAN OORD, J. 1996. Measurement of fully-developed turbulent pipe flow with digital particle image velocimetry. *Exp. Fluids*, **20**, 165–177.
- WYGNANSKI, I.J., & CHAMPAGNE, F.H. 1973. On transition in a pipe. Part 1. The origin of puffs and slugs and the flow in a turbulent slug. *J. Fluid Mech.*, **59**, 281–335.

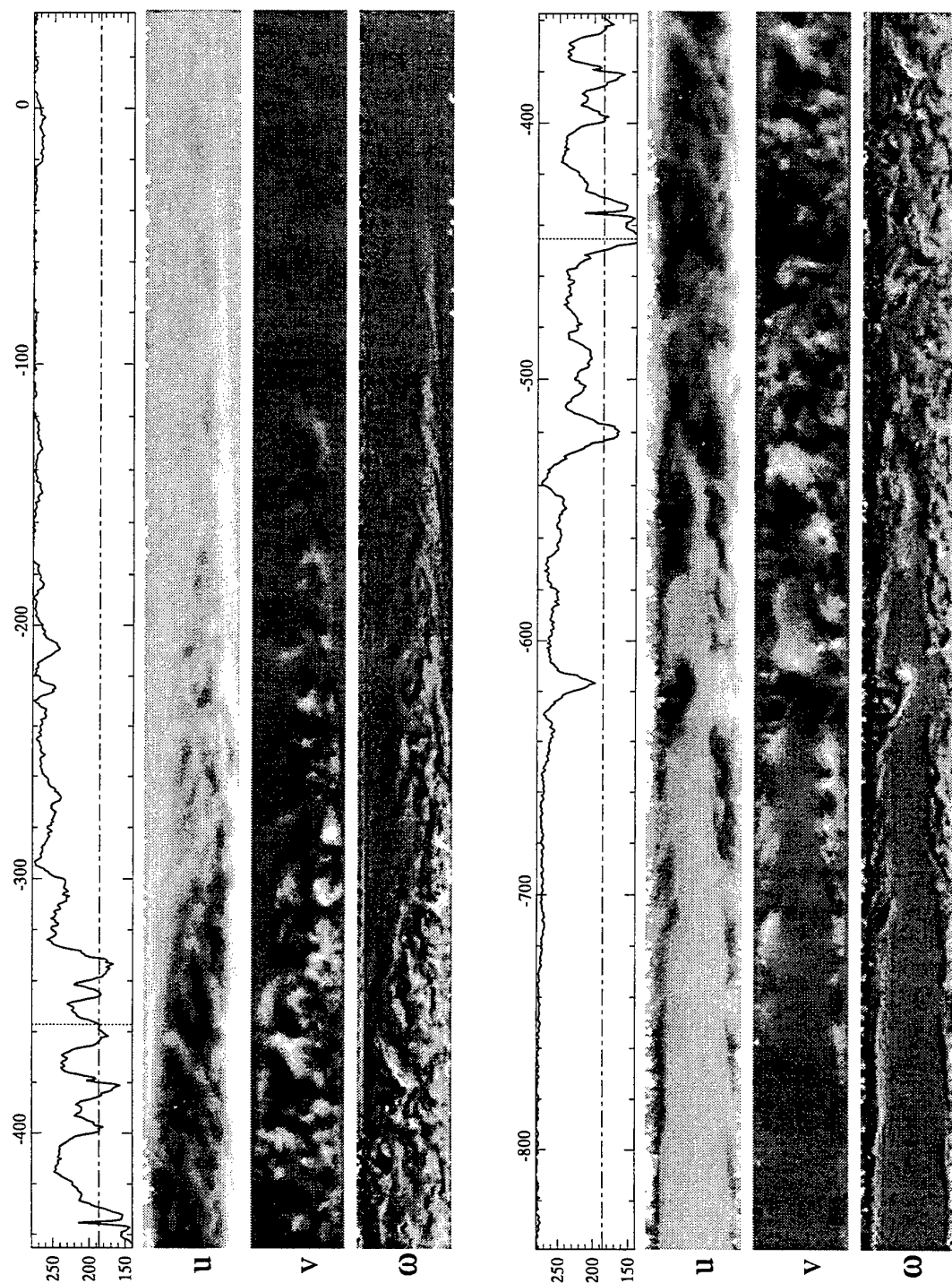


Figure 5: The (quasi-) instantaneous structure of a turbulent slug as compiled from about 60 overlapping PIV measurements. In this figure are shown the axial velocity at the centerline (in mm/s), and maps of the fluctuating axial and radial velocities (u and v respectively), and of the fluctuating vorticity (ω). For reference the dash-dotted line represents the mean centerline velocity for a fully-developed turbulent flow.

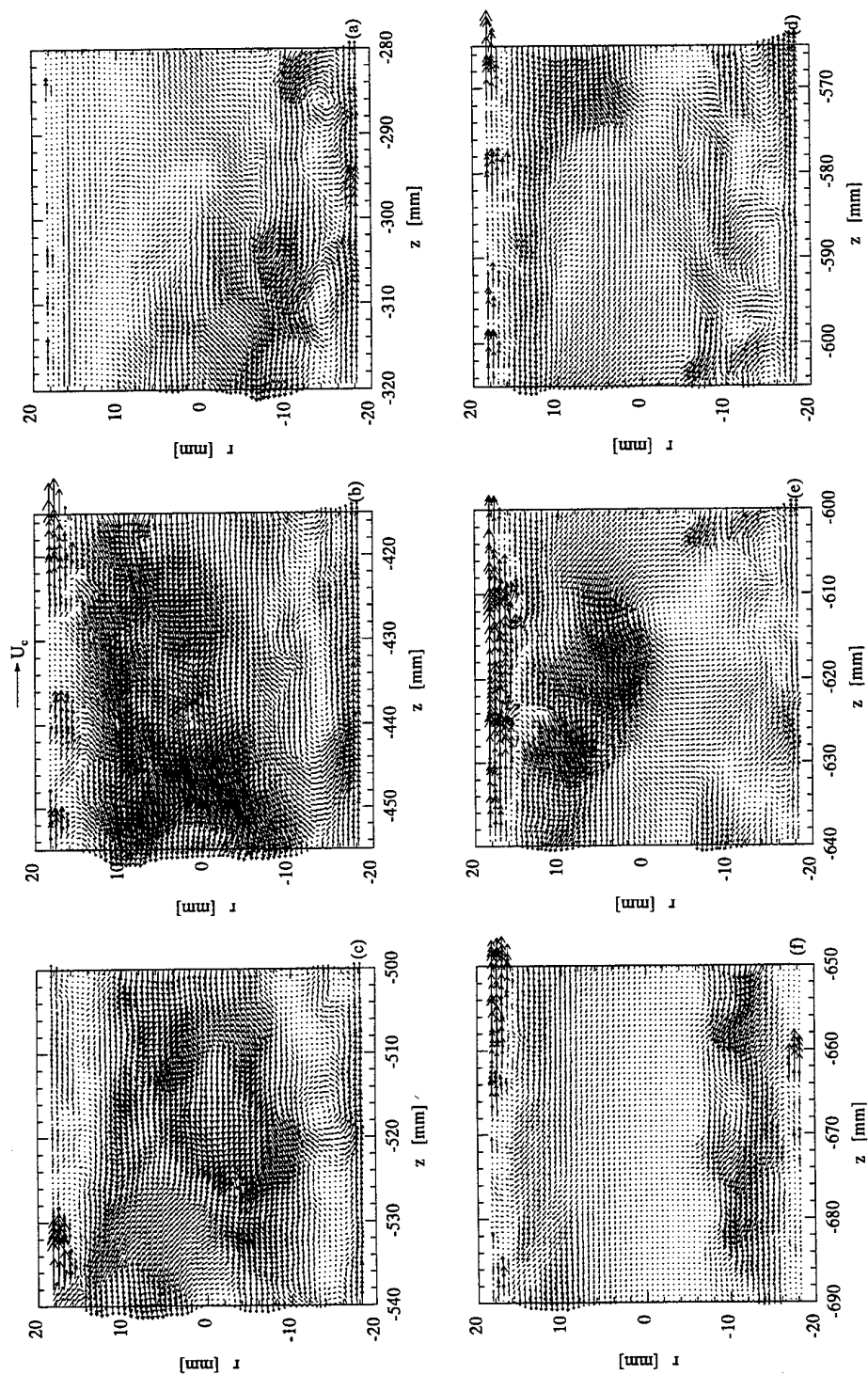


Figure 6: Details in the form of arrow plots from the compiled data set shown in Fig. 5. The arrows represent the velocity relative to the laminar velocity profile. The arrow above (b) represents the direction and magnitude of the centerline velocity in the laminar flow state.

TURBULENT TRANSPORT MECHANISM IN A DRAG REDUCING FLOW WITH SURFACTANT ADDITIVE INVESTIGATED BY TWO COMPONENT LDV

Y. Kawaguchi*, Y. Tawaraya**, A. Yabe*
K. Hishida** and M. Maeda**

*Mechanical Engineering Laboratory
AIST, MITI
Tsukuba, Japan

**Department of Mechanical Engineering
Keio University
Yokohama, Japan

ABSTRACT

It is known that frictional drag in turbulent flow can be reduced considerably by adding a small amount of surfactant to the fluid. In order to investigate the mechanism of this phenomenon, the turbulent characteristics of surfactant/water solution flow in a planar two-dimensional channel have been investigated by two-component LDV. The surfactant and counter ion used in this study were Cetyltrimethyl ammonium chloride (CTAC) and the sodium salicylate, respectively.

Profiles of two components of turbulent fluctuation intensity, u' and v' , and Reynolds shear stress are presented. It was found that u' and v' were suppressed and Reynolds shear stress was drastically decreased in the reduced-drag flow. The latter comes from de-correlation of u and v . Flow visualization showed that small scale turbulence was diminished and fluctuation had large time and length scales even at high Reynolds number. At moderate Reynolds number, the turbulence characteristics were almost the same for 50ppm and 100ppm surfactant concentration. When the Reynolds number exceeded a critical value, Reynolds shear stress near the wall increased sharply and turbulence characteristics approached those in water without surfactant.

1. INTRODUCTION

In recent years, the energy demand for residential air conditioning and water heating has been increasing in developed countries. This energy comes mainly from sources having high thermodynamic availability, such as fossil fuel or electric power. In contrast to this demand, large amounts of heat is commonly emitted to the sea or air in industrial factory areas. If this waste heat could be recovered by a very long district heating /cooling (DHC) system, more economical use of energy will be achieved.

Among the various efforts for energy economization of DHC systems, the addition of friction reducing additives (FRAs) to the fluid has a very low cost/benefit ratio (Gyr & Bewersdorff 1995). For the case of straight pipe, the reduction in pumping power sometimes approaches 80% and heat transfer reduction reaches 85%. Much research has been done on reduced-drag flows using polymer additives,

including investigation of the turbulent structure near the wall (Tiederman, 1990). But the usage of surfactant solutions instead of polymers is attractive because it has the advantage that no degradation occurs over long time periods (Zakin & Lui 1983, Ohlendorf 1986). There is not much work on turbulent characteristics of surfactant solution. Chara et. al. (1993) carried out single component LDV measurements of turbulent properties in surfactant solution flow in a pipe.

The authors are continuing our experimental study on the thermo-physical aspects of drag reduction phenomenon for the purpose of applying this phenomenon to economizing DHC systems. Park et. al. (1996) have reported turbulence characteristics of surfactant solutions in channel flow. They discussed effect of surfactant species and concentration. Kawaguchi et. al. (1996) have carried out investigation to see the heating effect on the flow in the purpose of controlling the reduced-drag flow.

The major point of the present work is determine how the turbulence characteristics are modified by surfactant additives. The effect of surfactant concentration in the dilute range as well as the effect of Reynolds number is discussed. As the surfactant solution exhibits complicated dynamical and thermal response, hot-film or other intrusive methods are unsuitable to measure the detailed flow characteristics. Therefore, in this study, two component LDV measurements are made to investigate the precise turbulent characteristics in reduced drag flow. At the same time, flow visualization was made to gain a qualitative understanding of the flow.

2. EXPERIMENTAL APPARATUS AND PROCEDURE

2.1 Water Channel

The present experiments were carried out in a closed loop fluid flow facility which is shown schematically in Figure 1. As shown therein, the system contains a reservoir tank (2.0 m³), a pump, a settling chamber equipped with a nozzle, a two-dimensional channel, a diffuser and an electro-magnetic flow meter. The test section is 40mm high (H), 500mm wide and 6m long (inside measurements). The surfactant solution is circulated by the pump and supplied to the settling chamber. The chamber is equipped with perforated pipe,

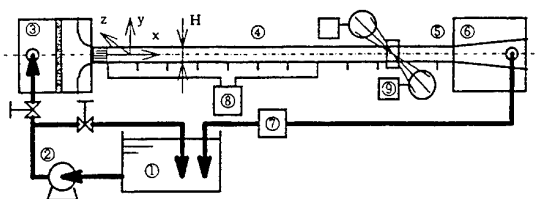


Fig. 1 Schematic diagram of closed flow loop

① Storage tank ② Pump ③ Contraction ④ Two dimensional channel ⑤ LDV measuring section ⑥ Diffuser ⑦ Flow meter ⑧ Pressure gage ⑨ LDV

nonwoven fabric sheet and 1/12.5 contraction nozzle. At the entrance of test section, a honeycomb of 150mm length having 10mm and 10mm rectangular openings was used to remove large eddies. The LDV measurement position is 5000mm ($=125H$) downstream from the inlet of the test section, and measurements were made across the half height ($H/2$) at the midway of 500mm width. Both sides of the LDV measuring position are fitted with rectangular glass windows. For measurement of pressure drop, a high-precision differential pressure meter was used. The flow rate was measured by an electro-magnetic flow meter. The reading provided by the flow meter and the flow rate calculated from the velocity profile measured by LDV coincided within 5%.

For the flow visualization, black Indian ink was supplied to the channel through an injection needle perpendicular to the wall. The flow rate of ink was carefully adjusted to equalize the injection and local flow velocity. These photograph showed qualitative details of the flow.

2.2 Laser Doppler Velocimeter System

The LDV measurement system consists of an argon-ion laser, standard DANTEC 55X optics working in a two-color three-beam mode, two photomultipliers, and two counter-processors. A double beam expander was used to minimize the measurement volume size. The probe volume has a length of 1.3 mm and a beam waist diameter of 0.08 mm. One beam in each component was frequency shifted 2MHz. The LDV was used in the forward scatter mode. Coincidence between the two channels was required for the data to be validated and transferred to the acquisition computer. For the measurement at each location, 20000 data points were recorded and analyzed.

The LDV and water channel configurations and axes are shown in Figure 2. The transmitting optics are inclined approximately 3deg with respect to the horizontal wall of the channel to improve optical access near the wall. The measurement volume was positioned by a two-axis traverser equipped with two planer mirrors. An one-axis traverser was used for the photomultiplier unit. Both unit were driven by a stepping motor controlled by a personal computer. For the scattering particle, polyethylene beads (Seitetsu Kagaku Co., flow Beads 1013) were used, which had a diameter of 5 μ m and density of 0.95.

2.3 Surfactant Solution

The surfactant used in this study was cetyltrimethyl

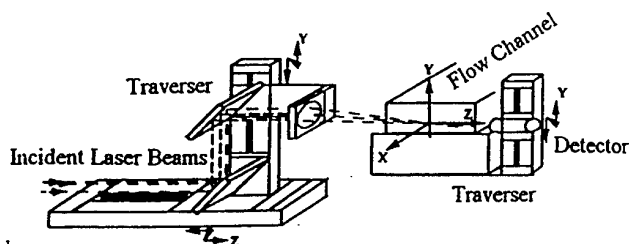


Fig. 2 LDV measurement system showing the coordinate frames and traverser directions

ammonium chloride ($C_{19}H_{42}NCl$) dissolved in tap water. The reason for using a CTAC, belonging to cationic surfactant group is that the rod-like micelle of the cationic surfactant is not greatly affected by calcium or sodium ions naturally found in tap water. Therefore, much attention has been paid for cationic surfactants in application and basic study for DHC system (Usui & Saeki 1993). The same weight concentration of sodium salichlate (NaSal) counter ion was added to the solution. In the case of surfactant, the rod-like micelle formation is thought to be the key to give visco-elasticity to the fluid. NaSal acts to stabilize the rod-like micelle structure of the surfactant. For the sake of simplicity, the composition of solution is designated by the surfactant concentration. It is not designated explicitly but the same weight concentration of NaSal is always included in the solution. Reynolds number was calculated based on the bulk mean velocity, channel height and dynamic solvent viscosity.

Prior to the channel experiments, viscosity of the solution was measured by a coaxial cylindrical viscometer. At concentrations of 50ppm and 100ppm, the apparent viscosity μ_a of the solution at a shear rate of 10 s^{-1} were 3.0 and 10.1 mPas respectively, and showed stress thinning. In addition to stress dependent viscosity, recoil was observed and it suggests the solution has elasticity. Time dependency was also found in the shear response of the solution. A detailed explanation is given in Kawaguchi et. al. (1995).

3. RESULTS AND DISCUSSION

3.1 Effect of Surfactant Additive to Turbulent Characteristics

Experimentally determined friction factors for water with and without additives are presented in Figure 3. Friction factors were obtained from pressure distribution measurements along the channel length. The Reynolds number was estimated from the bulk mean velocity U_b , channel height H and solvent viscosity ν_0 . The treatment of Reynolds number for non-Newtonian turbulent flow varies from researcher by researcher. From the preliminary study, it was obtained that the apparent viscosity of surfactant solution ν_a can be approximated as power-law fluid at low shear rates, but this is not valid at the wall where the shear rate reaches $1.0 \times 10^4 \text{ s}^{-1}$ at high Reynolds number cases. Therefore, in this study, the Reynolds number was estimated from the solvent viscosity.

The friction factor of the surfactant solution changes in a complicated way. The phenomena that friction factors rises at

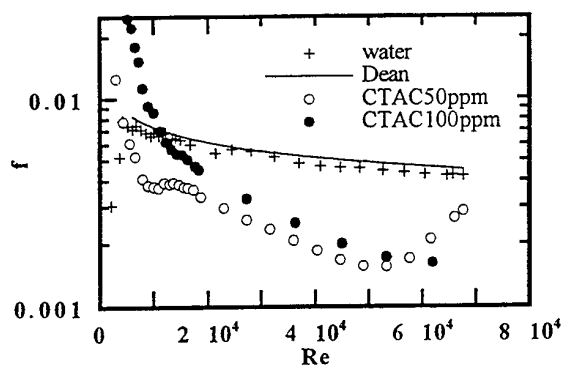


Fig. 3 Friction factor behavior for flows with and without surfactant additive (line ; experimental formula for Newtonian flow by Dean (1978))

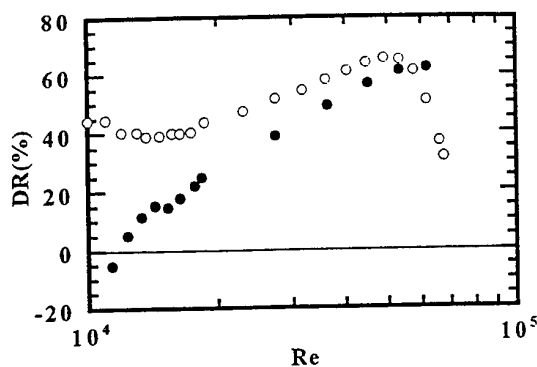


Fig. 4 Drag reduction rates for CTAC 50ppm and 100 ppm solution

certain Reynolds numbers will be discussed in section 3.3. Figure 4 shows the percentage drag reduction (DR) with Reynolds number and is defined by the following formula

$$DR = 100 \times \frac{f - f_0}{f_0}$$

where f is the friction factor for solution flow and f_0 is for water flow at the same Reynolds number. It is seen from Figure 4 that DR is dependent on Reynolds number and the largest reduction occurs at $Re = 4.8 \times 10^4$ where DR reached 70% for 50ppm concentration. Unfortunately, measurements for 100ppm concentration at $Re > 6.5 \times 10^4$ could not be made due to structural pressure limitations of the resisting pressure of the channel but the increasing trend looks like it continues to higher Reynolds number.

As the first step of our velocity measurements, the effect of surfactant additive on streamwise mean velocity profile was examined. Reynolds number was 5.2×10^4 for both cases and it means the flow rates of the channel is identical. Figure 5 shows mean velocity profiles normalized by the bulk mean velocity U_b . The horizontal axis shows the distance from the wall surface, with $H/2$ being the half-height of the channel. Open symbols correspond to the 50ppm surfactant solution and closed symbols correspond to 100ppm. The solid line corresponds to water only. All the flows have the same solvent Reynolds number of 5.2×10^4 . It is seen that the

velocity gradient of the surfactant solution flow near the wall is smaller than for the water flow. The surfactant solution velocity profile lies between the 1/7 power law profile for Newtonian turbulent flow and a parabolic profile for Newtonian laminar flow. Figure 6 shows the same data with a different scale using frictional velocity and solvent viscosity. The velocity profiles for surfactant solution obey a logarithmic law different from that of a Newtonian fluid, where Prandtl and von Karman's velocity profile is valid.

Figures 7 to 9 show effects of surfactant additive on turbulent characteristics by comparing flows of surfactant solution and water. Figures 7 and 8 show a comparison of two components of turbulence fluctuation intensity (u' and v') and Figure 9 shows a comparison of Reynolds shear stress ($-\overline{uv}$), all normalized by the friction velocity u_τ . The intensity u' normalized by the friction velocity in the surfactant solution remains on the same order as for the water-only case. It is worth noting that since the friction velocity is much smaller in the surfactant solution due to the drag reduction effects, u'/U_b has a much smaller value in the surfactant solution than in water. A mild peak far from the wall is observed in the surfactant solution case, and u'/u_τ has a larger value than water case for $y/(H/2) < 0.5$ but u'/u_τ is smaller than the water case over the entire region. Usually, the ratio v'/u' is 0.6 for most of the region of the water-only flow. In contrast with this, v'/u' is much smaller near the

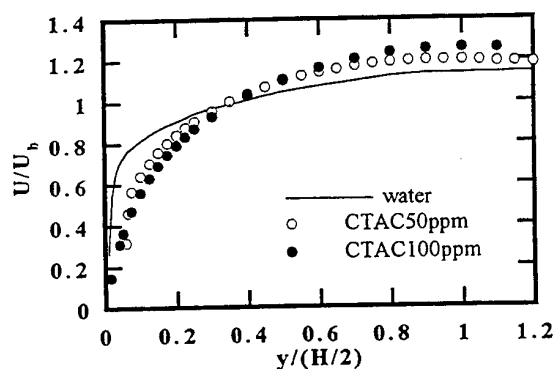


Fig. 5 Effect of surfactant solution additive for channel flow $Re = 5.2 \times 10^4$, Mean streamwise velocity profiles

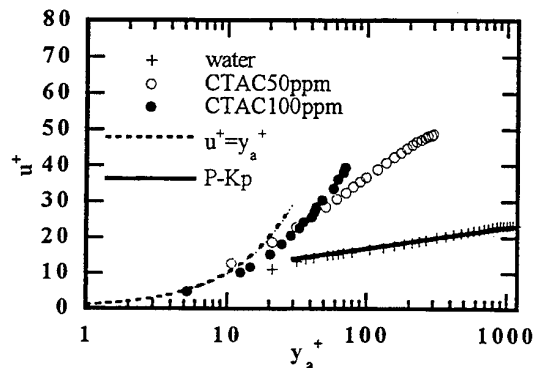


Fig. 6 Mean streamwise velocity profiles (dotted line ; $u^+ = y_a^+$, solid line ; $u^+ = 2.5 \ln y_a^+ + 5.5$)

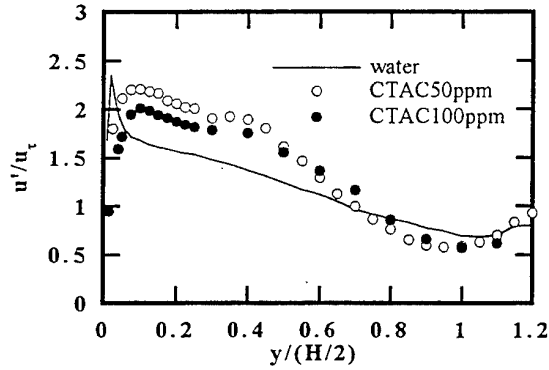


Fig. 7 Turbulence intensity u' profiles

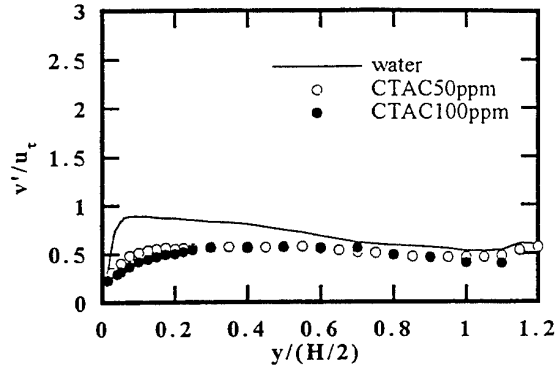


Fig. 8 Turbulence intensity v' profiles

wall in the surfactant solution case.

Figure 9 shows a comparison of Reynolds shear stress profiles in surfactant solution and water. Figures 9(a), 9(b) correspond to surfactant concentrations of 0ppm(water-only) and 50ppm, respectively. The result for 100ppm was almost the same with 50ppm case. In these figures, viscous stress estimated by the mean velocity gradient and apparent viscosity are plotted by the open symbols. The most striking finding is the fact that the Reynolds shear stress is almost zero over the whole channel height. As is well known, the total shear stress, i.e. sum of viscous stress and Reynolds shear stress in fully developed channel flow is proportional to the distance from the axis of symmetry ($H/2-y$). As seen in Figure 9(a), this is true for the water flow but not for the surfactant solution shown in Figure 9(b), which suggests that another type of stress is present in this condition. More detailed discussion will be given in the next section.

To close this section, it is worth noting that the effect of the surfactant is almost unchanged for surfactant concentrations of 50ppm and 100ppm. This is interesting because the apparent viscosity is different in each case.

3.2 Reynolds Shear Stress Deficit

In polymer additive based reduced-drag flows, it has been reported that the Reynolds shear stress becomes very small compared to the shear stress at the wall (Durst et. al. 1985, Bei & Willmarth 1992) and sometimes take small negative

value. In the present study, the same observation was made in the present surfactant solution flow. Some questions arise from the observation that Reynolds shear stress diminishes. The first question is how the stress are balanced in the fully developed channel flow. The imbalance term sometimes called shear stress deficit or elastic stress. Bewersdorff (1989) is making discussion that fluid elasticity acts to increase the effective viscosity. But the mechanism of momentum transport by fluid elasticity was not suggested. At the same time, this approximation cannot treat the case that the elastic stress become negative in high Reynolds number, which is shown in the section 3.3.

A possible explanation for the transport process in a visco-elastic fluid is as follows. In a Newtonian fluid, stress can be perfectly correlated to the velocity field, but this conventional idea is no longer valid for visco-elastic fluid turbulence. One aspect of elasticity is its time dependency. In spite of the fact that all visco-elastic fluids do not have hysteresis, they can store history through their storage modules. This means that stress applied to the fluid can be stored via a property change, which is undetectable from velocity measurements. Figure 10 shows the schematic picture explaining the following discussion. When a large shear stress is applied to an fluid element near the wall, the element stores energy. By random fluid motion, once the element is transported away from the wall, the mean shear rate in the new position is smaller and the eddy "emits" energy. Therefore, this process can transfer momentum

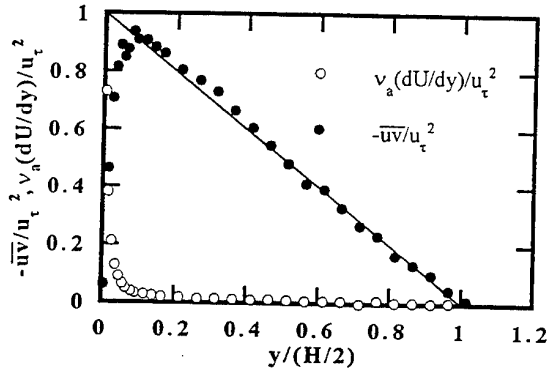


Fig. 9(a) Reynolds shear stress ($-\overline{uv}$) and viscous stress profiles, $Re=5.2 \times 10^4$ - water

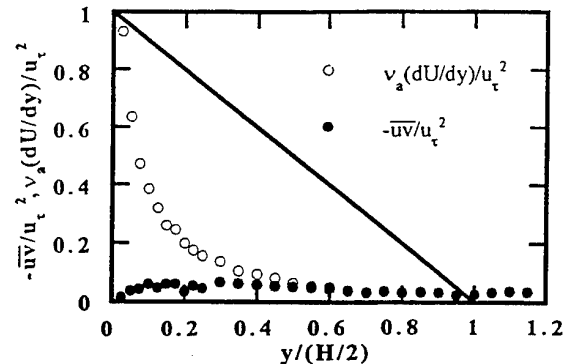


Fig. 9(b) Reynolds shear stress ($-\overline{uv}$) and viscous stress profiles, $Re=5.2 \times 10^4$ - CTAC 50ppm

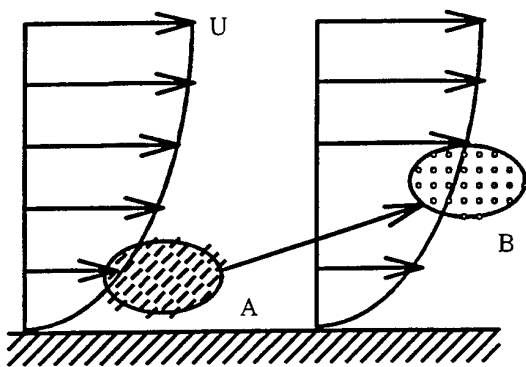


Fig. 10 Schematic figure of momentum transport by property change

similar to the way a passive scalar is transported by turbulent motion. For the better understanding of the transport phenomena in visco-elastic fluid, the investigation is needed focused on the inhomogeneous fluid property. At the same time, more detailed discussion on the relaxation time scale of the fluid and flow will be necessary.

We can however, suggest some future work to evaluate this explanation. If the normal component of turbulence is not

present or the mean shear rate is homogeneous, this transport process can not be present. Therefore, in such flows, the stress will be perfectly correlated to the mean and turbulent velocity fields. To have more positive, though still not direct, some properties relating to storage modules in turbulent field may be helpful. One candidate of such a property is the flow birefringence or another measure of fluid property anisotropy.

The second point is how the Reynolds shear stress deficit is related to coherent motion near the wall. In order to investigate this point, the joint probability density function (JPDF) of u and v was calculated at five channel positions for flows with and without surfactant. The results are shown in Figures 11(a) and 11(b). Figures 11(a) and 11(b) show JPDFs for the same Reynolds number flows without and with 50ppm surfactant additive, respectively. In each figure, the horizontal axis shows u and the vertical axis shows v . The probability density $P(u, v)$ is displayed by contours having equal values of $P(u, v)$. Except for the neighborhood of the channel centerline, most of the contours can be approximated by ellipsoids which corresponds to the unequal u' and v' intensities. Let us define the inclination angle α as the angle between the major axis of the contour and the horizontal axis. For the case of water flow, α has a positive value near the wall, as seen in Figure 11(a). This means most of the intense positive u fluctuations are accompanied by negative v fluctuations. At the same time, intense negative u fluctuations

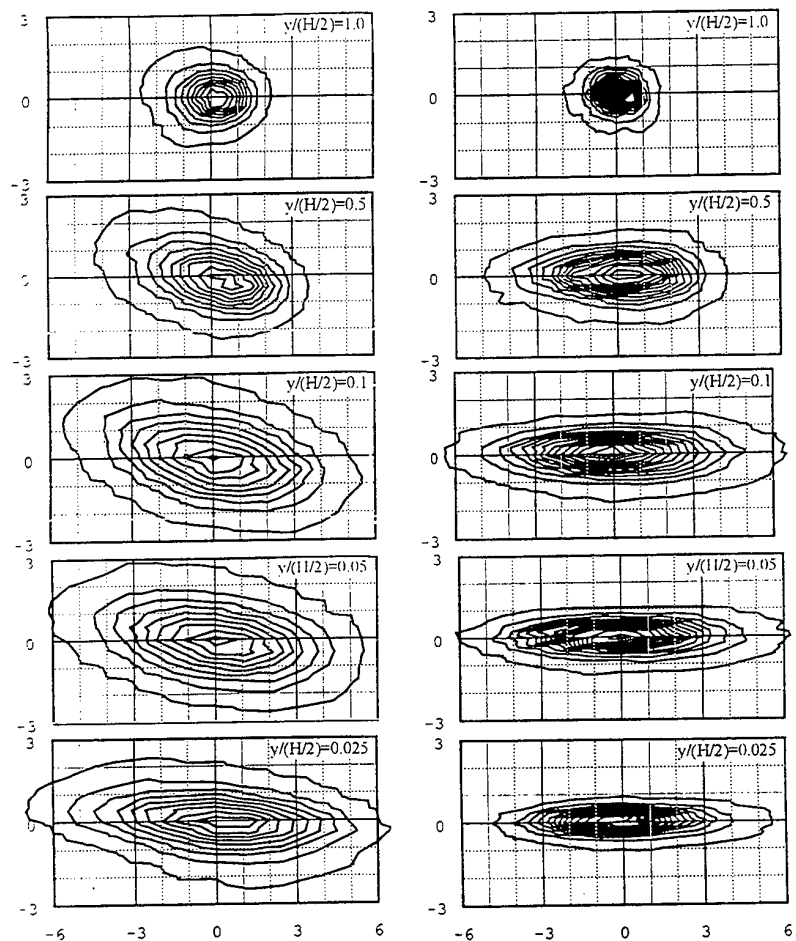
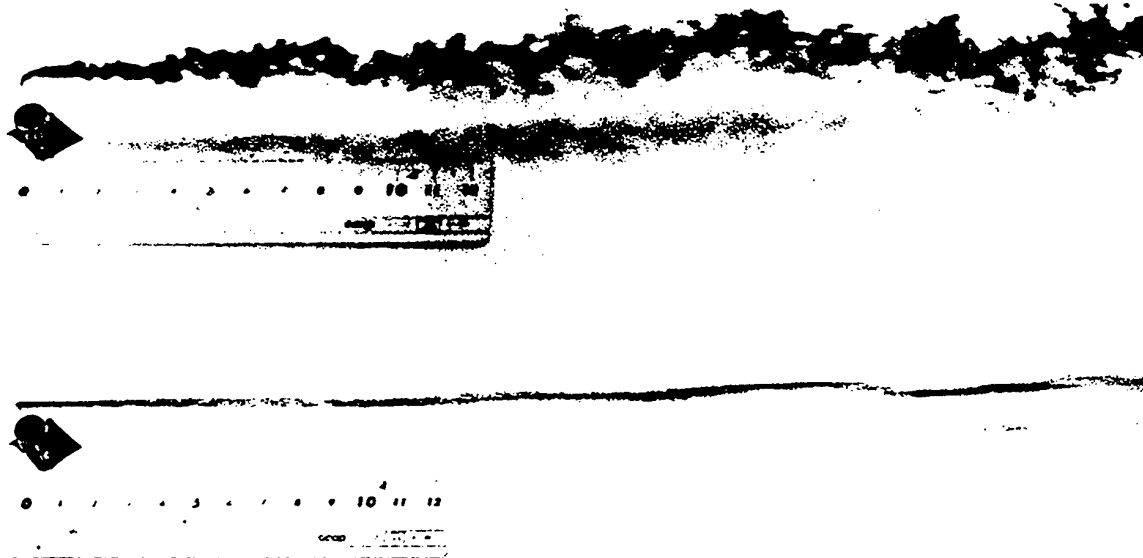


Fig. 11(a) Joint probability density function, $Re=5.2 \times 10^4$ - water (left)

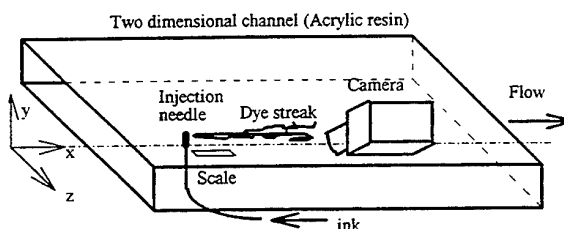
Fig. 11(b) Joint probability density function, $Re=5.2 \times 10^4$ - CTAC 50ppm (right)



Picture 1 Dye streak in channel, $Re=1.75 \times 10^4$
- water (top)

Picture 2 Dye streak in channel, $Re=1.75 \times 10^4$
- CTAC 100ppm, (bottom)

schematic diagram of camera position (right)



are associated with positive v fluctuations. This observation is consistent with the investigations of coherent motion near a wall. At the same time, this motion is reasonable from the view point of the mixing length hypothesis in turbulent shear flows.

Figure 11(b) shows the JPFDs for the case of adding surfactant. All JPFD contours obtained near the wall are ellipsoidal. The ratio of the major axis to minor axis is larger compared to the water-only case. This means that a greater unbalanced nature between the two directional components of fluctuation is present in the surfactant solution flow. The most unusual thing found in this figure is that the inclination angle α is almost zero and the major axis of the ellipsoids coincide with the horizontal axis. This means the coherent motion near the wall is not dominant, and that the flow can not be approximated by a mixing length hypothesis. This special kind of turbulence has one more unusual property in that there should be no turbulence production, in the classical definition, if the Reynolds shear stress is zero. According to an energy balance of the turbulence intensity, we cannot expect fully developed flow if the production rate is zero and the dissipation rate is positive. One explanation may be the effect of elasticity on the stress balance. If the elastic stress is taking the place of turbulent shear stress, the turbulence production rate would, in effect, positive.

Further information about time and length scales of the turbulence may be important. Pictures 1 and 2 show flow visualization results by dye injection. Both pictures were taken at the same Reynolds number, $Re=1.75 \times 10^4$ and correspond to cases without surfactant and with 100ppm

surfactant respectively. Picture 1 shows that the dye streak is diffused by the turbulence in a conventional manner. There are variety of eddies having different sizes. In contrast, figure 2 shows a thread-like dye streak with very little diffusion or deformation of the streak. The shape of the streak is slowly curved and it suggests that there are only large eddies. This may be the reason that turbulent energy is not dissipated quickly.

3.3 Critical Phenomena of Loss of Drag Reduction

In the application of FRA to DHC, the flow behavior over a wide range of Reynolds number is of interest because the flow rate in the DHC piping system is changing constantly depending on the required thermal load. More importantly, loss of drag reduction can cause trouble for the DHC if it was designed under the assumption of constant DR. The loss of drag reduction can be seen around $Re=6.0 \times 10^4$ in Figure 3 for the case of 50ppm surfactant concentration and it is believed that this comes from mechanical degradation of solution near the wall. To investigate this point in more detail, the variation of turbulent quantities was examined.

Figure 12 shows the variation of Reynolds shear stress normalized by the friction factor measured at $y/(H/2)=0.075$ and friction factor. As seen in the previous section, the Reynolds shear stress approaches zero at moderate Reynolds numbers and drag reduction is observed. When the Reynolds number exceeds some critical value, Reynolds shear stress increased sharply. In comparison with this, the increase of the wall shear stress is slow. In this higher Reynolds number

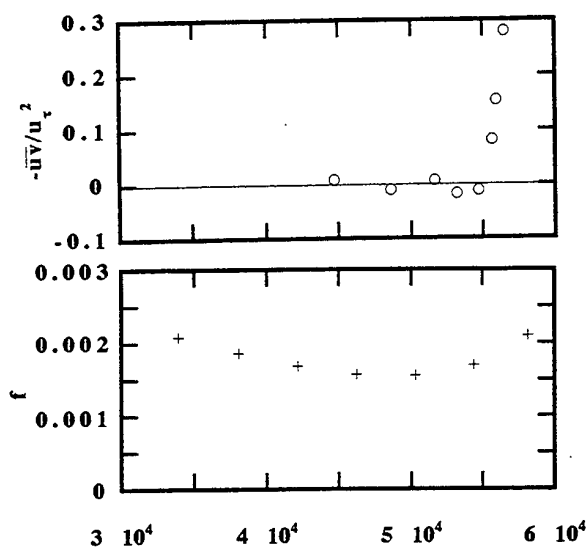


Fig. 12 Reynolds number dependency of Reynolds shear stress measured at $y/(H/2)=0.075$ and friction factor

region, the imbalance of shear stress again occurs, but in the opposite manner as the drag reduction case. At moderate and subcritical Reynolds numbers, elastic stress has a positive sign. Above the critical Reynolds number, the Reynolds shear stress recovers quickly and the wall shear stress remains at a lower level. Therefore, elastic stress has a negative sign in this region. In other word, this phenomena suggests that the Reynolds shear stress varies independently from the shear stress at the wall.

4. CONCLUSION

A statistical study of turbulence was made of a surfactant solution flow in a two-dimensional channel. The surfactant has a very long life compared to water soluble polymers, so it is suitable for application to closed circuit systems such as a DHC system. In association with wide-area energy economization, the importance of investigating surfactant solution drag reduction mechanisms increasing.

Results of two-component LDV measurements in a surfactant-based reduced-drag flow demonstrated that the Reynolds shear stress normalized by friction velocity drastically decreased over the whole range of the channel. This change corresponds to a de-correlation of the two components of velocity fluctuation, because each component of fluctuation intensity remained at the same order as in a similar flow without additives. This characteristic suggests the presence of an alternative momentum transport mechanism in the visco-elastic fluid. Suggestion of future research on elastic stress was made. Discussion of the joint probability density function was made in relation to coherent motion near the wall. The decline in drag reduction performance at high Reynolds number was also discussed.

ACKNOWLEDGMENT

The authors are thankful to Mr. H. Daisaka of Keio University whose assistance was invaluable in these experiments.

REFERENCES

- Bei, T. & Willmarth, W.W., 1992, Modifying turbulent structure with drag-reducing polymer additives in turbulent channel flows, *J. Fluid Mechanics*, vol. 245, pp. 619-641
- Bewersdorff, H. W. 1989, Drag Reduction in Surfactant Solutions, in *Structure of Turbulence and Drag Reduction*, ed. Gyr A., pp. 293-312, Springer-Verlag, Berlin
- Chara, Z., Zakin J. L., Severa M. & Myska J., 1993, Turbulence measurements of drag reducing surfactant systems, *Experiments in Fluids*, Vol. 16, pp. 36-41
- Dean, R.B., 1978, Reynolds number dependence of skin friction and other bulk flow variables in two-dimensional rectangular duct flow, *J. Fluid Engineering*, vol. 100, pp. 215-223
- Durst, F., Keck T. & Kleine, 1985, Turbulence Quantities and Reynolds Stress in Pipe Flow of Polymer Solutions, *Proc. Int. Conf. Laser Anemometry - Advances and Application. Manchester*, pp. 31-52
- Gyr, A. & Bewersdorff H. W., 1995, *Drag Reduction of Turbulent Flows by Additives*, Kluwer Academic Publishers, Dordrecht
- Kawaguchi Y., Tawaraya Y. & Tanaka M., 1995a, Viscosity Measurements of CTAC:NaSal/W Micelle Solution - Temperature Effect and Wall Effect of Viscometer, *J. of Mechanical Engineering Laboratory*, Vol. 49-4, pp. 12-21 (in Japanese)
- Kawaguchi Y., Tawaraya Y., Yabe A., Hishida K. & Maeda M., 1996, Active Control of Turbulent Drag Reduction in Surfactant Solutions by Wall Heating, *Proc. ASME Sym. Turbulence Modification and Drag reduction*, (in printing)
- Ohlendorf D., Intherthal W. and Hoffmann H., 1986, Surfactant Systems for Drag Reduction: Physico-chemical Properties and Rheological Behavior, *Rheologica Acta*, Vol. 26, pp. 468-486
- Park S.R., Kawaguchi Y. & Yoon H.K., 1996, Experimental Study of Turbulent Characteristics in Drag Reducing Channel Flow with 2D-LDV, *Proc. 3rd KSME/JSME Thermal Engineering Conf.*, (in printing)
- Tiederman W. G., 1990, The Effect of Dilute Polymer Solutions on Viscous Drag and Turbulent Structure, in *Structure of Turbulence and Drag Reduction*, ed. Gyr A., pp. 187-200, Springer-Verlag, Berlin.
- Usui H. & Saeki, T., 1993, Drag Reduction and Heat Transfer Reduction by Cationic Surfactants, *J. Chem. Engng. Japan*, vol. 26-1, pp. 103-105
- Zakin J.L. and Lui H.L., 1983, Variables Affecting Drag Reduction by Nonionic Surfactant Additives, *Chemical Engineering Communications*, Vol. 23 p.77

SESSION 30

Free Flows I

ON THE RELATIONSHIP BETWEEN THE FORMATION NUMBER AND PASSIVE SCALAR PINCH-OFF IN STARTING JETS

H. Johari,* D. Dabiri,[†] A. Weigand,[†] and M. Gharib[†]

*Mechanical Engineering Department, Worcester Polytechnic Institute, Worcester, MA 01609

[†]Center for Quantitative Visualization, Graduate Aeronautical Laboratories
California Institute of Technology, Pasadena, CA 91125

ABSTRACT

A series of experiments were conducted in a water tank to investigate the behavior of starting vortex in starting jets at Reynolds numbers up to 2×10^4 . The starting vortex of a jet separates from the rest of jet in the near-field. The velocity field was measured via the digital particle image velocimetry while the passive scalar concentration was observed by the laser-induced fluorescence technique. The measured Formation number was in the range of 4.5 to 5.5, consistent with previous low Reynolds number results. The passive scalar separation of starting vortex from the jet could not be measured, due to the lack of adequate run time. The Formation number appears to be a robust parameter for characterizing the pinch-off of vorticity in starting jets.

1. INTRODUCTION

Steady, round jets have been investigated extensively in the past because of their wide ranging applications in industrial settings as well as their utilization in scientific studies. The starting process for jets is much less well-understood and only a few studies have attempted to characterize impulsively-started jets. Abramovich and Solan (1973) examined experimentally laminar starting jets and modeled the flow as a laminar jet combined with a spherical vortex cap. Their experimental data corroborated the model predictions and the speed of the jet front was found to be about one half of the steady jet at the same location. Numerical studies conducted by Kuo et al. (1986) of laminar starting jets produced a Reynolds number scaling different than that of Abramovich and Solan. A model for the turbulent starting jet was developed by Witze (1980); it was based on Turner's (1962) model for a starting plume. The model, in agreement with measurements, indicated that the jet tip in the turbulent case also advances at one half speed of a steady jet at the same location. Lahbabi et al. (1993) have verified this scaling using non-intrusive image processing techniques applied to images of a passive scalar being carried by the jet.

In a number of recent experiments on starting jets, it has been observed that the starting vortex pinches off and

separates from the rest of the flow. It is interesting that this phenomenon has not been reported previously in the literature on starting jets, presumably due to the lack of data on velocity (vorticity) field. The pinch-off and subsequent separation of the starting vortex from the rest of the jet has been characterized by two different means. Gharib et al. (1994) have utilized the Digital Particle Image Velocimetry (DPIV) method to quantify the total circulation ejected from the source as well as that contained within the vortex core, and to follow these quantities in time. At a certain point in time, the circulation associated with the vortex core reaches a constant value while the total circulation in the flow field is increasing (due to the continued ejection of fluid at the source). Since the pinch-off time cannot be very accurately estimated from the vorticity contours extracted from the DPIV data, the time τ that corresponded with the total ejected circulation equal to the starting vortex circulation has been selected as the characteristic pinch-off time. The (running) average velocity of the source $\bar{V}(t)$ divided by the source diameter d has been used to non-dimensionalize the characteristic time τ , as indicated below.

$$\frac{\bar{V}\tau}{d} = \frac{1}{d} \left[\frac{1}{\tau} \int_0^\tau V(t) dt \right] \tau = \frac{1}{d} \int_0^\tau V dt$$

This dimensionless time is referred to as the Formation number F . For a variety of operating conditions and nozzle velocity time-histories, the measured Formation number has a mean value of approximately 4. For an impulsively-started flow of velocity V_0 , the Formation number will have a form of $V_0 \tau / d$. A plot of circulation against time is shown Fig. 1 along with the vorticity contours before and after pinch-off.

In a separate effort, the planar laser-induced fluorescence (LIF) technique was utilized by Kourou et al. (1993) and Johari et al. (1995) to investigate the dispersion of a passive scalar in starting jets. For the case of impulsively-started flow, nozzle Reynolds numbers, $V_0 d / \nu$, ranging from 5 000 to 20 000 were achieved in a pressure-driven system with nozzle diameters of 0.64, 1.3, 2.5 cm. In these experiments, it was also observed that the starting vortex, as marked by a passive scalar (fluorescent dye),

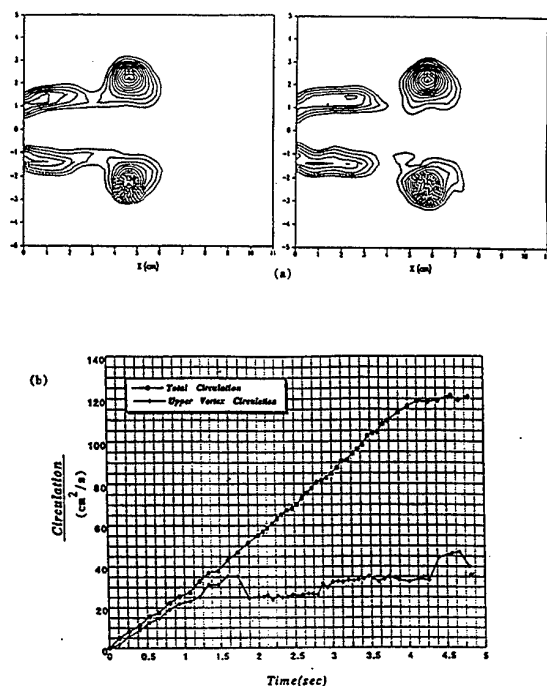


Fig. 1 (a) Vorticity contours of a starting jet before and after pinch-off, (b) temporal evolution of vortex core and total circulation

separated from the ensuing jet. LIF images of the starting vortex just after the pinch-off and separation is shown in Fig. 2. The separation time was chosen at the instant that pure ambient fluid existed across the entire width of the flow and the starting vortex was completely isolated from the rest of the jet. The normalized time for the separation of the starting vortex, derived from the passive scalar images, had values ranging from 10 to 40 and appeared to vary significantly among the different set of runs in the these experiments (Johari et al. 1995).

Interestingly, the normalized time derived from passive scalar experiments does not concur with the Formation number obtained from the circulation data. In fact, the former exhibits strong (jet) Reynolds number dependence, whereas the Formation number does not appear to vary strongly with the Reynolds number, based on the vortex core circulation, in the range of a few thousands (Gharib et al. 1994). There are two plausible reasons why the observed Formation numbers differ substantially from the normalized pinch-off time of passive scalar. First, the Formation number may exhibit strong Reynolds number dependence once it is varied over a considerable range. Second, the two distinct definitions used for the Formation number and the passive scalar pinch-off time may make any direct comparison between the two inappropriate.

To resolve these issues, a piston-driven apparatus was designed which was capable of achieving higher Reynolds numbers, i.e., comparable to those in the impulsively-started pressure-driven case. At the same time, the exit diameter

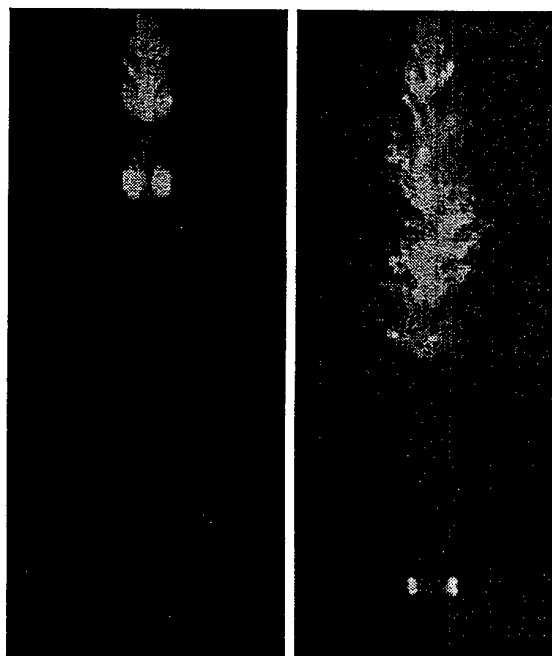


Fig. 2 LIF images of an impulsively-started jet

was made large enough so that accurate DPIV measurements could be attained. In this manner, both DPIV and LIF measurements could be performed on the flow generated from the same apparatus. The primary objectives of this project were: (i) to investigate the Formation number resulting from high Reynolds number starting jets, and (ii) to examine any possible relationship between the Formation number and the pinch-off of a passive scalar in starting jets.

2. EXPERIMENTAL SETUP

2.1 Apparatus

The experiments were conducted in a horizontal free-surface water tank having a 90 cm width and 60 cm depth. The dimensions of the tank were much greater than the vortex ring so that wall effects were negligible. The flow generating apparatus is shown in Fig. 3 and consists of three main sections, a piston-cylinder assembly, a plenum, and an ejection tube. The piston has a 10.2 cm diameter and is driven by a stepping motor. The maximum piston travel is also 10 cm; however, only about 8 cm of travel were utilized in the present experiments. The piston forced the fluid into the plenum; the fluid escaped through a perforated PVC tube. The PVC tube had a fill factor of unity such that the sum of perforated area was equal to the cross-sectional area of the tube. The flow passing through the PVC tube then entered the ejection tube via a honeycomb-screen element. The ejection tube was made of clear acrylic and had a 5.1 cm internal diameter and a length of 52 cm. The last 2.4 cm of the tube was tapered on the outside, creating a 15° angle with the tube wall. This last section will be referred to as the

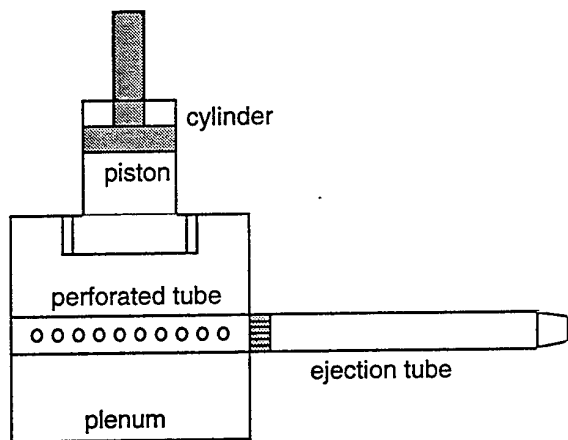


Fig. 3 Schematic of the apparatus

'nozzle' even though the tube inside diameter was constant.

The piston motion was controlled by a computer such that a constant acceleration was maintained until the piston reached the end of its travel. A linear variable displacement transducer was used to record the piston motion. Thus, the piston velocity increased linearly with time. Since the ejection tube's diameter was one-half of the piston-cylinder diameter, the velocity at the tube exit was also linear with time and 4 times greater than the piston velocity. Two piston 'ramp' rates of 6.63 and 2.63 cm/s² ($\pm 2\%$) were selected in the present study. The piston travel durations were 1.5 and 2.4 s for the two ramp rates, respectively, corresponding to fluid slug lengths of approximately 5.9d and 6.0d.

2.2 Optical Setup

The flow was seeded either with fluorescent dye for the passive scalar runs or with silver-coated glass spheres with an average diameter of 14 μm for the DPIV runs. The flow was illuminated by a 1 mm thick light sheet, generated by an argon-ion laser and a cylindrical lens, which revealed side views of the starting jet. The laser beam was shuttered to reduce blurring of the images. The image exposure times were 1.5 and 2 ms for the large and small piston ramp rates, respectively. Flow images were acquired by a CCD camera (768 \times 480) and recorded on laser disk. The area imaged was 2.1d in the axial direction and 2.7d transverse to the tube exit. Either the immediate near-field, from tube exit to 2.0d, or farther downstream, 2.2d to 4.3d, were imaged on the camera.

The particle images were interrogated in pairs using the cross-correlation method of Willert and Gharib (1991). The time differences between consecutive exposures were 2 and 5 ms for the large and small piston ramp rates, respectively. A window size of 32 \times 32 pixels and a step size of either 8 \times 8 (75% window overlap) or 16 \times 16 (50% window overlap) pixels were chosen, resulting in 96 \times 60 or 48 \times 30 velocity vectors, respectively. Circulation measurements obtained from the same images processed by the two different step sizes were quite consistent. According to Willert and Gharib (1991), the location of cross-correlation

peak can be resolved with an accuracy of 0.01 pixels. Then, velocity vectors and vorticities could be measured with uncertainties of 1 and 3 percent, respectively. The sampling rate of the current measurements was 15 Hz.

The primary quantity of interest in the present study is the circulation Γ ejected from the source and that associated with the starting vortex. Circulation was calculated by taking the line integral of velocity along a closed path. Two different closed paths were chosen in order to observe any differences between the circulation values resulting from the choice of path. The first path consists of a rectangle originating from the nozzle center and extending along the axis of symmetry to an axial position beyond the starting vortex. The radial extent of the rectangle was about 6 cm from the origin at nozzle center for the near-field images and 8 cm for the downstream images. As the flow evolved, the axial extent of this path also increased to always include the starting vortex completely.

The second method of determining circulation takes advantage of the calculated vorticity contours. The vorticity contour at 10% of the local peak vorticity was chosen as the path for the small piston ramp rate (8% contour for the large ramp rate). These contour levels provided circulation values which were quite consistent with the values resulting from the rectangular path. The overall accuracy of circulation values is estimated to be better than 5% of the local value. Incidentally, Reynolds number for the present experiments was based on the ratio of starting vortex circulation at 3d over the kinematic viscosity, i.e., $\text{Re} = \Gamma/\nu$. The Reynolds number for the small and large piston ramp rates were 2×10^4 and 4×10^4 , respectively.

3. RESULTS

3.1 DPIV Data

For each of the two piston ramp rates at least 10 runs were performed and among these, five runs with optimum seeding were selected for further processing. The vorticity contours of a starting jet with the small piston ramp rate are shown in Fig. 4 at three different time instances. The time was measured from the first image pair with non-zero velocity at the nozzle exit. The first contour level is at $\pm 2 \text{ s}^{-1}$ and the difference between the contours is also 2 s^{-1} . The solid contours indicate positive (counter-clockwise) vorticity and dashed contours negative (clockwise) vorticity. The origin is at the nozzle center and the tic marks are in centimeter. The first plot is at 1.5 s after the initiation of flow and only the vortex core with negative vorticity can be observed completely. The nearly circular contours with peak vorticity of 20 s^{-1} in the core center are noteworthy. The vortex core is at 2.8 cm from the nozzle. As the starting vortex core moves away from the nozzle, a secondary (toroidal) vortex in the (round) shear layer bounding the jet is evident. The total circulation ejected from the nozzle at this time is $91 \text{ cm}^2/\text{s}$, using either of the two closed paths.

The contour plot in Fig. 4 (b) depicts the starting jet at a time of 2.1 s after flow initiation. The starting vortex core is at 5.6 cm from the nozzle and the entire flow is still

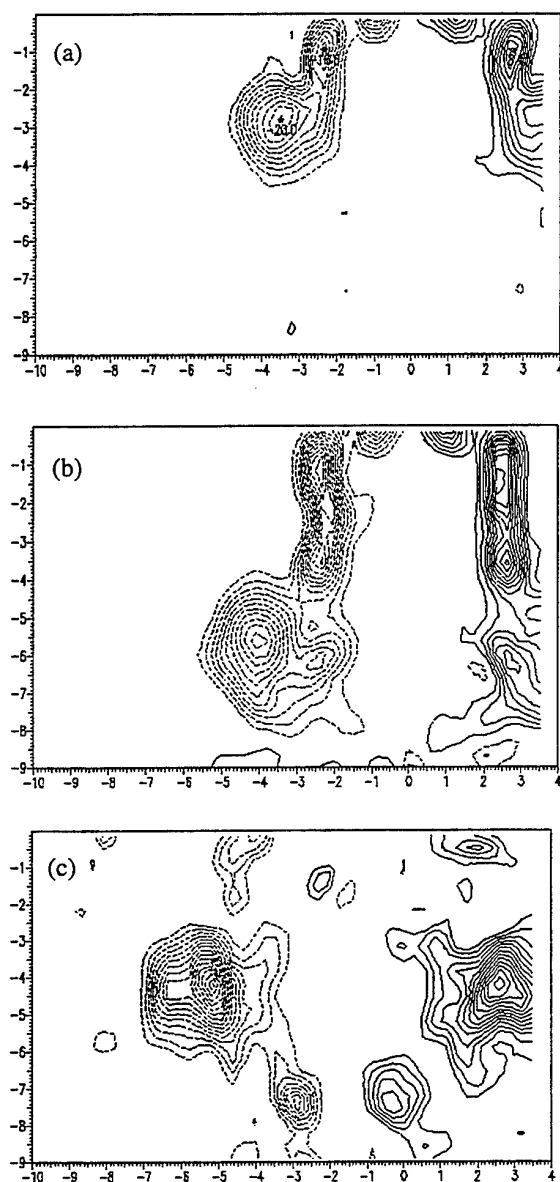


Fig. 4 Vorticity contours of a low ramp rate starting jet at 1.5 s in (a), 2.1 s in (b), and 3.2 s in (c). The flow is from top to bottom.

relatively symmetric. The vorticity within the starting vortex is segregated into a primary zone with peak vorticity of 23 s^{-1} and a secondary zone with peak vorticity of 13 s^{-1} . A possible explanation for the secondary vorticity within the starting vortex at this early time is the engulfment of the first shear layer vortex by the starting vortex. Furthermore, there are now two vortices in the jet shear layer. The total circulation, which is still increasing due to the continued fluid release, is $191 \text{ cm}^2/\text{s}$. The circulation values computed using either of the two closed paths is within $\pm 1\%$ of this average value.

The plot in Fig. 4 (c) shows the vortex ring after the nozzle flow had ceased, at a time of 3.2 s. The image corresponds to the downstream position of the camera, where the vortex core is 13 cm away from the nozzle. Clearly the starting vortex has separated from the rest of the jet. Note the appearance of separate vorticity regions ahead and behind the primary vortex core. The circulation computed from the vorticity contour path is $206 \text{ cm}^2/\text{s}$, whereas the rectangular path resulted in a value of $230 \text{ cm}^2/\text{s}$ due to the extra vorticity outside the primary zone. The vortical parcels behind the vortex core are postulated to have been shed from the main vortex ring, similar to those in turbulent vortex ring studies (Maxworthy 1974, Glezer and Coles 1990).

In order to calculate the Formation number for this run, circulation was plotted against time in Fig. 5 for both paths. The portion of data indicating the rapid increase of circulation with time comes from the runs with the camera viewing the region immediately downstream of the nozzle, and the data indicating relatively constant values of circulation from the downstream camera position. Note the close correspondence between the circulation values obtained from the two different closed paths, throughout the near-field. To arrive at the Formation number, time has to be normalized with the (running) average velocity and the nozzle diameter. Since the nozzle velocity increased linearly with time at a known rate, the average velocity as a function of time is readily found. Multiplying the average velocity with time is the effective fluid slug length ejected from the nozzle and is denoted by L .

The graph in Fig. 5 (b) is a plot of circulation against L/d for the near-field portion of the run. The horizontal line is at a value equal to the mean circulation of separated vortex, obtained from downstream data. The cross-section of this line with the near-field circulation data provides the Formation number for this run. The value for this run is about 4.6. It is important to realize that near-field data contain all the circulation ejected from the nozzle, i.e. the starting vortex circulation as well as that in the jet shear layer. The farther downstream data contain only the circulation associated with the separated starting vortex core. Therefore, a Formation number of 4.6 indicates that the circulation of the final vortex ring is equal to that derived from the first $4.6d$ long slug of fluid ejected from the nozzle.

The Formation number was found for a number of runs with both the small and large piston ramp rates. In all cases, the Formation number was in the range of 4.5 to 5.5. These values are quite consistent with those of earlier studies (Gharib et al. 1994) with Reynolds numbers smaller than the present runs by an order of magnitude. Then, it appears that the Formation number is a robust method of characterizing the separation and pinch-off of vorticity in starting vortices. The passive scalar experiments are described next.

3.2 Passive Scalar Visualization

The main purpose of passive scalar runs was to investigate whether the pinch-off of the starting vortex, as revealed by the separation of dyed vortex, can be corroborated with the Formation number. Sample LIF

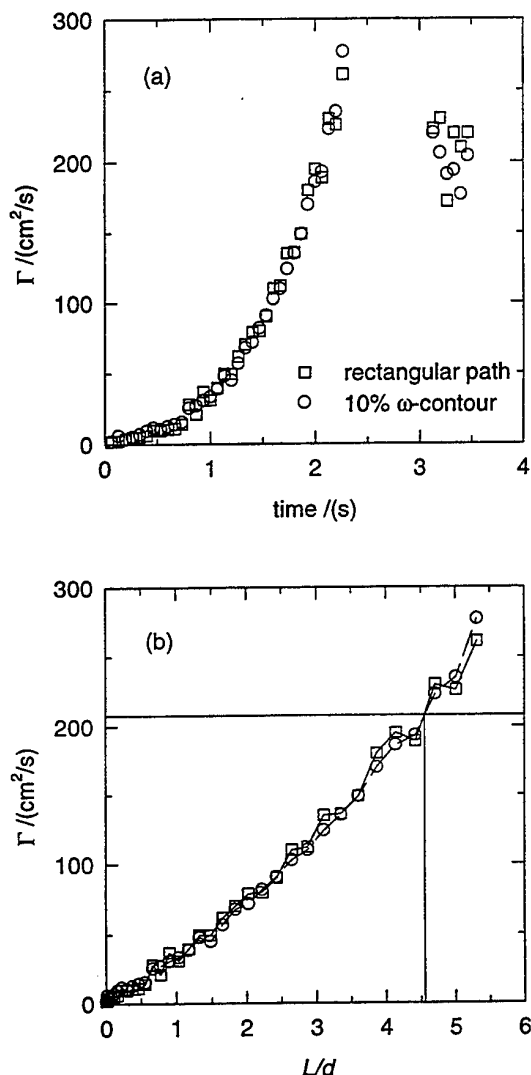


Fig. 5 Circulation as function of time in (a) and slug length in (b)

images of the flow at the large ramp rate is shown in Fig. 6. The dyed fluid has traveled $1.9d$ after 1.2 s in the first image. Of particular interest is the development of the Kelvin-Helmholtz instability of the jet shear layer. It is important to note that the velocity in the potential core increased linearly with time. The second image shows the flow at 1.3 s where the tip has extended beyond the field of view. Roll up of the shear layer vortices and their subsequent ingestion into the vortex core are remarkable. Shear layer vortices observed in this manner correspond approximately with the vorticity contours in Fig. 4 (b), although the piston ramp rates are different. The waves on the separating streakline in the first image took about one second to develop for both ramp rates.

The pinch-off and separation of the passive scalar took place only after the piston had reached its final position, i.e.,

after the supply had ceased. Based on the previous observations, it is believed that the dye within the starting vortex would have pinched-off and separated from the rest of the jet flow had the supply been continued. Unfortunately, the present apparatus was limited in this manner and the time for passive scalar pinch-off could not be directly measured. However, it was clear that the passive scalar pinch-off time would not correspond with the time associated with the Formation number. The latter time was clearly smaller than the time of each run, whereas the former time was certainly larger than the run time by an appreciable amount. The discrepancy associated with the passive scalar pinch-off time and the time associated with the Formation number appears to originate from their respective definitions and it does not appear to be due to the Reynolds number differences in the past experiments.

4. SUMMARY

The present results indicate that the Formation number is a consistent parameter for characterizing the pinch-off of vorticity not only at low Reynolds numbers but also at vortex Reynolds numbers extending to about 4×10^4 . Remarkably, the Formation number was nearly constant with a value between 4.5 and 5.5 for the case of constant acceleration piston motion in the present setup. This range of values is compatible with prior experiments with different nozzle velocity time-histories. At the same time, the definition used for the Formation number does not appear to be quite compatible with that employed for the quantification of passive scalar pinch-off. The latter is defined in terms of the local time when the complete separation of the starting vortex is observed. In contrast, the former definition goes back in time to the instant the starting vortex circulation has just been generated by the jet. For this reason, the two normalized times cannot be the same. Lastly, the Formation number can be used to predict the amount of circulation which will accumulate in the separated starting vortex core if the nozzle velocity time-history is known.

REFERENCES

- Abramovich, S. & Solan, A. 1973, The Initial Development of a Submerged Laminar Round Jet, *J. Fluid Mech.*, vol. 59, pp. 791-801.
- Gharib, M., Rambod, E., Dabiri, D., Hammache, M., Shiota, T. & Sahn, D. 1994, Pulsatile Heart Flow: A Universal Time Scale, *Proc. 2nd Int. Conf. Exp. Fluid Mech.*, Lovrotto and Bella, Torino, Italy.
- Glezer, A. & Coles, D. 1990, An Experimental Study of a Turbulent Vortex Ring, *J. Fluid Mech.*, vol. 211, pp. 243-283.
- Johari, H., Rose, M., Bourque, S. & Zhang, Q. 1995, Experiments on Impulsively Started Turbulent Jets, ASME FED-207, pp. 9-16.

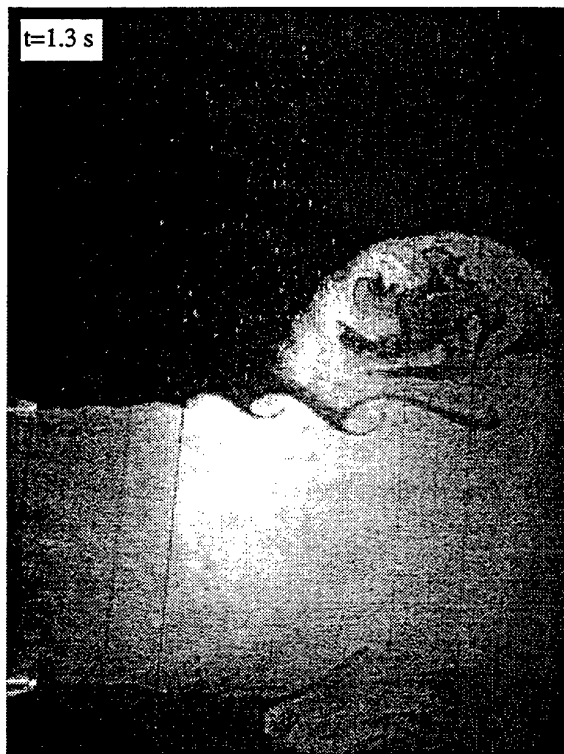
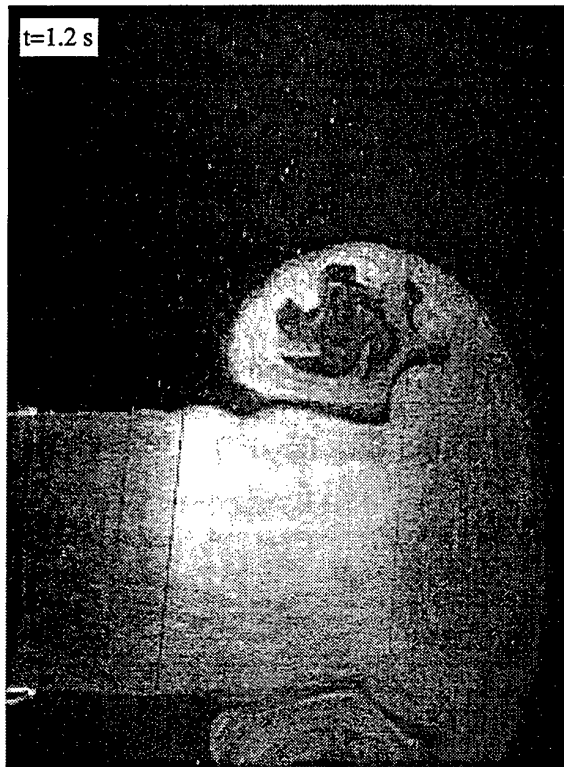


Fig. 6 Close-up LIF images of a large ramp rate starting jet

Kouros, H., Medina, R. & Johari, H. 1993, Spreading Rate of an Unsteady Turbulent Jet, *AIAA J.*, vol. 31, no. 8, pp. 1524-1526.

Kuo, T-W., Syed, S. A. & Bracco, F. V. 1986, Scaling of Impulsively Started, Incompressible, Laminar Round Jets and Pipe Flows, *AIAA J.*, vol. 24, no. 3, pp. 424-428.

Lahbabi, F.Z., Boree, J., Nuglisch, H.J. & Charnay, G. 1993, Analysis of Starting and Steady Turbulent Jets by Image Processing Techniques, *Third Symposium on Experimental and Numerical Flow Visualization*, ASME FED-172, New York.

Maxworthy, T. 1974, Turbulent Vortex Rings, *J. Fluid Mech.*, vol. 64, pp. 227-239.

Turner, J. S. 1962, The 'Starting Plume' in Neutral Surroundings, *J. Fluid Mech.*, vol. 13, pp. 356-368.

Willert, C. & Gharib, M. 1991, Digital Particle Image Velocimetry, *Exp. Fluids*, vol. 10, pp. 181-193.

Witze, P. O. 1980, The Impulsively Started Incompressible Turbulent Jet, Sandia Laboratories Report SAND80-8617.

LARGE SCALE VORTICAL STRUCTURES IN A TURBULENT COAXIAL JET

A. Talamelli¹, G. Buresti¹, A. Mordacci² and G. Tanzini³

¹Dipartimento di Ingegneria Aerospaziale, Università di Pisa, Italy

²S.M.C. Pisa, Italy

³ENEL-CRT (Centro Ricerche Termiche), Pisa, Italy

ABSTRACT

The mixing characteristics of a naturally-developing turbulent coaxial jet are investigated by means of LDA, in terms of the statistical moments of the axial and radial velocity components, for inner to outer velocity ratios $U_i/U_o = 0.30$ and $U_i/U_o = 0.67$. Measurements are carried out by alternatively seeding only one jet, and the results are compared with previous measurements obtained with a global seeding of the two streams. Flow visualizations permit to obtain further qualitative information on the jet evolution and on the dynamics of the vortical structures in the shear layers.

1. INTRODUCTION

It is well known that shear-layers rapidly become unstable, and roll-up in discrete vortices, which grow, merge and finally become turbulent. This evolution has been widely studied in the past for axisymmetric single jets, but less effort has been devoted to study the effect of the presence of an annular jet on the near-field dynamics of the vortical structures.

The characterization of such a coaxial jet flow field is considerably complex due to the high number of parameters involved in the definition of a given configuration. Indeed, the evolution of the flow and the mixing between the inner and outer jets are controlled by the sign, strength, mutual position and consequent dynamics of the vortical structures that are present in the shear layers developing between the two jets and between the outer jet and the ambient fluid. All these features depend primarily on the inner to outer velocity and diameter ratios, U_i/U_o and D_i/D_o , and secondarily on the thickness of the inner duct wall and on the conditions of the boundary layers at the outlet.

The study of the flow field produced by coaxial jets is of great interest in many applications, from

the control of mixing and of noise production, to the design of new-generation, low-pollution combustors. Moreover, the characterization of coaxial jets may also give a contribution to the basic research on developing turbulent flows, and in particular to the understanding of the dynamics of the different vortical structures that originate in the two shear-layers.

Several investigations have documented through hot-wire measurements the influence of the velocity ratio on the general characteristics of the mean and fluctuating flow fields, see Champagne and Wygnanski (1971), Ko and Kwan (1976), Kwan and Ko (1977), Ko and Au (1985) and Au and Ko (1987). In these works an interpretation of the results in terms of independent trains of vortices in the inner and outer shear layers has been attempted. However, using flow visualizations, Dahm and Tryggvason (1992) demonstrated that a high level of interaction exists between the vortex structures of the inner and outer shear layers, and many different near-field patterns were shown to arise in a coaxial jet with $D_i/D_o=0.71$, as a function not only of the velocity ratio, but also of the absolute velocities of the two streams. More recently, the near-field vortex structure has been investigated by Wicker and Eaton (1994) for a configuration with a larger outer diameter ($D_i/D_o=0.33$) at different velocity ratios. Instantaneous visualizations confirmed the possibility of a strong coupling between the shear layers, and showed the dominance of the vortical structures of the outer jet, at least for $U_i/U_o=0.81$ and $U_i/U_o=0.69$. In particular the presence of two different typologies of vortex pattern has been detected: a "shear-like pattern", involving vorticity of the same sign, and a "wake-like" pattern, where vorticity of opposite signs is present.

A long-term research on coaxial jets is being carried out at E.N.E.L. C.R.T. (Thermal Research Centre of the Italian Electricity Board) in

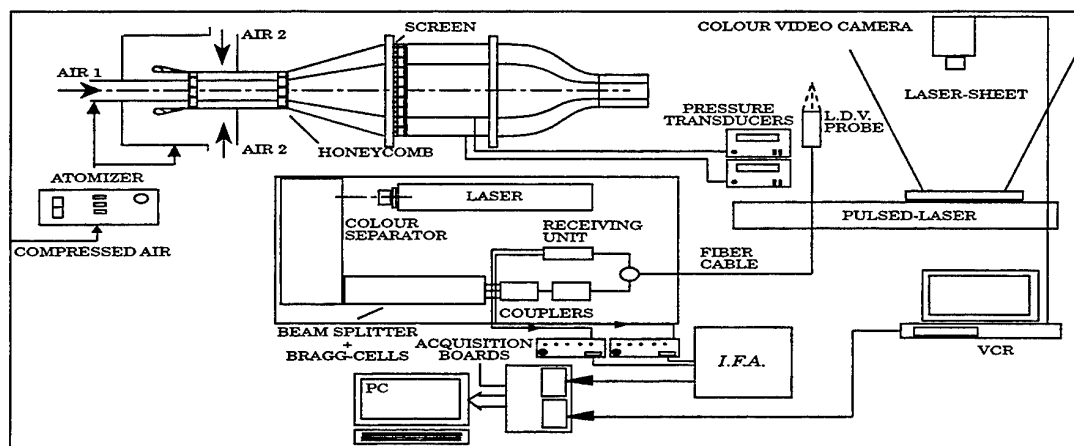


Fig. 1 - Sketch of the experimental setup

collaboration with DIA (Department of Aerospace Engineering) of Pisa. The experiments are performed in a facility designed and constructed for the purpose, by means of Laser Doppler and hot-wire anemometry.

The tests have been carried out on a configuration with an inner to outer diameter ratio $D_i/D_o \approx 0.5$, $D_i = 76.2$ mm, a thickness of the inner duct wall $t = 5$ mm, and inner to outer exit velocity ratios $U_i/U_o = 0.30$ and $U_i/U_o = 0.67$; the influence of varying the inner duct outlet to a sharp one, with a 2.5° angle, has been also analysed.

In Buresti et al. (1994, 1996) a complete description is given of the statistical moments up to fourth order for the axial and radial velocity components, obtained by means of two-component LDA at Reynolds numbers Re_i (based on inner velocity and diameter) of 0.47×10^5 and 1.04×10^5 , respectively for the two velocity ratios; hot-wire measurements were also performed to obtain the time variations of the two velocities for spectral analyses.

In the present work further results, obtained with a particular technique, are described. The test procedure is based on the fact that LDA can detect only the velocity of the seeding particles conveyed by the flow, so that, if only one jet is seeded, a sort of "conditional sampling" is obtained, and only velocity data from particles originating from the seeded jet are detected. The technique, which is called hereinafter "partial seeding", may be useful to characterize the mixing process. The results obtained in the coaxial jet facility are compared with those obtained with global seeding, and are discussed in connection with the information resulting from an extensive use of flow visualizations.

2. EXPERIMENTAL SET-UP

The experimental facility (CAT) and the instrumentation are described in detail in Buresti et al. (1994). A general layout of the test set-up is shown in Fig. 1. The LDA system is a TSI two-component, back scatter, optical fiber system, with a 5 W Argon-Ion Laser. The fiber probe (TSI 9832 type) has a beam spacing of 50 mm and is fitted with a front lens having a focal length of 350 mm and 83 mm of aperture; the resulting measuring volume is 1.6 mm long and 0.11 mm wide, with a fringe spacing of $3.6 \mu\text{m}$. The signal processing is carried out with a TSI IFA 750 Digital Burst Correlator, and a data acquisition system controlled by a 80486 PC. The seeding is a 50% mixture of water and glycerine produced by a six-jet atomiser (TSI 9306 model) fed with compressed air at 35-45 psi. The data are then processed to characterize statistically the flow, and to obtain the time variations of the velocity components.

The light source used in the flow visualisations was provided by a Continuum pulsed, Q-switched, frequency-doubled, Nd-YAG laser (model NY61-10), emitting at 532 nm, with a maximum pulse energy of 300 mJ. It delivers pulses 10 ns wide at a rate of 10 Hz. The laser output is forwarded to an optical system, which forms the light into a sheet of about 1 mm. The video camera is a JVC TK-1070E, which uses a $2/3$ " CCD device, with 756×581 effective pixels. The camera sees an area of about 400×300 mm, so that the resolution is about 0.5 mm per pixel. Although the video signal can be connected directly to a digital frame grabber, a conventional video recorder was used in the present tests for maximum flexibility, and to permit the storage of

a greater amount of data compared to the full digital solution. The data were processed off-line using a Macintosh Quadra 900 computer, equipped with a Perceptics PixelPipeline and PixelStore real time digital image processing and acquisition boards.

In order to obtain a good visualization of the turbulent structures in the shear layers, the requirements of the seeding particles are quite similar to those for LDA measurements: they must be sufficiently small to be able to follow the velocity fluctuations, but not too small, as this would reduce the scattered light intensity. Therefore, the same atomisers of the routine LDA measurements were used also in the visualizations. Two atomisers were used, with a total of 12 jets, to maximize the particle density and obtain a greater light scattering. Increasing scattered light intensity as much as possible allowed the diaphragm aperture to be reduced, obtaining a better focus. The pulse is short enough to allow the flow field to be considered as static: in such a short time, even a mean velocity of 100 m/s would produce a displacement of 1 μ m, which is much less than the space resolution. Besides, from previous measurements the velocity fluctuations are known to have frequencies lower than 3000 Hz, so that a "freezing" of the motion of the turbulent structures is obtained. The visualization tests were carried at the maximum velocities which allowed the vortical structures to be detected. The corresponding Reynolds numbers are $Re_i=6340$ and 14000 respectively for the $U_i/U_o = 0.30$ and $U_i/U_o = 0.67$.

However, the Reynolds number based on the diameter and velocity of the external jet, Re_o , which is probably more significant as regards the dynamics of the outer mixing layer, is 42500.

3. RESULTS AND DISCUSSION

3.1 Partial seeding

The two velocity ratios were obtained by keeping the outer jet velocity at the same value (30 m/s) and by changing the velocity of the inner jet. This permitted to vary only the "strength" of the inner shear layer, keeping the outer one unchanged.

Considering the lengths of the potential cores and the spreading rate of the flow field, the following longitudinal cross-sections were chosen in order to have similar fluid-dynamic conditions for both velocity ratios: $x/D_i=2.0, 3.0, 5.0$ for $U_i/U_o=0.3$ and $x/D_i=3.0, 5.0, 8.0$ for $U_i/U_o=0.67$. These sections correspond to the middle and final parts of the inner potential core and to a position upstream the reattachment point, i.e. the point where the maximum sectional velocity reaches

the axis. Preliminary tests were carried out in order to assure that the data-rate was similar to the one obtained with the global seeding.

The analysis of the partial seeding measurements presents some difficulties, connected with the definition of a level of mixing between the two streams. For this reason a physical interpretative scheme has to be introduced, which should be verified to be consistent with the observed results.

The mass transport between the jets is the result of a number of particles travelling across the mixing layer, in connection with the dynamics of the vortical structures in the shear-layer region. A possible, simplified, mechanism is schematically described in the sketch of Fig 2, which shows how high velocity particles coming from the external part of the inner mixing layer can be convected to the slower region by the downstream part of the vortical structures. Conversely, the upstream part is responsible of a transport of particles from the lower velocity side to the higher one. Only after a certain amount of time these particles adapt their velocity to the local one, corresponding to the stream into which they have migrated.

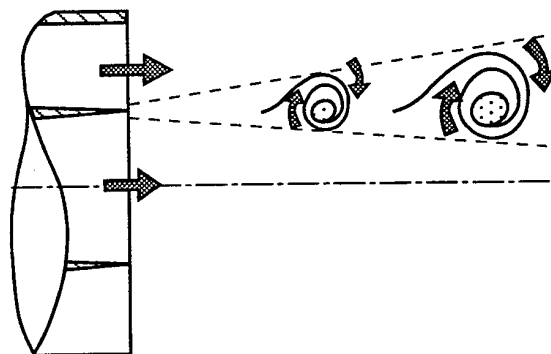


Fig. 2 - Scheme of mechanism of mixing due to vortical structures in a shear-layer

This scheme is no longer valid at the end of the potential cores, where stronger interactions between the different structures from the two mixing-layers occur. In this region the axisymmetry was observed to rapidly disappear and the jet appears to possess new longitudinal instability modes. Nevertheless, even this extremely simplified scheme may allow us to explain some of the results obtained in the present investigation.

Fig 3 a) and b) show radial profiles of the axial and radial components of the mean velocity measured by seeding only the inner or the external jet. In the same figures the profiles obtained with a global seeding are reported. From

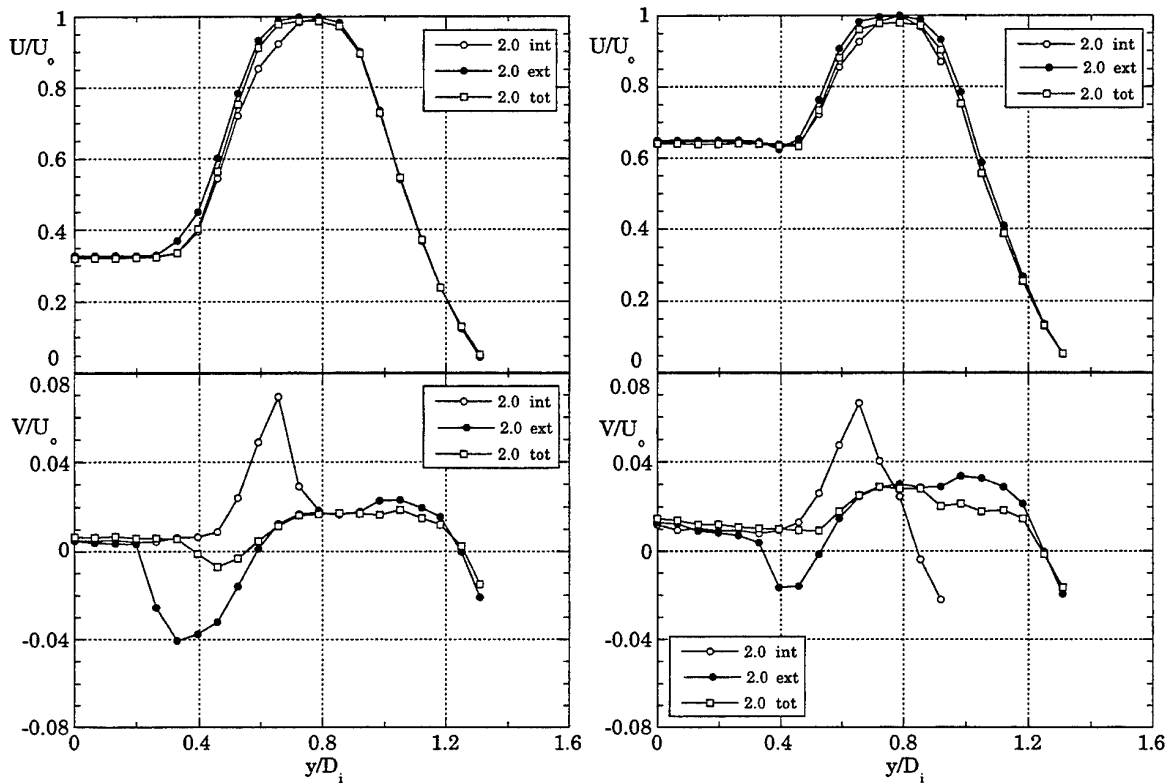


Fig. 3 - Profiles of the axial and radial components of the mean velocity at $x/D_i = 2$ (int: inner jet seeded; ext: outer jet seeded; tot: both jets seeded) - a) $U_i/U_0=0.3$; b) $U_i/U_0=0.67$.

these data it can be inferred that, for both velocity ratios, particles coming from the outer jet are able to reach the axis adapting their mean velocity to the local one of the inner jet. However, this does not mean that a significant mixing has occurred; indeed, the data-rates obtainable in the inner core when only the outer jet is seeded are much lower than those corresponding to a completely seeded flow, suggesting that only a small amount of particles is capable of reaching that region. On the other hand, particles coming from the slower jet are not able to penetrate so deeply in the outer potential core, probably due to their lower energy. From the same figures it can also be seen that a sort of enlargement of the mixing layer occurs on the side opposite to the seeded stream; i.e. higher (lower) axial velocities are measured in the inner (outer) part of the shear layer when the outer (inner) jet is seeded.

The effects of the partial seeding are clearly evident in the profiles of the mean radial velocities. The seeding of the external jet produces significant negative values (i.e. towards

the axis) of this velocity component in the inner and central parts of the shear layer. This is consistent with the fact that only the particles carried by the vortical structures and coming from the outer jet are detected. The opposite situation is found when only the inner jet is seeded.

As for the second order moments, Figs 4 a) and b) show trends similar to those obtained for the mean components, but a physical interpretation of the results is not as straightforward. For instance, it is not obvious why there is an increase of the fluctuation intensity on the side opposite to the seeded jet. This may probably be connected with an increase of the sampling time, which causes an alteration in the shape of the probability density function. Furthermore, the limited variation of the profiles in the middle of the inner shear-layer has to be justified. In this case this phenomenon may be connected with the fact that the vortical structures are the result of an inviscid inflexional instability mechanism acting on the free shear-layer produced by the merging of the two boundary layers coming from the inner and outer sides of the inner duct wall.

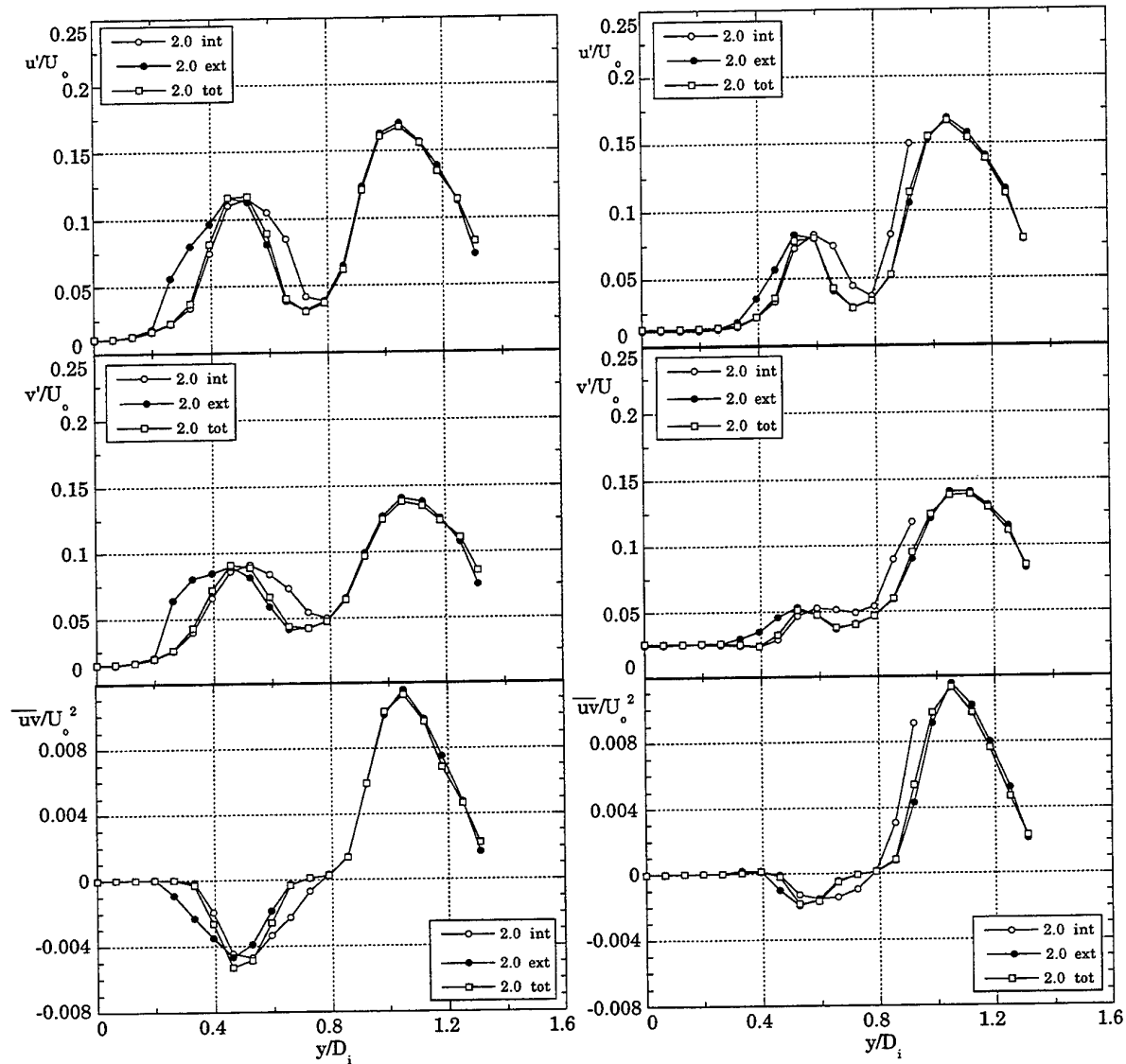


Fig. 4 - Profiles of the axial and radial fluctuations and of the Reynolds stresses at $x/D_i = 2$ (int: inner jet seeded; ext: outer jet seeded; tot: both jets seeded) - a) $U_i/U_o = 0.3$; b) $U_i/U_o = 0.67$.

This process ends up with the roll-up of vortical structures, whose cores contain particles coming from the boundary layers of both jets. While these structures are convected downstream, the seeding has the time to diffuse and to spread uniformly inside the cores. Therefore, even if only one of the jets is seeded, a similar level of the fluctuations in the middle of the shear-layer may be justified by the passage of the cores of these structures, where the seeding is nearly as uniform as when both jets are seeded. On the contrary, moving apart from the centre, there is a

prevailing passage of portions of unmixed fluid engulfed and dragged downstream by the external parts of the structures, where more irregularities are present, so that the already described alteration of the velocity profile takes place.

The same conclusions can be drawn for the measurements obtained, for both velocity ratios, more downstream, where the profiles, which are not shown here for simplicity, exhibit qualitatively the same behaviour. Nevertheless, as could be expected, the capability of the

particles to penetrate deeply inside the other jet increases. This is clearly evident if we analyse the profiles of the mean axial velocity component, which by moving downstream tend to become more and more similar to those for global seeding. However considerable differences are still discernible for the radial component.

Regarding shear-stresses and higher order moments (in terms of skewness and kurtosis) the profiles show interesting features, but their physical interpretation is much more involved (see Buresti et al., 1996).

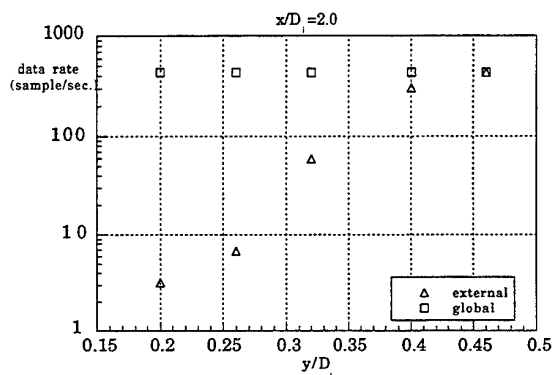


Fig. 5 - Data-rates obtained at $x/D_i = 2$ (external : outer jet seeded; global: both jets seeded)

Some characteristics of mixing may be assessed by analysing the radial profiles of the mean data-rate. In Figure 5 a comparison between data-rates obtained by seeding both jets or only the external one is presented, for $U_i/U_o=0.30$ and $x/D_i=2.0$. Corresponding profiles of mean velocity and fluctuation components may be found in Figs 3-4. Several features can be appreciated from Figure 5. The data-rate starts to change its value at $y/D_i=0.4$, where significant differences between statistical quantities are already present. The maximum of these differences is positioned at $y/D_i=0.3$ where the data-rate is approximately 10% of the one corresponding to global seeding. As expected, in the inner region of the potential core ($y/D_i=0.2$) the data-rate is extremely reduced, to about 1%. This is consistent with the fact that only few particles coming from the external jet penetrate inside the inner core.

The profiles of Figure 5 might allow us to define some sort of mixing parameter. For instance, the ratio between data-rates measured with partial and global seeding provides an indication of the percentage of passage of fluid coming from the external jet in the measurement point. However, as these profiles are the result

of a statistical analysis, they cannot provide any information on the effective temporal features of the mixing between the two jets. In this case it must be pointed out that a statistical and spectral analysis of the time lags between successive LDA data (i.e. the time Δt which divides the detection of two consecutive bursts) might give some further information. However, preliminary tests on the present data have demonstrated that the signals are too noisy and that some further processing should be accomplished, as, for instance, some type of conditional sampling.

3.2 Flow visualizations

Figs. 6 show some representative side views of the jet illustrating the natural jet development for three different configurations. Previous hot-wire measurements have shown that both coaxial streams are free of driven oscillations at the jet exit. The pictures are obtained by seeding only the outer jet, which appears in black in the pictures, in order to evidence the behaviour of both shear layers. The analysis of the whole set of images (of which Figs. 6 are only typical examples) shows that the outer layer seems to be hardly affected by the dynamics of the inner large scale structures. The shear layer rolls-up in almost axisymmetric ring vortices which are conveyed downstream, where they finally breakdown. The roll-up position is relatively stable, and the resulting vortex seems to remain axisymmetric over its entire life. As expected there is no evidence of stable pairing. For the two velocity ratios the structures appear to have a constant wavelength. This fact leads us to conclude that the outer shear-layer is not influenced by the inner one. Similar results have been found by Wicker and Eaton (1994) for lower Reynolds numbers.

Conversely, the structures in the inner mixing layer depend strongly on the velocity ratio and exit geometry. As the velocity jumps across the shear-layers have opposite sign and different magnitude, the sign of the inner layer vorticity is opposite to the outer one, and vortices roll towards the inner jet. For the 5 mm thick inner duct, the inner shear-layer undergoes a "wake-like" instability, and rolls-up in large structures which migrate downstream without any evident pairing. The effect of the wake in the near field region of the coaxial jet is more evident for $U_i/U_o=0.67$, for which Buresti et al. (1994) have shown, by means of hot-wire measurements, that a regular shedding of vortices from the inner duct wall is present.

The vortex shedding from the inner wall may be removed using a sharp inner duct outlet.



Fig. 6 a - Side view $U_i/U_o=0.67$; $t = 5 \text{ mm}$

For this configuration (Fig. 6b), Buresti et al. (1996) found a remarkable reduction of the radial velocity fluctuations and a significant change of the Reynolds stress profiles. These differences tend to decrease moving downstream and are smaller for the lower velocity ratio.

With the sharp outlet, the vortices are weaker and the pattern is quite irregular both in time and in space. The roll-up position is not fixed and the structures moving downstream undergo successive pairings and tearings. There is no clear interaction with the larger external structures, at least for the first three inner diameters from the jet exit.

Figures 6a and 6b show that the effects of the wake vortical structures are confined in the first two inner diameters from the jet exit. More downstream the two configurations exhibit the same behaviour. In conclusion, the configuration with a finite thickness clearly produces a moderately quicker mixing in the near exit region of the streams, specially for the higher velocity ratio, at which regular vortex shedding is present.

The effects of a different velocity ratio are shown in Fig. 6c. In particular, the length of the inner potential core decreases for $U_i/U_o=0.30$;

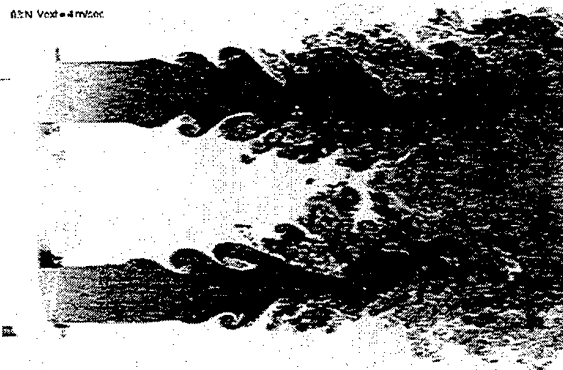


Fig. 6 b - Side view $U_i/U_o=0.67$; sharp outlet

the outer one remains practically unchanged, due to its dependence only on the outer jet diameter and velocity. The configuration with the lower velocity ratio is thus characterized by two cores of comparable size, a condition that seems to favour a more rapid and intense mixing of the flows (see Buresti et al., 1996). Nevertheless the growth rate of the wake instability depends strongly on the wake deficit, which is clearly reduced, and no regular shedding of vortices seems to be detectable (see Figure 6c).

Figures 7 a and b show cross-sectional images of the jet, for $U_i/U_o=0.67$, obtained at two different streamwise distances from the exit $x/D_i=1.0$ and $x/D_i=2.0$, still inside both potential cores. Discrete portions of fluid coming from the annular jet are injected both into the inner core and into the quiescent fluid, forming three dimensional structures, which are not discernible from the longitudinal views. The same phenomenon may be observed if the inner jet is seeded. In this case clear bursts of internal fluid are injected in the annular jet. More downstream, these structures form distinct mushrooms, which are probably originated by the presence of strong double counter-rotating axial vortices. The formation and the evolution of these structures has been well described by Liepmann and Gharib (1992) and Romano (1996). The number and dimensions of the mushrooms depend on the streamwise distance from the jet exit. At variance with what reported by Romano (1996), they are not clearly stable, and this may be due to the higher Reynolds numbers of the present tests, and to the different exit conditions as regards boundary layers and the free-stream turbulence. The presence of the "mushroom" structures may drastically affect the entrainment processes and the mixing features between the two streams, even in the near-field region. The sharpening of the inner wall does not seem to produce any distinct qualitative effect.

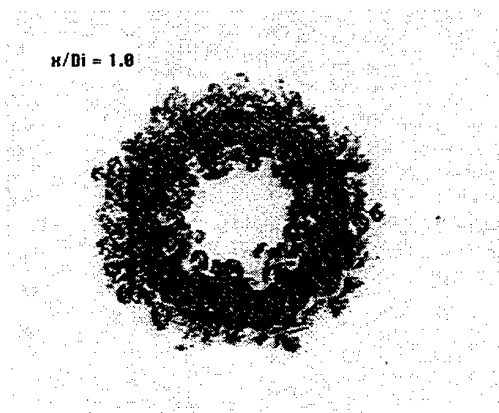


Fig. 7a - Cross view $U_i/U_o=0.67$; $t = 5$ mm, $x/Di=1.0$

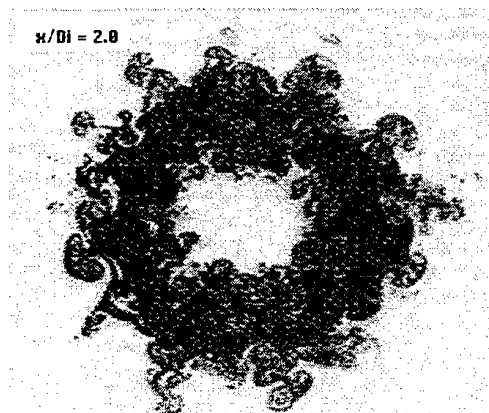


Fig. 7b - Cross view $U_i/U_o=0.67$; $t = 5$ mm, $x/Di=2.0$

CONCLUSIONS

A new technique that might be useful to characterize mixing between two streams has been described. Measurements have been done by means of LDA in a coaxial jet configuration by alternatively seeding only one stream. The profiles of the statistical moments have been compared with those obtained with global seeding and some significant features of mixing have been assessed. From the profiles of the mean velocities it can be inferred that particles coming from the outer jet are able to reach the axis, adapting their mean velocity to the local one of the inner jet. Regarding axial and radial fluctuations the profiles show interesting features but their physical interpretation is more involved, even if the observed behaviours may in part be interpreted on the basis of a simplified physical scheme. Furthermore, some aspects of the mixing process can be appreciated by analysing the radial profiles of the mean data-rates, which, however, cannot provide any information on the effective temporal features of the jet mixing.

Further information has been obtained by means of flow visualizations. They qualitatively confirm the results of previous experimental analysis on naturally developing jets. The outer layer appears to be hardly affected by the dynamics of the inner large scale structures which on the opposite depend strongly on the velocity ratio and exit geometry.

A regular vortex shedding, which may be removed using a sharp inner duct outlet, has been detected in the inner mixing layer of the configuration with $U_i/U_o=0.67$.

Finally the presence of three dimensional structures originated by secondary instabilities may drastically affect the entrainment processes and the mixing features between the two streams.

REFERENCES

- Au H. and Ko N.W.M. 1987, Coaxial Jets of Different Mean Velocity Ratios, Part 2, J. Sound and Vibrations, Vol. 116, pp. 427-443.
- Buresti G., Petagna P. and Talamelli A. 1994, Experimental Characterization of the Velocity Field of a Coaxial Jet Configuration, Exp. Thermal and Fluid Sci., Vol. 9, pp. 135-146.
- Buresti G., , Petagna P., Talamelli A. 1996, Experimental Investigation on the Turbulent Near Field of Coaxial Jet Configurations, in Eng. Turb. Modelling and Exp. 3, eds. Rodi W. and Bergeles G., pp.541-550, Elsevier.
- Champagne F.H. and Wygnanski I.J. 1971, An Experimental Investigation of Coaxial Turbulent Jets, Int. J. Heat & Mass Transfer, Vol. 14, pp. 1445-1464.
- Dahm W.J.A., Frieler C.E. and Tryggvason G. 1992, Vortex Structure and Dynamics in the Near Field of a Coaxial Jet, JFM, Vol. 241, pp. 371
- Ko N.W.M. and Kwan A.S.H. 1976, The Initial Region of Subsonic Coaxial Jets, JFM, Vol. 73, pp. 305-332.
- Ko N.W.M. and Au H. 1985, Coaxial Jets of Different Mean Velocity Ratios, J. Sound and Vibrations, Vol. 100, pp. 211-232.
- Kwan A.S.H. and Ko N.W.M. 1977, The Initial Region of Subsonic Coaxial Jets, Part 2, JFM, Vol. 82, pp. 273-287.
- Liepmann D. and Gharib M. 1992, The role of streamwise vorticity in the near-field entrainment of round jets, JFM, Vol. 245, pp. 643-668.
- Romano G.P. 1996, Investigation on particle trajectories and Lagrangian Statistics at the Outlet of a Circular Jet, in Eng. Turb. Modelling and Exp. 3, eds. Rodi W. and Bergeles G., pp.411-420, Elsevier.
- Wicker R.B. and Eaton J.K. 1994, Near Field of a Coaxial Jet With and Without Axial Excitation, AIAA Journal, Vol. 32, pp. 542-546.

SIMULTANEOUS VELOCITY AND CONCENTRATION MEASUREMENTS IN CONFINED COAXIAL JETS

M.M.C.L. Lima, J.M.L.M. Palma and N.A. Silva
Faculdade de Engenharia da Universidade do Porto, Portugal *

Abstract

The state of development of an experimental set-up for simultaneous measurements of velocity and concentration is described. The Laser Doppler Velocimetry (LDV) and Laser Induced Fluorescence (LIF) were used jointly, as a means for studying the transport mechanisms of momentum and mass in a flow made up of 2 coaxial streams enclosed in a duct. This is a configuration typical of many fluid mixing devices, and the experimental information available here is also relevant for development and validation of mathematical models.

1 Introduction

The main objective of the present paper is to report on the developments of an experimental set-up for simultaneous measurements of velocity and concentration, using Laser Doppler Velocimetry (LDV) and Laser Induced Fluorescence (LIF). The experimental configuration used as the basis for this work was the flow of 2 confined coaxial jets enclosed in a cylindrical duct.

Although the LIF is a long established technique within the chemistry field (Guilbault (1990)), it is far from being common as a fluid mechanics technique. There are still some difficulties in the use of LIF and the works of, for instance, Owen (1976), Johnson and Bennett (1981), Koochesfahani and Dimotakis (1985), Walker (1987), Arcoumanis *et al.* (1990) and Dahm *et al.* (1991) are contributions towards a deeper understanding and increased confidence in the use of LIF as a fluid mechanics technique.

Coaxial jet flows can be found in many fluid mixing and injection devices as used for instance

in the aeronautical and automotive industries. Studies of confined jets can be found in the literature of the sixties and seventies, but they are mainly concerned with confined jets discharging into an open environment (see Gibson (1986), for a review). Here the aim was the study of the development of 2 parallel coaxial streams into a single stream, with the downstream distance from the nozzle.

The flow used as the basis for our work has been the testbench for previous studies on LIF (Owen (1976) and Johnson and Bennett (1981)). This flow provides a significant test to the joint utilization of the LDV and LIF techniques, because of its fair degree of complexity and practical relevance also.

2 Experimental Rig and Measurement Equipment

Experimental Rig

The flow geometry (Figure 1) was made of 2 coaxial water flows enclosed in a cylindrical duct constructed from perspex. The test section was 2 m long (42 mm internal diameter) with optical access made through an optical box, filled in with water to reduce refraction effects.

The rig could be operated either as a closed or an open circuit (when taking LIF measurements). Both the inner and the annular flow were fed by one single centrifugal hydraulic pump. The flow rates were controlled separately by a set of valves and monitored by 2 different rotameters. The inner flow was established within an accuracy of 2% of the rotameter full scale (i.e. about 30 l/h); whereas the rotameter for the annular flow guaranteed a flow setting within an accuracy of about 144 l/h (1% of the rotameter full scale).

Before entering the test section, the annular

*Departamento de Engenharia Mecânica e Gestão Industrial, Secção de Fluidos e Calor, Rua dos Bragas, 4099 Porto Codex, Portugal (e-mail: jpalma@fe.up.pt).

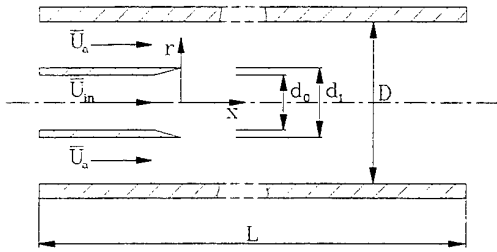


Figure 1: Flow configuration ($d_0 = 17$ mm; $d_1 = 19$ mm; $D = 42$ mm; $L = 2000$ mm)

flow went through a plenum chamber 600 mm long and 400 mm diameter, containing a series of honeycomb screens and grids, and terminated by a converging nozzle with an area ratio of 90.7:1. This guaranteed a uniform velocity profile with 6% axial turbulence intensity at the inlet of the test section. The inner flow was a fully developed pipe flow with a turbulence intensity of 8% on the axis. This was achieved by a brass tube positioned along the axis of the plenum chamber and terminated 97 mm downstream of the converging nozzle; the end section (straight) of this tube was $100d_0$ long.

The injection system was made up of a constant head tank and an electronic diaphragm metering pump (Cole Parmer G74110-15), operated at a maximum stroke frequency of 125 strokes per minute (i.e. a flow rate between 2.3 and 2.6 l/h, depending on the experimental conditions, and set to an accuracy of 2%). The mixture inside the tank was kept under uninterrupted stirring and its concentration was such that once injected into the inner flow line (220 tube diameters (d_0) upstream of the test section) led to a final concentration inside the test section where linear response between the incident and emitted light could be found and enabled us to neglect the light absorption along the beam path. This was between 2×10^{-5} and 0.1 mg/l, an interval asserted by performing measurements inside a vessel with a homogeneous concentration of rhodamine B. The minimum value was set by the sensitivity of the instrumentation, and depended also on the intensity of the incident light, voltage of the PM power supply and electronic amplification of the concentration signal. All measurements were performed with the test section protected from the ambient light.

The use of rhodamine B is justified because its fluorescence characteristics do not change over a period of several hours when continually stirred

in water (Arcoumanis *et al.* (1990)), as opposed to other fluorescent dyes. In addition because of its low molecular diffusivity of about 2×10^{-5} (from Reid *et al.* (1987)) and corresponding high Schmidt number it is particularly suitable for studies of turbulent mixing.

Measurement Equipment

The light source was an argon-ion laser (Spectra-Physics, Stabilité 2017) operating in power stability mode at 514.5 nm and a power of 600 mW. The optical system consisted of a conventional one-component laser Doppler Dantec 55× modular optics in backscatter configuration, with a 40 MHz Bragg cell (frequency shifter, Dantec 55N11) and a 310 mm front lens. The control volume of dimensions $0.075 \times 0.075 \times 0.73$ mm was moved along the test section, by moving the laser and optics mounted on a traversing table. A colour separator split the collected light into 2 wavelengths, above and below 590 nm, which were filtered before reaching the corresponding photomultipliers for velocity (514.5 nm interference filter, Dantec 55×37) and concentration (high pass filter, OG570 Melles Griot) signals. The photomultipliers (Dantec 57×08) were fed by 2 separate power supplies, both originated from Dantec and purposely built for this application. Particular care was taken in the design and assembling of the PM power supply for concentration signal, to avoid interference and reduce the electronic noise to levels below the intensity of the concentration signal.

Data acquisition was performed using a TSI Counter (1990C) and a velocimetry board Zechs Electronics (1400A) together with an Analogic Digital Converter module, interfaced to a personal computer (Dell, 325 SX). Both signals (velocity and concentration) were acquired simultaneously, whenever the counter validated velocity.

3 Discussion of Results

Experiments (Table 1) were performed for 4 velocity ratios (\bar{U}_a/\bar{U}_{in}) in a range between 0.8 and 3.2. The flow was always turbulent with a Reynolds number of about 3×10^4 , based on the bulk velocity and outer tube internal diameter (D).

The experimental data in this paper includes the centreline plots (flow conditions 1, 2, 3 and 4) and radial profiles (flow condition 1) of time averaged and fluctuating quantities of axial velocity and concentration at 9 axial locations ($x/d_0=0.14$,

Table 1: Experimental flow conditions

Exp. Conditions	1	2	3	4
\bar{U}_a/\bar{U}_{in}	3.2	2.0	1.1	0.8
\bar{U}_a	0.83	0.83	0.76	0.83
Re_a	9450	9450	8653	9450
\bar{U}_{in}	0.26	0.42	0.69	1.08
Re_{in}	4376	7069	1414	18230
Re	29380	30452	29898	34993
$\bar{U}_{a,Max}$	0.93	0.93	0.89	0.93
$\bar{U}_{in,Max}$	0.33	0.52	0.87	1.33
$\bar{U}_{a,Max}/\bar{U}_{in,Max}$	2.8	1.8	1.0	0.7

\bar{U}_a : average axial velocity in the annulus [m/s];
 $\bar{U}_{a,Max}$: maximum axial mean velocity in the annulus [m/s]; \bar{U}_{in} : average axial velocity at the outlet of the inner tube [m/s]; $\bar{U}_{in,Max}$: maximum axial mean velocity at the outlet of the inner tube [m/s]; Re_a : Reynolds number based on \bar{U}_a and size of the annular passage; Re_{in} : Reynolds number based on \bar{U}_{in} and d_0 ; Re : Reynolds number based on the bulk axial velocity and D

1, 2, 4, 8, 16, 32, 64 and 100). The mean quantities are simple statistical unweighted averages with no velocity-bias correction. In case of the concentration measurements no correction was made accounting for light absorption along the beam path, contrary to the practice of for instance Koochesfahani and Dimotakis (1985).

The results are displayed in nondimensioned form using as characteristic scales the centreline values of the mean velocity (\bar{U}_{in}) and concentration (C_{in}) measured at $x/d_0=0.14$, the diameter (d_0) of the inner flow and the inner radius of the outer tube ($R=D/2$).

Velocity Field

Based on Johnston (1978) and Gibson (1986), different flow regimes (Figure 2) can be identified, as the effect of the inlet conditions is reduced with the downstream distance. The flow evolves from the initially distinct 2 parallel coaxial streams to the classical fully developed turbulent pipe flow, which in terms of the mean concentration is nothing but a uniform radial distribution. For the velocity ratios under study (Table 1), no recirculation region was present.

At the first measured radial profile of mean axial velocity ($x/d_0=0.14$ in Figure 2a), the 2 coaxial (inner and annular) flows can easily be identified. The annular flow with a relatively flat profile and the inner flow (for radial positions $r/D < 0.4$), where the velocity profile shows a shape typical of a fully developed pipe flow, as it

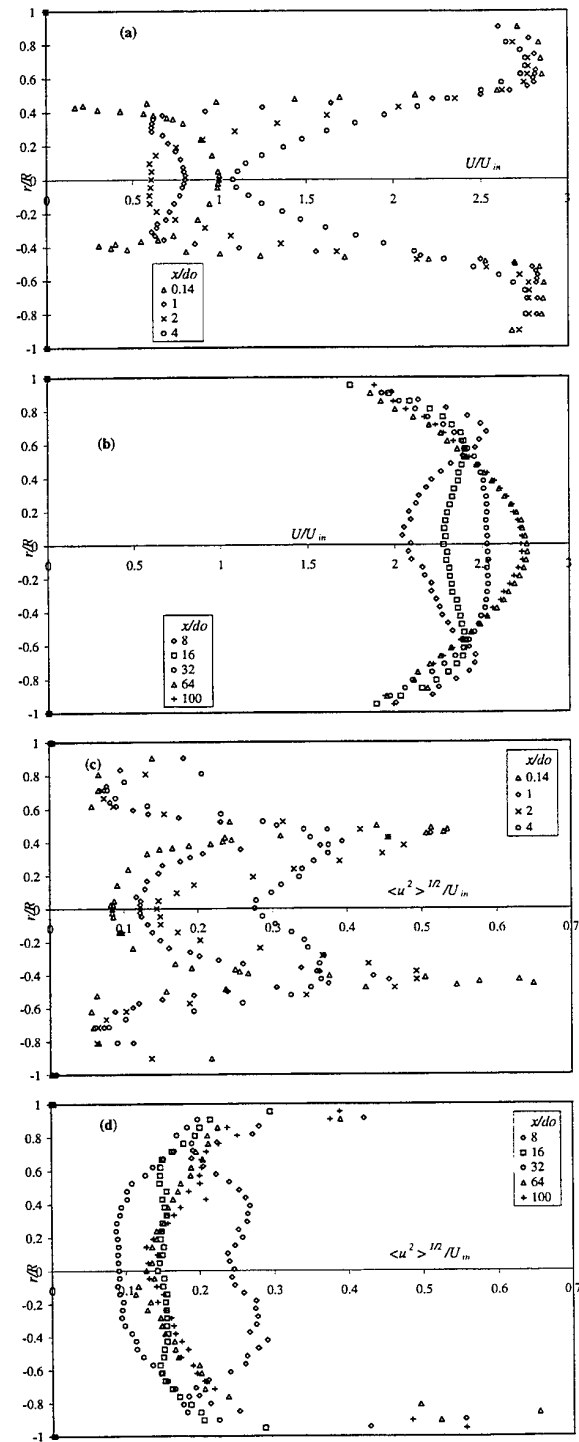


Figure 2: Radial profiles of mean axial velocity and turbulence intensity at 9 axial locations for flow condition 1

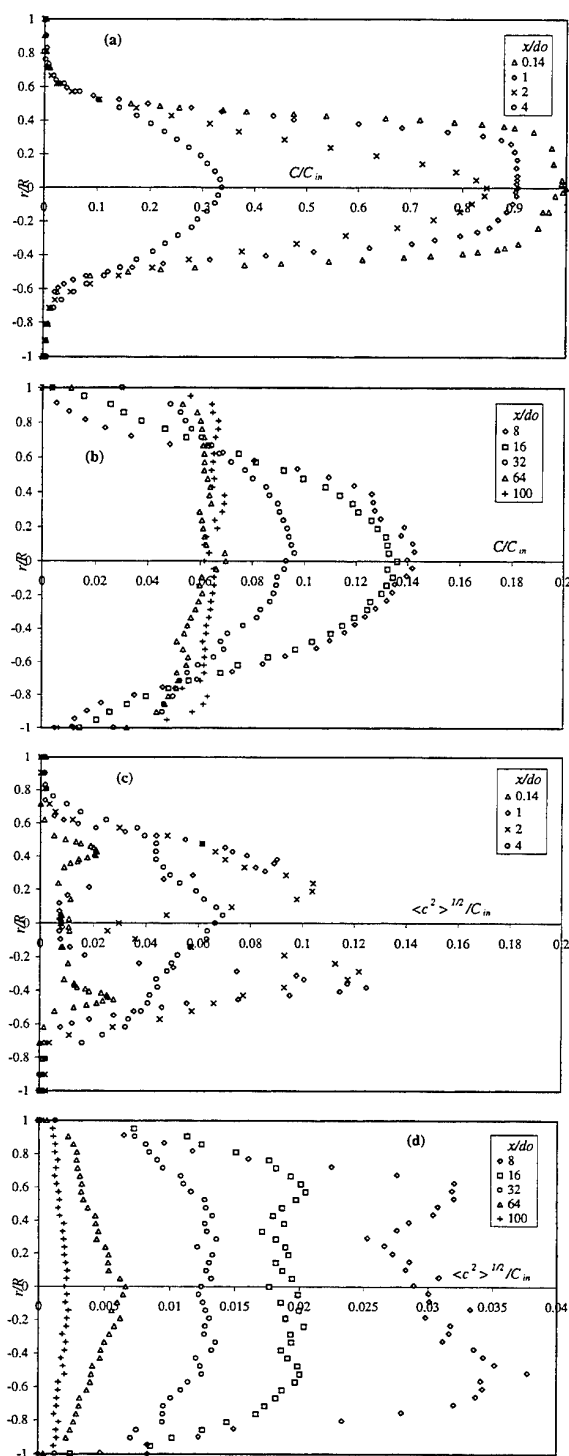


Figure 3: Radial profiles of mean and instantaneous concentration at 9 axial locations for flow condition 1 (Note that the horizontal scale in Figures b and d is magnified by a factor of 5, with respect to Figures a and c)

emerged from the inner tube. The annular flow denotes a wall boundary layer close to the outer diameter which is thin compared to the free shear layer developed between the 2 coaxial streams.

Note that a free shear layer will arise between the inner and annular flows always. The wall boundary layer and the finite thickness of the inner tube will contribute to a mean shear, even in case of $\bar{U}_a/\bar{U}_{in}=1$.

The growth of the free mixing layer is such that at $x/d_0=2$ (Figure 2a) the mean flowfield shows already no traces of the wall boundary layer associated with the inner flow. The mean velocity profile looks as if the 2 coaxial flows were both initially flat velocity profiles. The minimum value of the mean axial velocity moved from $r/R=0.4$ towards the centreline, and there is a deceleration of the central core of the inner flow which is most obvious for experimental condition 1, as can be seen from the centreline plot (Figure 4).

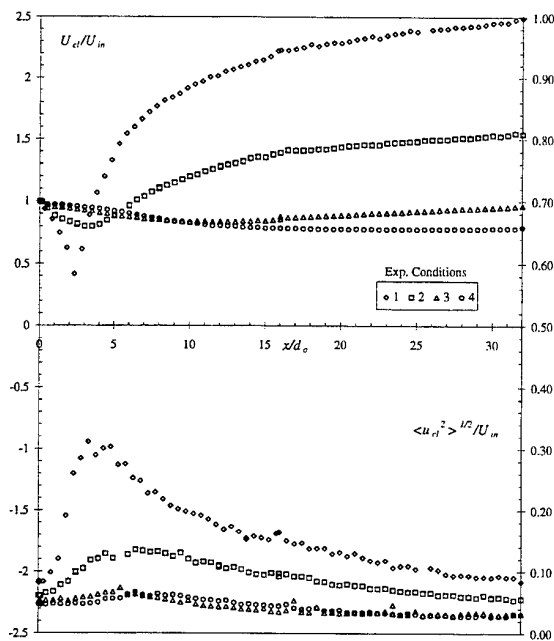


Figure 4: Centreline plot of mean and turbulence intensities along the axial direction for 4 flow conditions

After $x/d_0=2$ the flow accelerates in the centreline (see also Figure 4) as the growth of the

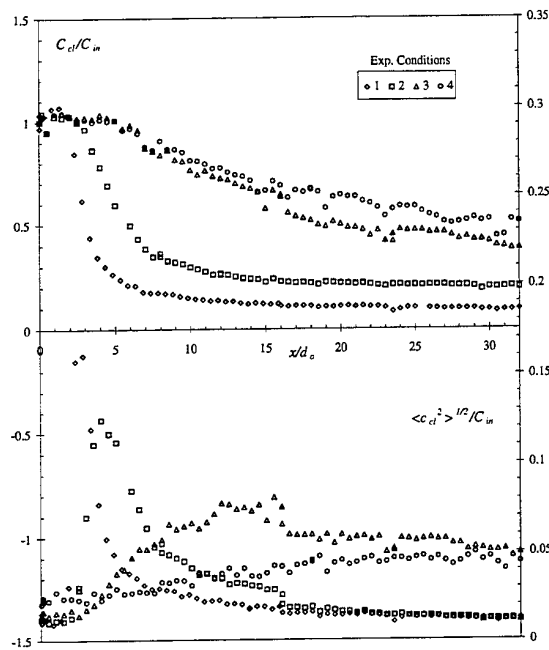


Figure 5: Centreline plot of mean and fluctuating concentration for 4 flow conditions

mixing layer continues, leading to the merging of the initially isolated coaxial free shear layers (at $x/d_0=4$). The mixing layer growth occurs here under the constraint of the pipe walls, opposed to previous studies of coaxial jets discharging into stagnant surroundings (e.g.: Ribeiro and Whitelaw (1976); Durao and Whitelaw (1973)); the flux of axial momentum is mainly directed towards the centreline, because $\bar{U}_a > \bar{U}_{in}$ and bounding of the pipe wall and corresponding boundary layer.

After $x/d_0=16$ (i.e., 6.5 pipe diameters, D) the central core of the flow is almost flat (Figure 2b). This is the so-called mixed-out condition in the ejector literature, for which Johnston (1978) indicates a value between 5 and 10 pipe diameters where this usually occurs. After $x/d_0=16$ the development to a fully developed pipe flow occurs without the marked individuality of the mixing layers in opposed sides of the axis.

Figure 4 shows that for experimental condition 4 the flow always decelerates along the centreline. In case of conditions 1, 2 and 3 the deceleration is terminated at $x/d_0=2, 4$ and 10, reaching a mini-

mum centreline velocity of 0.4, in case of condition 1. Conditions 1, 2 and 3 approach the fully developed state asymptotically by acceleration of the flow central core, as it would be expected from their velocity ratios (all above 1).

The description above has its counterpart in terms of the turbulence field. The main aspects to be mentioned are that the maximum turbulence intensity (about 0.6) is found at the first measured axial location (Figure 2c) in the free shear layer. The signatures of the free shear layer can be seen until $x/d_0=8$ (Figure 2d), through the 2 peak values of $\sqrt{u^2}/U_{in}$. After $x/d_0=16$, only the peak values related to the wall boundary layer persist. Concerning the centreline distribution (Figure 4), the high axial mean shear gives rise, in case of condition 1, to a peak value 2.4 times as high compared to the peak value of condition 2, or 4.4 times if compared to the peak value of condition 4.

The maximum centreline axial turbulence intensity (Figure 4) occurs at $x/d_0=3.3$ ($x/D=1.3$) and is 0.31, or 0.35 if nondimensioned by the local centreline velocity. This can be an indication of the effect of the flow confinement by the pipe walls, if one compares with the value of 0.15 located at $x/D=3.0$, measured by Durao and Whitelaw (1973) for confined jets with a velocity ratio of 4.3 (defined as the ratio between the maximum velocities of the annular and inner flows) discharging into stagnant surroundings.

The flow conditions reached at $x/d_0=64$ and 100, (i.e. about 26 and 40 pipe diameters), if nondimensioned by the pipe diameter and local axial centreline velocity, compare well with the values of fully developed turbulent pipe flow. The radial profile of mean axial velocity has reached self-similarity and the axial turbulence intensity in the axis is 4.7%, compared for instance to the values of 4.5% indicated by Eggels *et al.* (1994) and 2.8% indicated by Laufer (1954). This is an indication that the turbulent flowfield (opposed to the mean flowfield) may have not reached the fully developed state yet, a conclusion that is supported by Figure 3d where a decay of the instantaneous concentration field can be observed between the profiles at $x/d_0=64$ and 100.

Concentration Field

The fluorescent dye was mixed with the inner flow and measurements of mean concentration at $x/d_0=0$, not included here, show that it was fully mixed.

The mean concentration (Figure 3) develops

from a top hat radial profile at $x/d_0=0$, through a bell shape (sections $x/d_0=2, 4, 8$ and 16) to a uniform radial profile, typical of complete mixing.

Table 2: Mixedness parameter

Exp. Conditions	1	2	3	4
\bar{U}_a/\bar{U}_{in}	3.2	2.0	1.1	0.8
$ \bar{U}_a/\bar{U}_{in} - 1 $	2.2	1.0	0.1	0.2
C_∞/C_{in}	0.06	0.09	0.16	0.21
$\eta(x/d_0=10)$	42%	30%	21%	26%

To illustrate the state of mixing obtained for our 4 experimental conditions, Table 2 includes the mixedness at axial location $x/d_0=10$. Mixedness is a nondimensional parameter defined accordingly to:

$$\eta = C_\infty/C_{cl}$$

where $C_\infty (= C_{in}Q_{in}/(Q_{in} + Q_a))$, is the concentration obtained after complete mixing of both inner and annular flows. C_{cl} is the mean concentration in the centreline, and Q_{in} and Q_a are the flow rates of the inner and annular flows.

From Figure 5 and Table 2, one can see that the flow configuration 1 is the most efficient concerning mixing. A value of 42% is obtained compared to 21% in configuration 3, the least favourable of all experimental conditions presented in this study.

The mixing level attained is proportional to the velocity difference between the annular and inner flows. The higher strength ($|\bar{U}_a/\bar{U}_{in} - 1|$) of the free mixing layer originated between the 2 coaxial streams, i.e. higher mean shear and consequently high intensities of turbulence, leads to higher turbulence intensities and promotes mixing.

4 Conclusions

Measurements of simultaneous velocity and concentration in confined coaxial jets in an enclosed duct were performed by laser Doppler velocimetry and laser induced fluorescence. The results include both mean and instantaneous quantities and show that accurate results can be obtained, relevant for studies of turbulent mixing in liquid flows.

Based on the results of 4 different flow conditions with velocity ratios between 0.8 and 3.2, one could conclude that the scalar field seems to evolve to fully developed flow conditions at a lower rate, compared to the velocity field. Furthermore, for

increased mixing the velocity ratio (\bar{U}_a/\bar{U}_{in}) must be different from 1, and mixing seems to scale with the strength of the shear layer created between the 2 coaxial streams.

Acknowledgments

This work was carried out as part of a research programme supported jointly by JNICT and the Ministry of Environment (PEAM/C/APR/132/91).

M. Lima is a PhD Student under grants from programme *CIÊNCIA* (BD/2033/92/RN) and *PRAXIS XXI* (BD/5623/95). N. Silva participated in this work as part of his training programme under a grant from *PEDIP II*.

The authors are also grateful to the technical assistance of Mr. J. Sousa, and the interest of their colleague Dr. F. Proença during the various stages of the work.

References

- Arcoumanis, C., McGuirk, J., and Palma, J. (1990). On the use of fluorescent dyes for concentration measurements in water flows. *Experiments in Fluids*, **10**, 177–180.
- Dahm, W., Southerland, K., and Buch, K. (1991). Direct, high resolution, four-dimensional measurements of the fine scale structure of $Sc \gg 1$ molecular mixing turbulent flows. *Physics of Fluids A*, **3**(5), 1115–1127.
- Durão, D. and Whitelaw, J. (1973). Turbulent mixing in the developing region of coaxial jets. *Journal of Fluids Engineering*, **95**, 467–473.
- Eggels, J., Unger, F., Weiss, M., Westerweel, J., Adrian, R., Friedrich, R., and Nieuwstadt, F. (1994). Fully developed turbulent pipe flow: a comparison between direct numerical simulation and experiment. *Journal of Fluid Mechanics*, **268**, 175–209.
- Gibson, M. (1986). Hydrodynamics of confined coaxial jets, pages 367–390. Chapter 14 of *Dynamics of Single-Fluid Flows and Mixing*, Vol. 2 of *Encyclopedia of Fluid Mechanics*, Edited by N.P. Cheremisinoff, Gulf Publishing Company.
- Guilbault, G. (1990). *Practical Fluorescence*. Marcel Dekker, Inc., New York, 2 edition.
- Johnson, B. and Bennett, J. (1981). Mass and momentum turbulent transport experiments with

confined coaxial jets. Technical report, NASA-CR-165574 and UTRC Report RB1-915540-9.

Johnston, J. (1978). Internal Flows, pages 109-165. Chapter 3 of *Turbulence* (1978), Edited by P. Bradshaw, Vol.12 of Topics in Applied Physics Series, Springer-Verlag, Berlin.

Koochesfahani, M. and Dimotakis, P. (1985). Laser-induced fluorescence measurements of mixed fluid concentration in a liquid plane shear layer. *AIAA Journal*, **23**(11), 1700-1707.

Laufer, J. (1954). The structure of turbulence in fully developed pipe flow. Technical report, NACA.

Owen, F. (1976). Simultaneous laser measurements of instantaneous velocity and concentration in turbulent mixing flows. pages 27.1-27.7. AGARD-CP193.

Reid, R., Prausnitz, J., and Polling, B. (1987). *The Properties of Gases and Liquids*. McGraw-Hill Inc., New York, 4 edition.

Ribeiro, M. and Whitelaw, J. (1976). Turbulent mixing of coaxial jets with particular reference to the near-exit region. *Journal of Fluids Engineering*, **98**, 284-291.

Walker, D. (1987). A fluorescence technique for measurement of concentration in mixing liquids. *Journal of Physics E: Scientific Instruments*, **20**, 217-224.

SESSION 31

LDV - Signal Processing

DEVELOPMENT OF A PC-BASED MINIATURE SIGNAL PROCESSOR FOR LDA AND PDA MEASUREMENTS

MA Zhongming and SHEN Xiong

Department of Engineering Mechanics
Tsinghua University, Beijing, China, 100084

ABSTRACT

An advanced miniature signal processor for LDA and PDA applications is described. It is based on a PC-486 computer incorporated with two signal processing cards and a signal preprocessing device. One card is a two-channel high-speed data acquisition circuit board. It has two analog to digital converters with 50MHz sampling rate, $32K \times 2$ bytes of buffer memory, pre-triggering or post-triggering facility and ring storage manner. A single-chip FFT processor has been incorporated which is capable of executing complex Fast Fourier Transforms (FFT) of up to 1024 points in $514 \mu s$, 20 times faster than TMS320c25. This FFT card is also plugged in the computer to make the system compact. Outside the computer, there is a preprocessing circuit which performs amplifying, filtering and signal detecting. The signal identification mechanism can detect Doppler burst from comparatively lower SNR signal. A signal simulator of PDA has been developed for the examination and testing of the signal processor. The results of experimental measurements are also reported.

1. INTRODUCTION

Laser Doppler Anemometry (LDA) and Phase Doppler Anemometry (PDA) have been commercially available as instruments and widely used in various spray and combustion applications for simultaneous measurements

of particle size and velocity[1]. Optics, signal processing and data analysis are the basis of the instrument. To optimize the performance of the instrument, firstly it is important to maximize the SNR and seeding quality, then to select a suitable signal processing method[3]. The development of signal processing method can greatly improve their liability and area of applications.

There are basically two kinds of method, the time domain processor (namely the counter and the covariance processors) and the frequency domain processor (for the actual signal or for its correlation function). Counters are widely used for measuring frequency and time intervals of the signals with higher SNR. The average signal period can be measured by counting the number of zero crossings within the burst. The phase can be obtained by measuring the time interval between the positive going edges of the signals from the two detectors and then dividing it by the signal period. Counters are relatively simple and convenient. But it can not process signal with low SNR. The frequency domain signal processors usually consist of a fast analog to digital converters (ADC) and software or hardware array processor to compute the DFT using the FFT algorithm. Fourier analysis provides the optimum single tone parameter estimation (in terms of maximum likelihood criteria) in the presence of noise . The method is well applicable for noisy signals distorted by multiple scattering in a dense particle low and/or dusty window. Although the Fourier analysis provides the optimum estimation, the method is computationally intensive and requires a relatively large size data sample to be

transferred and stored[2]. As in many applications such as the low speed flow measurement, the signal quality is relatively good and the dynamic range is small, then a less powerful, portable and low-cost signal processor can be used to meet the requirement of measurement and it has been developed by ourselves.

The Doppler signal processor based on personal computer consists of a two-channel high speed data acquisition card, a hardware FFT processor card, an amplifier-filter circuit and a burst detection circuit. The schematic diagram of the system is shown in Fig.1. The test and evaluation of the processor have been carried out using Doppler signal generator. The results demonstrate that the processor has a good measuring precision and an acceptable data rate.

2. TWO-CHANNEL HIGH SPEED DATA ACQUISITION CARD

The FFT based signal processor requires a digitized Doppler signal. This can be done by the use of high speed analog to digital converters (ADC's). Fast ADC's are now available that can sample the Doppler burst with a sampling frequency larger than 300MHz. But the faster the ADC, the more expensive the sampling system is. In consideration of the price, performance, device supply and work load of design, we chose a sampling rate of 50MHz. The SRAM on the board should have an access time less than 20ns. In consideration of the time delay of the surrounding circuits and the effect of multi-level connection, the SRAM we used is CY7C185-15, which has an access time equal to 15ns. The block diagram of the high-speed data acquisition system is shown in Fig.2. The data acquisition board has two channels, each of them has a buffer capacity of 32k bytes, with pre-triggering and post-triggering facility and ring storage manner. As the input capacity of this ADC is very low, it causes little phase shift to the input signal, so it is very suitable to the sample of PDA signals.

A voltage follower is set in front of the ADC to increase the input impedance while separating the analog input from the ADC. The RAM is high performance CMOS

static RAM without clock control. The data bus is connected to the ADC and computer through the three-state bus transceiver 74F245. The address bus is connected to the output of the address multiplexier. Two sets of input of the multiplexier are connected to the address bus of the computer and ADC respectively. As for sampling, the RAM is associated with ADC and address generator unit. While transmitting data, the RAM is controlled by the computer. The address generator unit is a kind of counter whose output is used as the addressing control of the ADC. The clock of the counter also generates the converting pulses to ADC and the writing pulses to the RAM. It can be generated from the on-board clock source, outer clock or the random pulses controlled by the computer. The A/D card plugged in the XT-bus slot of the computer are controlled by means of the interface circuit. It decodes the address line to generate the port control and to coordinate all the circuit units. It also performs the interrupted procedure and the data transformation.

3. HARDWARE FFT PROCESSOR

The Discrete Fourier Transform (DFT) is considered to be one of the most efficient method for frequency estimation. It can be done by software or hardware. The software method costs cheaper but is slower. To increase the data rate, we adopt the hardware approach. We designed a FFT processing PC plug card using TMC2310 FFT chip. The TMC2310 is an advanced integrated circuit which is capable of executing complex FFT, forward or inverse of up to 1024 points, with or without data windowing. At the maximum clock pulse rate of 20MHz, the device will execute radix-2 butterflies in 100ns, and 1024 points complex transforms (5120 butterflies) in 514 μ sec. The TMC2310 provides the arithmetic, control, coefficient memory and address generation logic for a variety of signal processing. External memory is used for storage of complex data and window or filter coefficients. Each data port is bi-directional and the device can be used with one or two banks of memory for either in-place or bank switched memory configurations allowing the user to overlap I/O operations with arithmetic execution. All

functions utilize the same basic system architecture for ensuring maximum flexibility.

The block diagram of the FFT processor is shown in Fig.3. In our circuit, the memory for storage of complex data and window coefficients is $2k \times 19$ bit, using five IMS1423-25 chips. The device is programmed by initializing two internal configuration registers to set device parameters such as function, transform length, data addressing modes, single or bank switching memory architecture and other options. Once initialized, the device generates data address and control for external memory, transfers data, executes the algorithm, and provides a DONE flag to indicate completion.

The technique used in the present case, to obtain signal frequency and phase difference between the two channel signals, is based on the cross-spectral density (CSD) function, so as to yield high processing speed and to process signals with low SNR. As the TMC2310 FFT system can execute complex FFT, we join the two-channel signals into a complex sequence. We define $X(n \cdot \Delta t)$ and $Y(n \cdot \Delta t)$ as the two channel PDA signals, $Z(n \cdot \Delta t) = X(n \cdot \Delta t) + jY(n \cdot \Delta t)$. After FFT calculation of $Z(n \cdot \Delta t)$, we get Z_k . According to the theory of digital signal processing, we have $X''k''\% = (Z''k''\% + Z''N-K''\%)/2$, $Y''k''\% = (Z''k''\% - Z''N-K''\%)/2$, where $X''k''\%$, $Y''k''\%$ and $Z''k''\%$ are the FFT results $X(n \cdot \Delta t)$, $Y(n \cdot \Delta t)$ and $Z(n \cdot \Delta t)$ respectively. Hence the CSD function is

$$G_{xy}(f_k) = \frac{2 \cdot \Delta t}{N} |X_k^* Y_k|, \quad k=0,1,2,\dots,N-1$$

With this procedure, the processing speed are nearly two times faster than calculating $X''k''\%$ and $Y''k''\%$ separately. The accuracy of the method depends strongly on the length of the sample for the FFT and sampling period. A large total sampling time will increase the accuracy, but also will reduce the processing speed considerably.

4. DOPPLER SIGNAL CONDITIONER AND BURST DETECTION

The Doppler signal conditioner consists of an amplifier

and a filter. As the flow fields are much complex and the particle velocities change greatly, a wider frequency range is necessary and the amplitude of PDA signal may be very small. The amplifier we used is a low-noise, wide band and high slew rate one. The signal is first amplified with a trans-impedance amplifier that provides a flat gain response over the bandwidth of 20KHz to 20MHz. Bandpass filters are used to remove the pedestal and high frequency disturbance from the burst signal. This also prevents the errors due to the aliasing which occurs when the signal is undersample (sampled at less than twice the highest signal frequency) and the high frequency signals then appear to be at a much lower frequency.

A burst detection circuit is used after the low-pass filter to identify when a potential signal is present. An ideal burst detector should identify every signal and produce no false alarms so that every Fourier transform computation could yield an usable information. Besides, the sampling should be triggered near the central part of the Doppler burst where the SNR is the greatest, thus resulting in significant gains in accuracy and ensuring maximum performance of the instrument, meanwhile considerably reducing the trajectory dependent phase errors. The burst detection mechanism we used is a time domain one. Although this method suffers from a large false detection rate due to noise and performs not so well as the frequency domain detector at low SNR, it is relatively easy to implement and costs less on hardware. We combine the pedestal and envelope of the PDA signal to determine the triggering time and adjust the threshold dynamically, thus remove off the uncertainties in setting a define trigger level. The operating principle of the circuit is shown in Fig.4. It is rather simple and can be satisfied in the most common applications.

5. RESULTS

With the DFT method, the frequency resolution is given by $\Delta f = \frac{1}{N \cdot \Delta t}$, here N is FFT length and Δt is the sampling period. A higher accuracy may be achieved by interpolating between the discrete frequency lines to obtain the peak in the CSD, i.e. using fitting functions to

the discrete frequency lines of the CSD. A number of interpolation methods have been introduced in previous publications which aim to obtain high accuracy without increasing the calculation time. The commonly used functions are parabola, Gaussian, sine and centroid curve etc[4]. We have tested these methods and found that the modified Gaussian function is the most acceptable.

To test the signal processor, we have designed a phase Doppler signal simulator[5]. It applies the direct digital synthesis technique to produce two channel signals. All the frequency, amplitude and phase can be changed arbitrarily. The noise can be added to generate waveforms with different SNR. The frequency range of the output signal is from 100Hz to 10MHz. With the signal simulator, a rather comprehensive test was made, the response of the processor was investigated. About 64 realizations of a burst with the same SNR have been used to calculate the statistics of the frequency and phase estimates. Standard deviation and mean value of the testing parameters are shown as a function of the SNR. The effect of different interpolation algorithms were also evaluated. The test results shown in Fig.5 - Fig.7 show that the processor can be used satisfactorily at a SNR greater than 4dB. The choice of the signal processing method and its implementation is a compromise among the various factors, namely the processing speed, accuracy, efficiency and cost. The PC-plug board based signal processor we designed has the most remarkable advantage of having a large flexibility and the possibility of implementing different software for processing, also it is comparatively cheaper.

REFERENCES

- [1] Amir Naqwi, Franz Durst, Xiaozhi Liu, (1991), Extended Phase-Doppler System for Characterization of Multi-phase Flows, Part. Syst. Charact. 8, pp.16-22.
- [2] Ibrahim K. M., Werthimer G. D. and W. D. Bachalo, (1990), Signal Processing Considerations for Laser Doppler and Phase Doppler Applications, Proceedings of the 5th International Symp. on Appli. of Laser Techniques to Fluid Mechanics, Lisbon.
- [3] Kobashi K., K. Hishida and M. Maeda, (1990), Measurement of Fuel Injector Spray Flow of I.C. Engine by FFT Based Phase Doppler Anemometer-An Approach to the Time Series Measurement of Size and Velocity, Proceedings of the 5th International Symp. on Appli. of Laser Techniques to Fluid Mechanics, Lisbon.
- [4] Qiu, H.H., Sommerfield, M. and Durst, F., (1991), High Resolution Data Processing for Phase-Doppler Measurements in a Complex Two-phase Flow, Measurement Science and Technology, 2, pp 455-463.
- [5] Ma Zhongming and Sun Jiazi, (1994), Signal Simulator of Phase-Doppler Anemometry, Proceedings of the 2nd International Conf. on Fluid Dynamic Measurement and Its Applications, Beijing, pp85-88.

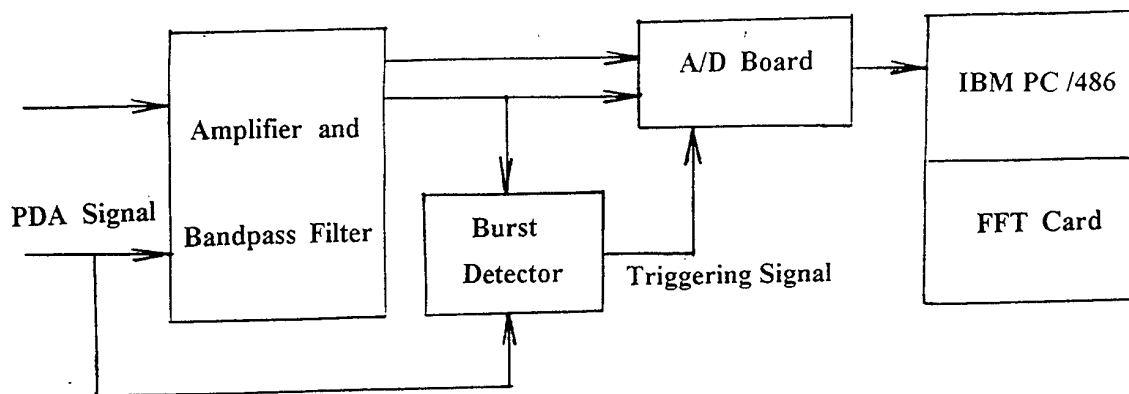


Fig.1 Schematic diagram of the LDA signal processor

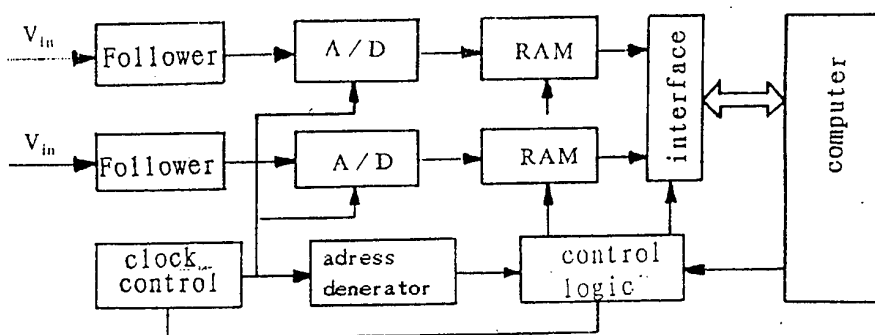


Fig.2 High speed A/D card

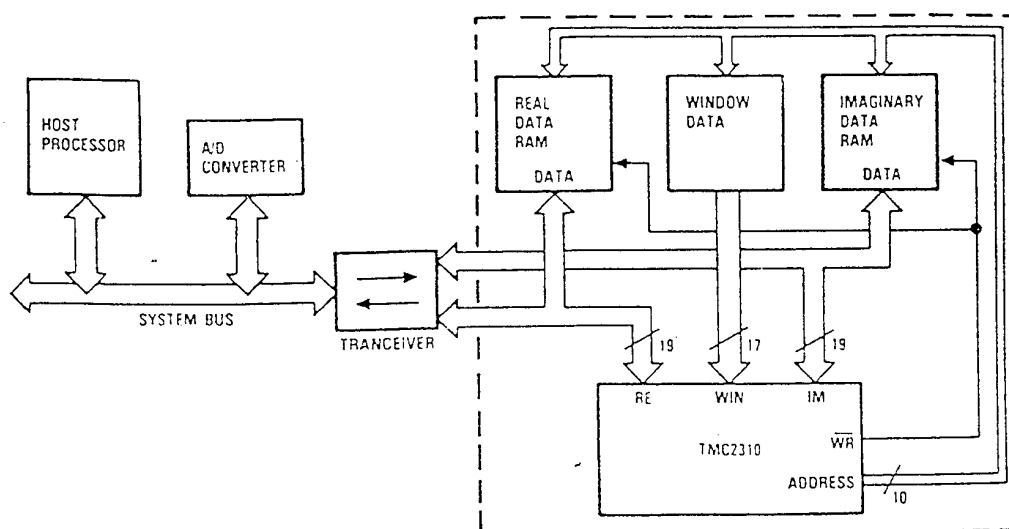


Fig.3 Hardware FFT processor card

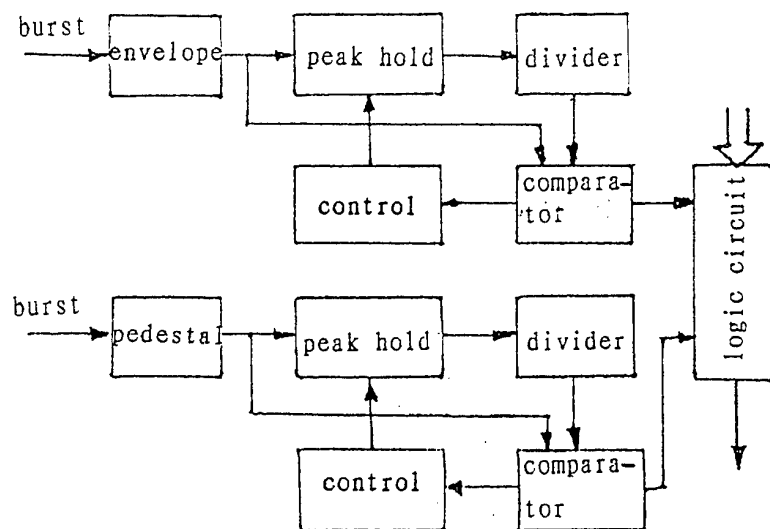


Fig.4 Principle of the burst detector

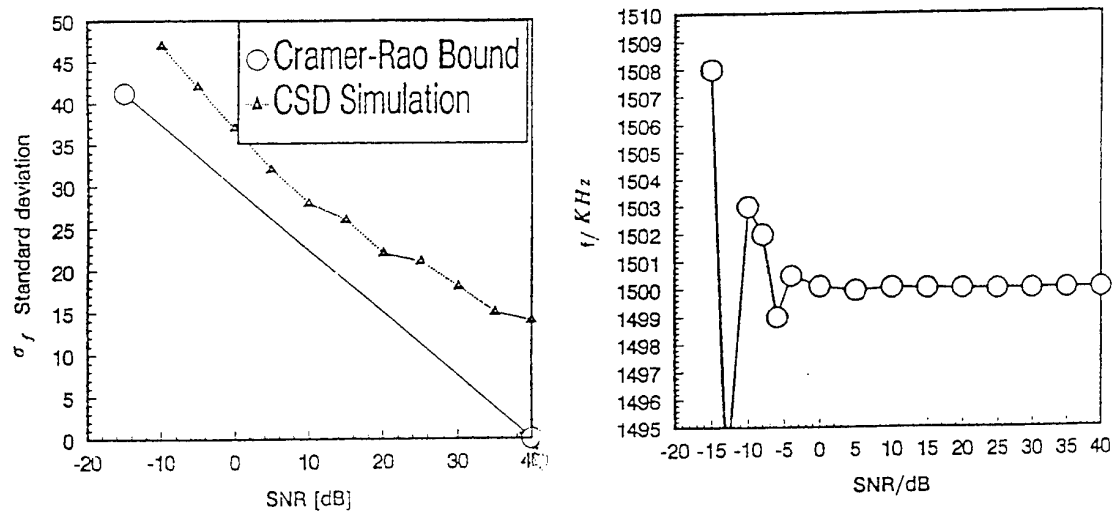


Fig.5 Performance of frequency(velocity) measurement

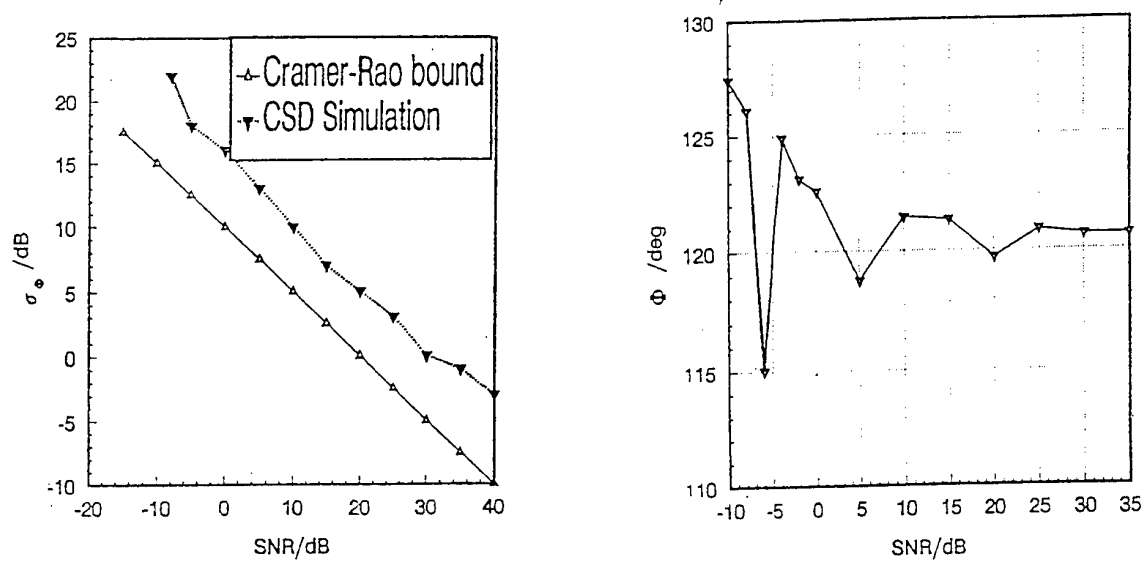


Fig.6 Performance of phase(diameter) measurement

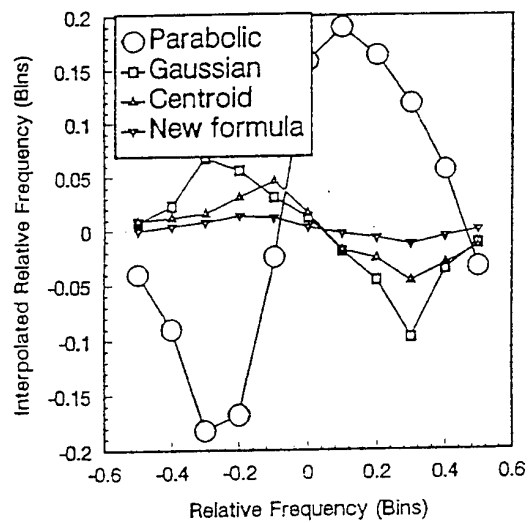


Fig.7 Comparison of different interpolating method

VELOCITY DOPPLER MEASUREMENTS IN A HIGH SPEED WATER FLOW USING A FABRY-PEROT INTERFEROMETER

by

B. Leporeq, J.F. Le Roy
Institut de Mécanique des fluides de Lille
Office National d'Etudes et de Recherches Aérospatiales
5, Boulevard Paul Painlevé, 59045 Lille cedex - FRANCE

B. Pinchemel, C. Dufour
Laboratoire de Dynamique Moléculaire et Photonique
Centre d'Etudes et de Recherches Lasers et Applications
Université de Lille 1
59655 Villeneuve d'Ascq cedex - FRANCE

G. Houssaye
Laboratoire de Fabrication Mécanique - Département Productique
Ecole des Mines de Douai
941, Rue Charles Bourseul, B.P. 838 - 59508 Douai cedex - FRANCE

ABSTRACT

Velocity Doppler measurements using a Fabry-Pérot interferometer has been tested in transsonic wind tunnel. A good agreement between the derived velocity and that obtained from a Pitot tube reading, renewed the interest in such a technique. Most of the jet cutting technologies involve a water flow seeded by abrasive particles. The simultaneous velocity measurements for water droplets and abrasive particles remain critical and often beyond any L.D.V classical technique. The need to validate computed velocities and to optimize parameters in an industrial machine led us to test and perform some measurements using this revived method.

1. INTRODUCTION

Numerous non intrusive techniques have been developed in order to qualify flows either by using the physical properties of the fluid in motion, or by following the tracer particles seeding it. In the most of common models for predicting the depth of cut with abrasive water jet, the cutting performance is a function of the total mass of impinging particles and the square of their velocity.

Experimentally the mass of impacting particles can be measured and the velocity of the water jet itself can be calculated from Bernouilli's law. The gaseous phase (air 95% volume of the jet [1] more complicates the search of a good theoretical model for the variation of particles velocity as a function of the distance inside the focusing tube. As it is impossible to find a model for the acceleration of the abrasive particles into the focusing tube, the actual velocity of the abrasive particles must be inferred. First investigation to measure the velocity of abrasive particles were done in 1987 [2]. A mixture of conventional garnet with magnetic particles was injected into a abrasive cutting head and the resulting cutting stream directed through a pair of current-carrying coils spaced a fixed distance apart. The abrasive particle velocity measurements were in the

range of 120m/s. In 1991, U. Himmelreich and W. Riess [3,4] used a laser-2 Focus for the measurement of phase velocities and turbulence and a Laser light sheet technique for the investigation of mass distribution and additional abrasive particle velocity measurement. They mentioned a dual peak in the TOF distribution of an abrasive water jet with parameters : 1g/s abrasive load rate, pressure 100 MPa and focusing tube length 30 mm. The peak associated to the lowest velocity corresponds to the abrasive particle and the other to the water. As they increased the length of the focusing tube from 10 mm, the two peaks have moved closer together, due to an enhanced mixing process. For U. Himmelreich and W. Riess [3, 4], the separate water peak had nearly vanished and it is assumed that the data of the droplet and abrasive phase are covered by one widely broadened peak. In 1992, Neusen [5, 6] used a forward-scatter LDV system to measure abrasive particles velocity. Most of the measured velocities clustered around 250 m/s. Due to the three phases of the jet (95% air, 4% Water, 1% abrasive [1]), it was not possible to discriminate between the velocities of particles and water drop.

Improvements in laser techniques made it possible to bring a method already known for long into use again [7]. A confocal Fabry-Perot spectrometer (C.F.P.) gives access to the Doppler shift between the light from the laser and that scattered by the particles seeding the flow under observation. The limits put into evidence by Seasholtz [7] arise from the lack of stability of the laser frequency, from mechanical vibrations and from the acoustic noises induced by the wind tunnel. The use of a stabilized narrow bandwidth (500 kHz) laser and of optical fibers for transmitting the signal to the C.F.P allows to turn these difficulties. This method is specially suited for measurements in high speed water flows such as used in cutting devices.

2. EXPERIMENTAL SET UP

The purpose of this experiment is to record simultaneously the signal of a narrow laser line and the signal, shifted by the Doppler effect, of the light scattered by the flowing water jet. The narrow laser line is emitted by a longitudinal single mode commercial CW ring dye laser, COHERENT 899-29 pumped by a COHERENT INNOVA 100 Argon-ion laser.

In the emission part of the experiment, the light of the dye laser is focused onto the tracer particles flowing in the probe volume (typically 0.03 mm^3). The scattered light is collected on an optical fiber through a 10cm - diameter lens, the focal length of which is 12 cm. At the exit of the optical fiber, the light is mixed with a few percents of the laser light. The two beams are focused on the aperture of a 10 cm long Confocal Fabry-Pérot (noted C.F.P.). The C.F.P. is an high resolution interferometer able to discriminate two frequencies 25 MHz apart. The C.F.P. interferometer is built with two 99% reflective coated confocal mirrors. This two mirrors form an optical cavity in which the incident light undergoes numerous reflexions. A laser beam is allowed to go through the interferometer along the optical axis when its wavelength is a multiple of the optical thickness between the two mirrors. The free spectral range (F.S.R.) of such an interferometer is narrow (750 MHz for a 10 cm long C.F.P.).

Such a device is generally well adapted when only a few numbers of discrete frequencies have to be discriminated. In this experiment the C.F.P. is used as a Spectrum Analyser. The rear mirror is fastened to a piezo-electric ring in order to scan over at least one F.S.R. The light transmitted through the C.F.P. is collected by a photomultiplier tube, the signal of which is recorded on a Nicollet digital oscilloscope to determine the Doppler shift between the reference and measured lines. The experimental set up is described on figure 1. Due to the transparency of the water jet it is possible to collect the scattered light symmetrically to the incident laser beam, as a consequence the incident and the observation angles can be chosen equal. When the two vectors make an angle of 60° with the water jet, a speed range of 30 m/s to 800 m/s with a resolution closed from 5m/s is obtained. The acquisition rate of the data is about 0.002 s, and depends only of the voltage scanning supply of the piezo-electric ring. The oscilloscope picture can be readily interpreted, a record of these data is presented on figure 2. The interferometer is built with two 99% reflective coated confocal mirrors. These two mirrors form an optical cavity in which the incident light undergoes numerous reflexions. A laser beam is allowed to go through the interferometer along the optical axis when its wavelength is a multiple of the optical thickness between the two mirrors. The free spectral range

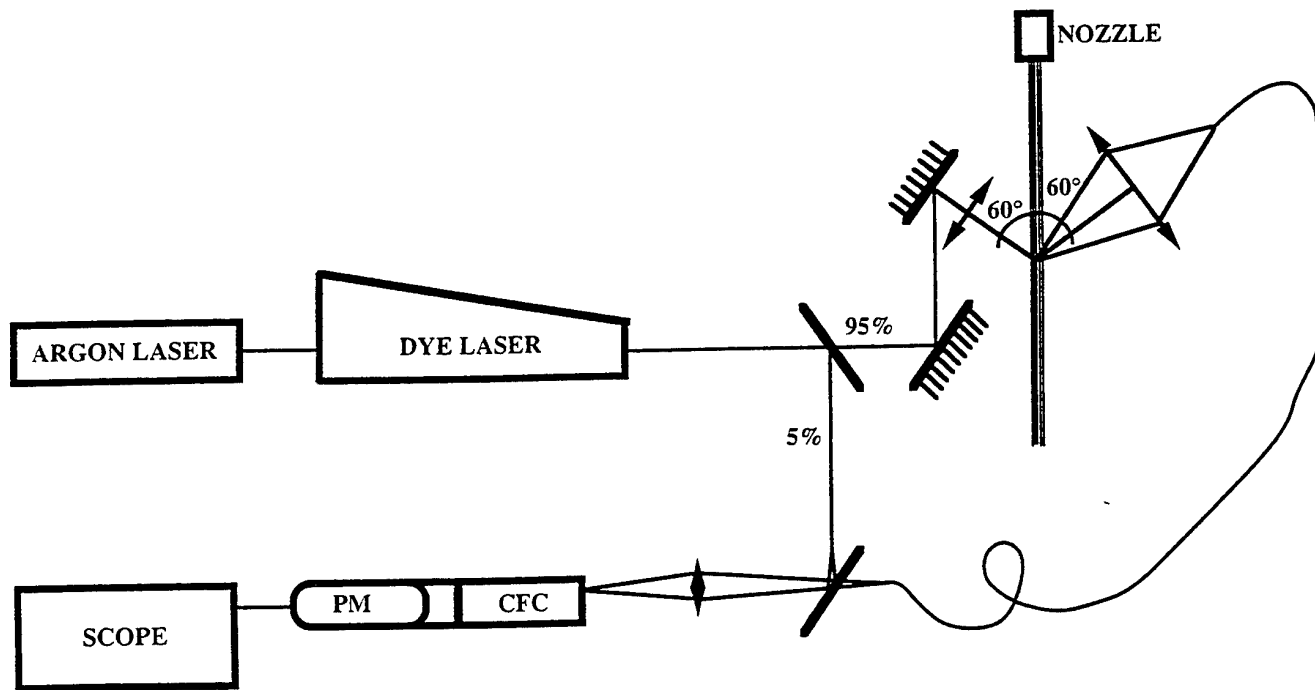


Figure 1 : EXPERIMENTAL SET UP

3. RESULTS

3.1. Description of the abrasive water jet cutting

The elements of a high pressure abrasive water jet are :

- a high pressure water pump capable of producing 400 MPa water jet with a flow rate of $0.05 \text{ dm}^3/\text{s}$.
- a primary nozzle to produce a pure water jet
- a mixing chamber where air and abrasive are entrained by the pure water jet
- a mixing tube where the abrasive particles are accelerated.

3.2. Experimental velocity of a pure water jet

For a pure water jet in absence of the mixing chamber and the focusing tube, the inner diameter of the sapphire nozzle is about .2 mm. The water pressure is adjustable from 50 to 400 MPa. Along the coherence length (20 to 30 mm), the jet diameter is less than 1 mm. The water velocity under the above pressure conditions is in the 300 - 800m/s speed range, in good agreement with Bernoulli equation (figure 4).

The influence of the distance from the nozzle exit on the velocity has been put into evidence allowing the determination of the geometrical location of the maximum velocity (figure 5).

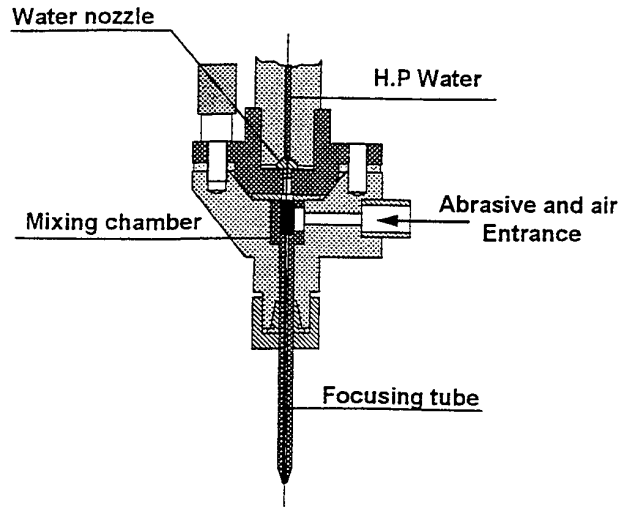


Figure 2 : ABRASIVE WATER JET CUTTING HEAD

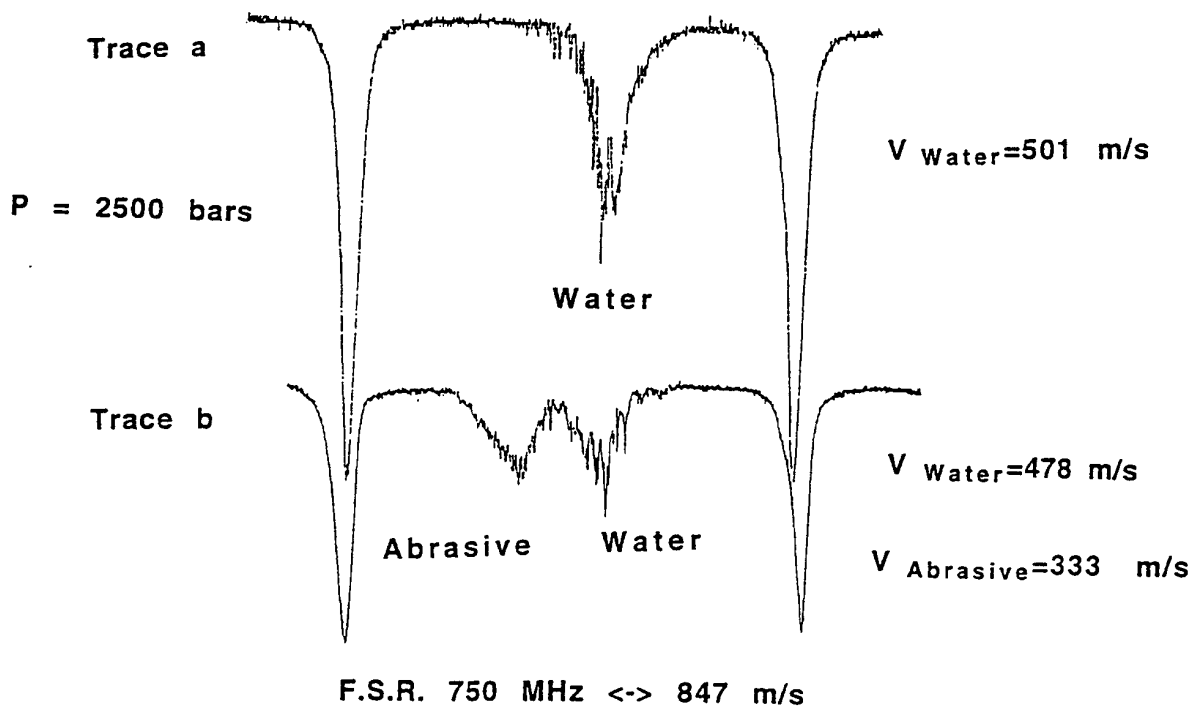


Figure 3 : EXPERIMENTAL RECORDING OF A DOPPLER SHIFT INDUCED

TRACE A : CASE OF A PURE WATER JET

TRACE B : CASE OF ABRASIVE SEEDED WATER JET

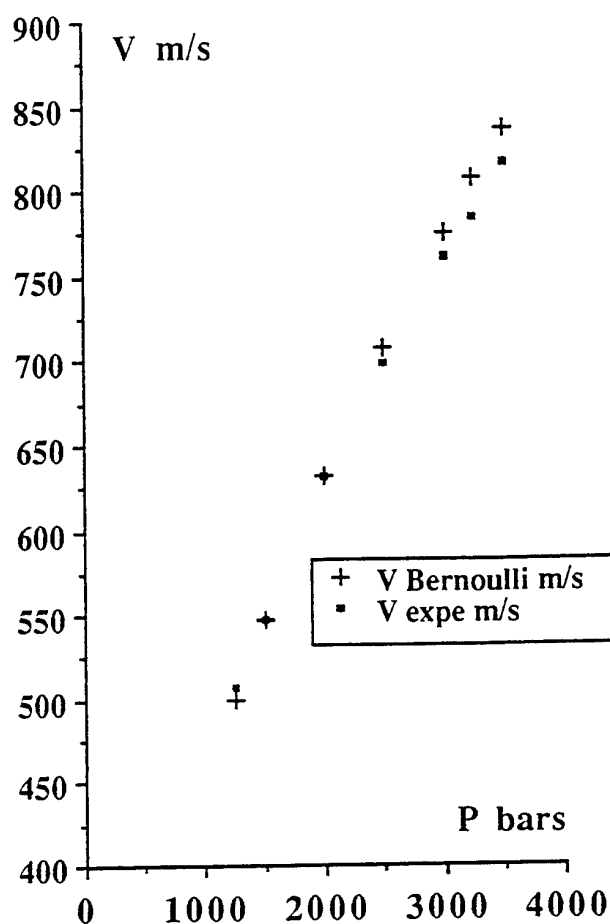


Figure 4 - COMPARISON OF THE EXPERIMENTAL VELOCITIES OF A PURE WATER JET TO THE THEORETICAL BERNOULLI VALUES VERSUS PRESSURE

3.3. Experimental velocities of abrasive seeded water jet

Abrasive particles are introduced into the mixing chamber located downstream of the nozzle and are carried away by a Venturi effect into a tube. Several tubes of inner diameter close to 1 mm have been tested, having different lengths larger than the jet coherence length. Under these conditions the slightly divergent jet is a ternary mixture of air, abrasive particles and water, inducing a significant velocity scattering. Moreover, these experimental velocities are lower than in the case of pure water (figure 2). The first recordings exhibit a weak and spreaded out signal. For high pressures, the signal is split in two lines which can be attributed to the water and to the abrasive particles. The injection of particles by suction has for consequence the presence of air in the mixture of water and abrasive. This had for effect to divide into fragment the jet and make it diffuse. The dynamic viscosity of water becomes lower as well as the interfacial forces (drag, virtual mass force,...) which are on the particles.

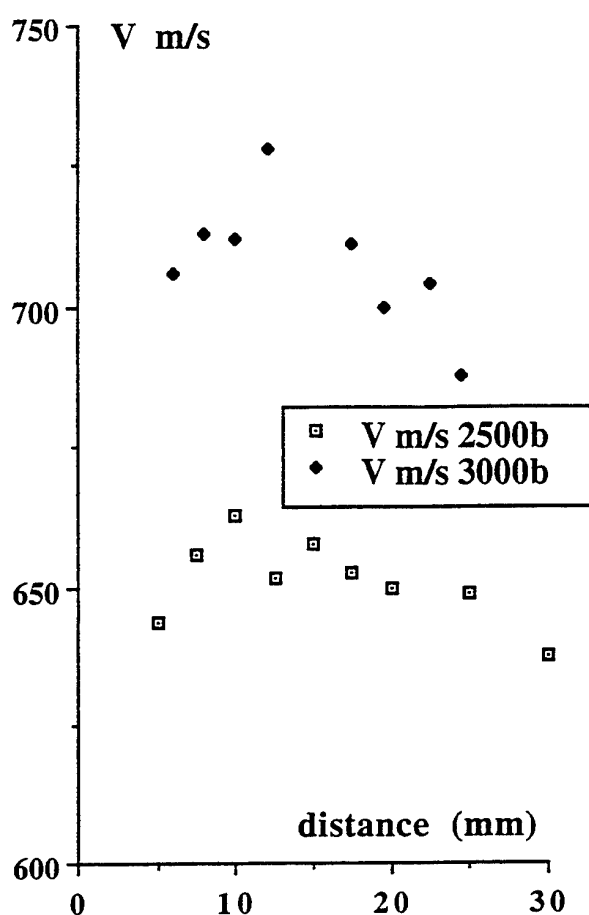


Figure 5 - DETERMINATION OF THE GEOMETRICAL LOCATION OF THE MAXIMUM VELOCITY FOR A PURE WATER JET AS A FUNCTION OF THE DISTANCE TO THE EXIT OF THE NOZZLE

4. CONCLUSION

After being calibrated in a transonic wind tunnel, a velocity Doppler technique using a Fabry-Pérot interferometer has been successfully applied to determine the velocity of pure water jet and abrasive seeded water jet. In a first step a good agreement has been obtained when comparing the experimental velocity in the case of a pure water jet to the theoretical Bernoulli value. When abrasive particles are injected in water, we evidenced a reduction of the mean velocity of the water of about 5%. A second signal which only appears in the presence of abrasive can be possibly attributed to the particles. Further systematic experiment should be done to confirm this hypothesis.

ACKNOWLEDGMENTS

The authors thank Mr. J.-P. Bourez, A. Osman and G. Leporecq for assistance in the experimental part of this work.

REFERENCES

- [1] A. TAZIBT
Hydrodynamic investigation and prediction of abrasive acceleration process in abrasive water jet cutting
12th International Conferences on jet cutting technology, BHR Group, October 1994, Rouen, France
- [2] R. K. SWANSON, M. KILMAN, S. CERWIN, W. TARVER
Study of particle velocities in water driven abrasive jet cutting
4th U.S. Water Jet Conference, August 26-28, 1987, University of California, Berkeley
- [3] U. HIMMELREICH, W. RIESS
Laser-velocimetry investigation of the flow in abrasive water jets with varying cutting head geometry
6th American Water Jet Conference, August 24-27, 1991, Houston, Texas
- [4] U. HIMMELREICH, W. RIESS
Hydrodynamic investigations on abrasive water jet cutting tools
10th International Conferences on jet cutting technology, BHR Group, October 1991, Amsterdam, The Netherlands
- [5] K. F. NEUSEN, T.J. GORES, T.J. LABUS
Measurement of particle and drop velocities in a mixed abrasive water jet using a forward-scatter LDV system
11th International Conferences on jet cutting technology, BHR Group, Sept 1992, St. Andrews, Scotland
- [6] K. F. NEUSEN, T.J. GORES, R.S. AMANO
Axial variation of particle and drop velocities downstream from an abrasive water jet mixing tube
12th International Conferences on jet cutting technology, BHR Group, October 1994, Rouen, France
- [7] R. G. SEASHOLTZ, L. J. GOLDMAN
Three Component Velocity Measurements using Fabry-Pérot Interferometer
Proceedings of the "Second International Symposium on Application of Laser Anemometry to Fluid Mechanics " 2-5 Juillet 84, Lisbonne, Portugal

NEW PROCESSING METHODS FOR LDA SIGNALS

Anders Høst-Madsen[†] & Palle Gjelstrup[‡]

[†] Kwangju Institute of Science and Technology, Dept. of Information and Communication,
572 Sangam-dong, Kwangsan-ku, Kwangju, Republic of Korea 506-303.

[‡] Dantec Measurement Technology A/S, Tonsbakken 16-18, 2740 Skovlunde, Denmark

ABSTRACT

The paper investigates a number of new methods for processing of LDA signals both theoretically and experimentally. For the theoretical analysis, Cramér-Rao bounds for signals with a Gaussian envelope are calculated. Two new processing methods are introduced and analyzed: the *adaptive burst length multibit FFT* processing and *variable spectral validation*. These processing methods are applied to signals with known and repeatable characteristics, and the effect analyzed.

1. INTRODUCTION

There are many crucial aspects to obtain accurate and reliable LDA measurements. Good optics and lasers are necessary to obtain high quality Doppler signals; advanced accurate processing of the Doppler signal is needed to estimate the Doppler frequency with high precision; and, finally, the data analysis techniques applied to the measurements should give optimal and reliable results. Processing of the Doppler signal plays a pivotal role, since this determines the accuracy in any subsequent processing. This processing should use the information in the Doppler signals to the fullest extent, otherwise optimization in other links of the chain is wasted. In this paper we will consequently concentrate on this part of the LDA measurement.

2. LDA SIGNALS

After quadrature mixing and sampling the LDA signal can be written

$$\begin{aligned} X_n &= b_0 b(\eta(t_n - t_0)) \cos(\omega t_n + \theta) + w(t_n) \\ Y_n &= b_0 b(\eta(t_n - t_0)) \sin(\omega t_n + \theta) + \hat{w}(t_n) \end{aligned} \quad (1)$$

We use the following notation:

ω : circular frequency.
 θ : initial phase.
 b : envelope function.

b_0 : amplitude of the signal.

t_0 : time of arrival.

$1/\eta$: duration of burst.

w, \hat{w} : noise (with Hilbert transform).

σ : RMS value of noise.

The noise is assumed to be white Gaussian additive noise.

The envelope function b may have different forms. However, for LDA signals the most common envelope is the Gaussian envelope because seeding particles usually are small compared to the measurement volume, and we will assume this envelope in the following.

Both the frequency of and the duration of the burst vary from burst to burst, and there is no deterministic relationship between the quantities. The frequency depends solely on the velocity of the particle in the fringe direction, while the burst duration depends on a combination of velocity in all three dimensions and particle trajectory. An optimal processing method therefore has to determine frequency and duration independently.

3. CRAMÉR-RAO BOUNDS FOR BURSTS WITH GAUSSIAN ENVELOPE

The Cramér-Rao (CR) bound gives a limit on how accurate burst parameters can be determined, and is therefore a basis of evaluating processing methods. The CR lower bound is a theoretical lower bound for the variance on frequency and other burst parameters for any *unbiased* estimator, i.e. no algorithm for calculating the frequency from the available samples can do better (Kendal and Stuart (1963) and Papoulis (1988)).

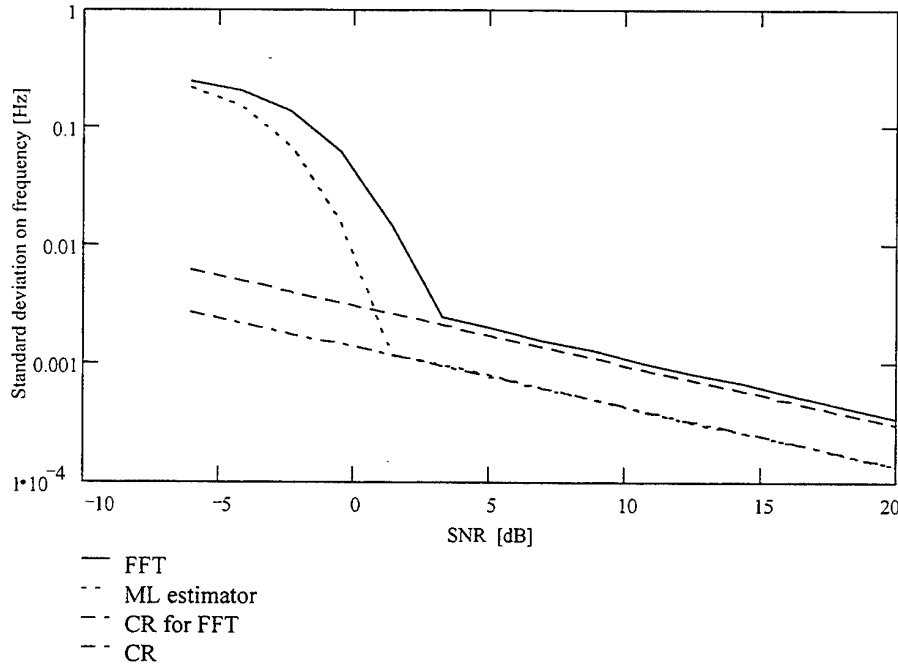


Figure 1. Estimation of frequency for sinusoidal signal with Gaussian envelope. The burst has a Gaussian width of 50 samples. Two estimators have been used on a simulated signal: a FFT on the 32 central samples and a ML estimator. It is seen that the simple FFT almost reaches the CR lower bound for constant envelope, while the ML estimator reaches the CR lower for Gaussian envelope.

The Cramér-Rao bounds for the constant envelope have been calculated in [1]. We have derived the CR bounds for the Gaussian envelope, comparable to [2] with a different noise model. The result is

$$S_{CR}[\omega] = \sqrt{\frac{8}{\sqrt{2\pi}}} \frac{1}{\sqrt{SNR}} \frac{1}{N\sqrt{N}\Delta t}$$

$$S_{CR}[b_0] = \sqrt{\frac{2}{\sqrt{2\pi}}} \frac{\sigma}{\sqrt{N}}$$

$$S_{CR}[t_0] = \sqrt{\frac{2}{\sqrt{2\pi}}} \frac{1}{\sqrt{SNR}} \sqrt{N}\Delta t$$

$$S_{CR}[\eta] = \sqrt{\frac{2}{\sqrt{2\pi}}} \frac{1}{\sqrt{SNR}} \frac{1}{N\sqrt{N}\Delta t}$$

where Δt is the sampling interval and N is the burst duration, $N\Delta t \equiv 1/\eta$, and $S_{CR}[\cdot]$ is the Cramér-Rao lower bound for the standard deviation.

4. ADAPTIVE BURST LENGTH PROCESSING

As seen in the previous section and also in the paper [1], the standard deviation on velocity measurements decrease with $N\sqrt{N}$. Thus, the record length has a significant influence on the accuracy of velocity

measurements. Therefore it is important that the full length of the burst is used, and to accommodate this we have made a new processing scheme: the adaptive burst length processing.

The adaptive burst length processing adapts the record length to the duration of the burst. Combined with true multibit FFT processing this gives a very high accuracy.

The advantages of adaptive burst length processing are in particular pronounced when the burst length varies considerably during a data acquisition. Examples are transient phenomena such as explosions, where the processor should be able to handle a large velocity range, or cyclic flows, where the average burst length varies through a cycle.

In adaptive burst length processing, a burst is divided into a number of blocks, each of which can be from 8 to 64 samples long. Each block is processed by a multibit FFT, and the results from the individual blocks are then validated and combined to give a total frequency estimate for the whole burst. The processing is outlined in Figure 2.

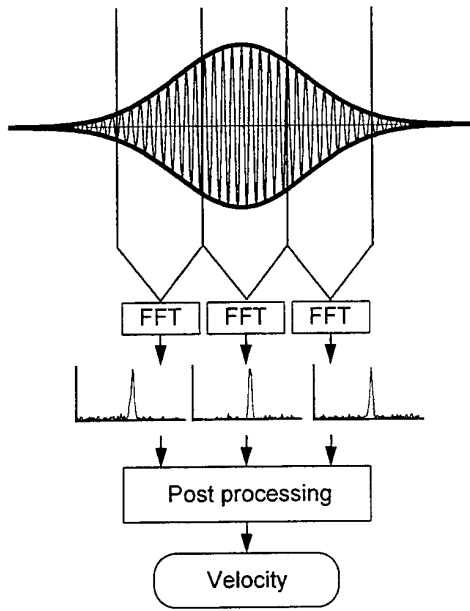


Figure 2. Adaptive burst length processing.

5. BIAS EFFECTS

In adaptive burst length processing, the uncertainty in the measurements depends on the velocity. Since the accuracy increases with burst length, and the average burst length is inversely proportional to the velocity, low velocities will be measured more accurately than high velocities. When measuring on turbulent flows, where there is a broad distribution of velocities, this will 'skew' velocity histograms, and it can make symmetric histograms asymmetric. Nonetheless, it will neither affect mean nor variance.

To see this, consider a distribution of velocities given by the function $f_{\mu,\sigma}$, with mean μ and standard deviation σ . Due to uncertainty, measurements at a velocity v do not give the value v , but a number of values distributed around v , and we call this distribution g_v . The variance in measurement at v is M_v , that is

$$\int_{-\infty}^{\infty} (x - v)^2 g_v(x) dx = M_v$$

We assume that the measurement at a given velocity is unbiased, so that

$$\int_{-\infty}^{\infty} x g_v(x) dx = v$$

In adaptive burst length processing the function g_v and the variance M_v depend on the velocity, while with a fixed record length g_v and M_v are the same for all v .

The distribution of measured velocities is given by a kind of convolution

$$h(v) = \int_{-\infty}^{\infty} f_{\mu,\sigma}(x) g_x(v) dx$$

From this the measured mean velocity can be found by

$$\begin{aligned} E[v] &\stackrel{\text{def}}{=} \int_{-\infty}^{\infty} h(v) v dv = \int_{-\infty}^{\infty} \int_{-\infty}^{\infty} f_{\mu,\sigma}(x) g_x(v) dx v dv = \\ &= \int_{-\infty}^{\infty} f_{\mu,\sigma}(x) \int_{-\infty}^{\infty} g_x(v) v dv dx = \int_{-\infty}^{\infty} f_{\mu,\sigma}(x) x dx = \mu \end{aligned}$$

Thus, the measured mean value $E[v]$ is identical to the true mean value μ , and the measurement with adaptive burst length is unbiased.

The measured variance, from which follows the turbulence intensity, can be calculated by

$$\begin{aligned} E[(v - \bar{v})^2] &\stackrel{\text{def}}{=} \int_{-\infty}^{\infty} h(v) (v - \bar{v})^2 dv \\ &= \int_{-\infty}^{\infty} \int_{-\infty}^{\infty} f_{\mu,\sigma}(x) g_x(v) dx (v - \bar{v})^2 dv \\ &= \int_{-\infty}^{\infty} f_{\mu,\sigma}(x) \int_{-\infty}^{\infty} g_x(v) (v - \bar{v})^2 dv dx \\ &= \int_{-\infty}^{\infty} f_{\mu,\sigma}(x) \int_{-\infty}^{\infty} g_x(v) [(v - x)^2 + (x - \bar{v})^2 + 2(v - x)(x - \bar{v})] dv dx \\ &= \int_{-\infty}^{\infty} f_{\mu,\sigma}(x) [M_x + (x - \bar{v})^2] dx = \int_{-\infty}^{\infty} f_{\mu,\sigma}(x) M_x dx + \sigma^2 \end{aligned}$$

Thus, for adaptive burst length processing, the measured variance is the true variance σ^2 plus a (positive) term $\int_{-\infty}^{\infty} f_{\mu,\sigma}(x) M_x dx$ due to the measurement

uncertainty. For fixed record length processing, M_x is independent of the velocity x , and the formula for the measured variance reduces to the standard formula

$$E[(v - \bar{v})^2] \stackrel{\text{def}}{=} M + \sigma^2$$

That is, true variance plus measurement uncertainty.

The formula $\int_{-\infty}^{\infty} f_{\mu,\sigma}(x) M_x dx$ is minimized when

M_x is minimized at each velocity x . This is exactly what adaptive burst length processing does. Therefore, *adaptive burst length processing introduces the minimum artificial turbulence*.

While adaptive burst length processing is optimal with respect to mean and variance, it does give a bias on higher order moments, such as skewness and flatness, because histograms may become more asymmetric. However, higher order moments are of minor importance and are in any case very uncertain measures, so this is a minor drawback of adaptive burst length processing.

What has not been taken into consideration in the above considerations is *detection bias*. At low SNR there is a higher probability that a long burst will be detected than a short burst. Therefore, there will be a larger proportion of the low velocity measurements than the high velocity measurements that are used in the calculation of moments, and inevitably this will bias the mean towards zero. This is true both for fixed record length processing and adaptive record length processing, but more pronounced for adaptive processing. However, the effect is difficult to evaluate, and it will not be done here.

6. VALIDATION

Validation of the measurements also play a crucial role in the accuracy that can be obtained and in the reliability of the results. The best validation is obtained in the spectral domain, where noise and signal are separated. Sometimes it can be an advantage to allow a few false measurements in order to get a higher data rate, while at other times only correct measurements should be validated. The false measurement can subsequently be removed by applying collective validation methods on the whole set of measurements. To allow the user to adapt the validation to the requirements of the experiment, we have therefore introduced a new spectral validation method: *the variable spectral validation method*.

The principle in FFT processing is to use the highest peak in the in the signal spectrum as an estimate of the frequency. The height of this peak, and the relative height of the highest peak to the second highest can therefore be used as a confidence measure of the measurement.

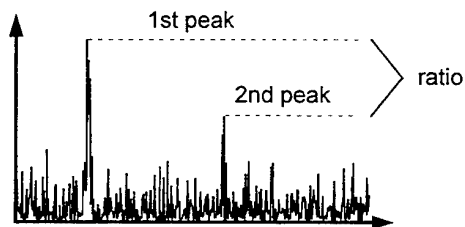


Figure 3. Variable spectral validation. The figure shows a typical spectrum for a noisy signal. The validation is done by comparing the absolute height of the 1st peak and the ratio of the 1st to the 2nd peak to some user selectable values.

7. MEASUREMENT RESULTS

7.1 Adaptive burst length processing

Simulated Doppler signals were used in order to quantify performance under repeatable conditions. A Dantec BSA enhanced processor operated with 40 MHz input filter bandwidth was used in both tests. The simulated signal was generated by combination of a fixed frequency sine wave signal, a white noise signal, an envelope modulation signal and a pedestal signal, all of which were individually adjustable. Bursts with 50 % modulation depth were used for all tests.

The sine wave signal amplitude was kept constant, whereas the noise signal level was varied. The RMS voltages of both the signal and the noise component were measured at each test condition in order to establish the signal to noise ratio, hereafter called the SNR. The RMS voltages were measured after the input filters of the processor in order to refer to the SNR that the processor actually encounters.

The effect of varying the SNR and burst length was investigated. Figure 4 shows the behaviour for the fixed burst length processing, and confirms that the measured turbulence intensity is independent of the burst length.

Figure 5 shows that the measured variance decreases with increasing burst length and with increasing SNR, as predicted above. It also shows that the adaptive burst length processing produces lower variance than fixed burst length processing, confirming the theoretical prediction from above that burst length adaptive processing gives the minimum artificial turbulence.

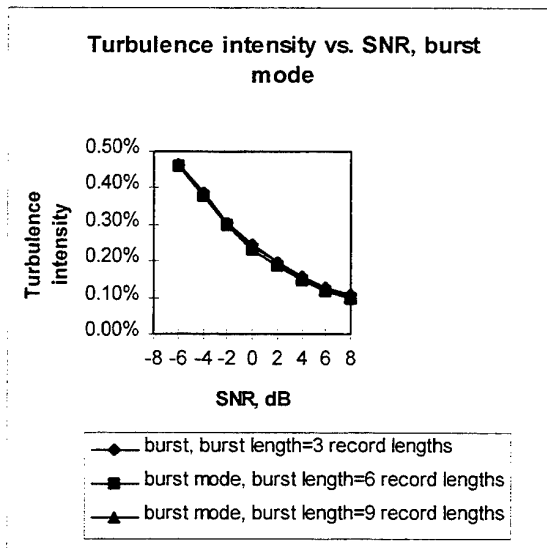


Figure 4. Burst mode: measured turbulence intensity versus SNR, with varying burst length

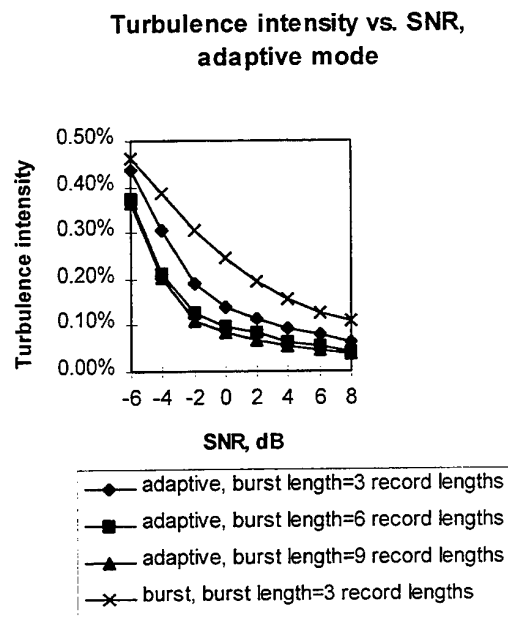


Figure 5. Adaptive mode: measured turbulence intensity versus SNR, with varying burst length (burst mode shown for comparison)

7.2 Variable spectral validation

The variable spectral validation method has been evaluated using simulated Doppler signals with known SNRs ranging from -14 dB to +4 dB.

A fixed burst repetition rate of 10 kHz was used, and the data rate at each test condition was recorded. The effective processor data rate was normalised by the burst repetition rate. Figure 6, Figure 7 and Figure 8 show the normalised data rate, the measured standard deviation and the measured mean value respectively, as functions of the SNR for three settings of the validation criterion:

1. The strictest setting (ratio 6) with an absolute peak level of 32 and a relative level of 6
2. The standard setting (ratio 4) with an absolute peak level of 32 and a relative level of 4
3. A very weak criterion (ratio 2) with an absolute peak level of 24 and a relative level of 2

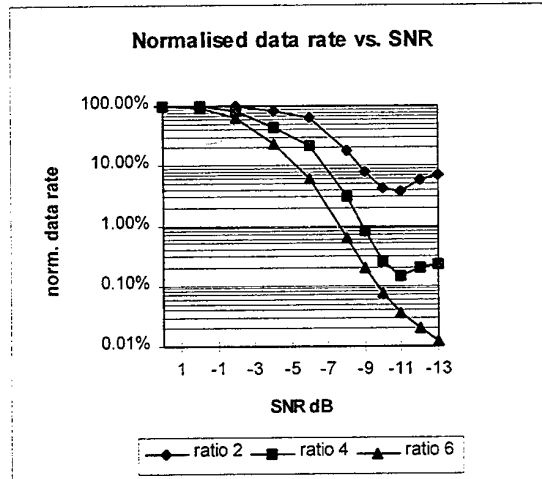


Figure 6. Normalised data rate versus SNR for three settings of the spectral level ratio.

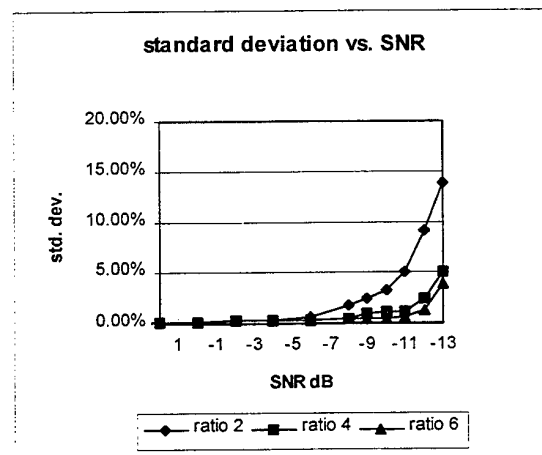


Figure 7. Measured standard deviation (in % of input filter bandwidth) versus SNR for three settings of the spectral level ratio.

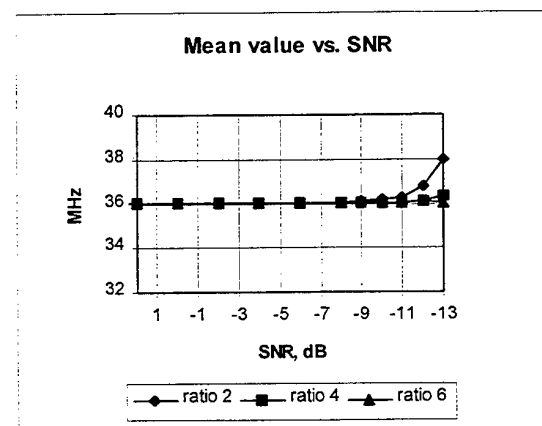


Figure 8. Measured mean velocity versus SNR for three settings of the spectral level ratio.

Several conclusions can be drawn from the figures:

1. The BSA can measure reliably at SNRs down to -13 dB, when a very strict validation is employed.
2. The effective data rate of the BSA can be tripled at -6 dB SNR without change in the standard deviation, using less restrictive validation than the standard setting.
3. The effective data rate can be increased more than ten times at -10 dB SNR, at the expense of increased standard deviation.
4. As one could expect, using a very relaxed validation criterion, the results are sensitive to noise.

Some implications for practical measurements are:

- Reliable results can be obtained under difficult experimental conditions with very noisy signals due to contamination of windows, small seeding particles or even natural seeding.
- The duration of experiments can be shortened due to increased effective data rate. This is particularly important in energy demanding facilities such as high speed wind tunnels and large cavitation tunnels.
- Temporal resolution can be improved by up to an order of magnitude. This opens new possibilities for the measurement of turbulence spectra and for studies of cycle-to-cycle variations in internal combustion engines.

8. CONCLUSION

The paper introduces two new processing methods. They are analyzed theoretically and applied to simulated Doppler signals with known SNR. The analysis shows that a further increase in accuracy, reliability and/or data rate is obtained. It is not possible to optimize all three parameters simultaneously, but using the present analysis a weighting of the parameters is possible based on the requirements of a specific application.

The results of the practical experiments show that adaptive burst length processing reduces the standard deviation of the measured velocities; the variable spectral validation can be used to significantly increase data rate without sacrificing accuracy, for SNR down to -6 dB, and to obtain useful data rates at SNRs as low as -10 dB.

Future work will include testing of the described methods in practical LDA measurements, where both the SNR, the signal amplitude, and the Doppler frequency vary at the same time.

The improvement in the Burst Spectrum Analyzer's performance is useful for many applications where the SNR is low due to experimental conditions such as small seeding particles, long measuring distance or contaminated windows.

9. REFERENCES

- [1] Lading, L. 1993: Signal processing for time resolved measurements, Summer School on optical diagnostics for flow processes (Risø 1993).
- [2] Rife, D. and Boorstyn, R. 1974: "Single-Tone Parameter Estimation from Discrete-Time Observations", IEEE Transactions on Information Theory, vol. IT-20, No. 5, p. 591-598.

APPLICATION OF THE WAVELET TRANSFORM TO LASER-DOPPLER SIGNAL PROCESSORS

H.R.E. van Maanen (*Shell Research and Technology Centre, Amsterdam*)
(*P.O. Box 38000, 1030 BN Amsterdam, Netherlands*)

and

F.J. Nijenboer (*University of Twente*)

Abstract.

Estimation of the frequency and arrival time of a Doppler burst are essential steps in LDA signal processing. The more accurate these estimators are, the more detail of the turbulence can be retrieved. We have used a numerical simulation to show that the Wavelet Transform yield an improvement of the estimates of both frequency and arrival time compared to current techniques. Required is, however, that the basic vector functions are Gaussian enveloped sine and cosine functions with a structure similar to the Doppler signal itself.

1. Introduction.

Several different techniques for the processing of Doppler signals from a Laser-Doppler Anemometer (LDA) have been developed (ref. 1 - 4). Most attention has been given to the estimation of the frequency of the Doppler signal, which is a direct estimate for the velocity. An essential problem that every processor has to deal with is the noise, accompanying the Doppler signal which translates as an error in the velocity estimation (ref. 5 and 6). Further processing of the data to e.g. a turbulence power spectrum leads to a "noise floor" which obscures the study of the small eddies in the dissipation range. Reconstruction of the turbulent velocity fluctuations is also hampered by this unavoidable noise problem (ref. 6, 7). However, not only the estimation of the **frequency** needs to be optimised, but also the **arrival time** of the tracer particle, as an error in the arrival time leads to an error in the velocity estimation:

- the actual velocity at the designated time will differ from the estimated velocity because of the change in velocity due to turbulence and
- a part of the Doppler signal is either ignored or replaced by noise because it is not possible to choose the optimum segment of the Doppler signal, decreasing the accuracy of the frequency estimation.

The processing of LDA signals should strive for an optimal estimation of both the frequency and arrival time of the Doppler signal.

2. The influence of noise on the estimators.

The photodetector signal consists of an ideal Doppler signal (fig. 1), accompanied by wide-band noise. Band-pass filtering improves the Signal-to-Noise Ratio (SNR) of the actual Doppler signal (fig. 2), but it does not necessarily improve the accuracy of the frequency estimation: for e.g. trackers, correlators and FT processors, the major part of the noise contribution is in some way suppressed. The noise contribution that determines the accuracy of the frequency estimation is the noise that is -spectrally speaking- indistinguishable from the Doppler signal itself (ref. 6): the accuracy of the estimation of the frequency of the Doppler signal depends on the "local" SNR and not on the "overall" SNR. A relatively simple way to understand the influence of the noise on the frequency estimate is to look at the high resolution spectrum of the actual Doppler signal. In fig. 3 the high resolution spectrum of an ideal and an actual Doppler signal are presented. The difference is caused by the noise contribution. This is an unavoidable, fundamental problem which is encountered by every type of processor. Note from fig. 2 that the apparent arrival time of the Doppler signal is shifted by approximately 250 μ s, which is an artefact from the noise contribution.

In this example the noise contribution is uniform (i.e. white noise), which means that its energy is *on average* independent of frequency in the band of interest. This would only lift the spectrum of the Doppler signal and give not rise to a shift in the estimated frequency, as illustrated in fig. 4.

However, this property manifests itself only over long averaging times and it is in general not true for short time intervals like the transit time of the tracer particle. The longer the averaging interval, the better white noise is approximated, so to use the complete Doppler signal is attractive. On the other hand are the weaker parts of the Doppler signals more vulnerable to noise. Optimisation is a difficult choice between a long averaging interval and elimination of the low SNR parts. Thus a **weighted** average seems the most appropriate. A Wavelet Transform (WT) in which the basic function is a (co)sine with an Gaussian envelope precisely does that. A short description of the WT will be given in the next section.

3. Wavelet transformation.

There is a certain similarity between the Fourier Transform (FT) and the WT. FT is basically a one-to-one projection from a time to a frequency space. The basic vectors in the frequency space are sine- and cosine functions. However, with FT all points within the transformation time window are equally important and the technique is thus not suited for arrival time estimation: the amplitude spectrum does not depend on the position of the Doppler signal in time (ref. 8). This is different with Wavelet Transforms (WT).

WT is a projection from time into a frequency-time space. The basic vectors (functions) are time-limited functions with a self similarity. This means that all the functions can be obtained from a single function by scaling (expansion/compression in time, equivalent to frequency) and shifting (in time) (ref. 9). The WT is a transformation into a two-dimensional space, in this case time-frequency. We will use as basic vector functions the Gaussian enveloped cosine and sine functions:

$$x_1(t) = \sqrt{a} e^{-\frac{1}{2}\left(\frac{at'}{\sigma_t}\right)^2} \cos[\omega_0(at')]]$$

$$x_2(t) = \sqrt{a} e^{-\frac{1}{2}\left(\frac{at'}{\sigma_t}\right)^2} \sin[\omega_0(at')]]$$

in which:

a = scaling factor

t' = t - t_s

t = time
t_s = shift in time
σ_t = sigma of Gaussian envelope
ω₀ = frequency

The factor √a is added for normalisation reasons. The WT can now be performed with the scaling factor (frequency) and the time shift as variables. The values of these variables which fit the signal best (highest value of the WT) yield an estimate for the frequency and the arrival time of the Doppler burst. Intuitively one would expect this is optimal because the functions used in the WT resemble the ideal Doppler signal better than those in the FT. They automatically reduce (but not neglect) the influence of the lower SNR parts and the choice of the time window is not critical because the functions are time-limited themselves. This is illustrated by applying the WT to the noisy Doppler signal of fig. 5, shown in fig. 6, which gives a clear "mountain" in the 3-D space.

To compare WT to e.g. FT based processors, we have used a numerical simulation, which will be discussed in the next section.

4. Numerical simulation.

To study the accuracy the different processing techniques for the frequency and arrival time estimations, a numerical simulation has been performed. For each simulation 10000 ideal Doppler signals of known frequency, as shown in fig. 1, have been generated and a white, Gaussian distributed noise contribution has been added. The thus obtained signal was fed through a band-pass filter (Butterworth 8th order high and low-pass), resulting in "actual" Doppler signals as shown in fig. 2. More details can be found in Appendix A. Using these signals the frequency was estimated using the FT (using the central part of the actual Doppler signal) by curve-fitting a parabola through the highest three points of the amplitude spectrum. The arrival time was estimated using the maximum of the envelope of the Doppler signal by using a similar fit to a parabola.

The estimations by the WT have been obtained by a similar parabola fit in both dimensions. The fit is applied alternating for the frequency- and the time-axis. The next fit gives a new and better value closer to the top. The distance between the new fit and the previous fit is taken as the error. When both the error of frequency and arrival time

drops below a certain value, it is assumed that the top is reached.

5. Results and discussion.

In fig. 7 the histograms of the frequency estimates of the FT on the central part of the Doppler signal (with known position in time) and the WT are shown. The variance of the WT is clearly lower than that of the FT, in this case the error of the FT is approximately 100 % higher than that of the WT. The use of the known position in time (arrival time) of the Doppler signal reduced the variance of the FT technique. However, the use of only the central part increased it. Thus there are different influences which partly cancel each other effects: the use of the central part and thus a shorter duration virtually eliminates the chance of just looking at noisy parts, but neglects the information contained in the weaker parts of the signal. Yet, in all cases that we have tried, the WT gave the lowest variance, although the reduction was relatively small ($\approx 30\%$) when the Doppler signals had a high SNR and FT over the full Doppler signal was used. The major advantage of the WT occurs when the SNR is lower. This is even more clearly illustrated by the arrival time estimation.

The distributions of the arrival time estimates are shown in fig. 8. The envelope detection of the time signal clearly has a larger variance than the WT estimator. This indicates that current processors do not estimate the arrival time very accurate. This is in agreement with measured time interval distributions, which often show a rounding in the vicinity of $\Delta t = 0$, as can be seen -amongst other deviations from the ideal distribution- in fig. 9. A Monte Carlo simulation of errors in the arrival time have shown a similar deviation in this distribution as can be seen from fig. 10.

6. Conclusions.

The estimation of frequency and arrival time of the Doppler bursts is an essential step in the processing of Laser-Doppler Anemometry. Any further processing of these raw data will take the errors in the estimates along. Therefore these errors should be as small as possible.

A numerical simulation has shown that the Wavelet Transform, in which the basic vector functions are Gaussian enveloped sine and cosine functions with a structure similar to the Doppler

signal itself, yields an improvement of the estimates of both frequency and arrival time compared to current techniques. Application of a processor, based on a Wavelet Transformation would result in a data-set with less variance and will thus increase the amount of detail of the turbulence that can be retrieved from it.

References

1. J.C.F. Wang, "Measurement accuracy of flow velocity via a digital-frequency-counter laser velocimeter processor", Proceedings of the LDA-Symposium Copenhagen 1975, pp. 150 - 176.
2. Chr. Caspersen, "The enhanced burst spectrum analyzer", DANTEC Information (June 1992) pp. 17 - 20.
3. T. Nakajima and Y. Ikeda, "Theoretical evaluation of burst digital correlation method for LDV signal processing", Meas. Sci. Technol. 1 (1990), pp. 767 - 774
4. W. Hösel and W. Rodi, "Errors occurring in LDA-measurements with counter signal processing", Proceedings of the LDA-Symposium Copenhagen 1975, pp. 251 - 258.
5. J. Adrian, J.A.C. Humphrey and J.H. Whitelaw, "Frequency measurement errors due to noise in LDV signals", Proceedings of the LDA-Symposium Copenhagen 1975, pp. 287 - 312.
6. R. Booij and J.M. Bessem (editors), Report on Workshop "User's Needs for Laser Doppler Anemometry", Supplement to the Proceedings of the Fifth International Conference on Laser Anemometry, held in Veldhoven (Netherlands) from 23rd-27th August 1993, pp. 13 - 50.
7. H.R.E. van Maanen and H.J.A.F. Tulleken, "Application of Kalman reconstruction to Laser-Doppler Anemometry data for estimation of turbulent velocity fluctuations", Proceedings of the Seventh International Symposium on Applications of Laser Techniques to Fluid Mechanics, July 11th to 14th 1994, Lisbon (Portugal), paper 23.1
8. A. Papoulis, "The Fourier Integral and its Applications", McGraw-Hill Book Company, New York (1962)
9. O. Rioul and M. Vetterli, "Wavelets and Signal Processing", IEEE Signal Processing Magazine, October 1991, pp. 14 - 38.

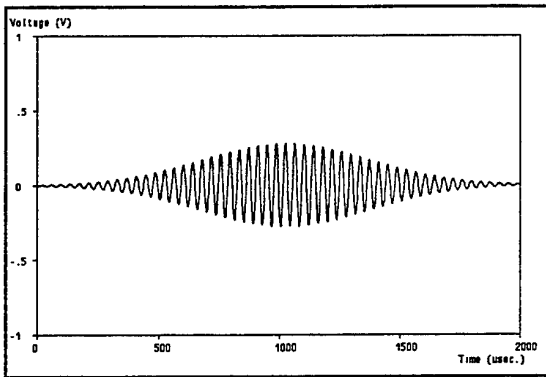


Figure 1: Doppler signal when no noise is present (ideal situation).

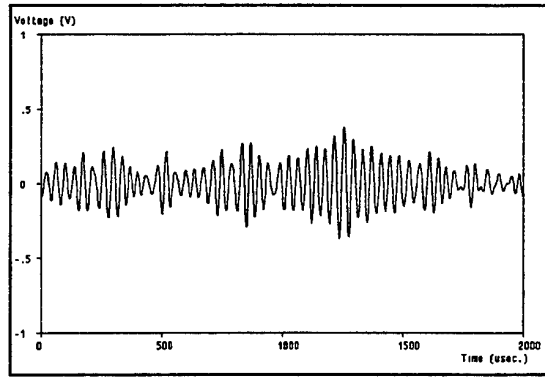


Figure 2: As figure 1, but with narrow band noise added (actual situation). Note the apparent shift in time.

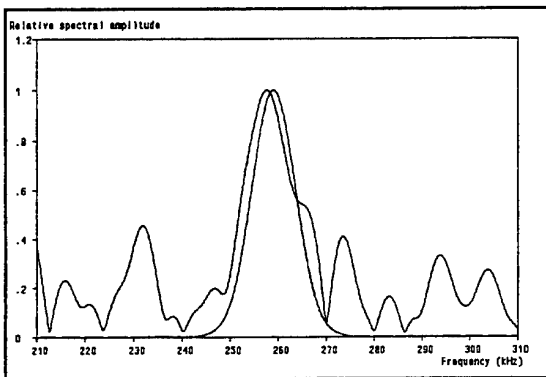


Figure 3: The high resolution spectrum of a noise free and a noisy Doppler signal. See also text.

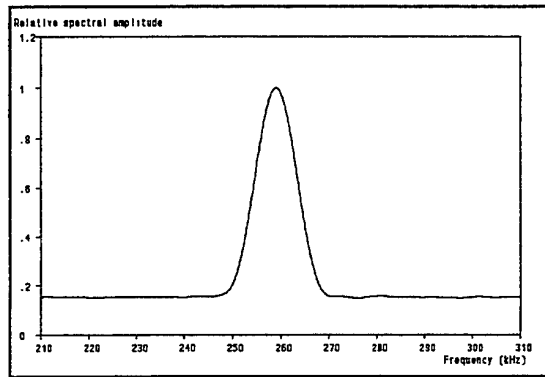


Figure 4: The white property of the noise only shows up in the average of a large number. Compare with figure 3.

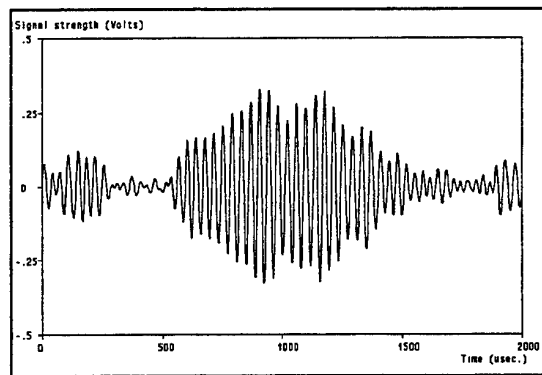


Figure 5: The Doppler signal that was used for the wavelet transformation of fig. 6.

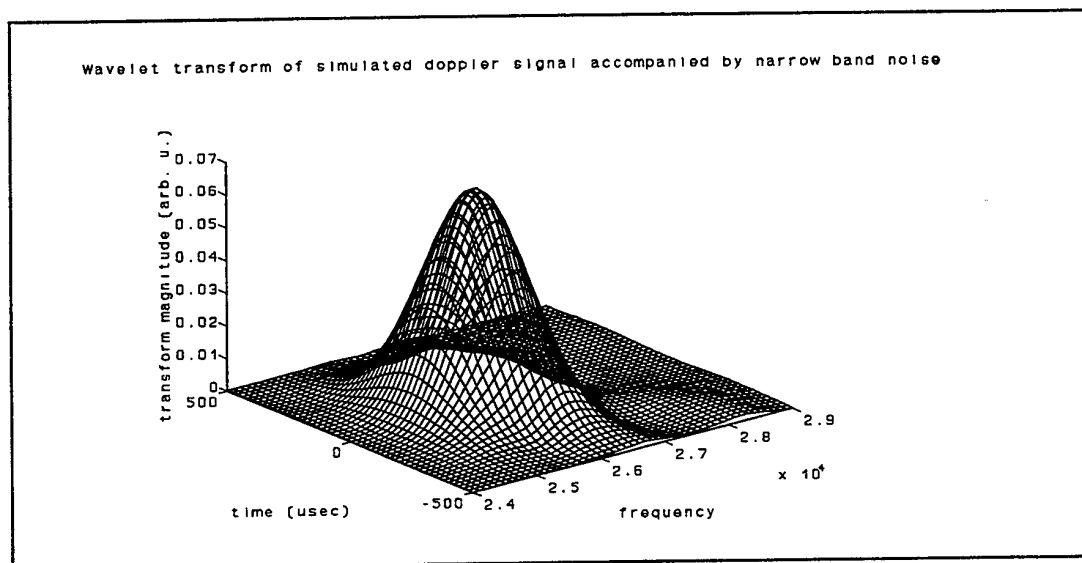


Figure 6: The 3-D plot of the Wavelet Transform of the noisy Doppler signal of fig. 5.

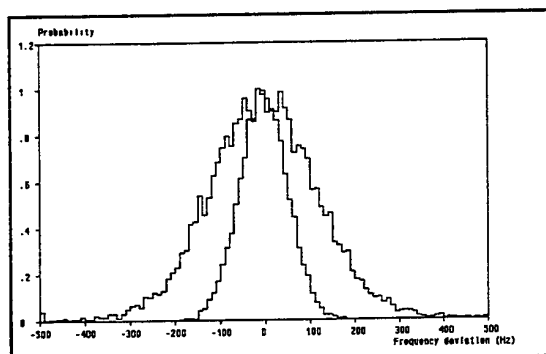


Figure 7: Histograms of the non-normalised frequency estimation distributions for FFT processing using 1/4 of the Doppler signal (outer curve) and wavelet transform (inner curve).

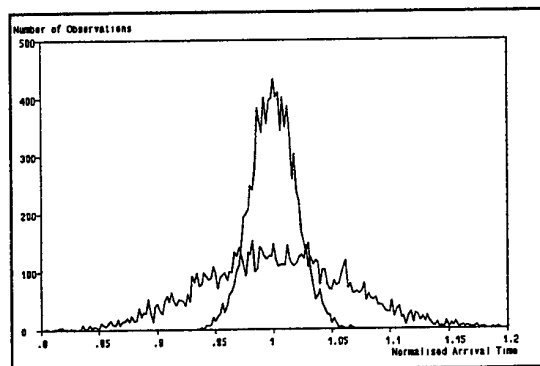


Figure 8: Comparison between parabola fit and wavelet transform method.

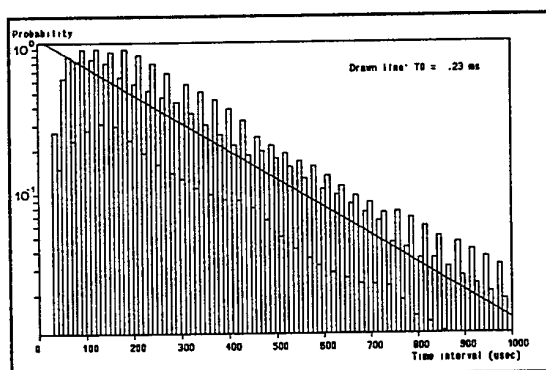


Figure 9: The time interval distribution as retrieved from the AHM4V data file and the result of the curve fit.

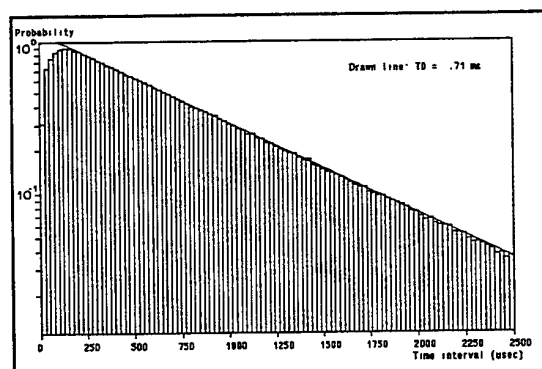


Figure 10: The time interval distribution when inaccuracies in the arrival time estimation of the Doppler bursts occur.

APPENDIX A

The generation of Doppler signals with a narrow-band noise contribution.

Simulated Doppler signals with a narrow-band noise contribution have been generated in the following way:

A cosine wave with a predetermined frequency (which is chosen as a non-integer fraction of the sampling frequency) is multiplied by a Gaussian envelope function. This envelope function is chosen such that the number of cycles in the signal with an amplitude above $1/e^2$ of the maximum amplitude is approximately 30, so that it corresponds with common values for the number of cycles in ordinary LDA systems. This signal is sampled with a frequency which is approximately 20 - 30 times as high as the frequency of the cosine. The number of samples is chosen at either 1024 or 2048. The result is the signal shown in fig. A-1 and we will refer to it as the ideal Doppler signal.

To each of the samples of the ideal Doppler signal is a Gaussian noise contribution added with a variance which is chosen according to the required Signal-to-Noise Ratio (SNR), which is found

by trial-and-error. The result is shown in fig. A-2. The Doppler signal is now completely hidden in the noise.

The signal of fig. A-2 is Fourier Transformed and the resulting amplitude spectrum is shown in fig. A-3. The peak, generated by the Doppler signal, is clearly visible.

The spectrum is multiplied by the (complex) transfer function of a band-pass filter (as is usually applied in LDA practice). The spectrum after this filtering operation is shown in figure A-4. Inverse Fourier Transformation of the filtered spectrum yields a Doppler signal accompanied by narrow-band noise as is shown in figure A-5.

The use of different random numbers for the noise contributions leads to different signals and the effect of the noise on the output of the different estimation algorithms can be found.

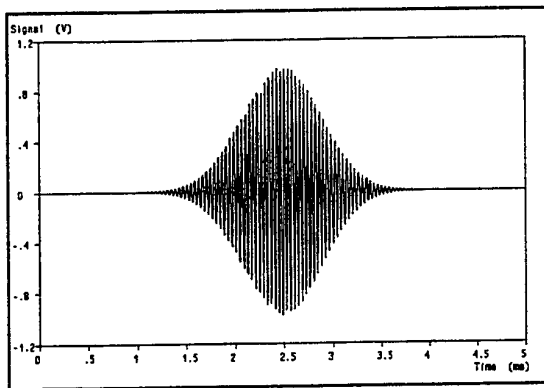


Figure A-1: Ideal Doppler signal.

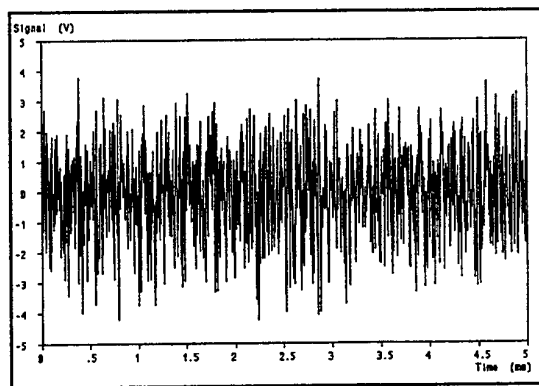


Figure A-2: The ideal Doppler signal with white noise added.

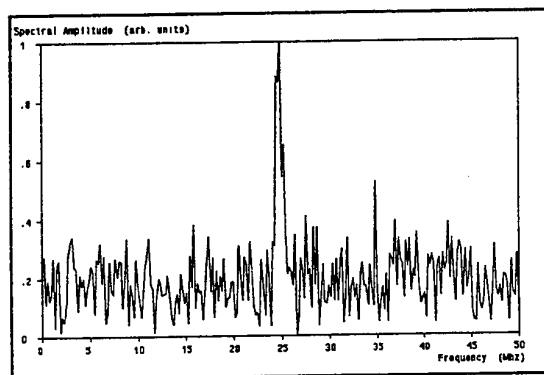


Figure A-3: Modulus of the spectrum of the signal of fig. A-2.

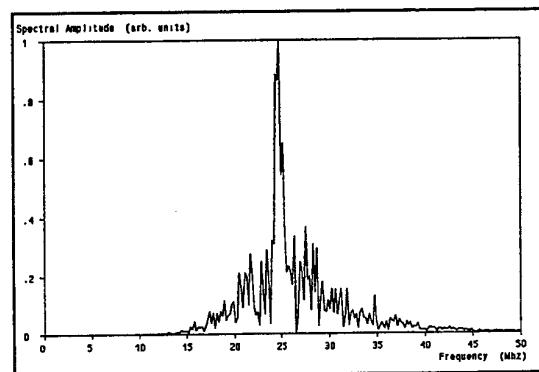


Figure A-4: Spectrum after applying a bandpass filter.

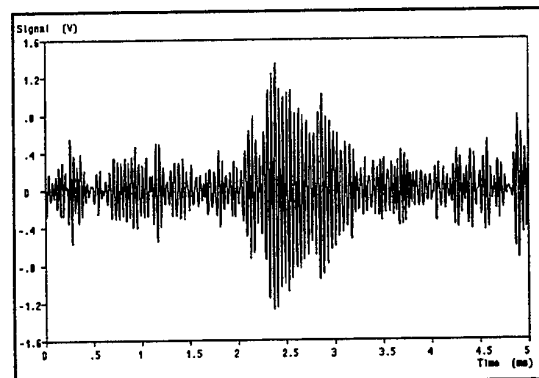


Figure A-5: Doppler signal with narrow-band noise.

Development of a Velocity Profile Monitor in an Unsteady Flow by using Semiconductor Laser Velocimeter with FFT-based Multi-channel Signal Processing

Tadashi Hachiga^{*1}, Noriyuki Furuichi^{*2}, Jyunji Mimatsu^{*2}, Koichi Hishida^{*3} and Masaya Kumada^{*2}

^{*1}Dept. of Automotive Engineering, Takayama College, Shimobayashi 1155, Takayama, Gifu 506, Japan

^{*2}Dept. of Mechanical Engineering, Gifu University, 1-1, Yanagido, Gifu 501-11, Japan

^{*3}Dept. of Mechanical Engineering, Keio University, 3-14-1, Hiyoshi, Kohoku-ku, Yokohama 223, Japan

ABSTRACT

An advanced LDV with a FFT-based multi-channel signal processing using a 1-bit FFT approach has been developed. A semiconductor laser light sheet, a 96-channel plastic optical fiber array, 16-Si APDs and a 2-channel capacious memory system with 8 bit were used in order to attain 16 individual Doppler frequencies simultaneously. Several experiments were conducted in this study to test the performance of the advanced LDV. We confirmed that the advanced LDV could be a useful, compact and inexpensive optical measuring instrument for obtaining a velocity profile.

1. INTRODUCTION

A detailed spatial information of fluid motion is required to analyze the mechanism of fluid flow and heat transfer in turbulent flows. Up to now, there were a few possible instrumentation of line sensing, such as an ultrasonic velocity profiler (Takeda, 1991 and 1995), flow visualization techniques (Sakakibara et al, 1993), multi point laser Doppler velocimeter (LDV) (Nakatani et al., 1978, 1984, 1986 and 1987), and scanning laser Doppler techniques (Durst et al., 1989, and Tanaka et al, 1993). However, such a instrumentation is still very expensive and the processes are time consuming.

The conventional LDV can only furnish an instantaneous velocity at a single point in a fluid. This paper deals with the development of a velocity profile monitor in an unsteady flow by using an advanced multi-point LDV. The signal processing technique of multi-point LDV has been developed by Nakatani et al (Nakatani et al, 1984 and 1986). In this study, the software Fourier transform method using a 1-bit quantization of Doppler signals was utilized in order to increase the flexibility of the signal processor of the advanced multi-point LDV, which enables measurements of the velocity to be in more points and in a wider range. The FFT based approach had an ability to accept signals with relatively low SNR. The software processing algorithm was optimized without changing hardware. The use of 1- bit quantization reduces the size of data storage requirement

significantly (Ibrahim et al, 1990).

The following improvements on an advanced multi-point LDV, which is a compact and inexpensive optical measuring instrument, were made in order to turn a pointwise measurement into a linewise measurement with the FFT-based multi-channel signal processing using a 1-bit FFT approach :

(1) A semiconductor laser light sheet was utilized as a planar light source by replacing the pointwise laser beam. A plastic fiber array, with output ends installed with an optical plug, and Silicon Avalanche Photodiodes (Si APD) with an optical receptacle installed, were used in order to detect the scattered light signal from tracer particles passing through at different points separately in a linewise measuring volume.

(2) The Fourier transform method using 1-bit quantization of Doppler signals was utilized in order to accomplish measurements under the low SNR condition and to increase the flexibility of the signal processor of the advanced multi-point LDV.

Several experiments were conducted in this study to test the performance of the advanced LDV. Measurement of the laminar velocity profile of water in a pipe flow and the Karman vortex behavior in the wake behind a cylinder were taken by using an advanced LDV.

Furthermore, we confirmed that an advanced semiconductor LDV with FFT-based multi-channel signal processing using a 1-bit quantization of Doppler signals is a useful, compact and inexpensive optical measuring instrumentation for obtaining a velocity profile in an unsteady flow.

2. OPTICAL ARRANGEMENT

The specification of the Semiconductor Laser Unit is given in Table 1. A Semiconductor Laser unit which had a visible laser diode with a maximum power of 40 mW and a wavelength of 685 nm was employed as a laser light sheet source. The ambient temperature was not precisely controlled during these measurement. Although the stimulated wavelength

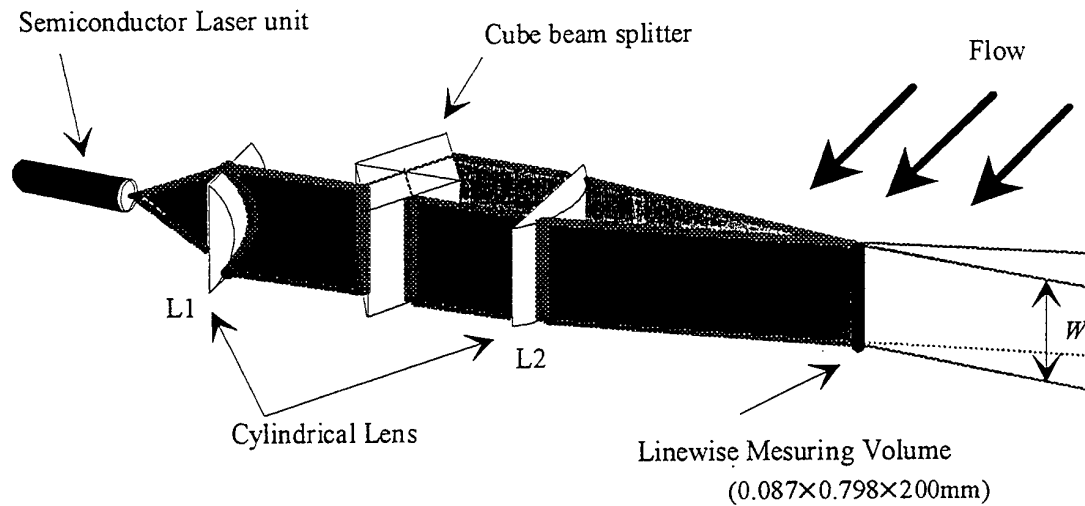


Fig. 1(a) Arrangement of transmitting optics

of the laser diode depends on temperature, it is estimated that the operating temperature changes by as much as 5 °C during the experiments. When using the laser diode under an operating temperature change within ± 5 °C, change in the signal frequency broadening may be smaller than 1 % (Bopp et al, 1988, Durst et al, 1989). Therefore, it is also not essential to

Table 1 Specification of semiconductor laser unit

Production Name	SU-38C/P-40 (Audio-technica Inc.)
Visible Laser Diode	TOLD 9160 (Toshiba Inc.)
Wave Length	685 nm
Beam Power	40 mW

stabilize the wavelength using thermoelectric cooling, provided that the ambient temperature during the measurement could be maintained within ± 5 °C of the temperature at which the LDV system is aligned.

The optical arrangement, which includes the transmitting and receiving modules of an advanced LDV system, is illustrated in Figure 1 (a), (b) and (c). The laser light sheet of the Semiconductor Laser Unit forms a fan-like shape. The laser light sheet passes through cylindrical lens L1 (focal length $F_1 = 25.4$ mm) in order to change the fan-like light sheet into the rectangular-like light sheet and for altering the width (W) of the laser light sheet (as shown in figure 1 (a)). A cube beam splitter (edge length of a cube $L = 50.8$ mm) is used to split the laser light sheet and to make the two laser light sheets parallel to each other. The two parallel light sheets, which pass through the cylindrical lens L2 (focal length $F_2 = 100$ mm), intersect in line segments at the focal line. Namely, the two laser light sheets were focused and crossed in a linewise measuring volume where a fringe pattern was formed. The intersection of line segments of the two incident light sheets defines the measuring region in the flow field. The cross angle of the laser light sheet was 12.554 ° and the core diameter of the optical fiber was 0.24 mm, which corresponds to about 40000 μm^3 of the measuring volume. The velocity components, perpendicular to the direction of the line intersection of the two incident laser light sheets, can be measured.

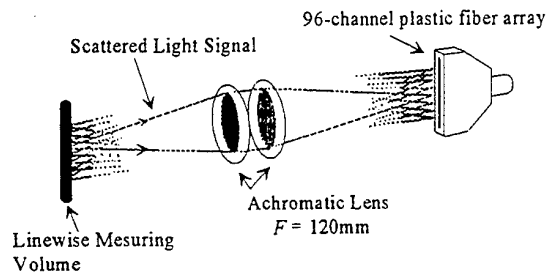


Fig. 1(b) Arrangement of receiving optics

As shown in figure 1 (b), the linewise measuring volumes are focused on the 96-channel receiving linear plastic fiber array of 24 mm in length. The scattered light signal from tracer particles, passing through at different points separately in a

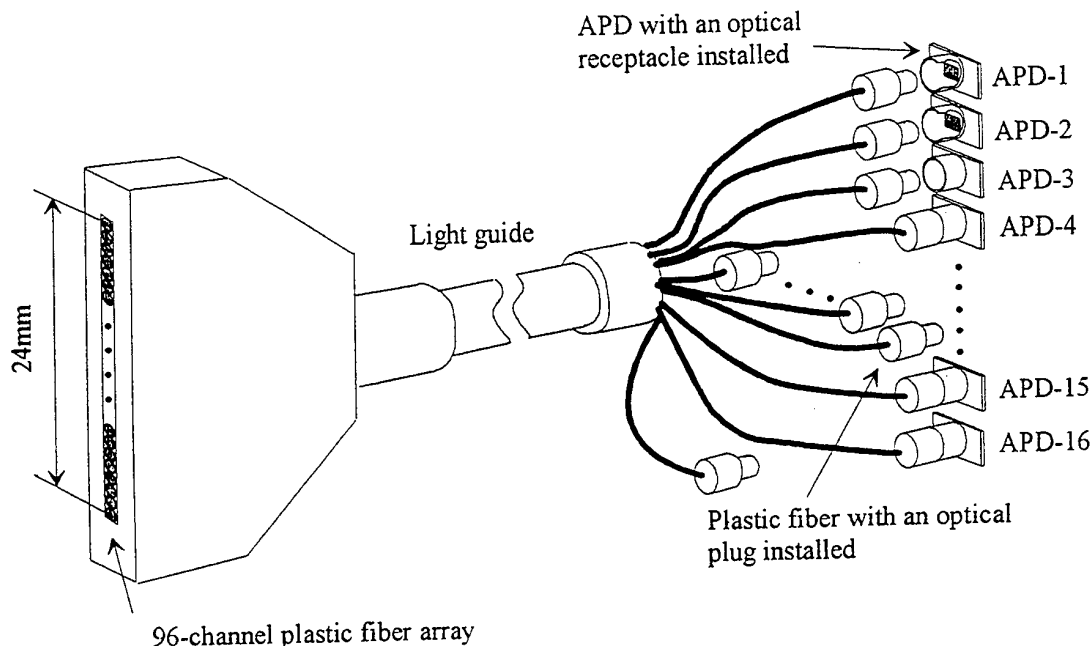


Fig. 1(c) Arrangement of receiving fiber unit

linewise measuring volume, is collected by the achromatic lens (focal length $F = 120$ mm) and received using plastic optical fiber array. As shown in figure 1 (c), the linear optical plastic fiber array had 96 plastic optical fiber and we can select any of fibers of the 96 plastic fibers as an active channel for measuring objectives. Their numerical aperture is about 0.5 and their diameter is 0.25 mm. The receiving plastic fibers were equally spaced in 1 mm length in this study. The output ends of receiving plastic fibers are installed with optical plugs. The optical plugs may be installed arbitrarily on any of plastic fibers of the 96 plastic fibers. 16-Si APDs are used as a photodetector. Any 16 scattered light signals from the scattered light signals, which are received with the optical fibers with an optical plug installed, can be transmitted to the 16-Si APDs with an optical receptacle installed. A plastic fiber array, with output ends installed with an optical plug, and Silicon Avalanche Photodiodes (Si APD) with a receptacle installed were used in order to ease the system construction and to increase flexibility.

3. SIGNAL PROCESSING

LDV signal processing has always encountered the difficulty of discrimination of Doppler burst signal from electronic and optical noises. Various noise sources prevent the signal processor from acquiring low SNR signals, especially in measurements using a semiconductor laser.

The FFT based signal processor usually provides more

accurate information than other types of signal processors for LDV in an insufficient noise environment. In the present study, a transient memory system of 1M word capacity was employed to accomplish measurements under the low SNR condition with FFT-based multi-channel signal processing using a 1 bit FFT approach in order to attain multi-channel individual Doppler frequencies simultaneously.

Hardware system

Figure 2 schematically illustrates the hardware system block diagram of an advanced LDV used in the present study. The hardware system consists of 16-Si APDs, a 16-channel pre-amplifier, a 16-channel active loop filter unit, a 16-channel comparator with amplifier and a 2-channel First-In First-Out (FIFO) memory system for 1M word capacity with 8 bit. Offering non-stop continuous collection of 16 input signals on parallel channels at the same time, the FIFO memory hardware system was placed on the host computer bus under software control.

The hardware system accepts 16 input signals, digitizes them at 1-bit resolution, passes them onto an on-board FIFO data memory and then places them on the computer bus interface under software control. The host computer in the present system is designed to be compatible with an IBM-PC/AT microcomputer system. Data may then be stored in the host-computer memory, saved on disk, and processed by FFT software. The calculated results were saved on disk, or displayed on the

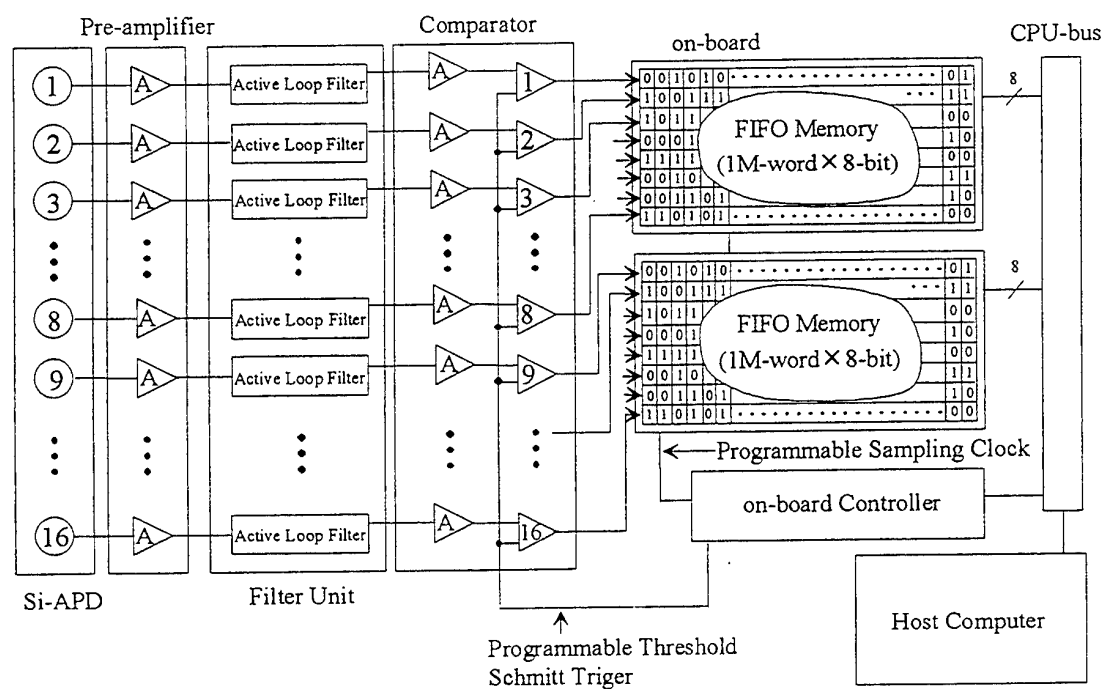


Fig. 2 Hardware system block diagram

screen or printer.

In the present study, photo-detector and amplifiers were optimized with a lower noise design. It was, of course, significant that the technique for signal processing with a poor signal had to be discussed to improve the performance of the signal processor. The photo-detector and pre-amplifier used a Si-APD S2383 (Hamamatsu Photonics.) and an instrumentation amplifier module with high common mode rejection using an AD847 or an AD797 (Analog Device) operational amplifier.

The 16 scattered light signals were converted into 16 individual Doppler burst voltage signal by 16 Si-APDs. These voltage signals were transferred to 16 pre-amplifiers with their gain constant. These signals, after filtering, were used as the Doppler burst signal for LDV, and led to 16 comparators via amplifiers. The gain of each amplifier is adjustable with external variable resistance. The peak amplitude of signals from the 16 Si-APDs is dependent on the Gaussian intensity distribution of the incident laser light sheet and varies along the detector due to the gain of 16-APD under the same bias voltage. Because the amount of dispersion of the gain of 16 Si-APD under the same bias voltage cannot be disregarded, the amplitude of signals from the 16 Si-APD by the use of such a laser light sheet was required to be made equal by the gain adjustment of the each

amplifier.

Figure 3 shows the schematic of signal processing. The digitized data at the programmable threshold Schmitt trigger level using comparators passes to an on-board First-in First-out (FIFO) data memory bank under software control. These 16 digitized signals were stored by a programmable sampling clock as two word data of 8 bits in 2-channel FIFO memory for 1M-word \times 8-bit capacity (as shown in figure 2), which corresponds to 0.1 sec storage at 10 MHz sampling rate, with which the performance was enough for the measurement of the present study. The sampling frequency was variable up to 20 MHz under software control. FIFO data was then transferred to the host computer bus interface under software control.

Software processing

It has recently become important to employ a method for detecting burst signals from real signals including noise. Hishida et al (Hishida et al, 1989 and Kobashi et al, 1990 and 1992) had discussed this method of frequency detection using FFT based signal processing. In this study, the Doppler burst signal detected by the APD was analyzed to obtain velocity information using a one-bit FFT method (Ibrahim et al, 1990) in addition to the method of frequency detection which is the software signal processing based on FFT burst analyzer

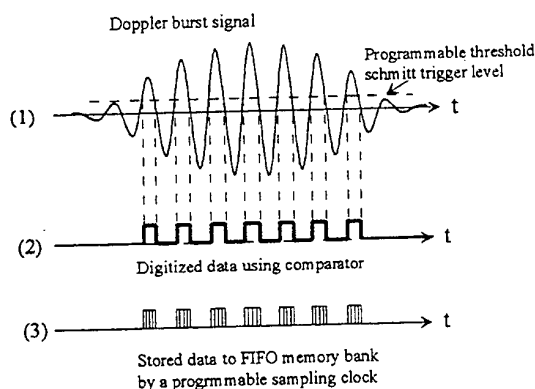


Fig. 3 Schematic of signal processing

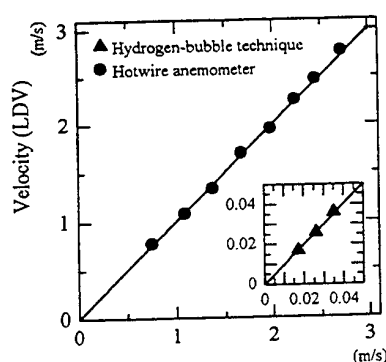


Fig. 4 Comparison of velocity measurement using LDV with other techniques

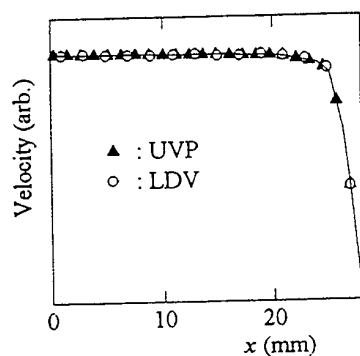


Fig. 5 Velocity profile in the entrance region of laminar pipe flow

x : the distance from the center axis of the pipe in the direction perpendicular to the centerline

technique. In most cases, when a photo-detector can obtain Doppler burst signals clearly, it will also be able to detect burst signals. After using these methods, an adjusted Gaussian interpolation scheme in frequency space was used in order to reduce the influence of amplitude modulation of the burst signals. The determination of whether, or not, the sampling data was a Doppler burst signal was validated using the procedure described by Hishida et al (Hishida et al, 1989 and Kobashi et al, 1990 and 1992).

The Fourier transform method using 1-bit quantization of Doppler signals was utilized in order to accomplish measurements under the low SNR condition and to increase the flexibility of the signal processor of the advanced multipoint LDV, which enables measurements of the velocity to be in more points and in wider range. Because of the software approach, the processing algorithm was optimized without having to change hardware. Furthermore the use of 1-bit quantization reduces the size of the data storage requirement significantly.

As for the algorithm for signal detection, the processing of all parts of the storage memory data needs plenty of FFT calculations, although the method has benefit for velocity measurement in an unsteady flow.

4. MEASUREMENTS IN A FLUID FLOW

Several experiments were conducted in this study to test the performance of the advanced LDV system. The laminar velocity profile of water in a pipe flow and the Karman vortex behavior in the wake behind a cylinder were measured in a pipe fluid flow. The flow was marked with tracer particles for velocity measurement. Polystyrene particles of 5 μm mean diameter were used as the tracer particle in measurements of velocity in the flow of water. In case of flow of air, fine water droplets produced by a nebulizer were used.

Comparison of the other techniques

The reliability of the LDV system is confirmed by comparing the performance of LDV with other techniques using a hotwire anemometer or a hydrogen-bubble technique. The measurement of the various reference velocities were taken by using an advanced LDV and a hotwire anemometer at high velocity (0.8 to 3 m/s) in air flow, and flow visualisation techniques using a hydrogen-bubble technique at low velocity (up to 0.5 m/s) of water in pipe flow. The results are shown in figure 4. The comparison of LDV with hotwire anemometer as well as a hydrogen-bubble technique indicated a good agreement within an accuracy of 3.1 %.

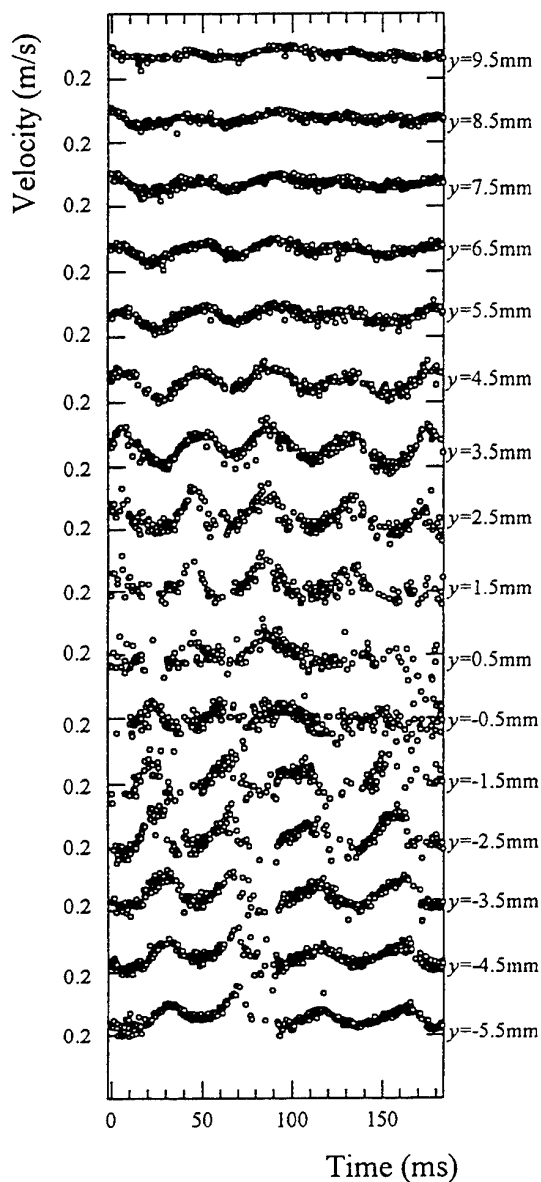


Fig. 7 Typical time series variation of velocity in the wake behind a cylinder

cylinder diameter $d=3$ mm, $x=3d$.

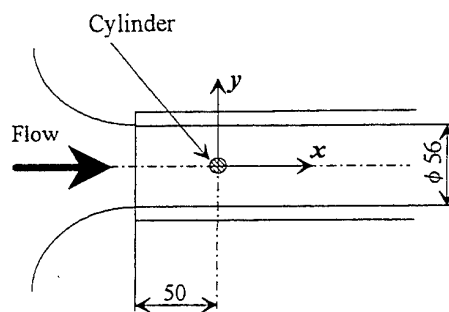


Fig. 6 Coordinate in flow

The laminar velocity profile of water in a pipe flow

The laminar velocity profile in a straight pipe of 56 mm diameter was measured at 65 mm from its entrance, connected with a nozzle. Measurements of the velocity profile in the entrance region of laminar pipe flow were taken by using an advanced LDV and an ultrasound velocity profile monitor (UVP). The results are shown in figure 5. The comparison of LDV with UVP indicated a good agreement with both techniques within an accuracy of 3 %.

Karman vortex flow

The measurement results of the Karman vortex flow demonstrated that the advanced LDV is a powerful tool in fluid mechanics. Vorticities in the Karman vortex flow were measured. The coordinate axes in the flow are shown in Figure 6. The fluid was water. The influence of the distance y along each measuring point on vorticity in the Karman vortex flow was investigated. Typical example patterns are shown in Figure 7. The experimental data of the Karman vortex frequencies n in cycles per second were in good agreement with the calculated value of n from the equation $nd/V=St$, where St is about 0.207 for the circular cylinder V is a velocity and d is a cylinder diameter.

Since we can obtain the information of the velocity field as a function of time and position, this method could have significant advantages as a tool of fluid flow and heat transfer.

5. CONCLUSION

We have developed an advanced multi-point LDV, which enables measurements of the velocity to be in more points and in a wider range, using a FFT-based multi-channel software signal processor. The FFT-based signal processor using 1-bit quantization of Doppler signals enabled the advanced multi-

channel LDV to accomplish measurements under the low SNR condition and to increase flexibility of the signal processor. This method enables measurements of the flow field as a function of position and time. An advanced multi-point LDV using a capacious memory system could be a useful compact and inexpensive optical measuring instrument for obtaining a velocity profile in an unsteady flow.

6. ACKNOWLEDGMENT

The authors are grateful to Prof. M. Maeda for his useful discussions. We also thank Dr. H. Morikita for his advice on construction of the hardware.

7. REFERENCE

- Ibrahim, K. M., Werthimer, G. D. and Bachalo, W. D., "Signal Processing Considerations for Laser Doppler and Phase Doppler Applications", 5th Int. Symp. on Applications of Laser Techniques to Fluid Mechanics, Lisbon, (1990), pp. 291-316.
- Bopp, S., Durst, F., M Durst, Müller, R., Naqwi, A., Tropea, C. and Weber, H., "Small laser-Doppler anemometers using semiconductor lasers and avalanche photodiodes", Proc. 4th Int. Symp. on Applications of Laser Anemometry to Fluid Mechanics, Lisbon, Portugal, 1988, July 11-14, pp. 315-337
- Durst, F., Müller, R., and Naqwi, A., "A semiconductor Laser-Doppler-anemometer for applications in aerodynamic research", IEEE (1989), pp. 215-225
- Kobashi, K., Hishida, K. and Maeda, M.; "Measurement of fuel injector spray flow of I.C. Engine by FFT Based Phase Doppler Anemometer", Proc. of 5th International Symposium Applications of Laser Technique to Fluid Mechanics, Lisbon (1990) pp. 21.2.
- Kobashi, K., Hishida, K. and Maeda, M.; "Multi-Purpose High Speed Signal Processor for LDA/PDA Using DSP Array", 1992, Sixth International Symposium Applications of Laser Technique to Fluid Mechanics, 21.6.1-21.6.6
- Hishida, K., Kobashi, K. and Maeda, M., "Improvement of LDA/PDA using a digital signal processor (DSP)", 3rd International Symposium on Laser Anemometry Advances and Applications/ Swansea, (1989), S2.1-S2.10
- Nakatani, Y., Yorisue, R., and Yamada, T., "Simultaneous Measurement of flow velocities in multipoint by the laser Doppler velocimeter", proceeding of the Dynamic Flow Conference, (1978), pp. 583-589
- Nakatani, N., Uehara, A., Tokita, M., and Yamada, T., "Simultaneous measurement of flow velocity at several points in premixed flame by the LDV using phase diffraction gratings", Proc. 2nd Int. Symp. on Applications of Laser Anemometry to Fluid Mechanics, Lisbon, Portugal, 1984, July 2-5, paper 13.2
- Nakatani, N., Maegawa, A., Izumi, T., and Yamada, T., "Advancing multipoint optical fiber LDVs-Vorticity measurement and some new optical systems", Proc. 3rd Int. Symp. on Applications of Laser Anemometry to Fluid Mechanics, Lisbon, Portugal, 1986, July 7-9, paper 8.4
- Nakatani, N., Yamada, T., and Sakabe, T., "Measurements of turbulent structures in premixed flame with multi-point LDVs", (1987), pp. 11.-19
- Sakakibara, J., Hishida, K., and Maeda, M., "Measurements of thermally stratified pipe flow using image-processing techniques", Experiments in Fluids 16, 82-96 (1993)
- Takeda, Y., "Development of an ultrasound velocity profile monitor", Nuclear Engineering and Design Vol. 126, (1991), 277-284
- Takeda, Y., "Instantaneous velocity profile measurement by ultrasonic Doppler method", JSME International Journal, Series B, Vol. 38, No. 1, (1995), 8-16
- Tanaka, S. and Murata, S., "Scale effect in cross flow fans", Trans. JSME (in Japanese), Vol. 59, No. 560, (1993-4), pp. 151-158

SESSION 32

Two-Phase Flows I

PARTICLE DISPERSION IN AN ACOUSTICALLY EXCITED ROUND JET

R. Hoffmann and A.L.N. Moreira

Instituto Superior Técnico
Dept. of Mechanical Engineering
Av. Rovisco Pais, 1096 Lisboa Codex, Portugal

ABSTRACT

The polydispersion of solid particles in the near field of an acoustically-excited unconfined round jet is studied based on simultaneous time-resolved measurements of velocity, size and particle concentration together with qualitative information obtained from laser sheet visualisation. The jet issues from a long pipe with a Reynolds number based on the average velocity of 1.5×10^4 and is laden with a mass load of 65% of spherical glass beads with a normal size distribution with a number-average particle diameter of 50 μm and a standard deviation of 15 μm . The flow is excited by a loudspeaker at $95 < f < 500\text{Hz}$, which gives rise to a nearly longitudinal wave at the nozzle exit with local intensities of velocity fluctuations about 35%.

The results identify the occurrence ring vortices released at the nozzle exit which lost their coherence at about three nozzle diameters, downstream of which the flow may be dominated by a helical mode. The effect of the coherent structures is to move the particles radially as they fly through the vortex centers, thus providing a way to control particle concentration in practical systems. However, comparison of the present results with others published in the literature shows that, even for favourable conditions of small Stokes number and high forcing amplitudes, the process of actively control particle dispersion is strongly dependent on boundary conditions.

1 - INTRODUCTION

Large-scale flow structures have been shown to have an important role in the mechanisms of fuel droplet dispersion, vaporisation and gaseous phase mixing in combustion systems (e. g., Gutmark et al., 1988, Jarosinski et al., 1988, Lázaro and Lasheras, 1992, Wen et al., 1992, Yu et al., 1991). When the flow field is dominated by these structures, combustion rates are likely to depend on their characteristic times and made suitable to burn solid and low calorific fuels are to be burnt. To achieve this, actively controlled oscillations have been

used to perturb the flow and to form large scale structures with optimised size and time scales (e. g., Smith et al., 1990, Marchant et al., 1992, Schadow et al., 1992, Schadow and Gutmark, 1992). In this context, the present work considers a particle laden turbulent jet because it reproduces the main features of the fuel injection devices used in most of solid fuel combustion systems.

The influence of a forcing frequency in the process of particle dispersion in mixing layers has been addressed in planar shear layers (e. g., Lázaro and Lasheras, 1992 and Wen et al., 1992) and in turbulent round jets (e. g., Longmire and Eaton, 1992 and 1994). Most of the works reported in the literature consider low particle mass loadings ($< 12\%$) due to the limitations imposed by the performance of the experimental techniques available. However, it was speculated that higher mass loadings, which are more representative of real conditions, may lead to particle-particle interactions in particle clusters even under moderate overall particle loadings (Longmire and Eaton, 1994). Furthermore, previous works have considered forcing waves with amplitudes giving rise to longitudinal velocity fluctuations up to 10-12%. Larger velocity fluctuations may, however, alter particle dispersion since the energy fed into the flow is higher.

More fundamental work is, therefore, required to understand the influence of the amplitude of the forcing waves on particle dispersion in actively controlled jet flows. The present study considers particle mass loadings up to 65% and forcing amplitudes yielding velocity fluctuations up to about 40%.

The remaining of the paper is organised in three sections as follows: the next section describes briefly the experimental arrangement; the results are presented and discussed in section 3 and the main findings are summarised in section 4.

2 - EXPERIMENTAL ARRANGEMENT

The flow configuration considered in the present study consists of a jet issuing vertically downward from a pipe ($L/D = 76$) with 23 mm in diameter, Figure 1. Glass

beads are introduced in the jet by gravity with a steady mass loading up to 65%, as controlled by calibrated pipettes issuing from a container located within the air stream upstream of the pipe. The particle loading is varied by changing the number of operating pipettes from one to five.

The glass beads used in the present study follow closely a normal size distribution with a number-average particle diameter of 50 μm and a standard deviation of 15 μm . The air flow to the jet is supplied at a steady rate of $4.15 \times 10^{-3} \text{ m}^3/\text{s}$ and the corresponding Reynolds number at the jet exit is 1.5×10^4 , based on a bulk velocity equal to 10 m/s.

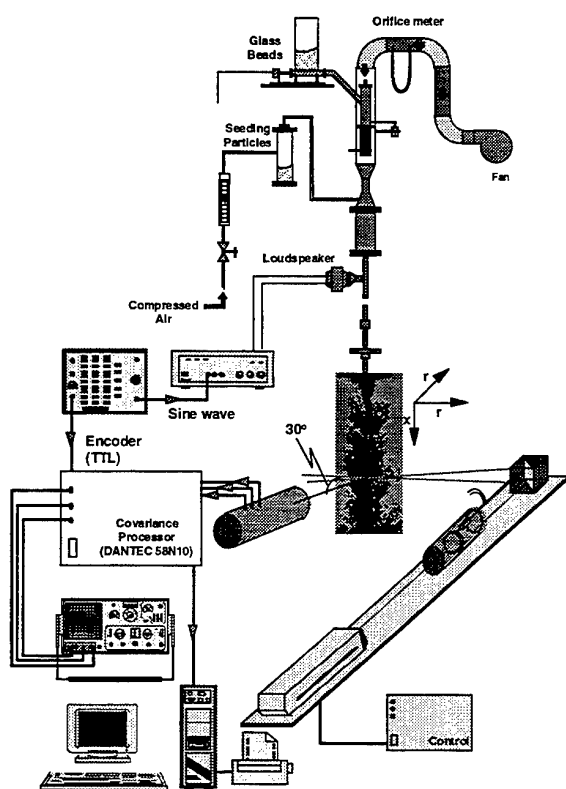


Figure 1 - Experimental set-up

The forcing device consists of a standard 100 mm diameter 16 W loudspeaker (Uni-Power). The speaker mouth is covered with a converging nozzle with a diameter of 8,5 mm, which is attached normally to the pipe about 1000 mm upstream of the exit plane. The analogue signal to control the oscillatory motion of the speaker membrane consists of a pure sinusoidal wave produced by a signal generator and sent to the membrane through a low-pass filter and a standard audio amplifier.

Simultaneous measurements of velocity, size and volume flux of particle concentration are obtained with a Dantec Particle Dynamics Analyser based on an argon-ion laser light source at 514.3 nm (400 mW nominal). The transmitting optics (DANTEC 55x) are in the standard single component form and included a Bragg cell operating at 40 MHz to provide the necessary light-frequency shifting for sensitivity to flow direction. A 310 mm front lens were used in the current experiments, resulting in a fringe pattern of 2.67 microns spacing. The receiving optics (DANTEC 57 x 10) are placed at 30° to the forward direction, which implies that the scattered light was predominantly of first order refraction for the glass beads. Furthermore, polarisation of the incident beams is used to eliminate the contributions of surface reflection to the scattered light. For the experiments reported here, polarisation normal to the plane defined by the beams is used to decrease the magnitude of the oscillations on the phase calibration curve (e. g., Saffman, 1986). Signal processing is performed with an analogue covariance processor operated in real time for both frequency and phase measurements (DANTEC 58N10) and interfaced with a 16 bit microcomputer.

For the measurements of the gaseous phase velocity, the air is seeded with aluminium oxide particles (nominal 1,0 μm) introduced into the airflow upstream of the jet tube by cyclone generators. Although the sizes of both, the glass and the alumina particles, cannot be measured simultaneously, it is shown that the optical sizes of the alumina particles fall outside the size range of the glass beads, thus allowing to discriminate the gaseous phase velocity from the particulate velocity. Therefore, the gas-phase velocity was identified with that of particles with a measured optical size under 5 μm .

The behavior of the particulate phase is characterised based on the analysis of three size classes, say 30-40, 40-50 and 50-60 μm . Each measurement is performed to acquire at least 1500 samples in each of these size ranges, for which a total of around 50 000 samples is required for a validation rate of around 75%.

Apart from the signal processing technique used for the unforced flow, phase-resolved measurements are also conducted in the present study. This is performed by using the encoder of the PDA processor and driven by software typical of rotating machinery. The loudspeaker wave form is used to trigger a set of synchronised TTL pulses, which are used as a phase reference to tag the data during data acquisition. Phase-locked measurements are obtained within a phase window of 10°, which corresponds to a duration of about 150 μs . In this case, the number of forcing cycles used to form the conditional measurements depends on the total number of samples required by the signal processor and on the number of samples acquired during each window, which in turn depends on the rate of particles passing through the control volume leading to a validated Doppler burst. For the flow conditions considered here and for a population of 50000 samples,

the number of cycles used to form the phase averages are usually over 700.

Flow visualisations is also obtained in this paper to provide qualitative information about the effect of the forcing acoustic wave on the formation of coherent structures along the jet flow and their influence on particle dispersion. The airflow was marked with either Titanium (IV Propoxide, 98%) smoke or alumina particles which were introduced upstream of the jet tube. A cylindrical lens was used to spread a continuous 1,5 mm Argon-Ion laser beam (2W) and the resultant light sheet aligned perpendicularly to the jet axis. The flow was photographed with a Nikon F801S 35 mm camera aligned perpendicular to the light sheet and registered on a Kodak Tmax 3200 ASA film. The time exposure could be varied up to 1/8000 seconds, which corresponds to 1/42 of the period of the most amplified forcing frequency (190Hz).

3 - RESULTS AND DISCUSSION

Prior to the analysis of particle-laden jets, the acoustic behavior of the air jet was carefully analysed with the ultimate objective of identifying the forcing frequency which maximises the amplitude of the oscillatory motions. The analysis was carried out up to forcing frequencies of 500Hz and Table 1 lists sample results for selected frequencies in terms of the resulting axial (u') and radial (v') velocity fluctuations measured at the centreline of the nozzle exit. In these tests, the amplitude of the electrical signal was kept close to the maximum limit at which the loudspeaker could be operated (1,5 Volt) and only forcing frequencies above 95 Hz are considered, because lower frequencies would require large amplitude of the forcing waves.

Table 1 - Axial and radial velocity fluctuations measured at the center of the nozzle (amplitude of the signal = 1,5 V)

Frequency (Hz)	Strouhal (fD/U_j)	u'/U_j (%)	v'/U_j (%)
Unforced	-	4,91	3,60
95	0,15	11,43	5,57
190	0,30	34,53	12,00
285	0,45	25,83	11,87
380	0,60	12,89	10,35
500	0,75	11,21	10,80

Table 2 - Axial and radial velocity fluctuations measured at the nozzle exit for different forcing amplitudes of the loudspeaker (forcing frequency = 190 Hz)

Forcing Amplitude (Volts)	u'/U_j	v'/U_j
Unforced	4,91%	3,60%
0,5	16,04%	7,11%
1,0	24,57%	10,97%
1,5	34,53%	12,00%

The results show that maxima velocity fluctuations occur for a forcing frequency of 190Hz, which is close to the second harmonic of the natural frequency of the pipe, for a half wave between the plenum and the nozzle exit. For these conditions, the Strouhal number, St , defined with the jet diameter, D , and the bulk velocity, U_j is about 0,3. It is worth noting that this forcing frequency also causes a minimum anisotropy ratio between the radial and the axial velocity fluctuations (v'/u'). The results also show that this ratio decreases as the forcing amplitude increases and, therefore, it is likely that the wave propagates at the exit of the jet tube as a longitudinal planar wave.

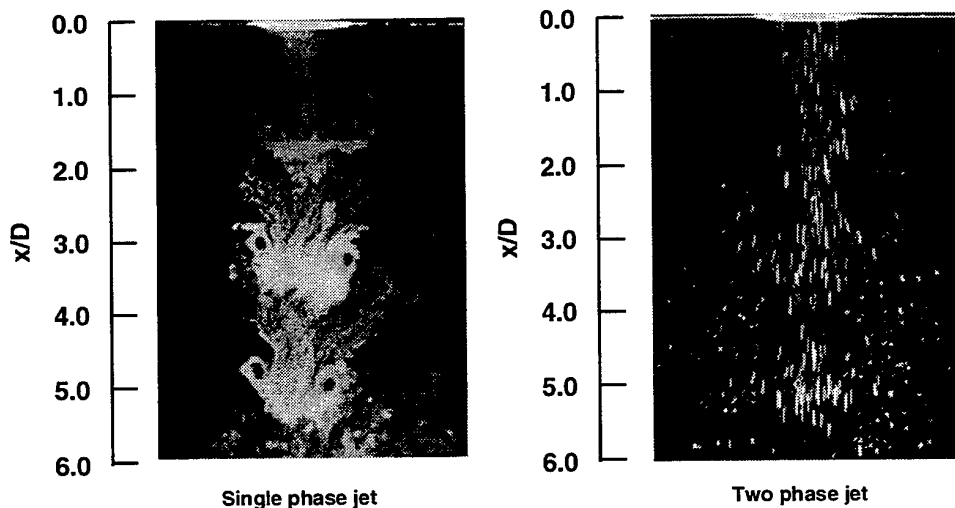


Figure 2 - Visualization of the acoustically forced air jet and of the acoustically forced particle-laden jet ($f = 190\text{Hz}$, $St = 0.3$)

Figure 2 shows photographs of the single-phase and of the particle-laden flows obtained with the flow forced at 190Hz (Strouhal = 0,3) and allow to visualise the main features of both flows up to six jet diameters. The photographs were obtained with a time exposure of 1/4000 which corresponds to 1/21 of the period of the forcing wave. The results for the single-phase air jet show the formation of large vortex rings which move downstream with a constant separation of about two jet diameters. These structures strongly affect the dispersion of particles in the two-phase flow, where dense clusters of particles are identified as reported by Longmire and Eaton (1992) for a round jet excited at $St = 0,26$ with a forced velocity fluctuation around 11%. The images suggest that some particles flung out from the jet downstream of the vortex rings due to the radial momentum acquired from the fluid motion, while others are pulled inward due to a stretching effect caused by the vortex rings in the core flow. This effect results in the black holes observed in the particle-laden jet, which should correspond to regions with very few particles as in other experiments reported in forced mixing layers, e. g., Lázaro and Lasheras (1992) and Wen et al. (1992).

Figure 3 shows the cyclic variation of the axial velocity along the centerline of the particle-laden jet up to $x/D = 5.5$ and quantifies the behavior described before. The analysis considers the gaseous and the particulate phases, namely for three size classes of particles (30-40, 40-50 and 50-60 μ m) for which the Stokesian relaxation time is 9.8, 16.2 and 24.3 ms, respectively. The plots show that the acoustic oscillations dominate the gas and particle flows of up to a distance of about three nozzle diameters, but further downstream the flow coherence is lost and the flow may be dominated by a helical mode.

Phase averaged values of particle concentration and axial velocity along the centreline are shown in Figures 4 and 5, respectively. The results in Figure 4 quantify the trends observed in the photographs, in that particles accumulate in clusters downstream of the vortex rings, as identified by the peaks in the curves. The first cluster forms at $x/D=0.5$, but the separation between clusters is not constant and depends on particle size in contrast with other results reported in the literature (e. g., Longmire and Eaton, 1992).

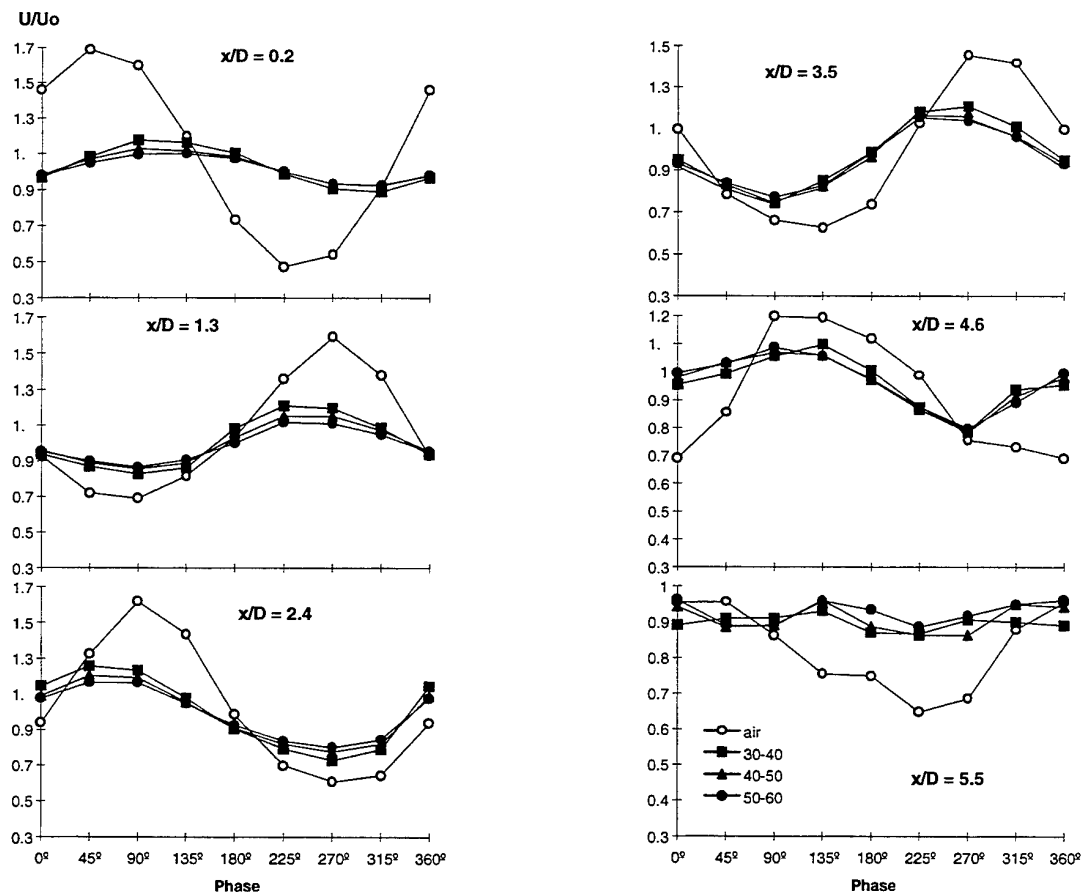


Figure 3 - Time variation of the axial velocity along the centerline of the particle-laden acoustically forced jet ($St = 0.3$)

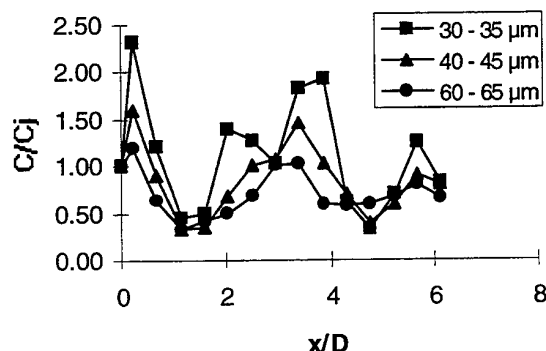


Figure 4 - Centerline variation of the phase averaged particle concentration (forcing frequency = 190 Hz)

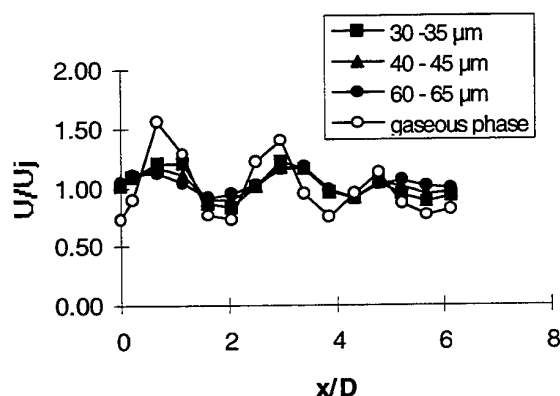


Figure 5 - Centerline variation of the phase averaged axial velocity (forcing frequency = 190 Hz)

The results in Figure 5 show that, although the velocity of the particles varies along the axial distance with an amplitude smaller than that of the gaseous phase (namely due to the effect of particle inertia) all the particle sizes has the same velocity as they move downstream. It is worth noting that the periodic fluctuations in the mean particle velocity are correlated with the local flow structures and have amplitudes about twice those reported by Longmire and Eaton (1992) in a similar flow excited at about 1/3 of the amplitude used here. Furthermore, the peaks in the particle velocity distribution occur in the regions between clusters, while the valleys occur near the clusters. Therefore, the maximum particle concentrations occur in the region where the air flow has been decelerated down to the minimum velocity in the axial direction.

Figure 6 shows the variation of the time averaged particle concentration along the centerline for the the three size classes considered before. The results show that the

smallest particles accumulate in a very short distance downstream the jet exit up to about 2.4 diameters, where they reach a concentration 2.5 times larger than the concentration at the exit of the jet. A qualitatively similar trend is observed for larger particles, but the distance at which their concentration is maximum is larger and the peak value is smaller. This may be a result of the axial accelerations and deceleration experienced by the particles, as they move along the core flow, thus producing regions of stagnation where the concentration increases. However, measurements of the time averaged axial velocity fluctuations along the centreline for the three size classes (and not shown here) showed that all particle sizes are too large to respond to the velocity fluctuations, although smaller particles still have larger velocity fluctuations due to their smaller response time.

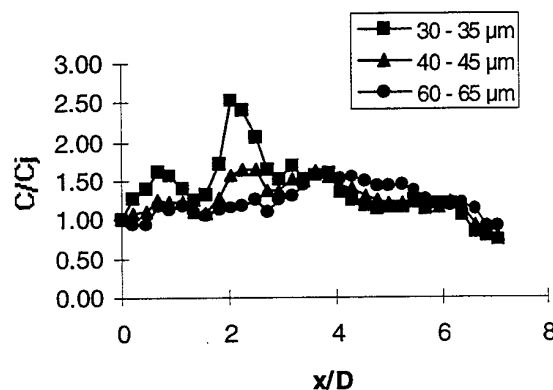


Figure 6 - Centerline variation of the time averaged particle concentration (forcing frequency = 190 Hz)

The present results show the strong interaction between the forced large structures of the flow and the particle dispersion process. In order to quantify the influence of acoustically forcing the flow on particle dispersion, radial profiles of time averaged statistics of particle concentration, mean velocity and standard deviation of velocity, respectively, were measured at five axial stations downstream of the nozzle exit ($x/D = 0.2, 1.3, 2.4, 3.5$ and 4.6). Figure 7 shows the axial location of the radial profiles relatively to the vortex rings and the results are depicted in Figures 8 to 10.

In terms of boundary conditions, when the measurements at $x/D=0.2$ are compared with those obtained in the unforced flow with the same Reynolds number (reported by Heitor and Moreira, 1994), it is observed that forcing alters the distribution of particle concentration from a nearly flat typical of a vertical downwards pipe flow to an off-center peaked distribution. Also, the mean and standard deviation of particle velocity

are smaller than those for the fluid, although the time resolved measurements depicted in Figure 3 show that the axial velocity of particles upon exiting the nozzle oscillates with the forcing frequency.

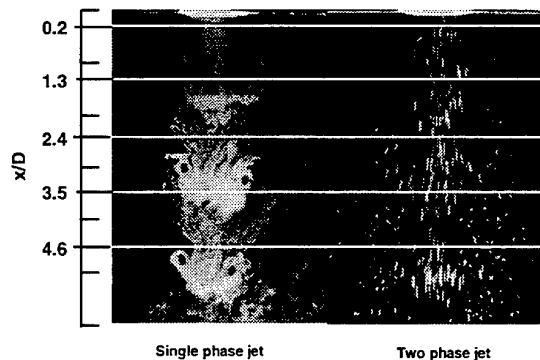


Figure 7 - Relative axial locations of the measured radial profiles

This is important when the present results are compared with others published in the literature, since it is known that the effects of growing vortices on particle dispersion depends on initial particle location and slip velocity. Following the analysis of Chung and Troutt (1988) and Wen et al. (1992), the fact that particles in the present work are released off-center will make them prone to be acted radially inwards by the initially growing vortices, while the fact that particles initially lag the fluid make them to respond faster. This would explain the high values of particle concentrations measured along the centerline so close to the nozzle exit (see Figure 4).

The most obvious effect of forcing the flow is to move the peak of the particle concentration distribution outwards and inwards as the vortices propagate downstream. The off-center peaks attain maximum values at axial locations where particle concentration at the centerline has a local minimum, showing that the particles are dispersed from the core region of the jet by the outwardly moving fluid downstream of the vortex rings. However, at $x/D=3.5$, the particles have not dispersed outwards more than 1.2 nozzle diameters, suggesting that, although the vortices move the particles radially, they do not allow, at least a significant portion of the particles to escape from the main flow. This may be contrasted with observations by Longmires and Eaton (1992 and 1994) despite the Stokes number of the particles in the current experiments are significantly smaller and the amplitude of velocity fluctuations comparatively higher. If the fluid time scale used to compute the Stokes number is defined as the distance, L , between successive vortices ($L=2D$ from Figure 5) divided by their convection velocity, U_c (taken as one half the jet core velocity) one would obtain Stokes number of about 1.0, 1.9 and 2.9 for the three size classes considered in the present analysis. The fact that particle ejection in the jet near field is not significantly enhanced, may then be attributed to the present

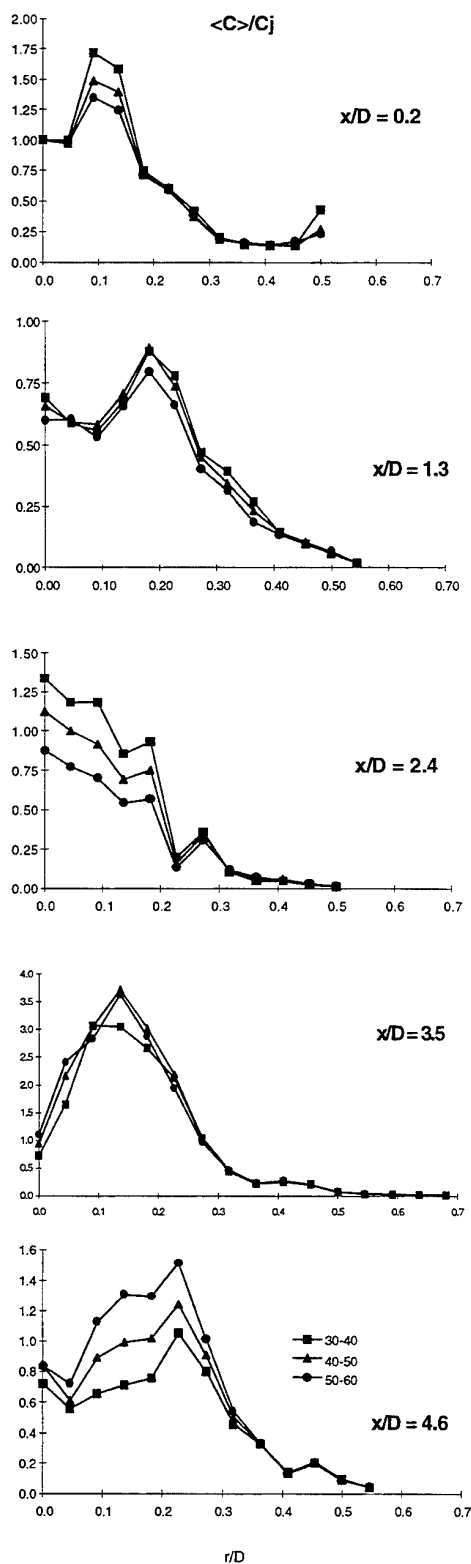


Figure 8 - Radial profiles of the time averaged particle concentration (forcing frequency = 190 Hz)

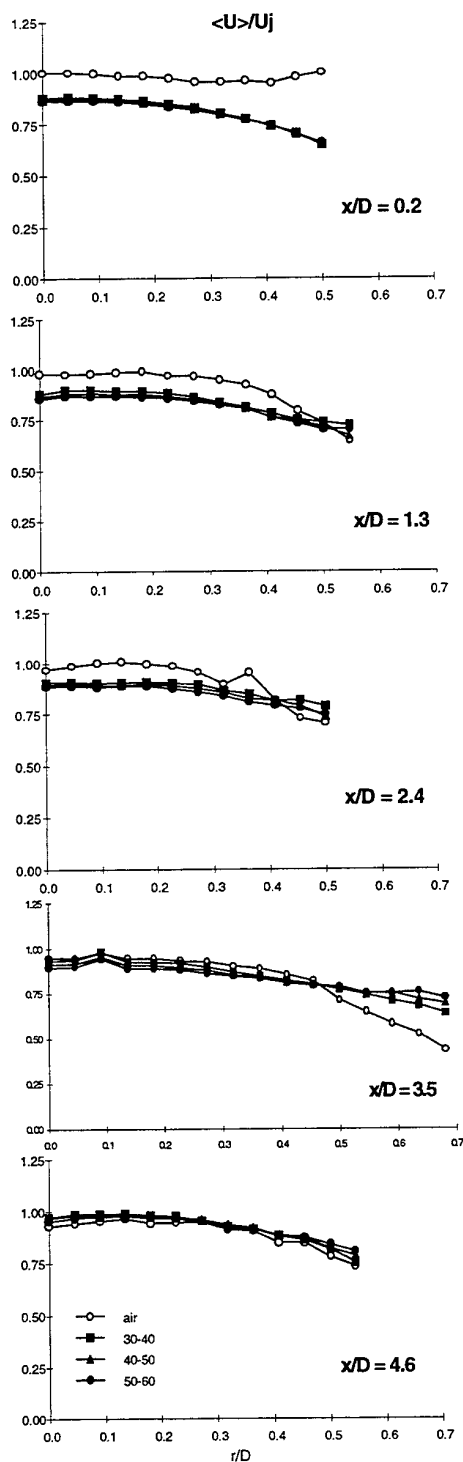


Figure 9 - Radial profiles of the time averaged mean velocity (forcing frequency = 190 Hz)

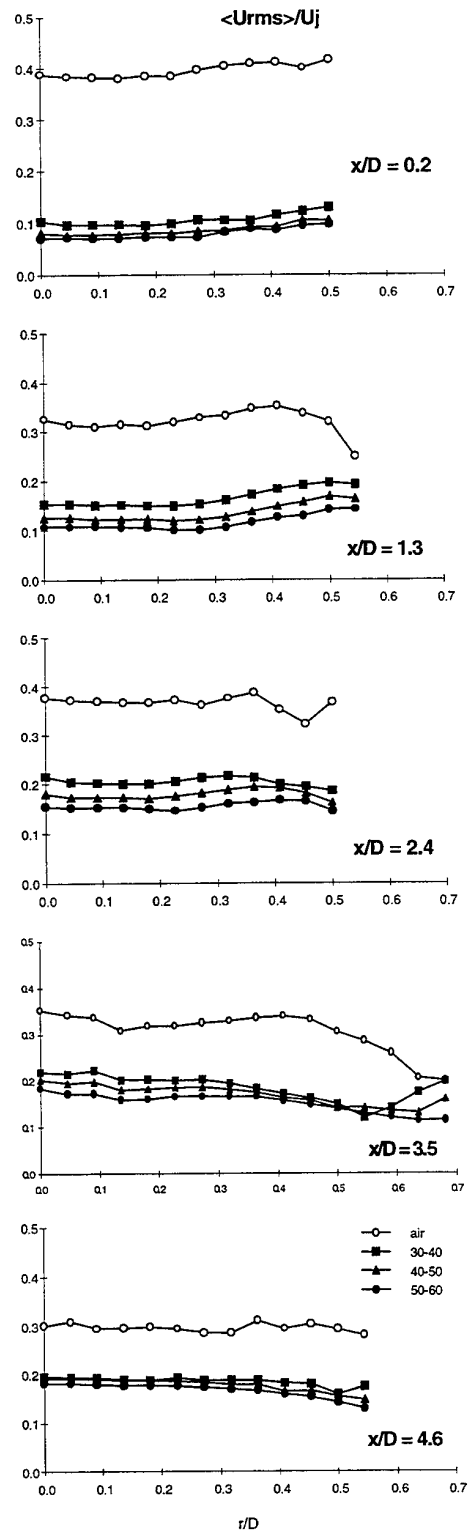


Figure 10 - Radial profiles of the time averaged standard deviation of velocity (forcing frequency = 190 Hz)

boundary conditions. In the present work, although the particles exit the nozzle off-center and, therefore, closer to the center of the vortex ring, they move with a mean velocity larger than the convection velocity of the vortices by about 3 m/s, meaning that particles fly over the vortices without having sufficient time to be accelerated outwardly. The particles fly from the region downstream one vortex where they are accelerated outwardly to the region upstream of the next vortex, where they are moved inwards, without having time to be ejected.

4 - SUMMARY

An experimental study was undertaken to characterize the polydispersion of solid particles in the near field of an acoustically-excited unconfined round jet with a Reynolds number of 1.5×10^4 and laden with a mass load of 65% of spherical glass beads. Dispersion was characterised based on the behavior of size classes, namely in the ranges 30-40, 40-50 and 50-60 μm . The Stokes number of these particles, computed with a fluid time scale defined as the distance between successive vortices divided by their convection velocity (taken as one half the jet core velocity) varies between 1 and 3.7.

The results show that particle dispersion is clearly modified by the ring vortices periodically formed at the nozzle exit up to a distance of about three nozzle diameters. Further downstream the vortical structures lose their coherence and the flow begins to be dominated by a helical mode. Despite the comparatively high amplitude of the forcing wave and the small Stokes number, particle ejection from the core flow is not significantly enhanced as compared with other results in the literature. In fact, although the particles accumulate in the straining regions downstream of vortices, they do not have enough time to be accelerated and pulled outward. This is attributed to the comparatively high velocity of the particles in a reference frame moving with the ring vortices, suggesting the predominant role played by the flow boundary conditions.

REFERENCES

- Chung, J. N. and Troutt, T. R., 1988, "Simulation of particle dispersion in an axisymmetric jet", *J. Fluid Mech.*, Vol. 186, pp. 199-222.
- Eaton, J. K. and Fessler, J. R., 1994, "Preferential concentration of particles by turbulence", *Int. J. Multiphase Flow*, Vol. 20, pp. 169-209.
- Gutmark, E., Parr, T. P., Parr, D. M. and Schadow, K. C., 1988, "Evolution of vortical structures in flames". 22nd Symp. (Intl.) on Combustion, The Combustion Institute, pp. 523-529.
- Heitor, M. V. and Moreira, A. L. N., 1994, "Experiments on Polydisperse Two-Phase Turbulent Jets" 6th International Conference on Liquid Atomization and Spray Systems. Rouen, France, 18-22 July, paper XI-5.
- Jarosinski, J., Lee, J. H. S. and Knystautas, R., 1988, "Interaction of a vortex ring and a laminar flame". 22nd Symp. (Intl.) on Combustion, The Combustion Institute, pp. 505-514.
- Lázaro, B. J. and Lasheras, J. C., 1992, "Particle dispersion in the developing free shear layer. Part 2. Forced Flow". *J. Fluid Mech.*, Vol. 235, pp. 179-221.
- Longmire, E. K. and Eaton, J. K., 1992, "Structure of a particle-laden round jet". *J. Fluid Mech.*, Vol. 236, pp. 217-257.
- Longmire, E. K. and Eaton, J. K., 1994, "Active open-loop control of particle dispersion in round jets", *AIAA J.*, Vol. 32, No. 3, pp. 555-563.
- Marchant, R., Hepler, W., Smith, O. I., Willis, J., Cadou, C., Logan, P. and Karagozian, A. R., 1992, "Development of a two-dimensional dump combustor for the incineration of hazardous wastes", *Combust. Sci. and Tech.*, Vol. 82, pp. 1-12.
- Smith, O. I., Marchant, R., Willis, J., Lee, L. M., Logan, P. and Karagozian, A. N., 1990, "Incineration of surrogate wastes in a low speed dump combustor", *Combust. Sci. and Tech.*, Vol. 74, pp. 199-210.
- Saffman, M., 1986, "The use of polarised light for optical particle sizing". Third Intl. Symp. on Appl. of Laser Anemometry to Fluid Mechanics, Lisbon, paper 18.2.
- Schadow, K. C., Gutmark, E. and Wilson, K. J., 1992, "Active combustion control in a coaxial dump combustor", *Combust. Sci. and Tech.*, Vol. 81, pp. 285-300.
- Schadow, K. C., and Gutmark, E., 1992, "Combustion instability related to vortex shedding in dump combustors and their passive control", *Prog. Energy Combust. Sci.*, Vol. 18, pp. 117-132.
- Wen, F., Kamalu, N., Chung, J. N., Crowe, C. T. and Troutt, T. R., 1992, "Particle dispersion by vortex structures in plane mixing layers", *J. of Fluids Eng.*, Vol. 114, pp. 657-666.
- Yu, K. H., Trounev, A. and Daily, J. W., 1991, "Low-frequency pressure oscillations in a model ramjet combustor", *J. Fluid Mech.*, vol. 232, pp. 47-72.

INFLUENCE OF CAVITATION ON THE WATER FLOW IN A PIPE WITH A SUDDEN EXPANSION

G. Wigley¹, R. Klasinc², R.H. Logar³ and T. Dum²

¹FMCS, A-8062 Kumberg, Austria

²Institut für Wasserbau and ³Institut für Hydraulische Strömungsmaschinen
Technische Universität, A-8010 Graz, Austria

ABSTRACT

There is a great potential for energy, and therefore cost, savings in the optimization of hydraulic systems operating at high Reynolds numbers. Computational fluid dynamics codes are seen as the future way of predicting hydraulic system performance but codes capable of handling single phase and cavitating flows are still under development. As the existing empirical relationships for hydraulic system design are insufficient for checking such numerical codes an experimental series using laser anemometry for the determination of the flow patterns in specific hydraulic system components has been planned. In this initial study the flow through a pipe with a sudden expansion has been characterized in the horizontal symmetry plane under non-cavitating and cavitating flow conditions for Reynolds numbers of 1 and 2×10^6 respectively. No differences were found however, neither in the mean and rms flow velocity profiles nor in the Reynolds stress profile. The flow profiles were found to scale with Reynolds number.

1. INTRODUCTION

In the optimization of the hydraulic design of closed pipe systems for hydro-power schemes, cooling and irrigation schemes, many comparative investigations into the hydraulic losses of the pipe system components have to be carried out. In the subject of Pipe Hydraulics most existing flows are considered as turbulent, one-dimensional processes with a square law relationship between the hydraulic loss, ΔH , and the fluid mean velocity, U . The total loss of head, H , in a hydraulic system consists of the sum of the friction losses through the whole system and the form dependent losses of the individual components. The friction losses, ΔH_f , are continuous losses dependent on the surface structure of the pipes:

$$\Delta H_f = \lambda \frac{L}{D} \frac{U^2}{2g}$$

where: λ is the friction coefficient
 L length of the pipe
 D diameter of the pipe
 g gravity

The form losses, ΔH_f , are local losses incurred by pipe bends, sudden expansions and valves

$$\Delta H_f = K \frac{U^2}{2g}$$

where: K is the form dependent loss coefficient.

The empirical determination of these loss coefficients is costly for complex hydraulic systems, particularly at Reynolds number above 10^6 where variations in loss coefficients can be smaller than at lower Reynolds numbers and yet where major energy and cost savings can be achieved by optimizing the hydraulic design, Miller (1978).

These optimization studies could be carried out using computational fluid dynamics codes rather than the existing empirical relationships, but there is a trade off between costs and the limitations to the hydraulic system complexity and numerical accuracy particularly where pipe geometries and flow conditions can generate cavitation. In comparing the performance of such a numerical code with the fluid system the use of the loss coefficients is not sufficient, the detailed flow field must be known.

A major investigation is now underway in which experimental fluid mechanics data are to be measured in simple geometric pipe models, with and without cavitation, to provide an understanding of the flow processes at high Reynolds numbers. No equivalent data have so far been found in the literature. These are to be compared with the data obtained from a numerical model, currently under development, designed for single phase and cavitating flows in hydraulic systems. The work described here is the first experimental study of the flow behaviour, in terms of the flow profiles, hydraulic losses and cavitation, in a straight pipe with a sudden expansion. The main question to be answered was: What is the influence of cavitation on the flow pattern and the turbulent fluctuations compared with the single phase flow?

2. EXPERIMENTAL PARAMETERS

This investigation was carried out in the large closed loop test facility of the Institute for Hydraulic Machinery, University of Technology, Graz. The loop consists of a 9,000 litre water reservoir, a 0.25 MW centrifugal pump, a venturi tube and throttling valve to measure and control the flow rate through the test section. The air pressure above the water level in the reservoir could be regulated from 0.9 bar below atmospheric pressure, to 5 bar above. In this manner the pressure level in the whole circuit could be varied to induce and control the level of cavitation in the recirculation zone downstream from the sudden expansion independent of flow rate.

The test section was made as long as possible, a total length of 6.5 m, with a 2.5 m straight pipe upstream and another 4 m downstream of the sudden expansion. This was to help produce near fully developed flow conditions either side of the sudden expansion. The sudden expansion was formed by using two plexiglass pipes of different internal diameters, 140 mm (D_0) and 172 mm (D_1), an aspect ratio of 1:1.23. The wall thickness was 5 mm. Static wall pressure tapings were available at $2D_0$ intervals, either side of the sudden expansion. It was not intended to provide a detailed fluid mechanical characterisation of the flow in the neighbourhood of the sudden expansion but data at certain key planes that would define the initial and developing flow conditions principally for comparison with the CFD calculations. The measurement planes and a schematic of the geometry of the sudden expansion are given in Figure 1.

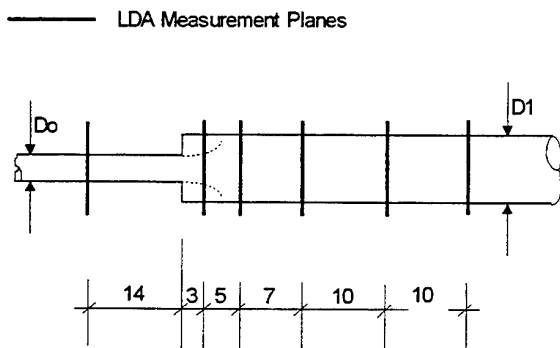


Figure 1. Sudden Expansion and Measurement Planes

The main experimental parameters defining the test conditions were the Reynolds number, upstream of the sudden expansion, the flow rate, which was kept constant throughout the tests, and the cavitation parameter as defined below.

Reynolds number: $Re = U_0 D_0 / \nu$

Cavitation parameter: $\sigma = (p_0 - p_v) / (\rho U_0^2 / 2)$

U_0 [m/s] mean velocity in the upstream pipe
defined as: $Q / D_0^2 \pi / 4$

Q [m³/s] volume flow rate

D_0 [m] diameter upstream of the expansion

ν [m²/s] kinematic viscosity
 p_0 [N/m²] reference pressure at the expansion
(a linear extrapolation from the wall pressures measured at $8D_0$ and $2D_0$ upstream, from the sudden expansion)
 p_v [N/m²] vapour pressure of the water
 ρ [kg/m³] water density (taken as 997 kg/m³ for the temperature range 15°C to 30°C)

Velocity measurements were made under three different test conditions:

a) Single phase flow,

$Q = 0.100$ m³/s, $Re = 1 \times 10^6$, $\sigma = 4.70$

b) At the onset of visible cavitation,

$Q = 0.210$ m³/s, $Re = 2 \times 10^6$, $\sigma = 0.31$

c) Strong cavitation,

$Q = 0.210$ m³/s, $Re = 2 \times 10^6$, $\sigma = 0.14$

This latter limit was set to allow LDA measurements to be made in the regions of the strongest cavitation just downstream from the sudden expansion and therefore at all measurement locations. The mass flow rate was controlled to within $\pm 1\%$, frequent corrections were necessary to account for the rise in the system operating temperature during the course of the measurements.

3. MEASUREMENT TECHNIQUE

Laser anemometry measurements are often made in water flows using low power Helium-Neon lasers but when consistent data rates are needed and two component velocity measurements are required the use of an Argon-Ion laser is essential. A Coherent *Innova* 90-5 was used, operated at 22 amps with an inter-cavity aperture setting of 5, it provided a total, all-lines, power output of 0.80 Watts with a Gaussian beam intensity profile for the output beam. The power in each of the 514.5 nm and 488 nm beams at the 2-component measurement volume was ~ 80 milliwatts and ~ 60 milliwatts respectively.

A 2-component Dantec *FiberFlow* LDA system was used in this study, the main components comprised of Transmitter Optics (60X41) with a 60 mm *FiberProbe* (60X67) and a 400 mm focal length front lens (60X21). The back-scattered light was re-collimated by the front lens and coupled through a multi-mode optical fibre to the colour splitter (55X35), to separate the blue and green components of the scattered light which were then directed to their respective photo-multipliers (57X08) and input to the signal processor.

The Signal Processor, a Dantec *Particle Dynamics Analyzer* (58N50) was used in its 'velocity only mode' to provide, in 1-component configuration, measurements of the axial velocity, and, in 2-component configuration, coincident measurements of both the axial and radial velocity, components of the instantaneous seed particle/cavitation bubble velocity through the measurement volume.

The technical specifications for the LDA hardware are given in Tables 1 and 2 where the data in the two columns refer to the parameters for determining the axial and radial components of the water flow in the pipe.

Table 1 Optical Parameters for the *FibreProbe*

Optical Parameters	U(Axial)	V(Radial)	
Laser Wavelength	514.5	488.0	nm
Beam Diameter	1.7	1.7	mm
Beam Expansion	1	1	
Beam Separation	38.0	38.0	mm
Lens Focal Length	400.0	400.0	mm
Fringe Spacing	5.422	5.143	um
Measurement Volume			
Diameter	0.154	0.146	mm
Length	3.25	3.08	mm

Table 2 Electronic Parameters for the *Particle Dynamics Analyser*

Electronic Parameters	U(Axial)	V(Radial)	
Bandwidths			
Frequency	12	4	MHz
Velocity	-32 / +32	-10 / +10	m/s
Burst Detector	0.2	0.2	MHz
Gains			
Amplifier	High	High	
Photo-Multiplier	800 / 950	800 / 950	Volts

The test section was enclosed in a rectangular plexiglass box full of water with the access for the laser beams through the base of the box. This arrangement is shown in Figure 2 and was implemented in order to:-

- minimise refraction effects on the input laser beams at the cylindrical pipe surfaces
- allow 2-component coincident velocity measurements of the axial and radial flow
- make noise free measurements in the near wall region
- place the small circular cross-section of the measurement volume in the measurement plane
- allow a simple solution to enable the LDA measurement volume to be traversed in the vertical plane.

The *FibreProbe* and the 45 degree mirror were both mounted on horizontal traverse mechanisms. They were coupled in such a way that either, the *FibreProbe* alone or, the *FibreProbe* and mirror as a unit, could be traversed to traverse the measurement volume in the vertical or horizontal planes respectively. The arrow through the measurement volume indicates the flow direction that would be measured as a positive radial flow.

The 45 degree mirror and probe were first positioned so that the plane of the laser beam pairs were not only normal to the base of the plexiglass box, and the free water surface, but also so that the individual back-reflections from the base and the top and bottom of the cylindrical pipe were co-linear and symmetrical about the input beams. The measurement volume must then lie on the vertical diameter, 1 to 2, and on the horizontal axis, 3 to 4, of the water pipe. Furthermore, the plane of the input laser beam pairs must lie parallel and normal to the axes of the plexiglass pipe.

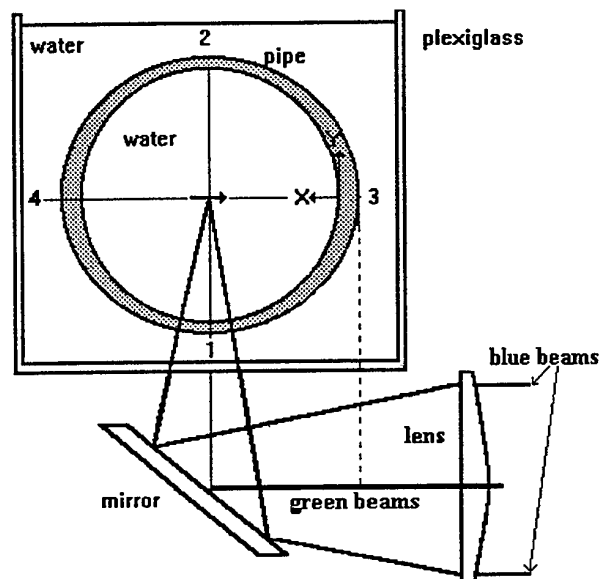


Figure 2 Vertical cross-section through the flow rig and LDA probe.

The horizontal (X) traverse was then positioned until the green beams were at the glancing angle with the outer wall of the cylindrical pipe i.e. at location 3. The horizontal (X) traverse was then repositioned by an amount equal to the wall thickness of the cylindrical pipe to place the (green) measurement volume at the reference point $X = 0$ mm, i.e. the free space position of the inner wall of the cylindrical pipe.

Refraction of the input laser beams in this near wall region causes two effects that need discussion as they affect the potential for 2-component velocity measurements and modify the spatial co-ordinate system of the traverse relative to the pipe.

There is a differential refraction between the input beam pairs which causes the green and blue measurement volumes to be displaced from each other. This is due to the different angles of incidence for each beam at the cylindrical plexiglass wall, their will also be a small difference due to the variation of refractive index with wavelength.

Simultaneous and coincident 2-component velocity measurements are only possible when a particle is present in the combined green and blue measurement volume. Coincident data ensures a high spatial resolution and provides data for the calculation of the Reynolds stresses. When the measurement volumes are separated simultaneous 2-component measurements can still be obtained when each measurement volume has a different particle travelling through it. A high seeding level would increase the probability of this occurring. However, for the cavitating flow the cavitation bubbles were large enough to be in side both measurement volumes at the same time in which case simultaneous and coincident 2-component velocity measurements are again possible.

The spatial co-ordinate system, or measurement volume location within the pipe is referenced to the traverse position $X = 0$ mm as defined above. However, as shown in Figure 3, refraction in the near wall region causes an input beam to be deflected such that the measurement volume would actually lie within the pipe itself at the reference $X = 0$ mm.

The location of the measurement volume will, in general, be different to the position defined by the traverse location. Only at the centre of the pipe will the two be identical but for practical purposes a correction need only be considered for the traverse positions closer than 5 mm to the wall. A simple raytrace for this geometry has been performed, see Figure 3, and the position at which the ray meets the cylinder axis calculated with respect to the X traverse location. This does not represent the position of the measurement volume from the cylinder wall. This will be greater than the distance for the ray location on the cylinder axis since the measurement volume will occur before the rays meet the cylinder axis due to the greater light path-length in the plexiglass with increasing angles of incidence. A more realistic estimate of the position of the measurement volume from the wall is obtained by calculating the height of the ray, at the mid-point of its path inside the cylinder. These data are presented in Table 3. Of course, such calculations are only valid in this application if- the plexiglass pipes are perfect cylinders, the base of the plexiglass box is flat and the laser beams normal to the base.

Table 3 Traverse location relative to ray location and measurement volume position from the wall

X Traverse position (mm from wall)	2	4	6	8	10
Ray location on cylinder axis	1.77	3.91	5.95	7.97	9.99
Measurement volume from wall	2.23	4.10	6.05	8.03	10.02

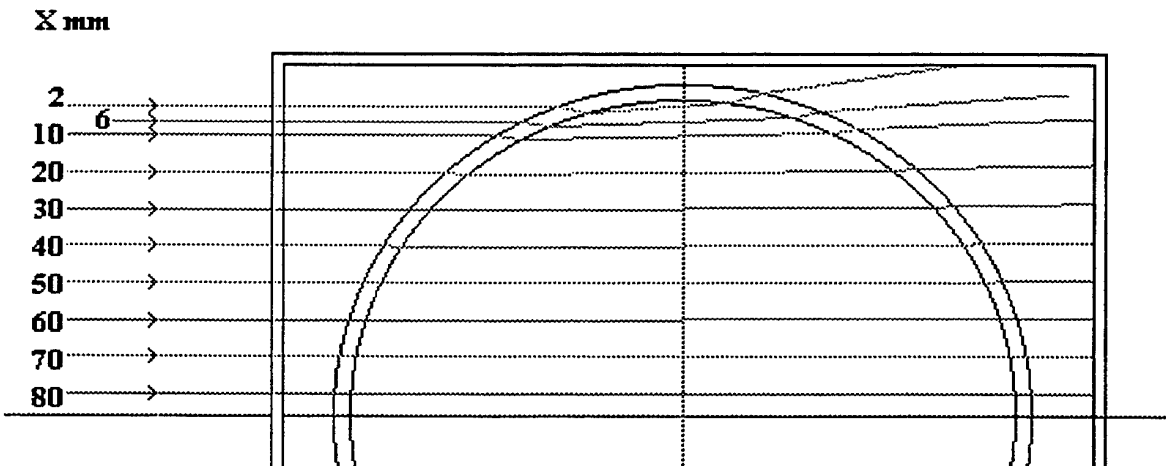


Figure 2 Raytrace through the plexiglass cylinder

Data were obtained for three flow conditions (a) without cavitation, (b) for the flow at the onset of cavitation and (c) for strong cavitation. The high level of cavitation was fixed such that velocity measurements could still be obtained throughout the cavitation region even though the transmission of the beams through the test section was highly intermittent. For each of the three flow conditions velocity profiles were measured at seven locations along the pipe corresponding to the following co-ordinates:-

$Z = -140, 0, 30, 80, 150, 250, 350$ and 956 mm
with $Z = 0$ mm located at the sudden expansion between the 140 and 172 mm diameter pipes.

Two-component velocity data were obtained over the whole profile while 1-component data were obtained for the near wall region and with one measurement on the pipe centre line. A small quantity of Toray SP-500 nylon seed particles of approximately 5.0 microns diameter and specific gravity of 1.02 were added to the water. For the cavitating flow conditions the cavitation bubbles would be the principal light scatterers, i.e. data for the gaseous bubble phase would totally dominate the flow data obtained.

Although 2-component velocity measurements were taken without cavitation at $X = 4$ mm the sample number was low, generally less than 100 samples. By $X = 10$ mm data were coincident and the data rate high. To improve the sample number and check on the statistical significance of the 2-component data a second measurement was made in which only the axial velocity component was recorded. With only 1-component of velocity to measure high data rates were always recorded, even for the $X = 2$ mm position.

Data acquisition parameters had to be chosen with some care in order to record a statistically significant number of data samples over an acceptable measurement. A time that was longer than the longest expected flow time scales and yet short enough to maintain consistent experimental flow parameters and result in practical experimental measurement times for the flow profile across the cylinder diameter.

One thousand validated samples generally represents the lowest sample number necessary for statistically significant data. However, in this particular experiment the data rate was found to vary dramatically as the measurement volume traversed the pipe diameter with high sample rates in the recirculation zones when containing the cavitation bubbles and low sample rates for the flow containing seed particles only, as in the middle of the pipe. It was therefore useful to introduce a 'dead time', 12.5 milliseconds, in the data acquisition. This also removed the need for a velocity bias correction to be made when ensemble averaging the velocity samples. When data rates were very low an 'elapsed time' of 90 seconds determined the end of the data acquisition at that point. The experimental time required for one profile consisting of 2-component velocity measurements at 34 positions was approximately 30 minutes.

Data reduction followed Reynolds decomposition of the instantaneous velocity in terms of the mean and the fluctuating velocities. The unweighted time averaged U , axial and V , radial mean and fluctuating (rms) velocities and the uv cross moment were calculated.

4. RESULTS AND DISCUSSION

A schematic of the sudden expansion with the extent of the recirculation zone and an impression of the appearance of the cavitation is shown in Figure 4a and 4b for the flow at the onset of cavitation and for strong cavitation respectively. In each case the zone containing the gaseous phase was the same length and varied from 80 to 100 mm downstream from the sudden expansion. At the onset of cavitation bubbles and voids were only to be seen in the core of the recirculation zone, depicted by the dashed line indicating the locus of the zero radial velocity point. With strong cavitation the whole of the recirculation zone up to wall contains bubbles and voids. The bubble sizes were estimated to be smaller than 0.5 mm and although slug shaped voids were also present these would quickly implode to produce bubbles. However, it must be emphasised that these are only qualitative observations and it was not possible to see through the pipe in the case of the strong cavitation.

For clarity the velocity data presented are limited to the positions $z = 30, 80, 150$ and 250 mm down stream from the sudden expansion. Data are included for the 3 flow conditions: a) single phase flow, b) at the onset of cavitation and c) with strong cavitation. The data for the single phase condition has been scaled up by 2, the ratio of the different Reynolds numbers.

The mean axial velocity profiles across the pipe diameter are presented in Figure 5. The scale for the pipe diameter indicates the X traverse position. The most surprising aspect is the very close agreement in the profiles for the 3 flow conditions. Small differences can be found for the single phase flow condition where a lower axial velocity appears between approximately 0.5 and 0.75 of the pipe radius. Due to the scaling of this data this difference cannot be uniquely attributed as due to the single phase flow condition. The profiles exhibit a high degree of symmetry about the pipe

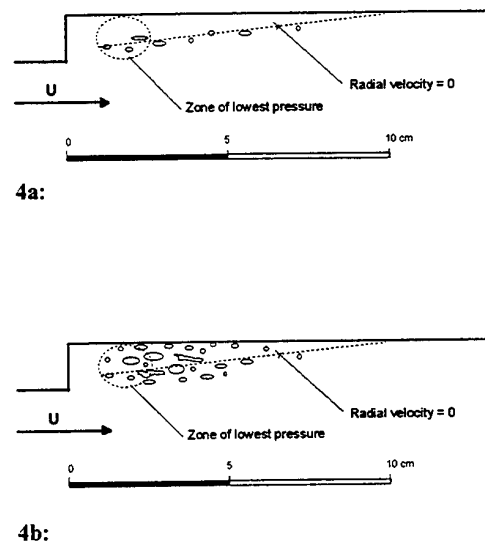


Figure 4 Schematic of the cavitation in the recirculation zone

axis although differences can be seen in the near wall regions. The recirculation zones at $Z = 30$ and 80 mm are smaller on the left-hand side of the profile with zero axial velocity occurring at 10 and 6 mm from the wall respectively whereas it is at 12 and 7.5 mm respectively for the right-hand side of the profile. The consistency of the data for the 3 flow conditions suggests that this is solely a function of the pipe geometry. The axial flow profiles upstream from the sudden expansion, at $Z = -140$ mm, were all symmetrical about the pipe axis.

The radial flows at this position and at $Z = 30$ mm were not symmetrical, they showed a significant departure from the accepted norm where the radial component should be zero on the pipe centre-line. The profiles indicated a near bulk fluid motion towards the wall at $X = 0$ mm with maximum values of between 0.2 and 0.6 m/s between the single phase flow and the flow at the onset of cavitation respectively. Due to the high axial velocity component, 15 m/s, along the pipe axis misalignments of 0.8 and 2.4 degrees would produce the above radial velocities values on the pipe axis. However, the method described earlier for the alignment of the laser beams with the pipe axis should guarantee a high alignment accuracy. It was therefore considered that small asymmetries in the flow existed, probably due to the position of the sudden expansion relative to the entrance pipe, diffuser and flow straighteners being located only 18 pipe diameters upstream.

Further downstream from the sudden expansion the symmetry of the radial flow profiles was much better and departures from the norm decreased. Since these flow conditions were specific to this hydraulic system and would be difficult to compare with CFD calculations the radial velocity profiles presented in Figure 6 have been adjusted, using velocity vector transformations, to force the condition of zero radial flow on the pipe axis. The effect

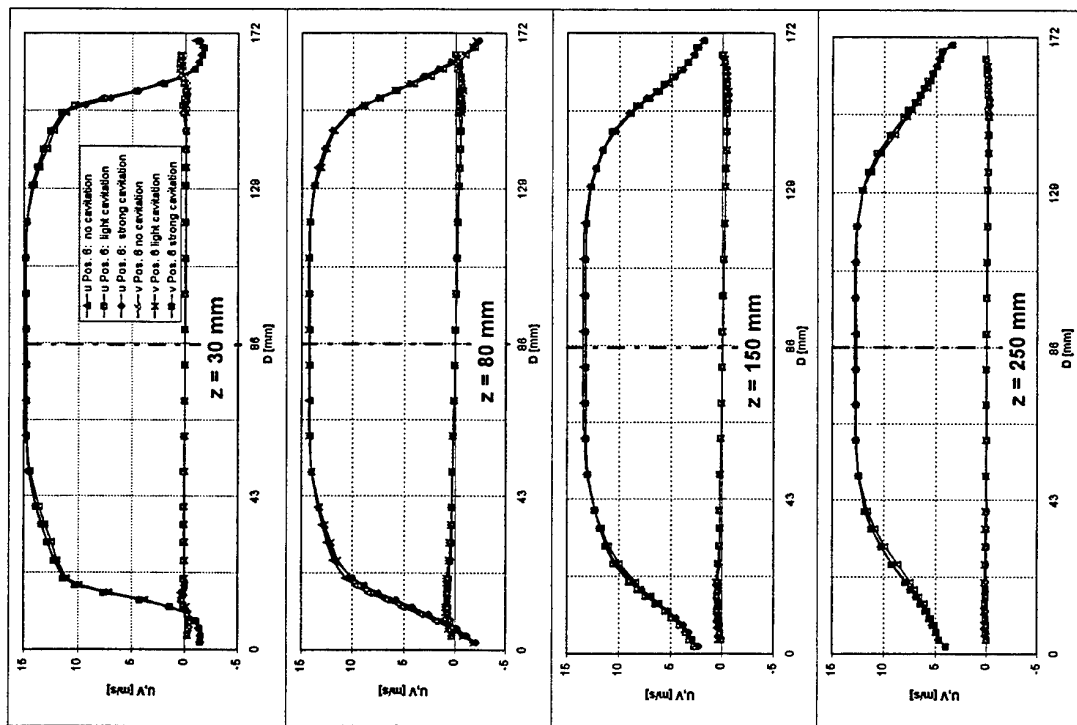


Figure 5 Axial and Radial Velocity Profiles

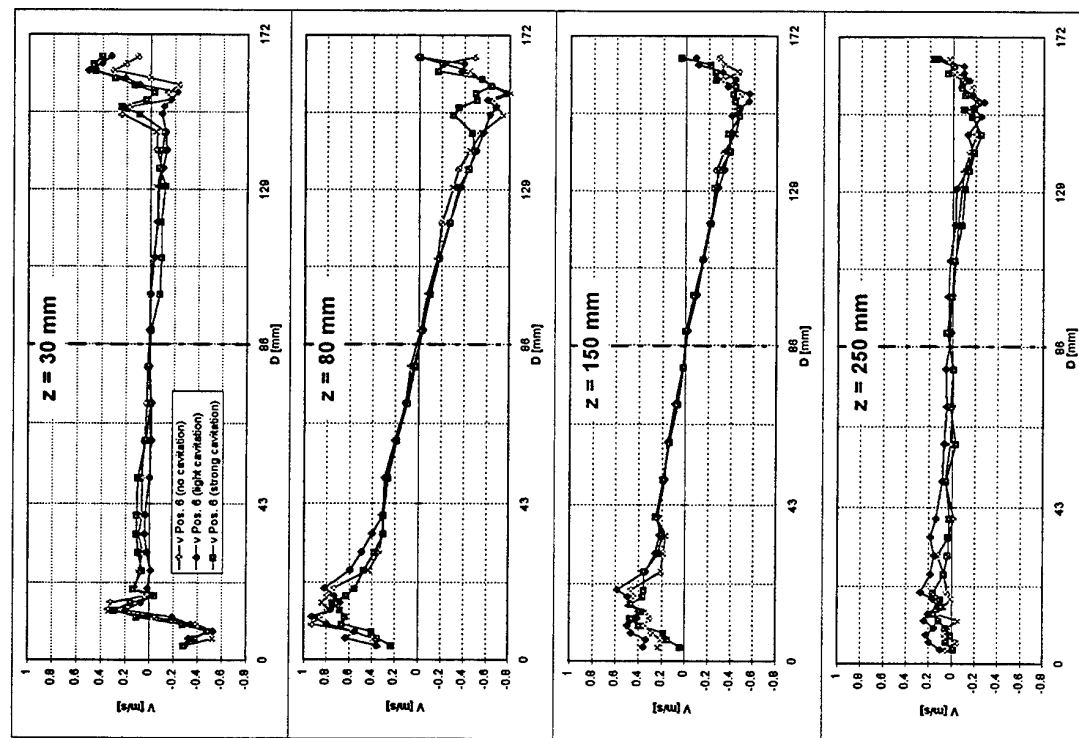


Figure 6 Radial Velocity Profiles

on the radial flow profiles in the wall region is reduced as the axial flow velocity reduces. It is clear that radial flow asymmetries exist at $Z = 30$ mm but after that they decrease. Once again no significant differences can be found between the single phase and the two cavitating flow conditions. The highest radial velocity profiles are to be found at the position $Z = 80$ mm after which the axial flow reattaches to the wall. The data show excellent consistency even though the data sample number is reduced in the near wall region and the velocity scaling has a high resolution.

The rms velocity profiles for the axial and radial flow components are of a similar magnitude so are presented together in Figure 7. The turbulent fluctuations approach isotropy in the centre of the pipe but in the near wall region the axial rms velocities are approximately 1.5 times greater than the radial rms velocities. The highest turbulent fluctuations are found at $Z = 80$ mm and peak closest from the at approximately 11.5 mm.

Considering the resolution of the velocity scale and the tendency for the mean square data to show a higher statistical variance than the previous data then the conclusion is that the cavitation has had no effect on the turbulent fluctuations in the flow.

As the 2-component velocity data was coincident the axial /radial cross moment, or Reynolds stress can be calculated. This data is shown in Figure 8. Data are presented for one half of the pipe diameter to improve the resolution of the radial distribution of the Reynolds stress. This highlights how consistent the data are for the single phase and the two cavitating flow conditions. Some scatter of the data are present at $Z = 80$ mm but this can be attributed to the lower statistical significance of the data here at this position where the greatest turbulent fluctuations in the flow can be found.

5. CONCLUSIONS

It was found that cavitation had no influence on the mean, rms and Reynolds stress profiles measured downstream from the sudden expansion. This result was unexpected especially considering the observed aspects of the flow with strong cavitation where the laser beam transmission was highly intermittent and the pipe vibration and cavitation acoustic levels were high. The laser anemometer data shows that the cavitation bubbles and voids must behave as seeds that have a good flow fidelity i.e. they are transported downstream capable of following the turbulent fluctuations of the continuous water phase. This was only the first experiment of the series planned and it would be unwise to generalise this finding.

6. REFERENCES

Miller, D.S. 1978, Internal Flow Systems , Vol. 4, Fluid Engineering Series, British Hydromechanics Research Association.

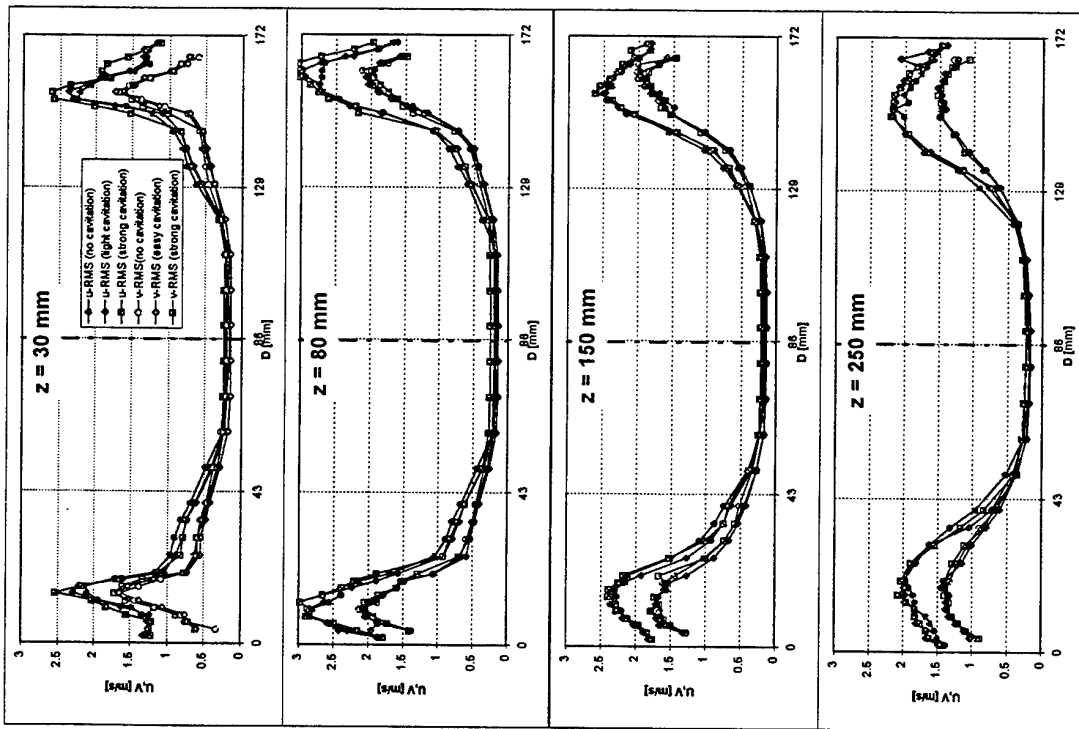


Figure 7 Axial and Radial RMS Velocity Profiles

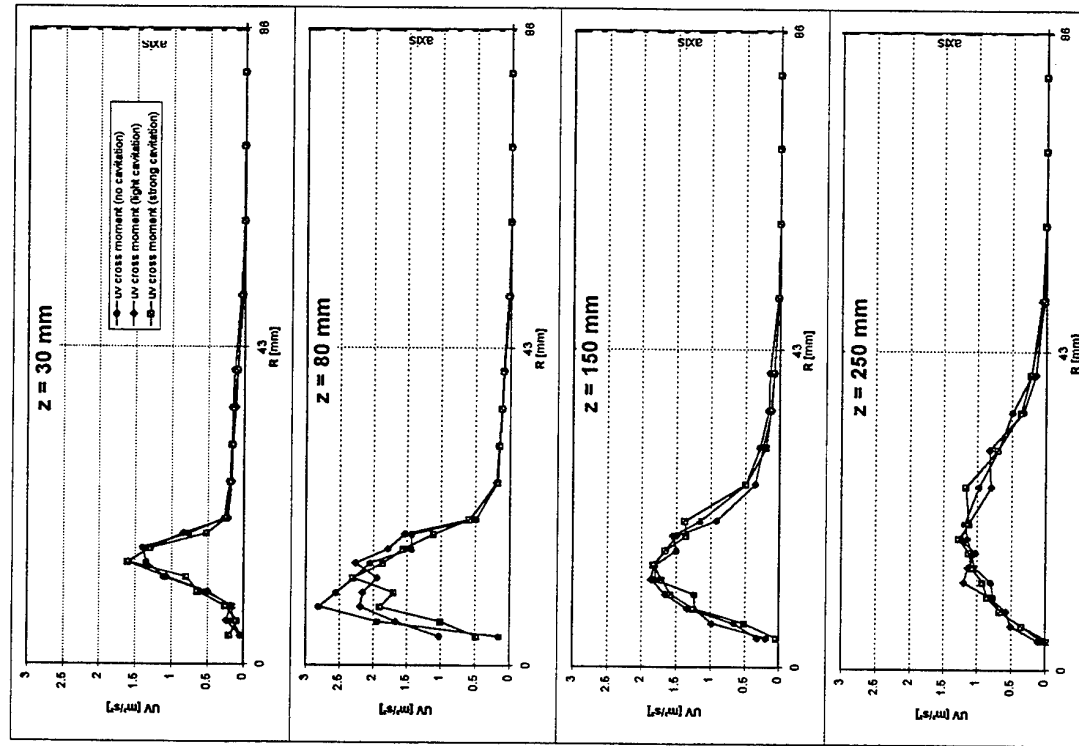


Figure 8 Reynolds Stress Profiles

Eddy Diffusivity of Liquid Droplets in a Vertical Flow of Vapor Produced at Boiling Liquid Surface

Kazuhiro Ohtake

Suntory Limited

Technological Development Center

1023-1, Yamazaki, Shimamoto-cho, Mishima-gun, Osaka 618, Japan

Tatsuhiko Miyata and Fumimaru Ogino

Department of Chemical Engineering

Kyoto University, Kyoto 606-01, Japan

ABSTRACT

Diameter, velocity and concentration of liquid droplets in a vertical flow of vapor produced at boiling liquid surface were measured by using PDA (Phase Doppler Anemometer or Particle Dynamic Analyzer). The result indicates that the droplet size distribution is represented by the logarithmic normal distribution and the turbulence intensity of the vapor flow decays in the same way as that generated by grids, although the value of the turbulence intensity is larger than that of the grid turbulence. A correlation equation of the eddy diffusivity of the droplets has been obtained.

1. INTRODUCTION

When bubbles at a boiling liquid surface burst, small liquid droplets are usually generated from the bubbles and rise with vapor flow. The droplets are called entrainment droplets. The quantity of the entrainment droplets is usually restricted to low level, for example, in a boiler of nuclear power plant to ensure the safety or in a solvent refining plant to prevent contamination into chemicals.

In a distillation process of whisky or brandy, the quantity of the entrainment droplets should be controlled in a range of concentration, because the liquid droplets include non-volatile fragrant substances. Therefore it is important to know the concentration of the liquid droplet at the inlet of condenser of vapor.

However, little is known about the number of the liquid droplets produced at the burst of the bubbles and the behavior of the droplets in the flow of vapor which are essential to determine the droplet concentration of the distillate in the still.

Garner et al. (1954) and Newitt et al. (1954) investigated size distribution of droplets and ejection velocity from the bursting bubbles using photographic technique and microscopic technique. They have distinguished two families of droplets: film drops (under $20\text{ }\mu\text{ m}$ in diameter) generated from bursting bubble films and jet drops (over $200\text{ }\mu\text{ m}$ in diameter) generated from the breakup of the water jet that is formed when the internal cavity of the bubble collapses.

Ramiretz and Marvillet (1991) measured the size distribution of droplets, velocity and number of the droplets in the range from about $1\text{ }\mu\text{ m}$ to $86\text{ }\mu\text{ m}$ in the flow generated from air-bubbling water surface by using the PDA. The result indicated that the size distribution was expressed by a logarithmic-normal probability function and the mean diameter was $7.49\text{ }\mu\text{ m}$ at 50 cm distant above the bubble surface. This showed that the large droplets fell down before reaching that height and, in a larger pot still, height of which is larger than 50 cm , the film drops play a dominant part of entrainment. Therefore we focus on the behavior of droplets of smaller diameters.

Correlations for the droplet entrainment from the bubbling or boiling liquid surface have been developed by Kataoka and Ishii (1984) based on a mechanistic

model with several researchers' experimental data. They have showed that there exist three regions of entrainment in the axial direction from the liquid surface: near surface, momentum controlled and deposition controlled regions. The deposition controlled region lies in the farthest distance from the boiling liquid surface. In this region, only the film drops rise with the vapor flow and are deposited to the still wall by diffusion. The correlation equation for the droplet entrainment in this region obtained by Kataoka and Ishii (1984), however, is not so reliable, because it has been based on considerably scattered experimental data.

Tchen (1947) showed that, for long diffusion time, the diffusivity for discrete particle is equal to that for fluid particle. However, experiments by Snyder and Lumley (1971) in a grid-generated turbulent flow carried out with discrete particles of different size and different density ratio resulted in smaller values of the diffusivity for discrete particles. On the other hand Ahmadi and Goldschmidt (1970) and Goldschmidt et al. (1972) obtained larger values of the diffusivity of discrete particles from experiments with small oil droplets in a plane air jet and with small gas bubbles in a round water jet.

The purpose of this paper is to present an

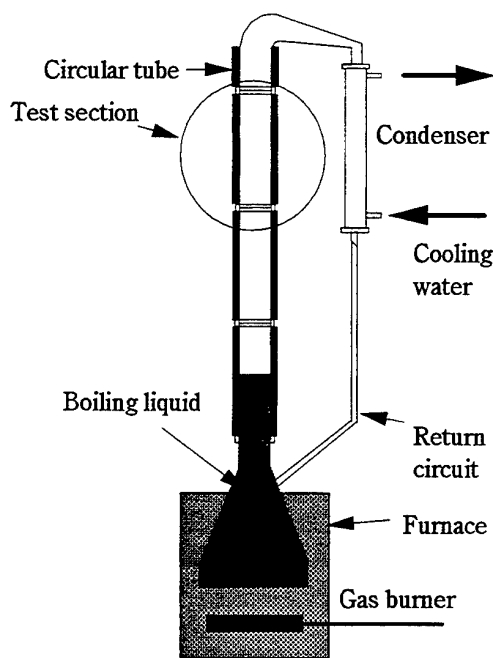
experimental result on the behavior of the liquid droplets in the flow of vapor above the boiling liquid surface in a vertical tube. The study on the concentration of the liquid droplet at the bursting bubbles is in progress.

2. EXPERIMENTAL APPARATUS

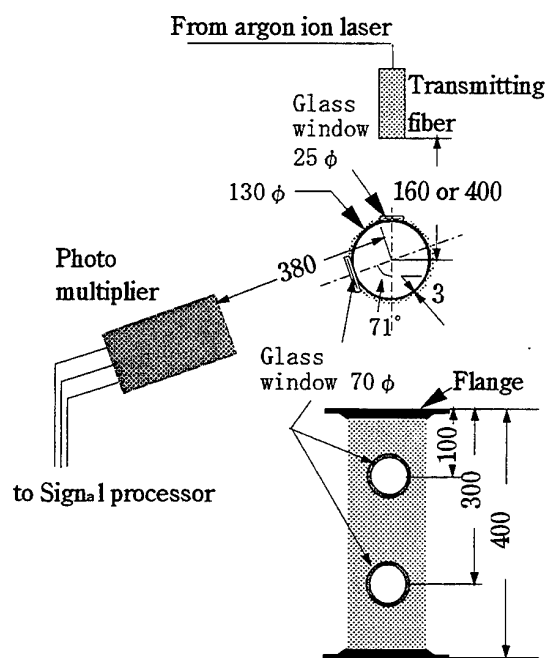
2.1 Test Section

Schematic diagram of the experimental apparatus and the detail of the test section are shown in Fig. 1. The vertical test tube consists of several interchangeable circular copper pipes of 400 mm long and 124 mm in diameter, so that the height of the test section can be varied. The wall of the test tube is insulated with a paper insulator.

The liquids used are water, 9.6mol% aqueous solution of ethanol, pure ethanol, methanol and Freon HCFC-141b, which are heated in a furnace. The vapor rises in the test tube and condenses in a condenser. The condensate returns into the liquid reservoir. The volume of the liquid reservoir is about 40 liters. The bubble surface is always set in the lowest pipe.



(a) Outline of flow system



(b) Test section

Fig. 1 Experimental apparatus.

2.2 Laser Instrumentation

The test section has two glass windows to pass laser beam as shown in Fig. 1(b). The Particle Dynamic Analyzer (PDA assembled by DANTEC) was used to measure the diameter, velocity and concentration of the droplets on the centerline of the test tube. The PDA consists of a transmitting fiber (60X) optics with 400 mm or 160 mm focal length lenses, Bragg cell which shifts the beam frequency by 40 MHz and a 100 mW Ar-ion laser. The scattered beam is received by a receiving optics (57X10) with 310 mm focal length lenses and three photomultipliers (57X08). The output signals from the photomultipliers are transmitted to a signal processor (58N10) with DMA (Direct Memory Access) interface for data transfer to a PC-AT computer by which we can measure the particle size, one-dimensional velocity, and the concentration of the particles. The transmitting and receiving optics are mounted on an L bench system which can be traversed along the test section in the vertical direction.

During experiment, the windows for the transmitting laser and scattered light are sometimes covered by condensed mist. To minimize the amount of the mist, hot air is blown on the windows for keeping them at high temperature.

The droplet size is obtained from a phase difference of the frequency of Doppler burst between two detectors at different scattering angles, namely the spatial frequency of the interference fringe pattern (Saffman et al. (1984), Bachalo and Houser(1984)). The scattered light by refraction, reflection and diffraction at the droplet is collected to the photomultipliers located at an angle of 71° from the optical axis of the transmitting optics as shown in Fig. 1(b). At this angle, for droplets of used liquid, the first order refraction has the highest energy, so that the contributions of reflected and diffracted lights can be neglected compared with that scattered by the refraction. Thus, this optical arrangement resulted in a linear relation between the diameter and the phase difference. The measurement of the phase difference requires the use of two detectors separated by a fixed spacing. Any two of the three photomultipliers are used depending on size range sensitivity.

Table 1 Principal characteristics of PDA

Diameter range	
0.0 to 41.905 μ m (Lens focal length : 160 mm)	
0.0 to 104.09 μ m (Lens focal length : 400 mm)	
Velocity range	-0.54 to 1.63 m/s
TRANSMITTING OPTIC PARAMETERS	
100 mW Ar-ion laser wave length	0.5145 μ m
Gaussian beam diameter of laser	1 mm
Shift frequency due to a Bragg cell	40.0 MHz
Beam separation	38.0 mm
Lens focal length	160.0 or 400.0 mm
Polarization orientation	parallel to fringes
Calculated dimensions of beam intersection volume	
Lens focal length	f=400 mm f=160 mm
Delta X	0.2623 mm 0.1055 mm
Delta Y	0.2620 mm 0.1048 mm
Delta Z	5.5227 mm 0.8888 mm
Fringe spacing	5.4219 μ m 2.1815 μ m
Calculated number of fringes	48 48
RECEIVING OPTIC PARAMETERS	
Location of o. ti. s from forward scatter	71.0 degrees
Lens focal length	310.0 mm
Phase factors, 1st Refraction	
Photomultipliers U1-U2	-4.995 deg./ μ m
Photomultipliers U1-U3	-2.497 deg./ μ m
Maximum particle concentration	
1.0E11(f=400 mm), 9.0E11(f=160 mm) drops/m ³	
Angle adjustment [0.0;2.0]	2.0 mm
Polarization angle	0.0 degree
Direction of fringe motion (Flow \uparrow)	negative(\downarrow)
Particle/medium refractive indexes	see Table 2
ELECTRONIC PARAMETERS	
Photomultipliers	U1 U2 U3
High voltage	1400 1400 1400 Volts
	1.00 1.00 Balance
Bandwidth	0.4 MHz
Burst detector bandwidth	0.010 MHz
Arrival time	564 μ s/bit
Transit time	56.4 μ s/bit

Table 2 Properties of the used fluids at vapor or liquid phase

	Water	9.6mol%Ethanol	Ethanol	Methanol	Freon HCFC-141b
Liquid phase					
Boiling point (B.P.) [K]	373	359	351	338	305
Refractive index at B.P.	1.318	1.332	1.293	1.280	1.400
Density at B.P. [kg/m ³]	958	929	736	740	1220
Surface tension [N/m]	0.588	0.330	0.173	0.186	0.180
Vapor phase at B.P.					
Equilibrium concentration [mol%]	100	43	100	100	100
Refractive index [-]	1.00	1.00	1.00	1.00	1.00
Density [kg/m ³]	0.590	1.010	1.594	1.15	4.64
Kinematic viscosity [m ² /s]	21.0×10^{-6}	11.1×10^{-6}	6.5×10^{-6}	9.2×10^{-6}	2.2×10^{-6}

The velocity of droplets is calculated from the frequency of the Doppler burst, namely the temporal frequency of the fringe pattern from one detector. The concentration of the droplets is calculated from the occurring frequency of the Doppler burst. A more complete typical documentation of optical and electronic parameters utilized in the present research is presented in Table 1.

The software for calculating the velocity and the concentration of droplets is "Size Ware version 2.2" programmed by DANTEC.

Properties of used fluids are calculated using empirical equations (Sato (1968), Ooe (1985)) and are listed in Table 2.

3. EXPERIMENTAL RESULT

Measured results of the size distribution of the water droplets at several vapor velocities are shown in Fig. 2 and those at several distances from the boiling liquid surface are shown in Fig. 3. Figures 2 and 3 indicate that the distribution function is approximately expressed by the logarithmic-normal distribution and the shape of the distribution curve does not change with the vapor velocity and the distance from the liquid surface.

The logarithmic mean diameter of the water droplets is $2.1 \mu\text{m}$ which indicates that the water droplets are film droplets. Similar results have been obtained for the other fluids as shown in Fig. 4. Although the logarithmic mean diameter may depend on the physical properties of the liquid and the boiling

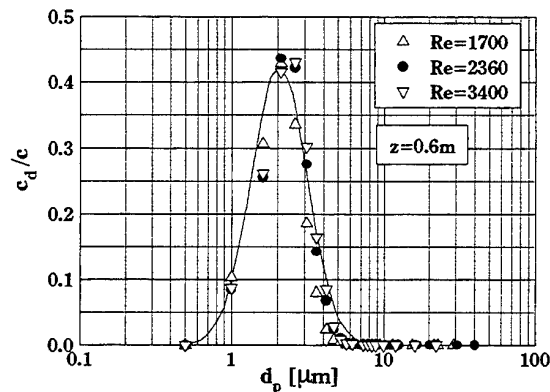


Fig. 2 Size distribution of water droplets for various velocities.

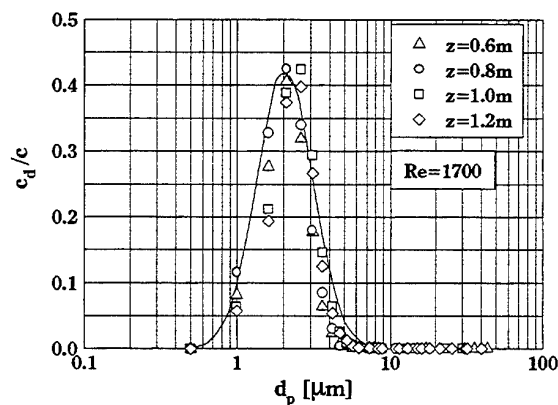


Fig. 3 Size distribution of water droplets for various distances from boiling surface.

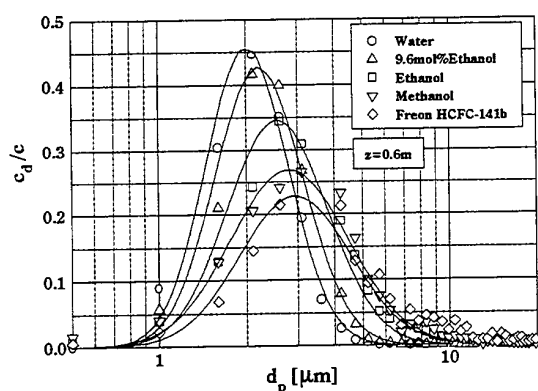


Fig. 4 Size distribution of various liquid droplets.

condition, the relation between them is not yet clear. However, all mean diameters of the liquid droplets used in the present experiment are smaller than $4 \mu\text{m}$.

The terminal velocity of the Freon droplet of $4 \mu\text{m}$ is $8.1 \times 10^{-4} \text{ m/s}$. The value of the frequency below which the Freon droplet of $4 \mu\text{m}$ responds to the velocity fluctuation of vapor within the accuracy of 1% is about 300 Hz. Therefore, the measured velocity of the droplet smaller than $4 \mu\text{m}$ can be assumed to represent the velocity of the energy-containing eddies of the turbulent flow of vapor.

The measured turbulence intensity of the flow of water vapor is plotted against the distance from the boiling water surface in Fig. 5. The diameter of bubbles, d_B , at the water surface has been measured by photographic method.

The experimental result indicates that the turbulence intensity in the flow above the boiling water surface decays in a similar manner to that in the final period of the turbulent flow downstream from grids, that is, $(U/u')^{4/5} \propto z/d_B$ (Batchelor and Townsend (1947)(1948)). Figure 6 shows that the same relationship exists for the other fluids, although the values of the relative turbulence intensity are different each other. The values of the relative turbulence intensity obtained in the present experiment are much larger than those in the turbulence generated by grids. For example, the value of u'/U of water vapor are $0.2 \sim 0.3$ at $z/d_B = 200 \sim 450$ for the present experiment and those in the grid turbulence are in the order of 10^{-2} to 10^{-3} at $z/M = 100 \sim 200$ where M denotes the mesh size of the grid.

The variation of the measured concentration of the

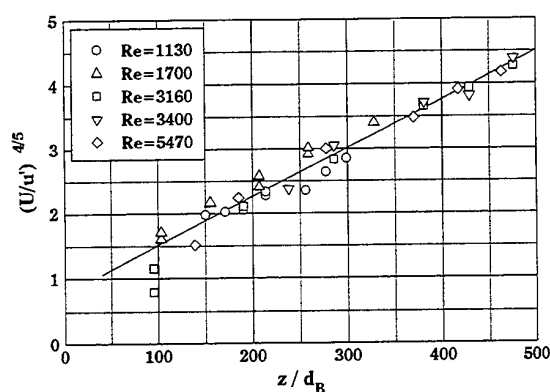


Fig. 5 Decay of turbulence intensity for water vapor flow.

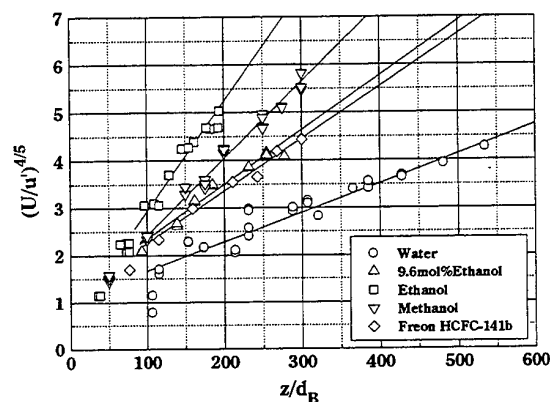


Fig. 6 Decay of turbulence intensity for various vapor flow.

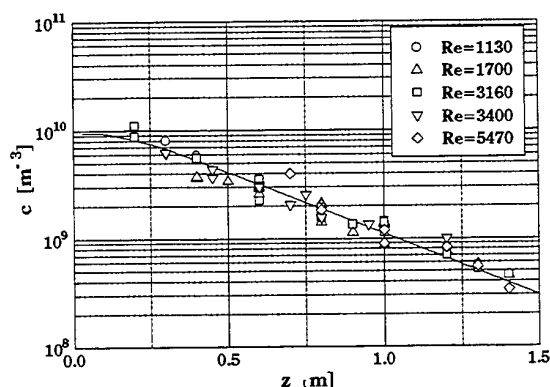


Fig. 7 Variation of concentration of water droplets with distance from the boiling water surface.

water droplet with the distance from the boiling water surface is shown in Fig. 7.

The result indicates that the concentration of the droplet decreases with increasing distance from the boiling water surface. The similar variation of the concentration of the droplets of other liquids has been obtained. The fact that the diameter of droplet dose not vary and the concentration of droplet decreases with the distance from the liquid surface indicates that the liquid droplets diffuse in radial direction and are deposited at the tube wall.

If we assume that the eddy diffusivity of the droplet is constant, the variation of the concentration of the droplet can be expressed by

$$U \frac{\partial c}{\partial z} = \varepsilon_p \frac{1}{r} \frac{\partial}{\partial r} \left(r \frac{\partial c}{\partial r} \right) \quad (1)$$

The boundary conditions are given by

$$z = 0 ; c = c_0 \quad (2)$$

$$r = 0 ; \frac{\partial c}{\partial r} = 0 \quad (3)$$

$$r = R ; c = 0 \quad (4)$$

where the concentration of the droplet is assumed to be zero at the tube wall.

If we further assume that the velocity of the vapor is uniform in the cross section of the tube, we obtain the following solution for the concentration of the droplet in the vapor flow.

$$\frac{c}{c_0} = \frac{2}{R} \sum_{n=1}^{\infty} \frac{J_0(\alpha_n r)}{\alpha_n J_1(\alpha_n R)} \exp \left(-\alpha_n^2 \frac{\varepsilon_p}{U} z \right) \quad (5)$$

where J_0 and J_1 are Bessel functions of zero and first order. The values of α_n are determined by $J_0(\alpha_n R) = 0$. The values of the eddy diffusivity ε_p are obtained by substituting the measured concentration of droplet into Eq. (5). The result is depicted in Fig. 8.

The measured eddy diffusivity of the droplet is correlated by

$$\varepsilon_p / \nu = 0.10 \text{ Re } \lambda^{1/2} \quad (6)$$

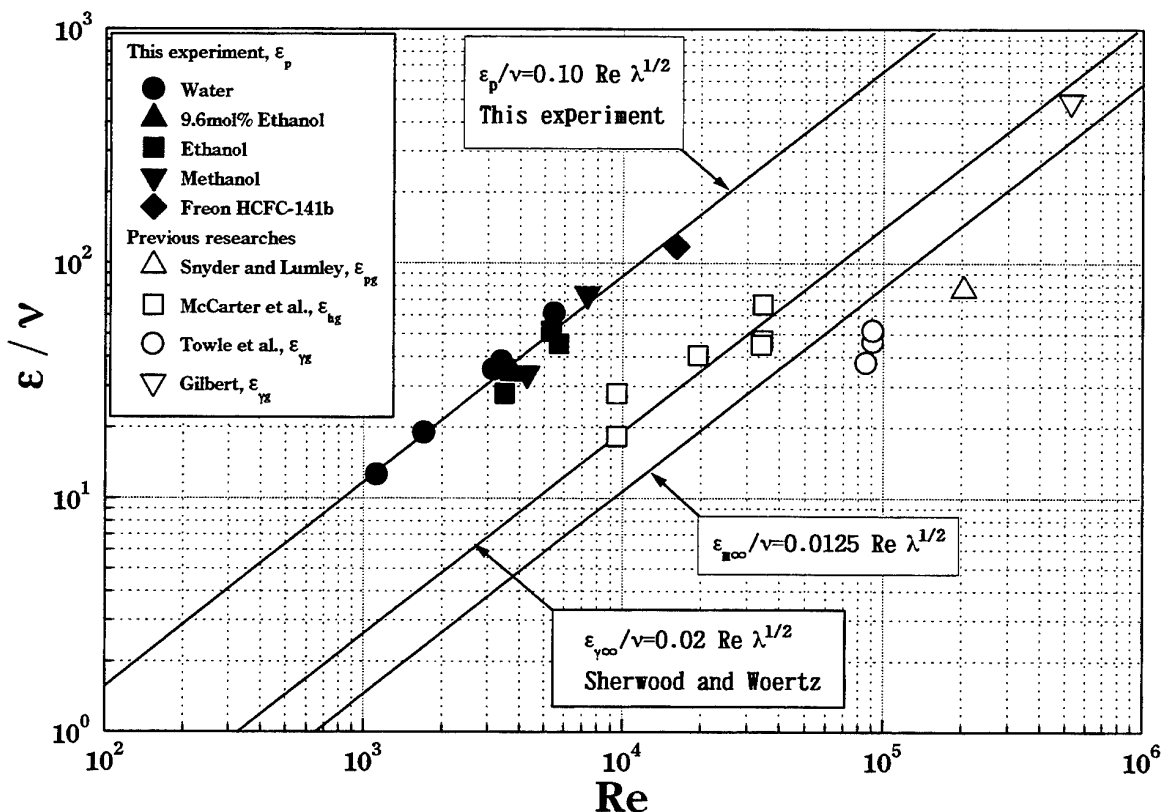


Fig. 8 Comparison of eddy diffusivity of droplet with those of momentum, heat and mass.

For comparison, experimental result obtained by Snyder and Lumley (1971) is shown in Fig. 8 along with the measured values of the eddy diffusivities for heat (McCarter et al. (1949)) and mass (Towle et al. (1939), Gilbert (1980)) in a turbulent flow behind a grid. Furthermore, the eddy diffusivities of momentum calculated from the velocity profiles measured by Laufer (1954) and that of mass obtained by Sherwood and Woertz (1939) in a fully developed pipe flow are also shown in Fig. 8. The subscripts m, h and γ denote respectively momentum, heat and mass. In addition, the subscripts g and ∞ represent grid turbulence and fully developed turbulent flow in the pipe, respectively.

The present experimental values of the eddy diffusivity of droplet are much higher than those of momentum and mass in the fully developed turbulent flow, whereas the eddy diffusivities of particle by Snyder and Lumley (1971) obtained in the flow downstream from a grid are smaller than those of momentum and mass in the fully developed flow. The values of the eddy diffusivity of mass obtained by Towle et al. (1939) in the flow downstream from a grid are also smaller than those in the fully developed pipe flow. However, the eddy diffusivity of heat by McCarter et al. (1949) and that of mass by Gilbert (1980) for the grid generated turbulence are in good agreement with that obtained by Sherwood and Woertz (1939) for the fully developed pipe flow.

On the whole, we can see that the values of the eddy diffusivity of particle as well as those of heat and mass for the grid generated turbulent flow are almost the same as those for the fully developed flow in tube, whereas those of droplet in the flow from boiling liquid surface are larger than those of momentum and mass for the fully developed flow.

Since the eddy diffusivity is usually expressed as the product of the turbulence intensity and the scale of turbulence, the higher values of the present experimental data can be considered to result from the larger value of the turbulence intensity. On the other hand, the lower value of those by Towle et al. (1939) can be attributed to small scale of the turbulence produced by the grids than the scale of turbulence in the fully developed turbulent flow in the tube.

4. CONCLUSION

1. The droplet size distribution shows a logarithmic normal distribution. The log-mean diameter of the droplets is constant regardless of the velocity of vapor and the distance from the boiling liquid surface.
2. The turbulence intensity decays in accordance with the decay law for the final period of the decay process in the flow downstream from grids.
3. The turbulence intensity in the flow of vapor generated at the boiling liquid surface is much larger than that generated by grids.
4. The eddy diffusivity of liquid droplet in the flow from boiling liquid surface is given by

$$\varepsilon_p / \nu = 0.10 \text{ Re } \lambda^{1/2}$$

NOMENCLATURE

c	concentration of droplets [m^{-3}]
c_d	concentration of droplets of the diameter d_p [m^{-3}]
c_0	concentration at boiling liquid surface [m^{-3}]
d_B	bubble diameter at boiling liquid surface [m]
d_p	liquid droplet diameter [μm]
J_0	Bessel function of zero order [-]
J_1	Bessel function of first order [-]
M	mesh length of grid [m]
R	inner radius of test section [m]
r	radial distance from center line of test section [m]
Re	Reynolds number [-] $\text{Re} = 2RU/\nu$
U	mean vapor velocity in tube [m/s]
u'	turbulent fluctuation [m/s]
z	distance from boiling liquid surface to measuring point
α_n	root of $J_0(\alpha_n R) = 0$ [m^{-1}]
ε_p	eddy diffusivity of droplet [m^2/s]
ε_{pg}	eddy diffusivity of particle in grid turbulence [m^2/s]
ε_{hg}	eddy diffusivity of heat in grid turbulence [m^2/s]
$\varepsilon_{\gamma g}$	eddy diffusivity of mass in grid turbulence [m^2/s]
$\varepsilon_{m\infty}$	eddy diffusivity of momentum in fully developed pipe flow [m^2/s]

$\varepsilon \rightarrow \infty$ eddy diffusivity of mass
in fully developed pipe flow [m^2/s]
 λ friction factor in pipe flow [-]
 ν kinematic viscosity [m^2/s]

REFERENCES

- Ahmadi, G. & Goldschmidt, V.W. 1970, Techn. Rep. F.M.T.R.70-3, Purdue Univ..
- Bachalo, W.D. & Houser, M.J. 1984, Phase/Doppler spray analyzer for simultaneous measurements of drop size and velocity distributions, Optical Eng., vol.23, pp.583.
- Batchelor, G.K. & Townsend, A.A. 1947, Decay of vorticity in isotropic turbulence, Proc. Roy. Soc. London, vol.190A, pp.534.
- Batchelor, G.K. & Townsend, A.A. 1948, Decay of turbulence in the final period, Proc. Roy. Soc. London, vol.194A, pp.527.
- Garner, F.H., Ellis, S.R.M. & Lacey, J.A. 1954, The size distribution and entrainment of droplets, Trans. Instn Chem. Engrs, vol.32, pp.222.
- Gilbert, B. 1980, Diffusion mixing in grid turbulence without mean shear, J. Fluid Mech., vol.100, pp.349.
- Goldschmidt, V.W., Householder, M.K., Ahmadi, G. & Chuang, S.C. 1972, Turbulent diffusion of small particles suspended in turbulent jets, Progress in Heat and Mass Transfer, vol.6, pp.487, Pergamon Press, New York.
- Kataoka, I. & Ishii, M. 1984, Mechanistic modeling of pool entrainment phenomenon, Int. J. Heat Mass Tran., vol.27, pp.1999.
- Laufer, J. 1954, The structure of turbulence in fully developed pipe flow, Natl. Advisory Comm. Aeronaut. Tech. Repts. No.1174.
- McCarter, R.J., Stutzman, L.F. & Koch Jr., H.A. 1949, Temperature Gradients and Eddy Diff. sivities in T. rbulent Fluid Flow, Ind. Eng. Chem., vol.41, pp.1290.
- Newitt, D.M., Dombrowski, N. & Knelman, F.H. 1954, Liquid entrainment: 1. The mechanism of drop formation from gas or vapour bubbles, Trans. Instn Chem. Engrs, vol.32, pp.244.
- Ooe, S. 1985, Bussei Jyousuu Suisanhou ed. Ooe, S., Nikkankougyoushinbunsha, Tokyo.
- Ramirez De Santiago, M. & Marvillet, C. 1991, Pool entrainment phenomenon: Measurement of size and velocity distributions of droplets at several distances above the bubbling surface, Int. Comm. Heat Mass Transfer, vol.18, pp.207.
- Saffman, M., Buchhave, P. & Tanger, H. 1984, Simultaneous measurement of size, concentration and velocity of spherical particles by a laser Doppler method, Proc. Sec. Int. Sym. on Appl. of Laser Anemometry to Fluid Mech., Lisboa, Paper 8.1.
- Sato, K. 1968, Bussei Jyousuu Suisanhou, ed. Sato, K., Maruzen, Tokyo.
- Sherwood, T.K. & Woertz, B.B. 1939, Mass Transfer between Phases, Ind. Eng. Chem., vol.31, pp.1034.
- Snyder, W.H. & Lumley, J.L. 1971, Some measurement of particle velocity autocorrelation functions in a turbulent flow, J. Fluid Mech., vol.48, pp.41.
- Tchen, C.M. 1947, Mean Value and Correlation Problems Connected with the Motion of Small Particles Suspended in a Turbulent Fluid, Ph.D. thesis, Delft University of Technology.
- Towle, W.L., Sherwood, T.K. & Seder, L.A. 1939, Effect of a Screen Grid on the Turbulence of an Air Stream, Ind. Eng. Chem., vol.31, pp.462.

SESSION 33

Flows with Unsteadiness

MEASUREMENTS OF UNSTEADY VELOCITY AND HEAT TRANSFER FOR CYLINDERS IN CROSS FLOW

J.W. Scholten, D.B. Murray and J.A. Fitzpatrick

Department of Mechanical Engineering,
Trinity College, Dublin 2, Ireland.

ABSTRACT

This paper describes the results of a study in which unsteady velocity and time dependent heat transfer are simultaneously recorded both for a single cylinder in cross flow with two turbulence levels and for a cylinder located within a small cluster of cylinders. Laser Doppler anemometry is used for the velocity measurements and fluctuations in heat flux are obtained from a hot film sensor mounted on the surface of a heated cylinder. The results obtained from both single cylinder and cylinder cluster tests demonstrate the strong dependence of surface heat transfer on local fluid dynamics.

1. INTRODUCTION

Detailed information on the heat transfer and flow characteristics of cylinders in cross flow is essential for the design of tubular heat exchangers. Studies of time-averaged heat transfer and flow parameters for cylinders in cross flow have been widely reported, as reviewed by Zukauskas and Ziugzda (1985). Time-resolved velocity and heat flux data are more useful, however, as tube arrays operate under turbulent flow conditions. For heat transfer, Mancuso and Diller (1991) used a microfoil sensor to measure fluctuations in surface heat flux for a periodic flow impinging on a flat plate. Heat transfer variations on the surface of an oscillating cylinder in cross flow were measured by Rosiczkowski and Hollworth (1991), but this was limited to low frequencies. For the front stagnation point of a cylinder in cross flow, Ching and O'Brien (1991) recorded the unsteady heat flux for high freestream turbulence conditions. The flow field around cylinders has also been studied extensively, using either hot wire or laser Doppler anemometry. For example, both Meyer and Larsen (1994) and Balabani et al. (1994) used laser Doppler anemometry to investigate the local flow magnitude and direction and the local turbulence intensity for flows through tube arrays.

This paper describes the results of a study in which unsteady velocity, measured using laser Doppler anemometry, and time dependent heat transfer are

simultaneously recorded both for a single cylinder in cross flow with two turbulence levels and for a cylinder located within a small cluster of cylinders. For the flow measurements, the tangential velocity is measured close to the cylinder surface, directly above the location for which the heat transfer rate is determined.

2. EXPERIMENTAL SET-UP

The test facilities consisted of a low turbulence (0.5%) wind tunnel with a perspex test section of 127 mm x 127mm. The test cylinder was installed horizontally and consisted of a thick walled copper tube of 25mm diameter, with an internal cartridge heater, approximating a uniform wall temperature boundary condition. The ends of the tube were constructed of tufnol to reduce axial heat loss. In addition to the low turbulence test, a turbulence grid was used to generate a flow with a mainstream turbulence intensity of 7% immediately upstream of the cylinder. For the cluster test, 2 unheated cylinders of the same diameter were located upstream, forming a triangular configuration similar to a staggered tube array with pitch to diameter ratio of 2.

Midway along the heated tube length, a thin constantan wire was embedded flush with the surface, and the tip of the wire was electrically connected to the copper of the tube to form a type T thermocouple junction. A Dantec 55R47 hot film sensor was mounted directly above this thermocouple junction in such a way that the hot film itself was aligned with the axis of the cylinder, giving a spatial resolution in the circumferential direction of 0.9° . All leads were brought out of the test section through one of the tufnol end pieces. The hot film was connected to a Dantec 55M10 standard bridge, which maintained the temperature of the hot film at a specified value. The estimated uncertainty in the absolute temperature of the hot film and of the tube surface is $\pm 0.3^\circ\text{C}$. However, the uncertainty in temperature difference between the hot film and the tube surface is $\pm 0.1^\circ\text{C}$. The 90% frequency response for the hot film was found to be about 10 kHz by using a square wave test.

For velocity measurements in the vicinity of the test tube, hot wire anemometry is inappropriate because of the temperature gradients close to the heated tube surface. Thus, laser Doppler anemometry was used for the velocity measurements. The laser Doppler system consisted of a 32 mW HeNe laser with Bragg cell for frequency shifting, and was used in forward scatter mode. The photomultiplier signal was processed by a TSI 1980B counter type processor which outputs velocity data points together with the time between successive data points.

3. DATA ACQUISITION AND ANALYSIS

For the heat transfer rate, the output from the bridge and the output from the embedded thermocouple junction were logged on a Pentium P5-60 computer through 2 channels of an Amplicon PC-30PGL AtoD board. The heat transfer rates were then calculated by dividing the amount of power dissipated in the hot film sensor:

$$Q_{diss} = (V_{Bridge}^2 - V_0^2) \frac{R_{sensor}}{(R_{arm} + R_{op})^2}$$

by the surface area of the sensor:

$$q_{diss} = \frac{Q_{diss}}{A_{eff}}$$

where A_{eff} is the surface area needed to take account of lateral conduction (see Beasley and Figliola, 1988). The contribution of conductive heat transfer between tube and sensor has been accounted for by use of the embedded thermocouple:

$$q_{cond} = k_{kapton} \frac{(T_{tube} - T_{tube,0})}{\delta}$$

where δ refers to the thickness of the sensor substrate. So the total heat flux that is being used for convective heat transfer equals:

$$q_{conv} = q_{diss} + q_{cond}$$

To non-dimensionalise the heat transfer rate, the Nusselt number is calculated as:

$$Nu = \frac{q_{conv} D}{k_{air} (T_{sensor} - T_{amb})}$$

Data acquisition for the combination of LDA and heat transfer rates was performed by simultaneous recording through the direct memory access technique (DMA) into the computer, and AtoD conversions were started by a triggering pulse from the LDA-counter processor in such a manner that a heat transfer data point is taken each time a LDA-point is taken. The velocity and heat flux data, which

both consist of discrete data points and time-between-data points, were resampled at equidistant time intervals by using a 1st order interpolation. This has been shown by Simon et al. (1995) to reduce bias in spectral estimates from randomly sampled data.

The degree of correlation between turbulence and heat flux was estimated using coherence functions rather than the usual cross-correlation function. The coherence function gives the degree of correlation as a function of frequency and is considered to provide more insight into the underlying mechanisms of turbulent heat transfer. In addition, the phase difference between velocity and heat flux signals provides further information on the heat transfer mechanisms. The auto spectra for the turbulence and heat transfer data were calculated using FFT based procedures and the coherence function, which is a normalised form of the cross spectrum (e.g. Bendat and Piersol, 1986), was computed from these.

4. RESULTS

Fluctuations in heat flux on the surface of a cylinder in cross flow originate in local unsteadiness of the flow. For a single cylinder in cross flow the velocity fluctuations result

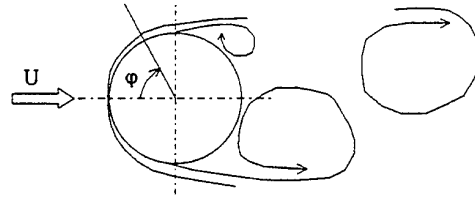


Figure 1: Typical flow pattern around a cylinder.

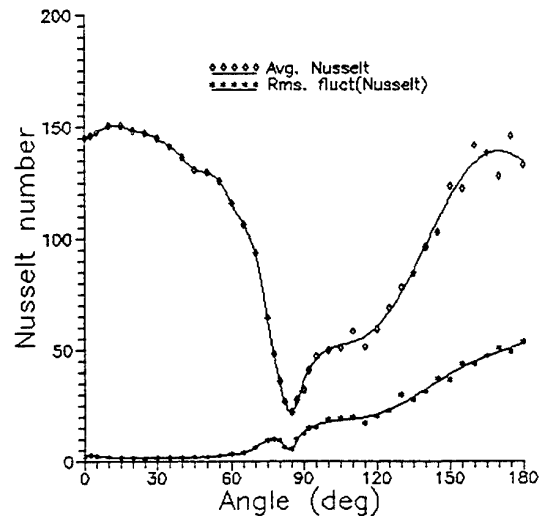


Figure 2: Local Nusselt number and Nusselt number fluctuations for a single cylinder in cross flow.

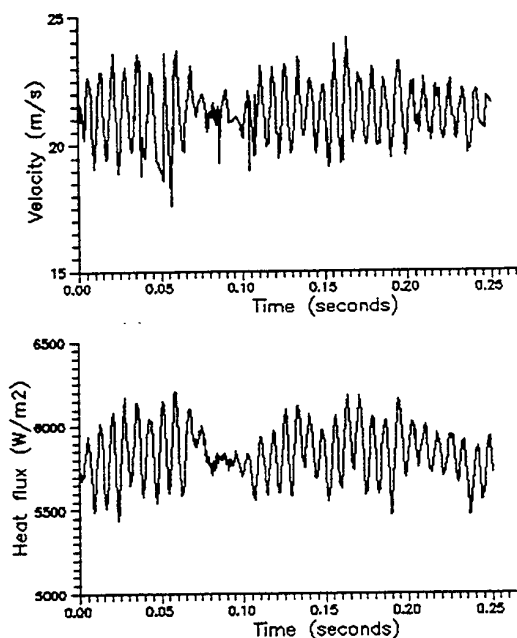


Figure 3: Simultaneous traces of velocity and heat flux.

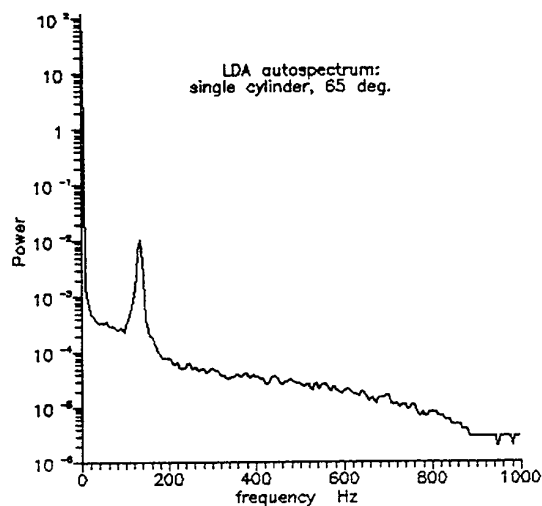


Figure 4(a): Velocity auto spectrum for single cylinder.

from the shedding of vortices at the back of the cylinder. Figure 1 shows a typical flow pattern with a boundary layer developing from the front stagnation point (0°). This boundary layer separates at around $80-90^\circ$, depending on flow Reynolds number, and alternate vortex shedding takes place from each side of the cylinder. The pattern shown is characteristic of subcritical Reynolds numbers where transition to turbulence has not taken place within the boundary layer.

Figure 2 shows the time-averaged local Nusselt numbers, obtained from the hot film data, for a single cylinder with a main stream velocity of 15 m/s,

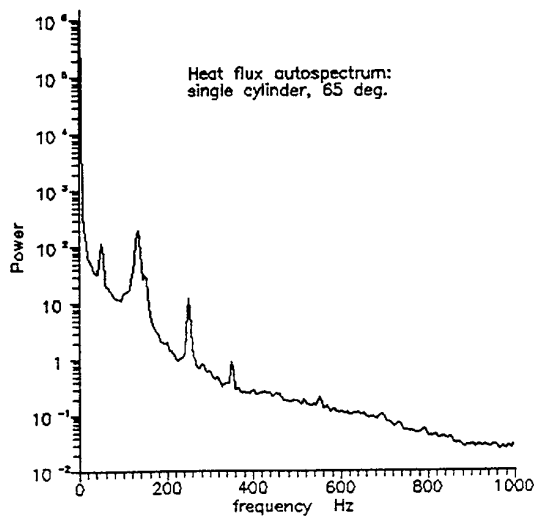


Figure 4(b): Heat flux auto spectrum for single cylinder.

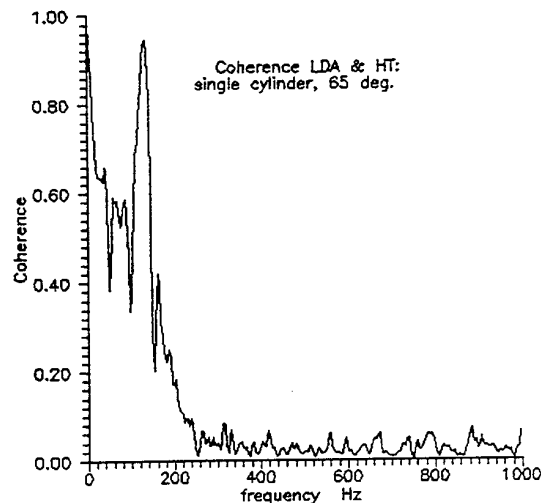


Figure 5: Coherence for single cylinder case.

corresponding to a tube Reynolds number of 24000. The pattern observed is typical for subcritical Reynolds numbers, with the minimum Nusselt number corresponding to separation of the laminar boundary layer at 85° . In addition to the time-averaged Nusselt number, the rms values of the unsteady heat transfer are shown. It can be seen that the fluctuations at the front of the tube are very small, whereas the fluctuations measured over the rear of the tube are large due to extensive mixing and recirculation in the wake.

Figure 3 shows simultaneous time records for heat flux at the cylinder surface and velocity 1mm above this point. The measurements were taken at 65° from the front stagnation point for the single cylinder in cross flow with a Reynolds number of 24000. It is clear that the two time traces show the same trend of strong fluctuations at the

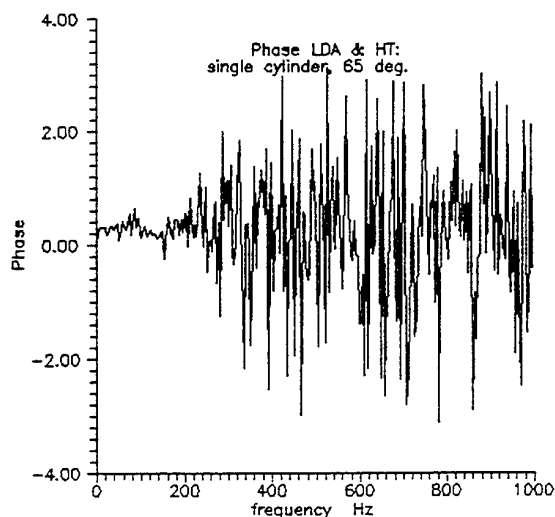


Figure 6: Phase difference for single cylinder case.

vortex shedding frequency. Figures 4(a) and 4(b) show the auto spectra for velocity and heat flux at 65° , with both graphs containing a strong peak at the vortex shedding frequency (130 Hz). The additional peaks evident on figure 4(b) originate in mains noise. Figure 5 shows the coherence between the 2 signals. A maximum coherence of 0.96 is reached for the shedding frequency, confirming the strong dependence of surface heat flux on local velocity. The low coherence for the remainder of the frequency range results from the very low level of fluctuations at frequencies other than 130 Hz. Figure 6 shows the phase difference between the velocity and heat flux signals for this set-up. The phase difference at the vortex shedding frequency, taking some signal variance into consideration, is zero, indicating that there is no time delay between the velocity and heat transfer fluctuations.

Figure 7 shows the auto spectra of velocity and heat flux for the test conducted with the upstream turbulence grid. From figure 7(a), it can be seen that although the general level of velocity fluctuations has increased, as compared with the low turbulence case, there is still a strong peak at the vortex shedding frequency. In contrast, for the heat transfer case, figure 7(b) shows that the rise in the general level of fluctuations is so significant that the peak associated with vortex shedding cannot be detected. Despite this, the peak in coherence at the vortex shedding frequency, shown in figure 8, indicates that the surface heat flux is still influenced by velocity fluctuations linked to vortex shedding. Unlike the low turbulence case, figure 9 shows that there is a phase difference between the surface heat flux and the velocity measured 1 mm away from the cylinder. The reasons for this phenomenon will be addressed later.

For the cylinder located within the small cluster, Figure 10 shows the time traces for velocity and heat flux at 65° . It can be seen that the correspondence is not as good as for the single cylinder low turbulent case, but some similarity is evident. Figures 11(a) and 11(b) show the auto spectra for the same conditions. In contrast to the single

cylinder cases, multiple dominant frequencies can be seen in both the velocity and the heat transfer spectra. All peaks in the heat flux spectrum can be seen to match those present in the velocity spectrum, with the exception of the first harmonic of the lowest dominant frequency. This peak cannot be found in the velocity data. The lowest dominant frequency (92 Hz) is due to vortex shedding from the second row whereas first row vortex shedding results in a peak at 316 Hz. The auto spectra peak at 224 Hz is thought to result from interaction between first and second row shedding, similar to that described by Oengoren & Ziada (1995). The highest peak at 408 Hz is a consequence of local boundary layer effects for the cluster case, as confirmed by hot wire measurements. Figure 12 shows the coherence between the two signals for the cluster. Apart

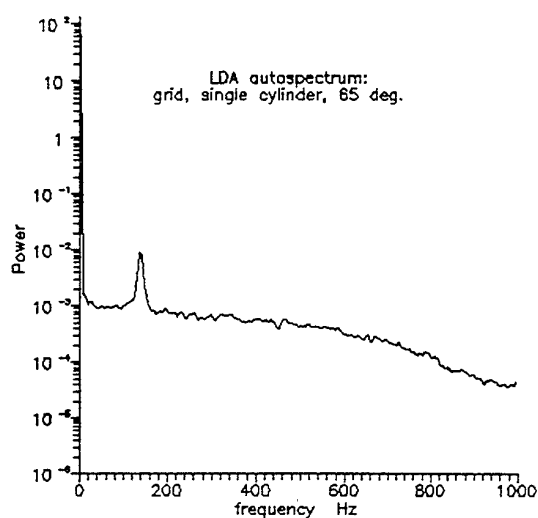


Figure 7(a): Velocity auto spectrum for the single cylinder, high turbulent case.

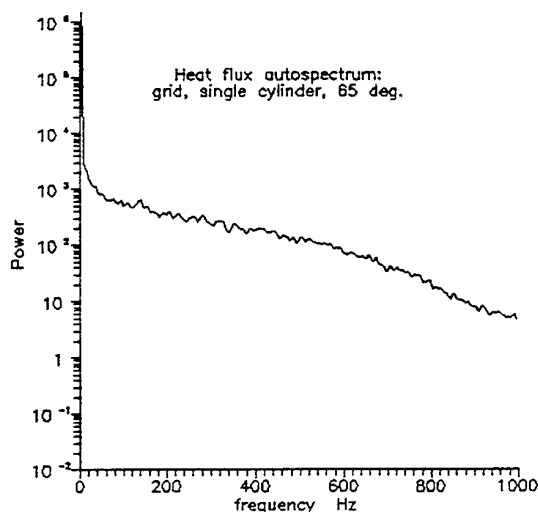


Figure 7(b): Heat flux auto spectrum for the single cylinder, high turbulent case.

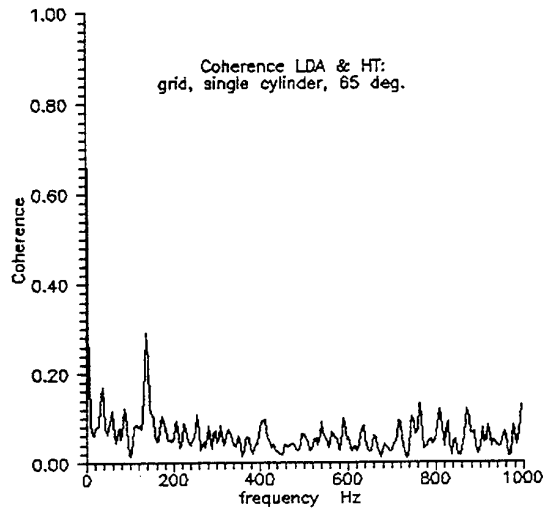


Figure 8: Coherence for the single cylinder, high turbulence case.

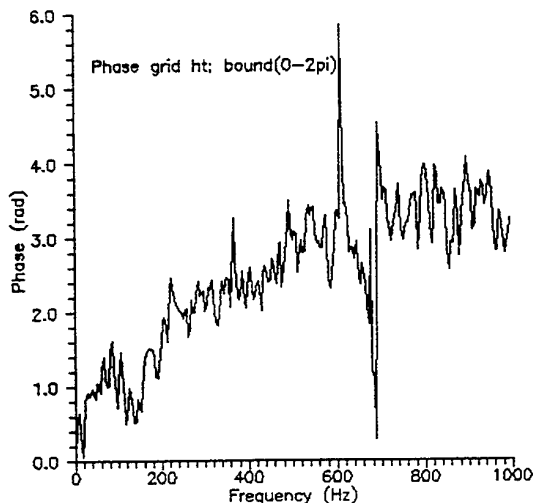


Figure 9: Phase difference for the single cylinder, high turbulence case.

from the above mentioned harmonic all peaks in the auto spectra appear in the coherence plot. Figure 13 shows the phase difference between the velocity and heat flux signals for the cluster test. As in the high turbulence case, there is a rise in phase difference with increasing frequency indicating a time delay between the measured fluctuations.

5. DISCUSSION OF PHASE DIFFERENCE

For the low turbulence case, the velocity fluctuations originate in pulsation of the entire flow field as a consequence of vortex formation and shedding. This is true even in the case of the present measurements which were

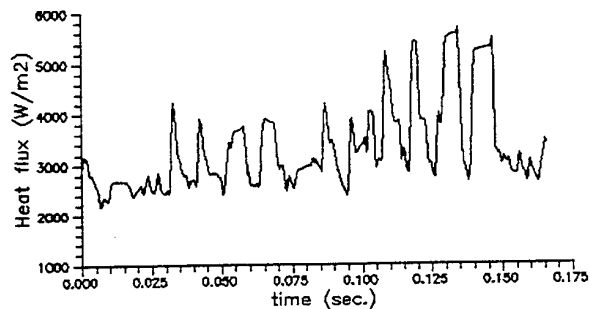
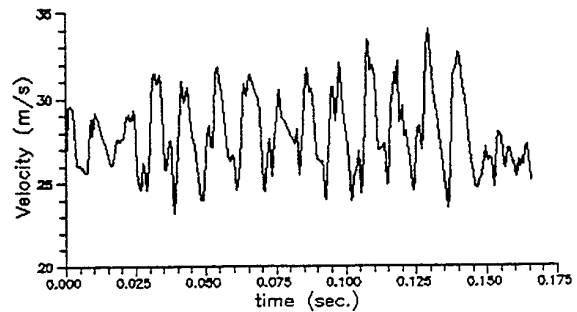


Figure 10: Velocity and heat flux time traces for the cylinder cluster case.

obtained at 65° which is upstream of the flow separation point. This is indicated by the zero phase lag between the velocity and heat flux fluctuations. Further confirmation that the velocity fluctuations originate in a pulsating flow field can be obtained from figure 14 which shows the phase difference between surface heat flux at 65° and velocity measured 15mm from the surface at 90° . It can be seen that the phase difference is again zero suggesting that the velocity outside of the wake region changes everywhere at the same time. The coherence value for this distant measurement, at the vortex shedding frequency, equals the value obtained in figure 5.

In contrast, for the high turbulence case, the velocity fluctuations are due to the transport of small turbulent eddies. The radial motion of these eddies has a significant influence on surface heat flux, but the low radial velocity results in a time delay between the velocity and heat transfer fluctuations. This shows up in the steep slope of the phase difference plotted in figure 9. Beyond a frequency of around 600Hz, the phase difference flattens out as a consequence of the zero phase difference from the higher content of interpolation noise in this frequency range.

For the cluster case, the rise in phase difference with increasing frequency suggests that a significant part of the heat transfer fluctuations result from turbulent eddy transport similar to that described for the high turbulence case. This is despite the fact that the multiple peaks evident in the coherence plot of figure 12 result from vortex shedding from the different cylinders.

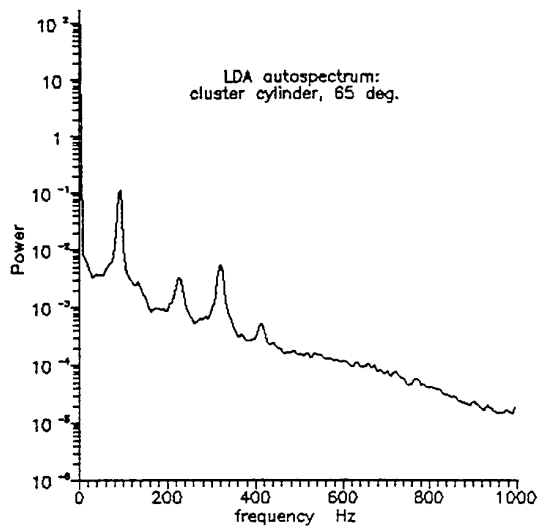


Figure 11(a): Velocity auto spectrum for the cylinder cluster case.

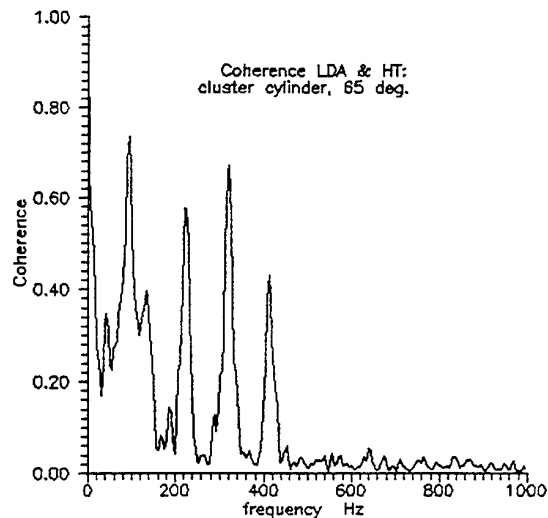


Figure 12: Coherence for the cylinder cluster case.

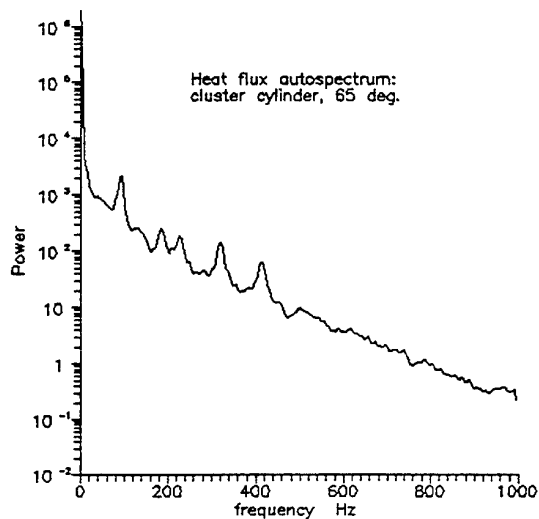


Figure 11(b): Heat transfer auto spectrum for the cylinder cluster case.

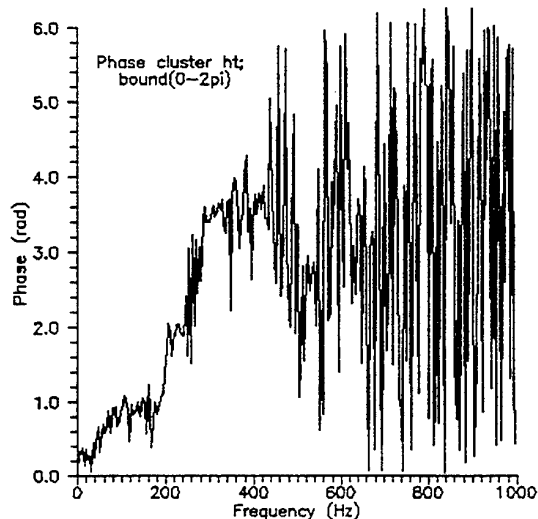


Figure 13: Phase difference for the cylinder cluster case.

6. CONCLUSIONS

A method has been developed for making simultaneous measurements of time-resolved velocity and local heat flux at the surface of a cylinder in cross flow. The results obtained from both single cylinder and cylinder cluster tests demonstrate the strong dependence of surface heat transfer on local fluid dynamics.

7. ACKNOWLEDGEMENT

The authors would like to acknowledge Laurent Simon (Laboratoire d'Acoustique de l'Université du Maine, Le Mans, France) for his major contribution to the MATLAB data processing procedures.

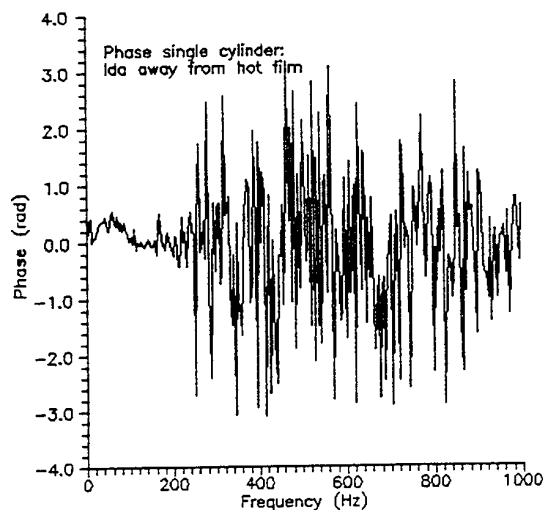


Figure 14: Phase difference for the single cylinder case, but with the LDA measurement volume located away from the location of surface heat transfer.

8. NOMENCLATURE

A_{eff}	: Effective surface area of the hot film sensor [m^2],
D	: Tube diameter [m],
$k_{kapton,air}$: Thermal conductivity of kapton, air [W/mK],
Nu	: Nusselt number,
Q_{diss}	: Dissipated electrical energy [W],
q_{cond}	: Conductive heat flux [W/m^2],
q_{conv}	: Convective heat flux [W/m^2],
q_{diss}	: Electrical energy dissipation heat flux [W/m^2],
R_{arm}	: Resistance of the active arm of the wheatstone bridge that controls the hot film [Ω],
R_{sensor}	: Hot film sensor resistance [Ω],
R_{top}	: Top resistance in the wheatstone bridge [Ω],
T_{amb}	: Ambient temperature [K],
T_{sensor}	: Hot film sensor temperature [K],
T_{tube}	: Tube surface temperature [K],
V_0	: Bridge voltage at the no flow condition [V],
V_{bridge}	: Bridge voltage with flow [V].

9. REFERENCES

- Balibani, S., Bergeles, G., Burry, D., and Yianneskis, M., 1994, Velocity Characteristics of the Crossflow over Tube Bundles, *Proc. 7th Int. Symposium on Applications of Laser Anemometry to Fluid Mechanics*, Lisbon, pp. 39.3.1-39.3.7.
- Beasley, D.E., and Figliola, R.S., 1988, A Generalised Analysis of a Local Heat Flux Probe, *J. Physics E*, vol. 21, pp. 316-322.
- Bendat, J.S. and Piersol, A.G., 1986, *Random Data: Analysis and Measurement Procedures*, Wiley Intersc., New York.
- Ching, C.Y., and O'Brien, J.E., 1991, Unsteady Heat Flux in a Cylinder Stagnation region with High Freestream Turbulence, *Fund. Exp. Meas. in Heat Transfer*, ASME, HTD-vol.179, pp. 57-66.
- Mancuso, T., and Diller, T.E., 1991, Time-resolved Heat Flux Measurements in Unsteady Flow, *Fund. Exp. Meas. in Heat Transfer*, ASME, HTD-vol.179, pp. 67-74.
- Meyer, K.E., and Larsen, P.S., 1994, LDA Study of Turbulent Flow in a Staggered Tube Bundle, *Proc. 7th Int. Symposium on Applications of Laser Anemometry to Fluid Mechanics*, Lisbon, pp. 39.4.1-39.4.7.
- Oengoren, A. and Ziada, S., 1995, Vortex Shedding, Acoustic Resonance and Turbulent Buffeting in Normal Triangular Tube Arrays, *Proc. 6th Int. Conf. on Flow Induced Vibration*, London, pp.295-313.
- Rosicskowski, J., and Hollworth, B., 1991, Local and Instantaneous Heat Transfer from an Isothermal Cylinder in Cross-Flow, *Fund. Exp. Meas. in Heat Transfer*, ASME, HTD-vol.179, pp. 49-56.
- Simon, L., Scholten, J., and Fitzpatrick, J., 1995, Velocimétrie Laser: Amélioration du Traitement des Données Expérimentales par Interpolation d'Ordre 1, *Proc. Congrès Français de Mécanique*, Strasbourg, pp.321-324.
- Zukauskas, A., and Ziugzda, J., 1985, *Heat Transfer of a Cylinder in Cross Flow*, pp. 97-127, Springer-Verlag.

MEASUREMENTS OF FLOW AROUND TWO-DIMENSIONAL CIRCULAR CYLINDER BUNDLES WITH LDV

Kazumi Tsunoda, Shiki Okamoto, Masamichi Kijima, Shinobu Higashi

Department of Mechanical Engineering,
Shibaura Institute of Technology, Tokyo, Japan

and

Nobuaki Abe

Morinaga Milk Industry CO., LTD., Tokyo, Japan

ABSTRACT

Velocity vectors and turbulence intensity around two-dimensional circular cylinder bundles arranged in a single row or three rows were measured by using a laser Doppler velocimeter(LDV). The experiments were conducted for various spacing ratios which were defined as the ratio of the spacing between two adjoining circular cylinders to the circular cylinder diameter. The existence of a biased flow between two streamwise circular cylinders was shown by the feature of velocity vector field for small spacing ratio. In the case of three rows arrangement, alternate peaks of the streamwise and spanwise components of turbulence intensity appeared behind the first and second row for small spacing ratio, whereas symmetric double peaks appeared behind first, second and third row for large spacing ratio. Measurements of the frequency of vortex shedding from circular cylinders were also carried out by using an LDV. The characteristics of vortex shedding were discussed for various spacing ratio.

1. INTRODUCTION

Studies on fluid forces acting on circular cylinder bundles recently attracts the attention in many engineering applications. With the development of energy equipment, the investigation on the mechanism of fluid-elastic vibrations becomes particularly important issue to counteract the vibration of circular cylinder bundles installed in various types of heat exchangers. It is therefore necessary in such circumstances to discuss flow structure around circular cylinders in detail. Understanding the fluid forces acting on a single circular cylinder has been the primary focus of early experimental research. However, when many circular cylinders are placed perpendicular to the streamwise direction, the interference between separated flows from adjoining circular cylinders gives rise to complexity of the flow-field, thus characteristics of the flow-field would markedly changed compared with those for a single circular cylinder.

In relation to this problem, Zdravkovich(1977) cited many references and discussed the general subject of flow interference between two circular cylinders in various arrangements. Moreover investigations of the flow-field around several circular cylinder bundles positioned at right angles to the approaching flow direction have been done by many researchers. Zukauskas(1972) reported the investigations of tube banks of various arrangements and a single tube in cross-flow and discussed the surface pressure, drag, velocity distribution and flow pattern around a tube in a bank. Ishigai and Nishikawa(1974) observed flow structure over circular cylinder rows for various arrangements by Schlieren method. In addition to this Nishikawa and Ishigai(1977) reported the pressure loss induced by circular cylinders arranged in five or six rows. In the references mentioned so far no systematic information is presented on the detailed flow structure and shedding vortex. Weaver and Abd-Rabbo(1985) studied the flow behavior in tube arrays in water crossflow and presented the turbulence, vortex shedding and fluid-elastic instability including visualization photographs under the square array with a spacing ratio of 1.5. Abd-Rabbo and Weaver(1986) reported the similar result for a spacing ratio of 1.41. Nishimura et al.(1993) measured the surface shear stress distributions and mass transfer rates and performed flow visualizations in a staggered array and an in-line array in tube banks. Balabani et al.(1994) presented the velocity characteristics of the cross-flow over tube bundles in a staggered arrangement in water flow and compared them with the numerical result based on the $k-\epsilon$ turbulence model. Okamoto et al.(1994) reported systematic studies on the effect of the ratio of spacing between two adjoining circular cylinders to diameter on flow properties.

The present paper describes an experimental study of flow structure around the circular cylinder bundles arranged in a single row namely, side by side arrangement or three rows. In order to obtain detailed flow structure around the circular cylinder bundles, we used LDV thus the information of flow field, turbulence intensity and shedding vortices would be comprehended even in the narrow region among adjoining circular cylinders.

2. EXPERIMENTAL APPARATUS AND MEASUREMENT PROCEDURES

The experiment was carried out in a circuit type wind tunnel of a 200mm × 200mm working section and 2000mm in length. Two-dimensional circular cylinders with diameter $D = 20\text{mm}$ or 30mm were aligned at regular space S in square array, and the first row of them was placed at 500mm downstream of the leading edge of the ground plate as shown in Fig.1. The spacing ratio between two adjoining circular cylinders was varied as $S/D = 1.3, 1.5, 1.7, 2.0, 2.3, 2.5, 3.0$ and ∞ . The time-mean velocity and turbulence intensity were measured by LDV. The LDV used in this experiment is as follows (forward scattering dual beams mode, 2 colors 4 beams, power: 4 watt argon-ion, operating power: 300mW, wave length: green 514.5nm, blue 488nm, beam spacing: 50mm, focal distance: 500mm, measurement region: diameter 0.16mm, length 3.2mm). The smoke of the joss stick was used for seeding the air flow. Flow properties were measured under the condition of $Re = U_\infty D / \nu = 9.4 \times 10^3$.

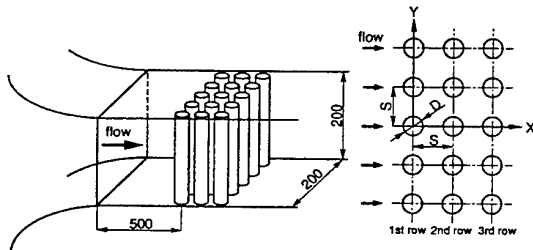


Fig.1 Experimental apparatus and nomenclature.

3. EXPERIMENTAL RESULTS AND DISCUSSIONS

3.1 Flow structure past a single two-dimensional circular cylinder

We first examined the flow structure past a single two-dimensional circular cylinder, since the wake behind a row which is composed of many circular cylinders is closely related to that behind a single one in general. Figure 2 shows

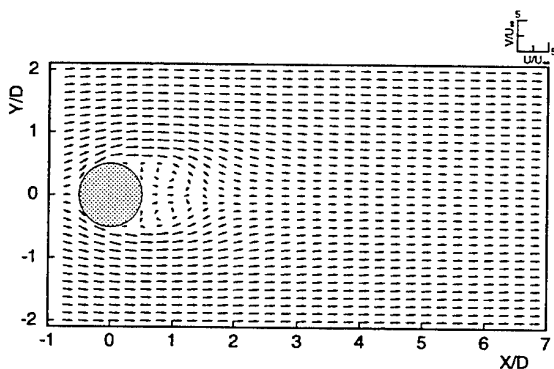


Fig.2 Distribution of velocity vectors in horizontal center plane for a single circular cylinder.

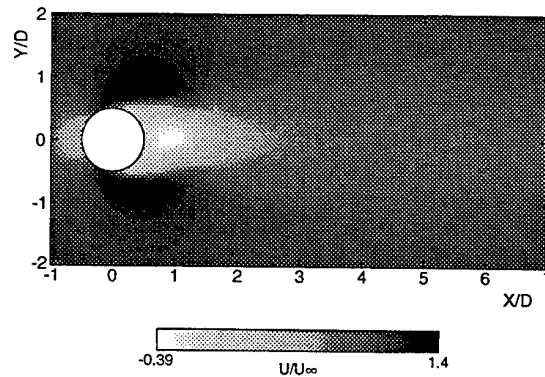


Fig.3 Contour of mean streamwise velocity in horizontal center plane for a single circular cylinder.

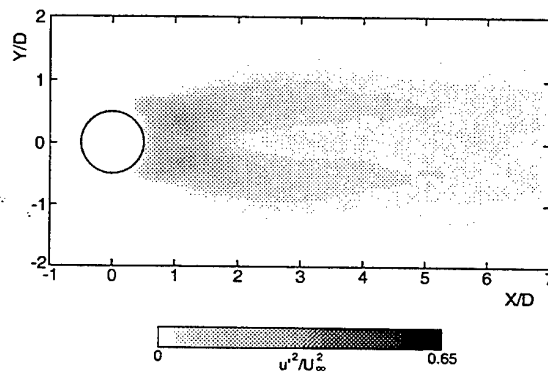


Fig.4 Contour of X-component of turbulence intensity in horizontal center plane for a single circular cylinder.

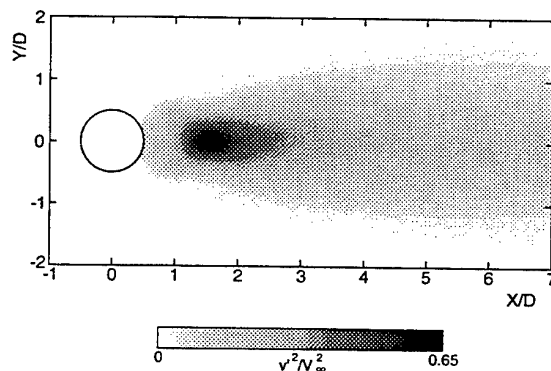


Fig.5 Contour of Y-component of turbulence intensity in horizontal center plane for a single circular cylinder.

the distribution of velocity vectors which are measured in the horizontal center plane and nondimensionalized by the free stream velocity of U_∞ . As we shall see in Fig.15, the power spectrum measured behind the single two-dimensional circular cylinder has a peak at a frequency corresponding to that of the vortex shedding in the present experiment. However, a regular vortex street cannot be observed in Fig.2 since instantaneous velocities were averaged with respect to time. The

contour of mean streamwise velocity in the horizontal center plane is presented in Figure 3. This figure clearly shows that a stationary reverse flow region exists near the rear face of circular cylinder and its longitudinal length of the reverse flow region reaches about $1.4D$ along the line of $Y/D = 0$.

Figure 4 illustrates the contour of X -component of turbulence intensity. We can see that there are two peaks in the distribution of the turbulence intensity and their locations are symmetrical with respect to the center line of $Y/D = 0$. The values of the turbulence intensity become maximum near $X/D = 1$ and $Y/D = \pm 0.4$. On the other hand the distribution of Y -component of turbulence intensity differs from that for X -component one, as shown in Figure 5. For Y -component of turbulence intensity, the distribution with one peak appears behind the circular cylinder and its magnitude attains maximum near $X/D = 1.5$ on the center line of $Y/D = 0$. It means that the wake has a relatively strong tendency to spread transversely in this region.

3.2 Flow structure around the circular cylinders arranged in a single row

The flow separating from one circular cylinder is capable of interacting with another one, which causes to change the flow-pattern around them. Therefore, in order to confirm the basis of the flow-field which is necessary to discuss the flow behavior around the circular cylinder bundles, we have to measure the flow properties around the circular cylinders arranged in a single row. Okamoto et al.(1994) reported that a flow-pattern around circular cylinders changed with spacing ratio of S/D and was characterized for the case of small spacing ratio and large one. In accordance with this result, two parameters of $S/D = 1.5$ and 2.5 were selected to discuss the detailed flow structure in the present paper.

Figure 6 represents the velocity vectors around the circular cylinders placed in a single row for the case of $S/D = 1.5$ and 2.5 . We can see that the flow passing through the gap between adjoining cylinders goes downstream along the streamwise direction. Moreover, in the case of $S/D = 1.5$, a reverse flow can be observed in the region of $X/D < 2.0$. It is found from the comparison of Fig.6(a) with Fig.6(b) that the size of reverse flow region behind a cylinder decreases with increase in spacing between cylinders, and the reverse flow exists in the region of $X/D < 1.5$ when the spacing ratio achieves $S/D = 2.5$.

The contour maps of streamwise velocity for $S/D = 1.5$ and 2.5 are shown in Figure 7. For both cases, the flow velocity increases in the gaps of two adjoining circular cylinders and decreases to negative value in the reverse flow region behind each circular cylinder. From the comparison of Fig.7 with Fig.3, the longitudinal length of reverse flow region behind circular cylinder becomes longer and the wake is decelerated stronger than those for single circular cylinder. The velocity profile in the near wake behind the circular cylinder is seen almost symmetric with respect to the center line even for $S/D = 1.5$.

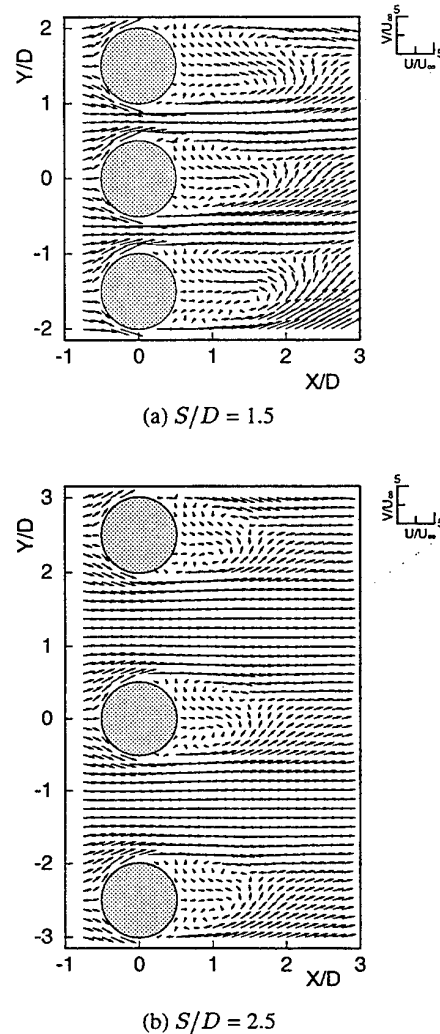


Fig.6 Distribution of velocity vectors around the circular cylinders in a single row.

Spatial distributions of X - and Y -component of turbulence intensity are given in Figure 8 and 9, respectively. It can be seen in Fig.8 that for both spacing ratios the distribution of X -component of turbulence intensity has two symmetric peaks with respect to the lines parallel to X -axis through centers of circular cylinders. For $S/D = 2.5$ this distribution is similar to that for single circular cylinder as seen in Fig.4. In the case of Y -component of turbulence intensity, we can recognize from Fig.9 that there appears one peak behind each circular cylinder for $S/D = 1.5$ and 2.5 . The peak position locates on the streamwise direction center line and shifts to upstream with increase in spacing ratio. Moreover, as shown in Fig.8 and 9, the X - and Y -component of turbulence intensities are weakened as the spacing is increased from $S/D = 1.5$ to 2.5 .

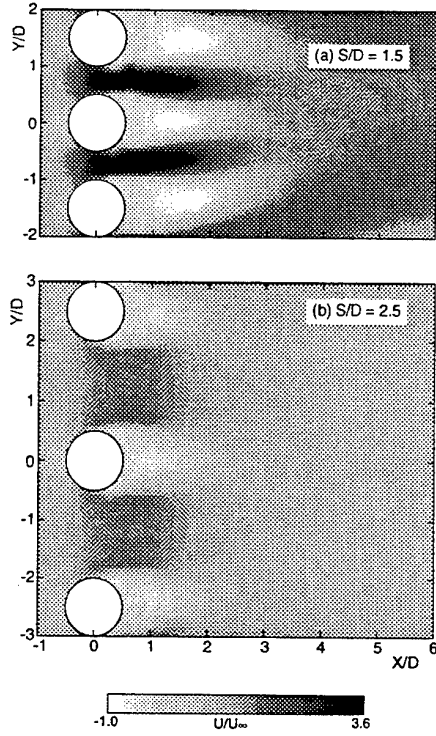


Fig.7 Contour of mean streamwise velocity around the circular cylinders in a single row.

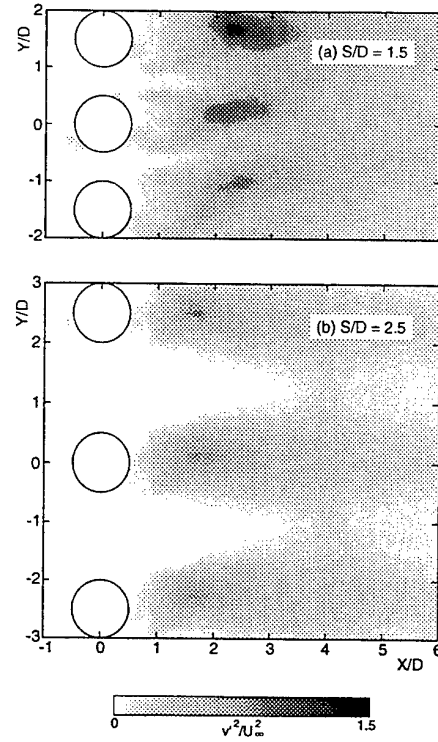


Fig.9 Contour of Y-component of turbulence intensity around the circular cylinders in a single row.

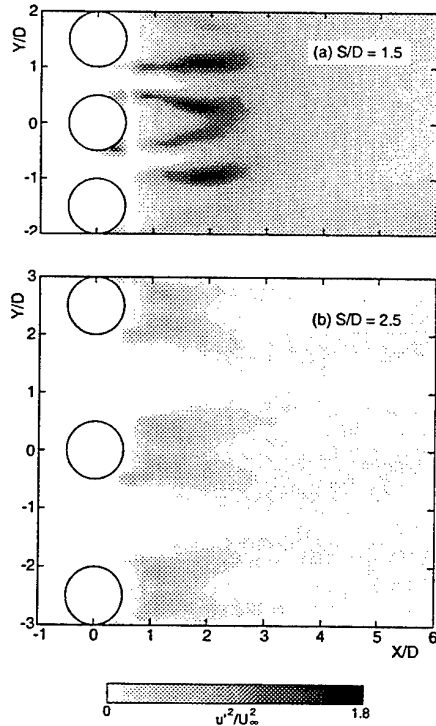


Fig.8 Contour of X-component of turbulence intensity around the circular cylinders in a single row.

3.3 Flow structure around the circular cylinders arranged in three rows

Figure 10 indicates the velocity vectors around the circular cylinders arranged in three rows. For the case of $S/D = 1.5$, in the region between first and second row, the flow goes to negative Y -direction. On the contrary, the flow goes to positive Y -direction in the region between second and third row. These streams generate clockwise circulating flow behind the first row and counter-clockwise one behind the second row, respectively. This type of biased flow was observed in the case of $S/D \leq 1.7$. Therefore the velocity profile in the near wake behind each circular cylinder becomes asymmetric with respect to the center line. It causes the generation of the lift. On the other hand, for the case of $S/D = 2.5$, it is clear that the main stream goes downstream along the streamwise direction and two circulating flows occupy the entire region between first and second row, and between second and third row. The sizes of these circulating flows are comparable to that for the case of single circular cylinder as seen in Fig.2.

In order to investigate the flow structure quantitatively, we show the contour of the streamwise velocity in Figure 11. For the case of $S/D = 1.5$, reverse flow regions appear on the downstream side of the first and second rows. These locations are antisymmetrical with respect to the line connecting the centers of the circular cylinders along the streamwise direction because of the existence of biased flow. For the case of $S/D = 2.5$, negative values of the streamwise ve-

locity can be seen symmetrically along the streamwise line connecting the centers of circular cylinders behind each row. In this case, positive values of the streamwise velocity occur in the part of the region between second and third row, which fact means the change of flow-pattern around the circular cylinders. From the results shown in Fig.10 and 11, the two flow-patterns, which are inferred from the surface-pressure distribution measurements and the power spectrum analyses of vortex shedding in our previous researches, are confirmed also by the velocity distribution measurements with LDV.

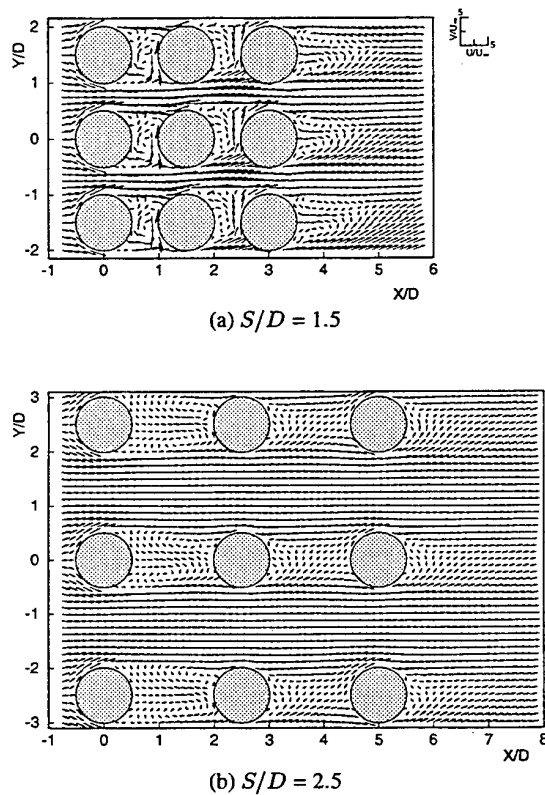


Fig.10 Distribution of velocity vectors around the circular cylinders in three rows.

The distributions of the X-component of turbulence intensity are shown as contour maps in Figure 12. For small spacing ratio($S/D = 1.5$), alternate peaks of turbulence intensity can be identified behind the first and second row. The distribution with two peaks behind the third row is similar to that observed in the near wake of a single circular cylinder. On the other hand, for large spacing ratio($S/D = 2.5$), two peaks appear behind first, second and third row, and these values are smaller than that for the case of $S/D = 1.5$.

Figure 13 illustrates the contour of the Y-component of turbulence intensity. For small spacing ratio($S/D = 1.5$), the distribution of the Y-component of turbulence intensity has also alternate peaks behind the first and second row. Although this distribution is similar to that for the X-component of

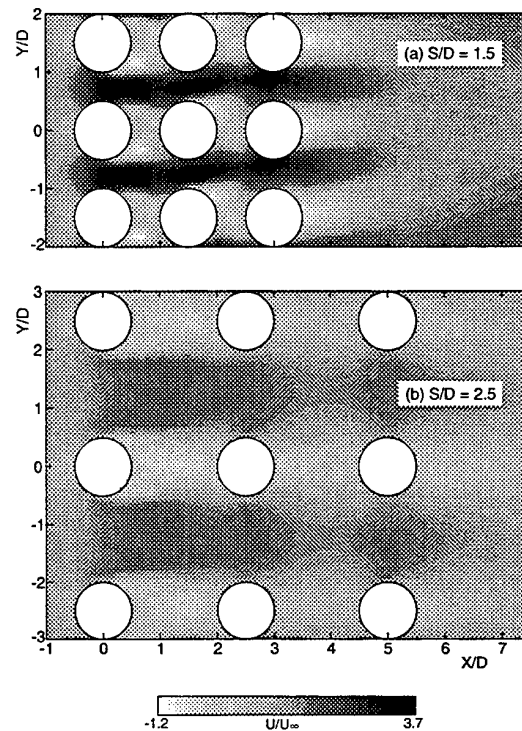


Fig.11 Contour of mean streamwise velocity around the circular cylinders in three rows.

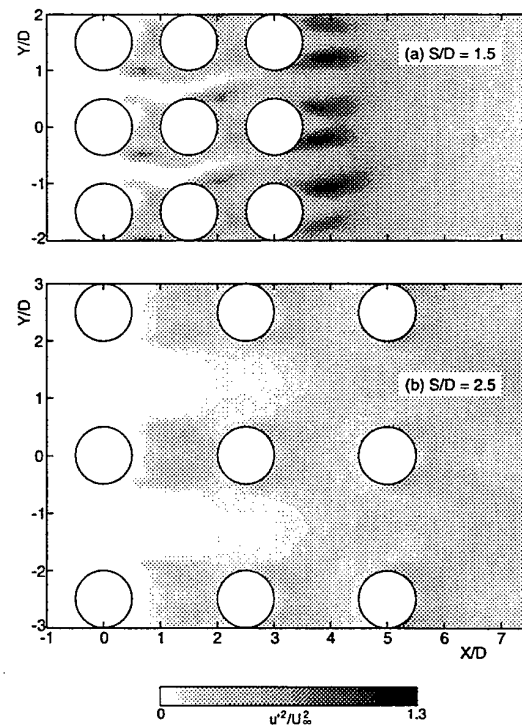


Fig.12 Contour of X-component of turbulence intensity around the circular cylinders in three rows .

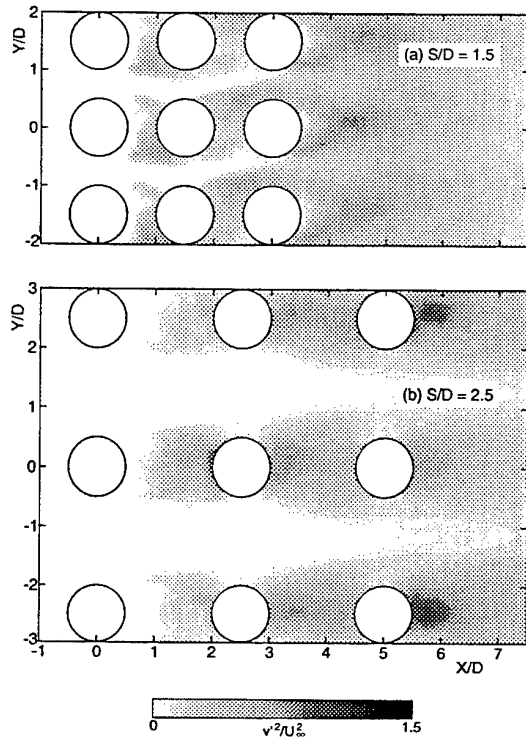


Fig.13 Contour of Y-component of turbulence intensity around the circular cylinders in three rows .

turbulence intensity, peak positions are slightly difference compared with those for X-component of turbulence intensity. It can be found from the comparison of Fig.13(a) and Fig.10(a) that the magnitudes of the spanwise turbulence intensity become maximum at the location where the flow going along the frontal surface of the circular cylinder joins the main stream. In contrast to the case of small spacing ratio, the Y-component of the turbulence intensity increases just ahead of the circular cylinder in the second row for large spacing ratio ($S/D = 2.5$).

3.4 Vortex shedding from circular cylinders

It is well known that Kármán vortex street forms in the wake of a single circular cylinder. Whether shedding vortices exist or not is of great importance to characterize flow patterns. Thus in order to examine the vortices shed from the circular cylinders, the power spectrum was measured using an LDV. The measurements of frequency of vortex shedding were conducted at the locations shown in Figure 14.

Figure 15 shows the power spectrum for various spacing ratios in the case of single row arrangement. A feature of the power spectrum for the single circular cylinder at the same Reynolds number is given in Fig.15 for comparison. In the range of $S/D \geq 2.3$, a steep peak appears in the spectra and the frequency where the power spectrum attains maximum shifts to lower frequency with increase in spacing ratio. On the contrary to the case of $S/D \geq 2.3$, a noticeable peak

profile cannot be recognized in the range of $S/D \leq 2.0$. In particular, power spectrum simply decreases in terms of frequency for $S/D \leq 1.7$. It can be found from these results that the vortices are periodically shed from the circular cylinder for $S/D \geq 2.3$, whereas the periodic vortex shedding behind circular cylinders is not produced for $S/D \leq 2.0$.

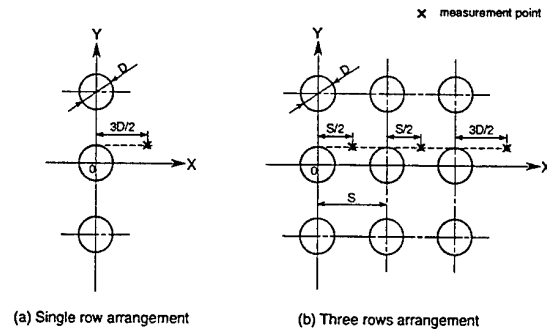


Fig.14 Measurement positions for frequency of vortex shedding.

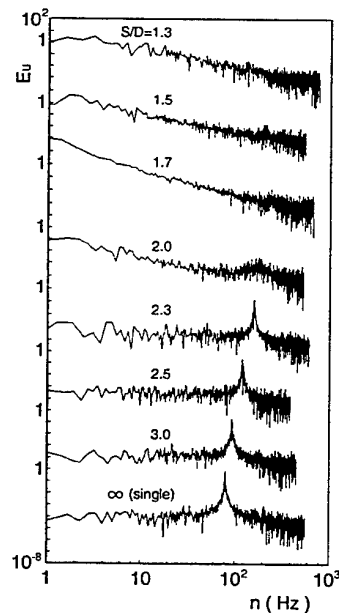


Fig.15 Power spectrum for a single row arrangement.

Figure 16 indicates the power spectrum as a function of the frequency for three rows arrangement. There are no vortex shedding detectable behind the circular cylinder up to $S/D = 1.7$. As seen in Fig.16(a), (b) and (c), when the spacing ratio reaches $S/D = 2.0$, steeply increase in power spectrum is observed behind three rows, and their magnitude become large with increasing downstream distance. In the case of $S/D = 2.0$, frequencies at which the power spectrum

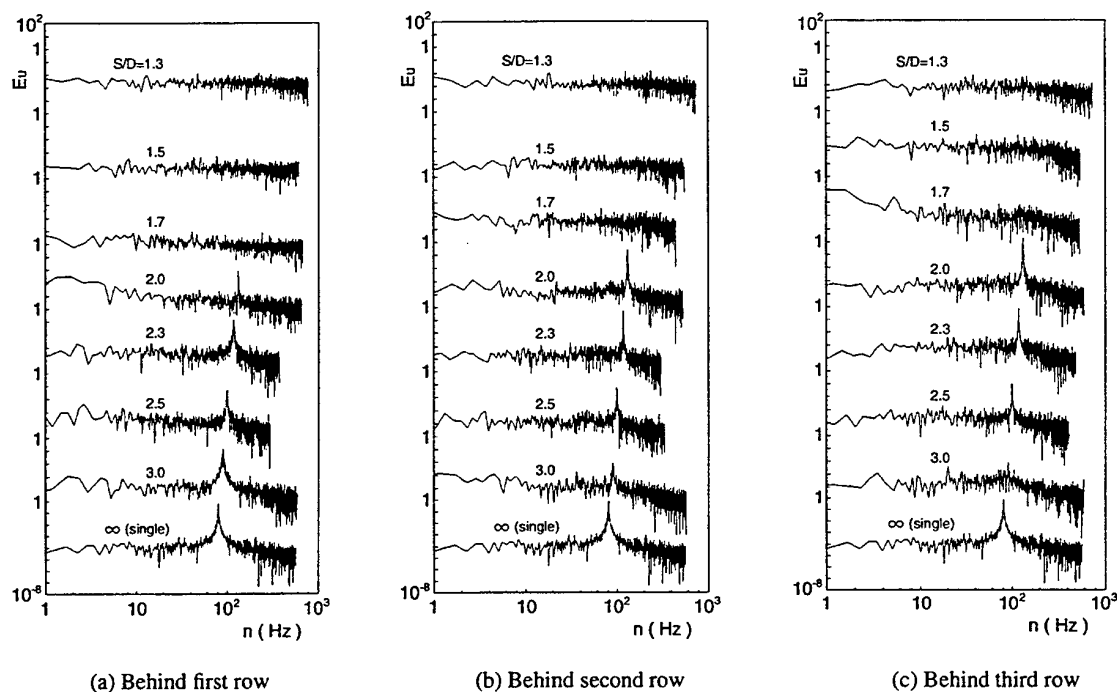


Fig.16 Power spectrum for three rows arrangement.

achieves maximum are almost the same value of $n = 130\text{Hz}$ at all locations. For larger spacing ratio ($S/D \geq 2.0$), the frequency of vortex shedding shifts to lower side with spacing ratio. Apparently these results indicate that the periodic vortex shedding from circular cylinder occurs for $S/D \geq 2.0$ and disappears for $S/D \leq 1.7$ in the case of three rows arrangement.

Therefore, it may be suggested from the comparison of the characteristic of power spectrum with the distribution of flow properties that the two typical flow-patterns are generated around circular cylinders arranged in three rows. The first type of flow-pattern appears for small spacing ratio, namely $S/D = 1.5$. In this case, there is no periodic vortex shedding behind the circular cylinder and exists a biased flow between two streamwise circular cylinders. This biased flow can cause unsymmetrical distributions of the streamwise velocity, and X - and Y -component of turbulence intensity. On the other hand, the second type of flow-pattern appears for large spacing ratio, namely $S/D = 2.5$. This flow-pattern has a periodic vortex shedding between two streamwise circular cylinders. The feature of velocity field and turbulence intensities are similar to those for a single circular cylinder and the symmetric distribution develop in the flow field.

4. CONCLUSIONS

The experimental results presented here on flow structure around circular cylinder bundles arranged in a single row and

three rows lead to the following conclusions:

- (1) The details of the flow-pattern around circular cylinder bundles were obtained with LDV. In particular occurrence of the biased flow between two streamwise circular cylinders was shown by the distribution of velocity vectors for small spacing ratio.
- (2) In the case of a single row arrangement, distributions of X - and Y -component of turbulence intensity behind a circular cylinder are basically similar to that for a single circular cylinder. There is a double peak in the distribution of X -component of turbulence intensity, and a single peak in that of Y -component of turbulence intensity behind a circular cylinder regardless of spacing ratio. On the other hand, in the case of three rows arrangement, alternate peaks of the X - and Y -component of turbulence intensity appear behind the first and second row for small spacing ratio, whereas there are symmetric double peaks behind first, second and third row for large spacing ratio.
- (3) The turbulence intensities become small in the near wake behind circular cylinders with increase in the value of spacing ratio in the case of a single row and three rows.
- (4) The vortices are periodically shed from the circular cylinder for $S/D \geq 2.3$ in the case of single row arrangement. Furthermore there are no vortex shedding detectable behind the circular cylinder up

to $S/D = 1.7$, while the periodic vortex shedding from circular cylinder in the range of $S/D \geq 2.0$ for the case of three rows.

NOMENCLATURE

D	: diameter of circular cylinder
Eu	: power spectrum function for fluctuating velocity u'
n	: frequency of vortex shedding
Re	: Reynolds number $= U_{\infty} D / \nu$
S	: spacing between the two adjoining circular cylinder
St	: Strouhal number $= Dn / U_{\infty}$
U	: time-mean velocity
U_{∞}	: velocity in free stream
u', v'	: X and Y -component of fluctuating velocity
X, Y	: co-ordinates with origin at the center of the base of central circular cylinder at 500mm from the leading edge of the ground plate (see Fig.1). X is chosen along the ground plate, and Y for the horizontal directions respectively
ν	: kinematic viscosity of air

REFERENCES

- Abd-Rabbo, A. & Weaver, D.S., 1986, A Flow Visualization Study of Flow Development in a Staggered Tube Array, Journal of Sound and Vibration, 106-2, pp.241-256.
- Balabani, S., Bergeles, G., Burry, D. and Yianneskis, M., 1994, Velocity Characteristics of the Crossflow over Tube Bundles, Proceedings of the Seventh International Symposium on Applications of Laser Techniques to Fluid Mechanics, 2, pp.39.3.1-39.3.8.
- Hill, R.S. & Armstrong, C., 1962, Aerodynamic Sound in Tube Banks, Proc. Phys. Soc. 79-1, pp.225-227.
- Ishigai, S. & Nishikawa, E., 1974, Experimental Study of Structure of Gas Flow in Tube Banks with Tube Axes Normal to Flow (Part 2. On the Structure of Gas Flow in Single Column, Single Row and Two Rows of Tubes), Transactions of the JSME, 40-337, pp.2599-2608.
- Nishikawa, E. & Ishigai, S., 1977, Structure of Gas Flow and Its Pressure Loss in Tube Banks with Tube Axes Normal to Flow, Transactions of the JSME, 43-373, pp.3310-3319.
- Nishimura, T., Itoh, H. & Miyashita, H., 1993, The Influence of Tube Layout on Flow and Mass Transfer Characteristics in Tube Banks in the Transitional Flow Regime, International Journal of Heat and Mass Transfer, 36-3, pp.553-563.
- Okamoto, S., Sato, I., Shiina, M. and Tamura, M., 1994, Effect of spacing between two adjoining circular cylinders on flow around two-dimensional circular cylinder rows (1st report, a single row in side-by-side arrangement), Transactions of the JSME, 60-573B, pp.1568-1574.
- Okamoto, S., Sato, I., Shiina, M. and Tamura, M., 1994, Effect of spacing between two adjoining circular cylinders on flow around two-dimensional circular cylinder rows (2nd report, two and three rows of transverse arrangement), Transactions of the JSME, 60-578B, pp.3336-3344.
- Weaver, D.S., & Abd-Rabbo, A., 1985, A Flow Visualization Study of a Square Array of Tubes in Water Crossflow, Journal of Fluids Engineering, 107, pp.354-363.
- Zdravkovich, M.M., 1977, Review of flow interference between two circular cylinders in various arrangements, Transactions of the ASME, Journal of Fluids Engineering, 99-4, pp.618-633.
- Zukauskas, A.A., 1972, Heat Transfer from Tubes in Crossflow, Advances in Heat Transfer (Edited by T.P. Irvine, Jr and J.P. Hartnett), Academic Press, 8, pp.93-160.

TURBULENCE SCALES AND SPECTRA IN STAGGERED TUBE BUNDLE FLOWS

S. Balabani and M. Yianneskis

Centre for Heat Transfer and Fluid Flow Measurement
Department of Mechanical Engineering
King's College London, University of London,
United Kingdom.

ABSTRACT

Time-resolved LDA measurements of the axial and transverse velocity components were performed in the first 6 rows of a staggered tube bundle with relative transverse and longitudinal pitch ratios of 3.6 and 1.6 respectively. Measurements were carried out in flow of water at a Re_d of 12,858. A flow periodicity with a Strouhal number equal to 0.26 was detected which is in agreement with published data. This periodicity was found to broaden the turbulence levels by up to 50% in some locations. Agreement between the experimental results and the turbulence levels predicted using the $k-\epsilon$ model by Bouris (1995) improved when this periodic component was removed from the spectra using appropriate filtering techniques. In an attempt to describe turbulence more accurately time-, length-scales and dissipation rates were estimated from the filtered time-resolved data. Integral timescales were on average equal to 4 ms and Taylor microscales 0.7 ms. Despite the approximations and uncertainties involved in the estimation of the length scales and dissipation rates, the present estimates provide the only published data in relation to the tube bundle flows known to the authors. Comparisons of the data with numerical predictions show promise for more extensive evaluation of CFD predictions in future than has been possible hereto.

1. INTRODUCTION

Recent studies have shown clearly that alternate vortex shedding occurs in the first rows of staggered tube bundles and symmetric or anti-symmetric jet instabilities in in-line arrays (Weaver et al., 1993; Ziada and Oengören, 1991). These instabilities, or vorticity shedding excitation, may incite tube vibrations in liquid and acoustic resonance in gas flows. They manifest themselves by a constant Strouhal number flow periodicity which depends on the tube arrangement, the spacing between the tubes, Re_d , the location within the array (Collinson and Robinson, 1991) and, according to a recent study (Oengören and Ziada, 1995), on the number of rows and columns in the tube bundle. There may even be multiple Strouhal numbers (St) at a given Re_d in the first rows of an array (Weaver et al, 1993; Oengören and Ziada, 1995).

The presence of such a flow periodicity introduces a 'pseudo-turbulence' contribution to the measured velocity fluctuations due to the variation of the mean flow, which broadens the random turbulence levels. As a result, the turbulence levels determined by ensemble-averaged techniques may overestimate the true amount of turbulence in the flow. An earlier study (Balabani et al, 1994) showed that the turbulence levels in a 3.6 x 1.6 staggered tube bundle were underestimated by the $k-\epsilon$ model. This may be attributed partly to the well known shortcomings of the $k-\epsilon$ model in recirculating flows (Bergeles et al, 1996; Rodi and Scheuerer, 1986; Gosman and Ahmed, 1987) and partly to the presence of discrete periodicities in the flow which were not accounted for in the modelling. Ensemble-averaged measurements in the same configuration also showed evidence of the presence of flow instabilities as bimodal probability distributions of the transverse velocity component were observed.

The vortex shedding phenomena in tube bundles have attracted considerable attention due to their implications for the design of heat exchangers. Most of the relevant studies such as those mentioned earlier employed hot wire anemometry to estimate spectra and therefore identify dominant frequencies. Flow visualisation studies have also been performed to reveal the nature of the observed flow periodicities. On the other hand, LDA studies reported previously on tube bundle flows (for example, Simonin and Barcouda, 1986, 1988; Halim and Turner, 1986 etc.) have been concerned with ensemble-averaged measurements. It appears from the published literature that the effect of the flow periodicity on the turbulence content has not been quantified and the turbulence structure has not been fully characterised.

To this end, time-resolved LDA measurements were taken in a staggered tube bundle - previously studied by means of ensemble-averaged measurements (Balabani et al, 1994) - with the aim of identifying dominant frequencies, quantifying their effect on the turbulence levels and estimate quantities such as turbulence scales and dissipation rates. The present work forms part of a research programme investigating the effects of fouling on the efficiency of heat exchangers in lignite utility boilers. The configuration investigated is typical of heat exchangers in utility boilers where severe fouling is encountered mainly in the first 2-3 tube rows and in conjunction with the

present experimental work, CFD predictions of the flow were carried out in the National Technical University of Athens (Bergeles et al, 1996).

2. FLOW CONFIGURATION AND MEASUREMENT TECHNIQUE

The experiments were performed in a water tunnel which has been described in detail in Balabani et al (1994). A square test section, made of Perspex, was used as working section. It comprised a staggered tube bundle with 6 transverse rows and 5 columns of acrylic rods, of 10 mm diameter (d). Two of the tube columns comprised half rods which were fixed in alternate rows along the side walls to simulate an infinite tube bundle and minimise boundary layer effects. The transverse pitch ratio, S_T/d , was 3.6 and the longitudinal one, S_L/d , 1.6. The rods were fixed horizontally in the test section and they were rigidly mounted on the Perspex plates to eliminate possible resonance effects that might interfere with the flow parameters measured. The aspect ratio of the rods was equal to 7.2 which was sufficient to ensure the presence of two-dimensional flow conditions over the central part of the span (Fox and West, 1990). A cross-sectional view of the test section is shown schematically in Figure 1. The co-ordinate system employed as well as the measurement locations are shown on the same figure.

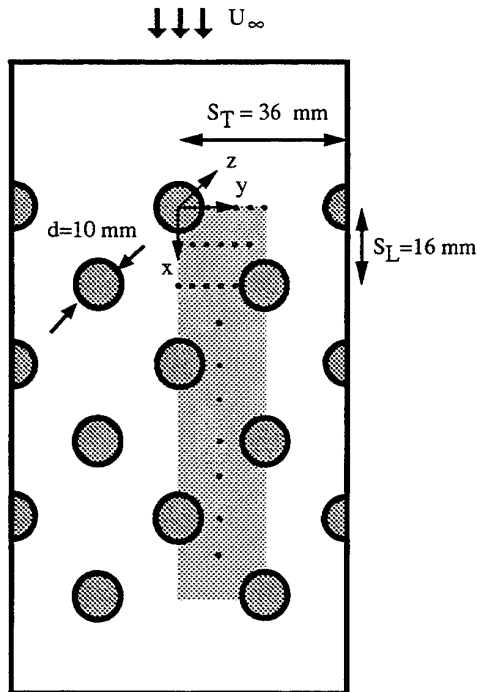


Figure 1. Cross-section of the staggered configuration investigated.

The flow and optical characteristics of the experimental facility were identical to those employed for the ensemble-

averaged measurements reported by Balabani et al (1994) and Balabani and Yianneskis (1996). The laser Doppler system consisted of a single component 10 mW He-Ne laser operating in forward-scatter. The diameter and length of the control volume were 48.8 μm and 466 μm respectively. The photomultiplier signal was processed using a TSI model 1990B frequency counter interfaced to a PC equipped with appropriate data acquisition software. The frequency shift and filter settings were kept the same as those employed for the ensemble-averaged measurements in order to facilitate comparisons.

Instantaneous values of the axial and transverse velocity components were recorded at regular time intervals. All measurements were taken at the plane of symmetry ($z/d = 0.0$) and tap water was used as the working fluid. The Re_d , defined by the tube diameter and the gap velocity, was 12,858. The validated data rates obtained with the impurities in the water and/or by introducing a few drops of diluted milk in the flow varied from 1 to 5 kHz and sampling rates in the range of 1 to 4 kHz were used. These sampling rates were sufficient to resolve the timescales in most parts of the flow. Blocks of 6000 velocity data points were acquired at each location. Velocity data points lying outside $\pm 3\sigma$ from the mean value were removed from the records. The number of these data was very small, well below 1%, and therefore they were not expected to affect the spectral estimates (Srikantaiah and Coleman, 1985). A numerical algorithm was developed using the commercial software *Mathematica* in order to process the data and obtain amplitude and power spectra, autocorrelation functions, filtering of periodic components and estimation of turbulent scales and dissipation rates.

3. EXPERIMENTAL RESULTS AND DISCUSSION

Figure 2 shows a typical short record of the axial instantaneous velocities obtained in the second row ($x/d = 1.6$

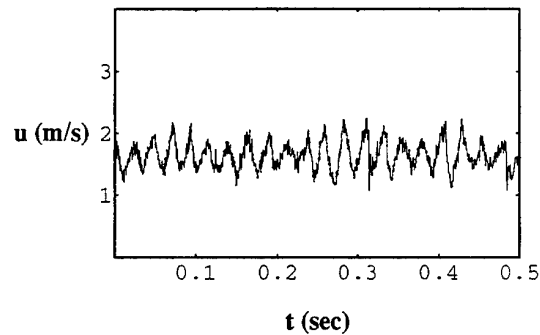


Figure 2. Characteristic variation of the axial instantaneous velocity with time ($x/d = 1.6$ and $y/d = 0.6$; $Re_d = 12,858$).

and $y/d = 0.6$). A typical autocorrelation function, $R(\tau)$, for the same location is shown in Figure 3. $R(\tau)$ was calculated from:

$$R(\tau) = \frac{\overline{u(t)u(t+\tau)}}{u'^2} \quad (1)$$

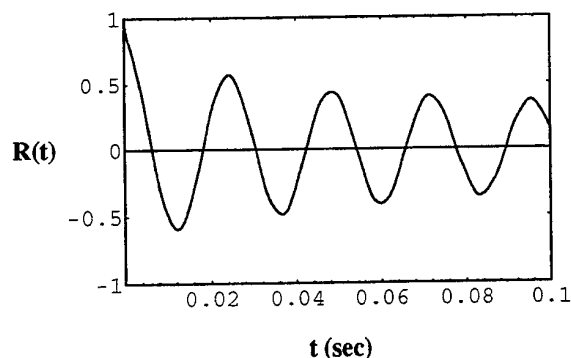


Figure 3. Autocorrelation function of velocity trace of Figure 2 ($x/d=1.6$ and $y/d=0.6$; $Re_d = 12,858$).

where $u(t)$ and $u(t+\tau)$ are the instantaneous fluctuating velocities at times t and $(t+\tau)$ and τ is the separation in time. Both figures show evidence of a discrete flow periodicity. Amplitude spectra obtained through a Fast Fourier Transform of the velocity time series revealed a dominant frequency peak at an average frequency of 34 Hz. According to the published literature this dominant frequency may be attributed to alternate vortex shedding from the first row of the tube bundle. The development of the vortex shedding frequency through successive rows can be observed in the amplitude spectra shown in Figure 4. The amplitude of the vortex shedding frequency varies significantly from row to row: it increases considerably after the first row, reaching a maximum between the third and fourth rows and decreases further downstream. Transverse velocity spectra - not shown here - showed the same trends with the axial ones. However, the amplitude of the dominant frequency was considerably lower. Similar trends have been reported by other investigators (Weaver et al, 1991, 1993, Polak and Weaver, 1995). However, in contrast to the present study they observed a maximum vorticity shedding in the second row.

A harmonic is discernible in the axial velocity spectrum obtained between the third and fourth rows (Figure 4). Harmonics have also been observed by other investigators (McDonnell and Fitzpatrick, 1992; Ziada and Oengören, 1991). According to the non-linear hydrodynamic instability theory (Ziada and Oengören, 1991) the occurrence of this higher harmonic is due to the fact that the amplitude of the dominant frequency exceeded about 4 % of the mean flow. This harmonic was not present in the transverse velocity spectra.

The Strouhal number (St) corresponding to the dominant frequency detected was 0.26. St is defined by the tube diameter and the gap velocity (equal to $1.38 U_\infty$). The measured St lies within the range given by published St charts (Chen, 1977), but it is higher than the value of 0.20 reported for a single cylinder under subcritical flow conditions (Massey, 1983; Roshko, 1961) despite the relatively large spacings employed. Although there are many published St data and correlations in the literature, these usually refer to standard geometries such as normal triangular or rotated square arrays etc. (e.g. Weaver et al, 1993; Oengören and Ziada, 1995; Polak and Weaver, 1995). For example, a single St number at around 0.50 was reported by Weaver et al (1991) and McDonnell and Fitzpatrick (1992) for normal triangular arrays with pitch ratios of 1.71 and 2

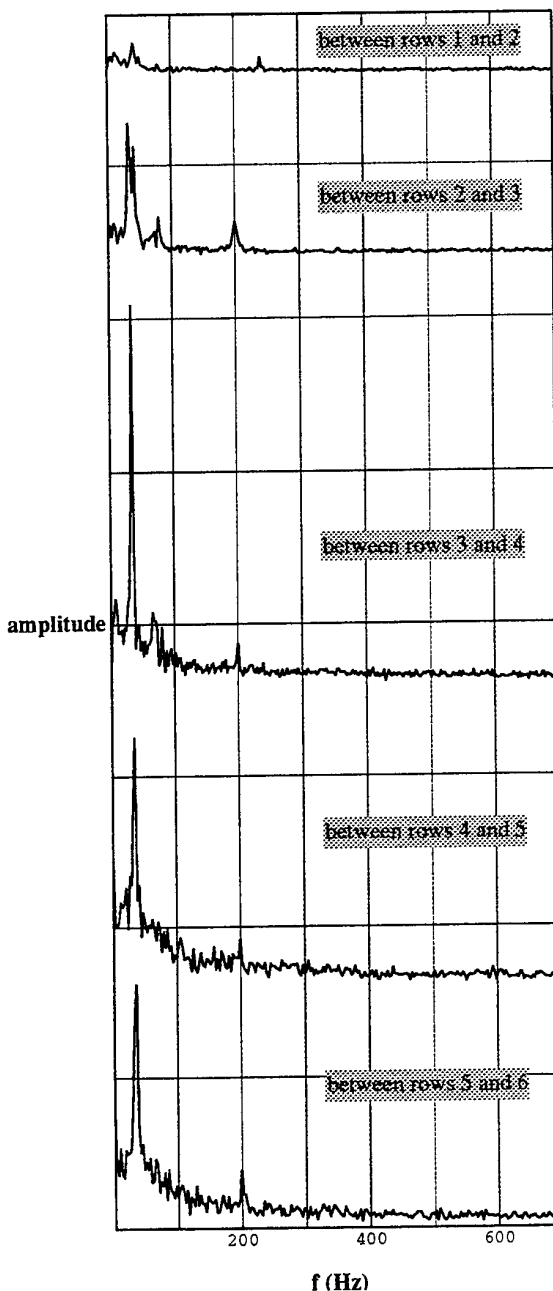


Figure 4. Development of the dominant vortex shedding frequency in successive rows.

respectively. Multiple St numbers have been reported for normal triangular geometries (Hill et al, 1986; Polak and Weaver, 1995; Oengören and Ziada, 1995) and rotated square arrays (Weaver et al, 1993) with intermediate to relatively large spacings. These were attributed to alternate vortex shedding at two different frequencies from the first and second rows and possible non-linear interaction between the two. The multiple-frequency nature of vortex shedding and the relative importance of each component has been found to depend strongly on Re_d , pitch ratio, location within the array and in some cases the

number of rows and columns in the tube bank.

The aforementioned published data emphasise the significant effect of the bundle geometry on the formation of coherent flow structures in staggered tube bundles. First row alternate vortex shedding appears to occur in every pitch ratio while second row-vortex shedding may occur in some geometries. In general, smaller pitch ratios result in higher *St* numbers while a trend towards the vortex shedding from an isolated cylinder is expected for large spacings.

It is difficult to compare the present findings with the previously published ones since the present arrangement is different. However, it can be roughly approximated by a rotated square array with a pitch ratio of 2.41, i.e. equal to the diagonal pitch in the present array. Empirical correlations (Weaver et al, 1987) predict a *St* of 0.25 for such a rotated square array which is very similar to the *St* of 0.26 found in the present investigation.

Power spectra were also estimated from the time-resolved velocity data using the periodogram technique. The spectra reported in Balabani and Yianneskis (1996) showed that at the higher (turbulent) frequencies and for locations characterised by nearly isotropic turbulence, the slope of the spectrum was approximately -5/3, which is typical of the inertial subrange region.

In order to remove the periodic component due to vortex shedding from the spectra three filtering techniques were applied: notch filtering, moving window averaging and low-pass filtering. The notch filtering technique was found to be the most appropriate since it removed only the narrow vortex shedding band. In contrast, the moving window and low-pass filtering techniques removed some of the low-frequency turbulence content of the spectrum as well. Furthermore, the results were found to be sensitive to the selected cut-off frequency or window sizes respectively. Therefore, the data presented below were obtained using the notch filtering technique.

The axial r.m.s. velocities obtained after filtering out the dominant frequency peak are shown in Figure 5, reproduced

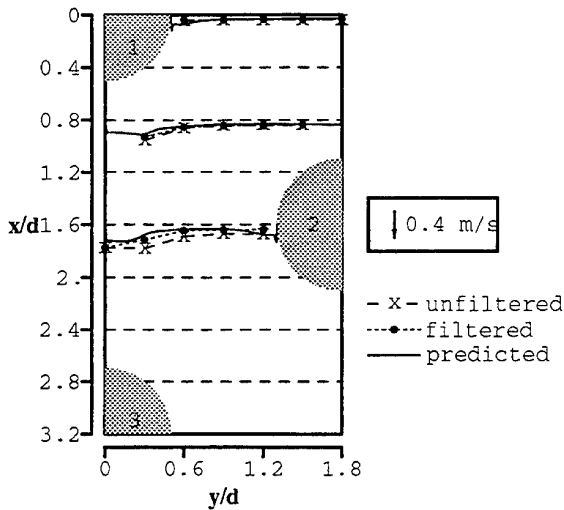


Figure 5. Comparison between unfiltered, filtered and predicted axial r.m.s. velocities.

from Balabani and Yianneskis (1996). The data are compared with the unfiltered values and corresponding numerical predictions using $u' = (2k/3)^{0.5}$ (Bergeles et al, 1996, Balabani et al, 1994; Bouris, 1995). Significant differences, up to 50 %, between filtered and unfiltered data can be seen at $x/d = 1.6$ where pronounced vortex shedding was observed. The filtered values are closer to the predicted r.m.s. levels than the unfiltered ones, suggesting that the vortex shedding phenomena should be accounted for in numerical modelling of flows over tube bundles.

In order to characterise the turbulence structure more fully and to be able to estimate the rate of dissipation of k , ϵ , the turbulence time and length scales were calculated from the filtered time-resolved data. Estimates of the integral timescale, T_E , and the micro timescales, τ_E , are shown in Figures 6(a) through (c). The integral timescales, T_E , were determined by integrating the autocorrelation function, $R(\tau)$, up to the first zero crossing:

$$T_E = \int_0^{\infty} R(\tau) d\tau \quad (2)$$

The autocorrelation function was computed from the filtered data, unlike the one shown in Figure 3. The micro timescales, τ_E , were calculated from (Hinze, 1975):

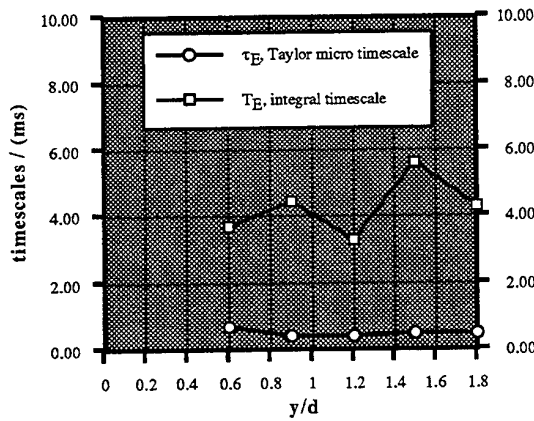
$$\frac{1}{\tau_E^2} = \frac{1}{2u'^2} \left(\frac{\partial u}{\partial t} \right)_{t=0}^2 \quad (3)$$

where u is the filtered axial instantaneous velocity value, i.e. the high-frequency velocity fluctuation and u' the axial r.m.s. velocity.

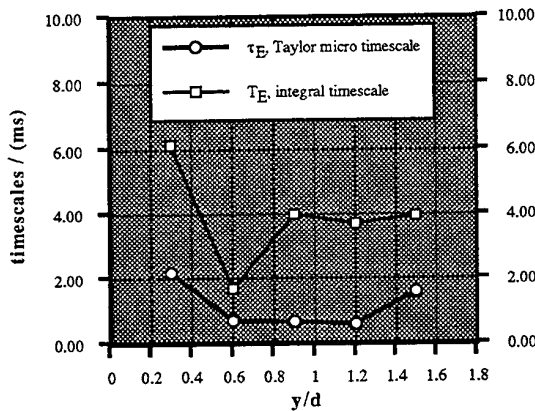
The measured T_E values range from 1.5 to 8 ms with an average value of 4 ms whereas τ_E range from 0.4 to 2.2 ms with an average of 0.7 ms. On average, T_E differ from τ_E by a factor of 7 which is reasonable (Tennekes and Lumley, 1972). The distributions of T_E and τ_E show in general similar trends i.e. higher values in areas of low velocities and smaller in the mainstream flow. However, the τ_E distributions appear more uniform.

Comparisons of the estimated T_E values with numerical predictions (Bouris, 1995) based on the k - ϵ model (Balabani and Yianneskis, 1996), showed good quantitative agreement in some locations, but qualitative differences were found in some locations, e.g. predicted values were lower in areas of low velocities (i.e. in the wake regions) and higher in the flow passages between tube columns. Given the uncertainties and approximations involved both in the experimental and numerical determinations of T_E the comparisons were very encouraging. The authors are not aware of any similarly extensive comparisons in the literature, mainly due to the difficulties involved in measuring T_E .

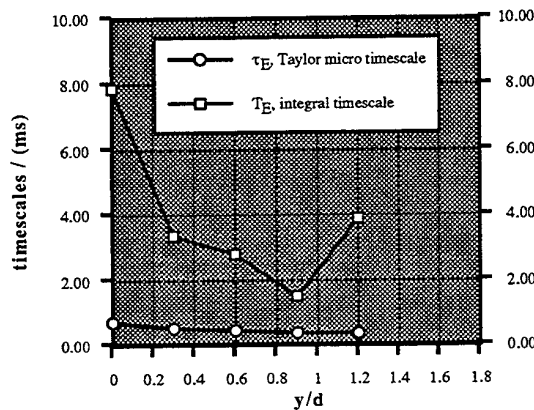
Macro (Λ_f) and micro length (λ_f) scales were estimated by multiplying the calculated τ_E and T_E values with the mean velocity \bar{U} at each location. The results are shown in Figures 7(a) through (c). Macro length scales, Λ_f , vary from 0.1 to 8 mm



(a) $x/d = 0.0$



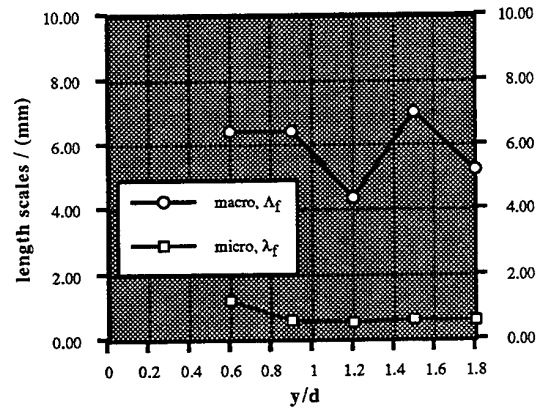
(b) $x/d = 0.8$



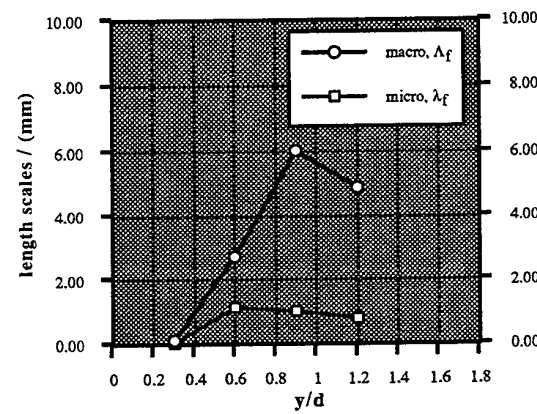
(c) $x/d = 1.6$

Figure 6. Estimates of the integral and Taylor micro timescales.

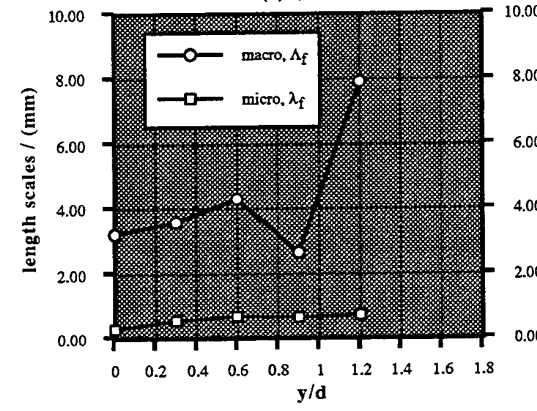
with an average value of 4.6 mm, i.e. around half the cylinder diameter, whereas λ_f values vary from 0.04 mm to 1.6 mm with an average value of 0.74 mm. Both the micro and macro length scales were found to be lower in the wake regions and higher in the flow lanes between tube columns although the opposite distribution would be expected. This may be partly due to the



(a) $x/d = 0.0$



(b) $x/d = 0.8$



(c) $x/d = 1.6$

Figure 7. Estimates of the macro and micro length scales obtained from the timescale estimates using the mean velocity as convective velocity.

fact that Taylor's hypothesis that relates the partial time and space derivatives in the momentum equation is not expected to be valid in areas of high turbulence intensity, i.e. in the wake region of the first cylinder where \bar{U} values are smaller or similar to the r.m.s. velocities. As a result the use of \bar{U} as a convective

velocity may not be appropriate (Heskestad, 1965). Similarly unexpected length scale distributions were reported for the flow past an axisymmetric poppet valve by Yianneskis et al (1991) and it may therefore be more appropriate to determine length scales from velocity traces obtained simultaneously at 2 locations in the flow. According to the generalised Taylor's hypothesis suggested by Heskestad (1965) for highly turbulent shear flows a convective velocity given by :

$$U_c = \sqrt{\bar{U}^2 + u'^2 + 2v'^2 + 2w'^2} \quad (4)$$

would be more appropriate. Since only the axial velocities were measured in detail in this investigation such a convective velocity could not be determined from the time-resolved data without some postulation about the other two transverse fluctuating components v' and w' . Therefore, the use of an alternative U_c would yield little constructive information. However, a simplified version of U_c can be used by neglecting the two transverse fluctuating components, i.e. using:

$$U_c = \sqrt{\bar{U}^2 + u'^2} \quad (5)$$

as suggested by Wu et al (1989). The use of this convective velocity results in higher timescale estimates in the wake regions (for example at $x/d = 0.8$ and $y/d = 0.3$) as can be seen from Figure 8. However, the trends exhibited are similar.

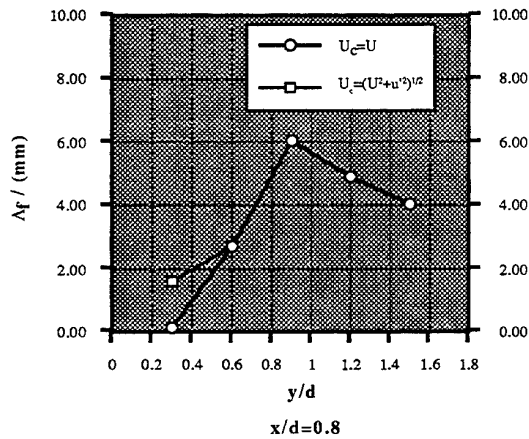


Figure 8. Comparison between length scale estimates obtained using different convective velocities.

No data from similar flows are available to allow quantitative comparisons to be made. Estimated timescales have been reported for a number of other flow configurations. For example, $T_E = 0.7$ ms was measured by Absil (1988) in the wake of a 2 mm single cylinder in crossflow at a distance of 125 d from the cylinder and $Re_d = 1,300$. Yianneskis et al (1991) reported time- and length-scales of the flow past a poppet valve. On average, τ_E values were found to be around one order of magnitude lower than T_E , in agreement with the present data. Cenedese et al (1992) estimated timescales in the boundary layer of the flow in duct. T_E values in the axial direction were found approximately

equal to the duct dimension divided by the mean velocity. T_E values were significantly lower in the other two directions. τ_E estimated by counting the number of zero crossings per unit time of the fluctuating velocity component were found to be around one order of magnitude lower than T_E . Gould and Benedict (1994) carried out spatial- and auto-correlation measurements using LDA in an axisymmetric sudden expansion. Timescales were found to be lower in locations of low turbulence and higher in the shear layer, while length scales obtained from the timescales using Taylor's hypothesis were overestimated in low turbulence locations and underestimated in the shear layer. Their findings therefore are in agreement with those of the present study.

The dissipation rate of the turbulence kinetic energy, ϵ , was determined using three alternative techniques. The dimensional relationship:

$$\epsilon = A \frac{u'^3}{L} \quad (6)$$

with $A = 1$, the filtered axial r.m.s velocity u' as a characteristic velocity scale u' and the cylinder diameter $d = 10$ mm or the integral length scale Λ_f as a characteristic length L , and the relationship (Hinze, 1975):

$$\epsilon = 30\nu \frac{u'^2}{\lambda_f^2} \quad (7)$$

The estimated ϵ values are shown in Figure 9 together with the CFD predictions of Bouris (1995). In general measured dissipation rates are very low in the flow passages between tube columns where the turbulence levels are small and high in the

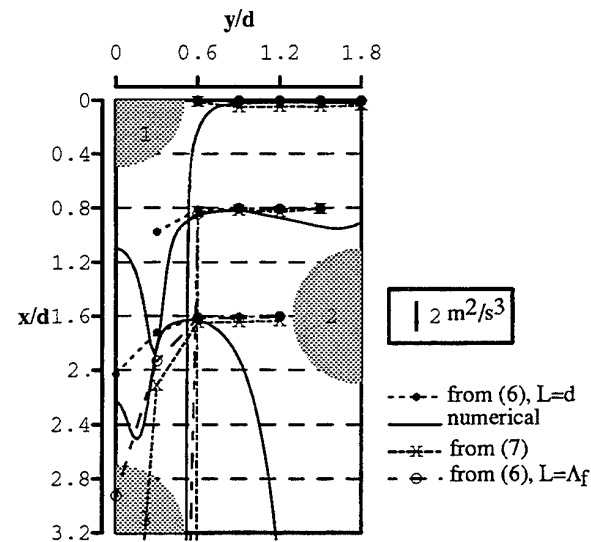


Figure 9. Estimates of the dissipation rate of k and comparison with numerical predictions.

wake region where high r.m.s. velocities are present. All three techniques produce similar estimates in the main flow. However, the techniques based on length scales are subject to the uncertainties involved in the estimation of these scales mentioned above. As a result high values of ϵ are found in the wake region due to the small length scale values estimated there. Predicted dissipation rates are low in the flow between tube columns - in agreement with the measured ones. They increase sharply in regions with steep velocity gradients and decrease thereafter. Extremely high numerical values are observed close to the cylinders. The agreement between the experimental and predicted values is poor in the wake region downstream of the first cylinder and close to the second cylinder.

All three methods used to estimate ϵ are subject to uncertainties. Clearly, the use of d as a characteristic length scale is only an approximation while those employing λ_f and Λ_f may not be appropriate for the reasons explained earlier for the length scale estimates. Furthermore, the use of the axial fluctuating velocity as a characteristic velocity scale assumes that the turbulence is isotropic, which is not true in the wake regions. On the other hand, the well-known shortcomings of the k- ϵ model in regions of recirculation or with strong streamline curvature are likely to affect predicted ϵ results. These arguments are supported by the similarity of values estimated with all three methods and the predicted ones over most of the $x/d = 0.0$ profile for $0.6 < y/d < 1.0$ at $x/d = 0.8$ and for $0.3 < y/d < 0.6$ at $x/d = 1.6$. At these locations the assumptions employed in estimating ϵ are more appropriate and streamline curvature/recirculation effects are likely to have a smaller influence on the ϵ values predicted with the k- ϵ model. As in the k- ϵ turbulence model formulation ϵ is linked very strongly to the local mean strain field, but relatively weakly to the small scale eddies where dissipation takes place (Habib and Whitelaw, 1979) it might be expected that ϵ is overpredicted in some regions, as indicated by the above comparisons.

In conclusion, although comparisons of predicted and measured values of ϵ should be made with great care due to the approximations involved in both experiment and calculation, the present results provide the only published comparison of ϵ data known to the authors and provide not only a useful assessment of the levels of ϵ in the flow but also show promise for more extensive evaluation of CFD predictions in future than has been possible hereto.

4. CONCLUSIONS

Time-resolved LDA measurements of the axial and transverse velocity components were performed in the 6 first rows of a staggered tube bundle with relative transverse and longitudinal pitch ratios of 3.6 and 1.6 respectively. Measurements were carried out in flow of water at a Re_d of 12,858. Turbulence spectra revealed the existence of a flow periodicity with a Strouhal number equal to 0.26, which is in agreement with published data. This periodicity is expected to result from alternate vortex shedding from the first row cylinders. Due to the variation of the mean flow caused by this periodicity the random turbulence levels are broadened by up to 50% in

some locations. The agreement between experimental and numerical turbulence levels based on the k- ϵ model was better when the periodic component was removed from the spectra using appropriate filtering techniques such as notch filtering. In an attempt to describe turbulence more accurately time-, length-scales and dissipation rates were estimated from the filtered time-resolved data. Integral timescales were on average 4 ms whereas Taylor microscales 0.7 ms. Length scales estimated using the mean velocity as a convective velocity were found inappropriate due to the fact that Taylor's hypothesis was not satisfied in all locations in the flow. Estimates of the dissipation rates were also subject to same uncertainties due to the definitions employed. The measured estimates demonstrated the need for the determination of an appropriate convective velocity or spatial correlation measurements if accurate length scale estimates are to be obtained.

ACKNOWLEDGEMENT

The authors are pleased to acknowledge financial support from the Commission of the European Union under contract JOU2-CT92-0014 for the work carried out for this paper.

REFERENCES

- Absil, L.H.J. 1988, Laser Doppler measurements of mean turbulence quantities, time- and spatial correlation coefficients in the wake of a circular cylinder, Proc. 4th Int. Symp. Applications of Laser Anemometry to Fluid Mechanics, Lisbon, pp. 1.1-1.6.
- Balabani, S. & Yianneskis, M. 1996, An experimental study of the mean flow and turbulence structure of cross-flow over tube bundles, Proc. IMechE, Part C, Journal of Mech. Eng. Science (In press).
- Balabani, S., Bergeles, G., Burry, D. & Yianneskis, M. 1994, Velocity characteristics of the crossflow over tube bundles, Proc. 7th Int. Symp. Applications of Laser Anemometry to Fluid Mechanics, Lisbon, vol. II, pp. 39.3.1 - 39.3.8.
- Bergeles, G., Yianneskis, M., Kravaritis, A., Balabani, S., Bouris-Burry, D. & Itskos, S. 1996, Effects of fouling on the efficiency of heat exchangers in lignite utility boilers, Final Report, Joule II Research Programme, Contract No. JOU2-CT92-0014.
- Bouris, D. 1995, Personal communication.
- Cenedese, A., Costantini, A. & Romano, G.P. 1992, LDA spectral measurements in a turbulent boundary layer, Experimental Thermal and Fluid Science, vol. 5, pp. 281-289.
- Chen, Y.N. 1977, The sensitive tube spacing region of tube bank heat exchangers for fluid elastostatic coupling in crossflow, in ASME Symposium Fluid Structure Interaction Phenomena in Pressure Vessel and Piping Systems, ed. M.K. Au-Yang &

S.J. Brown, pp. 1-18.

Collinson, A.E & Robinson, R.G.J. 1991, Cross-flow Strouhal numbers in square and triangular pitch tube arrays at Re from 0.8-3.5 x 10⁵, in Flow Induced Vibrations, I.Mech.E, Paper C416/083, pp. 217-229.

Fox, T.A. & West, G.S. 1990, On the use of end plates with circular cylinders, Experiments in Fluids, vol. 9, no. 4, pp. 237-339.

Gosman, A.D. & Ahmed, A.M.Y. 1987, Measurement and multidimensional prediction of flow in an axisymmetric port/valve assembly, SAE Paper 870592.

Gould, R.D. & Benedict, L.H. 1994, Comparison of length scale estimates for a sudden expansion flow estimated from spatial and auto correlation LDV measurements, Experiments in Fluids, vol. 17, no. 4, pp. 285-287.

Habib, M.A. & Whitelaw, J.H. 1979, Velocity characteristics of a confined coaxial jet, Trans. ASME, J. Fluids Engineering, vol. 101, pp. 521-529.

Halim, M.S. & Turner, J.T. 1986, Measurements of cross flow development in a staggered tube bundle, Proc. 3rd Int. Symp. Applications of Laser Anemometry to Fluid Mechanics, Lisbon, paper 21.7.

Heskestad, G. 1965, A generalised Taylor's hypothesis with application for high Reynolds number turbulent shear flows, Trans. ASME, J. Applied Mech., vol. 32, pp. 735-739.

Hill, R.S., K.C. Shim & R.I. Lewis 1986, Sources of excitation in tube banks due to vortex shedding, Proc. Instn Mech. Engrs., vol. 200, no. C4, pp. 293-301.

Hinze, J.O. 1975, Turbulence, 2nd ed., McGraw-Hill, New York.

Massey, B.S. 1983, Mechanics of Fluids, 5th ed., Van Nostrand Reinhold, UK.

McDonnell, C. & Fitzpatrick, J.A. 1992, Spectral analysis of turbulent flows from LDA measurements, Proc. 6th Int. Symp. Applications of Laser Anemometry to Fluid Mechanics, Lisbon, pp. 8.3.1 - 8.3.5.

Oengören, A. & Ziada, S. 1995, Vortex shedding, acoustic resonance and turbulent buffeting in normal triangle tube arrays, in Flow-Induced Vibration, ed. Bearman, Balkema, Rotterdam, pp. 295 - 313.

Polak, D.R. & Weaver, D.S. 1995, Vortex shedding in normal

triangular tube arrays, J. Fluids and Structures, vol. 9, pp. 1-17.

Rodi, W. & Scheurer, G. 1986, Scrutinising the k-e turbulence model under adverse pressure gradient conditions, Trans. ASME, J. Fluids Engineering, vol. 108, pp. 174-179.

Roshko, A. 1961, Experiments on the flow past a circular cylinder at very high Re number, J. Fluid Mech., vol. 10, no. 3, 345-356.

Simonin, O. & Barcouda, M. 1986, Measurements of fully developed turbulent flow across tube bundle, Proc. 3rd Int. Symposium Applications of Laser Anemometry to Fluid Mech., Lisbon, paper 21.5.

Simonin, O. & Barcouda, M. 1988, Measurements and prediction of turbulent flow entering a staggered tube bundle, Proc. 4th Int. Symposium Applications of Laser Anemometry to Fluid Mech., Lisbon, paper 5.23.

Srikantaiah, D.V. & Coleman, H.W. 1985, Turbulence spectra from individual realization laser velocimetry data, Experiments in Fluids, vol. 3, pp. 35-44.

Tennekes, H. & Lumley, J.L. 1972, A first course in turbulence, MIT Press, Cambridge (Mass.).

Weaver, D.S., Fitzpatrick, J.A. & El-Kashan, M. 1987, Strouhal numbers for heat exchanger tube arrays in crossflow, Trans. ASME, J. Pressure Vessel Technology, vol. 109, pp. 219 - 223.

Weaver, D.S., Lian, H.Y. & Huang, X.Y. 1991, A study of vortex shedding in a normal triangular tube array, in Flow Induced Vibrations, I.Mech.E, Paper C416/091, pp. 511 - 515.

Weaver, D.S., Lian, H.Y. & Huang, X.Y. 1993, Vortex shedding in rotated square arrays, J. Fluids and Structures, vol. 7, pp. 107 - 121.

Wu, H., Patterson, G.K. & Van Doorn, M. 1989, Distribution of turbulence energy dissipation rates in a Rushton turbine stirred mixer, Experiments in Fluids, vol. 8, pp. 153-160.

Yianneskis, M., Tindal, M.J. & Nadarajah 1991, Measurement of turbulence scales, moments, and spectra in engine flows, Proc. I.Mech.E., Experimental Methods in Engine Research and Development, pp. 127-133.

Ziada, S. & Oengören, A. 1991, Vorticity shedding and acoustic resonance in an in-line tube bundle. Part one: vorticity shedding, in Flow Induced Vibrations, I.Mech.E., paper C416/047, pp. 497-509.

PULSATILE FLOW BEHAVIOUR NEAR CARDIAC PROSTHESES: APPLICATION AND LIMITATION OF LASER AND MRI TECHNIQUES

F. Hirt, K. Eisele, Z. Zhang, E. Jud

Fluid Dynamics Laboratory, Sulzer Innotec AG
CH-8401 Winterthur, Switzerland

R. Botnar and P. Boesiger

Institute of Biomedical Engineering, Federal Institute of Technology, ETHZ
CH-8492 Zurich, Switzerland

J. Kepner and T. Baldwin

CarboMedics Inc., Austin, U.S.A.

ABSTRACT

The present investigation focuses on the significance of *in vitro* flow measurements in the vicinity of prosthetic bileaflet heart valves. In a preliminary study, the widely used Laser Doppler Anemometry (LDA) technique has been compared with the novel Magnetic Resonance Imaging (MRI) technique. The latter has been developed at ETHZ and University Hospital Zurich and was applied to *in vivo* and *in vitro* flow studies. Measurements with both techniques were conducted in two unique pulse duplication systems and using a blood analog fluid. The MRI results reveal a high resolution of the flow field in space and time as long as the statistical velocity fluctuations are small compared to the mean flow velocity. The good agreement between MRI and LDA test results makes the examination of *in vitro* and *in vivo* pulsatile flow behaviour of cardiac prostheses possible for the first time.

INTRODUCTION

The prediction of thrombus-formation in the vicinity of cardiac prostheses plays a crucial role in the modern product development process. For this purpose there is a need for systematic *in vitro* and *in vivo* investigations to establish a correlation between deposited blood cell mass near a surface and the predominated flow pattern.

Recent developments of cardiac prostheses have been made mainly on the basis of *in vitro* hydrodynamics. Thereby the optical LDA-technique has become a valuable tool for analysing the effect of small design changes on the amount of turbulence generated. Recently a fast imaging PTV-technique for *in vitro* applications was published by Eisele *et al.* (1996). Another novel tool to visualize real blood flow in large vessels is the MRI-technique. Major contributions concerning the methodology of mean flow analysis and the optimi-

zation of the data-processing have been made by Boesiger *et al.* (1992) and Botnar *et al.* (1996) at ETHZ. One of the first applications of MRI-technique to prosthetic heart valves has been reported by Walker *et al.* (1995). The objective of the present study is to validate the MRI-technique for mean flow measurements in the vicinity of prosthetic heart valves. For this purpose the pulsatile mean axial flow velocity was measured at specified downstream locations in the aortic test section of a pulse duplication system. These data were compared with the corresponding results gained by LDA technique. As a result, it is demonstrated that the MRI-measurement strategy developed at ETHZ is very efficient in resolving the 3D-blood flow field in space and time.

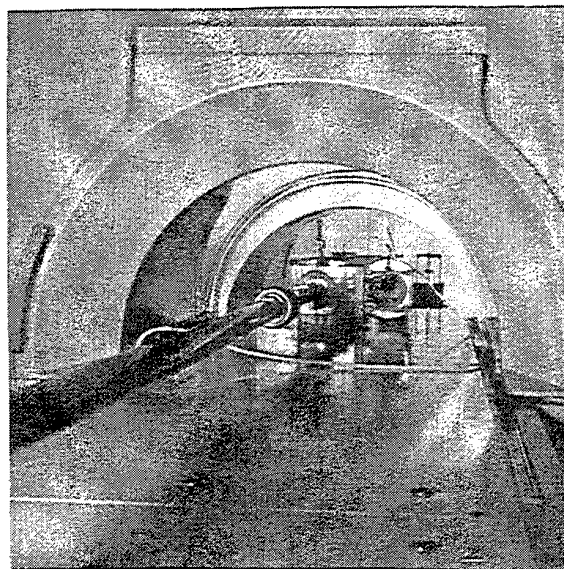


Figure 1. Arrangement of the experimental pulse duplication system used in the MRI-scanner at ETHZ.

PULSE DUPLICATION SYSTEMS

In vitro investigations of the pulsatile flow field in the vicinity of prosthetic heart valves have been conducted in two different 1:1 scaled pulse duplication systems. One system was designed for the application of optical techniques (LDA, PTV). This system was operated with a refractive index matched Newtonian blood analog fluid and has been described by Hirt *et al.* (1994 a,b). The other system was prepared for the application of the MRI-scanner and consisted of the same components but with different design of the left ventricle. In order to avoid magnetic interference effects of the MRI-scanner and the power control unit of the pump, the pump head was connected to the left ventricle via a long tube. The complete pulse duplication system was mounted on the patient table of the MRI-scanner as shown in **Figure 1**. Pulsatile velocity measurements have been conducted in both systems under the same physiological flow conditions. These were defined by the ratio of the upper to the lower aortic pressure (120/80 mmHg), by the cardiac output (5 l/min) and by the heart beat rate per minute (72 BPM).

APPLIED MEASUREMENT TECHNIQUES

LDA - Technique

A commercially available Laser Doppler Anemometry system (LDA) was used to measure the instantaneous velocities of seeded particles (diameter 1.5 μm) which followed the flow of the blood analog fluid. The optical system consisted of a two colour *Dantec* fiber optical device and a PDA signal processor.

The LDA system was capable of correlating collected velocity data with the cardiac cycle phase. The beginning of each cycle was initiated by a 5V TTL trigger pulse which was provided by the power control unit of the displacement pump. This pulse was divided in 1500 equally spaced pulses within the cardiac cycle at 72 BPM. These pulses were used to define time windows for the unsteady velocity data collection during one cycle. The resulting time resolution was therefore about 0.55 ms.

Magnetic Resonance Imaging (MRI) Technique

The Magnetic Resonance (MR) measurements were performed with a 1.5 Tesla *Philips Gyroscan ACS II* whole body scanner. In order to achieve a higher signal to noise ratio, either a surface coil ($\varnothing = 150 \text{ mm}$) or a cardiac coil was used. The investigation of the pulsatile flow field near prosthetic heart valves required optimized measurement conditions of the system. Since the influence of higher order effects becomes stronger as the echo time is increased, different measurement strategies have been developed in order to take into account the high demand on the echo time. The velocity measurements were taken on a long axis image. In order to collect data on the fully 3D-time resolved velocity field near the prosthetic heart valve, a volume of $30 \times 200 \times 200 \text{ mm}$ was covered by 10 equidistant transversal slices, each of a thickness of 6 mm. The synchronization of the MR measurements and the displacement pump of the pulse duplicator was achieved with a 5V TTL trigger signal which was provided by the control unit of the displacement pump.

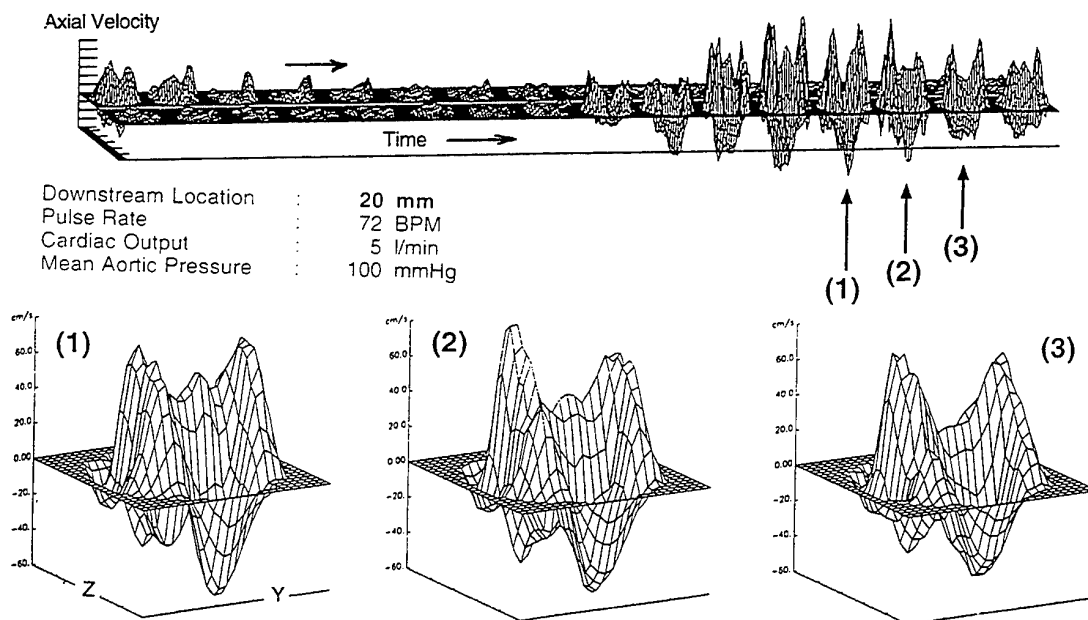


Figure 2. MRI-measurements of the axial mean velocity profiles during the cardiac cycle of an aortic bileaflet valve

Each cross sectional slice provided a two dimensional velocity map for one of the three velocity components. In order to achieve a higher time resolution, only one co-ordinate direction was velocity encoded per scan. The time resolution of the cardiac cycle was 35 ms yielding to 32 frames throughout the cycle at 72 BPM. With a field view of 200 x 200 mm a pixel resolution of 0.78 x 0.78 mm was obtained. The processed MRI-data of the axial mean velocity near a prosthetic aortic heart valve are presented in **Figure 2**.

bulence on the phase of the MR-signal has been investigated and it was found that the calibration relation may be affected by the effect of turbulence. Further improvements are needed to achieve a higher time resolution of the accelerated flow phase where the relative turbulence level becomes very high. During the diastolic phase of the cardiac cycle the valve is closed and small regurgitant leakage jets are generated which flow backwards into the ventricle. The power of MRI-technique was also demonstrated by visualizing these jets.

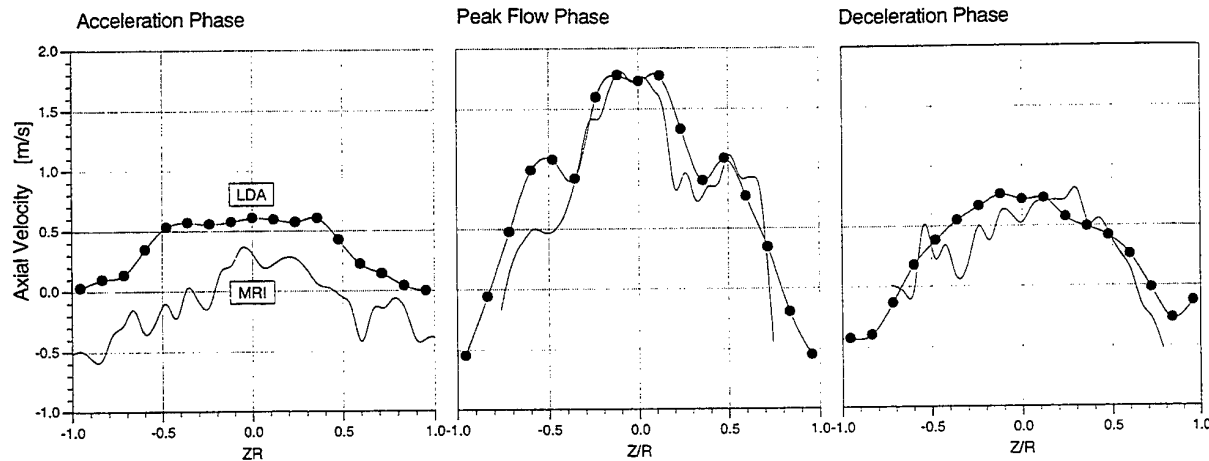


Figure 3. Comparison of pulsatile MRI and LDA data of the axial mean velocity near a bileaflet heart valve at the aortic position and at a downstream distance of $x = 11$ mm.

DISCUSSION OF THE RESULTS

The comparison of the LDA and MRI velocity measurements was established for the same bileaflet valve at the same pulsatile tuning conditions and for the same downstream location of the aortic test section. The number of collected LDA data points per cycle was $7'000 < N < 10'000$ and a single specified time phase was represented by more than 700 data points. The post processor allowed a decomposition of the measured flow velocity into mean value and statistical fluctuation. However, the problem is one of the measurement of turbulent fluctuations. In fact errors may occur due to the acceleration or deceleration of the flow. In the present work, an investigation concerning the effect of the time window size on the magnitude of the major turbulent Reynolds shear stresses was carried out and will be published by Zhang *et al.* (1996). Accordingly the time window for post-processing was 7 ms. Using the described arrangement under optimized measurement conditions, reliable measurements were carried out during the whole cardiac cycle. As a result a good agreement between the LDA and MRI measurement techniques has been found for the peak flow and the deceleration phase (cf. **Figure 3**). The most significant difference between the two techniques is recognized at the mid-acceleration phase. There, the influence of tur-

CONCLUSIONS

Two different pulse duplication systems have been built for the application of LDA and MRI measurement techniques. Using both techniques under the same pulsatile flow conditions, the MRI-technique has been validated as a valuable tool to analyze the blood flow in large vessels and at low turbulence levels. Besides the collection of mean velocity data, the application of the optical techniques was focused on the statistical turbulence quantities. In particular the Reynolds stresses under pulsatile flow conditions were of interest. Based on the flow behaviour over one cardiac cycle, it was found that behind the valve the relative turbulence intensity (axial RMS velocity/mean velocity) becomes larger as the flow speed is increased. At peak flow, the turbulence level is about 5%.

ACKNOWLEDGEMENTS

The authors thank the Swiss National Science Foundation for the financial support which made the MRI-experiments at the ETHZ possible. Continuing support and valuable comments by Drs. M.V. Casey and S. Ziada, Sulzer Innotec AG, are gratefully acknowledged.

REFERENCES

Boesiger, P., Maier, S.E., Kecheng, L., Scheidegger, M.E., Meier, D. (1992). Visualization and Quantification of the Human Blood Flow by Magnetic Resonance Imaging. *J. Biomechanics* Vol.25, No.1, 55-67.

Botnar, R., Ringgaard R., Hirt, F., Pedersen, E., Scheidegger, M.B., Boesiger P. (1996). Assessment of Velocity Fields Downstream of Prosthetic Heart Valves: In Vivo and In Vitro Studies. Fourth Scientific Meeting of the Society of Magnetic Resonance.

Eisele, K., Zhang, Z., Hirt, F., Perschke, N. (1996). Fast Imaging Techniques Promise Low-Cost Flexible Flow Visualization without Pulsed Lasers. *Laser Focus World & Laser Report*.

Hirt, F., Jud, E., Zhang, Z. (1994a). Investigation of the Local Flow Topology in the Vicinity of a Prosthetic Heart Valve Using Particle Image Velocimetry. Proceedings of 7th International Symposium on Applications of Laser Techniques to Fluid Mechanics, Lisbon.

Hirt, F., Baldwin, T., Casey, M.C. and Jud, E. (1994b). Cardiac Valves in a Model Circulatory System. *Sulzer Medica Journal*.

Walker, P.G., Pedersen, E.M., Oyre S., Flepp, L., Ringgaard S., Heinrich, R.S., Walton, P., Hasenkam, J.M., Jorgensen, H.S., Yoganathan, A.P. (1995). Magnetic Resonance Velocity Imaging: A New Method for Prosthetic Heart Valve Study. *J Heart Valve Dis*, Vol. 4. No.3.

Zhang, Z., Eisele, K., Hirt, F. (1996). The influence of phase-averaging window size on the determination of turbulence quantities in unsteady turbulent flows. Submitted to *Experiments in Fluids*.

SESSION 34

Optics I

POWER AND SENSITIVITY IMPROVEMENT OF LDA-SYSTEMS BY FIBER AMPLIFIERS

H. Többen, H. Müller, D. Dopheide

Physikalisch-Technische Bundesanstalt (PTB)
Laboratory for Fluid Flow Measuring Techniques
D-38116 Braunschweig, Bundesallee 100, Germany

ABSTRACT

A new concept is presented where fiber amplifiers are used in fiber optical LDA-systems as booster amplifier to magnify the laser power in the measuring volume as well as preamplifier to increase the sensitivity of detector units.

1. INTRODUCTION

Scattered light of low intensities is produced by particles with small dimensions, particles in high speed flows and in LDA-systems with a great working distance. In these cases powerful lasers like Argon-ion and Nd:YAG-laser are preferred in LDA-systems. Because the emission wavelengths of the Nd:YAG and of the Argon laser are aside of the maxima of responsivity from Si-, InGaAs- and Ge-detectors, the output power of these lasers can not be completely yielded for the LDA-system. In example, Arndt et. al. (1996) have demonstrated that twice the laser power of a 830 nm diode laser LDA must be applied at 1064 nm Nd:YAG LDA to obtain the same sensitivity for the whole system for particles sizes smaller than 1 μm .

As shown here, a drastical increase of the sensitivity can be obtained by optical preamplification with fiber amplifiers placed in front of photodetectors. This offers a very interesting possibility of improving the performance of LDA-systems, specially of LDA-systems with working wavelengths at low responsivities of commonly used conventional photodiodes like diode pumped Nd:YAG lasers at 1064 nm.

A further interesting application of fiber amplifiers is the optical post amplification of laser radiation produced by laser sources with small emission linewidths and low output powers like longitudinal single mode laser diodes as DFB- (distributed feedback), DBR- (distributed Bragg reflector) or well tuneable TTG (tunable-twin-guide)-lasers. This lasers are used in newly developed shift LDA-systems as presented by Müller and Dopheide (1993), where the output beams of two DFB-laser diodes are focused directly into the measuring volume.

The most advantage of post or booster amplification using fiber amplifiers is the increase of the signal source output power without changing the spectral characteristics by pumping with a pump source with low requirements on its spectral characteristics.

Fiber amplifiers can also be used in already existing fiber optical LDA-systems, i.e. multicomponent LDAs where the waveguiding takes place in fibers. In this case it is easy to amplify the laser radiation by simply inserting fiber amplifiers.

2. FUNDAMENTALS OF FIBER AMPLIFIERS

The basic function principle of a fiber amplifier which is placed between standard fibers is shown in figure 1. A fiber amplifier consists essentially of a pump laser diode, a fiber coupler and a short fiber doped with rare earth ions. The pump power of pump laser diode supplies the amplifier with energy. The doped fiber core creates the active medium, its dopant is excited to higher energy levels by pump power.

Amplification occurs if the excited energy level of an ion is depleted by an incident photon which induces, or stimulates, the emission of a second photon, as shown in figure 2. Because the emitted photon has the same frequency, phase and polarization as the stimulating photon it is an exact replica of the photon already present. The radiation remains coherent and the spectral emission characteristic doesn't change. A fiber coupler combines the

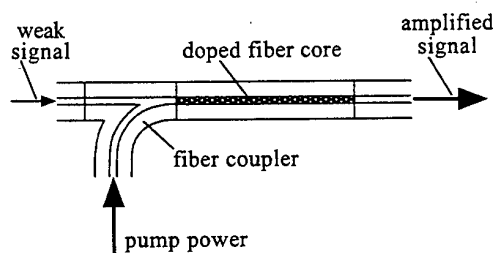


Fig. 1 Basic function principle of a fiber amplifier

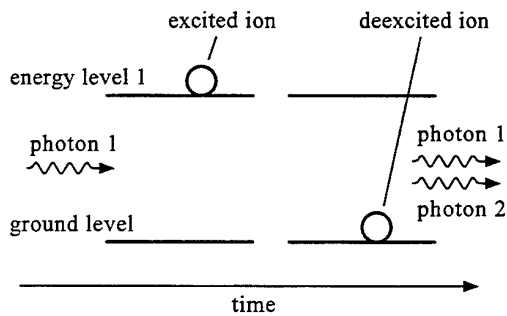


Fig. 2 Principle of stimulated emission

pump and the signal radiation in the doped fiber. The coupler can be placed in front of or behind the active fiber for backward or forward pumping.

The greatest efforts in developing optical amplification with fiber amplifiers have been done in the optical telecommunication technique for realizing long distance transmission systems with transmission rates of Gbit/s at a wavelength of 1,55 μm . The mostly developed fiber amplifier is the EDFA (Erbium doped fiber amplifier). The EDFA, which can be pumped by 980 nm or 1480 nm broadband emitting multimode laser diodes, amplifies laser radiation in the wavelength range between 1520 nm and 1560 nm. A record amplification value of 54 dB (factor: 250.000) was achieved with an EDFA for small signal amplification reported by Laming et. al. (1992). Further well developed fiber amplifiers have been realized for the wavelength range around 1,3 μm with Neodymium or Praseodymium doped fibers. The experiences gathered from these fiber amplifiers, specially from the EDFA, can be transferred to other fiber amplifier set-ups to realize amplification at preferred wavelength.

3. CHARACTERISTICS OF FIBER AMPLIFIERS

Fiber amplifiers placed behind a laser source with low output power (mW or sub-mW range) can be used as booster (post) amplifier. They work in the saturated regime and convert pump power delivered from broadband sources into signal power of high precision lasers. With an EDFA

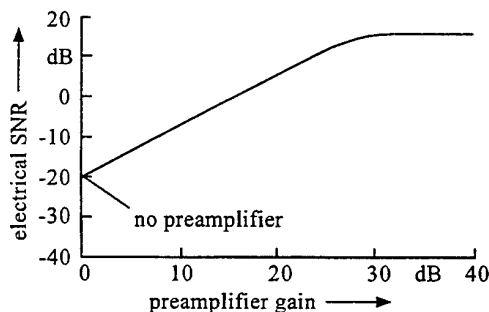


Fig. 3 SNR as function of preamplifier gain

as booster amplifier a pump-to-signal conversion efficiency of 59 % was realized by Laming et. al. (1991).

Behind fiber coupled lasers, booster amplifiers give the chance to use high quality sources like DFB or DBR laser diodes with low output power and low price. Specially to realize fiber optical multicomponent LDA-systems utilizing the optical frequency difference of two separate laser sources for the generation of each LDA-beam booster amplifiers simply inserted as „black box“ can be used to increase the power in the measuring volume.

As preamplifiers in front of photo detectors fiber amplifiers can be used to increase the signal-to-noise ratio (SNR). Specially, aside of the maxima of responsivity at 900 nm in Si-detectors and at 1,55 μm in InGaAs- or Ge-detectors, for example at 1064 nm or 532 nm which are emission wavelengths of powerful Nd:YAG solid state lasers, the minimum detectable signal level can be drastically reduced by broadband optical preamplification.

SNR calculations made by Desurvire (1994) have shown that the SNR of the electrical current delivered from a PIN photodiode can be drastically improved by optical preamplification with an EDFA. The calculations have demonstrated that:

- The electrical SNR of signal detection with a PIN photodiode can be increased of about 36 dB (factor: 4000) in combination with optical preamplification in an EDFA for typical values used for amplification of 1,55 μm signals. The result is shown in figure 3.
- If a SNR of 20 dB (factor: 100) should be required for the detection unit, an enhancement of minimum detectable power or detector sensitivity of 25 dB (factor: 316) can be achieved by using optical preamplification.
- In comparison with an APD photodiode the PIN photodiode with optical preamplification delivers the best results.

Thus, the conclusion is that this optical preamplification technique is a very valuable tool in laser Doppler anemometry.

4. FIRST EXPERIMENTS

Figure 4 shows the experimental set-up used for our first examinations of optical amplification with a fiber amplifier as booster amplifier to be applied in a fiber optical frequency shift LDA-system. An Erbium-doped silica fiber of 15 m length was used as active part in the

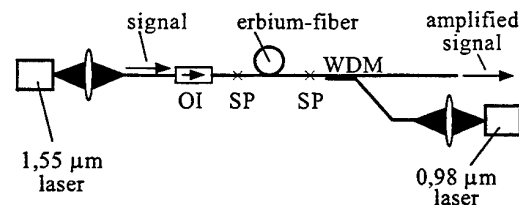


Fig. 4 Set-up of a booster fiber amplifier for 1,55 μm laser radiation in an Erbium-doped fiber

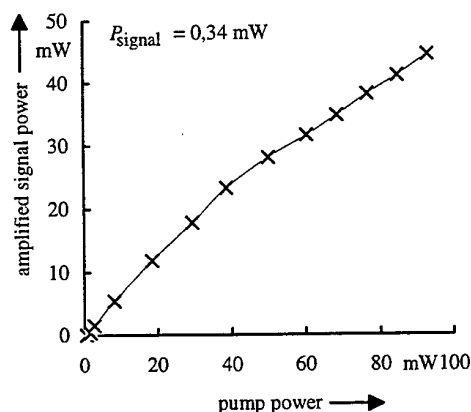


Fig. 5 Amplification of 340 μ W input signal power at 1,55 μ m with a 980 nm pump as shown in fig. 4

system. The Erbium-doped fiber was connected to the standard single mode fiber components with mechanical splices (SP).

A low power tunable TTG-laser diode with an emission wavelength near 1,55 μ m and an emission linewidth of a few MHz was used as the signal source. A 980 nm laser diode was used as pump. The output radiation of the pump and the signal laser source was focused into the core of standard fiber components. The WDM-fiber coupler (WDM: wavelength division multiplexer) selects or combines the pump and signal radiation. Due to backscattered light and amplified spontaneous emission radiation generated in the doped fiber, the optical isolator (OI) with fiber pigtails in front of the 1,55 μ m-laser diode

ensures a stable operation of the signal source.

Figure 5 shows one of the first results of booster amplification with the set-up shown in figure 4. The launched 1,55 μ m-signal power was 340 μ W. It can be observed that the amplified signal power at 1,55 μ m increases approximately linear with increasing pump power at 0,98 μ m. At a launched pump power of 93 mW the signal power started with 0,34 mW was amplified up to 44 mW. This corresponds to an amplification factor of 129 (21 dB) and a pump-to-signal conversion efficiency of 34 %. By optimization of fiber parameters and pump configuration improvements of these first results are possible.

4. CONCEPT OF A FIBER OPTICAL SHIFT-LDA WITH FIBER AMPLIFIERS

Figure 6 shows the concept of a fiber optical shift-LDA-system which combines the post and pre amplification of optical radiation with fiber amplifiers. Two laser diodes (LD1 and LD2) with an emission frequency difference and emission linewidths in the MHz range produce the LDA radiation (P_{LD1} and P_{LD2}). Booster fiber amplifiers behind each source increase the laser radiation to higher power levels ($P_{LD1, ampl.}$ and $P_{LD2, ampl.}$). Therefore, low power laser diodes i.e. conventional pigtailed well tunable DFB laser diodes can be used as LDA sources.

A fiber coupler combines small parts of the laser radiation (P'_{LD1} and P'_{LD2}) to produce a beat signal in the photodiode 1 (PD1) as reference signal, which will be used for the signal evaluation unit. Miniaturized focusing optics

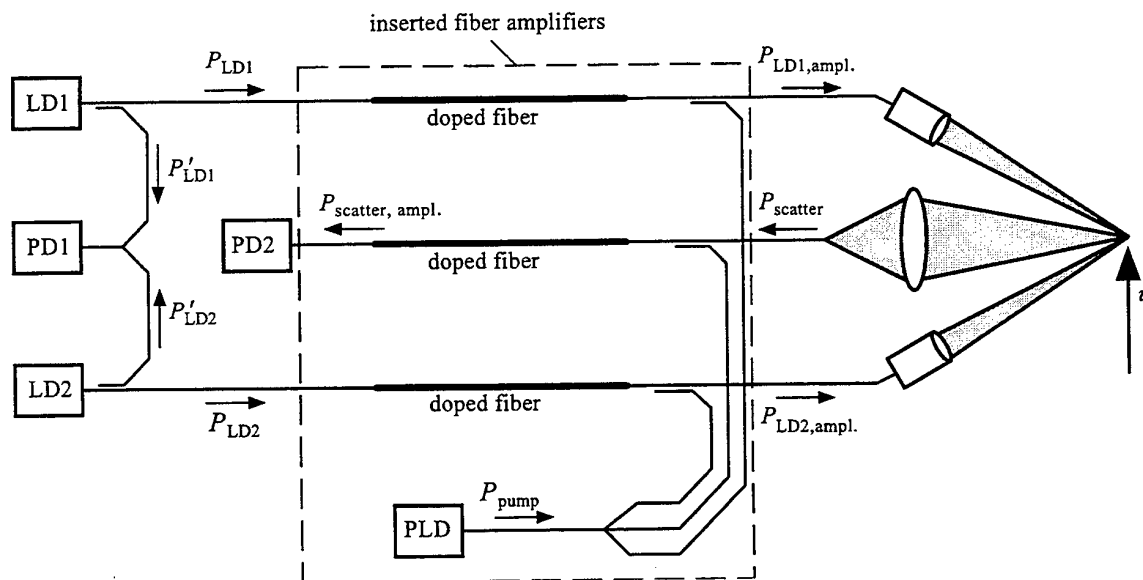


Fig. 6 Schematical set-up of a fiber optical shift-LDA system with fiber amplifiers for post and pre amplification

with fiber pigtails focus the amplified laser radiation into the measuring volume.

The scattered light of tracer particles in the flow is focused into the fiber core of a third fiber amplifier in front of the photodiode 2 (PD2) which is used as preamplifier. For enhancing the SNR of the measuring signal the preamplifier amplifies the launched scattered light (P_{scatter}) to higher power levels ($P_{\text{scatter, ampl.}}$).

A fiber coupler splits up the output power (P_{pump}) of the pump laser (PLD) in three parts, which are coupled into the doped fibers by WDM fiber couplers. A powerful multimode laser diode can be used as pump source. To keep away disturbing radiation, e.g. pump radiation, from laser diodes and photodiodes optical filters or optical isolators can be placed in front of these devices.

By mixing the measuring signal, delivered from PD2, with the simultaneously detected reference signal, delivered from PD1, by quadrature signal processing technique, presented earlier by Müller et. al. (1994), the shift frequency f_{sh} with all its frequency fluctuations and bandwidth influences is eliminated, the directional information is retained and the Doppler frequency f_D is obtained in the base band. Figure 7 shows the schematical diagram of the quadrature demodulation unit.

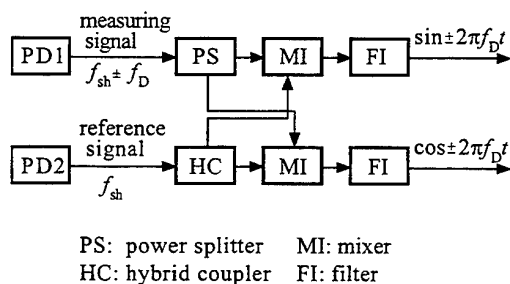


Fig. 7 Quadrature detection unit for signal processing of fiber optical shift LDA-system according to fig. 6

CONCLUSION

A new concept was presented for increasing the power in the measuring volume and improving the sensitivity of LDA-systems with fiber amplifiers.

As booster amplifiers they offer the possibility to increase the output power of DFB- or DBR-laser sources with low cost broadband emitting pump lasers. In a first experiment an amplification factor over 100 (20 dB) was realized.

As preamplifier in front of a PIN-photodiode fiber amplifiers enhance the SNR of the detected signals and allow to detect extremely weak burst signals. Enhancement over 36 dB (factor: 4000) are predicted using Erbium-doped fiber amplifiers. Such a fiber amplifier can enhance the sensitivity of LDA-receivers dramatically and allows to set novel impetus to diode pumped solid state lasers and photo diode receivers.

REFERENCES

- Arndt, V., Müller, H. & Dopheide, (1996), Comparison measurements for selection of suitable photodetectors for use in Nd:YAG LDA systems, Experiments in Fluids, vol. 20, pp. 460-465
- Desurvire, E., 1994, Erbium-doped fiber amplifier, pp. 167-174, John Wiley & Sons, New-York.
- Laming, R.I., Townsend, J.E., Payne, D.N., Meli, F, Grasso, G. & Tarbox, E.J., 1991, High-power Erbium-doped-fiber amplifiers operating in the saturated regime, Photonics Tech. Letters, vol. 3, pp. 253-255.
- Laming, R. I., Zervas, M. N. & Payne, D. N., 1992, Erbium-doped fiber amplifier with 54 dB gain and 3,1 dB noise figure, Photonics Tech. Letters, vol. 4, pp. 1345-1347.
- Müller, H. & Dopheide, D., 1993, Direction sensitive laser Doppler velocimeter using the optical frequency shift of two stabilize laser diodes. Proc. SPIE Vol. 2052 Laser Anemometry Advances and Applications, pp. 323-330
- Müller, H., Czarske, J., Kramer, R., Többen, H., Arndt, V., Wang, H. & Dopheide, D., 1994, Heterodyning and quadrature signal generation: advantageous technique for applying new frequency shift mechanisms in the laser Doppler velocimetry. Proc. 7th Int. Symp. on Appl. of Laser Techniques to Fluid Mechanics, 11-14 July 1994, Lisbon, pp. 23.3.1-23.3.8

TWO-COMPONENT DIRECTIONAL LASER DOPPLER ANEMOMETER BASED ON A FREQUENCY MODULATED ND:YAG RING LASER AND FIBER DELAY LINES

J. W. Czarske¹ and H. Müller²

¹ Laser Zentrum Hannover e. V., Hollerithallee 8, D-30419 Hannover, Germany

² Physikalisch-Technische Bundesanstalt, Laboratory for Fluid Flow Measuring Techniques, Bundesallee 100, D-38116 Braunschweig, Germany

ABSTRACT

A novel method for the directional multicomponent laser Doppler anemometry, based on the generation of different carrier frequencies by means of a frequency modulated diode-pumped Nd:YAG miniature ring laser is presented. The realized laser Doppler anemometer makes it possible to determine precisely the sign and magnitude of two orthogonal fluid flow velocity components.

1. INTRODUCTION

The laser Doppler anemometry (LDA) is an established technique for the velocity measurement of fluid flows (Tropea (1995)). Especially studies of turbulent flows require the measurement of multiple velocity components with directional discrimination. Conventional multicomponent LDA systems employ optical wavelength multiplexing techniques, involving multiple-line Argon ion lasers with emission lines at 488 nm and 514.5 nm wavelength, together with components for the wavelength separation of the laser beam as well as of the received scattering light onto different detectors. Additionally, optoelectronic elements, usually Bragg cells, are involved in LDA systems for the generation of electrical carrier frequencies in order to ensure the directional discrimination. However, such LDA systems exhibit a high expense, large dimensions, a high alignment effort and are in consequence not suited for special fluid flow measurement situations. The application of the carrier frequency multiplexing techniques by employing Bragg cells to generate different carrier frequencies allows to save the optics for expensive wavelength multiplexing technique. Employing fiber optics simplified LDA systems with flexible measuring heads were realized, but the high alignment effort, especially by applying Bragg cells in combination with fiber optics remained.

In this contribution we propose a novel multicomponent heterodyne fiber-optic LDA system based on different carrier frequencies without having to use additional frequency shift elements. Thus it is possible to realize a simple and optomechanical robust LDA system. The employed diode-pumped Nd:YAG ring laser (Freitag et al. (1995)) has a compact, efficient design and emits a high single-frequency power, enabling the realization of a portable, precise LDA system.

2. METHOD

The realization of a heterodyne LDA system requires the generation of LDA beams with slightly different optical frequencies. In general, four different methods can be used: (1) The application of external frequency shift elements (e.g. Bragg cell, electro-optical modulators (Drain (1986))), (2) the use of a dual-frequency laser (Czarske (1994), Kramer (1994)), which emits two waves of different frequency and orthogonal polarization, (3) the use of several lasers (Müller (1994)), stabilized on constant difference frequencies and (4) the generation of a chirp frequency modulated laser in combination with optical delay lines (Jones (1982)).

The generation of the different carrier frequencies is based on a well defined time delay of frequency modulated optical waves (Jones et al. (1982), Jones et al. (1984), Schröder (1987), Aoshima and Ohtsubo (1992), Yamaguchi and Hamano (1995), Czarske and Müller (1995)), see fig. 1.

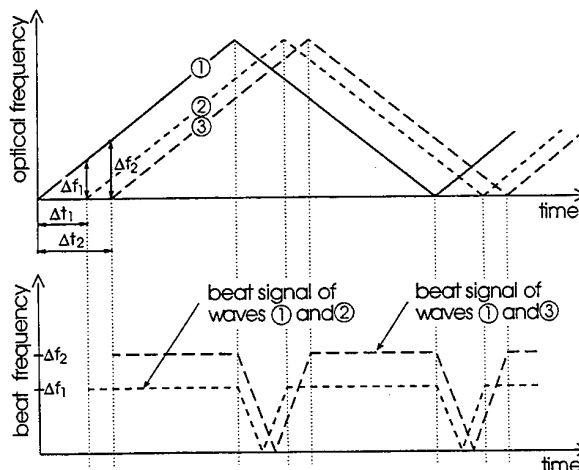


Fig. 1 Principle of the carrier frequency generation by a chirp laser modulation in combination with occurring time delays.

A chirp frequency modulated laser wave is splitted up into three waves, having relative time delays of Δt_i , $i = 1, 2$, realized by fiber delay lines with a resulting path length difference

of Δl_i , $i = 1, 2$. The time delays result in the difference frequencies Δf_i of the optical waves, which are equal to the carrier frequencies of the generated electrical beat signals. Assuming a triangular frequency modulation function, the carrier frequencies Δf_i are given by Czarske and Müller (1995):

$$\Delta f_i = \Delta l_i \frac{df_L(t)}{dt} = \frac{4l_i f_M \Delta u}{c} \frac{df_L(t)}{du(t)}$$

where l_i are the optical delay lengths, f_M is the modulation frequency, Δu is the modulation amplitude (half of the modulation peak to peak voltage), c is the light velocity and $df_L(t)/du(t)$ is the laser modulation coefficient.

3. OPTICAL ARRANGEMENT

In fig. 2 the configuration of the heterodyne LDA system is shown. The used fiber-pigtailed diode-pumped monolithic Nd:YAG miniature ring laser emits 160 mW at 1319 nm wavelength and is piezomechanically frequency modulated. The modulated laser wave is guided via a 1 x 3 fused fiber coupler, three delay fiber lines (a), (b), (c) of different lengths and three gradient index lenses (Grin) into the measuring volume. The Mie scattered light waves from scattering particles passing through the measuring volume, are imaged onto an avalanche InGaAs photodiode and generate the carrier frequency measuring signal. The resulting measuring frequencies are given by $f_{Mi} = \Delta f_i \pm f_{Di}$, where the indices $i = 1, 2, 3$ correspond to the different velocity components. Δf_i are the carrier frequencies, given by the optical frequency differences and f_{Di} are the Doppler frequencies, corresponding to the velocity components v_i , given by $v_i = f_{Di} \cdot d_i$, with d_i as the fringe spacings in the measuring volume.

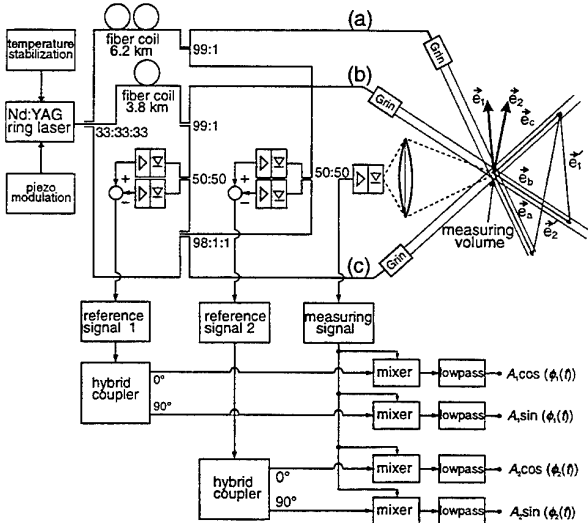


Fig. 2 Arrangement of the two-dimensional differential laser Doppler velocimeter with directional discrimination;

$$\Phi_i(t) = 2\pi f_{Di} \cdot t$$

Fig. 3 shows the frequency spectrum of a typical measuring signal for the parameters:

modulation frequency $f_M = 4$ kHz, modulation amplitude $\Delta u = 15$ V, modulation coefficient $df_L/du \approx 4.8$ MHz/V, optical delay lengths $l_i = n \cdot l_{Fi}$, with the LP_{01} mode refraction index $n = 1.45$ and the fiber path differences $l_{F1} = 3.8$ km, $l_{F2} = 6.2$ km, $l_{F3} = 2.4$ km.

In the future, it is planned to reduce the high lengths of the preliminary realized fiber delay lines, since besides the appearing technical effort high time delays Δt_i result, which give a loss of the available measuring time, see fig. 1.

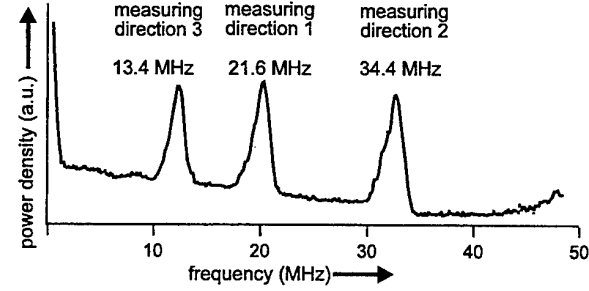


Fig. 3 Frequency spectrum of the measuring signal for a non-moving scattering particle.

Only two of the three available measuring directions are linear independent (Czarske and Müller (1995)). The two directions $\pm \vec{e}_1$ and $\pm \vec{e}_2$, given by $\vec{e}_1 = \vec{e}_c - \vec{e}_b$, $\vec{e}_2 = \vec{e}_c - \vec{e}_a$ with $\vec{e}_a, \vec{e}_b, \vec{e}_c$ as unit vectors of the three LDA beams and $\vec{e}_i = \vec{e}_i / e_i$, $i = 1, 2$, as measuring direction unit vectors, have been evaluated. As shown in fig. 3 and 4, the carrier frequencies have fluctuations. To eliminate the carrier frequency fluctuations, the measuring signal is correlated with reference signals for each measuring component, given by the beat signals of the LDA beam pairs. The reference signals are generated by out-coupling of a small part of the LDA waves onto balanced pin InGaAs photodiodes, see fig. 2.

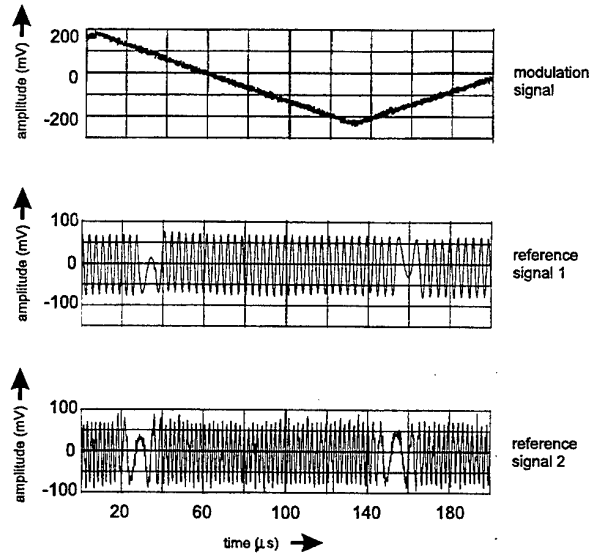


Fig. 4 Time functions of the triangular modulation signal and the reference beat signals. The laser modulation frequency is 4 kHz and the piezo modulation amplitude is 200 mV.

The triangular function is the best suited modulation type, because of the resulting small carrier frequency variations, especially compared to the sinusoidal modulation type. A sawtooth modulation would cause problems concerning the different slopes, resulting in different carrier frequencies. Additionally a sawtooth modulation allows only to generate the half carrier frequency amount compared to triangular modulation, assuming the same laser frequency modulation amplitude.

4. SIGNAL PROCESSING TECHNIQUE

The employed quadrature demodulation signal processing technique allows to determine the magnitude and sign of the Doppler shifts of the measuring directions in the baseband (Agrawal (1984), Skolnik (1980), Czarske and Müller (1995), Czarske (1996)). Besides the optical arrangement figure 2 also shows the block diagram of the quadrature demodulation unit for evaluating two measuring components (1, 2). The measuring signal is correlated by two-stage mixer/filter units with the reference signals, containing the carrier frequencies of the measuring components 1 and 2, respectively. To retain the directional information when eliminating the carrier frequencies, quadrature signal pairs in the baseband are generated by employing a hybrid coupler in order to achieve a broadband 90° phase shift. The bandwidth for ensuring a constant 90° phase shift defines the allowed fluctuations of the carrier frequencies. Since the signal processing is accomplished in the baseband it should be noted that the carrier frequency signals are auxiliary signals for the realization of (i) the frequency multiplexing of different measuring components and (ii) the realization of a constant 90° phase shift, necessary for the quadrature signal pair generation.

As a preliminary result, in fig. 5 signal pairs with nearly ±90° phase difference are shown, measured for the same fluid flow direction, but for opposite signs of the triangular modulation signal slope. The phase difference of the signal pairs alternates from -90° to +90°, caused by the change of the sign of the frequency difference between the corresponding LDA beam pair (b), (c) of the measuring direction 1.

The quadrature signal pairs can be regarded as the real and the imaginary parts of the complex signals

$$\underline{a}_i(t) = A_i \exp i\Phi_i(t) = A_i (\cos \Phi_i(t) + i \sin \Phi_i(t)), i = 1, 2,$$

where A_i are the signal amplitudes and $\Phi_i = 2\pi x_i(t)/d_i$ are the phase angles with $x_i(t)$ as scattering particle positions in the measuring volume and the d_i as fringe spacings of the two measuring directions $i = 1, 2$. Employing a four-channel transient recorder and a signal processor, the signal pairs are digitized and evaluated by using the expression

$$\Phi_i(t) = \arctan \frac{A_i(t) \sin \Phi_i(t)}{A_i(t) \cos \Phi_i(t)} \pm 2\pi n_i, i = 1, 2,$$

where n_i are the incrementally counted periods of the burst signal. This technique allows the determination of two phase angle time series. In order to achieve the information about the scattering particle velocity, an evaluation of the phase angle series by means of the least squares method is accomplished. The averaged velocity in the measuring volume can be estimated with the regression straight line $\Phi_i(t) = 2\pi b_i t$, where \hat{b}_i is the esti-

mated regression slope. The estimated magnitudes $|\hat{b}_i|$, $i = 1, 2$ are equal to the averaged frequencies of the two burst signal pairs and proportional to the averaged velocity in the directions 1 and 2. In order to determine the fluid flow direction, the triangular modulation signal has to be simultaneously detected by the employed signal processor. In dependence on the sign of the modulation slope, the measured signs of the regression slopes are multiplied by ±1 to determine the fluid flow direction.

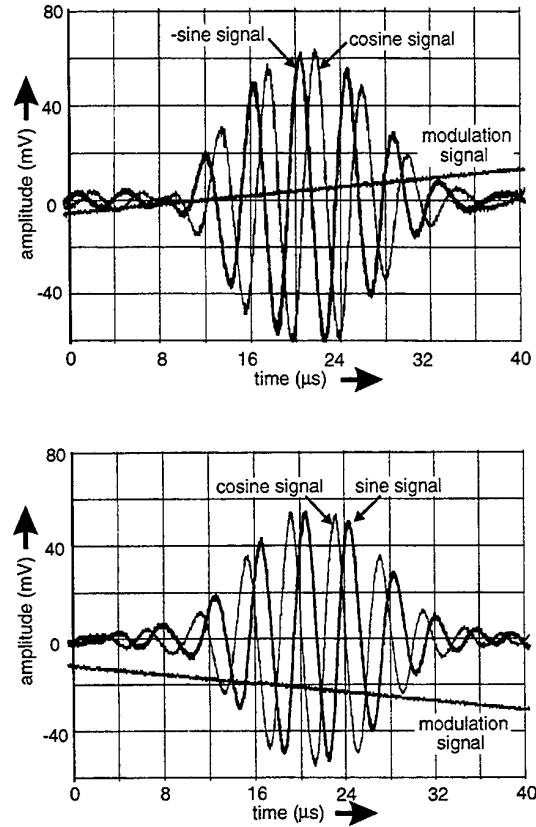


Fig. 5 Quadrature burst signal pairs of the measuring direction 1 for opposite slopes of the triangular modulation signal.

5. DISCUSSION ON THE MEASURING UNCERTAINTY

On the one hand quadrature signals can advantageously be evaluated by linear regression of the phase angle time series, especially if directional measurements of velocities and accelerations with high temporal resolution are required. On the other hand quadrature demodulation by linear regression is a helpful tool for the discussion of the measurement uncertainty of LDA signals in order to optimize of the LDA measuring volume by an appropriate optical design.

The first part of this chapter gives a brief description of the measurement uncertainty analysis method based upon the evaluation of the phase angle time series resulting from the digitized quadrature signal. In the second part of the chapter the method is exemplarily used for the optimization of the LDV measuring volume. The presented uncertainty analysis method of the differential LDV system is based upon

- (i) the derivation of the mean velocity measuring uncertainty as function of LDV burst signal parameters and
- (ii) the determination of the LDV signal parameters in dependence on the parameters of the optical LDV system, e.g. the dimensions of the LDV measuring volume.

Assuming a scattering particle movement with constant fluid velocity v_0 , the measured LDV signal phase is given by

$$\Phi_M(t) = (2\pi v_0/d)t + \Phi_N(t),$$

where $2\pi v_0/d$ is equal to the angular frequency ω_0 and $\Phi_N(t)$ represents the occurring phase noise in the measurement. The phase is sampled with the constant period T . Thus, the sampling times are given by $t_i = t_0 + iT$, $i = -(N-1)/2 \dots (N-1)/2$, where N is an odd number of phase values. The sampling frequency $1/T$, as well as the phase number N are restricted by the employed transient recorder for the beat signal digitalization. Furthermore, the measuring duration $\tau = (N-1)T$ should be set equal to the LDV burst signal duration, which is given by the transit time of scattering particles passing the measuring volume. The measured phase series Φ_{Mi} contains the fundamental information of the movement of the scattering particle, since the phase time function describes the time dependent position of the scattering particle. Hence, based on phase series, different LDV measuring parameters and their uncertainty can be effectively determined. In order to achieve the aim to estimate the mean velocity uncertainty $\Delta\langle\hat{v}\rangle$, which is assumed to be proportional to the estimated center frequency uncertainty $\Delta\langle\hat{\omega}\rangle$, first an estimation of the signal center frequency is accomplished. The measured phase values Φ_{Mi} are fitted to a straight regression line $\hat{\Phi}_i = \langle\hat{\omega}\rangle t_i$ by using the least squares method (Czarske (1996), Seber (1977)). The estimated center frequency of different burst signals exhibits a fluctuation around the true center frequency ω_0 , because of the influence of the occurring phase noise Φ_N . Considering an ensemble of burst signals, the uncertainty $\Delta\langle\hat{\omega}\rangle$ is determined, involving the error propagation law (Czarske (1996)). Assuming a statistical independent Gaussian heteroscedastic white noise process and a deterministic sampling, the standard deviation is given by (Czarske (1996), Seber (1977)):

$$\Delta\langle\hat{\omega}\rangle = \frac{\Delta\Phi_{\min}}{\left[\sum_{i=-(N-1)/2}^{(N-1)/2} t_i^2 w_i\right]^{1/2}},$$

where $w_i = (\Delta\Phi_{\min}/\Delta\Phi_{Mi})^2$ is the weighting of the phase values, with $\Delta\Phi_{\min}$ as the minimal standard deviation of the phase series. The assumed statistical independence of the phase values is valid, if the sampling frequency is lower than the noise bandwidth of the photo detection. The used least squares method meets the necessary properties of an efficient estimator, often referred to BLUE (Best Linear Unbiased Estimator). In the sim-

plified case of a constant phase variance, i.e. a weighting of $w_i = 1$, the standard deviation can be written as

$$\Delta\langle\hat{\omega}\rangle = \Delta\Phi_{\min} / \left\{ \tau \{N(N+1)/[12(N-1)]\}^{1/2} \right\},$$

where τ is the averaging time or burst signal duration and N is the number of uncorrelated phase values. This result is identical to the Cramer-Rao lower uncertainty bound of the maximum likelihood frequency estimation and it is in agreement with Heisenberg's uncertainty relation (Czarske (1996)).

In the following, the relationship between the signal parameters (equation above) and the LDV system will be investigated. The phase standard deviation $\Delta\Phi_M(t) = \Delta\Phi_N(t)$ and hence the weighting w_i and minimal phase deviation $\Delta\Phi_{\min}$, respectively, are dependent on the LDV signal amplitude $S(t)$ and can be simply expressed by:

$$\Delta\Phi_M(t) = [c_1 + c_2 S(t)]^{1/2} / S(t),$$

where c_1 is the proportionality constant of the signal independent noise process, which is mainly caused by the detector thermal noise and amplifier noise, and c_2 is the proportionality constant of the signal dependent noise process, which is mainly determined by the detector shot noise, equal to the photon quantum noise. The signal amplitude $S(t)$ should be analysed by a chain of proportionalities. The amplitude $S(t)$ is proportional to the detected light power $P(t)$, which is on the other hand proportional to the intensity $I(x, t)$ in the measuring volume and the Mie scattering cross section. The intensity is given by $I \sim P_L/a^2$, where P_L is the laser power and a is the lateral diameter of the measuring volume. Hence, it results $S = \alpha/a^2$, with α as LDV system constant. The phase number N is proportional to the signal duration τ , assuming a constant sampling frequency (see above). The duration τ is dependent on the diameter α of the measuring volume and the fluid velocity v_0 : $\tau = \alpha/v_0$.

The briefly described method will be used exemplarily for the optimization of the LDV measuring volume. Because of the Gaussian profile of the generally used TEM₀₀ laser beams, the lateral intensity distribution in the measuring volume can be described by

$$I(x) \sim \exp\left[-(x/a)^2\right] \cos(2\pi x/d).$$

The intensity has a fringe structure in x -direction with the constant fringe spacing d and the fringe number $N_F = a/d$. The measuring volume diameter has two well known fundamental influences on the frequency uncertainty, see fig. 6: On the one hand, the phase variance increases with an enlarged diameter, implying a great frequency uncertainty. On the other hand, an extended diameter causes a larger burst signal duration, enabling a great averaging time and hence a small frequency uncertainty. An optimization of the diameter can be accomplished by the presented method and the proportionality $\Delta\langle\hat{\omega}\rangle \sim \Delta\Phi_{\min}/(\tau\sqrt{N})$ can be derived. The expressions above give the relationship of the used signal parameters with the diameter a : $\Delta\Phi_{\min} = (c_1 + \alpha c_2/a^2)^{1/2} a^2/\alpha$ and $\tau\sqrt{N} = \beta\alpha^{3/2}$, assuming fixed LDV system constants α , β , because of a constant laser power, a constant sampling frequency $1/N$ and a phase

sample number $N \gg I$, provided that a suitable transient recorder is employed. The resulting proportionality for the center frequency uncertainty is then given by:

$$\Delta(\hat{\omega}) \sim (\alpha^{-2}\beta^{-2}c_1a + \alpha^{-1}\beta^{-1}c_2a^{-1})^{1/2}.$$

Figure 7 shows this dependence for the exemplary chosen parameters $\alpha^{-2}\beta^{-2}c_1 = 1 \text{ m}^{-1}\text{s}^{-2}$ and $\alpha^{-1}\beta^{-1}c_2 = 10^4 \text{ ms}^{-2}$. In this case the minimal uncertainty is achieved, if a measuring volume with a diameter of $100 \mu\text{m}$ is realized, see fig. 7. It should be noticed, that this realization results in an equal variance of shot and thermal noise. Interpretation: It can be concluded that the optimized diameter of LDV measuring volume is dependent on the function between phase variance and the LDV signal amplitude. Of course, a more detailed discussion has to consider further noise processes, e.g. quantization noise, the demodulation threshold of the phase measurement and the flow properties, e.g. velocity gradients in the measuring volume (Drain (1986), George (1993), Durst and Whitelaw (1992)).

In consequence, based on quadrature demodulation and regression as maximum-likelihood estimators some generally guilty results on the optimized design of LDA systems were presented.

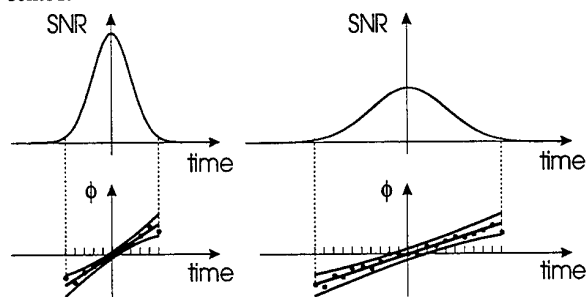


Fig. 6 Illustration of the diametrical relationship of the signal-to-noise-ratio (SNR) and the signal duration to the measuring volume diameter, assuming constant laser power and sampling frequency.

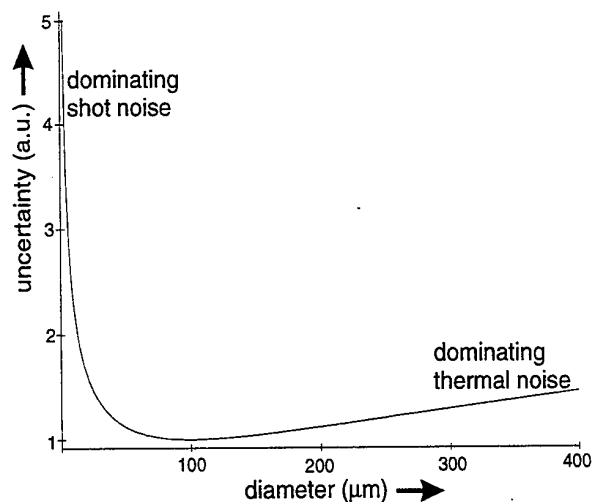


Fig. 7 Exemplary dependency of the center frequency standard deviation on the measuring volume diameter.

6. CONCLUSIONS

A novel fiber-based heterodyne laser Doppler anemometer (LDA) for the directional two-dimensional velocity measurement of fluid flows has been described. The presented LDA system has the following advantages:

- (i) The employed diode-pumped Nd:YAG ring laser type delivers a high single-frequency power of up to 1.8 Watt (Freitag (1995)), which is significantly higher than the optical power of single-mode diode lasers. Hence, a high signal-to-noise ratio and in consequence a high measurement accuracy can be achieved.
- (ii) The compact design and the high efficiency of the Nd:YAG ring laser gives a high portability of the LDA system, especially compared to LDA systems, employing argon ion lasers.
- (iii) The used fiber-optics enables an alignment insensitive realization of defined delaying, splitting and combining of the LDA waves, necessary for the employed heterodyne technique. Since the carrier frequency generation is achieved without additional optoelectronic elements, the heterodyne LDA system can be significantly simplified. The generation of stimulated Brillouin scattering (Cotter (1982)) in the fiber lines, as one of the most important mechanisms causing optical losses, can be eliminated by generating a high laser frequency modulation amplitude or by using small fiber lengths.
- (iv) The generated high carrier frequencies enable wide-range velocity measurements.
- (v) The applied heterodyne technique guarantees a precise velocity measurement without influence of carrier frequency fluctuations. Due to the quadrature demodulation processing in the baseband, quasistatic scattering particle movements can be measured with high velocity resolution. Additionally, velocity fluctuations can be directionally evaluated with a high resolution in time.

Acknowledgments: The authors thank Dir. und Prof. D. Dopheide and Prof. H. Welling for support.

7. REFERENCES

- Agrawal, Y. 1984, Quadrature demodulation in laser Doppler velocimetry, *Appl. Opt.*, vol. 23, pp. 1685-1686.
- Aoshima, T. and Ohtsubo, J. 1992, *Opt. Commun.*, vol. 92 p. 219.
- Cotter, D. 1982, *Electron. Lett.*, vol. 18, p. 638.
- Czarske, J. and Müller, H. 1994, Heterodyne interferometer using a novel two-frequency Nd:YAG laser, *Electron. Lett.*, vol. 30, pp. 970-971.
- Czarske, J. and Müller, H. 1995 (a), Multicomponent heterodyne laser Doppler anemometer using chirp-modulated Nd:YAG ring laser and fiber delay lines, *Electron. Lett.*, vol. 31, pp. 1428-1430.

- Czarske, J. and Müller, H. 1995 (b), Birefringent Nd:YAG microchip laser used in heterodyne vibrometry, Opt. Commun., vol. 114, pp. 223–229.
- Czarske, J. 1996 (a), Method for the Analysis of the Measuring Uncertainty of Laser Doppler Velocimeters, Opt. Lett., 1. April issue.
- Czarske, J. 1996 (b), Verfahren zur Messung und Auswertung der Interferenzphase in der Laser-Doppler-Velocimetrie, VDI-Fortschritt-Berichte, Serie 8, no. 530, VDI, Düsseldorf, Germany.
- Drain, L. 1986, The Laser Doppler Technique, Wiley, Chichester, UK.
- Durst, F. and Whitelaw, J. 1992, in Proceedings of Heat Transfer Conference, American Society of Mechanical Engineers, New York, p. 1.
- Freitag, I., Tünemann, A. and Welling, H. 1995, Power scaling of monolithic miniature Nd:YAG ring lasers to optical powers of several watts, Opt. Commun., vol. 115, pp. 511–515.
- George, W. 1993, in Laser Doppler Velocimetry, ed. R. A. Adrian, SPIE Milestone Ser. 78, p. 135.
- Jones, J., Corke, M., Kersey, A. and Jackson, D. 1982, Miniature solid-state directional laser Doppler velocimeter, Electron. Lett., vol. 18, pp. 968–969.
- Jones, J., Chan, R., Corke, M., Kersey, A., Jackson, D. 1984, Conference Proceedings Fiber Optics, Sira SPIE, vol. 468, p. 229.
- Kramer, R., Müller, H., Dopheide, D., Czarske, J. and Schmitt, N. 1994, LDV-System with frequency shift using two modes of a Nd:YAG micro crystal laser in Proceedings of the 7th International Symposium on Applications of Laser Techniques to Fluid Mechanics, Lisbon, vol. I, pp. 14.4.1–14.4.4.
- Müller, H., Czarske, J., Kramer, R., Többen, H., Arndt, V., Wang, H. and Dopheide, D. 1994, Heterodyning and quadrature signal generation: advantageous techniques for applying new frequency shift mechanisms in the Laser Doppler velocimetry in Proceedings of the 7th International Symposium on Applications of Laser Techniques to Fluid Mechanics, Lisbon, vol. II, pp. 23.3.1–23.3.8.
- Schröder, J. 1987, Electron. Lett. 23, p. 114.
- Seber, G. 1977, Linear Regression Analysis, p. 193, Wiley, New York.
- Skolnik, M. 1980, Introduction to radar systems, chap. 3, McGraw-Hill, New York.
- Tropea, C. 1995, Laser Doppler anemometry: recent developments and future challenges, Measurement, Science & Technology, vol. 6, pp. 605–619.

FIBRE OPTICAL MULTICOMPONENT LDA-SYSTEM USING THE OPTICAL FREQUENCY DIFFERENCE OF POWERFUL DBR LASER DIODES

H. Müller, H. Wang, D. Dopheide

Physikalisch-Technische Bundesanstalt (PTB)
Laboratory for Fluid Flow Measuring Techniques
Bundesallee 100, D-38116 Braunschweig

ABSTRACT

A fibre optical directional two component LDA utilizing the optical frequency differences of three fibre coupled 100 mW DBR laser diodes is presented. The resulting frequency shifts are used for the channel separation as well as for the directional discrimination. Additionally the use of one laser source for each LDA beam allows to multiply the laser power in the measuring volume.

First experimental results of two dimensional directional velocity measurements with the realized adjustment insensitive powerful LDA set-up are presented.

1. INTRODUCTION

The generation of a frequency shift by utilizing the optical frequency difference of two stabilized monomode laser diodes allows in principle the realization of simple and compact directional LDA set-ups (Müller and Dopheide (1993), Müller et al. (1994)), when the resulting beat signal of the laser diodes is used as reference signal which is correlated with the detected carrier frequency LDA measuring signal. Thus the resulting frequency shift is exclusively used as an auxiliary carrier frequency with drastically reduced requirements on stability and bandwidth (Müller et al. (1994)).

In any way laser diodes with almost equal emission frequencies are required. Up to now it was necessary to select appropriate monomode laser diodes by measuring the spectral characteristics of numerous laser diodes depending on the current and the temperature. Recently available powerful DBR laser diodes have output powers in the 100 mW range and additionally a wide wavelength tuning range so that the selection problem of appropriate laser diodes vanishes.

Using the optical frequency differences of three DBR laser diodes to generate two shift frequencies which are exclusively used as auxiliary carrier frequencies for the channel separation as well as for generation of two quadrature signal pairs in the baseband containing the directional velocity information one gets a powerful two component LDA set-up.

The directional two component LDA-system has been realized by employing fibre optics. By the use of three fibre coupled DBR lasers, fibre coupled photodiodes, fibre couplers for the generation of the reference signals by optical heterodyning and a back

scatter optic for the detection of the LDA signal, it was possible to realize a compact and adjustment insensitive LDA-system.

2. EXPERIMENTAL SET-UP

The concept is based upon the application of three appropriate monomode laser diodes with almost equal emission frequencies and overlapping tuning ranges without mode hopping. Therefore DBR (distributed Bragg reflector) laser diodes have been used, one for each LDA beam. In contrast to conventional laser diodes having a Fabry Perot resonator structure (see figure 1a), these DBR laser diodes employ a phase grating structure (Bragg grating) in the laser resonator (see figure 1b) which guarantees a dynamic single mode operation (Amann (1991)) and allows to adjust the emission wavelength without mode hopping by varying the current or temperature of the laser diode.

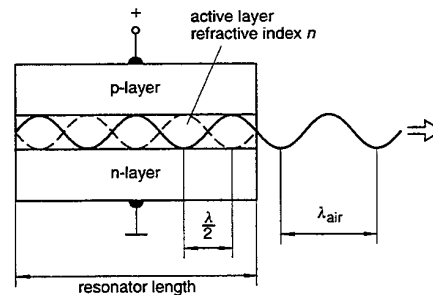


Fig. 1a: Conventional monomode laser diode having a Fabry Perot resonator structure.

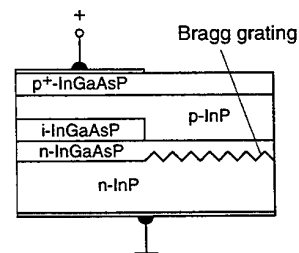


Fig. 1b: Resonator structure of a DBR laser diode.

A typical wavelength tuning characteristic depending on the temperature for different diode currents is shown in figure 2 for both laser diode resonator structures shown in figure 1.

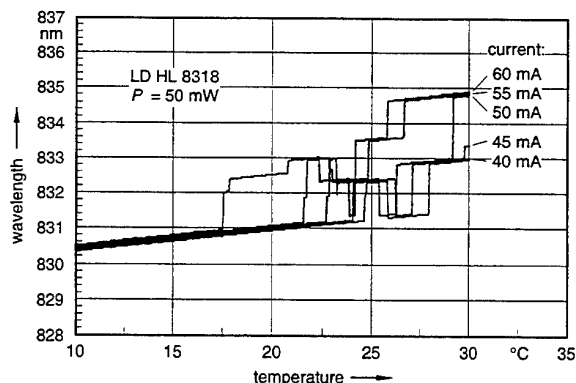


Fig. 2a: Wavelength characteristic of a conventional monomode laser diode with a Fabry Perot resonator structure showing a critical wavelength tuning behaviour caused by mode hopping effects.

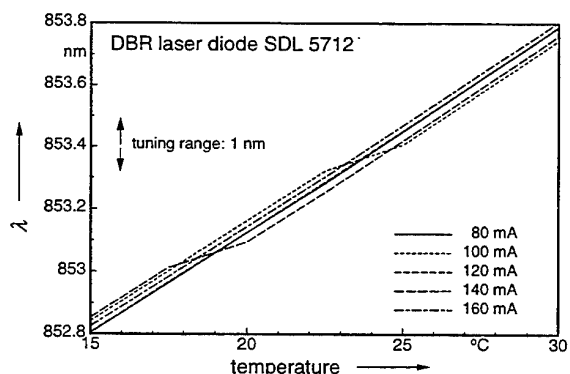


Fig. 2b: Wavelength characteristic of a DBR laser diode for several diode currents depending on the temperature. The wavelength characteristic shows wide tuning ranges without any mode hopping.

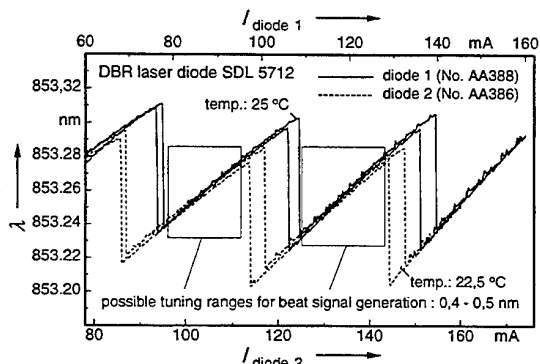


Fig. 3: Wavelength characteristic of two arbitrarily chosen DBR laser diodes, almost equal emission frequencies are marked as possible tuning ranges for the generation of beat signals.

Figure 3 shows useable tuning ranges for the generation of a beat signal with an arbitrarily chosen DBR laser diode pair of the SDL 5712 type (wavelength 852 nm, optical output power 100 mW). Without having to perform any laser diode selection one easily can get a beat signal in the hundred MHz range which can be used as an auxiliary carrier frequency for the quadrature signal generation.

To realize a two component directional LDA system using the optical frequency differences of three LDA beams as carrier frequencies for the channel separation and the quadrature signal generation, fiber coupled optical devices can advantageously be applied (Wang et al. (1994)). To avoid external resonator effects by reflections at fiber ends or connectors, optical isolators should be inserted between the DBR laser diode and the fiber coupling device. Figure 4 shows the frequency spectra of the beat signal of two DBR- laser diodes whose output beams were superimposed by a fiber coupler a) without and b) with the use of an optical isolator. Thus, optical isolators should be integrated to ensure a stable operation of the system.

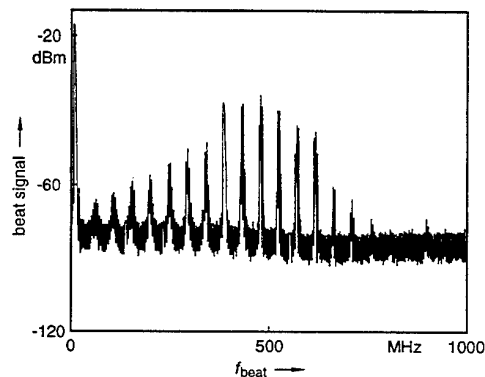


Fig. 4a: Beat signal generation of two DBR laser diodes using a fiber coupler **without optical isolator** between laser diode and fiber coupling device. Reflections at the fiber facets cause external resonator effects resulting in multiple longitudinal modes given by the optical path lengths in the fiber.

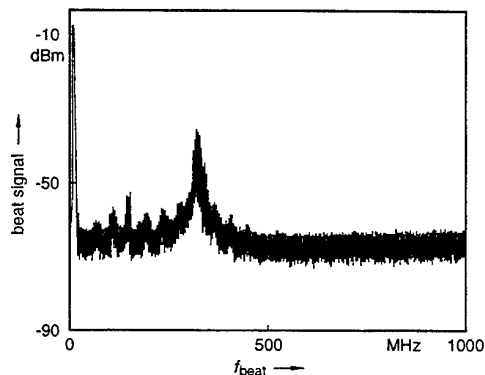


Fig. 4b: Beat signal generation of two DBR laser diodes using a fiber coupler **with optical isolator** between laser diode and fiber coupling device. By eliminating reflections into the DBR laser diode one gets a stable beat frequency operation.

Figure 5a shows the experimental set-up of the two component frequency shift LDA system based on the application of three fibre coupled DBR laser diodes and the utilization of their optical frequency differences. The optical frequency differences between the LDA beams result in a carrier frequency measuring signal containing one carrier frequency for each velocity component to be measured. In order to use the carrier frequencies exclusively for the separation of the different components as well as for the quadrature signal generation in the baseband containing the directional information, the LDA measuring signal has to be correlated with one carrier frequency reference signal for each velocity component (see reference 1 and reference 2 in figure 6).

The reference signals were easily obtained by optical heterodyning of the LDA beams employing fibre couplers and pigtailed PIN photo diodes (see figure 5a) and the correlation was performed by the mixer/correlator unit shown in figure 6.

As the resulting carrier frequencies are completely eliminated by the correlator unit when separating the components and generating quadrature signal pairs in the base band containing the directional information in the phase relationship of the quadrature signal pair, arbitrary frequency shifts higher than the occurring Doppler shifts can be used for a channel separation without having any influences on the evaluation of the measuring information.

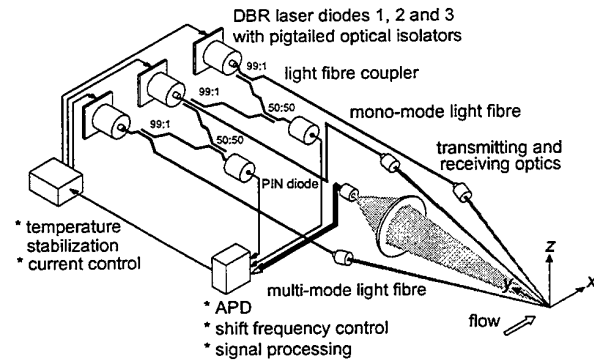


Fig. 5a: Block diagram of a directional two component LDA system based on fibre optics utilizing the optical frequency difference of DBR-monomode laser sources as frequency shift.

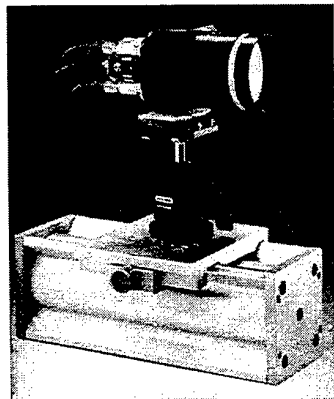


Fig. 5b: Fiber coupled transmitting and receiving optics.

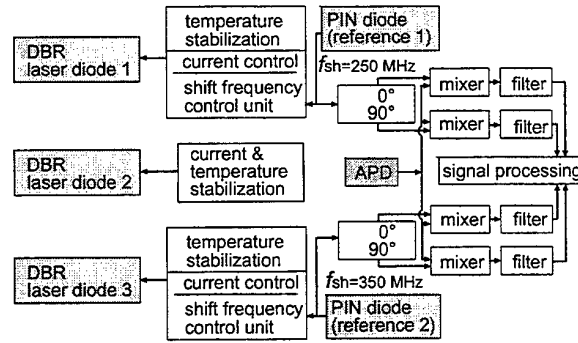


Fig. 6: Block diagram of the laser diode driver and the correlator unit.

3. EXPERIMENTAL RESULTS

Figure 7 represents typical burst signal pairs from the measurement of two orthogonal velocity components in a free jet.

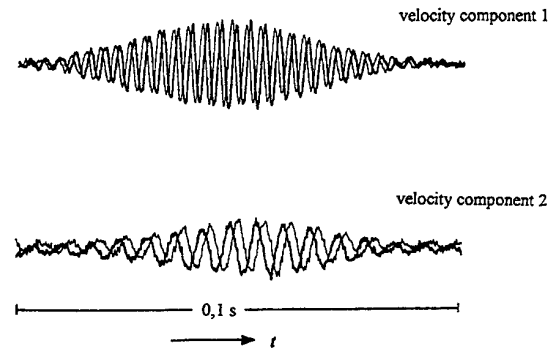


Fig. 7: Typical quadrature signal bursts of the two orthogonal velocity components at the output of the mixer unit in figure 6 measured simultaneously in a free jet.

Figure 8 shows the quadrature signals of each velocity component resulting from particles with different flow orientations in a two dimensional flow. From a) to c) the velocity direction was changed about 90 degrees. As the phase relationship between the signals in the quadrature signal pairs (+90° or -90°) corresponds to the sign of the velocity component to be measured, the sign of the first velocity component still remains whereas the sign changes for the second velocity component when the flow direction is changed by about 90 degrees.

It has to be pointed out that having quadrature signals in the baseband also quadrature demodulation techniques based upon the evaluation of the phase angle time function can be applied advantageously (Czarske et al. (1993), Czarske et al. (1994)).

Especially if at least two velocity components have to be determined simultaneously, the evaluation of the phase angle time function additionally allows to determine velocities for low numbers or fractions of LDA signal periods resulting from particles passing nearly parallel through the fringe systems in the measuring volume (Müller et al. (1995)).

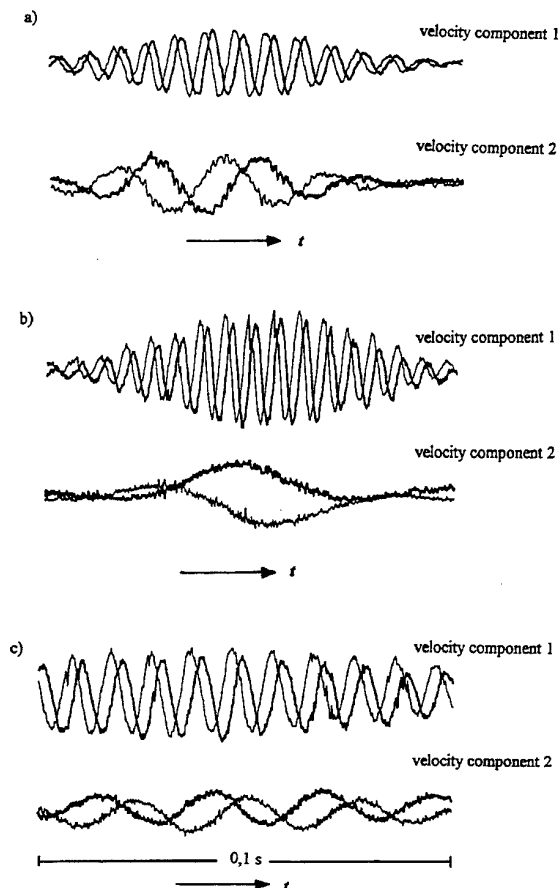


Fig. 8: Quadrature signal pairs of the two measured velocity components for different flow directions

4. CONCLUSIONS

The advantages of a novel LDA concept using separate monomode laser diodes for each LDA beam and quadrature demodulation techniques for the burst signal evaluation have been presented. Some typical experimental results show the application of the LDA system in a two component flow.

The advantages of described LDA system consist in

- the increase of the laser power in the measuring volume by the use of one laser source for each LDA beam,
- the utilization of the beat signal of the laser diodes which is exclusively used as auxiliary carrier frequency for the quadrature signal generation,
- the possible application of quadrature demodulation techniques in the base band concerning:
 - * directional discrimination
 - * the measurement of very small velocities
 - * the drastically reduced requirements on number of signal periods which has to be evaluated for a precise velocity determination.

Additional advantages are:

- the enlarged velocity measuring range starting from quasistatic up to high speed flows,
- the simple extension to multicomponent systems by applying fibre optics separating the velocity components by carrier frequency techniques,
- the utilization of fluctuating frequency shifts without deteriorating the measuring accuracy.

5. REFERENCES

- Amann, M. Ch. 1991, Wavelength tuneable single mode laser diodes, *Advances in Solid State Physics*, vol 31, pp. 201–218
- Czarske, J., Hock, F. and Müller, H. 1993, Quadrature demodulation — A new LDV - Burstsignal Frequency Estimator, Proc. 5th Int. Conf. Laser Anemometry — Advances and Applications, Koningshof, Veldhoven, *SPIE VOL. 2052*, pp. 79–86
- Czarske, J., Hock, F. and Müller, H. 1994, Minimierung der Meßunsicherheit von Laser-Doppler-Anemometern, *tm — Technisches Messen*, vol. 61, no. 4, pp. 168–182
- Müller, H. and Dopheide, D. 1993, Direction sensitive Doppler velocimeter using the optical frequency shift of two stabilized laser diodes, Proc. 5th Int. Conf. Laser Anemometry — Advances and Applications, Koningshof, Veldhoven, *SPIE VOL. 2052*, pp. 323–330
- Müller, H.; Többen, H.; Arndt, V.; Strunk, V.; Wang, H.; Kramer, R.; Dopheide, D. 1994, New frequency shift techniques in laser anemometry using tunable semiconductor lasers and solid state lasers. In: *Modern Techniques and Measurements in Fluid Flows: The Proceedings of The Second International Conference on Fluid Dynamic Measurement and Its Applications* (edited by Shen Xiong; Sun Xijiu, International Academic Publishers Beijing, 1994), pp. 3–19
- Müller, H.; Czarske, J.; Kramer, R.; Többen, H.; Arndt, V.; Wang, H.; Dopheide, D. 1994, Heterodyning and quadrature signal generation: advantageous techniques for applying new frequency shift mechanisms in the laser doppler velocimetry, *Proc. 7th Int. Symposium on Application of Laser Techniques to Fluid Mechanics*, Lisbon, 1994, Vol. I, pp. 23.3.1–23.3.8
- Müller, H., Többen, H., Strunk, V., Arndt, V., Dopheide, D. 1995, Quadrature demodulation in novel frequency shift LDV systems as an alternative to fringe biasing. In: *Laser Anemometry — 1995* — presented at the 1995 ASME/JSME fluid engineering and laser anemometry conference and exhibition, Hilton Head, South Carolina, *FED-Vol. 229*, pp. 455–458
- Wang, H.; Müller, H.; Arndt, V.; Strunk, V.; Dopheide, D. 1994, Experimental realization of a direction sensitive two-dimensional LDA using frequency-shifted diode lasers. In: *Modern Techniques and Measurements in Fluid Flows: The Proceedings of The Second International Conference on Fluid Dynamic Measurement and Its Applications* (edited by Shen Xiong; Sun Xijiu, International Academic Publishers Beijing, 1994), pp. 126–129

Integrated Laser Doppler Velocimeter made by Ion-exchange in Glass Substrate

P. L.-Auger¹, A. Cartellier, P. Benech¹ and I. Schanen Duport¹

LEGI, UJF-CNRS-INPG, BP 53 X, 38041 GRENOBLE CEDEX, FRANCE

¹ LEMO, UMR 5530 INPG-UJF-CNRS, 23 Avenue des Martyrs, BP 257, 38016 GRENOBLE CEDEX, FRANCE

ABSTRACT

A fully integrated laser Doppler velocimeter made by ion-exchange in a glass substrate is presented. Thanks to the integration of emission and reception systems, no optical adjustments are required. Beside, when flush mounted on a wall, this LDV does not collect unwanted reflected light : it is thus well suited for velocity measurements in boundary layers. In this paper, the fabrication technique is thoroughly described, and some qualifications are commented. Beside, in the prospect of wall shear stress measurements, it is shown that, by optimizing the waveguide structure, highly localized velocity measurements are accessible.

1. INTRODUCTION

Measurements of velocity gradients in the viscous sublayer is not an easy task. Among the non intrusive possible techniques, laser Doppler anemometry is probably the best one.^[1-3] Such apparatus made in classical volume optic are found in research laboratories and industries despite their elevated cost. For such systems, both the emission and the reception system are outside the fluid flow and requires the presence of transparent walls. Their spatial resolution depends mainly on the size of the measuring volume formed by the intersection of the two lasers beams. The smallest one are comprise between $30 \times 20 \times 20 \mu\text{m}^3$ and $200 \times 200 \times 300 \mu\text{m}^3$ ^[4-7] and requires rather complex lenses system which are relatively big. The shortest distance between the measuring volume and the channel wall doesn't go under 100 to 200 μm .^[8-10] The reason for this is that diffused light is reflected from the wall and degrades the optical signals received. If

the measuring volume touches the wall, then unwanted reflection of the volume itself will also cause a degradation of the signals.^[11-12]

Partially integrated anemometer were also developed.^[13] In that case, the emission system was introduced through the channel wall but the reception system was still exterior to the fluid flow. Direct velocity gradient were measured with such a partially integrated captor.^[13] The fringe spacing varied linearly with the distance. However, rather long optical adjustments were required and the uncertainty was quite large ($\pm 50\%$).

In the present paper, we propose a first prototype of a fully integrated anemometer (emission + reception) able to be introduced inside a channel wall. Reception is done on the same side as the emission. For this anemometer, no adjustments of any kind by an operator are required. The final aim of the project is to produce an anemometer with a very high spatial and temporal resolution. The measuring volume will be located inside the viscous sublayer ($y^+ \leq 6$). So indirect measurements of the velocity gradient and the skin friction by the same way could be done.

The fabrication of the anemometer is first presented. Then, a description of the anemometer is given. Finally, measurements with an optical fiber as the reception element of the optical signals are presented and discussed.

2. FABRICATION

The main part of the anemometer is the system producing the fringes. It is realized by integrated optic techniques on a glass substrate. The choice of that substrate was governed by the fact that

glass is well suited to realize passive components.^[14] It is indeed a cheap material with good optical properties. Also, the technique of ion-exchange - the most widely used technique to produce waveguides on glass - is well controlled.^[14-16]

To realize the actual anemometer prototype, Mentzel soda-lime glass is utilized. It is first clean in a tensio-actif industrial soap solution (Decon soap) that takes out organic as well as inorganic contaminants. Then, a layer of approximately 150 nm of aluminum is evaporated on it. Afterwards, standard photolithographic process employed in the fabrication of integrated circuits is used. Positive photoresist is spun over the aluminum (0.5 μm thick). The guiding structure is reproduced from the photolithographic mask to the resist by exposition to U.V. light, see figure 1a. Exposed resist will be dissolved in a developer solution, contrarily to the unexposed one. Aluminum can then be locally chemically attacked with an acid solution. All of the remaining photoresist is removed with acetone after that. As the final result, the guiding structure is present on the aluminum layer.

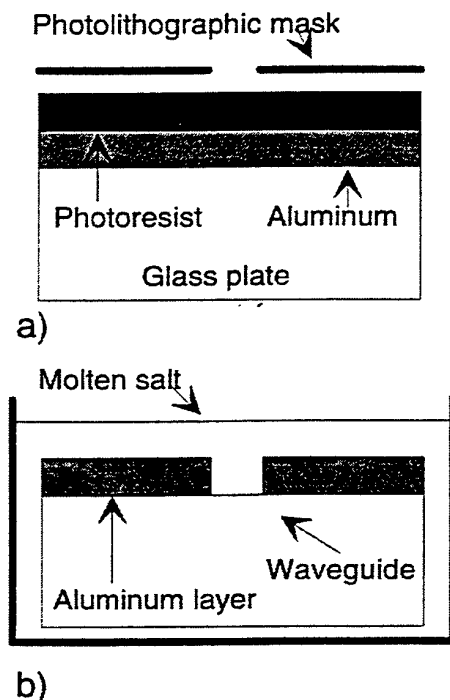


Fig. 1 The photolithographic process, a) U.V. exposition, b) Ion-exchange step.

The glass plate with his aluminum coating is immersed in a pure molten salt of potassium nitrate (KNO_3). An exchange between the potassium ions present in the salt and the sodium ions contained in the glass takes place over specific regions where there is no aluminum present, see figure 1b, the latter blocking the diffusion of ions. A specific waveguide pattern is thus created by this way. Indeed, due to the difference between the size of the sodium and potassium ions, local constraints are created in the glass that give rise to an increase of the refractive index.

For the sample fabricated, the exchange took place for 4 hours at a temperature of 350 $^{\circ}\text{C}$. In those conditions, the maximum index change is 0.11.

Finally, the aluminum layer is removed and both edges of the glass plate are mechanically polished.

An optical fiber connected to the pigtail laser diode is glued inside a small metal cylinder which is attached to the sample by soldering it to a small copper piece glued on a support plate, like can be seen in figure 2. The procedure is relatively easy to do but rather long. Nevertheless, the attachment is mechanically very solid, it resists to water and humidity and it is quite stable in time. No coupling power change could be observed for a 6 months old sample.

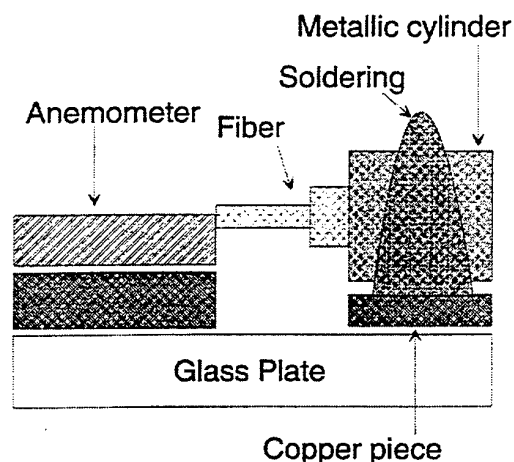


Fig. 2 Scematic representation of the connection between the optical fiber and the glass sample.

3. DESCRIPTION OF THE INTEGRATED ANEMOMETER

The integrated guiding structure used for the emission of the fringes is shown on

figure 3. The first part of it is a singlemode straight waveguide which is coupled to the optic fiber of the pigtail laser diode which wavelength is 832 nm. The guided light is then divided into two equal parts in the Y-junction. Each arm of the interferometer that follows has the same length and is terminated by a taper structure.^[17] The purpose of the latter is to excite only the fundamental mode of a multimode waveguide of 40 μm width (this width is the photolithographic mask opening). The size of a single waveguide, 2 μm , is small and the beam produced by such an optical waveguide would strongly diverge in free space, while the beam issued from the fundamental mode of a 40 μm waveguide will act like a quasi-collimated beam. The divergence of the latter is on the order of 1.5°. The output beams of the two tapers will travel in a slab waveguide, where light is confined in one dimension only, and will produce the interference pattern^[18]. Half of the latter exist inside the glass plate while the other half is outside the exterior medium. In both cases, it is easy to demonstrate that fringe spacing (Δx) is given by :

$$\Delta x = \frac{\lambda_0}{2N_{\text{eff}} \sin \gamma}, \quad (1)$$

where λ_0 is the wavelength in free space, N_{eff} is the effective index of the slab waveguide and γ is the half angle between the two beams. It is worth noting that the fringe spacing is independent of the refractive index of the exterior fluid. The position of the measuring volume (in the case where it would entirely be outside the glass plate) and its dimensions do depend however upon the fluid index. Ulrich and Martin^[19] have demonstrated that light, when guided in a slab waveguide, follows Snell law of refraction with the effective index instead of the refractive index of the bulk material.

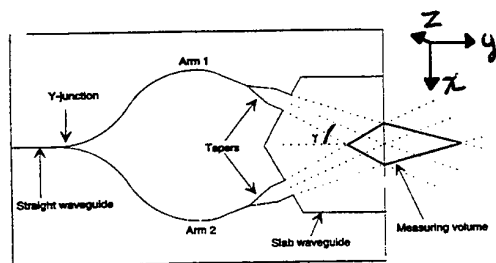


Fig. 3 Schematic representation of the integrated emission system

For the present prototype, the angle between the two beams inside the glass is 1.8 °, the fringe spacing 8.77 μm . The width of the output beam produced by the taper is 40 μm . In those conditions, the size of the measuring volume (half of the whole interference region) is approximately 60 μm x 1000 μm x 50 μm , as shown in the calculation of figure 4. The present configuration is therefore not adapted for measurements in the viscous sublayer. Nevertheless, it demonstrates the feasibility of such an anemometer.

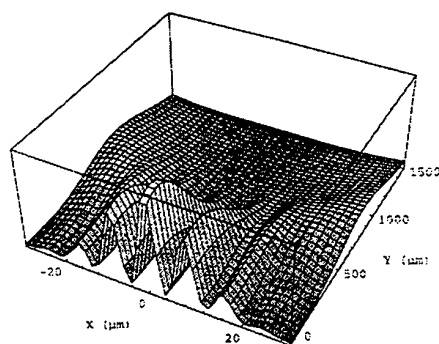
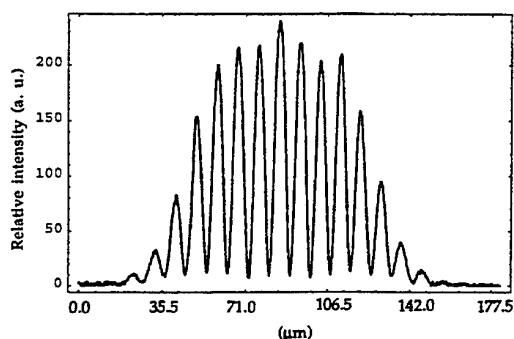


Fig. 4 Computed measuring volume

An image of the fringe pattern observed with a digital camera on the edge of the glass is given in figure 5a and the corresponding intensity profile in figure 5b. The contrast ratio being only 0.9 is explained by the fact that the middle of the fringe pattern is not exactly located on the edge of the glass. The geometry of the tapers explains the fact that the envelope (fig. 5b) of the fringes is not a Gaussian type. Other taper produces Gaussian type envelope, like shown on fig. 6, but due to the small angle available between the beams, the number of fringes is not sufficient enough for a laser Doppler anemometer. This will be corrected in future configurations.





b)

Fig. 5 a) Image of the fringe pattern on the edge of the glass, b) corresponding intensity

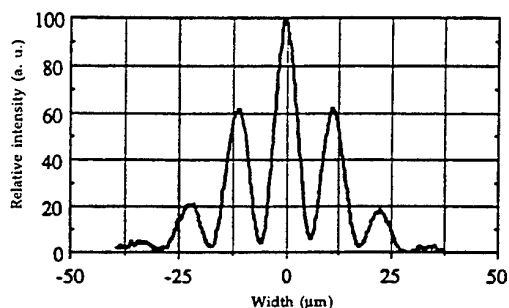


Fig. 6 Fringe pattern produced with a different taper and having a Gaussian envelope

The total optical output power of the sample for an input power of 30 mW is 0,95 mW, corresponding to 15 dB optical loss in the sample. The propagation losses are estimated to 1 dB/cm, so the major part of those losses (11 dB) comes from the connection between the optical fiber and the sample. Great care must then be taken when connecting the fiber to the sample.

Finally, an optical fiber, that can easily be glued on the glass plate, collects the light scattered by particles passing in the measuring volume and transmits it to a photomultiplier. The scheme of the complete integrated anemometer is given in figure 7. Because the laser diode and the photomultiplier can both be several meters apart from the head of the anemometer, measurements can be done in places of difficult access.

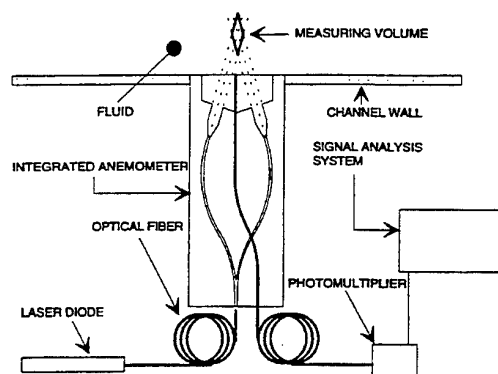


Fig. 7 Scheme of the complete integrated anemometer

4. FIRST EXPERIMENTAL VALIDATIONS

To test the anemometer, a metallic cylinder of 500 μm diameter is used as the diffusing particle. It is placed on the side of a rotating disk of 4.3 cm diameter, making two complete revolutions per minute. The speed of the diffusing element is thus 0,90 cm/s. The extremity of the emitting system was placed at a distance of approximately 0.5 mm away from the cylinder.

First, a plastic fiber was used to collect the retrodiffused light. It was allowed to move freely in regard to the glass plate. Study of the Doppler signal as a function of the position of the fiber was done that way. The longitudinal distance between the fiber extremity and the glass edge was varied. For each position, the ratio between the amplitude of the high frequency Doppler signal and the amplitude of the low frequency Doppler signal was measured. An example of the signals obtained on an oscilloscope is given in Fig 8. A low-pass filter was used to lower the noise produced by the amplification circuit following the photomultiplier. The measured Doppler frequencies (1.02 kHz) correspond to a velocity of 0,894 cm/s, which is almost the same value as the one calculated above.

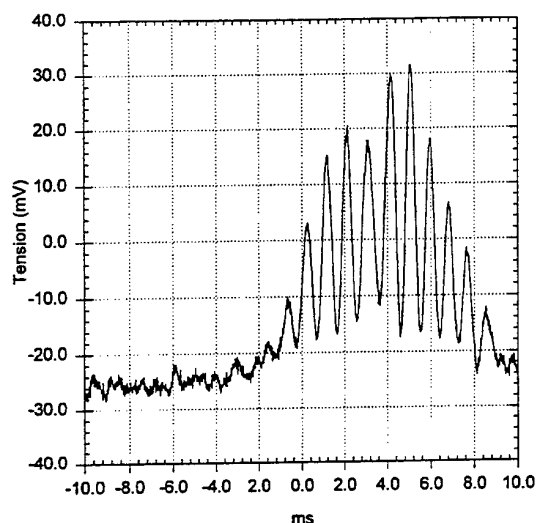


Fig. 8 Example of Doppler bursts obtained with the plastic fiber as the reception element. Longitudinal distance is 24 mm. A low-pass filter (2.5 kHz) was used.

Figure 9 shows the results of that study. It can be seen from the graph that a distance of 24 mm gives the maximum ratio, 0.8. For greater distances, it becomes difficult to discern the signal from the noise. Also, one has to keep in mind that the center of the measuring volume is located near the side of the glass plate, so a ratio of 1 is impossible to get in those conditions. The conclusion of that first study is that plastic fiber is inadequate because its extremity cannot be placed next to the edge of the glass. This is essential if the anemometer is to be placed inside the wall of a channel.

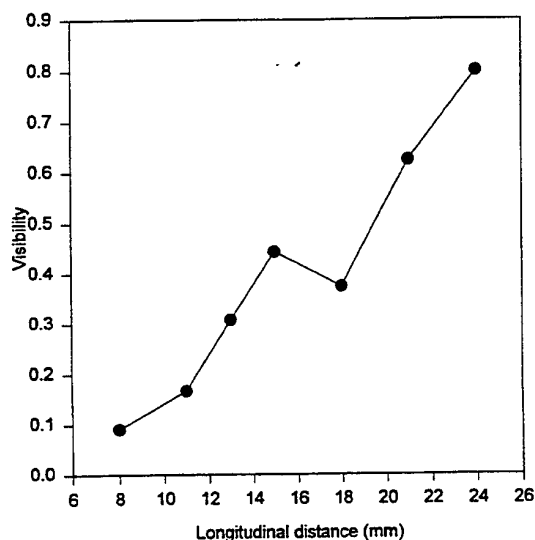


Fig. 9 Visibility as a function of the longitudinal distance between the fiber and the glass edge.

The same study was done but with a multimode silica fiber (100/140 μm) this time. In that case, Doppler frequency could be observed for a distance varying from 0 to at least 4 mm between the fiber extremity and the glass side. Example of filtered and non filtered signals are given in figure 10. The lateral position of the fiber is however critical for a nul longitudinal distance. It has to be placed within $\pm 100 \mu\text{m}$ from the symmetry axis of the integrated guiding structure. Signal merging from a measuring volume located between 0 and 500 μm of the glass side can be collected with that multimode fiber glued on the glass plate.

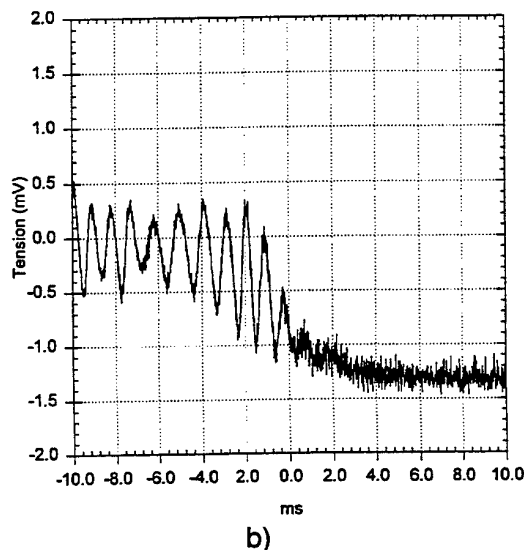
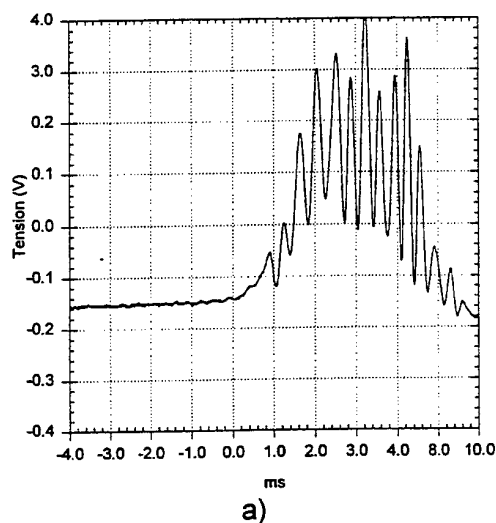


Fig. 10 Example of signals obtained with the silica multimode fiber, a) low-pass filter (2.5 kHz) used, b) no electric filter used.

5. NEW GENERATION OF PROTOTYPE

The measuring volume of our first prototype is however too large for accurate velocity measurements in the viscous sublayer. To improve the spatial resolution, a new design of the waveguide structure has been imagined. Optical simulations show that it should provide a probe volume of $12\ \mu\text{m} \times 33\ \mu\text{m} \times 40\ \mu\text{m}$, located at a distance ranging between 0 up to $500\ \mu\text{m}$ from the glass side. The probe volume extend along the direction normal to the wall is $33\ \mu\text{m}$. This design is well adapted to wall shear stress measurements. Some of these new prototypes have been manufactured and are currently under test in terms of optical performances. In the near future, their performance with respect to wall shear stress measurements will be checked in various well controlled flow conditions, both in air and water flows.

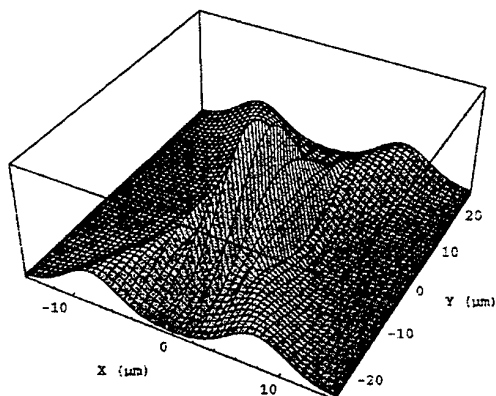


Fig. 11 Computed measuring volume of the new prototype.

6. CONCLUSION

A first prototype of an integrated laser Doppler velocimeter has been presented. Its emission system has been made by integrated optics techniques on a glass substrate. Using a reception consisting in a multimode silica fiber, Doppler bursts from retrodiffused light and with a good visibility have been recorded. The feasibility of this technique has thus

been demonstrated, indicating that the combination of an integrated optical interferometer and a multimode guide is an easy and efficient way to produce cheap velocimeters free of optical adjustments. Future works will be devoted to the qualification of wall shear stress measurements using a new generation of prototypes allowing a much better spatial resolution.

ACKNOWLEDGEMENTS

The first author would like to thank the FCAR organisation of the Quebec government for a doctoral research grant. Authors are grateful to PIR Ultimatech for financial support under grant 94 N-II.4.1.

6. REFERENCES

- [1] Hanratty TH. J., Campbell J.A., 1983, "Chapter 11 : Measurement of wall shear stress", in Fluid Mechanics Measurements, Golstein R.J. Ed., Hémisphère Publishing Corp., distributed by Springer-Verlag, pp.559-611.
- [2] SaeTRAN L.R., 1987, "Comparison of five methods for determination of the wall shear stress, AIAA J., 25, 11, 1524-1527.
- [3] Gasser D., Thomann H., Dengel P., 1993, "Comparison of four methods to measure wall shear stress in a turbulent boundary layer with separation", Experiments in Fluids, 15, pp.27-32.
- [4] Martin S.R., Bates C.J., 1992, "Small-probe-volume laser Doppler anemometry measurement of turbulent flow near the wall of a rib-roughened channel", Flow Meas. Instrum., Vol. 3, No. 2, 81-88.
- [5] Leprince F., Riethmuller M.L., 1986, "LDV Measurements in a viscous sublayer : determination of skin friction", Laser Techniques and Applications in Fluids Mechanics - Proceedings of the 3th International Symposium, Lisbon, Portugal, 1-6.
- [6] Aizu Y., Ushizaka T., Asakura T., 1985, "Measurement of the Velocity Gradient Using a Laser Doppler Phenomenon", Appl. Phys. B 36, 155-161.
- [7] Keveloh C., Staude W., 1983, "Determination of velocity gradients with scattered light cross-correlation

- measurements", *Appl. Opt.*, Vol. 22, No. 2, 333-338.
- [8] Wernet M.P., Edwards R.V., 1986, "Implementation of a new time of flight laser anemometer", *Appl. Opt.*, Vol. 25, No 5, 644-648.
- [9] Dybbs A., Edwards R.V., 1987, "Refractive index matching for difficult situations", 2nd Int. Conf. Laser Anemometry - Advances and Applications Glasgow, UK, BHRA, Cranfield, 1-22.
- [10] Durst F., Keck T., Kleine R., 1985, "Turbulence quantities and Reynolds stress in pipe flow of polymer solutions", 1st Int. Conf. Laser Anemometry - Advances and Applications Manchester, UK, BHRA, Cranfield, 32-52.
- [11] Mishina H., Vlachos N.S., Whitelaw J.H., 1979, "Effect of wall scattering on SNR in laser Doppler anemometry", *Applied Optics*, 18, 14, pp.2480-2485
- [12] Cline C., Deutsh S., 1993, "On elevated RMS levels in wall-bounded turbulent flows when measured by laser Doppler velocimetry", *Experiments in Fluids*, 15, 130-132.
- [13] Petrik S., Naqwi A.A., Durst F., 1992, "Fiber optic dual-cylindrical wave sensor for measurement of flow velocity gradients", 2nd French-German workshop on Optical Measurement Techniques - Fibers Optics and Instrumentation, 13-14 Octobre, St. Etienne, France.
- [14] Johansson, J. Djanta, G., and Coutaz, J.-L., 1992, "Optical waveguide fabricated by ion exchange in high-index commercial glasses", *Applied Optics*, Vol. 31, No. 15, pp.2796-2799.
- [15] Ramaswamy, R.V. and Srivastava, R., 1988, "Ion-Exchanged Glass Waveguides : A Review", *Journal of Lightwave technology*, Vol. 6, No. 6, pp.984-1001
- [16] Findakly, T., 1985, "Glass waveguides by ion exchange : a review", *Optical engineering*, Vol. 24, No. 2, pp. 244-250.
- [17] Duport I., Benech P., Kahlil D., Rimet R., 1992, "Study of linear tapered waveguides made by ion exchange on glass", *J. of Physics, D :Applied Physics*, 25, pp. 913-918.
- [18] Schanen Duport, I., Benech, P. Rimet, R., 1994, "New integrated-optics interferometer in planar technology", *Applied Optics*, Vol. 33, No. 35, pp. 5954-5958.
- [19] Ulrich, R. and Martin, R.J., 1971, "Geometrical optics in thin film light guides", *Applied Optics*, Vol. 10, pp. 2077-2085.

LASER RESONANCE ANEMOMETER OPTICS

Noboru Kurihara and Masaki Takamoto

National Research Laboratory of Metrology (NRLM)
Fluid Measurement Section
Mechanical Metrology Department
1-1-4, Umezono Tsukuba 305 Japan
AIST, MITI, JAPAN

ABSTRACT

New type laser anemometer optics to be built in an industrial flow meter is developed. A principle of laser resonance anemometer (LRA) optics and some results of primary tests are reported. Although the optics has a LDA like measuring control volume, LRA is not an application of interference but sharp focusing of laser light. Mode number, fringe number on LDA, was not less than 7 under the dynamic range of tested LD light source.

LRA has quite a simple and robust structure to make laser anemometer to be economy and miniature enough to build in industrial equipment. With the L2F like optics, a signal from photo detector is completely processed by a conventional LDA processor.

1. INTRODUCTION

There are some needs for trading the residue heat transferred with exhaust gas or dirty hot water as a recycles. In managing such kind of fluids, we have to measure their flow rate precisely to know its enthalpy transfer rate. Most of the flow meters have not fill the needs enough because they have been made for clean and isothermal source fluids. Optical technique such as laser Doppler anemometer (LDA) is suitable for this application, because they have little dependence for thermo-physical properties of medium. Since equipment has to be simple, robust and low cost to supply them for industrial workshop, no LDA is applied for industrial equipment.

There are many reports on miniaturized LDA. Tropea (1995) have reviewed LDA using laser diode (LD) as a light source. Several works have been done to achieve shift frequency for determination of flow direction. Kramer et al. (1994) and Müller et al. (1995) reported interference of individual LD light sources. Többen et al. (1994) applied Brillouin scattering. Dopheide et al. (1990) and Wang et al. (1994) developed multicomponent system with pulsated single LD light. It seems that state-of-the-art of an experimental measurement with miniaturized LDA has been established.

Durst et al. (1990) has reported a significant problem in accuracy caused by miss collimating on semiconductor LDA. This ambiguity does not occur if we apply a laser-two focus-velocimeter (L2F) established by Schodl (1980) or laser four-focus velocimeter developed by Ikeda et al. (1991), because these are using time-of-flight on particles passing through a series of sharp focused spots. Azzazy et al. (1995) developed diode array velocimeter (DAV) similar to L2F as a robust optics. DAV measures a particle velocity not in time-of-flight but in frequency from only four pulses. The number might not be enough to determine the signal frequency precisely. Schmidt et al. (1992) reported novel LDA sensor with grating to overcome an ambiguity caused by mode hopping. These two reports have shown us new direction of development in near future.

The presented optics has a simple configuration because its measuring principle is based upon an emitting mechanism of LD. Temporal variation of the light scattered from a dust particle passing through its measuring control volume is a burst signal quite similar to that of LDA. The light source of the optics is one of the conventional LD for compact disk players and magneto optical disk drives. In principle, its calibration factor is stable enough to the alignment changing, and homogeneous in the measuring control volume. As above described reason and that the presented optics does not employ any stabilization or isolation for LD, it is expected to be low cost and reliable.

The purpose of this study is the basic examination to check the availability of new type optics. In this report, we describe novel principle and discuss some results of the basic examinations of the presented optics.

2. METHOD

2.1 A Resonance of Laser Cavity

The principle of presented optics is based upon a longitudinal multimode oscillation in laser cavity.

Concerning a laser without stabilization element such as etalon, it is normally observed some oscillating modes

inside its gain band of cavity medium. The existence of longitudinal multimode is useless for interferometry because it wastes the visibility and shortens the coherent length of lasers.

The oscillation probability density of the laser cavity is distributed on wavelength space in an amplification gain width of the medium. The resonance of the cavity is given by the length, medium index and wave length. This is quite similar to a sonic resonance inside a closed long pipe. In this reason, the following formula is available for each oscillation mode:

$$q \frac{\lambda}{2n} = L$$

where

- λ : wave length of the observed modes
- n : index of cavity medium
- q : order of observed mode
- L : cavity length

It is easy to understand the requirement on optical spectrum analyzer with Fabry-Perot interferometer to observe the longitudinal modes of gas lasers. For example, Ar-ion laser with 1m cavity has a resonance in the frequency order of only 150MHz for each neighboring modes.

A longitudinal multimode and transverse single mode LD have been produced to eliminate optical feed back from optical recording disk. We can observe the longitudinal mode by spectroscopy with grating, because of its wide gain band more than 1nm and tiny cavity length less than 1mm. Figure 1 shows a typical saw tooth spectrum of longitudinal multimode LD observed by a spectroscopy. Even in such cavity length, the number of stable waves in the LD is more than a few thousand. It means that there is a series of spots in nearly the same distances on the outlet slit of the spectroscopy when the observed LD is in multimode.

In this report, the authors apply this optical phenomenon as a measuring control volume of an LD anemometer optics to be very simple structure. We name the optics laser resonance anemometer (LRA), because it is a unique application of the saw tooth spectrum of laser resonance.

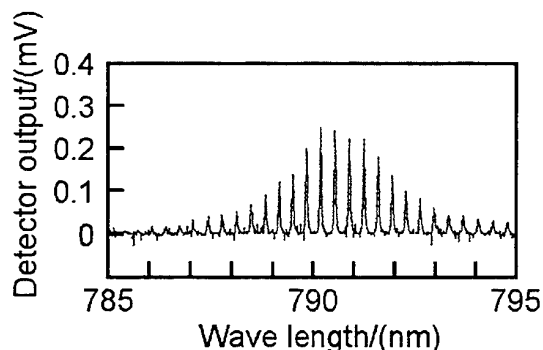


Figure 1: Typical saw tooth spectrum of longitudinal multimode LD detected by a spectroscopy.

2.2 Principle of Measurement

A series of spots of each oscillating mode would be formed by a focusing lens and any kinds of optical element for spectroscopy, such as prisms or gratings. The angular changing of diffraction with wavelength is about 10 times larger than that of refraction at normal operation. Thus we chose grating to realize LRA optics.

It is well known that the following equation exists for blazed gratings:

$$\sin \alpha + \sin \beta = Nm\lambda$$

where

- N : number of ruling in the unit length
- m : diffraction order
- α : incident angle
- β : diffraction angle

To get a maximum efficiency, the grating alignment was optimized with the wavelength of LD. It is possible to eliminate higher or lower order of diffraction with the optimization of N value and alignment of α . Under the following limitation, we can achieve the region with only 0 and +1 order diffraction.

$$\frac{2}{3} < N\lambda < 1$$

We can estimate an angular difference of neighboring beams with angular dispersion, a differential of angle β :

$$\Delta\beta = \frac{d\beta}{d\lambda} \Delta\lambda = \frac{Nm\Delta\lambda}{\sqrt{1 - (Nm\lambda - \sin \alpha)^2}}$$

where

- $\Delta\beta$: angular difference of neighboring beams
- $\Delta\lambda$: wave length difference of neighboring modes

The resolving power of grating depends on the number of ruling on the grating plane. Thus, the diameter of collimated beam on the grating plane should be larger than the Rayleigh criterion W_L :

$$\frac{\lambda}{\Delta\lambda} = mNW_L$$

In this way, a measuring control volume is generated in front of the lens system. Several spots are formed in parallel when the grating is placed on the focal plane backward of the lens. A light scattered by individual particles, such as sand in dirty water, passing through most of the spots are received with some kinds of detector. The speed of particle u is estimated by the signal frequency f and the mean distance of spots Δx determined by focal length F and the $\Delta\beta$ value:

$$u = f\Delta x = f \cdot F \tan \Delta\beta$$

The basic structure of LRA is quite similar to conventional L2F. The signal from photo detector is analyzed by any kinds of frequency processor for LDA because the number of spots is large enough to be estimated.

2.3 Realization of prototype optics

From these optimizations described above, a prototype optics is realized.

It has been reported gain guiding type TAPS laser by Mamime et al. (1983). This laser has longitudinal multimode and transverse single mode. In this reason, we used TAPS laser, SLD104AUL (SONY), as a light source of LRA. This LD is mass-produced for compact disk player in these years. A blazed holographic grating was used to separate the longitudinal multimode beam into individual modes at different angle. Figure-2 shows a schematic apparatus of LRA. The collimated laser light is diffracted by a grating and the beam is separated to several different angles with each mode. With lens system assembled by a beam expander and single lens, these beams are sharp focused into a series of spots in almost the same distances between each neighboring spot.

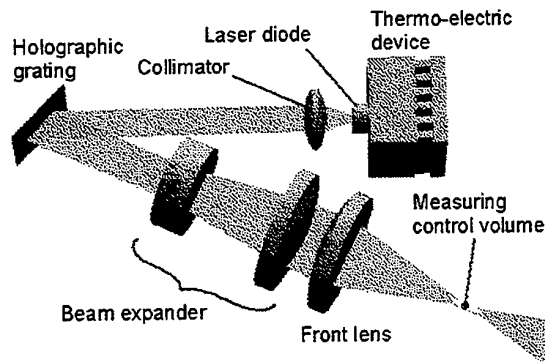


Figure 2: Schematic apparatus of LRA transmitting optics.

Figure 3 is a cross-sectional photo image of the measuring control volume. We can observe fringe like pattern rather than a series of spots. It is because astigmatism of the elliptic beams make their focused spots to be panel like shapes. The spots are formed as a set of parallel planes similar to fringe, when the long radius of the elliptic beam is parallel to diffraction plane. The intensity distribution of measuring control volume forms Gauss distribution. Light intensity distribution in the measuring control volume is quite similar to LDA. Thus all the signal processing techniques for traditional LDA are available to LRA.

LRA does not use interference but sharp focusing of laser diode. When the oscillating condition is in multimode completely, the beam intensity is quite stable to the temperature changing or anode current variation. It is because every mode shares the emitting energy with each other in the gain distribution of semiconductor medium.

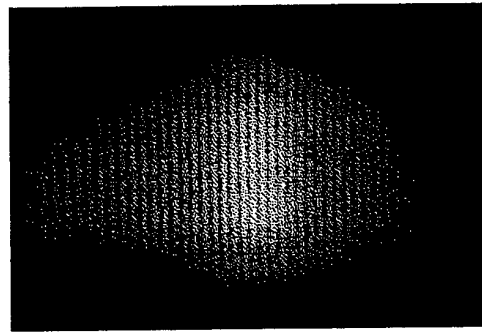


Figure 3: Cross sectional photo image of a series of vertical plane spots focused on the measuring control volume.

There is no need to put optical isolator, because multimode oscillation eliminates the instability caused by optical feed back. The changing of mean wavelength is easy to predict from operating condition. Thus LRA does not require any stabilization or isolation techniques. The disadvantage is the lack of reverse flow determination, but it is regardless if we limit the application for only a flow rate measurement inside the pipe line in plant.

3. BASIC EXAMINATION

3.1 Optical Properties of LD Light Source

An ambiguity of the burst signal from the measuring control volume depends on the number of modes. That is given not only by the gain width of semiconductor medium but by the output power of the LD. Now we define the mode number for LRA in 4 spans of standard deviation on the saw tooth spectrum distribution. With this definition, mode number has just the same meaning as the fringe number on LDA. Figure 4 shows the variations of the mode number with change of output power and device temperature. Here illustrated a property for LRA that the mode number is related only to the output power. Mode number is a decreasing function of the output power of LD while the signal to noise ratio is an increasing function.

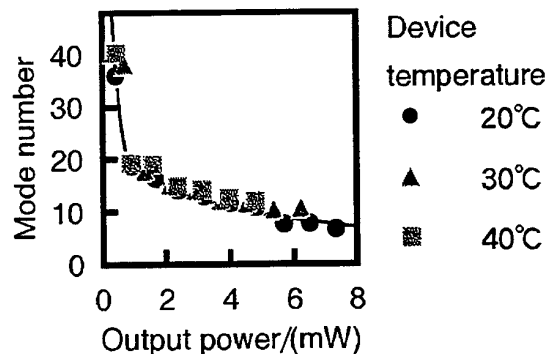


Figure 4: Mode number variation with the changing of output power and device temperature.

This means that LRA may have a peak performance with the output power and the flow to be measured. In practice, the mode number of the optics is kept by simple circuit monitoring the output power by photo diode in the LD package. This LD has 7 modes at the maximum output. To use conventional LDA processor, 3 to 4 mW is the upper limit of output power with this optics and LD.

Figure 5 shows the relationship between wave length difference of neighboring modes and mean wave length of the spectrum distribution. Although the wave length differences are nearly constant in broad band with any condition, these differences have a reducing trend less than 2% in precisely. They are negative proportional to square of the wavelength in theoretically. Referring to Figure 5, some ripples are found plotted with the uncertainty from numerical error with resolution limit of spectroscop. It was observed a functional relationship between wavelength and variation of the device conditions in the experiment. This means that we can correct the changing of calibration factor from a pre-mapped table of wave length with temperature and anode current.

In our current step, its calibration factor is not predictable enough. It is very important to determine the calibration factor with known kinetic object.

3.2 LRA Measurement

Conventional receiving optics, photo detectors, and processors for LDA have used to test the optics. We tested the behavior of the light source and coordinate an optimized optics. The calibration factor is determined with a moving wire. Primary tests have been done with dry fog of water.

Figure 6 is the schematic apparatus of the calibration test of LRA with known velocity of moving wire. Calibration factor is checked with such simple procedure. A platinum wire in the diameter of 5mm for hot wire anemometer is used for the calibrator. A burst spectrum analyzer is used to process the signal of photo-multiplier put in front of the optics. The revolution is set to be slow

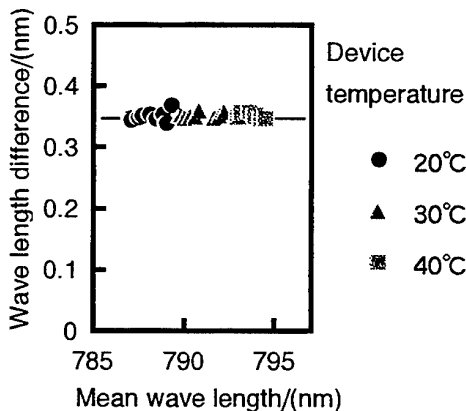


Figure 5: Relationship between wave length difference of each neighboring mode and mean wave length variation at different device temperature.

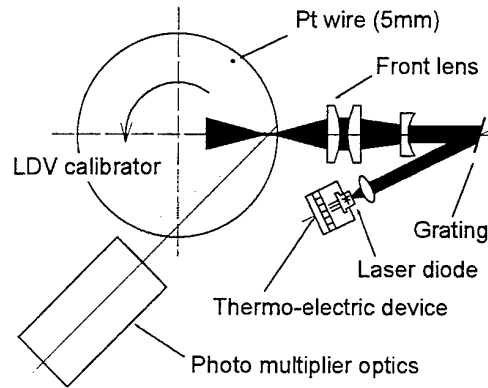


Figure 6: Schematic apparatus of the calibration test for LRA with moving wire.

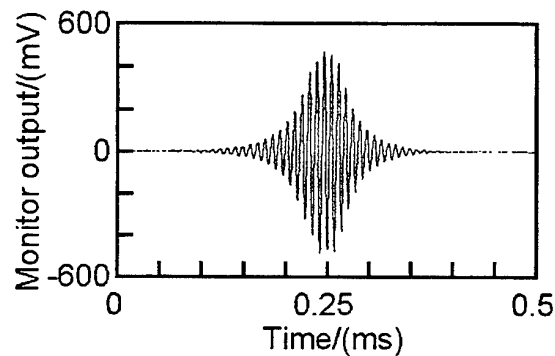


Figure 7: Complete burst signal wave form of LRA

speed less than 8π rad/s to eliminate the vibration of the wire. In this test, individual signal of the light scattered by the metal wire is observed for each rotation. Figure 7 shows the typical burst signal of LRA at the angular velocity of 4π rad/s. Temporal variation of the light scattered from the wire passing through the spots becomes quite a similar wave form to Doppler burst signal on LDA. Table-1 is a result of the calibration test. In this measurement, rms value was 0.2% for all settings. The measured frequencies are proportional to known velocities. Thus we can measure the velocity of object precisely like LDA. From this test, calibration factor is determined as 16.181m/s/MHz for focal length 50mm, diffraction angle 15.8° with incident angle of 41.5° on the grating of 1200 lines/mm and collimated diameter of 15mm in long radius.

Table 1: A result of calibration test for LRA with moving wire.

Radial position	(mm)	100.46			
Angular velocity	(*2 π rad/s)	1.000	2.000	3.000	4.000
Mean velocity	(m/s)	0.6312	1.2624	1.8936	2.5248
Mean Frequency	(MHz)	0.03921	0.07832	0.11707	0.15632
Calibration factor	(m/s/MHz)	16.181			

Figure 8 is an example of a series of burst signals logged in the test using stagnated water mist in dry fog condition. In that testing flow, signal to noise ratio was not very high because the number density of the water droplet was quite high. Even in such condition, The Doppler like burst signal is observed clearly. Burst spectrum analyzer and photomultiplier is used to acquire the burst signals. The validation ratio indicated on the processor was 70% to 80% on this experiment.

4. CONCLUSION

In this report, the principle of the LRA optics and the results of the primary tests have reported. The LRA has a LDA like measuring control volume, but the optics is not an application of interference but sharp focusing. The mode number, fringe number on LDA, was not less than 7 under the dynamic range of tested LD light source. The wave length differences of longitudinal multimode LD was nearly constant at any conditions. For precise measurement, the calibration factor is to be corrected by a reappearing wavelength. Burst signal nearly the same wave form as Doppler burst signal is detected from a moving wire or dry mist particle of water passing through the measuring control volume.

LRA has quite a simple and robust structure to make laser anemometer to be economy and miniature enough to build in industrial equipment. The optics is a kind of multifocus anemometer such as L2F, but LRA has a measuring control volume quite similar to LDA. In this reason, the collected burst signals are completely processed by all the LDA signal processor, not by the specialized processor. This means that the LRA stands upon an open design concept developing with LDA in the future.

REFERENCES

- Azzazy, M; Potts, R. L. & Ben Rosow 1995, Flow Velocity Measurements Using Laser Diode Array, Proc. 6th Int Conf. on Laser Anemometry, ASME, FED-Vol. 211, pp.129-135.
- Durst, F.; Müller, R. & Naqwi, A. A. 1990, Measurement accuracy of semiconductor LDA systems, Exp. Fluids, vol. 10, pp. 125-137.
- Dopheide, D.; Strunck, V. & Pfeifer, H. J. 1990, Miniaturized Multicomponent Laser Doppler Anemometer Using High-Frequency Pulsed Diode Lasers and New Electronic Signal Acquisition Systems, Exp. Fluids, vol. 9, pp. 309-316.
- Ikeda, Y.; Nishimura, M. & Nakajima, T. 1991, Laser Four-Focus Velocimeter, Proc. 4th Int Conf. on Laser Anemometry, ASME, pp.449-455.
- Kramer, R.; Müller, H.; Dopheide, D.; Czarske, J. & Schmitt, N. P. 1994, LDV-System with Frequency Shift Using Two Modes of a ND:YAG Micro Crystal Laser, Proc. of 7th Int. Sym. on Applications of Laser Techniques to Fluid Mechanics, Lisbon, pp. 14.4.1-14.4.4.

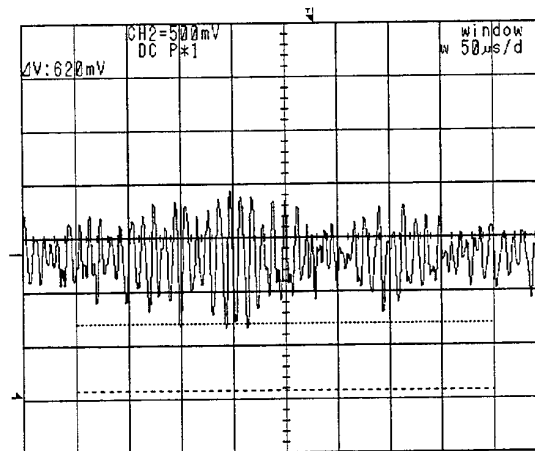


Figure 8: An example of actual burst signals of LRA logged in the stagnated dry mist.

- Mamine, T.; Oda, T. & Yoneyama, O. 1983, New Class Gain Guiding Laser with a Tapered-stripe structure, J. Appl. Phys., vol. 54, pp. 4302-4304.
- Müller, H.; Többen, H.; Strunck, V.; Arndt, V. & Dopheide, D. 1995, Quadrature Demodulation in Novel Frequency Shift LDV System as an Alternative to Fringe Biasing, Proc. 6th Int Conf. on Laser Anemometry, ASME, FED-Vol. 229, pp.455-458.
- Schmidt, J.; Völkel, R.; Stork, W.; Sheridan, T.; Schwider, J.; Streibl, N. & Durst, F. 1992, Diffractive Beam Splitter for Laser Doppler Velocimetry, Opt. Lett., vol. 17, pp. 1240-1242.
- Schodl, R. 1980, A Laser-Two-Focus (L2F) Velocimeter for Automatic Flow Vector Measurements in the Rotating Components of Turbomachines, Trans. ASME, J. Fluids Eng., vol. 102, pp. 412-419.
- Többen, H.; Müller, H. & Dopheide, D. 1994, Brillouin Frequency Shift LDA, Proc. of 7th Int. Sym. on Applications of Laser Techniques to Fluid Mechanics, Lisbon, pp. 14.2.1-14.2.4.
- Tropea, C. 1995, Laser Doppler Anemometry: Recent Developments and Future Challenges, Meas. Sci. Technol., vol. 6, pp. 605-619.
- Wang, H.; Strunck, V.; Müller, H. & Dopheide, D. 1994, New Technique for Multi-Component Flow Velocity Measurements Using a Single HF-Pulsed Diode Laser and a Single Photodetector, Exp. Fluids, pp. 36-40.

SESSION 35

Free Flows II

TWO-SCALE GRID TURBULENCE MIXING

Marco Gottero, Gaetano Iuso and Michele Onorato

Dipartimento di Ingegneria Aerospaziale, Politecnico di Torino, Italy

ABSTRACT

Turbulence analysis of a mixing region, due to the interaction of two quasi homogeneous grid flows, having different turbulence intensities and scales, is shown. Results obtained using hot wire in air and DPIV in water are presented. DPIV technique shows its potentiality to contribute to give better interpretation to the well time resolved hot wire measurements.

1. INTRODUCTION

The non-linear interaction between different scales is a typical feature of many turbulent flows of interest for industrial, aeronautical and ambient applications. Examples may be the mixing of flows in combustion chambers, the mixing of two different streams at the trailing edge of an airfoil and the interaction between a jet normal to the wall and a turbulent cross flow. Such flows can not be simply modelled, and a better understanding and description of the evolution and interaction of the turbulent structures are needed.

A research is being conducted at the *Modesto Panetti* Aeronautical Laboratory of the *Politecnico di Torino*, having as object the study of the interaction of two turbulent flows with different intensities and scales, but with the same mean velocity. This shearless mixing flow is produced by two sets of parallel bars, each having the same solidity and geometrical shape, but different dimensions. The mixing flow is therefore dominated by turbulent transport between the two adjacent nearly homogeneous turbulence, with scales determined by the sizes of the two grids.

Physically, this lateral transport can be brought about two mechanisms:

- gradient diffusion, which is associated with small eddies and with turbulence transport down the kinetic energy gradient in the mixing region, similar to the molecular diffusion;
- bulk convection, which is associated with large eddies and is related to the levels of turbulent kinetic energy present in the two streams.

The relative importance of the two mechanisms to lateral transport in the mixing region is not clear yet, but does appear to be dependent on the ratio of the two turbulence intensities and lengthscales.

In previous experiments, Gilbert (1980), using grids with a low ratio of turbulent intensities, found that only diffusion transport appeared to be present, Veeravalli et al. (1989), Heenan et al. (1994), using grids of larger turbulence intensity ratios, produced evidence that both mechanisms were present.

The first part of the present research has been done in air flow, performing turbulence measurements with single and X hot wire probes. However, the statistical approach based on single-point or multi-point traditional velocimetry (Hot Wire, LDV), even if it provides important information about the dynamics of turbulent flows, has a clear limitation. The highly three-dimensional nature of the coherent structures, responsible of most of the dynamic behaviour of turbulent flows, can not easily be observed by punctual measurements. For this reason and in order to give better interpretation of the hot wire results, experiments have been initiated in a water tunnel, applying quantitative flow visualisation technique.

Before starting the measurements in the region of interest, data have been collected downstream a uniform grid, in order to assess the measurement technique and the data analysis procedure, comparing the results with the well known behaviour of the homogeneous decaying turbulence.

In this paper results from the hot wire measurements are

reported and preliminary results obtained applying D.P.I.V. (Digital Particle Imaging Velocimetry) technique to the homogeneous flow and to the mixing flow are shown.

2. WIND TUNNEL EXPERIMENTAL LAYOUT

The wind tunnel used for the air flow experiment is an open-return type, having the working section length equal to 6.34 m and the cross section dimension $H=90$ cm and $B=130$ cm.

The flow uniformity, in terms of dynamic pressure, in the test section is less than 0.75%, while the turbulence intensities is less than 0.1%.

The two sets of bars were mounted at the entry of the working section. The large and small bars have a square section, with dimensions respectively equal to $L_1=18$ mm and $L_2=6$ mm. The solidity is equal to 0.33 for both sets of bar, in order to have the same pressure drop.

The mean velocity in the test section has been set to 7.7 m/sec, with an average gradient in the direction normal to the bar equal to 0.4 /sec.

The experimental investigation has been performed using a constant temperature anemometer system, Dantec 55M, with single and X wires probes. A Metrabyte data acquisition board, with 12-bit resolution has been used to sample the amplified signals. In each measurement point the statistical analysis has been computed over 10 data blocks, each containing 30000 samples, collected at a sample rate of 16 kHz. Measurements have been taken every 5 cm from 17 cm to 72 cm along the y axis, in the direction transversal to the bars.

3. WATER TUNNEL EXPERIMENTAL LAYOUT

The experiments were performed in a vertical water tunnel whose test-section is 0.15 m x 0.15 m x 1.1 m. To provide complete optical access, the test section walls are made in plexiglass. A maximum operating speed of around 0.3 m/s is allowed. The grids are mounted between the contraction and the entry of the test chamber. The uniform grid used for the preliminary experiments in homogeneous turbulence is made up of bars having diameter equal to 2 mm, separated 8 mm from each other. The grid used for the mixing flow was characterized by large bars having a diameter equal to 3 mm and small bars of 1 mm diameter. The solidity of the two sets of bars was equal to 0.33.

Metallic coated particles with 12 μ m diameter were used as a tracer. The seeding density was sufficiently high in order to allow autocorrelation technique for the analysis of the images.

A pulsating light sheet was generated by scanning a 4W

Argon-Ion laser beam by means of a polygonal rotating mirror. The lighted vertical plane was recorded by a CCD video camera, 25 frames per second, 768 x 512 pixels, and by a 24 mm x 36 mm film photographic camera. The imaged flow field was 2 cm x 1.33 cm for the video camera and 12 cm x 8 cm for the photo camera. The video camera was mounted on a transversing mechanism in order to scan the test-section, downstream the grid, in the central plane along the x direction. In each measurement region the image acquisition time was 5 minutes, in order to permit proper statistical analysis. The speed of the rotating polygonal mirror was adjusted to allow in each frame two or three superimposed particle images. Autocorrelation technique was used to extract the velocity field from the images, Adrian (1991), Kompenans (1989), Willert et al. (1991). All the acquisition and analysis software was written in LabView.

The mean velocity downstream the grid, nominally uniform across the grid, has been set to 200 mm/sec. Due to difficulties in positioning the bars in the water tunnel, the best average gradient achieved for the uniform and mixed bar grids was respectively equal to 0.4 sec⁻¹ and 0.8 sec⁻¹.

4. RESULTS AND COMMENTS

Hot wire data will be first shown. The complete set of results has been presented in Heenan et al. (1994). Here only basic results will be shown to highlight the physical problem.

In figure 3 the profiles of the longitudinal component of the turbulence intensity are shown at different distances, x/M_1 (M_1 is the large bar separation) from the grid. Two distinct levels of turbulence, associated with the two regions of the grid, the small grid and the large grid, are evident. In the large scale region the turbulent intensity is more than twice as great as that behind the small scale grid. Between the two streams there is a region of gradually varying turbulent intensities as the two streams diffuse and penetrate into one another from the boundary of the two scales. Moving downstream the grid, the decaying evolution of the turbulence is observed. For the two homogeneous regions, the turbulence evolution shows a decaying law typical to those found with grid turbulence Batchelor (1953), Comte-Bellot (1980), Kolmogoroff (1941).

In figures 2 and 3, the skewness and flatness profiles of the longitudinal velocity component are presented. In the mixing region skewness and flatness profiles demonstrate strong deviations from the homogeneous values of zero and three respectively. The large departures from Gaussian values, in the mixing region, imply that significant mechanisms are operating in addition to diffusion. It is

interesting to notice that in all cases the extreme values for skewness and flatness are reached for $y=36$ cm, below the grid geometric centre located at $y=43$ cm; this is a sign of the dominant effects of the large scale that propagates towards the small scale region.

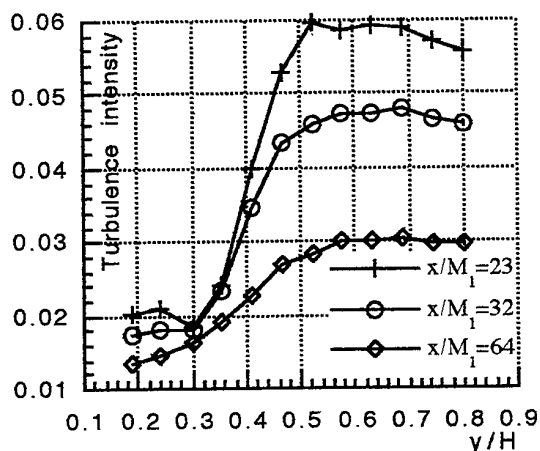


Fig.1 Profiles of turbulence intensity.

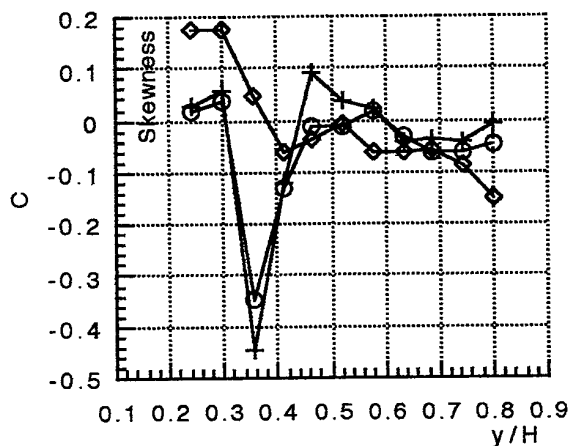


Fig.2 Profiles of skewness. Same symbolism as figure 1.

In figure 4, The u^2v triple correlation coefficient, R_{uvv} , represents the transport of the u -component normal turbulent stress by the transverse to the grid v -component velocity; as the v -component is strongly negative skewed in the mixing region this correlation is strongly negative. The minimum value is reached for $y=36$ cm, below the grid geometric centre located at $y=43$ cm, this is again a sign of the propagation of the large scale towards the small scale.

Water tunnel preliminary results, obtained with DPIV technique, will be shown here. Starting with the homogeneous grid flow, the decay of the square of the turbulence intensity downstream the grid is shown in figure 5. Results for the longitudinal, T_u^2 , and the transversal,

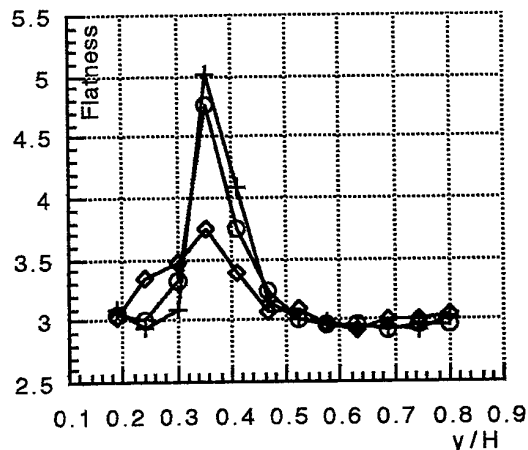


Fig.3 Profiles of flatness. Same symbolism as figure 1.

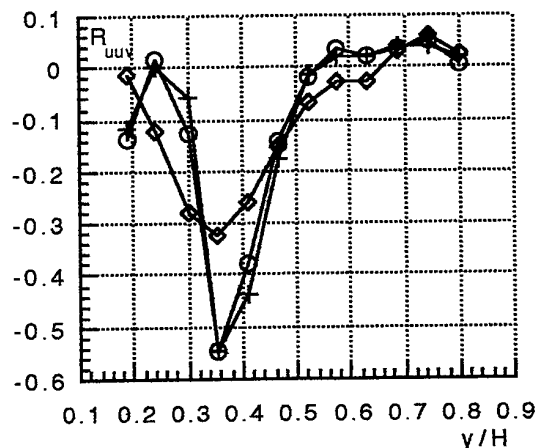


Fig.4 Profiles of triple correlation coefficient. Same symbolism as figure 1.

T_v^2 , components are displayed. The exponential decaying law obtained interpolating the experimental results shows exponents slightly smaller than those measured with hot wire probes or with LDV. The smaller values found may be attributed to a small velocity gradient present in the mean flow, responsible of turbulence production, rather than to the technique adopted. Skewness and flatness of the longitudinal fluctuant velocity component, figures 6 and 7, show also expected values for homogeneous grid flow, respectively near 0 and 3. In figure 8, the degree of anisotropy, defined as the root square of the ratio between the longitudinal and the transversal components of the turbulence intensity, is presented. Values close to 1.3 are observed, not far from the values measured in the wind tunnel experiment. In figure 9 the spatial lateral correlation coefficient is reported as a function of the lateral displacement λ , for two different distances from the grid. The area under the curves is proportional to the integral macro scale length presented in figure 10, were the

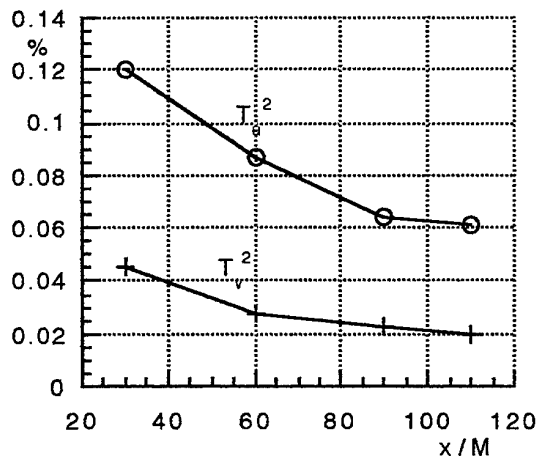


Fig.5 Turbulence intensity decay law.

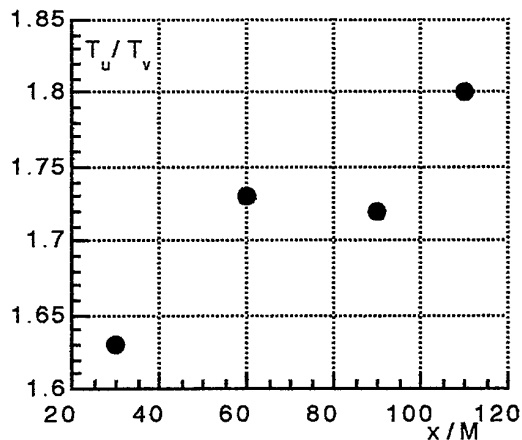


Fig.8 Degree of anisotropy downstream the grid

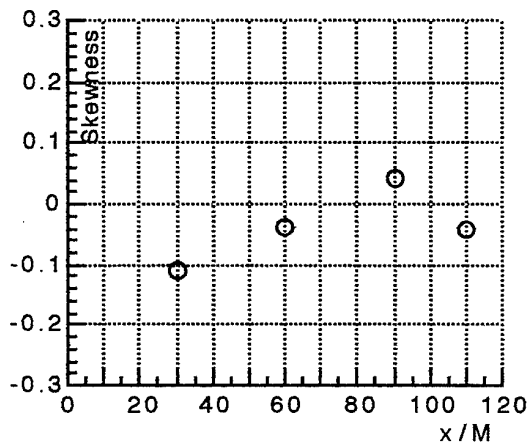


Fig.6 Skewness downstream the grid.

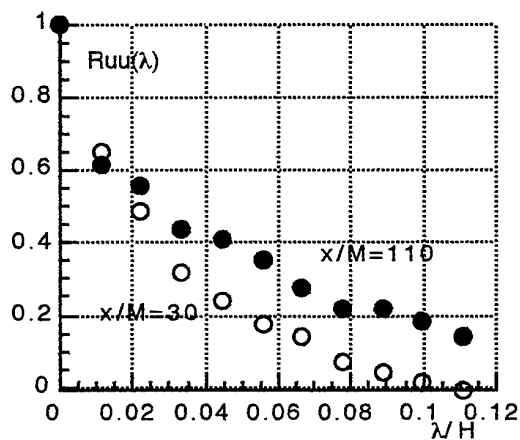


Fig.9 Spatial lateral correlation coefficient.

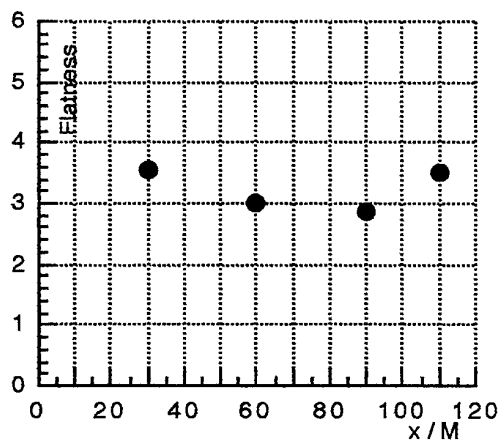


Fig.7 Flatness downstream the grid.

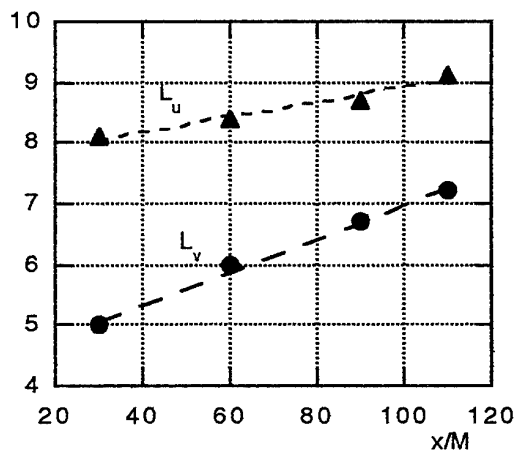


Fig.10 Integral macro scale length downstream the grid.

expected slopes and the quasi-linear evolution downstream the grid is shown, Hinze (1975). L_u and L_v are

respectively the longitudinal and the transversal components.

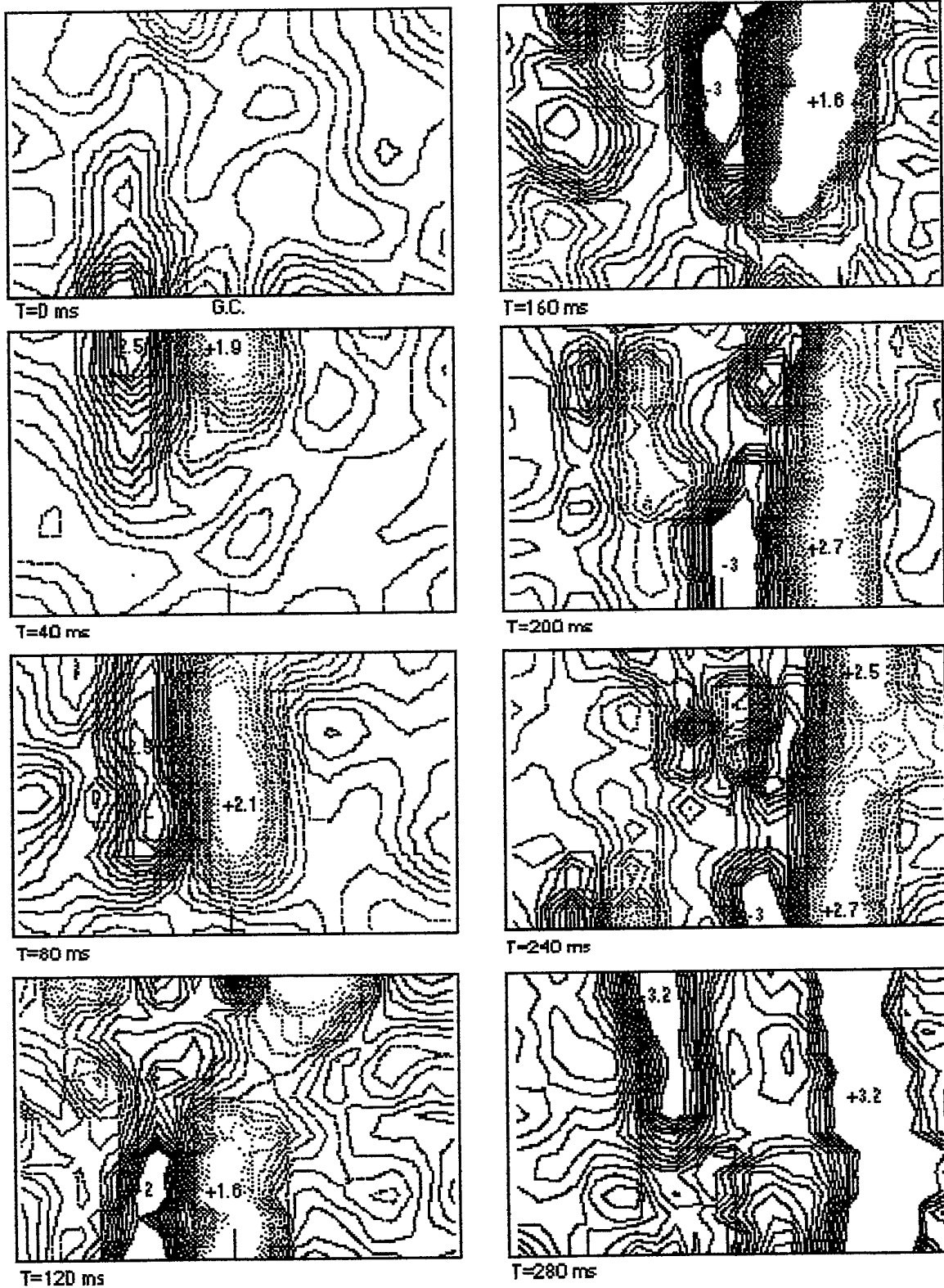


Fig.11 Sequence of vorticity isocontour maps.

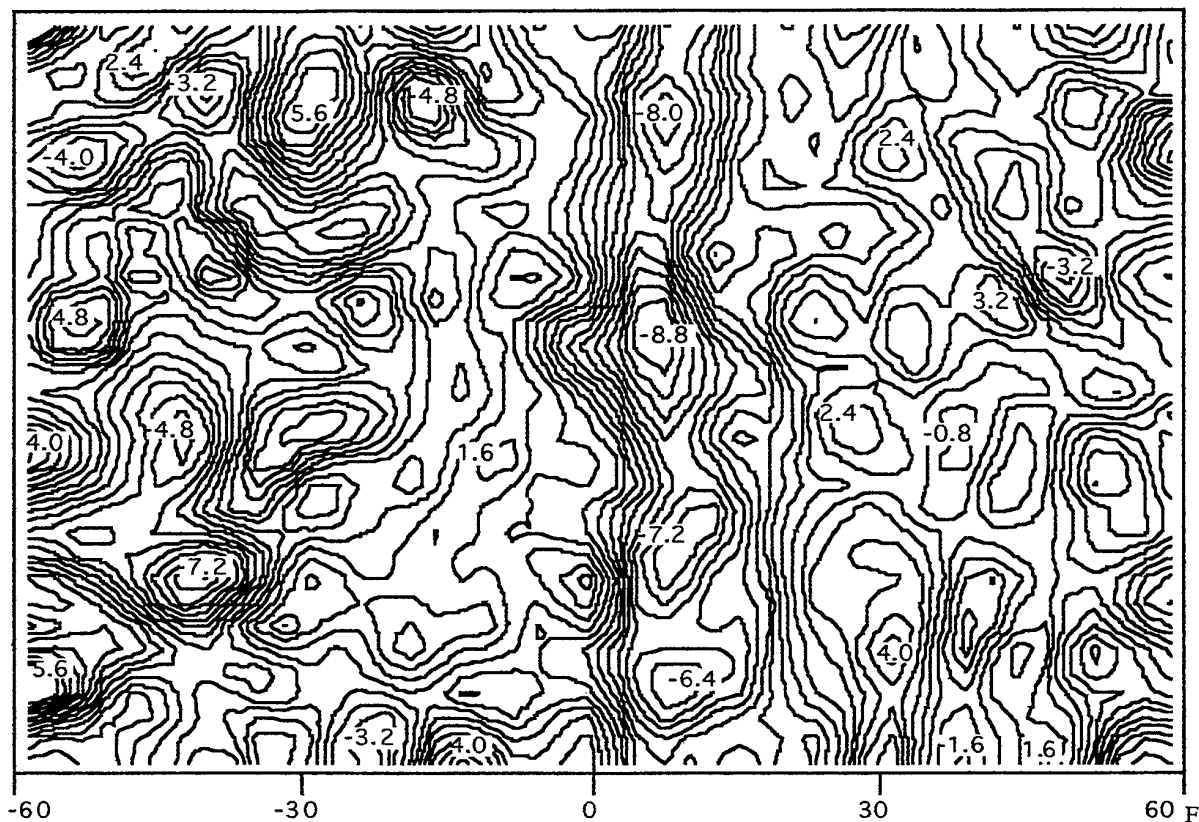


Fig.12 Instantaneous dimensional isovorticity map (dimensions in mm)

5. CONCLUSIONS

The results obtained measuring flow velocities in the mixing region of two nominally shearless grid flows, having different turbulence intensity and scales, have been presented.

The main measurements have been done in air flow using hot wire technique. The potentiality of DPIV to contribute to a complete understanding of this flows has been shown.

Results have been also presented applying the DPIV to a homogeneous turbulent grid flow. The obtained results are in reasonable agreement with the well documented results on the subject.

ACKNOWLEDGEMENTS

The authors are grateful to Umberto Testa for the great help given in collecting and analysing all data and to Alastair Macquarrie for his precious collaboration. They would like to express their gratitude to Mr Marco Grivet and Marcello Masili for their technical support. This research is in part sponsored by the E.N.E.A. and in part by the Centro Studi Dinamica Fluidi - C.N.R.

REFERENCES

- Adrian, Ronald J., Particle Imaging Techniques for Experimental Fluid Mechanics, *Ann. Rev. Fluid Mechanics*, 23, 261-304, 1991
- Batchelor, G.K. (1953), *The theory of homogeneous turbulence*, Cambridge Univ. Press
- Comte-Bellot, G. (1980), The use of a contraction to improve the isotropy of grid generated turbulence, *J.Fluid Mech.*, vol.25, p.657.
- Gilbert, B. (1980), Diffusion mixing in grid turbulence without mean shear, *J.Fluid Mech.*, vol.100, pp.349.
- Heenan, A.F., Morrison, J.F., Iuso, G. & Onorato, M. (1994), Evolution of two-scale, shearless grid turbulence, *Proc. II International Conference on Experimental Fluid Mechanics*, Torino, pp.321-330.
- Hinze, J. O. (1987), *Turbulence*, McGRAW-HILL Publishing Company.
- Kolmogoroff, A.N. (1941, On the degeneration of isotropic turbulence in an incompressible viscous liquid, *C.R. Akad. SCI. SSSR (Dokl.)*, vol.31, p.538.
- Kompenhans J., Höcker, R., (1989), Investigation of turbulent flows by means of P.I.V., paper from the 5th Int. Symp. On Flow Vis., Prague.
- Veeravalli, S. & Warhaft, Z. (1989), The interaction of two distinct turbulent velocity scales in absence of mean shear, *J.Fluid Mech.*, vol.207, p.191.
- Willert, C., Gharib, M. (1991), Digital Particle Image Velocimetry, *Exp. in Fluids* 10.

THE EFFECT OF A SINGLE BUBBLE ON TURBULENCE STRUCTURE IN GRID TURBULENCE FLOW BY COMBINED SHADOW-IMAGE AND PIV TECHNIQUE

A. Tokuhiko*, M. Maekawa**, K. Iizuka**, K. Hishida** and M. Maeda**

*formerly at Paul Scherrer Institute, CH-5232 Villigen PSI, Switzerland

**Department of Mechanical Engineering, Keio University, 3-14-1 Hiyoshi, Kohoku-ku, Yokohama, 223 Japan

ABSTRACT

An experimental investigation on flow around a quasi-stationary bubble and its solid counterpart, one-half a hemisphere, was conducted. A single bubble was attached to a small disk (~2mm) at the end of a needle suspended across a square channel (100 mm) by piano-wire while water flowed downward. A dynamic balance between the buoyant upward tendency of the bubble and the downward flow of water while attached by surface tension forces to the small disk kept the bubble approximately stationary within the measurement region. The solid model was suspended across the square channel in the same manner. The flowrate was held constant while one bubble sizes was used. Velocity measurements were made using Digital Particle Image Velocimetry (DPIV) around the flow field centered on the bubble which oscillated with the flow, but remained attached to the disk. A novel technique was devised wherein the laser sheet was viewed from the back camera through a LED-array outlining a square so that the front camera recorded the bubble's shadow simultaneously. In this way both the flow-field and the boundary of the bubble (solid) were measured. The recorded images were processed so that a vector flow field was generated while distinguishing the average interfacial boundary of the bubble. A comparison of results with previous studies revealed some of the benefits and limitations of the present measurement techniques. These will be described in this work.

1. INTRODUCTION

The study of flow around a solid body such as a hemisphere or that around a single rising gas bubble in a volume of liquid are two classic examples of problems in fluid mechanics of multi-phase flows. It goes without saying that our understanding of such rudimentary systems can be and is often extrapolated and applied to larger scale systems such as fluidized-beds, bio-reactor bubble columns and other equipment involving solid-

liquid and gas-liquid flows. Our base of knowledge on the fundamental aspects of these types of flows over many years are contained in such texts as by Levich (1962) and Clift et al. (1978).

With regard to velocity measurement techniques employed in past experimental investigations, they mainly encompass a wide variety of (classic) flow visualization techniques and pointwise measurement by such methods as hot-film/hot-wire and laser Doppler anemometry.

In the present work we first sought to apply a number of recent measurement techniques (in contrast to the classic) in unison to the fundamental problem of flow around bubbles and in this case, its corresponding solid counterpart. Our objectives were thus two-fold: 1) to explore the applicability of DPIV, LIF and a specifically developed shadow technique to find the contour of the bubble to this problem and 2) to evaluate the information content produced by our measurement system; that is, measurement of the differences between flow around a solid and a bubble.

2. MEASUREMENT METHOD

In order to detect the interaction between the bubble motion and the turbulent flow field around it we implemented a Digital Particle Image Velocimetry (DPIV) system previously described by Sakakibara et al. (1993). Our original intent was to simultaneously capture both the bubble and tracer particle motions, the latter of which was approximately 1000 times smaller in size than the bubble. However, it became clear that the intensity of light reflected from the bubble's surface saturated the CCD camera such that the intensity of light from the tracer particles was overwhelmed. We thus resorted to application of Laser Induced Fluorescence (LIF) using fluorescent particles (1-10 μm) with a specific density 1.02 along with a light-sheet produced by a argon-ion laser; that is, by mixing these particles

with rhodamine-B we could detect the fluorescence emitted by the particles through a color filter (to cut reflections) into our CCD camera. The fluorescence particles we prepared by mixing MMA, a monomer, with rhodamine-B and then polymerizing the two together. Since the resulting product does not fluoresce we mix the MMA with i-PrOH. We found that with this set-up we could detect the motion of tracer particles in the vicinity of the bubble-liquid interface.

Next in order to measure the bubble's cross-sectional shape we supplemented the DPIV-LIF system with an infrared shadow-image technique (IST) specifically prepared for recognizing the contour of bubble. Figure 1 thus depicts our arrangement consisting of two CCD cameras; one for DPIV-LIF (rear camera) and the other for IST(front). A shadow was produced from infrared LEDs outlining a square and located behind the bubble. The emitted light passed through a filter attached to the CCD camera that only recorded the shadow and the infrared-light. By shadow we mean the projected image produced by a positioned rear light source such that the CCD's close-up lens recorded only the front or unilluminated side of the bubble. In order to capture both the bubble shape and the flow field around it closely at the bubble surface we synchronized the triggering of both the laser and the LEDs.

As for the experimental apparatus it consisted of two rectangular tanks, a lower and upper, connected in between by a vertical, channel of $100 \times 100 \text{ mm}^2$ and 1000 mm in length. A schematic is shown in Figure 2. At the top of the channel there is a entrance section with a grid in order to generate a homogenous incoming flow. The test medium was water and flowed freely down through the channel to the lower tank where it was pumped back up to upper tank. The mid-region of the channel was our

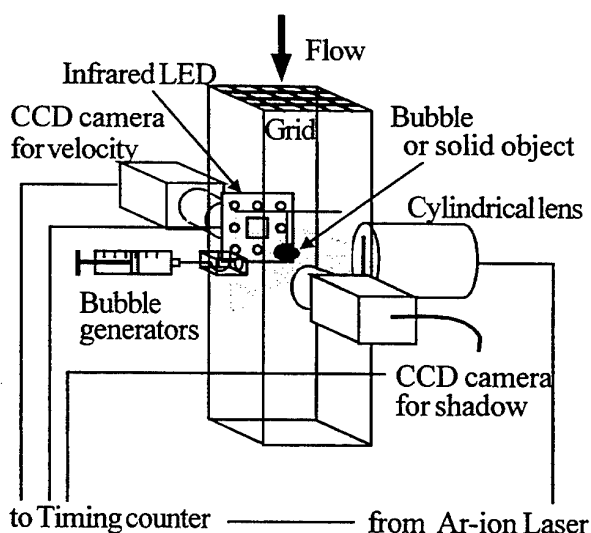


Figure 1. Schematic of measurement section.

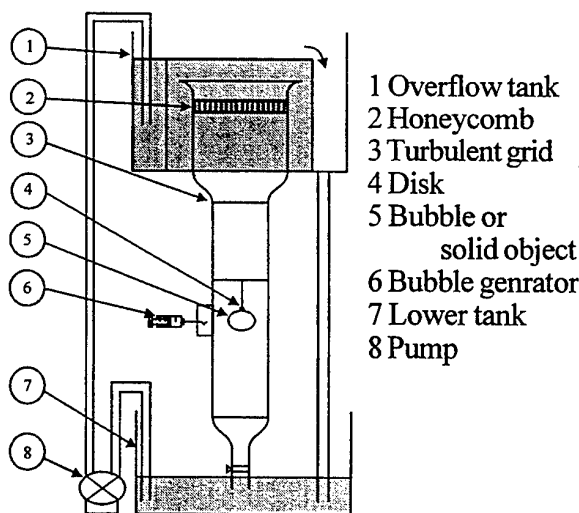


Figure 2. Schematic of experimental loop.

measurement section and consisted of a port from where either a bubble or its equivalent solid could be introduced. The bubble or solid was attached to a small disk (dia. $\sim 2 \text{ mm}$) located at the end of a needle suspended across the channel by a piano-wire. We note that in the case of the bubble it was thought that the surface tension kept the bubble attached to this small disk even as water flowed downward. We did take note of the fact that placement of the small disk in the flow field and the attachment of the bubble to it was not exactly equivalent to a freely rising bubble. However, since our objective was to study the flow field around the bubble, a nearly stationary bubble was both a necessity and an experimental compromise. The operational flowrate was held constant at $U_o = 0.245 \text{ m/s}$ while the corresponding turbulent intensity level due solely to grid-generated turbulence was 5 % in the channel. This level was measured separately by laser Doppler anemometry. As for the reference bubble size used in the presentation of our data, we used the breadth of the bubble $D = 12 \text{ mm}$. This figure was supported by a calculation of the breadth from a correlation put forth by Tadaki and Maeda (1961) based on the flow and physical properties.

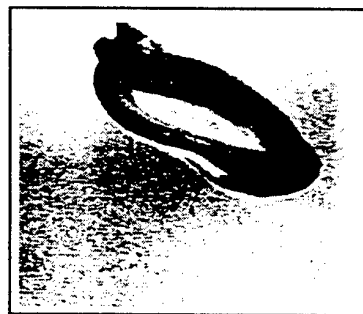


Figure 3. Typical shadow image of bubble as digitized from video.

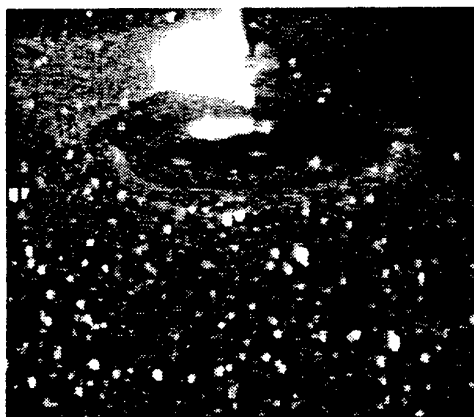


Figure 4. Typical snapshot of particle image around the suspended bubble as digitized from video.

3. RESULTS

Figure 3 shows a representative still image of the bubble's image taken by the illuminating from the back side (in black) as imposed on a grayscale background. The bubble in the figure is right-shifted in a descriptive sense and has been captured at one instant of a continuous oscillatory motion in all three axial directions. The bubble is attached at the top (center) to a small disk that is marked by a white dot within a black region. Figure 4 depicts a representative image of the tracer particles, including a partial outline of the bubble boundary and the region inside which contain fewer speckles. Note especially in the latter figure that there is a white-out region located at the top. This appears to be a region of high light reflectance resulting from, in general, the bright laser light and multiple reflections from various surfaces.

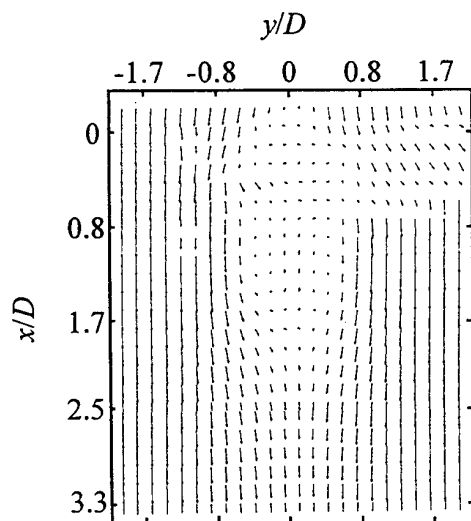


Figure 5. Representative vector field plot of the flow around the solid.

Due to this difficulty which hinders simultaneous measurement of both the bubble's boundary and its velocity field, use was made of Fig. 3 which by comparison clearly identifies the shape and boundary of the bubble. We thus obtained boundary and velocity information simultaneously but separately through the use of two CCD cameras.

Based on these and similar images for the equivalent solid, we extracted velocity information from a collection of more than 1000 images. Other velocity-related informations were subsequently calculated. For initial comparison, we present in Figures 5 and 6 an enlarged section of the measured flow field around the bubble and solid. In the figures the laser sheet enters from the left and introduces a region of relatively larger uncertainty with respect to the calculated vectors to the right of the solid or bubble; that is, due to total and partial shading respectively in the cases of the solid and bubble, the error in this right region is higher relative to the rest of the field. We henceforth will show data from only the left side of the measured flow field. As for differences in their respective flow fields, upon close scrutiny we note that the flow pattern and the spatial extent of flow in the wake regions are different; that is, in the case of the solid there is a longer wake region and recirculating flow area in comparison to the bubble. Of course the non-slip boundary condition at the solid's surface and the slip condition at the bubble's surface influences this wake flow. The generation of vorticity at some separation point along the edge of their respective boundaries, the conveyance of vorticity along the nearby free shear layer, the formation of a circular vortex (two-dimensional) or vortex ring (three-dimensional) and eventual shedding of vortices by an entrained cross-flow are nevertheless common mechanisms in both the solid and bubble. However, since the bubble oscillates substantially with the flow, there is

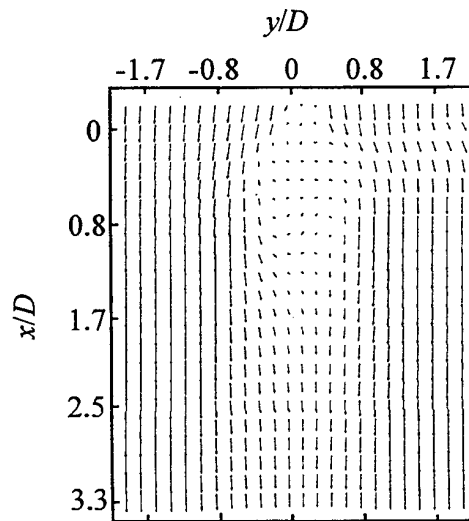


Figure 6. Representative vector field plot of the flow around the suspended bubble.

also a contribution from this motion (to the flow field); that is, it is likely that turbulence is generated from the oscillatory motion of the bubble whereas it is not significant in the case of the solid.

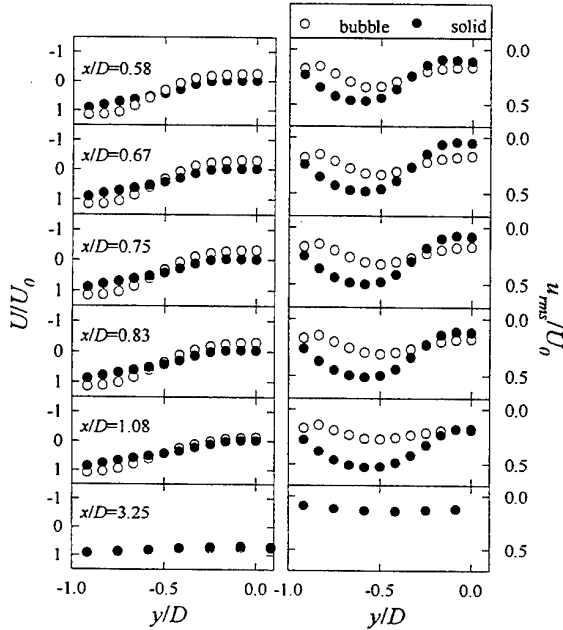


Figure 7. Streamwise variation of the average velocity and RMS velocity distributions. Only one-half of the profile is shown due to symmetry.

Figure 7 shows the cross-stream distribution of the average (U/U_0) and normalized RMS (u_{rms}/U_0) velocities respectively to the left and right of the figure. Here U_0 represents the average velocity without bubble or solid as measured by LDV. To facilitate our discussion, 4 axial locations close to the solid and bubble and 2 locations further away ($x/D = 1.08, 3.25$) have been selected. In each of these figures the blank and filled circles represent respectively the bubble and solid data. Note that although the on-average velocity defect is slightly larger for the bubble at close range ($x/D < 1.08$), u_{rms}/U_0 has a larger variation and extends further downstream for the solid. The data at $x/D = 3.25$ essentially shows that flow is identical for both flow parameters at this downstream location. In Figure 8 we show the corresponding cross-stream average (V/U_0) and normalized RMS (v_{rms}/U_0) velocities. Whereas one-half of symmetric distributions in Fig. 7 were shown, the half-profiles here are symmetric but of opposite sign about the centerline since the flow are directed in both directions. In fact, due to the bubble's oscillatory motion notice that V/U_0 and v_{rms}/U_0 are generally larger for the bubble in contrast to the solid.

While Figs. 7 and 8 show relative magnitudes of u_{rms} and v_{rms} with respect to U_0 Figure 9 shows a direct comparison of the

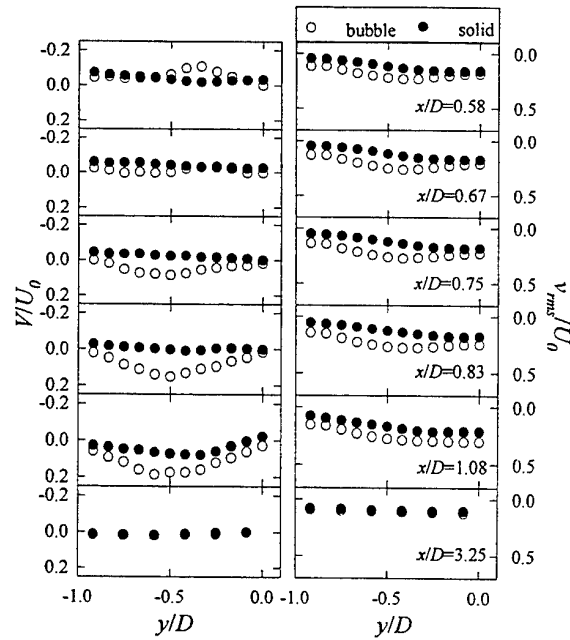


Figure 8. Streamwise variation of cross-stream average and RMS velocity distributions.

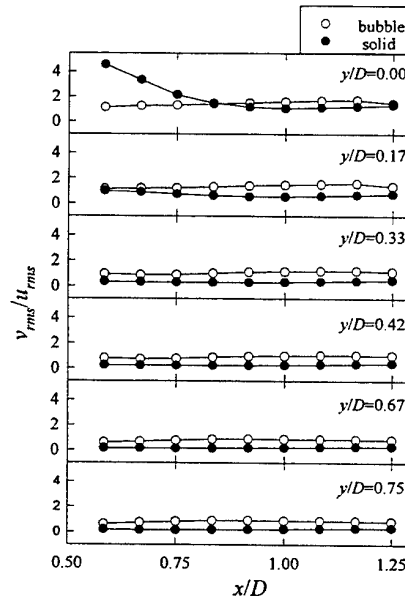


Figure 9. Ratio of cross-streamwise to streamwise RMS values for solid and bubble.

RMS values along the streamwise direction with the cross-stream direction as parameter. Note that except at the centerline for $x/D < 0.85$ the bubble's oscillatory motion again contributes to a consistently larger v_{rms} than the solid. On the other hand the reversed flow just along the centerline typically appears to show as much as 4 times more fluctuation in the case of the

solid in contrast to the bubble. In other words the cross-stream flows are spatially confined behind the solid in comparison to the oscillating bubble.

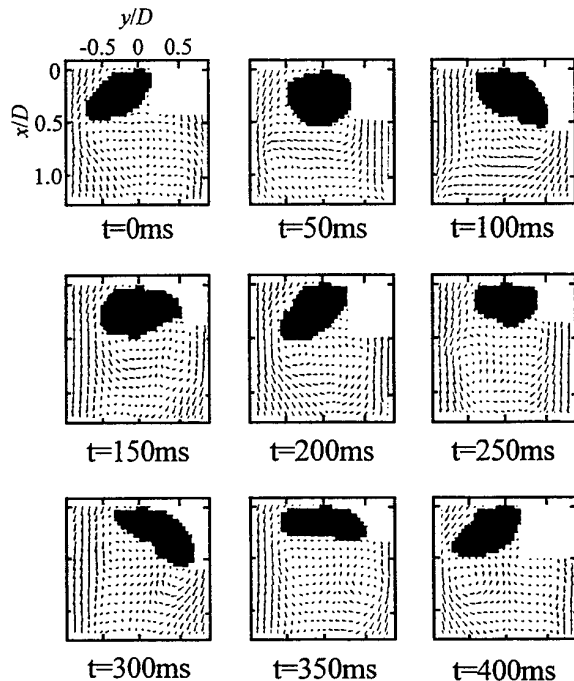


Figure 10. Sequence of shadow-images of the bubble's oscillatory motion taken at 50 ms intervals.

The data presented thus far show averaged quantities calculated from a multiple number of images. While these figures provide some insight, details of the flow field as dictated by the bubble's motion is overlooked. We present in Figures 10 and 11 a sequence of vector field plots, respectively with the identified bubble's shadow image and that of the solid superimposed at 50 ms intervals. The sequence which was recorded with a normal speed (30 fps) CCD camera, although clearly depicts the change in shape and position of the bubble, only captures snapshots of the bubble's continuous oscillatory motion which we judged to be approximately periodic every 200 ms. Note the change in the flow field with respect to the bubble's position at each 50 ms interval. In fact upon close scrutiny of the vector field in the figure, one can approximately identify the formation and shedding of the vortices. Notice that the shedding is not necessarily at the spatially extreme (right or left) positions of the bubble. In fact upon scrutinizing the average velocity, *RMS*-velocity, *u* and *v* *RMS* ratio and vector field plots we think it likely that the bubble's motion locally produces regions of large Reynolds stresses but also spatially distributes any generated turbulence much more evenly than the solid.

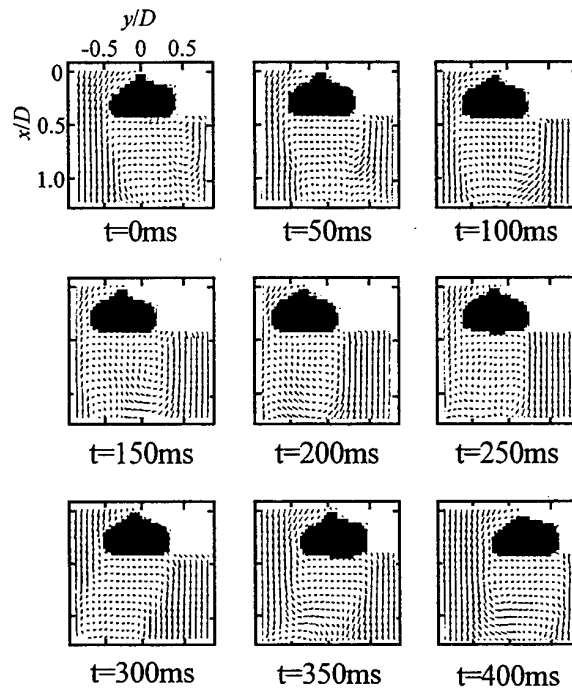


Figure 11. Equivalent sequence at times as indicated for solid.

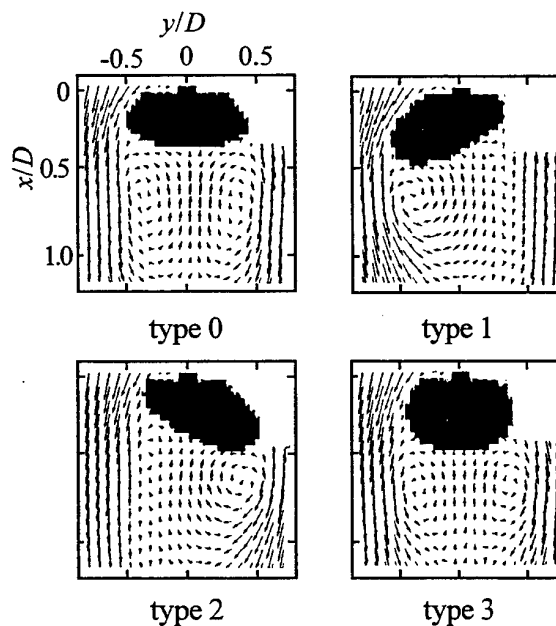


Figure 12. The 4 selected shapes of the bubble.

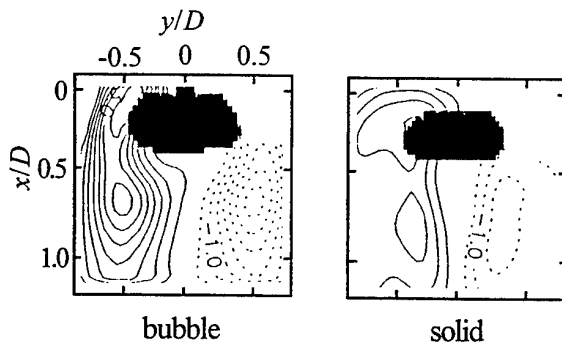


Figure 13. Vorticity contour contrasting the bubble and the solid.

Figure 11 shows a similar sequence for the solid. Notice that here that the body is consistently identified in shape but, also exhibits some sideways motion most easily detected with respect to the outline of the square measurement area. Although this motion may influence the solid's wake velocity field, we observed that in comparison to the bubble the oscillation frequency was much smaller and in addition thought the deformation of the bubble-shape would strongly influence its wake flow-field. In fact, because the bubble shape does change so drastically in time, we selected four representative types of shadow images from the sequence shown in order to selectively study its corresponding flow field. We show these four types (type 0, 1 2 and 3) in Figure 12 and note that they typically represent the time events in Figure 10 as follows: 1) type 0 [flat] 350 ms, 2) type 1 [left-shifted] ~ 200 ms, 3) type 2 [right-shifted] ~ 300 ms and 4) type 3 [full] ~ 250 ms. The word in brackets gives their short descriptive names.

We next show in Figure 13 the vorticity contours contrasting the bubble and solid. The sense of positive and negative vorticity are noted respectively by solid and dotted lines. One can see that besides the nearly symmetric distribution of vorticity about the central axis for both the bubble and solid, the contrasting feature is the large vorticity values in the case of the bubble. Since large velocity gradients, typically from free shear and vortical flows, are known to have large vorticity the distribution as shown is at least qualitatively consistent with the vector field plots comparing bubble versus solid in Figs. 10 and 11. Next in Figure 14 we show the vorticity contours corresponding to the four bubble types shown in Fig. 12. Note here that the left (type 1) and right (type 2) bubble orientations distort or respectively "pinch" the otherwise symmetric (type 0 and 3) vorticity distribution. The concentration of vorticity, however, from the unspecified separation point just aft of the bubble does not appear to change in location.

In Figures 15 and 16 we display the turbulent energy distribution

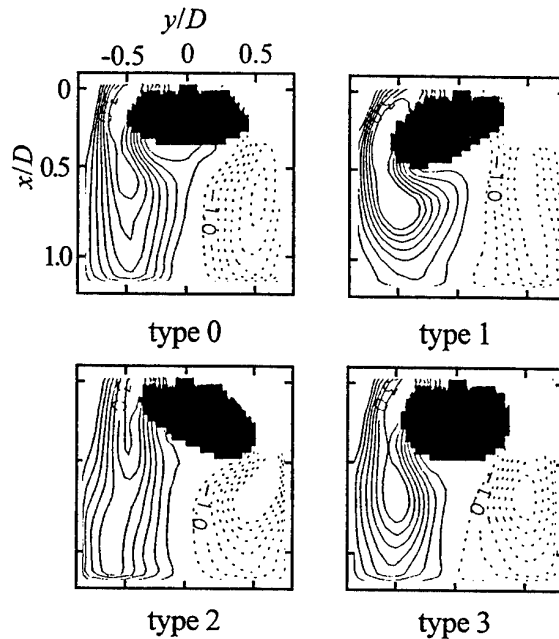


Figure 14. Vorticity contours corresponding to the four selected bubble types.

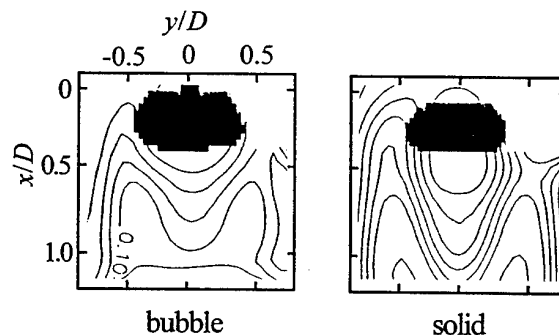


Figure 15. Turbulent kinetic energy contour contrasting the bubble versus the solid.

contours corresponding to Figs. 13 and 14; that is, at first contrasting the bubble/solid and subsequently, for each of the four selected bubble types. The turbulent energy is here defined as $k = 1/2 (u'^2 + v'^2 + w'^2) / U_0^2$ as v' and w' have been assumed to be equivalent. Note that once again the contours are generally similar in shape but, not in detailed trends nor in magnitude. In fact, although the bubble appears to generate more vorticity than the solid (Fig. 13), the turbulent energy is not analogously distributed. In fact, the energy is certainly evenly distributed in the case of the bubble in comparison to the solid. This is clearly indicated by the contours for the four types where right and left orientations show equally shifted energy distributions.

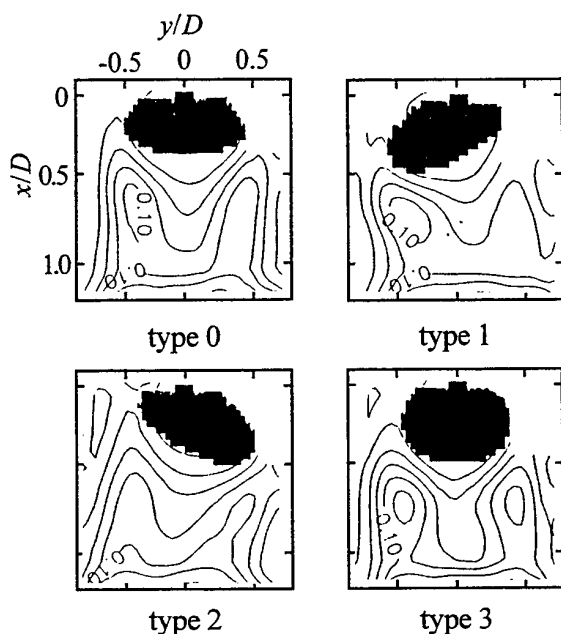


Figure 16. Turbulent energy distribution corresponding to the four selected bubble types.

Finally in Figures 17 we depict the spanwise profiles of, respectively, the turbulent kinetic energy and Reynolds stress of the bubble and solid at the same streamwise locations as previously shown data. Note that consistent with Figs. 13 and 14 the Reynolds stress for the bubble shows a peak at $y/D \sim -0.5$ ($x/D < 1.08$) while for the solid a peak doesn't appear until $x/D = 1.08$. Again at $x/D = 3.25$ there is no difference between the two.

4. DISCUSSION

The results as presented appear to fulfill much of our first objective; that is, the combined use of DPIV, LIF and the above-described infrared shadow technique enables one to identify both the shadow of a body and the flow field around the body simultaneously. Recall that while it has been called a shadow, the boundary of the object was identified by proper placement of back-lighting and use of the CCD's close-up lens such that the unilluminated front cross section was recorded. In addition, based upon close scrutiny of the measured velocity vector field and subsequent velocity derived plots, we are able to elucidate and verify a number of phenomenological facts regarding the differences in the wake flow produced by a bubble and a solid.

First in order to facilitate our discussion, we refer to Fan and Tsuchiya (1990) who describe in detail many of the physical mechanisms observed in this experiment regarding the bubble and its wake flow field. If we use for instance the observed breadths of the bubble and average channel velocities, the

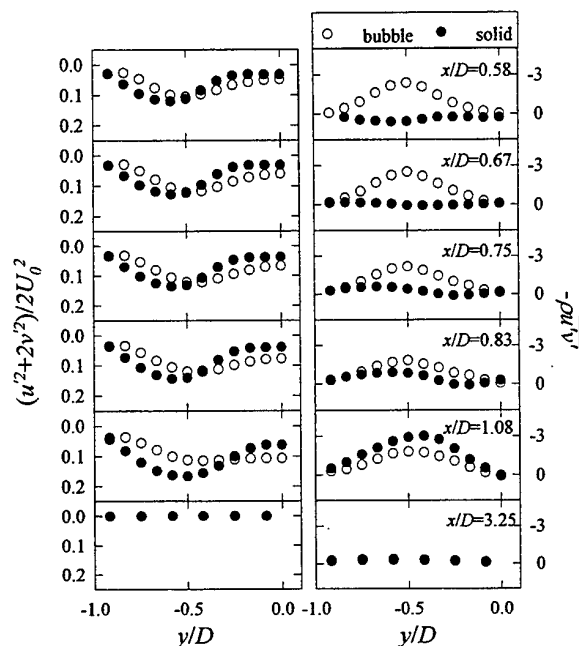


Figure 17. Turbulent kinetic energy and Reynolds stress distributions for selected streamwise locations contrast the bubble versus the solid.

estimated bubble Reynolds number range is 1800 to 2700. Note that contrary to most experiments where the bubble rise velocity is measured, we have an oncoming flow toward a fixed bubble. With an estimate of the Reynolds number, we see from a plot of past experimental data of Strouhal versus Reynolds numbers [Cf: Fan and Tsuchiya (1990)] that our corresponding Strouhal number for vortex shedding is approximately 0.15 to 0.20. An equally separate calculation of the Strouhal number based on an estimate of the bubble's oscillation frequency from high-speed video images yields $0.16 < Sr < 0.245$. The oscillation frequency from high-speed video-images were estimated visually and at present could not be resolved to better than 4-6 Hz. This then roughly confirms the proper range of the relevant mechanisms.

Although the details of the vortex shedding mechanism especially for a bubble are of great interest, due to the great difficulties in direct measurement, most of the experimental evidence has been accumulated from photographic and visualization techniques that are non-intrusive in nature. In reviewing this data Fan and Tsuchiya assert that the wake flow behind a bubble is characterized as follows: 1) the bubble tends to oscillate in order to reduce its wake size; 2) by reducing its wake size the bubble also minimizes the pressure loss behind the bubble and thereby its drag; and 3) this reduction in wake size is best realized when the vortex shedding and bubble oscillation frequencies are near unity.

In other words in comparison to the solid, the bubble's oscillatory motion generally serves to minimize the energy loss while rising through the liquid phase or in our case as the water flows past it. It is therefore not surprising to see in Figures 15 that the iso-contours are less densely spaced for the bubble. The turbulent kinetic energy is evenly distributed throughout the flow field for the bubble whereas the iso-contours for the solid are more densely spaced. The overall shape of the iso-contours as well as the order of magnitude of the turbulent energies are, however, similar for both objects. This latter result may be slightly surprising since typically the production of turbulence is concurrent with large Reynolds stresses and strain fields. From Fig. 17 (right) it is clear that at distances less than a diameter, the bubble has a larger Reynolds stress in the vicinity of $y/D \sim -0.5$ than the solid. An equally large stress does not appear for the solid until $x/D = 1.08$. These trends are consistent with the spatial distribution of vorticity in Figs. 13 and 14. Figure 17 then leads us to believe that in spite of the aforementioned contrasts, since the turbulent kinetic energies are roughly equal, flow around a solid versus that around a bubble must have inherently different energy dissipation mechanisms. Part of the difference is likely attributable to the internal flow (air) of the bubble which of course does not exist for the solid. The primary reason, however, must be that due to the interaction of the bubble's oscillatory motion with its own wake flow field. While the vortex shedding mechanism is common to both object, the interaction between the bubble's oscillatory motion and fluid motion surely produces turbulence. The turbulent kinetic energy distribution is however similar.

5. CONCLUSIONS

Using DPIV supplemented by LIF and an infrared shadow-image technique (IST) produced by an array of LEDs shining through a translucent window, two CCD cameras were used to simultaneously identify the boundary (shape) and flow field around a bubble and its corresponding solid equivalent. The bubble or solid was suspended in the middle of a square channel in which water flowed downward through a grid arrangement. From a collection of more than 1000 images, boundary and velocity information were extracted.

A comparison of first the vector flow field around the solid and bubble revealed differences in the wake flow structure as expected; that is, the implemented measurement system was able to detect differences in the flow field resulting from, respectively the non-slip surface boundary condition in the case of the solid versus the slip condition at the bubble-liquid interface for the bubble. We additionally noted that the oscillatory motion of the bubble appeared characteristic under the given experimental conditions. Upon scrutinizing the average velocity, RMS-velocity, u and v RMS ratio, vorticity and finally,

the Reynolds stress distributions, we noted that indeed the interaction between the bubble's motion and its wake region distinguishes its flow field from that of the solid, that is, turbulence beyond that produced in case of the solid originates from the concurrent interaction of the bubble's oscillatory motion with the fluid motion.

ACKNOWLEDGMENTS

The first author expresses his sincere appreciation to Professor P. S. Lykoudis for his ideas on the experimental techniques of relevance to this experiment.

REFERENCES

- Clift, R., Grace, J. R. and Weber, M. E. 1978, Bubbles, Drops, and Particles, Academic Press, New York.
- Fan, L.-S. and Tsuchiya, K. 1990, Bubble wake dynamics in liquids and liquid-solid suspensions, Butterworth-Heinemann Series in Chemical Engineering, Boston (USA) isbn 0-409-90286-1
- Levich, V. G. 1962, Physicochemical Hydrodynamics, Prentice-Hall, Englewood Cliffs, NJ (USA)
- Sakakibara, J., Hishida, K. and Maeda, M. 1993, Measurement of thermally stratified pipe flow using image-processing techniques, Experiments in Fluids, 16, pp. 82-96.
- Tadaki, T. and Maeda, S. 1961, On the Shape and Velocity of Single Air Bubbles Rising in Various Liquids, Chemical Engineering, (in Japanese), 25-4, pp. 254-264.

THE SEPARATION OF LARGE-SCALE AND SMALL-SCALE TURBULENCE IN A SHALLOW MIXING LAYER

Jan Tukker and Robert Booij

*Faculty of Civil Engineering, Delft University of Technology,
P.O. Box 5048, 2600 GA Delft, The Netherlands*

1. INTRODUCTION

In turbulent shallow-water flow, transverse gradients in the horizontal velocity generate large-scale, nearly two-dimensional, horizontal turbulent structures. They give rise to some problems in modelling the turbulent flow with standard turbulence models. The essence of these problems arises from the shallowness of the flows considered, which introduces two phenomena which are not encountered in unbounded flows. On the one hand, the relatively small depth restricts the large turbulent motions to basically two-dimensional horizontal motions. In contrast to three-dimensional turbulence, two-dimensional turbulence has as characteristic properties the suppression of vortex stretching and the transfer of turbulence energy from small to large scales. This last property is known as the 'inverse energy cascade'. Consequently, these characteristic properties result in the formation of large, two-dimensional turbulent structures. On the other hand, the bottom friction gives rise to small-scale three-dimensional turbulence. This system of coexisting different turbulent length scales (Chu and Babarutsi, 1988) cannot be modelled with conventional turbulence models, because they use a single length scale and a single scalar eddy viscosity.

The large-scale turbulence and the small-scale turbulence interact with each other. The small-scale turbulence generated by the bottom friction dissipates turbulence energy of the large-scale turbulence. Besides, the presence of the large-scale, horizontal turbulent structures leads to a, relatively small, change of the local small-scale turbulence energy, and these large-scale structures convect small-scale turbulence.

Experimental research on transverse mixing layers in shallow water was started in the Laboratory of Fluid Mechanics of the Delft University of Technology last year. The aim of the present research are two-fold. First, to gain insight into the influence of the depth on the evolution of large, horizontal turbulent structures in a transverse mixing layer in a shallow free-surface flow. Second, to detect the various length scales present in the considered flow and the presumed gap between large two-dimensional structures and

small-scale three-dimensional turbulence in the turbulence energy spectrum of the considered shallow water flow.

2. EXPERIMENTAL SET-UP

Experiments were executed in a glass-bottom shallow water flume with a length of 20 m, a width of 3 m and a height of 0.20 m (Figure 1). The presence of the glass bottom makes Laser-Doppler measurements from below possible. This was chosen because the width and the shallowness of the flow preclude measurements from the flume sides. The flow chosen in this investigation is a developing transverse mixing layer between two adjacent turbulent streams with an initial flow velocity of 0.10 m/s and 0.30 m/s respectively, and an initial water depth of 0.06 meter. The width of the mixing layer δ in a cross-section is defined as the maximum-slope thickness in the following way

$$\delta \equiv \frac{U_f - U_s}{\left(\frac{\partial U}{\partial y}\right)_{\max}}$$

in which U_f and U_s are the mean longitudinal velocity of the fast stream and of the slow stream respectively. Turbulence data were obtained with a fibre-backscatter Laser-Doppler-Anemometer system, including a 4W-Argon laser and three Burst Spectrum Analyzer processors (Dantec). The optical system consists of a one-dimensional probe and a two-dimensional probe, which allow measurements of spatial correlations. The measuring system can be traversed automatically in the longitudinal (x), the transverse (y) and the vertical (z) direction. Further, the distance between the two probes can be varied automatically. With this system automatic measurements can be executed without aligning the probes between two measurements. The combination of four independent movements is required to be able to measure spatial or two-point correlations with separations in the x-, y- and z-direction. For spatial correlations over vertical separations the two-dimensional probe can also be traversed vertically by hand, independently of the position of the one-

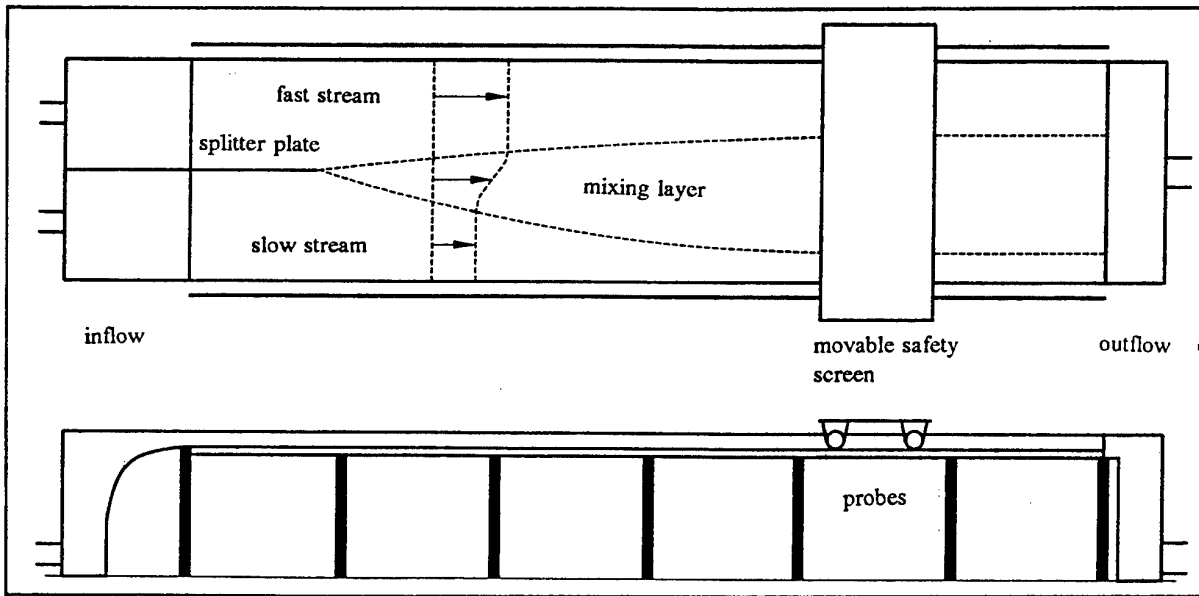


Figure 1 Top and side view of the shallow-water channel of Laboratory of Fluid Mechanics, Delft University of Technology, with a shallow-mixing layer.

dimensional probe.

To simplify aligning of the laser beams only horizontal velocities and their spatial correlations were measured in the first part of this investigation. To maximize the range of correlation distances between measuring points two different probe configurations were used. In the first configuration both probes were positioned vertically (Figure 2a), to measure correlations between horizontal velocities for the range of distances between the two measuring volumes from 0.18 m to 0.5 m. For smaller distances the dimensions of the probes necessitated another configuration. In this second configuration the 1D-probe made an angle of 30° with the vertical (Figure 2b). With this probe configuration spatial correlations with horizontal distances between the measuring points from -0.10 m. to 0.2 m were measured. The 1D-probe was positioned in such a way that a horizontal velocity component was measured.

Despite the slanting position of the 1D-probe both incident beams of this probe form a joint volume in the flow: the measuring volume. This can be realized, because both incident beams have the same angle to the bottom. Therefore, both intersecting beams remain symmetric to the optical axis of the probe. The volume of intersection is displaced both horizontally and vertically, and its orientation is changed as a result of refraction. Relationships for these displacements can be derived from the optical law of refraction. If the angle between both incident beams, θ_a , is much smaller than the angle between the beam and the bottom, the orientation of the measuring volume can be described with simple, approximated relationships. The orientation of the measuring volume is

expressed in the angle ψ_w , which is the angle between the longitudinal axis of the measuring volume and the normal to the bottom after refraction. This angle depends on the similar angle ψ_a before refraction in the following way

$$n_w \sin(\psi_w) = n_a \sin(\psi_a)$$

Here, $n_a (= 1.0)$ and $n_w (= 1.33)$ are the refractive indices of air and of water respectively. Further, the angle between both refracted beams, θ_w , obeys a similar relation

$$n_w \sin\left(\frac{\theta_w}{2}\right) = n_a \sin\left(\frac{\theta_a}{2}\right)$$

Note that the angle θ_w does not depend on the orientation angle ψ_a of the probe. Therefore, the calibration factor between the Doppler-frequency and the flow velocity is independent of the orientation angle of the probe, provided that only horizontal velocities are measured. For measurements of vertical velocities a more complex optical set-up is necessary, because in that case special devices have to be used to correct for effects of refraction. An example of such device is a water-filled prism, used in 3D-measurements by Booij and Tukker (1994).

Up to now horizontal velocities in three cross-sections of the mixing layer were measured at a distance of about 6 m, 11 m and 15 m respectively in the streamwise direction from the origin of the mixing layer, at the end of the splitter plate. Further, transverse spatial correlations between horizontal velocities were measured at $x = 15.4$ m with the reference probe in the centre of the mixing layer and with the measuring probe placed at several distances from 0 to +0.5 m off this centre in both transverse directions. Long measuring times of about 10

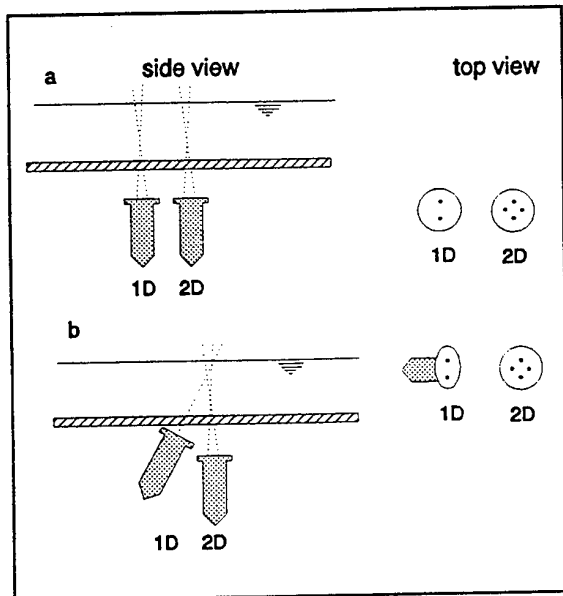


Figure 2 Used probe configurations: a. for large, and b. for small horizontal separations between the two measuring volumes.

minutes for each measuring point were used, because the largest time-scale present in the mixing layer was about 10 seconds.

3. SPATIAL CORRELATIONS

A method to investigate the presence of two different turbulent length scales is the measuring of spatial or two-point correlations, defined as

$$R_i(\vec{r}, \Delta\vec{r}) = \frac{u_i(\vec{r})u_j(\vec{r} + \Delta\vec{r})}{\sqrt{u_i^2} \sqrt{u_j^2}}$$

with u_i and u_j are a component of the velocity fluctuation vector in the reference point and in the measuring point respectively, \vec{r} is the position vector of the reference point, $\Delta\vec{r}$ is the separation vector. Transverse spatial correlations ($\Delta\vec{r} = (0, \Delta y, 0)$) between longitudinal turbulent velocities were measured far from the splitter plate (at $x = 15.4$ m) at two levels: $z/h = 0.5$ and 0.9 in shallow water with h is the water depth which is about 0.06 m (see Figure 3). In this cross-section the width of the mixing layer δ is about 13 times the water depth. For these measurements the reference point was fixed in the centre of the mixing layer and the second measuring point was placed at various positions in both transverse directions. The data was filtered with a coincidence window of 0.3 ms for spatial separations smaller than 0.2 m, or of 3 ms for larger separations. In Figure 3 the peak in the correlation for small distances (smaller than the water depth) represents the small-scale turbulence, which is superposed on the

large-scale turbulence apparent over all distances. The sharpness of the small-scale peak in the correlation makes it possible to extrapolate the large-scale part of the correlation to zero-distance (Townsend, 1976), and so to separate the turbulence energy and the spatial correlation in a large-scale contribution R_{H_i} and in a small-scale contribution R_{h_i} . A measure of the transverse dimensions of the large-scale structures is the integral length scale L , defined here as the integral of the entire large-scale contribution in the transverse spatial correlation function, R_{H_i} , in the following way

$$L = \int_{-\infty}^{\infty} |R_{H_i}| d(\Delta y)$$

Here the absolute value of the correlation coefficient is used, because a negative correlation coefficient at a certain distance means coherence over this separation in the flow. Therefore, this correlation coefficient should contribute positively to the integral scale. The measured spatial correlations functions presented in Figure 3 yield about the same integral length scale L of the large-scale structures of 0.6δ for both levels, which confirms the idea of the large-scale structures as (quasi-)two-dimensional, horizontal structures.

4. TIME-CORRELATIONS

Another method in which the presence of large-scale turbulence can be observed is the time-correlation (or autocorrelation) of a velocity signal, defined as

$$R_i(\tau) = \frac{u_i(t)u_i(t+\tau)}{u_i^2}$$

Time-correlations of turbulent transverse velocities at four vertical elevations in the centre of the mixing layer in the cross-section at $x = 15.4$ m are presented in Figure 4. These autocorrelations were calculated with an algorithm based on the slotting technique (Tummers, 1994), because the velocity signals were sampled nonequidistantly in time. The peaks in these autocorrelations around the origin (say, below 0.5 s) represent the small-scale turbulence, which is superposed on the large-scale turbulence apparent over all time differences.

5. TIME-SPACE-CORRELATIONS

Due to the differences in convection velocity the large-scale, horizontal structures are stretched in flow direction. A sketch of a stretched large-scale structure in a mixing layer is presented in Figure 5. The spatial orientation of the large-scale structures can be measured by the means of spatial correlations with both a transverse shift and a streamwise shift between the measuring points. Measuring a whole horizontal field with two-point measurements is time-consuming. Therefore, a streamwise spatial shift is simulated by a time-shift of a measured signal, multiplied

with the mean convection velocity. This is possible, if the passing time of a structure is much smaller than the life-time of the structure. In this case the turbulence structure can be considered as been 'frozen' turbulence. This 'frozen-turbulence' hypothesis can be applied in our considered shallow mixing layer flow, because the life-time of the large-scale structures is of the order of magnitude of a few minutes, while the passing time is of the order of magnitude of 10 seconds.

Our spatial correlation measurements consist of pairs of measuring points with the reference probe in the centre of the mixing layer and the other measuring point placed at different transverse positions at the same level. For each spatial shift Δy the correlation function $R_{rr}(\Delta y, \tau)$ was calculated as function of a time-lag τ ,

$$R_{rr}(\Delta \vec{r}, \tau) = \frac{\overline{u_i(\vec{r}, t) u_j(\vec{r} + \Delta \vec{r}, t + \tau)}}{\sqrt{u_i^2} \sqrt{u_j^2}}$$

To this end the measured velocity time series were filtered with a filter-frequency of 12.5 Hz and resampled with a sample frequency of 25 Hz, because the raw data was randomly sampled and we were mainly interested in the spatial orientation of the large-scale structures. The correlation coefficients were calculated by shifting the time axis of the velocity signal measured by the second measuring probe was shifted. The maximum (absolute)

value of the correlation function $R_{rr}(\Delta \vec{r}, \tau)$ as a function of time-lag τ at a certain separation will be related to a positive time-lag for spatial separation in the positive transverse direction (in the direction of the fast stream), and to a negative time-lag for separation in the opposite direction. First we discuss the measured correlations between two longitudinal velocity components. For this case Figure 6 shows the time-lag at which the maximum correlation occurs, measured at $x = 15.4$ m and $z/h = 0.5$, where Δy varies between 0 and about 0.5 m. These data show clearly that the time shift increases with the transverse spatial shift. Furthermore, the data follows a line corresponding to an orientation angle of 20° with the x-axis of the flow. This means that the averaged longitudinal dimension of the large-scale structures is about three times its transverse dimension. This indicates the importance of the convective stretching of the horizontal, large-scale structures. Further, for spatial lags smaller than 0.03 m ($=1/2h$) the maximum correlation coefficient coincides with the correlation coefficient at zero time-lag, because in this region the small-scale turbulence dominates the correlation coefficients. At larger distances the contribution of the small-scale turbulence to the correlation diminishes, and here the large-scale structures dominate the correlation coefficients

The values of the maximum correlation coefficients are presented in Figure 7, together with the correlations

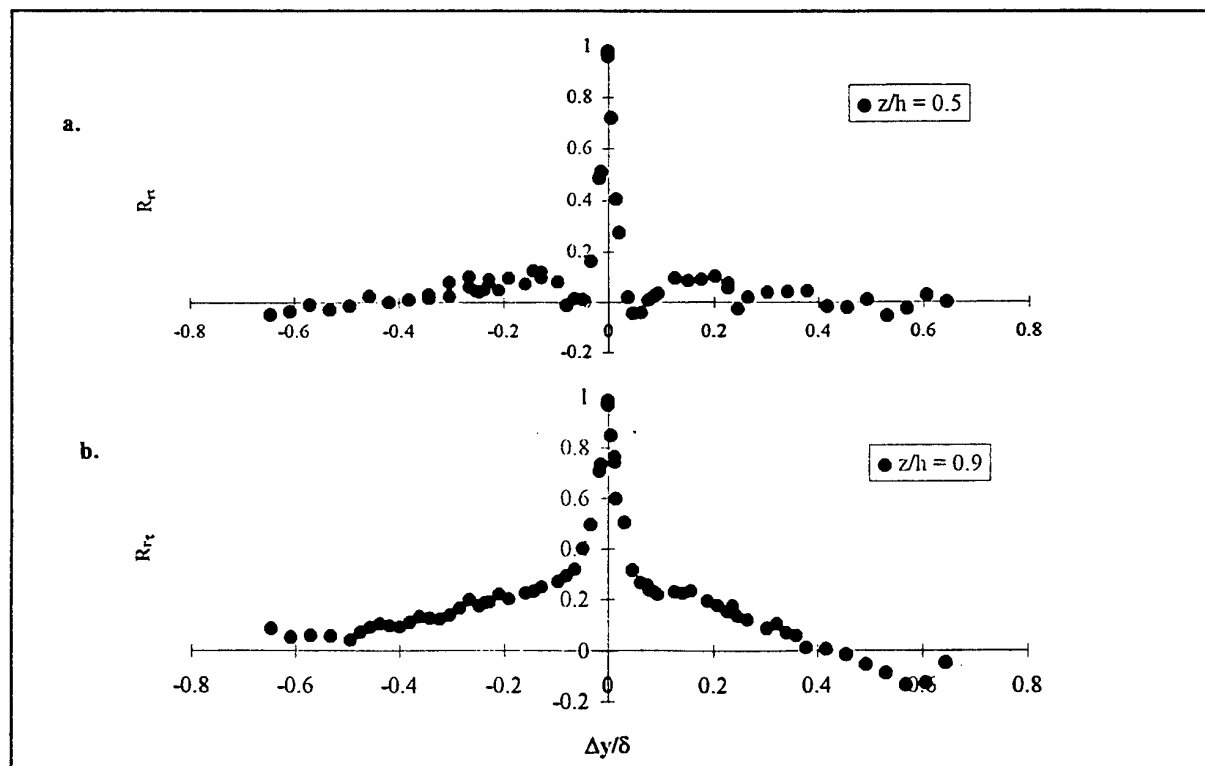


Figure 3 Transverse spatial correlation function between longitudinal velocities $R_r(\Delta y)$, as function of $\Delta y/\delta$ ($\delta = 0.79$ m), measured at $x = 15.4$ m. and a. $z/h = 0.5$, and b. $z/h = 0.9$.

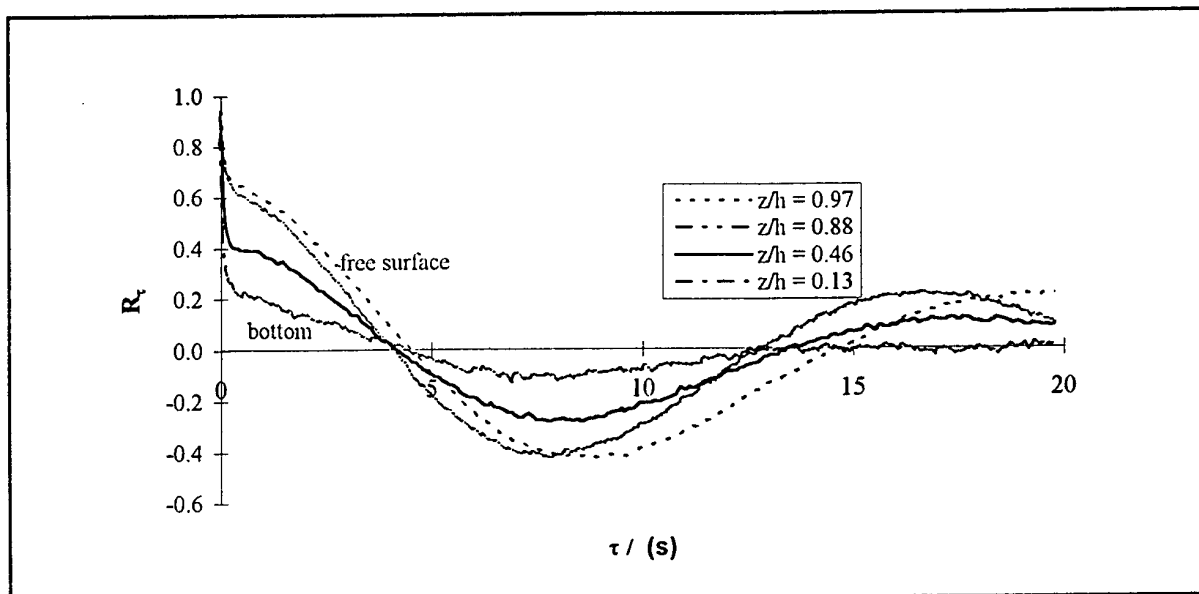


Figure 4 Time-correlations of transverse velocity component at four elevations, in the centre of the mixing layer in the cross-section at $x = 15.4$ m.

without time shift. For small spatial lags (say smaller than $\frac{1}{2}h$) these correlation functions coincide. For all spatial lags the maximum time-shifted correlation function remains positive, whereas the unshifted correlation function is negative for spatial shifts of about 0.05 m and larger than 0.35 m. Therefore, the integral length-scale obtained from the shifted correlation function will be larger than the length-scale of the unshifted correlation function. Hence the measurement of mere (unshifted) transverse correlation functions yields a too small transverse integral length scale which means an underestimation of the transverse extension of the large-scale structures.

Figure 8 shows measured correlation coefficients between longitudinal and transverse velocity components for positive spatial shifts, measured at $x = 15.4$ m and $z/h = 0.5$. Here, the longitudinal velocity was measured in the

centre of the mixing layer and the transverse velocity at a position shifted in the direction of the fast stream. These negative correlations are dominated by the horizontal large-scale structures for spatial shifts larger than 0.06 m ($=h$). This means that this correlation function is about constant for spatial shifts up to about 0.35 m and its magnitude decreases for larger spatial shifts. Figure 8 shows the correlation function without time shift and with maximum magnitude after shifting in time. For positive spatial shifts smaller than 0.35 the time-unshifted correlation coefficients are about -0.11 and the time-shifted coefficients are about -0.17.

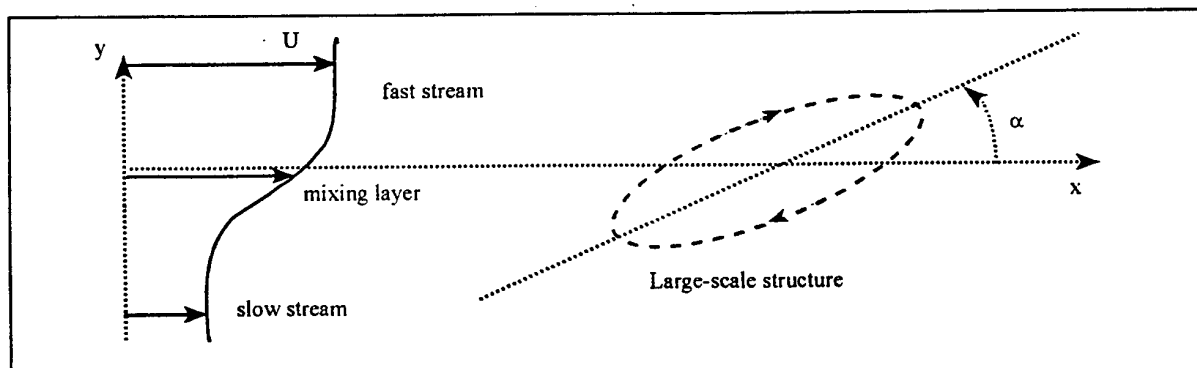


Figure 5 A sketch of a stretched large-scale turbulence structure with the orientation angle α .

6. TURBULENCE INTENSITIES

The velocity fluctuations in the shallow mixing layer, u_i , consists of two contributions: a contribution u_l of the large-scale structures and a contribution u_s of the small-scale turbulence. In case of distinct separation of scales the large-scale and the small-scale velocity fluctuation will show hardly any correlation. In that case the variance of the velocity fluctuations is the sum of the variances of u_l and of u_s ,

$$\overline{u_i^2} = \overline{u_l^2} + \overline{u_s^2}$$

The total variance follows directly from the measured velocity time series. The large-scale and the small-scale can be determined in various manners. One method is the extrapolation of the correlations function for large time-lags or large spatial shifts to zero time-lag or zero spatial shifts (discussed above). Another method is to estimate the small-scale contribution from measurements outside the mixing layer where large-structures are absent. Then the large-scale contribution is the difference between the measured total variance and the estimated small-scale contribution. By the way, the small-scale contribution can also be estimated with a general relation for uniform turbulent shallow free-surface flows, which for example is presented by Nezu and Nakagawa (1993). Both methods were applied to determine the turbulence intensity of the large-scale structures, which is the square root of the corresponding variance.

The measured turbulence intensity of the large-scale turbulence is of the order of magnitude of the transverse-shear velocity of the mixing layer, u_{sh} , which is defined as follows

$$u_{sh} \equiv \sqrt{\frac{\tau_t}{\rho}}$$

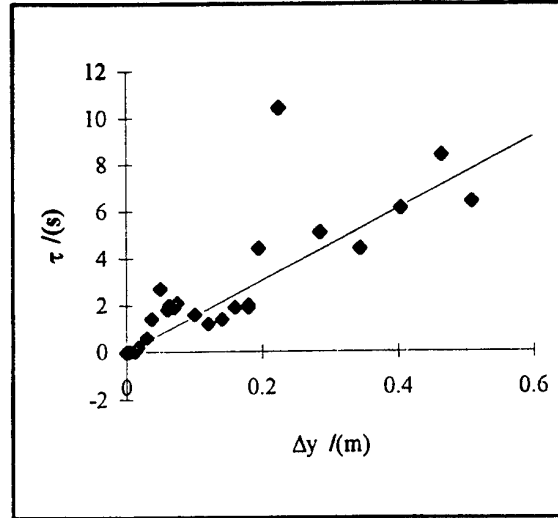


Figure 6 The time-lag τ corresponding to maximum correlation between longitudinal velocity components, at $x = 15.4$ m and $z/h = 0.5$. The line corresponds to an orientation angle of 20° .

with τ_t the maximum transverse shear stress in a cross-section, and ρ the density of fluid. This transverse shear stress τ_t is proportional to ΔU^2 ,

$$\tau_t = \chi \rho (\Delta U)^2$$

in which ΔU is the velocity difference between the two ambient streams at both sides of the mixing layer, and χ a proportionality constant. The value of this constant χ is about 0.01 for free mixing layers (in sufficiently deep water), with which the transverse-shear velocity u_{sh} is about

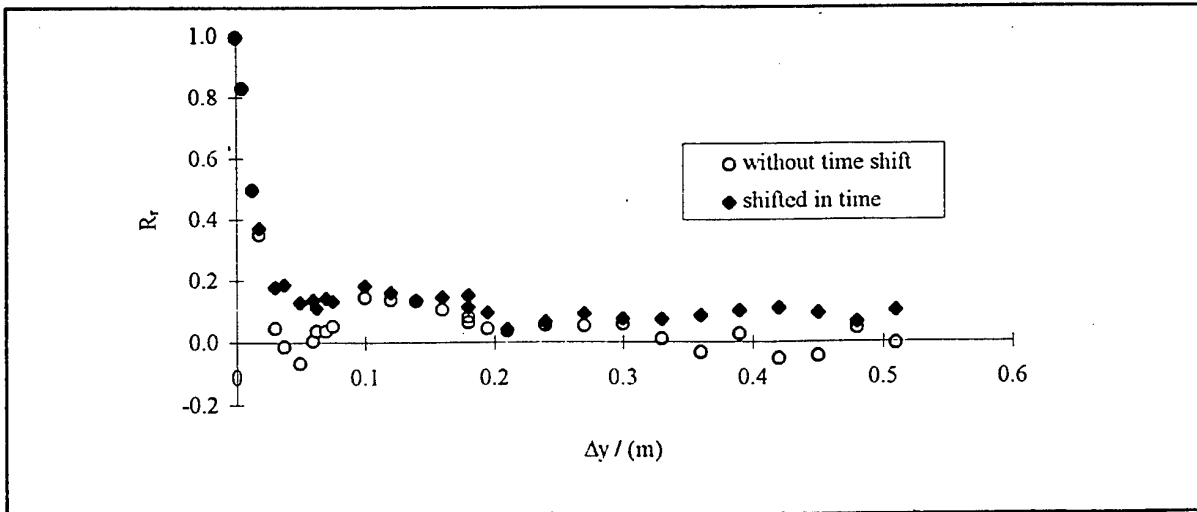


Figure 7 Spatial correlations between longitudinal velocity components as function of transverse separation, \circ without time shift, \bullet maximum correlation coefficient shifted in time ($x = 15.4$ m; $z/h = 0.5$).

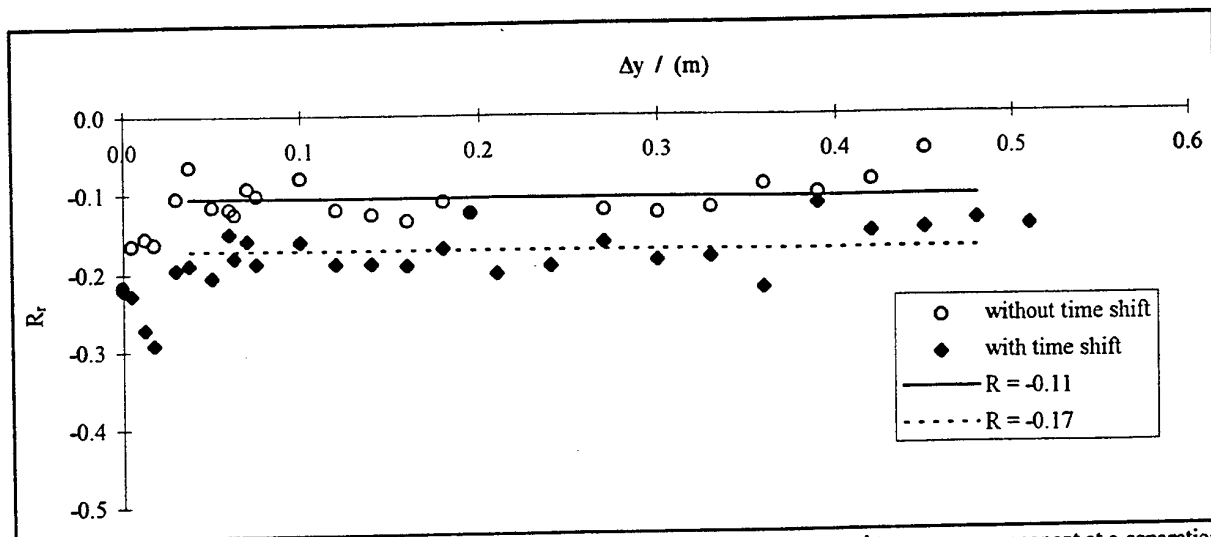


Figure 8 Spatial correlations between longitudinal velocity component in layer centre and transverse component at a separation Δy , \circ without time shift, \blacklozenge maximum correlation coefficient shifted in time ($x = 15.4$ m; $z/h = 0.5$).

$\Delta U/10$. In turbulent uniform free surface flows the intensity of the small-scale turbulent fluctuations is analogously of the order of magnitude of the friction velocity u_* , which depends in a similar way on the bottom friction.

In shallow mixing layers the turbulence intensity of the large-scale fluctuations decreases in the direction of flow, because of the streamwise decrease of the velocity difference across the mixing layer, and the dissipation due to the bottom friction. In shallow-water flows above a horizontal bottom the small-scale turbulence, generated by the bottom friction is responsible for a decrease of the momentum of the mean flow. The influence of the bottom friction is compensated by a longitudinal slope of the free surface resulting in a longitudinal pressure gradient. In shallow mixing layers the transverse variation of the longitudinal slope will be small, because the transverse slope of the free surface is much smaller than the longitudinal one. However, the bottom friction of the fast stream is much larger than the bottom friction of the slow stream. Hence the fast stream is decelerated and the slow stream accelerated, resulting in a streamwise decrease of the velocity difference ΔU . Furthermore, the small-scale turbulence slows down the large-scale turbulence structures, in this way dissipating energy from the large-scale structures. The importance of this energy loss increases with the scale of the structures.

Both phenomena result in a streamwise decrease of the intensity of the large-scale velocity fluctuations. This was confirmed with our measurements which shew a decrease of the maximum intensity of the longitudinal large-scale fluctuations. In the first part of the shallow mixing layer, up to 11 m from the origin of the mixing layer, the maximum intensity scaled with the local velocity difference remains constant at about 0.148, measured at $z/h = 0.8$. This confirms the suggestion that the intensity of the large-

scale structures mixing layer adapts to the local velocity difference. The value of this scaled maximum intensity is smaller than the value 0.18 measured in two-dimensional free mixing layers (Wynanski and Fiedler, 1970). Beyond 11 m this scaled intensity decreases to 0.086 at $x = 15.4$ m and $z/h = 0.8$. The decrease of the scaled intensity between $x = 11.1$ and 15.4 m is the result of the transfer of turbulence energy from the large-scale structures to the small-scale turbulence by the bottom friction.

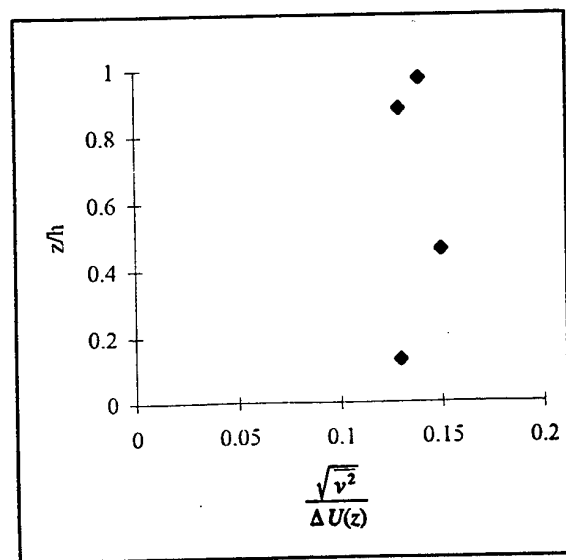


Figure 9 Scaled turbulence intensity of transverse velocity components of large eddies, varies over depth. Measured in the centre of the mixing layer at $x = 15.4$ m.

Further, a vertical distribution of the scaled turbulence intensity of the large-scale, transverse velocity component, v , is shown in Figure 9. Here the turbulence intensity is scaled with the slightly depth-dependent velocity difference across the mixing layer, $\Delta U(z)$:

$$\frac{\sqrt{v^2}}{\Delta U(z)}$$

This data was measured in the centre of the mixing layer at $x = 15.4$ m. This scaled turbulence intensity is nearly constant in the mixing layer, in accordance with the notion of quasi-two-dimensional structures. The scaling with the depth-dependent velocity difference $\Delta U(z)$ corrects for the influence of the bottom friction. The vertical profile of the intensity of this large-scale turbulence corresponds to the vertical velocity profile of the mean flow as is expected when both are slowed down by the bottom friction through small-scale turbulence. The contribution of the large-scale structures to the work done by the bottom friction and hence to the production of small-scale turbulence is small in shallow water. Hence, the intensity of small-scale turbulence depends on the local depth-averaged velocity U . The measured distributions of the small-scale turbulence intensity over depth agree well with the expressions presented by Nezu and Nakagawa (1993) for uniform, free surface flows.

7. CONCLUSIONS

- In a turbulent shallow mixing layer with a layer width much larger than the water depth distinctly separated scales of turbulence are present.
- The large-scale turbulence motions have a horizontal, two-dimensional structure, and the small-scale turbulence motions have a three-dimensional structure

- Time-correlations and spatial correlations can both be used to measure the distribution of energy over the large-scale and the small-scale turbulence.
- Correlation techniques are useful tools to measure the structure of the large-scale turbulence.

REFERENCES

- Booij, R. & Tukker, J. 1994, 3-Dimensional Laser Doppler measurements in a curved flume, Proceedings of Seventh International Symposium on Applications of Laser Techniques to Fluid Mechanics, Lisbon, pp. 28.5.1-8.
- Chu, V.H. & Babarutsi, S. 1988, Confinement and Bed-Friction Effects in Shallow Turbulent Mixing Layers, Journal of Hydraulic Engineering, vol. 114, no. 10, pp. 1257-1274.
- Nezu, I & Nakagawa, H. 1993, Turbulence in Open-Channel Flows, IAHR Monograph series, Rotterdam.
- Townsend, A.A. 1976, The structure of turbulent shear flow, second edition (first edition: 1956), Cambridge University Press, Cambridge.
- Tummers, M.J. Passchier, D.M. and P.A. Aswatha Narayana 1994, Three-component LDA measurements of mean turbulence quantities, time- and spatial correlation functions in the wake of a flat plate in an adverse pressure gradient, Proceedings of Seventh International Symposium on Applications of Laser Techniques to Fluid Mechanics, Lisbon, pp. 25.1.1-7.
- Wynanski, I. & Fiedler, H.E. 1970, The two-dimensional mixing region; Journal of Fluid Mechanics, vol. 41, part 2, pp 327-361.

DAMPING OF A VORTEX RING IN A STRATIFIED FLUID

D.R. McCluskey[†], T. S. Laursen[‡], J. J. Rasmussen[‡] and B. Stenum[‡]

[†]Dantec Measuring Technology A/S, Tonsbakken 16-18, DK-2740 Skovlunde, Denmark

[‡]Risø National Laboratory, Optics and Fluid Dynamics Department, DK-4000 Roskilde, Denmark

ABSTRACT

The temporal evolution of the flow field produced by a vortex ring ejected horizontally into a stratified fluid has been studied in a vertical cross-section by Particle Image Velocimetry. The formation of a propagating vortex ring in a stratified fluid was found to be similar to that in a homogeneous fluid. In the stratified fluid, the propagation speed of the vortex ring is initially slowed due to formation of secondary vortical structures. Later the motion of the vortex ring couples to internal waves, energy is radiated away from the ring and the propagation speed of the vortex ring further decreases. Finally, the vortex ring breaks down and the fluid flow collapses into a horizontal motion.

1. INTRODUCTION

In stratified fluids, such as salt water with a salinity which increases with depth, vertical motion is suppressed by the effective gravity. Thus forcing the flows to become two-dimensional. In two-dimensional flows, the formation of coherent vortical structures is supported by the so-called inverse energy cascade and almost any disturbance to the fluid self-organises into vortical structures. In three-dimensional flows, the energy cascade to smaller scales tends to break down coherent structures and vortical structures have to be formed directly as the result of well defined external forcing. Nonetheless, vortex rings are known as long lived coherent structures in three-dimensional flows (e.g. Batchelor 1967).

Vortex rings are well-known coherent structures and have been studied for more than a century both for fundamental and engineering interest (Batchelor 1967, Shariff 1992, Maxworthy 1977). Vortex rings can be described as a ring core with a concentrated vorticity surrounded by a volume with a decaying vorticity (Maxworthy 1977). In a homogeneous fluid, the whole structure propagates at an almost constant velocity along

the axis of symmetry. This propagation induces movements in the ambient fluid. According to a simplified description, in the reference frame of the moving vortex ring, the fluid elements inside the vortex ring structure follow closed streamlines while the streamlines of fluid outside the vortex ring are open (Batchelor 1967). In more physical descriptions, fluid exchange between the vortex ring and the ambient fluid must be taken in account (Shariff 1992).

The damping of a three-dimensional vortex ring ejected horizontally into a stratified fluid has been studied by means of a shadowgraph technique (van Atta and Hopfinger 1989). In this paper, the dynamics of this damping process are studied quantitatively by acquiring a time sequence Particle Image Velocimetry (PIV) data sets. PIV studies of both the internal structure and the evolution a vortex ring flow in a homogeneous fluid have been obtained previously (McCluskey et al. 1995).

2. EXPERIMENTAL SET-UP

The experiments were carried out in a glass tank with a length of 800 mm, a width of 500 mm and a depth of 500 mm. The stratified fluid - salt water with a salinity which increased with depth - was produced by means of two reservoirs, one filled with salt water and the other with fresh water. While pumping water from the salt water reservoir into the experimental tank, the salt water in the reservoir was continuously mixed with water from the fresh water reservoir. In the experimental tank, the incoming water was gently layered on top of previous layers by a floating spreading device. The experimental tank was filled to a depth of about 400 mm with stratified water. The stratification measured by a refractometer was found to be linear with a buoyancy frequency of

$$N = \sqrt{-(g/\rho)(d\rho/dz)} = 1.47 \text{ Hz}.$$

Vortex rings were produced by a gravity induced horizontal inlet from a water column. The water column

was contained in a vertical tube connected to a horizontal tube section, with an inner diameter of 44 mm, via a 90 degree bend. During the experiments, the axis of the horizontal tube section was placed about 110 mm below the surface of the stratified water, close to the mean density of the seeding particles (see below). The surface was found not to influence the damping of the vortex ring significantly. Before inlet from the water column, water was sucked into the tube ensuring that the density of the fluid in the inlet corresponded to the density of the stratified water. A schematic of the set-up is shown in figure 1.

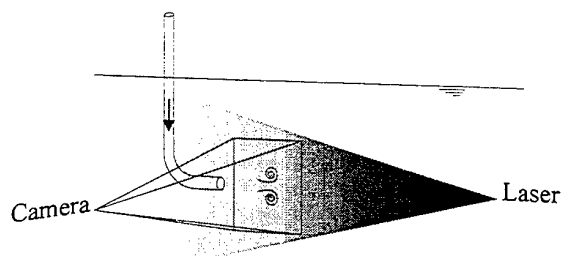


Figure 1. Schematic of the experimental set-up.

The duration of the inlet was defined by a timer valve and the inlet velocity of the water puff controlled by an air flow resistor, consisting of a small tube with an inner diameter of 3 mm and a length of 30 mm. An opening time of 0.4 s for the valve results in inlet of a water column of 40 mm from an initial level of 150 mm above the tank level. The speed of the water column was almost constant during inlet. The initiation of the experiments ($t = 0$) is defined as the opening of the valve controlling the inlet.

The velocity fields were measured by a FlowMap PIV system (McCluskey et al 1995). A 5W argon-ion laser beam was scanned through a section of the fluid flow by means of a polygon scanner. A laser shutter ensured each frame of the PIV camera was exposed to only a single sweep of the laser beam. A cross-correlation camera was used since this unambiguously provides velocity direction as well as magnitude. The illumination system and camera were controlled automatically by a synchronisation board in the PIV 2000 processor which processed images into vector results in real-time. The size of the interrogation area and magnification were selected so that the spatial resolution of velocity structures was around 4.5 mm. Successive vector maps were captured at intervals of 0.16 to 0.32 s and covered an area of approximately 9 cm x 6 cm. The camera was moved to study the flow field at various distances downstream of the inlet pipe. The stratified water was seeded with polycrystalline polymer particles (Optimage PIV Seeding Powder) with a mean diameter of 30 μm and a density of $\approx 1.03 \times 10^3 \text{ kg/m}^3$.

To assess the effects of stratification, vortex ring formation and propagation were studied both in a stratified and in a homogeneous (fresh water) fluid. The experimental method used in the homogeneous fluid case was a dye study. Fluorescent dye was added to the water inside the tube and the flow field illuminated by a light sheet produced by a slide projector.

3. RESULTS AND DISCUSSION

The velocity fields for the vortex rings ejected horizontally in the stratified fluid were measured in the vertical cross-section through the axis of the vortex ring.

3.1 Vortex ring formation

Figure 2 shows a sample of the time sequence covering the generation of the vortex ring. Vorticity maps have been calculated from four different vector maps. The vorticity component is perpendicular to the vertical measuring plane. This corresponds to the azimuthal component in cylindrical co-ordinates.

At $t = 0.64 \text{ s}$ (figure 2 a), the formation of the vortex ring has started and vorticity is building up in and around the vortex ring core. The generation of vorticity is a result of rolling up of the out-coming fluid column and a simultaneous entrainment of ambient fluid (McCluskey et al 1995, Nitshe and Krasny 1994). Initially, the formation of the vortex ring in the stratified fluid seems to be similar to that in a homogeneous fluid. The vorticity contours are approximately circular.

At $t = 0.96 \text{ s}$, as well as the vortex ring, additional vorticity is observed. This is located at the rear of the vortex ring, close to the propagation axis. From the homogeneous flow studies, it was observed that the water column oscillated around its final height and one or two small additional vortex rings are formed by these oscillations. The additional rings are significantly smaller and weaker than the primary vortex ring.

Later (figure 2 c), the relatively weak additional vortex ring moves through the orifice of the primary vortex ring. When in front of the primary vortex ring, the diameter of the additional vortex ring increases as a result of the outward movement of flow in front of the primary vortex ring.

Finally, the additional vortex ring is shed off as a weak structure behind the primary vortex ring. A similar interaction - known as "leap-frogging" - between two identical vortex rings has been reported (Yamada and Matsui 1979). Simultaneous to the increase of the diameter, vorticity signed oppositely to the additional vortex ring is generated ahead of this ring (figure 2 d), as a result of the reduced gravity force acting against the vertical motion.

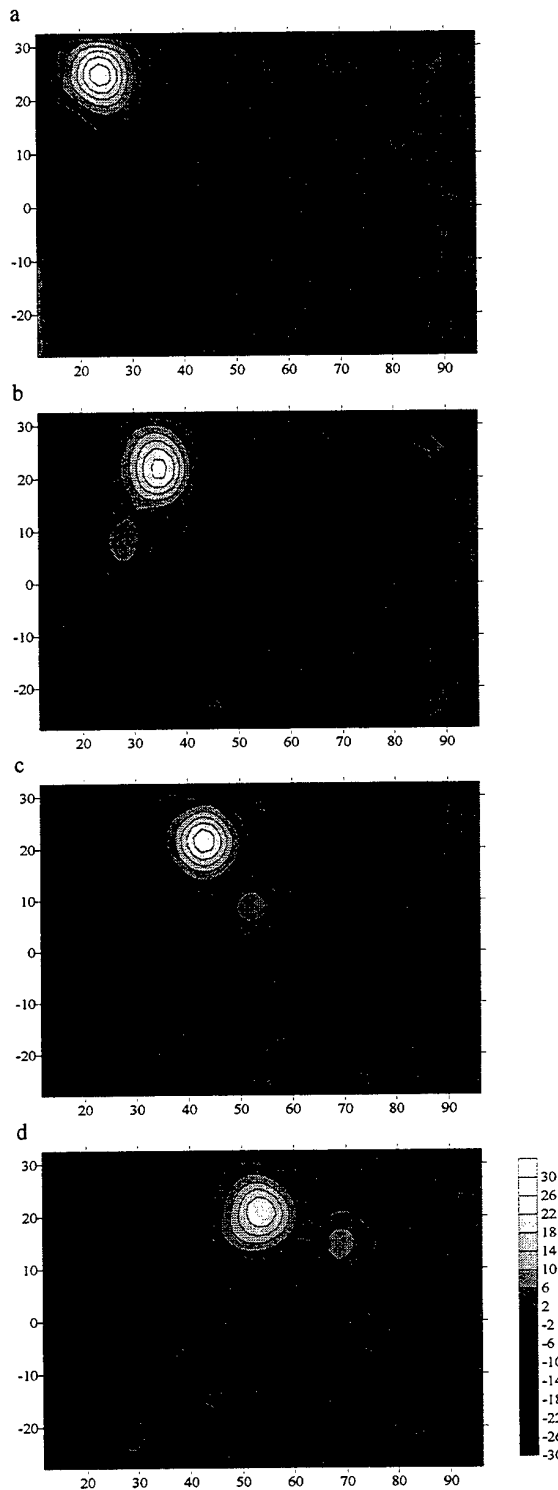


Figure 2. Sequence showing the vorticity component (s^z) perpendicular to the vertical measuring plane at $t = 0.64$ s (a), $t = 0.96$ s (b), $t = 1.28$ s (c) and $t = 1.60$ s (d).

3.2 Vortex Propagation

Figure 3 shows the propagation distance of a vortex ring both in a stratified and in a homogeneous fluid. In the stratified fluid the propagation distance was determined as the mean value of the distance from the nozzle edge to the two *extrema* observed in the vorticity contour. In the homogeneous fluid case the core was located by means of the characteristic dye spirals (McCluskey et al. 1995).

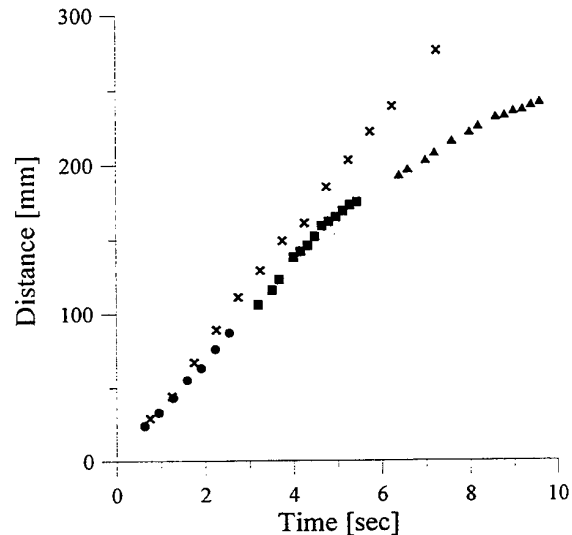


Figure 3. The propagation distance for identical vortex rings ejected into stratified (closed circles, squares and triangles) and homogeneous fluid (crosses) versus time. The circles, squares and triangles indicate different runs and camera positions.

The evolution of the flow field of a vortex ring in the stratified fluid was found to be qualitatively reproducible. In figure 3 it is seen that the propagation distance for three different experimental runs follows the same curve. As discussed, the formation of a propagating vortex ring in the stratified fluid is almost similar to its formation in a homogeneous fluid. Initially, the propagation speed is slightly slower than in a homogeneous fluid. From 140 mm downstream of the nozzle ($t \approx 4.2$ s), the vortex ring propagation in the stratified fluid is significantly lower than in the homogeneous fluid. A further deceleration of the propagation of the vortex ring is observed at $t \approx 9$ s.

This is in sharp contrast to the homogeneous case where the vortex ring propagates at a steady speed after its formation. (The formation is completed after the vortex ring has translated a distance of about five times its radius (Saffman 1975) corresponding to about 100 mm.)

3.3 Internal waves

About 100 to 150 mm downstream some vortical structure inside, slightly ahead of the vortex ring is again observed (figure 4 b below). This is most likely a result of the stratification since no vortical structure is observed in the homogenous fluid were only some oscillations in the drifted distance can be seen (figure 3). The secondary vortical structure may be formed as a result of the effective gravity acting against the vertical motion in the stratified fluid. This baroclinic generation of secondary vorticity explains the initial slowing of the vortex ring propagation (van Atta and Hopfinger 1989).

Figure 4 shows the velocity fields in the co-moving frame at $t = 1.60, 4.32$ and 7.60 s. In the moving frame the fluid parcels oscillate as they pass the vortex ring. Similar behaviour is observed when fluid parcels pass a bottom perturbation. Such a perturbation may excite internal waves downstream of the flow. Internal waves generated behind an obstacle are known as "lee waves" (Kundu 1990).

The dispersion relation for internal waves in a drifting, stratified fluid induced by a bottom perturbation is:

$$U = \frac{N}{\sqrt{k^2 + m^2}}$$

where U is the flow speed
 k is the horizontal wavenumber
 m is the vertical wavenumber, and
 N is the buoyancy frequency.

With the horizontal wavenumber given as $k = 2\pi/\lambda$, the dispersion relation can only be fulfilled when $U/\lambda < N/2\pi$, where λ is the wavelength of the perturbation induced by the obstacle. When the dispersion relation is unfulfilled, excitation of internal waves is unexpected (Kundu 1990).

For the given situation, the speed is the propagation velocity of the vortex ring (in the laboratory frame) and the largest possible perturbation wavelength can be assumed to be twice the width of the vortex ring. In this description, the movements of the fluid parcels passing the vortex ring corresponds to half a period. Taking the width of the vortex ring as the distance between the stagnation

points in front of and behind the vortex ring (figure 4 a), λ is about 80 mm and the propagation velocity, v_d , of the vortex ring (determined as local linear fit) is 33 mm/s at $t = 1.60$ s. Thus, $U/\lambda \approx 0.41 \text{ s}^{-1}$, which is significantly larger than $N/2\pi \approx 0.23 \text{ s}^{-1}$ and so generation of internal waves is unexpected in this region.

At $t = 4.32$ s (figure 4 b), the propagation velocity of the vortex ring has decreased to about 28 mm/s while the width of the whole vortical structure (including the secondary structure) has increased to about 46 mm. Here, $U/\lambda \approx 0.26 \text{ s}^{-1}$, thus the dispersion relation is nearly fulfilled and excitation of internal waves is expected. The internal waves may radiate energy away from the vortex ring resulting in a further slowing of the vortex ring propagation as observed in figure 3 (at $t \approx 4$ s). In figure 4 c, at $t = 7.60$ s, the propagation velocity of the vortex ring has decreased to 17 mm/s while the size of the vortical structure has reduced to about 38 mm, indicating that the coupling to the internal waves is maintained.

The internal waves can be seen in figure 5 which shows contour plots of the vorticity component perpendicular to the measuring plane at $t = 8.0, 9.0, 10.0$ and 11.0 s. In the vorticity maps, the internal waves show up as vorticity concentrations along lines of constant phase associated with the internal waves. As expected, initially the internal waves are generated behind the primary vortex ring (figure 5 a). Later waves are also emitted ahead of the vortex ring, and the vortex ring structure breaks down (figure 5 b and c).

At the break up of the vortex ring around $t \approx 9$ s, the propagation velocity of the remaining structure is again reduced (figure 3). According to the dispersion relation, the reduced propagation velocity of the wave generating structure is balanced by an increase of the vertical wavenumber m , resulting in more horizontally directed constant phase lines and hence vorticity contours as seen in figure 5. Finally, all vertical motion seems to collapse and the flows moves only in the horizontal direction. At this stage, the residual motion de-couples from the internal waves since their generation by vertical movements becomes less efficient.

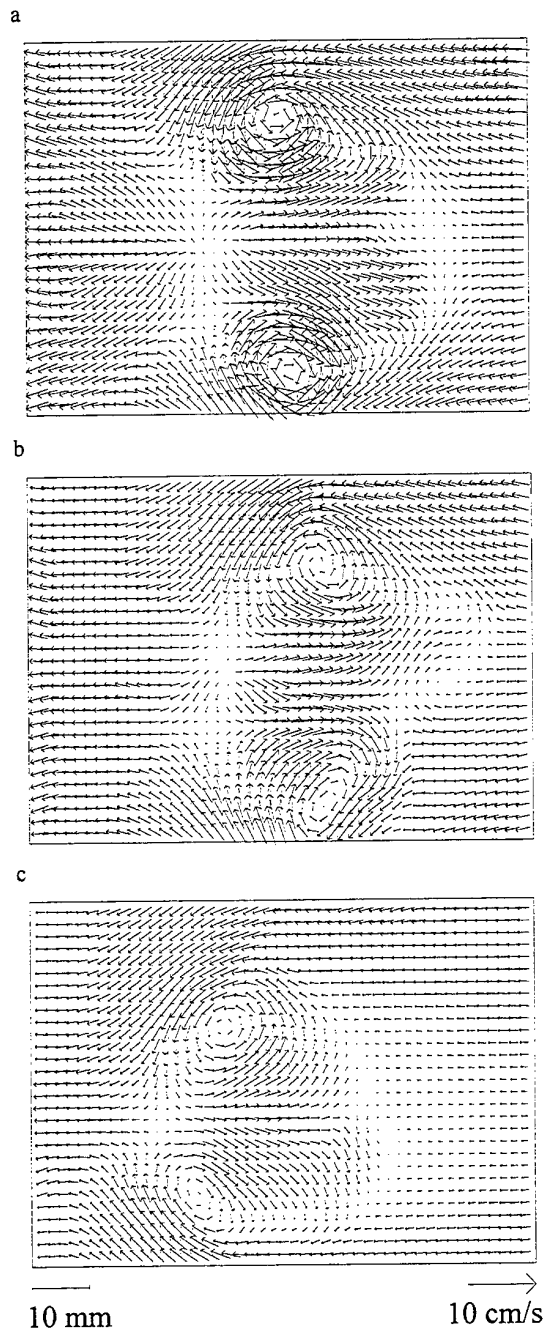


Figure 4. The velocity fields in the co-moving frame at $t = 1.60$ s, $t = 4.32$ s and $t = 7.60$ s. The velocity fields were measured at different runs and camera positions. a) 10 - 98 mm, b) 96 - 184 mm and c) 184 - 262 mm downstream.

3.4 Vortex ring collapse

During the damping process, the size of the vortex ring was found to be reduced (figure 2 and 5). This is probably a result of a vertical compression by the effective gravity and radiation of energy via the internal waves reducing the kinetic energy of the rotating ring structure.

Preliminary studies (de Nijs 1994) have shown that the time scale for the collapse of a vortex ring in a stratified fluid is shorter than the time scale for the collapse of a turbulent jet (Fonseka et al. 1995). This may be a result of the efficient coupling to internal waves of the whole vortex ring structure propagating through the stratified water. When the motion has collapsed in a horizontal motion, the preliminary studies (de Nijs 1994) showed that a dipole is formed. This dipole continues to propagate horizontally with a circulation much less than that of the initial vortex ring. The formation of a dipole seems to be similar to that after injection of a turbulent jet in a stratified fluid (van Heijst and Flor 1989).

4. CONCLUSION

The evolution of the flow field of a vortex ring ejected horizontally into a stratified fluid has been studied. Two-dimensional vector maps were measured by a real-time PIV system in the vertical cross-section. During the formation of vortex rings, small additional vortex rings were induced by oscillations of the water column around its final height and these were resolved by the PIV measurements. The formation of vortex rings in the stratified fluid was almost similar to that in a homogeneous fluid. In the stratified fluid the propagation of the vortex ring was slowed. Initially, the energy loss of the propagation of the vortex ring seems mainly to be caused by formation of secondary vortical structures. After propagating about seven times its radius, the propagation of the vortex ring is further slowed due to coupling to internal waves. This coupling is a result of the reduced propagation velocity as well as a broadening of the vortex ring structure. At this stage, additional energy is radiated away via the internal waves. Gradually, the primary vortex ring loses energy and the motion collapses into a horizontal motion. Subsequently, a plane dipole is formed. This dipole continues to propagate horizontally at a velocity which is much less than that of the initial vortex ring.

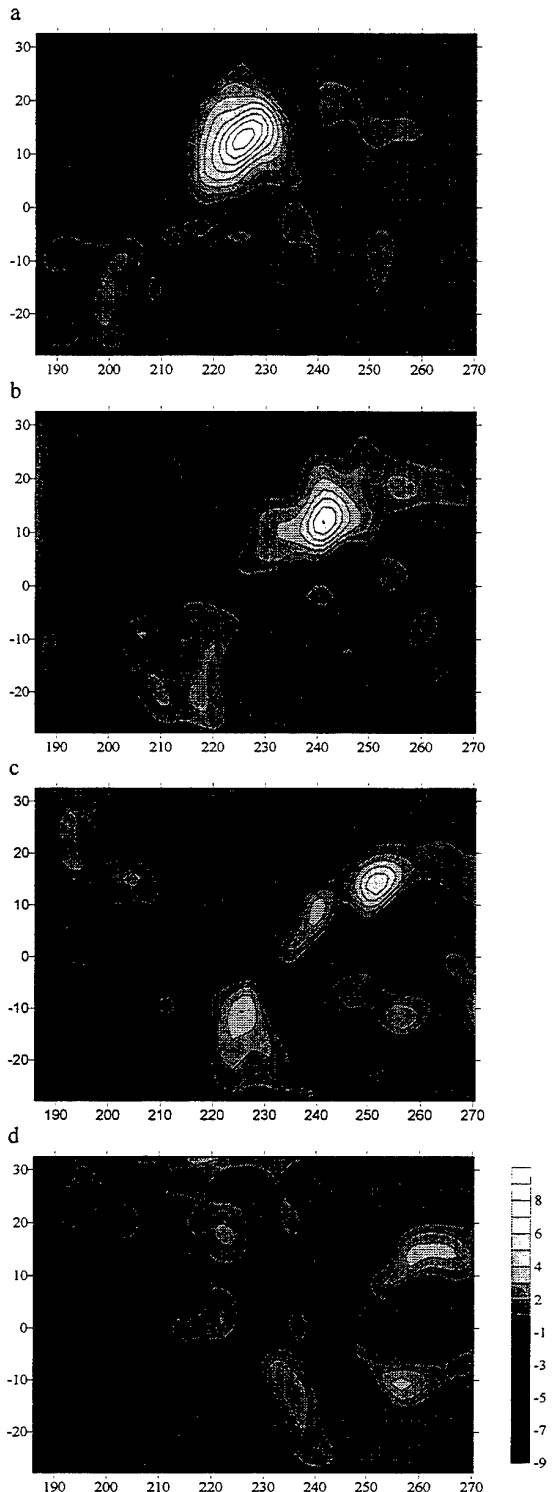


Figure 5. Contour plots of the vorticity component (s^{-1}) perpendicular to the measuring plane during the slowing down of the vortex ring after coupling to internal waves. a) $t = 8.0$ s, b) $t = 9.0$ s, c) $t = 10.0$ s and d) $t = 11.0$ s.

5. ACKNOWLEDGEMENTS

We gratefully thank the Department of Combustion, Risø National Laboratory for making laboratory and laser facilities available, Bjarne Sass for technical assistance during the measurements and GertJan van Heijst, Eindhoven University of Technology, for fruitful suggestions and discussions.

6. REFERENCES

- C.W. van Atta and E.J. Hopfinger: Vortex ring instability and collapse in a stable stratified fluid, *Exp. in Fluids* 7 (1989) 197-200.
- G.K. Batchelor: *An Introduction to Fluid Dynamics*, Cambridge University Press, Cambridge, 1967.
- S.V. Fonseka, H.J.S. Fernando and G.J.F. van Heijst: The evolution of an isolated turbulent region in a stratified fluid, (unpublished manuscript 1995)
- G. J. F. van Heijst and J.B. Flor: Laboratory experiments on dipole structures in a stratified fluid in: *Mesoscale/Synoptic Coherent Structures in Geophysical Turbulence* eds. J.C.J Nihoul and B.M. Jamart, Elsevier Science Publishers, Amsterdam, 1989, pp. 591-608.
- P.K. Kundu: *Fluid Mechanics*, Academic Press, New York, 1990, p. 525.
- J. Maxworthy: Some Experimental Studies of Vortex Rings, *J. Fluid Mech.* 81 (1977) 465
- D.R. McCluskey, T. S. Laursen, J.J. Rasmussen and B. Stenum: Evolution of vortical flow fields measured by real time PIV system, *FED-Vol. 229* (1995) 313-318.
- R. de Nijs: Vortex rings in a homogeneous and in a stratified fluid, R-1325-S, Eindhoven University of Technology, Eindhoven 1994.
- M. Nitshe and R. Krasny: A numerical study of vortex ring formation at the edge of a circular tube, *J. Mech.* 276 (1994) 139-279.
- P.G. Saffman: On the formation of a vortex ring, *Studies in Appl. Math.* 54 (1975) 261-268.
- K. Shariff and A. Leonard: Vortex rings, *Annu. Rev. Fluid Mech.* 24 (1992) 235-279.
- H. Yamada and T. Matsui: Mutual slip-through of a pair of vortex rings, *Phys. Fluids* 22 (1979) 1245-1249.

FLOW OF SHEAR-THINNING FLUIDS AROUND A CYLINDER: VORTEX SHEDDING AND DRAG CHARACTERISTICS

P. M. Coelho, F. T. Pinho, A. H. Rodrigues

Departamento de Engenharia Mecânica e Gestão Industrial
Faculdade de Engenharia, Rua dos Bragas, 4099 Porto Codex, Portugal

ABSTRACT

Measurements of the vortex shedding frequency in the wake of a cylinder and of the pressure profile around its surface were carried out for various elastic, shear-thinning fluids and compared with those of Newtonian fluids. The results obtained so far show that the normalised vortex shedding frequency increases with polymer concentration for flows pertaining to the subcritical regime. This effect is due to the thinning of the boundary layer associated with a shear-thinning viscous behaviour, whereas the elasticity of the fluids was found to have the opposite effect.

The form drag coefficient was calculated from the measured pressure profiles at the surface of the cylinder, and it was found that its reduction could be accounted for by both the shear-thinning and the fluid elasticity.

1. INTRODUCTION

The flow around a cylinder is a basic flow, whose knowledge is fundamental to a comprehensive understanding of the more complex flow around rod bundles, this one of particular relevance in tube-shell heat exchangers. Many engineering processes of the food, detergent and allied industries, amongst others, involve heat transfer with non-Newtonian fluids of low viscosity, but the information pertaining to these flows is scarce in the literature. This is the motivation for this work, which starts by investigating the hydrodynamics of the cross flow of shear-thinning fluids around a cylinder.

As far as Newtonian fluids are concerned, there has been extensive work due to the relevance of the flow for similar purposes and in other practical situations, such as in hydraulics, and two important references on the subject are the paper of Cantwell and Coles (1983) and the recent review of Telionis *et al.* (1992). However, for non-Newtonian fluids most of the work is theoretical and numerical, and is mainly concerned with creeping flows.

Shah *et al.* (1962) were among the first to experimentally investigate cross flows of non-Newtonian fluids around cylinders, up to Reynolds numbers as high as 12000. They found that the circumferential pressure profile on the cylinder laminar-boundary layer, with shear-thinning, elastic aqueous solutions of CMC, were independent of the power law of the viscosity consistency (k) and power (n) indices.

The measurements of the hydrodynamic and heat transfer characteristics of elastic fluids of constant viscosity of James and Acosta (1970) and James and Gupta (1971) were limited to lower maximum Reynolds numbers of 50 and 200, respectively. Both works reported that, at the high Reynolds number range, the drag coefficient and Nusselt number were independent of the Reynolds number but not of the Weissenberg number.

On the vortex shedding phenomena from a circular cylinder, it is important to refer the work of Gerrard (1966), who proposed a mechanism to explain its hydrodynamic characteristics based on two characteristic lengths, the formation and the diffusion lengths. According to Bloor (1964), the formation region (l_f) goes from the rear stagnation point up to the location where fluid from outside the wake first crosses the flow symmetry plane, as it is entrained by the opposite shear layer. The second characteristic length, which he termed the diffusion length (L), is the thickness of the free shear layer measured at the end of the formation region. Thus, the Strouhal number varies inversely with l_f and L.

In this work, results of measurements of the static pressure around the cylinder and of the frequency of the vortices shed in the wake of the cylinder, for various aqueous polymer solutions and two Newtonian fluids, are presented and discussed.

The next section describes the rig, the instrumentation and the corresponding uncertainties. Then, the rheological characteristics of the fluids are presented, before the results are shown and discussed. A summary of the main conclusions closes the paper.

2. EXPERIMENTAL FACILITY

The measurements were carried out in a water tunnel, shown schematically in figure 1, which had a 6 to 1 contraction before a transparent test section 197 mm high and 120 mm wide. The cylinder had a diameter of 19.7 mm, leading to a blockage of 10%, an aspect ratio of 6:1 and it was located 7 diameters downstream of the test section entrance. In order to reduce vibrations the test section and the settling chamber were isolated from the rest of the rig by means of flexible rubber pipes. The maximum mean velocity in the test section was about 2 m/s, corresponding to a maximum flow rate of 170 m³/h, regardless of the fluid. The mean velocity profile at the test section inlet, outside the wall boundary layers, was cons-

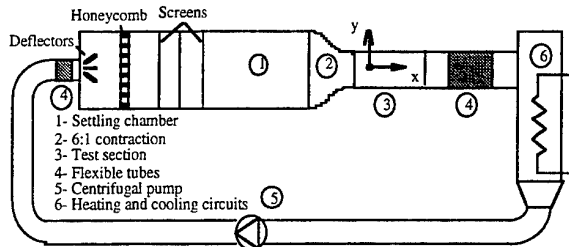


Figure 1 - Schematic representation of the water tunnel.

tant to within 1% and the free stream turbulence was equal to 3.9% at a flow rate of 85 m³/h.

In order to reduce the level of free stream turbulence, a long settling chamber with a large cross section would have been required, thus increasing enormously the volume of the rig. Budgetary constraint also imposed the purchase of a centrifugal pump, known to cause a much more intense mechanical degradation than that of a volumetric pump, Pinho and Whitelaw (1991).

The intense degradation of the polymer molecules requires frequent fluid substitution, of about 6 to 20 h, depending on the fluid resistance. Therefore, the volume of the rig of around 450 l, was a compromise between a reasonable flow condition at the test section, an affordable water tunnel and an easy and not to expensive fluid substitution procedure.

The heat exchanger, where tap water was the coolant and electrical resistances provided the heating, allowed the temperature to be maintained at 25°C during the whole test, with a variation never exceeding 0.5°C.

A diode fibre-optic laser-Doppler system from INVENT, model DFLDA, was used for the velocity measurements in the wake of the cylinder. A full description of this anemometer can be found in Stieglmeier and Tropea (1992). The S30 optical probe, with a 120 mm focusing lens, was used and the LDA main characteristics are listed in table 1. The output of the avalanche photodiode was processed by a 1990C TSI counter with 2⁵ cycles using the single measurements per burst mode and the validation criteria set to 1% comparison. The large number of cycles was possible since, according to Tropea (1993), the frequency shift adds N_{sh} fringes to the measuring volume equivalent in number to:

$$N_{sh} = \frac{f_{sh} d_{mcv}}{U_p} \quad (1)$$

where f_{sh} is the shift frequency and d_{mcv}/U_p is the residence time of the particle (d_{mcv} - control volume diameter; U_p - particle velocity). The frequency information from the counter was then sent to a computer via a DOSTEK 1400A interface card for further statistical and numerical analysis. In order to minimise velocity bias effects the data was acquired at a predefined frequency, rather than on the basis of the arrival data rate, which was higher than the timer frequency.

The high data rate signal measured downstream of the cylinder was processed by the FFT routines included in the software from DOSTEK to output the vortex shedding frequency. Note that for these measurements, the acquisition frequency was always at least 5 times higher than the frequency of the shedding. Figure 2 is a typical example of the measured power spectral density distribution (PSD) as a function of the frequency, plotted in log-log coordi-

Table 1- Main characteristics of the Laser Doppler anemometer

Laser Wavelength	827 nm
Laser power	100 mW
Measured half angle of beams in air	3.68°
Measuring volume size in water (e ⁻² intensity)	
minor axis	37 µm
major axis	550 µm
Fringe spacing	6.44 µm
Frequency shift	2.0 MHz

nates.

The velocimeter was mounted on a milling table with movement in the three orthogonal directions and the estimated maximum uncertainty of the mean velocity and frequency measurements, at a 95% confidence level was always better than 1.5%, calculated following Durst *et al.* (1981). As far as the positional uncertainty is concerned, it was of ± 20 µm in the x-z horizontal plane and of ± 10 µm in the vertical direction.

The pressure measurements were carried out with three different P305D Validyne differential pressure transducers, diaphragm numbers 30, 24 and 20 with full scale values of 880, 200 and 80 mm H₂O, respectively.

One pressure tap of 0.3 mm in diameter was drilled on the surface of the cylinder, which could rotate about its axis. The small size of the tap meant that for the more viscous fluids (0.4% CMC and 0.6% Tylose), the response time was slow, of about two minutes, in spite of the fact that the connecting tubes were filled with water.

The pressure transducers were connected to a 386 PC via a data acquisition Metrabyte board DAS8 and a Metrabyte ISO4 multiplexer board. For each angular location a sample size of 2000 measurements was taken and the statistical quantities were calculated by purpose-built software, with an estimated overall uncertainty of 4.3%, 0.8% and 1.2% for the pressure transducers number 30, 24 and 20, respectively.

3. FLUIDS CHARACTERISTICS

Two different polymers, of high and low molecular weights, were dissolved in water to manufacture elastic

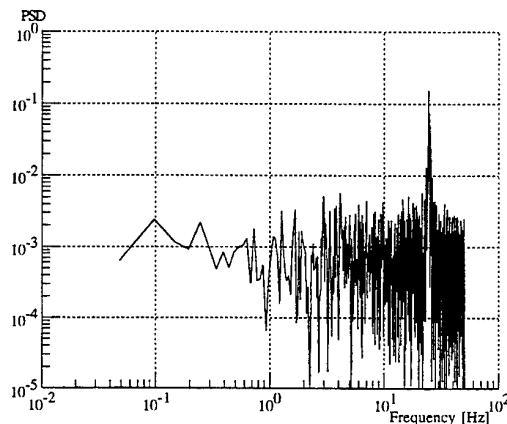


Figure 2 - PSD versus frequency for 0.6% Tylose and Re=848.

and weakly elastic shear-thinning fluids, respectively, and the results compared to those of two Newtonian fluids of different viscosity.

The weakly elastic fluids, Pereira and Pinho (1994), were aqueous solutions of 0.2, 0.3, 0.4 and 0.6% by weight concentration of a methyl hydroxyethyl cellulose called Tylose, grade MH 10 000K from Hoechst, which had a molecular weight of 6 000 kg/kmol. The more elastic aqueous solutions were manufactured from carboxy methyl cellulose sodium salt, (CMC) grade 7H4C from Hercules, which had a molecular weight of 300 000 kg/kmol, at concentrations of 0.1, 0.2, 0.3 and 0.4% by weight. A biocide, Kathon LXE 1.5% from Rohm & Haas, at a concentration of 0.02% by weight, was added to all solutions of CMC, to prevent bacteriological growth and degradation.

The Newtonian fluids were water and a mixture of 40% water and 60% glycerin with a viscosity of 0.0073 Pa.s.

The densities and refractive indices of all non-Newtonian fluids were unchanged from those of water ($\rho=998 \text{ kg/m}^3$, $n=1.333$) at 25°C , whereas for the glycerin-water mixture they were of 1148 kg/m^3 and 1.409, respectively. Figure 3 shows the viscosity of all non-Newtonian solutions as a function of the shear rate.

An assessment of some elastic material functions for the Tylose solutions is given in Pereira and Pinho (1994) and for the CMC solutions in Escudier *et al.* (1996).

4. RESULTS AND DISCUSSION

The minimisation of blockage corrections in wind and water tunnels usually requires the use of large test sections. In spite of being an old issue, e.g. Allen and Vicenti (1944) as quoted by Roshko (1961), Maskell (1963) and Farrel *et al.* (1977), there is not yet a widely accepted procedure for correcting for blockage effects. According to West and Apelt (1982), for a 10% blockage as in here the usual correction leads to a poorer drag coefficient (C_d), and the correction of the Reynolds number increases its value by at most 4%. Therefore, and considering also the unknown effects of the non-Newtonian characteristics of the fluids on what concerns this issue, no blockage corrections will be applied to the present experimental data.

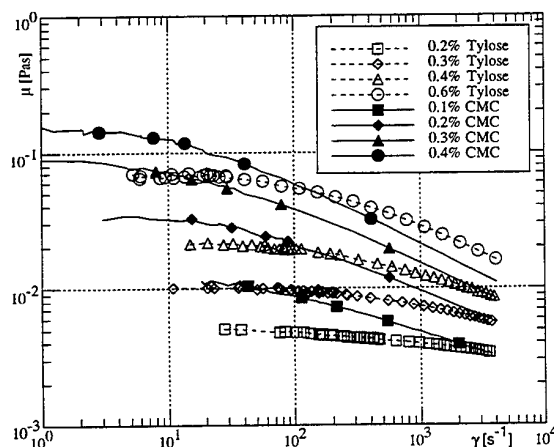


Figure 3 - Viscosity versus shear rate at 25°C .

In non-Newtonian fluid mechanics the pertinent issue of the adequate viscosity for normalisation arises. In simple flows, such as in a turbulent boundary layer over a flat plate, the argument for selecting the wall viscosity is relatively straightforward, but in more complex flows, such as this one, the decision is not so easy.

Selecting a proper viscosity is equivalent to selecting a characteristic shear rate that dominates the main flow hydrodynamic features. One of the advantages of dimensional analysis is the possibility it gives of comparing similar flows with different fluids and sizes without knowing *a priori* their detailed flow characteristics. This suggests that one should base the characteristic shear rate on integral, general quantities and geometrical dimensions, rather than on measured local quantities.

The obvious selection for the cylinder cross flow is the ratio of the free stream velocity to the cylinder radius (U_∞/R), but the work of Gerrard (1966) on Newtonian cylinder flows has shown that the important flow characteristics downstream of the cylinder depend of the shear layer thickness at the end of the formation region. Then, a more appropriate characteristic viscosity could be somehow related to this shear rate, but this requires the detailed knowledge of the flow field.

If the issue is irrelevant for Newtonian flows, it becomes important once the viscosity varies. In this work, the contradictions between these two approaches will come to light and a first attempt to solve it will be proposed and discussed.

Initially, a Reynolds number of

$$Re = \frac{\rho U_\infty D}{\mu_{ch}} \quad (2)$$

where ρ , U_∞ , D and μ_{ch} are the fluid density, freestream mean velocity, cylinder diameter and characteristic viscosity, will be defined with the characteristic shear rate set as the ratio of the free stream mean velocity to the cylinder radius. Later on, an alternative based on an estimate of local shear rates at the boundary layer will be discussed.

Figure 4 shows a plot of the Strouhal number ($Sr = f \cdot D / U_\infty$), where f stands for the vortex shedding frequency, as a function of the Reynolds number for all the solutions. The broken line represents the Newtonian data of Norberg (1994) without blockage or end plate effects. The fact that our measurements with Newtonian fluids are below those of Norberg, for Reynolds numbers under 5300, can be explained by the influence of the boundary layer at the tunnel side walls on the mechanism of vortex shedding, according to Gerich and Eckelmann (1982) and Stäger and Eckelmann (1991). To reduce this effect, end plates on the cylinder edges are commonly use, thus replacing the boundary layer on the tunnel wall by a thinner boundary layer on the end plates surface. In the present case, since the cylinder is located at 7 cylinder diameters from the entrance of the test section the tunnel walls behave roughly like end plates, except that the flow at the connection between the test section and the contraction is different from that at the leading edge of a real end plate.

According to Stäger and Eckelmann (1991) the end plates reduce the affected area to the edges of the cylinder, a region that decreases as the Reynolds number increases. Since the aspect ratio of the current experiments is not

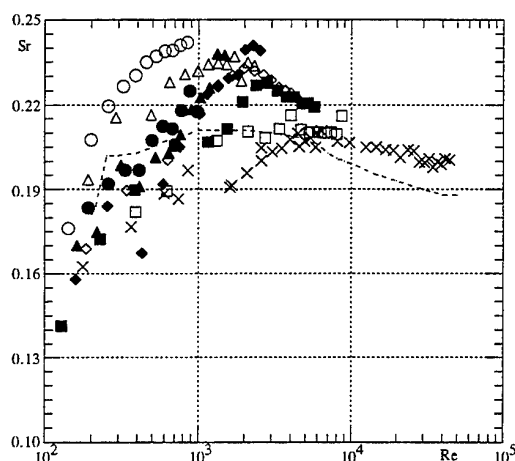


Figure 4 - Strouhal number versus Reynolds number for all solutions. \square 0.2% Tylose; \diamond 0.3% Tylose; Δ 0.4% Tylose; \circ 0.6% Tylose; \blacksquare 0.1% CMC; \blacklozenge 0.2% CMC; \blacktriangle 0.3% CMC; \bullet 0.4% CMC; \times Newtonian; --- Norberg (1994)

very high, at low Reynolds number flows the end plate effect can span all the cylinder length. In the affected region, the shedding frequency is always smaller than that in the unaffected region, represented by the Norberg values in figure 4. According to Stäger and Eckelmann (1991), for an end plate with dimensions similar to ours the Reynolds number above which the end plate effects cease to exist is approximately 3 000, but since truly end plates were not used, it is reasonable to expect that this critical Reynolds number value is different from 3 000. The measured Strouhal number values start to be higher than those of Norberg (1994), for Reynolds numbers above 5 300, therefore one may conclude that above this number the end plate effects become negligible.

At the high Reynolds number range, higher Strouhal number values relative to those of Norberg (1994), at the high Reynolds number range, were expected because they are the outcome of the blockage effect, following West and Apelt (1982). According to them, a 10% blockage at a Reynolds number of 10^4 corresponds to an increase in the Strouhal value of 0.005, whereas our data is 0.015 higher than the situation of no blockage. At this Reynolds number range the aspect ratio does not affect the Strouhal number (negligible end plate effects according to West and Apelt, 1982), so the extra difference between ours and Norberg's data can only be explained by the higher freestream turbulence intensity.

The values of the Strouhal number for the non-Newtonian fluids are well above those for Newtonian fluids, but they follow the same pattern, i.e. the Strouhal number increases first at low Reynolds numbers, reaching a maximum of 0.24, decreasing afterwards towards a constant value of around 0.2 at higher Reynolds numbers. So, the major difference in the value of the Strouhal number is at the low Reynolds number range, with the non-Newtonian fluids exhibiting a higher frequency of vortex shedding, which also increases with the polymer concentration. Note, however, that this Reynolds number effect may not exist, because it depends of the definition of the viscosity, as will be shown later.

The formation length, the boundary layer and shear layer thicknesses for these non-Newtonian fluid flows were not measured yet, therefore we are still unable to confirm the following tentative theory. According to Gerrard (1966), the formation length mainly depends of the turbulent entrainment by the shear layer, of fluid coming from the opposite shear layer, most of which bears opposite signed vorticity. This latter fluid will influence the vortex strength, and consequently the flow that goes into the formation region (reverse flow), thus reducing its length, i.e., a smaller reversed flow will induce a shorter formation region. This argument means that the formation length should increase, and according to Roshko (1954 b) as quoted by Gerrard (1966) the frequency decrease, the higher the capability of the fluid to delay the transition to turbulence, i.e., the higher the concentration of polymer.

The observed tendency is the opposite, so, still following Gerrard's (1966) theory, it must be the other characteristic length (the diffusion length) which is playing here the most important role, even when the shear layers are completely laminar (Reynolds numbers below 700 for flows with low free-stream turbulence, according to Gerrard, 1978). Serth and Kiser (1967) have shown that the boundary layer thickness in the flow over a flat plate is thinner with shear-thinning fluids than with constant viscosity fluids. The same effect is bound to occur in the flow around a cylinder, i.e. the shear layer will be thinner for higher polymer concentrations, which is the same as saying that the diffusion length will be thinner and the Strouhal number higher. The Tylose solutions emphasize this effect: as the polymer concentration is raised, the shear-thinning is intensified, thinning the boundary and shear layers and increasing the shedding frequency.

The decrease of the Strouhal number at higher Reynolds numbers could be explained by the same mechanism acting in the opposite way; shear layers (diffusion lengths) are thickening by virtue of the increased flow turbulence and the shedding frequency decreases. Quoting Gerrard (1966) "...when the layer is diffused it will take longer for a sufficient concentration of vorticity (of opposite sign) to be carried across the wake and initiate shedding. So we expect the shedding frequency to decrease as the diffusion length L increases.". Obviously this effect should be stronger than the attendant reduction in the formation length in order to justify the Strouhal number decrease.

The behaviour of the weakly elastic Tylose solutions agrees with this theory, but the data pertaining to the more elastic aqueous solutions of CMC do not confirm it so well. Although an increased Strouhal number is still observed, its systematic increase with the polymer concentration is not so intense as with the Tylose solutions, for a similar progression of the power law index (n). This different behaviour of the CMC solutions will be confirmed later by the drag coefficient measurements and the reason for it could be attributed to elasticity effects in the boundary and shear layers.

Metzner and Astarita (1967) have shown that by virtue of the great resistance which the elastic fluids manifest when they are subjected to sudden changes in the flow and consequently to high shear rates, they develop a thicker boundary layer, that extends to the forward stagnation point in the case of flow around bodies. This

forces the potential-flow velocity field outside the boundary layer to adjust to a larger radius of curvature. The higher the elasticity of the fluid, the more prone will be the fluid to this effect.

There are many demonstrations of the elasticity of CMC solutions, as in the experiments of Pinho and Whitelaw (1990), especially in the presence of turbulence. The experimental work on the laminar flow of elastic and inelastic non-Newtonian fluids around spheres of Acharya *et al.* (1976 a and b) and Adachi *et al.* (1977/78) have clearly demonstrated that on account of fluid elasticity the separation bubble behind the sphere was shorter than for inelastic fluids, and that there was an upstream shift of the streamlines, in agreement with the theory put forward by Metzner and Astarita (1967). As far as the drag coefficients were concerned, the elasticity was seen to reduce these values relative to those pertaining to inelastic fluids.

The relative constancy of the Strouhal number with polymer concentration for the CMC solutions can then be related to the opposite effects of the elasticity and shear-thinning upon the shear layer thickness, and consequently upon the diffusion length. The recent rheological measurements of Escudier (1996) have shown that to higher concentrations of CMC correspond higher intensities of shear-thinning and of elastic quantities, so their effects may somehow cancel each other.

Whereas the increased Strouhal number of non-Newtonian fluids is independent of the definition of the characteristic viscosity and is truly a non-Newtonian effect, the shift in the curves plotted in figure 4 to lower Reynolds number, depends on that choice.

If the arguments put forward by Gerrard (1966) on the role of the diffusion length are accepted, which we did to explain the increased shedding frequency, then the characteristic shear rate should be somehow related to the diffusion length, which is to say to the shear layer thickness in the formation region. However this quantity was not measured and had to be estimated. In addition, a method which does not require an *a priori* knowledge of the detailed flow field should be preferred.

In this attempt to quantify more realistically the shear rates encountered by the fluids following a general procedure, the choice was the well-known integral method of Thwaites based on Newtonian fluids, as explained by White (1991). According to this work, the value of the shear rate over a circular cylinder, at an angle of 70° from the forward stagnation point, represents reasonably well in order of magnitude the shear rates near the separation for the case of a laminar boundary layer flow over a circular cylinder.

The Thwaites method was used in conjunction with Hiemenz potential flow velocity field to calculate the wall shear stress at 70° (using equations 4-132 to 4-139 of White 1991) and yielded values of the characteristic shear rate 13 to 50 times higher than U_∞/R , corresponding to the lowest and highest flow rates tested. The order of magnitude of those shear rates also compared well with values calculated in a set of numerical simulations that were performed for the same flow around a cylinder, assuming symmetry of the flow. These calculations were carried out using a finite-volume based code, described by Oliveira (1992), with CDS and LUDS

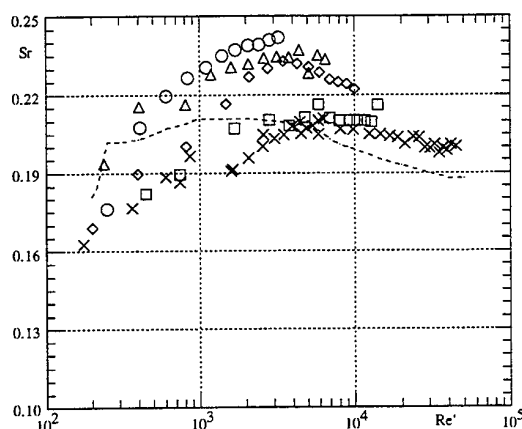


Figure 5 - Strouhal number versus Reynolds number calculated with the characteristic shear rate based on Thwaites method. \square 0.2% Tylose; \diamond 0.3% Tylose; Δ 0.4% Tylose; \circ 0.6% Tylose; \times Newtonian; ---- Norberg (1994)

as differencing schemes for diffusion and convection, respectively.

Using these characteristic shear rates a new Reynolds number designated by Re' was defined, and the Strouhal number data pertaining to the negligibly elastic Tylose solutions of figure 4, were plotted again in figure 5.

With this new Reynolds number the Strouhal number curves moved closer to each other, with its maximum value for the 0.3%, 0.4% and 0.6% Tylose solutions, occurring at basically the same Reynolds number, and with all the data spanning now roughly the same range of Reynolds numbers. It is now necessary to measure the velocities in the boundary and shear layers in order to quantify the real shear rate and definitely validate and/or improve this procedure, a task which will be carried out in the near future.

In figure 6 a typical non-dimensional pressure distributions around the cylinder is shown. By definition, the pressure coefficient is 1 in the forward stagnation point, it decreases until the minimum pressure coefficient (C_{pm}) at around 70° to 73° , and increases again to an approximately constant value (C_{pb}) at the back of the cylinder. The tunnel static pressure was calculated from the total pressure measured at the forward stagnation point of the cylinder, and the approach velocity measured by LDV. Small differences in the symmetry of the pressure distribution around the cylinder were found in the range 70° - 100° , never exceeding 7% for the Tylose solutions and 3% for CMC and Newtonians solutions. A small perturbation in the oncoming flow could be responsible for this behaviour.

The pressure distribution around the cylinder was processed to evaluate various quantities: its integration all around the cylinder with a Newton-Cotes formula quantified the form drag coefficient (C_d), the mean value of the pressure coefficient between 120° and 240° degrees defined the base pressure coefficient (C_{pb}), the minimum pressure value quantified the minimum pressure coefficient (C_{pm}), and the approximate location of the beginning of the wake region (θ_w) was defined as suggested by

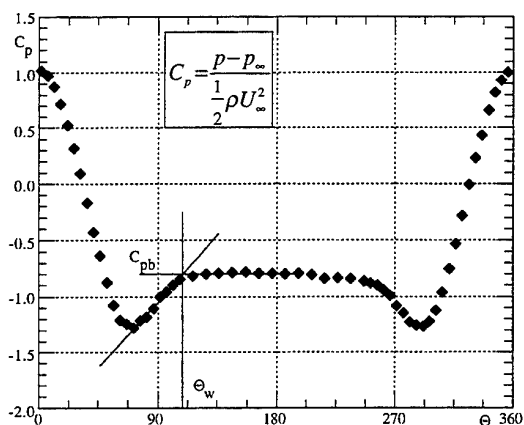


Figure 6- Typical non-dimensional pressure distributions around the cylinder for a Reynolds number ($Re \approx 800$). ♦ 0.2% CMC

Niemann, according to Guven *et al.* (1980) (see sketch on figure 6). The pressure rise coefficient ($C_{pb} - C_{pm}$) is a measure of the pressure rise sustained by the boundary layer prior to separation and it was also calculated. It is an important parameter, because it is insensitive to the blockage ratio, as explained by Farell *et al.* (1977).

The form drag coefficient is shown in figure 7 as a function of the two Reynolds numbers defined in this paper, with the full line representing the Newtonian values of C_d measured by Wieselsberger, as presented in Roshko (1961). Figure 8 shows the pressure rise coefficient for the same solutions and in figure 9, values of the wake angle calculated as the averaged value of the wake angles from the two sides of the cylinder following the procedure outlined above, are presented.

The Newtonian curve for the C_d pertains to the total drag coefficient whereas data measured in this work only refers to the pressure contribution. The range of Reynolds numbers covered by the current measurements is not so extensive as that pertaining to the data from the literature, therefore the typical U-shaped curve is not observed clearly for all the fluids. Bearing this in mind and that the

data in the figure was calculated rather than measured, it is not surprising the degree of scatter observed in it.

The Tylose solutions show a reduction of the minimum form drag coefficient with polymer concentration. The shift of the curves to lower Reynolds numbers in figure 7a) is associated with using U_∞/R as the characteristic shear rate for the calculation of viscosity, and it disappears if the alternative Reynolds number based on Thwaites method is used (figure 7b).

The aqueous solution of 0.2% Tylose behaves similarly to the Newtonian fluids, not just in the shedding frequency but also in the C_d , which is not surprising since it is the least shear thinning and elastic of all non-Newtonian fluids.

As far as the CMC solutions are concerned, they exhibit a lower form drag than the correspondingly similar shear-thinning weakly elastic solutions, as was also observed for the total drag in the sphere flows of Adachi *et al.* and Acharya *et al.*, and in agreement with the reported tendencies associated with elastic behaviour, namely a delayed flow separation.

For Reynolds numbers smaller than 700, the solutions of 0.6% Tylose and 0.4% CMC have a fairly constant C_d , but lower than the Wieselsberger Newtonian curve, a result that contradicts the measurements of James and Gupta (1971). One possible explanation for this discrepancy is that we have measured the pressure drag of elastic shear-thinning fluids, whereas James and Gupta measured the total drag with elastic fluids of constant viscosity. Achenbach (1971) has demonstrated that in the subcritical regime, and for Reynolds numbers above 2×10^4 , the friction forces contribute with less than 2% to the total flow resistance. However, we could not find any reference in the literature to the contribution of frictional drag for lower Reynolds numbers, but it is reasonable to expect that here it will be higher, because the separation occurred later, at an angle above 100° for Reynolds number below 1 000 (figure 9), and also because the velocity gradients at the wall are higher on account of the pseudo-plasticity of the fluids, Serth and Kiser (1967). Another possible reason for this can be the end plate effects, which according to Norberg (1994) measurements substantially increases the base pressure coefficient (C_{pb}) thus decreasing the drag coefficient (C_d).

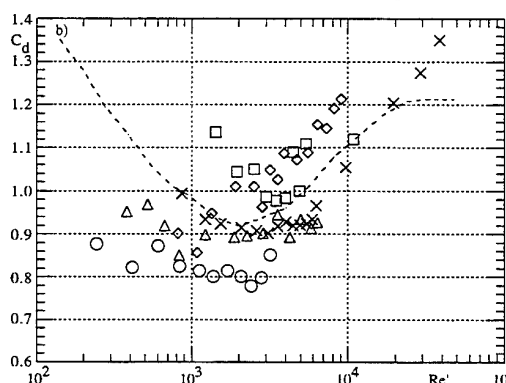
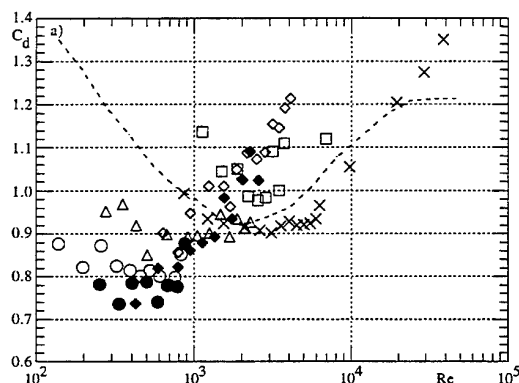


Figure 7 - Pressure drag for all solutions as a function of the two different Reynolds numbers: a) Re b) Re' . □ 0.3% Tylose; △ 0.4% Tylose; ○ 0.6% Tylose; ♦ 0.2% CMC; ● 0.4% CMC; X Newtonian; ---- Wieselsberger.

The pressure rise coefficient ($C_{pb}-C_{pm}$) shown in figure 8 changes slowly with the Reynolds number for each fluid, therefore the Reynolds number definition is not so important in this plot. One can see in the figure that the more elastic solutions, represented by the CMC, exhibit higher pressure rises before separation. In this region the polymer molecules are being subjected to a compression and it is known (Bird *et al.*, 1987) that elastic fluids resist more to the normal deformations, so they can sustain a larger pressure rise. If this is true, then the more concentrated Tylose solutions are exhibiting some elasticity as their pressure rise coefficient are above those of Newtonian fluids, but not so intense as for the CMC solutions. This is a speculative argument, but Pereira and Pinho (1994) have found out that all solutions of Tylose exhibited some elongational elasticity effects under the presence of turbulence, in spite of their low molecular weight, and in this flow the free-stream turbulence is in excess of 3%.

With a fairly constant pressure rise with the Reynolds number, especially with the polymeric solutions, the wake angle should not vary as much as depicted in figure 9.

In the subcritical regime the wake angle should be less than 90° , but as shown in figure 9 for the lower Reynolds numbers the separation occurs at more than 115° , decreasing to less than 85° as the Reynolds number increases above 10 000, a result also confirmed by flow visualisation experiments using dyes.

There are two possible causes for this: first, the end plate effect, which decreases as the Reynolds number increases and is thus responsible for an earlier separation and larger drag. Secondly, the turbulence of the free-stream flow was found to increase from about 3% at the higher Reynolds numbers to 4% at lower Reynolds numbers. The higher turbulence could bring some fluid into the boundary-layer raising its capability to resist adverse pressure gradients, thus helping to delay flow separation.

The use of the alternative Reynolds number based on Thwaites method was not used here to replot the data of figures 8 and 9, because it did not bring any additional information.

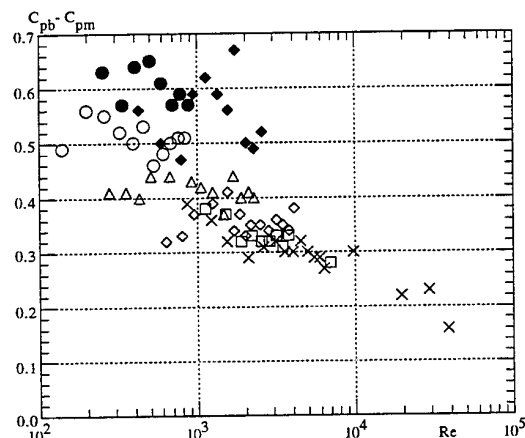


Figure 8 - Pressure rise coefficient for all solutions studied. \square 0.2% Tylose; \diamond 0.3% Tylose; Δ 0.4% Tylose; \circ 0.6% Tylose; \blacklozenge 0.2% CMC; \bullet 0.4% CMC; \times Newtonian.

5. CONCLUSIONS

Measurements of the vortex shedding frequency and form drag were carried out with various shear thinning weakly elastic polymer solutions and Newtonian fluids over a wide range of Reynolds numbers pertaining to the subcritical regime.

Pseudoplasticity was found responsible for reducing the boundary layer thickness over the cylinder and the shear layer thickness in the formation region, thus raising the maximum Strouhal number from the typical value of 0.2 for Newtonian fluids to about 0.24 for a power law index fluid of 0.56. Elastic fluids exhibited the opposite effect, because of the increased resistance of their molecules to be strongly deformed, thus thickening the boundary and shear layers.

An estimative of the real shear rates within the boundary layer over the cylinder was attempted following a procedure based on Thwaites integral method. The viscosity corresponding to this shear rate defined a new Reynolds number which provided less scatter of all the measured data than the use of a viscosity based on the free-stream velocity divided by the cylinder radius. Reynolds number effects associated with non-Newtonian fluids were also removed by this new definition of the characteristic viscosity.

The minimum form drag coefficient dropped by at most 15% when the power law index of weakly elastic Tylose solutions decreased from 1 to about 0.56. The elasticity further reduced the form drag coefficient so that with the 0.4% CMC solution the minimum C_d was of about 0.73, against a Newtonian value of 0.93. The observed behaviour of the CMC solutions agreed with results reported by other authors relative to flows around spheres.

The angle of flow separation decreased with the Reynolds number and was always higher than 90° for the non-Newtonian solutions. However, following the observed trend with Newtonian fluids at Reynolds numbers higher than those measured here, the separation is expected to occur on the forward half of the cylinder.

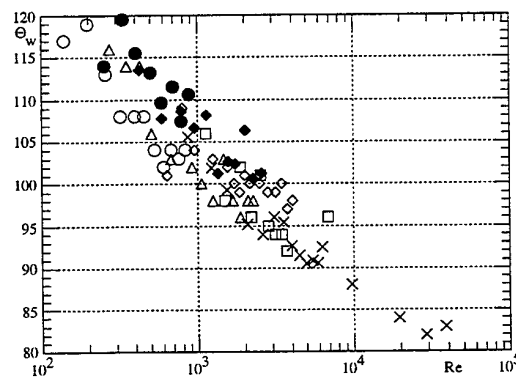


Figure 9 - Estimated wake angle for all solutions studied. \square 0.2% Tylose; \diamond 0.3% Tylose; Δ 0.4% Tylose; \circ 0.6% Tylose; \blacklozenge 0.2% CMC; \bullet 0.4% CMC; \times Newtonian.

ACKNOWLEDGMENTS

The authors wish to thank JNICT for the financial support through project PBIC/C/CEG/1370/92 and the equipment lent by INEGI and IDMEC. P. M. Coelho also wishes to thank the University of Porto for the leave of teaching duties over the last three years which made this work possible.

Finally, we gratefully acknowledge the helpful comments of Prof. M. P. Escudier.

REFERENCES

- Adachi, K., Yoshika, N. & Sakai, K. 1977/78, An investigation of non-Newtonian flow past a sphere, J. Non-Newt. Fluid Mech., Vol. 3, pp 107-
- Acharya, A., Mashelkar, R. A. & Ulbrecht, J. 1976 a), Flow of inelastic and viscoelastic fluids past a sphere. I Drag coefficient in creeping and boundary layer flows, Rheol. Acta, Vol. 15, pp 454-470
- Acharya, A., Mashelkar, R. A. & Ulbrecht, J. 1976 b), Rheol. Acta, Vol. 15, pp 471-478
- Achenbach, E. 1971, Influence of surface roughness on the cross-flow around a circular cylinder, J. Fluid Mech. Vol. 46, pp 321-335.
- Bird, R. B., Armstrong, R. C. & Hassager, O. 1987, Dynamics of Polymeric Liquids. Volume 1: Fluid Mechanics, pp 1- 649, John Wiley & Sons.
- Bloor, S. M. 1964, The transition to turbulence in the wake of a circular cylinder, J. Fluid Mech. Vol. 19, pp 290-304.
- Cantwell, B. & Coles, D. 1983, An experimental study of entrainment and transport in turbulent near wake of a circular cylinder, J. Fluid Mech. Vol. 136, pp 321-374.
- Durst, F., Melling, A. & Whitelaw, J. H. 1981, Principles and Practice of Laser-Doppler Anemometer, Pergamon Press, London.
- Escudier, M. P. 1996, Private communication on measurements of viscosity, oscillating material functions and first normal stress difference with CMC solutions, University of Liverpool
- Farrell, C., Carrasquel, S., Güven, O. & Patel, V. C. 1977, Effect of wind-tunnel on the flow past circular cylinders and cooling tower models, J. Fluids Engineering Vol 99, pp 470-479.
- Gerich, D. & Eckelmann, H. 1982, Influence of end plates and free ends on the shedding frequency of circular cylinders, J. Fluid Mech. Vol. 122, pp 109-121.
- Gerrard, J. H. 1966, The mechanics of the formation region of vortices behind bluff bodies, J. Fluid Mech. Vol. 25, pp 401-413.
- Gerrard, J. H. 1978, The wakes of cylindrical bluff bodies at low Reynolds number, Phil. Trans. R. Soc. Lond. Ser. A, 288, pp 351-382.
- Güven, O., Farrel, C. & Patel V. C. 1980, Surface-roughness effects on the mean flow past circular cylinders. J. Fluid Mech. Vol. 98, pp 673-701.
- James, D. F. & Acosta, A. J. 1970, The laminar flow of dilute polymer solutions around circular cylinders, J. Fluid Mech. Vol. 42, pp 269-288.
- James, D. F. & Gupta, O. P. 1971, Drag on circular cylinders in dilute polymer solutions, Chem. Engng. Prog. Symp. Ser. Vol. 67, 111 pp 62-73.
- Maskell, E. C. 1963, A theory of blockage effects on bluff bodies and stalled wings in a closed wind tunnel, R. & M. N° 3400.
- Metzner, A. B. & Astarita, G. 1967, External flow of viscoelastic materials: fluid property restrictions on the use of velocity-sensitive probes, AIChE J. Vol. 13, pp 550-555.
- Norberg, C. 1994, An experimental investigation of the flow around a circular cylinder: influence of aspect ratio, J. Fluid Mech. Vol. 258, pp 287-316.
- Oliveira, P. 1992, Computer modelling of multidimensional multiphase flow and application to T- junctions. PhD thesis. Imperial College, University of London, UK.
- Pereira, A. S. & Pinho, F. T. 1994, Turbulent pipe flow characteristics of low molecular weight polymer solutions, J. Non-Newt. Fluid Mech. Vol. 55, pp 321-344.
- Pinho, F. T. & Whitelaw, J. H. 1990, Flow of non-Newtonian fluids in a pipe, J. Non-Newt. Fluid Mech. Vol. 34, pp 129-144.
- Pinho, F. T. & Whitelaw, J. H. 1991, Flow of non-Newtonian fluids over a confined baffle, J. Fluid Mech. Vol. 226, pp 475-496.
- Roshko, A. 1961, Experiments on the flow past a circular cylinder at very high Reynolds number, J. Fluid Mech. Vol. 10, pp 345-356.
- Stieglmeier, M. & Tropea, C. 1992, A miniaturized, mobile Laser-Doppler Anemometer, Applied optics, Vol. 111, pp 4096-4099
- Serth, R. W. & Kiser, K. M. 1967, A solution of the two-dimensional boundary-layer equations for an Ostwald-deWaele fluid, Chem. Eng. Sci. Vol. 22, pp 945-956.
- Shah, M. J., Petersen, E. E. & Acrivos, A. 1962, Heat transfer from a cylinder to a power-law non-Newtonian fluid, AIChE J. Vol. 8, pp 542-549.
- Stäger, R. & Eckelmann, H. 1991, The effect of endplates on the shedding frequency of circular cylinders in the irregular range, Phys. Fluids A3 (9), pp 2116-2121.
- Telionis, D. P., Gundappa, M. & Diller, T. E. 1992, On the organisation of flow & heat transfer in the near wake of a circular cylinder in steady and pulsed flow, Trans. A.S.M.E., J. Fluids Engng. Vol. 114, pp 348-355.
- Tropea C. 1993 DFLDA Technical Reference Manual, INVENT GmbH, appendix B
- West, G. S. & Apelt, C. J. 1982, The effects of tunnel blockage and aspect ratio on the mean flow past a circular cylinder with Reynolds number between 10^4 and 10^5 , J. Fluid Mech. Vol. 114, pp 361-377.
- White, F. M. 1991, Viscous Fluid Flow, pp 1-614, McGraw-Hill, New York.

TURBULENT NATURAL CONVECTION AROUND A HEATED VERTICAL SLENDER CYLINDER

N. J. Persson and R. I. Karlsson

Vattenfall Utveckling AB, S-814 26 Älvkarleby, Sweden
and

Royal Institute of Technology, Department of Mechanics, Faxén Laboratory
S-100 44, Stockholm, Sweden

ABSTRACT

This paper reports on two new experiments regarding turbulent natural convection on a vertical heated circular cylinder in air. Simultaneous two-component LDV measurements are performed to determine U , V , u' , v' and uv . In one experiment the velocity and temperature fields were measured separately, and in the second experiment simultaneous velocity- and temperature measurements were made, so that the u and v contributions to the turbulent heat flux could be determined. Particular attention was given to the near-wall region.

We find in both experiments, in contradiction to some previous hot-wire measurements, that there exists a region close to the wall ($y^+ < 20$) where the turbulent shear stress uv is negative. A disturbance of mainly the normal velocity V by the presence of the temperature probe makes the quantitative results of the simultaneous velocity and temperature measurements containing V in the second experiment somewhat uncertain. A redesign of the temperature probe can eliminate this problem.

1. INTRODUCTION

Turbulent natural convection is of great importance in many industrial and environmental processes such as in nuclear reactors and in copper refining and heating in buildings. In numerical modelling of such processes the near wall behaviour of the turbulence quantities is essential in determining the relations between temperatures, heat fluxes and velocities. Modelling of turbulent natural convection is still quite a challenge (see Dathieu et al. 1996).

The early measurements of turbulent natural convection used the HWA technique and different types of corrections for separating the measured velocities from effects of the varying temperature (Cheesewright 1968). It is very difficult to get reliable data with good spatial resolution using this technique (Tsuji and Nagano, 1988, 1989, Cheesewright and Ierokipiotis, 1982), particularly close to the wall. Moreover, the high local turbulence intensities both near the wall and outside of the velocity maximum contribute to a lower measurement accuracy. Using LDV with enhanced spatial resolution (Karlsson and Johansson 1988, Karlsson et al. 1993, Kato et al. 1993) gives the possibility to perform high resolution velocity measurements without contaminating the velocity measurements with temperature.

Turbulence data from the near-wall region of turbulent natural convection boundary layers are scarce in the literature, and moreover, there are some discrepancies between different data sets. Here we will discuss the data of Tsuji and Nagano (1988), Tsuji et al. 1991, and Kato et al. 1993. Tsuji et al. used hot-wire anemometry with a specially designed V-shaped hot-wire for measuring uv and v' , while Kato et al used LDV. Both experiments were made on heated vertical flat plates in air, and the Grashof numbers were high enough to secure fully turbulent flow. The main discrepancies between the two data sets concern the results on uv and v' near the wall ($y^+ < 15$, the so-called buoyant sublayer). Tsuji et al. find that $uv > 0$ all the way to the wall, while Kato et al. find a region of negative shear stress. There is also a difference in v' in this region. The data of Tsuji and Nagano show an approximately constant level of v'^+ between $10 < y^+ < 25$ and a small decrease for $y^+ < 10$. On the other hand, the data of Kato et al show lower values and a more gradual decay when the wall is approached. The absence of a region of negative shear stress close to the wall indicates a negative production of k by the mean shear in this region. This finding made Tsuji et al. (1991) develop an elaborate theory of energy transfer in the near-wall region of the natural convection boundary layer.

The present contribution aims to resolve the above-mentioned discrepancy by presenting results from two experiments: one experiment where velocity and temperature measurements were made separately, and a first attempt to simultaneously measure two velocities and the temperature in one "point" in a simple set-up which was specially designed to permit near-wall measurements.

2. EXPERIMENTAL SET-UP AND MEASUREMENT SYSTEM

The velocity measurements were performed with a standard TSI fiberoptical system. Because of the geometry of the set-up a 1200 mm transmitting lens was needed. The measuring volume dimensions were kept reasonably small by using beam expansion ($l = 2.7$ mm, $d = 0.07$ mm for the vertical component and $l = 1.3$ mm, $d = 0.07$ mm for the horizontal component). The great difference in the measuring volume lengths is due to the use of a centre-side configuration in the normal component to improve the possibility for near-wall measurements.

The LDV-system was combined with a Data Link (TSI) in test 2 which gives the possibility to measure eight

additional quantities simultaneous with the velocities. The Data Link was used to add the local temperature, measured with a standard Dantec platinum hot wire ($l = 1 \text{ mm}$, $d = 1 \mu\text{m}$) (Dantec 55R31), to the velocity measurements.

The case studied is natural convection along a slender vertical heated cylinder. The cylinder ($l = 2.2 \text{ m}$, $d = 0.10 \text{ m}$) was placed in a $1.8 \times 1.8 \times 2.2 \text{ m}$ enclosure, which has an open slot (height: 50 mm) along the floor which enables the cool air to get in. Seeding in the form of small oil droplets from a disco-type atomizer was added to the air flow in the slot. A point-outlet was placed just beneath the ceiling on one of the sides and $190 \text{ m}^3/\text{h}$ was sucked out through the outlet, which gave a steady stratification in the enclosure with a sharp temperature interface 1.8 m above the floor. Below that level the temperature gradient was about $1^\circ\text{C}/\text{m}$. The set-up, shown in figure 1, was in principle identical for test 1 and test 2.

The LDV measuring volume could be positioned at the very top of the temperature probe using the reflection from the probe and its shadow on the wall behind as indications. Interference between the measuring volume and the temperature probe leads to an increase in temperature and wall-signal in the LDV response. The LDV measuring volume was then traversed towards the cylinder until no indication of interference could be observed neither on the temperature- nor on the LDV signal. Then the measuring volume was traversed 0.1 mm towards the cylinder and 0.05 mm downwards to ensure that the systems did not interfere. This procedure results in a distance between the temperature probe and the LDV measuring volume which is smaller than the smallest length scale in the boundary layer ($\nu/u^* = 0.21 \text{ mm}$). Figure 2 shows the position of the measuring volume and the temperature probe.

The origin of the coordinate system is situated at the floor and on the surface of the vertical cylinder with the x-axis directed vertically upwards along the cylinder surface. The y-axis is horizontal and perpendicular to the wall, pointing outwards from the wall. U and V are thus the axial (vertical) and the normal (horizontal) velocity components, respectively.

The measurements in test 1 were made at a height of 1.1 above the floor, which gave $Ra = 7.0 \cdot 10^9$. Here, the temperature was measured separately, and no mixed velocity-temperature moments could be measured. All measurements in test 2 were done on a height of 1.5 m above the floor, which in this case corresponds to $Ra = 1.4 \cdot 10^{10}$. Temperature and velocity were measured simultaneously in this case. Typical temperature differences between the cylinder surface and the ambient temperature were about 80°C for both tests.

A problem in using LDV-technique for studying turbulent natural convection is the change in refractive index that comes with a change in temperature, which leads to beam refraction and -wandering (Karlsson, 1988). These effects are limited when measuring in air, and the test case of a slender cylinder gives the additional advantage of a shorter path in the thermal boundary layer for the beams compared with a flat plate.

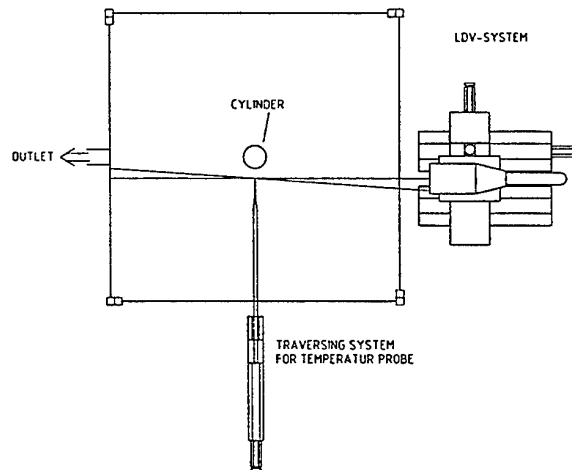


Figure 1. Experimental set-up seen from above.

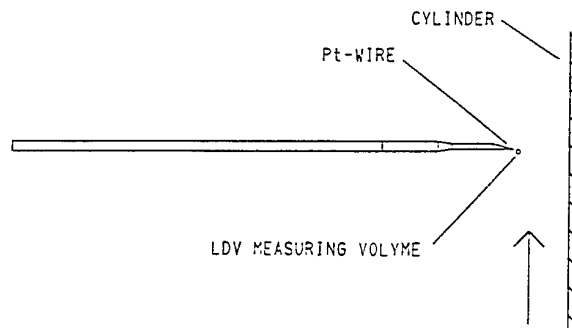


Figure 2. Close-up of the temperature probe and the LDV measuring volume.

3. DATA REDUCTION

In the analysis of data in a flow situation with high local turbulence intensities, velocity bias is a major cause of error. Since only two components were measured, it was not possible to apply the McLaughlin & Tiederman correction. Other weighting methods based on the velocity was excluded because of uncertainties concerning uniform seeding concentration.

It was decided to use an even time sorting of the data in order to get a conservative correction that not is affected by non-uniform seeding. It was implemented in the so called controlled processor form (Fuchs et al., 1992). The time step was varied and it was found that for time steps larger than 10 ms the mean values were unaffected by the change of time step. The time step of 10 ms was finally chosen for the data reduction which means that $40 - 70 \%$ of the data was excluded and $15000 - 30000$ samples were used when calculating the statistical quantities. The resulting statistical

quantities did not differ much when compared to the ones that was corrected with transit time weighting.

The intention was to use independently sampled temperature measurements to compare with different bias corrections methods to see in what sense the correction method effected the temperature measurement. The effect of the even time correction on the mean and standard deviation of the temperature was too small to make such conclusions.

4. RESULTS

4.1 Test 1

Results from test 1 are presented in Figures 3-7. Although the Ra number is low, the flow is turbulent, and the general character of the results is in agreement with previous work (Tsuji and Nagano 1988, Kato et al. 1993). The mean velocity and temperature profiles are shown in Fig. 3, and the corresponding RMS values are shown in Fig. 5. The data are presented in dimensionless form in inner scaling by using the kinematic viscosity ν , the friction velocity u^* and the friction temperature t^* as scaling parameters. Such dimensionless variables are denoted with superscript (+). Fluid properties were evaluated at the bulk temperature. The friction velocity was determined from the velocity gradient at the wall, see Fig. 4.

The main difference in results from previous hot-wire measurements is seen in the shear-stress distribution. Fig. 6. An enlarged view of the turbulent shear stress in the near-wall region is shown in Fig. 7, and the data show clearly that there is a region close to the wall ($y^+ < 15$) where \overline{uv}^+ is negative. Although there is some scatter in the data, we think that the results are conclusive: there exists a small region close to the wall where the shear stress is negative. Although the present measurements are made along a vertical circular cylinder, we do not expect any significant difference compared to a vertical flat plate. Our results on the turbulent shear-stress distribution in the near-wall region are thus in agreement with the LDV results by Kato et al. 1993 but disagree with the hot-wire results of Tsuji and Nagano 1988.

4.2 Test 2

In test 2 we measured velocity and temperature simultaneously at a slightly higher Ra number than in test 1. The profiles of the mean values and standard deviations of the temperature and the velocities in wall variables are shown in Figure 8 and 9. The scatter in the data in the outer layer is large, which is a result of the long time scales in the outer low-velocity region where the flow pattern is unstable, but it also reflects the difficulties in obtaining uniform seeding. Even though the measurements were taken over a time of 20 min this scatter could not be avoided. This indicates that velocity variations of extremely low frequency are present in the outer flow.

The main outline of the curves corresponds well with the vertical flat-plate convective boundary layer (Tsuji and Nagano 1988, Cheesewright and Ierokipiotis 1982, Kato et al. 1993), except for the normal velocity component V which obviously is contaminated by the larger axial velocity U . An attempt was made to correct the normal velocity for this non-orthogonality effect by the method of Karlsson et al. 1993, but there is still a remaining uncertainty in variables

containing V . It should be noted that the angle between the beam pairs were very close to 90 degrees, so that the effect is probably a result of an unfortunate design of the probe which modifies the flow (we used a standard straight probe). This effect is also essential when evaluating the correlation between the two velocity components and between the normal velocity and the temperature. The results on \overline{uv}^+ , \overline{ut}^+ , and \overline{vt}^+ , which are shown in Fig. 10, are therefore only qualitatively correct. In particular, the negative value of \overline{vt}^+ near the wall should be taken with some caution. A close-up of the near-wall results are shown in Fig. 11.

Fig. 12 shows short time records of velocity and temperature at different distances from the cylinder. In the position closest to the cylinder, $y^+ = 1.9$, all fluctuations are small as a result of damping from the wall.

At the position $y^+ = 6.2$ the magnitude of the fluctuations in U and T increases considerably, while the V -fluctuations still are quite small. The temperature fluctuations appears to be symmetric around the mean value, compared to closer to the cylinder where it has short negative peaks and further away where the peaks are positive.

At the position $y^+ = 32$, which is close to the maximum mean velocity, the correlation between U and T is obvious. Further out at $y^+ = 85$ and 245 the temperature appears to be dominated by occasional outward bursts of high temperature fluid. These events show up as positive peaks in the V -velocity which are correlated with positive peaks in the temperature signal.

Regarding the frequency contents of the signals, it is apparent that the temperature signal contains a smaller amount of high-frequency fluctuations than the velocity signals. This may be interpreted as that the hot/cold fluid parcels have a larger size than the smaller turbulent eddies in the flow.

Even though the present set-up gave some errors in the results it was concluded that the technique worked very well for simultaneous velocity and temperature measurements. Further measurements will be made with a modified temperature probe in order to minimize blockage effects.

5. CONCLUSIONS AND FUTURE WORK

Turbulent natural convection along a heated vertical circular cylinder has been experimentally studied in two different tests by using a two-component LDV system and a resistance thermometer. The two velocity components U and V were measured simultaneously, but the temperature was measured separately in test 1. Thus, no blockage effects affected the velocity measurements. It was found that there exists a small region close to the wall where the turbulent shear stress \overline{uv}^+ is negative ($y^+ < 15$), in contradiction to previous hot-wire measurements.

In test 2, the two velocity components and the temperature were measured simultaneously in a "point", with the thin cold hot-wire placed just downstream of the LDV measuring volume. This technique has proven useful in the characterisation of the turbulent natural convection boundary layer. However some improvements of the experimental set-up must be made before correct measurements can be carried out:

- 1 The HWA-probe support has to be redesigned in order not to influence the flow. Velocity measurements without the HWA-probe present should be carried out to prove undisturbed flow.
- 2 The enclosure dimensions should be smaller in order to stabilise the secondary flow. That will also give the possibility to use a transmitting lens with shorter focal length which will improve the spatial resolution.
- 3 The seeding equipment and procedure has to be improved in order to get a more uniform seeding concentration in the enclosure during each measurement.
- 4 Measurements should be carried out at different heights in order to determine the energy balance.

6. REFERENCES

- Cheesewright, R. "Turbulent natural convection from a vertical plane surface". J. Heat Transfer. Vol 90, pp. 1-8, 1968.
- Cheesewright, R. & Ierokipiotis, E. "Velocity Measurements in a Turbulent Natural Convection Boundary Layer". Proceedings 7th Int. Heat Transfer Conf., Munich, F.R.G. vol. 2, pp. 305- 3309. 1982.
- Dathieu, I., Laurence, D. & Richoux, S. "Proceedings of the 5th ERCOFTAC/IAHR Workshop on Refined Flow Modelling". EDF/LNH, Chatou (Paris). April 25-26, 1996.
- Fuchs, W., et al, "Simulation and Experimental Verification of Statistical Bias in Laser Doppler Anemometry including Non - Homogeneous Particle Density", Sixth Int.Symp. on Applications of Laser Techniques to Fluid Mechanics, July 20th - 23rd, Lisbon, Portugal. 1992. Paper 8.2.
- Karlsson, R. & Johansson, T.G., "LDV Measurements of Higher Order Moments of Velocity Fluctuations in a Turbulent Boundary Layer", Laser Anemometry in Fluid Mechanics III, Eds. R.J. Adrian et al. Ladoan - Instituto Superior Tecnico, 1096 Lisbon Codex, Portugal 1988, pp. 273-289.
- Karlsson, R., "Experimentella studier av naturlig konvektion i inneslutningar", Rapport UL-FUD-B-88:1, Vattenfall Älvkarlebylaboratoriet. 1988. (In Swedish)
- Karlsson, R.I., Eriksson, J. & Persson, N.J. "LDV Measurements in a Plane Wall Jet in a Large Enclosure". In: Laser Techniques and Applications in Fluid Mechanics, Eds. R.J Adrian et al., Springer-Verlag 1993, pp. 311-332.
- Kato, S., Murakami, S. & Yoshie, R. "Experimental and Numerical Study on Natural Convection with Strong Density Variation along a Heated Vertical Plate". Ninth symposium on "Turbulent Shear Flows". Kyoto, Japan, August 16-18, 1993.
- Tsuji, T. & Nagano, Y. "An anemometry technique for turbulence measurements at low velocities". Experiments in Fluids vol.7, pp. 547-559, 1989.
- Tsuji, T. & Nagano, Y. "Turbulence measurements in a natural convection boundary layer along a vertical flat plate". Int J Heat Mass Transfer. Vol. 31, No. 10, pp. 2101-2111, 1988.
- Tsuji, T., Nagano, Y. & Tagawa, M. "Thermally Driven Turbulent Boundary Layer". Eight Symposium on Turbulent Shear Flows. Technical University of Munich. September 9-11, 1991.
- Tummers, M. J., et al, "An Experimental Investigation of Velocity Bias in a Turbulent Flow", Sixth Int.Symp. on Applications of Laser techniques to fluid mechanics, July 20th - 23rd, Lisbon, Portugal. 1988. Paper 5.4.

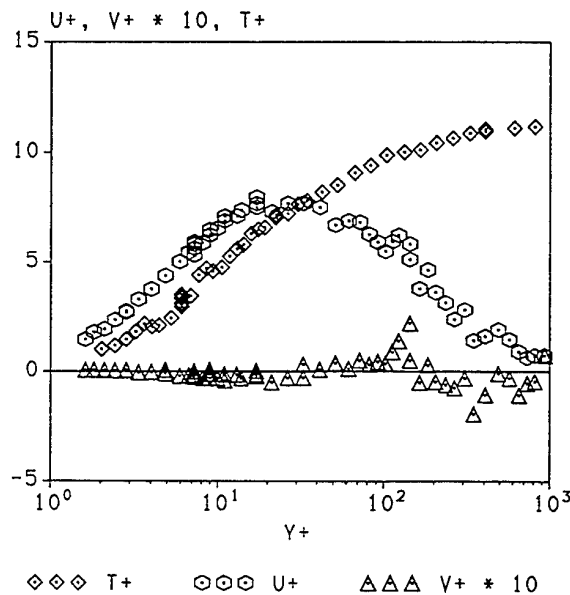


Figure 3. Measured mean velocity and mean temperature profiles, test 1.

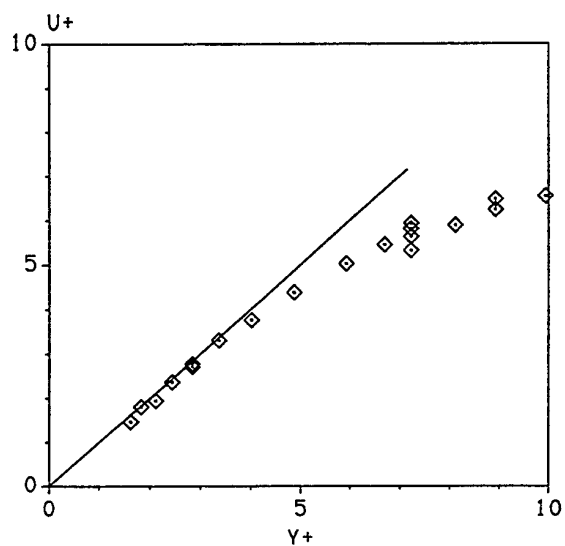


Figure 4. Measured mean velocity close to the wall.

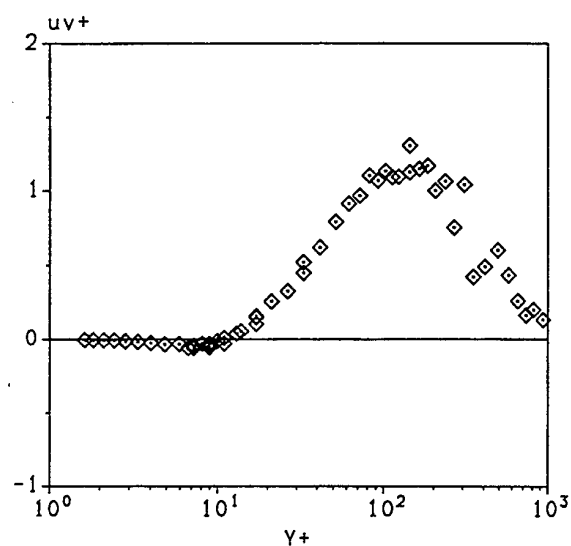


Figure 6. Measured distribution of turbulent shear stress, test 1.

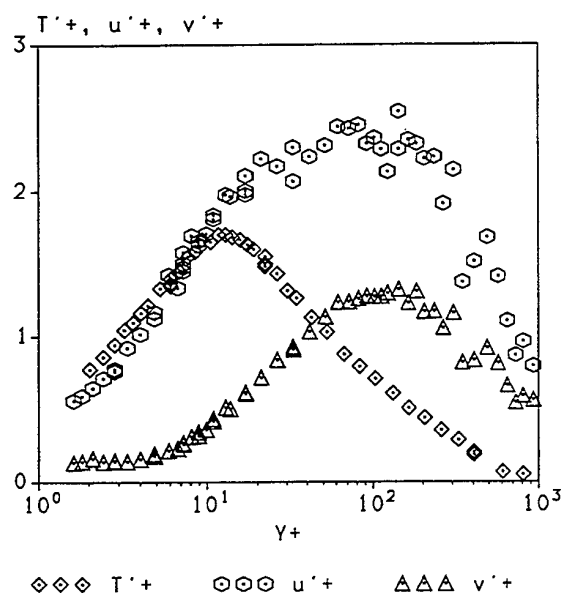


Figure 5. Measured intensities of velocity and temperature fluctuations, test 1.

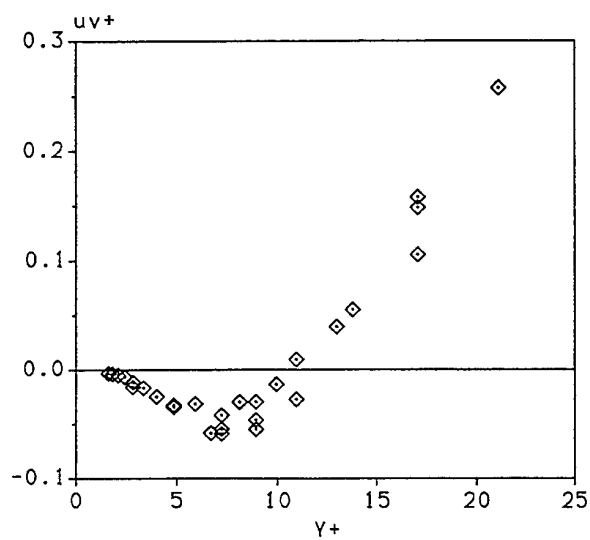


Figure 7. Close-up of the turbulent shear stress close to the wall.

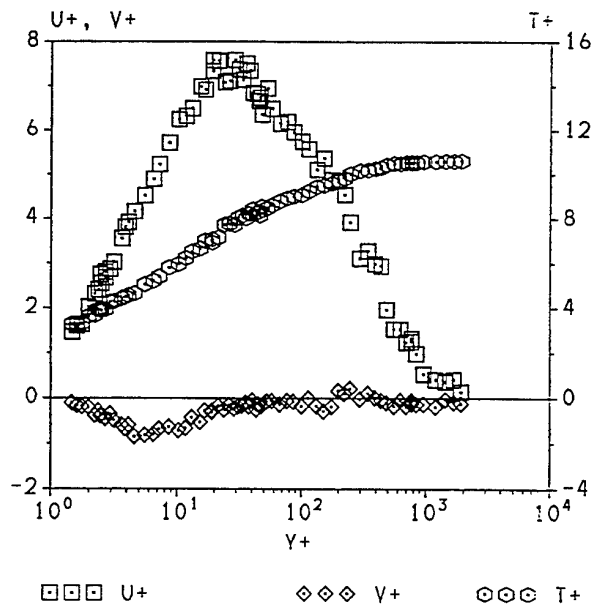


Figure 8. Measured mean velocity and mean temperature distributions, test 2.

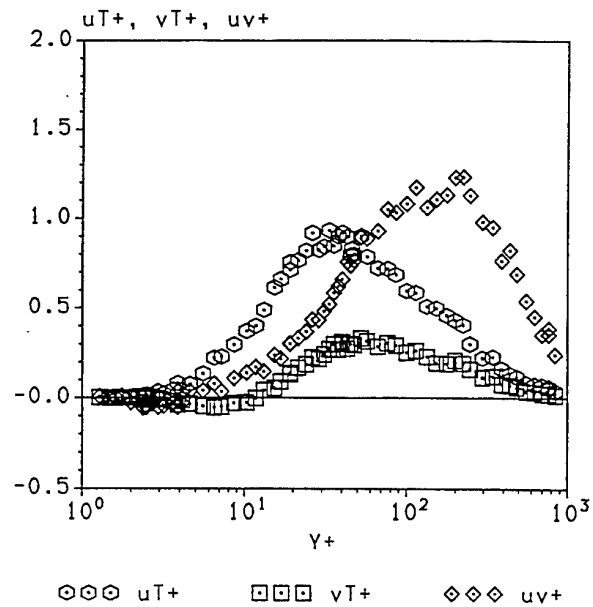


Figure 10. Measured shear stress and turbulent heat flux distributions, test 2.

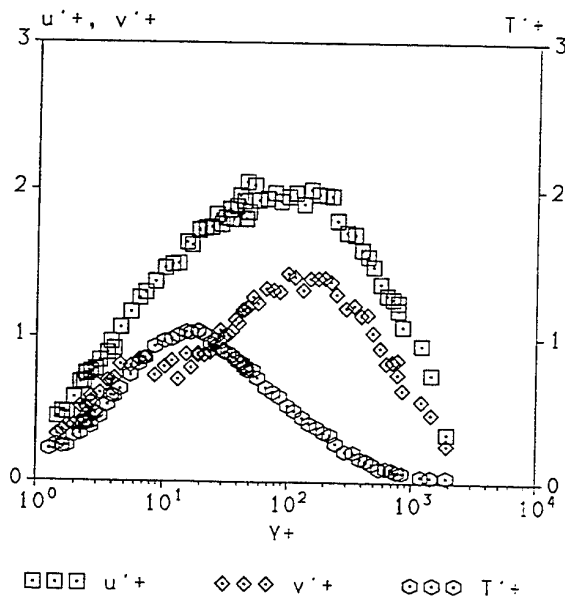


Figure 9. Measured intensities of velocity and temperature fluctuations, test 2.

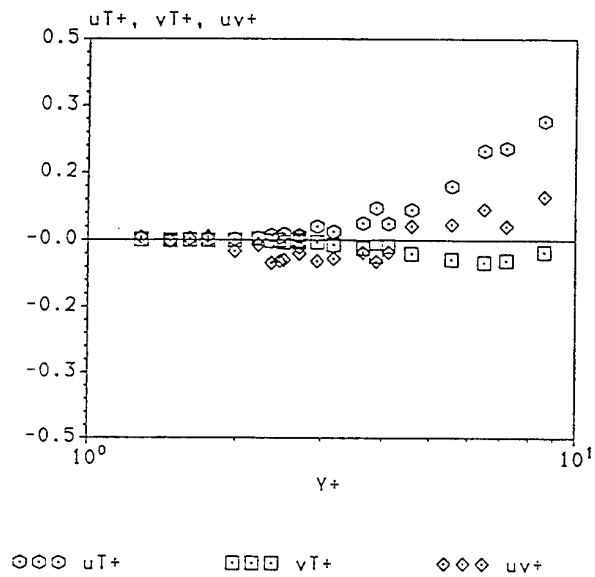


Figure 11. Close-up of turbulent shear stress and heat flux distributions close to the wall, test 2.

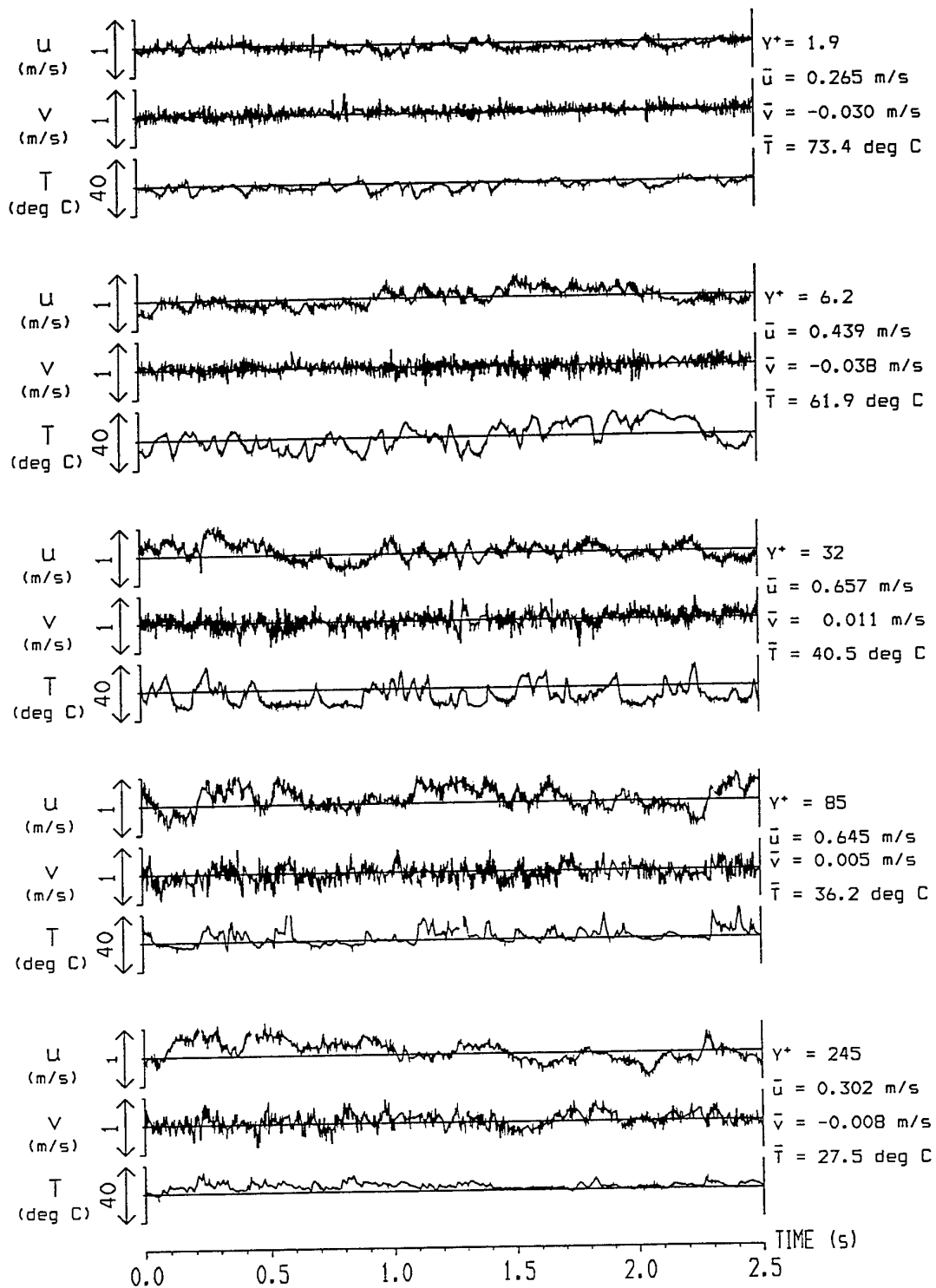


Figure 12. Typical time records of velocity and temperature close to the wall, test 2.

SESSION 36

LDV Data Processing

UNCERTAINTY ESTIMATES FOR ANY TURBULENCE STATISTIC

L. H. Benedict and R. D. Gould

Department of Mechanical & Aerospace Engineering
North Carolina State University
Raleigh, NC 27695, USA

ABSTRACT

Methods for calculating the statistical uncertainty associated with the sampling of random processes such as those which occur in turbulence research are given. In particular, formulas based on normal distribution assumptions and on any general distribution shape are given for means, variances, Reynolds stresses, correlation coefficients, homogeneous and mixed turbulent triple products and fourth order turbulence moments. In addition, two resampling algorithms, the "bootstrap" and "jackknife", are presented and compared using actual turbulence data. The availability of these methods will allow turbulence data to be presented with statistical uncertainty error bars on *all* turbulence quantities.

1. INTRODUCTION

Uncertainty analysis in the context of single sample experiments and the planning or design of experiments has been addressed by Kline and McClintock (1953), Kline (1985), Moffat (1982, 1985, 1988) and Abernethy et al. (1985). These works discuss: estimation of instrument uncertainties, facility variability, instrumentation bias, human error, and the propagation of these individual uncertainties into overall uncertainties for experimental results. They touch upon random processes only in the sense that repetition of readings from an instrument or repetition of an entire experiment leads to a random process that can be considered normally distributed without correlation between repetitions. Thus the uncertainty in the mean estimated from a group of independent observations is the highest order statistic treated by the above references.

George (1978) gives a good account of the basic uncertainty principles governing the statistics of correlated time series with emphasis on the differences between equal-time and Poisson sampling. Statistics treated by George include the mean, variance, autocorrelation and power spectrum.

There remains a need to provide researchers with a convenient accurate method for determining uncertainties of higher order statistics. This need is especially felt by

experimentalists attempting to validate complex turbulence models who wish to know and report the accuracy of higher order turbulence correlations. It is also surely felt by computationalist trying to decide whether it is their model or rather the experimental data which needs reworking! This communication seeks to introduce to the turbulence community some results from large sample theory and two useful resampling algorithms, now widespread in the field of statistics, the use of which could lead to more precise uncertainty estimates for turbulence statistics and a more realistic appraisal of the accuracy of experimental data.

2. STATISTICAL VARIANCE OF HIGHER ORDER MOMENTS

Most experimentalists are familiar with the determination of a confidence interval for the sample mean. For the sake of introduction we repeat here that for uncorrelated samples where $N > 30$, the statistic

$$z = \frac{\bar{x} - \mu_x}{[s_x^2/N]^{1/2}} \quad (1)$$

has a standardized normal distribution (regardless of the underlying distribution of x) where N is the number of samples, μ_x is the true mean of x , \bar{x} is the sample mean, and s_x^2 the sample variance of x . The quantity s_x^2/N is the variance of the estimated mean, \bar{x} . A 95% confidence interval then follows where we say that we are 95% certain the true mean, μ_x , falls within the interval, $\bar{x} \pm 1.96(s_x^2/N)^{1/2}$ (see Bendat and Piersol (1986) for further information). For a 99% confidence interval the 1.96 factor would be replaced with 2.58. This confidence interval is symmetric about the estimate and simple to calculate.

Unfortunately in the study of turbulence, statistics up to at least third order moments are required and it is for such statistics that the determination of confidence limits is not so clear. A simple formula based on the Chi squared, χ^2 , statistic for the uncertainty of the sample variance is also

widely known. It is valid only for variables with a normal distribution, however, whereas most turbulent flow quantities are *not* normally distributed. Formulas for moments above the second are difficult to find in the literature. Castro (1989) gives a good discussion of uncertainties for higher order moments again under the assumption of a normally distributed variable.

To find techniques suitable for assessing the uncertainty of turbulence correlations of arbitrary order, one must delve deeply into the statistics literature. Stuart and Ord (1994) and Kendall and Stuart (1958) present general formulas for the sampling variance of univariate and bivariate central moments based on large sample theory. Specifically, if the exact r^{th} central moment, μ_r , of a distribution is given by

$$\mu_r = \int_{-\infty}^{\infty} (x - \mu_x)^r dF \quad (2)$$

where dF is the cumulative distribution function of the variable, x , and if the r^{th} central moment sampling statistic, m_r , is given by

$$m_r = \frac{1}{N} \sum_{i=1}^N (x_i - \bar{x})^r \quad (3)$$

then the sampling variance of m_r is given by

$$\text{var}(m_r) = \frac{1}{N} (\mu_{2r} - \mu_r^2 + r^2 \mu_{r-1}^2 \mu_2 - 2r \mu_{r+1} \mu_{r-1}) \quad (4)$$

where terms of order N^{-2} have been neglected. Note that $\mu_1 = \mu_1 = 0$. 95% confidence intervals may then be constructed as $m_r \pm 1.96 [\text{var}(m_r)]^{1/2}$.

Equation (4) relies on the asymptotic tendency to normality of the central moment statistic in question. This tendency is realized only for large N where the actual number associated with "large" becomes greater for higher order moments and variables with significant deviations from normality in their distribution functions. For turbulence studies, 1000 can be considered a "safe" number to ensure close adherence to normality for moments through fourth order. Note also that equation (4) is in terms of the exact central moments, μ_r , and not the central moment sampling statistics, m_r . Once again, large sample theory arguments are used to justify replacing these μ_r 's with m_r 's in the practical computation of uncertainties.

Extension of equation (4) to the bivariate case is straightforward. Defining the exact $r^{\text{th}}, s^{\text{th}}$ mixed central moment as

$$\mu_{r,s} = \int_{-\infty}^{\infty} \int_{-\infty}^{\infty} (x - \mu_x)^r (y - \mu_y)^s dF_x dF_y \quad (5)$$

and the $r^{\text{th}}, s^{\text{th}}$ central moment statistic, $m_{r,s}$, by

$$m_{r,s} = \frac{1}{N} \sum_{i=1}^N (x_i - \bar{x})^r (y_i - \bar{y})^s \quad (6)$$

results in the sampling variance of $m_{r,s}$ as

$$\text{var}(m_{r,s}) = \frac{1}{N} \left(\begin{aligned} &\mu_{2r,2s} - \mu_{r,s}^2 + r^2 \mu_{2,0} \mu_{r-1,s}^2 + \\ &s^2 \mu_{0,2} \mu_{r,s-1}^2 + 2rs \mu_{1,1} \mu_{r-1,s} \mu_{r,s-1} - \\ &2r \mu_{r+1,s} \mu_{r-1,s} - 2s \mu_{r,s+1} \mu_{r,s-1} \end{aligned} \right) \quad (7)$$

From equation (7) the variance of a bivariate central moment of arbitrary order may be determined. Note that $\mu_{10} = \mu_{01} = 0$, $\mu_{r,-1} = \mu_{-1,s} = 0$, $\mu_{20} = \text{var}(x_i)$, and $\mu_{02} = \text{var}(y_i)$. For $s = 0$, equation (7) reduces to equation (4).

Equations (4) and (7) are valid for variables of arbitrary distribution function (i.e., non normal variables) so long as N is large, as presumably it will be for studies of turbulence. Simplified formulas assuming normally distributed x_i and y_i can be derived from equations (4) or (7) using relations between the central moments of normal variables. Specifically, all odd moments in equations (4) and (7) are zero for a normal distribution and the 2nd, 4th, 6th and 8th moments in equations (4) and (7) are 1, 3, 15 and 105 times σ^2 , respectively, for a normal distribution. In this investigation, formulas derived from equations (4) and (7), valid for any distribution, as well as formulas based on a normal distribution assumption were applied to actual turbulence measurements made using a laser Doppler anemometer (LDA) to compare uncertainty estimates for specific higher order fluctuating velocity correlations. The variances of the statistics considered herein are presented in Table 1 using the nomenclature familiar to turbulence research. Formulas for $\sqrt{u^2}$, the standard deviation and R_{uv} , the shear stress correlation coefficient are included as they are also of interest to turbulence researchers. Note that the formulas given in Table 1 are *multiplied by N*. As an example, the 95% confidence bounds for the third central moment of U for any probability distribution shape would be

$$\bar{u}^3 \pm 1.96 \left\{ \left[\bar{u}^6 - (\bar{u}^3)^2 - 6(\bar{u}^4)(\bar{u}^2) + 9(\bar{u}^2)^3 \right] / N \right\}^{1/2} \quad (8)$$

This equation is constructed by setting $r = 3$ in equations (3) and (4) and $x = U$ in equation (3). Note that $U \equiv \bar{U} + u$ and $V \equiv \bar{V} + v$ in this discussion where the overbar denotes sample mean and the lower case letter denotes fluctuation about the mean. Similarly, the confidence interval for the mixed triple product \overline{uvu} is found by setting $r = 2$, $s = 1$, $x = U$ and $y = V$ in equations (6) and (7) and is given in Table 1 for reference. Confidence intervals for any combination of moments can be constructed using equation (4) or (7). Use of the formulas in Table 1 (or any other derived from equations (4) and (7)) requires independence between samples. Practically speaking, the data rate must be less than $1/2T$ where T , is the integral time scale of the quantity being

Table 1. Estimator variances multiplied by N

Statistic	Valid for any distribution	Normal assumption
\bar{U}	\bar{u}^2	\bar{u}^2
$\sqrt{\bar{u}^2}$	$\left[\bar{u}^4 - (\bar{u}^2)^2 \right] / 4\bar{u}^2$	$\bar{u}^2/2$
\bar{uv}	$\bar{u}^2\bar{v}^2 - (\bar{uv})^2$	$(1 + R_{uv}^2)(\bar{u}^2)(\bar{v}^2)$
$R_{uv} = \frac{\bar{uv}}{(\bar{u}^2)^{1/2}(\bar{v}^2)^{1/2}}$	$R_{uv}^2 \left[\frac{\bar{u}^2\bar{v}^2}{(\bar{uv})^2} + \frac{1}{4} \left(\frac{\bar{u}^4}{(\bar{u}^2)^2} + \frac{\bar{v}^4}{(\bar{v}^2)^2} + \frac{2\bar{u}^2\bar{v}^2}{(\bar{u}^2)(\bar{v}^2)} \right) - \left(\frac{\bar{u}^3\bar{v}}{(\bar{uv})(\bar{u}^2)} + \frac{\bar{uv}^3}{(\bar{uv})(\bar{v}^2)} \right) \right]$	$(1 - R_{uv}^2)^2$
\bar{u}^2	$\bar{u}^4 - (\bar{u}^2)^2$	$2(\bar{u}^2)^2$
\bar{u}^3	$\bar{u}^6 - (\bar{u}^3)^2 - 6(\bar{u}^4)(\bar{u}^2) + 9(\bar{u}^2)^3$	$6(\bar{u}^2)^3$
\bar{vuu}	$\bar{u}^4\bar{v}^2 - (\bar{u}^2\bar{v})^2 + (\bar{u}^2)^2\bar{v}^2 + 8\bar{u}^2(\bar{uv})^2 - 2\bar{u}^2(\bar{u}^2\bar{v}^2) - 4(\bar{uv})(\bar{u}^3\bar{v})$	$2(1 + 2R_{uv}^2)(\bar{u}^2)^2(\bar{v}^2)$
\bar{u}^4	$\bar{u}^8 - (\bar{u}^4)^2 - 8(\bar{u}^5)(\bar{u}^3) + 16(\bar{u}^3)^2\bar{u}^2$	$96(\bar{u}^2)^4$

measured, i.e., $T = \int R_{xx} dt$ (see George (1978)). This should not be a great limitation for as George points out, it is inefficient from the standpoint of minimizing uncertainty to sample any faster than this rate. It is imperative, however, that reliable estimates of the integral time scale be made prior to any experiment to ensure that samples will be independent of one another. (Some practical guidelines for making autocorrelation measurements using an LDA can be found in Benedict and Gould (1995).) If the sampling rate is too high to ensure independence of samples, N should be adjusted to reflect the number of integral scales in the total sampling time, not the actual number of samples. Otherwise confidence bounds based on N would be too narrow.

3. RESAMPLING ALGORITHMS

The reader may note that compilation of formulas suitable for estimating the uncertainty of higher order statistics can be quite tedious. Additionally, researchers may have an interest in statistics for which there are no readily available formulas. Two resampling algorithms are available in the statistics literature, however, which should be applicable to any of the statistics measured in turbulence research. They also require independence between samples. The first of these is referred to as the *jackknife*, named by Tukey (1958), who first recognized its potential for estimating standard errors. Miller (1974) provides a review of jackknife research while Efron and Tibshirani (1993) discuss practical implementation.

Given a data set $\mathbf{x} = (x_1, x_2, \dots, x_N)$ and some statistical estimator, $\hat{\theta}$, determined from this original data set \mathbf{x} , the jackknife makes use of the N data subsets that leave out one measurement at a time from the original data set giving $i = 1, 2, \dots, N$ new jackknife data sets

$$\mathbf{x}_{jack,i} = (x_1, x_2, \dots, x_{i-1}, x_{i+1}, \dots, x_N) \quad (9)$$

called *jackknife samples*. These new data sets are used to form N *jackknife replications*, $\hat{\theta}_{jack,i}$, of the statistical estimator of interest, $\hat{\theta}$. The jackknife estimate of variance for $\hat{\theta}$ is defined as

$$\text{var}(\hat{\theta})_{jack} = \frac{N-1}{N} \sum_{i=1}^N \left(\hat{\theta}_{jack,i} - \bar{\hat{\theta}}_{jack} \right)^2 \quad (10)$$

where

$$\bar{\hat{\theta}}_{jack} = \frac{1}{N} \sum_{i=1}^N \hat{\theta}_{jack,i} \quad (11)$$

and an approximate 95% confidence interval for the estimator, $\hat{\theta}$, is then given by $\hat{\theta} \pm 1.96 \left(\text{var}(\hat{\theta})_{jack} \right)^{1/2}$.

According to Efron and Tibshirani, the jackknife may be viewed as an approximation to a more general resampling algorithm, the *bootstrap*, introduced by Efron (1979). Its implementation consists of drawing randomly, with replacement B independent *bootstrap samples* $\mathbf{x}_{boot,1}, \mathbf{x}_{boot,2}, \dots, \mathbf{x}_{boot,B}$, each consisting of N data values from the original data set, \mathbf{x} . (Replacement implies that each bootstrap sample is always drawn from the entire original data set, \mathbf{x} .) For each bootstrap sample, a *bootstrap replication*, $\hat{\theta}_{boot,i}$, $i = 1, 2, \dots, B$, of the desired statistic is calculated. The bootstrap estimate of variance is defined as

$$\text{var}(\hat{\theta})_{boot} = \frac{1}{B-1} \sum_{i=1}^B \left(\hat{\theta}_{boot,i} - \bar{\hat{\theta}}_{boot} \right)^2 \quad (12)$$

where

$$\hat{\theta}_{boot} = \frac{1}{N} \sum_{i=1}^N \hat{\theta}_{boot,i} \quad (13)$$

An approximate 95% confidence interval for the estimator, $\hat{\theta}$, follows as $\hat{\theta} \pm 1.96 \left(\text{var}(\hat{\theta}_{boot}) \right)^{1/2}$. The number of bootstrap replications required for satisfactory results is investigated in section 4.

4. A NOTE ON IMPLEMENTATION

The bootstrap algorithm requires $B \times N$ calculations per statistic. As will be shown in section 5, below, $B=100$ is usually a sufficient number of bootstrap replications so that the algorithm can be said to require roughly $100N$ calculations per variance estimate. The jackknife in its general form requires N^2 calculations per variance estimate. Thus for $N > 100$, the jackknife would appear much the slower of the two algorithms, requiring roughly the computing time of a power spectrum *without* benefit of the fast Fourier transform.

At the expense of generality, however, the jackknife may be structured so as to reduce the number of calculations from N^2 to N . This is a very significant reduction in computing time (when N is measured in thousands) and, in many cases, is well worth the added programming chore. This reduction in computation is accomplished by expanding the individual jackknife centralized moment statistics to create a series of summations composed entirely of noncentralized variables. A simple example is afforded by the jackknife estimate of the variance for \bar{u}^2 . First, the variance for jackknife sample i is written as

$$\hat{\theta}_{jack,i} = \bar{u}^2_{jack,i} = \frac{1}{N-1} \sum_{j=1, j \neq i}^N (U_j - \bar{U}_{jack,i})^2 \quad (14)$$

where the summation is over $N-1$ samples since each jackknife replication leaves out one sample from the data set. Equation (14) may be expanded as

$$\bar{u}^2_{jack,i} = \frac{1}{N-1} \left[\sum_{j=1, j \neq i}^N U_j^2 - 2\bar{U}_{jack,i} \sum_{j=1, j \neq i}^N U_j + (N-1) \left(\bar{U}_{jack,i} \right)^2 \right] \quad (15)$$

and simplified further giving

$$\bar{u}^2_{jack,i} = \frac{1}{N-1} \sum_{j=1, j \neq i}^N U_j^2 - \left(\frac{1}{N-1} \sum_{j=1, j \neq i}^N U_j \right)^2 \quad (16)$$

Note that the mean for each jackknife data set, $\bar{U}_{jack,i}$, is given as

$$\bar{U}_{jack,i} = \frac{1}{N-1} \sum_{j=1, j \neq i}^N U_j \quad (17)$$

An efficient way to calculate $\bar{u}^2_{jack,i}$ is to first find the sum of U_j^2 and U_j for the entire sample set ($j=1, 2, \dots, N$). Then these sums in equation (16) are merely decremented by U_j^2 and U_j , respectively, for each jackknife replication.

The jackknife replications determined in this fashion are used in equations (10) and (11) to determine the variance of \bar{u}^2 . Equation (10) can be expanded, similar to what was done with equation (14), so that the calculations can be made in one pass as follows

$$\text{var}(\bar{u}^2) = (N-1) \left(\frac{1}{N} \sum_{j=1}^N (\bar{u}^2_{jack,i})^2 - \left(\frac{1}{N} \sum_{j=1}^N \bar{u}^2_{jack,i} \right)^2 \right) \quad (18)$$

where the second term in brackets is

$$\overline{\bar{u}^2_{jack,i}} = \frac{1}{N} \sum_{i=1}^N \bar{u}^2_{jack,i} \quad (19)$$

This procedure may be carried out for any statistic based on central moments. The cost, of course, being that a single jackknife algorithm no longer applies to every statistic. New sum variables must be programmed for each new statistic of interest. An example of this streamlined procedure is given in the partial FORTRAN code listed in the APPENDIX.

5. APPLICATION TO LDA DATA

LDA data from flow over a backward-facing step have been used to compare the performance of the uncertainty formulas from Table 1 and the resampling algorithms presented above. Details concerning the facility and data acquisition are available in Benedict (1995). In the figures that follow, x is the streamwise direction (U velocity component) with its origin at the plane of the backstep face and y is the normal direction (V velocity component) with its origin on the bottom wall. Thus, the separation point of the step is at $x/h=0$ and $y/h=1$ where $h=25.4$ mm is the step height.

A controlled processor sampling in approximate equal-time increments at 100 Hz was used to ensure independence between samples. The necessary data rate was determined from extensive autocorrelation measurements which determined integral time scale estimates throughout the flow. The controlled processor was also operated according to the criteria set by Winter et al. (1991) to ensure an unbiased data set.

The upper plots in Figure 1 show measurements of $\overline{u^2}$, $\overline{u^3}$, and $\overline{u^4}$ at $x/h = 4.0$ (reattachment at $x/h = 6.4$) with $N = 6000$. The lower axes of the upper plots give the absolute magnitude of these statistics normalized by the centerline velocity ($U_{ref} = 15.75$ m/s) at $x/h = -0.5$. The upper axes for the plots of $\overline{u^3}$ and $\overline{u^4}$ also give the skewness, $\overline{u^3}/(\overline{u^2})^{3/2}$, and kurtosis, $\overline{u^4}/(\overline{u^2})^2$, of the U distribution, respectively (3.0 is the kurtosis for a normal distribution). Error bars in the upper plots indicate the 95% confidence bounds of these statistics and were calculated using the formulas in Table 1 valid for any distribution. The upper plots show that uncertainties vary widely across a profile. Although the relative uncertainties are highest for quantities of small absolute magnitude, their absolute uncertainties are insignificant at these locations. Thus it is clear that $\overline{u^3} \approx 0$ for $y/h \geq 1.5$ at $x/h = 4$ even though the relative uncertainty at this location is 40%. It is also evident that the precise measurement of higher order correlations requires a vast number of measurements. Uncertainty levels of 2% in the peak triple product measurements would require $N \approx 200000$.

The lower plots compare the absolute uncertainties determined from the four methods presented above. Various

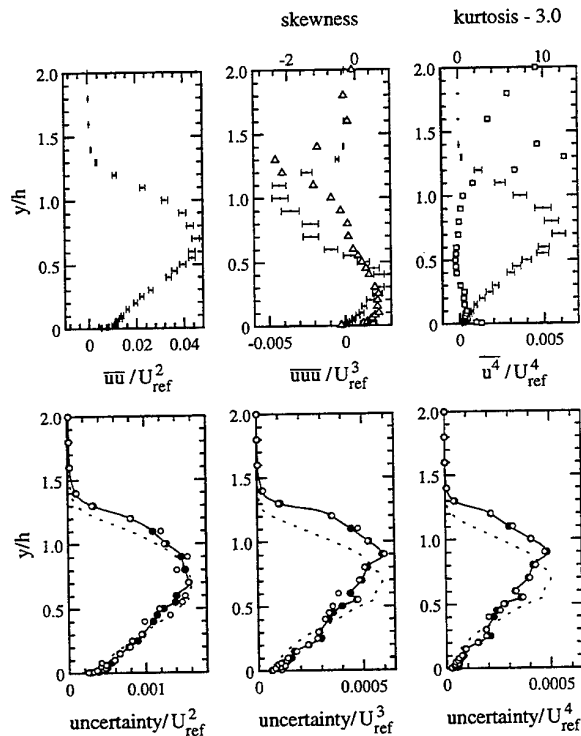


Figure 1 Comparison of uncertainties at $x/h = 4.0$
 normal assumption (Table 1 formulas)
 — any distribution (Table 1 formulas)
 ● jackknife, ○ bootstrap, 100 replications
 △ skewness, □ kurtosis - 3.0

line types are used for some of the error estimates, as opposed to symbols, in order to make the plots clearer. These lines *do not* imply that errors estimates have been made at any values of y/h other than those at which measurements were made. The formulas based on a normal distribution assumption underestimate the uncertainty in regions where the skewness or flatness of the velocity distribution is high, e.g. $y/h = 1.2$. They can also overestimate the uncertainty if the distribution is very narrow, e.g. $y/h = 0.55$. At this location the skewness ≈ 0 while the kurtosis < 3.0 . The jackknife uncertainty estimates agree with the formulas valid for any distribution to at least 3 significant digits. It can be shown theoretically that the jackknife is biased slightly high in its estimation of uncertainty. Thus the jackknife will never underestimate the uncertainty of a statistic. This bias is negligible however for the sample sizes presented here and commonly used in turbulence research. The bootstrap algorithm using 100 bootstrap replications performs well in all cases with values falling near those determined using Table 1 formulas valid for any distribution.

In answering the question as to how many bootstrap replications B are necessary, Efron and Tibshirani suggest that $25 \leq B \leq 200$ suffices for most statistics. Figure 2 explores this question by presenting the deviation of bootstrap uncertainties, in percent, from those calculated with Table 1 formulas valid for any distribution. The number of replications necessary to achieve accuracy to within about 10% of the Table 1 formulas is 100 for all three statistics. Note that the bootstrap can err on the low side so that overly "optimistic" uncertainty estimates are possible with this algorithm in contrast to the jackknife.

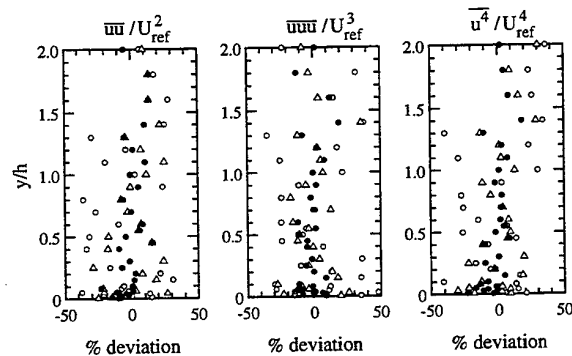


Figure 2 Bootstrap deviation from general formula for
 ○ $B = 10$, △ $B = 25$, ● $B = 100$

Figure 3 illustrates results for measurements of the Reynolds stress, shear correlation coefficient, and a mixed triple product with $N = 12000$, also from the backstep flow at $x/h = 4$. Results are similar to those of Figure 1, however, it is interesting to note the behavior of the shear correlation coefficient uncertainties. Firstly, the normal assumption (Table 1 formulas) performs very badly for skewed or flat distributions. The skewness of V is roughly minus that shown for U in Figure 1 while its kurtosis is similar to that of U in

Figure 1. Additionally, whereas most statistics have a higher absolute uncertainty when the statistic is large, R_{uv} displays an opposite trend. Its absolute uncertainty is smallest when its magnitude is greatest. This behavior stems from the correlation between the two velocity components. The reduction of uncertainty for large values of R_{uv} is of practical importance in terms of making accurate turbulence measurements, for although \overline{uv} itself may be a highly uncertain quantity, R_{uv} can be determined with relatively high accuracy when it attains values typical of turbulent flows (roughly -0.4).

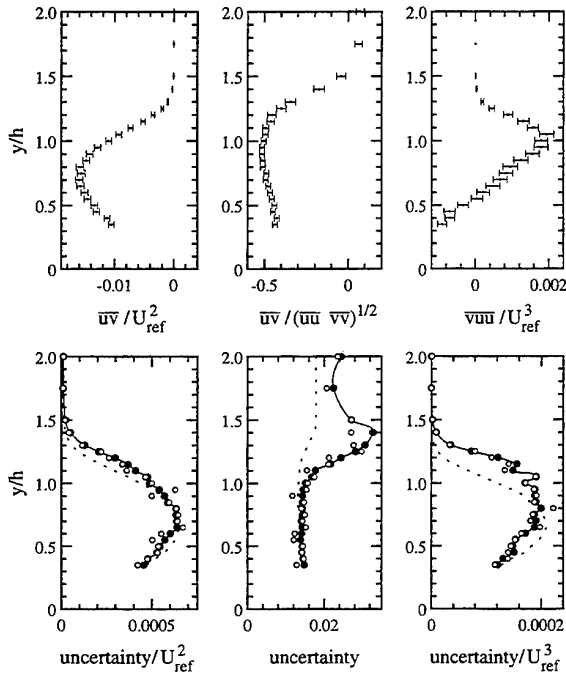


Figure 3 Comparison of uncertainties at $x/h = 4.0$
 normal assumption (Table 1 formulas)
 ——— any distribution (Table 1 formulas)
 • jackknife, ○ bootstrap, 100 replications

When the statistical uncertainty of each measurement can be reliably calculated, the task of combining uncertainties of individual terms in an equation to estimate the overall uncertainty of the result is easily accomplished according to the guidelines of Kline and McClintock (1953). Figure 4 presents the results of such computations for a turbulent kinetic energy (TKE) balance made using measurements in the backstep flow ($N=12000$). All terms in the TKE equation were normalized by h/U_{ref}^3 . As is typical of TKE balances, the pressure-velocity diffusion term has been assumed negligible and the dissipation determined through balance of the TKE equation (see for example, Gould et al. (1990)). No smoothing of the data has been done prior to differentiation. It is clear that uncertainties in the measured quantities, amplified by the process of differentiation, have led to significant uncertainty in the various terms of the energy

balance. The turbulent diffusion terms (consisting of triple products) have the greatest uncertainty. Obviously the dissipation, determined by balance of the other terms, is a highly uncertain quantity. In practice, each measured profile would have been smoothed prior to differentiation leading to less scatter in the terms of the energy balance; however, smoothing amounts to assuming a shape for the measured profile. It is questionable whether an energy balance determined in this way, although more pleasing to the eye, is any more accurate.

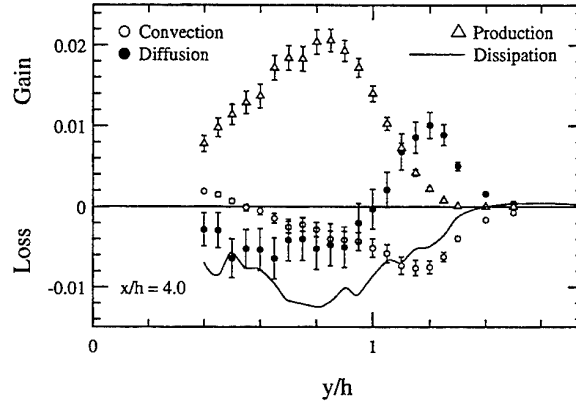


Figure 4 Energy balance uncertainty analysis

Finally, Figure 5 presents measurements of the longitudinal spatial correlation $R_{11}(x,0,0)$ in the recirculation zone ($x/h = 2.0$, $y/h = 0.4$) of the backstep flow ($N=12000$). Formulas for R_{uv} from Table 1 are applicable to this statistic although the same velocity component is measured at two locations in this case. Also, included on this figure are the uncertainties estimated using the four methods described above. Bootstrap uncertainties have been calculated using 100 bootstrap replications. Spatial correlation measurements are currently of interest in direct measurements of the turbulent dissipation rate and for the determination of turbulence length scales. One method for estimating the dissipation or micro length scale is to fit a parabola to the spatial correlation function near zero separation. The location where this parabola intersects the Δx axis is defined as the spatial microscale. It is thus useful to analyze the uncertainty of such measurements in the context of fitting a parabola to the data near $\Delta x/h = 0$. A parabolic fit to the data near $\Delta x/h = 0$ is also shown in Figure 5. It can be seen that the uncertainty decreases markedly near $\Delta x/h = 0$. This is, of course, the same effect mentioned with regard to the shear stress correlation coefficient above. This can be understood from the definition of the spatial correlation coefficient

$$R_{11}(x,0,0) = \frac{\overline{u(x)u(x+\Delta x)}}{\sqrt{\overline{u^2(x)}}\sqrt{\overline{u^2(x+\Delta x)}}} = \frac{\overline{u_1 u_2}}{\sqrt{\overline{u_1^2}}\sqrt{\overline{u_2^2}}} \quad (16)$$

As $\Delta x \rightarrow 0$ the correlation between u_1 and u_2 increases so that it can be stated approximately

$$R_{11}(0,0,0) \approx \frac{\overline{u_1^2}}{\overline{u_2^2}} = 1 \quad (17)$$

This condition is without uncertainty. It is fortuitous that uncertainties in the spatial correlation coefficient decrease substantially near zero separation. Otherwise the prospect of fitting parabolas in order to determine microscales would be remote. Even with this advantage it must be cautioned that there remains considerable uncertainty in making parabolic fits to spatial correlation functions for a variety of reasons (Benedict (1995)).

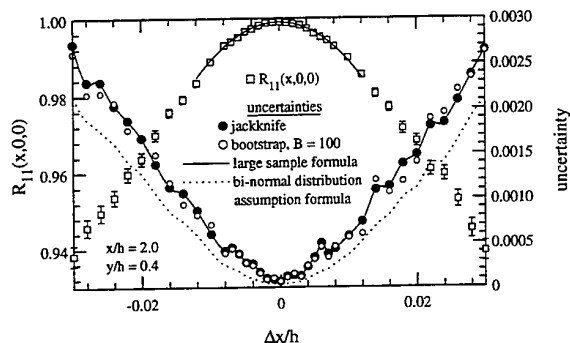


Figure 5 Statistical uncertainty in spatial correlation measurements

6. SUMMARY

It remains to be said which approach is best in the estimation of uncertainties for higher order statistics. Clearly it has been shown that formulas based on normal distribution assumptions for the measured variables are highly inaccurate when the distributions of these variables deviate from normality. In the context of turbulence research therefore they cannot be recommended. Even so, they are very simple and might be useful for grid turbulence studies or similar work in which the distributions of the measured variables can be shown not to deviate significantly from normality. Choosing between the remaining three methods discussed in this work depends on the application and amount of data to be processed. Formulas valid for any distribution of the measured variables, when available, are quick, however, a new formula is required for each statistic of interest. The resampling algorithms presented offer generality and accuracy with the bootstrap requiring $100N$ calculations per statistic and the jackknife N^2 calculations per statistic in its most general form. Jackknife algorithms tailored to individual statistics (see section 4) require only N calculations per statistic and are thus favored by the authors, especially for real time data processing. The jackknife has the additional advantage that its estimate of variance is always greater than or equal to the true variance of a statistic.

In closing it should be remarked that this paper has dealt with the uncertainty associated with the sampling of a random

process. Additional uncertainties due to the particular character of each measuring instrument or those related to the experimental facility as a whole must also be accounted for in a thorough accounting of data accuracy. For instance, positioning uncertainty could contribute significantly to the uncertainties in measurements of $R_{11}(x,0,0)$ near $\Delta x/h = 0$ in Figure 5. The rules governing this process are well established by Kline and McClintock (1953) and Moffat (1988) among others. It is hoped that this work will complement that which has preceded it.

ACKNOWLEDGMENTS

The authors wish to express their thanks to Dr. Dennis D. Boos of the Department of Statistics, North Carolina State University for directing them to the literature pertinent to this topic and for many helpful discussions. Thanks are also given to the United States Air Force Office of Scientific Research for the partial support of this work through the Summer Research Extension Program.

REFERENCES

- Abernethy, R.B., Benedict, R.P. & Dowdell, R.B. (1985) "ASME Measurement Uncertainty," *J. Fluids Eng.*, **107**, pp. 161-164.
- Bendat, J.S. & Piersol, A.G. (1986) *Random Data, Analysis and Measurement Procedures*, John Wiley & Sons, New York.
- Benedict, L.H. (1995) "Direct Measurements of Turbulent Dissipation Rate in Flow Over a Backward-Facing Step using LDA," Ph.D. dissertation, North Carolina State University, Raleigh, North Carolina.
- Benedict, L.H. and Gould, R.D. (1995) "Concerning Time and Length Scale Estimates made from Burst-mode LDA Autocorrelation Measurements," to appear in *Exp Fluids*.
- Castro, I.P. (1989) *An Introduction to the Digital Analysis of Stationary Signals*, Adam Hilger, Bristol, England.
- Efron, B., 1979, Bootstrap Methods: Another Look at the Jackknife, *Ann Statist.*, vol. 7, pp. 1-26.
- Efron, B. & Tibshirani, R.J. (1993) *An Introduction to the Bootstrap*, Chapman and Hall, New York.
- George, W.K., Jr. (1978) "Processing of Random Signals," *Proc. of the Dynamic Flow Conf.*, Skovlunde, Denmark.
- Gould, R.D., Stevenson, W.H. and Thompson, H.D. (1990) "Investigation of Turbulent Transport in an Axisymmetric Sudden Expansion," *AIAA Journal*, **28**, pp. 276-283.
- Kendall, M.G. and Stuart, A. (1958) *The advanced theory of statistics, Vol 1, distribution theory*, Charles Griffin & Co. Limited, London.

Kline, S.J. (1985) "The Purposes of Uncertainty Analysis," *J. Fluids Eng.*, **107**, pp. 153-160.

Kline, S.J. and McClintock, F.A. (1953) "Describing Uncertainties in Single-Sample Experiments," *Mechanical Eng.*, **75**, pp. 3-8.

Miller, R.G. (1974) "The Jackknife -- A Review", *Biometrika*, **61**, pp. 1-15.

Moffat, R.G. (1982) "Contributions to the Theory of Single Sample Uncertainty Analysis," *J. Fluids Eng.*, **104**, pp. 250-260.

Moffat, R.J. (1985) "Using Uncertainty Analysis in the Planning of an Experiment," *J. Fluids Eng.*, **107**, pp. 173-182.

Moffat, R.J. (1988) "Describing the Uncertainties in Experimental Results," *Exp Thermal and Fluid Science*, **1**, pp. 3-17.

Stuart, A. and Ord, J.K. (1994) *Kendall's Advanced Theory of Statistics*, Edward Arnold, London.

Tukey, J.W. (1958) "Bias and Confidence in Not-Quite Large Samples(Abstract)," *Ann Math Statist.*, **29**, p. 614.

Winter, A.R., Graham, L.J.W. and Bremhorst, K. (1991) "Velocity Bias Associated with Laser Doppler Anemometer Controlled Processors," *J. Fluids Eng.*, **113**, pp. 250-255.

APPENDIX

```

c      program jackknife
c
c      real*8 u,ubar,u2,sum_u,sum_uu,sum_uj
c      &      ,sum_uuj,ubarj,uuj,samp,sampml
c      &      ,uuj_sum,uuj2j_sum,uuj_bar,var_uu
c      &      ,uu95j
c      integer*4 isamp,j
c      dimension u(5000)
c
c      *****
c      Example of jackknife uncertainty
c      estimate for uu normal stress.
c
c      First read u velocities into an array
c      dimensioned u(isamp). It is assumed that
c      all outliers have been removed from the
c      data set prior to loading this array.
c      isamp is the number of "good" samples.
c
c      The authors give permission for the free
c      use of this code segment for all
c      non-commercial uses.
c
c      This code segment should not be relied on
c      for solving a problem whose incorrect
c      solution could result in injury to a
c      person or loss of property. The authors,
c      publisher, and North Carolina State Univ.
c      disclaim all liability for direct or
c      consequential damages resulting from the
c      use of this code segment.
c
c      Copyrighted: R.D. Gould and L.H. Benedict
c      May 1, 1996
c      *****

```

```

c      *****
c      initialize sum variables
c      *****
c
c      sum_u=0.0
c      sum_uu=0.0
c      sum_uj
c      sum_uuj=0.0
c      uuj_sum=0.0
c      uuj2j_sum=0.0
c      samp=float(isamp)
c      sampml=samp-1.0
c
c      *****
c      calculate sums for entire sample set once
c      *****
c
c      do 100 j=1,isamp
c      u2=u(j)*u(j)
c      sum_u=sum_u+u(j)
c      sum_uu=sum_uu+u2
c      100 continue
c
c      =====
c      main loop follows
c      =====
c
c      do 200 j=1,isamp
c      u2=u(j)*u(j)
c
c      *****
c      remove one sample from original data
c      set and sum moments for each jackknife
c      sample set
c      *****
c
c      sum_uj=sum_u-u(j)
c      sum_uuj=sum_uu-u2
c
c      *****
c      calculate equations (17) and (16) for
c      each jackknife sample set
c      *****
c
c      ubarj=sum_uj/sampml
c      uuj=sum_uuj/sampml-ubarj*ubarj
c
c      *****
c      calculate sum and sum squared of
c      uu,jack,i used in equation (18)
c      *****
c
c      uuj_sum=uuj_sum+uuj
c      uuj2j_sum=uuj2j_sum+uuj*uuj
c
c      200 continue
c
c      =====
c      main loop completed
c      =====
c
c      *****
c      calculate equations (19) and (18)
c      *****
c
c      uuj_bar=uuj_sum/samp
c      var_uu=sampml*(uuj2j_sum/samp-uuj_bar**2)
c
c      *****
c      calculate 95% confidence interval for uu
c      *****
c
c      uu95j=1.96*(var_uu)**0.5
c
c      stop
c      end

```

REFINED RECONSTRUCTION TECHNIQUES FOR LDA DATA ANALYSIS

H. Nobach, E. Müller

Universität Rostock, Fachbereich Elektrotechnik
Institut für Nachrichtentechnik und Informationselektronik
Richard-Wagner-Straße 31, 18119 Rostock, Germany

C. Tropea

Lehrstuhl für Strömungsmechanik, Universität Erlangen-Nürnberg
Cauerstraße 4, 91058 Erlangen, Germany

ABSTRACT

A new spectral estimator for LDA data is introduced, based on one-point reconstruction techniques, but employing a refinement which accounts in a statistical manner for the velocity change between a particle arrival and the sample instant. The technique successfully eliminates the low-pass filter behavior associated with reconstruction techniques in general and is therefore particularly interesting for the estimation of spectra at low data rates. The new estimator is demonstrated using experimental data and simulations. The evaluation is supplemented by comparisons with low-noise, hot-wire data.

1. INTRODUCTION

LDA data analysis, especially spectral estimation, has often been performed using a signal reconstruction, yielding data with equal time spacing between measurements. The statistical properties of such reconstructed data can differ significantly from the those of the physical process being measured. Among other effects, conventional reconstruction techniques introduce a finite correlation time to the originally uncorrelated noise component of the velocity time history, which is equivalent to a low-pass filter. This effect has been well documented for specific reconstruction schemes and is easily observable in measured power spectral densities (Adrian, Yao; 1987). In fact, this appears to be the dominating effect of reconstructed signals, meaning that even among reconstruction schemes, it is often difficult to give a general preference (Müller et al.; 1994).

The present work examines the possibility of improving autocorrelation and spectral estimates from reconstructed signals, using knowledge about the particle arrival statistics to *correct* the raw estimates. The techniques discussed here are applicable only for one-point interpolation schemes, i.e. interpolation between LDA data points irregularly spaced in time, which use only the last valid data point for interpolation within that interval. This would include the widely used *sample and hold interpolation* (S+H) (Adrian, Yao; 1987) or the *single exponential interpolation* (Høst-Madsen; 1994). The technique is not suitable for use with a linear interpolation or, for instance,

a fractal reconstruction, in which two or more data points are used to interpolate missing intervals of the data set.

As in many previous suggestions for estimating power spectra, the goal is to reduce the effect of noise in LDA data sets as well as the variance of the estimates — goals which are usually compatible with one another [2,10,13,18]. Furthermore, interest lies in achieving these goals also under the constraint of low data rates.

The refined reconstruction technique is introduced in section 2 including details of the solution algorithms. A brief description of the simulation procedure and experiments used to test the technique is given in section 3. The performance of the technique is then studied in section 4 with some conclusions and outlook for further work given in section 5.

2. ESTIMATION PROCEDURE

The estimation of the power spectral density (PSD) function of turbulent velocity fluctuations can be broadly subdivided into *non-parametric* and *parametric* methods, as illustrated in Fig. 1. The present technique is classified as non-parametric and uses as a starting point, existing methods of one-point signal reconstruction, re-sampling and equal time sampled PSD estimators. This PSD estimate is then refined on the basis of knowledge about the mean time between velocity samples and the distribution of the interarrival times. The approach is to derive an expression for the resampled autocorrelation function in terms of the true autocorrelation function, in a manner very similar to that presented by Adrian and Yao (1987). This relation is then inverted to estimate the true autocorrelation function from the measured resampled autocorrelation. The PSD estimate follows using a Fourier transform.

2.1 Expression For Resampled Autocorrelation Function

The derivation begins by examining the time periods involved in LDA data acquisition and resampling, as illustrated in Fig. 2 for the case of a sample and hold reconstruction. There are basically three superimposed processes: 1) the arrival of validated LDA data at the times, $t_{LDA,i}$; 2) the resolution of time measurement in the ac-

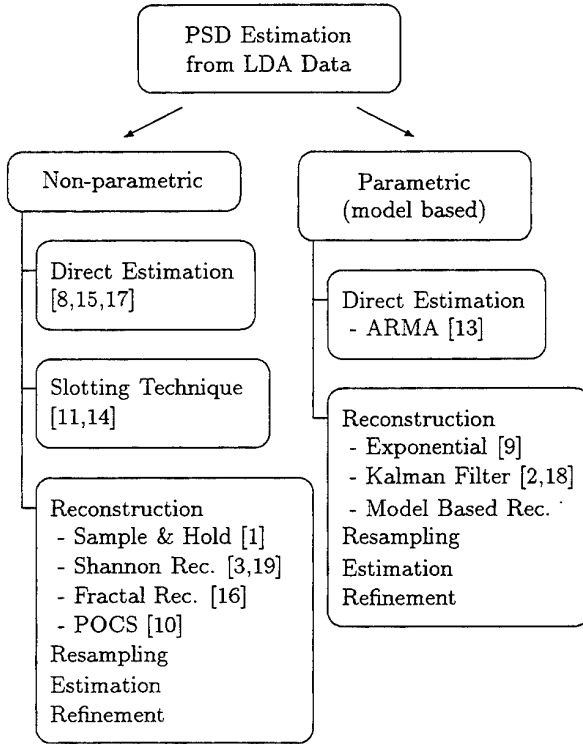


Figure 1: Overview of estimation techniques for power spectral density from LDA Data

Table 1: Possible reconstruction functions. ρ_{model} is the autocorrelation coefficient of the model process.

Reconstruction technique	$f_{rec}(\xi_j - t_i)$
Sample and hold (S+H)	1
Autoregressive 1st order (AR1) (Exponential)	$\phi_1^{\xi_j - t_i}$
Model based reconstruction	$\rho_{model}(\xi_j - t_i)$

quisition system, t_i ; 3) and the resample times ξ_j . The resample times are necessarily coincident with the time resolution steps and for present purposes these steps are assumed to be unity ($\xi_j = j$). Furthermore, this primary time resolution is assumed to be so high, that the time difference $t_{LDA,i} - t_i$ is negligible in terms of flow dynamics, i.e. $t_{LDA,i} = t_i$ and $u_{LDA,i} = u(t_i)$. In principle this time resolution will limit the spectral resolution at the high frequency end, however other factors prohibit this limit from being reached, as shown below.

Quite generally the reconstructed velocity signal can be expressed for one-point reconstruction techniques as:

$$u_{rec}(\xi_j) = u_{LDA,i} f_{rec}(\xi_j - t_i) \quad (1)$$

where $t_i - 1 \leq t_{LDA,i} < t_i \leq \xi_j \leq t_{i+1} - 1 \leq t_{LDA,i+1} < t_{i+1}$. The function f_{rec} depends on the selected reconstruction method, several possibilities are summarized in Table 1.

The autocorrelation of the reconstructed velocity signal

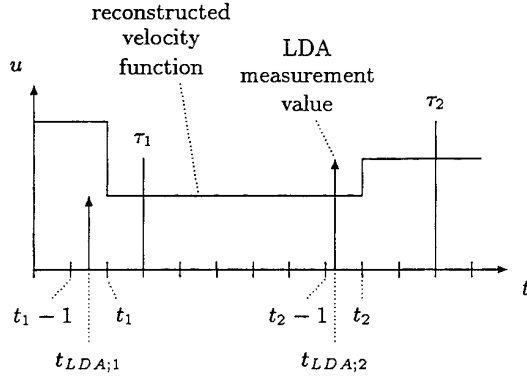


Figure 2: Principle relationship between arrival times and resample times

is given by

$$R_{rec}(\tau_1; \tau_2) = E\{u_{rec}(\tau_1)u_{rec}(\tau_2)\} \quad (2)$$

Assuming stationarity this definition becomes time independent and can be written as

$$R_{rec}(\tau) = E\{u_{rec}(\xi_j)u_{rec}(\xi_j + \tau)\} \quad (3)$$

which can be estimated from a finite data set as

$$\hat{R}_{rec}(\tau) = \frac{1}{N} \sum_{j=1}^N u_{rec}(\xi_j)u_{rec}(\xi_j + \tau) \quad (4)$$

where τ is simply the number of primary time steps between resample instances. Before proceeding to evaluate this expression, it is now necessary to examine the statistics of the time periods $\xi_j - t_i$.

The statistics of particle arrivals have been thoroughly studied [4,5] in the past. For a random spatial distribution of the seed particles, the time between particle arrivals is exponentially distributed with an exponent equal to the instantaneous particle rate

$$\dot{n}(t) = cA(\vec{u})|\vec{u}| \quad (5)$$

where c is the volume concentration and $A(\vec{u})$ is the detection area of the measurement volume projected normal to the velocity vector \vec{u} .

The probability of no particle arrival in the time interval $[t_i; \xi_j]$ is therefore

$$p(n=0; t_i; \xi_j) = e^{-\int_{t_i}^{\xi_j} \dot{n}(\tau) d\tau} \approx e^{-\dot{n}(\xi_j - t_i)} \quad (6)$$

The second expression assumes time invariance of \dot{n} over short intervals. Conversely the probability of receiving at least one particle arrival in the same interval becomes

$$p(n \geq 1; t_i; \xi_j) = 1 - e^{-\dot{n}(\xi_j - t_i)} \quad (7)$$

To now derive an expression for the autocorrelation function of the reconstructed velocity signal in terms of the true autocorrelation function, it is necessary to examine the velocity values at two times τ_1 and τ_2 and their probability of occurrence. Two different situations must be examined.

1. one measurement value at $t_{LDA;1}$ such that $t_1 - 1 \leq t_{LDA;1} < t_1 \leq \tau_1$ no further measurement value between t_1 and τ_1 and one further measurement value such that $\tau_1 \leq t_2 - 1 \leq t_{LDA;2} < t_2 \leq \tau_2$ and no further value in the interval $[t_2; \tau_2]$. In this case

$$\begin{aligned} u_{rec}(\tau_1) &= u_{LDA;1} f_{rec}(\tau_1 - t_1) \\ u_{rec}(\tau_2) &= u_{LDA;2} f_{rec}(\tau_2 - t_2) \end{aligned} \quad (8)$$

with an occurrence probability denoted by p_1 .

2. one measurement value at $t_{LDA;1}$ such that $t_1 - 1 \leq t_{LDA;1} < t_1 \leq \tau_1$ and no further measurement value in the interval $[t_1; \tau_2]$. In this case

$$\begin{aligned} u_{rec}(\tau_1) &= u_{LDA;1} f_{rec}(\tau_1 - t_1) \\ u_{rec}(\tau_2) &= u_{LDA;1} f_{rec}(\tau_2 - t_1) \end{aligned} \quad (9)$$

with an occurrence probability denoted by p_2 .

The probabilities of these two situations are respectively

$$\begin{aligned} p_1 &= (1 - e^{-\hat{n}})^2 e^{-\hat{n}(\tau_1 + \tau_2 - t_1 - t_2)} = p_1(\tau_1; \tau_2; t_1; t_2) \\ p_2 &= (1 - e^{-\hat{n}}) e^{-\hat{n}(\tau_2 - t_1)} = p_2(\tau_1; \tau_2; t_1) \end{aligned} \quad (10)$$

The autocorrelation function given by Eq. (2) can now be written

$$\begin{aligned} R_{rec}(\tau_1; \tau_2) &= \sum_{t_1=-\infty}^{\tau_1} \sum_{t_2=\tau_1+1}^{\tau_2} E\{u(t_1) f_{rec}(\tau_1 - t_1) u(t_2) f_{rec}(\tau_2 - t_2)\} p_1 \\ &+ \sum_{t_1=-\infty}^{\tau_1} E\{u(t_1) f_{rec}(\tau_1 - t_1) u(t_1) f_{rec}(\tau_2 - t_1)\} p_2 \end{aligned} \quad (11)$$

These equations can be simplified somewhat by setting $\tau_1 = 0$, which assumes an arbitrary reference time of a stationary process.

$$\begin{aligned} p_1' &= p_1'(\tau; t_1, t_2) = p_1(0; \tau; t_1, t_2) \\ &= (1 - e^{-\hat{n}})^2 e^{-\hat{n}(\tau - t_1 - t_2)} \\ p_2' &= p_2'(\tau; t_1) = p_2(0; \tau; t_1) \\ &= (1 - e^{-\hat{n}}) e^{-\hat{n}(\tau - t_1)} \end{aligned} \quad (12)$$

A final expression for the autocorrelation function of the reconstructed velocity signals can now be written

$$\begin{aligned} R_{rec}(\tau) &= \sum_{t_1=-\infty}^0 \sum_{t_2=1}^{\tau} E\{u(t_1) f_{rec}(-t_1) u(t_2) f_{rec}(\tau - t_2)\} p_1' \\ &+ \sum_{t_1=-\infty}^0 E\{u(t_1) f_{rec}(-t_1) u(t_1) f_{rec}(\tau - t_1)\} p_2' \\ &= \sum_{t_1=-\infty}^0 \sum_{t_2=1}^{\tau} R_{uu}(t_2 - t_1) f_{rec}(-t_1) f_{rec}(\tau - t_2) p_1' \\ &+ \sum_{t_1=-\infty}^0 R_{uu}(0) f_{rec}(-t_1) f_{rec}(\tau - t_1) p_2' \end{aligned} \quad (13)$$

which is in fact now expressed in terms of the true autocorrelation function $R_{uu}(\tau)$.

This expression has been verified using simulation techniques described briefly in the next section. A velocity time series with known spectrum (autocorrelation function) was generated and used to simulate LDA particle arrivals at a mean data rate of 0.316 and for 10000 time units. Fig. 3 compares the input spectrum with the spectrum deduced from Eq. (13) (after applying a Fourier transform) and with the estimated spectrum directly from Eq. (4) over the finite sample size for a sample and hold reconstruction. Clearly Eq. (13) describes the autocorrelation function of the reconstructed signal well. Fig. 3b illustrates similar performance using an AR1 reconstruction.

2.2 Refinement Of The Estimate

Using the transformation $\xi = t_2 - t_1$, Eq. (13) can be written as

$$\begin{aligned} R_{rec}(\tau) &= R_{uu}(0) \sum_{t_1=-\infty}^0 f_{rec}(-t_1) f_{rec}(\tau - t_1) p_2'(\tau; t_1) \\ &+ \sum_{\xi=1}^{\infty} R_{uu}(\xi) \sum_{t_2=1}^{\min(\tau; \xi)} f_{rec}(\xi - t_2) f_{rec}(\tau - t_2) \cdot p_1'(\tau; t_2 - \xi; t_2) \end{aligned} \quad (14)$$

which is a linear system of equations

$$R_{rec}(\tau) = \mathfrak{F} R_{uu}(\tau) \quad (15)$$

By inverting the matrix \mathfrak{F} , a *corrected* or *refined* estimate of \hat{R}_{rec} can be obtained

$$\hat{R}_{rec}^*(\tau) = \mathfrak{F}^{-1} \hat{R}_{rec}(\tau) \quad (16)$$

which is now a non-biased and consistent estimator of $R_{uu}(\tau)$. This is illustrated in Fig. 4 for the previous example, in which the PSD deduced from $\hat{R}_{rec}^*(\tau)$ is compared with the input spectrum (an AR2 process: $\phi_1 = 1.5$, $\phi_2 = -0.75$). The improvement in the spectral estimate is dramatic, at least at the lower frequencies.

3. SIMULATION TECHNIQUES AND DESCRIPTION OF THE EXPERIMENT

Both simulations and experiments have been used to investigate the performance of the refined PSD estimate, as illustrated in Fig. 5.

The simulations were based on signal generation as described by Fuchs et al. (1994). Typically a 1st or 2nd order autoregressive process is used to generate a time series, after which particle arrivals are simulated using a refined conveyor-belt model. Thus, all statistics of the underlying process are known, including the PSD, however the data is available as would be measured by an LDA, albeit without noise. The reliability of these simulations has been thoroughly investigated previously [6,7]. These simulations are used to investigate the performance of the estimators as a function of all system parameters,

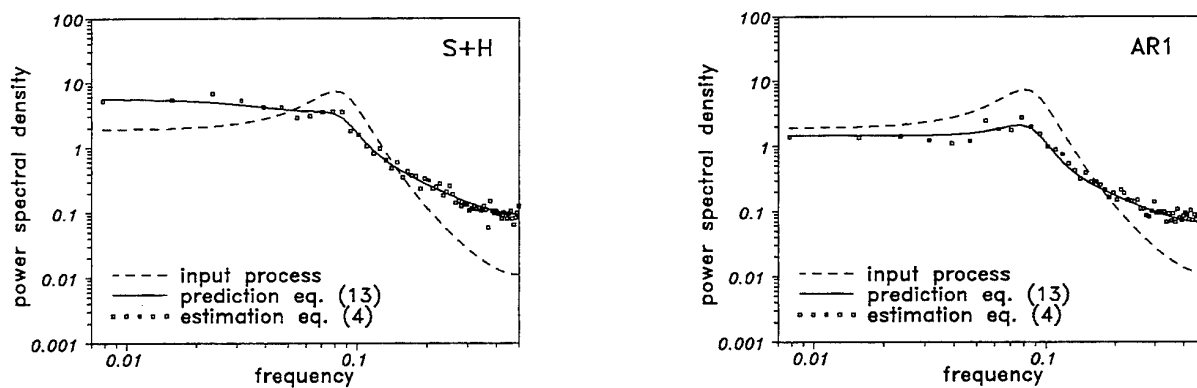


Figure 3: Power spectral density of input process, according to Eq. (13) and according to Eq. (4): a) S+H reconstruction, b) AR1 reconstruction.

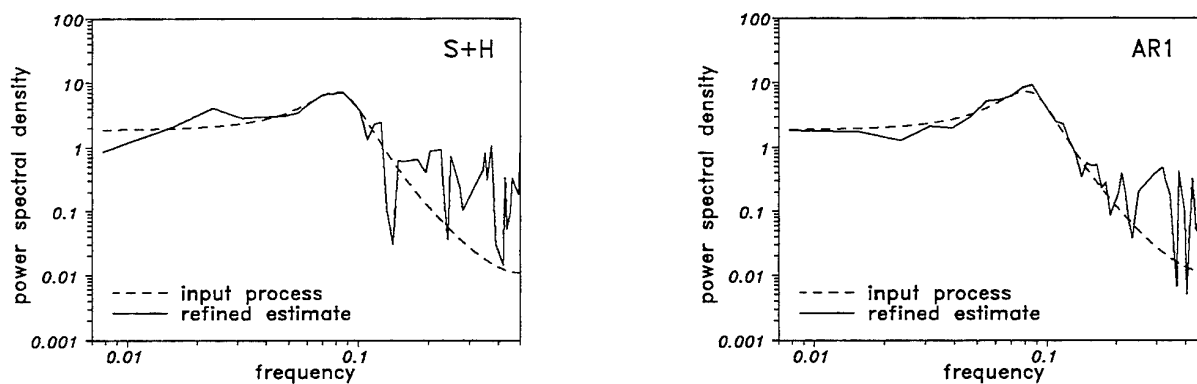


Figure 4: Power spectral density of input process and refined estimate: a) S+H reconstruction, b) AR1 reconstruction.

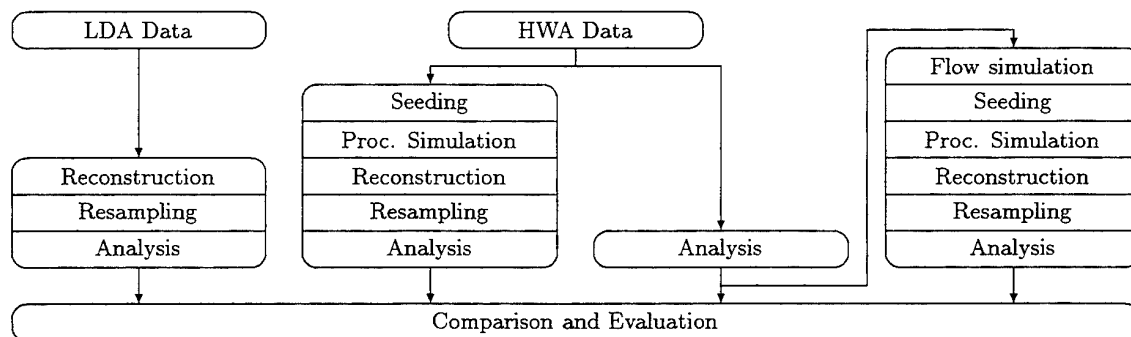


Figure 5: Use of simulations and experiments to evaluate estimator performance

Table 2: Flow specifications

z/D	x/D	Re	$I/(ms)$	$Tu/(%)$
6	3	40 000	2	24
Re - based on jet outlet diameter and velocity				

Table 3: LDA specifications

Optics	
Power	10 mW
Wavelength	632.8 nm
Mode	forward scatter
MV diameter	70 μm
MV length	470 μm
Shift	5 MHz
Processor	
Model	Counter TSI 1980
Min. Fringes	16
Mode	Total Burst

including data density (particles/integral time scale), turbulence level, etc. The simulation can be extended by adding white noise to the individual velocity samples, designed to mimic various noise sources present in the LDA system (van Maanen, Tulleken; 1994).

Alternatively, the simulation can use an analog signal sampled at a high rate as an input series. In the present case a hot-wire signal was sampled at 20 000 Hz for this purpose. The statistics of this signal can still be known within the certainty of the noise in the analog signal.

LDA and hot-wire measurements were performed in an axisymmetric free jet. The integral time scale (I) and turbulence level (Tu) could be selected according to the measurement position as summarized in Table 2. The data density of LDA measurements (N_D number of data samples per integral time scale) was varied either through the seed rate or through signal amplification.

A counter processor (TSI 1980) interfaced (DOSTEK 1400A) to a PC computer was used to process the LDA signals. Specifications of the LDA system are summarized in Table 3. The particle seeding was turned off while HWA measurements were performed at the same measurement position and flow conditions. A DANTEC 55M01 anemometer with a 55P01 single wire probe was used. The signal was filtered at 10 kHz and sampled at 20 kHz. The HWA signal was used to determine the integral time scale of the flow fluctuations and also as a reference PSD function.

4. EVALUATION OF THE ESTIMATOR

In the following evaluation only the S+H reconstruction will be examined, since preliminary investigations revealed little difference in comparison to other one-point reconstruction techniques.

The first set of results are presented in Fig. 6 in which the LDA spectral estimate with and without refinement is compared to the HWA spectra for four cases. These cases correspond to the conditions a) high data density ($N_D = 14$); b) high data density but also high noise level ($N_D = 16$); c) and d) low data density ($N_D = 0.63$), short

and long data sets respectively.

Examining, first the spectral estimate at a high data density (Fig. 6a), it is apparent that the S+H reconstruction estimate is not capable of resolving the second slope in the spectrum indicated by the HWA data. The second slope in the spectrum is associated with dissipative scales of turbulence. The first slope is termed the inertial subrange. The refinement does not improve the estimate noticeably. The S+H estimate appears smoother at high frequencies than the refined estimate. The S+H yields a systematic error which in this case dominates the random error (noise) in the LDA data set. The refined estimate in fact recovers a portion of this random error, which appears to lead to a larger variance of the estimate, but is probably more realistic of the true spectral content.

The increased noise level of case 2 (Fig. 6b) is apparent both in the raw and the refined spectral estimate, whereby the refined estimate shows a marginal advantage in the range $200 \text{ Hz} < f < 500 \text{ Hz}$.

The refined estimate shows a distinct advantage, especially at the low data rate of 314 Hz (Fig. 6c and d). The S+H estimate exhibits a low-pass filter behaviour with a cutoff frequency of $314/2\pi \approx 50 \text{ Hz}$, whereas the refined estimate appears reliable up to about 1000 Hz (Fig. 6d). Comparing Figs. 6c and d allows the influence of the record length to be evaluated, specifically the estimator variance, which will decrease with increasing record length. The estimation in Fig. 6c extends reliably only to about 500 Hz, whereas in Fig. 6d this limit is increased by factor of 2. Correspondingly, the noise level at high frequency also decreases.

The interpretation of the spectrum in Fig. 6d is hindered somewhat because the actual noise level existing in the LDA signal is not known beforehand. To circumvent this difficulty the HWA signal, which clearly has a much lower noise level, was used as the primary input signal for an LDA signal simulation. A high ($N_D = 14$) and low ($N_D = 0.63$) data density was simulated with the respective spectra estimates shown in Fig. 7.

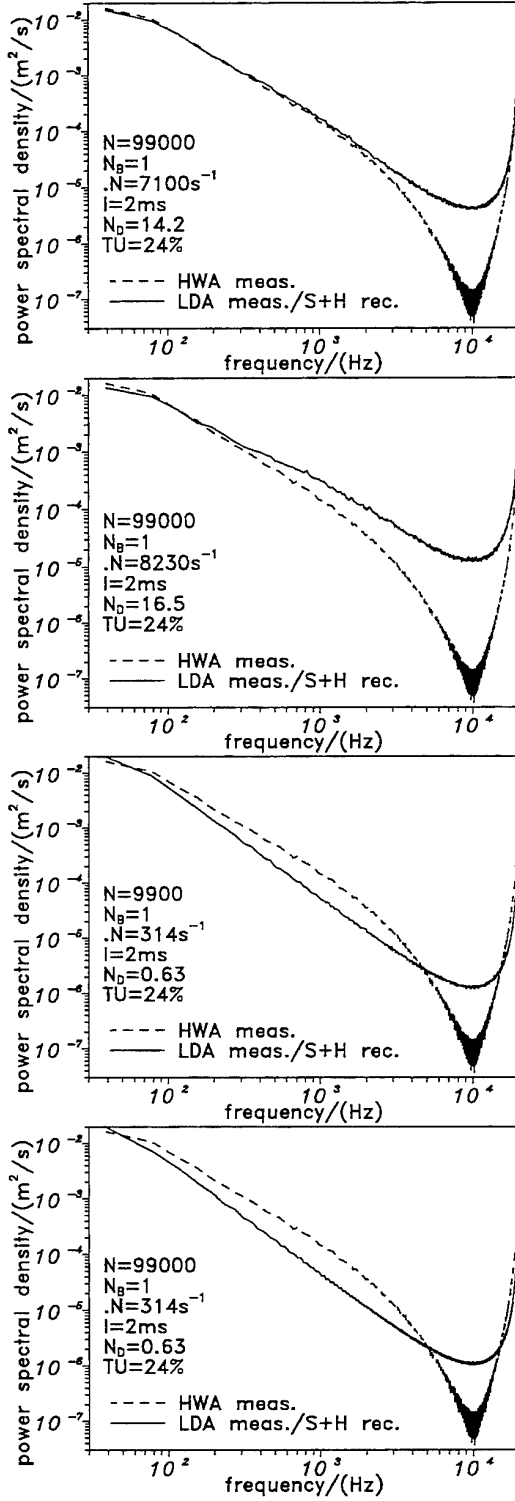
Fig. 7a shows clearly that the refined estimate is very successful in capturing even a portion of the dissipation range of the spectra whereas the raw estimate is filter dominated above 1 kHz. The approximate agreement with the true spectrum is only fortuitous in the case of the raw estimate, a situation which has often been misinterpreted in the past. These results indicate that the noise level in Fig. 6a was indeed preventing resolution of the refined spectral estimator.

The same simulation procedure at the low data rate (Fig. 7b) results in estimates in astounding agreement with the original LDA data (Fig. 6c). This is because a rather short data record has been used, in which case the estimator variance is again dominating the estimate at high frequencies.

5. CONCLUSIONS

A new spectral estimator has been introduced which builds on conventional one-point reconstruction estimators and refines these using knowledge about the particle arrival statistics. The above results on a selected number of data sets appear to be at most a modest improvement of LDA spectral estimation. On the other hand a very

S+H



S+H with refinement

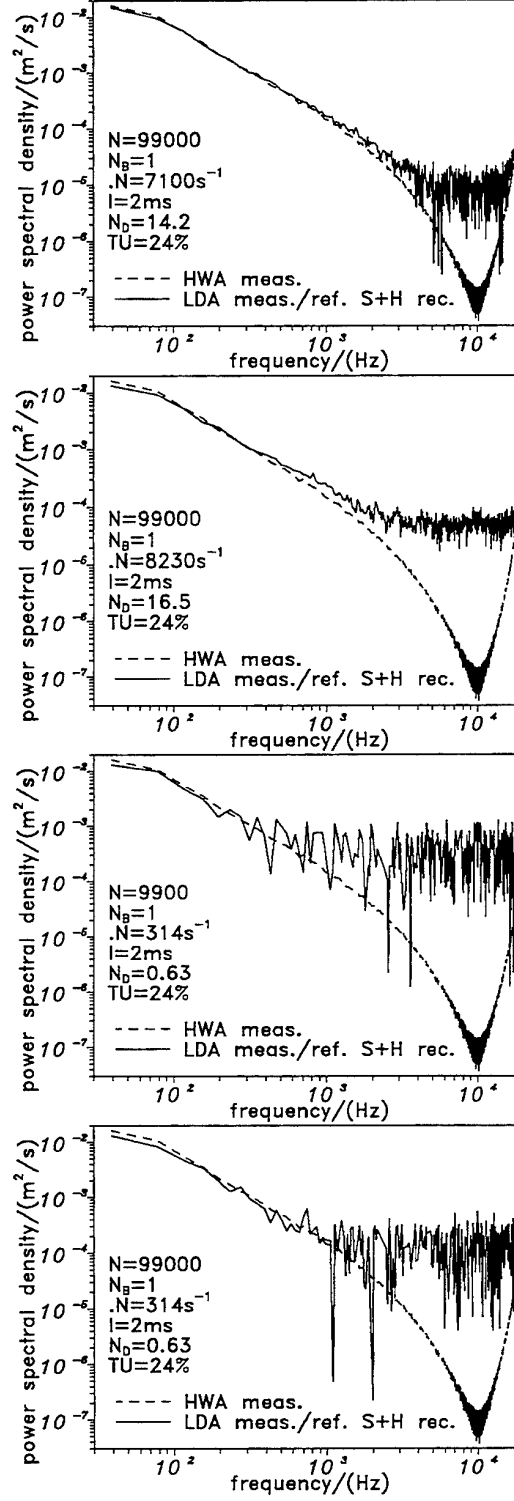


Figure 6: Raw and refined spectra estimates (S+H) compared to HWA spectrum, $Re = 40\,000$: a) $N_D = 14$; b) $N_D = 16$, high noise level; c) $N_D = 0.63$ short data set; d) $N_D = 0.63$ long data set

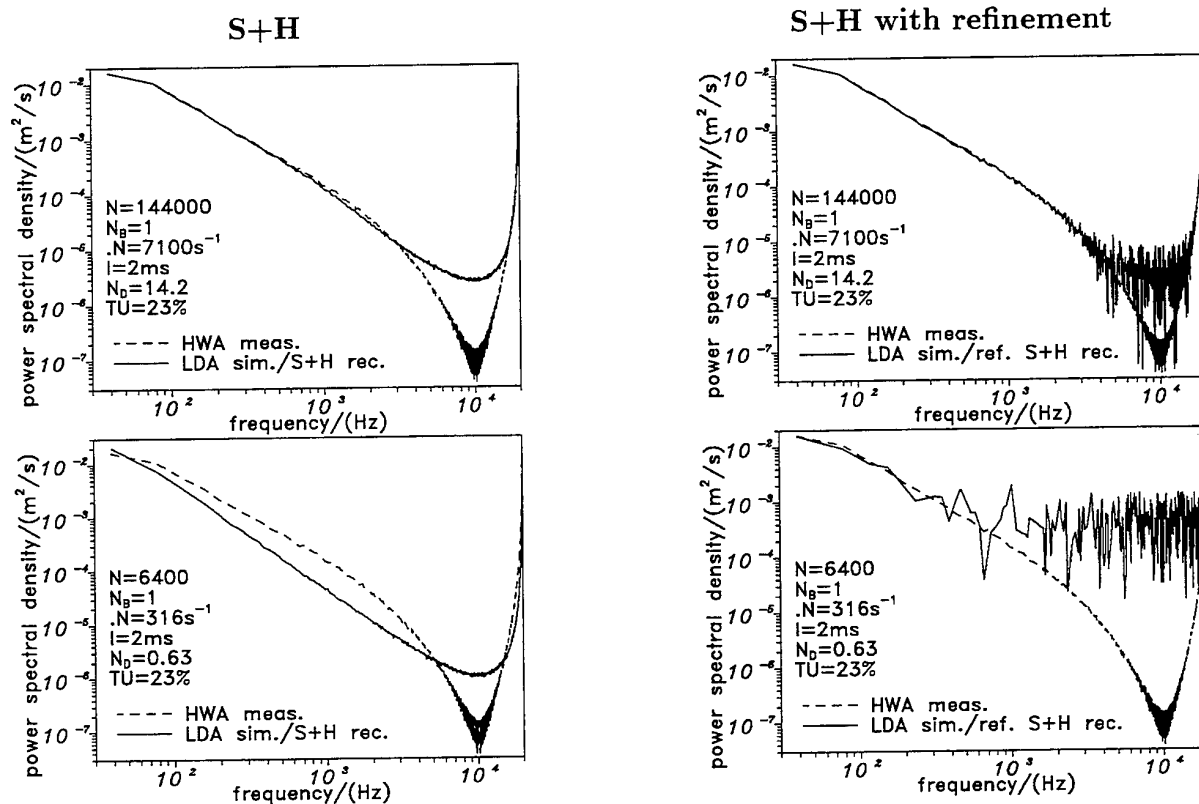


Figure 7: Spectral estimates from simulated LDA data using HWA data as primary input series: a) high data rate
b) low data rate

basic feature of reconstruction techniques in general has been overcome, namely the low-pass filter associated with the mean particle rate. It is therefore not surprising that the merits of this new approach become especially apparent at low data rates.

Nevertheless, the presence of noise in the data set will ultimately determine the resolution of the estimator at high frequencies and the remarks concerning the minimizing of these noise sources given in van Maanen and Tulleken (1994) can only be reiterated. In the case of very low noise levels however, all other reconstruction techniques, including the Kalman filter will suffer from filter dominated estimates at low data rates. This is the major advantage of the new, refined estimator.

6. ACKNOWLEDGEMENTS

This work has been carried out with the financial support of the Deutsche Forschungsgemeinschaft under grants Tr 194/9 and Mu 1117/1. Also the help of Mr. T. Unger in taking the hot-wire and LDA measurements at LSTM is acknowledged.

REFERENCES

- [1] Adrian, R.J. & Yao, C.S. 1987, Power Spectra of Fluid Velocities Measured by Laser Doppler Velocimetry, *Exp. in Fluids*, vol. 5, pp. 17-28.
- [2] Benedict, L.H. & Gould, R.D. 1995, Experiences Using Kalman Reconstruction for Enhanced Power Spectrum Estimates, *Proc. 6th Int. Conf. on Laser Anemometry, Hilton Head*.
- [3] Clark, J.J., Palmer, M.R. & Lawrence, P.D. 1985, A Transformation Method for the Reconstruction of Functions from Nonuniformly Spaced Samples, *IEEE Trans. of Acoustics, Speech, and Signal Processing*, vol. ASSP-33, No. 4, pp. 1151-1165.
- [4] Edwards, R.V. & Jensen, A.S. 1983, Particle-Sampling Statistics in Laser Anemometers: Sample-and-Hold Systems and Saturable System, *Journal of Fluid Mechanics*, vol. 133, pp. 397-411.
- [5] Erdmann, J.C. & Tropea, C. 1982, Statistical Bias of the Velocity Distribution Function in Laser Anemometry, *Proc. 7th Int. Symp. on Appl. of Laser Techn. to Fluid Mechanics, LADOAN, Lisbon*, paper 16.2.
- [6] Fuchs, W., Albrecht, H., Nobach, H., Tropea, C. & Graham, L.J.W. 1992, Simulation and Experimental Verification of Statistical Bias in Laser-Doppler Anemometry Including Non-Homogeneous Particle Density, *Proc. 6th Int. Symp. on Appl. of Laser Techn. to Fluid Mechanics, LADOAN, Lisbon*.
- [7] Fuchs, W., Nobach, H. & Tropea, C. 1993, The Simulation of LDA Data and its Use to Investigate the Accuracy of Statistical Estimators, *AIAA Journal*, vol. 32, pp. 1883-1889.
- [8] Gaster, M. & Roberts, J.B. 1975, Spectral Analysis of Randomly Sampled Signals, *J. Inst. Maths Appls*, vol. 15, pp. 195-216.
- [9] Høst-Madsen, A. 1994, A New Method for Estimating Turbulence Spectra for Laser Doppler Anemometry, *Proc. 7th Int. Symp. on Appl. of Laser Techn. to Fluid Mechanics, LADOAN, Lisbon*, paper 11.1.
- [10] Lee, D.H. & Sung, H.J. 1992, Turbulent Spectral Bias of Individual Realization of LDV, *Proc. 7th Int. Symp. on Appl. of Laser Techn. to Fluid Mechanics, LADOAN, Lisbon*.
- [11] Mayo, W.T. Jr. 1975, Modelling of Laser Velocimeter Signals as Triply Stochastic Poisson Process, *Proc. of Minnesota Symp. on Laser Doppler Anemometry, Bloomington*.
- [12] Müller, E., Nobach, H. & Tropea, C. 1994, LDA Signal Reconstruction: Application to Moment and Spectral Estimation, *Proc. 7th Int. Symp. on Appl. of Laser Techn. to Fluid Mechanics, LADOAN, Lisbon*, paper 23.2.
- [13] Müller, E., Nobach, H. & Tropea, C. 1995, Model Parameter Estimation from LDA Data at Low Particle Densities, *Proc. 6th Int. Conf. on Laser Anemometry, Hilton Head*.
- [14] Roberts, J.B. & Ajmani, D.B.S. 1986, Spectral Analysis of Randomly Sampled Signals Using a Correlation-Based Slotting Technique, *IEEE Proceedings*, vol. 133, Pt. F, No. 2, pp. 153-162.
- [15] Roberts, J.B., Downie, J. & Gaster, M. 1980, Spectral Analysis of Signals from a Laser Doppler Anemometer Operating in the Burst Mode, *J. Phys. E: Sci. Instrum.*, vol. 13, pp. 977-981.
- [16] Strahle, W.C. 1991, Turbulent Combustion Data Analysis Using Fractals, *AIAA Journal*, vol. 29, No. 3, pp. 409-417.
- [17] Tropea, C. 1987, Turbulence-Induced Spectral Bias in Laser Anemometry, *AIAA Journal*, vol. 25, pp. 306-309.
- [18] van Maanen, H. & Tulleken, H. 1994, Application of Kalman Reconstruction to Laser-Doppler Anemometry Data for Estimation of Turbulent Velocity Fluctuations, *Proc. 7th Int. Symp. on Appl. of Laser Techn. to Fluid Mechanics, LADOAN, Lisbon*, paper 23.1.
- [19] Veynante, D. & Candel, S.M. 1988, A Promising Approach in Laser Doppler Velocimetry Data Processing: Signal Reconstruction and Nonlinear Spectral Analysis, *Signal Processing*, vol. 14, pp. 295-300.

ANALYSIS OF RANDOMLY SAMPLED DATA USING FUZZY AND NONLINEAR TECHNIQUES

Amilcare Porporato and Luca Ridolfi

*Department of Hydraulics, Transports and Civil Infrastructures
Polytechnic of Turin, Italy*

ABSTRACT

This work deals with the analysis of non-uniformly sampled signals, with special attention given to signals measured with Laser Doppler Anemometer (LDA). We propose a reconstruction procedure which combines two relatively new techniques, namely the fuzzy delay technique (Breedon & Packard, 1992) and the noise reduction technique of Schreiber and Grassberger (1991). Beside giving a reconstruction which is physically meaningful, the method also provides very good noise reduction, thus avoiding possible problems that may be caused by low-pass filtering signals generated by nonlinear dynamics.

In the second part a preliminary application of the method to a signal measured using an LDA is presented. Although the technique has still not been optimized and many open questions remain, the results are good and encouraging.

1. INTRODUCTION

It is a well-known fact that, because sampling is tied to the discontinuous and random transit of particles in the measurement volume, the LDA provides a discrete and non-equispaced time series. Since usually most analyses require equispaced signals, this means that the first problem in analysing LDA data is to evaluate the various quantities being dealt with, starting from the series provided by the acquisition.

Many studies (both analytical and numerical) have dealt with this far from easy problem, focusing on statistical (Leneman & Lewis, 1966) and, in particular, on spectral analysis (regarding LDA signals cf. e.g. Gaster & Roberts, 1977; 1980; Mayo, 1979; George et al., 1979; Adrian & Yao, 1987; Tropea, 1987; Veynante & Candell, 1988; Lee & Sung, 1992; Butera et al., 1994; Porporato & Ridolfi, 1994; and further references in the above). For these kind of analysis it is possible in some cases to treat the non-equispaced signal directly, without having to reconstruct an equivalent equispaced signal. For the spectral analysis, in particular, Gaster and Roberts (1977; 1980) and Mayo (1979) have proposed two estimators for randomly sampled data. These last however turn out to be

quite limited (Porporato & Ridolfi, 1994). Therefore for the spectral analysis, as well as for many other kinds of analysis, the reconstruction of an equivalent (or of a better quality) equispaced signal is often necessary. This happens, for example, with nonlinear time sequence analysis (e.g. Grassberger et al., 1991).

When a signal is sampled non-uniformly in time, there are zones where information is lost with others where the signal is well sampled. This means that a random sampling may be better than a uniform one. In spectral analysis this is particularly evident. In fact, for poissonian sampling the estimator of Gaster and Roberts (1977) has no high frequency limits. For equispaced signals the limitation of the Nyquist frequency is always present.

When the sampling is of good quality (i.e. with high mean data rate and low noise level) the loss of information is not very significant. The signal is then interpolated with a simple function (sampling and holding, linear, etc.) and the new signal is resampled at a constant rate (usually the mean data rate of the original non-equispaced signal). In general, this is sufficient. But, when the sampling is poor or when the detailed nonlinear structure of the signal is important for the analysis, it may be inadequate, adding no information during the non-acquisition periods. Even worse is the fact that the interpolators cause a bias in the signal that corresponds to a rough low-pass filter. As a result, spectral estimation is distorted in the high frequency range and further problems may arise with nonlinear analysis (Badii et al., 1988; Rapp et al., 1993; Lawkins et al., 1993).

To avoid this it is necessary to reconstruct a new equispaced signal using as much information gained by acquisition as possible.

In this regard the approach proposed by Clark et al. (1985; see also the work of Sandberg, 1994) is worth noting. This is based on an extension of the Shannon's theorem and is adopted in the context of LDA data analysis by Veynante and Candell (1988). They suggest that for a band limited signal it is possible to obtain a perfect reconstruction, provided that there is an infinite number of data and an infinite amount of calculation. In practice this method consists of interpolating the non-equispaced signal with Sinc functions (Lund & Bowers, 1992). Veynante and Candell (1988) have shown that its application also gives good results for small data sets, even if the low-pass

filtering remains fairly pronounced. This has been confirmed by some unpublished tests we have performed on larger signals. Moreover the Sinc interpolation gives rise to spurious oscillations just before and after the strongest gradients, as happens with the spline interpolation.

In this work a different approach to the signal reconstruction is followed. This is based on methods of nonlinear time sequences analysis which stem from chaos theory (e.g. Schuster, 1995).

The time asymptotic dynamics of many dissipative deterministic systems (chaotic or not) lives on attractors whose dimensions are much inferior to those of the relevant phase space. If we can model the dynamics on the attractor, then the dynamics of the whole system can be known. Being able to reconstruct the attractor means that the complete time history of one of the variable of the system can be reconstructed.

For the equispaced measurement of a single scalar component of the system the reconstruction of the attractor can be accomplished using the delay time method of Takens (1981). The method does have some limitations due to noise and the finite number of data (Casdagli et al., 1991). More importantly however, it is not directly applicable for non-equispaced signals and the reconstruction must then be done iteratively.

Provided that the measurement is sufficiently extended, the system (on the attractor) will pass sufficiently close to a missing portion of trajectory to permit the use of this new information for the reconstruction of the dynamics lost by the acquisition.

Naturally, the more complex the system, the larger the information holes, the greater is the time required for measurement. From this it emerges that what is important is not so much a high sampling frequency as a sufficient exploration of the attractor.

Based on these concepts Breeden and Packard (1992) proposed the fuzzy delay technique to allow the use of the Takens method for non-uniformly sampled signals. A complete reconstruction based on the same concepts and using the fuzzy technique as the first step of the procedure is described below.

2. THE METHOD

Starting with the non-equispaced signal provided by the measurement, the aim is to reconstruct an equivalent equispaced signal, from which reliable estimates of the various quantities being studied are obtained.

The reconstruction is realized by the following steps:

- i) the first step is the application of the fuzzy-delay technique (Breeden & Packard, 1992) to the non-equispaced signal;
- ii) then an interpolator is used to fill the gaps between data, obtaining a new equispaced signal;
- iii) the last step is the application of a noise reduction technique (e.g. Schreiber & Grassberger, 1991).

2.1 The fuzzy technique

The fuzzy delay technique, proposed by Breeden and Packard (1992), is used so as not to waste the information

acquired. Given a non-uniformly sampled signal,

$$x_0 = x(t_0), \quad x_1 = x(t_0 + \Delta t_1), \quad \dots, \quad x_i = x(t_{i-1} + \Delta t_i), \quad (1)$$

$i=1, \dots, N-1$, where $\Delta t_1 \neq \Delta t_2 \neq \dots \neq \Delta t_i$, the technique entails the construction of a new signal of $M \leq N$ data, still non-equispaced, yet with data spaced of multiples of a certain fuzzy time, Δt_f . Fixed a tolerance window of with 2δ , the value (if there any) of the closest point in time within a distance of δ to the various equispaced instant of the fuzzy grid is associated to that instant (Fig. 1). In other words, the i -th original value is accepted as the j -th of the new series if

$$|(t_{i-1} + \Delta t_i) - j\Delta t_f| \leq \delta. \quad (2)$$

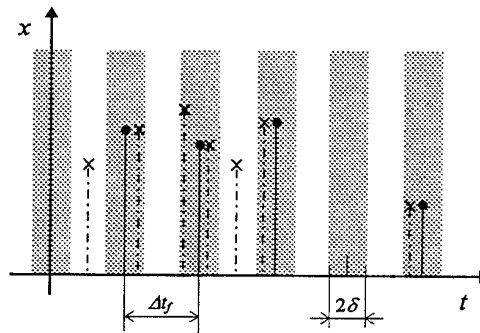


Fig. 1. Scheme of the fuzzy delay technique.

The number M and the quality of the reconstruction depend on the two parameters, Δt_f and δ , which have to be determined by trial and error.

It is important to note that whilst the method maximizes the use of the available data, it does not directly smooth the data. On the other hand, the time shift introduces errors into the series. For random sampling the effect is that of adding stochastic noise. This lack of a particular structure in the added noise is important for the subsequent application of noise reduction.

2.2 Interpolation

The second step of the reconstruction has the function of filling the gaps in the series obtained using the first step described above. Since the interpolator is not directly used for the reconstruction, the interpolator can be of any kind. It can range from being very simple (such as sampling and holding or linear) to being more refined.

However, it is possible that, because a simple interpolator acting as a low-pass filter systematically biases the signal, its use is not very appropriate for the subsequent application of the noise reduction. A more careful choice of the interpolator might well be appropriate. Notwithstanding its importance this problem is not dealt with here but will be discussed in a future work. The present paper limits itself to considering simple interpolators.

At this point an equispaced signal of a better quality than the signals resulting from standard techniques has

been obtained. In some cases this better quality signal may be advantageous even without proceeding to step 3.

2.3 Noise reduction

In this step the geometric structure of the dynamics in phase space is reconstructed. In order to do this we use the recent noise reduction techniques. Loosely speaking, they are non linear filters that eliminate additive noise from deterministic signals by recognizing the deterministic dynamics and reconstructing the real hidden trajectories in phase space.

In our context their use is twofold: to eliminate measurement and fuzzy-introduced errors and to give appropriate corrections to interpolated data using dynamical information present in the signal.

There are many methods proposed up to now to eliminate additive noise (e.g., Kostelich and Yorke, 1988; 1990; Hammel, 1990; Farmer and Sidorovich, 1991; Schreiber and Grassberger, 1991; Sauer, 1992; Schreiber, 1993; Grassberger et al., 1993; and Davies, 1994). They all have a common root which can be summarised as follows. In general, measured time series are univariate and disturbed; the generic i -th scalar element can then be seen as the sum of the true value y_i , plus a disturbance ε_i , that is

$$x_i = y_i + \varepsilon. \quad (3)$$

Besides of the measurement errors present in the original signal, the disturbance ε here consists principally of the distortions caused by the fuzzy technique and by the subsequent interpolation.

In order to reconstruct the dynamics in an embedding space with a dimension which is high enough to allow us to obtain a single deterministic description, the above relation is joined to the equation which defines the dynamics in the delay coordinates (assuming for simplicity $\tau=1$)

$$y_{i+m} = f(y_i, y_{i+1}, \dots, y_{i+m-1}), \quad (4)$$

with m embedding dimension. Rewriting the above in implicit form $f(y_i, y_{i+1}, \dots, y_{i+m-1}) - y_{i+m} = 0$, we find that, in a space having $(m+1)$ coordinates, the noise-free dynamics would be constrained to an m -dimensional hypersurface. In reality this does not happen for the measured values x_i , and the extension of the cloud of experimental points perpendicular to this hypersurface is the width of the noise level. It follows that, if we can reconstruct this surface starting from the disturbed data (step 1) and subsequently correct it by projecting it onto the subspace relative to the clean data (step 2), it is possible to reconstruct a time series much closer to the real system than the $\{x_i\}$ might be.

The present work considers the algorithm proposed by Schreiber and Grassberger in 1991 (see also, Grassberger et al., 1993; and Kantz, 1993). The basic idea of this algorithm is to consider locally the information on both the past and the future evolution, reconstructing the dynamics in a $(\alpha+1+\beta)$ -dimensional phase space with α delay coordinates and β forward coordinates

$$\mathbf{x}_i = (x_{i-\alpha}, x_{i-\alpha+1}, \dots, x_i, \dots, x_{i+\beta-1}, x_{i+\beta}). \quad (5)$$

Considering then a $(\alpha+1+\beta)$ -dimensional boundary $\mathfrak{T}^{(i)}$ of each point \mathbf{x}_i , the dynamics can be approximated locally in it with a linear model and the corrected value can be obtained through

$$x_i = \sum_{j=-\alpha}^{\beta} a_j^{(i)} x_{i+j} + b^{(i)} = \mathbf{a}^{(i)} \mathbf{x}_i + b^{(i)}, \quad (6)$$

where $\mathbf{a}^{(i)}$ and $b^{(i)}$ are coefficients dependent on the position in the phase space, i.e. time, obtained by minimizing the quantity

$$\sum_{\mathbf{x}_s \in \mathfrak{T}^{(i)}} (\mathbf{a}^{(i)} \mathbf{x}_s + b^{(i)} - x_s). \quad (7)$$

The above, which accomplishes the first step of the correction, links the correction to the local dynamics of the system by trying to reconstruct it from the information contained in the neighborhood $\mathfrak{T}^{(i)}$ of each point \mathbf{x}_i . Relation (6) represents the second step of the correction.

The noise reduction may therefore be seen as a locally linear filter in the phase space. The nonlinearity comes from the fact that for every point \mathbf{x}_i there is a different neighborhood and different values of $\mathbf{a}^{(i)} \in b^{(i)}$. The tight link with the nonlinear prediction with local approximation (see e.g. Farmer & Sidorovich, 1987) is clearly evident.

As the approximation is locally linear, and the values involved (the forward coordinates and all the neighbors \mathbf{x}_s which follow \mathbf{x}_i in the multidimensional series) are still to be corrected, the value x_i is only partially corrected and the entire procedure must be iterated on the previously-corrected series until convergency is reached. The interpolation performed at step two gives the initial condition to the iterative procedure of reconstruction in the zones where points are lacking. The more appropriate it is, the better will be the convergency of the reconstruction.

There are four parameters to be selected in applying the method and since precise indications are lacking, it is necessary to proceed by trial and error. The first of these concerns the neighborhood $\mathfrak{T}^{(i)}$, which is assumed to be constituted by a fixed number k' of neighbors, strictly greater than $\alpha+\beta+1$. There are then the parameters α , β and a_0 . The latter is not deducible from (7) and must be $0 < a_0 < 1$: the closer to the unit the smaller is the correction applied each time. Based on our experience a good choice for k' is a value around twice $\alpha+\beta+1$, while for a_0 is around 0.9-0.95.

3. APPLICATION

In this preliminary study we applied the above procedure to a tract of 15.000 data measured using an LDA. The signal is the longitudinal velocity component of an hydraulically-smooth turbulent pipe flow. The Reynolds number, based on the mean global velocity and the pipe diameter is 197.000 and the measurement point was at $y^+ = yu_* / \nu \sim 100$ (y is the wall distance, u_* is the friction velocity and ν the kinematic viscosity). The 15 mW, He-Ne LDA was set in

Forwardscatter and in Continuous Mode. The mean data rate was 1.03 kHz obtained without seeding the flow.

Fig. 2 shows in detail the first part of the non-equispaced signal obtained by the measurement.

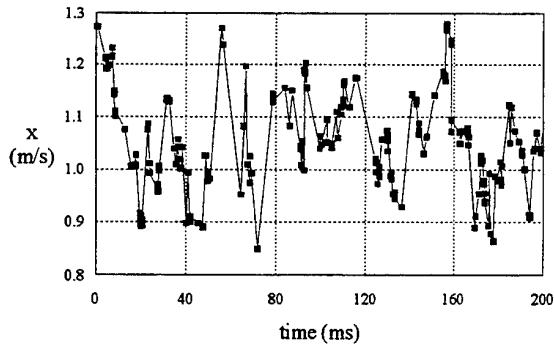
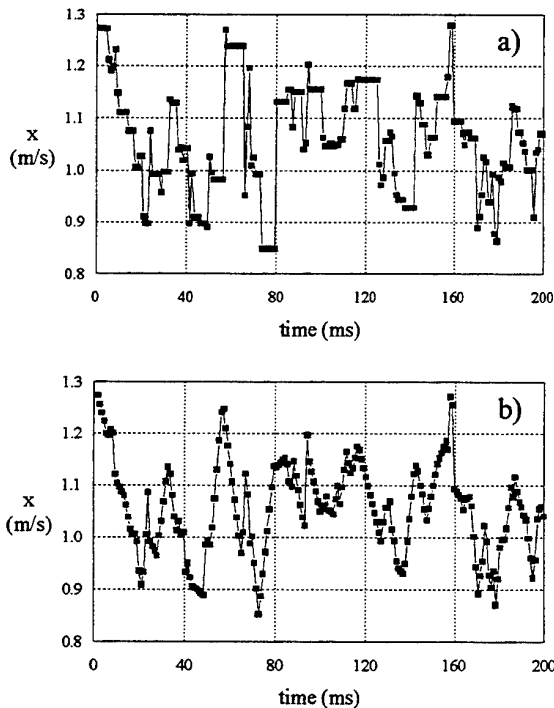


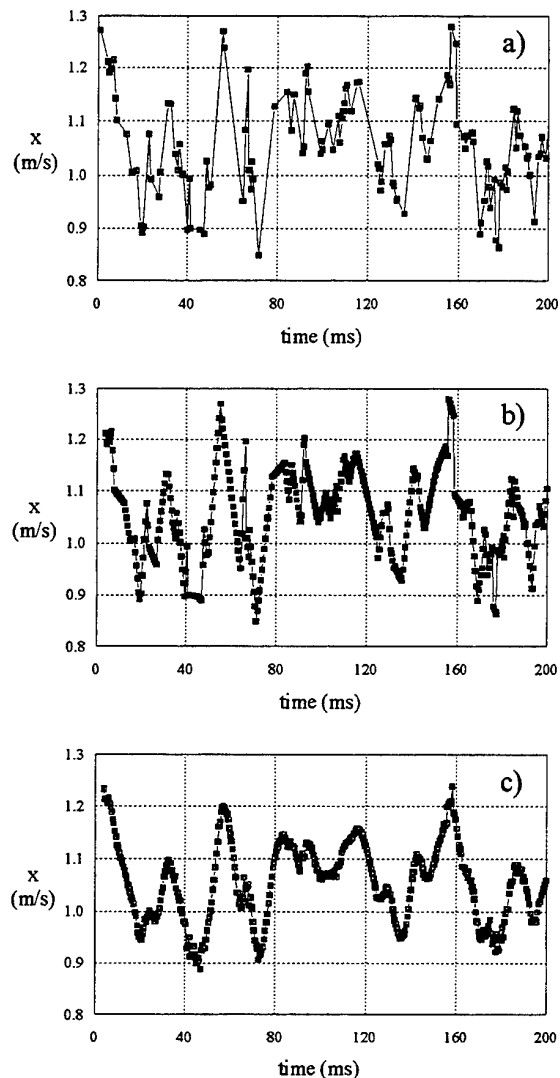
Fig. 2. Tract of the signal obtained by the measurement.

In order to have a reference point for the subsequent analysis, the usual procedure is first applied. The original signal is interpolated using the sampling and holding and the linear interpolators. The resulting continuous signals are then resampled at the mean sampling rate, 0.97 ms. The initial part of the signals thus obtained is shown in Figs. 3a-b. The low-pass filtering (especially for the linear interpolator) and the step noise caused by the sampling and holding interpolation (Adrian & Yao, 1987) are clearly visible.



Figs. 3a-b. Signals reconstructed using the usual procedure: (a) sampling and holding and (b) linear interpolation.

The procedure discussed is now applied. Due to the preliminary character of the application we will not dwell on the optimization of the fuzzy delay technique and simply adopt $\Delta t_f = 0.5$ ms and $\delta = 0.25$ ms, as it seems to be a good compromise between number of data and quality of the reconstruction. The obtained signal consist of 8455 data: its behaviour is very similar to that of the original non-equispaced signal, showing a negligible information loss (Fig. 4a).

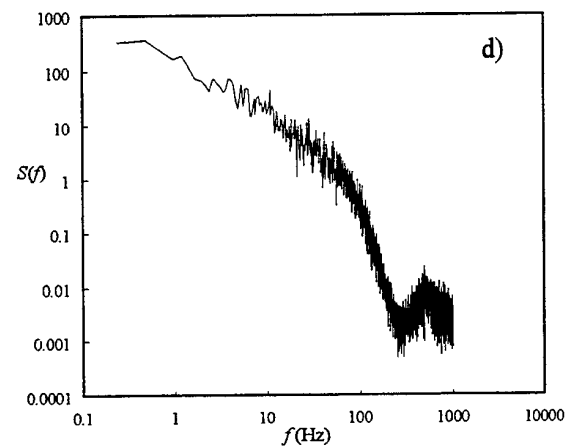
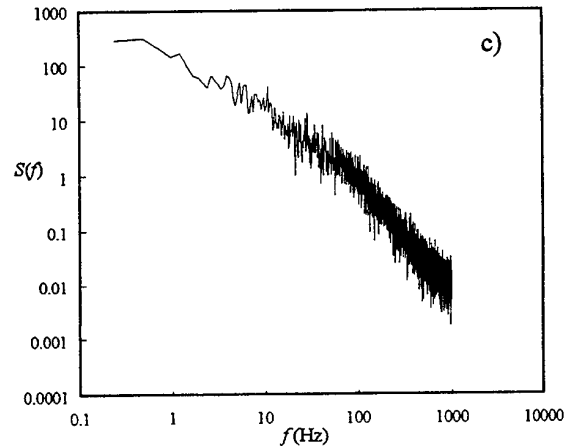
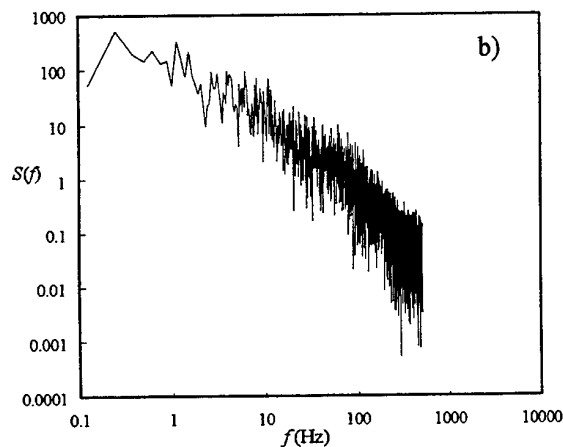
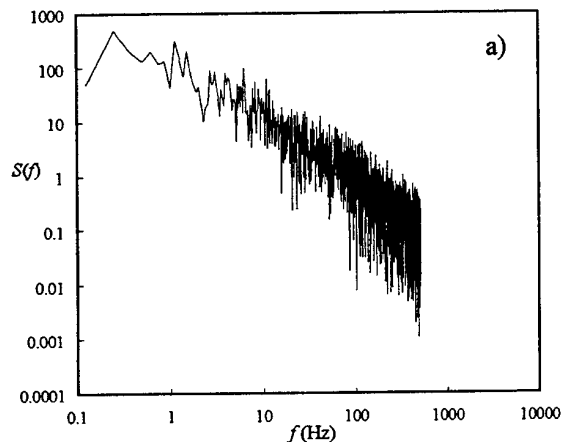


Figs. 4a-c. Tract of the signal after the three steps of the reconstruction.

For the second step of the reconstruction the simple linear interpolator (Fig. 4b) is adopted, leaving to a subsequent work the use of a more refined one. The number of points is raised to 29102. At this point the resulting signal may already be a good alternative to that obtained with the usual technique.

The result of the last step is reported in Fig. 4c. The noise reduction is implemented with $\alpha_0 = 0.9$, $\alpha + \beta + 1 = 7$ ($\alpha = \beta$) and $k = 15$. Even if here and there residuals of the original noise remain, due to the limited number of iterations, the refined smoothing, which preserves the characteristic strong gradient of the turbulence, is evident.

Figs. 5a-d show the spectra obtained with the usual procedure (sampling and holding and linear) and those obtained after the second and the third step of our procedure, averaging out the spectra calculated on blocks of 4096 data with the FFT and applying the Hanning window. With respect to the usual procedure (Figs. 5a-b), Fig. 5c already reveals a certain improvement. The Nyquist frequency is shifted towards higher frequencies and the variance of the estimate is reduced for the increasing of the number of data. Finally, the noise reduction lowering the measurement and fuzzy-introduced noise and the effect of the interpolation, provides a spectrum which is typical of fully developed turbulence. The behaviour over 200 Hz is probably due to the incomplete noise reduction stopped at the 11th iteration. Below this the spectrum seems to be reliable, but of course the actual interplay between reconstruction and smoothing remains to be checked in order to be sure that at least the bigger scale motions are indeed reconstructed.



Figs. 5a-d. Spectra obtained with different methods: usual procedure with (a) sampling and holding and (b) linear interpolation and after the second (c) and the third (d) step of our procedure.

4. CONCLUSIONS

In this work a possible approach for the reconstruction of non-equispaced signals has been proposed. At the present stage the three steps of the method have not yet been optimized and a lot of work still has to be done to check its effective potentials. Nevertheless the preliminary results are quite good and the calculation burden may be justified by the many advantages it should give. The fuzzy delay technique enables the use of as many data as possible without the loss of the high frequency content of the measurement. Noise reduction lowers the error level and improves interpolation. Moreover it is particularly appropriate for this kind of problem because of the white random character of the optical and fuzzy-introduced noises. Furthermore, compared to more common procedure of applying a simple interpolator, equispacing and low-pass filtering, the use of noise reduction causes less disturbance to the underlying nonlinear dynamics (Badii et al., 1988; Rapp et al., 1993; Lawkins et al., 1993).

The research currently being undertaken deals with optimizing each step of the procedure. Possible future improvements include the use of an interpolator more suitable to the subsequent application of the noise reduction, and the optimization of the noise reduction technique, starting by weighting the original values more than the values introduced by the interpolation. It is also planned to extend the elaborations to other signals (different LDA measurement conditions and different kind of numerically simulated signals) and to test not only the spectral analysis but also the most common estimates of nonlinear analysis.

REFERENCES

- Adrian, R. J. & Yao, C. S. 1987, Power spectra of fluid velocities measured by laser Doppler velocimetry. *Exp. in Fluids* **5**, 17.
- Badii, R., Broggi, B., Derighetti, B., Ravani, M., Ciliberto, S., Politi, A. & Rubio, M. A. 1988, Dimension Increase in Filtered Chaotic Signals. *Phys. Rev. Lett.*, **60** (11), 979.
- Breeden, J. L. & Packard, N. H. 1992, Nonlinear analysis of data sampled nonuniformly in time. *Physica D* **58**, 273.
- Butera, L., Porporato, A., Ridolfi, L. & Sordo, S. 1994, Autocorrelation and related quantities of the longitudinal turbulent velocity component. An experimental investigation in a water flow in a smooth pipe. *Proc. 2nd Int. Conf. on Exp. Fluid Mech.* Turin, 2-6 July, 1994.
- Casdagli, M., Eubank, S., Farmer, J. D. & Gibson, J. 1991, State space reconstruction in the presence of noise. *Physica D* **51**, 52.
- Clark, J. J., Palmer, M. R. & Lawrence, P. D. 1985, A transformation method for the reconstruction of function from nonuniformly spaced samples. *IEEE Trans. Acoust. Speech. Signal Process* **33**, 1151.
- Davies, M. 1994, Noise reduction schemes for chaotic time series. *Physica D* **79**, 174.
- Farmer, J. D. & Sidorowich, J. J. 1987, Predicting Chaotic Time Series. *Phys. Rev. Lett.* **59**(8), 845.
- Farmer, D. J. & Sidorowich, J. J. 1991, Optimal shadowing and noise reduction. *Physica D* **47**, 373.
- Gaster, M. & Roberts, J. B. 1977, Spectral analysis of randomly sampled records by a direct transform. *Proc. Royal Soc. A* **354**, 27.
- Gaster, M.; Roberts, J. B. 1980, On the estimation of spectra from randomly sampled signals: a method of reducing variability. *Proc. R. Soc. Lond. Ser. A* **371**, 235.
- George, W. K., Beuther, P. D. & Lumley J. L. 1979, Processing of random signals. *Proc. of the Dynamic Flow Conference*. 1978. Skovlunde, Denmark, 757.
- Grassberger, P., Schreiber, Th. & Schaffrath, C. 1991, Nonlinear time sequence analysis. *Int. Journ. of Bifurcation and Chaos*, **1**(3), 521.
- Grassberger, P., Hegger, R., Kantz, H., Schaffrath, C. & Schreiber, Th. 1993, On noise reduction methods for chaotic data. *Chaos* **3**(2).
- Grebogi, C., Hammel, S. M., Yorke, J. A. & Sauer, T. 1990, Shadowing of Physical Trajectories in Chaotic Dynamics: Containment and Refinement. *Phys. Rev. Lett.* **65**, 1527.
- Hammel, S. M. 1990, A noise reduction method for chaotic systems. *Phys. Lett. A* **148**(8, 9), 421.
- Kantz, A. 1993, Noise reduction by local reconstruction of the dynamics. In *Time Series Prediction*. Eds. Weigend, A. S. & Gershenfeld, N. A. SFI Studies in the Sciences of Complexity, Proc. vol. XV, Addison-Wesley.
- Kostelich, E. J. & Yorke, J. A. 1988, Noise reduction in dynamical system. *Phys. Rev. A* **38**, 1649.
- Kostelich, E. J. & Yorke, J. A. 1990, Noise reduction: finding the simplest dynamical system consistent with the data. *Physica D* **41**, 183.
- Lawkins, W. F., Daw, C. S., Downing, D. J. & Clapp, N. E. Jr. 1993, Role of low-pass filtering in the process of attractor reconstruction from experimental chaotic time series. *Phys. Rev. E* **47**(4), 2520.
- Lee, D. H. & Sung, H. J. 1992, Turbulent spectral bias of individual realization of LDV. *Proc. 6th Int. Symp. on Appl. of Laser Techniques to Fluid Mech.* Lisbon, July 20-23, 1992.
- Leneman O. A. Z. & Lewis J. B. 1966, Random sampling of random processes: mean square comparison of various interpolators. *IEEE Trans. on Automatic Control*, 396.
- Lund, J. & Bowers, K. 1992, *Sinc Methods*. SIAM Publ. Philadelphia.
- Mayo, W. T. Jr. 1979, Spectrum measurements with laser velocimeters. *Proc. of the Dynamic Flow Conference*. 1978. Skovlunde, Denmark, 851.
- Porporato, A. & Ridolfi, L. 1994, Confronto tra stime spettrali per segnali turbolenti misurati con LDA. *XXIV Convegno di Idraulica e C. I.* Napoli, 20-22 Settembre 1994 (in Italian).
- Rapp, P. E., Albano, A. M., Schmah, T. I. & Farwell, L. A. 1993, Filtered noise can mimic low-dimensional chaotic attractor. *Phys. Rev. E* **47**(4), 2289.
- Sandberg, I. 1994, The reconstruction of band limited signals nonuniformly spaced samples. *IEEE Trans. Circ. and Systems*, **41**, 64.
- Sauer, T. 1992, A noise reduction method for signals from nonlinear system. *Physica D* **58**, 193.
- Sauer, T. 1993, Time series prediction using delay coordinates embedding. In *Time Series Prediction*. Eds. Weigend, A. S. & Gershenfeld, N. A. SFI Studies in the Sciences of Complexity, Proc. vol. XV, Addison-Wesley.
- Schreiber, Th. & Grassberger, P. 1991, A simple noise reduction method for real data. *Phys. Lett. A* **160**, 411.
- Schreiber, Th. 1993, Extremely simple nonlinear noise-reduction method. *Phys. Rev. E* **47**, 2401.
- Schuster, H. G. 1995, *Deterministic chaos*. 3rd. Ed. Physic Verlag. Weinheim.
- Takens, F. 1981, Detecting strange attractors in turbulence. In *Lectures notes in Mathematics* vol. **898**. Springer.
- Tropea, C. 1987, Turbulence-induced spectral bias in laser anemometry. *AIAA Journal* **25**(2), 306.
- Veynante & Candell 1988, Application of nonlinear spectral analysis and signal reconstruction to Laser Doppler velocimetry. *Exp. in Fluids* **6**, 534.

ESTIMATION OF THE AUTO CORRELATION FUNCTION OF TURBULENT VELOCITY FLUCTUATIONS USING THE SLOTTING TECHNIQUE WITH LOCAL NORMALISATION

by

H.R.E. van Maanen (*Shell Research and Technology Centre, Amsterdam*)
(P.O. Box 38000, 1030 BN Amsterdam, Netherlands)

and

M.J. Tummers (*Delft University of Technology, Faculty of Aerospace Engineering*)

Abstract.

The auto correlation function (ACF) of randomly sampled turbulent velocity fluctuations can be estimated using the slotting technique. However, the obtained ACF has a relatively high variance which obscures the shape at small lag times. In case of velocity bias the estimates can grow larger than 1, eliminating the possibilities to separate noise and turbulence and to estimate the Taylor time scale. This paper analyses a modified slotting technique that has a much smaller variance at small time lags and is less susceptible to velocity bias. The modified algorithm is evaluated using a numerical simulation and yields satisfactory results, even in case of strong velocity bias, enabling the estimation of Taylor time scales and turbulence power spectra.

1. Introduction.

Retrieval of the properties of turbulence using Laser-Doppler Anemometry (LDA) could be achieved by estimation of the Auto Correlation Function (ACF) which is defined as:

$$R_{u'u'}(\tau) = \frac{\overline{u'(t) \cdot u'(t+\tau)}}{\overline{u'^2}} \quad [1]$$

in which

$R_{u'u'}$ = Auto Correlation function of u'
 u' = fluctuating part of the velocity (average value of u' is zero)
 τ = time lag

The overbar denotes time averaging.

The ACF is a measure for the similarity of a signal with itself, shifted over the time lag τ . This can be used to determine a number of timescales of the turbulent fluctuations, such as the Taylor timescale T_λ which follows from the curvature of the ACF at zero lag time:

$$T_\lambda^2 = \frac{-2}{\left(\frac{d^2 R_{u'u'}(\tau)}{d\tau^2} \right)_{\tau=0}} \quad [2]$$

Eq. 2 shows that very accurate estimates of $R_{u'u'}$ at small time scales are required when the T_λ is to be determined from experimental data.

The application of LDA to gas and two-phase flows often results in mean data-rates that are too

low to apply velocity reconstruction (ref. 1 - 3). However, as was shown theoretically (ref. 4 and 5) the Poisson sampling process provides information on time scales much smaller than the mean time between samples. Mayo (ref. 6) proposed a practical algorithm for the estimation of the ACF from randomly sampled data that became known as the slotting technique. However, this technique suffers from several serious drawbacks:

- the variance in the estimator of the ACF in each slot is large compared to other techniques.
- the estimators can rise above 1 for $\tau > 0$ because of velocity bias (ref. 7).
- separation of noise and turbulence contributions is difficult because the above mentioned problems.

In this paper we will analyze a different normalisation approach, which has been proposed and applied by Tummers et al. (ref. 8). In the next section we will describe the algorithm, followed by an analysis of its properties by means of a Monte Carlo simulation. The properties will be verified on experimental data and the possibilities to obtain the Power Spectral Density (PSD) from a slotted ACF will be studied.

2. Description of the algorithm.

The algorithm for the slotting technique is given by (ref. 6):

$$R_{u'u'}(k\Delta\tau) = \frac{\sum (u_i u_j)_{(k\Delta\tau)}}{N_{k\Delta\tau} [\overline{u'^2}]} \quad [3]$$

in which

$\sum (u_i u_j)_{k\Delta\tau}$ = sum of all cross products $u(t_i)u(t_j)$ that are separated by a lag time in the interval $(k - \frac{1}{2}) \Delta\tau \leq (t_j - t_i) \leq (k + \frac{1}{2}) \Delta\tau$
 $N(k\Delta\tau)$ = number of products within the above defined slot (note that $\Delta\tau$ is the width of a slot)

The Mean Square value of the velocity fluctuations is estimated using:

$$[\overline{u'^2}] = \frac{1}{N} \sum_{i=1}^N [u'^2(i)] \quad [4]$$

However, if the flow is stationary then

$$[\overline{u'^2}] = \sqrt{[\overline{u'^2}]} \cdot \sqrt{[\overline{u'^2(t+\tau)}]} \quad [5]$$

Substituting [5] and [4] into [3], the ACF can be estimated as:

$$R_{u'u'}(k\Delta\tau) = \frac{\sum (u_i u_j)_{(k\Delta\tau)}}{\sqrt{\sum (u_i u_i)_{(k\Delta\tau)}} \cdot \sqrt{\sum (u_j u_j)_{(k\Delta\tau)}}} \quad [6]$$

This yields the modified ACF estimator which showed to be very promising, as reported by Tummers (ref. 8). Its properties will be discussed after the description of the numerical simulation in the next section.

3. Numerical simulation.

The numerical simulation consist of three essential parts:

1. Simulated turbulence.
2. Time interval generation according to an exponential distribution (without or with velocity bias).
3. A simulated noise contribution to the velocity samples.

Ad 1.

The simulated turbulence has been generated according to the "Bessem power spectrum" (ref. 9):

$$S(f) = \frac{S(0)}{1 + \left(\frac{f}{f_1}\right)^{\frac{5}{3}} \cdot \left[1 + \left(\frac{f}{f_2}\right)^4\right]^{\frac{4}{3}}} \quad [7]$$

in which:

S = Power spectral density

f = frequency

f_1 = first characteristic frequency (= 1 Hz)

f_2 = second characteristic frequency (= 50 Hz)

A with a continuous record of 10^6 samples has been generated with a sampling frequency of 1000 Hz, thus representing 1000 sec. of signal with a Gaussian amplitude distribution. The corresponding auto correlation function is shown in fig. 1. Each velocity estimate was calculated as the linear interpolated value between the latest sample before and the first sample after the selected "measurement" instant (see below). Because the sampling frequency is high compared to the characteristic frequencies, this interpolation leads to correct values. The Taylor time scale of this simulated turbulence is 27 msec.

Ad 2.

The velocity samples have been taken using an exponential time interval distribution. The time intervals, Δt , can be generated from

$$\Delta t = -t_0 \cdot \ln(RND) \quad [8]$$

in which

Δt = time interval

t_0 = mean time between samples (= 1/data-rate)

\ln = natural based logarithm

RND = random number in [0,1]

One-dimensional velocity bias has been introduced by adding a constant average velocity to the samples and taking the actual data-rate proportional to the instantaneous velocity. In the rare case that the actual data-rate would become lower than 0.01 of the average data-rate, the data-rate was set to 0.01 of the average data-rate to avoid excessive and thus unrealistic time intervals. The effect of velocity bias on the time interval distribution is illustrated in fig. 2.

Ad 3.

To each velocity sample a Gaussian distributed noise contribution has been added (ref. 10), the Signal-to-Noise Ratio (SNR) used was 5.

In these simulations a t_0 of 6 msec. has been used and the turbulence intensities ranged between 33 and 200 % when velocity bias has been

introduced. The simulated velocity data have been processed with slots of 0.2 and 1 msec. wide.

4. Results.

Applying the algorithm of eq. [6] results, especially in the vicinity of $\tau = 0$, in a variance which is noticeably smaller than the original estimator of eq. [3]. This is illustrated in fig. 3, in which the ideal, slotted and novel ACF estimators are shown simultaneously in the absence of velocity bias. Note that the ideal and the novel ACF are virtually identical for small values of τ . The variance depends on the **absolute value of the correlation coefficient** as is shown in fig. 4. This graph shows the ACF of a randomly sampled, periodic signal with 10% Gaussian distributed white noise added. The variance in the maxima and minima is clearly less than for low absolute values of the correlation coefficient. In fig. 5 the ACF of the same signal with the slotting technique of eq. [3] is shown. Note that the variance of these estimates is nearly **independent** of the value of the correlation coefficient. As a result, some of the estimates of fig. 5 rise above 1 although no velocity bias has been introduced. This is clearly visible in fig. 6, which shows the estimates according to eq. [3] and [6] close to $\tau = 0$. For small correlation coefficients the variance of both estimates is identical (as well as the estimates themselves) as is illustrated in fig 7.

A second advantage of the algorithm of eq. [6] is the disappearance of the increase in the ACF estimate **above 1** for $\tau > 0$ in the presence of velocity bias (ref. 7). This is illustrated in fig. 8 in which similar curves are shown as in fig. 3, but with the occurrence of velocity bias. The same can be found from real measured data as is shown in fig. 9.

Because of these properties the Taylor time scale can be estimated by least-squares fitting a parabola to the ACF at $\tau = 0$. When no velocity bias is present the estimated Taylor time scale is correct. The influence of velocity bias has been studied using 1-D velocity bias as described above. Some typical results of the estimated ACF's are shown in the figs. 10 - 13. It has been found that:

1. The Taylor time scale rises above the actual value (27 msec.) for turbulence intensities above 100 %.
2. The Taylor time scale is below the actual value for turbulence intensities below 100%.
3. The Taylor time scale is close to the actual value for turbulence intensities of 100% and

for the limiting case of the turbulence intensity going to 0%.

4. The noise peak at $\tau = 0$, indicative for the SNR of the velocity fluctuations, is too small for high turbulence intensities.

The results of 1 - 3 are presented in fig. 14 and in fig. 15 the SNR, estimated from the size of the noise peak at $\tau = 0$, is shown as a function of the turbulence intensity.

5. Discussion.

The retrieval of the turbulence properties of a stationary flow up to the smallest scale has proven to be difficult at low mean data-rates. The reasons are:

1. The noise contributions to each individual velocity estimate obscure the contribution of the small eddies.
2. The original slotting algorithm is sensitive to velocity bias and has a large variance in the individual ACF estimates.

Although the novel algorithm is still sensitive to velocity bias, it solves some of the above mentioned problems. Important is its low variance in the vicinity of $\tau = 0$ where the correlation coefficient is high. This not only enables an accurate determination of the Taylor time scale, but one may even go one step further. The PSD -and thus the eddy size distribution- can be obtained from the ACF by Fourier Transformation (ref. 11). However, the variance of the estimations, especially for the lower values, is still prohibitive and obscures the small eddies with a kind of "noise" floor, as can be seen from fig. 16. To circumvent this, the following approach has been used.

In literature an attempt has been made to reconstruct the ACF, based on the assumption that the velocity fluctuations can be described by an auto-regressive moving average (ARMA) approach (ref. 12). The disadvantage of the ARMA approach is that the slopes in the PSD are integer multiples of -2. A direct curve-fit of the ACF allows more degrees of freedom, which may be a more attractive approach. The critical part around $\tau = 0$, which is essential for correct determination of the PSD at higher frequencies -and thus small eddies- can now be estimated with low variance. Because a curve-fit will result in a continuous, smooth function, the parts of the ACF that contribute to the "noise" floor in the PSD are smoothed, thereby circumventing the problem of the higher variance in that part of the ACF. But any curve fit for a realistic ACF should avoid the pitfall of creating "self-fulfilling prophecies". This

can be done by using as little assumptions as possible and by selecting a set of functions that incorporate the general properties of an ACF of turbulent fluctuations.

The set of functions that has been selected are modified Gaussian functions. In fig. 1 one can see that the ACF has a Gaussian like behaviour. A curve fit could theoretically be obtained by introducing a parameter σ which is a function of τ . The subsequent function would then be:

$$R_{u'u'}(\tau) = e^{-\frac{1}{2}\left(\frac{\tau}{\sigma(\tau)}\right)^2} \quad [9]$$

in which:

σ = characteristic parameter of Gaussian function

Such a Gaussian-like ACF has as a derivative which is zero for $\tau = 0$. This property is required for the ACF of real turbulence: usually a parabola is fitted through that part of the ACF in order to estimate the Taylor time scale.

The curve fitting problem then shifts to $\sigma(\tau)$ and in order to see if this is a realistic option, the $\sigma(\tau)$ of the theoretical ACF of the Bessem spectrum has been calculated. The result is presented in fig. 17. This figure shows that the dependence of σ as a function of τ is rather simple and can be fitted. Using the multi-parameter error minimizing technique (ref. 13), the curve fittings have been done with a high weighting for the values for $\tau > 0$ (the noise contribution is located at $\tau = 0$) but with the correlation coefficient > 0.9 . A preliminary result is shown in fig. 18, in which the ACF, used to generate the PSD of fig. 16 is processed in this way and the theoretical Bessem spectrum is shown as well. We are working on further development of this approach, but from these results one can conclude that the technique seems feasible. As a second test, experimental data have also been processed. The result of the Fourier Transform of this shown in fig. 19 and it shows the expected properties of a PSD of turbulent velocity fluctuations. The data-rate of this experiment (≈ 1000 Hz) is well below the data-rate required for reconstruction ($\approx 35\,000$ Hz).

6. Conclusions and future work.

Using a different algorithm for the slotting technique, an improved estimation of the auto correlation function of turbulent velocity fluctuations, measured with a Laser-Doppler Anemometer, has

been obtained. The use of simulated turbulence has revealed that:

- The variance of the estimator is significantly lower than the estimator of the original algorithm for high absolute values of the correlation coefficient: the higher the absolute value of the correlation coefficient, the lower the variance.
- The novel estimator is identical to the estimator of the original algorithm when the absolute value of the correlation coefficient is close to zero.
- The erroneous result of the original algorithm in the presence of velocity bias (correlation coefficients > 1) does not occur with the novel algorithm.
- This new algorithm is also sensitive to velocity bias, albeit in a different way. The velocity bias affects the results for the values of the Taylor time scale and the Signal-to-Noise Ratio, derived from the estimated ACF.

The reduction of the variance, especially in the vicinity of $\tau = 0$ enables a curve-fit for the ACF. The use of a Gaussian function with a parameter σ which is a function of τ shows to be feasible. A major advantage of this approach is that only few assumptions about the turbulence are required, the most important being that the derivative of the ACF is zero in $\tau = 0$, which is actually a requirement. Application of the curve-fitting approach to both simulated and measured data demonstrate its potential, but more development is required on:

- a robust set of functions, suitable for the description of the ACF.
- the development of an efficient algorithm for the determination of the curve-fit parameters.
- the influence of velocity bias to the PSD.

References.

1. H.R.E. van Maanen and H.J.A.F. Tulleken, "Application of Kalman reconstruction to Laser-Doppler Anemometry data for estimation of turbulent velocity fluctuations", Proc. 7th Int. Symp. on Appl. of Laser Techniques to Fluid Mechanics, Lisbon (1994), paper 23.1
2. R. Booij and J.M. Bessem (editors), Report on Workshop "User's Needs for Laser Doppler Anemometry", Supplement to the Proc. of 5th Int. Conf. on Laser Anemometry, Veldhoven (Neth.) 1993, pp. 13 - 50.
3. R.J. Adrian and C.S. Yao, "Power spectra of fluid velocities measured by laser-Doppler

- velocimetry", *Exp. in Fluids*, Vol. 5 (1987), pp. 17 - 28.
4. H.S. Shapiro and R.A. Silverman, "Alias-free sampling of random noise", *J. Soc. Indust. Appl. Math.*, Vol. 8 (1960), no. 2, pp. 225 - 248.
 5. W.K. George and J.L. Lumley, "The laser velocimeter and its applications to the measurement of turbulence", *J. of Fluid Mechanics*, Vol. 60 (1973), pt. 2, pp. 321 - 362
 6. W. Mayo, "A discussion of limitations and extensions of power spectrum estimation with burst-counter LDV systems", *Proc. of 2nd int. workshop on laser velocimetry*, Purdue University, 1974, pp. 90 - 104.
 7. M.J. Tummers, L.H.J. Absil and D.M. Passchier, "An Experimental Investigation of Velocity Bias in a Turbulent Flow", *Proc. 6th Int. Symp. on Appl. of Laser Techniques to Fluid Mech.* Lisbon, 1992, paper # 5.4
 8. M.J. Tummers, D.M. Passchier and P.A. Aswatha Narayana, "LDA Measurements of Time- and Spatial Correlation Functions in and Adverse Pressure Gradient Wake", *Proc. of ASME/JSME Fluids Engng. and Laser Anemometry Conference*, Hilton Head Island, SC, USA, 1995, FED Vol. 229, pp. 347 - 355.
 9. J.M. Bessem and H.R.E. van Maanen, "Optimization of digital storage of random analogue data", *Meas. Sci. Technol.*, Volume 5 (1994), pp. 1331-1338.
 10. J.S. Bendat and A.G. Piersol, "Random Data, Analysis and Measurement Procedures", John Wiley & Sons, New York (1986)
 11. A. Papoulis, "The Fourier Integral and its Applications", McGraw-Hill Book Company, New York (1962)
 12. E. Müller, H. Nobach and C. Tropea, "Model Parameter Estimation from LDA Data at Low Particle Densities", *Proc. of ASME/JSME Fluids Engng. and Laser Anemometry Conference*, Hilton Head Island, SC, USA, 1995, FED Vol. 229, pp. 417 - 424.
 13. P.R. Aaby and M.A.H. Dempster, "Introduction to Optimization Methods", Chapman and Hall, London (1974).

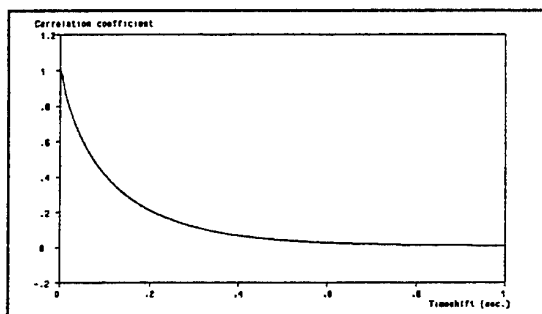


Figure 1: The theoretical auto correlation function, corresponding to the Bessem power spectrum.

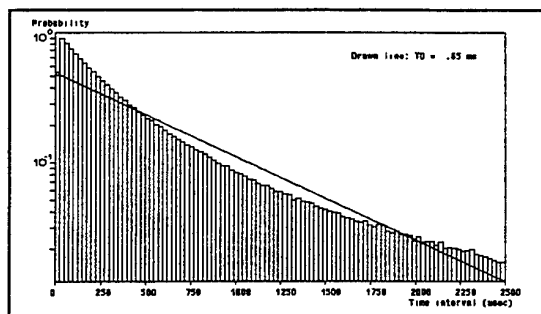


Figure 2: The time interval distribution when strong velocity bias occurs (turbulence intensity 100% and up).

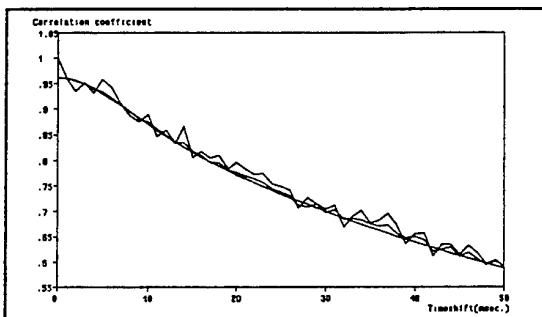


Figure 3: Comparison of Ideal, Slotted and Novel ACF estimates. Note that the Novel and Ideal ACF's almost coincide for small values of τ .

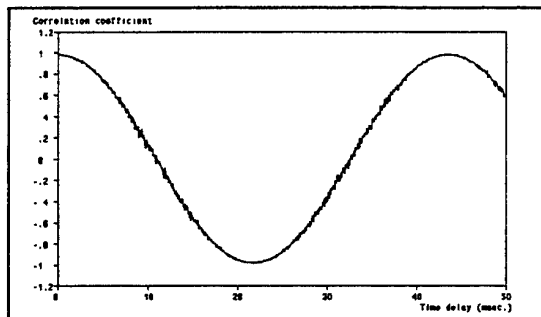


Figure 4: Slotted ACF using eq. [6] of periodic signal with 10 % Gaussian white noise added. Note that the variance depends on the absolute value of the correlation coefficient.

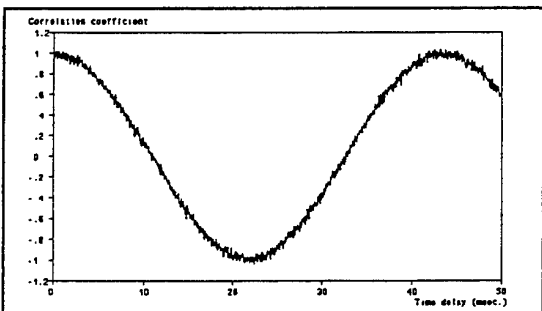


Figure 5: Slotted ACF using eq. [3] of periodic signal with 10 % Gaussian white noise added. Note that the variance is independent of the value of the correlation coefficient.

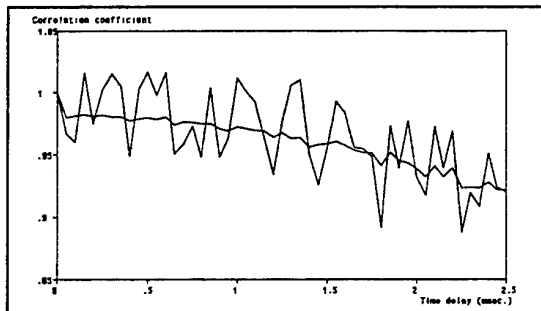


Figure 6: Enlargements of slotted ACF's of fig. 4 and 5. Note the difference in variance for large values of the correlation coefficient. Rise above 1 is caused by variance, not by velocity bias.

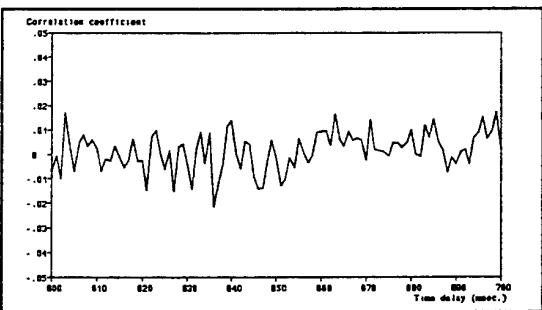


Figure 7: Comparison of the ACF estimates of eq. [3] and [6]. Note that the variances are identical for such low values of the correlation coefficient because the traces are virtually indistinguishable.

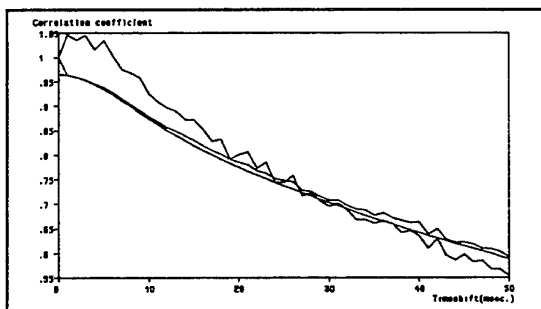


Figure 8: As figure 5, but with velocity bias introduced.

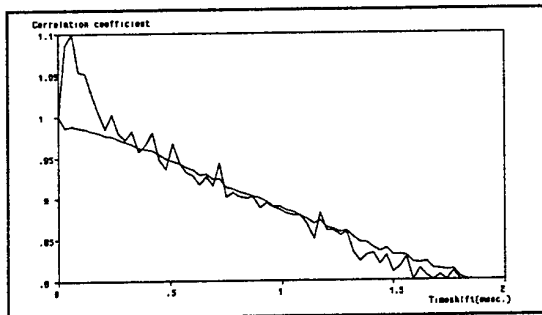


Figure 9: Comparison of estimations of ACF's on measured data.

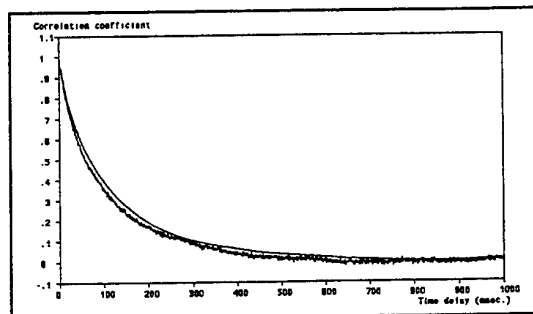


Figure 10: Estimate of the ACF using the algorithm of eq. [6] and the theoretical ACF, slot width 1 ms. Turbulence intensity 33 %, 1-dimensional velocity bias introduced.

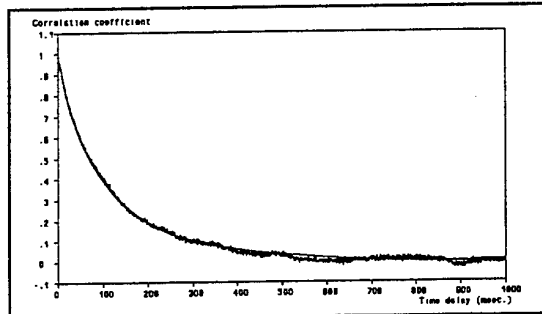


Figure 11: Estimate of the ACF using the algorithm of eq. [6] and the theoretical ACF, slot width 1 ms. Turbulence intensity 100 %, 1-dimensional velocity bias introduced.

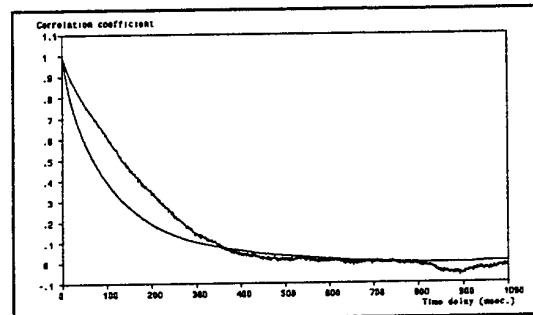


Figure 12: Estimate of the ACF using the algorithm of eq. [6] and the theoretical ACF, slot width 1 ms. Turbulence intensity 200 %, 1-dimensional velocity bias introduced.

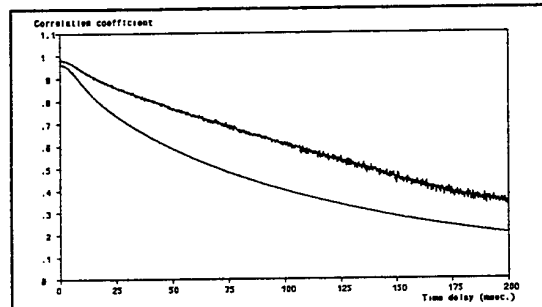


Figure 13: Estimate of the ACF using the algorithm of eq. [6] and the theoretical ACF, slot width 0.2 ms. Turbulence intensity 200 %, 1-dimensional velocity bias introduced.

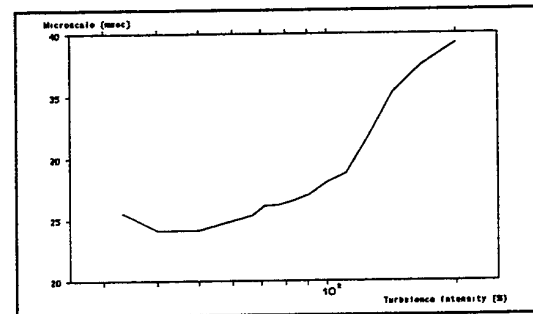


Figure 14: Taylor time scale as a function of the turbulence intensity.

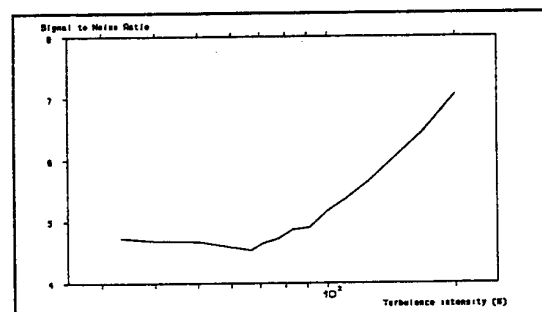


Figure 15: Signal to noise ratio as a function of the turbulence intensity (input value = 5).

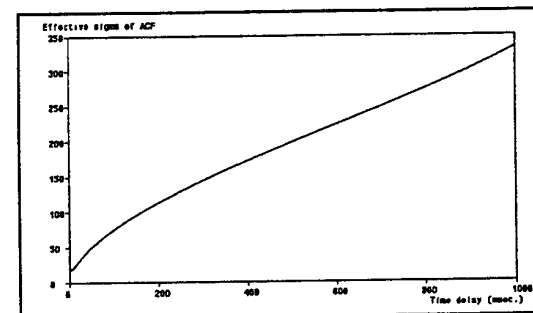


Figure 17: Effective σ of the auto correlation function of the turbulence according to the Bessem spectrum.

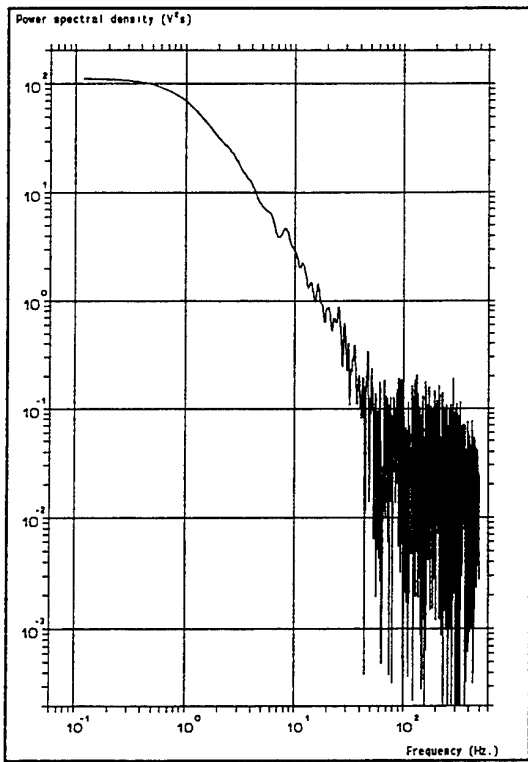


Figure 16: Power Spectral Density, obtained by Fourier Transformation of ACF estimated using eq. [6].

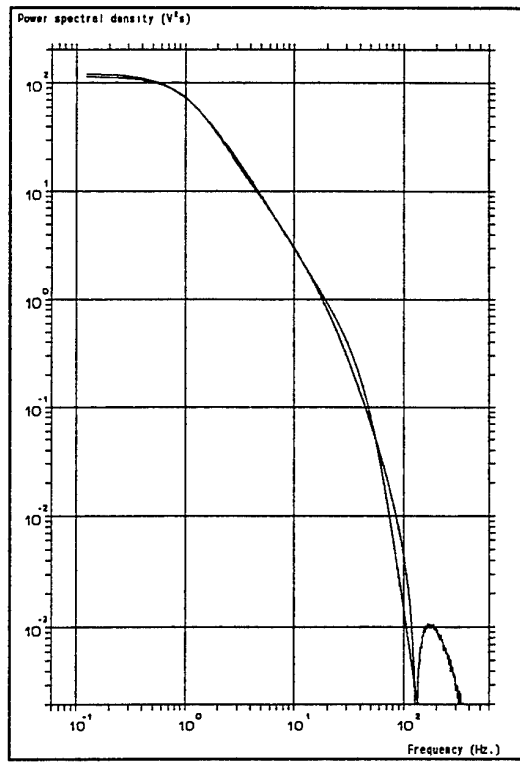


Figure 18: Turbulence Power Spectrum, obtained after curve fitting of the ACF and theoretical spectrum. Compare with fig. 16.

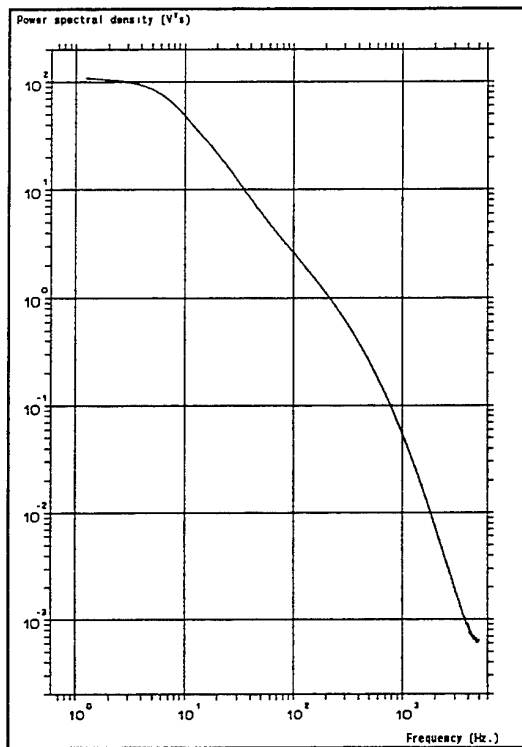


Figure 19: Turbulence power spectrum based on curve fit of experimental data.

MINIMISING ERRORS FOR CROSS SPECTRAL ANALYSIS USING LASER DOPPLER ANEMOMETRY MEASUREMENTS

J.Scholten, S.Dawson, J.A.Fitzpatrick
Department of Mechanical Engineering
Trinity College, Dublin, Ireland.

&

L.Simon
Laboratoire d'Acoustique de l'Universite du Maine
LeMans, France.

ABSTRACT

A linear interpolation method is shown to reduce the step noise inherent in the sample & hold process associated with LDA data acquisition and hence improve the estimates of autospectra, especially at high frequencies where the signal to noise ratio is low. Results from a series of experiments using a single component laser Doppler anemometer are compared with those from single and cross hot wires. It is shown that bias errors in coherence and phase measurements caused by small differences in time between the sample & hold method for the LDA and the regularly sampled data for the hot wire can be eliminated by using simultaneous sampling and reconstructing the time domain data using linear interpolation between measured data points for both hot wire and LDA data.

1. INTRODUCTION

The most commonly used method for the determination of autospectra from laser Doppler anemometry measurements is the sample & hold technique followed by direct transformation from time to frequency domain and hence spectra using FFT algorithms. Other methods include correlation slotting (Gaster & Roberts, 1975) and direct transform with adaptive filtering (Ajmani & Roberts, 1990), but they require significant data processing and have been shown by McDonnell & Fitzpatrick (1992) to be, at best, no better than sample & hold methods for medium sample rates. The errors associated with sample & hold procedures have been detailed by Adrian & Yao (1987) as step noise and a low pass filter effect. The former adds a constant level of noise across the spectrum and the latter serves to attenuate the signal at high frequencies. Both these effects can be calculated using error estimates from Adrian & Yao (1987) and corrected spectra can be obtained. However, this entails considerable additional signal processing for very little gain, especially if data rates are of the order of 4 times the maximum frequency to be resolved.

For many applications in fluid mechanics, fundamental understanding of turbulence related phenomena depends not only on the correct estimation of the turbulence frequency spectrum but also on accurate estimation of the spatial correlation of the turbulence and on the degree of correlation of the turbulence with other dynamic parameters. This is usually expressed as a normalised cross correlation or cross covariance function, but the use of the coherence function (normalised cross spectrum) and phase is becoming more popular as they contain frequency dependent information. Cross spectra are most efficiently determined from time domain data using FFT techniques. This necessitates reconstruction of the LDA data in the time domain, and it has been shown by Fitzpatrick & McDonnell (1994) that step noise in sample & hold procedures produces a predictable error in the estimation of coherence functions relating LDA data with regularly sampled data, whereas the low pass filter effect produces an error in the phase estimate. The results from a comparison of LDA and hot wire data (nominally at the same measurement location) from grid generated turbulence showed poor agreement over a wide range of frequencies. A linear interpolation scheme was shown by Simon et al. (1995) to reduce significantly the step noise and improve the estimates of coherence functions.

The objective of this paper is to identify the origins of the poor coherence measurements and to develop methods for cross spectral techniques using LDA measurements in combination with those from a hot wire (or indeed any conventional instrument providing an analogue output) which minimise bias errors. Results from hot wire measurements are compared with those from a single component LDA system using both sample & hold and interpolation methods. The effect of step noise on coherence and phase between the LDA and hot wire data is examined for grid generated turbulence and vortex dominated flows, and the results for both u and v components in a turbulent flow are compared with those from cross hot wire measurements. Finally, the effect of LDA measurement volume on the results is examined.

2. SIGNAL PROCESSING METHODS FOR LDA

2.1. Time Domain Reconstruction

Reconstruction of the time domain LDA data is required for cross spectral analysis. A linear interpolation scheme has been reported by Simon et al. (1995). The results for a series of simulated Kolmogorov type spectra are shown in figure 1(a) for the sample & hold method and in figure 1(b) for the linear interpolation for a number of different mean sample frequencies.

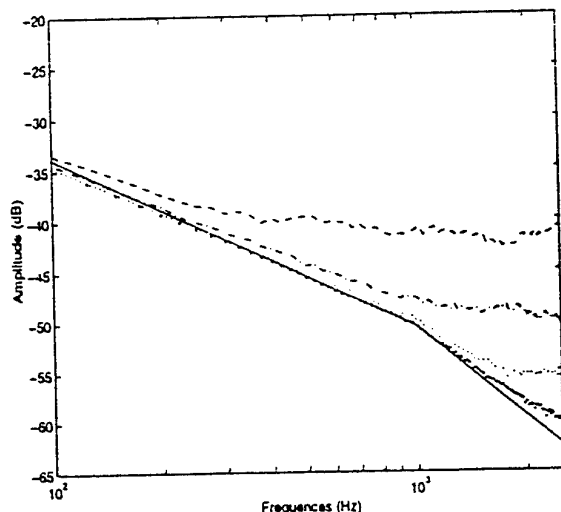


Figure 1(a): Simulated Kolmogorov spectra : sample & hold. $F_s = 2\text{kHz}$ (- -), 5kHz (- · -), 10kHz (· · ·), 20kHz (·)

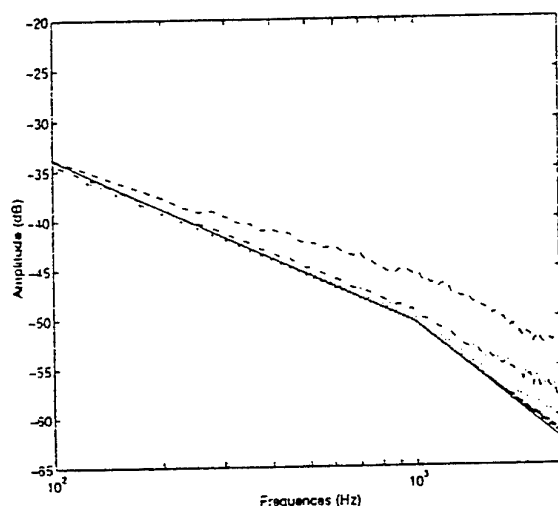


Figure 1(b): Simulated Kolmogorov spectra : linear interpolation. $F_s = 2\text{kHz}$ (- -), 5kHz (- · -), 10kHz (· · ·), 20kHz (·)

It can be seen that the linear interpolation method has reduced significantly the bias errors inherent in the sample & hold process, thus enabling better resolution at high frequency. The reduction in step noise bias was also evident in the estimates of coherence functions which were significantly improved for both white and pink noise when linear interpolation was used to reconstruct the data. The low pass filter effect was unchanged for the interpolation method, but the errors inherent in the linear interpolation method require further investigation.

2.2. Bias For Simultaneously Sampled Data

It will be seen in section 4 that the coherence between simultaneously sampled data can be improved by sampling the analogue data at the same time as the LDA data, using LDA data points as triggers. However, since this involves introducing the same step noise to both data sequences, coherence estimates will be biased upwards. The degree of bias will depend on the signal to step noise ratio and on the coherence of the original data. Figure 2 shows schematically the effect of using simultaneous sample & hold for both LDA, $u(t)$, and hot wire, $e(t)$, signals.

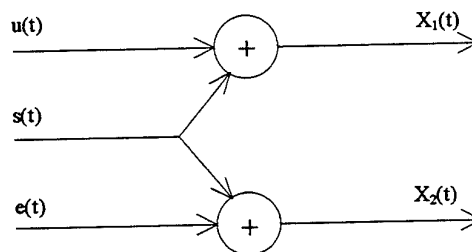


Figure 2: Schematic of Step Noise Effect

The bias in coherence measurements due to step noise can be determined as follows. The measured data are given by:

$$\begin{aligned} X_1(t) &= u(t) + s(t) \\ X_2(t) &= e(t) + s(t) \end{aligned} \quad (1)$$

Assuming that $s(t)$ is not correlated with either $u(t)$ or $e(t)$, the auto and cross spectra of $X_1(t)$ and $X_2(t)$ are given by:

$$\begin{aligned} G_1(f) &= G_u(f) + G_s(f) \\ G_2(f) &= G_e(f) + G_s(f) \\ G_{12}(f) &= G_{ue}(f) + G_s(f) \end{aligned} \quad (2)$$

From these, the measured coherence function is given by (omitting dependence on f):

$$\gamma_{12}^2 = \frac{|G_{ue} + G_s|^2}{(G_u + G_s)(G_e + G_s)}$$

$$\text{If } \gamma_{ue}^2 = \frac{|G_{ue}|^2}{G_u G_e}; \quad \gamma_{ue} \approx \frac{\text{Re}\{G_{ue}\}}{G_u}$$

$$\text{and } \alpha = \frac{G_s}{G_u} = \frac{G_s}{G_e}$$

then the measured coherence function is given by:

$$\gamma_{12}^2 = \left(\frac{\alpha + \gamma_{ue}}{1 + \alpha} \right)^2 \quad (3)$$

Thus, if the signal to noise ratio ($1/\alpha(f)$) is known, then the actual coherence $\gamma_{ue}^2(f)$ can be determined from the measured coherence $\gamma_{12}^2(f)$. The error in the measured coherence function is shown in figure 3 as a function of the actual coherence function with signal to noise ratio as a parameter.

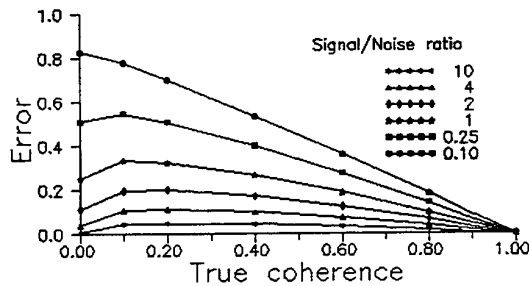


Figure 3 : Effect of step noise on Coherence estimates.

3. EXPERIMENTAL SET UP, DATA ACQUISITION & ANALYSIS

Tests were performed in a low turbulence wind tunnel, with a grid installed for the turbulence measurements and a single cylinder for the vortex dominated flow. A single channel laser Doppler system using a 32mW He-Ne laser in forward scatter mode was used in conjunction with a TSI 1980B counter interfaced to a Pentium type pc through a DMA board. Two lenses of focal length 350 mm and 120 mm respectively were used to investigate the effect of measurement volume on coherence estimates. A Dantec hot wire system using a 55P11 probe was used for the single wire and a 55P61 probe for the cross wire tests, with 55MO1 anemometer modules as required. The output from

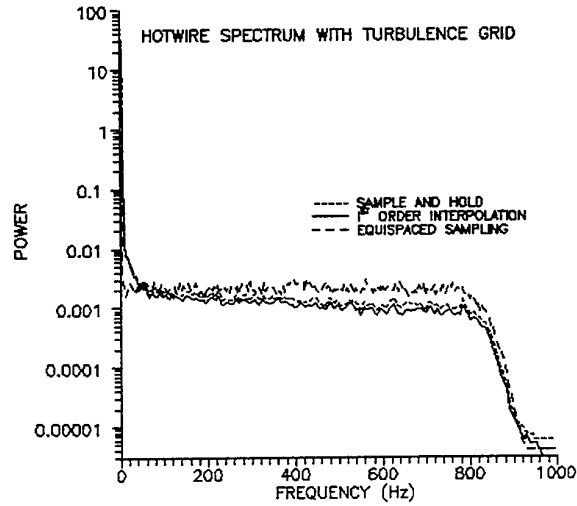


Figure 4(a): Hotwire autospectra with grid turbulence.

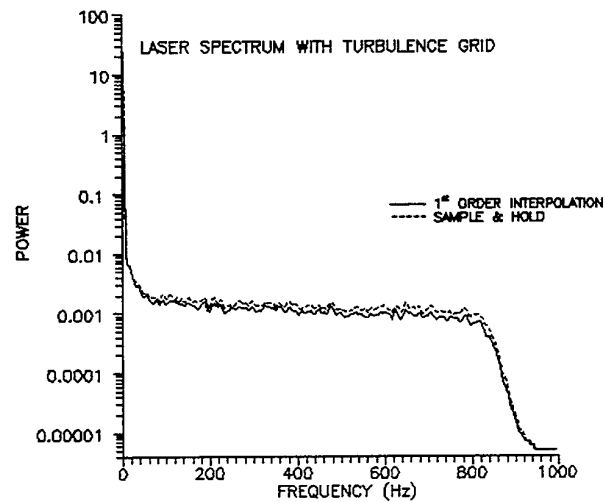


Figure 4(b): LDA autospectra with grid turbulence.

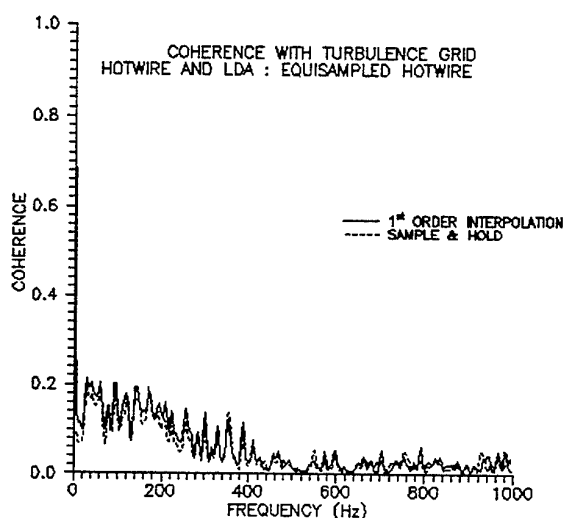
the hot wire modules was sampled using an A to D board. The LDA data was acquired in the usual way of validated data and time from the counter. The hot wire output was sampled, in the first instance, as equispaced data in blocks acquired at the same time as the blocks of LDA data. The non-equispaced data was acquired simultaneously for both the LDA and hot wire by using a trigger pulse from the counter to activate the A to D board, and sample the hot wire bridge. For the cross wire measurements, all data was acquired simultaneously, non-equispaced. The signal processing to yield auto and cross spectra was implemented using spectral analysis software written in MATLAB. The mean data rate for the LDA acquisition was 5 kHz. After reconstruction by either sample & hold or linear

interpolation at time intervals equivalent to 100 kHz, the data was low pass filtered using an 8 pole Chebyshev filter and resampled at 2 kHz with spectra computed up to 1 kHz.

4. EXPERIMENTAL RESULTS

4.1. Autospectra

Figures 4(a) & (b) show the results for spectra calculated from hot wire and LDA data using sample & hold and linear interpolation for both, with equispaced data also plotted for the hot wire. As can be seen from the results, there is little variation in the calculated spectra, as would be expected as the step noise level is small.



4.2. Coherence & Phase

The coherence and phase for the equispaced hot wire and LDA data is shown in figure 5. As reported by Fitzpatrick & McDonnell (1994), the results show very low levels of coherence and the phase estimates are almost random above 400 Hz. The use of the linear interpolation scheme shows little improvement on the results, indicating that there is virtually no bias due to step noise as this would produce different results for the two reconstruction methods. However, when the hot wire and the LDA data are sampled simultaneously, there is a dramatic improvement in the coherence and phase data, as can be seen in figure 6. The latter is shown to be increasing

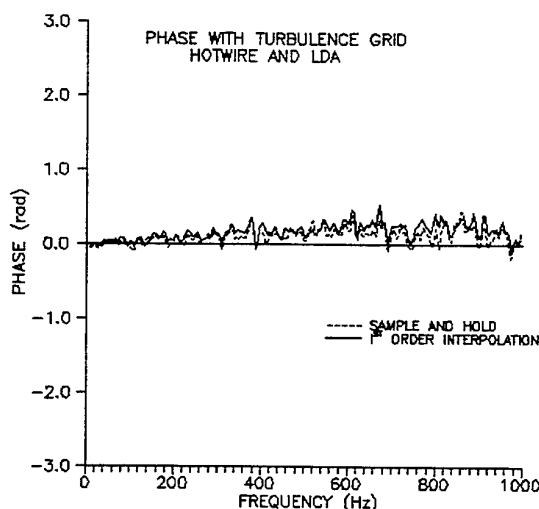
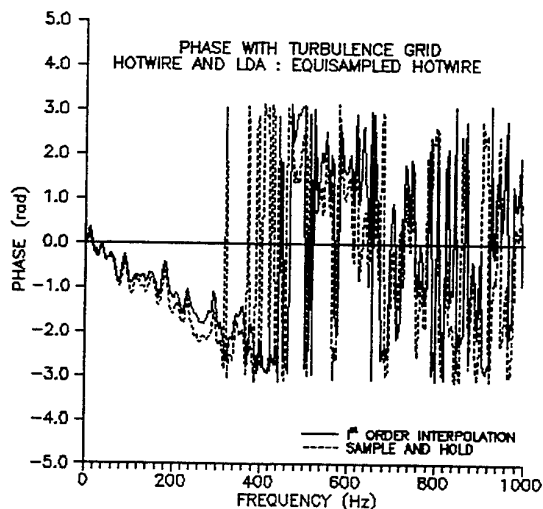
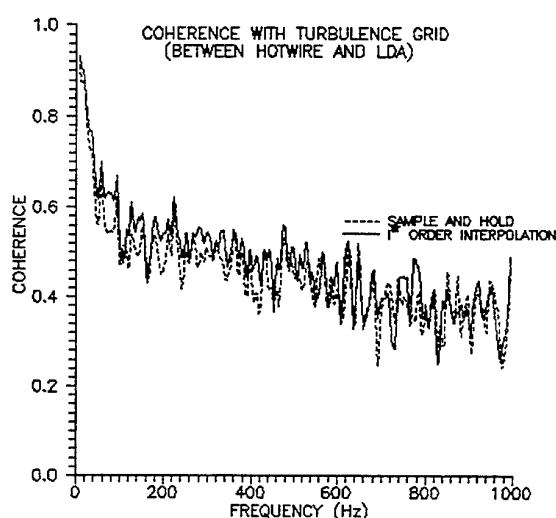


Figure 5: Coherence and Phase for LDA and equispaced hotwire.

Figure 6: Coherence and Phase for LDA and simultaneously triggered hotwire.

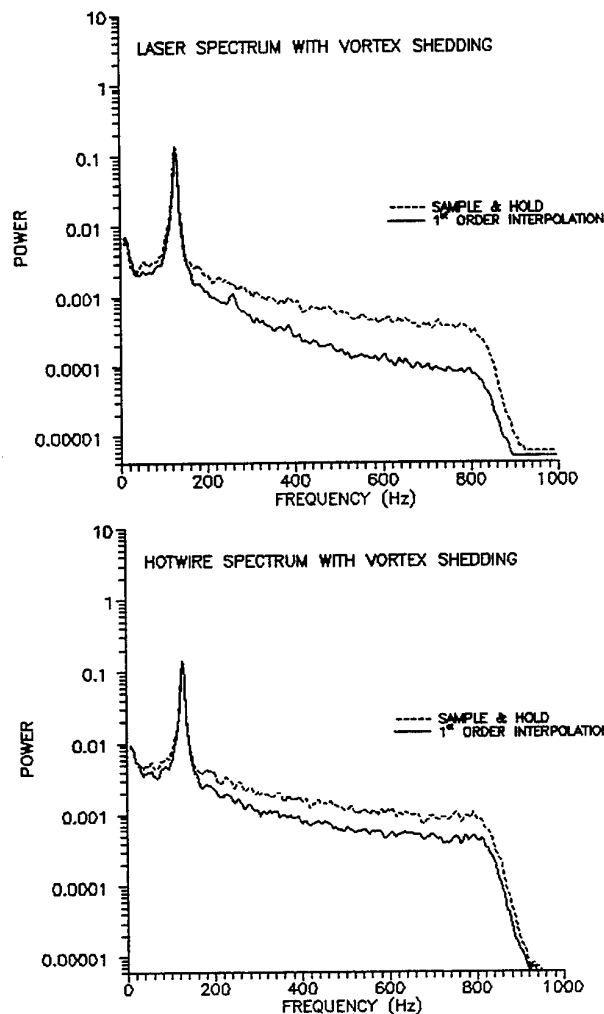


Figure 7: Autospectra for LDA and hotwire in shear layer behind cylinder.

slightly from zero indicating a phase lead between LDA and the hot wire as expected since the hot wire is located downstream. The phase is determined from the time lead which is estimated from the mean velocity of 15m/s and separation of 1mm between LDA and hot wire giving a lead of less than 0.1 ms. Again, the use of linear interpolation does not improve the data to any significant degree indicating that there has been virtually no positive bias of the coherence by step noise as suggested in section 2.2. Thus, the errors in the coherence estimates using equispaced data are due almost entirely to bias errors caused by time domain mismatch, which would be expected to be more pronounced at the higher frequencies. This indicates that data should be sampled simultaneously if cross spectral and phase estimates are required. The coherence and phase data of figure 6 is the correct estimate as the phase relationship has been estimated correctly. The coherence is typical of what would be expected from a grid flow using a one component LDA and a single hot wire.

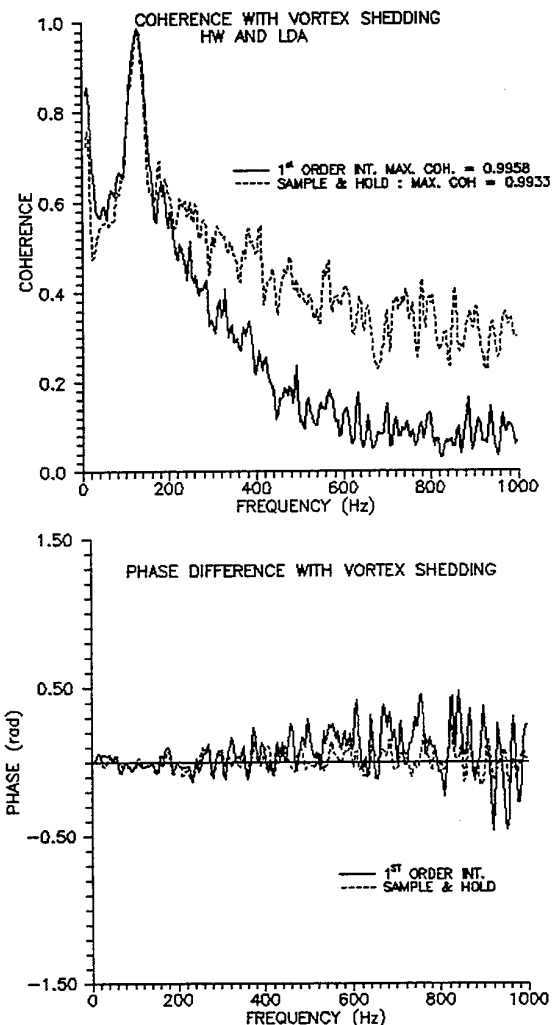


Figure 8: Coherence and Phase for LDA and hotwire in shear layer behind cylinder.

Thus, the spatial coherence of the turbulence can be estimated with minimal errors using the procedures described above. For turbulence data, the differences between the sample & hold and linear interpolation methods are small indicating minimal effect of step noise as expected for the mean sample rates achieved.

Figure 7 shows the auto spectra for the LDA and hot wire data for a test in which the measurements are taken at the edge of the shear layer behind a cylinder. As expected, the dominant peak in the spectra corresponds to the vortex shedding frequency and the results shown for both linear interpolation and sample & hold clearly show the step noise associated with the former at the higher frequencies. Figure 8 shows the coherence and phase for this data with coherence at the vortex shedding frequency close to unity, indicating a highly coherent structure. The coherence estimates also show clearly the positive bias predicted in section 2.2 and inherent in data reconstructed using the sample & hold method especially at the higher frequencies

where the step noise begins to dominate the spectrum. For this case, the sample & hold process is clearly inferior to linear interpolation.

4.3. Coherence & Phase for Cross Hot Wires

Further analysis of the grid generated turbulence was performed using cross wires in order to analyse the effect of using a single component LDA system. The objective was to investigate the coherence between the u & v components measured by the hot wires and the U component from the LDA. The coherence and phase between U (LDA) and u (hot wire) are shown in figure 9. It can be seen that the coherence values are lower than those of figure 6 from the LDA/single wire measurements. This can be explained by reference to the phase, which shows a larger lead time as the laser measurement volume was located further

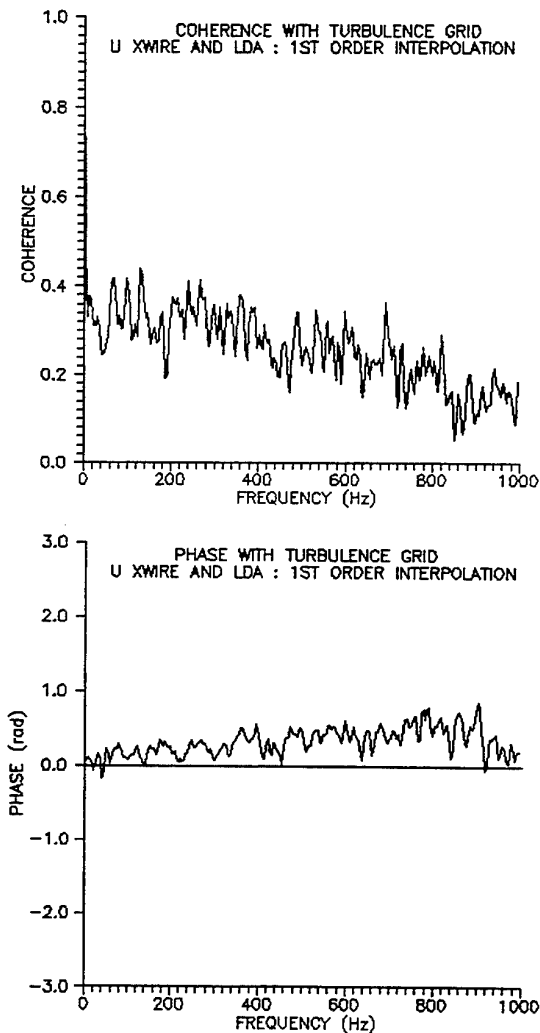


Figure 9: Coherence and Phase for U (LDA) and u (cross hotwire) with grid turbulence

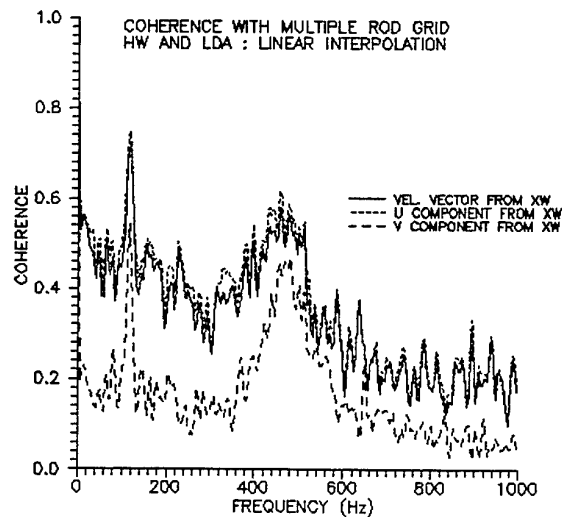


Figure 10: Coherence for U (LDA) and cross hotwire velocity components, for cylinder cluster

upstream from the cross wires. There was virtually no coherence between the U (LDA) and the v (hot wire) measurements as the hot wires were dominated by streamwise velocity components.

In order to create a flow in which the u and v components are significant, a cluster of cylinders of various diameters was used. The coherence between the LDA and the u and v hot wire components are shown in figure 10 together with coherence between the LDA and the velocity vector obtained from hot wire. It can now be seen that the highest coherence values are obtained for the combination of U (LDA) and the u (hot wire). The coherence obtained when using the velocity vector is marginally lower with the v (hot wire) at about half this level. Further analysis of this data is necessary before any significant conclusions can be drawn, as the u and v components are also correlated.

4.4. Effect of Measurement Volume

In order to investigate the effect of LDA measurement volume on the results, a different focal length lens was used to reduce the measurement volume. For the tests described above, the LDA lens with focal length of 350 mm and measurement volume 3.9 mm long was replaced by a lens with a focal length of 120 mm giving a measuring volume of length 0.5 mm. Figure 11 shows the coherence and phase obtained using the 120 mm lens together with that obtained with the original lens. It can now be seen that the coherence for the reduced measurement volume is significantly lower than that for the larger. This is again due to the increased distance between the laser measurement volume and the hot wire resulting from the increased angle of incidence of the beams. The phase data shows clearly this effect.

5. CONCLUSIONS

The use of linear interpolation to reconstruct time domain data from laser Doppler anemometry measurements significantly reduces the step noise inherent in the sample & hold method. The low pass filter effect is common to both. Errors arising when estimating cross spectra and hence coherence and phase between LDA data and conventional instruments can be minimised by sampling the latter at the same time as the former. Simultaneous sampling results in a bias in coherence function estimates which can be predicted when sample & hold methods are used. This error does not appear to be significant for linearly interpolated data.

Thus, to minimise errors in cross spectral analysis using LDA data, all data should be sampled simultaneously (i.e. triggered by the LDA data). Time domain signals should be reconstructed using linear interpolation, and FFT based analysis used to estimate the auto and cross spectra from which coherence and phase can be determined

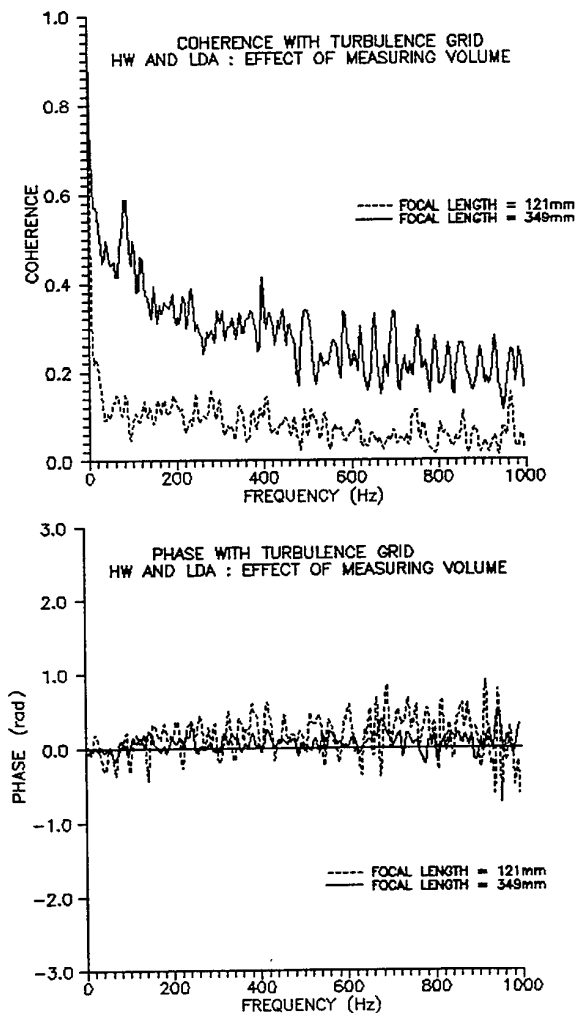


Figure 11: Coherence and Phase for different measuring volumes.

6. REFERENCES

- Adrian, R.J. and Yao, C.S., 1987, Power Spectra of Fluid Velocities Measured by Laser Doppler Velocimetry. *Experiments in Fluids*, vol. 5, pp. 17-28.
- Ajmani, D.B.S., and Roberts, J.D., 1990, Improved Spectral Estimation for Irregularly Sampled Data using Digital Filters. *Mech. Systems and Signal Processing*, vol. 4, pp. 77-94.
- Fitzpatrick, J.A., and McDonnell, C., 1994, Cross Spectral Analysis using Laser Doppler Anemometry. *Proc. 7th Int. Conf. on Applications of Laser Techniques to Fluid Mechanics, Lisbon*, paper 8.4.
- Gaster, M. and Roberts, J.D., 1975, Spectral Analysis of randomly Sampled Signals. *J. Inst. Maths. Appl.*, vol. 15, pp.195-216.
- McDonnell, C. and Fitzpatrick, J.A., 1992, Spectral Analysis of Turbulent Flows from LDA Measurements. *Proc. 6th Int. Symposium on Applications of Laser Techniques to Fluid Mechanics, Lisbon*, paper 8.3.
- Simon, L., Scholten, J. W. and Fitzpatrick, J.A., 1995, Velocimétrie Laser: Amélioration du Traitement des Données Expérimentales par Interpolation d'Ordre 1. *Proc. Congrès Français de Mécanique, Strasbourg*, pp. 321-324.

UNDERSTANDING BIASES IN THE NEAR-FIELD REGION OF LDA TWO-POINT CORRELATION MEASUREMENTS

L. H. Benedict and R. D. Gould
Dept. of Mechanical and Aerospace Engineering
North Carolina State University
Raleigh, NC 27695

ABSTRACT

Two-point LDA measurements have been found to be strongly affected by both geometric and coincidence timing parameters, some effects of which are akin to those previously documented for nonorthogonal three-component LDAs. High spatial resolution is shown to be a necessity for small scale two-point measurements. It is suggested that a maximum effective probe volume dimension of one Kolmogorov length be considered as an upper bound for lateral and spanwise correlation measurements if microscale estimates are intended. However, if the effective probe volume shape is roughly spherical and a proper coincidence window is chosen, the spatial resolution of longitudinal correlation measurements appear to be independent of probe dimension.

1. INTRODUCTION

A review of the literature concerning two-point laser Doppler anemometer (LDA) measurements suggests that researchers have easily achieved the goal of making coarse measurements pertaining to large scale structures. The small separation character of two-point correlations has remained elusive, however. This is unfortunate because accurate near-field correlation measurements could allow for determination of the turbulent dissipation rate in complex flows.

Reasons for the lack of progress in near-field two-point correlation measurements include: spatial resolution of the probes, geometric constraints affecting the design of dual LDA systems, particle detection difficulties, geometric biases arising from the interaction of the probes, and coincidence timing biases. These problems are all in addition to the considerable difficulties which arise in making accurate single-point LDA measurements in complex flows. An explanation of geometric and coincidence window biases affecting the spatial resolution of two-point correlation measurements is the primary goal of the present communication. The approach taken here is an intuitive explanation of these bias mechanisms followed by presentation of supporting experimental data from the shear layer and separation zone of a backward-facing step flow. A more detailed account of this work can be found in the dissertation of Benedict (1995).

2. LITERATURE REVIEW

Spatial averaging (Durst et al. (1995)) and virtual single particles (Boutier (1985)), both of which are directly related to the size of the probe volumes, are the main factors influencing the spatial resolution of single-point statistics (assuming that proper overlap of probes has been achieved for multi-component systems). As will be shown next there are several additional parameters to consider in evaluating the spatial resolution of two-point correlation measurements, namely, the presence or absence of a dominant velocity component in the flow (i.e., $|\bar{U}| \gg |\bar{V}|, |\bar{U}| \gg |\bar{W}|$), the magnitude of the local turbulence intensities (TIs) ($\sqrt{u^2}/\bar{U}, \sqrt{v^2}/\bar{V}, \sqrt{w^2}/\bar{W}$), the magnitude of the Reynolds stresses ($\overline{uv}, \overline{uw}, \overline{vw}$), and the relative orientation of the probe volumes to the mean flow. Furthermore, the choice of coincidence window and processor priority is very significant for two-point measurements.

The first studies to consider the consequences of coincidence window settings and overlapping probe volumes for two-point measurements were those of Absil et al. (1990) and Absil (1995) in the wake of a circular cylinder. One aspect of their work considered the variation in $R_{11}(0,0,z)$ with coincidence window for several separation distances. It was plainly shown that the coincidence window makes any spatial correlation measurements made by LDA actually *space-time* correlations. Thus an initial requirement for accurate spatial correlation measurements is that the coincidence window be kept short enough so that no appreciable change in correlation takes place over its duration.

Absil and Absil et al. also noted a geometric bias associated with measuring either lateral or spanwise spatial correlations in flows with a dominant longitudinal velocity. When probes partially overlap, measurements are most likely made on the *same particle, simultaneously* (i.e., single-particle burst-pairs), in the region of overlap because these particles automatically satisfy the coincidence timing limit; whereas, particle *pairs* arriving in other parts of the probe volumes and satisfying the coincidence timing limit are rare. This leads to correlation coefficients biased towards the zero-separation value.

Interestingly, Tummers et al. (1994, 1995), claim to have observed the same geometric bias in longitudinal correlations made in the wake flow of a flat plate in an adverse pressure gradient. Intuitively, however, one may reason that there should not be a geometric effect for longitudinal correlations because measurements only take place simultaneously in the same place when the probes are completely overlapping.

Recently Eriksson and Karlsson (1995) have investigated the spatial resolution requirements of two-point LDA measurements by analyzing the variation of correlation coefficients at zero separation, $R_{11}(0,0,0)$, with probe size. Such an experiment is tantamount to investigating the effect of virtual single particles on $R_{11}(0,0,0)$. It will be shown, however, that measurement of only the zero separation correlation coefficient provides insufficient information to determine the spatial resolution of a two-point LDA system.

It should be mentioned that two-point measurements in complex flows can also be expected to suffer from velocity bias. Whether or not the bias has a significant effect on the correlation coefficient remains a topic for debate; however, Trimis and Melling (1995) have recently published an analysis indicating that the correlation coefficient is, in fact, relatively insensitive to velocity bias. Benedict (1995) reported limited experimental data which appear to support such a claim.

3. TWO-POINT SINGLE-COMPONENT LDA

Two-point velocity statistics were measured using two single-component, traversing LDAs. A schematic of the system is shown in Figure 1. One set of beams from a two-component LDA (henceforth denoted LDA1) was blocked off so that the system functioned as a single-component LDA. A second single-component LDA (denoted as LDA2) was mounted to a traverse on the opposite side of the test section. Both beams of both LDAs were frequency shifted so that both systems utilized a net shift of 10 MHz in the upstream direction. The laser line of LDA2 could be changed from 514.5 nm to 488 nm and the orientation of the beams could be changed to make measurements of either axial or transverse velocity. Additionally, the test section could be rotated to allow either LDA to measure the spanwise velocity component. The probe volume diameters and lengths were approximately 140 μm and 1200 μm , respectively. TSI model 1990 counter processors were used with low and high filter settings of 2 and 50 MHz, respectively. For each measurement 32 fringes were counted with a 1% comparator setting. Data were transferred through a Dostek LDA interface with coincidence timing logic to an Intel-based 486 personal computer for storage and analysis.

All measurements were made with LDA2 stationary at a given location while LDA1 was traversed through this location over both positive and negative separation distances. Positioning accuracy of LDA1 with respect to LDA2 was determined by precision analog movement indicators, one with 10 μm divisions, the other two with 25 μm divisions. The indicator with the 10 μm divisions was always used to measure the distance along the separation coordinate with

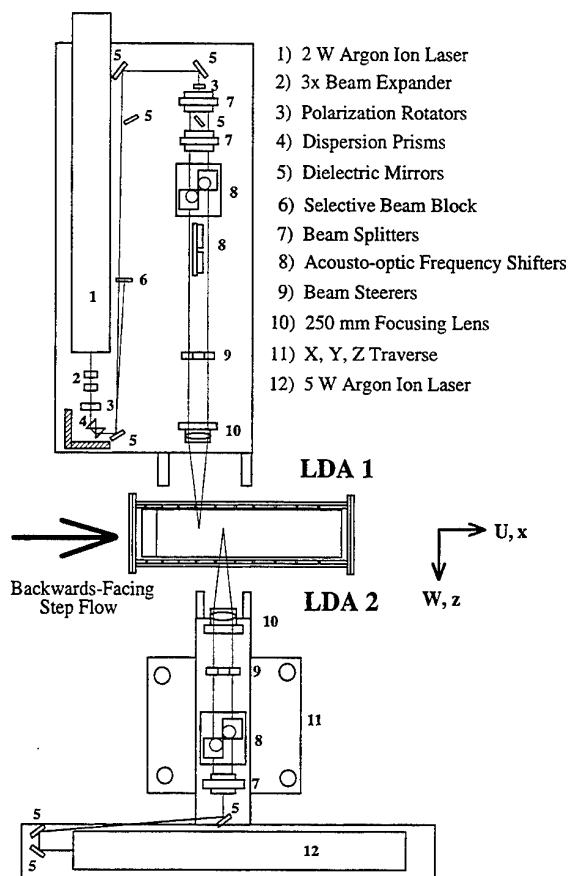


Figure 1 Two-point LDA schematic

$\pm 2 \mu\text{m}$ uncertainty while the indicators with 25 μm divisions were used to ensure zero separation in the other two coordinate directions with $\pm 5 \mu\text{m}$ uncertainty.

Very short traverses in all three coordinate directions were used to define the zero-separation location (i.e., total overlap of the two probes) prior to any set of measurements. The zero-separation location was considered to be the location for which both the correlation coefficient and the coincident data validation rate (DVR) reached their maximum values. It was felt that this method of determining zero-separation was superior to the pinhole alignment technique used for example by Tummers et al. (1994, 1995), Gould et al. (1992), and Trimis and Melling (1995). Certainly *in the plane* of the pinhole the probes may be brought to overlap one another quite accurately using this technique. However, the accuracy of this method is insufficient in the plane *perpendicular* to the pinhole. The relatively slow divergence of the beam waists allows for some misalignment along the separation vector perpendicular to the pinhole.

Because the two LDAs were oriented to face each other, signal collection in the forward direction was not possible; rather both LDAs were designed to utilize collection optics mounted at 90° to the incident beam direction (i.e., 90° side-scatter) as illustrated in Figure 2. Although signal strength is decreased substantially when collecting from 90° , there is a distinct advantage in that the effective probe volume dimensions can be reduced by allowing the

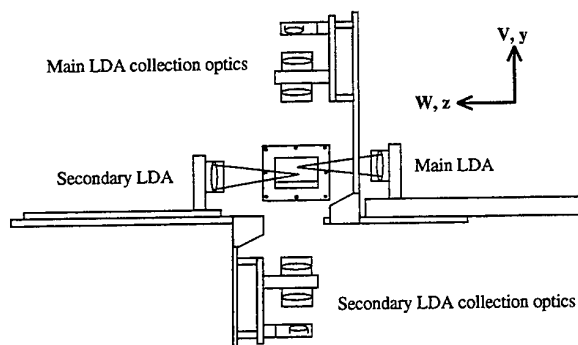


Figure 2 End view of test section depicting 90° collection

photomultiplier to "see" only a portion thereof. In fact, the effective dimensions can be manipulated to some extent simply by choosing pinholes of various sizes. This concept is illustrated (two-dimensionally) in Figure 3 for a typical dual beam LDA setup (i.e., $\approx 10:1$ length to diameter ratio). The collection optics used in this investigation had a magnification factor of 1.0 so the area of the probe volume projected onto the photomultiplier was determined by the physical diameter of the pinhole.

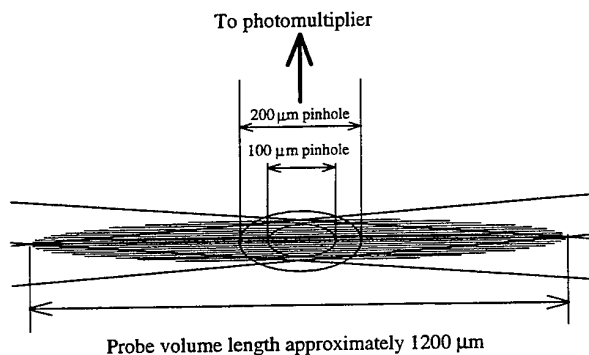


Figure 3 Probe volume reduction through 90° collection

Unfortunately, the pinhole cannot affect the effective probe dimension in the direction parallel to the collection optics (the y -direction for measurements of U and V , the z -direction for measurements of W). Thus in the case of 90° collection, there is little point in decreasing the pinhole size much below the physical diameter of the probe volume. Pinholes of 200 μm were thus used for all measurements resulting in the effective dimensions given in Table 1.

Table 1 Probe dimensions in side-scatter for R_{11}

Coordinate	Actual	Effective (200 μm pinhole)
x	140 μm	140 μm
y	140 μm	140 μm
z	1200 μm	200 μm

Measurements presented in Benedict (1995) show that master/slave priority mode coincidence logic (one of the probes is the master and initiates the coincidence timing trigger) leads to very sharp biases when both positive and

negative velocities are present in the velocity probability distribution function (PDF). In light of these results, nonpriority coincidence (i.e., either probe can initiate the coincidence timing trigger) was used for all two-point measurements presented here.

4. INTUITIVE EXPLANATIONS OF TWO-POINT MEASUREMENT BIASES

4.1 Geometric Bias

An important point to make regarding two-point LDA measurements is that the finite size of the measurement volumes, *in combination with* the orientation of the fringes to the separation vector and the mean flow direction, defines the spatial resolution of the system and can create a *geometric bias* error for near-field measurements. A detailed intuitive analysis of this bias phenomenon is attempted here under the assumption that 90° collection is used to limit the size of the measuring volume. This assumption allows the probe volumes to be considered roughly spherical in shape and eliminates the need to seriously consider the effects of virtual single particles which were the primary topic of concern of Eriksson and Karlsson (1995). Only measurements of R_{11} are considered here because the nature of the geometric bias should not be dependent on the velocity component measured. Thus there are three separation directions (along the x , y , and z coordinate axes), three classes of separation distance (i.e., near-field nonoverlapping, partial overlap, and total overlap), and two flow regimes (i.e., dominant velocity component or fully three dimensional) which require consideration.

Consider a flow with a dominant velocity component and then let this component arbitrarily be considered as the axial component, \bar{U} . This type of flow corresponds to a relatively low turbulence flow with $0\% < \text{TI} < 100\%$. The upper bound is somewhat arbitrary and chosen out of practical experience. Generally speaking, low turbulence is considered as $\text{TI} < 30\%$, but because the distinction here is between only "dominant mean flow direction" and "fully three-dimensional flow," the upper bound on "low turbulence" must be extended somewhat. Figure 4 depicts the probe orientations for measurement of $R_{11}(x,0,0)$, $R_{11}(0,y,0)$, and $R_{11}(0,0,z)$ with regard to the dominant flow direction. Arrows through the probes indicate whether a measurement most likely consists of a dual-particle (two arrows) or single particle (one arrow) burst-pair. Only separations on the order of a few probe diameters are under consideration, but it is necessary to consider the cases of nonoverlapping, partially overlapping, and totally overlapping probes separately. In Figure 4 all three types of separation are shown. *It is evident that for both lateral (i.e., $R_{11}(0,y,0)$) and spanwise (i.e., $R_{11}(0,0,z)$) correlations, the effective separation distance is zero as soon as the probes begin to overlap.* Thus in the case of a dominant axial velocity component there appears to be a limitation on the spatial resolution of the lateral and spanwise correlation measurements. Any correlation measurements made when the probes are partially overlapping will be biased high (i.e.,

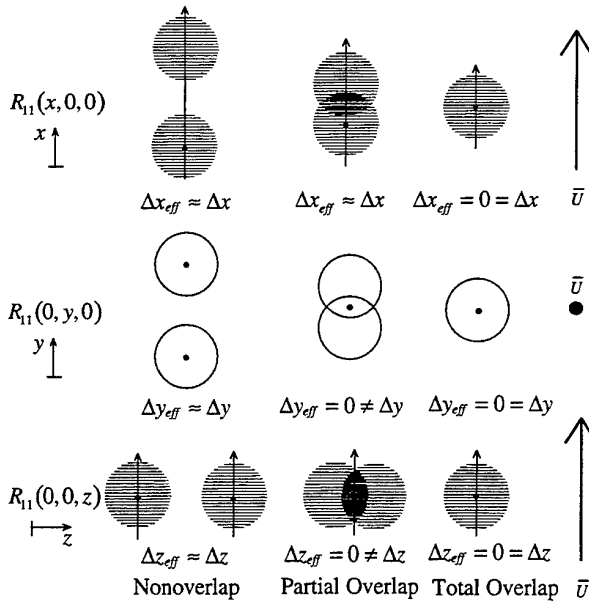


Figure 4 Two-point measurements with a dominant axial velocity component

toward perfect correlation). On the other hand, resolution for measurements with separation vector in the direction of the dominant velocity component (i.e., the axial direction in this discussion) appears to be infinite, an interesting result in light of the fact that separations in the direction of the mean flow cause the most difficulty for hot wires.

In the case of fully three-dimensional flow, more precisely described as isotropic turbulence with $\bar{U} = \bar{V} = \bar{W} = 0$, the direction of the separation vector no longer matters and both dual-particle and single-particle burst-pairs are likely to occur. Such a situation is illustrated in Figure 5.

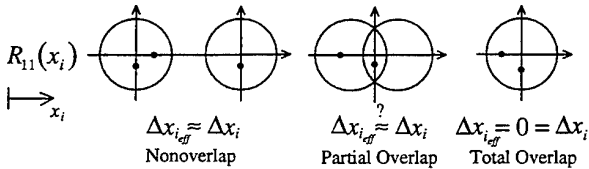


Figure 5 Two-point measurements in fully three-dimensional flow

Obviously for the nonoverlapping and totally overlapping cases the effective separation distance is equivalent to the physical separation distance of the probes. The important question is whether the single-particle burst pairs bias the partially overlapping case just as they do for certain orientations in Figure 4. The opinion of the present authors is that the entry surface area of the probes leading to dual-particle burst-pairs is much greater than the entry surface area leading to single-particle burst-pairs. If this assertion is true then the effect of the single-particle burst-pairs may not be enough to cause a significant bias in the correlation measurements when the flow is truly three dimensional. This is also an interesting concept which basically implies that the

spatial resolution becomes infinite as the local TIs tend toward infinity.

4.2 Coincidence Window Bias

Absil (1988) and Absil et al. (1990) recognized that the coincidence timing dictates that spatial correlation measurements are actually space-time correlations with the lag-time determined by the coincidence window duration. Researchers must be mindful of this when setting coincidence windows. The current authors suggest that autocorrelation measurements are the best means of determining the proper upper bound on the coincidence window for the purpose of measuring small scale structures. The window should be selected so that $R_{ij}(\tau_{cw}) \approx 1.0$. This implies that the coincidence window may be increased as the flow time scales increase, i.e., it should be considerably easier to make two-point measurements in flows with long time scales.

A more subtle problem of the coincidence timing logic is a bias which occurs when one probe is positioned closely downstream of the other with respect to the mean flow such that a large portion of the measurements consist of single-particle burst-pairs. The bias is the same as that discussed by Brown (1989) in the context of three-component LDAs. Essentially, the measurements are biased towards particles with a greater velocity in the direction of the separation vector. However, a clear distinction must be made in the case of two-point measurements, because this bias varies with the separation distance and is dependent on the alignment of the probe separation vector to the mean flow. Two-point measurements are also not well-suited to the channel-blanking technique advocated by Brown. This technique does eliminate any dependence on the coincidence window, but it can actually do more harm than good for two-point measurements. The reason is that the geometric bias described in §4.1 is incurred for all separations which require partial overlap of the probes. The directional dependence is also removed so that even the separation vector in the direction of the dominant velocity component incurs the geometric bias. Channel-blanking thus automatically limits the spatial resolution of the system to the effective probe diameter and would therefore *not* appear to be a useful solution (for small scale flows at least) to coincidence window bias in two-point measurements.

Clearly coincidence window bias can only occur when two-point measurements consist of single-particle burst-pairs processed at two different locations. By referring to Figure 4 it can be understood that if the flow exhibits a dominant velocity component (in this case the axial velocity), only measurements with separations along that component's coordinate axis (in this case $R_{11}(x, 0, 0)$) are influenced by coincidence window bias. In the case of fully three-dimensional flow (see Figure 5), coincidence window bias can be expected to affect measurements along all three coordinate axes. However, the effect should be the same in each direction, so that the discussion can be limited to measurements of $R_{11}(x, 0, 0)$.

Consider two probes separated to such an extent that all two-point measurements consist of two-particle burst-pairs,

in which case there is no coincidence window bias, and then consider the effect of the coincidence window as the probe separation is gradually reduced to zero. By decreasing the separation distance, a point is reached at which the fastest particles validated by the first probe can make it to the second probe within the coincidence time, i.e., the first single-particle burst-pairs are validated. These particles become over-represented in the velocity PDF because the arrival of these particles in both probes is determined only by one Poisson process and not two separate ones as it is for two-particle burst-pairs.

The first occurrences of single-particle burst-pairs are associated with particles having a very large velocity magnitude in the direction of the probe separation vector. The mean velocities measured at the two probes are thus biased towards greater magnitudes and the TIs begin to rise because the tails of the velocity PDFs are more heavily weighted. As the probe separation decreases further, however, the single-particle burst-pairs begin to outnumber the two-particle burst-pairs. The character of the velocity PDFs gradually change from having overly-weighted tails to a bimodal shape until, finally, the PDFs are very narrow. At this point, the mean velocities are still biased high but the TIs are biased low (i.e., low variance). The coincidence bias finally disappears when the probe separation is small enough that even particles with the smallest velocity magnitudes can make it to the second probe within the coincidence time.

5. EXPERIMENTAL VERIFICATION OF BIAS EFFECTS IN TWO-POINT MEASUREMENTS

Because the biases are dependent on the separation coordinate, but not on the velocity component measured, it was necessary to measure correlations in all three directions. The correlations, $R_{11}(x,0,0)$, $R_{11}(0,y,0)$, and $R_{11}(0,0,z)$ were chosen arbitrarily for this study. Of particular importance was a more definitive specification of the probe size required to resolve Taylor microscales than that given by Eriksson and Karlsson (1995).

To this end, two measurement locations in a backwards-facing step air flow ($Re_H = 26300$) were chosen for study with the step face located at $x = 0$, the bottom wall at $y = 0$ and the step height, $H = 25.4$ mm, measured from the bottom wall. The first location was $x/H = 3.0$, $y/H = 0.85$, roughly in the middle of the separated shear layer at the peak in the turbulent kinetic energy profile. Microscales are very small at this highly turbulent location, denoted as *station 1*, where unbiased single-point measurements indicated that $\bar{U} = 6.04$ m/s with $\sqrt{u^2} = 3.01$ m/s (see Benedict (1995) for detailed velocity statistics). A second location, *station 2*, was chosen in the recirculation zone at $x/H = 2.0$, $y/H = 0.4$, where the microscales could be expected to be somewhat larger. The unbiased statistics at this location were $\bar{U} = -2.01$ m/s and $\sqrt{u^2} = 1.51$ m/s. In the following figures, the stationary probe is referred to as LDA2; the traversing probe is designated LDA1.

5.1 Coincidence Window Bias Results

Measurements at station 1 were used to consider the effect of coincidence window bias on the longitudinal correlation coefficient, $R_{11}(x,0,0)$. Figure 6 shows the variation of the coincident data validation rate (DVR) in the near field (roughly plus or minus 3 probe diameters) for three different coincidence window widths. (The dimension of the probe in the direction of the separation vector is given by $l_{x,eff}$). When the probes completely overlap, the measurements are effectively single-point measurements so the coincident DVR is almost independent of the coincidence window duration. Virtually perfect overlap must be achieved to attain this result. In the far field, the DVRs reach their minima when all measurements are determined entirely by two-particle burst-pairs. The far-field DVRs increase with increasing coincidence window width; however, they are generally an order of magnitude less than the single-point DVRs. Between these two zones, the DVRs show different decay rates determined by the coincidence window's role in allowing single-particle burst-pairs at non-overlapping separation distances. A larger coincidence window allows more single-particle burst pairs and thus shows a more gradual decay in DVR with separation distance.

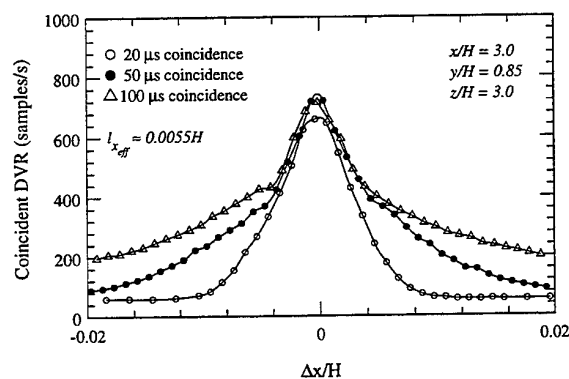


Figure 6 Coincident data validation rates in the near-field for several coincidence windows

Figure 7 shows that the choice of coincidence window width can have a profound effect on the near-field behavior of the correlation coefficient. The most obvious result is that 100 μ s is too large a coincidence window at this flow location to prevent the spatial correlation from becoming a space-time correlation. Evidently the autocorrelation at this location decays too rapidly to allow the use of such a large coincidence window. The differences between the 20 μ s and 50 μ s coincidence window results are more subtle; yet the rather narrow 20 μ s window results still do not show the proper parabolic behavior expected of spatial correlation measurements near zero-separation. As these window widths are short enough to allow for a good approximation of a pure spatial correlation, it can be inferred that coincidence window bias is affecting these measurements. Figures 8 and 9 support this claim. The statistics of the stationary probe (LDA2) over the range of separations change dramatically. Figure 8 shows the variation of \bar{U} where it can be seen that

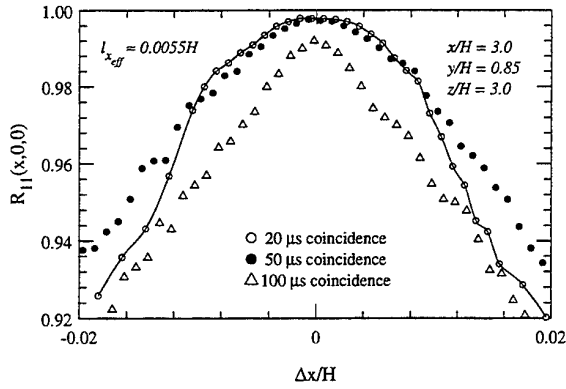


Figure 7 $R_{11}(x,0,0)$ for several coincidence windows

\bar{U} increases rapidly away from zero-separation until reaching a peak before it decays away to its far-field value. As the coincidence window decreases, the peak moves closer to zero-separation and covers a narrower range of separations. The standard deviations (Figure 9) drop initially as the probes are separated, reaching a minimum, then rise to a maximum before decaying to a constant value in the far-field. All uncertainties (denoted by error bars) presented in these figures and those following were determined using the jackknife estimator of variance as described in Benedict and Gould (1996).

Some further elaboration is necessary concerning the various horizontal lines appearing in these figures. Solid lines represent the *unbiased* single-point statistics at this location. Dotted lines indicate the data ready (i.e., biased) single-point statistics of the traversing probe, LDA1, while the dashed lines correspond to the single-point data ready statistics of the stationary probe, LDA2. Recall that the two-point statistics presented are those of LDA2. A curious phenomenon occurs in these measurements which is related to the DVR ratio defined as: $\text{DVR ratio} = [\text{DVR LDA1}]/[\text{DVR LDA2}]$. For these measurements, the DVR ratio was roughly 0.2 so that LDA2 was validating many more particles than LDA1. When the probes overlap, this implies that LDA2 "sees" all of the particles in the velocity PDF of LDA1 plus many more. At zero-separation, LDA1 effectively determines which particles are validated on both systems because LDA1's particles are a subset of those validated by LDA2. The net result is that the statistics of LDA2 are forced to match those of LDA1 at zero-overlap. Furthermore, the statistics are the same as the single-point data ready statistics of LDA1. When the probes are well separated, however, the probes validate totally different particle sets, and because in the far-field there is no correlation between the two locations, each LDA determines its own statistics.

Readers may be puzzled as to why two LDAs produce such different results at the same flow location. Actually, they both measure the same single-point statistics when an unbiased sampling technique is used (i.e., the solid lines in Figures 8 and 9). In lower turbulence regions of the flow, both LDAs give the same single-point statistics with any sampling technique. The data ready statistics are only different in highly turbulent regions which implies that one

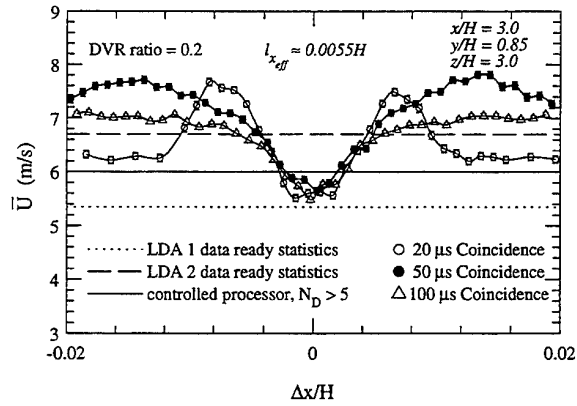


Figure 8 Mean axial velocity, stationary probe (LDA2)

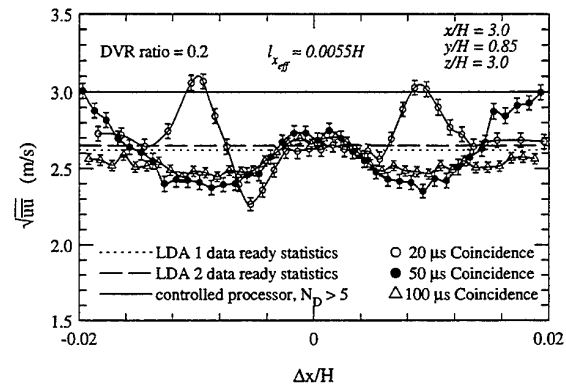


Figure 9 Axial velocity standard deviation, stationary probe (LDA2)

processor is perhaps making more multiple validations than the other, or that one LDA sees predominantly particles of one size or velocity trajectory, while the other sees predominantly particles of a different size or velocity trajectory. These results should be a reminder to all LDA practitioners that data ready statistics (i.e., biased) are not to be trusted in highly turbulent flows.

The effects are better understood from Figure 10 and Figure 11 which show the overall trend in \bar{U} measured by LDA2 in relation to the correlation coefficients. The general trend from the LDA2 data ready statistics to the LDA1 statistics is clearly evident, with the coincidence window biases limited to very small separation distances. Evidently the correlation coefficient must be close to 1.0 before LDA1 exerts much influence on the statistics of LDA2.

It would appear from Figures 8 and 9, that the 20 μs window gives stronger coincidence bias effects than the 50 μs window which shows a relatively gentle transition in the near-field statistics. The 50 μs window excludes less of the velocity PDF in this region, i.e., more of the slower particles reach the second probe before the coincidence time expires. There is still some bias in the mean and standard deviation values in the near field, but the correlation coefficients are well-behaved with a parabolic region evident in the near field.

Essentially, as the coincidence window is reduced, single-particle burst-pairs are only possible for very small

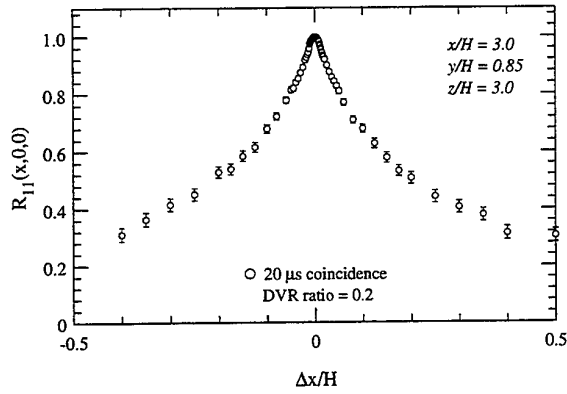


Figure 10 Correlation coefficients in the far-field, station 1

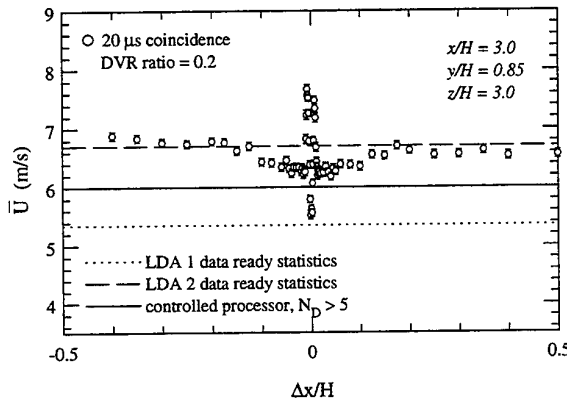


Figure 11 Mean velocity, stationary probe (LDA2)

separations. If the coincidence window is reduced to something on the order of one probe transit time or less, the effect becomes similar to that of channel-blanking and all measurements with partially overlapping probes have an effective separation distance of zero. Obviously this situation must be avoided. Otherwise the spatial resolution advantage of the longitudinal correlation is negated. The challenge then is to choose the largest window possible without allowing the spatial correlation to become a space-time correlation.

5.2 Geometric Bias

Whereas coincidence window bias affects the longitudinal correlation coefficient, geometric bias is a problem for both the lateral and spanwise correlation coefficients. To illustrate this bias phenomenon, measurements of $R_{11}(0,y,0)$ and $R_{11}(0,0,z)$ were made at station 1 using a 200 μm pinhole. The Kolmogorov scale was estimated to be roughly 40 μm at station 1 (based on the TKE balance estimate of ϵ , see Benedict (1995)) so geometric bias was likely to occur. The correlation coefficients are presented in Figure 12. Instead of a smooth parabolic variation near zero-separation, the correlation coefficients maintain a value of almost 1.0 for some distance before dropping precipitously. This effect is particularly strong for the measurements made with a 5 μs coincidence window. Recall from §4.2 that coincidence window bias

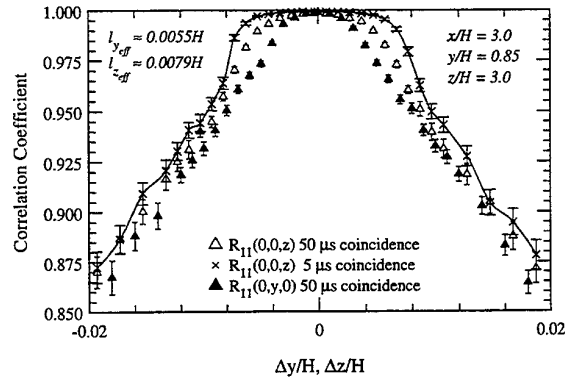


Figure 12 Geometric bias in lateral and spanwise correlation measurements

should not influence lateral and spanwise measurements in flow with a dominant axial velocity. In this case, however, lateral and spanwise fluctuations are strong enough to cause some coincidence window effects which mask the severity of the geometric bias. The 5 μs coincidence window effectively introduces a channel-blanking condition so as to isolate the geometric bias from the effect of the coincidence window. Thus for the measurements made with a 5 μs coincidence window the geometric bias can be clearly seen to influence all the measurements made with overlapping probes, i.e., $-0.0079 \leq \Delta z/H \leq 0.0079$. The geometric bias acts over a shorter span for $R_{11}(0,y,0)$ ($-0.0055 \leq \Delta y/H \leq 0.0055$) because the effective probe dimension in the y -direction is only 140 μm whereas the effective probe dimension in the z -direction is constrained by the pinhole at 200 μm . Evidently, both of these probe dimensions are too large to resolve either of the microscales, $\lambda_{11,2}$ or $\lambda_{11,3}$, at station 1.

Note that the zero-separation correlation coefficients in Figure 12 achieve values as great as 0.9993 and yet clearly the spatial resolution is insufficient for estimating microscales. These results reveal the inadequacy of the technique used by Eriksson and Karlsson (1995) to determine the spatial resolution requirements for accurate estimation of microscales. For the measurements of $R_{11}(0,y,0)$ presented in Figure 12, the ratio of maximum probe dimension to Kolmogorov length is approximately 3.5 and yet the spatial resolution is insufficient for microscale estimation. Measurements at station 2 with a ratio of only 1.9 (presented in Benedict (1995)) were also affected by geometric bias. This suggests that a maximum probe dimension of one Kolmogorov length be considered as the upper bound for lateral and spanwise correlation measurements if microscale estimates are intended.

Figures 13 and 14 present the mean velocities and standard deviations measured by LDA2 (stationary probe). Clearly some bias effects are evident for those measurements made with a 50 μs coincidence window. Although both \bar{V} and \bar{W} are small at station 1, turbulence levels are fairly high so coincidence window bias was suspected of influencing the measured velocity statistics. The set of $R_{11}(0,0,z)$ measurements with the 5 μs coincidence window was thus made in order to focus purely on geometric bias effects. This small coincidence time essentially created a

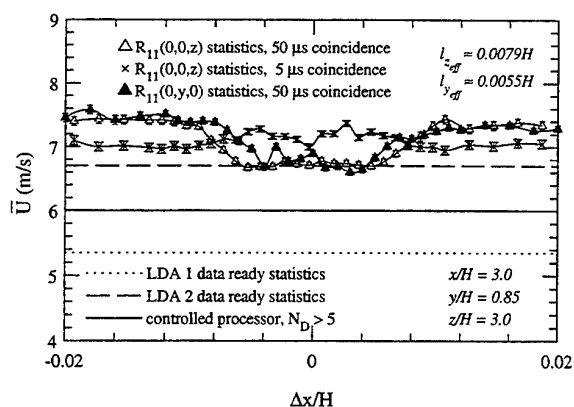


Figure 13 Mean axial velocity, stationary probe (LDA2)

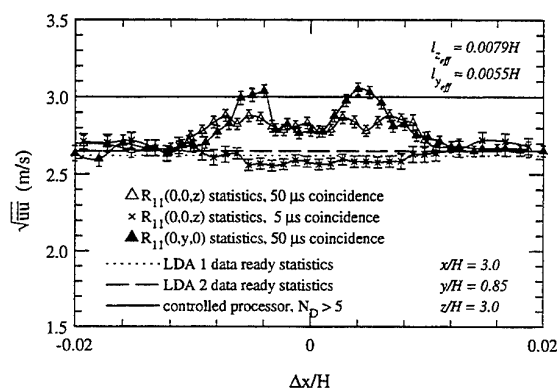


Figure 14 Axial velocity standard deviation, stationary probe (LDA2)

channel-blanking effect because its duration was less than one probe transit time for most of the velocity PDF. The results of these measurements, also shown in Figures 13 and 14, indicate that the coincidence bias has been eliminated and that the geometric bias has no effect on either the mean velocity or standard deviation.

6. CONCLUSIONS

Two-point LDA measurements are strongly affected in the near-field region by coincidence timing parameters. This coincidence window bias is a more general case of that which has been previously documented for nonorthogonal three-component LDAs. A geometric bias which limits the spatial resolution of lateral and spanwise measurements has also been documented. It is suggested that a maximum effective probe volume dimension of one Kolmogorov length be considered as an upper bound for lateral and spanwise correlation measurements if microscale estimates are intended. The spatial resolution of longitudinal correlation measurements, however, appears to be independent of probe dimension if the effective probe volume shape is roughly spherical and a proper coincidence window is chosen.

ACKNOWLEDGMENTS

The authors wish to thank the United States Air Force Office of Scientific Research for the partial support of this work through the Summer Research Extension Program.

REFERENCES

- Abail, L. H. J. (1995) "Analysis of the Laser Doppler Measurement Technique for Application in Turbulent Flows," Ph.D. dissertation, Delft University of Technology, Delft, The Netherlands.
- Abail, L. H. J., Steenbergen, W. and Passchier, D. M. (1990) "Time and Spatial-Correlation Measurements in the Turbulent Wake of a Circular Cylinder Using Laser Doppler Anemometry," *Applied Scientific Research*, **47**, 247–271.
- Benedict, L. H. (1995) "Direct Measurements of Turbulent Dissipation Rate in Flow over a Backwards-Facing Step Using LDA," Ph.D. dissertation, North Carolina State University, Raleigh, North Carolina.
- Benedict, L. H. and Gould, R. D. (1996) "Uncertainty Estimates for Any Turbulence Statistic," *Proc. Of the 8th Int. Sym. on Appl. of Laser Techniques to Fluid Mechanics*, Lisbon, Portugal, July 8–11.
- Boutier, A., Pagan, D., and Soulevant, D. (1985) "Measurements Accuracy with 3-D Laser Velocimetry," *Int. Sym. on Laser Anemometry*, ASME WAM, Miami Beach, Florida, Nov. 17–22, FED-Vol. 33, p. 305.
- Brown, J. L. (1989) "Geometric Bias and Time Coincidence in 3-Dimensional Laser Doppler Velocimeter Systems," *Experiments in Fluids*, **7**, 25–32.
- Durst, F., Jovanovic, J. and Sender, J. (1995) "LDA Measurements in the Near-Wall Region of a Turbulent Pipe Flow," *J. of Fluid Mechanics*, **295**, 305–335.
- Eriksson, J. G. and Karlsson, R. I. (1995) "An Investigation of the Spatial Resolution Requirements for Two-Point Correlation Measurements Using LDV," *Experiments in Fluids*, **18**, 393–396.
- Gould, R. D. and Benedict, L. H. (1992b) "A Comparison of Spatial Correlation and Autocorrelation Measurements in an Axisymmetric Sudden Expansion using LDV," *Proc. of the 6th Int. Sym. on Appl. of Laser Techniques to Fluid Mechanics*, Lisbon, Portugal, July 20–23, paper 7.1.
- Tummers, M. J., Passchier, D. M. and Aswatha Narayana, P. A. (1994) "Three-Component LDA Measurements of Mean Turbulence Quantities, Time- and Spatial Correlation Functions in the Wake of a Flat Plate in an Adverse Pressure Gradient," *Proc. of the 7th Int. Sym. on Appl. of Laser Techniques to Fluid Mechanics*, Lisbon, Portugal, July 20–23, paper 5.4.
- Tummers, M. J., Passchier, D. M. and Aswatha Narayana, P. A. (1995) "LDA Measurements of Time- and Spatial Correlation Functions in the Wake of a Flat Plate in an Adverse Pressure Gradient," *ASME/JSME Fluids Engineering and Laser Anemometry Conf.*, Hilton Head, South Carolina, Aug. 13–18, FED-Vol. 229, 347–354.
- Trimis, D. and Melling, A. (1995) "Improved Laser Doppler Anemometry Techniques for Two-Point Turbulence Flow Correlations," *Measurement Science and Technology*, **6**, 663–673.

SESSION 37

Complex Flows II

USE OF COMPLEMENTARY PIV AND LDV TECHNIQUES TO STUDY INDUSTRIAL COMPLEX FLOWS

C. Cahen, J. Bénard, M. Barcouda*, F. Hofmann*

Direction des Etudes et Recherches - Electricité de France -
REME, 25 allée privée 93206 Saint Denis, France

*LNH, 6 quai Watier, 78400 Chatou, France

ABSTRACT

Cracks detected in some nuclear vessels led to design a scale mockup in order to understand the origin of this problem and where experimental results and computation could be compared. Two methods, LDV and PIV, were used to measure the velocity field. It appeared that the two methods were complementary: LDV was dedicated to measure precisely the velocity and the turbulent energy fields, PIV was used to capture flow patterns as the location of stagnation point. If LDV is a local pointwise measurement, classical PIV is intrinsically a 2D image measurement. Consequently, a detailed analysis is done of the 3D effects upon the 2D measurements. The methodology of this analysis is presented. The results have demonstrated the capability of the code to predict such a complex flow eventhough some discrepancies were found. PIV needs some improvements especially in terms of an higher capacity of processing large set of data and a methodology to compute the actual measurement accuracy.

1. INTRODUCTION

Industrial complex flows usually feature a local 3D behaviour due to a complex geometry that complicates both modelling and experimental studies. When 3D modelling or capability measurement techniques are available, it is often necessary to use a step by step approach: first, the use of a more accurate 2D examination of the problem and, second, a full 3D computation.

Modelling the flow inside a nuclear reactor vessel falls in this category. The flow is locally 3D because of the presence of many obstacles. A careful experimental validation is needed for the complex flow structure.

This paper describes the strategy used to get the required validation of the computations. LDV is used to measure the mean velocity field while PIV is used to capture instantaneous flow patterns. If LDV is a local pointwise measurement, classical PIV is intrinsically a 2D image measurement. Consequently, a detailed analysis is done of the 3D effects upon the 2D measurements. The results obtained are then discussed. In conclusion, there

are recommendations to simultaneously use LDV and PIV in complex situations.

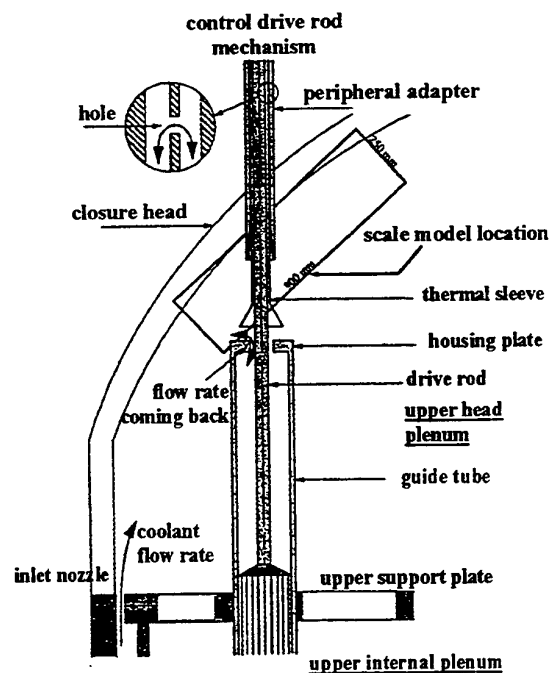


Figure 1 : view of the upper head with one adapter.
The location of the mockup is shown.

2. EXPERIMENTAL MOCK-UP AND MODELLING

Cracks detected in a number of vessel closure heads in nuclear power plants are related to the internal flow structure. Locally, close to the adapter, the main flow has a 3D behaviour because of the interaction between the incident wall jet and the inclined obstacle. Consequently, a recirculation zone and a stagnation point are present. The knowledge of the flow allows to estimate the temperature

inside the adapters that plays a predominant role in the kinetics of the corrosion leading to cracks. The finite element code, N3S CFD, was used to evaluate the flow in the upper head plenum and around as well as inside the adapters. This complex situation was rather challenging for CFD predictions and gave an opportunity to validate the N3S code for such a geometry. To validate the N3S CFD modelling of the upper head of the reactor, a transparent scale mock-up, named TRAVERSIN, was constructed and described by Hofmann et al. (1995). This allowed experimental investigations as shown in Fig. 1. The channel had a parallelepiped shape (900 mm length \times 250 mm \times 350 mm rectangular section). The adapter and the thermal sleeve were taken as concentric cylinders (resp. diameter 103 mm and 62 mm). It was difficult to correctly predict the flow because of the presence of the inclined obstacle and the impingement of the secondary flow circulating inside the adapter.

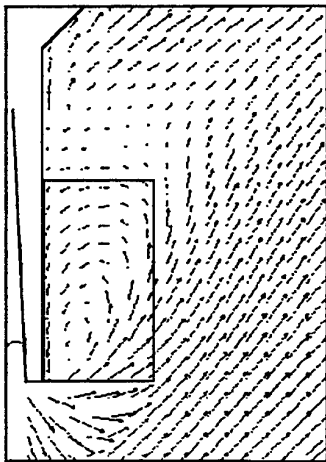


Figure 2 : N3S predictions of the flow around the adapter. The superimposed rectangle shows the LDV and PIV measurement zone (60 mm \times 80 mm).

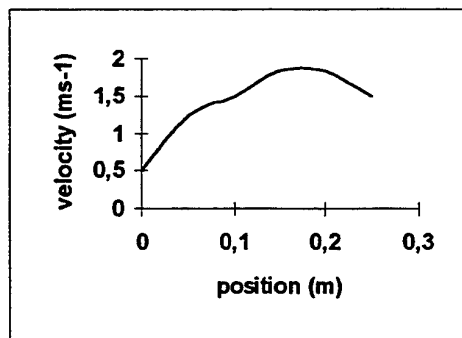


Figure 3 : input velocity profile measured by LDV in the plane of symmetry

An example of the predicted flow pattern in the symmetry plane is shown in Fig. 2. There was a recirculation zone inside a zone of 60 mm \times 80 mm behind the obstacle. Note also that the secondary flow created a complex flow pattern at the exit of the adapter leading to an unsteady solution of the computational code. Consequently, the results presented here represent a quasi-converged solution. The confidence on the CFD code relies on its ability to predict correctly the size of the recirculation zones and the location of the stagnation point. At first to get a straightforward comparison, pressure measurements were taken. They indicated that some adjustments were still needed. Eventhough there are small discrepancies, the computation seems reliable enough to undergo a more sophisticated validation. To check these predictions, two techniques for velocity field measurement were used: LDV to accurately measure the velocity field, PIV to capture the flow structure, especially in low velocity regions.

3. LDV RESULTS AND DISCUSSION

First, LDV was used to measure the input velocity field that was used as input data for the computation. An example of the measured profiles is shown in Fig. 3. The mockup was designed to get a flat input velocity profile. However, this was not exactly obtained and it emphasized the necessity to use the actual measured velocity field as the input data for the computation.

Second, the computations were used to prepare the experimental validation. The LDV exploration zone was sized according to the code predictions: 60 mm \times 80 mm with a step of 5 mm as shown in Fig. 2. Eventhough LDV has a 3D capability, the 2D configuration was used for convenience.

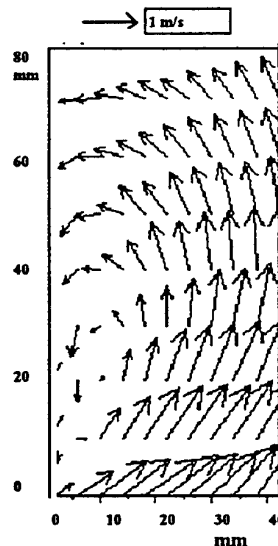


Figure 4 : LDV measurements inside the recirculation zone

The LDV system was controlled by an home-made software, CAIMAN, to acquire and process the data. This software made it possible to check the convergence of the acquisition with a real-time weighted average of the measurements as recommended by Oliver (1980). It also offered a direct link with the CFD N3S post processor for easy comparison. The acquisition for a given position could be stopped when the desired accuracy was reached, usually 1% uncertainty on the computed velocity.

The LDV velocity field is shown in Fig.4. The results compared favorably to the code prediction. The size and major axis of the recirculation zone were correctly predicted even though the location of the vortex centre was underevaluated. This was one of the difficulties in computing such a complex flow. The transverse width of the recirculation zone was measured ≈ 2 cm. The velocity of the unperturbed flow was 1.65 ms^{-1} .

4. PIV RESULTS AND DISCUSSION

4.1. Preparation of PIV measurements

The consequences of the experiment on the intrinsically 2D PIV measurements had to be examined. We used the N3S CFD predictions to simulate PIV images. An example of the transverse component field for a given image is shown in Fig.5.

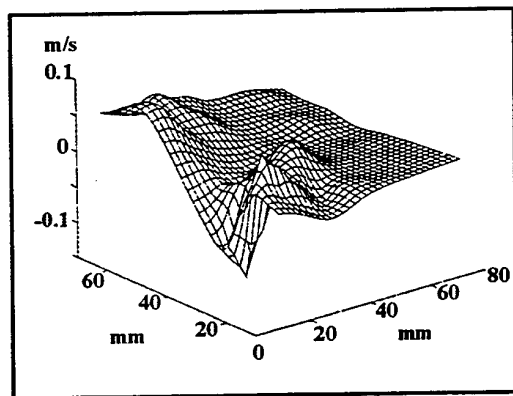


Figure 5 : out-of-plane velocity component to simulate a PIV image.

Using this simulation, we were able to determine an acceptable trade-off. In a PIV experiment, the adjustable parameters are the seed (shape and density), the light sheet width, the size of the image and the time delay between the two exposures. The size of the image was controlled by the captured flow pattern ($60 \text{ mm} \times 80 \text{ mm}$ in our case). The time delay between the double exposure was a trade-off between the maximum expected velocity (2 ms^{-1}) and the null velocity. This delay was set at $500 \mu\text{s}$. The seed characteristics and the light sheet width should be more carefully examined. On the one hand, the seed density had to be at least 10 particles per elementary

subimages (32×32 pixels) to reach a 10% error (Fig.6). Higher the density, higher the accuracy. The size of the subimage for the intercorrelation procedure was imposed by the PC computer capability. This size combined with the size of the image defined the spatial resolution of the measurements (7.5 mm). To increase spatial resolution, the size of the interrogation zone in the intercorrelation procedure would be decreased by at least a factor 2 that would hit the time and memory consuming limits of our system.

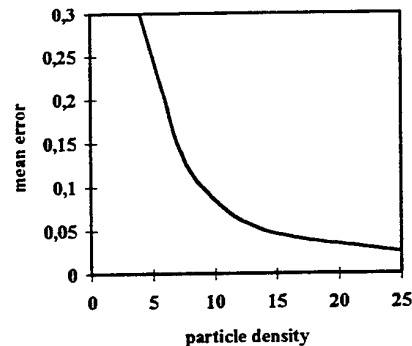


Figure 6 : particle density needed within an elementary subimage to reach a given mean error

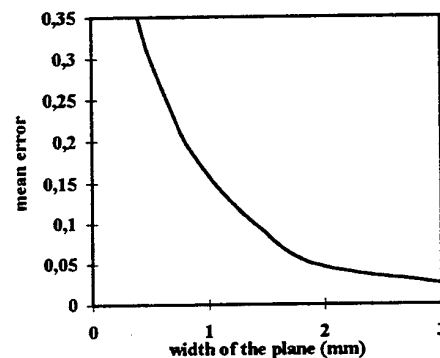


Figure 7 : influence of the the lightsheet's width of on the mean error (a 10% mean error corresponds to a 1.5 mm width)

On the other hand, the light sheet width must be as large as 1.5 mm to reach an acceptable 10 percent error on the ultimate velocity field (Fig.7). Obviously, the increase of the light sheet width spatially averaged the out-of-plane effects.

To meet these requirements the corresponding optics were designed to take into account the desired size of the PIV image similar to the LDV exploration zone and constraints of optical access. PIV was a home-made system using a double frequency, a two pulses Nd YAG laser, a double CCD camera and the MATLAB environment to

process the images. The light routine was done with the usual mirrors and lens. To meet the seeding requirements of the flow rate (148 l.s^{-1}), eriodine faceted particles were used. This was done because the flow circulation was a semi-open loop and it was impossible to recycle the usual more expensive sphere particles. According to these features, the images suffered from three main disturbances: 1) measurement noise due to digitisation, 2) various shapes and sizes of the seed (eriodine faceted particles in our case) and 3) out-of-plane motion of some particles due to the transverse velocity component. The best trade-off in all the possible signal processing was the necessary binarisation of the image after pre-processing in order to enhance the amplitude and contrast as described by Utami and Blackwelder (1991) or Keane and Adrian (1993). This processing is barely available in commercial PIV software where real-time processing using grey level images is emphasized.

4.2. PIV results

Recirculation zone. The LDV exploration zone matching the image size for a straightforward comparison was not adapted to this PIV experiment. The recirculation zone featured a 2 cm width corresponding to only 2 computed velocity vectors in the PIV image. The recirculation zone barely appeared due to this poor spatial resolution.

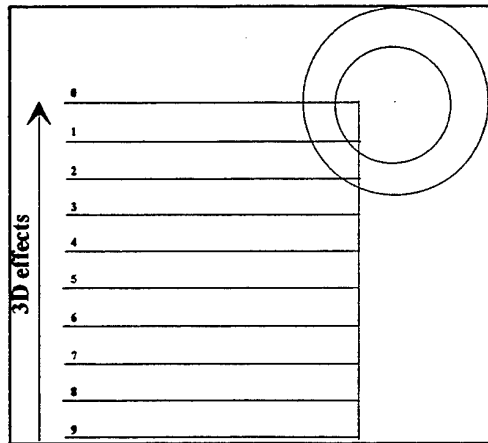
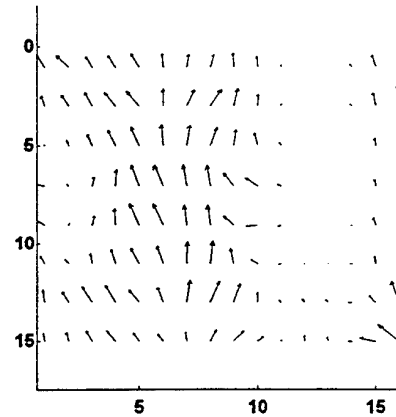


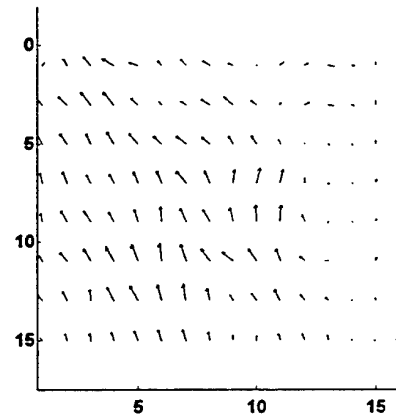
Figure 8 : position of the different planes of measurement (the planes are separated by 1 cm)

PIV was then used to evaluate the spatial extent of the obstacle's influence on the main flow. Figure 8 shows the location of the different cross section measurements in the flow channel. The expected influence of the obstacle was computed by analysing the progressive 3 D behavior of the velocity field.

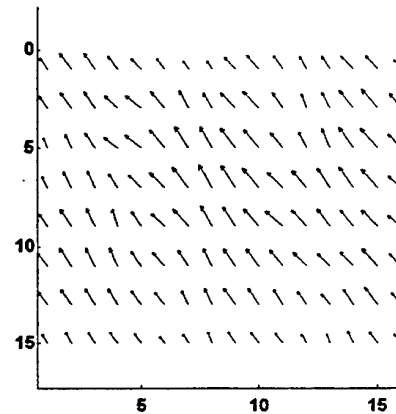
Figure 9 shows a series of average measurements. The labelling corresponds to the label of the stored files. The co-ordinates correspond to the rows and columns of the CCD processed images



Position # 0



Position # 4



Position # 9

Figure 9 : different cross sections of the flow. The labeling corresponds to the figure 8

The extent of the obstacle's influence was directly retrieved and features a length of a diameter and half. The unaffected image (position # 9) made it possible to check the measurement correctness. The almost constant velocity field made it possible to average the velocities upon the whole domain. This check led to a mean velocity of 1.74 ms^{-1} corresponding accurately to the controlled flow rate. It gave confidence in our measurements. The flow field was progressively distorted. For position # 0, a recirculation zone was apparent but the spatial resolution was not high enough to correctly size the zone. Eventhough on the same image, locating the sleeve and the adapter (absence of velocity vectors) made it possible to scale the image.

Stagnation point. PIV was also used to locate the stagnation point, which was difficult to observe with LDV (drawback for the null velocity). Figure 10 shows the PIV image position in the channel.

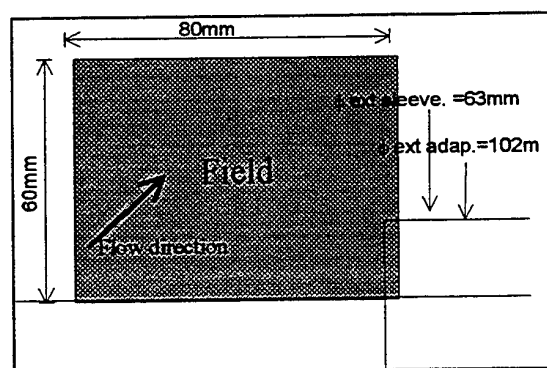


Figure 10 : location of the PIV image

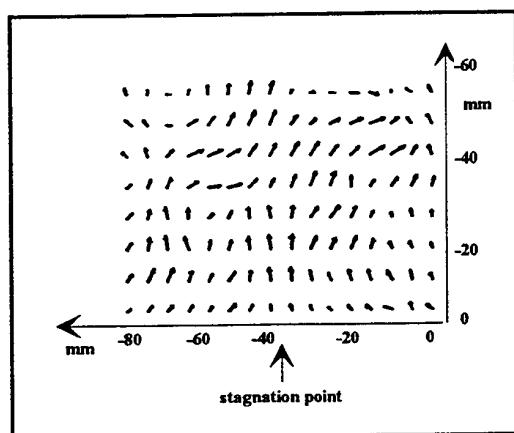


Figure 11 : instantaneous PIV image showing evidence of the presence of a stagnation point

Figures 11 and 12 show an instantaneous record of the velocity field, revealing chaotic behavior as expected. The stagnation point could be seen and had a slow erratic motion within a range 1.5 cm, extending the size of the

potential corrosion zone. Since the flow was predicted unsteady only conditional averaging could lead to a correct prediction. As expected, the time average LDV measurements led to a more precise interpretation. On the other hand, the time to time varying PIV images could lead to some confusing interpretations. The PIV led to an instantaneous velocity field instead of local velocity as a function of time as in the LDV method.

These two methods were naturally complementary. PIV addresses the structure and low frequency features of the flow while LDV addresses the turbulent energy estimate. However, averaging the PIV images led to an erroneous constant velocity field. This was because the average was not done from a large set of images.

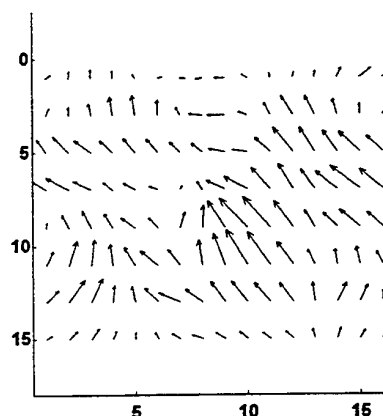


Figure 12 : an other example of an instantaneous PIV image revealing the chaotic behavior of the flow

5. CONCLUSION

The use of these two methods is indispensable. Although the limitations of the LDV are well known, LDV's capability to give access to reliable measurements is not still challenged by the PIV method. In PIV, improvements are needed in software handling large data software and time-resolved capability to compute true average measurements. The commercially available systems provide some improvements in this area but are not necessary designed to analyse accurately the influence of the 3D local behavior of the flow upon the data processing. A strategy is needed comparing experimental results and theoretical predictions: first, using the predictions to prepare the measurements, second using at least two experimental methods enabling conditional averaging of the obtained data. Such a strategy would greatly improve the validation of CFD for complex flows. This combined information is necessary for validating the finite elements N3S CFD code on the geometry of the scale mock-up. These improvements will be accounted for and further studies will be performed in the next coming months.

REFERENCES

Hofmann F., Daubert O., Bertrand C., Hecker M., Arnoux-Guisse F., Bonnin O., 1995, Some thermohydraulics of closure head adapters in a 3 loops PWR, Proc. Int. Meeting on Nuclear Reactor Thermohydraulics, Saragota Springs, NY.

Keane R. D., Adrian R. J., 1993, Theory of cross correlation analysis of PIV images in Flow visualisation and image analysis, Kluwer Academic Publishers.

Oliver C.J., 1980, Accuracy in laser anemometry, J. Phys. D: Appl. Phys., 13, pp. 1145-59.

Utami T., Blackwelder R. F., 1991, A cross correlation technique for velocity extraction from particle visualisation, Experiments in Fluids, 10, pp. 213-223.

LDA-STUDY FOR MODELLING FLOWS THROUGH SCREENS

U.Ullum, J.P.Frederiksen, E.Akoh*, N.F.Nielsen and P.S.Larsen

Dept. of Energy Engineering, Fluid Mechanics, Building 404
Technical University of Denmark, DK-2800 Lyngby, Denmark

* Now at Danish Maritime Institute, DK-2800 Lyngby, Denmark

ABSTRACT

Flow through three types of commercial screens has been studied experimentally by LDA-technique. The measurements provide detailed information of the turbulent kinetic energy downstream of the screens and indicate that the kinetic energy is independent of screen inclination and upstream turbulence level. The main interest of the present study is to model source terms to the turbulent kinetic energy, k , and dissipation, ϵ , of the widely used k,ϵ model in order to study turbulence alteration for two-dimensional flow through screens. The experimental results suggest a simple relation between turbulent kinetic energy and pressure drop given by equation (7). The dissipation is modelled by rapid distortion theory, equation(10). Numerical investigations of diffuser flow including a single screen, applying the source terms of the present study for k and ϵ , indicate that separation can be reduced by turbulence generation. Applying drag forces, lift forces and turbulence generation separately by including source terms in momentum equations and the turbulent transport equations shows that the dominating factor is drag forces. A computational example also shows the use of a variable porosity screen to manage a large-angle diffuser flow.

1. INTRODUCTION

Screens and vaned screens are often used in industrial process equipment to manage flows to obtain desirable distributions despite undesirable configurations dictated by space and cost savings. Examples include wide-angle diffusers, abrupt bends, etc. resulting in short-circuit flows, large regions of recirculation or poor mixing, rather than uniform dis-

tributions with good mixing and controlled hold-up times.

In traditional wind tunnels, the moderate pressure drop across several fine-mesh screens is designed to produce a uniform velocity field with only small-scale turbulence of low intensity that quickly decays (Seltsam, 1995). However, in industrial diffusers, which are common in internal flow systems, coarse screens produce large-scale turbulence of often considerable intensity that delays or suppresses separation and produces more uniform flows (Kline *et al.*, 1959). Although many possibilities exist to prevent diffuser flow separation, eg. swirl flow generators (Goenka *et al.*, 1990), splitters (Kline, 1959), wall suction (Yang and El-Nasar, 1975), wall shape modification (Carlson *et al.*, 1967) etc., the most common way to obtain uniform velocity profiles is installation of screens where separation occurs (Metha, 1977).

Currently, the traditional approach of cut-and-try paired with past experience or simple empirical procedures is being replaced by CFD-modelling. For this to be reliable it is necessary to have experimentally verified correlations for source terms that represent screens on relatively coarse computational grids of practical use in design calculations. Existing data and correlations on pressure drop (Idelchik, 1994) and change of direction (Simmons and Cowdrey, 1945) for flow approaching a screen obliquely can provide source terms to the momentum equations. On the other hand, data on turbulent kinetic energy, k , and the scale of turbulence, say $l \sim k^{3/2}/\epsilon$, or the dissipation ϵ , are not available for commercial screens.

The present experimental and theoretical study is focussed on providing a set of source terms for the balance equations of momentum, as well as source terms for the kinetic energy and the dissipation

equations of the k, ϵ -turbulence model by Jones and Launder (1972), which is still widely used in engineering practice. Specifically, given local variables ($u_0, v_0, p_0, k_0, \epsilon_0$) upstream, the effective change or the resulting values ($u_1, v_1, p_1, k_1, \epsilon_1$) downstream of a given screen are required.

2. EXPERIMENTS

The laboratory facility is a 0.3 x 0.3 m low turbulence wind tunnel, giving a uniform velocity profile with 1 - 2% turbulence intensity at the inlet to the test section. The test section is a 0.75 m long perspex channel (Figure 1) prepared for installing screens in different angles of inclination relative to the direction of flow.

A detailed experimental study has been carried

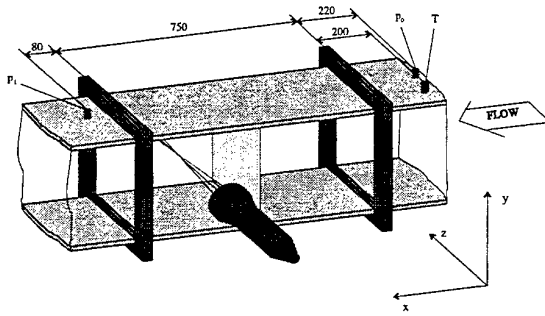


Figure 1: Windtunnel test section.

out upstream and downstream of the screens using a two-component backscatter LDA-system from DANTEC with counter processors. Each data point consists of 2000 samples with a sampling frequency of approximately 20-50 Hz. The sample frequency is found from the Nyquist criterion with integral time scales derived from time series. The integral time scale is found to be approximately $2.27 \text{ ms} < \Lambda_t < 18.5 \text{ ms}$ yielding sampling frequencies less than 220 Hz and 27 Hz, respectively, and uncorrelated samples are assured. Also, the static pressure upstream, p_0 , and downstream, p_1 , as well as the temperature, T , are measured (Figure 1). Furthermore, two-dimensional flow is assumed by fixing the z -position in the center of the channel throughout the experiments.

The study has considered 3 commercial screens with both square and circular holes and porosities $\phi = 0.30, 0.40$ and 0.49 defined as the ratio of the open area to the total screen area (Figure 2), angles of inclination relative to flow direction being $\theta = 90^\circ$ and 60° , and Reynolds numbers based on the

screen mesh $Re_M = UM/\nu = 875, 1595$ and 2750 , U denoting the mean bulk velocity, M the spacing between centers of screen holes (Figure 2), and ν the kinematic viscosity.

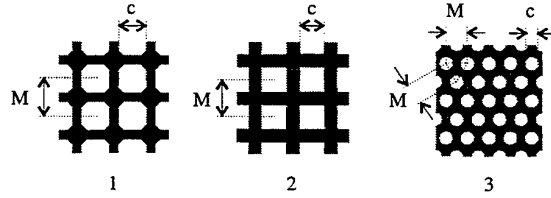


Figure 2: Three different types of commercial screens used in the study, with porosity $\phi = 0.49, 0.40$ and 0.30 for screen 1, 2 and 3 respectively. The mesh M ($= 8.36, 4.0$ and 2.0 mm) denotes spacing between centers of the screen holes and c a characteristic length of the hole.

Prior to the measurements, a flow visualization at $Re_M = 500$ was performed in order to provide a qualitative impression of the flow (Figure 3). Injected dye was illuminated with a laser sheet and recorded with a conventional black and white video camera. Figure 3 shows the deflection of flow upstream and downstream of the screen and the fact that the screen jets are fully mixed approximately 5 mesh spacings downstream of the screen suggesting uniform conditions.

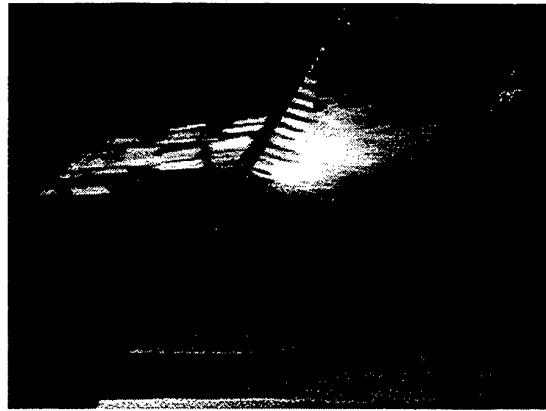


Figure 3: Light sheet visualization of jet mixing. $\theta = 60^\circ$, $\phi = 0.40$, $Re_M \simeq 500$. Flow from left to right.

Next, traversing axially behind a hole and behind a solid cross of the screen (Figure 4) LDA-data show uniform conditions to be established at approximately $x/M = 6$ in good agreement with flow visualization of Figure 3, now at Reynolds number

$Re_M = 1595$. Also, Figure 4a shows the existence of a non-turbulent jet core with relatively high velocities. A few spacings downstream, Figure 4b shows that the turbulent kinetic energy increases as a result of the interaction with the neighboring jets. Despite uniform conditions for $x/M > 6$ no power law fits the turbulent kinetic energy at this early stage of decay.

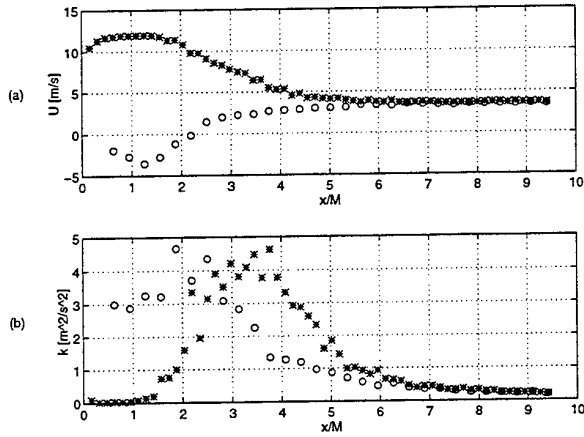


Figure 4: Axial velocity, U , and turbulent kinetic energy, k , versus downstream position, x/M ; behind screenhole (*) and solid cross. $\theta = 90^\circ$, $\phi = 0.40$, $Re_M = 1595$.

The turbulent kinetic energy is computed from $k = (\overline{u^2} + 2\overline{v^2})/2 = (1 + 2/I)\overline{u^2}/2$, where $I = \overline{u^2}/\overline{v^2}$ denotes the anisotropy. The present results indicate decreasing I with increasing porosity (Figure 5), taking values $I = 1.41, 1.16$ and 1.03 for $\phi = 0.3, 0.4$ and 0.49 , respectively. It is noted, that I is calculated as the mean value at all downstream positions and no coincidence filter is imposed during sampling. The anisotropy for the present screens can be compared with Bradshaw (1971) who obtained $I = 1.35$ for wire-screen turbulence.

The effect of screen inclination was investigated by traversing downstream of both a perpendicular and an oblique screen, maintaining the same screen Reynolds number. Figure 6, upper part, shows only small differences on the downstream turbulence level of $\theta = 90^\circ$ compared to $\theta = 60^\circ$ screen inclination.

Finally, introducing an extra identical screen at $x/M = -15.7$ ($\theta = 90^\circ$, $\phi = 0.40$) the effect of enhanced upstream turbulence level has been studied. Figure 6, lower part, shows that the downstream turbulence level is unaffected by the extra screen, hence, the upstream turbulence level seems to be without importance regarding the increase of turbulent kinetic energy over the screen, suggesting

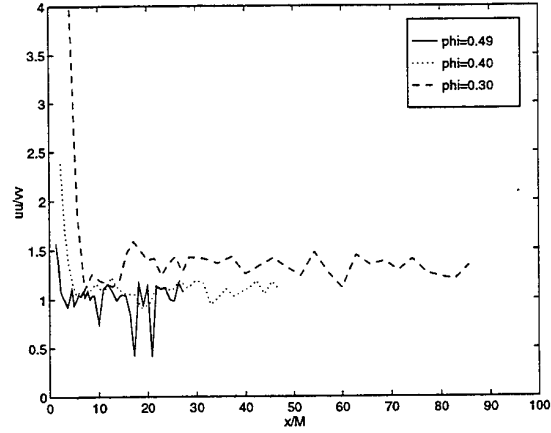


Figure 5: Degree of anisotropy $\overline{u'^2}/\overline{v'^2}$ versus x/M downstream of the 3 screens of Figure 2, $\theta = 90^\circ$, $Re_M = 875, 1595$ and 2750 for $\phi = 0.3, 0.4$ and 0.49 , respectively.

that the latter screen dictates the downstream turbulence level. This experiment could be repeated with two non-identical screens disproving that turbulence with different spatial scales would survive through the next screen. The latter observation suggests use of a Diriclet condition on k at the screen rather than a source term in the modelling procedure.

In conclusion, modelling a source term for the turbulent energy equation the present experimental study indicates that the kinetic energy is independent of screen inclination and upstream turbulence. Furthermore, the results indicate decreasing anisotropy of approximately 27% for increasing porosity from $\phi = 0.3$ to $\phi = 0.49$, and that jet mixing behind the screen disappears at approximately $x/M = 6$. Further investigations show that the turbulent kinetic energy obeys the power law fit downstream of approximately $x/M = 25$.

3. THEORETICAL MODELLING

Introducing a screen into fluid flow causes three basic effects: (1) pressure drop due to screen resistance, (2) change of flow direction due to viscous effects and (3) production of turbulent kinetic energy and dissipation. The pressure drop or the drag force, F_D , which is perpendicular to the screen and the change of direction or the lift force, F_L , which is parallel to the screen are defined as:

$$F_D = C_D \frac{1}{2} \rho U_l^2 A, \quad (1)$$

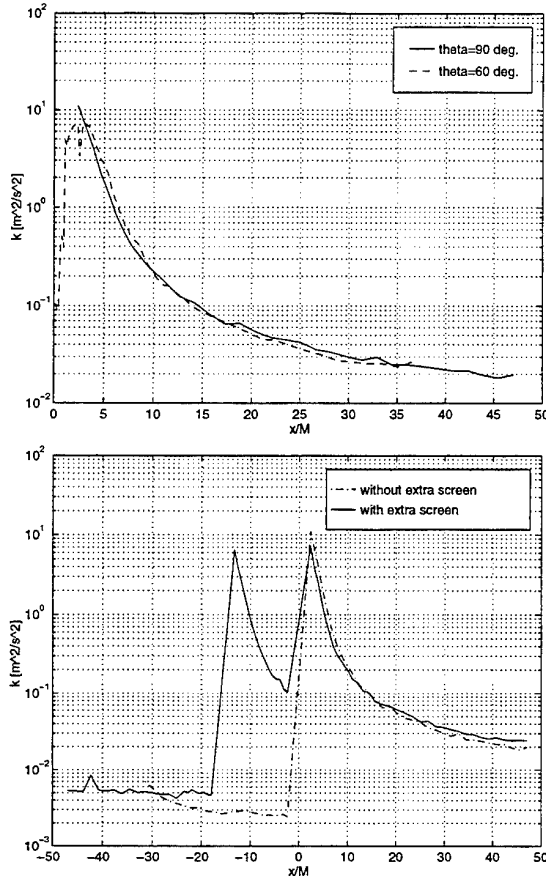


Figure 6: Upper part, Turbulent kinetic energy k versus downstream position x/M showing insensitivity to angle of inclination, $\theta = 60^\circ$ and 90° , $\phi = 0.4$, $Re_M=1595$. Lower part, Turbulent kinetic energy k versus downstream position x/M , with and without extra screen placed upstream at $x/M = -15.7$; $\theta = 90^\circ$, $\phi = 0.4$, $Re_M=1595$.

$$C_D = C_P(1 - \phi), \quad (2)$$

$$F_L = C_L \frac{1}{2} \rho U_l^2 A, \quad (3)$$

where C_D , C_P and C_L denotes non-dimensional drag, pressure and lift coefficients, respectively, ρ fluid density, U_l local mean speed based on the local speed before and after the screen, A the solid screen area and ϕ the screen porosity defined above.

Both drag and lift forces are governed by the momentum equations by introducing source terms according to eq. (1) and (3) (see for example Seltsam (1995) for further details). Now, concentrating on modelling source terms for the turbulent transport equations, which is the main interest of the present study, the balance of total energy for

steady, incompressible and uniform flow through a screen is given by:

$$\dot{m} \left[\underbrace{(\tilde{u}_1 - \tilde{u}_0)}_{\text{internal energy}} + \underbrace{\frac{p_1 - p_0}{\rho}}_{\text{potential energy}} + \underbrace{\frac{U_1^2 - U_0^2}{2}}_{\text{kinetic energy}} + \underbrace{(k_1 - k_0)}_{\text{turb. kin. energy}} \right] = 0, \quad (4)$$

where subscript 0 and 1 indicate upstream and downstream variables, respectively. Applying the equation for conservation of mass, equation (4) reduces to:

$$\frac{p_1 - p_0}{\rho} = -(\tilde{u}_1 - \tilde{u}_0 + k_1 - k_0), \quad (5)$$

stating that the pressure drop across a screen equals the sum of increase of turbulent kinetic energy and the loss of mechanical energy as converted into internal energy. Considering only the turbulent kinetic energy and the pressure drop, the dimensionless variable $\Delta k / (\Delta p / \rho)$ can be plotted versus the downstream position as shown in Figure 7 for the 3 screens of Figure 2. Of course, the ratio $\Delta k / (\Delta p / \rho)$

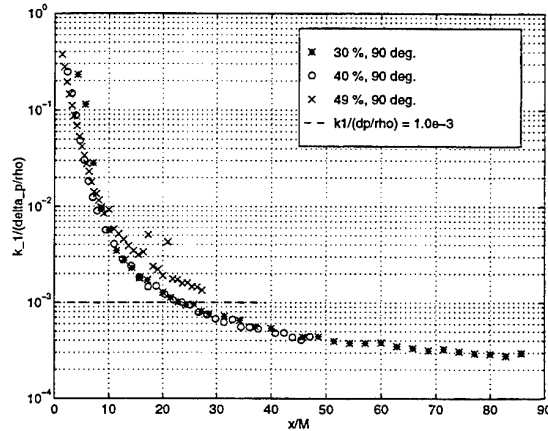


Figure 7: Dimensionless variable $k_1 / (\Delta p / \rho)$ versus x/M . $\theta = 90^\circ$, $Re_M=875$, 1595 and 2750 for $\phi=0.3$, 0.4 and 0.49 respectively.

(or $k_1 / (\Delta p / \rho)$ since the upstream value k_0 is without importance), continues to decrease downstream due to dissipation, but in a rather universal way as indicated by Figure 7. Neglecting production and diffusion in the transport equations for the turbulent kinetic energy and dissipation of turbulent kinetic energy the solution to the k and ϵ equations

can be given as:

$$k = A \left(\frac{x}{M} \right)^{1/(1-C_{\epsilon 2})}, \quad (6)$$

where $C_{\epsilon 2}$ ($=1.92$) is a model constant and A a proportionality constant. Now, referring to Figure 7, as the decay does not obey the power law in the nearfield a relation between the pressure drop and the turbulent kinetic energy at $x/M = 25$ is suggested, despite the slight deviations for $\phi = 0.49$,

$$k_1 \{x/M = 25\} \simeq 0.001 \left(\frac{\Delta p}{\rho} \right). \quad (7)$$

In the modelling procedure eq. (6) is used to extrapolate k and ϵ to the screen position yielding the prescribed turbulence alteration at that point. This approach results in slightly underestimated values of k compared to experimental results in the screen plane.

Estimates of the dissipation ϵ based on length scale measurements from random sampled counter processed time series proved to be impossible due to limited data-rates. Instead, ϵ_1 corresponding to k_1 has been determined by applying rapid distortion theory to the k, ϵ -model across a screen. Neglecting dissipation and diffusion at the screen position the turbulence transport equations for steady flow are given by:

$$\frac{\partial}{\partial x_j} (\rho U_j k) = \mu_T \frac{\partial U_i}{\partial x_j} \left(\frac{\partial U_i}{\partial x_j} + \frac{\partial U_j}{\partial x_i} \right), \quad (8)$$

$$\frac{\partial}{\partial x_j} (\rho U_j \epsilon) = C'_{\epsilon 1} \frac{\epsilon}{k} \mu_T \frac{\partial U_i}{\partial x_j} \left(\frac{\partial U_i}{\partial x_j} + \frac{\partial U_j}{\partial x_i} \right), \quad (9)$$

yielding the solution

$$\epsilon_1 = \epsilon_0 \left(\frac{k_1}{k_0} \right)^{C'_{\epsilon 1}}, \quad (10)$$

where $C'_{\epsilon 1}$ is a model constant to be determined. In the standard version of the k, ϵ model the value of $C_{\epsilon 1}=1.45$ is determined by considering a homogeneous shearlayer quite different from the present flow. Modelling one unit cell of a screen with inlet and outlet boundary conditions on west and east boundaries, respectively, and with symmetric boundary conditions on upper and lower boundary a detailed parametric study has been carried out. The result of this study yields a value of 2.1 of $C'_{\epsilon 1}$

and the values of k and ϵ upstream of the screen are fitted to experimental results.

4. NUMERICAL RESULTS

The experimental and theoretical study above provides source terms to the turbulent kinetic energy and dissipation equations of the standard k, ϵ turbulence model by applying equations (7) and (10) with the model constant $C'_{\epsilon 1} = 2.1$. In the numerical study the two-dimensional incompressible Navier-Stokes code EllipSys2D (see Michelsen (1992), Michelsen (1994) and Sørensen (1995) for further details), extended with momentum and turbulent source terms, is used. It employs a general non-orthogonal curvilinear coordinate system, finite-volume discretization, a full multigrid method, and among other turbulence models the standard k, ϵ model using logarithmic wall functions in the viscous sublayer near walls.

Two geometrical configurations with simulated screens have been considered, that of a simple channel flow identical to the experimental setup of Figure 1 (Figure 8) and that of a symmetric diffuser (Figure 9).

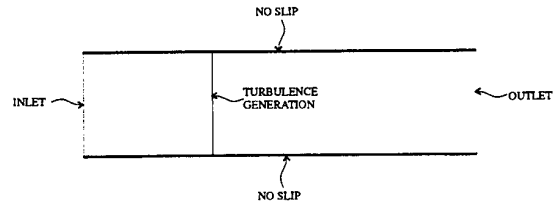


Figure 8: Geometry and boundary conditions for channel case.

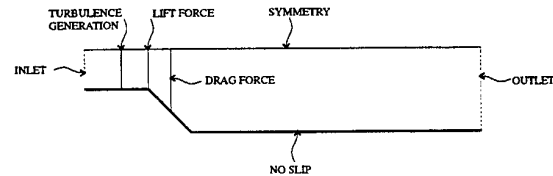


Figure 9: Geometry and boundary conditions for diffuser case. Three screen positions, as used in the diffuser case, are shown in order to study separate effects of drag forces, lift forces, and turbulence generation.

The former configuration, denoted 'channel case', is studied in order to demonstrate the reliability of the turbulent source term model by validating

against experimental results of section 2. The latter configuration, denoted 'diffuser case', is an application of wide industrial interest.

CHANNEL CASE

Plane two-dimensional channel flow is investigated with special attention to turbulent kinetic energy arising from source terms in the k transport equation. A nonuniform 320×64 cartesian computational grid (refined near the source locations) is used and the source terms are prescribed by values calculated from eq. (7) and (10) using experimentally known values for pressure drop, Δp , and upstream turbulence level, k_0 .

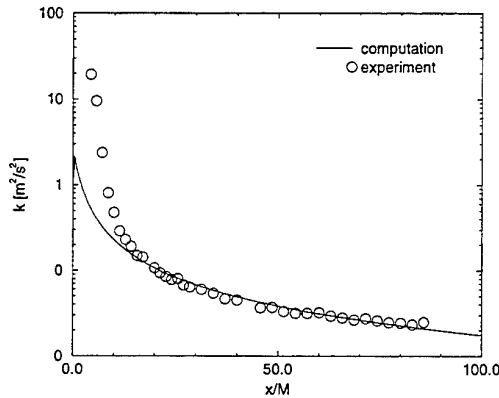


Figure 10: Comparison of numerical and experimental values of k downstream of screen. $C_p=11$, $\phi=0.3$, $Re_M=875$ and $Re_H=75573$ (H denoting the channel width).

Figure 10 shows experimental and numerical results of turbulent kinetic energy, k , versus downstream position, x/M for screen 3 of Figure 2 ($\phi=0.30$). Good agreement is found at the downstream positions of $x/M=15$ by using the prescribed value of the k -source term. As discussed in section 3 the turbulent source term is based on the experimental value of k at $x/M=25$ in order to obey the power law of the intermediate phase starting approximately at that point. In the near field, $x/M < 25$, the numerical values naturally differ from the experimental results because of the non-power law behaviour but the downstream values seem satisfactory.

DIFFUSER CASE

A two-dimensional 45° symmetric diffuser flow at $Re_H = 1 \times 10^6$, H denoting the inlet width, with a single screen is studied. A boundary fitted 288×32 computational grid refined near source locations is used and momentum source terms as well as source terms for k and ϵ in the turbulent transport equations are applied. Special attention is given to the separate effect of drag forces, lift forces and turbulence generation.

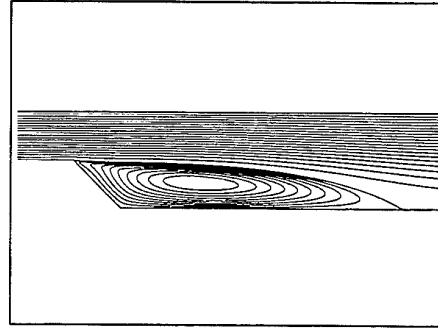


Figure 11: Streamlines for computation results without source terms, $Re_H = 1 \times 10^6$.

Figure 11 shows a diffuser flow with no source terms simulating a diffuser without screens. The flow separates near the diffuser entrance and, as expected, a large separation bubble is generated.

Now investigating the separate effect of including drag forces, lift forces and turbulence generation the reduction of the recirculating region and overall flow pattern can be studied for these three basic effects.

First, Figure 12a shows a streamline plot for a calculation with a screen placed in the middle of the diffuser. Clearly, the separation bubble after the screen is removed, but separation remains in front of the screen. This separation bubble could of course be removed by placing a second screen at the diffuser inlet.

Next, including only lift forces with a linear distribution at the diffuser inlet of $C_L=2$ at the wall to $C_L=0$ at the centerline, Figure 12b shows that separation is suppressed. This simulates vanes with variable angles of attack instead of a screen. Clearly, introducing vanes in the middle of the diffuser for this case would have no effect which has also been demonstrated by numerical calculations (not shown).

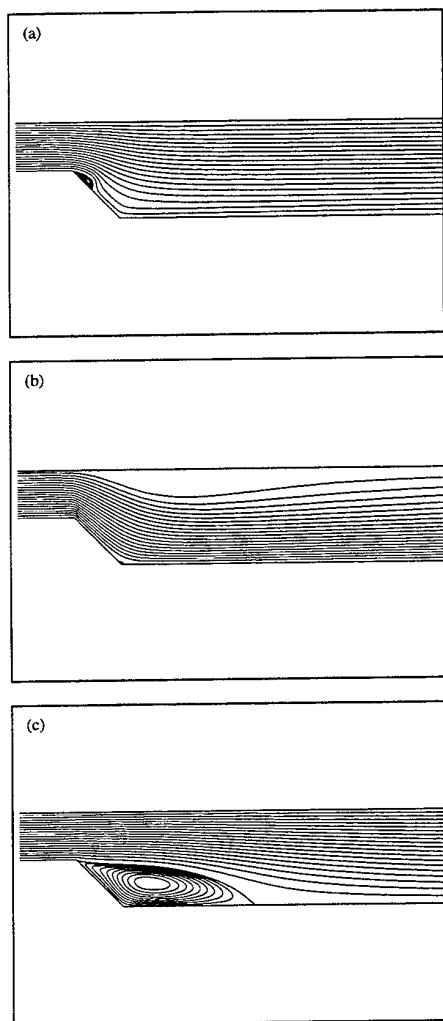


Figure 12: Streamline plots for numerical diffuser calculation at $Re_H = 1 \times 10^6$. (a) momentum source term with $C_p=3.5$. (b) momentum source term with linear distribution of $C_L=2$ at wall to $C_L=0$ at centerline. (c) turbulent source term with $k_1 = 2.9 \times 10^{-1} m^2/s^2$ and $\epsilon_1 = 2.5 \times 10^1 m^2/s^3$. For screen location of (a)-(c) see Figure 9.

Finally, including only source terms in the turbulent transport equations, Figure 12c shows a reduction of the recirculating region of approximately 54%. The turbulence generator (coarse screen) is placed in the section before the diffuser (see Figure 9) in order to ensure a highly turbulent boundary layer before the point of separation at diffuser inlet. In the calculation the following values of upstream (k_0, ϵ_0) and downstream (k_1, ϵ_1) kinetic energy and dissipation has been used: $k_1 = 2.9 \times 10^{-1} m^2/s^2$, $\epsilon_1 = 2.5 \times 10^1 m^2/s^3$, $k_0 = 6.5 \times 10^{-3} m^2/s^2$ and

$$\epsilon_0 = 8.0 \times 10^{-3} m^2/s^3.$$

5. CONCLUSIONS

Flow management by screens or guide vanes, being of great practical importance in the engineering design of flow systems, can be simulated by distributions of discrete sources of drag, lift and turbulent kinetic energy and dissipation. Data on drag and lift are available for many commercial screens. The present study has provided a semi-empirical scheme for handling source terms of kinetic energy and dissipation in a standard k, ϵ -model calculation. The scheme has been verified experimentally for three screens. Clearly a numerical study provides detailed information of velocity, pressure and turbulent quantities, however, streamline results are presented here for brevity in order to obtain a qualitative understanding of diffuser flow with screens.

A model study of turbulent flow in a 45° diffuser shows that adding a coarse screen in the diffuser (Figure 12a) has clear beneficial effects in suppressing a large recirculation region and providing nearly uniform flow downstream. Further improvements can be achieved by guide vanes (sources of lift) (Figure 12b) as well as a variable porosity screen (variable drag). The separate effect of sources in the k - and ϵ -equations also proves to affect the flow (Figure 12c), but according to the present study drag forces is the dominating factor. From a practical point of view screens are most readily handled, however in some cases screens that give adequate flow management may introduce excessive pressure drop. Guide vanes, on the other hand, require more experimental data to provide reliable discrete sources of lift and may not readily adapt to three-dimensional flow. Anyway a principle approach is suggested by the present study, in which various lay-outs of screens can quickly be tested for the resulting flow by numerical means in order to determine an optimal design.

REFERENCES

- Bradshaw, P. (1971). *An Introduction to Turbulence and its Measurement*. Pergamon Press.
- Carlson, J. J., Johnston, J. P., and Sagi, C. J. (1967). Effect of wall shape on flow regimes

- and performance in straight, two-dimensional diffusers. *Journal of Basic Eng.*, pages 151-160.
- Goenka, L. N., Panton, R. L., and Bogard, D. G. (1990). Pressure and three-component velocity measurements on a diffuser that generates longitudinal vortices. *Journal of Fluids Engineering*, **112**, 281-288.
- Idelchik, I. E. (1994). *Handbook of Hydraulic Resistance*. CRC Press Inc.
- Jones, W. P. and Launder, B. E. (1972). Some properties of sink flow turbulent boundary layers. *Journal of Fluid Mech.*, **56**, 337-351.
- Kline, S. J. (1959). On the nature of stall. *Journal of Basic Eng.*, **81**(D), 305-320.
- Kline, S. J., Abbott, D. E., and Fox, R. W. (1959). Optimum design of straight-walled diffusers. *Journal of Basic Engineering*, **81**(Ser. D), 321-331.
- Metha, R. D. (1977). The aerodynamic design of blower tunnels with wide-angle diffusers. *Prog. Aerospace Sci.*, **18**, 59-120.
- Michelsen, J. A. (1992). *Basis3D - a platform for Development of Multiblock PDE Solvers*. AFM 92-05. Department of Fluid Mechanics, Technical University of Denmark.
- Michelsen, J. A. (1994). *Block structured Multigrid solution of 2D and 3D elliptic PDE's*. AFM 94-06. Department of Fluid Mechanics, Technical University of Denmark.
- Seltsam, M. (1995). Experimental and theoretical study of wide-angle diffuser flow with screens. *AIAA Journal*, **33**(11), 2092-2100.
- Simmons, L. G. F. and Cowdrey, D. F. (1945). Measurements of the aerodynamic forces acting on screens. *Aeronaut. Res. Council. Reports and Memoranda*, **2276**.
- Sørensen, N. N. (1995). *General Purpose Flow Solver Applied to Flow over Hills*. Ph.D. thesis, Risø National Laboratory, Roskilde, Denmark. Dissertation presented at the Technical University of Denmark, Department of Fluid Mechanics.
- Yang, T. and El-Nasar, A. M. (1975). Slot suction requirements for two-dimensional griffith diffusers. *Journal of Fluids Engineering*, **97**, 258-260.

FILTRATION OF DIRTY GASES BY CERAMIC CANDLE FILTERS

K Simmons, A Aroussi and SJ Pickering

Department of Mechanical Engineering,
University of Nottingham

ABSTRACT

Combined cycle technologies offer the potential to generate power from coal at higher thermal efficiencies. A prerequisite to such systems is a filtration system capable of removing particulate material from the coal-derived combustion products in order to protect the gas turbine from damage. Ceramic candle filters are generally accepted as the most suitable technology. Continued satisfactory operation of ceramic candle filter units is dependent on satisfactory removal of the filter cake which builds up during operation. This project is concerned with the way particles deposit on the surface of the filter, and looks specifically at particle trajectories around a single filter in cross-flow, as a function of particle size, filter face velocity and free-stream velocity. This information is fundamental to an understanding of the formation and subsequent removal of the filter cake. Computational Fluid Dynamics (CFD) and the experimental technique Particle Image Velocimetry (PIV) are used to further the investigation.

In the CFD investigation, particles in the diameter range 1 to 800 microns are tracked through the domain. The radius of convergence defines the critical trajectory for particles just impinging on the filter. The radius of convergence is plotted as a function of Stokes' number for different inlet to filter face velocity ratios.

Experimentally, 30 micron particles are tracked in the vicinity of a fabric filter using PIV. The images are processed to give the radius of convergence and these are compared with the numerical predictions.

1. INTRODUCTION

Pulverised coal is currently an important fuel source in the power generation industry. Estimates of the world reserves of primary fossil fuels continue to show its dominance.

Environmental considerations and legislation coupled with the availability of other economical processes have forced some countries to develop techniques to reduce pollution from fossil fuel combustion.

Combined cycle technologies offer the potential to generate electricity from coal at higher thermal efficiencies with lower emissions of pollutants. The higher thermal efficiencies are possible because, in addition to the conventional steam

cycle, the hot combustion gases are also expanded through a turbine to generate power. However, combustion gases are dirty and contain particles which would erode the turbine blades and hence reduce efficiency. In order to reduce the particulate material to a satisfactory level (both in terms of emissions standards and turbine wear) it is necessary to filter the combustion gases. Conventionally, cyclones have been used. However, even several cyclone stages do not meet current requirements and an alternative technology is sought. In the quest for a suitable method of hot gas filtration several technologies have been investigated: ceramic fabric filters or baghouses (e.g. Chang et al (1986), Foote (1986) and Lippert et al (1986)), electrostatic precipitation (e.g. McEvoy (1986) and Rinard et al (1986)), cross flow filtration (e.g. Lippert et al (1986)), pulsating pressure filtration (e.g. Kerr and Probert (1985)), and granular bed filtration, as well as ceramic candle filters (e.g. Drencker et al (1987) and Eggerstedt & Zievers (1986)). Ceramic candle filters are robust and resistant to conditions of high temperature and have a high collection efficiency. For these reasons the technology which stands out as the most promising is that of the ceramic candle filter.

A ceramic candle filter generally consists of a long slender hollow tube closed at one end. It is typically made from porous silicon carbide of grain size 200-500 micron, with a microporous 'skin' (EPRI (1992)), such that the hot gases can pass through and the particulate material cannot. The filter elements are combined into a filter unit, the number of elements required being dependent on the desired flow rate. Ceramic filters are used in one of two ways; either the dirty gases flow past the outside of the filter with cleaned gas passing to the inside, or the dirty gases flow up through the middle of the filter and cleaned gas passes through the filter to the outside. In the majority of work done to date, the dirty gases have been on the outside of the filters. As the hot gases are filtered, the particulate material deposits on the outside of the filter forming a filter cake. The cake is periodically removed by back-pulsing the filter, causing the filter cake to break up and fall away. The 'cleanability' of the filters is one of the fundamental design considerations, and is clearly affected by whether the particulate material is deposited evenly around the filter.

There are two main candle filter experimental test programs reported in the literature. The first was undertaken at Aachen (EPRI (1992)a). An array of six candle filters was mounted downstream of a combustor. Ash from an

Atmospheric Fluidised Bed Combustor was injected upstream of the filter unit. The second, larger investigation took place at Grimethorpe (EPRI (1992)b). An array of 130 Schumacher candle filters was mounted downstream of a Pressurised Fluidised Bed Combustor. The filter unit was tested over a range of operating temperatures and pressures. Investigations were also made into the pressure, duration and cycle time of the cleaning pulse.

The work described in this paper scrutinises particle trajectories around a single filter in cross-flow as a function of particle size, filter face velocity and free-stream velocity. This information is fundamental to an understanding of the way the filter cake forms during filtration. Both computational and experimental methods are used to further the investigation.

2. EXPERIMENTAL WORK

2.1 Experimental test rig and procedure

The experimental work is conducted at atmospheric temperature and pressure using a purpose-built experimental rig. The rig was designed to cover the range of flow rates investigated at Grimethorpe (EPRI (1992)). In the Grimethorpe filter unit there were 130 candle filter elements hung in square array from a tubesheet within a cylindrical filter vessel. The dirty gases entered the filter vessel through a pipe just below the bottom of the filter elements. A notional cylinder can be placed around the filter elements to give an indication of the

velocities incident on the filter elements. In this way, the flow incident on the filter could be parallel or perpendicular to the element, or a mixture of both. In this project, the cross flow is the first case investigated. The maximum face velocity found at Grimethorpe was 0.07 m/s although the bulk of the work was done with 0.03-0.05 m/s.

It is not necessary to reproduce the actual dust loading since this project is only concerned with tracking particles to the filter face, not with forming a realistic filter cake.

Actual ceramic candle filter elements cannot be used in the experimental rig as they create a differential pressure of the order of 100 mbar when the filtration velocity is of the order of 0.05 m/s. This is far higher than is available from a conventional fan. Instead, fibre filters of the correct diameter are used throughout the experimental work.

A schematic diagram of the test rig is shown on figure 1. The body of the rig is constructed from 0.5m MDF cubes and has a perspex working section to allow visual access. The rig is modular in design such that parallel and angled incident flow can be investigated later. Flow through the filter element and the body of the rig is controlled via butterfly valves, and measured using orifice plates. A fabric filter protects the fan and orifice plates from particles in the rig. A 90 micron wire mesh and a 6 mm cell honeycomb are used to condition the flow into the tunnel, which enters via a circular inlet, and contraction (ratio 4:1, designed according to Rouse & Hassan (1949)).

Particles are injected into the rig from a fluidised bed particle feeder. Compressed air is fed into a plenum beneath a

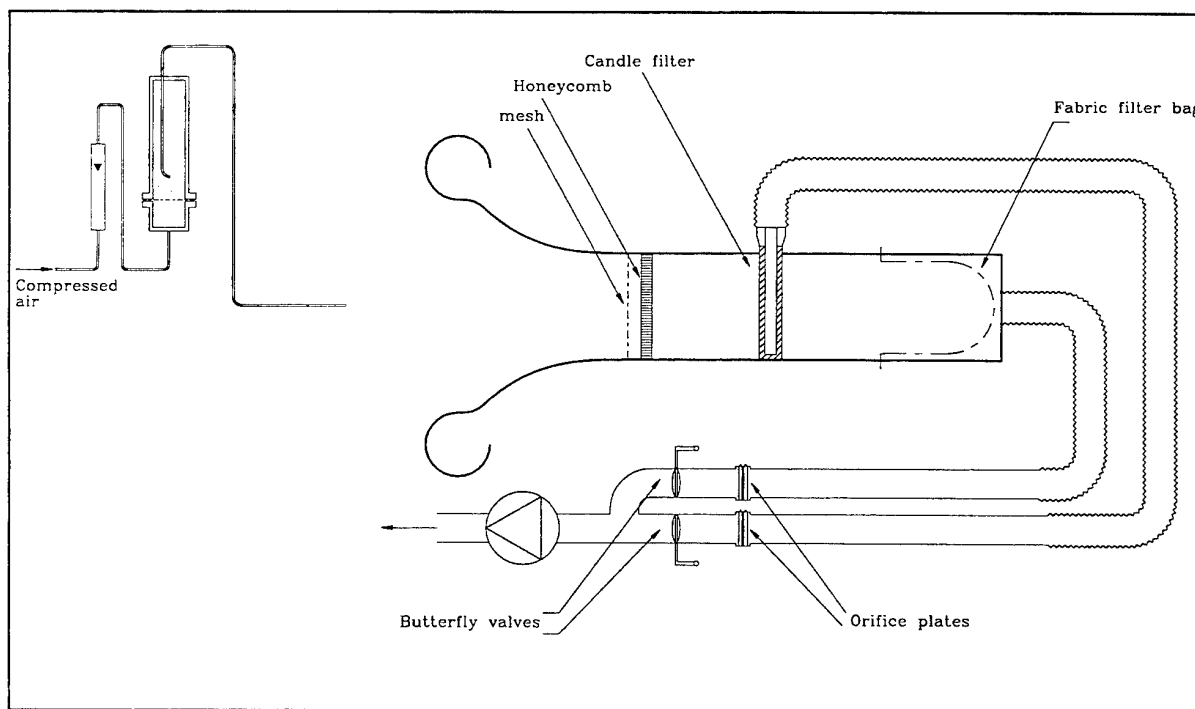


Figure 1 Schematic diagram of experimental test rig

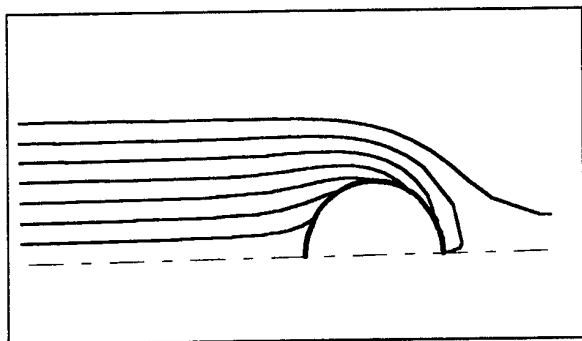


Figure 2 Radius of convergence

porous plastic distributor. The particles above the distributor are fluidised, and an 0.003 m diameter off-take tube is used to deliver the particles to the rig. The fluidised bed was chosen because it gives a continuous and even flow of particles. To date, proprietary seeding particles have been used, but it is anticipated that flyash will be used for later tests.

The particle trajectories and corresponding velocity field is acquired using Particle Imaging Velocimetry (PIV). A mechanically-chopped 20W continuous-wave Argon-ion laser is fanned into a sheet of the order of 0.003 m wide by a cylindrical lens. The sheet is positioned at the mid point of the filter and perpendicular to it. A 35 mm SLR camera is placed perpendicular to the laser sheet and is used to capture the flow field, which is analysed using a commercial PIV analysis package, or in-house software.

2.2 Radius of convergence

A parametric study into the effect of different inlet and filter face velocities was carried out. As a comparative parameter, the radius of convergence (R_c) was chosen. The radius of

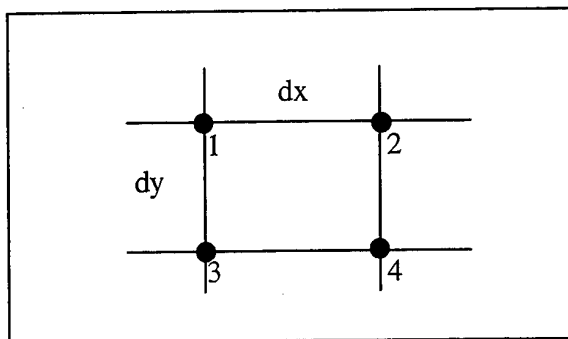


Figure 4 Calculation of stream function field

convergence has been used in similar studies on the flow past non-porous cylinders (Hedley et al (1965) and Davies & Peetz (1956)), where it is described as the collection diameter or the critical trajectory.

The radius of convergence is defined as the farthest starting distance from the cylinder centreline from which a particle would collide with the cylinder. It is specific to the inlet velocity, particle size, and in this case, the filtration velocity. Figure 2 shows the potential flow solution for a porous cylinder in cross flow, where the filter face velocity is 0.032 m/s and the inlet velocity is 0.057 m/s, and is used to illustrate the radius of convergence. The critical trajectory is characterised by its radius of convergence.

A particle-laden gas stream impinging on a filter would have a given particle size distribution. Each particle size within the distribution has its own radius of convergence. It is therefore possible to calculate the mass flow rate of particles colliding with the filter. The deposition of particles of diameter d , for unit duct height, is given by:

$$D_d = 2R_{c,d}M_d v_{in}$$

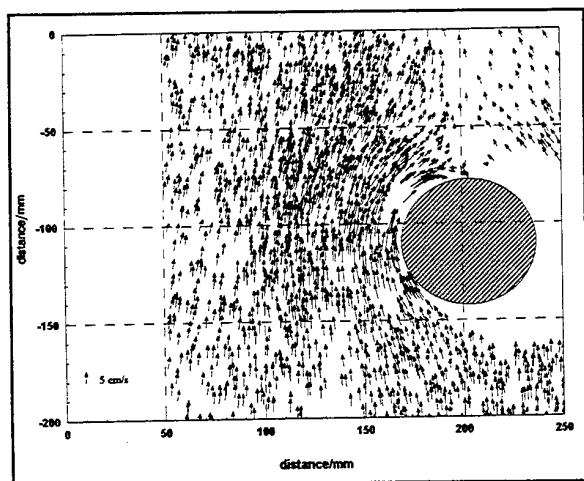


Figure 3 A typical vector field

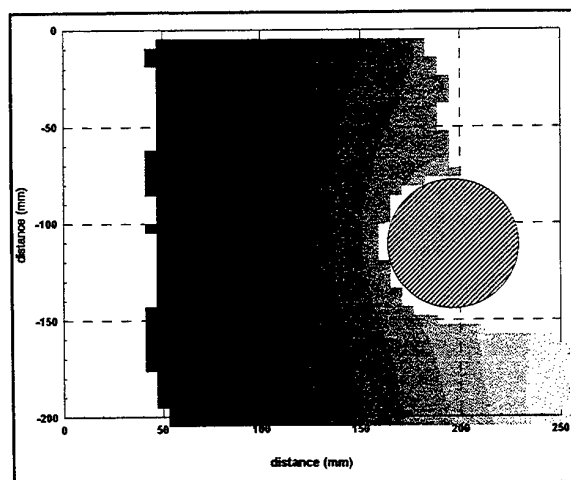


Figure 5 Field stream function values

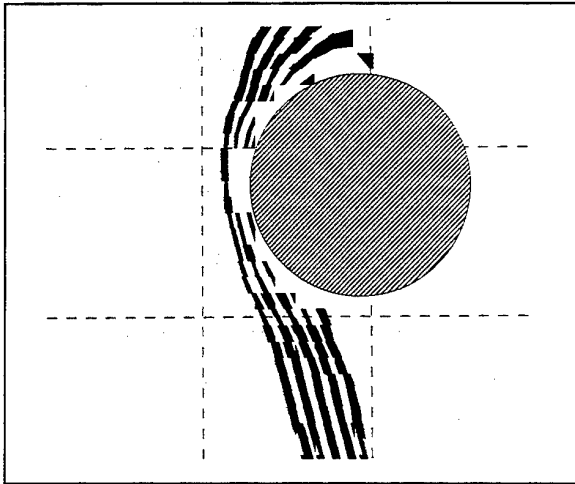


Figure 6 Stream function detail in the vicinity of the filter

Thus by integrating over the range, the radius of convergence can be used to calculate the total dust loading on a filter element:

$$D_{total} = \sum_{d_{min}}^{d_{max}} 2R_{c,d} M_d v_{in}$$

2.3 Analysis of data

The random vector field obtained by analysis of a typical image is shown in figure 3. The radius of convergence can be obtained approximately by visual inspection of the vector field. However, a rigorous analytical method is more desirable, and has been developed. The random vectors are interpolated onto a regular grid using in-house software. Two

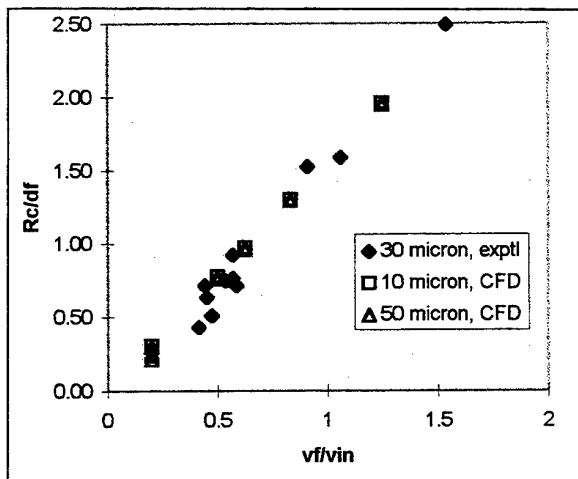


Figure 7 Variation in R_c with velocity ratio v_f/v_{in}

different methods of interpolation have been investigated, an inverse distance weighted scheme and Delaunay triangulation. The inverse distance weighted scheme is found to be the most suitable as it is less sensitive to the presence of erroneous vectors. In Delaunay triangulation, each interpolated vector is calculated using only data at the vertices of the surrounding triangle (Hatem & Aroussi (1996)). In the inverse distance weighted scheme a notional radius is drawn around each interpolation point. Within this radius, vectors nearer the interpolation point have more influence than those further away. This scheme guarantees a complete set of interpolated vectors.

The interpolated flow field is used to calculate values of stream function at each of the grid points. The top left corner of the interpolation grid is arbitrarily assigned a stream function value of zero ($\psi_1=0$), see figure 4. Values of ψ along the x-axis and y-axis through that point are calculated using:

$$\psi_2 = \psi_1 + v_2 dx \quad \psi_3 = \psi_1 + u_3 dy$$

The stream function values over the rest of the grid are then calculated by sweeping diagonally across the grid successively applying

$$\psi_4 = \psi_1 + u_4 dy + v_4 dx$$

Around the filter it is necessary to obtain some of the values by sweeping in the x or y direction rather than diagonally as the corresponding diagonal value may not be present. This method of obtaining these values was applied first to the potential flow solution for the flow field near a porous cylinder to check its validity. The method was found to be adequate and there is no need to apply more complicated schemes for filling in the missing numbers. The stream function values can be plotted as filled contours, giving pseudo streamlines as in figure 5.

Detailed examination of the stream function values in the vicinity of the filter allows the critical streamline, and therefore the radius of convergence, to be obtained. Strictly, this is not the true radius of convergence, since the flow field does not extend sufficiently far upstream for there to be no curvature of the streamlines. However, the information can still be compared directly with the computational results if the equivalent radius of convergence is used instead of the true radius of convergence. The variation of stream function in the vicinity of the filter is shown in figure 6. The critical trajectory can then be identified with its corresponding radius of convergence.

2.4 Experimental Results

Four different filter face velocities were investigated, 0.05 m/s, 0.04 m/s, 0.03 m/s and 0.02 m/s. Ratios of filter face velocity to inlet velocity (v_f/v_{in}) in the range 0.4 to 1.5 were investigated. A graph showing the variation of non-dimensional radius of convergence with velocity ratio (v_f/v_{in}) is shown on figure 7. Broadly, as the ratio v_f/v_{in} increases, the radius of convergence increases. The experimental results are for one nominal particle diameter only, and within the experimental

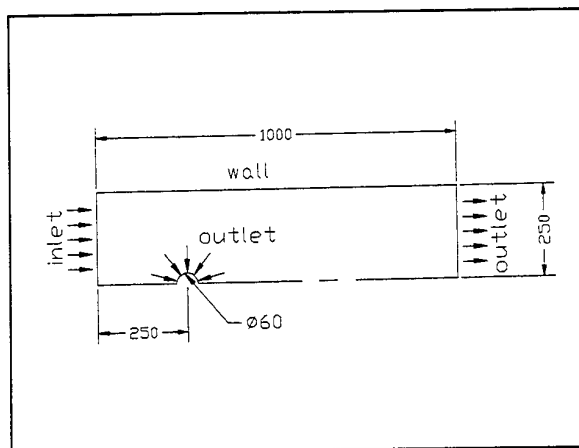


Figure 8 Dimensions of computational domain

uncertainty it is not possible to see the effect of variation in face velocity for a given velocity ratio. In a slower overall velocity field, particles are better able to respond to flow field curvature. It is anticipated, and borne out computationally, that there will be a small effect arising from this factor.

3. COMPUTATIONAL WORK

3.1 Introduction

A commercial computational fluid dynamics (CFD) code CFD-Flow3D is used to predict the flow field for a two-dimensional slice of the flow around a single filter in cross-flow. It is intended that the experimental work will validate the computational work. The CFD investigation therefore concentrates on a geometry as close as possible to that on the test rig.

3.2 Geometry and Boundary Conditions

The computational domain models the working section of the test rig. As the investigation is concerned only with the trajectories of particles until they impact the surface of the filter it is not necessary to model the filter as a porous solid, but simply as a boundary through which the flow can leave the computational domain. The computational domain is shown in figure 8.

A uniform velocity is set at the inlet plane, and a uniform face velocity is set as an outlet condition around the filter face. The outlet is modelled as a dirichlet boundary. For grid dependence tests the geometry symmetry plane was applied to the computational model, but for later work involving particle tracking it was necessary to model the entire plane as under certain conditions particles cross the symmetry plane during computation. This causes the particle tracking algorithm to fail, even when the particle does not cross the symmetry plane in the converged solution.

3.3 Grid Independence

The same initial boundary conditions were applied to three successively finer grids, of 1 125 (coarse), 4 500 (fine) and 18 000 (very fine) cells. In all grids there was a higher cell density near the filter face, with the grid expanding away from the filter with a maximum expansion ratio of 1.27.

The criteria of comparison used to confirm grid independence are: the position of pressure and speed contours in the computed flow fields, and the impact point of ten differently sized particles starting from ten different locations on the inlet plane. It is found that there is very little difference between the flow fields computed on the fine and very fine grids, and the impact positions of the particles, although there is significant difference between the results for the coarse and fine grids. As a compromise between true grid independence and increased computing time, the fine grid was used for all the computational work.

3.4 Radius of convergence

A parametric study into the effect of variation in inlet velocity, filter face velocity and particle size was carried out. As a comparative parameter, the radius of convergence (R_c) was chosen. The radius of convergence was obtained from computed particle tracks for particles of diameter 1, 5, 10, 50 and 100 micron, filter face velocities of 0.02, 0.03, 0.04 and 0.05 m/s and inlet velocity to filter face velocity ratios of 0.8, 1.2, 1.6, 2.0 and 5.0. In order to present the results in non-dimensional form a Buckingham- Π analysis was carried out on the variables involved. This yielded the following dimensionless ratios: d_p/d_f , v_{in}/v_f and ρ_p/ρ_a and one dimensionless group involving μ . For particles dispersed by turbulent flows a Stokes number can be defined as the ratio of the aerodynamic response time of a particle, τ_p , to the flow time constant, τ_a (Roco (1993), Banin (1992) and Chung & Trout (1988)).

The particle and flow response times are given by:

$$\tau_p = \frac{\rho_p d_p^2}{18\mu}, \quad \tau_a = \frac{v_{in}}{d_f}$$

$$St = \frac{\tau_p}{\tau_a} = \frac{\rho_p d_p^2}{18\mu} \frac{v_{in}}{d_f}$$

Although in this case the flow is not turbulent, it seemed appropriate to use this Stokes' number as the non-dimensional group because it is a measure of the way the particles respond to streamline curvature.

3.5 CFD Results and discussion

An example of the computed particle trajectories is shown in figure 9, for the case where the inlet velocity is 0.057 m/s and the filter face velocity is 0.032 m/s. The start position of the particles is adjusted until any further displacement from the centreline causes the particles to pass the filter instead of

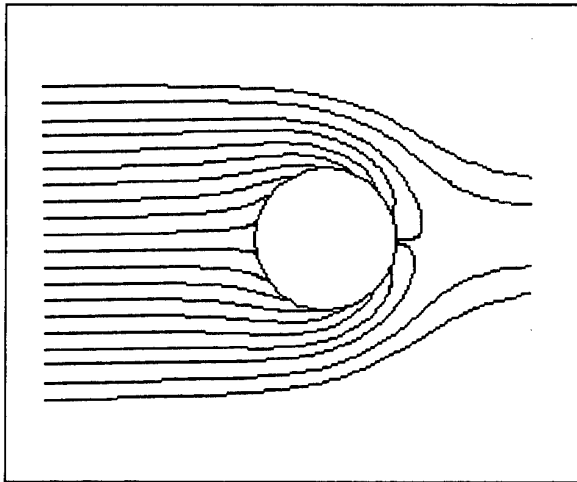


Figure 9 Particle trajectories for $v_f=0.032$ m/s and $v_{in}=0.057$ m/s

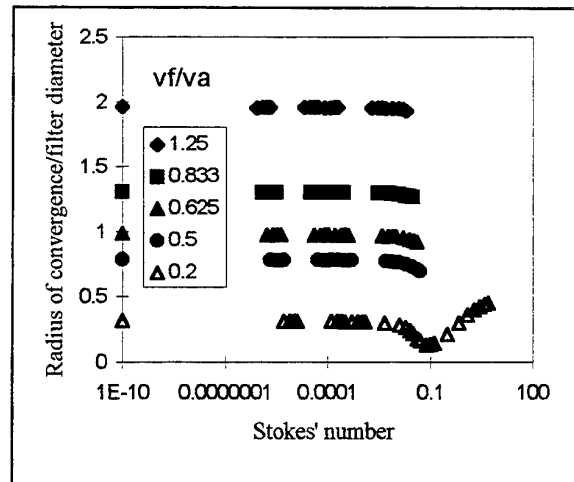


Figure 10 Variation of non-dimensional radius of convergence with Stokes' number

colliding with it. The start position is then the radius of convergence for that particle size.

The results of the computational investigation into the variation of radius of convergence with Stokes' number are shown on figure 10. For the velocity ratio 0.2, a number of larger particle diameters, 200, 300, 400, 500, 600, 700 and 800 microns, were also computed to extend the range of the graph. It is found that the data form a family of curves, for each velocity ratio. As the velocity ratio increases, the radius of curvature increases. For the smaller particles (lower Stokes' number) it can be seen from figure 10 that it does not appear to matter whether the velocity field is the result of a low face velocity and a low inlet velocity or a high face velocity and a high inlet velocity. However, as the particle size increases, their ability to respond to flow field curvature is diminished as the actual velocity values are higher.

For all the cases investigated, the effect of increasing Stokes' number was initially to decrease the radius of curvature.

For the velocity ratio $v_f/v_{in}=0.2$, further increase in Stokes' number caused an increase in radius of convergence. It is thought that this is because with this velocity ratio particles start from within the extension of the filter diameter ($R < d_f/2$) and are swept outwards around the filter. Larger particles are less deflected, and therefore collide with the filter where a smaller particle would not.

All these curves shown on figure 10 are theoretically asymptotic to $R_c/d_f=0.5$ (or to be strictly accurate $0.5+d_p$ to allow for the particle diameter), since in the limit the particle paths are undeflected by any streamline curvature. For larger particles and higher inlet velocities the deflected particle trajectory starts from a radius inside the filter radius and the asymptote is approached from below. For smaller particles and lower inlet velocities the deflected particle trajectory starts from a radius outside the filter radius and the asymptote is approached from above. It is worth noting that the result for the special case when there is no filtration velocity, i.e. flow past a

solid cylinder (Davies & Peetz (1955)) forms a curve consistent with the family of curves shown on figure 10, the traditional 'S' shaped curve asymptotic to $R_c/d_f=0.5$.

4. DISCUSSION

An experimental and computational investigation has been made into the flow of particles around a porous cylindrical filter element in cross flow. A radius of convergence has been defined, and investigated as a function of inlet velocity, face velocity and particle size (computationally). The radius of convergence gives the dust loading on the filter for a given particle size. If the total dust loading and particle size distribution within it are known, summation over the range allows the total particle loading on the filter to be calculated.

Computationally it is found that the radius of convergence is a function of Stokes' number and the face to inlet velocity ratio. The resultant family of curves is asymptotic to $R_c/d_f=0.5$, approaching from above if the streamline curvature is 'into' the filter and below if the streamline curvature is 'away' from the filter.

Experimentally, PIV has been used to investigate the variation in radius of convergence for 30 micron spherical (nominally) PIV particles. The results are compared on figure 7 with the computational results for 10 micron and 50 micron particles. Although there is some experimental scatter, the agreement is very good both in trend and numerical values.

The experimental work validates the computational investigation and it is now possible to predict filter cake growth in terms of particulate loading for a single filter element in cross flow. The work can now clearly be extended to allow for multiple filters in more complex flow fields. It will also be possible to look in detail at the distribution of particles around the filter to investigate non-uniformity of deposition. This is important because it will show whether, as is currently assumed,

the particles deposit evenly around the filter. If they do not, then it may be possible to condition the flow such that even deposition is achieved. This in turn would lead to increased cleaning efficiency for the filter elements.

The different inlet velocities modelled represent the differing flow conditions a filter will see dependent on its position within the filter array. Filter elements towards the outside of the array will clearly see higher approach velocities than those in the centre of the array. This work shows that if all filters have the same face velocity, the radius of convergence is greater for smaller particles. It would be reasonable to infer that more of the larger particles, proportionately, will be found towards the centre of the array than at the edge. This also has implications for filter cleaning, as it may be possible to clean the inner filters less frequently than those at the edge of the array.

5. CONCLUSIONS

An investigation has been made into particle trajectories around a ceramic candle filter element. The flow around a single, cylindrical, porous filter element in cross flow has been investigated computationally using CFD and experimentally using PIV. The experimental results validate the CFD predictions for 30 micron particles. For a given filter face velocity, more particles will be collected from a slower approach flow than a faster one. It is also found that the radius of convergence is smaller for larger particles if the streamline curvature is into the filter, and vice versa when the streamline curvature is away from the filter. These results have implications for the design of ceramic candle filter systems.

6. FUNDING

The project is funded through EPSRC/ERCOS Grant reference GR/J08195 and has industrial collaboration from CTDD and Powergen.

7. NOMENCLATURE

D	Deposition of particles (kg/s)
M	Loading of particles (kg/m ³)
R_c	Radius of convergence (m)
Ψ	Stream function (m ² /s)

7.1 Subscripts

in	at the inlet plane
f	at the filter face
a	fluid phase
p	particulate phase
d	for particles of diameter d

8. REFERENCES

- Banin, M.P. 1992, Optical measurements of particle size, velocity and number density in two-phase pulverised coal flames, Ph.D. thesis, Bringham Young University.
- Chang, R., Sawyer, J., Lips, H., Bedick, R. & Dellafield, R. 1986, The testing and evaluation of ceramic fabrics, 6th Symposium on the transfer and utilisation of particulate control, New Orleans, vol. 1, paper 11.
- Chung, J.N. & Troutt, T.R. 1988, Simulation of particle dispersion in an axisymmetric jet, J. Fluid Mech., vol. 186, pp. 199-222.
- Davies, C.N. & Peetz, C.V. 1956, Impingement of particles on a transverse cylinder, Proc. Roy. Soc. A234, pp. 269-295.
- Drencker, S.G., Stringer, J.S. & Tassicker, O.J. 1987, Pilot scale development of ceramic filters for PFBC power plants, Proceedings of the 9th international conference on FBC, vol. 2, pp. 1008-1012.
- Eggerstedt, P. & Zievers, J.F. 1986, Hot gas clean-up by means of porous ceramic filter elements, 6th Symposium on the transfer and utilisation of particulate control, New Orleans, vol. 1, paper 12.
- EPRI 1992, High-temperature gas filtration. Vol. 2: Operating performance of a pilot-scale filter. EPRI Rept. GS-6489 vol. 2, October.
- EPRI 1992, Grimethorpe high-pressure/high-temperature gas filter experimental program, vol. 1: Design, commissioning and modification of a large hot-gas filter on the Grimethorpe PFBC. EPRI Rept. TR-100-499 vol. 1, September.
- Foote, J.P. 1986, Design of baghouse and electrostatic precipitator for the coal-fired flow facility, 6th Symposium on the transfer and utilisation of particulate control, New Orleans, vol. 1, paper 14.
- Hatem, A.B. & Aroussi, A. (1996), Improved histogram based methods for PIV vector extraction, IMechE, pp. 259-265.
- Hedley, A.B., Brown, T.D. & Shuttleworth, A. 1965, Available mechanisms for the deposition from a combustion gas stream, ASME paper 65-WA/CD-4.
- Kerr, K. & Probert, D. 1985, Pulsating pressure filter for fluidised bed combustion gas clean up, Applied Energy (UK), vol. 20, n. 2, pp. 85-101.
- Lippert, T.E., Ciliberti, D.F., Tassicker, O.J. & Drencker, S.G. 1986, Test and development of woven ceramic bag and ceramic candle filters for the HTHP application, Symposium of cleaning at high temperatures, Surrey, pp. 215-231.

McEvoy, L.T., Parker, K.R. & Russel-Jones, A. 1986, The collection of fine particulates in power plant electrostatic precipitators, 6th Symposium on the transfer and utilisation of particulate control, New Orleans, vol. 1, paper 6.

Rinard, G.A., Dugg, D.E., Durham, M. & Armstrong, A. 1986, Advanced energy applications II - Results of parametric tests on an electrostatic precipitator operating at high temperature and pressure conditions, 6th Symposium on the transfer and utilisation of particulate control, New Orleans, vol. 1, paper 6.

Roco, M.C. 1993, Particulate two-phase flow, chapter 18, Butterworth-Heinemann.

Rouse, R. & Hassan, H. 1949, Mechanical Engineering, Cavitation free inlets and contractions, March .

THE HOLOGRAPHIC DETERMINATION OF THE PARTICLE DYNAMICS IN AN ELECTRO-HYDRODYNAMIC FLOW-FIELD

H.-J. Schmid and H. Umhauer

Institute of Mechanical Process Engineering and Mechanics
University of Karlsruhe (TH), Kaiserstr. 12, D-76128 Karlsruhe, Germany

ABSTRACT

An electro-hydrodynamic (EHD-) flow-field is formed by the superposition of the motion of gas ions in an electrical field and a conventional gas flow. Such a flow occurs for instance in an electrostatic precipitator, widely used for the separation of particles from gases. Experimental investigations are important to understand the fluid mechanics and the particle transport in this complex two-phase flow.

Double-pulse holography was used to examine the dynamic behaviour of a particle collective in a laboratory-scale electrostatic precipitator. This experimental method allows to determine the location, size and velocity of each individual particle within a specified volume at a distinct moment. In this paper frequency distributions of particle velocities as well as velocity profiles were determined and the momentary particle motion was visualised. The results help to clear substantial aspects of the particle motion and the secondary gas flows within the electro-hydrodynamic flow field.

INTRODUCTION

Electrostatic precipitators are very important industrial devices for cleaning great amounts of particle laden gases. The separation of particles is based on the unipolar charging in a corona discharge and withdrawing them from the gas flow by means of an electric field.

A wire-duct electrostatic precipitator is the most frequently used type in industry. It consists of parallel plates which form a series of ducts. Within each duct there is a row of wires (fig. 1). When high voltage is applied to the wires, a corona discharge takes place. This process generates ions, which causes a current flow from the discharge wires to the plates, whereby the particles are charged and hence transported by the electric field towards the collecting plates (White 1963).

Although the geometry of the separation zone is rather simple, there is a complex behaviour of the fluid flow: The fluid consists of the neutral gas molecules and the ions, produced by the corona discharge. These ions drift along the electric field lines. Due to collisions with neutral gas molecules there is a momentum transfer to the turbulent flow by the electric field and this specific flow is therefore called 'electro-hydrodynamic (EHD) flow'.

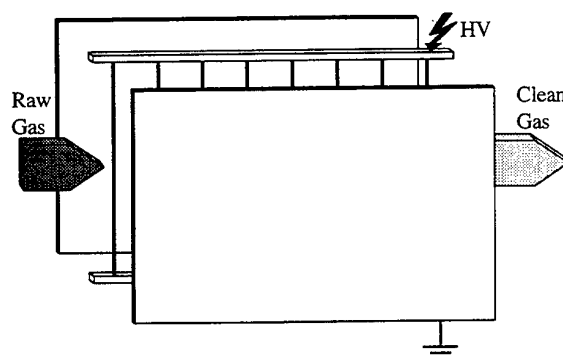


Fig. 1: Sketch of a single duct of an electrostatic precipitator

Opposite of the discharge wires there is the highest concentration of ions and therefore a secondary flow towards the collecting plates at this location will be formed. On the other hand for the sake of continuity there must be a reversal secondary flow in the regions between the discharge wires (fig. 2). This is well known from the literature as the so called 'ionic wind' (Yabe et al. 1976, Yamamoto and Velkoff 1981, Riehle and Löffler 1993, Bernstein and Crow 1979, Liang and Lin 1994, Shaughnessy et al. 1985). Furthermore a production of turbulence due to the electric field has to be assumed. Finally in combination with the particles as dispersed phase present in the gas, there exists a complex two-phase-flow.

Based on some assumptions, a comparison of experimental results with theoretical values is possible. An equilibrium of the hydrodynamic drag force with the electrostatic force on the particle leads to the stationary particle drift velocity relative to the fluid flow w_D :

$$w_D = \frac{Q_P \cdot E}{3 \cdot \pi \cdot \eta \cdot d_P} \quad (1)$$

The particle charge accumulated on a particle exposed to a homogeneous external electric field E may be calculated for particles larger than $1 \mu\text{m}$ according to the field charging theory (Pauthenier and Moreau-Hanot 1932):

$$Q_P = \pi \epsilon_0 \left(1 + 2 \frac{\epsilon_r - 1}{\epsilon_r + 2} \right) d_P^2 E \cdot \frac{t}{t + \tau} \quad (2)$$

where t is the residence time and τ is a characteristic time, which may be calculated with the current related to the area of the collecting electrodes j_{CE} :

$$\tau = \frac{4 \epsilon_0 E}{j_{CE}} \quad (3)$$

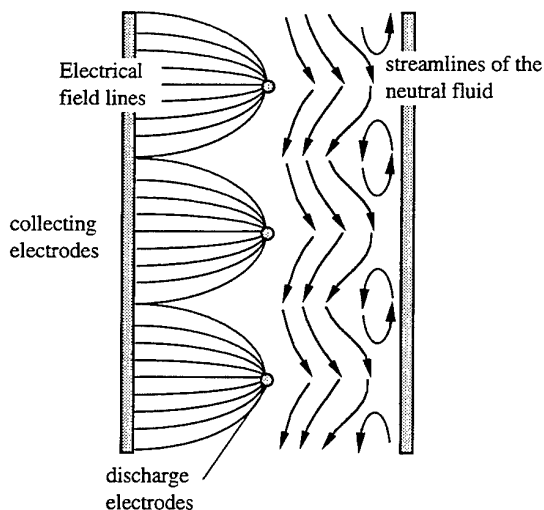


Fig. 2: Sketch of electric field lines and streamlines of the fluid flow in a single duct.

The aim of the investigations presented in this paper is to examine the particle dynamics in a laboratory-scale precipitator and how it is affected by the electrohydrodynamic flow field.

EXPERIMENTAL SETUP

As experimental approach pulsed-laser holography has been chosen. It is a short-time, whole-field photographic imaging technique producing a spatial image. If particle concentrations are not too high, an 'in-line' arrangement has proven as most suitable for the investigation of the dynamic behaviour of dispersed phases (Schäfer and Umhauer 1987, Schäfer 1986). Hereby a parallel coherent beam emitted by a pulsed ruby laser, expanded to a diameter of 80mm traverses the two phase flow and forms by superposition with the diffracted light the hologram on the hologram plate (fig. 3a). In this way a comparatively large flow field volume (up to 10^3 cm^3) may be imaged. The application of two short pulses allows to record all particles within that volume twice.

The systematic evaluation of a hologram (fig. 3b) leads to the knowledge of the 2x3 coordinates and the size of each individual particle within a specified volume. This evaluation is conducted semi-automatically which is time-consuming but very reliable. Because the time interval between two pulses is known (in these investigations between 40 and 100 μs), the particle velocity can be calculated. In addition with the known size and mass density also more complex quantities such as kinetic energy or momentum of individual particles may be derived.

From these quantities, frequency distributions as well as profiles across the gap may be derived. Furthermore it is possible to examine the spatial distribution of the dispersed phase in the flow (Neumann and Umhauer 1991). Because pulse holography is a concentration related measuring technique, the results are always based on spatial averaging (Raasch and Umhauer 1977)

From these quantities, frequency distributions as well as profiles across the gap may be derived. Furthermore it is possible to examine the spatial distribution of the dispersed phase in the flow (Neumann and Umhauer 1991). Because pulse holography is a concentration related measuring technique, the results are always based on spatial averaging (Raasch and Umhauer 1977)

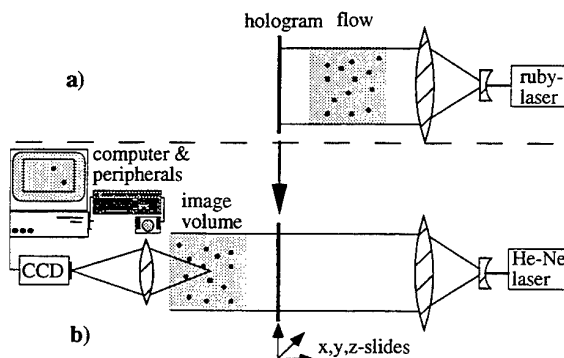


Fig. 3: Scheme of the optical arrangement for holographic recording of particle ensemble (a) and evaluation of holograms (b).

The experimental setup for recording the holograms is shown in fig. 4.

A single vertical duct with a cross section of $100 \times 100 \text{ mm}^2$ is used to model an electrostatic precipitator. The precipitation zone with a length of 250 mm and 5 round wires with a diameter of 0.3 mm as discharge electrodes is following an inlet zone with a length of 500 mm.

The particles are fed into the channel by an ultrasonically stimulated sieve with a mesh size only a little larger than the particle size. To inhibit deposition of dust on the lens and the hologram plate the particles are fed

only in the middle of the channel in a slit perpendicular to the electrodes. In addition this causes the particles to be in a flow region, which is not disturbed by the lens and the hologram plate.

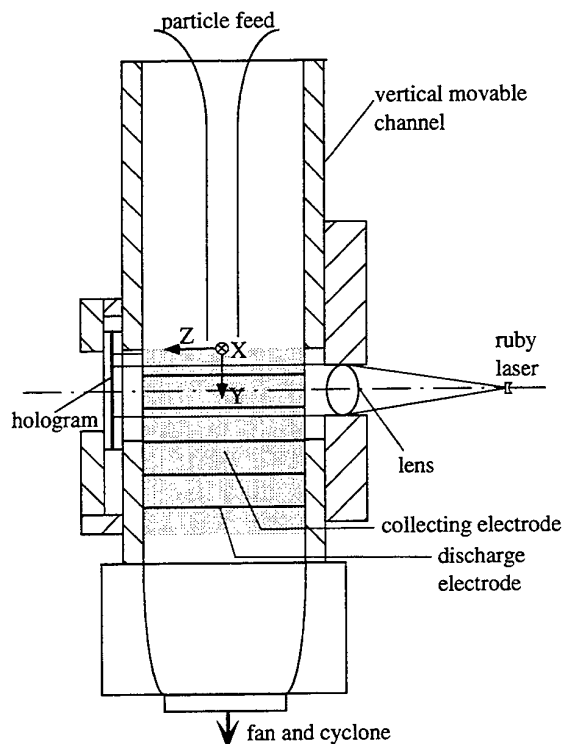


Fig. 4: Schematic view of the experimental setup for holographic recording

The holographic images allow to access in x-direction the whole region between the centre of the duct and one of the collecting electrodes. In flow- (y-) direction a region long from the inlet to the third discharge electrode is accessible (fig. 5).

The particles which leave the electrostatic precipitator are collected in a suction fan which is positioned downstream, ahead of a cyclone.

Most of the data presented in this paper is gained by evaluation of very flat volumes, thin layers, perpendicular to the mean flow direction (compare with fig. 5). The first layer is at the position of the first discharge electrode ($y=25\text{mm}$), the second layer is situated between the first and second discharge electrode ($y=50\text{mm}$).

As dispersed phase a narrow fraction of glass beads with a mean diameter of $20\text{ }\mu\text{m}$ were used, large enough to allow a very good holographic detection of the particles.

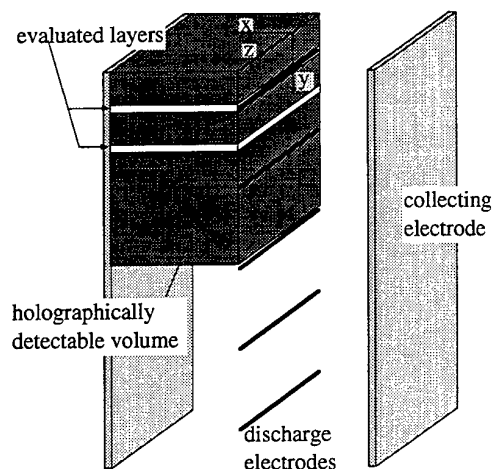


Fig. 5: Holographically accessible volume and evaluated volumes for data presented here.

EXPERIMENTAL RESULTS

Experiments were conducted with fluid velocities typical in electrostatic precipitators, ranging from 0.5 to 2.0 m/s. The applied voltages are varying from corona onset voltage up to 30 kV, which corresponds with a mean electric field strength of 6.0 kV/cm.

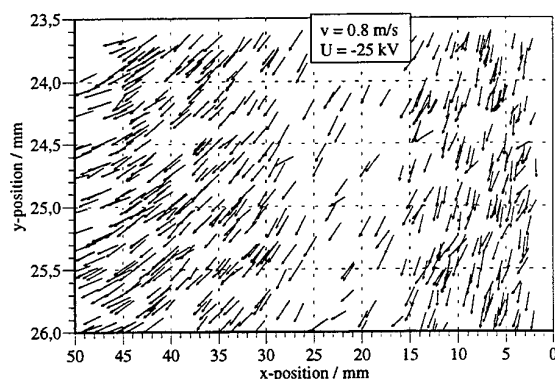


Fig. 6: Vector plot of particle velocities. Projection in z-direction.

The data gained by evaluation of the holograms may be analysed in many different ways. To visualise the influence of the electric field on the particle motion as well as the spatial distribution of the particles two-dimensional vector plots, as shown for example in fig. 6, are very suitable. In fig. 6 a projection of the particle ensemble in z-direction is shown, with each arrow representing one particle, where the foot of the arrow indicates the position and the arrow itself the velocity of the particle.

This representation gives a good qualitative impression of the particle motion in the EHD-flow. It should be especially noticed, that even particles in the near wall region are detectable.

Furthermore momentary local fluctuations of the particle concentration, which may be caused for example by small irregularities of the particle feed, can easily be detected. This is a specific feature of this whole-field method, which is hard to attain by other experimental techniques.

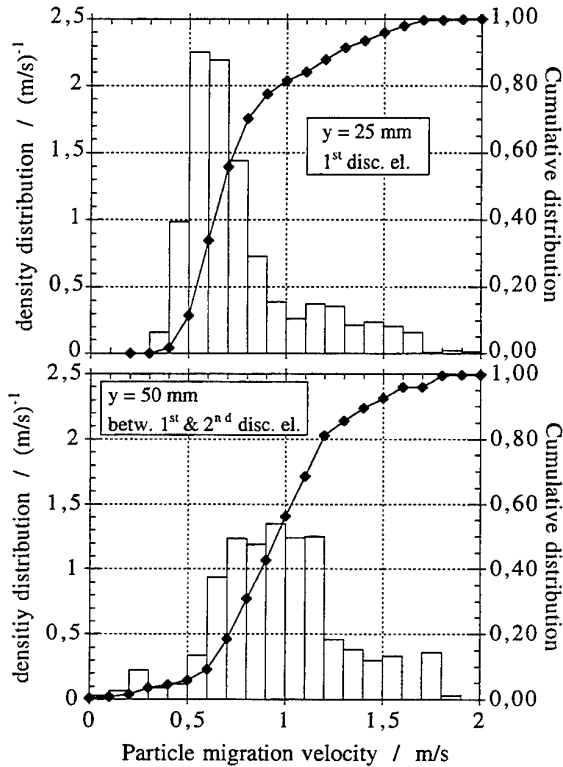


Fig. 7 a&b: Normalized number distributions of particle migration velocities. $U = -25$ kV; $v = 1$ m/s.

To achieve a quantitative analysis of the results, distributions of particle velocities within a specified volume can be evaluated. In fig. 7 frequency distributions based on the whole ensemble within the two already mentioned layers (compare fig. 5) are shown. These are significantly broader than the local distributions because of the local variations of the velocities (compare fig. 8).

In fig. 7a, for the first layer, one can recognise a rather narrow distribution in comparison to fig. 7b, representing the result gained from the second layer. This corresponds with a distribution of the electric field strength declining from a value of about 5kV/cm at the wall to 0kV/cm in the middle of the channel for the second layer. On the other hand for the first layer the field strength decreases from almost the same value at the wall to a mini-

mum of about 4.4 kV/cm at $x=15$ mm and then increases again towards the discharge electrode. This explains the broader distribution in fig. 7b. Furthermore a shift to higher migration velocities in fig. 7b may be observed, which is due to the increasing charge on the individual particles with increasing residence time (eq. 2).

The same data as in fig. 7a&b is shown in fig. 8a but now represented as velocity profiles across the gap from the middle of the channel ($x=0$ mm) to the wall ($x=50$ mm). Here a local averaging over small sectors is necessary to evaluate such profiles. The error bars indicate the standard deviation within each averaging sector.

At a x -position of approximately 10mm the mean value of the local migration velocity is about 0.6m/s in the case of $y=25$ mm. As can be seen from fig. 7a, this value is also the modal value of the frequency distribution.

The measured profiles correspond very well with calculated electric field strength. At $y=25$ a minimum of the migration velocities at about $x=15$ mm can be observed, whereas at $y=50$ mm the migration velocity decreases monotonously towards the middle of the channel.

Once more the influence of residence time on particle charge and hence migration velocity can be shown by comparing the profiles for different mean fluid velocities. For a mean fluid velocity of 2m/s the migration velocities are significantly slower than for 1m/s.

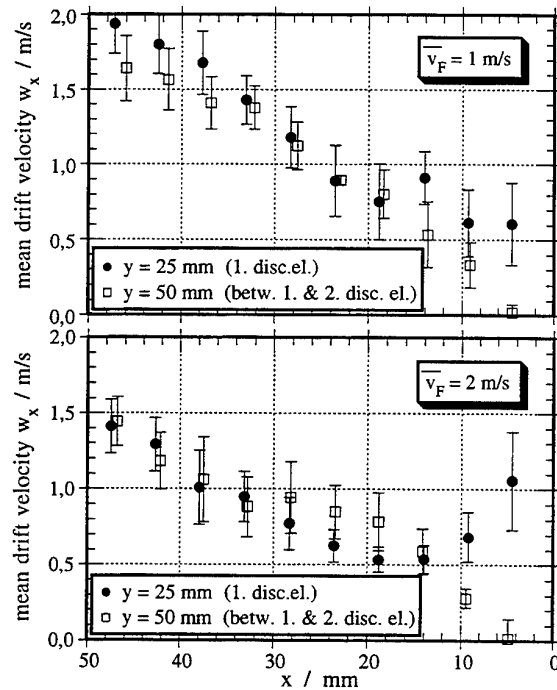


Fig. 8 a & b: Profiles of velocity component perpendicular to the collecting electrode. $U = -25$ kV.

A comparison of the migration velocities in the near-wall region for different fluid velocities and different

locations ($y=25\text{mm}$ and $y=50\text{mm}$ respectively) show very interesting details of the ionic wind of the EHD-flow.

In this near-wall region the electric field strength is virtually independent from the position in flow direction. Therefore the migration velocities may be well compared with theoretical calculations of expected velocities. This is shown in fig. 9 for an applied voltage of -25kV and different mean fluid velocities.

Opposite of the discharge electrode ($y=25\text{mm}$) the experimentally determined migration velocities are always higher than theoretically predicted according to equation 1. On the other hand at the symmetry plane between two discharge electrodes the measured values are very similar to the predicted ones. This has to be blamed on the influence of the ionic wind, as explained in the introduction. The quantity denoted Δv in fig. 9 is computed according to eq. 4:

$$\Delta v = (w_{\text{meas}} - w_{\text{theor}})_{y=25\text{mm}} - (w_{\text{meas}} - w_{\text{theor}})_{y=50\text{mm}} \quad (4)$$

Δv may be used as a measure for the strength of the ionic wind. Although Δv scatters significantly for the three fluid velocities, it can be stated that the secondary flow towards the wall, commonly called ionic wind, is about several 10 cm/s .

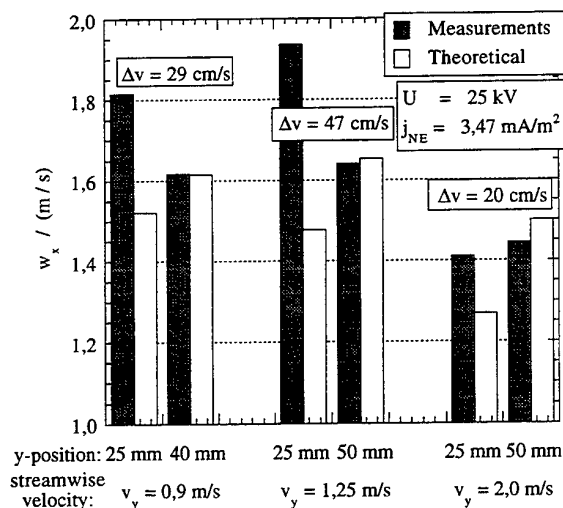


Fig. 9: Comparison of measured and theoretical migration velocities near the wall.

SUMMARY AND CONCLUSIONS

The presented examples show, that pulsed laser-holography is well suited to study the complex electrohydrodynamic flow-field in an electrostatic precipitator.

The holographic image contains the instantaneous spatial arrangement of a particle ensemble. A systematic evaluation of parts of the hologram yields a very detailed description of the dispersed phase. The size, location, ve-

locity of every particle can be calculated. These data may be represented as vector plots, profiles or frequency distributions.

The visualisation of the particle motion by vector plots give a good impression of the dynamic behaviour of the dispersed phase in the EHD-flow.

The representation of the data as frequency distributions shows a significantly broader distribution of the migration velocities between two electrodes than at the electrodes itself.

The profiles of the migration velocities correspond very well with the electric field strength.

The evaluation of the near-wall region shows the influence of secondary flows. It can be shown, that the ionic wind causes an increase of the migration velocities at the discharge electrodes about some 10 cm/s .

Although the evaluation is time consuming, only few holograms taken until now lead to very detailed informations. Additional holograms, taken at identical conditions should be recorded, to further increase statistical reliability, especially for evaluating velocity fluctuations.

REFERENCES

- Bernstein, S. and Crow, C.T. 1979: Interaction Between Electrostatics and Fluid Dynamics in Electrostatic Precipitators, 2nd Sympos. On the Transfer and Utilization of Particulate Control Technology, July 1979, Cnover, Colorado.
- Liang, W.-J. and Lin, T.H. 1994: The Characteristics of Ionic Wind and its Effect on Electrostatic Precipitators, Aerosol Sc. and Techn., vol. 20, pp. 330-344.
- Neumann, P. and Umhauer, H. 1991: Characterization of the Spatial Distribution State of Particles Transported by a Turbulent Gas Flow, Experiments in Fluids, vol. 12, pp. 81-89.
- Pauthenier, M.M. and Moreau-Hanot, M. 1932, Charging of Spherical Particles in an Ionizing Field, J. de Physique et le Radium, vol. 3, pp. 590-613.
- Raasch, J. and Umhauer, H. 1977: Grundsätzliche Überlegungen zur Messung der Verteilungen von Partikelgröße und Partikelgeschwindigkeit disperser Phasen in Strömungen., Chem. Ing. Techn., vol. 49, pp. 931-941
- Riehle, C. and Löffler, F. 1993: Particle Dynamics in an Electrohydrodynamic Flow Field Investigated with a Two-Component Laser-Doppler Velocimeter, Part. Syst. Charact., vol. 10, pp. 41-47.
- Schäfer, M. 1986: Determinierte Beschreibung des Zustands disperser Phasen in Strömungen durch Aufnahme und vollständige Auswertung von Doppel-Impulshologrammen. Fortschrittberichte der VDI-Zeitschriften 3: Verfahrenstechnik, Nr. 126, VDI-Verlag, Düsseldorf.

- Schäfer, M. and Umhauer, H. 1987: Realization of a Concept for the Complete Evaluation of Double Pulse Holograms of Particulate Phases in Flows, Part. Charact., vol. 4, pp. 166-175.
- Shaugnessy, E.J.; Davidson, J.H.; Hay, J.C. 1985: The Fluid Mechanics of Electrostatic Precipitators, Aerosol Sc. and Techn., vol. 4, pp. 471-476.
- White, H.J. 1963, Industrial Electrostatic Precipitation, Addison-Wesley Co., Pergamon Press, Oxford.
- Yabe, A. ; Mori, Y.; Hijikata, K. 1978: EHD Study of the Corona Wind Between Wire and Plate Electrodes, AIAA Journal, vol. 16, pp. 340-345.
- Yamamoto, T. and Velkoff, H.R. 1981: Electrodynamics in an Electrostatic Precipitator, J. Fluid Mech., vol. 108, pp. 1-18.

ACKNOWLEDGEMENT

The authors would like to thank the 'Deutsche Forschungsgemeinschaft (DFG)' for friendly supporting this work. (Lo 142/23-1 and Schm 810/11-2)

LDA EXPERIMENTS ON A MULTIPLE SPLIT FLOW AT 90°

G. Bräumer(*); V.A. Campos(**) and J.C.F. Teixeira(**)

(*) Fachhochschule Aalen, Aalen, Germany

(**) Universidade do Minho, 4800 Guimarães, Portugal

ABSTRACT

The present paper reports an experimental investigation, using laser anemometry, on the patterns observed in the upstream chamber of a turbulent flow split over multiple ducts are oriented at 90° to the main flow. The velocity profiles show the occurrence of a recirculation zone at the end of the chamber which is larger in the centre than at the edges. This appears to be linked with the observation of an even flow split through the outlet tubes. In addition there is evidence of a shift in the turbulence structure along the chamber from an upstream region of energy production near the inlet to a mainly dissipative region downstream the flow.

1. INTRODUCTION

The flow through multiple holes is of great importance in many engineering applications. As examples, one may refer the problem of fuel injection into the combustion chamber in gas turbines and the flow distribution on the tube side of shell and tube heat exchangers. In the former, most of the studies reported have concentrated on the flow patterns inside and downstream of the holes and the jet interaction with a flow stream at 90°. Measurements have been carried out using hot wire anemometry such those reported by Andreopoulos and Rodi (1984) and Moussa et al (1977) and laser velocimetry as referred by Martins (1996). Velocity profiles and turbulence patterns are reported with great detail for various hole configurations (length/diameter ratios) and layouts (number of holes and their relative location). Cho and Goldstein (1993 a,b) have investigated the flow patterns in great detail inside the holes. These were inferred from the local mass transfer rates occurring between the naphthalene walls and the air flow. Regarding the flow distribution in heat exchangers, the main problem

concerning a multiple flow split is that associated with possible maldistributions into the tube bundle. In understanding the hydrodynamics in heat exchangers some attention has been paid to the flow on the shell side, in particular around the baffles and through the internal leakages between the baffles and the tubes which is affected by the thermal expansions during the exchanger operation, as described by Haseler et al (1988). In this context, it becomes evident that a key point regarding the overall performance of a heat exchanger is an adequate flow distribution through the various tubes. Obviously, in such a situation, the upstream flow patterns characteristics are of paramount importance to the flow distribution. Very little knowledge is available for the upstream behaviour of the flow and this is of great importance to the heat exchanger performance and its design. In the present work, the flow distribution and patterns were investigated upstream of the tube array.

2. EXPERIMENTAL DETAILS

For the purpose of measuring the flow distribution upstream of a multiple 90° split, an experimental rig, as shown in Figure 1, was built. Basically, a centrifugal

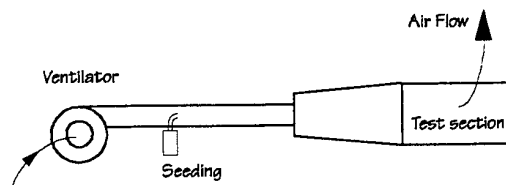


Figure 1 - Basic scheme for the test rig

ventilator drives an air stream into a duct which is connected to the test section through a 5° half angle diverging section. The duct contains honeycomb grids and

meshes to stabilise the flow. In addition, a bank of low pressure atomisers used for seeding the flow are located along the duct.

Both the test and divergent sections are made of Plexiglas 6 mm thick in such a way that the air stream at atmospheric pressure entering through the side (x direction as shown in Figure 2 for the coordinate system referred

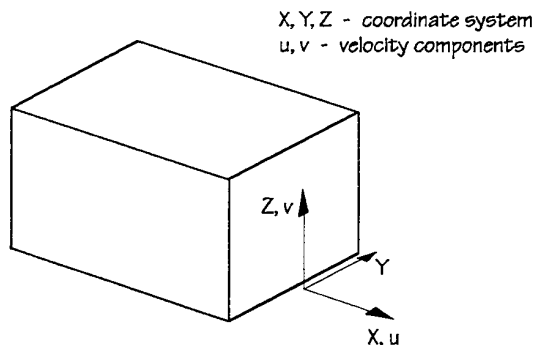


Figure 2 - Coordinate system for the test section

throughout the paper) of a square chamber is split into an array of 81 (9x9) tubes (y direction). These are arranged into a regular square pitch of $2D$, D being the internal diameter of each tube (16 mm). The test section is 300 mm (x direction) long and has a cross section 280 mm (z direction) and 140 mm (y direction). In order to achieve a good flow distribution, various meshes and honeycomb grids are placed upstream of the test section. The construction details of the test section are shown in Figure 3. Measurements were carried out over the entire chamber

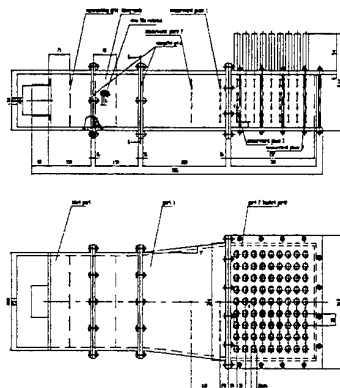


Figure 3 - Test section details

using a two component Dantec LDA system operating in back scatter. In this, the two components (blue and green) from a 5W argon ion laser were frequency shifted by means of 40 MHz Bragg cells in order to handle reverse flows.

Processing was carried out by a pair of burst spectrum analysers enabling good acceptance ratios and, therefore, high data acquisition rates as mentioned by the constructor's specifications. 1 μ m polystyrene latex particles were used for flow seeding. In addition to both mean and high order moments from the velocity *pdfs*, cross moments and the velocity spectrum were obtained from the experimental runs.

3. RESULTS AND DISCUSSION

Measurements of two simultaneous velocity components (u and v , according to Figure 2) were carried out throughout a comprehensive set of points inside the distribution chamber. In the stream wise direction (x), the control volume was always located below a row of tubes; in the crosswise direction (z), data was collected both below the outlet tubes and in between them. The flow Reynolds number was approximately 20,000.

3.1 Mean Velocity

Figure 4 shows the v component of the velocity

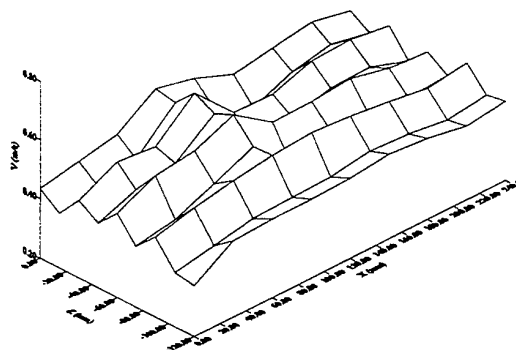


Figure 4 - Outlet mean velocity in the vicinity of the tubes ($y=123$ mm)

(outlet direction) in the vicinity of the array of tubes. The peaks correspond to points located just below the entrance to each of the tubes and, therefore, enables the identification of possible flow maldistributions among them. Although the flow distribution is fairly uniform (as observed in Figure 5 from the contour plot for the vertical central plane, $z=0$), it is noticed that tubes located in the central region of the test section show a slightly higher outlet velocity as opposed to those closer the entrance of the chamber and the lateral walls. This observation shows that in terms of heat transfer coefficient, all the tubes perform similarly. The effect of fluid removal on the variation of the v component of the velocity (Figure 4) is 'damped' further

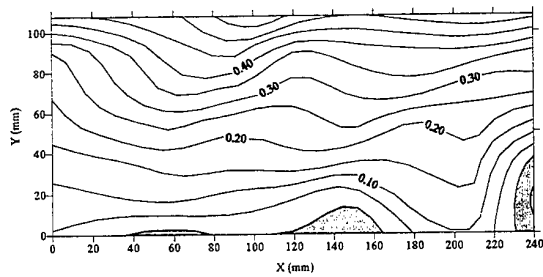


Figure 5 - Contour plot for the v component of the velocity in the central plane ($z=0$ mm)

below the outlet tubes, as shown in Figure 6. This is particularly evident near the entrance of the test section

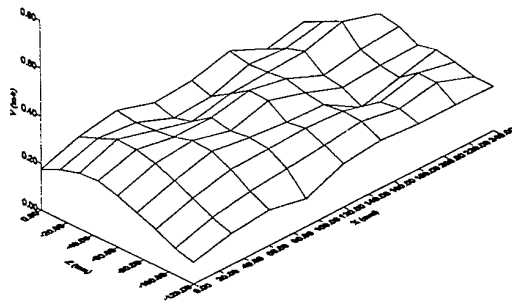


Figure 6 - v velocity for $y=69$ mm

although further downstream fluctuations in v occur but due to another reason, as will be discussed below.

The axial component of the velocity (x) shows a steady decrease along the chamber (and this reduction being more evident at the bottom of the chamber) as a result of fluid removal through those tubes located upstream (Figure 7 for the central plane, $z=0$ mm). This occurrence resulted in a significant decrease in the data rate

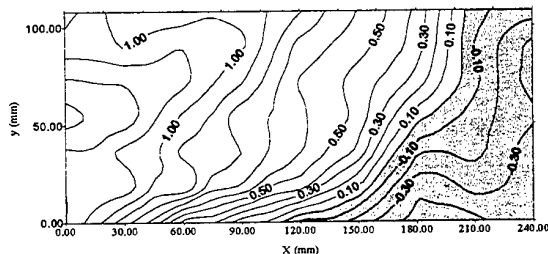


Figure 7 - Axial velocity in the central plane ($z=0$)

during acquisition. Due to fluid deceleration along the flat surface at the bottom, a situation of zero shear stress occurs, leading to a large region of flow recirculation inside the test section, represented by the shadowed area in the plot (Figures 5 and 7). The point of flow detachment occurs approximately at mid-distance along the chamber ($x=120$ mm), which is roughly the region of maximum outlet

velocity (Figures 4 and 5). It is therefore suggested that these occurrences are related; the existence of a recirculation zone reduces the effective cross section area and drives the fluid outwards at an approximately constant rate. This very fact contributes to the occurrence a nearly uniform flow distribution among the tubes as observed in Figure 4. In fact, the observation reported with Figure 6 is related to the flow recirculation which is accompanied by a drop of the mean velocity to values close to zero.

Figure 8 shows the flow pattern in the central plane

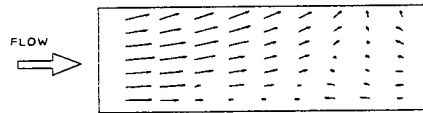


Figure 8 - Flow pattern for the central plane ($z=0$ mm)

($z=0$ mm) where the recirculation area and associated patterns becomes evident. Because the axial deceleration is stronger at the centre of the chamber, the recirculation zones get smaller from the centre to the periphery, as shown in Figure 9 ($z=60$ mm) and Figure 10 ($z=120$ mm)

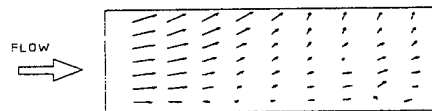


Figure 9 - Flow pattern for a vertical plane ($z=60$ mm)

where it is virtually non-existent. This observation suggests a far more complex flow pattern inside the chamber. Because the flow is not reversed at the edges of the test section, once the fluid reaches the end of the chamber, it is directed towards the centre (z direction), recirculated and

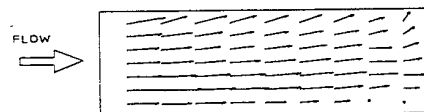


Figure 10 - Flow pattern for a vertical plane ($z=120$ mm)

driven outwards. This mechanism explains the backwards movement of the fluid near the front end of the chamber in the central plane observed in Figure 8.

3.2 Turbulence

Figure 11 shows that the velocity cross moments are approximately zero for most of the length of the chamber

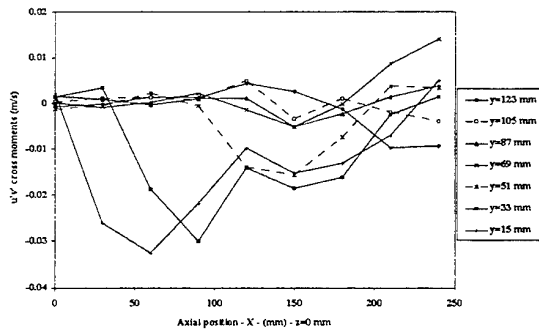


Figure 11 - Cross moments along the test section ($z=0$ mm)

(central plane). However, it is observed that near the flat wall ($y=0$) in the vicinity of the entrance, turbulent stresses ($-\rho \overline{u'v'}$) do occur in the flow. As the flow is increasingly retarded near the wall, the shear stresses approach zero near the recirculation zone ($x=120$ mm). The same pattern is found for other planes xz . This behaviour suggests that production of turbulent energy ($-\rho \overline{u'v'} \partial u / \partial y$) occurs near the wall in the absence of reverse flows. The observation of the turbulent fluctuations of velocity ($\sqrt{u'^2}$ in Figure 12

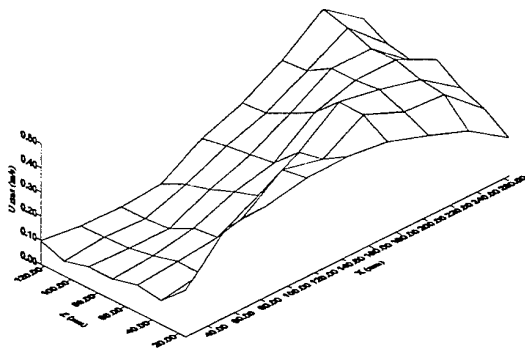


Figure 12 - Turbulence in the axial direction ($y=123$ mm)

and $\sqrt{v'^2}$ in Figure 13) in the central plane shows that turbulence enhancement in the chamber spreads from the wall, upstream in the chamber (where the turbulent stresses are higher), throughout its full volume. An increase in turbulence levels by a factor of ≈ 10 from the entrance to the recirculation zone is observed and this fact is coupled with a profound change in the velocity *pdf*'s: the distribution flatness (4th order moment) increases from a value

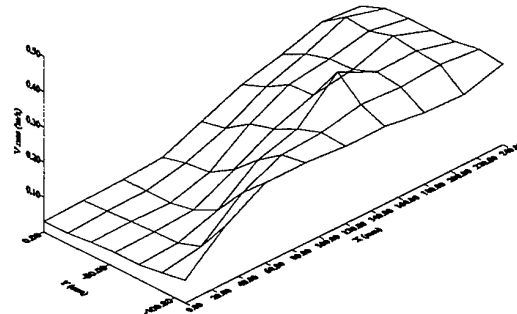


Figure 13 - Cross wise turbulence ($y=123$ mm)

typically around 3 near the entrance to values as high as $\approx 6-7$ in the recirculation areas.

Figure 14 shows the ratio $\sqrt{u'^2} / \sqrt{v'^2}$ in the

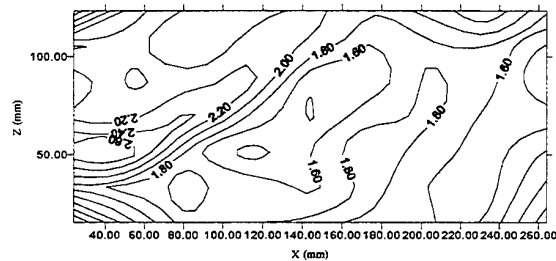


Figure 14 - ratio $\sqrt{u'^2} / \sqrt{v'^2}$ for $z=0$ mm

central plane ($z=0$). Near the entrance, this ratio is very high, though in the recirculation zone turbulence approaches a state of isotropy. This shows that near the inlet the stream wise component is dominant and

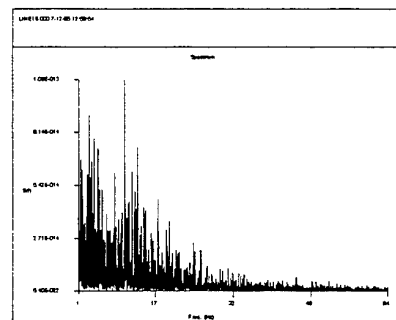


Figure 15 -a) - Frequency spectra for $(x,y,z)=(24,123,0)$

turbulence production occurs.

Being the energy dissipation process associated with small scale eddies which do not have preferred orientation (isotropic turbulence, Hinze, 1975) it can be concluded that the recirculation zone is a region of energy

dissipation. This shift in the structure of turbulence from production at the inlet to dissipation in the recirculation zone can also be inferred from the frequency spectra. As shown in Figure 15 a) and b), it is observed change in the contribution from the low frequency eddies (at the entrance, Figure 15-a) to the high frequency eddies (dissipatives) in Figure 15-b).

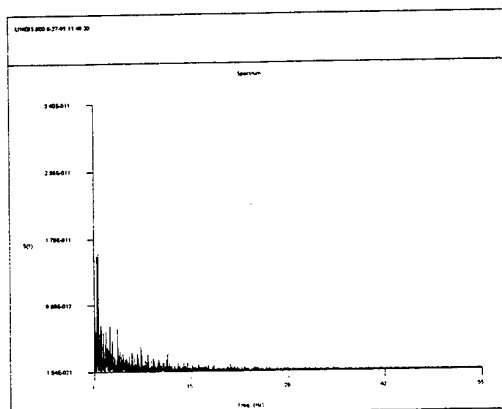


Figure 15 -b) - Frequency spectra for
(x,y,z)=(204,51,0)

4. CONCLUSIONS

From the results reported above some comments may be highlighted. Firstly, which is important from the heat transfer point of view, the flow distribution into the outlet tubes is fairly uniform. Although the fluid is being removed along the chamber, this behaviour is due to the occurrence of a recirculation zone which in practice reduces the available cross flow area. The variations in the shape of this recirculation zone from the centre to the periphery, suggests a complex 3D flow inside the chamber. Obviously, further investigation is required to properly characterise this phenomenon. The turbulence analysis show that turbulence levels increase by a factor of ≈ 10 along the test section. In addition, turbulence approaches isotropic conditions in the recirculation zone which is in agreement with frequency spectra analysis.

ACKNOWLEDGEMENTS

G Bräumer acknowledges the Fachhochschule Aalen for the leave of absence in order to carry this work at the Universidade do Minho.

The authors are grateful to Mr V Braga for his assistance during the course of the experimental work.

REFERENCES

- Andreopoulos, J. & Rodi, W 1984, Experimental Investigation of Jets in a Crossflow, *J. Fluid Mech.*, vol. 138, pp. 93-127.
- Cho, H.H. & Goldstein, R.J. 1993 a), Heat (Mass) Transfer and Film Cooling Effectiveness with Injection through Discrete Holes Part 1: Within Holes and on the Back Surface, *ASME Winter Annual Meeting, New Orleans, LA*, paper 93-WA/HT-58
- Cho, H.H. & Goldstein, R.J. 1993 b), Heat (Mass) Transfer and Film Cooling Effectiveness with Injection through Discrete Holes Part 1: On the Exposed Surface, *ASME Winter Annual Meeting, New Orleans, LA*, paper 93-WA/HT-59
- Haseler, LE Murray, P and Owen, D 1988, Flow velocities on the shell side of a shell and tube heat exchanger', *2nd UK National Heat Transfer Conf.* Vol. 1, pp 801-814
- Hinze, JO 1975, *Turbulence*, McGraw Hill
- Martins, LB 1996, *Private communication*
- Moussa, Z.M., Trischka, J.W. & Eskinazi, S. 1977, The Near Field in the Mixing of a Round Jet with a Cross-Stream, *J. Fluid Mech.*, vol. 80, part 1, pp. 49-80.

PULSATILE FLOW THROUGH TAPERED U-BENDS AS SIMULATED AORTIC ARCH (VELOCITY FIELD MEASUREMENTS BY LASER-INDUCED FLUORESCENCE METHOD)

K. Ohba, A. Sakurai, S. Ikedo, T. Urabe and K. Sawa

Department of Mechanical and Systems Engineering
Kansai University
Suita, Osaka, JAPAN

ABSTRACT

Velocity fields in pulsatile flows through a tapered U-bend as simulated aortic arch was visualized using a laser-induced fluorescence (LIF) method, and analyzed, after the velocity field in the same pulsatile flow through a tapered straight tube, of which inlet and outlet diameters and taper angle were same as the tapered U-bend, was accurately determined by the LIF measurements and the numerical calculations. As a result, the followings were elucidated. Firstly, for a tapered straight tube the measured and calculated instantaneous velocity profiles agreed well with each other. At the inlet, velocity profiles had parabolic shape and had rather gentle gradients at the tube wall. On the other hand, at the outlet they became on near rectangular shape and had steep gradients at the wall. Secondly, for a tapered U-bend velocity profile along the centrifugal direction was almost flat and furthermore had a dent in the central region. An inverse flow appeared near the inner wall at the phases of decreasing flowrate.

INTRODUCTION

In the biomedical field, knowledge of the detailed velocity field in the pulsating blood flow at stenoses, bends and bifurcations has been required, because such flow fields has been considered to play an important role in cardiovascular diseases like atherosclerosis. Several experimental studies have been made primarily to understand the changes in the blood flow pattern due to bends and bifurcations by Ku and Giddens (1987). It has only been recently, however, that the distribution of lesions in given anatomical regions of human subjects has been correlated with quantitative fluid dynamic measurements, thus allowing a sharper focus upon the potentially relevant hemodynamic factors such as high and/or low wall shear stress, high and/or locally low pressure, turbulence and oscillating wall shear *etc.* Thus, for the experimental study in this field the quantitative measurements of the local and temporal velocity field over the whole flow field are required.

Hence, in order to simulate the blood flow in the aortic arch by physical models of blood vessel and blood flow *in vitro*, pulsatile water flow through a tapered U-bend was investigated experimentally. A laser-induced fluorescence (LIF) method by Ohba et al. (1990 and 1992) was used to visualize and quantitatively measure instantaneous velocity profiles in pulsatile water flow through a 180 deg. curved tapered tube (U-bend).

APPARATUS AND PROCEDURE OF EXPERIMENTS

Figure 1 shows the outline of a tapered U-bend used in this experiment and a co-ordinates system for the U-bend. The inlet and outlet diameters of the U-bend were 22.0 mm and 15.6 mm, respectively. The radius of curvature was 37.6 mm, and the ratio of the radius of curvature to the mean radius 9.4 mm of the tube was 4. Straight 1,000 mm long circular tubes of which diameters were same as the inlet and outlet diameters of the U-bend, respectively, were attached to those. The z -axis was taken in the main flow direction, and the y -axis was taken in the direction of the centrifugal force. The x -axis was taken in the direction perpendicular to the z - and y -axes.

Figure 2 shows an apparatus for the visualization and measurement of the flow velocity distribution as used in these experiments. A Nd:YAG laser was used for exciting the fluorescence (phosphorescence) particle, thus making it fluoresce. The 3rd harmonic wave of the emitted light from the laser was used, which was an ultraviolet light of 10 nanosecond in pulse width. For the fluorescence particles, a zinc sulfide particle of about 8 micrometer in mean diameter and 4.1 g/cc in density was used. It was intermixed into water in a concentration of 0.1 to 0.2 % by weight. The ZnS particles, irradiated by a well collimated pulse ultraviolet laser light, emit a green fluorescence light of about 1 second in life time. As a row of fluorescing particles moves with a flow, a time line representing a velocity profile along the laser beam is formed. The motion of the time line so generated was photographed and tracked by a high speed video camera having a time resolving power of 200 frames per second in the direction perpendicular to both the laser beam and the flow. The camera was equipped with an image intensifier for amplifying the weak fluorescence light.

Figure 3 shows a schematic diagram of a generator of sinusoidal pulsatile flow and a system for triggering of the pulse laser synchronized with the pulsatile flow. The pulsatile flow was generated by periodically pressing a part of the flow duct made of a natural rubber tube as shown in Fig. 3. A sinusoidal wave form of the flowrate Q generated in such a method is shown in Fig. 4. Arrow marks below the number represent the times at which measurements were made in one cycle of the pulsatile flow.

CHARACTERISTICS OF PULSATILE FLOW

In order to know the characteristics of the pulsatile flow

through the tapered tube used in this experiment, its instantaneous and local flow field was measured and numerically analyzed in the case of a tapered straight tube of which taper angle was same as that of the tapered U-bend used in this experiment and in consequence same as the averaged angle of the human aortic arch.

Figure 5 shows the size of a tapered straight tube used, of which inlet and outlet diameters as well as taper angle are approximately same as those of human aortic arch.

In the present numerical analysis, flow was assumed to be an axisymmetrical two-dimensional one, and to be a pulsatile flow of which wave form of the flowrate is shown in Fig. 6. This wave form was the measured one of the actual pulsatile flow which was generated by the flow generator shown in Fig. 3. Numerical characters written beside dots on the wave form curve in Fig. 6 represent the phases at which visualization and measurements of velocity profiles were made, and numerical calculation were also made.

The governing equations are the equation of continuity, the equations of motion in the axial and radial directions, i.e. x and r . They are expressed as follows:

$$\frac{\partial}{\partial x}(ru) + \frac{\partial}{\partial r}(rv) = 0 \quad (1)$$

$$\begin{aligned} \frac{\partial u}{\partial t} + u \frac{\partial u}{\partial x} + v \frac{\partial u}{\partial r} \\ = -\frac{1}{\rho} \frac{\partial p}{\partial x} + \frac{\mu}{\rho} \left[\frac{\partial^2 u}{\partial x^2} + \frac{1}{r} \frac{\partial u}{\partial r} + \frac{\partial^2 u}{\partial r^2} \right] \end{aligned} \quad (2)$$

$$\begin{aligned} \frac{\partial v}{\partial t} + u \frac{\partial v}{\partial x} + v \frac{\partial v}{\partial r} \\ = -\frac{1}{\rho} \frac{\partial p}{\partial r} + \frac{\mu}{\rho} \left[\frac{\partial^2 v}{\partial x^2} + \frac{1}{r} \frac{\partial v}{\partial r} - \frac{v}{r^2} + \frac{\partial^2 v}{\partial r^2} \right] \end{aligned} \quad (3)$$

The above equations were discretized by the finite volume method. The SIMPLE method by Patankar was used for numerical calculation. Spaces in the upstream, tapered and downstream regions were divided into 30 elements, 50 elements and 20 elements, respectively. Field was divided into 86 elements in the radial direction. Convergence criterion of the numerical calculation was that the maximum residual of mass flowrate was smaller than 10^{-6} .

The results of the experiments and the numerical calculation are shown and are compared with each other in Fig. 7. The parameters $\phi 1$ to $\phi 8$ represent the phases in one cycle of pulsation which correspond to the numerical characters in Fig. 6. The quantity X_0 to X_6 represent the axial positions of the tapered tube, which are located at same intervals. The positions X_0 and X_6 represent, the inlet and the outlet of the tube, respectively. It is seen that the measured and calculated instantaneous velocity profiles agree well with each other. At the inlet, velocity profiles, which are shown in the

upper left and upper right figures in Fig. 7, have parabolic shape and have rather gentle gradients at the tube wall. On the other hand, at the outlet they, which are shown in the lower left and lower right figures, become of near rectangular shape and have steep gradients at the wall.

VELOCITY FIELD IN PULSATILE FLOW THROUGH TAPERED U-BEND

Visualization of instantaneous velocity profiles across the tube was made at eight different phases in a period of the pulsatile flowrate wave form at the position of $\theta = 0, 45, 90, 135$ and 180 degs., where θ was taken as shown in Fig. 1.

Figure 8 shows the equi-velocity curves in the case of a steady flow (top figures) and in the case of a pulsatile flow (the rest). Figure 9 also shows the stereographs of instantaneous velocity profiles corresponding to Fig. 8. The flowrate Q was 1.0 l/min. These were obtained by making picture analysis of the instantaneous velocity profiles visualized by the LIF method. It is seen from Fig. 8 that the height of the velocity peak near the outer wall was not so prominent compared with that in the case of a cylindrical U-bend, and the velocity profile along the y -axis was almost flat at the positions of $\theta = 45, 90$ and 135 degs. Hence, the velocity gradient and therefore the wall shear stress on the inner wall was much greater than that of the cylindrical U-bend. At $\theta = 45, 90$ and 135 degs., the velocity profiles along the y -axis were seen to have a rather sharp dent in the central region of the cross-section. In the case of the pulsatile flow, an inverse flow region appeared near the inner wall at the phases of $\phi 3$ and $\phi 5$.

CONCLUDING REMARKS

Velocity fields in pulsatile flows through a tapered U-bend as simulated aortic arch was visualized using a laser-induced fluorescence (LIF) method, and analyzed, after the velocity field in the same pulsatile flow through a tapered straight tube, of which inlet and outlet diameters and taper angle were same as the tapered U-bend, was accurately determined by the LIF measurements and the numerical calculations. As a result, it was elucidated that velocity profile along the centrifugal direction was almost flat and furthermore had a dent in the central region. An inverse flow appeared near the inner wall at the phases of decreasing flowrate.

REFERENCES

- Ku, D. N., and Giddens, D. P., 1987, "Laser Doppler Anemometry Measurements of Pulsatile Flow in a Model Carotid Bifurcation," *Journal of Biomechanics*, Vol. 20, pp. 407-431.
- Ohba, K., Sato, M., Sakaguchi, S. and Sakurai, A., 1990, "Visualization and Measurement of Detailed Velocity Field in U-Bend and Branched Tube Using Laser-

Induced Fluorescence Method," *Applications of Laser Techniques to Fluid Mechanics*, Adrian R. J. et al. eds., Springer-Verlag, pp. 537-552.

Ohba, K., 1992, "Visualization of Velocity Profile in Blood-Related Flow by Laser Technique," *Flow Visualization VI, Proceedings, 6th International Symposium on Flow Visualization*, Springer-Verlag, pp. 119-124.

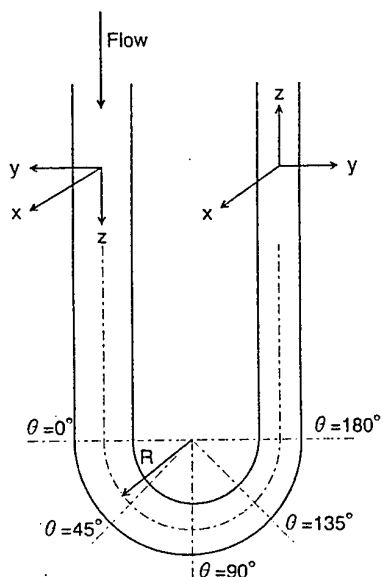


Fig.1 The form of a tapered U-bend and a co-ordinates system.

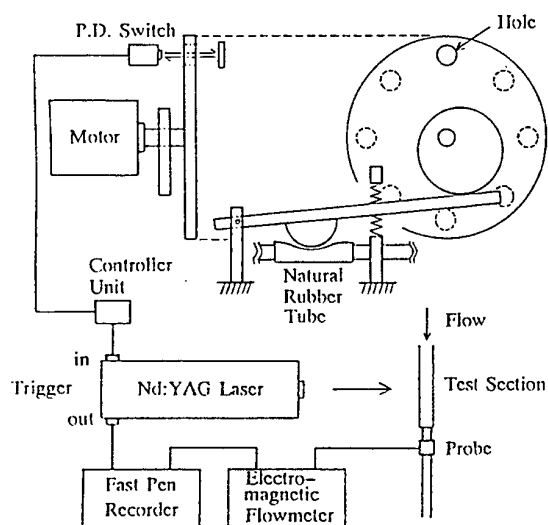


Fig.2 Schematic diagram of a pulsatile flow generator and laser trigger system.

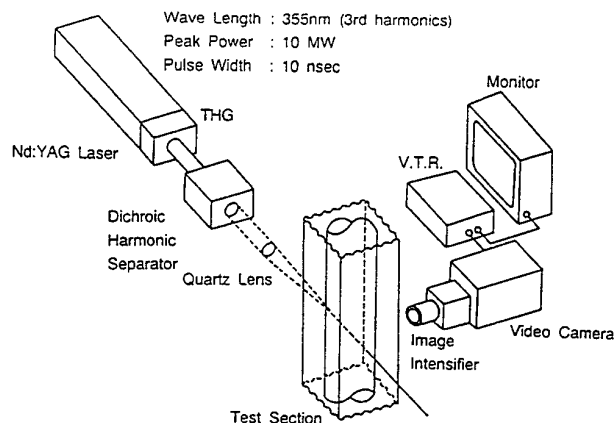


Fig.3 Experimental apparatus of a laser-induced fluorescence method.

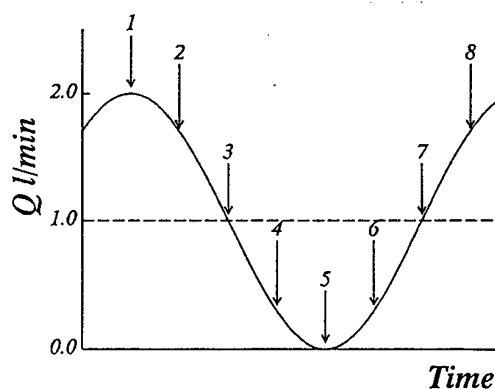


Fig.4 Waveform of flowrate.

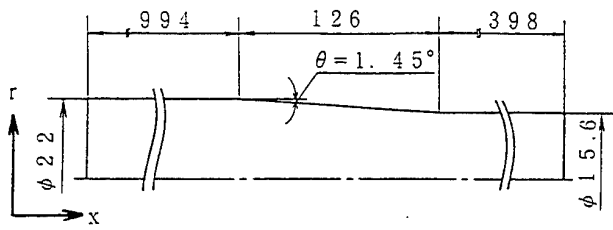


Fig.5 Tapered straight tube.

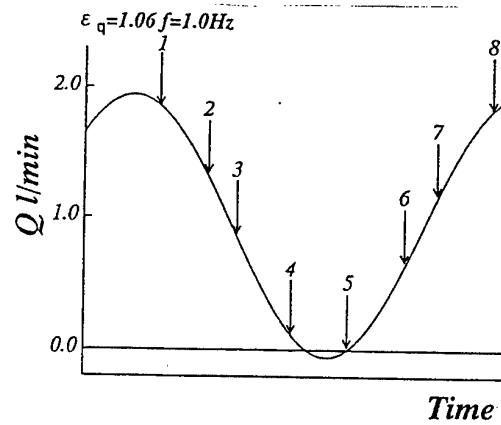


Fig.6 Waveform of the flowrate of a pulsatile flow.

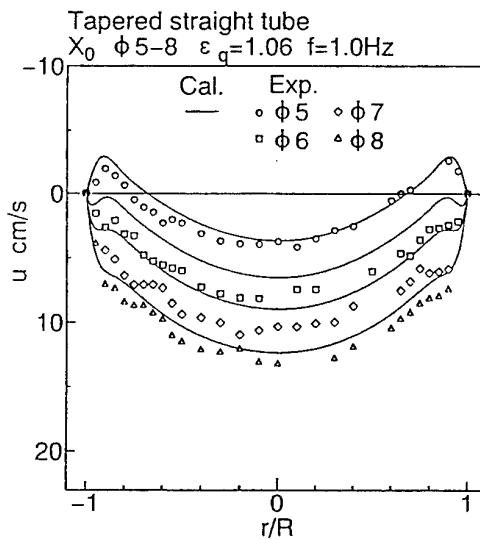
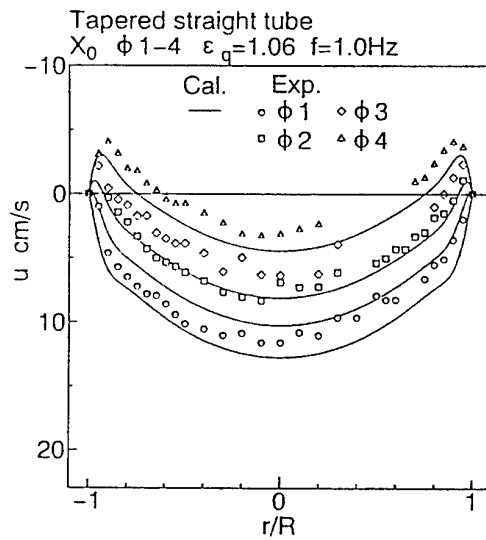
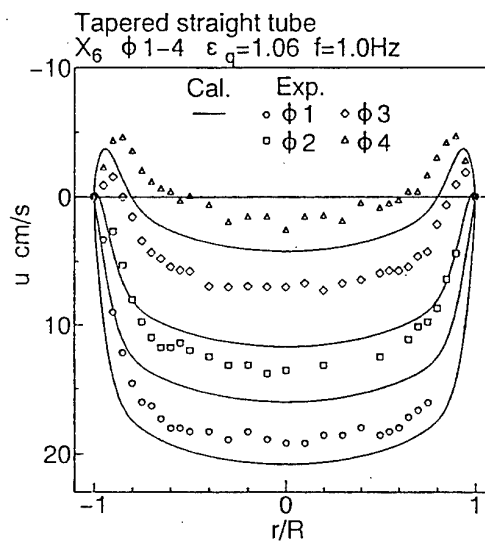
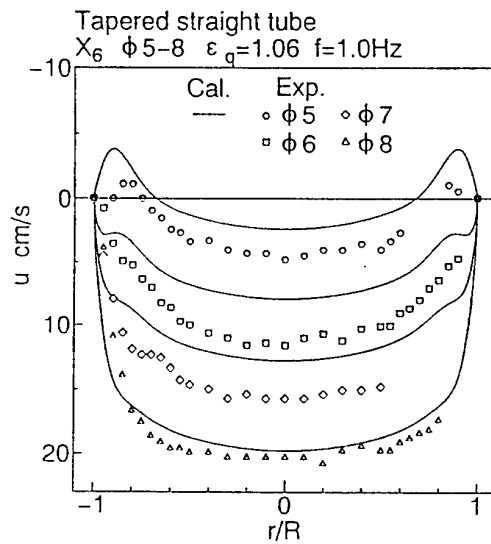


Fig.7 The numerical results and the experimental data of velocity profiles in a pulsatile flow through a tapered straight tube.

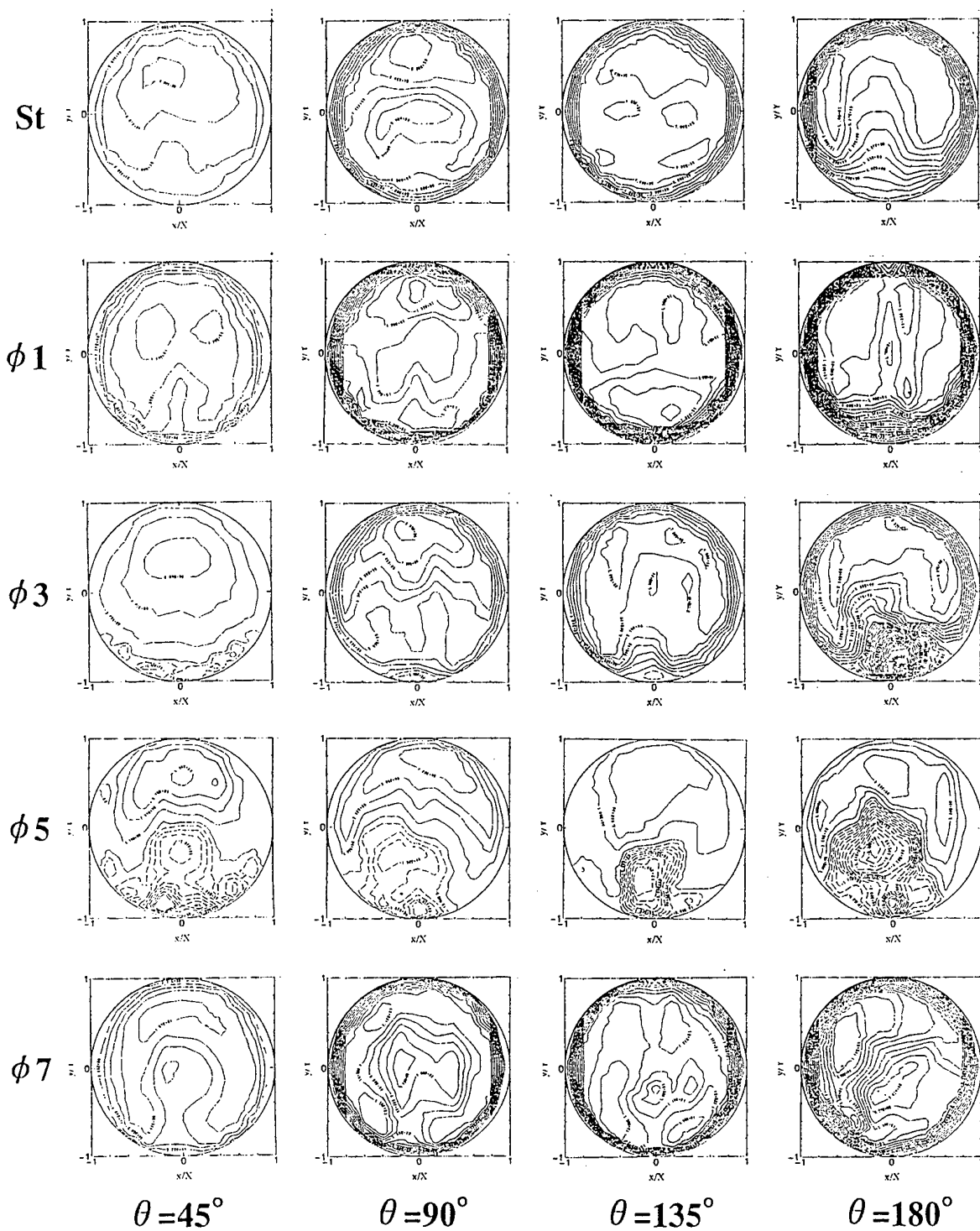


Fig.8 Equi-velocity curves in steady and pulsatile flows. $Q = 1.0$ l/min.

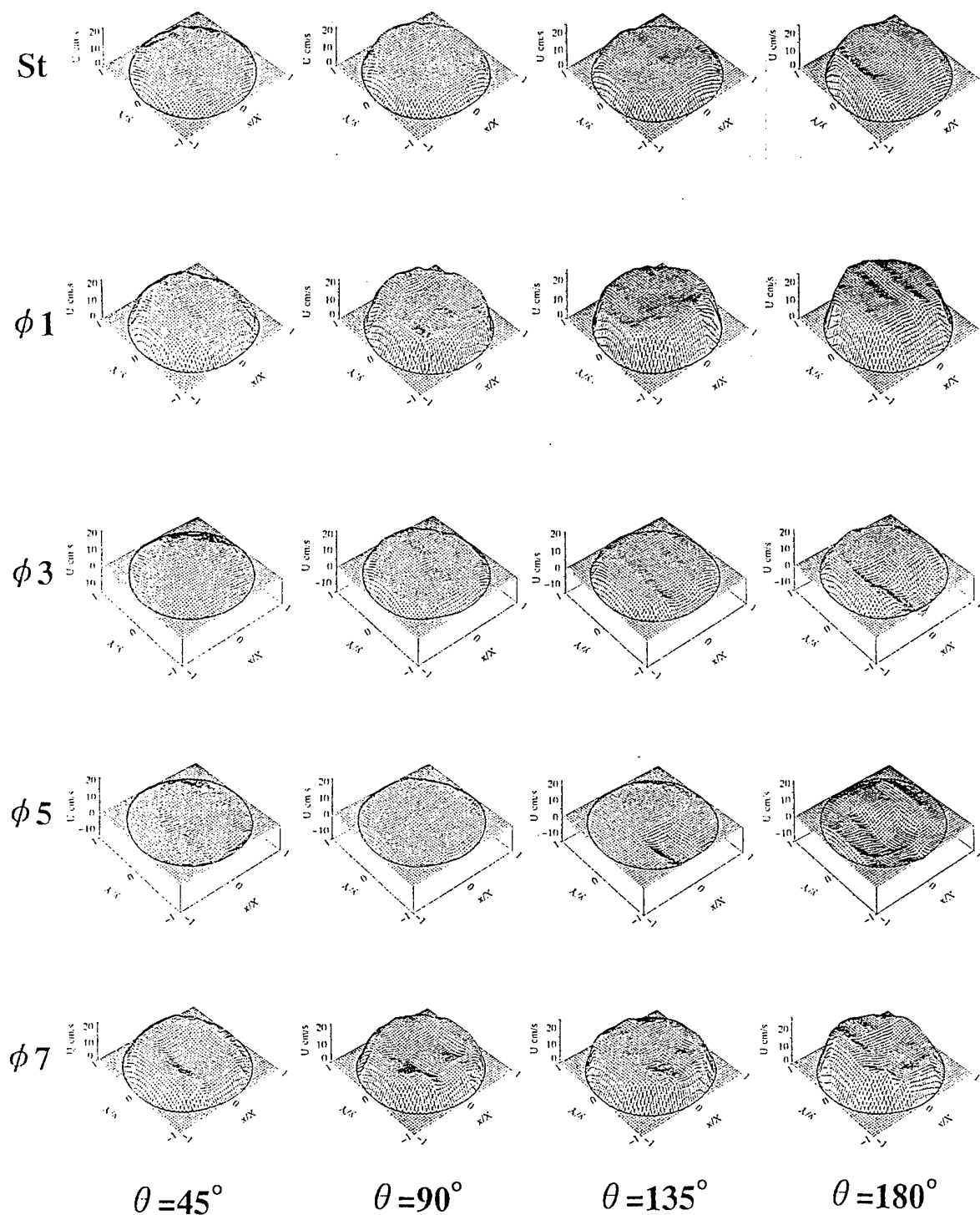


Fig.9 Stereographs of instantaneous velocity profiles in steady and pulsatile flows.

SESSION 38

Two Phase Flows II

APPLICATION OF LASER-DOPPLER ANEMOMETRY TO FLOWS IN LIQUID/LIQUID AND SOLID/LIQUID-EXTRACTION COLUMNS

G. Wigley^{*)}, C. Weiß^{**)} and R. Marr^{**)}

^{*)} Flow Measurement Consulting Service
Birkenweg 4, A-8062 Kumberg, Austria

^{**)} Institut of Thermal Process Engineering and Environmental Engineering
Graz University of Technology
Inffeldgasse 25, A-8010 Graz, Austria

ABSTRACT

The flow characteristics of a liquid/liquid dispersion and of a solid/liquid suspension in stirred extraction columns of the Rotating Disk Contactor (RDC) type were analysed by means of laser anemometry. For the assessment of the extraction efficiency under the constraints of column geometry and operating conditions the knowledge of the flow pattern and of the turbulence intensity in the extraction column is a necessary prerequisite. Experiments comparing single-phase and two-phase operation were performed. Axial and tangential velocity components of both phases were measured along a radial traverse in a representative column compartment. An analysis of the data shows that the solid particles do not modify the flow patterns as obtained for the continuous phase only but do enhance the turbulent fluctuations. Contrary to these findings is that the liquid droplet swarm totally rearranges the flow pattern in the column and that the turbulent fluctuations are damped and is associated with a significant loss in turbulence isotropy.

1. INTRODUCTION

Liquid/Liquid extraction is a separation process used in chemical, pharmaceutical, food and environmental process engineering to transport a product component, or waste species, from a liquid feed stock to an immiscible or partially miscible solvent stream. Usually one liquid phase is dispersed in the other, the continuous phase, to maximize the interfacial contact and therefore the mass transfer intensity between the two phases. The phase contact is performed in vertical extraction columns where the dispersion is maintained by pulsing or stirring the liquid feed stock in the column. The most commonly used operation mode for the extraction process is to establish a countercurrent flow between the dispersed and continuous phase through the column, Figure 1a. Within a certain ratio of the volume flow rates this is possible due to the density difference between the phases. The aqueous feed stock is pumped to the top of the column, moves downward in the apparatus and leaves at the bottom of the column as the raffinate. The lighter solvent stream is pumped to the inlet distributor at the bottom of the

column and moves upward as a swarm of droplets. At the column top the droplets aggregate in a dense dispersion layer and then coalesce to form an homogeneous extract phase leaving the column. For some special extraction problems cocurrent operation is applied. Even in this case the buoyancy generated flow of the lighter phase induces a slip velocity between the dispersed phase and the continuous phase.

The applied column operating conditions generate a certain level of dispersed phase volume fraction in the column, which is usually termed 'holdup'. Investigating the hydrodynamics in an extraction column involves characterization of the continuous and dispersed phase volumetric throughputs, dispersed phase holdup, interfacial area and mixing behaviour. When combined with a mass transfer model a fluid-mechanical description can be established for the basis of column extractor design, Godfrey & Slater (1994). Generally extraction columns with small flow cross-sectional area provide a long contact time between the phases and therefore a high efficiency but small throughput. Increasing the free area of the stator cross-section increases throughput but decreases contact time and extraction efficiency. The goal in the design of extraction columns is to find the optimum between the opposing requirements of throughput and extraction efficiency.

Ideally one wishes to establish a flow pattern, where the continuous and the dispersed phase elements move countercurrent at a constant interfacial slip velocity throughout the column. In practice extraction column operation is usually far from the ideal. Various flow irregularities influence the behaviour of both phases. Backmixing occurs in the continuous phase, due to vortex shedding and circulation caused by the rotor elements and the column internals. 'Short cut' streams and channeling effects produce a maldistribution of the continuous phase velocity in the column cross-section. Continuous phase entrainment takes place in the wake of the rising droplet swarm and small droplets of the dispersed phase are entrained in the eddies and in the mean flow of the continuous phase. To evaluate the influence of the flow irregularities on column performance investigations into the overall spatial flow structure in the column compartments are required.

The knowledge of the flow pattern and the turbulent fluctuation level in the extraction column is

necessary to assess the extraction efficiency under the constraints of column geometry and operating conditions. This is particularly important when trying to scale up from pilot size plant to industrial size plant.

In the recent literature there have been found only few attempts to apply LDA-techniques to liquid/liquid two-phase flows in extraction columns. Among these the contributions of Masbernat et al. (1993) and of Abid & Godfrey (1993) are of considerable interest concerning the measurement technique. In both works a matched refractive index two-phase system was used to enable the LDA-measurements in dense liquid/liquid dispersions. However these authors obtained their measurements in model flow configurations and did not investigate real extraction columns. The present research activity aims to investigate the mean flow patterns and the turbulence characteristics of the moderately dense two-phase flows in two pilot sized extraction columns of the Rotating Disk Contactor (RDC) type by laser anemometry. The question to be answered is: What is the influence of the dispersed phase motion on the flow pattern and the turbulence intensity of the continuous phase in the flows appearing in the extraction column?

2. FLOW CONFIGURATION AND EXPERIMENTAL TECHNIQUES

2.1 The Pilot Sized Extraction Columns

The mean flow patterns and turbulence characteristics of the two phase flow were measured by laser anemometry in two pilot sized RDC-columns. A section of a typical column geometry is shown in Figure 1b. The outer wall of each column was made from QVF pyrex® glass and was fitted with stator rings which are interleaved with discs mounted on a central rotating shaft. The first column studied had an inner diameter of 150 mm and was operated with a dispersed phase of kerosene droplets in a continuous phase of water, i.e. a density difference of 230 kg/m³. The second column, with an inner diameter of 200 mm, was operated with a dispersed phase of solid polypropylene particles in water, i.e. a density difference of 100 kg/m³. The exact kerosene droplet size distribution was unknown, but the mean drop diameter was estimated to be 2 mm diameter, whereas the polypropylene particles were prepared with a specified size range of between 0.2 and 0.5 mm diameter.

Column geometry data and operating conditions are summarized in Table 1. The solid/liquid system provided a two phase flow of known characteristics and a dispersed phase volume fraction that was constant over the height of the column. This avoided the additional complexities of droplet coalescence and breakup occurring which are associated with a liquid dispersed phase. In the case of the liquid/liquid system the drop interaction events produce a time varying drop size distribution over the column height. In relationship to the size specific drop rising velocity, the change in drop size distribution causes a specific holdup profile. In the case of the breakup dominated system kerosene/water, where coalescence in the dispersion was of minor importance, the dispersed

phase holdup increases with column height, due to the decreasing mean drop size and the lower rising velocity of the smaller drops.

For the solid/liquid suspension special attention was given to the phase separation in the settling zone at the column top. From there a dense particle slurry was recirculated to the dispersed phase inlet at the column bottom.

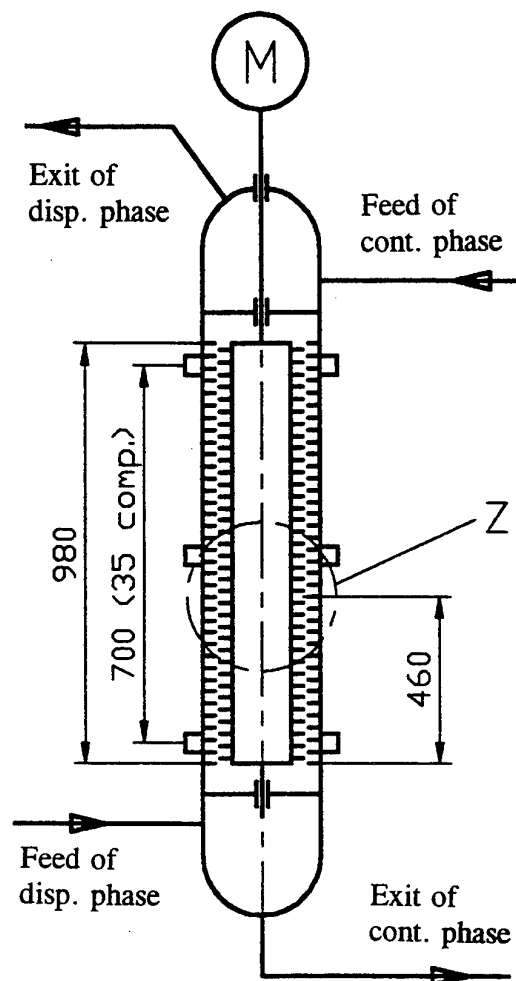


Fig. 1a RDC-column geometry

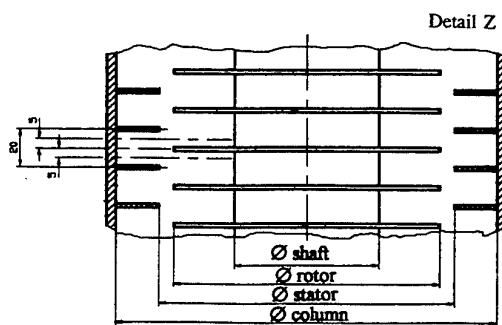


Fig. 1b Geometry of the column compartments

Table 1 RDC-column geometry and investigated range of operating conditions

	liquid/liquid dispersion of kerosene droplets in water column: RDC-150	suspension of PP-particles in water column: RDC-200
column geometry:		
inner diameter	148 mm	200 mm
stator diameter	105 mm	155 mm
rotor diameter	90 mm	140 mm
shaft diameter	54 mm	76 mm
compartment height	30 mm	20 mm
column height (active section)	2012 mm	980 mm
operating conditions:		
phase transport	countercurrent	cocurrent, countercurrent
continuous phase throughput	120 l/h	50 - 400 l/h
dispersed phase throughput	10 l/h	5 - 30 kg/h
rotor speed	300 rpm	250 - 550 rpm
dispersed phase holdup	5 %	4 - 15 %
LDA measurement technique	one-component LDA fibre optic system back scatter mode	two-component LDA back scatter mode

A mass flow meter was used to measure the flux and the density of the suspension flow.

The suspended polypropylene particles had a tendency to aggregate around entrained air bubbles. The resulting clusters had a different rising velocity compared to the freely suspended particles. Therefore the clusters may significantly influence the flow behaviour. For correct operation it was necessary to avoid this particle aggregation. This was achieved by operating the column section as a closed loop without free liquid surfaces.

2.2 Instrumentation and Measurement Techniques

Two different laser anemometer systems were used in this work with each chosen to suit the specific measurement application. For the liquid/liquid dispersion in the 150 mm diameter RDC a DANTEC one-component, Argon-ion, fibre-optic LDA probe, with back scatter collection was used since the measurement planes were located nearly 5 metres above floor level and physical access to the column was very restricted due to the scaffolding supporting the RDC. In the case of the solid/liquid suspension in the 200 mm diameter RDC where more complex measurements were to be attempted, but at 1.5 metres above floor level, a two-component, Argon-ion, radial diffraction based, back-scatter laser anemometer system was preferred. Both LDA systems are specified in Table 2.

The two-component LDA system has been described in detail by Pitcher and Wigley (1991) but the essentials will be given here with regard to this particular application where low mean velocities exist, less than 0.5 m/s, a correction for the differential refraction of the different wavelengths was made and a method for optical phase discrimination was found.

The principal components of the opto-mechanical system are the independent transmitters for the 488/514 nm wavelengths and a common receiver unit. The function of each transmitter is to split the incoming laser beam into two parallel, expanded output beams of equal intensity with a frequency shift between them. Each transmitter consists of three lenses arranged as a Newtonian beam expander with a rotating radial diffraction grating placed in the focal plane. The transmitters are identical, apart from the wavelength specific lens positions and the orthogonal orientation of the radial diffraction gratings and, therefore, of the output beam planes. The measurement volume is formed by the final focusing lens bringing each pair of beams together in a common focal spot.

The back-scattered light from the measurement volume is collected only through the central area of the final focusing lens. It is then reflected by a mirror into the receiver module. The receiver consists of two lenses, arranged as a Galilean telescope, to produce a magnified image of the measurement volume's cross-section on the adjustable pinhole before the photo-detector assembly. In front of the pinhole is a polarizing prism which is used to select either the vertical or horizontal polarized component of the received light.

After the scattered light has passed through the pinhole a wavelength separating prism splits the 488 and 514 nm wavelengths and directs them to their respective photo-detectors. The signals obtained from the photo-multipliers were processed by Frequency Counters. In calculating the mean velocity components each velocity sample was weighted with its residence time to overcome the velocity bias. The essential specification and operating characteristics of the laser anemometer system are summarised in Table 2.

Table 2. Specification of the Laser Anemometer System

	liquid/liquid dispersion of kerosene droplets in water column: RDC-150	suspension of PP-particles in water column: RDC-200
Laser Wavelength	514 nm	488 and 514 nm
Laser Power	100 mwatts	300 and 600 mwatts
Beam Diameter	1.35 mm	1.35 mm
Transmitter		
Beam Separation at final focusing lens	38 mm	50 mm
Beam Diameter	2.2 mm	5 mm
Focal Length of final focusing lens	160 mm	450 mm
Beam Intersection Angle	13.5 degrees	6.34 degrees
Fringe Spacing	2.07 μm	4.41 and 4.65 μm
Measurement Volume Diameter	50 μm	75 μm
Measurement Volume Length	510 μm	1080 μm
Number of Fringes	22	17 and 16
Receiver		
Measurement Volume Magnification	-	3.33
Pinhole Diameter	-	200 μm
Wavelength Separator	-	DANTEC 55X35
Photo-detectors	DANTEC 55X08s	DANTEC 55X08s
Frequency Processor	Covariance DANTEC 58N10	Counter, DANTEC 55L90a
Bandwidth	1.20 MHz	1 to 2 MHz

2.3 Measurement Techniques

The measurement of the mean and fluctuating velocity components and their profiles involved traversing the measurement volume, from 1 mm from the inside surface of the glass column to 2 mm from the rotor or the central shaft. At each measurement point 1,500 velocity samples were recorded. From these the mean and fluctuating (rms) velocity, the turbulence intensity and the skewness of the velocity distribution were calculated.

In performing this work 3 specific topics merit discussion here; they are the optical geometry of the RDC, the precision and accuracy of the velocity measurements and the discrimination between velocity measurements of the particle and liquid phases.

Optical Geometry. Cylindrical glass test sections, particularly when filled with a liquid, pose a problem for the application of optical diagnostics as they behave as cylindrical lenses and cause deviations and aberrations of the light transmitted into and out of the curved wall test section. In laser anemometry the plane of incidence of the beams must be either parallel to or normal to the column axis for the beams to intersect fully. However, the beam pairs will incur different deviations and aberrations such that the beam pairs would not come to a common measurement volume nor would the beam cross-section be circular. A simple method to alleviate this problem was to cement a square glass tank to the side of the glass column. The problem is reduced and is then dominated by refraction at the first flat glass interface.

The refraction of each input beam pair at the different optical interfaces results in a displacement of the measurement volumes inside the glass column. However,

since the refractive index is dependent on the wavelength of light there will be different displacements for the two measurement volumes formed by the 488 and 514 nm laser wavelengths. There will not be a constant displacement between the two measurement volumes as the final focussing lens is traversed due to the varying angle of incidence of the horizontal, 488 nm beams at the curved glass / water interfaces. With this laser anemometer system the small relative displacements between the two measurement volumes was corrected for by adjustment of the beam expander lenses in the 488 nm transmitter optics.

When the measurement volume was close to solid surfaces, e.g. the walls or rotor of the RDC, a high proportion of the received light can consist of surface reflected light. This reflected light will have the polarization of the input laser beam whereas the back-scattered light from the individual particles in the flow will be elliptically polarized. The polarizing prism in front of the pinhole was used to reject the horizontally polarized reflected light (the noise) and transmit only the vertically polarized component of the scattered light (the signal).

Precision and Accuracy. The frequency to velocity conversion factors for the wavelengths 488 and 514 nm are 4.41 and 4.65 metre/sec/MHz respectively. The accuracy with which these values can be determined is dependent only on the beam intersection angle which can be estimated to with +/- 0.5%.

The accuracy of the frequency measurement is determined by the stability of the frequency shift imposed by the rotating diffraction grating, the signal quality (signal/noise ratio) and the discretization of the frequency output from the Counter Processor. The diffraction grating motors were driven at their lowest stable speed, nominally a

rotation of 50 Hz. However, in practice each motor had slightly different speeds and stabilities. The best way of determining, not only the frequency shift value, but also the effects of signal quality and Counter Processor discretization, i.e. a reference of the system performance, was to perform a velocity measurement on a static surface. In performing this two-component reference measurement up to 5,000 coincident velocity data samples were collected and the mean and fluctuating velocity components calculated. These values were subtracted from the measured flow velocities to obtain accurate flow velocities. The motor speed controls had a slight temperature dependence so the offset values were recorded before and after a velocity measurement scan inside the RDC.

As stated above the lowest stable motor speed was 50 Hz, this produced a frequency shift of 1.6 MHz. This was in fact an optimum choice for the frequency bandwidth of 1.0 to 2.0 MHz that was available on the Counter Processor. This translates to a maximum velocity range of -2.78 to +1.86 metre/second. Whereas this velocity range easily accommodated the maximum horizontal and vertical mean and fluctuating velocity components measured, 0.2 and 0.4 m/s respectively, it unfortunately incurred a poor discretization resolution in the Counter Processor output due to the relatively high frequency shift value. An input signal frequency of 1.6 MHz would be recorded as 40,000 clock pulses for the 8 cycle measurement. The output resolution of the Counter Processor at this frequency is 64 clock pulses, i.e. the velocity resolution with which one sample would be obtained was 0.012 m/s. This does not represent the accuracy with which the mean and fluctuating velocities were measured since 1,500 velocity samples were collected at each measurement point and due to the turbulent nature of the flow a distribution of signal frequencies was spread over many frequency 'bins'. In general the mean flow velocity should be within 1%, with the fluctuating flow velocity better than 5%. Even if it had been possible to maintain a perfectly stable frequency shift at lower frequencies it would have brought little benefit since the optical noise frequency spectrum, caused by particle/laser beam interactions at high particle loadings, extended up to 0.5 MHz.

Discrimination Between Particle / Liquid Phases.

In the study of multi-phase flows it is essential to try to separate the flow data from the different phases. In this two-phase work it was necessary to devise a technique by which one could discriminate between signals coming from a seed particle, that was representative of the continuous liquid phase, and those coming from the particulates of the dispersed phase. The seeds were essential for the continuous liquid phase, the water supply was very clean. Toray SP-500 nylon particles of mean diameter 5 microns and specific gravity 1.02 were used while the dispersed phase consisted of polypropylene particles with diameters in the range 200 to 500 microns.

The ideal technique would be Phase Doppler Anemometry (PDA) where the velocity and size of particles can be measured simultaneously. However, many attempts

at phase discrimination have been made with LDA. Many of these have relied on the fact that the scattered signal is a squared function of the particle size so the problem reduces to one of signal amplitude discrimination. Another method has considered the modulation depth, or visibility, of the signals; seeds smaller than the fringe spacing would give well modulated signals whereas particles approaching the size of the measurement volume diameter would generally give a poorly modulated signal. It was also considered that the signal transit time, or the number of fringes crossed, be used to discriminate between the phases.

In practice it was found that the seed and particle signals, i.e. the AC components, were of a similar amplitude and that the envelope of a particle signal could fluctuate above and below the signal validation threshold. A single particle would therefore produce multiple velocity measurements each with a low fringe count. Furthermore, it must be noted that the multiple velocity measurements were not necessarily single valued. It was suggested that particle translation and rotation were both contributing to the signal frequency.

So, while it was easy to discriminate the seed and particle signals by monitoring them on an oscilloscope it was not possible with the present hardware setup, or in software, to discriminate data from the different phases. However, it was found that a slight misalignment of the pinhole in the receiver with the image of the measurement volume could discriminate against the seed signals. This is due to the nature of the Gaussian intensity distribution across the measurement volume and that its diameter has to be considered as a function of the particle size. Particles travelling through the outer regions of the measurement volume will produce a validated signal; seeds will not. The phase discrimination therefore consisted of two measurements, the first, with the pinhole centred on the measurement volume image, and the second, with it off-centred. The former measures the behaviour of the two-phase flow, seeds plus particles, while the latter measures only the particle flow. A comparison of the two measurements then allows the flow of the two different phases to be inferred. In principle the seeds could have been removed from the system to achieve a better two-phase discrimination.

3. CHARACTERISTIC PROPERTIES OF THE INVESTIGATED TWO-PHASE SYSTEM

Particle motion in two-phase flows can result in modification of the turbulence fluctuations in the continuous phase and may even influence the mean flow pattern; Alajbegovic et al. (1994). Turbulence, damping or enhancement may occur according to the phase density difference and to the specific particle inertia and particle drag force regime; Yarin & Hetsroni (1994).

Therefore it is important to classify the dispersed flows under investigation by quantifying the dynamics of the droplet and the particle transport relative to the continuous phase motion. The physical properties and the transport

Table 3: Physical properties and fluid-mechanic characteristics of the two-phase flows.

	liquid/liquid dispersion of kerosene droplets in water column: RDC-150	suspension of PP-particles in water column: RDC-200
dispersed phase droplet-, particle diameter density	kerosene 0.5 - 5.0 mm 760 kg/m ³	polypropylene particles 0.2 - 0.5 mm 910 kg/m ³
continuous phase	water	water
representative droplet-/particle diameter	2 mm	0.4 mm
volume fraction of dispersed phase, ϵ []	0.05	0.05
particle number concentration	1.2×10^7	7.6×10^8
mean dimensionless particle distance l_{av}/d_p	2.5	2.5
particle relaxation time, τ_p [s]	0.175	0.010
particle terminal velocity, v_p [m/s]	0.08	0.006
particle Reynolds number, $Re_p = d_p v_p / \nu_c$	1160	2
Eulerian integral length scale, Λ [mm]	ca. 2	ca. 0.2
Eulerian integral time scale, $\tau_{E,f}$ [s]	ca. 0.02	ca. 0.003
Stokes number $St = \tau_p / \tau_{E,f}$ []	9	3

characteristics of both two-phase flows are summarized in Table 3. In the calculations the representative drop diameter was taken as $d_p = 2.0$ mm for the dispersion and $d_p = 0.4$ mm for the particles respectively. For the experiments performed at a fixed dispersed phase volume fraction of $\epsilon = 0.05$ the dimensionless particle distance $l_{av}/d_p = 2.5$ remains identical for the particles and the droplets. Due to their small density difference and their small size the single particle terminal velocity is much lower than the corresponding velocity of the droplets. This is also reflected in the particle Reynolds number, indicating that the drag force of the particles is still in the Stokes regime. The particle relaxation time was calculated by taking into account only the contribution of the Stokes drag for the particles as well as for the droplets. The relaxation time of the droplets is one order of magnitude higher than that of the particles. This is due to their large inertial force and their small drag coefficient (approx. unity) compared to the particles ($C_D \approx 20$). This preliminary quantification demonstrates that the small particles can be expected to follow the carrier fluid flow more closely than the larger kerosene droplets.

From the quantities given in Table 3 it follows, that the kerosene droplets move, within their relaxation time, a distance of 10-15 mm relative to the carrier fluid, that is about 5-10 times their diameter. The equivalent distance for the particles is only in the order of 0.05 mm, a fraction of the particle diameter.

4. EXPERIMENTAL RESULTS

4.1 Compartment Flow-Patterns

The velocity measurements were made on a radial traverse of the column and confined to one representative compartment, i.e. between a pair of stator rings close to the half height of the column, see Figure 1b. Velocity

measurements were obtained for both columns each operating with the continuous phase only and then with the two phase flow.

In the case of the suspension in the RDC-200 comparing single-phase and two-phase flow operation, the overall mean flow patterns remain identical. This demonstrates that the PP-particles with their low density difference follow the continuous phase flow rather closely. The continuous phase axial velocity profiles for the RDC-200 at rotor level are shown in Figure 3 for three different rotor speeds. A close similarity of the single-phase and the corresponding suspension two-phase flow patterns was found.

Contrary to what one would expect from the analogy to stirred tank flow patterns, the flow field in the RDC-compartment is dominated by only one circulation region filling the outer space between rotor edge and column wall. Increasing rotor speed clearly shows a tendency to enhance the circulatory motion, see Figure 3a, as it shifts the tangential velocity component as well as the axial and tangential fluctuation velocity components towards higher values, see Figure 3b and 3c. Data for the the axial and tangential fluctuation, Figure 3c indicate the turbulence to be locally isotropic for the three rotor speeds investigated. This also holds in the case of single-phase operation.

Contrary to the findings for the particle motion in the suspension the motion of the droplet swarm modifies the continuous phase flow pattern. For the RDC-150 column the flow pattern in the axial/radial plane in the dispersion is dominated by one circulation region only. Comparing the profiles of the mean axial velocity components at rotor level for the single-phase and the two-phase case a change in the direction of the circulation region is observed; Figure 4a. In single-phase flow the fluid motion is directed downward at the rotor edge and upward near the column wall, opposite to the behaviour that occurs in the two-phase case. Under the chosen operating conditions the dispersion is rather dilute. In this case the droplet swarm moves along prevered paths.

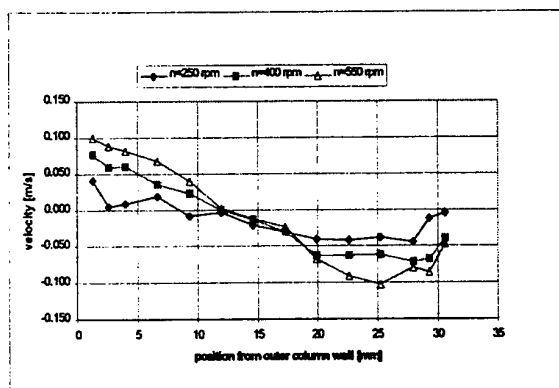


Fig. 3a Mean axial velocity of the continuous phase in the suspension

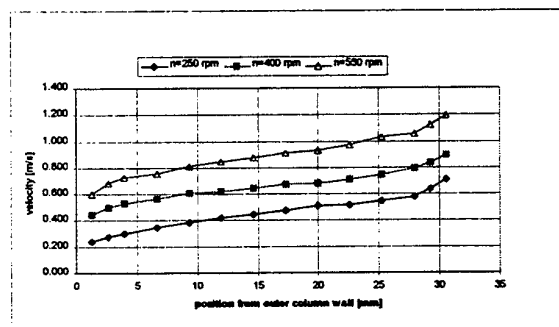


Fig. 3b Mean tangential velocity of the continuous phase in the suspension

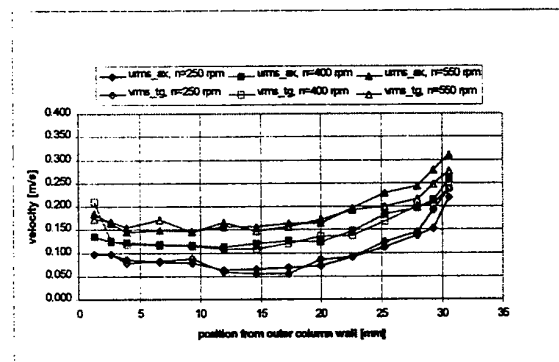


Fig. 3c Axial and tangential velocity fluctuations of the continuous phase in the suspension

Figure 3 Velocity profiles at rotor level for RDC-200 for three different rotor speeds.

Visual observation shows the droplets to accumulate under the stator rings and partially also under the rotating disks, where they are centrifuged outward. From there the droplets take the shortest way upward, round the rotor edge, to the next stator ring. This results in a kind of zig-zag motion of the drops through the column compartment and leads to an inhomogeneous distribution of the drop volume fraction. The flow pattern shift from single-phase to two-phase flow

operation is associated with a shear force acting on the continuous phase by the rising droplets near the rotor edge.

In single-phase flow again local isotropic turbulence is found in the fluid bulk; Figure 4b. Deviation from isotropy exists only in the close vicinity of the rotor edge. In the two-phase case the deviation from isotropy increases near the rotor; Figure 4c. As mentioned before the upward movement of the rising droplet swarm occurs in exactly that region. It is important to notice, that the turbu-

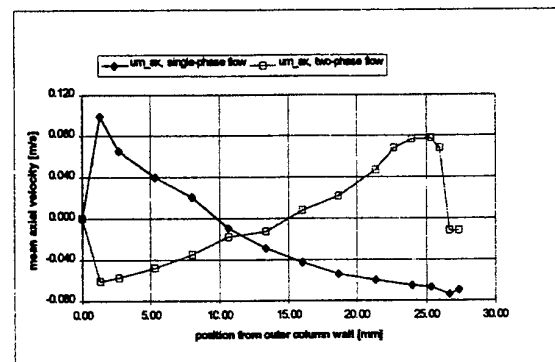


Fig. 4a Mean axial velocity components of single-phase and of liquid/liquid two-phase flow operation; rotor speed $n=300$ rpm

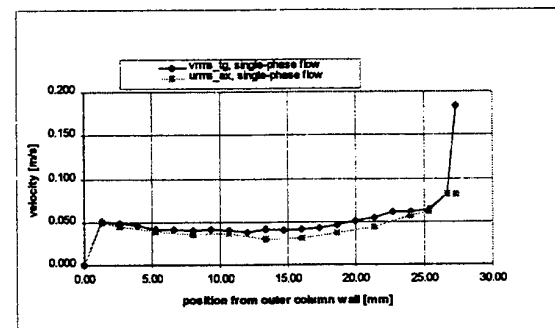


Fig. 4b Axial and tangential velocity fluctuations of single-phase flow; radial profiles at rotor level

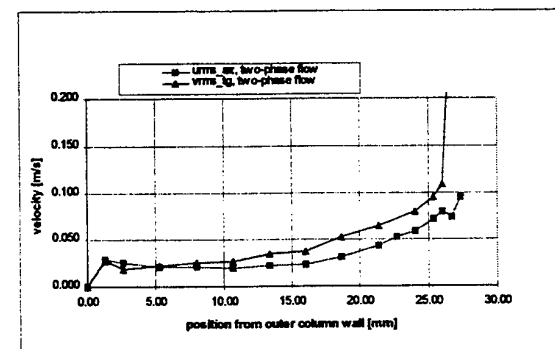


Fig. 4c Axial and tangential velocity fluctuations of the continuous phase in the dispersion

Figure 4 Radial profiles at rotor level; column RDC-150

lence level in the compartment, related to the profile of the mean axial velocity component, is at least 50% and locally reaches 100% magnitude. This demonstrates that the overall flowpattern in the axial/radial cross-section has a strong superimposed fluctuating velocity component and therefore the instantaneous flowfield in the compartment shows a stochastic nature.

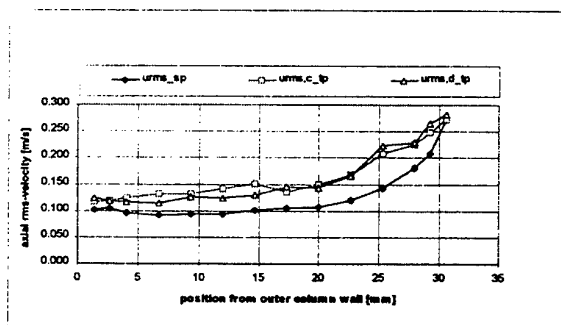


Fig. 5a Column type: RDC-200, rotor speed $n=400$ rpm;

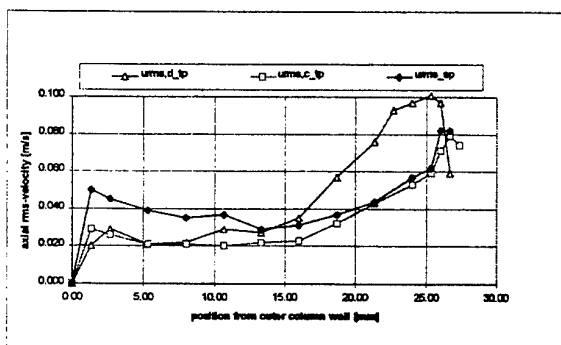


Fig. 5b Column type: RDC-150, rotor speed $n=300$ rpm;

Figure 5 Radial profiles of turbulent axial velocity fluctuations at rotor level in single-phase and two-phase operation; $urms_{sp}$, rms-velocity of single-phase flow; $urms_{c,tp}$, rms-velocity of the continuous phase at the two-phase flows; $urms_{d,tp}$, rms-velocity of the particles (Fig. 5a) and the droplets (Fig.5b) at two-phase flow

4.2 Comparison of the Turbulence Intensity of the Single-Phase and the Two-Phase Operation

The suspension in the RDC-200 experiment clearly exhibits an enhancement effect on the continuous phase turbulence. This is demonstrated in Figure 5a which shows the profiles of the axial fluctuation velocity component for the single-phase flow and for the continuous phase as well as for the particulate phase in two-phase flow. Although the particles seem to follow the carrier fluid motion closely, they have a significant impact on the turbulence level. The same effect was experimentally demonstrated also for rotor speeds of 250 rpm and 550 rpm. The corresponding profiles for the liquid/liquid-dispersion are shown in Figure 5b. The turbulence intensity of the continuous phase in the two-phase case is lower or approaches the maximum for the single-phase level near the rotor. The large droplets move in the vicinity of

the rotor and their fluctuation intensity is higher than that of the carrier fluid. The detected dispersed phase velocity signals in the outer column region are mainly caused by small droplets, which are entrained in the continuous phase eddies. Therefore the fluctuation intensity of the dispersed phase approaches that of the continuous phase in the outer column region.

5. DISCUSSION AND CONCLUSION

Two different kinds of dispersed flows in pilot sized extraction columns of the rotating disc contactor (RDC) type have been analyzed by means of laser anemometry. A kerosene/water system was used as a two-phase flow model to study the behaviour of liquid/liquid dispersions in the extraction column. These findings have been compared with the results for a suspension flow of particles in water.

The particle swarm shows a negligible influence on the continuous phase flowpattern in the compartments of the column. The particle motion does not induce a deviation from the clearly established local isotropy of the carrier fluid flow. The rotor speed seems to be the dominant factor for the generation of the overall compartment flow pattern. Surprisingly the particle/fluid relative movements lead to a clear enhancement in the continuous phase turbulence. Although the particles have a small density difference compared to the continuous phase and therefore exhibit a small stationary slip-velocity.

Contrary to that the kerosene droplet swarm totally rearranges the column flow pattern. This is associated with turbulence intensity damping and with a significant loss of turbulence isotropy.

REFERENCES

- Abid, K.H. & Godfrey, J.C. 1993, Requirements for Liquid-Liquid Dispersion Studies with a Matched Refractive Index System, *Proceedings of Int. Solvent Extraction Conf.*, York, vol. 1, pp. 499-505
- Alajbegovic, A., Assad, A., Bonetto, F., Lahey Jr., R.T. 1994, Phase Distribution and Turbulence Structure for Solid/Liquid Upflow in a Pipe, *Int. J. Multiphase Flow*, vol. 20, pp. 453-479
- Godfrey, J.C. & Slater, M.J., eds. 1994, *Liquid-Liquid Extraction Equipment*, John Wiley, Chichester
- Masbernat, O., Gourdon, C. & Casamatta, G. 1993, Local Measurements in a Dense Two-Phase Liquid Flow, *Chem. Eng. Sci.*, vol. 48, pp. 3225-3242
- Pitcher, G. & Wigley, G. 1991, The design and application of a two-component LDA system to study engine flows, *Proceedings of Laser Anemometry - Advances and Applications ASME, Cleveland*, vol. 1, pp.179-189
- Yarin, L.P. & Hetsroni, G. 1994, Turbulence Intensity in Dilute Two-Phase Flows 3. The Particle-Turbulence Interaction in Dilute Two-Phase Flows, *Int. J. Multiphase Flow*, vol. 20, pp. 27-44

INSIGHTS INTO GRAIN ENTRAINMENT USING PARTICLE IMAGE VELOCIMETRY

M.W. Gallagher and I.K. McEwan

Department of Engineering
Fraser Noble Building, University of Aberdeen, UK

ABSTRACT

One of the key elements in achieving accurate prediction of grain entrainment rates is the understanding of the near bed flow structures. Research has revealed that the turbulent boundary layer structure over smooth beds is not random but shows some degree of coherence. Questions arise as to whether similar patterns of flow structure occur over natural river beds, where the influence of roughness elements and mobile grains may be of relevance. The aim of the work reported here was to conduct experiments which would identify key flow structures over sediment beds and thus examine their influence on grain entrainment.

Flow field measurements were made over natural and fixed sediment beds using Particle Image Velocimetry (PIV). A short time series of near instantaneous velocity field measurements has been recorded to aid the identification of flow structures and the study of their evolution. Analysis has identified two scales of flow structure, one possibly scaling with grain size or bed features and the other with flow depth, and has also enabled assessment of the potential of each of these scales to entrain grains. The distribution of these flow structures appears to be related to the transport rate.

1. INTRODUCTION

Sediment movement can cause permanent changes in the form and character of a river. It is therefore of great importance to be able to predict the movement of sediment resulting from the flow conditions. There are a number of existing formulas which have been developed to predict sediment transport rate but results can be highly inconsistent even when applied to similar problems. This level of uncertainty would in many engineering disciplines be considered unsatisfactory and could potentially have serious consequences for river engineering works. One of the reasons for the wide scatter of results found, is the lack of understanding of the processes involved in grain entrainment. This is a complex problem involving many

important factors such as bed roughness, particle shape and flow character, including turbulence. It is acknowledged that turbulent fluctuations occurring over a sediment bed are important in the grain entrainment process (Grass, 1970). Many experiments conducted in a natural rivers have reinforced this point and shown the importance of temporal and spatial variations in the near bed flow regime. Experiments conducted by Drake *et al* (1988), using motion picture photography, studied the different modes of sediment transport. The results showed that 70% of the total bedload transported was due to frequent but apparently random sweep events which effected localised areas of the bed. This suggested that grain entrainment is predominately effected by fluid forces rather than other processes such as the impact of moving grains.

Grain entrainment occurs when the forces produced by the fluid exceeds the resisting forces of the grains in the bed. Grass (1970) used this concept to introduce a novel idea that the entrainment rate could be determined from the overlap of two probability distributions as shown in figure 1. The first probability distribution is of the fluid shear

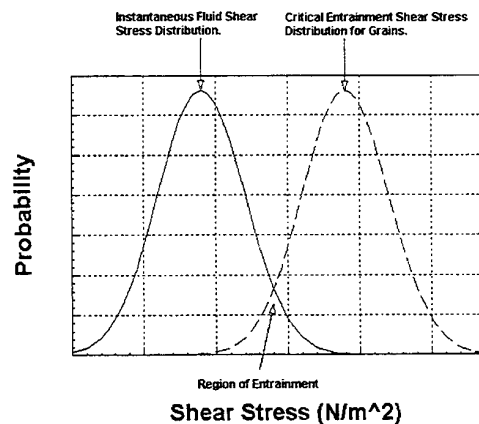


Fig. 1 The probabilistic concept of entrainment introduced by Grass (1970)

stress applied to the bed by the turbulent flow. The value of fluid shear stress is dependant on the type turbulent fluctuation experienced by bed. The second distribution is the critical shear stresses needed to entrain a given particle size from a mixed grain size surface. This variation in critical shear stress is due to differences in the surface topography of mixed grain sized sediment beds. Therefore entrainment is not only dependant on grain size but on location so that significant variability in threshold conditions is found within a given grain size class. The entrainment rate depends on the extent of the overlap between the two distributions and in particular the detailed shape of their tails. This concept has not yet been used in engineering calculations because neither distribution has yet been adequately quantified. More research is needed on the turbulent flow structures near the bed before a probability distribution of the important fluctuations can be determined.

The work presented here firstly describes experiments conducted to investigate the spatial behaviour of the turbulent flow field close to a sediment bed, and secondly identifies potential key flow structures in the grain entrainment process.

2. THE NEAR BED FLOW STRUCTURE

It was initially thought that the turbulent flow structure consisted of random fluctuations which were imposed on an otherwise steady flow. Research on the structure of turbulent boundary layers (Kline *et al* (1967) ; Grass (1971)) has revealed that the temporal and spatial variations in the flow are not entirely random but show some degree of coherence. This had resulted in the discovery of a number of organised events in the flow which are now more commonly known as coherent flow structures. From the literature on this subject Best (1993) has categorised what he perceives to be the main structural features within a turbulent boundary layer.

(i) Low speed streaks which are said to have a velocity of approximately half the mean local velocity. These structures are laterally spaced and occur within a region of 10 wall units above the boundary (where a wall unit $\equiv yU^*/\nu$, y is the height above the boundary, U^* is the shear velocity and ν is the kinematic viscosity). Observations of the streaks have shown that they meander with this tendency increasing with height (Kline & Robinson 1990). The streaks are also very persistent lasting for a distance of hundreds of wall units in the streamwise direction. The majority of observations of this have been over smooth beds although Grass *et al* (1991) has observed similar features over a organised rough bed of 12mm marbles.

(ii) Regions of low speed fluid rising from the boundary, known as ejections. The occurrence of this structure is thought to be due to the rising of the low speed streaks.

(iii) Regions of high speed fluid moving towards the wall, known as sweeps. It has been stated that a possible relationship exists between sweeps and ejections. (Offen & Kline, 1974,1975)

(iv) Large scale vortical structures which comprise a wide range of structures such as the horseshoe or hairpin vortices as reported by many researchers (e.g. Head & Bandyopadhyay (1981), Smith *et al* (1991)).

These coherent flow structures have been categorised using experimental data mainly obtained from smooth beds and therefore the structure of the near bed flow is likely to be due to instabilities within the viscous sublayer. However in natural rivers there is additional complexity due to particulate transport and a deformable boundary. In this case the structure of the near bed flow is dominated by pressure variations created by the roughness elements. This would suggest that flow structures created in this way should be scaled with the roughness elements. The two different methods of flow structure production have raised doubts over whether the behaviour of the structures is similar in the smooth and rough wall experiments.

3. EXPERIMENTAL WORK

A series of flume experiments have been conducted to examine the spatial variations of the flow over mixed sized sediment surfaces, and to determine the key coherent flow structures involved in grain entrainment. The first series used a technique known as particle image velocimetry to record flow field measurements over a fixed bed. A second series of experiments were conducted over the same fixed bed which involved the introduction of sediment grains into the flow upstream of the measurement area. The same techniques were used to examine the flow in this case, thus enabling significant changes between the two series to be identified. Both horizontal and vertical planes of the flow were investigated in these series (at different times) in order to obtain an understanding of the three dimensional nature of the flow. A third series of experiments was also conducted over a natural sediment bed involving a different flow condition to the previous experiments.

3.1 Measurement Technique

In the past observations of coherent flow structures have been obtained using single point measurement techniques such as laser doppler anemometry. These have yielded useful results on the temporal behaviour of the near bed flow structure. However using techniques such as this make it difficult to interpret how the temporal variations at one point immediately effect fluid in the surrounding areas. Therefore a measurement technique was adopted which enables near instantaneous spatial measurements of the flow field to be obtained. This technique is called particle image velocimetry. This system relies on a laser light sheet

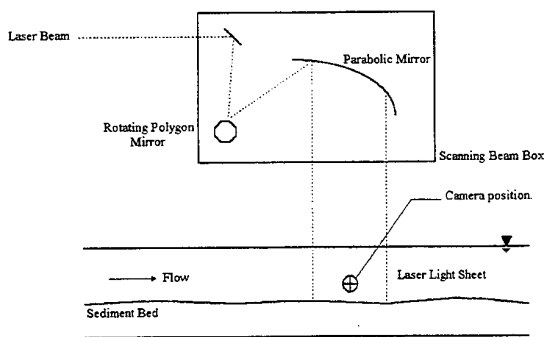


Fig. 2 A schematic diagram of the scanning box system

illuminating an area of flow which has been seeded with small neutrally buoyant particles. Figure 2 shows the scanning beam system used to produce the laser light sheet. A camera was placed at right angles to the light sheet and due to a selected shutter speed the particles were captured several times during each frame. This provided a displacement record of each particle as can be seen in figure 3. The time interval between the illuminated particles was dependant on the speed of the rotating mirror, enabling velocities to be calculated from the image.

3.2 Experimental Set-Up

A recirculating glass sided flume 12.5 m long and 0.3 m wide was used for the experimental work. The first experiment was conducted over a fixed bed so that flow structures identified could be attributed to the roughness elements. The fixed bed comprised of a number of sections which were made using cement. A sediment mixture was then placed on the surface of the cement and allowed to set. The sediment mixture had an average grain diameter of 1.92 mm and its distribution can be seen in figure 4, grade 1. Each of these sections were 0.5 m long and 0.3



Fig. 3 A typical Particle Image Velocimetry image

m wide and were pushed firmly together to fill the whole of the flume. The slope of the channel was adjusted to 1/500 and uniform flow conditions set with a flow depth of approximately 78 mm and discharge of 10 l/s. The flow was then seeded with conifer pollen with a diameter of 50 μ m. The laser light sheet scanned across the centre line of the flume, and the camera was positioned to record an experimental flow area immediately above the bed of approximately 65 mm in the streamwise direction and 49 mm in the vertical direction. The camera had a resolution of 752 by 582 pixels and recorded 25 frames a second. All the images were time coded and recorded on video tape for subsequent analysis. This enabled a time series of spatial images to be analysed which aided the study of the temporal evolution of flow structures. A second set of measurements were made in the presence of mobile grains with a mean diameter of 0.8 mm. These were fed into the flume 3.6 m upstream of the measurement area at a rate of 0.003 kg/s/m. Differences between the two sets of results could then be attributed to the influence of the mobile grains.

Turbulent flow is three dimensional and so it was decided to obtain spatial images in a near bed horizontal plane. In the horizontal case the scanning beam box was placed on its side and the laser light sheet scanned horizontally across the flow at a height of 5 mm above the bed. The camera was positioned such that the line of sight was vertical and thus normal to the horizontal light sheet, the viewing area was 73 mm in the streamwise direction and 55 mm in the transverse direction. The above procedure was repeated and flow measurements were once again taken before and during the feeding

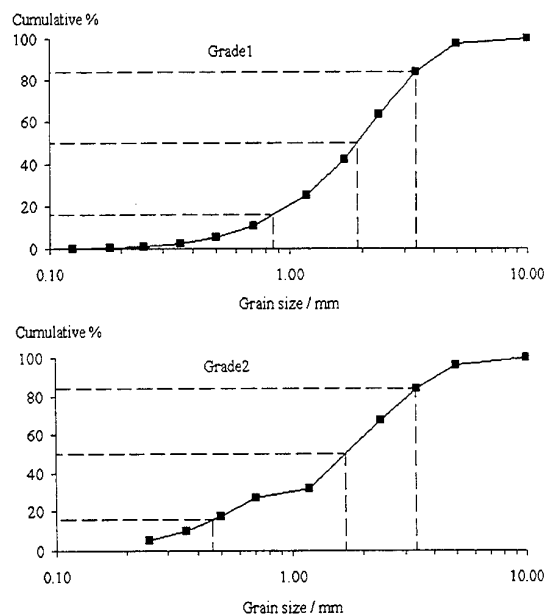


Fig. 4 Sediment distribution curves

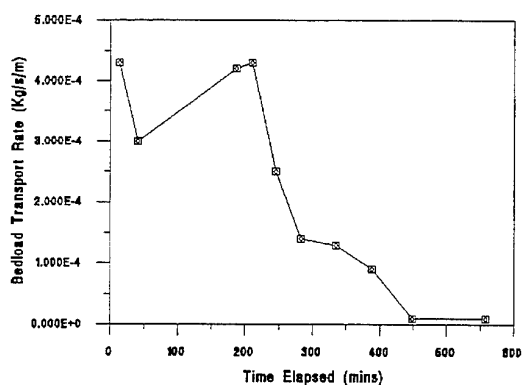


Fig. 5 Plot showing transport rate against time for experiments conducted over natural sediment mixture.

process.

Associated experiments were also conducted over a natural sediment mixture and are described in detail in Tait S.J. , Willetts B.B. & Gallagher M.W. (1996). In these experiments the sediment had an average grain diameter of 1.64 mm and its distribution can be seen in figure 4, grade 2. The slope of the channel was adjusted to 1/750 and the sediment was laid along the base of the flume and levelled. Uniform flow conditions were set with an average water height of approximately 63.6 mm and a discharge of 7.0 l/s. The sediment transport rate reduced with time due to the bed armouring, see figure 5. Again PIV was used to take flow field measurement along the centre line of the channel this time for an area of 45 mm in the streamwise direction and 30 mm in the vertical direction. Flow measurements were taken at 25 minutes and 275 minutes into the experiment. These times corresponded to high and low transport rates respectively.

3.2 Image Analysis

The recorded images were digitised for use in a PIV analysis package (Gray, 1994) which allowed a grid of near instantaneous velocity vectors to be calculated for any given frame. The analysis procedure involved splitting a digitised image into a grid of interrogation areas. The interrogation areas were 32 by 32 pixels in size corresponding to a physical flow area of the order of 2 mm by 2 mm and each overlapped the adjacent areas by 50%. This resulted in each image consisting of 1598 interrogation areas. Each area was then analysed using correlation techniques developed by Gray (1994). The correlation routine found the average displacement of the particles within an area. Division of the value by the time interval between each particle resulted in a flow velocity vector which was positioned at the centre of the interrogation area. Therefore on completion of the analysis each image consisted of 1598 near instantaneous flow velocity vectors. However errors did occur in some of the

vectors calculated due to the correlation routine incorrectly computing the average displacement. This was usually due to a low concentration of seeding within an interrogation area. The image analysis software incorporates a validation routine to eliminate suspect vectors. The routine works by selecting each vector and calculating a comparative value from surrounding values using the least squares method. Any vector which varies from the comparative value by a selected deviation is considered erroneous and deleted. In the experiments conducted 5% of the values were erroneous in the vertical slice images and 13% in the horizontal images.

To aid visual inspection of the flow field, horizontal slice vector maps were split into streamwise and transverse components and vertical vector maps were separated into streamwise and vertical components. This information was used to produce a time series of contour maps which aided the identification of flow structures. The time series for experiments conducted over the fixed bed consisted of 125 frames of experimental data, covering an interval of 5 seconds. In experiments conducted over the natural bed 25 frames were studied covering an interval of 1 second.

4. EXPERIMENTAL RESULTS

4.1 Horizontal Slice Experiments

The first condition studied was the horizontal plane experiments conducted over the fixed bed. Inspection of the streamwise velocity components revealed that longitudinal strips of low and high speed fluid existed. These structures were observed both before and during the grain feeding process. This type of structure can be seen in figure 6, where the height is representative of the streamwise velocity component. The diagram shows a distinct trough which represents a strip of low speed fluid

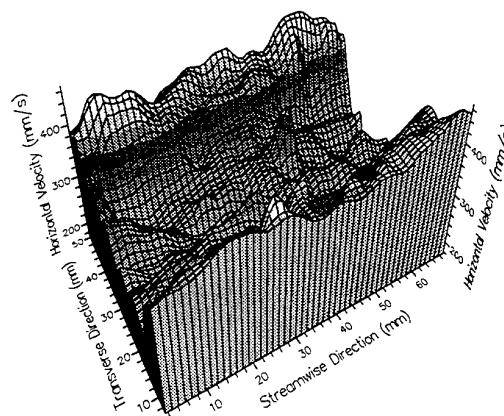


Fig. 6 A typical streamwise low speed velocity strip.

which has a velocity of approximately 310 mm/s. This is bounded on its outer edges by higher speed fluid moving at approximately 410 mm/s. As this diagram shows the length of the strips were in some instances longer than the analysis image length of 68 mm. The structures were not particularly persistent over any localised areas of the bed and could not be identified in all images. Therefore a particular region of the bed experienced both high and low speed fluid throughout the analysis periods. This meant the vertical slice experiments were not dominated by particular persistent flow structures and thus measurements taken along the centre line of the flume are representative of the general flow.

With respect to grain entrainment it was likely that the high speed velocity strips are important but it was also interesting to note the potential importance of transverse velocity fluctuations. In some instances the transverse velocities were as much as 20 % of the streamwise velocities. These transverse fluctuations may be important in respect to grain entrainment as a grain may be relatively stable in the streamwise direction but relatively unstable in the transverse direction due to the orientation of the supporting grains. It is therefore desirable to obtain a full understanding of these transverse fluctuations as many current sediment transport models do not take them into account.

4.2 Vertical Slice Experiments

Examination of the time series from the vertical plane experiments showed the existence of a number of organised flow structures. There were two types of variation observed, the first being areas of downward moving fluid which may be related to the reported sweep events, and the second being areas of upward moving fluid which may be related to the reported ejection events. The sweeps and ejections were observed to occur at two different scales over the bed. At the smaller scale sweeps and ejections are millimetres in size, possibly scaling with grain size or bed features and occur close to the bed. Figure 7 is a vertical velocity contour map which reveals a small scale ejection from the bed occurring at position [A]. The structure is rising at a speed of approximately 20 - 40 mm/s at an angle of approximately 18 degree's and is about 10 mm in height at the instant of observation. The second scale involves much larger structures such as the large scale sweep shown in figure 8. The centre of the structure is at position [B] and is moving downwards at approximately 20 - 40 mm/s. As the figure shows this type of structure could fill the whole of the analysis measurement area (32 mm, 22 mm) and is possibly scaled with the flow depth. The correlation between vertical and streamwise velocities revealed that large

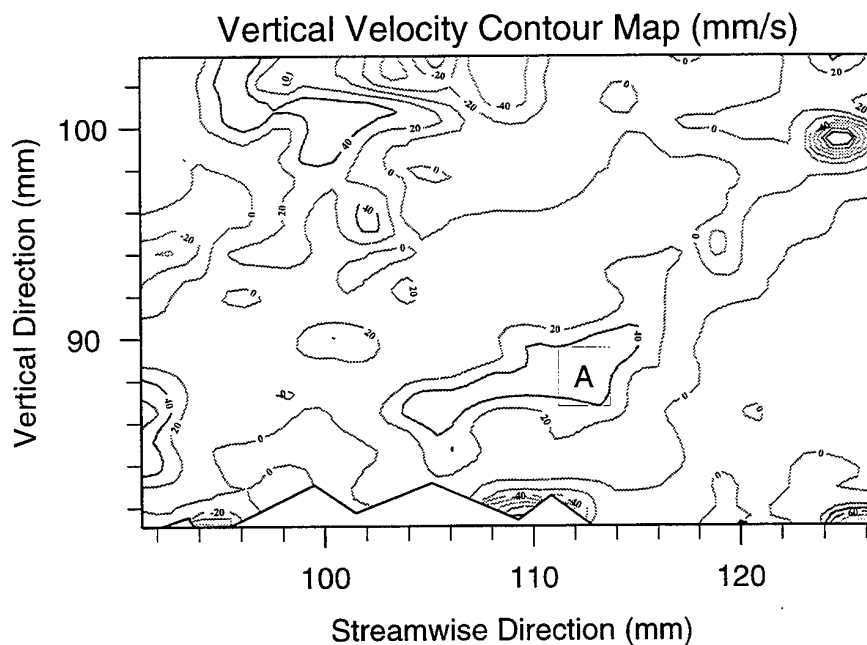


Fig. 7 Vertical velocity contour map showing a small scale ejection.
Note part of the bed can be seen positioned at the bottom of the flow measurement area.

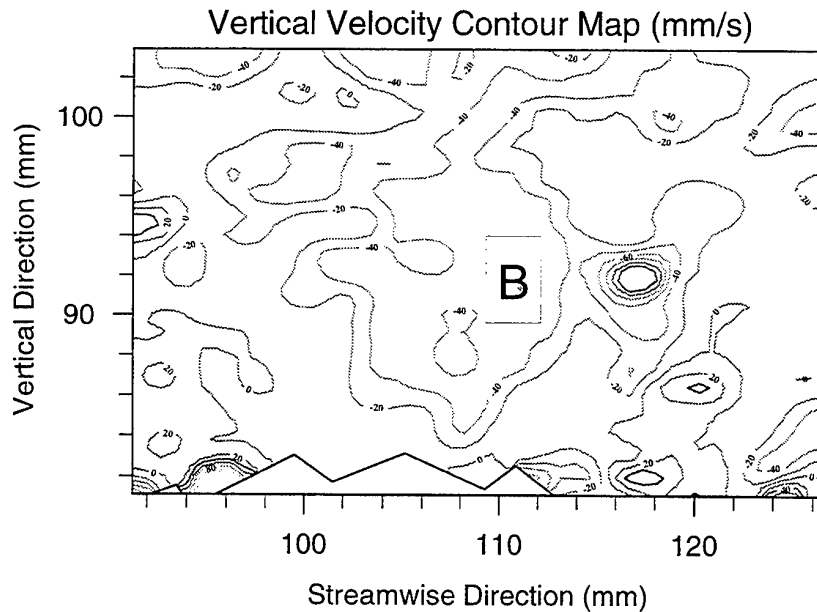


Fig. 8 Vertical velocity contour map showing a large scale sweep.
Note part of the bed can be seen positioned at the bottom of the flow measurement area.

scale sweeps were associated with high streamwise velocities, and the large scale ejections were associated with low streamwise velocities. This can be seen in figure 9 where the average horizontal velocity has been plotted with the average vertical velocity for each frame. The average horizontal and vertical velocities were obtained by summing the respective components of each vector in a frame and dividing these values by the number of vectors. A positive average vertical velocity component indicates a

net movement upwards whereas a negative value indicates a net movement downwards. The data clearly shows that a peak in the average horizontal velocity corresponds with a trough in the average vertical velocity component and vice-versa. It is for this reason that the large scale sweep is possibly the most influential flow structure in terms of grain entrainment. Experiments by Drake *et al* (1988) have indicated the importance of these sweep structures. He observed that 70 % of the total bedload moved was due to frequent, localised random sweep events.

The small scale structures showed some degree of coherence with small scale ejections being followed by small sweeps of similar magnitude. This pattern is to be anticipated if continuity is to be satisfied. Although only a short time series is shown figure 9 demonstrates this concept by showing the cyclic behaviour of net movements up and down, indicating an almost periodic interchange between ejections and sweeps. However this pattern is disrupted when the larger structures come close to the bed. The larger structures also shared some agreement with continuity but there were some instances when a series of large scale sweep and ejections occurred without the appropriate return of fluid. Instances such as this emphasise how care must be taken with interpretation of the results as the flow is three dimensional and the experimental data is two dimensional. This reinforces the need for a better understanding of the transverse fluctuations and their connection with vertical fluctuations.

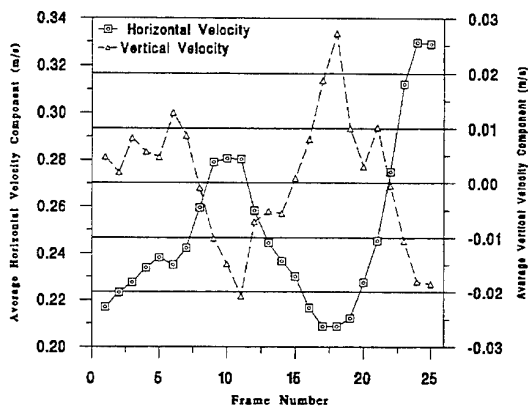


Fig 9. Correlation between Horizontal and Vertical velocities

Preliminary experimental results so far have indicated that the large scale sweep events occur more frequently over the mobile bed. This would suggest that the distribution of flow structures change with differing sediment activity, however this is based only on a relatively short time series.

5. CONCLUSIONS

The series of experiments presented here has identified a number of flow structures which are present over a sediment bed and are likely to be important in the process of grain entrainment. Experiments revealed that the flow field in the vertical plane over a sediment bed consists of two types of structure, the first being areas of downward moving fluid which may be related to the reported sweep events, and the second being areas of upward moving fluid which may be related to the reported ejection events. Both of these structures occur at two different scales above the bed, one possibly scaling with grain size or bed features and the other possibly scaling with flow depth. The most influential flow structure in respect to grain entrainment is probably the large scale sweep as these were accompanied by higher than average horizontal velocities. There was evidence to suggest that these flow structures became more frequent in periods of high transport. Even though only a short time series was analysed, the suggestion is that the distribution of flow structures is related to the transport rate.

Further experiments are needed to investigate the significance of transverse fluctuations as instances have been observed where the magnitude of the transverse velocities has been as much as 20% of the streamwise velocities. Fluctuations of this magnitude may be potentially important in respect to grain entrainment.

More images covering a wider range of conditions need to be examined before a more complete description of the origin and frequency of important flow structures is attained, and improvements can therefore be made to current transport rate prediction methods.

REFERENCES

Best, J. 1993, On the interactions between turbulent flow structure, sediment transport and bed form development:

- Some considerations from recent experimental research, in Turbulence: Perspectives On Flow and Sediment Transport, ed. Clifford, N.J., French, J.R. & Hardisty, J., pp. 61-92, John Wiley & Sons Ltd.
- Drake, T.G., Shreve, R.L., Dietrich, W.E., Whiting, P.J. & Leopold, L.B. 1988, Bedload Transport observed by motion-picture photography, J. Fluid Mech., vol. 192, pp. 193-217.
- Grass, A.J. 1970, Initial instability of fine bed sand, J. Hydraul. Div., ASCE, vol 96, pp. 619-632
- Grass, A.J. 1971, Structural features of turbulent flow over smooth and rough boundaries, J. Fluid Mech., vol. 50, pp. 233-255.
- Grass, A.J., Stuart, R.J. & Mansour-Tehrani, M. 1991, Vortical structures and coherent motion in turbulent flow over smooth and rough boundaries. Phil. Trans. Roy. Soc. Lon. A, vol 336, pp 35-65.
- Gray, C. 1994, Vipiv for Microsoft Windows: Analysis tools for Particle Image Velocimetry, Optical Flow Systems, University of Edinburgh, pp 1-63.
- Head, M.R. & Bandyopadhyay, P. 1981, New aspects of turbulent boundary layer structure, J. Fluid Mech., vol. 107, pp 297-338.
- Kline, S.J., Reynolds, W.C., Schraub, F.A. & Runstadler, P.W. 1967, The structure of turbulent boundary layers. J. Fluid Mech., vol. 30, pt. 4, pp. 741-773.
- Kline, S.J. & Robinson, S.K. 1990, Quasi-coherent structures in the turbulent boundary layer. Part 1: status report on a community-wide summary of the data, in Near Wall Turbulence. Proceedings of the 1988 Zoran Zaric Memorial Conference, ed. Kline, S.J. & Afgan, N.H., pp 200-217, New York, Hemisphere.
- Offen, G.R. & Kline, S.J. 1974, Combined dye streak and hydrogen bubble, visual observations of a turbulent boundary layer, J. Fluid Mech., vol 62, pp 223-239
- Offen, G.R. & Kline, S.J. 1975, A proposed model of the bursting process in turbulent boundary layers, J. Fluid Mech., vol 70, pp 209-228
- Smith, C.R., Walker, J.D.A., Haidara, A.H. & Sobrun, U. 1991, On the dynamics of near wall turbulence. Phil. Trans. Roy. Soc. Lon. A, vol 336, pp 131-175.
- Tait, S.J., Willetts, B.B. & Gallagher, M.W. 1996, The Application of Particle Image Velocimetry to the Study of Coherent Flow Structures over a Stabilising Sediment Bed, in Coherent flow structures in Open Channels, ed. Ashworth, P.J., Bennett S.J., Best, J.L. & McLelland, S.J., pp 185-201, John Wiley & Sons Ltd.

Flow and particle aerodynamic properties in aerial dispersion of pathogen spores

Alecsandra Rambert*, Pierre Gougat*, Laurent Huber**

*C.N.R.S. Meudon, France

** Laboratoire de Bioclimatologie, INRA Grignon, France

ABSTRACT

The processes by which spores and pollen are dispersed are: release or separation of the spores from the biological surface (leaf), transport by the wind and deposition (by sedimentation in still air and by impaction). This paper describes laser Doppler measurements reported to the flow field of Lycopodium spores. Particle release was observed for a minimum wind speed of 2.3 m/s and occurred in discrete and intermittent events. Particle transport was characterised by the air flow and spore velocity gradient. The settling speed of single particles and different-sized clusters was determined in still air. The average terminal velocity was 0.036 m/s. The settling speed of a cluster of N particles was determined as a function of the number of particles per cluster.

1. INTRODUCTION

Spore dispersal may be important in the initial infection of fields and the spread of disease over short or large distances. This biophysical process can be divided into three stages: release, transport and deposition.

The study of the removal or liberation stage requires methods for quantify several physical and biological parameters. All particles placed on a surface are subject to the following forces: gravity, buoyancy, drag

and adhesion. The relative magnitude of these forces depends on the local velocity flow. Spore liberation results of interaction between these forces. Above a minimum wind speed threshold, aerodynamic forces exceed the adhesion force and spores are removed with increasing wind speed (Grace, 1976). The time needed to dislodge the spores is dependent on the duration of the applied force beyond which spore liberation occurs.

The main parameters experimentally studied for characterising spore liberation were the count of removed particles and the mean wind speed threshold outside the leaf boundary layer. Most methods employed were intrusive and measurements of the local flow conditions near the leaf surface were approximate.

Physics of transport depends on both turbulence and particle characteristics. Just after release spores are submitted to a velocity gradient inside the leaf boundary layer and dispersion of spores can be described by diffusion equation (Chamberlain, 1975). It is usual to assume that the cloud of spores is advected at the mean wind velocity, however when turbulence intensity is high, spore velocity may be a factor of two or more above the mean wind speed (Legg, 1983).

The spores are liberated into the air not only as single spores but also as spore

clusters. To calculate the transport of spore clusters in the natural environment, we need to know the settling speed and the relation between cluster diameter and number of spores in the cluster. Spore sedimentation was investigated by several authors (Aylor, 1984) without possibility to consider variability in size and speed of individual spores or clusters.

In this paper we shall focus our discussion on the potential of laser velocimetry to characterise mean parameters for use in a dispersal model. Lycopodium spores (spherical particles $d \sim 30 \mu\text{m}$) were studied in controlled wind tunnel experiments with particular reference to wind speed and diameter variability.

2. MATERIAL AND METHODS

Laser Doppler Velocimetry (LDV) was used for velocity measurements.

Phase method was employed for the measurement of particle size.

For measuring the airflow velocity, particles of dyoctyl phtalate (spherical particles with diameter about $4 \mu\text{m}$) were used as seeding.

2.1 Particle Release

Leaves bearing spores were held vertically inside a glass tube. A compressed air source created the air flow inside the tube measured by a flow meter. The probe volume was located at 30 mm from the leaf.

For all leaves there was a threshold wind speed below which spores were not removed from the biological structure. This minimum wind speed required to dislodge the spores was detected by increasing the flow rate progressively and corresponded to the first spores detected.

The air flow velocity determined with the flow meter was an average velocity. The

local air flow description inside the tube was obtained by measuring the mean air velocity and air velocity fluctuations in the absence of spore liberation.

2.2 Transport of Particles

To describe the spore transport inside the leaf boundary layer, the experimental device shown on figure 1 was used.

Two independent flows were generated. The main flow contained seeding particles (2) and was generated by a fan (6) inside the tube (3). The secondary flow contained the spores (1) and was generated by a compressed air source (5) inside the tube (4). Two flowmeters (7) were used. A region of mixed flows was obtained downward the tubes in the probe volume (8) at 30 mm from the tube bottom. Tube (4) placed inside tube (3) was considered as a particle injector.

Simultaneous measurements of spore velocity and stream wind velocity were done using seeding with uniform smaller size particles for the air flow in the region of mixed flows.

By adjusting the velocity inside the tubes (3) and (4), injected spores were submitted to a variable velocity gradient.

2.3 Particle Sedimentation

Spore settling speed was studied inside a glass settling tube ($d=0.02 \text{ m} \times l=0.8 \text{ m}$). Spores were introduced and allowed to fall through a porous membrane at the top of the tube.

After entering the settling tube particles were allowed to settle for about 50 cm in the tube. The relaxation time is about 10^{-3} seconds, the settling speed was less than 0.05 m/s, therefore spores reached their terminal velocity after a vertical displacement of less than 0.001 m.

3. RESULTS

3.1 Particle Release

By increasing the air flow velocity progressively every 30 seconds (average wind speed steps: 2.3 m/s; 2.8 m/s; 3.1 m/s; 3.5 m/s; 4.1 m/s; 4.6 m/s; 5.1 m/s), we found an average threshold wind speed for the spores of 2.3 m/s (figure 2).

Both experimental conditions and cumulated number of spores are presented on figure 2a. We can see that the source exhaustion was not reached during this time.

Spore velocity with respect to time is plotted on figure 2b. The first removed spores were detected about 10 seconds after the beginning of the experiment. During the first 150 seconds we notice instantaneous particle release. At the end of the experiment particle release was more homogeneous over time. During the first step of the experiment ($t=0-30$ seconds) the average spore velocity was 3.68 m/s and RMS=1.62 m/s (figure 3a). Spore velocity fluctuations can be explained by local airflow velocity fluctuations. The histogram corresponding to the threshold wind velocity presented on figure 3b shows an important fluctuation rate relatively to the mean velocity about 15 %.

The importance of the mean velocity airflow in particle release is related to the time period while the aerodynamic force was applied.

Airflow rate fluctuations can also explain the instantaneous liberation of spores.

3.2 Transport of Particle

In order to describe the particle transport in the airflow, simultaneous measurements of spore and mean air flow velocities were done (figure 4).

Local main air flow velocity histogram and seeding particle size histogram are presented on figure 4a.

The measurements corresponding to the two mixed flows (main airflow and secondary flow containing the spores) were made at the same location than for the main flow. The velocity and diameter histograms are presented on figure 4b.

The results presented on a velocity-diameter diagram (figure 4c) show two distinct clouds corresponding to the two types of diameters ($4\mu\text{m}$ and $60\mu\text{m}$) directly related to two average velocities (0.98 m/s and 1.4 m/s).

3.3. Particle sedimentation

In order to relate the settling speed of spore clusters and their size, simultaneous measurements of velocity and diameter were obtained (figure 5). We present measured values of diameter and velocity for single particles or clusters: histogram of spore settling speed (figure 5a) and histogram of particle size (figure 5b). The average settling velocity is 0.036 m/s. The settling velocity for a single particle is 0.018 m/s. These results reduce to a standard curve, the normalised settling speed V_{ns} of a cluster of N particles (equal to the ratio of the settling speed of a cluster to that of a single particle) as a function of the number of spores in clusters. With simultaneous velocity and diameter measurements, the standard curve can be used to estimate the number of spores in each cluster (assuming one spore being equivalent to a sphere of diameter $35.7\mu\text{m}$ and N spores together as a sphere of diameter $35.7 \times N^{1/3}$).

Figure 5c shows the normalised average settling speed V_{sn} for a cluster containing N particles as a function of the number of particles N . This result agree very well with previous measurements made by Aylor (1984).

The evolution of spore size over time is presented on figure 6a. At the beginning the greatest clusters sedimented. At the end of

the experiment the single particles sedimented.

In order to explain the observed spectrum of particle diameters we tried to better characterise the sedimentation processes. We used five microscope slides, placed at the bottom of the settling tube. As seen on figure 6a, spores were collected every 5 seconds. The photographs on figure 6b confirmed that the first falling particles were the greatest spore clusters and the last ones the single particles.

4. CONCLUSION

This experimental investigation tried to examine if laser velocimetry could be successfully applied in order to determine main aerodynamic parameters necessary to construct a spore dispersal model (threshold wind velocity for particle release, settling velocity in still and turbulent air, particle diameter and particle concentration).

For a better characterisation of the liberation processes we propose a study of the exhausting of the source.

REFERENCES

- Aylor D.E., Ferrandino J.F., 1984, Settling speed of clusters of spores, Phytopatology 74:969-972.
- Chamberlain A.C., 1975, The movement of particles in plant communities in Vegetal and Atmosphere 155-203, Academy Press, London.
- Grace, Collins, 1975, Spore liberation from leaves, Microbiology of Aerial Plant, Academy Press, NY, 185-193.
- Legg B.J., 1983, Movement of plant pathogens in crop canopy, Philosophical Transaction of the Royal Society, London, B302, 559-574.

FIGURES:

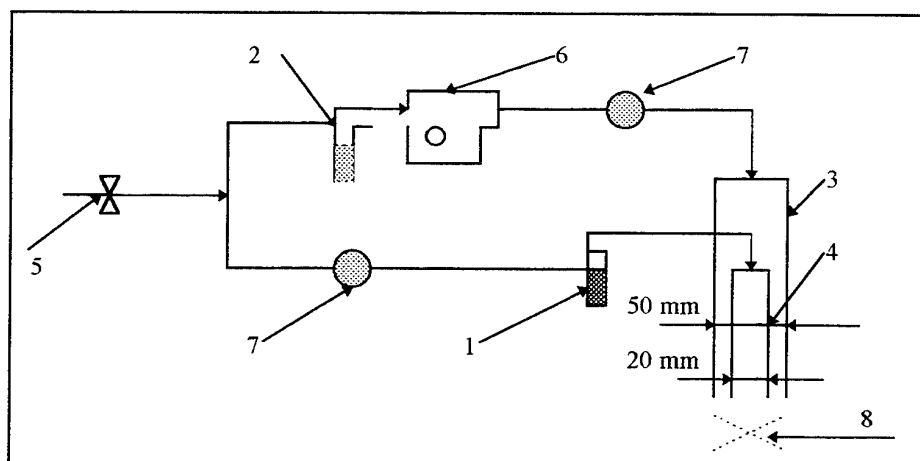


Fig. 1 Device used in spore transport experiments for simultaneous measurements of spore size, spore velocity and air flow velocity.

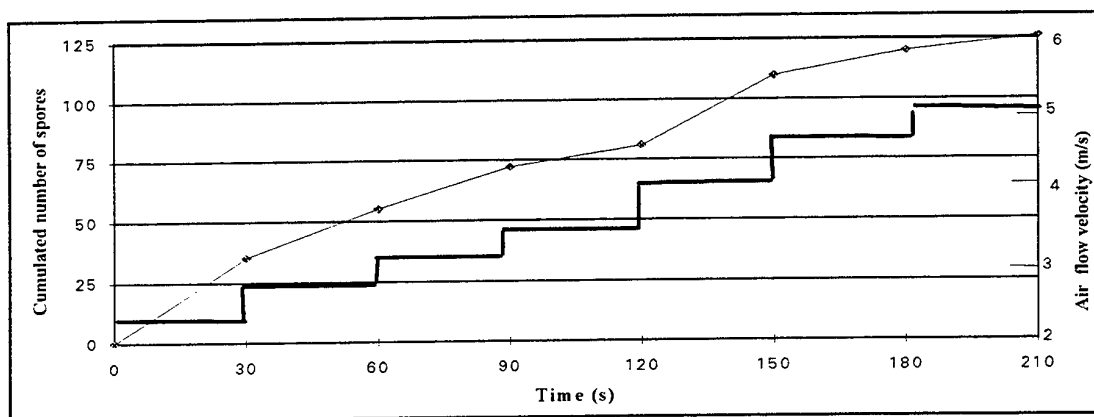


fig.2a

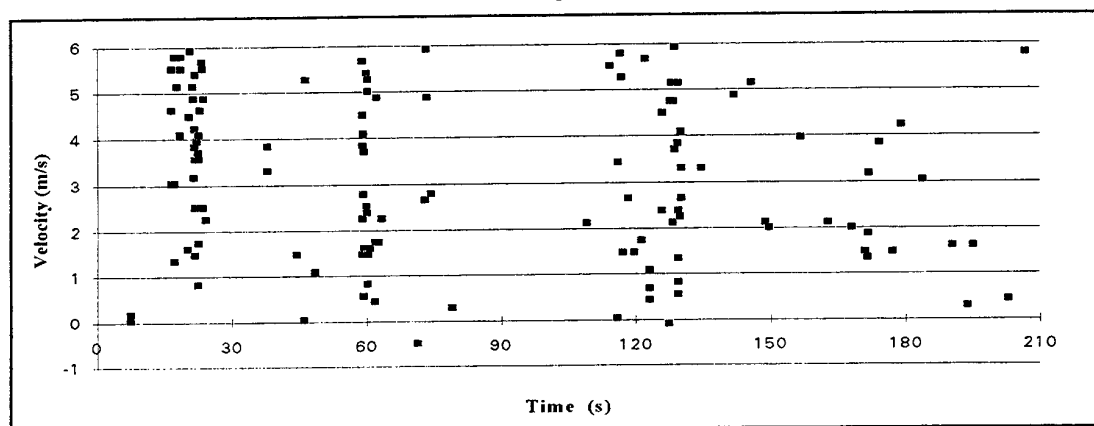


fig.2b

Fig.2 Cumulated number of spores (a) and time change of spore velocity (b) in a spore release experiment. The mean airflow velocity increased from 2.3 m/s to 5.1 m/s step by step every 30 seconds (2.8 m/s; 3.1 m/s; 3.5 m/s; 4.1m/s; 4.6 m/s).

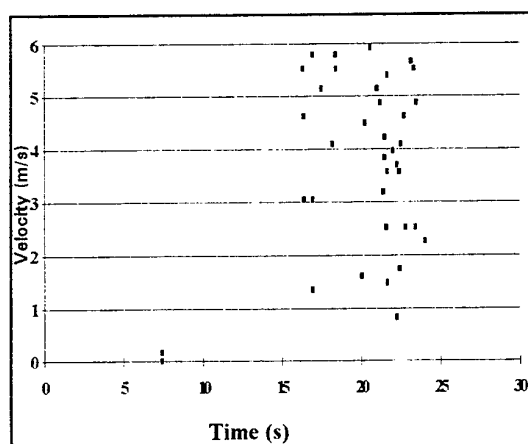


fig.3a

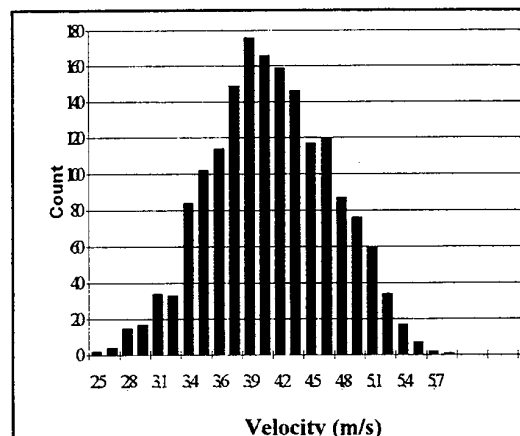


fig.3b

Fig.3 Spore velocity (a) and air flow velocity histogram (b) corresponding to the first 30 seconds duration of spores release (mean spore velocity: 3.68 m/s. RMS=1.62 m/s; mean air flow velocity : 4.18 m/s. RMS=0.57 m/s).

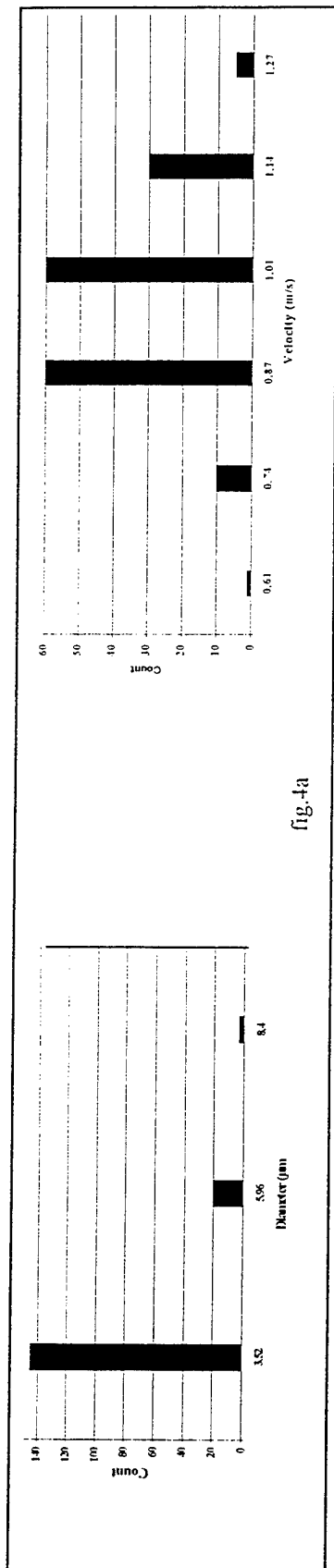


fig.4a

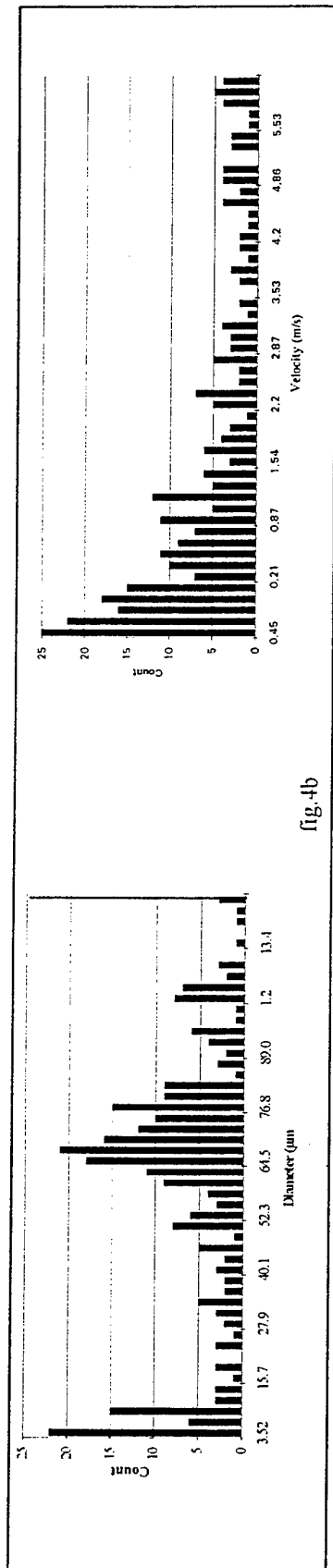


fig.4b

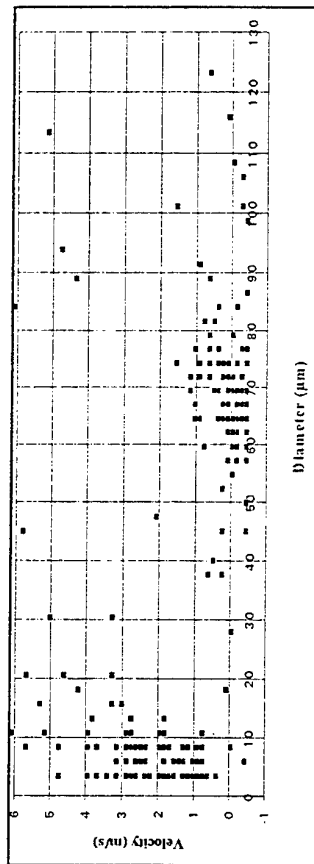


fig.4c

Fig.4 Spore transport experiments made in controlled conditions of seeding particle diameter (4 μm) and velocity of main air flow (0.97 m/s) (a).

(b) Particle size and velocity histograms in the mixed flows region (mean size: 58 μm ; mean velocity: 1.2 m/s).

(c) Particle velocity versus particle diameter for mixed flows.

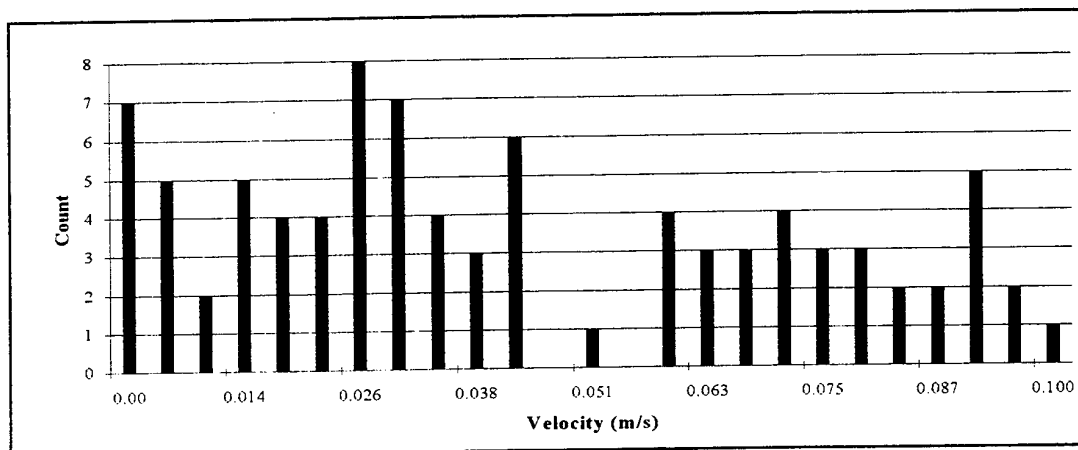


fig.5a

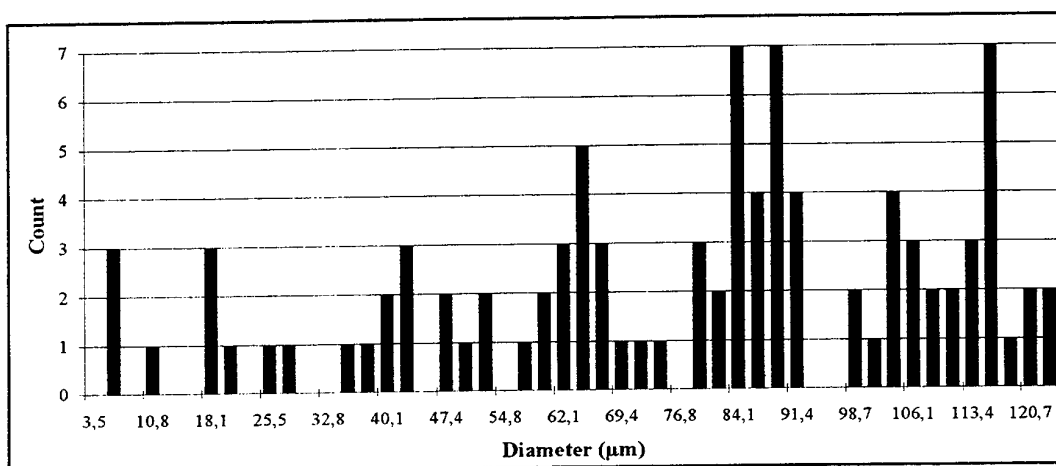


fig.5b

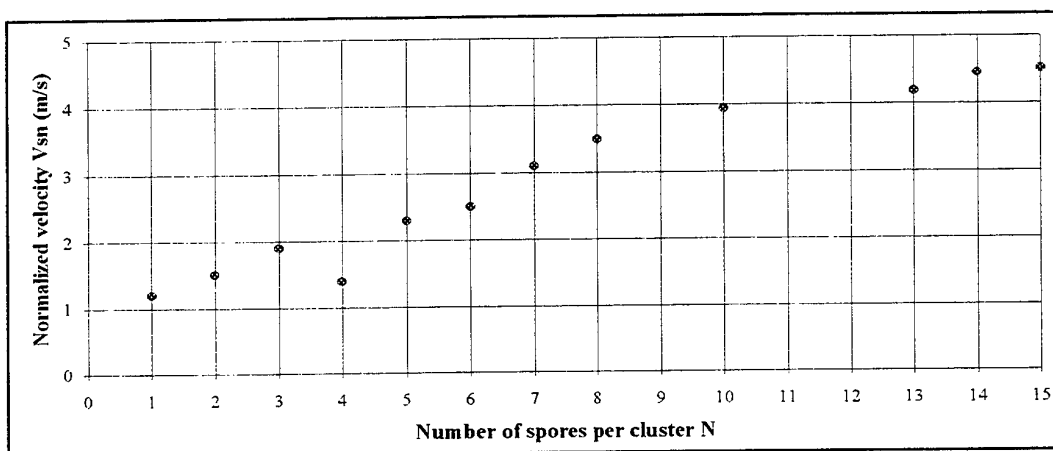


fig.5c

Fig.5 Spore sedimentation in still air: particle velocity (a) and particle size (b) histograms.

(mean settling velocity: 0.036 m/s; mean particle size: 77 μm)

(c) Normalised settling speed of a cluster of N particles, assuming a power law relationship between cluster diameter and the number of particles: $V_{sn}=1.01 \cdot N^{0.54}$ ($r^2=0.897$).

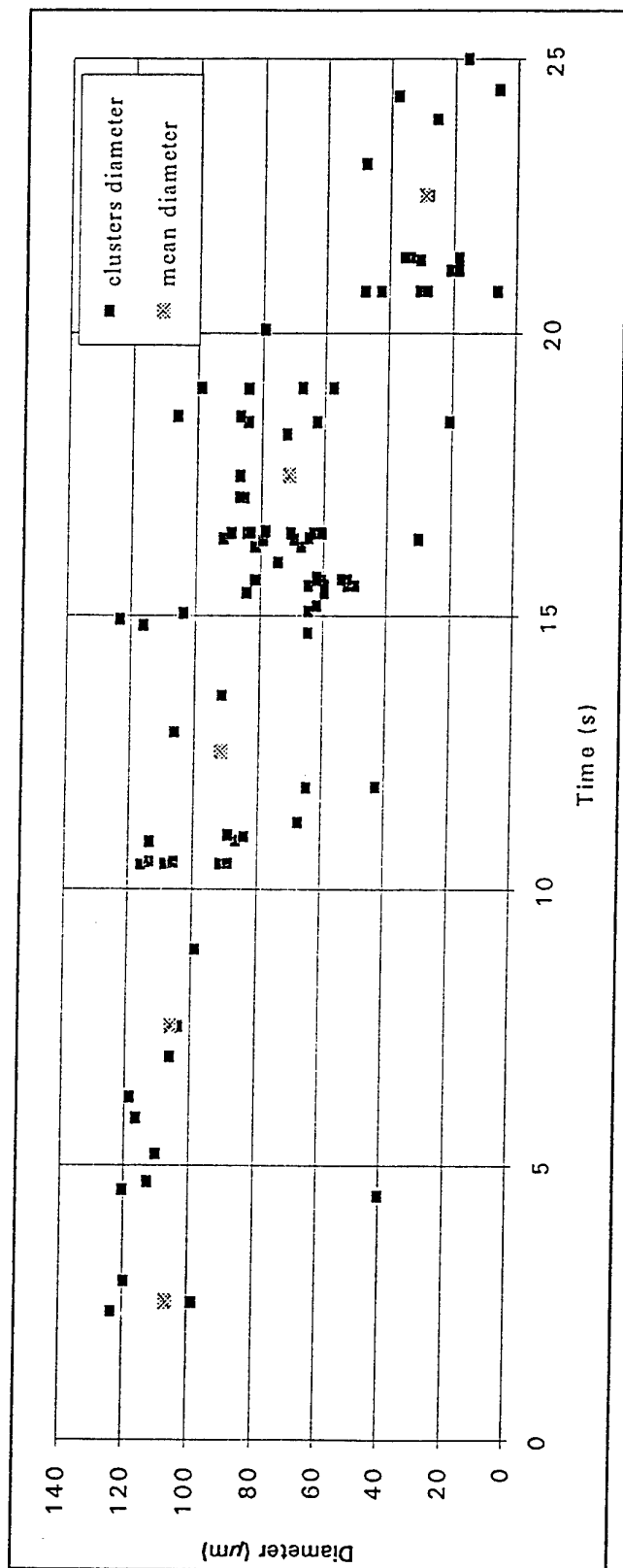


fig. 6a

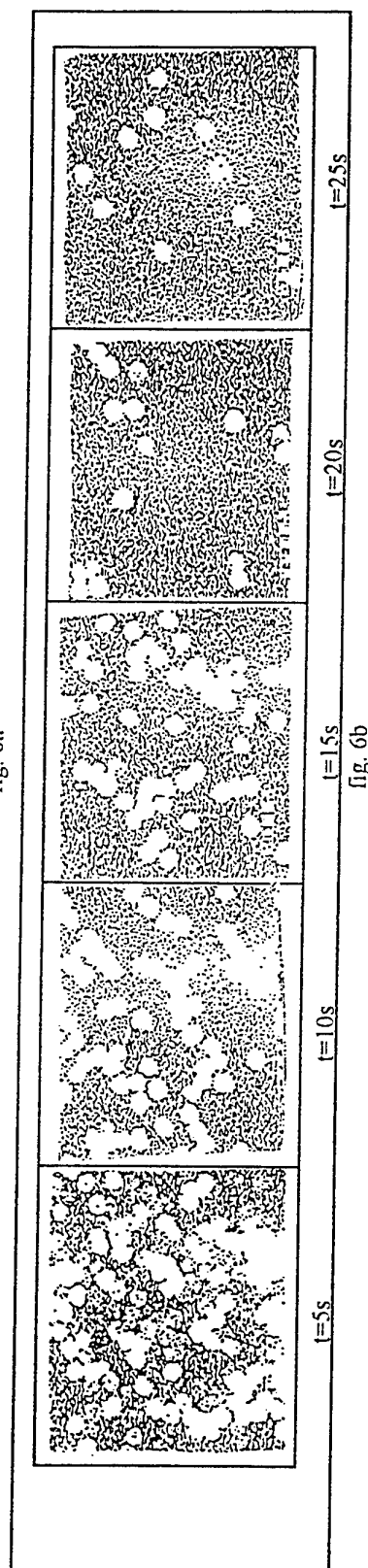


fig. 6b

Fig.6 Sedimentation experiments in still air: (a) single particles and clusters diameter versus time.
(b) Photographs of Lycopodium single particles and clusters during sedimentation every 5 seconds.

AN EXPERIMENTAL STUDY OF THE AERODYNAMIC BREAK-UP OF LIQUID DROPS USING LASER DIFFRACTION TECHNIQUE

S.H. Zaidi and B.J. Azzopardi

Department of Chemical Engineering,
University of Nottingham,
University Park, Nottingham NG7 2RD, U.K.

ABSTRACT

New measurement of the distribution of drop sizes formed by secondary atomisation are presented in the context of the available knowledge of the subject. The data appear to show little effect of gas velocity. The drop size distribution is seen to be multiple peaked. When compared with the experimental data and correlations of Hsiang & Faeth, the new data show similar trends.

1. INTRODUCTION

Drops, if too large, can break-up under the influence of gas flows or shock waves. This can be important in creating fine sprays. This can occur in some atomisation processes where coarse atomisation produces large drops which are disrupted by aerodynamic forces and create smaller drops. This stage is known as secondary atomisation. The processes can be important in the exacerbation or mitigation of hazards. An example of the former might occur in liquid hydrocarbon leaks. These might produce a coarse spray with large drops which would vaporise slowly. However, should a small explosion occur, the shock wave would shatter the large drops into much smaller droplets with a large specific surface area. These would produce higher evaporation rates and hence make the accident worse. If water sprays are used for explosion suppression, the opposite could occur. Coarse water sprays could be shattered by a preliminary explosion and thence create fine drops which would suppress any further detonation or deflagration.

The break-up of drops is also of interest in gas cleaning. In wave plate demisters, it is believed that a significant part of the liquid which passes through these units causing their efficiency to be low comes from re-entrainment of liquid which has already deposited and formed a film on the channel walls. Local accumulation of liquid can lead to protrusions on the film which are then broken up by the aerodynamic forces to create very small drops.

Another motivation for the study of aerodynamic

driven drop break-up comes from interest in gas/liquid two-phase flow in pipes. In the stratified and annular flow patterns, entrainment of liquid from the wall film to create drops carried by the gas is one of the most important phenomena which occurs. Azzopardi (1983) has shown the mechanisms of entrainment to be very similar to those of drop break-up.

In this paper, the stability of drops, the mechanisms of break-up and the sizes of the drops formed are considered. In particular new data on residual drop sizes are presented.

2. STABILITY OF DROPS

The fact that drops can break-up under aerodynamic forces has been known since the turn of the century, Lenard (1904). The critical conditions for drops to break-up were determined by Hinze (1949) to depend on a dimensionless group, the Weber number $= \rho_g U^2 d_0 / \sigma$. Here, U is the velocity difference between gas and drop, ρ_g the gas density, d_0 the original drop diameter and σ the surface tension. From an examination of the data obtained by Merrington and Richardson (1947), Hinze determined the critical value of Weber number to be 13. Lane (1951) suggested a value of 10 from his experiments. Recently, Wierzbka (1990), indicates that the variation in critical Weber number may be due to a probabilistic effect. Figure 1 shows that at Weber numbers near critical a varying percentage of the drops studied broke up by a bag type mechanism.

The above all relate to water drops. For more viscous liquids, Hinze (1955) proposed that an additional dimensionless group, the Ohnesorge number $= \eta_l / (\rho_l \sigma d_0)$, had to be taken into account. Hinze's relationship was

$$We = We_c (1 + K On) \quad (1)$$

with η_l being the liquid viscosity and K is a constant. Brodkey (1969) suggested

$$We = 12(1 + 1.077 On^{1.6}) \quad (2)$$

Pilch and Erdman (1987) give support to Brodkey's equation whilst more recently, Cohen (1994) showed that Hinze's linear relationship was well fitted by data.

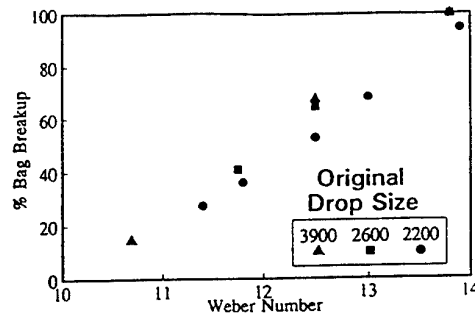


Figure 1 Percentage bag break-up observed by Wierzbna (1990), variation with Weber number

3. MECHANISMS OF BREAK-UP

The break-up of drops at conditions beyond the minimum can occur by a number of mechanisms. These depend on Weber and Ohnesorge numbers. The earliest recorded description of break-up is by Hochschwender (1919) who reported that in observing drops falling into an upward current of air, some were seen to be turned inside out. This is an obvious reference to the mechanism reported thirty years later by Lane (1951) - bag break-up. This occurs at Weber number just above critical and is illustrated in figure 2. The drop is initially deformed into a disc or ellipsoid with the major dimension in the direction perpendicular to the flow. The pressure difference on either side of the drop then squeezes liquid from the centre to the edges. In the next stage of deformation, the centre is inflated to give the characteristic bag shape. The thin film forming the bag ruptures forming

small drops. The thicker rim then breaks into a smaller number of larger drops. For cases where the original drop was falling under gravity, the rim is characterised by a small number of lobes (2-4) which themselves form the larger residual drops.

For high Weber numbers, Simpkins (1971) first reported an alternative mechanism which has been labelled umbrella or bag and stamen break-up. In this the bag is formed around a central filament of liquid. Beyond this the shear or stripping mechanism comes into play. Initially, the drop deforms into a disc as for bag break-up. Subsequently, liquid is torn off the edges, or at higher velocities, off waves which form on the upstream face of the distorted drop.

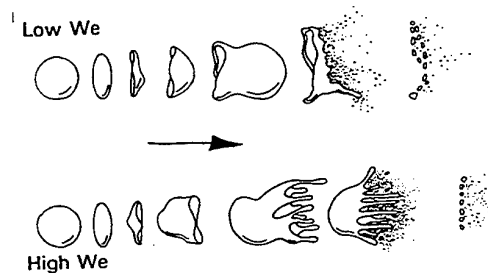


Figure 2 The two main mechanisms of liquid drop break-up

Information about the conditions at which each mechanism occurs has been published by Sarjeant (1979), Krzeczowski (1980), Pilch & Erdman (1987) and Hsiang & Faeth (1995). Most show that the transition lines depend on both Weber and Ohnesorge number, with the effect of the latter only becoming important at for $On > 0.5$. However, there is now always agreement between the published works. The variation is seen in Table 1.

Table 1 Weber number ranges for different mechanisms of break-up

	Sarjeant	Krzeczowski	Pilch/Erdman	Hsiang/Faeth
Bag	12-25	12-20	12-50	14-32
Umbrella	25-50	20-30	50-100	32-72
Transition	-	30-65	-	
Shear or stripping	> 50	> 65	100-350	> 72

There have only been two analyses proposed to determine the transitions between the mechanisms. In the first, Azzopardi and Hutchinson (1983) note that the drop distorts to a disc irrespective of the mechanism by which break-up occurs. Therefore, they suggest that the actual mechanism which occurs will be governed by the reaction of the disc shaped package of liquid to the shear and pressure drag components. The pressure or form drag will be felt predominantly at the centre of the disc. In contrast, the shear force will be felt most strongly at the edges. However, here it is resisted by a surface tension force greater than might have been expected for the original drop as the local curvature at the edge of the disc is greater than for the sphere. They suggested that the shear mechanism will predominate if the shear force is sufficient to overcome the surface tension force at the edge of the disc. When the surface tension force predominates, distortion and break-up are by bag break-up caused by the pressure acting on the centre of the disc. Here the surface tension forces are less than at the edge because of the gentler curvature. If a balance is written between the shear and surface tension forces at the edge of the disc

$$A \frac{2c_D}{3} \frac{\rho_g U^2}{2} = \frac{B \sigma}{d_o} \quad (3)$$

Here c_D is the drag coefficient, A is a constant to relate the local and overall values of shear and B is a factor relating the local curvature at the edge of the disc to the original diameter. Shear break-up is expected if the LHS > RHS. If the drag coefficient is expressed as

$$c_D = \frac{24}{Re} + 0.44 \quad (4)$$

then equation (3) can be rewritten as

$$We = \frac{6.66 B}{A} - 53.3 \frac{U \eta_g}{\sigma} \quad (5)$$

Using the suggested values of $A = 1$ and $B = 6$ yields a transition Weber number of 40, close to the upper limit for bag break-up in Table 1.

An alternative approach has been put forward by Hsiang & Faeth (1995) who differentiate between two types of distortions of drops, bowl and dome shaped, i.e., with convex side facing upstream and downstream respectively. Obviously, the former will be associated with the shear mechanism and the latter with bag break-up. Hsiang & Faeth (1995) note that the shapes suggest that the boundary between them depends on the balance of the shear force and surface tension forces. Using boundary layer arguments to specify the shear force results in a relationship of $We = CRe^{1/2}$ which provides a reasonable description of the boundary between the regions at which the different distortions occur.

Hitherto, there has been no complete analysis of the

entire complex process of drop break-up. However, there have been attempts to model some of the stages, particularly for bag break-up. Hinze (1949) and Haas (1964) have looked at the initial stage of deformation, distortion of sphere to disc. They concentrated on the stagnation region, described the pressure distribution over the front face and obtained an expression for the time to maximum deformation, which was a linear function of the group $d_o(\rho_l/\rho_g)^{1/2}/2U$. Azzopardi & Hutchinson (1983) have shown that this gives a good prediction of the time to flattening, figure 3.

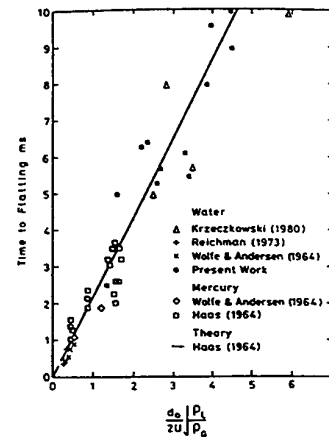


Figure 3 Time for first stage of distortion during drop break-up

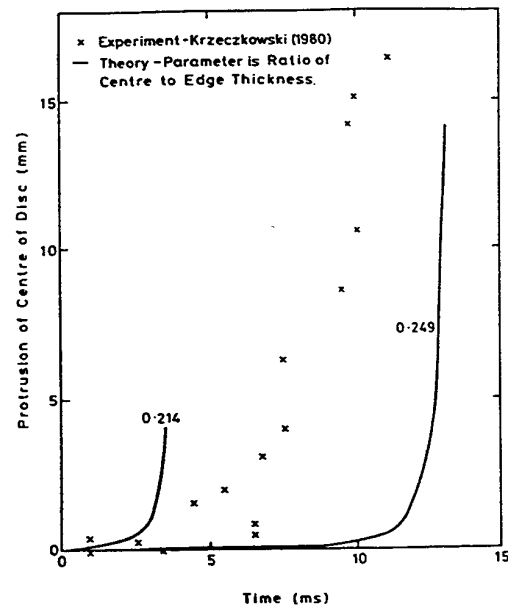


Figure 4 Growth of bubble stage in bag break-up, comparison of model of Azzopardi & Hutchinson (1983) with measured distortion

Azzopardi & Hutchinson (1983) considered the third stage of bag break-up, the blowing up of the centre (thinned) portion of the distorted drop. Using Newton's second law they calculated the differential acceleration of the centre and rim. They found that solutions depended on the degree to which the drop centre had thinned and that unless the centre was less than 1/4 of its original thickness, the rim accelerated faster than the centre. An example of the predicted protrusion of the disc centre and its comparison with experimental data is shown in figure 4. The parameter is the ratio of thickness at start of protrusion to original thickness.

3. RESIDUAL DROP SIZES

Though there have been a significant number of studies of the aerodynamic break-up of drops, data on the sizes of the new drops formed are much more limited. Some publications give maximum or median sizes, e.g., Lane (1951), Wolfe & Anderson (1965), Craig (1984). Others, such as Fournier d'Albe & Hidayettulla (1955), Magarvey & Taylor (1956), Kombayasi *et al.* (1964), Alusa & Blanchard (1973) and Hsiang & Faeth (1993) give the information about the distribution of sizes. Though data is presented for many different liquids, only Hsiang & Faeth have a very systematic study. Many other papers present data for only a very limited number of conditions.

From this information we can determine a number of relationships and trends. For studies in the bag break-up region, Fournier d'Albe & Hidayettulla (1955), Magarvey & Taylor (1956), Kombayasi *et al.* (1964), there is evidence of a bimodal size distribution. The smaller drops are formed from the bag, the larger ones from the rim. The ratio of mass median diameter to original diameter varies from 0.8 to 0.01. The corresponding ratio for the Sauter mean diameter (d_{32}/d_0) is smaller. However, this parameter is sensitive to drops of a particular size being missed out. For example, Magarvey & Taylor (1956) present data for drops with an original diameter of 0.015 m falling through air. Here velocity of the drop relative to the still air can be estimated from the work of Laws (1941), Gunn & Kinzer (1949) and van der Leeden *et al.* (1955) to be about 9.2 m/s. From the data given a d_{32}/d_0 of 0.3 is calculated. However, the authors note that they did not measure all fragment. Examination of their data shows that 15% were not accounted for. If these were taken to be at the smallest size, the value of d_{32}/d_0 drops to 0.137.

Methods for prediction of the sizes of the drops formed by secondary atomisation have been produced by Mayer (1961), Anderson & Wolfe (1965), Hsiang and Faeth (1993) and Wert (1995). The first three model the shear break-up regime whilst the last looked at bag break-up. Mayer considered the gas flow to induce disturbances on the surface of the fluid. He suggested that when waves of the fastest growing wavelength reach an amplitude comparable with the wavelength they form ligaments and thence drops whose size is proportional to the wavelength.

The wavelength was obtained from stability analysis. Anderson & Wolfe's is based on the idea that a sheet of liquid is created from the edge of the distorted drop. This sheet is assumed to break-up due to circumferential and axial instabilities. This gave them the volume of the packet of liquid formed and thence its diameter. Hsiang & Faeth (1993) proposed that drops would be comparable to the thickness of the boundary layer formed on the liquid along the front surface of the distorted original drop. This resulted in a correlating equation which linked the Weber numbers based on the original and residual drop sizes, as well as the Reynolds number.

$$We_s = 6.2 \left(\frac{\rho_l}{\rho_g} \right)^{\frac{1}{4}} \frac{We}{\sqrt{Re}} \quad (6)$$

The last two show good agreement with their own data.

Wert (1995) proposes that the residual drop size in bag break-up mainly arise from the rim of the bag. He argues that it depends on the growth of disturbances and that the magnitude to which these grow depends on the available time - defined as the time to break-up. To provide the required times they use the difference between the time to the first flattening of the drop and the time to total break-up as given by Pilch & Erdman (1987). However, much of the time to break-up is taken up by the extension of the bag which is accompanied by the radial stretching of the rim. During such a stretching process it might be expected that the usual Rayleigh type instabilities are suppressed. Thus, alternative time scales are required.

5. EXPERIMENTAL ARRANGEMENT

The drop break-up experiments were carried out in an open circuit wind tunnel whose cross section at the point at which measurements were made was 0.07 m x 0.2 m. Gas velocities at the throat ranged from 16 to 42 m/s. Measurements had shown the velocities to be very uniform across the throat.

Drops were introduced into the wind tunnel through a 10 mm diameter glass tube which protrudes mm from the top of the tunnel. This was used to ensure that drops were not torn off the needle from which they were produced and that they were exposed suddenly to the gas stream. Different size needles were used to produce drops. Both single and multiple needle arrangements were used. The latter was employed because the former did not produce a sufficient signal to noise ratio in the measurement techniques. The sizes of the original drops were measured from photographs. Figure 5 shows an example to these drops.

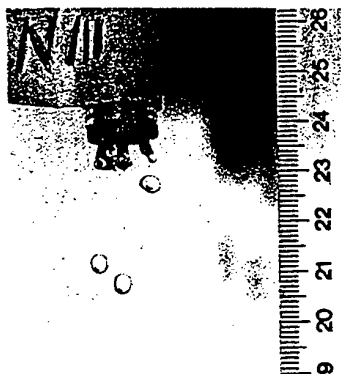


Figure 5 Drops produced from the multiple needle arrangement.

Drop sizes and concentrations were measured using the laser diffraction technique developed by Swithenbank *et al.* (1976). The basis of the technique is as follows: when a spherical particle is illuminated by a parallel beam of monochromatic, coherent light, a diffraction pattern is formed. If a lens is placed in the light path after the particle and a screen placed at the focal plane, then the undiffracted light is focused at a point on the axis and the diffracted light forms a pattern of rings around the centre spot. Movement of the particle does not cause movement of the diffraction pattern since light diffracted at an angle will give the same radial displacement in the focal plane irrespective of the particle's position in the illuminating beam. The "far field" diffraction pattern thus produced is known as the Fraunhofer diffraction pattern for which the intensity pattern is known. If an ensemble of drops with a distribution of sizes is examined and a detector consisting of concentric annular rings is used then the energy (integral of intensity over the detector area) falling on each ring is a function of the geometry of the annulus, the Fraunhofer diffraction pattern and the drop size distribution. A set of equations can be derived which can be expressed in the form of a matrix equation, $L=WT$, where L is the light energy distribution vector, W is the drop weight distribution and T is the matrix of coefficients which define the light energy distribution curves for each particle.

Normally the equation would be inverted to give W explicitly using the inverse of T . In practice this is not done because the large dynamic range of the coefficients which can result in considerable computational difficulties and non-physical solutions. In these experiments, a model-independent approach was used. In this the volume fractions in fifteen size classes were adjusted until the error between calculated and measured energies was minimised. An instrument based on this technique is available from Malvern Instruments. It comprises a 3mW HeNe laser whose beam is expanded to 18mm diameter. This is directed at the drop sample and the angular distribution of scattered light is monitored by an array of photosensitive detectors placed at the focal plane of the 1000 mm Fourier transform lens used in this technique. A computer samples the detectors and converts the information to a drop size distribution. The instrument has been checked by a

number of different techniques and found to be accurate, Azzopardi (1984, 1992).

In applying the technique to this particular study, a number of precautions had to be taken to eliminate the extraneous vibrations from disturbing the measurement technique. These included mounting the instrument on a separate frame from the wind tunnel and sitting the instrument on anti-vibration mountings.

6. RESULTS

Measurements were made of the drop size distribution for seven positions from the injection point (10, 20, 30, 45, 60, 75 & 90 mm), five gas velocities (16, 26, 35, 40, 42 m/s) and three initial drop sizes (2.5, 2.8 & 4 mm). For each combination ten measurements were made, each one involving 1000 sweeps of the detector array. Measurements were made with drops being created from single needles as well as arrays containing six or seven needles. However, only the results from the multiple needle experiments will be considered as the in the single needle runs, the drop concentration and thence signal to noise ratio were too small.

A typical distribution is shown in figure 6. This shows the characteristic form found in many of the measurements, more than one peak. In this case the peaks occurred at about 150, 350 and 730 μm . If the 10 runs carried out at these conditions are examined, all are seen to contain three peaks with the first lying within 135 - 195 μm , the second 330 - 390 μm and the third 620 - 780 μm . The variability found between runs is illustrated in figure 7, where the cumulative volume fraction undersize for all ten runs is plotted. In these cases the entire drop size distribution fell within the operational range of the instrument.

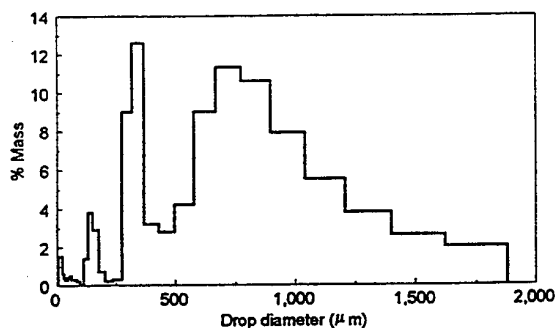


Figure 6 Typical drop size distribution - initial drop diameter = 2.5 mm, velocity = 26 m/s

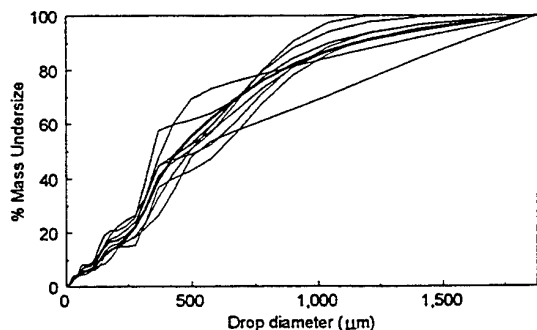


Figure 7 Illustration of variability between runs - initial drop diameter = 2.5 mm, velocity = 26 m/s

The evolution of the size distribution of the newly formed drops can be inferred from the variation of Sauter mean diameter with distance downstream from the injection point, figure 8. This data can only be taken as indicative as, in many cases, there was evidence that there were drops present larger than the upper limit of the instrument. Nevertheless, the figure shows that the drop ensemble seemed to have arrived at something approaching steady state.

The effect of initial drop size and gas velocity on Sauter mean diameter are shown in figure 9. Interestingly, there appears to be little effect of gas velocity. There is some effect of initial drop size, though two of the sizes were rather close together.

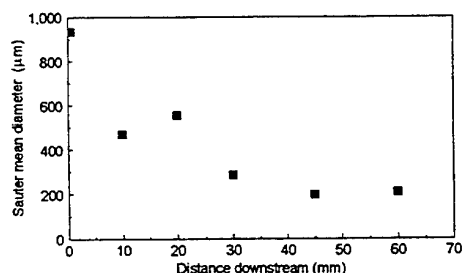


Figure 8 Development of mean drop size with distance from injection point

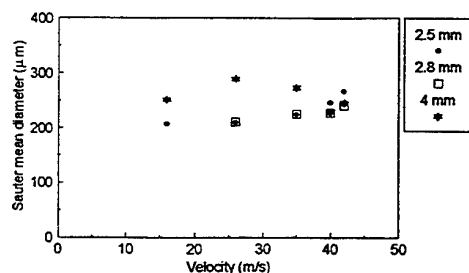


Figure 9 Effect of initial drop size and gas velocity on Sauter mean diameter of drops formed

7. DISCUSSION

In considering the new results presented above for the distribution of drop sizes and consequent means, some questions need to be considered. Are the multiple peaks observed in the distribution a true effect or some artefact of the measuring technique? If it is a true effect, what is the physical reason for its occurrence? What are the effects of initial drop size and gas velocity on the Sauter mean diameter and are there models or correlations which can predict these?

It is noted that the multiple peaks occurred consistently. They were present in measurements made with single needles as well as in the multiple needle cases reported here. Though the single needle results did suffer from low obscuration and hence signal to noise ratios, the same was not true of the multiple needle case. It was thought that vibration of the wind tunnel windows and instrument might be causing the multiple peaks. However, as described above, adequate precautions have been taken to remove effects of vibration. Evidence of multiple peaks does exist in other data, e.g., Fournier d'Albe & Hidayettulla (1955), Magarvey & Taylor (1956) & Kombayasi *et al.* (1964). These data were from the bag break-up region and many of our data are from Weber numbers which encompass that region. Thus it can be concluded that the multiple peaks observed are a real phenomenon.

The effects of initial drop size and gas velocity have been modelled by Andersen & Wolfe (1965) and correlated by Hsiang & Faeth (1993) for the shear break-up mechanism and Wert (1995) has presented a correlation for the bag break-up mechanism. The present data span both mechanisms. However, if data is considered in terms of the correlating groups suggested by Hsiang & Faeth, figure 10, it is seen that the new data show reasonable agreement at higher velocities but deviate more at those lower velocities corresponding to bag break-up.

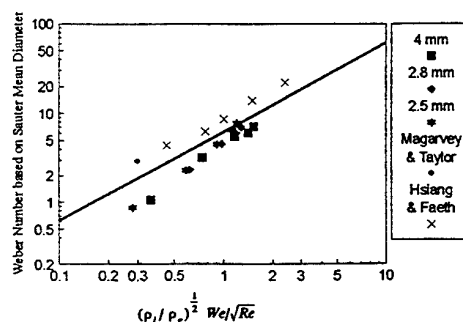


Figure 10 Present data plotted using correlation parameters of Hsiang & Faeth (1993)

The different behaviour with breakup mechanism can be seen in figure 11 where the data and corresponding predictions of Hsiang & Faeth (1993) are plotted. Though there might be differences in absolute value, the high velocity data follow the trends but then there is a break off

at velocities which might be expected given the transition Weber numbers listed in Table 1. The predictions of the model of Andersen & Wolfe (1965) show similar trends to the Hsiang & Faeth correlation though with lower absolute values. However, Andersen & Wolfe did not specify that they were predicting Sauter mean diameters and there might be a missing scaling factor. The correlations suggested by Wert (1995) predict larger diameters than measured. However, inspection of the trends with gas velocity indicate a decrease of drop size with decreasing gas velocity as seen in figure 11. For example, for an original drop size of 4 mm, Wert predicts 777 μm at 35 m/s, 1064 μm at 26 m/s and 985 μm at 16 m/s.

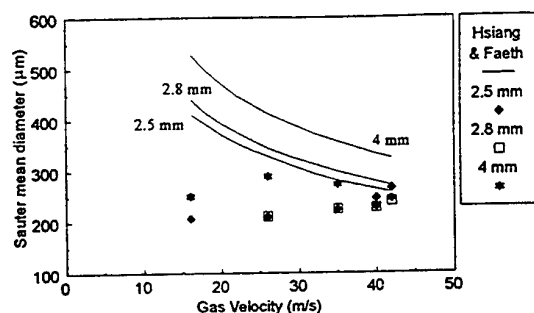


Figure 11 Comparison between present data and predictions of Anderson & Wolfe (1965) and Hsiang & Faeth (1993)

6. CONCLUSIONS

From the material presented here we can conclude that:

- (i) The aerodynamic break-up process can occur by one of a number of mechanisms. The transition between these mechanisms depends on Weber and Ohnesorge numbers.
- (ii) Within one of the mechanisms, e.g., bag break-up, several steps can be identified. Models are available for a number of these.
- (iii) There are not many data for the sizes produced by the aerodynamic break-up process. Significant errors can be produced in the Sauter mean diameter if the smaller drops are not accounted for.
- (iv) The correlation suggested by Hsiang & Faeth (1993) gives a reasonable description of new drop size data presented here.

Acknowledgements

This work was carried out as part of an EPSRC funded project (GR/J52143) on annular flow in inclined pipes.

REFERENCES

- Alusa, A.L. & Blanchard, D.C. 1973, Drop size distribution produced by the break-up of large drops under turbulence, *J. Rech. Atmos.*, vol 7, pp 1-9.
- Andersen, W.H. & Wolfe, H.E. 1964, Aerodynamic break up of liquid drops - I - Theoretical, *Proc. Int Shock Tube Symp*, Naval Ordinance Lab., White Oak, Maryland, USA.
- Azzopardi, B.J. 1983, Mechanisms of entrainment in annular two-phase flow, UKAEA Report AERE R11068.
- Azzopardi, B.J. 1984, A diffraction drop sizing technique: its testing and application to confined sprays, *Filtration and Separation*, vol. 21, p 415-419.
- Azzopardi, B.J. 1992, Instrumentation of particle size analysis by far field diffraction: accuracy, limitations and future, in *Particle Size Analysis*, Ed N.G. Stanley-Wood and R.W. Lines, Royal Society of Chemistry, Cambridge, pp 108-132.
- Azzopardi, B.J. & Hutchinson, P. 1983, The disintegration of liquid droplets, UKAEA Report AERE R10929.
- Brodkey, R.S. 1969, *The Phenomena of Fluid Motions*, Addison-Wesley, Reading, MA
- Cohen, R.D. 1994, Effect of viscosity on drop breakup, *Int. J. Multiphase Flow*, vol. 20, pp 211-216.
- Craig, J.E. 1984, Conventional and liquid metal droplet break-up in aerodynamic nozzle contractions, *A.I.A.A. 22nd Aerospace Sciences Meeting*, 9/12 January, Reno, Nevada.
- Faeth, G.M., Hsiang, L.-P. & Wu, P.-K. 1995, Structure and breakup properties of sprays, *Int. J. Multiphase Flow*, vol. 21 supp., pp 99-127.
- Fournier d'Able, E.M. & Hidayetulla, M.S. (1955), The break-up of large water drops falling at terminal velocity in free air, *Quart. J. Roy. Met. Soc.*, vol. 81, pp 610-613.
- Gunn, R. & Kinzer, G.D. 11949, The terminal velocity of fall for water droplets in stagnant air, *J. Meteor.*, vol 6, pp 243-248.
- Haas, F.C. 1964, Stability of droplets suddenly exposed to a high velocity gas stream, *A.I.Ch.E.J.*, vol. 10, pp 920-924.
- Hinze, J.O. 1949, Critical speeds and sizes of liquid globules, *App. Sci. Res.*, vol. A1, pp 263-288.
- Hinze, J.O. 1955, Fundamentals of the hydrodynamic mechanism of splitting in dispersion processes,

- A.I.Ch.E.J., vol. 1, pp 289-295.
- Hochschwender, E. 1919, Dissertation, University of Heidelberg.
- Hsiang, L.-P. & Faeth, G.M. 1993, Drop properties after secondary breakup, Int. J. Multiphase Flow, vol. 19, pp 721-735.
- Hsiang, L.-P. & Faeth, G.M. 1995, Drop deformation and breakup due to shock wave and steady disturbance, Int. J. Multiphase Flow, vol. 21, pp 545-560.
- Kombayasi, M., Gonda, T. & Isono, K. 1964, Lifetime of water drops before breaking and size distribution of fragment drops, J. Meteor. Soc. Japan, vol. 32, pp 330-340.
- Krzczkowski, S.A. 1980, Measurement of liquid droplet disintegration mechanisms, Int. J. Multiphase Flow, vol. 6, pp 227-239.
- Lane, W.R. 1951, The shatter of drops in streams of air, Ind. Eng. Chem., vol. 43, pp 1312-1317.
- Laws, J.O. 1941, Measurement of the falling velocity of water-drops and rain-drops, Trans Am. Geophys. Union, vol. 22, pp 709-721.
- Lenard, P. 1904, , Met. Z., vol. 5, p 175.
- Magarvey, R.H. & Taylor, B.W. 1956, Free fall break-up of large drops, J. Appl. Phys., vol. 27, pp 1129-1135.
- Mayer, E. 1961, Theory of liquid atomisation in high velocity gas streams, A.R.S.J., vol 31, pp 1783-1785.
- Merrington, A.C. & Richardson, E.G. 1947, The break-up of liquid jets, Proc. Phys. Soc., vol. 59, pp 1-13.
- Pilch, M. and Erdman, C.A. 1987, Use of break up time data and velocity history data to predict the maximum size of stable fragments for acceleration induced break up of liquid drops, Int. J. Multiphase Flow, vol. 13, pp 741-757.
- Sarjeant, M. 1979, Drop break-up by gas streams, 3rd European Conf on Mixing, York, 4/6 April.
- Simpkins, P.G. 1971, Non-linear response of deforming drops, Nature, vol. 233, pp 31-33.
- Swithenbank, J., Beer, J.M., Taylor, D.S., Abbot, D. and McCreath, G.C. 1976, A laser diagnostic for the measurement of droplet and particle size distributions, Progress in Astronautics and Aeronautics, vol. 1, p 421-.
- van der Leeden, P., Liem Djan Die & Suratman, P.C. 1955, The velocity of free falling droplets, Appl. Sci. Res., vol A5, pp 338-348.
- Wert, A rationally-based correlation of mean fragment size for secondary breakup, Int. J. Multiphase Flow, vol. 21, pp 1063-1071.
- Wierzbza, A. 1990, Deformation and break up of liquid drops in a gas stream at nearly critical Weber numbers, Experiments in Fluids, vol. 9, pp 59-64.
- Wolfe, H.E. & Andersen, W.H. 1964, Aerodynamic break up of liquid drops - II - Experimental, Proc. Int Shock Tube Symp, Naval Ordnance Lab., White Oak, Maryland, USA.

EXPERIMENTAL INVESTIGATION AND VISUALISATION OF PARTICLE MOTION IN A MODEL OF A BEATER WHEEL MILL MODEL

Maria A. Founti, Thomas J. Achimastos, and Demetrios A. Dimopoulos

National Technical University of Athens
Mechanical Engineering Department, Thermal Engineering Section
Patisision 42, Athens - 10682, Greece

ABSTRACT

The paper presents particle-velocity measurements obtained with a one component fibre optic, back scatter laser Doppler anemometer and visualisation of the flow in a model of a lignite beater wheel mill. The mill-model has been constructed with the aim to retain the same particle motion characteristics as in the mills used by the Greek Public Power Corporation (P.P.C.) for the pulverization and drying of lignite.

An analysis of the particle motion characteristics and the adopted scaling down procedure for the design of the model mill, which retains geometrical and fluid dynamic similarity, are presented. The real and model beater wheel mills are described and the simplifications adopted are discussed. The experimental results shed light into the particle motion inside the mill and allowed to locate areas, where particles tend to accumulate and where erosion-wear is expected to be high.

1. INTRODUCTION - DESCRIPTION AND OPERATIONAL CHARACTERISTICS OF BEATER WHEEL MILLS

Grinding and pulverization of solid fuels are crucial processes in large coal power plants. Pulverization of the solid fuel can be accomplished under continuous motion inside the mill, by crushing the lignite-particles against the blades of the mill without them being compressed. In the beater wheel mills used by Greek P.P.C., the impingement of the coarse lignite particles takes place on the blades of a fast rotating fan, which also acts as suction pump and pneumatic conveyer for both the solid fuel and drying flue gases. The size distribution of the lignite particles at the mill outlet affects their physical and chemical behavior inside the furnace, by determining the particle residence time into the flame and the total fuel area exposed to chemical reaction. Additionally, Greek lignite, is characterized by a 50 -60 % moisture content which has to be reduced, i.e. the fuel has to be dried before it enters the combustion chamber. The drying and milling process are

accomplished simultaneously in the beater wheel mill.

For the drying process, hot flue gases are sucked from the top of the combustion chamber and they are then mixed with cold air and with the solid fuel (lignite) coming from a silo, thus achieving gradual vaporization of the surface moisture.

A typical beater wheel mill used by the Greek P.P.C. consists of (Petrourgakis, 1994):

1. A pulverizer beater wheel (impeller) with steel blades, which acts as a suction fan for the flue gases and simultaneously as the feeding fan for the mixture of flue gases, vapor and dried solid fuel.
2. The mill volute.
3. An intermediate duct leading to the classifier.
4. The classifier which controls the amount of lignite to be recycled for further pulverization.
5. A shutter for isolation (i.e. a damper of the flue gases), which achieves isolation of the mill in case of maintenance.
6. The chamber of recirculation for the mixing of lignite and flue gases.
7. A gate for replacement of the pulverizer wheel.
8. Dampers of hot and cold air, and recirculation dampers.

An operational mill pulverizes about 100 tons of lignite per hour, with a rotational speed of 450 rpm. The lignite enters the mill, transported by the flue gases via a suction duct and impinges on twelve fan blades fixed on the beater wheel. In this section the big lignite particles are centrifuged radially to enter the space between the rotating blades. They impinge and get crushed on the blades. The produced smaller particles are centrifuged radially, pass through the mill volute, which is in fact a spiral shell, to the intermediate convergent duct and are finally directed to the classifying chamber. The classifier captures the bigger particles and leads them through a convergent duct, back to the mill for further grinding.

The problems arising in the operation of such beater-wheel mills are associated with the mill design, with variations in the mineral composition of ore lignite, and

with variations in feed rate conditions: For example, the quantity and size range of particles that are recirculated inside the mill via the classifier affects mill efficiency. The latter also affected by the deterioration of surface material, and especially of the fan blades surface. The damage is generally due to the wear properties of the abrasive mineral species (i.e. SiO_2) contained in the impinging lignite-particles and necessitates frequent replacement of blades (after about 2000 operation hours).

Experimental investigation of the flow field inside the mill could:

- demonstrate the operational limits for an efficient operation.
- lead to useful suggestions for improved design of some parts, in order to minimize the erosion wear and lengthen the required time between consecutive mill maintenance.
- lead to suggestions for modification of the flow conditions in the classifier, in order to regulate the amount of particulates that recycles back to the mill.

Numerical investigations of the grinding process, particle motion, fuel moisture evaporation and erosion wear inside the same P.P.C. mill and classifier have been performed by Anagnostopoulos and Bergeles (1993a,b). Their numerical results quantified the fraction of particles that is captured in the classifier and recycle back to the mill for further grinding.

Recently, Gehrke and Stegelitz (1995) have conducted experimental and numerical investigations in order to evaluate a new classifier design developed by the Energie und Verfahrenstechnik GmbH, (E.V.T.) Germany, in connection with an E.V.T. beater wheel mill. Flow visualization experiments have been conducted in a water duct simulating the mill duct and classifier and in a test rig for gas-solid flows. In connection to the above experimental studies, numerical simulations of the gas-solid flow in the mill classifier system have also been performed. Their numerical results, although they refer to the mills of the power station "Schwarze Pumpe" and not to the mills of the Greek P.P.C., agree in general with the findings of Anagnostopoulos and Bergeles (1993a,b). They confirmed that flow irregularities caused by the beater wheel of the mill are continued via the mill volute and the intermediate duct to the classifier, where they are further enhanced by the classifier inclinations. Gehrke and Stegelitz (1995) proposed the installation of guiding elements in the classifier to improve the local flow conditions.

In the present work a model mill has been constructed in order to investigate the particle motion inside the mill and to locate areas, where particles tend to accumulate and where erosion-wear is expected to be high. The particle-velocity measurements, conducted with the use of laser Doppler anemometry, can serve as inlet conditions and for the validation of the performance of computational codes, such as the ones developed by Bergeles et al (1993a,b) and Gehrke and Stegelitz (1995).

2. DESIGN AND CONSTRUCTION OF A PROTOTYPE BEATER WHEEL MILL MODEL.

The design of the model mill has been based on the operational characteristics of the real beater wheel mill. Geometric and dynamic similarity of the flow field and also similarity of the aerodynamic behaviour of the fuel particles entering the mill, have been retained in the design of the model mill.

In order to achieve dynamic similarity between the flow in the real and in the model mill, the ratio of the inertia to the viscous forces should be equal for both cases. For this purpose, similarity in the values of:

- Reynolds number, $Re = U_{bulk} \cdot d/v$, where U_{bulk} : bulk velocity, d : characteristic length, v : kinematic viscosity of the gas
- Mach number, $M = U_{bulk}/a$, where a : speed of sound and
- Froude number, $F = U_{bulk}/(g \cdot d_p)^{1/2}$,

has been achieved based on experimental data and the operational conditions of the real mill, provided by the Greek P.P.C. (Kloukinitis and Hatzifotis, 1993). The density and dynamic viscosity of the flue gases and air, in the real and model mills respectively have been taken equal to:

$$\rho_{real} = 0.726 \text{ Kg/m}^3, \mu_{real} = 19.497 \text{ } \mu\text{Pa}\cdot\text{s and} \\ \rho_{mod} = 1.17 \text{ Kg/m}^3, \mu_{mod} = 19.83 \text{ } \mu\text{Pa}\cdot\text{s at } 27^\circ\text{C,}$$

where the subscripts "real" and "mod" refer to the real mill and the model mill respectively. The width of the intermediate converging duct has been considered as the characteristic length, (d) for the calculation of the Reynolds and Froude numbers in the two cases.

It has been considered that the particle size distribution in the real mill follows a Rosin-Ramler-Sperling-Bennet distribution (RRSB-distribution). The characteristic mean lignite-particle diameter has been estimated using data from the Greek P.P.C. power station at "KARDIA"-Ptolemais, (Kloukinitis and Hatzifotis, 1993) to be equal to ca. 159 μm .

For the aerodynamic similarity of the particle motion between the real and model mill, the following characteristics numbers have been considered:

- Particle Reynolds number, $Rep = \rho_F \cdot D_p \cdot |U_F - U_p|/\mu$, where ρ_F : fluid density, in our case the flue-gases or air, D_p : particle diameter, U_F : velocity of the fluid, U_p : mean characteristic velocity of the particles, μ : dynamic viscosity of the fluid
- Stokes number, $St = T_E/\tau_p$, where T_E : characteristic time scale of the turbulent eddies of the gas-phase, τ_p : particle relaxation time ($= \rho_P \cdot d_p^2/18\mu$)
- Constant value of $(\rho_F/\rho_P)_{real} = (\rho_F/\rho_P)_{mod}$

Figure 1 shows the geometrical layout of both the real and model mill. The dimensions of the real mill and those

deduced after dynamic similarity for the model mill are tabulated, according to the notation of Fig. 1, in Table 1.

Figure 2 presents the layout of the set-up where the experiments have been performed, which consists of the model mill, a cyclone to separate and retain the glass particles used in the experiment and a tank for particle collection.

The particles are sucked, due to the vacuum developed during the fan operation, are mixed with air, and then they are transported in the mill. At the exit of the mill the mixture of air and particles are transported to the cyclone for separation.

Tables 2 and 3 tabulate the operational characteristics for the gas and solid-particle phases, as they have been realized in the model mill and are compared to the real-mill operational data.

The main differences between the two mills (the prototype and the model) are the following:

- In the real mill the working medium are the furnace flue gases, whereas the working medium in the model is air.
- In the real mill lignite is dried and pulverized, whereas in the model the cold air acts only to convey the glass-particles inside the mill, without pulverization and moisture retention.

Table 1. Dimensions of the real and model mill

Dimensions	Real mill (mm)	Model Mill (mm)
a	2830	370
b	2135	360
c	3700	540
d	2400	205
e	2070	340
f	2335	320
g	1900	282
h	2100	308
i	2600	352
j	3000	408
k	3000	270
l	3225	280
m	6120	550
n	11190	1280
o	4200	447.5

Table 2. Characteristics of continuous phase

	Real mill (flue gases)	Model mill (air)
m (Kg/h)	260867	1011
V (m ³ /h)	359321	864
U _{bulk} (m/s)	22	5.71
Re	1.97 · 10 ⁶	6.9 · 10 ⁴
Fr	0.31 · 10 ⁶	0.078 · 10 ⁶
μ (μPa·s)	19.497	19.83

Table 3. Characteristics of dispersed phase

	real mill (particles of lignite)	model mill (glass particles)
m _p (Kg/h)	78474	210.85
V _p (m ³ /h)	56	0.084
d _p (μm)	159.3	42.84
ρ _p (Kg/m ³)	1400	2500
τ _p (ms)	101.23	12.85
T _E (ms)	109	36
St	1.077	1.08
Re _p	-	3.8
C _D	-	6.3

3. DESCRIPTION OF MEASURING PROCEDURE

The flow visualisation has been performed with a PANASONIC CAM-CORDER MS4 Video Camera and with a 135 CLR EOS-1N camera. The glass particles have been fed in the model mill and the flow field has been uniformly lit with a 2000W lamp. Traces of the particle motion have been video recorded and photographed.

The laser-Doppler anemometer used for the velocity measurements is the Dantec/Invent "FlowLite" system consisting of an integrated laser-optical unit for back scattering measurements, a signal processor (Flow Velocity Analyzer-FVA) and oriented software (FLOware/graphics), (Dantec/Invent, 1994). The FlowLite integrated 1D laser-optical unit comprises a 10mW He-Ne laser, a 40 MHz Bragg cell and lenses. The unit is connected to a 60mm diameter optical probe by a fiber optic cable. A 160mm focal length lens is used in the probe resulting to a measuring volume size 75μm×630μm. The beam separation has been 38.4mm with 1.7mm beam diameter.

A constant shift frequency of 40MHz has been produced from a Bragg cell driver, incorporated into the signal processing unit. The FVA covariance signal processor employs special detection and validation techniques. A frequency detector, incorporating a phase detector, and a burst detector based on signal intensity use analogue correlation to analyze the detected signals and determine the flow characteristics. The covariance processor comes with a dedicated interface board that connects it to a P.C. All the settings and functions of the processor are controlled from the P.C. Six different band-pass filters ranging from 120kHz to 36MHz can be selected. The FVA can analyze low signal-to-noise ratio signals, and provides higher data rates than processors based on the counter principle. Velocities ranging from -16 to +80m/s can be measured. The system has a burst validation based on signal-to-noise ratio and the number of fringes in the measuring control volume and it uses a threshold down to -6dB. The detected data rate can be up to 150,000 samples/s with continuous trigger (800Hz or 26KHz). The arrival

time resolution is 1 μ s and the dead time varies from 500ns (typical) to 800ns (maximum).

The FLOWare software provides on-line monitoring of data acquisition and processing. Mean and rms velocities, turbulence intensity, flatness and skewness, histograms of velocity, transit time, arrival time, and the energy spectrum have been measured at different locations in the model of the lignite mill.

For the measurements presented here glass particles ($\rho_p=2500\text{Kg/m}^3$) have been used of 45 μ m average diameter (size distribution 0-60 μ m). Mean and rms quantities and particle arrival rates have been measured at each location based on 10000 collected samples per measuring location. Systematic and random errors in the mean velocities have been estimated to be of the order of ± 0.3 m/s and $\pm 2.5\%$ of the local value respectively. Random errors incorporated in the measurement of the particle arrival rates are about $\pm 15\%$. Errors due to the collected sample size were less than 1% in the mean velocities for 40% turbulence intensity and 95% confidence level and less than 2% in the turbulence quantities for 99% confidence level (Yanta, 1973).

4. RESULTS

4.1 Mean Velocity Profiles

As already discussed in the previous section the particle motion in the "blade" part of the mill is complex, involving crushing of the particles, heat and mass transfer due to the evaporation of the moisture contained in the fuel and consequent drying of the particles. Even in the model mill, where crushing of the particles and heat and mass transfer effects were neglected, the performance of laser Doppler anemometry velocity measurements required special instrumentation, which has been not available.

Hence the measurement emphasis has been placed in investigating the behaviour of the simulated lignite particles as they pass through the intermediate duct connecting the spiral mill volute to the classifier. The video recording of the particle motion indicated that particles impinge on the blades when they enter the beater wheel section. In the sequence they pass through the spiral mill volute, where they collide several times with the volute internal walls (photo 1). Particles tend to concentrate in the outer wall area, until they reach the convergent intermediate duct. The particle motion in the intermediate duct is a dilute two-phase flow of suspended solid particles mainly governed by gravity, drag, inertia and friction forces acting on the particles. The calculated Stokes numbers for the real and model mills (table 3) are close to unity, and particles are expected to follow closely the gas-phase motion. In the classifier the flow is 3D, strongly swirling and the local particle void fraction is affected by the position of the dampers (photo 2) that control the amount of gas that recirculates in the mill.

Representative measurements of the axial velocity component have been performed in the various sections of the mill in order to define the local gas flow rates and the mass balance of the flow. The results are shown in table 4.

Table 4. Mass Balance

SECTION	Air Velocity U _{max} (m/s)	V (m ³ /s)
SUCTION	5.5	0.24
OBLIQUE SECTION	3.36	0.237
RECIRCULATION angle of dampers (deg)		
0	11.74	0.023
45	12.67	0.0248
90	7.83	0.015
OUTLET DUCT angle of dampers (deg)		
0	13	0.23
45	11.1	0.196
90	5.2	0.0918

Errors involved in the mass balance are of the order of 20%. As the table shows the sum of the volumetric flow rate of gas that goes through the recirculation section and the outlet duct is approximately equal to the volumetric gas flow rate at the suction when the dampers are totally open (i.e. angle equal to zero). Measurements of the streamwise and normal mean velocities of the particles have been obtained in the vertical mid-span plane for nine different horizontal planes along the axis (z-axis) of the duct, and are shown in Fig. 3 and Fig. 4 respectively. The profiles measured at z=0mm correspond to the entrance of the classifier section. Video recording indicated that the flow was directed upwards coming from the spiral mill volute, and the profiles from z=600mm, to z=0mm present the particle motion in the convergent intermediate duct. The profiles at z=-100mm and z=-215mm present the characteristics of the motion of the particles before they enter the classifier, as they tend to pass through the dampers. The streamwise velocity profiles of Fig. 3 indicate that the particle flow enters this part of the mill deformed. At z=600mm the highest streamwise mean velocities have been measured close to the duct outer wall, it is visual that the particles tend to accumulate towards the outer wall of the convergent intermediate duct whereas at z=80mm the particle flow is directed towards the duct inner wall, with highest streamwise and normal mean velocities (Fig. 3 and Fig. 4 respectively) measured close to the inner duct walls. Figures 3 and 4 include also four additional profiles of axial and normal mean velocities, measured along and across the

vertical mid-span plane. The profiles demonstrate the two-dimensional nature of the flow in the intermediate duct. The profiles measured at the outlet duct are also included in figures 3 and 4, and indicate the local flow symmetries.

The measurements indicated that the convergent intermediate duct acts to re-direct and smooth-out the irregularities of the particle motion as they come from the spiral mill volute. Nevertheless, the mill classifier caused the particle flow to get once more distorted as the particles exit the intermediate duct to enter the classifier, that could be clearly seen in the video recording. The measured high values of the mean streamwise and normal particle velocities close to the dampers at $z=0\text{mm}$, $z=-100\text{mm}$ and $z=-215\text{mm}$ demonstrate the flow distortion. Visual observation, combined with the measured particle data rates (Fig. 6), suggests that a small amount of particles impinges on the upper wall. Most of them follow the upward gas flow and are directed towards the dampers.

4.2 Erosion Wear

The mechanisms and parameters governing mechanical erosion wear caused by impinging particles on solid surfaces have been extensively investigated, e.g. Humphrey (1990), Raask (1988). Erosion is widely defined as the ratio of mass removed from a surface over the total mass of particles impinging on a surface, and it depends markedly on the speed of the incident particles and the impact angles (angle formed between a plane tangent to the surface at the impact location and the direction of motion of the incident particle). It has been empirically found (Humphrey, 1990) that for ductile materials maximum erosion is caused when a particle strikes a surface with impact angle among 10° and 30° . Evidently, control of particle trajectories and impact speeds offers means for controlling mechanical erosion wear.

Particle velocity vector plots, shown in Fig. 5 indicate that particles enter ($z=600\text{mm}$) the intermediate duct with a small vector angle, directed away from the mill walls, probably due to the change in the preceding mill volute curvature. The inclined wall, at the lower inner part of the duct is exposed to direct impingement of particles ($z=425\text{mm}$ and $z=330\text{mm}$), which move towards the inclined wall with a considerable speed and angle (as shown in Fig. 5). Hence erosion wear is expected to be significant in the inclined part of the intermediate duct. This is further confirmed by the particle arrival data rates, selectively shown in Fig. 6, for $z=330\text{mm}$ at the inclined wall, and at $z=-215\text{mm}$ at the upper part of the duct before the classifier entrance. The measured data rates at $z=330\text{mm}$, indicate two peaks. One peak is located close to the outer vertical wall, where particles move with high velocities, but low impact angle and hence erosion wear is expected to be low. Contrary the second peak located close to the inner inclined wall, corresponds to high particle velocities (Fig. 3), high and impact angles. Measured impact angles in this area have been ranging among 20° to 30° , suggesting increased erosion wear. Along the duct, measured particle data rates indicated no preferential concentration of the particles. The vector plots of Fig. 5 indicate

that particles, although they move with relatively high speeds along the duct, they impact on the wall with small angles resulting to low erosion wear. Along the duct the measured streamwise and normal velocities, shown in Fig. 3 and 4, indicate a uniform distribution of the two components (e.g. at $z=270\text{mm}$ and 160mm).

Further downstream in the duct ($z=160\text{mm}$, or $z=80\text{mm}$) both the streamwise and normal velocity components attain high values towards the inner wall of the duct (Fig. 3 and 4 respectively). In this region, the angle of impact increases to values close to 30° at the outlet corner of the convergent duct joining it to the entrance of the classifier section, indicating that erosion wear is again expected to be high in this region of the flow. At $z=-100\text{mm}$ and $z=-215\text{mm}$, the velocity vectors in Fig. 5, show high values of particle speeds and impact angles as they are directed to the recirculation dampers, suggesting once more high erosion wear.

5. CONCLUSIONS

Velocity measurements, obtained with a fiber-optic laser Doppler anemometer and video recording have served in describing the particle motion in a model of a beater wheel mill. Velocity profiles and particle data rates have been measured in the convergent intermediate duct connecting the spiral mill volute to the classifier section. The results indicated that this part of the mill re-directs the flow from the outer mill casing walls to the inner walls towards the classifier section. The measured velocity vectors and measurement of the particle mean impact angles indicated that erosion wear is expected to be high at the inclined wall connecting the convergent duct to the mill spiral section and at the duct outlet, at the connection with the mill classifier. Erosion wear in these two parts can be reduced by design modifications that alter the angle of impact of particles on the walls. For example, increasing the angle of inclination of the inclined wall, will modify the particle impact angles to values above 30° , which will lead to reduced mechanical erosion wear.

Further parametric experimental investigations, e.g. for various particle sizes, different damper angles etc. can support the understanding of flow characteristics in beater wheel mills. The obtained data can support the validation of CFD codes.

6. ACKNOWLEDGMENTS

The authors would like to acknowledge the support of Dantec/Invent Measurement Technology and the cooperation of the Greek branch, E.Gavala-Larigou & Co representatives, for making available the FlowLite system. Also the significant technical contribution of the cameraman Constantinos Markoulakis for the visualisation work is acknowledged.

The project has been financed by the Greek General Secretariat of Research and Technology and the Greek Public Power Cooperation.

7. REFERENCES

Anagnostopoulos, J., and Bergeles, G. 1993, "Numerical investigation of grinding process in power plants, Part I: Calculations inside a fan-type mill," NTUA-Mech. Eng. Dept., Fluids Section, Technical Report.

Anagnostopoulos, J., and Bergeles, G. 1993, "Numerical Investigation of grinding process in power plants, Part II: Calculations inside the classifier," NTUA-Mech. Eng. Dept., Fluids Section, Technical Report.

Dantec/Invent. 1994, "Flow Lite reference guide"

Gehrke, B., and Stegelitz, P., 1995, "Mühlen für das KW 'Schwarze Pumpe' Sonderdruck aus EVT-Register 53/1994," EVT-Bericht, EVT Energie und Verfahrenstechnik GmbH., 112/95.

Humphrey, J. A. C., (1990), Review: "Fundamentals of fluid motion in erosion by solid particle impact," *Int. J. Heat and Fluid Flow*, vol. 11., No. 3, pp. 170-195.

Kloukiniotis, A., and Hatzifotis, D., 1993, "Private Communication", Greek Public Power Corporation, Athens, Greece.

Petrougakis, L., 1994, "Dimensional analysis, design and construction of an experimental lignite beater wheel model mill for the investigation of the mill operational characteristics," Diploma thesis, N.T.U.A., Mech. Eng. Dept., Thermal Section.

Raask, E., 1988, "Erosion wear in coal utilisation," Hemisphere Publishing Corporation, New York.

Yanta, W. J., 1973, "Turbulence measurements with a laser Doppler Velocimeter, Report NOLTR-73-94, NOL, White Oak, Silver Spring, Maryland.

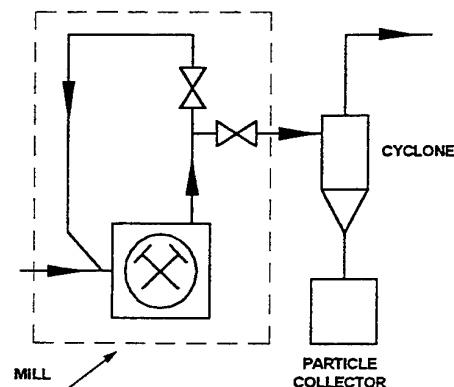


Figure 2. Layout of the experimental set-up.

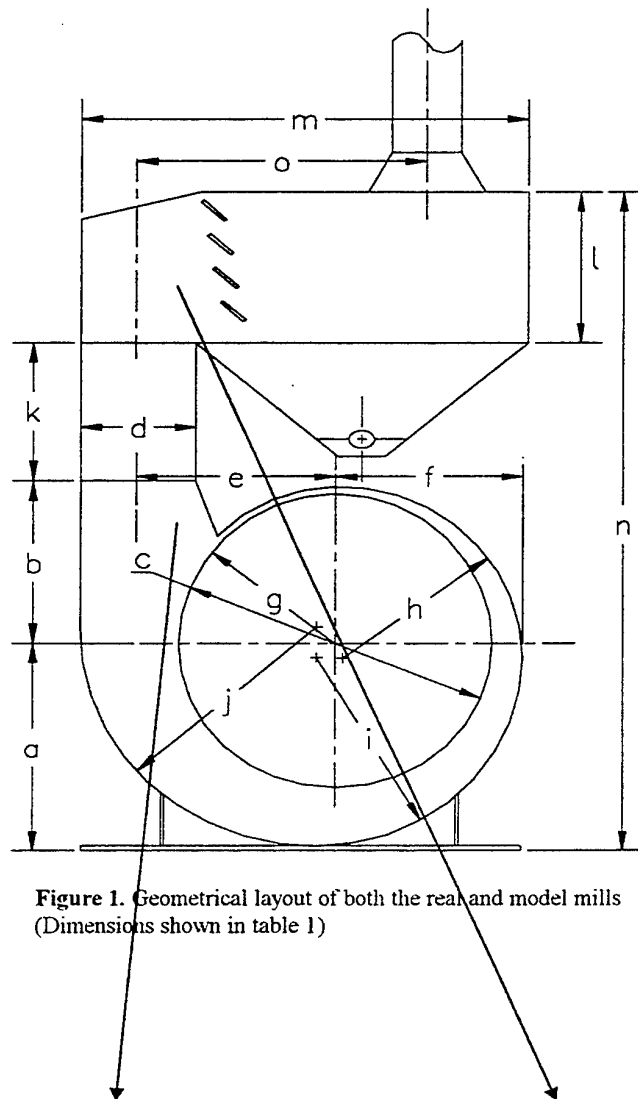


Figure 1. Geometrical layout of both the real and model mills (Dimensions shown in table 1)



Photo 1.

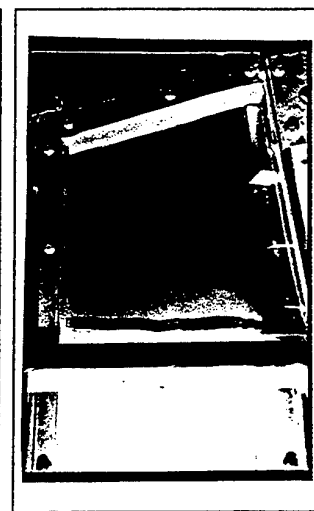


Photo 2.

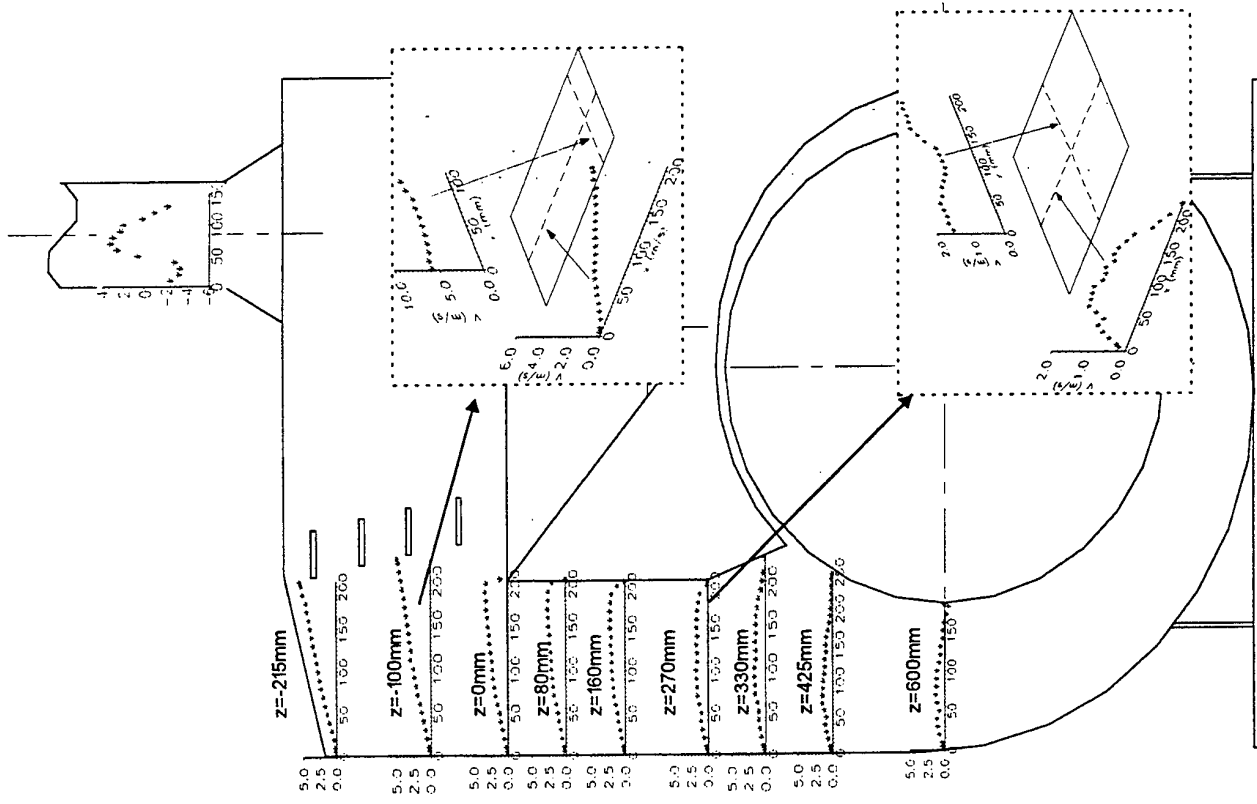


Figure 3. Measured particle streamwise mean velocity profiles in nine different horizontal planes along the duct.

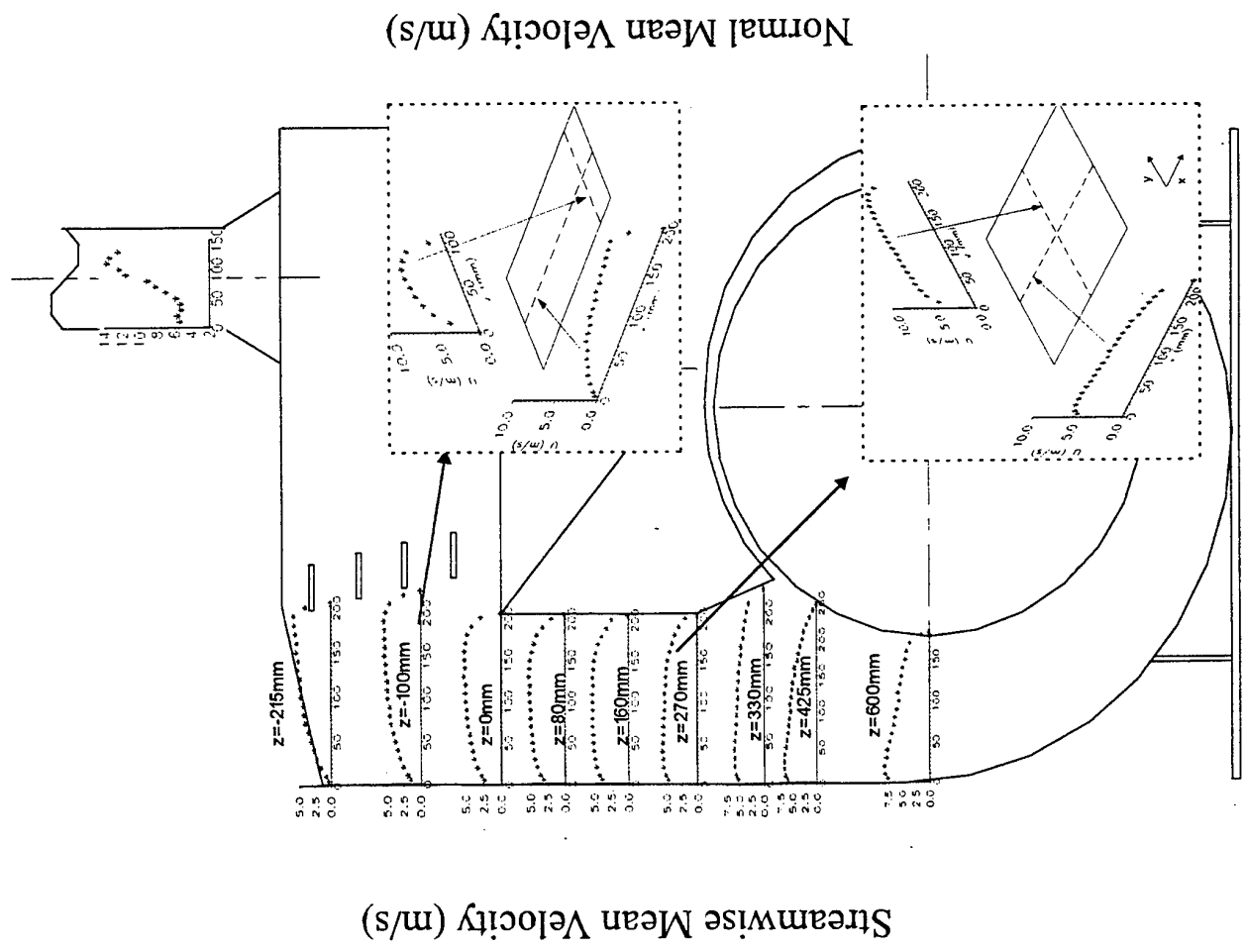


Figure 4. Measured particle normal mean velocity profiles in nine different horizontal planes along the duct.

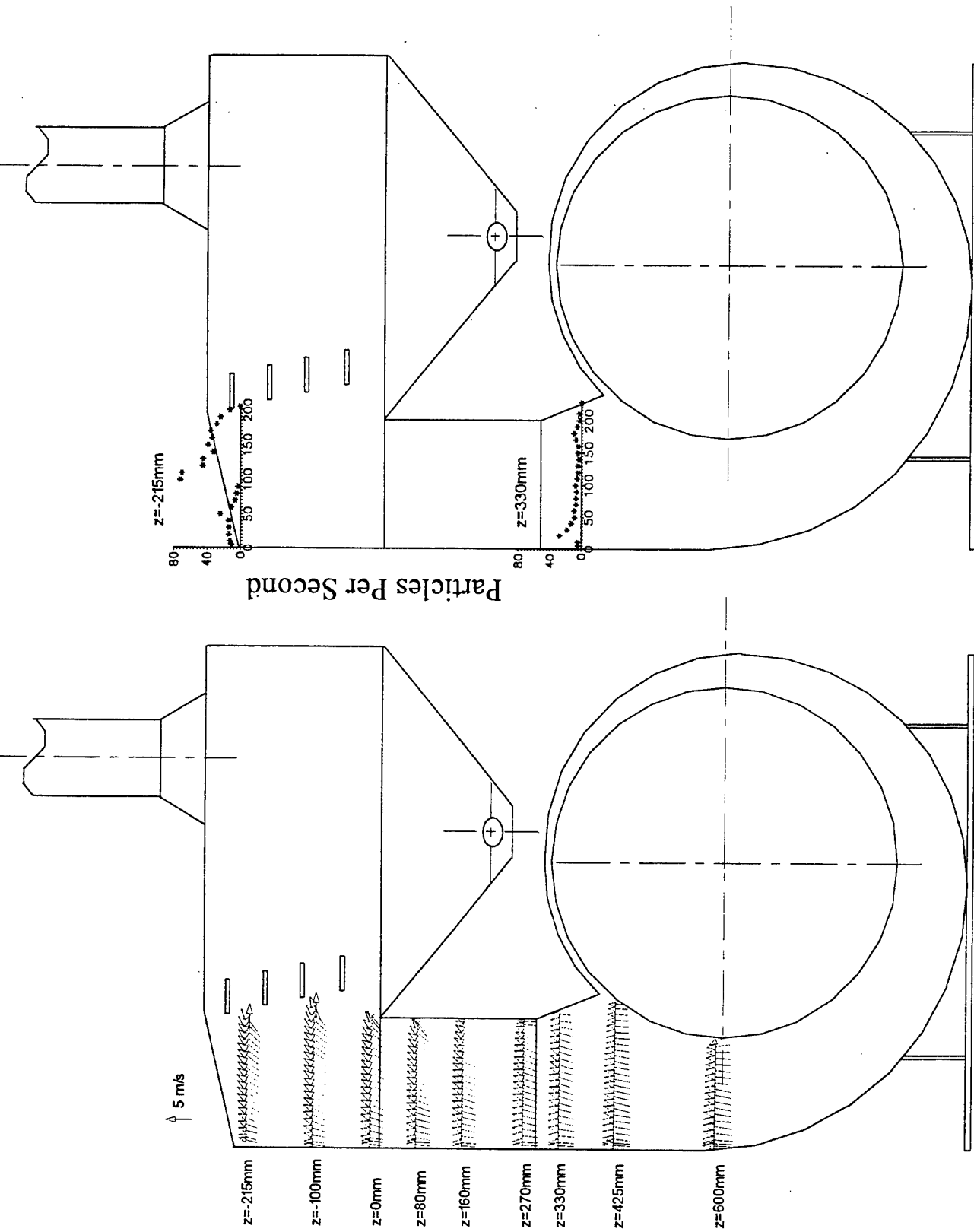


Figure 5. Measured particle mean velocity vectors plots.

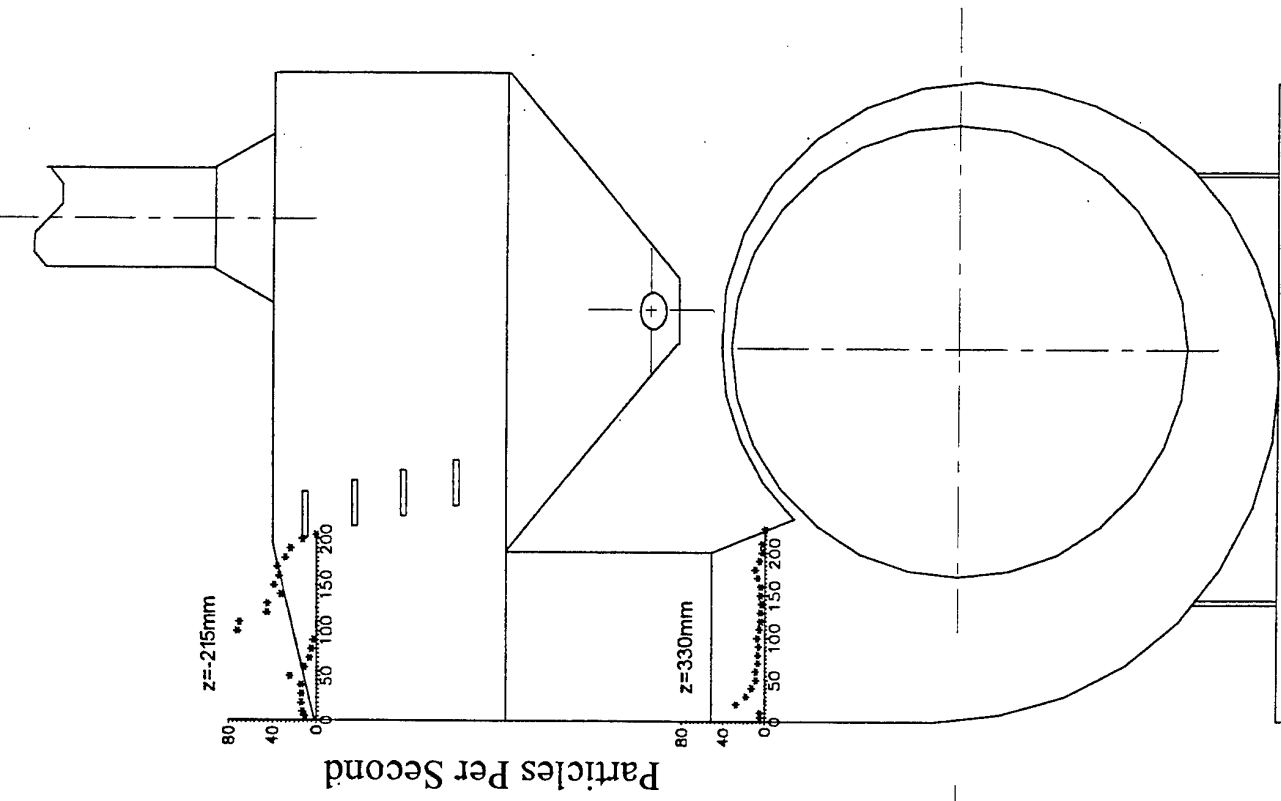


Figure 6. Measured particle data rates

SESSION 39

Oscillating Flows and Flames

VELOCITY, PRESSURE AND HEAT RELEASE CHARACTERISTICS OF A PREMIXED PULSED FLAME

D.F.G. Durão, E.C. Fernandes and M.V. Heitor

Instituto Superior Técnico
Mechanical Engineering Department
Av. Rovisco Pais, 1096 Lisboa Codex
Portugal

ABSTRACT

The use of a laser-Doppler velocimeter has been extended to the analysis of the coupling mechanisms between pressure, velocity and heat release fluctuations typical of pulsed flames downstream of a pipe flow, through its combination with the chemiluminescent emissions of free radicals in the flames and the pressure oscillations in the upstream flow. The procedures which allow the laser-Doppler data to represent the pulsed flame are identified in terms of the energy associated with its predominant frequency of oscillation of 265 Hz, which is shown to occur for data ready frequencies above 2.3kHz. The results quantify coherent motions between pressure and heat release oscillations, which are about 45° out-of-phase with the velocity oscillations in the flame front.

1. INTRODUCTION

A continued, but renewed, attention has recently been given to pulsating combustion because of its attractive features recognised in the search of fuel savings, increased productivity and reduced emissions (Zinn, 1996). However, the ability to predict and, hence, design practical pulsating systems has been challenging because of the complex coupling of the various controlling parameters and the lack of a well-founded theory for the phenomena involved. This paper is aimed to contribute for this discussion and to help clarifying the current understanding of the coupling mechanism between pressure, velocity and the related heat release fluctuations on combustors of practical interest. To achieve these objectives, a recirculating flame is analysed at the end of long pipe, as produced by stabilising a propane/air flame downstream of a cylindrical baffle.

In the analysis of pulsed combustion systems, it is important to distinguish the two main types of thermoacoustic devices. First, those where the thermoacoustic interaction occurs spontaneously at the natural modes of oscillation of the combustion chamber, with the Rijke tube being the most important example (Raun et al, 1987); second, those where the fuel/air supply are controlled by mechanical or aerodynamical valves (Keller et al, 1987). For the former, a further distinction can be made based on the heater type and, consequently, on the coupling mechanisms that support the

oscillations. If an electrical device (constant current supply) or solid fuel bed (Carvalho et al, 1989) is used, then we are in the presence of a trully Rijke tube and the oscillations are driven by the oscillatory convection/conduction heat transfer from the heat source to the air flow. On the other hand, for gas-fired burners where chemical reaction is the main source of energy, the oscillations are flame-driven and the specific coupling mechanisms may include changes in turbulent mixing rate, flames area variation, periodic air/gas supply and hydrodynamic instabilities (Fernandes and Heitor, 1996).

Although the processes mentioned above have been shown to be influenced, among other parameters, by the air and gas flow rates and the blockage and burner type (e.g. Heitor et al, 1984, Sivasegaram and Whitelaw, 1987, Sivasegaram and Whitelaw, 1991), attention is given in this paper to the coupling mechanisms between pressure fluctuations and the other time-resolved flow variables, which explain the on-set of combustion-induced oscillations. Since the chemical reaction is the main source of energy driving the pressure field, the related response of the heat release rate is of essential importance, being largely controlled by the local availability of the air-to-fuel mixture ratio, together with the status of instantaneous pressure, temperature and velocity. However, to complete the analysis, it should be noted that, work on acoustic driven-oscillation (Keller et al., 1989) has shown that the coupling mechanisms depend on the characteristic time scales, which include those of the acoustic field, turbulence and chemical reaction. For example, if the time scale associated with the acoustic field is much higher than that of turbulent fluctuations, both fields are decoupled. In general, the coupling between the three main time scales mentioned above is not easily identified (e.g., McIntosh 1991) and the techniques described in this paper have been developed in order to improve understanding of the processes involved.

An additional difficulty in the interpretation of combustion-induced oscillations is the need to account for the dependence of the pulsations frequency upon the phase difference between the pressure and the heat release oscillations. This has unabled many past investigators to correlate measured pulse combustor frequencies with predicted acoustic modes of the system under analysis, but has been clearly analysed by Zinn (1992) and has contributed to the motivations of the present work.

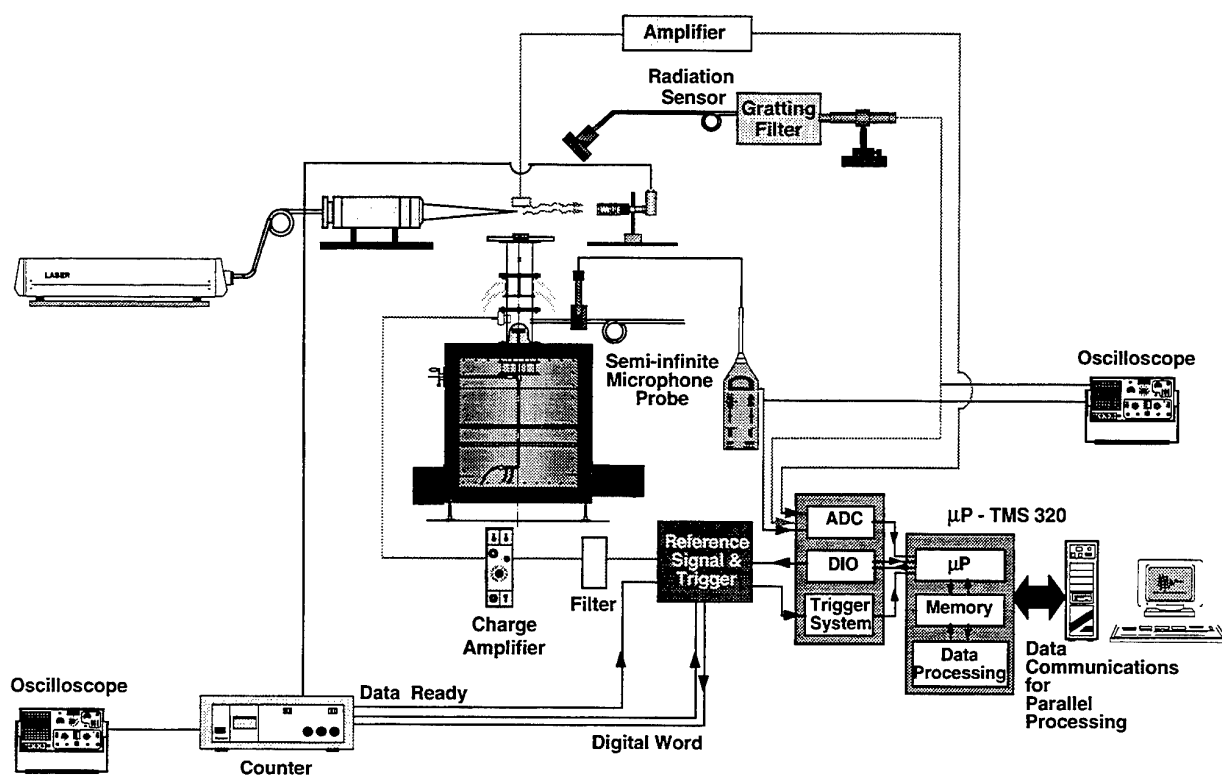


Fig. 1. Schematic drawing of experimental apparatus with identification of the instrumentation used.

The next section briefly described the flow configuration and the experimental techniques used. Sample results are presented and discussed in section 3 and the paper is concluded with a brief description of the main findings of the work.

2. EXPERIMENTAL APPARATUS AND PROCEDURES

2.1. Flow Configuration

The apparatus consists of cylindrical duct of stainless-steel with a variable length, an a diameter of 186mm, which was placed on the top of a cubic plenum of 3m³, figure 1. The tube was designed to work with two acoustically-opened ends with a length varying from .25mm to 3m in steps of .25mm, allowing the fundamental resonance frequency to range between 50Hz and 1kHz. The burner holder can be moved continuously inside the duct, in order to search for the optimum driving location for heat addition (e.g. Fernandes and Heitor, 1996), and several flame stabilisers can be assembled on the top of it. However, for most of the results described here, the pipe length was kept constant and equal to 0.52m and the flame holder was positioned 10mm downstream of the pipe exit. The resulting flame is open to the atmosphere, but offers the advantage of easy access to the techniques described below.

The primary air was injected with a velocity of 1.7m/s ($Re = 20000$) through the plenum, where it was seeded with powdered aluminum oxide (nominal diameter below 1.0μm before agglomeration) making use of a purpose-built cyclone generator. The burner consists of a cylindrical bluff-body ($\phi = 940$ mm, height=20 mm) surrounded by holes, with a diameter of .5 mm, through which a mixture of air and gas is injected, figure 2, with an equivalence ratio $\phi_i > 3$.

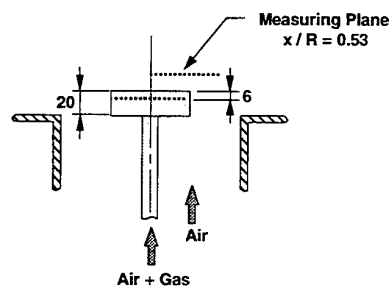


Fig. 2. Schematic diagram of flame holder and shape, together with identification of main measuring zone used throughout this work.

2.2. Experimental techniques

Figure 1 shows schematically the various experimental techniques used throughout this work. The radiated sound intensity from the flame was measured with a free-field condenser microphone (B&K 4130) together with a pre-amplifier (B&K 2130) with a flat response over a frequency band of 20Hz to 10kHz. The pressure fluctuations along the duct were measured with a semi-infinite probe with a flat response up to 1kHz. The signal output of the microphone was digitally sampled at a rate of at least 20kHz and post-processed in a 16-bit DSP board. The spectral content of the sound was determined by digital Fast Fourier Transforms with a resolution in the frequency domain of at least 2.44Hz. Figure 3 quantifies the acoustic characteristics of the flow in the pipe upstream of the flame and identifies a standing half-wave with a predominant frequency of 265 Hz. The flame is then located in a velocity antinode and the resulting time-resolved characteristics are described below.

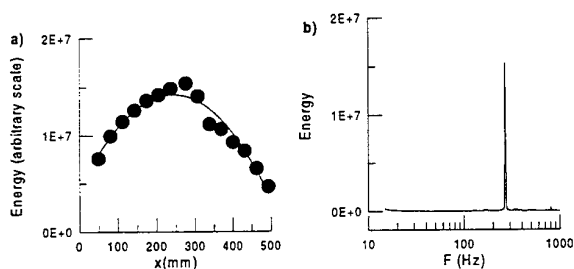


Fig. 3. Acoustic characteristic of the pipe flow upstream of the flame:

- local amplitude of pressure fluctuations along the pipe
- power spectral density of pressure fluctuations, with identification of predominant frequency at 265 Hz.

The light emitted from the flame was used as a signature of the rate of change of heat release (e.g. Willis et al, 1991, Keller and Saito, 1987) in terms of the chemiluminescence emission due to the radiative decay of electronically excited radicals existing in the reaction zone, such as $\langle \text{OH} \rangle$, $\langle \text{CH} \rangle$ and $\langle \text{C}_2 \rangle$ (Gaydon and Wolfhard, 1979). The light from the flame was collected by a 200mm focal length lens and guided through a fiber optic cable to the entrance slit of the a 125mm grating monochromator (Oriel 77250), which was equipped with a photomultiplier (EMI-9658 A).

The signal output of the photomultiplier was digitally sampled at a rate of at least 20kHz. The spatial resolution of the system and wavelength readout were evaluated and calibrated using the blue and green beams of an Argon-Ion laser and uncertainties in the measurements are estimated to be less than 10%, with a resolution of 7nm at half peak transmission.

Time-resolved velocity information was obtained with a laser-Doppler velocimetry which comprised an Argon-Ion

laser operated at a wavelength of 514.5 nm and a power of around 1W, a fiber optic (DANTEC) used to guide the beam to an optical unit arranged with a two beam system with sensitivity to the flow direction provided by light-frequency shifting from a Bragg cell at 40MHz, a 310 mm focal length transmission lens, and forward-scattered light collected by a 310 mm focal length lens at a magnification of 1.0. The half-angle between the beams was 5.53° and the calculated dimensions of the measuring volume at the e^{-2} intensity locations were 2.3 and 0.219 mm. The output of the photomultiplier was mixed with a signal derived from the driving frequency of the Bragg cell and the resulting signal processed by a commercial frequency counter (DANTEC 55296) interfaced with a 16-bit DSP board.

The complete LDV system was mounted in a three-dimensional traversing unit, allowing the positioning of the laser-velocimeter control volume within $\pm 0.25\text{mm}$. Measurements were obtained with the laser beams in the horizontal and vertical planes and by traversing the control volume along the horizontal and vertical directions to allow the determination of the axial, U, and radial, V, time-resolved velocities.

Although various weighting methods have been proposed to correct for velocity bias effects (e.g. Durst et al, 1981) no corrections were applied to the measurements reported here. The systematic errors that could have arisen were minimised by using high data acquisition rates in relation to the fundamental velocity fluctuation rate, as suggested for example by Dimotakis (1978) and Erdman and Tropea (1981). This could be easily achieved because the rate of naturally-occurring particles was sufficiently high for the flow conditions considered here.

Spectral analysis of LDV signals was carried out by resampling the time series after a linear interpolation with minimum interval time given by the mean data rate.

Figure 4 shows results obtained as a function of the data ready frequency, f_{DR} , of the counter for a typical location in the reacting shear layer studied through this work. The measurements were obtained for conditions corresponding to data ready signals associated with each new Doppler burst. The results show that the predominant flow frequency of 265Hz could be identified in the spectra of the velocity fluctuations for any data rate, although the energy associated with this frequency (in a band of ± 2.4 Hz) is independent of that rate only for $f_{DR} > 2.3\text{kHz}$. This agrees with the conditions given by, for example, Adrian and Yao (1989) for which the output of the counter yields a satisfactory spectral analysis for the frequency range considered here.

The paragraphs above described the different experimental techniques used throughout this work. We now describe briefly the procedures used to acquire the various signals simultaneously. The Doppler frequency and both scalars, namely pressure and heat release, were acquired simultaneously and post-processed making use of a microprocessor, Texas Instruments-TMSC320. The scalars were digitized with a sample-and-hold analog converter at a

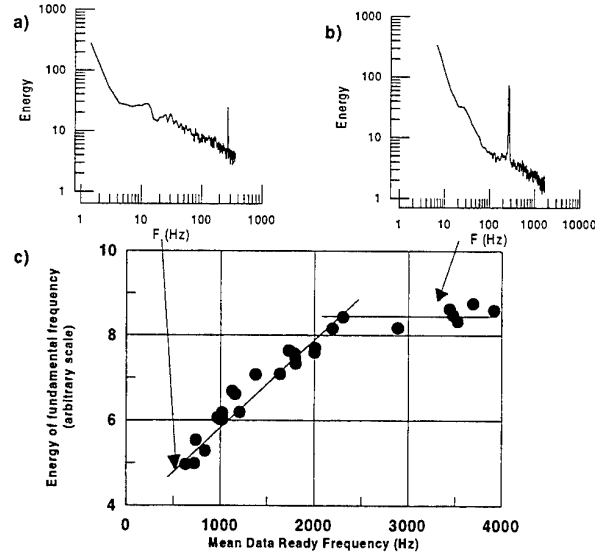


Fig. 4. Frequency analysis of measured axial velocity fluctuations as a function of data-ready frequency, f_{DR} , in the reacting shear layer ($x/R = 0.53$; $r/R = 0.91$):

- a) power spectral density of velocity fluctuations for $f_{DR} = 700$ Hz
- b) power spectral density of velocity fluctuations for $f_{DR} = 3800$ Hz
- c) energy of axial velocity fluctuations for $f = 265 \pm 2.4$ Hz, as a function of f_{DR}

rate of 50kHz/channel and stored in a circular memory buffer. The acquisition starts only when the pressure signal is zero-to-negative, which is given by a reference detector, and the buffer access, to collect data simultaneously with the occurrence of a burst, was made through an active pointer, sensitive to velocity data ready signals. The complete system can go up to 12.5kHz of data ready signals, the delay of the board to the data ready signal is less than 200ns and the window resolution between velocity and scalars is less than 1/50kHz

3. RESULTS AND DISCUSSION

The previous section has described the flow configurations, and the instrumentation used throughout this work. This section presents and discusses sample results of time-resolved pressure, velocity and emissions of $\langle C_2 \rangle$ radicals with the main objective of improving knowledge of the basic mechanisms associated with the on-set of combustion-driven oscillations.

As mentioned before, the flow under consideration is that resulting from the presence of a recirculation zone, surrounded by a reacting shear layer, located at a velocity antinode at the exit of a pipe flow, which is characterised by a longitudinal standing half-wave. The results presented here have been obtained for "rough" combustion, which is

characterised by a sharp increase in the sound pressure levels from around 80 dB to values in excess of 110 dB, when the equivalence ratio of the propane/air mixture released in the flame holder decreased under $\phi_i = 8.4$. The analysis is given for $\phi_i = 8.2$, corresponding to an overall equivalence ratio at the pipe exit of $\phi_T = 0.1$. For these conditions, the spectrum of the pressure fluctuations in any location of the pipe wall is associated with the excitation of a predominant frequency at 265 Hz, as in figure 2.

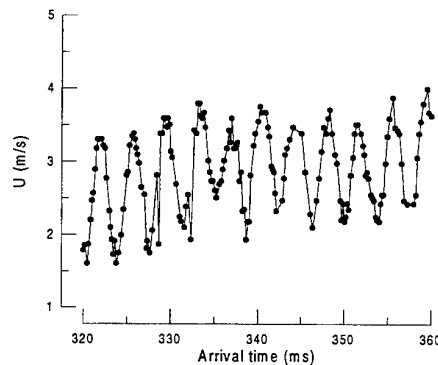


Fig. 5. Time-resolved axial axial velocity fluctuations in a typical point of the reacting shear layer ($x/R = 0.53$; $r/R = 1.17$)

Figure 5 shows typical time-resolved measurements of the axial velocity component in the reacting shear layer of the

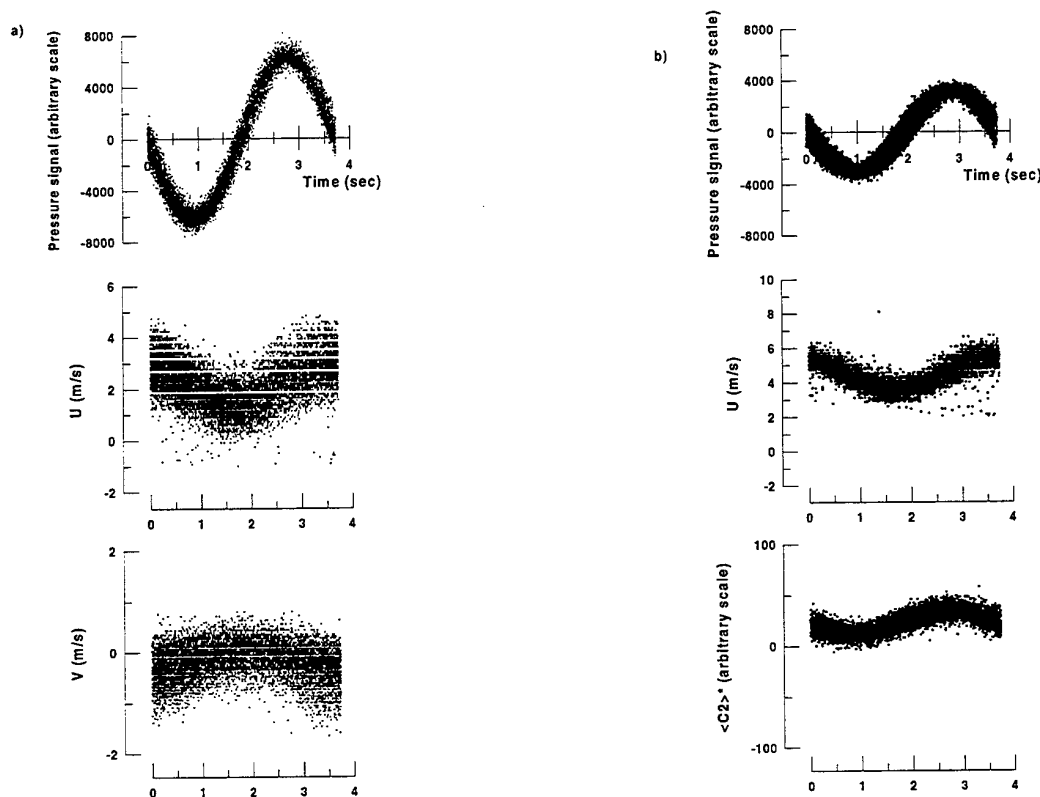


Fig. 6. Simultaneous, cycle-resolved measurement of instantaneous pressure, velocity (axial, U , and radial, V) and $\langle C_2 \rangle$ emissions in the flame ($x/R=0.53$)

- a) reacting shear layer, $r/R=0.91$
- b) reacting shear layer, $r/R=1.17$

pulsed flame considered throughout this work, which exhibits the expected periodic wave at a predominant frequency of 265 Hz, as in the related spectra of pressure fluctuations of figure 4b). The corresponding distribution of values, as measured for about 4000 cycles of oscillations, are plotted in figure 6a) over a period of oscillation (i.e., 3.7 msec), together with simultaneously acquired values of pressure, radial velocity and $\langle C_2 \rangle$ emissions. For comparison, Figure 6b) shows a similar analysis for a point located in the recirculation zone. In general, the results exhibit a periodic shape with strong coherence of the cycle-resolved values, as also verified by Lovett and Turns (1993) for an acoustically forced jet diffusion flame, which appears to be independent of the flame location under consideration. If the signals are filtered for the band of the fundamental frequency, the analysis shows a correlation coefficient above 0.90 between the pressure fluctuations and $\langle C_2 \rangle$ emissions, as well as between the fluctuations of the two velocity components, being the phase between these two sets of data about $45^\circ \pm 4^\circ$. Assuming that the measured $\langle C_2 \rangle$ emissions are linearly proportional to the time-resolved heat release in the flame (e.g. Price et al., 1969; Fernandes and Heitor, 1996),

our experimental evidence is that the instantaneous distribution of heat release from the flame fluctuates in phase with the standing wave in the pipe, contributing for its excitation through heat additions locally released in the velocity-antinode of the acoustic wave, as may be explained from the Rayleigh's criterion for heat driven oscillations (Fernandes and Heitor, 1996).

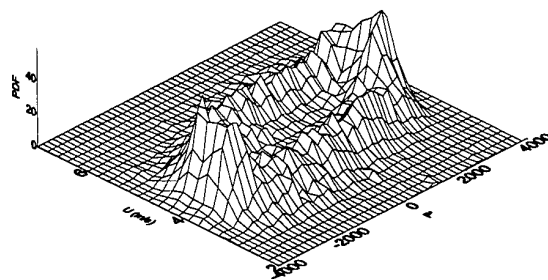


Fig. 7. Joint probability density function of pressure and axial velocity fluctuations for the conditions of figure 6b).

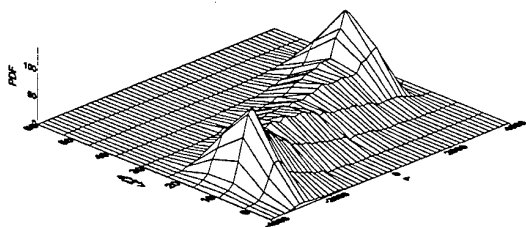


Fig. 8. Joint probability density function of pressure and $\langle C_2 \rangle$ radicals emission for the conditions of figure 6b).

The relative coherence of the two signals can be further analysed by the joint probability density function of figure 7, which is to be contrasted with that of figure 8 for the velocity and pressure signals. The latter characterizes the observed lag between pressure and pressure fluctuations, which is likely to be associated with a relative weak contribution of the velocity fluctuations to the fluctuating component of heat release. The explanation is that the periodic heat release is more likely to be driven through the oscillating pressure gradients, which determine directly the rate of reaction of premixed flames (e.g. Williams and Libby, 1995). This is because the reaction rate for the present flame conditions is expected to be controlled by the rate of turbulent mixing, which, in turn, is directly influenced by the instantaneous axial pressure gradient (e.g. Takagi et al., 1985; St rner and Bilger, 1986; Ferr o and Heitor, 1995).

The relative coherence of the time-resolved flame shape can be derived from the analysis of figure 9, which quantifies the correlation between pressure and velocity fluctuations across the reacting shear layer. The results should be analysed in terms of the relative lack of phase between the velocity and pressure signals in the flame and reflect the turbulent contribution to the periodic motions, as clearly identified in the distribution of figure 6.

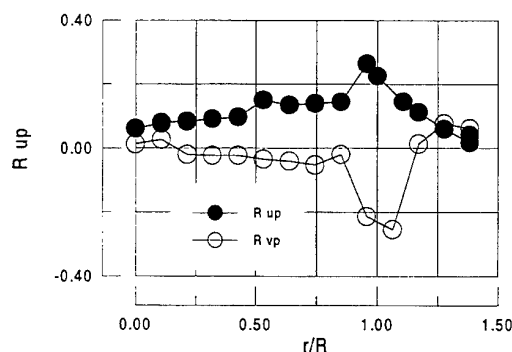


Fig. 9. Correlation coefficient for the pressure and velocity fluctuations across the recirculating flame, $x/R = 0.53$.

4. CONCLUSIONS

A laser-Doppler velocimeter has been used and combined with the chemiluminescent emission of $\langle C_2 \rangle$ radicals in a premixed flame to characterise the nature of thermoacoustic oscillations driven by a premixed flame located at the velocity antinode of a standing half-wave in a pipe flow. The analyses characterizes the acoustic behaviour of a pulsed unconfined flame and shows that the presence of an acoustic velocity antinode in the zone of energy release, together with the oscillatory pressure gradient associated with a recirculating flow, may influence the turbulence pattern and therefore the local mixture, causing the instantaneous heat release to fluctuate (Heitor et al, 1984) and therefore the expansion gas to transfer work for the velocity field. While some of the results can be analysed based on the existing theories, the full understanding of the coupling mechanisms that support the oscillations must be further analysed and based on the detailed characterisation of time-resolved flame front.

REFERENCES

- Adrian, R.J. and Yao, C.S. (1989). "Power Spectra of Fluid Velocities Measured by Laser-Doppler Velocimetry. ASME, Winter Annual Meeting, Miami Beach, Florida, November 17-22, 1995.
- Culick, F., Heitor, M.V. and Whitelaw J.H. (1996). Unsteady Combustion, Kluwer Academic Publishers, NATO/ASI Series, Vol . 306.
- Carvalho, J.A.Jr., Ferreira, M.A., Bressan, C. and Ferreira, J.L.G. (1989), "Definition of heater location to drive maximum amplitude acoustic oscillations in a Rijke pipe", *Combust. and Flame*, 76, pp.17-27
- Dimotakis, F. (1978). "Single Scattering Particle Laser-Doppler Measurement of Turbulence". AGARD CP 193, Paper 10.7.
- Durst, F., Melling, A. and Whitelaw, J.H. (1981). "Principles and Practice of laser-Doppler Anemometry", Academic Press.
- Erdman, J.C. and Tropea, C.D. (1981). "Turbulence-induced Statistical in Laser Anemometers". Proc. 7th Biennial Symp. on Turbulence, Rolla, Missouri.
- Ferr o, P. and Heitor, M.V. (1995) "Turbulent mixing and non-gradient diffusion in baffle-stabilized flame", in Turbulent Shear Flows, Eds. Durst et al, Springer
- Fernandes, E.C. and Heitor, M.V. (1996) "Unsteady flames and the Rayleigh criteria", in *Unsteady Combustion*, eds. Culick, F., Heitor, M.V. and Withelaw, J.H., Nato ASI Series, Series E: Applied Sciences- Vol. 306 ., Kluwer Academic Publishers, pp. 1-16

Gaydon, A.G. and Wolfhard, H.G. (1979) Flames- their structure radiation and temperature, Ed. Chapman and Hall, Fourth Edition, London

Heitor, M.V., Taylor, A.M.K.P. and Whitelaw, J.H. (1984) "Influence of confinement on combustion instabilities of premixed flames stabilised on axisymmetric baffles", *Combust. and Flame*, 57, pp. 109-121

Keller, J.O. and Saito, .K. (1987) "Measurements of the combustng flow in a pulse combustor", *Combust.Sci. and Tech.*, 53, pp. 137-163

Keller, J.O. , Barr, P.K. Bramlette, T.T, Dec, J.E. and Westbrook, C.K. (1989) "Pulse combustion: the importance of characteristic times", *Comb. and Flame*, 75, pp.33-44

Langhorne, P.J. (1988) "Reheat buzz: an acoustically coupled combustion instability. part1- experiment", *J. Fluid Mech.* 193 pp. 417-443

Lovett, J. A. and Turns, S. (1993) "The structure of pulsed turbulent nonpremixed jet flames", *Combust. Sci. Tech*, 94, pp. 193-217

Mandaram, H. (1981) "Thermally Induced Acoustic Oscillations in a Pipe", paper No. 195-15, *Bulletin of JSME*, 24, No. 195, September 1981,

McIntosh, A.C. (1991). "Pressure disturbances of different length scals intracting with conventional flames". *Combust. Sci. and Tech.*, 75, pp. 416-424.

Price, R.B., Hurle, I.R. and Suldin, I.M. (1969). "Optical studies of the generation of noise in turbulent flames". Twelfth Symp. (Intl.) on Combustion, The Combustion Institute, pp. 1093-1102.

Raun, R.L., Beckstead, M.W., Finlinson, J.C. and Brooks, K.P. (1993), "A review of Rijke tubes, Rijke burners and

related devices", *Prog. Energy Combust. Sci.*, 1993, 99, pp.313-364

Sivasegaram, S. and Whitelaw, J.H. (1987), "Combustion oscillations in ducts". *Instrumentation for Combustion and Flow in Engines*, eds. Durão, D.F.G., Whitelaw, J.H. and Witze, P.O., Kluwer Academic Publishers, pp.45-54

Sivasegaram, S. and Whitelaw, J.H. (1991), "The influence of swirl on oscillations in ducted premixed flames", *Combust. and Flame*, 85, pp. 195-205

Stärner, S.H. and Bilger, R.W. (1986) "Joint measurements of velocity and scalars in a turbulent diffusion flame with moderate swirl", 21st Symp. (Int'l) on Combustion, The Combustion Institute, pp. 1569-1577

Takagi, T, Okamoto, T, Taji, M and Nakasuji, Y. (1985) "Retardation of mixing and counter-gradient diffusion in a swirling flame", 20th Symp. (Int'l) on Combustion, The Combustion Institute, pp. 251-258

Willis, J., Cadou, C., Karagozian, A. and Smith, O. (1991), "Diagnostic methods for visualization of heat release in unsteady combustion", Paper WSS/CI 91-68, presented at the 1991 Fall Meeting of the Western States Section/The Combustion Institute, October, 14-15 1991, Los-Angeles-CA, USA.

Zinn, B.T. (1992): "Pulse cmbustion: recent application and research issues". Twenty-fourth symp. (Intl.) on Combustion. The Combustion Institute, pp. 1297-1305.

Zinn, B.T. (1996) "Pulse combustion applications: Past, Present and Futue", in *Unsteady Combustion*, eds. Culick, F., Heitor, M.V. and Withelaw, J.H., Nato ASI Series, Series E: Applied Sciences- Vol. 306 ., Kluwer Academic Publishers, pp.113-137

MEASUREMENT OF THE PERIODIC FLOW INSTABILITY DURING A SELF EXCITED COMBUSTION OSCILLATION BY LDV

P. Zangl, J. Hermann, A. Orthmann, D. Vortmeyer

Technische Universität München - Fakultät für Maschinenwesen

ABSTRACT

Self excited combustion oscillations originate from interactions and feed back processes between acoustic pressure waves, periodic heat release and unsteady flow being a superposition of steady, oscillatory and turbulent contributions. To investigate the behaviour of the periodically oscillating flow field in a 50 kW turbulent oil burner, unsteady flow velocities were measured by LDV in the combustion chamber. Customary signal processing methods for unsteady LDV-data like root mean square calculation, probability density function or averaging of conditionally sampled data turned out not to be sufficient to interpret these measurements. So a non-equidistant Fourier transformation was developed to derive accurate information about the unsteady flow. The applied methods and their results are described in this paper.

1 MODULATED FLOW AND COMBUSTION OSCILLATIONS

Fluctuating heat release is, according to the works of Rayleigh (1878) or Dowling and Ffowcs Williams (1983) a necessary requirement for self excited combustion oscillations. These can be induced by flow oscillations like sound particle velocity, a mechanism explained by Schimmer (1974), vortex-shedding, reported for example by Reuter et al. (1989) or Milosavljevic et al. (1990) and other phenomena.

Flow modulation may appear as a pure acoustic modulation, which has its velocity minima and maxima at fixed locations according to the shape of a standing acoustic wave. Another case, found in our burner and shown in figure 1, is a propagating modulation of the flow. Accelerated flow regions pass fixed locations alternately with delayed regions. Following a characteristic point of the propagating flow velocity oscillation, for example the maximum on its way downstream, the propagation speed is obtained.

This speed is an important parameter for empirical delay time models. Such a model is discussed by Hermann et al. (1995). An approach to determine the propagation speed is to express Δt in equation 1 as the product of the phase lag $\Delta\varphi = \varphi(x_1) - \varphi(x_2)$ between the flow velocity oscillations at the locations x_1 and x_2 and the period T of the flow velocity oscillation divided by 360° .

$$v_{\text{propagation}} = \frac{\Delta x}{\Delta t} = \frac{\Delta x}{(T \cdot \Delta\varphi)/360^\circ} \quad (\text{eq. 1})$$

2 NON EQUIDISTANT FOURIER ANALYSIS

Dealing with phases requires a reference. Phase relations $\varphi(x)$ between an appropriate reference signal and the flow oscillation at various locations x will result from processing the measured velocity data $v(x, t_n)$ for each location x applying a Fourier analysis. According to Bell (1986), the conventionally applied Fast Fourier Transformation (FFT) algorithm is not convenient because it needs equally spaced data. This is not reasonable for LDV measurements where each measured velocity $v(x, t_n)$ depends on stochastic burst events. A more general form of Fourier analysis that is capable to process randomly sampled data is a non equidistant analysis $v_{\text{fourier}}(x, t_n)$ of the measured velocities $v(x, t_n)$. It is given by equation 2 where k is a running variable related to the frequencies f_k , a_k and b_k are the Fourier coefficients at the frequency f_k obtained by equations 3 and 4.

$$v_{\text{fourier}}(x, t) = \frac{a_0}{2} + \sum_{k=1}^n a_k(x) \cdot \cos(2 \cdot \pi \cdot f_k \cdot t) + \sum_{k=1}^n b_k(x) \cdot \sin(2 \cdot \pi \cdot f_k \cdot t) \quad (\text{eq. 2})$$

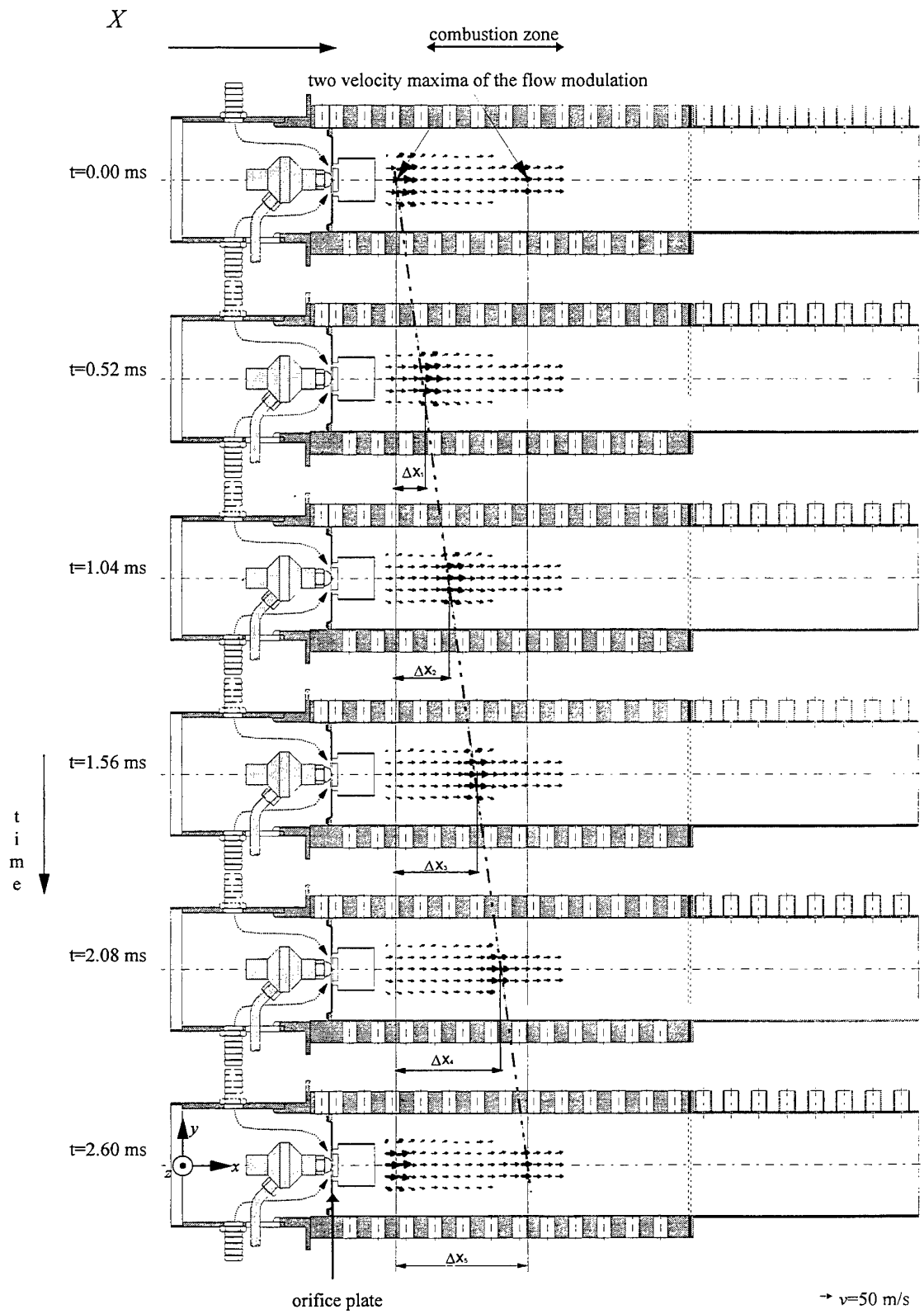


Figure 1: Modulated flow in the combustion chamber

$a_0/2$ represents the non oscillating part. It is equal to the average velocity $\bar{v}(x)$ and represents the steady part in the unsteady flow.

$$a_k(x) = \frac{1}{T_o} \int_{-T_o/2}^{T_o/2} v(x, t) \cdot \cos(2 \cdot \pi \cdot f_k \cdot t) dt \quad (\text{eq. 3})$$

$$b_k(x) = \frac{1}{T_o} \int_{-T_o/2}^{T_o/2} v(x, t) \cdot \sin(2 \cdot \pi \cdot f_k \cdot t) dt \quad (\text{eq. 4})$$

Having a record of N values of $v(x, t_n)$ for a fixed location x sampled during the time T_o , the integrals are approximated by the sums:

$$a_k(x) = \frac{2}{T_o} \cdot \sum_{n=1}^N v(x, t_n) \cdot \cos(2 \cdot \pi \cdot f_k \cdot t_n) \cdot \Delta t \quad (\text{eq. 5})$$

$$b_k(x) = \frac{2}{T_o} \cdot \sum_{n=1}^N v(x, t_n) \cdot \sin(2 \cdot \pi \cdot f_k \cdot t_n) \cdot \Delta t \quad (\text{eq. 6})$$

The time dt is expressed in the numerical approximation as Δt_n . During this investigation, it turned out that the expression

$$\Delta t_n = \frac{t_{n+1} + t_n}{2} - \frac{t_n + t_{n-1}}{2} = \frac{t_{n+1} - t_{n-1}}{2} \quad (\text{eq. 7})$$

delivered the best results.

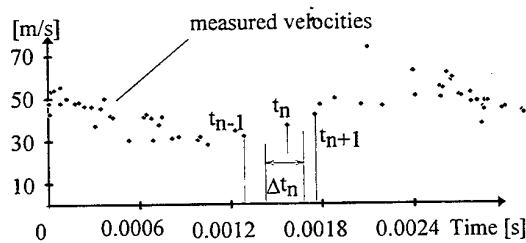


Figure 2: Measured Velocities and time interval Δt for the non equidistant Fourier transformation

As figure 2 shows, Δt_n means the time interval surrounding one measured velocity point. With this expression for Δt_n , a density weighting of the measured velocity data is obtained. If there are only few particles around t_n , Δt_n will become large and the measured velocity $v(x, t_n)$ that repre-

sents the rarely seeded interval is weighted by a large time. On the other hand, if there are many particles around t_n , Δt_n will become small and a measured velocity $v(x, t_n)$ in the interval with high particle density is weighted by a short time.

To attenuate the errors caused by sampling during a finite time T_o and to get sharp frequency peaks, the averaged velocity is subtracted from the measured velocity and the result $(v(x, t_n) - \bar{v}(x))$ then is multiplied by a hamming window $(0.54 + 0.46 \cdot \cos(\pi - (2\pi t_n/T_o)))$ before computing the Fourier coefficients. To correct the influence of the hamming window, the Fourier coefficients have to be divided by 0.54. Other windowing functions known in signal processing, which are reported by Schröder (1990), can also be applied. For the frequencies f_k this velocity amplitude

$$A(x, f_k) = \sqrt{a_k(x)^2 + b_k(x)^2} \quad (\text{eq. 8})$$

is calculated. If at a dominant frequency f_{kd} this value becomes high compared to other frequencies, the frequency is identified as the frequency of the velocity oscillation.

If only this frequency f_{kd} or any individual frequency of the spectrum $f_{1..k}$ is regarded, equation 2 reduces to the following relation

$$v_{\text{fourier}}(x, f_k, t) = A(x, f_k) \cdot \sin(2\pi \cdot f_k \cdot t + \varphi) \quad (\text{eq. 9})$$

with

$$\varphi(x, f_k) = \arctan\left(\frac{b_k(x)}{a_k(x)}\right) \quad (\text{eq. 10})$$

When there are several dominant frequencies f_{kd} in the spectrum, v_{fourier} can be approximately expressed as a sum of the term given in equation 9 using the dominant frequencies f_{kd} .

If there are different $\varphi(x_j, f_k)$ at different locations x_j , the oscillating flow is moving and the propagation speed can be derived from equation 1. If the velocity signal $v(x, t_n)$ includes an oscillation at the frequency f_k , the correct phase is found, even when the signal shows no obvious oscillation in the time domain.

3 EXPERIMENTAL SETUP

The unsteady flow was analyzed in a 50 kW turbulent ($Re \approx 88000$) diffusion flame laboratory burner shown in figure 3. It consists of a 864 mm long cylindrical prechamber with the diameter of 100 mm and a 515 mm long combustion chamber with a cross section area of 90 x 90 mm. This corresponds to the power density of a modern com-

bustion system. Both chambers are separated by the flameholder chosen from the MAN-Raketenbrenner®. This flameholder consists of an orifice plate with a diameter of 26 mm and a 32 mm long tube with a diameter of 36 mm mounted 5 mm in front of the orifice plate. At one side of that tube a small window allows optical access to the interior of the flameholder. Diesel oil serves as fuel and is supplied in the plane of the flameholder orifice plate by a HAGO DFN nozzle (0.65 USG, 60°, ES) at a pressure of 29.5 bar. It vaporizes on its way through the flameholder. The burner is operated at a fuel-air-ratio of $\lambda=1.1$. Air is supplied through the prechamber. Under these conditions the burner shows a self excited combustion oscillation with a single frequency of 384 Hz as investigated by Hermann et al. (1995).

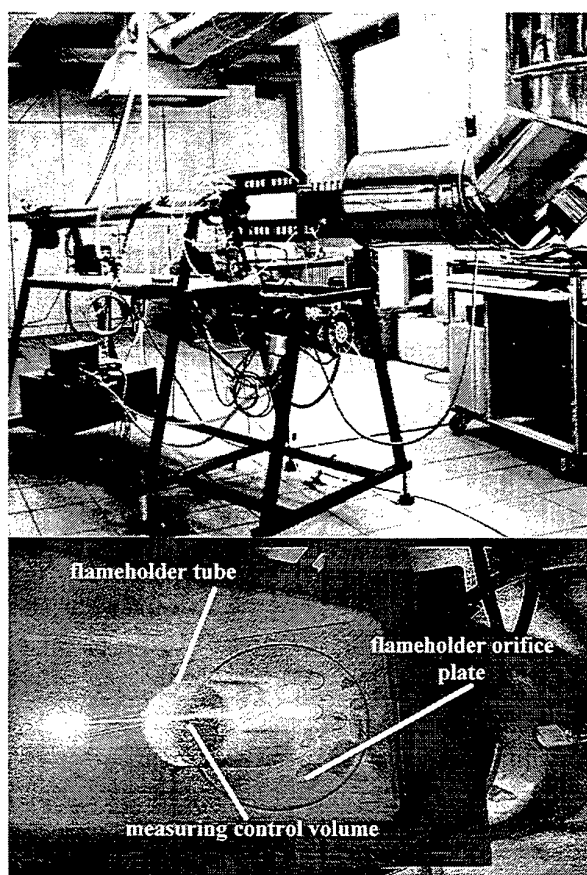


Figure 3: Laboratory burner and details of the flame holder

For optical access, 300 mm long vicor windows are mounted on both sides of the combustion chamber. The air flow is seeded at the flameholder orifice plate with a mixture of TiO_2 and SiO_2 particles for Laser-Doppler-Velocimeter measurements. The laser equipment consisted of an argon-ion-laser, usually operated at a power of 1 W, and of a three beam-two colour TSI-LDV operated in backscatter mode. The laser wavelength was 514.5 nm, if

only the horizontal channel was in operation and additionally 488 nm if horizontal and vertical channel were employed. The diameter of the measuring control volume was 0.11 mm and its length 3 mm. A TSI IFA 750 burst correlator analysed the bursts and delivered time dependent velocity data.

4 CUSTOMARY LDV-MEASUREMENTS IN THE COMBUSTION ZONE

Processing of the measured unsteady velocities delivered probability density functions at different locations of the burner flow field. Two examples for two locations are shown in figures 4 and 5. The first histogram in figure 4 reaching from 20 m/s to 70 m/s shows two peaks at 45 m/s and 33 m/s indicating oscillating flow. In the second histogram in figure 5, flow velocities of about 30 m/s to 60 m/s are encountered. The histogram in figure 5 exhibits a wide maximum at about 45 m/s. Regarding the whole combustion chamber, the average velocity accelerated from 43 m/s at the flameholder to 50 m/s at the end of the chamber.

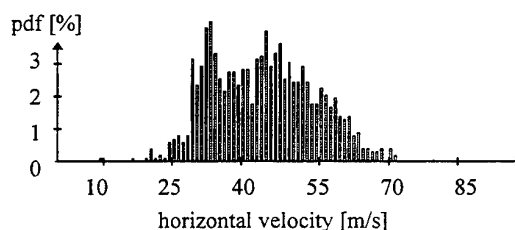


Figure 4: Probability density function 95 mm downstream of the flameholder orifice plate

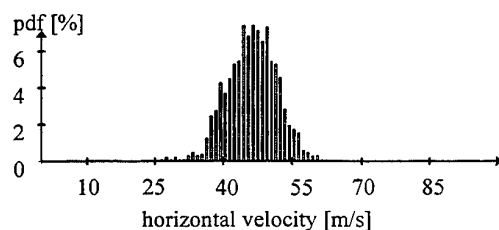


Figure 5: Probability density function 200 mm downstream of the flameholder orifice plate

The plots of the time dependent velocities in figures 2, 10 and 11 reveal, that the tracer-particle density is neither constant in time nor in space. For this reason, the peaks in the histograms 4 and 5 do not exhibit the true maxima and minima of the oscillating flow as it was found by Milosavljevic (1990). Nevertheless the frequency of the velocity oscillation can be obtained, using the slotted correlation method suggested by Bell (1986). It is the standard way of frequency analysis in the TSI-software. The frequency analysis in figure 6 shows that the velocity oscillates at 384 Hz. Also the double frequency of 768 Hz is

slightly visible. The slotted correlation method is optimised for a good frequency resolution but gives only qualitative results for the amplitudes. As this method is based on an autocorrelation, amplitude and phase information is lost during calculation.

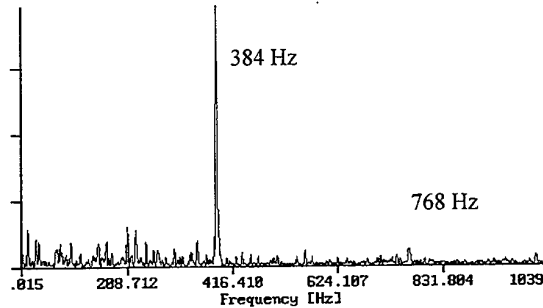


Figure 6: Frequency analysis using the slotted correlation method 50 mm downstream the flameholder orifice plate

5 ADVANCED LDV-MEASUREMENTS

5.1 Acoustic Pressure as Reference Signal for velocity measurements

With the methods discussed in chapter 4, it is not yet possible to decide, if or in which way the flow at different locations shows a propagating modulation.

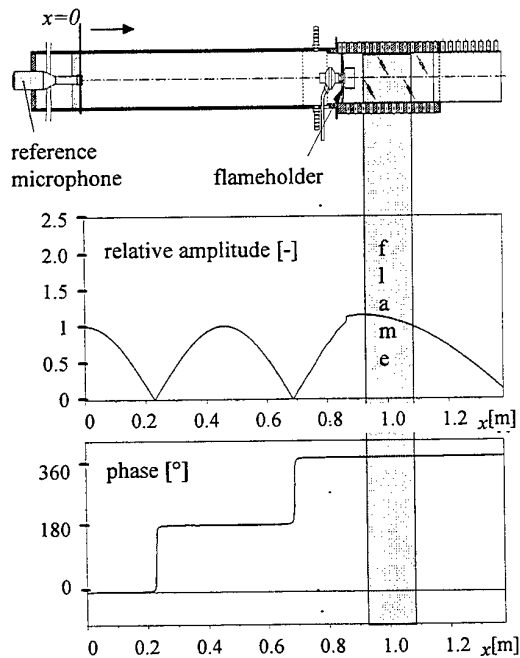


Figure 7: Burner acoustics (numerical modal analysis)

To investigate this behaviour, the time resolved velocity data at different locations of the combustion chamber has to be related to a well defined reference signal. Following Lang and Vortmeyer (1987) or Reuter et al. (1989), the acoustic pressure was taken for that purpose, because it also exhibits the 384 Hz frequency. According to figure 7, the laboratory burner is acoustically characterized by a standing longitudinal 5/4-wave. For this reason, we have a fixed phase relation between the sound pressure at $x = 0$ and at any other position in the pre- and combustion chamber. This reference point was chosen, because at $x = 0$ we have a pressure antinode with a high pressure amplitude. Furthermore, this location is far away from the combustion zone and free of seeding particles. Using a filtered microphone signal, a continuous sinusoidal signal is obtained to trigger the LDV measurement at the moment of a rising slope. Phase lags of 180° induced by the microphone and of 60° induced by the filter were taken into account in the following analysis.

5.2 Repetitive Sampling

Figures 8 and 9 show the time dependent velocities at two different locations. In figure 8 the particle density is sufficient to observe two periods of the 384 Hz oscillation while in figure 9 there are only three measured velocities during the same time. To avoid the undesirable effect of aliasing in frequency analysis, described for example by Bell (1986) or Schröder (1990), it is required that the sample time difference $\Delta t_n = t_n - t_{n-1}$ for each pair t_n, t_{n-1} is equal or shorter than half the period of the highest frequency that ought to be investigated. This requirement is fulfilled in figure 8 but not in figure 9.

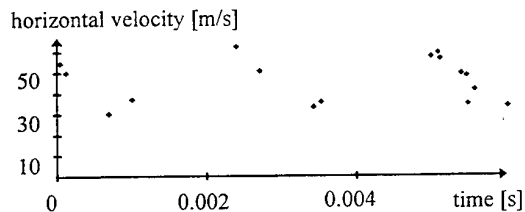


Figure 8: 2800 burst events per second at 95 mm downstream the flameholder orifice plate ($x=0.959$ m)

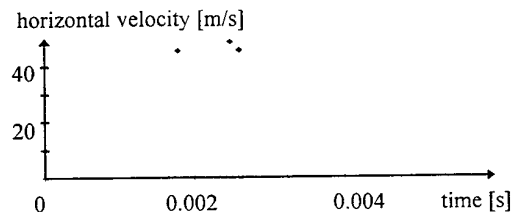


Figure 9: 500 burst events per second at 200 mm downstream the flameholder orifice plate ($x=1.064$ m)

Consequently the velocity measurements had to be adapted to a sample rate of at least twice the combustion oscillation frequency for each point of the chamber. If non-linear effects occur, also the double or triple frequencies appear and the sample rate has to be increased. However, due to the low particle density throughout the flame and particularly behind the flame front, the required sample rate could not be obtained. A solution of this problem would be to add more particles which however leads to a damping of the oscillation.

This dilemma was solved by repetitive data acquisition over n periods of the velocity oscillation. This method is applicable because only the combustion oscillation frequency and its higher harmonics appear. Therefore, the clock of the IFA 750 processor was reset after n oscillation periods. Figures 10 and 11 are two examples for repetitive sampling. Compared to figures 8 and 9, they show more velocity data and give a good picture of the oscillation.

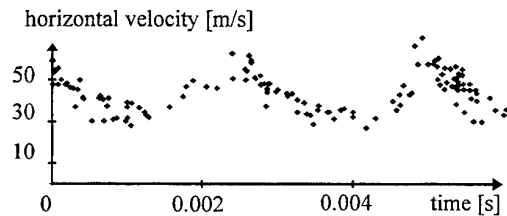


Figure 10: 28 000 burst events per second, achieved by repetitive sampling at 95 mm downstream the flameholder orifice plate ($x=0.959$ m)

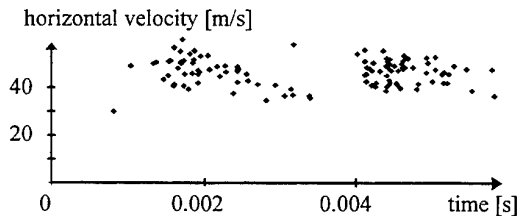


Figure 11: 17 000 burst events per second, achieved by repetitive sampling at 200 mm downstream the flameholder orifice plate ($x=1.064$ m)

5.3 Investigation of the Modulated Flow by Repetitive Sampling over one Period and Analysis in the time domain

We are now able to display the measured velocities at different times and locations. The visualized flow field of figure 1 is based on the method of repetitive sampling over one period of the combustion oscillation.

For each location, the oscillation period was divided into five intervals. In each interval the measured velocities were averaged following the method suggested by Reuter (1989). The low quality of the signal - mainly due to the

effects of turbulence in the combustion chamber - allows only a rough estimation of the propagation speed which in this case is about $50 \text{ m/s} \pm 9 \text{ m/s}$.

5.4 Investigation of the Modulated Flow by Repetitive Sampling over Twenty Periods and Analysis by the Non Equidistant Fourier Transformation

A considerable improvement is obtained, if the repetitive sampling is extended over twenty periods as in this work. Velocity data is analyzed by the non equidistant Fourier Transformation with $N=1024$ in equations 5 and 6. This analysis was performed for the horizontal velocities at 54 locations 5 mm apart from each other along the centre axis of the combustion chamber as shown in figure 12.

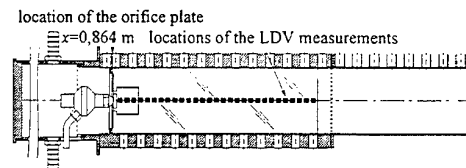


Figure 12: Locations of the LDV measurement

The non equidistant Fourier analysis delivers an amplitude spectrum $A(f_k)$ and a phase spectrum $\phi(f_k)$ at each of the 54 locations. For two locations, these spectra are plotted in figures 13 to 16. The corresponding time signals can be found in figures 10 and 11.

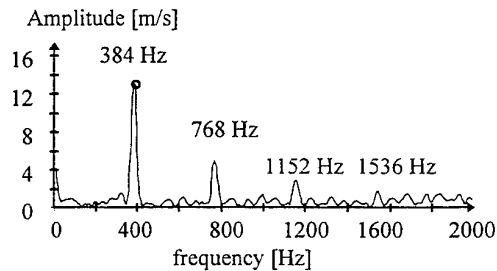


Figure 13: Amplitude spectrum at 95 mm downstream the flameholder orifice plate ($x=0.959$ m)

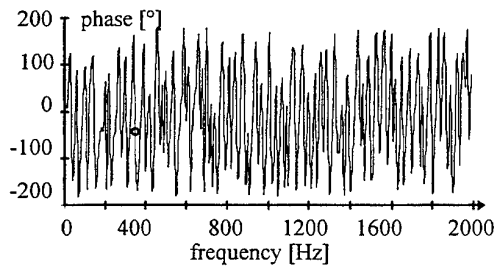


Figure 14: Phase spectrum at 95 mm downstream the flameholder orifice plate ($x=0.959$ m)

The amplitude spectrum obtained at a location 95 mm downstream the flameholder orifice plate in figure 13 exhibits oscillations at 384 Hz, 768 Hz, 1152 Hz and 1536 Hz. The phase lags against the reference acoustic pressure for these frequencies are plotted in figure 14.

For the second location 200 mm downstream the flameholder orifice plate, amplitudes and phases are shown in figures 15 and 16. The 384 Hz-peak in figure 15 decreased considerably compared to figure 13.

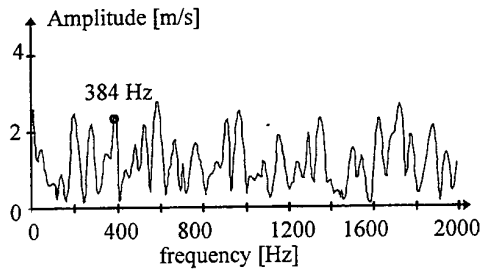


Figure 15: Amplitude spectrum at 200 mm downstream the flameholder orifice plate ($x=1.064$ m)

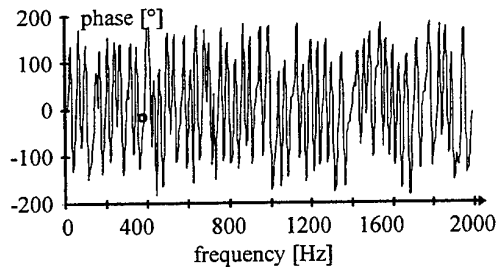


Figure 16: Phase spectrum at 200 mm downstream the flameholder orifice plate ($x=1.064$ m)

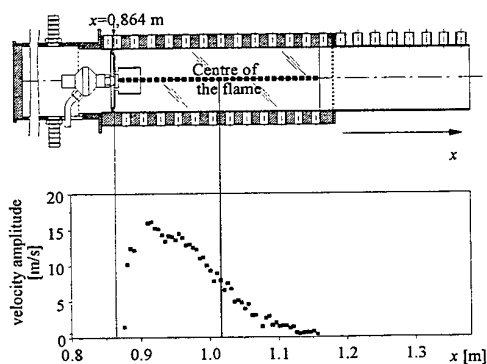


Figure 17: Flow velocity amplitudes in the combustion chamber

The 384 Hz oscillation amplitudes $A(x)$ are plotted in figure 17, and their phases $\phi(x)$ in figure 18 along the combustion chamber coordinate x . Figure 17 reveals, that the amplitudes of the oscillating flow increase from low

values inside the flameholder tube up to 17 m/s at the end of the tube. Downstream the amplitudes decrease.

According to figure 18, the phase $\phi(x)$ along the centre line of the combustion chamber is a linear function of x . The gradient $\Delta\phi(x)/\Delta x = 2624^\circ/\text{m}$ gives the necessary information to determine the propagation speed which in this case is $52.7 \text{ m/s} \pm 0.1 \text{ m/s}$.

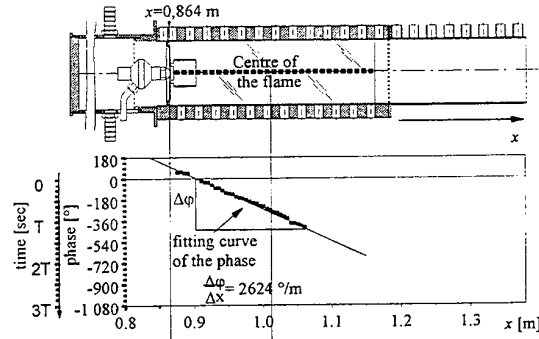


Figure 18: Determination of the propagation speed of the flow modulation from the phase

Figure 19 shows the measured velocities at the location 95 mm downstream of the flameholder and their approximation by the Non Equidistant Fourier Transformation according to equation 9.

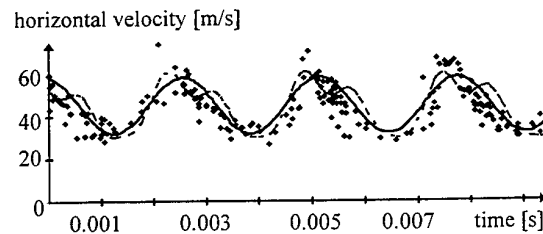


Figure 19: Approximation of measured velocities 95 mm downstream the flameholder ($x=0.959$ m)

The full line is the sinusoidal function, resulting from fitting the 384 Hz frequency. Taking also into account the higher harmonics at 768 Hz and 1152 Hz, the dotted line is obtained, which appears to be a slightly better approximation with regard to the measured points.

6 SUMMARY

In this work, theoretical and experimental methods have been developed to measure the flow modulation during self excited combustion oscillations. The standing acoustic wave was chosen as reference for LDV-measurements. The measured velocity data, acquired by repetitive sampling was processed by a non equidistant Fourier transformation. The resulting frequencies, their amplitudes and their phases lead to quantitative data on the behaviour of unsteady flow in the presence of self excited combustion oscillations.

7 NOMENCLATURE

a_k, b_k	Fourier coefficients	[m/s]
f_k	frequency in the spectrum	[Hz]
f_{kd}	dominant frequency	[Hz]
φ	phase	[°]
$\Delta\varphi$	phase difference	[°]
j, k, n	counting variables	[-]
N	number of sampled data	[-]
λ	fuel-air-ratio	[-]
t	time	[s]
t_n	time of the n-th measured velocity	[s]
$\Delta t, \Delta t_n$	time intervals	[s]
T	period of an oscillation	[s]
T_o	total sampling time	[s]
v	velocity	[m/s]
\bar{v}	averaged velocity	[m/s]
$v_{propagation}$	propagation velocity	[m/s]
$v_{fourier}$	velocity approximation by Fourier analysis	[m/s]
A	velocity amplitude	[m/s]
x	coordinate	[m]
x_i	certain coordinate	[m]
Δx	distance	[m]

8 REFERENCES

(Books)

Dowling, A. P.; Ffowcs Williams, J. E.: Sound and sources of sound, Chichester 1983;

Schrüfer, E.: Signalverarbeitung, numerische Verarbeitung digitaler Signale; München 1990;

(Journal Articles)

Milosavljevic, V. D.; Sivasegaram, S.; Whitelaw, J. H.: Velocity Characteristics of oscillating ducted premixed flames, Experiments in Fluids 9, 1990;

Rayleigh, J.: The Explanation of Certain Acoustical Phenomena, Nature, S. 319-321, July 18, 1878;

(Symposium Proceedings)

Bell, W. A.: Spectral analysis of laser velocimeter data with the slotted correlation method; AIAA/ASME 4th fluid mechanics plasma dynamics and laser conference 1986, Atlanta, Georgia;

Hermann, J., Zangl, P., Gleis, S., Vortmeyer, D.: Untersuchung der Anregungsmechanismen selbsterregter Verbrennungsschwingungen an einem Verbrennungssystem für Flüssigkraftstoff, 17. Deutscher Flammentag, Hamburg, 12. und 13. September 1995, VDI-Bericht Nr. 1193;

Lang, W.; Vortmeyer, D.: Messung der Schallschnelle in einer schwingenden Flamme mit einem Laser-Doppler Anemometer, 13. Deutscher Flammentag, 7. und 8. Oktober 1987, VDI-Bericht Nr. 645;

Reuter, D. M.; Hedge, U. G.; Zinn, B. T.: Flowfield Modifications of Combustion Rates in unstable Ramjets, 27th Aerospace Sciences Meeting, Reno, AIAA 89-0105, 1989;

(Thesis)

Schimmer, H.: Selbsterregte akustische Schwingungen in Brennräumen mit flacher Flamme. Dissertation, TU München 1974;

CHARACTERISTICS OF OSCILLATING CONTROL SPRAY FOR THE SUPPRESSION OF LOW FREQUENCY COMBUSTION INSTABILITIES.

Mr. Eugene Lubarsky and Assoc. Prof. Yeshayahou. Levy

Faculty of Aerospace Engineering, Technion, Haifa 32000, Israel.

ABSTRACT

Combustion instabilities often occur in the liquid fueled combustors using bluffbody or sudden-expansion for stabilization. From the practical point of view, the most severe oscillations are at 100-500 Hz. This low-frequency rumble is generally characterized by longitudinal acoustic oscillations. The main idea of the present study is to use the air from the oscillating flow of the unstable combustor for the atomization and distribution of part of the main liquid fuel to obtain the required oscillating phase shifted heat release for stabilization. The effervescent spray injection, at relatively low pressure, was investigated as a model for pressure dependent atomizer. Acoustic modulations were superimposed on the atomizing air stream using a rotating motion of the perforated disk. A special laser light sheet system was used to obtain an integral indication of spray oscillation. Phase Doppler Anemometry measurements were performed to determine the droplet velocity and droplet diameter oscillations with different phase shifts in respect to the oscillations of the atomizing air. Such data are integrated within the computer simulation. Preliminary results demonstrated successful suppression process using the pressure dependent fuel injection without the need of any external controllers.

1. INTRODUCTION

Combustion instabilities often occur in the liquid fueled combustors using bluffbody or sudden-expansion for stabilization. Several jet engines have exhibited excessively high

amplitude pressure oscillations which resulted in loss of the engine performance and/or excessive vibrational loads on the system. From the practical point of view the most severe oscillations are at the frequency of 100-500 Hz. This low-frequency rumble is generally characterized by longitudinal acoustic oscillations in the inlet sections and in the combustor. As the full understanding of the mechanisms controlling the low-frequency instability is still unknown, development program has to be performed for nearly every new engine design. Theoretical modeling typically used an assembly of point actuators, as the source for the additional oscillating and phase shifted heat release. The Fung et al. (1991) simulation of the instability suppression process predicted that only a small portion (0.1-0.3%) of the total fuel has to be injected in the oscillating manner for the successful suppression. In Langhorne (1990) experiments, with active controlled oscillating gas fuel injection, successful result was achieved at 3-4% additional fuel injection. However in an experimental design (Levy and Lubarsky, 1994) of a flameholder/injector combination within an actual kerosene fueled ramjet combustor, the suppression of longitudinal pressure oscillations was achieved only with a minimum of 10% additional pressure dependent fuel injection.

Difficulties exist in modeling the two-phase flow in a liquid fueled unstable combustor, and the required additional oscillating fuel spray for stabilization by the phase shifted heat release. This highlights the need for a joint experimental-theoretical study, directed towards the suppression of combustion instabilities in practical configuration.

2. METHOD.

Previous laboratory studies (Langhorne et al., 1990, Sivasegaram and Whitelaw, 1992, Schadow et al., 1992, and Wilson et al., 1992) are reported about suppression of low-frequency combustion instability. It has been shown that combustion oscillations can be stabilized by periodic addition of secondary fuel, usually in the form of premixed gas fuel. Control was applied by active modulation of the extra fuel flowrate according to signals of pressure transducers in the combustor with the required phase shift. The direct action solenoid valves, needle valve attached to a vibrator, acoustic drivers in the assisting air line of the injector, and spark ignition of the stoichiometric air-fuel mixture are the techniques used for heat release modulation. In spite of the progress in instability control with laboratory facilities, the application of these methods in real liquid fueled combustors is still not practical. The present work differs from previous studies by the following suggestions:

1. Using liquid spray, of the main liquid fuel, for the instability control.

2. The use of passive control method, that involves only air pressure sensitive fuel injection mechanism.

The principal idea is to use air from the oscillating host flow of the unstable combustor for atomization and distribution of the additional control fuel. Hence this method is based on the direct influences of the interchamber pressure oscillations on the additional heat release (without external controllers) and thus is referred as a passive control. Scheme that illustrates these principles is shown in the fig.1. The oscillating air flow in the combustor enter the atomizer of the additional fuel. The atomizer, which is sensitive to ambient pressure, produces an oscillating spray. As a result additional oscillating heat is released with a certain time delay relative to pressure oscillations. Hence the atomizer sense the pressure oscillations of the main flow and produces phase-shifted oscillating heat release as a response to those oscillations. It seems that proper atomizer design may result in spray modulation at frequency of the pressure oscillations and with phase-shift in accordance with the Rayleigh (1945) criterion, and lead to suppression of combustion instability.

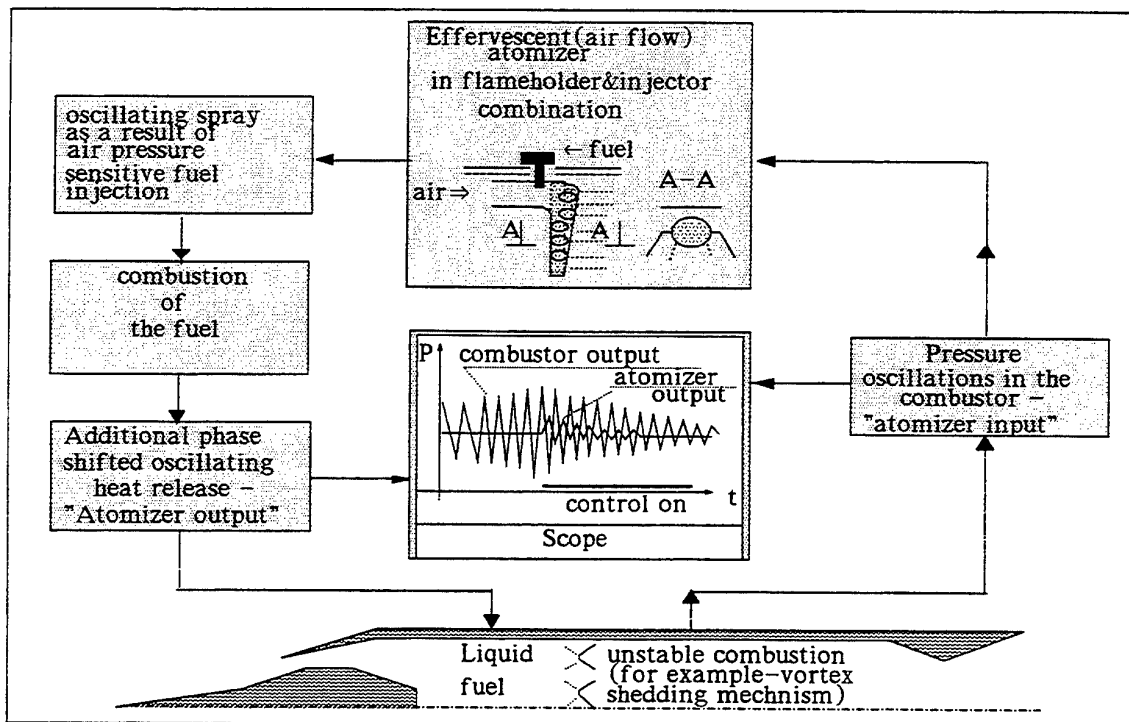


Fig.1. Schematic diagram of the control mechanism of suppression the low-frequency combustion instability using pressure dependent oscillating spray.

3. SUPPRESSION MECHANISM (THEORETICAL MODEL)

The theoretical model of suppression mechanism by the pressure dependent oscillating spray is based on the studies of Culick (1976 and 1992) about longitudinal combustion instabilities.

It is assumed that the medium in the combustion chamber consists of two-phase mixture. The gas phase contains inert species, reactance and combustion products. The liquid phase is composed of fuel droplets, and is treated as a fluid with density ρ_l mass per unit volume of the chamber. Conversion of the liquid phase to the gas may occur at the rate w_l due to droplet vaporization. If the droplets are considered to be uniformly dispersed, the conservation equations for a two-phase mixture in the combustor can be written as;

$$\frac{\partial \rho}{\partial t} + \nu_g \nabla \rho = W \quad (1)$$

$$\rho \frac{\partial \nu_g}{\partial t} + \rho \nu_g \nabla \nu_g = -\nabla p + F \quad (2)$$

$$\frac{\partial p}{\partial t} + \gamma p \nabla \nu_g = -\nu_g \nabla p + P \quad (3)$$

where ρ is the density of the two-phase mixture and ν_g is the velocity of the gas phase. The function W represents the mass conversion rate of condensed phases to gases per unit volume, F is the force of interaction between the gas and condensed phases, and P is the sum of heat release associated with chemical reactions and energy transfer between the two phases.

Whatever physical means are devised, control inputs must be theoretically treated as sources in the conservation equations. Therefore, Eqs. (1-3) are modified by adding control inputs W_c , F_c , and P_c to the W , F and P , respectively, on the right-hand sides. The subscript c represents the effect arising from the control inputs. As the actuator is associated with the heat released from the injected fuel, P_c in the eqs. (3) takes the form:

$$P_c = \frac{\bar{R}}{\bar{C}_v} Q_c = \frac{\bar{R}}{\bar{C}_v} \dot{w}_c \Delta H_c, \quad (4)$$

where \bar{R} and \bar{C}_v are the gas constant and the specific heat at the constant-volume for

two-phase mixture respectively, Q_c is the rate of energy release in the gas phase, \dot{w}_c is the burning rate of the control fuel, and ΔH_c is the heat of combustion per unit fuel mass.

A wave equation governing the unsteady fluid motions is derived. In the equation, decomposition of dependent variables as sums of mean and fluctuating parts is performed. Thus,

$$\begin{aligned} \rho &= \bar{\rho}(r) + \rho'(r, t) \\ \nu_g &= \bar{\nu}_g(r) + \nu_g'(r, t) \\ p &= \bar{p}(r) + p'(r, t) \end{aligned} \quad (5)$$

By substituting Eqs. (5) in Eqs. (1-3), collecting coefficients of similar powers, and rearrange the results, we obtain the following wave equation:

$$\nabla^2 p' - \frac{1}{\bar{a}^2} \frac{\partial^2 p'}{\partial t^2} = h + h_c \quad (6)$$

where \bar{a} is the speed of sound of mixture, p' —fluctuating pressure, h contains all physical processes of acoustic motions, mean flow, and combustion without the influence of external forces. The control source arising from combustion of the injected control fuel is

$$h_c = -\frac{1}{\bar{a}^2} \frac{\partial P_c}{\partial t} = -\frac{\bar{R}}{\bar{a}^2 \bar{C}_v} \frac{\partial \dot{w}_c}{\partial t} \Delta H_c, \quad (7)$$

where F_c was taken to be zero. Multiple effects of the control input, h_c on the original forcing term h are not considered here, since they represent high order (negligible) influences.

The term h_c is related to the mass flow rate of the fuel by means of the Crocco and Cheng (1956) time-lag theory. According to Yang et al. (1992) the distribution of heat release is:

$$\begin{aligned} h_c(r, t) &= -\frac{\bar{R} \Delta H_c}{\bar{a}^2 \bar{C}_v} \times \\ &\times \sum_{i=1}^M \left[\frac{\partial \dot{m}_{in}(t-\tau)}{\partial t} \mathcal{R}(r(\tau), t-\tau) \Delta V(r_i) \right] \delta(r-r_i) = \\ &= -\sum_{i=1}^M [b_i u_{in}(t-\tau_i)] \delta(r-r_i) = \\ &= -\sum_{i=1}^M \delta(r-r_i) u_i(t) \end{aligned} \quad (8)$$

where $\Delta V(r_i)$ denotes the (i) volume of the discretized control element at position r_i , $\delta(r-r_i)$ is the Dirac delta function and

$$u_{in}(t-\tau) = -\frac{\bar{R}\Delta H_c}{\bar{a}^2 \bar{C}_v} \left[\frac{\partial \dot{m}_{in}(t-\tau)}{\partial t} \right] \quad (13)$$

$$b_i = \mathcal{R}(r(\tau), t-\tau) \Delta V(r_i) \quad (14)$$

$$u_i(t) = b_i u_{in}(t-\tau) \quad (15)$$

Representation of the control source by a series of droplet groups is justified when: 1. the number of groups is sufficiently large to provide the required spatial resolution; 2. the characteristic lengths of oscillations are much longer than the dimensions of each volume cell.

The computer simulation, which made use of SIMULINK of MATLAB represents the model as a block diagram windows (Levy and Lubarsky, 1996). In this windows, models are created and edited principally by mouse driven commands. A typical preliminary result is given in fig.2a,b,c. The figures demonstrate the variations of pressure with time at different turbulence level and indicates an unstable behavior of the combustor. At a certain time additional fuel is supplied for the suppression of combustion instability at the appropriate amount, frequency and phase shift. The effect of the additional fuel is immediately observed, as indicated by the attenuation of the pressure oscillations. The effect of turbulence in the host gases was also investigated. It was seen that turbulence does not have significant effect on the suppression characteristics of the combustor. The maximum level of pressure turbulence, with which suppression is still possible, was found to be about 5%.

5. EXPERIMENT

A major part of this study is concerned with the analysis of air pressure dependent fuel atomization for the generation of oscillating and phase shifted heat release. Effervescent spray injection at relatively low pressure is investigated. Recently, sufficient results of spray modulation were obtained using an experimental model of pressure dependent

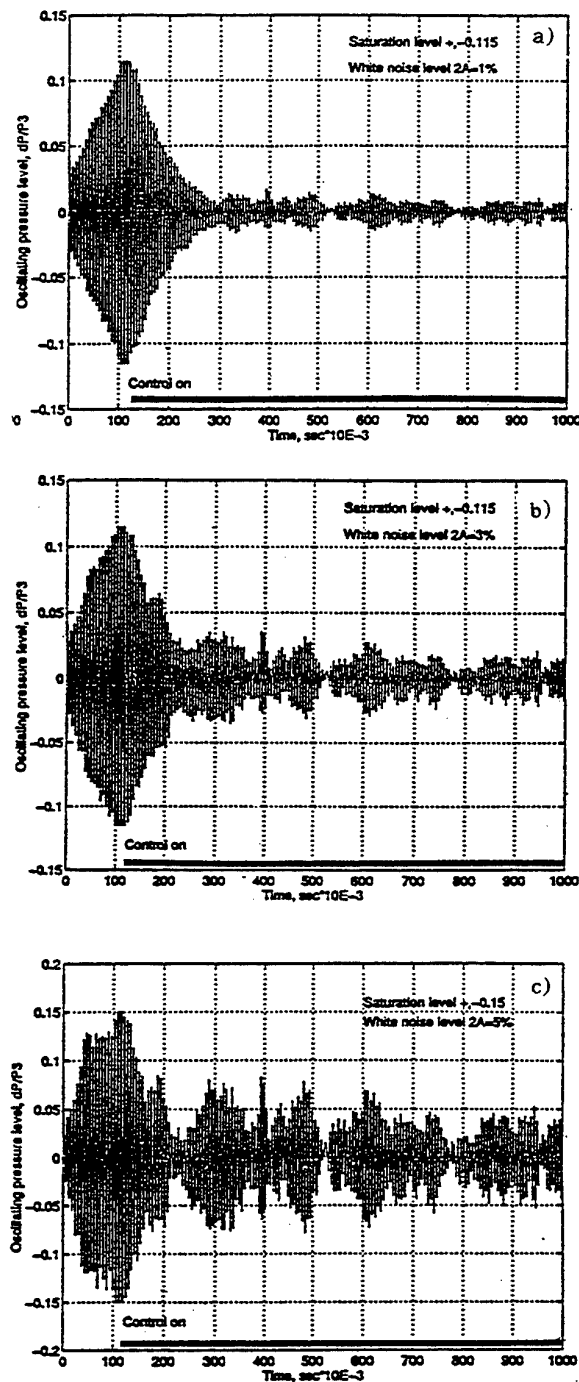


Fig.2. Computer simulation of the effect of additional oscillating heat release on the unstable combustor; a-1% turbulent noise; b-3% turbulent noise; c-5% turbulent noise.

atomizer. Schematics of the atomizer and the experimental setup are shown in Fig.3. It consist of the air assist (effervescent) atomizer, fueling arrangement, air supply, and source of acoustic modulation. The fuel was injected into the air cavity of the atomizer. Acoustic modulations are superimposed on the atomizing air stream. This is done by the special device that produce high pressure amplitude oscillations by a rotating motion of the perforated disk. A special laser light sheet

system, capable to detect spray oscillation was developed. The technique make use of a light sheet with width comparable to that of the spray and its plane aligned coaxial with spray axis. It is optimized to sense the spray modulation which varies in time, mainly along the principal axis. Figure 4 shows signals of pressure transducer which measures the atomizing air pressure inside the effervescent atomizer and signal of photodiode that is proportional to the light sheet diffusion by the droplets (i.e. proportional to

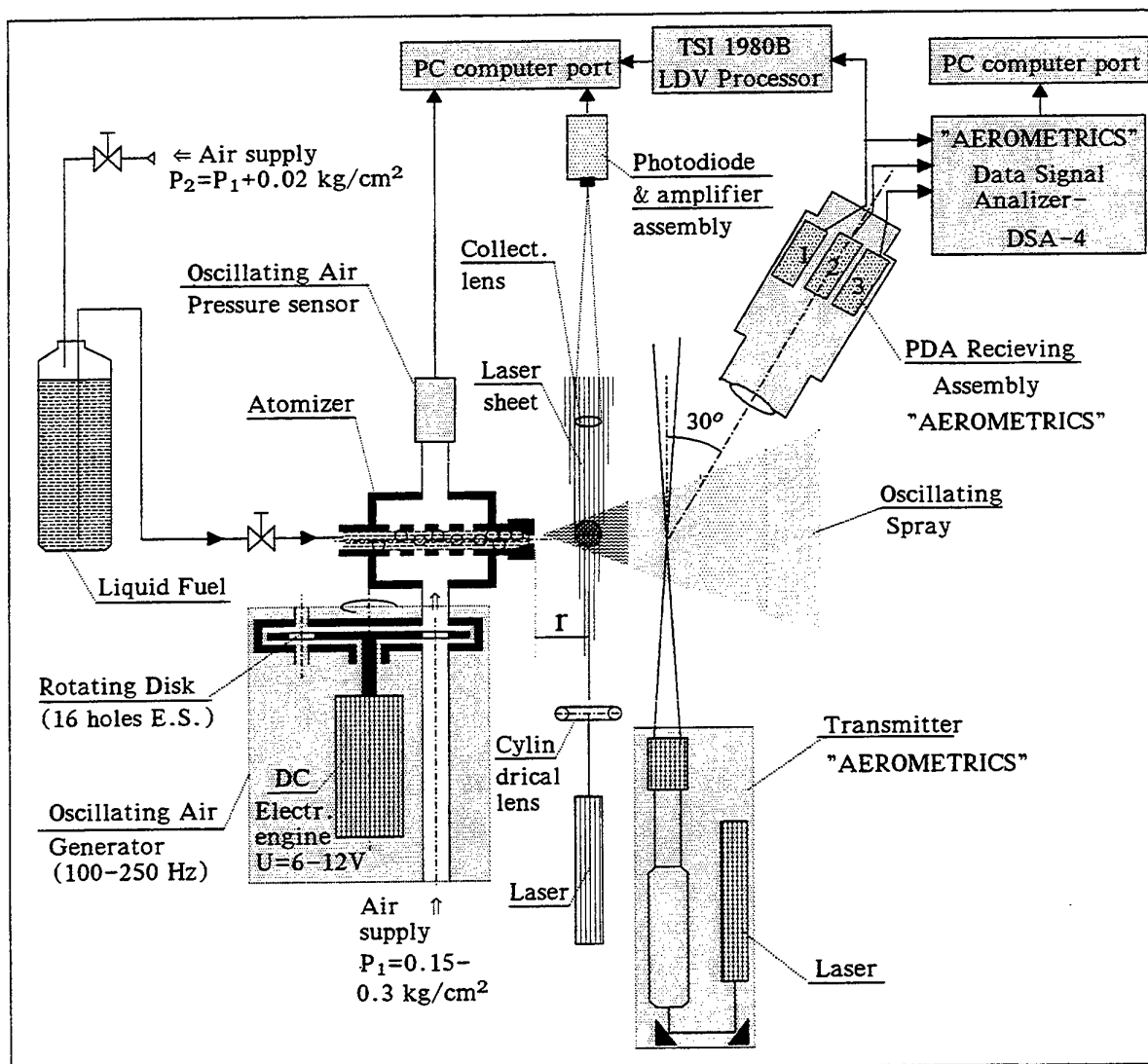


Fig.3. Schematic Diagram of the Experimental Setup for Oscillating Spray Investigation.

the spray density). The figure clearly indicates spray modulation by the oscillations of the atomizing air with different phase shifts, which corresponds to the mean velocity of the spray and the different axial locations. Measurements were also performed to determine the oscillating spray characteristics. This was done in order to determine the initial conditions and to confirm

the validity of the physical models. Phase Doppler Anemometry (PDA) was used to measure the diameters and velocities of droplets of the oscillating spray. These characteristics (fig.5) demonstrate droplet's velocity and diameter modulation by the pressure oscillations of the atomizing air. The figure consists of 4 parts. Parts *a* and *b* demonstrate typical time

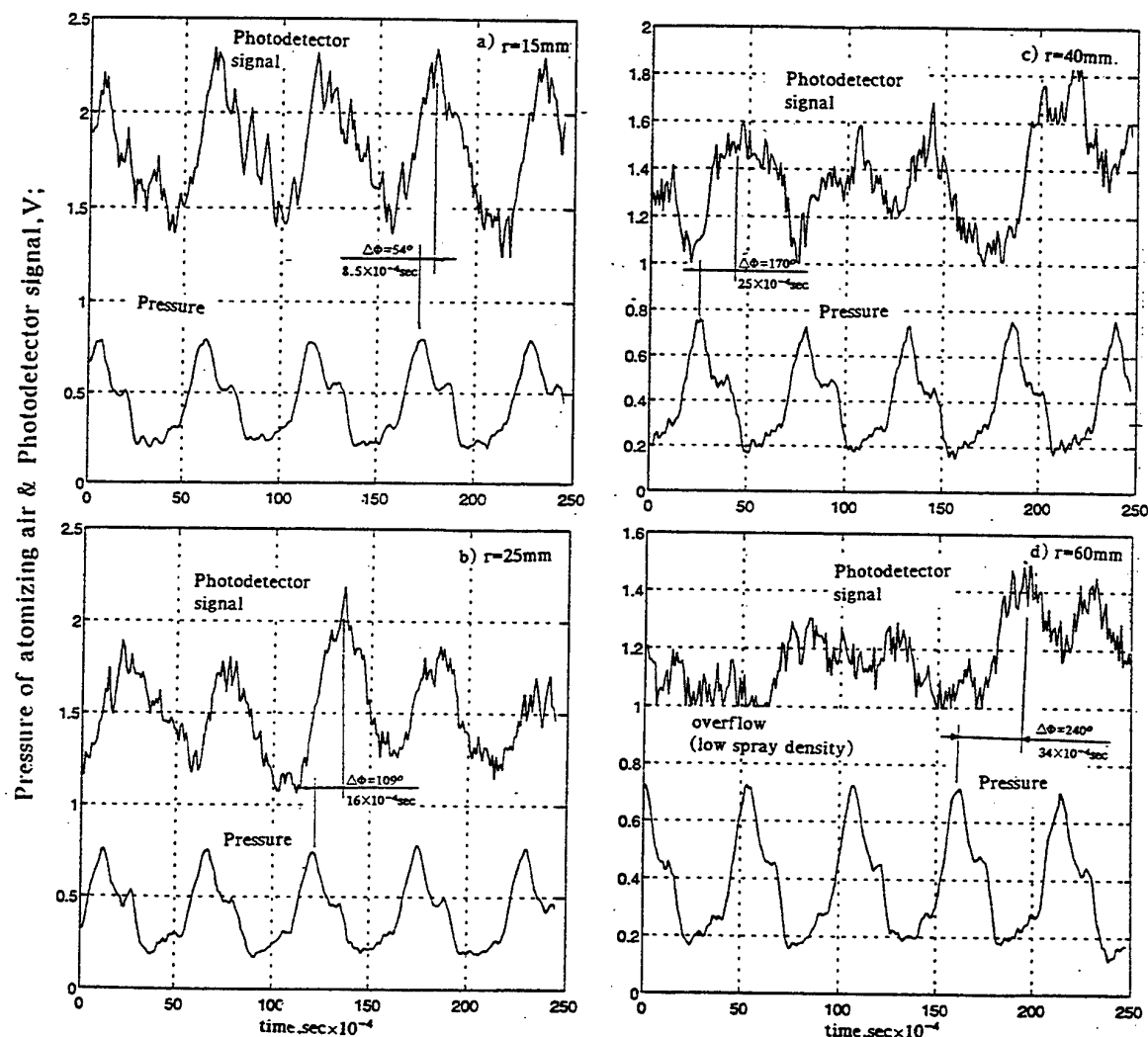


Fig.4. Spray oscillations as a result of atomizing air oscillations;

a) laser sheet crosses the spray at $r=15\text{mm}$ from the atomizer exit, b) $r=25\text{mm}$, c) $r=40\text{mm}$, d) $r=60\text{mm}$ (maximum of the photodetector signal corresponds to the maximum of the spray density).

it can be seen that they are at about 180° phase different. This indicates that period of high velocities is characterized by small droplets whereas the smaller velocity value periods are associated with larger droplets. However the size velocity correlation (fig.6) has triangular region which indicates that the maximum value of droplet size is related only to the period of low velocities whereas the minimum value remain nearly constant in time. From such type of information the variation of volume flux and size distribution with time is extracted, to be fed into the computer simulation.

variation of the droplet velocity and their Power Spectral Density. A very clear and distinct peak at 180 Hz is seen. This value corresponds exactly to the frequency of the atomizing air oscillation as generated by the perforated disk. Part c and d of the figure demonstrates time variation of the droplet size and the Power Spectral Density of droplet diameter variation. Even though it is very difficult to visualize an oscillating pattern in the droplet diameter variation, the Power Spectrum clearly reveal a distinct peak at the same frequency as the velocity. When correlating the velocity and diameter time series,

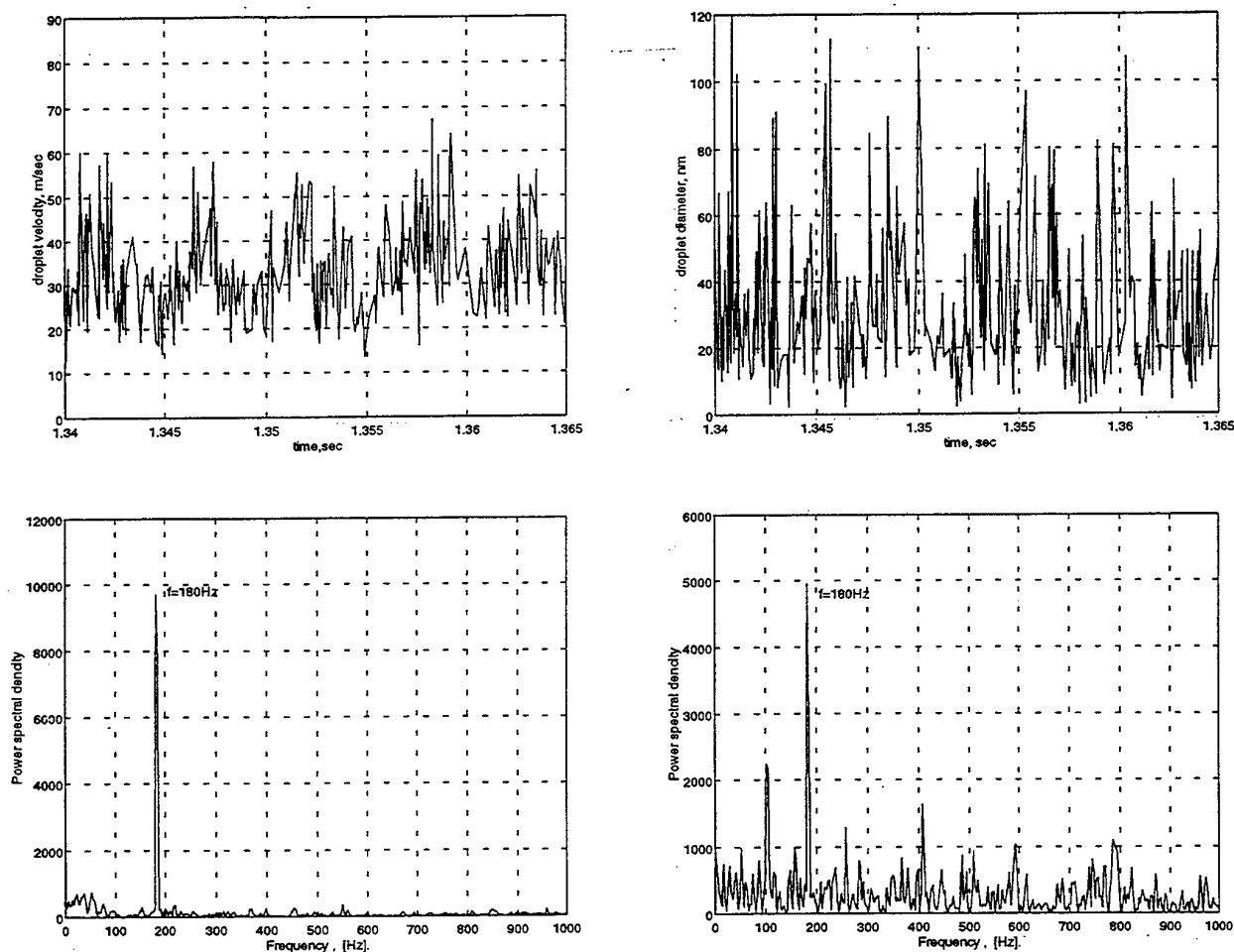


Fig.5. The pressure dependent oscillating spray characteristics – results of the PDA measurements; a–time variation of the droplet velocities; b–power spectral density of the droplet velocities; c–time variation of the droplet diameters; d–power spectral density of the droplet diameters.

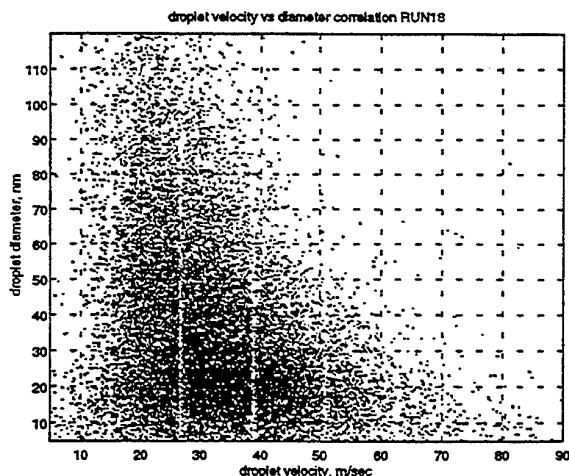


Fig.6. Droplet diameter & velocity correlation.

6. CONCLUDING REMARKS

An original method of suppression the low frequency combustion instability was suggested. The method is based on the usage of an additional pressure dependent oscillating spray which is part of the main liquid fuel. This lead to excitation of oscillating heat release which is phase shifted to the pressure oscillations in the combustor.

The potential validity of this method was successively demonstrated by the computer simulation and reported elsewhere.

The experimental investigation includes effervescent spray injection at relatively low pressure. The spray modulation by the oscillations of the atomizing air with different phase shifts was clearly demonstrated. This was shown through time variation and Power Spectrum of the velocity as well as the size of droplets. Hence the experimental part of the study confirmed the principal of the suggested method for suppression of the pressure oscillations; namely to generate oscillating phase shifted spray (and heat release) by ambient pressure dependent atomizer.

ACKNOWLEDGEMENT

This research was supported by the fund for the promotion of research at the Technion, Israel Institute of Technology.

REFERENCES

- Langhorne, P.J., Dowling, A.P. and Hooper N., 1990, Practical Active Control System for Combustion Oscillations, J. of Propulsion and Power, vol. 6.
- Sivasegaram, S. and Whitelaw, J.H., 1992, Active Control of Oscillations in Combustors with Several Frequency Modes, DSC. Vol. 38 Active Control of Noise and Vibration, ASME.
- Schadow, K.C., Gutmark E., and Wilson K.J., 1992, Active Combustion control in a Coaxial dump Combustor", Combust. Sci. and Tech., Vol. 81, pp. 285-300.
- Wilson K.J., Gutmark E., and Schadow K.C., 1992, Flame-Kernel Pulse Actuator for Active Combustion Control, Proc. ASME Winterannual meeting Nov. 8-13, Anaheim, Ca.
- Lord Rayleigh, 1945, The Theory of sound, Dover Publications, New York.
- Culick, F.E.C., 1976, Nonlinear Behavior of Acoustic Waves in Combustion Chambers-1 and 2, Acta Astronautica, vol. 3, pp. 715-757.
- Culick, F.E.C., 1992, Combustion Instabilities in Liquid-Fueled Propulsion Systems-an Overview", AGARD Conference Proceedings No-450, North Atlantic Treaty Organization
- Fung, Y.T., Yang V. and Sinha A., 1991, Active Control of Combustion Instabilities with Distributed Actuators, Combust. Sci. and Tech., Vol. 78, pp. 217-245.
- Yang V., Sinha A., and Fung Y-T., 1992, State-Feedback Control of Longitudinal Combustion Instabilities, J. Propulsion and Power, Vol. 8, No. 1.
- Crocco, L., and Cheng, S.I. 1956, Theory of Combustion Instability in Liquid-Propellant Rocket Motors, AGARDograf No. 8, Butterworths Scientific Publications, London.
- Levy Y. and Lubarsky E., 1994, Oscillating Control Spray for the Suppression of the Low Frequency Combustion Instabilities - Background, Faculty of Aerospace Engineering, Technion - Israel Institute of Technology, TAE No. 741.
- Levy Y. and Lubarsky E., 1996, Oscillating Control Spray for the Suppression of the Low Frequency Combustion Instabilities, Proc. 36th Israel Annual Conference on Aerospace Sciences, February 21-22.

ACOUSTIC VELOCITY MEASUREMENTS BY MEANS OF LASER DOPPLER VELOCIMETRY

P. Herzog(*), J.C. Valière, V. Valeau, G. Tournois

Laboratoire d'Acoustique, U.R.A. 1101 C.N.R.S.
Université du Maine, B.P. 535, F- 72017 Le Mans Cedex, FRANCE

(*) now: Centre de Transfert de Technologie du Mans
20 rue Thalès de Milet, F- 72000 Le Mans, FRANCE

ABSTRACT

Although LDV has been used for measurements in Acoustics since numerous years, the effective performances gained in this field have not been assessed yet. Specific aspects of the acoustic velocity have to be taken into account in order to achieve measurements at low levels or high frequencies, which requires some optimization of both the optics, the mechanical supports, and the signal processing.

This paper presents a first step toward a LDV setup dedicated to Acoustics in air, and presents the performances obtained using commercially available hardware. It also tries to point out where the main limitations are, especially as concerns the signal processing, and presents some solutions which are being developed now.

At this early stage of the work, results are quite encouraging as a significant part of the audio dynamic and frequency ranges seems to be covered. Much work remains however to be done in order to validate fully the setup, and to simplify its use in order to integrate LDV as a "standard" tool for daily measurements in airborne Acoustics.

1. INTRODUCTION

The use of LDV in Acoustics could be the starting point of many new developments concerning aspects such as the understanding of acoustic phenomena near sources or boundaries, or in inhomogeneous medium. This is especially true for sharp changes in the behaviour of the field, where the vector nature of the velocity may give much more information than a scalar variable such as pressure or temperature.

Indeed several techniques exist for the measurement of acoustic velocity or intensity in air, but most of them rely on an indirect evaluation which involves two or more pressure measurements. This has several drawbacks, among which the total size of the resulting sensor, which both perturbs the field and leads to an average over a large scale, and the limited frequency range due to inaccuracies of the relative calibration of the microphones. Some other tools are used, such as hot wire sensors, with the disadvantages of very non-linear characteristics and an inadequate dynamic range if used without flow.

Potential advantages of LDV are, inversely, its theoretical "non-invasive" nature, its ability to track very low frequencies (as it can deal with steady flows), a small measuring volume giving access to a very good spatial resolution, and a linear response. Its use in Acoustics could therefore seem obvious, at least for applications compatible with the total size and cost of commercial products.

In fact, many work have dealt with the measurement of acoustic velocity components, but most known results concern high levels and low frequencies, or signals superimposed upon flows. See, for instance, Taylor (1976), Taylor (1981), Davis and Hews-Taylor (1986), Eckmann and Grotberg (1991), Vignola *et al* (1991), and recently Lee *et al* (1993). Two main reasons may be proposed for this situation: first LDV is still a "heavy" tool which requires a great amount of know-how to be used efficiently; its use remains thus restricted in teams for which it is a key equipment, such as in fluid dynamics. Although cooperations with other teams exist, they may not be sufficient to "export" the technique. A second reason is that particle velocity is very different between acoustic fields and flows, and existing equipment is therefore not optimized for measurements without flow in the full audio range.

Because the technology of LDV has become more and more affordable, and that many theoretical works in Acoustics still lack a tool accurate enough for experimental validation, it has been decided to try to point out what is the actual potential of LDV for acoustic measurements, using either purely commercial components or more dedicated developments. The aim of this paper is to give the very first results of our investigations, both to show that significant results may already be obtained, and to collect as much remarks and informations as possible to speed up the path toward the "ideal" acoustic sensor.

2. SPECIFICITY OF ACOUSTIC VELOCITY

For plane waves far from boundaries, the acoustic field may be described as a spatial distribution of pressure and particle velocity, their amplitudes being proportional as described by the following relation:

$$p = \rho c \cdot \|\vec{v}\| \quad (1)$$

where ρ is the density (about 1.2 kg/m^3),
 c is the sound speed (about 345 m/s).

The sound pressure level p (SPL) is usually expressed in decibels as the ratio of p to the reference sound pressure $p_0 = 2 \cdot 10^{-5} \text{ Pa}$. For the audio dynamic range, the SPL values range from 0 dB to 130 dB, this maximum corresponding to 63 Pa. Obviously, acoustic pressure is a very small perturbation around the static state of air, and acoustic phenomena involve very small energies.

Similar figures may be given for the velocity: starting from relation (1), it is straightforward to find that acoustic velocities for audio plane waves range between 50 nm/s and 150 nm/s. These values cannot be much higher because nonlinearity would occur, but they can be lower near rigid boundaries or in resonant fields where acoustic velocity almost vanishes. The last figures of interest concern the acoustic displacement, and can be obtained roughly by dividing the velocity by 2π times the frequency f . The audio frequency range is usually taken as 20 Hz - 20 kHz, and the acoustic displacement thus ranges from 1.2 mm (130 dB at 20 Hz) to a theoretical $4 \cdot 10^{-13} \text{ m}$ (0 dB at 20 kHz). Although this last figure is not realistic because the microscopic nature of the gas should be taken into account in such a case, we can see that acoustic phenomena may not be measured in the full audio ranges, and that perturbation of the field is likely to occur with almost all sensor principles.

More reasonable specifications may be derived considering a normal laboratory environment: ambient noise of measurement rooms, or self noise of microphones and preamplifiers, limit the dynamic range for low levels. Measured acoustic velocities may therefore range between a few $\mu\text{m/s}$ and a few cm/s , values which are similar to the ones observed in natural convection. This points out another characteristic of the acoustic velocity: it is defined as the first order derivative of the particle velocity, and has therefore a zero mean value. All other air motions are thus considered as perturbations of the acoustic field, either interesting (e.g. Aeroacoustics) or not (low-frequencies noise). A side effect is the fact that any superimposed flow has a magnitude at minimum equal, and usually much higher than the acoustic velocity, therefore masking useful signals if the sensor output is not sharply filtered to remove the lower frequency components. Such a need is obviously not fulfilled in LDV, which is designed to track these flow components.

Last, usual sound sources have a level decreasing with frequency, leading to velocities smaller when the frequency is higher, that is for more rapid variations. As lower velocities can be tracked usually only with higher data rates and/or longer windows, a limit may be reached very early when increasing the frequency.

3. DESIGNING A SETUP FOR ACOUSTICS

As a first step, it had been decided to investigate the performances which could be reached using only commercially available equipment. The main part of this step was thus to select the elements which seemed the most appropriate for our need, trying also to keep enough

flexibility for further evolutions of the setup. Following are the main aspects which were considered at this time.

We assumed that the acoustic velocity had to be measured as the normal component of the field near a flat boundary. This case had been chosen as it seemed to concentrate most of the difficulties mentioned above, and would therefore be the most restrictive. More usual measurements (e.g. in waveguides) had however to be also possible.

In order to cope with the LF noise inherent to the LDV principle, we decided to consider only periodic acoustic signals, because suited signal processing techniques exist to select only the wanted frequency components in such a case. As a first step, we considered a sinewave excitation, associated to a synchronous demodulation ("lock-in") to get the amplitude and phase of the resulting acoustic response.

3.1 Optics and supports

Measurement of the near field of a boundary involves that the optics would be inside the acoustic field itself. This necessitates a compromise concerning the focal distance, as vibrations of the setup because of the acoustic pressure would become unacceptable at large distances, while diffraction of the acoustic waves on the optics and support would degrade the accuracy of measurement for shorter ones. Considering usually available equipments, two distances seemed adequate: 60 cm for waveguides, and 2 m for "half-space".

As the velocities to be measured are very small ones compared to the usual ranges in fluid dynamics, all had to be done to get sensitivities as high as possible. A simple mean was to increase the angle between incident beams, so that fringes get closer. This had also the advantage to lead to a more compact measuring volume, a very positive point as it increases the spatial resolution of the setup. A drawback is that it necessitates large lenses if used at small distances, and even separate optics for larger ones such as in our case.

Another problem, emphasized by the increased angle, is that for measurements close to the boundary, one of the incident beams must be almost parallel to the surface. The measuring axis is therefore not normal, but tilted of half the beams angle (see fig. 1). If this angle is larger, the measurement is perturbed by the tangential velocity component, which may be much higher than the wanted, normal one. This led us to select a two-components LDV, in order to be able to rotate the measured velocity and get the normal component alone. This could be avoided for many other acoustic problems.

The choice between front or back scatter is not so obvious: back scatter leads to a lower intensity of scattered light, thus needing a larger lens for the photomultiplier, or more laser power. Inversely, for a moving setup such as a scanning one, keeping two separate optics aligned at a several meters distance seemed a difficult challenge. First experiments done using a small laser showed that back scatter could give satisfying signal levels without needing huge lenses, and we chose this solution. The angle between the beams cannot however be increased too much, unless the backscatter is no more reliable. In our setup, it can be adjusted between about 30 and 80°, and is usually fixed at about 60°.

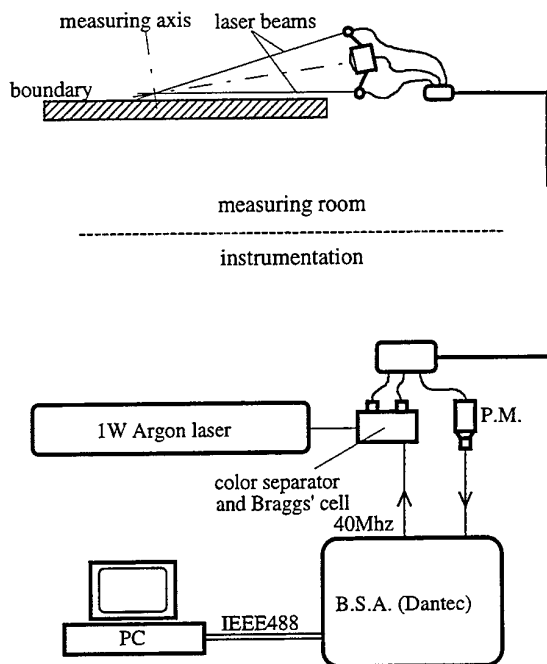


Fig. 1 : schematic description of LDV setup
(here for a single velocity component)

Still to permit a scanning setup, fiber optics seemed an evident choice. A supplementary constraint was that all noisy equipments had to be removed far from the measurement zone, especially the laser and its power supply. They were therefore installed in a separate room, which required a fiber length of about 15m. To be sure to get still enough power at the measuring volume for both wavelengths, without demanding too much of the laser capacity, a 1W argon laser was then chosen. It does not seem that this power is really needed, although some situations have occurred when we had to use a significant proportion of it. Obviously a simpler setup using front scatter for a single velocity component could use a much smaller laser.

3.2 Burst processor

The specifications of the burst processor are the consequences of the above figures. For a target velocity comprised between $1\mu\text{m/s}$ and 100mm/s , and with the optics described above, the doppler frequency ranges roughly from 1 Hz to 100 kHz. Because the acoustic velocity has a zero mean, a carrier is needed. It is provided by a Bragg's cell, driven at the usual frequency of 40 MHz. A shifter is therefore needed so that the frequency modulation index is sufficient to get a good resolution.

However, the actual frequency range of the doppler signal is almost identical to the audio frequency range. It would be possible to use a standard audio analyser to get the doppler spectrum, as is done e.g. for some convection studies. The problem is that the doppler frequency is modulated by the audio one, leading to a complex FM

spectrum because both frequencies are of the same order of magnitude.

The unit must also provide the Bragg drive signal and the shifter signal from a single clock, in order to avoid any jitter between them, as it could be of significant importance considering the above mentioned orders of magnitude for the doppler signal. Moreover, the unit should be able to provide an estimation of the instantaneous frequency using relatively short windows, even at low carrier frequencies. This seems to imply either an FFT processor, or a correlator, both with interpolation capability. Last, the wanted equipment should be able to process the results using as an external time reference the synchronization output of the sine generator, so that further synchronous demodulation of the audio velocity signal remains possible.

At the time we built our setup, only one manufacturer (DANTEC from Denmark) could propose an integrated solution, together with valuable help to adapt all elements to our problem. We therefore used a BSA processor (based on FFT analysis with some kind of interpolation, and also supplying the Bragg's cell and powering the PM). It is connected through an IEEE488 interface to a PC running the "Burstwar" software, using its "rotating machinery" feature to keep the time reference of the audio signal for further averaging. In parallel, we use the BSA shifter output to feed the A/D converter of a post-processing workstation running a real-time unix system ("Maxion" system from Concurrent Computer Corporation) in order to develop custom algorithms for signal processing.

3.3 Seeding

The particles to be tracked should have a size small enough to follow the acoustic movement, but large enough to scatter significantly the light. Several studies deal with these aspects, leading to criteria useful for selecting suitable seeding. Our practical problem was to be able to start our experiments without knowing exactly for which frequency range we would have to optimize the setup, and we therefore did not try to find a very sophisticated seeding. First experiments were conducted using a small lightshow smoke generator, which produces an aerosol of small oil drops. This principle, far from optimal in this case, has three disadvantages: the oil drops are too heavy, they are hot, and they spoil the setup and eventually the optics. Better realizations, designed specifically for LDV, could be used but we have not still enough experience to quantify the improvement which could be achievable.

A specific aspect of our problem is that there is almost no flow. The quantity of seeding needed is therefore very small, and it must be provided at a very low speed to avoid perturbing the acoustic field. Moreover the thermodynamic characteristics of the gas should not be modified too much by the presence of the particles.

To adapt our smoke generator to this problem, we had to build a very simple unit, consisting of two tanks one over the other. In the first, the smoke is fed and stays for a while, eliminating the biggest drops. Two fans (running at low speed) mix the resulting smoke and transmit it to the second tank, where it is stored with a slight overpressure. A small diameter flexible tube permits to conduct the seeding from this second tank to where it is needed.

The results obtained up to now show that this very rough generator is sufficient for many applications, although far from optimal. Further studies are needed to improve both the nature of the particles, the way to select the adequate sizes, and means to put them at the right place without generating too much parasitic flows.

4. INITIAL ACOUSTIC SETUP FOR VALIDATION

The problem of validating LDV for use in Acoustics is a difficult one, as we have no reliable mean to evaluate the velocity exactly at the same place as the beams crossing. We therefore tried to build a setup in which the structure of the acoustic field could be very well known, so that it would be possible to deduce the velocity from other measurements. A classical solution for that problem is to use a cylindrical tube, for which an analytical description of the field may be derived with some accuracy.

In order to design such a setup, one needs to have some experience of the problem. We therefore began by building a simplified version, which would permit to give some orders of magnitude, and to learn more about eventual difficulties. All results presented in the following sections have been obtained from this first version of the setup. An improved one is being tested now, but no definite measurement from it is still available at the date of this writing.

The initial setup is composed of a cylindrical tube made of PVC, excepted for the measuring section which is made of calibrated glass. The internal diameter of the tube is about 45 mm, so that the field is assumed to be described by plane waves up to 2-3 kHz (the eigenfrequency associated to the first next mode is about 4500 Hz). The measuring section is about 60 cm long, and a microphone permits to measure the acoustic pressure on the walls at each of its ends. The field is created by a loudspeaker situated about 60 cm away from the measuring section. Seeding is input near the loudspeaker, and goes out at the other side of the measuring section, again 60 cm away. These distances are kept so that local perturbations related to the seeding inlets would not create significant evanescent modes throughout the measuring section. This setup may be loaded by a one meter long diedre made of absorbing material, so that the field is almost propagative, or closed by a rigid wall to get stationary waves. This last case is interesting in order to get a larger dynamic range for the acoustic quantities.

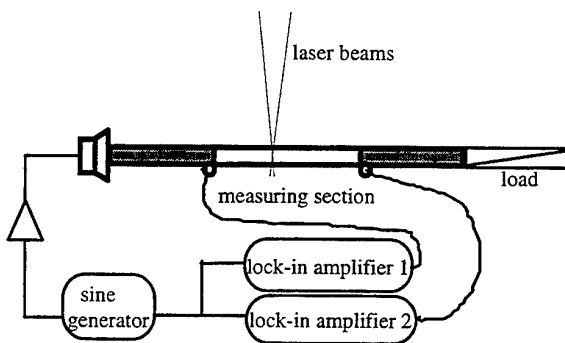


Fig. 2: schematics of acoustic setup for validation

The beam optics are adjusted so that the beams plane includes the setup axis, and that they cross almost exactly at the center. This way, the LDV signal is supposed to be the plane waves velocity v , which can be calculated from the two measured pressures p_1 and p_2 using the following relation:

$$v(x) = \frac{1}{\xi_{sh}(\Gamma\ell)} (p_1 ch(\Gamma x) - p_2 ch(\Gamma(\ell - x))) \quad (2)$$

where: Γ is the wavenumber in the tube,

ξ is the characteristic impedance of the tube,

ℓ is the distance between the microphones,

x is the distance from the first microphone.

As the measured pressures are parietal ones, any evanescent mode superimposed on the plane waves may lead to significant errors on the velocity estimation. The microphones themselves are a source of such coupling, so a great care must be taken to respect the boundary condition at their position: they must be carefully flush mounted, without any leakage. The microphone capsules used for the setup are electret ones, with a diameter of about 5 mm and an equivalent volume small enough to avoid significant perturbation. Their signals are amplified by custom preamplifiers which feed the inputs of two lock-in amplifiers whose phase references are directly taken from the sine generator supplying the loudspeaker.

The relative calibration of the two microphones is done using a reference source at 1 kHz, but it is however not so good, because no simple way exists to ensure it over a large frequency range with enough accuracy, especially concerning the phase. This lack of accurate microphone calibration therefore limits the validity of the existing results, which are however interesting in order to give a first idea of the functioning domain of the whole setup.

5. EXTENSIONS OF SIGNAL PROCESSING

5.1 Principle of existing processor / software

As stated above, the signal processing available now is the burst processing provided by the BSA itself. It consists of a FFT spectrum calculated from a window of data during each detected burst. A maximum frequency is searched for each of these spectra, and some criteria are applied to verify that these maxima may correspond to the "instantaneous" frequency corresponding to a velocity component. If these criteria are verified, the velocity is computed using different constants related to the optics.

The data are transferred to the PC together with the time of arrival referenced to the last clock signal ("rotating machinery" mode). This way, the software can accumulate several periods of signal on a single graph, which then reconstitutes the shape of the sinewave over the many bursts involved. All these evenements can be distributed into discrete classes of arrival time, and averaged in each of these classes, leading to an averaged waveform suitable for a further processing such as the synchronous demodulation. A drawback of this method is that it averages values which did

not occur exactly at the same instant in the period; this leads to an estimation error increasing as the number of classes decreases.

5.2 Improved processing using conventional hardware

Our first effort was to try to reduce such errors in order to get the best from the existing equipment. A least-squares method has therefore been developed to extract the amplitude and phase of the sinewave directly from the data sent by the BSA, including the "exact" arrival time. In the present implementation, we use however the "Burstwar" software to process the data for validation, and to export them as ASCII files.

This method suffers from the fact that the actual velocity may not be a pure sinewave, e.g. because of distortions in the source or during propagation. As it has no way to get rid of eventual harmonics, as was done by the synchronous demodulator, this estimator of the fundamental component may be biased for distorted signals. We did not however notice significant problems during our experiments.

A more severe limitation occurs because the velocity is a sinewave, and thus varies rapidly with time. As the BSA searches for a spectrum maximum, it requires the velocity to be constant during one window, and does not track the actual velocity evolution with time. In fact, the BSA can be seen as an instantaneous frequency detector based on a windowed Fourier transform, with no overlap between windows. This transform is not optimum for varying signal, which suggests to look at other time-frequency tools to build a more suited detector.

5.3 Direct Time-Frequency analysis : the CWV detector

To be able to test other processings, we used the shifted signal from the BSA, fed to the acquisition workstation described above. Different algorithms were tested, first on simulated signals, and then on a few samples of real bursts. The comparison of these methods has been given by Herzog *et al* (1995), and we thus just recall the conclusions.

Among various methods, the most suited was found to be the Cross-Wigner-Ville detector (CWV), which is based on a modified kernel for a Wigner-Ville transform. To build this detector, we start from the analytic signal $z(t)$, constructed from the real signal from the A/D converter and completed by an imaginary part obtained by Hilbert transform:

$$z(t) = e^{j\varphi(t)} = e^{j\omega_c t + j\alpha \sin(\omega_0 t + \phi)} \quad (3)$$

where ω_c is 2π times the carrier frequency,
 α is proportional to the velocity amplitude,
 ω_0 is 2π times the audio frequency f_0 ,
 ϕ is the phase of the acoustic velocity.

The aim is to detect the instantaneous frequency (IF), defined as

$$f_i(t) = \frac{1}{2\pi} \frac{d\varphi(t)}{dt} \quad (4)$$

on a current window. An iterative algorithm found out by Boashash and O'Shea (1993) is based on three steps :

1) An IF is set and an unit amplitude reference windowed signal, $r(t)$, is built from it.

2) The CWV transformation is calculated between the reference and the windowed signal $x(t)$ from $z(t)$, as following

$$CWV(t, f) = \int_{-\infty}^{+\infty} x(t + \tau) r^*(t - \tau) e^{-j\omega\tau} d\tau \quad (5)$$

A peak detection determine a new IF.

3) The procedure is repeated from step one until the IF estimate remains stable. The resulting value is taken as the IF of $x(t)$.

This detector could extract successfully simulated acoustic signals, even with low signal/noise ratios. It proved to be the best detector in the case of short windows, but as it assumes a linear frequency law during the window analysis, it is still limited to signals with a low modulation index.

5.4 Limits of the direct analysis principle

When increasing the audio frequency, the number of points inside a period decreases for a given sampling frequency. It is therefore necessary to decrease the number of windows per audio period to keep a constant doppler frequency resolution for each of them, or to reduce the window length, leading to a degraded resolution. Obviously a limit will occur when increasing the frequency or decreasing the velocity.

This limit may be expressed from the simple following considerations: to be able to evaluate correctly the sinewave parameters, one needs at least two values per period (Shannon theorem), and needs them to be around the maximum of amplitude in the period to get best resolution. The minimum velocity δv which can be detected can then be expressed as a function of the audio frequency f_0 from the incertitude principle given in a general case:

$$\sigma_t \cdot \sigma_f \leq \frac{1}{4\pi} \quad (6)$$

where σ_t is the standard deviation of the signal energy distribution and σ_f the frequency resolution.

In order to respect the Shannon criteria, $\sigma_t = 1 / 2f_0$ is the minimum window length. On the other hand, σ_f , the doppler frequency resolution, can be related to the minimum velocity δv as:

$$\sigma_f = \frac{2 \sin(\theta / 2)}{\lambda} \delta v \quad (7)$$

where θ is the beams angle and λ is the optical wavelength.

As a result, the minimum velocity and the audio frequency can be related as follows:

$$\delta_v \geq \frac{\lambda}{4\pi \sin(\theta/2)} f_0 \quad (8)$$

This last relation should only be taken as a rough estimate showing the absolute limits of a processor having no knowledge of the periodic nature of the audio signal.

5.5 Synchronous processing methods

A way to go further in processing the burst signal is to take into account the fact that the analytic form of the velocity is known (or supposed so). We therefore developed a different method which evaluates the parameters of the sinewave directly from the burst signal, and able to use longer windows by assuming a suited form for the time-frequency law; it was called the Global Demodulation Transformation by Valeau *et al* (1996):

$$GDT(t, f) = \int_{-\infty}^{+\infty} \left(s(t + \tau) s^*(t - \tau) \right)^{K\omega_0 \tau \sin(\omega_0 \tau)} \left(s \left(t + \tau + \frac{\pi}{2\omega_0} \right) s^* \left(t - \tau - \frac{\pi}{2\omega_0} \right) \right)^{K\omega_0 \tau \cos(\omega_0 \tau)} e^{-j\omega \tau} d\tau \quad (9)$$

It can be easily shown that the transformation of the following signal

$$s(t) = e^{j\alpha \sin(\omega_0 t + \phi)}, \quad (10)$$

becomes the signal

$$\delta(\omega - A \cos(\omega_0 t + \phi)), \quad (11)$$

which is the instantaneous frequency law of the Doppler signal, where $A=2K\alpha\omega_0$ is proportional to the acoustic velocity magnitude and K is an arbitrary parameter. In order to use this method, the real signal must be firstly converted into an analytic signal and, secondly, shifted around the 0 Hz frequency.

6. RESULTS

A first experiment has been achieved according to the description given in the fourth section, in order to compare the velocities deduced from the microphone measurements and those obtained by the Burst Spectrum Analyser of DANTEC. The figure 3 shows the ratio between both measurements for three different levels at a single point in the guide with an anechoic load.

At this stage, it can only be observed that the results are quite similar up to 3000 Hz, with about 5% discrepancy. After this limit, the difference increases significantly.

Another remark concerns typical bias which appears on the values below 3000Hz, for which the BSA values are always the lower. Until now, this bias can not be explained and further investigations have to be conducted in order to determine which technique gives results closer to the actual values.

In order to evaluate the dynamic ability of the BSA technique, two complementary experiments were achieved at 860 Hz, and then at the limiting value of 3000 Hz. We tried to use the lowest level possible, according to the laboratory environment. The BSA gave values similar to the evaluation from pressure measurements down to 50μm/s at 860 Hz, and down to 0.5 mm/s at 3000 Hz, even if the agreement was poorer than at higher levels. It should be noted that the dynamic limits implied by this figures are in rough agreement with eq. (8), although their actual significance is somewhat questionable.

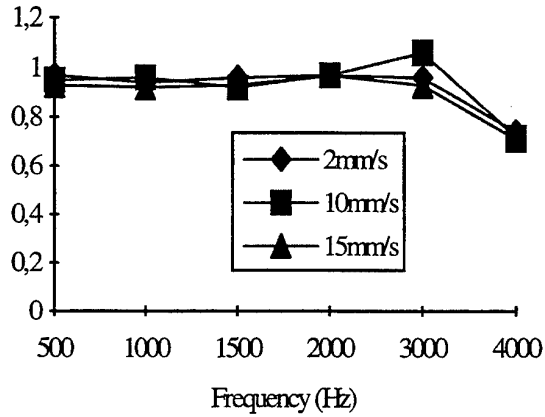


Fig. 3 : Ratio of the velocities obtained by microphone measurements to these obtained by the BSA

The second experiment concerns the extraction of the IF by means of the time-frequency techniques described above. The figures 4-a and 4-b are, respectively, the extracted IF from the CWV and from the GDT, for a 3000 Hz acoustic signal and with a velocity around 2.3 mm/s. The second one seems to follow the IF law more accurately, in spite of important low frequency disturbances. The figures 5-a and 5-b describe the same experiment, but with an approximative level of 0.5 mm/s. The improvement of the GDT is more evident in this case, and still emphasises the need to remove low frequency components at an early stage.

The third experiment consisted to scan one wavelength in the acoustic guide closed at the end. In this case, the wave is almost stationary and velocity or pressure nodes appear, leading to more extreme values of the velocity. The working frequency was still taken at 3000 Hz. The figure 6 shows the BSA measurements and the velocities deduced from the acoustic pressures. As the seeding modifies the value of the measured pressure (i.e. the acoustic field), both acquisition were made synchronously. We can still notice the under-estimation observed previously, but, furthermore, both

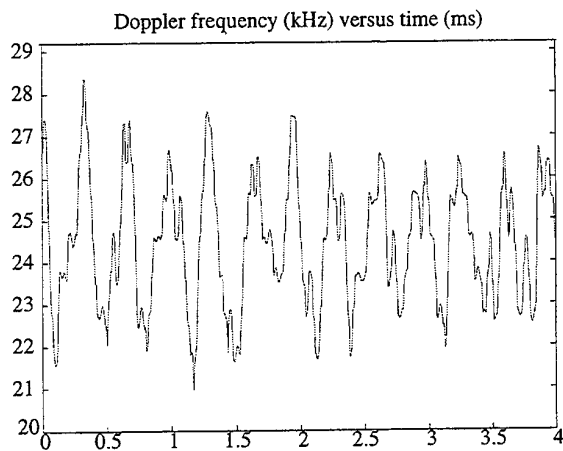


Fig 4-a: IF extraction of a 3000 Hz acoustic signal at 2.5 mm/s velocity by means of CWV technique.

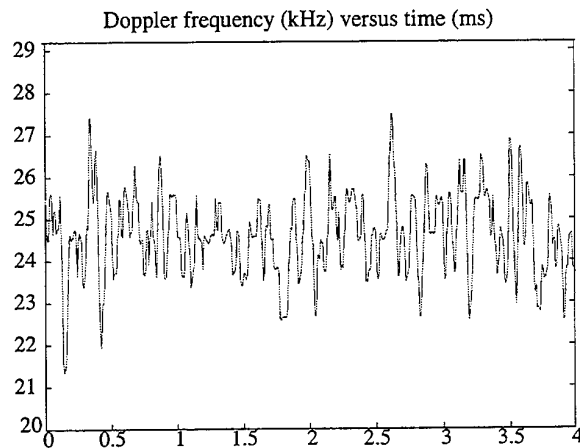


Fig 5-a: IF extraction of a 3000 Hz acoustic signal with a 0.5 mm/s velocity magnitude by means of CWV technique.

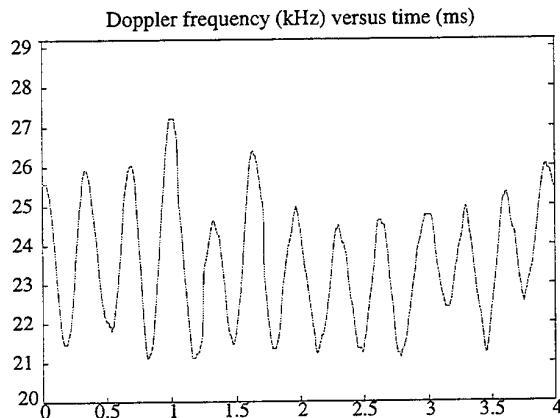


Fig 4-b: IF extraction of a 3000 Hz acoustic signal at 2.5 mm/s velocity by means of GDT technique.

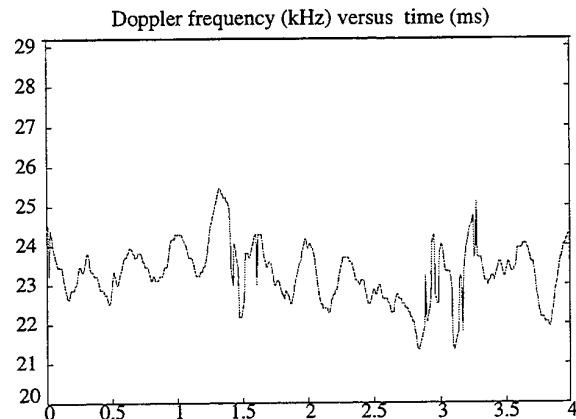


Fig 5-b: IF extraction of a 3000 Hz acoustic signal with a 0.5 mm/s velocity magnitude by means of GDT technique.

curves have a position-lag which can probably be due to the inaccuracy of the microphone phase estimation at this frequency.

This measurement has been repeated to test the time-frequency demodulator using fewer seeding. The figure 7-a and 7-b respectively show the results obtained by the CWV and the GDT techniques (solid lines), both compared to the values calculated from the pressure measurements (dashed lines). We can first note that the under-estimation observed previously with the BSA measurement is not so systematic. On the other hand, the position-lag still remains. A probable explanation could be that the BSA processing is responsible of the bias, but that the position-lag is actually related to a microphone phase error.

In all these comparisons between BSA and other processings, we noticed that the ideal amount of seeding was lower for the time-frequency methods. This fact is very positive for Acoustics, as the presence of particles seems to change significantly the properties of the medium, as could be seen from the microphone measurements.

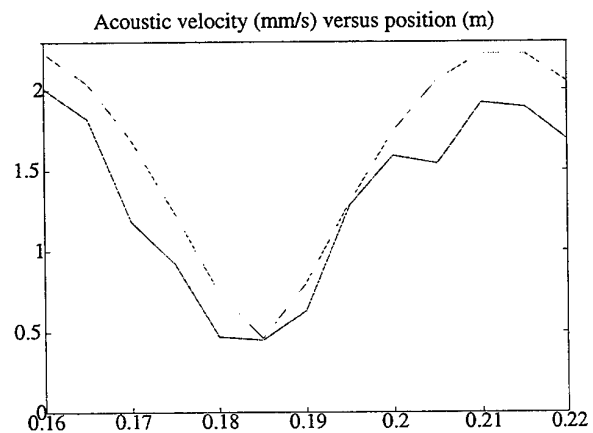


Fig 6: Measurement of velocity along a closed guide using the BSA (solid line) or acoustic signals (dashed line).

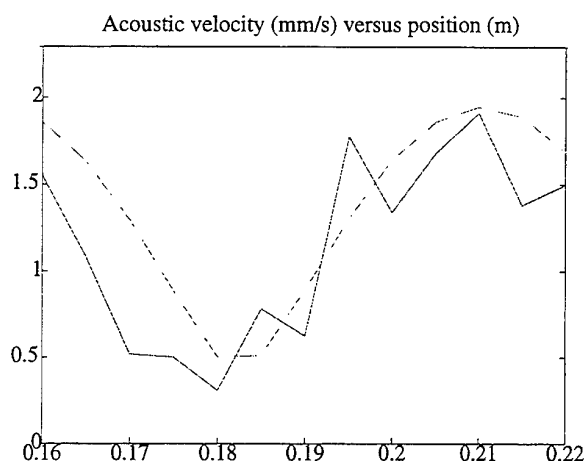


Fig 7-a: Measurement of velocity along a closed guide using the CWV (solid line) or acoustic signals (dashed line).

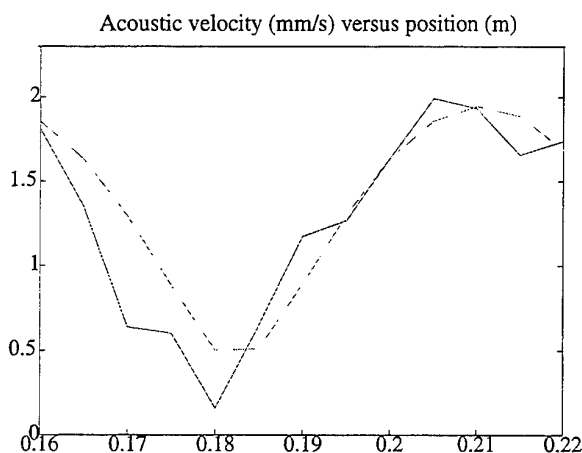


Fig 7-b: Measurement of velocity along a closed guide using the GDT (solid line) or acoustic signals (dashed line).

7. CONCLUSION

This work has proved the capability of commercial equipment to achieve acoustic velocity measurements with a large dynamic range, from 50 $\mu\text{m/s}$ to 5 cm/s at 860 Hz, i.e. between 60 and 120 dB SPL for plane waves. The frequency range is validated at least up to 3000 Hz, which is the limit of our experimental setup, but only for higher levels.

There seems to be a theoretical limit for these conventional tools as the velocity resolution achievable by direct analysis would reach a limit proportional to the audio frequency.

Proposed methods are likely to improve both the minimum velocity reachable and the limiting frequency, however this has to be validated by further measurements. Anyway, these methods already permit to use fewer seeding, thus limiting the perturbation of the acoustic field itself.

An intensive experimental work will now start based on an enhanced validation setup, in order to confirm and improve these results.

7. ACKNOWLEDGEMENTS

The authors wish to thank the engineers of the DANTEC company for their helpful contributions, and especially Mr Tanguy for its patience and support all along the starting of this project.

REFERENCES

Boashash, B. & O'Shea, P. 1993, Use of the Cross Wigner-Ville Distribution of the Signal, *IEEE Trans. on Signal Processing*, vol. 41 (3), pp.1439-1445.

Davis, M. & Hews-Taylor, K., 1986, Laser-Doppler Measurement of Complex Acoustic Impedance, *J. of Sound and Vibration*, vol. 107 (3), pp. 451-470.

Eckmann, D. & Grotberg, J. 1991, Experiments on Transition to Turbulence in Oscillatory pipe Flow, *J. Fluid. Mech.*, vol. 222, pp. 329-350.

Herzog, P., Valière, J.C. & Duffossé, S., 1995, Laser Doppler Velocimetry in Acoustics: Principle and Signal Processing, *Proc. 15 th. Int. Conf. Acous., Trondheim (Norway)*, pp.91-94.

Lee, D., Jarzynski, J. & Berthelot, Y., 1993, A Study of Wave Propagation on a Cylindrical Shell using Fiber Laser Doppler Velocimetry, *J. Acoust. Soc. Am.*, vol. 94 (1), pp.196-212.

Taylor, K., 1977, Absolute Measurement of Acoustic Particle Velocity, *J. Acoust. Soc. Am.*, vol. 59 (3), pp. 691-694.

Taylor, K., 1981, Absolute Calibration of microphones by a Laser-Doppler Technique, *J. Acoust. Soc. Am.*, vol. 70 (4), pp. 939-945.

Valeau, V., Valière, J.C., Herzog, P., Simon, L. & Depollier, C., 1996, Instantaneous Frequency Tracking of a Sine Wave Phase Modulation Signal., *Proc of the IEEE Int. Symp. on Time-Frequency and Time-Scale Analysis*.

Vignola, J., Berthelot, Y. & Jarzynski, J., 1991, Laser Detection of Sound, *J. Acoust. Soc. Am.*, vol. 90 (3), pp.1275-1286.

SESSION 40

Optics II

EVALUATION OF THE GAUSSIAN BEAM MODEL FOR PREDICTION OF LDV FRINGE FIELDS

Paul C. Miles and Peter O. Witze

Combustion Research Facility
Sandia National Laboratories, Livermore, CA, USA

ABSTRACT

A simple model is developed to estimate the fringe field geometry at the intersection of two gaussian laser beams. Comparison of the model results to experimentally measured fringe spacing demonstrates that while the model predicts the fringe geometry well when the beam waists are far from the intersection volume, it performs poorly under nominally ideal conditions—when the beam waists are located at the intersection. Data obtained with two different laser sources indicate that the discrepancies between the theory and experiment are likely due to deviations of the laser beam from an ideal gaussian beam. With a high quality laser, the details of the fringe field geometry are still not well duplicated by the gaussian beam model, although the magnitude of the variation in fringe spacing and the effect of the controlling system parameters are correctly predicted.

1. INTRODUCTION

Over the past thirty years, Laser Doppler velocimetry (LDV) has evolved into the technique of choice for obtaining accurate, non-intrusive measurements of fluid velocity. In the dual-beam, real-fringe configuration (Fig. 1), the frequency of the Doppler signal can be viewed as being due to passage of a scattering particle through a set of interference fringes created by two coherent laser beams which are brought to a focus (waist) and crossed by a single transmitting lens. Due to continuous improvements in optics, electronics, and signal processing techniques, the spatial uniformity of these interference fringes may now be the limiting factor in determining the accuracy with which flow velocities can be measured.

In recent experimental investigations, large variations in the spatial uniformity of the fringe field are observed along the coordinate directions defined by both the major and minor probe volume axes (Miles and Witze, 1994). These non-uniformities occur even under conditions of nominally ideal optical alignment—especially in regions off the probe volume axes. In attempting to understand the source of these variations we found that existing analytical models of the

fringe spacing variation provided limited guidance. These models are valid for gaussian beams with equal beam waist sizes and equal (or equal but opposite) distances of the beam waists from the measuring volume; the effects of differing waist sizes and positions on the fringe field uniformity cannot be ascertained. Additionally, the predicted fringe spacings are strictly valid only on the probe volume axes. Computed results from a more rigorous, general model are similarly available only for a restricted subset of conditions and only along the probe volume major axis.

Previous experimental measurements also provided few points for comparison—data obtained under conditions of near ideal alignment are sparse, and are generally limited to measurements along the longitudinal probe volume axis. In addition, these data were obtained with techniques that averaged over the transverse extent of the probe volume, a procedure that masks the details of the fringe field.

In view of the preceding discussion, the goals of this paper are outlined as follows:

- (1) To provide an alternative gaussian beam model which permits simple evaluation of the fringe field throughout the probe volume, for arbitrary beam waist sizes and positions.
- (2) To compare the model results with experimental data in order to a) determine the applicability of the models to the prediction of fringe fields in a dual-beam velocimeter and b) to understand the origin of the large variations in the fringe field which have been experimentally observed.
- (3) To provide guidance to the user or designer of LDV systems on how to minimize the effects of the fringe field non-uniformities on the accuracy of the data obtained.

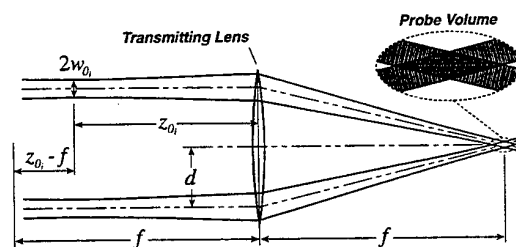


Fig. 1 Dual-beam, real-fringe LDV configuration

2. PREVIOUS LDV FRINGE FIELD STUDIES

Fringe field uniformity was first investigated by Hanson (1973), who demonstrated that misaligned LDV systems are characterized by a gradient in fringe spacing along the optical (longitudinal) axis. An expression for this gradient was obtained which is valid at the intersection of the two beam centerlines when the waists of the two beams have equal longitudinal positions. Comparison of the predicted gradient to experimental measurements demonstrated reasonable agreement, although data were obtained under conditions of rather severe misalignment.

Later, Hanson (1976) demonstrated the existence of a fringe spacing gradient along the transverse probe volume axis, which occurs when the two beam waists are located at equal distances from the intersection volume, but on opposite sides. His resulting expression is valid on the probe volume minor axis; no experimental verification was performed.

Durst and Stevenson (1979) extended Hanson's longitudinal analysis by referring the results to system parameters: the transmitting lens focal length and the location of the waists of the input laser beams. Implicit in the interpretation of their result is the assumption that the longitudinal gradient in fringe spacing is constant over the length of the probe volume. Extensive measurements of the longitudinal gradient were also obtained, and showed good agreement with the analytical result. As will be shown below, the assumption of a constant longitudinal gradient is appropriate under the experimental conditions employed. For these conditions, however, little structure in the fringe field is to be expected under near-ideal alignment conditions, and the large variations seen by Miles and Witze (1994) were not observed.

In addition, Durst and Stevenson obtained an alternate expression for the fringe spacing variation along the transverse axis; like Hanson's result, the analysis was restricted to equal but opposite distances of the beam waists from the intersection volume, and is valid only along the transverse axis. Qualitative confirmation of this effect is reported, but no quantitative verification of the result was possible.

A more recent, frequency-based analysis is given by Durst, *et al.* (1990), which allows for different beam waist sizes and positions and provides a framework for examination of the effects of non-gaussian beams. The expressions obtained are complex, and the effect of various system parameters on the longitudinal variation in fringe spacing is therefore computed and presented as a series of

graphs. Experimental verification of the computed results demonstrates fair agreement between theory and experiment under misaligned conditions; under near-ideal alignment conditions, however, the experimental variation in fringe spacing exceeds the theoretical variation by a factor of approximately three.

Collectively, the above cited studies have verified the applicability of gaussian beam models in predicting the longitudinal variation in fringe spacing under conditions in which the longitudinal gradient is nearly constant—this typically occurs when the beam waists are far from the probe volume. Although the variation in fringe spacing under near-ideal alignment conditions is also of interest, the existing data obtained under these conditions are few and tend to show a large discrepancy with theoretical predictions. Furthermore, until recently, experimental determination of the transverse variation in fringe spacing had not been achieved, and no comparison to gaussian beam model predictions has been made.

3. THE GAUSSIAN BEAM MODEL

There are at least two approaches by which a model for the fringe spacing in the intersection volume of two gaussian beams can be developed. The first approach, based on the difference in phase of the two beams expressed in beam coordinate systems, permits a rigorous analysis without approximation (Miles, 1996). The second approach, presented in this paper, has much in common with the earlier fringe-based models and is both intuitive and mathematically simple, although some implicit approximations must be made. The effect of these approximations, however, can be shown to be negligible simply by comparison with results obtained using the first approach. Although the following analysis is specific to gaussian beams, we believe that the indicated effects of various system parameters carry over, at least qualitatively, to the beams delivered by single-mode optical fibers as well.

An excellent discussion of the properties of Gaussian beams and their transformation by optical elements can be found in the text by Siegman (1986); here we review only those aspects relevant to the present work. Fig. (2) depicts the divergence of a Gaussian beam propagating away from its waist. At the waist, the surfaces of constant phase (wave fronts or phase fronts) are locally planar, and gradually acquire curvature and diverge as distance from the waist is increased. At any location z along the beam axis, the local radius of curvature and the local beam spot size (the radius defined by the $1/e^2$ intensity contour) are known solely in terms of the spot size at the beam waist w_0 . With the Rayleigh range z_R defined by

$$z_R = \frac{\pi w_0^2}{\lambda}, \quad (1)$$

the local radius of curvature, $R(z)$, and spot size, $w(z)$, can be found from

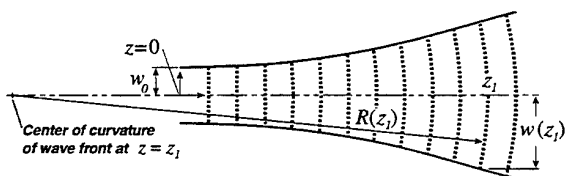


Fig. 2 Geometry of a gaussian beam

$$R(z) = z + \frac{z^2}{z_R} \quad (2)$$

and

$$w^2(z) = w_0^2 \left(1 + \left(\frac{z}{z_R} \right)^2 \right) \quad (3)$$

Note that the center of curvature lies on the beam axis. The usual sign convention is that positive $R(z)$ indicates a diverging beam.

In the following derivation, we consider a 'fringe' to be defined by the locus of all points for which the phase difference between the two beams is fixed. As a practical matter, this may correspond to a surface of maximum light intensity, minimum light intensity, or neither. The geometry to be considered is shown schematically in Fig. 3. The locations (x_{c_1}, z_{c_1}) and (x_{c_2}, z_{c_2}) refer to the locations of the centers of curvature of the wavefronts of each beam at an arbitrary location (x, z) within the measurement volume. The wavefront centers of curvature are known to lie along the lines $x_{c_1} = -z_{c_1} \tan \alpha$ and $x_{c_2} = z_{c_2} \tan \alpha$, where α is the usual half-angle of the beam crossing and the origin of the coordinate system is at the crossing of the beam centerlines. If the phase difference between the two beams at their centers of curvature is taken to be fixed (for convenience we take this difference to be the phase difference which defines a fringe), then the condition for the existence of a fringe at (x, z) is simply that the optical path length, R_p , between the two centers of curvature to (x, z) differs by an integral number of wavelengths. This optical path length can be identified as the radius of curvature of the phase front at (x, z) . The condition for the existence of a fringe can therefore be simply expressed as:

$$R_2 - R_1 = \sqrt{(x - x_{c_2})^2 + (z - z_{c_2})^2} - \sqrt{(x - x_{c_1})^2 + (z - z_{c_1})^2} = n\lambda \quad (4)$$

The spacing L between adjacent fringes in the x -direction is determined by differentiating Eq. (4) with respect to x and re-arranging to obtain

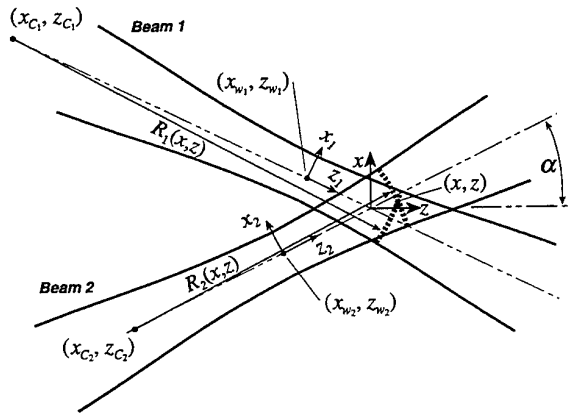


Fig. 3 Geometry and coordinate system for analysis of fringe spacing

$$L = \left(\frac{dn}{dx} \right)^{-1} = \frac{\lambda R_1 R_2}{R_1(x - x_{c_2}) - R_2(x - x_{c_1})} \quad (5)$$

Note that the fringe spacing given by Eq. (5) has a z -direction dependency which is implicit in the definitions of the R_i . It is also noteworthy that as x varies, the local phase of each beam at (x, z) varies, and the corresponding radius of curvature (and center of curvature) of the local phase front also varies. In deriving these equations, we have neglected this x -dependency of x_{c_i} and z_{c_i} . It can be shown (Miles, 1996) that neglecting the x -dependency of the wavefront center of curvature introduces an error of order $(\lambda/2\pi w_0)^2$, which is negligible for practical LDV systems.

It is interesting to examine some limiting cases of Eq. (5) to establish consistency with earlier studies. Along the optical axis ($x = 0$), when the beam waists are of equal sizes and are located at equal distances from the beam crossing (but on the same side of the crossing), $R_1 = R_2 = R$ and $x_{c_1} = -x_{c_2}$, so that Eq. (5) reduces to

$$L = \frac{\lambda R}{2x_{c_1}} \quad (6)$$

Eq. (6) is identical to the result obtained by Hanson (1973).

A second limiting case of interest occurs when the beam waists are equal distances from the crossing but on opposite sides. In the $z=0$ plane, $R_1 = -R_2 = R$ and $x_{c_1} = x_{c_2}$, so that

$$L = \frac{-\lambda R}{2(x - x_{c_1})} \quad (7)$$

This is identical to the expression obtained by Hanson (1976). Differentiating Eq. (7) with respect to x , the transverse gradients in fringe spacing are found to be

$$\frac{dL}{dx} = \frac{\lambda}{2(x - x_{c_1})} \left(\frac{R}{(x - x_{c_1})} - \frac{(x - x_{c_1})}{R} \right) \quad (8)$$

Accounting for the different coordinate systems used, Eq. (8) is the expression obtained by Durst and Stevenson (1979). All previously obtained fringe model results can thus be shown to be special cases of Eq. (5).

The fringe spacing at any location within the probe volume can be computed from Eq. (5) with R_i obtained from Eq. (2). The longitudinal beam coordinate z_i , for use in Eq. (2), can be determined from (see Fig. 3)

$$z_1 = (z - z_{w_1}) \cos \alpha - (x - x_{w_1}) \sin \alpha \quad (9)$$

and

$$z_2 = (z - z_{w_2}) \cos \alpha + (x - x_{w_2}) \sin \alpha \quad (10)$$

where (x_{w_1}, z_{w_1}) and (x_{w_2}, z_{w_2}) represent the coordinates of the beam waists. The x -coordinates of the wavefront centers of curvature, for use in Eq. (5), can be obtained from

$$x_{c_1} = x_{w_1} + (R_1 - z_1) \sin \alpha \quad (11)$$

and

$$x_{c_2} = x_{w_2} - (R_2 - z_2) \sin \alpha \quad (12)$$

By revisiting the simplified, limiting cases described

above, some insight into the geometry of the fringes can be gained. It is interesting to consider the changes in fringe spacing along the major axis of the probe volume ($x=0$), when the beam waists have equal sizes and z -coordinates z_w (as described by Eq. (6)). This corresponds to a typical, conventional LDA using a path compensated beam splitter (note that we do not assume that the input laser beam has been appropriately "collimated"). Under these conditions, Eqs. (2), (6) and (9)-(12) give

$$L = \frac{\lambda}{2\sin\alpha} \left(1 + \frac{z \cos^2\alpha (z \cos^2\alpha - z_w)}{z_R^2 \cos^2\alpha - z_w (z \cos^2\alpha - z_w)} \right). \quad (13)$$

From the form of Eq. (13), it is apparent that the fringe spacing gradients in the z -direction cannot be assumed constant unless $z_w \gg z$, that is, under fairly severe conditions of misalignment. Further note that for beams characterized by large z_R , the variation in fringe spacing can be small even for misaligned systems. With perfect alignment of the beam waists with the crossing ($z_w = 0$), Eq. (13) reduces to

$$L = \frac{\lambda}{2\sin\alpha} \left(1 + \left(\frac{z \cos\alpha}{z_R} \right)^2 \right), \quad (14)$$

from which the minimum possible variation in fringe spacing for a given α and waist diameter can be computed.

Eqs. (13) and (14) allow the longitudinal variation in fringe spacing to be determined in terms of properties of the focused beams near the intersection volume. While these properties can be readily measured, it is of greater value to understand how the fringe variation is affected by various system parameters, *e.g.*, input beam diameter or beam crossing angle. It is shown elsewhere (Miles, 1996) that, to a good approximation, Eq. (13) can be expressed as

$$L \approx \frac{\lambda}{2\sin\alpha} \left\{ 1 - \hat{z} \cos^2\alpha \left(\frac{w_0}{d} \right) \left(\frac{z_0 - f}{z_R} \right) + \hat{z}^2 \cos^4\alpha \left(\frac{w_0}{d} \right)^2 \right\}. \quad (15)$$

In Eq. (15), w_0 and d are the incident beam waist radius and offset from the optical axis, respectively, as defined in Fig. 1. The parameters z_0 and f in the "normalized mis-alignment" $(z_0 - f)/z_R$ are also defined in Fig. 1, and the coordinate \hat{z} is defined as the z -coordinate normalized by one-half of the probe volume length, $w_0/\sin\alpha$. With this definition, \hat{z} is constrained to the range $-1 < \hat{z} < 1$. Eq. (15) can be used with good accuracy for $w_0/d < 0.10$ and $(z_0 - f)/z_R < 2$, or alternatively, for arbitrary w_0/d when $(z_0 - f)/z_R \approx 0$. Note that the variation in fringe spacing under all alignment conditions is determined by the ratio w_0/d . In order for fringe spacing non-uniformities to be large, the beam offset d is typically small, which implies small α . It follows that for most applications in which the variation in fringe spacing is important, Eq. (15) can be further approximated by

$$L \approx \frac{\lambda}{2\sin\alpha} \left\{ 1 - \hat{z} \left(\frac{w_0}{d} \right) \left(\frac{z_0 - f}{z_R} \right) + \hat{z}^2 \left(\frac{w_0}{d} \right)^2 \right\}. \quad (16)$$

Like Eq. (13), Eq. (16) can be reduced under ideal alignment conditions to

$$L \approx \frac{\lambda}{2\sin\alpha} \left\{ 1 + \hat{z}^2 \left(\frac{w_0}{d} \right)^2 \right\}, \quad (17)$$

in which case the fringe spacing non-uniformity is determined solely by the ratio w_0/d .

In a similar manner, the situation in which the beam waists are equal distances from the crossing but on opposite sides can be revisited. Substituting Eq. (11) into Eq. (7) and expanding in a power series one obtains

$$L = \frac{\lambda}{2\sin\alpha} \left[1 + \left(\frac{x \cos\alpha}{R \tan\alpha} \right) + \left(\frac{x \cos\alpha}{R \tan\alpha} \right)^2 + \dots \right]. \quad (18)$$

After evaluating Eq. (9) at $z = 0$ and introducing the approximation $x \sin\alpha \ll z \cos\alpha$, Eq. (18) can be expressed as

$$L \approx \frac{\lambda}{2\sin\alpha} \left[1 - \frac{x z_w \cos^2\alpha}{(z_w^2 + z_R^2 \cos^2\alpha) \tan\alpha} \right]. \quad (19)$$

Eq. (19) expresses the transverse variation in fringe spacing in the $z = 0$ plane in terms of the properties of the focused beams. Like Eqs. (13) and (14), it is of greater interest to express this variation in terms of system variables, which results in (Miles, 1996)

$$L \approx \frac{\lambda}{2\sin\alpha} \left[1 - \hat{x} \cos^5\alpha \left(\frac{w_0}{d} \right) \left(\frac{z_0 - f}{z_R} \right) \right]. \quad (20)$$

The transverse variation in fringe spacing is thus shown to also be fully determined by the dimensionless ratios w_0/d and $(z_0 - f)/z_R$, and is approximately linear in the normalized transverse coordinate \hat{x} .

Although the above discussion has clarified the variation in fringe spacing observed along the longitudinal and transverse probe volume axes, we have not yet addressed the off-axis fringe spacing variations, nor the effects of differing beam waist sizes and arbitrary beam waist positions. These effects are considered by using Eq. (5), with Eqs. (9)-(12), to compute the fringe spacing at arbitrary (x, z) locations throughout the probe volume.

In general, the computed results show that the on-axis variation in fringe spacing, as given by Eqs. (13) and (19), can be used as a reasonable predictor of the fringe spacing throughout the probe volume, and that different waist sizes and positions do not dramatically vary the nature of the variation in fringe spacing.

For path-compensated (and ideally aligned) systems, when $z_{w1} = z_{w2}$, the longitudinal (z) variation in fringe spacing is found to have negligible dependence on the transverse coordinate x . Likewise, the transverse variation is essentially independent of z and is negligible throughout the probe volume.

In a similar fashion, when the beam waists are equal but opposite distances from the beam crossing ($z_{w1} = -z_{w2}$), we find that the longitudinal profile retains the parabolic form given by Eq. (14), but the total variation decreases with increasing $|z_w|$. The longitudinal profile remains nearly identical off-axis, although it is offset by an amount dictated by the expected lateral variation. The lateral profile is found

to be closely linear (*cf.* Eq. (19)), with a slope which does not change significantly with z (as required by the observed variation in the longitudinal profiles).

To a rough approximation, the computed results indicate that when the beam waists are at arbitrary locations, the longitudinal variation in fringe spacing can be estimated from Eq. (13) with $z_w = (z_{w1} + z_{w2})/2$, while the lateral variation can be estimated from Eq. (19), using $z_{w1} = -z_{w2} = (z_{w1} - z_{w2})/2$. Under no circumstances were longitudinal profiles observed which deviated from the approximately parabolic form dictated by Eq. (13). Similarly, the lateral profiles were observed to remain linear, with a slope which never exceeded the slope estimated from Eq. (19) as described above.

The effects of varying beam waist sizes are similar to the effects of arbitrary waist locations—both variables change the local evolution of the wavefront curvature and subsequently the spatial fringe spacing variation. For the present purposes, it suffices to note that for modest changes in waist size ($\pm 10\%$) the induced variation in fringe spacing was small compared to the longitudinal variation which exists under ideal alignment conditions, and negligible in comparison to the variation associated with non-ideal beam waist locations. Fringe spacing variation was computed for various combinations of different beam waist sizes and locations—none of these combinations resulted in departures in the longitudinal profiles from a nearly parabolic form or in a departure from linearity in the transverse profiles.

4. EXPERIMENTAL SET-UP AND PROCEDURE

Due to the desire to examine the variation in fringe spacing throughout the probe volume (including the transverse variation), a simple experimental technique in which the beat frequency of light scattered from a moving surface is measured cannot be employed. The signal frequency resulting from such a technique is an average over a cross-section of the probe volume, and additional difficulties are introduced due to random phase fluctuations associated with multiple scattering centers within the probe volume. To overcome these problems, a commercial beam profiling device (Photon Inc., Model 1180), consisting of a rotating drum surrounding a photodetector is employed. On the drum surface a small aperture is mounted which sweeps across the incident beam in front of the photodetector. The resulting signal is proportional to the intensity of the light falling on the aperture. By scanning the aperture through the probe volume, a signal is generated which is analogous to the Doppler burst that would be generated by a particle following the same trajectory of the aperture. This apparatus is similar in function to the scanning pinhole used by Durst, et al. (1990). Because the fringe spacing within the probe volume may be smaller than the available apertures, the measurement of the variation in fringe spacing is made in a magnified image of a cross-section of the probe volume. In earlier work, Miles and Witze (1994) demonstrated that the fringe field in the magnified image is related to the fringe

field in the object plane of the imaging system simply by the ray-optics magnification M . It was further found that this relationship can be achieved experimentally with good accuracy. Because the fringe spacing in the magnified image is considerably larger than in the probe volume (and the signal from the beam profiler of significantly lower frequency), the signal from the beam profiler can be sampled digitally and used to accurately determine the spacing between individual fringes. The need to use counter or FFT type signal processors to determine the signal frequency is thus eliminated, as is the bias due to an averaging over many fringes which is inherent in such schemes.

A full discussion of the experimental technique is given by Miles and Witze (1994), and only a summary is presented here. The beam profiler and imaging lens (20X microscope objective) are mounted on an optical rail with a fixed separation corresponding to the image distance which gives the desired magnification. Because the distance of the image plane from the imaging lens is fixed, translation of the entire optical rail simply changes the effective object plane at fixed magnification. The signal output by the beam profiler is digitally sampled at a rate of about 50 times the signal frequency. Digital filtering is used to remove the signal pedestal and high frequency noise without inducing skewing of the zero crossings due to non-linear filter phase characteristics. The fringe spacing is obtained from the time between zero-crossings, which are determined using linear interpolation between the two samples on either side of each zero crossing. A threshold signal modulation of approximately 10% of the maximum modulation is used to delimit the signal.

The experimental apparatus used to create the probe volume and position the waists of the input beams is shown in Fig. 4. The beam from the laser is split by an equal path length beam splitter and each beam passes through a Keplerian telescope. The telescope lenses have independent x - y - z adjustments, which enables placement of the waists of the laser beam at arbitrary locations and allows for precise beam positioning in the front focal plane of the transmitting lens. Various beam expansion ratios can be obtained by changing the telescope lenses and their spacing. Placement of the waists of the laser beams at the desired z -coordinate z_w is accomplished by placing the beam profiler within the beam path and adjusting the beam expander until the beam has equal diameters at $z_w \pm \Delta z$. The distance Δz is chosen such that the beam diameter has changed by a measurable amount, typically 5% of the waist diameter. Due to the rather

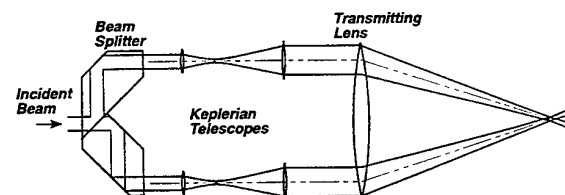


Fig. 4 Experimental configuration. The separate telescopes (collimators) permit adjustment of the location of each beam waist individually.

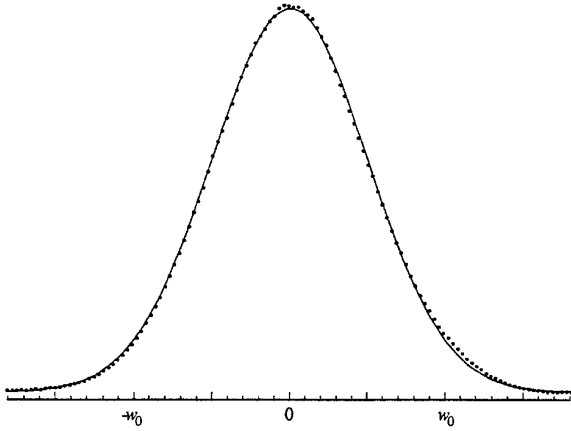


Fig. 5 Far-field intensity profile of the Ar⁺ laser beam. The symbols are the measured intensities, while the solid line is the gaussian function which best fits the data.

slow variation in beam size (or maximum intensity) near the waist this method appears to give the most repeatable results.

For most of the results presented below, a water-cooled Ar⁺ laser (Cooper Lasersonics Excel 5000) operating at 514.5 nm was employed. Even at low power, the near-field profile measured just at the beam exit was markedly non-gaussian, though characterized by a single central maximum in intensity. Diffraction rapidly smooths the profile to a near-gaussian shape in the far-field (approximately 20-30 cm from the laser exit), where the beam is round to better than 1%, and is very nearly gaussian, as shown in Fig. 5. Nevertheless, the near-field profile indicates that the beam must contain higher order hermite-gaussian modes. Although the theoretical model described above is for gaussian beams, it is appropriate to compare the model predictions to the measurements obtained with this laser due to the common use of such lasers for LDV and the prevalent assumption that their beams are closely approximated by a gaussian (TEM₀₀) beam. To more closely correspond to the model predictions, we have also obtained measurements of the fringe field with a low power HeNe laser with a near-field beam profile that is very closely approximated by a gaussian function.

5. GAUSSIAN BEAM MODEL ASSESSMENT

In Fig. 6 the variation in fringe spacing along the probe volume longitudinal axis is shown for three different alignment conditions: $z_{w1} = z_{w2} = -5.0$ mm[†], $z_{w1} = z_{w2} = 0.0$ mm, and $z_{w1} = z_{w2} = 5.0$ mm. The model predictions agree reasonably well with the data for the misaligned conditions—especially at locations within the probe volume which are furthest from the beam waists. At probe volume locations approaching the beam waists, however, the deviations between the model predictions and the data grow larger.

[†] With $w_0 = 47$ μ m, 5.0 mm corresponds to approximately 37% of the beam Rayleigh range.

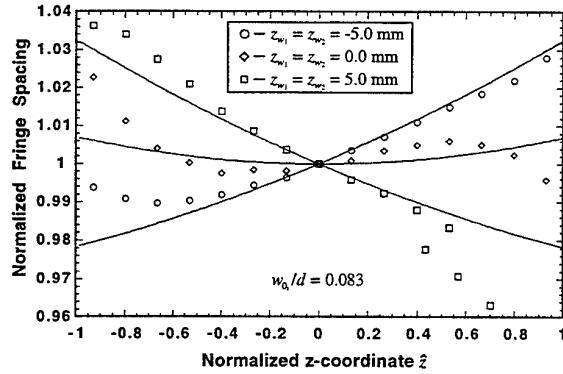


Fig. 6 Longitudinal variation in fringe spacing at $x = 0$ for beam waists before, at, and after the crossing. The solid lines indicate the model results, while the symbols indicate the experimental data. The z -coordinate has been normalized by the half-length of the intersection volume, $w_0/\sin\alpha = 1.13$ mm.

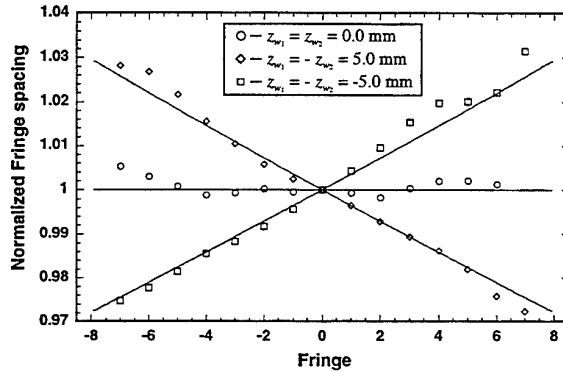


Fig. 7 Lateral variation in fringe spacing at $z = 0$ for both beam waists at the crossing and for waist positions on opposite sides of the crossing.

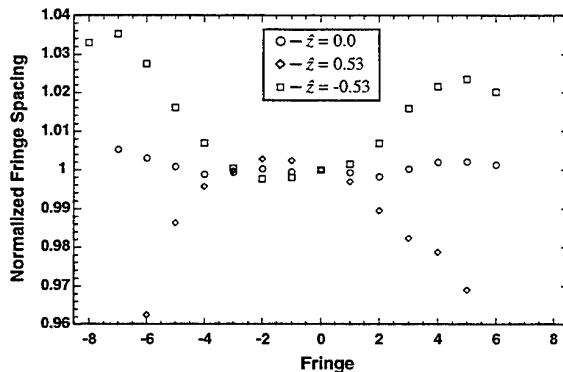


Fig. 8 Lateral variation in fringe spacing under ideal alignment conditions at different longitudinal locations within the probe volume. The model predicts negligible fringe spacing variation throughout the volume.

Despite this agreement for misaligned conditions, the model fails to predict both the magnitude and the trends in the data under conditions of near-ideal alignment. In particular, the presence of two local extrema in the longitudinal profile is a recurring feature in our experimental measurements which is not consistent with the single extremum near $z = 0$ given by the functional form of Eq. (13).

Fig. 7 presents the fringe spacing variation in the transverse coordinate direction along the probe volume minor axis ($z=0$), for $z_{w1} = z_{w2} = 0.0$ mm, $z_{w1} = -z_{w2} = 5.0$ mm, and $z_{w1} = -z_{w2} = -5.0$ mm. In contrast to the longitudinal profiles, these experimental lateral profiles appear to be well approximated by the Gaussian beam model. For $z \neq 0$, however, the transverse experimental profiles obtained with $z_{w1} = z_{w2} = 0.0$ mm do not agree well with the model predictions. These off-axis transverse profiles are shown in Fig. 8. Although the model predicts a negligible transverse fringe spacing variation throughout the probe volume, an overall variation of approximately 7% is observed. The characteristic shapes of these transverse profiles, concave up at negative z and concave down at positive z , are also recurring features in our measurements.

It is, perhaps, not surprising that the transverse variations are small along the minor axis but large elsewhere. Only along the minor axis are the transverse beam coordinates equal (i.e. $x_1 = x_2$, see Fig. 3), and deviations in the phase of the two beams from the ideal gaussian beam phase profile may be self-canceling when $z = 0$.

It is important to recognize that in obtaining the data presented in Figs. 6–8, great care was taken to ensure that aberrations in the beam profile were not introduced by the optical system employed. The (presumably innocuous) beam splitter was found to introduce measurable deviations from a gaussian profile into the beams; replacement with an alternate design which did not introduce these deviations did not materially affect the results. Nowhere in the optical system were beam aperturing effects significant, and replacement of the beam expanders with a Galilean design (in which lens aberrations are expected to cancel to some extent) did not change the results. The transmitting lens used was a high quality achromat, characterized by a marginal ray f-number of $f/12$. The possibility remains, however, that aberrations of this lens, though not significantly affecting the intensity profiles in the probe volume, introduced wavefront aberrations which led to the observed fringe non-uniformity.

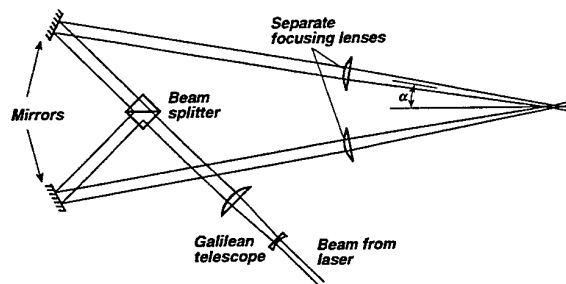


Fig. 9 Alternative LDV configuration

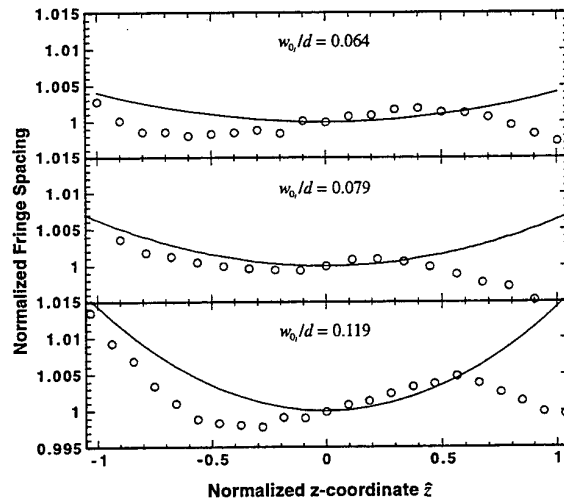


Fig. 10 Longitudinal profiles of the fringe spacing at $x = 0$ obtained using a HeNe with near gaussian near-field beam quality; for various values of the parameter w_0/d . Although the gaussian beam model (solid lines) is unable to correctly reproduce the shape of the profile, the magnitude of the overall variation appears to scale with w_0/d approximately as the model predicts.

This possibility was investigated with the apparatus shown in Fig. 9, where the transmitting lens was replaced with individual focusing lenses for each beam. Equivalent results were obtained.

In light of the above discussion, it is likely that the differences between the model predictions and the data are associated with the higher order hermite-gaussian modes in the Ar^+ laser beam. To investigate this hypothesis, fringe spacing measurements were obtained using the HeNe laser described above. Longitudinal profiles of the fringe spacing variation obtained with this laser are shown in Fig. 10, for three different values of the ratio w_0/d , under ideal alignment conditions ($z_{w1} = z_{w2} = 0.0$). Although the profiles retain the two extrema seen in Fig. 6, the gaussian beam model appears to correctly estimate the magnitude of the longitudinal fringe spacing variation, if not the details of the profile. Note in particular that the total variation seen for $w_0/d = 0.079$ is reduced to about 0.5%, as compared to the variation in Fig. 6 ($w_0/d = 0.083$) of over 2%. Transverse profiles are again observed to have significant departures from linearity, although of considerably lesser magnitude than seen in Fig. 8. By way of comparison, the overall variation in fringe spacing observed for $w_0/d = 0.079$ is about 2.5%, versus about 7% in Fig. 8. The observed lateral variation appears to scale with w_0/d , although the overall observed variation for $w_0/d = 0.079$ and $w_0/d = 0.064$ are similar. In addition, the characteristic concave up curvature for $z < 0$ and concave down for $z > 0$ is again observed, as well as very little transverse variation when $z \approx 0$.

6. SUMMARY, CONCLUSIONS, AND IMPLICATIONS FOR LDV SYSTEM DESIGN

A simple, yet general, analysis of the fringe field in the intersection of two gaussian beams has been presented and shown to reduce to all previously obtained fringe model results. By comparison with the results of a more rigorous analysis, the approximations inherent in this simple approach can be shown to be negligible.

Expressions for the variation in fringe spacing along both the longitudinal and transverse probe volume axes are provided in terms of the beam waist size and locations near the intersection volume. Referring these expressions to system parameters demonstrates that the dimensionless ratio w_0/d controls the overall fringe spacing variation for both properly aligned and mis-aligned systems. The model results are also used to compute the variation in fringe spacing for arbitrary (and different) beam waist locations and sizes, both on and off the probe volume axes. It is found that fringe spacing variation throughout the probe volume is generally well approximated by the on-axis results. Furthermore, the fringe spacing profiles calculated for arbitrary beam waist positions and differing waist sizes are found to be qualitatively similar to the profiles seen when the beam waists have equal or equal but opposite longitudinal locations.

Comparing the model results to measured spacing between the fringes formed by nominally gaussian Ar⁺ laser beams, it is found that the model adequately predicts the experimental data only when the beam waists are relatively far from the intersection volume. Under near ideal alignment conditions, large longitudinal and off-axis ($z \neq 0$) transverse variations in fringe spacing are observed. Neither the magnitude nor the characteristic shapes of the fringe spacing profiles can be reproduced from the gaussian beam model, even with mismatched beam waist sizes and arbitrary waist locations. Experimental fringe spacing profiles obtained with more nearly gaussian HeNe laser beams retained the same characteristic shapes observed using the Ar⁺ laser, but the magnitude of the variation was reduced to approximately the levels predicted by the gaussian beam model.

Both the theoretical and the experimental results obtained have implications for the design of LDV systems when highly accurate measurements of fluid velocity are required. Due to the large fringe spacing variation observed experimentally in the z -direction, we concur with the recommendation of Durst *et al.* (1990) that the collection optics should restrict the effective probe volume to the central half of the actual probe volume length. In particular, we observe the largest longitudinal (z) gradients in fringe spacing before the center of the probe volume ($\hat{z} < 0$), a region which should be avoided. The large x -direction variations which exist off the probe volume axes, however, indicate that the effective probe volume should be limited to the central portion of the probe volume height as well, provided that the number of available fringes and signal processing considerations permit this course.

Perhaps the single most significant improvement in fringe field uniformity, however, can be achieved by using a

laser with a more nearly gaussian beam profile. The peak variation in fringe spacing was found to decrease by a factor of approximately 4–5 by changing from an Ar⁺ laser to a HeNe, for similar values of the ratio w_0/d .

Provided that a high quality laser is used, the theoretical and experimental investigations indicate that the overall longitudinal variation in fringe spacing scales with the square of the non-dimensional ratio w_0/d . Reducing this parameter can reduce the overall variation in fringe spacing, though it must be recognized that this action can adversely affect other aspects of the measurement, such as signal-to-noise ratio and spatial resolution. Additionally, we observe experimentally that the off-axis lateral variation in fringe spacing is reduced as w_0/d is reduced, though the gaussian beam model predicts this variation to be negligible at all values of w_0/d .

ACKNOWLEDGMENTS

Support for this work from the U.S. Department of Energy, Office of Advanced Industrial Technologies and the Defense Programs Technology Transfer Initiative is gratefully acknowledged. This work was performed at the Combustion Research Facility of Sandia National Laboratories.

REFERENCES

- Durst, F., Müller, R., and Naqwi, A. 1990, "Measurement accuracy of semiconductor LDA systems," Exp. in Fluids, **10**, pp. 125-137.
- Durst, F. and Stevenson, W.H. 1979, "Influence of gaussian beam properties on laser Doppler signals," Applied Optics, **18**, 4, pp. 516-524.
- Hanson, S. 1973, "Broadening of the measured frequency spectrum in a differential laser anemometer due to interference plane gradients," J. Phys. D: Appl. Phys., **6**, pp. 164-171.
- Hanson, S. 1976, "Visualization of alignment errors and heterodyning constraints in laser Doppler velocimeters," The Accuracy of Flow Measurements by Laser Doppler Methods, Proceedings of the LDA-Symposium Copenhagen 1975, Skovlunde, Copenhagen, pp. 176-182.
- Miles, P.C. and Witze, P.O. 1994, "Fringe field quantification in an LDV probe volume by use of a magnified image," Exp. in Fluids, **16**, pp. 330-335.
- Miles, P.C. 1996, "Geometry of the Fringe Field Formed in the Intersection of Two Gaussian Beams", Submitted to Applied Optics.
- Seigman, A.E. 1986, Lasers, University Science, Mill Valley, CA.

MINIATURISING AND RUGGEDISING LASER ANEMOMETERS

Husain Imam and Bjarke Rose
Ibsen Microstructures A/S
Centre for Advanced Technology
Risø National Laboratory
DK-4000 Roskilde, DENMARK

Lars R. Lindvold, Steen G. Hanson and Lars Lading
Optics and Fluid Dynamics Department
Risø National Laboratory
DK-4000 Roskilde, DENMARK
E-mail: lading@risoe.dk

ABSTRACT

The possibility of miniaturising laser anemometers has been investigated. It is shown that diffractive elements may provide a substantial reduction in complexity and mechanical design. A system based on the incorporation of integrated vertically emitting lasers and detectors is also presented. The possibility of fully integrated systems based on a combination of waveguides and diffractive structures is discussed.

1. INTRODUCTION

Laser anemometers have traditionally been rather complicated, bulky and expensive. Several groups have demonstrated compact implementations based on semiconductor lasers and conventional refractive optics.^{1, 2, 3, 4, 5, 6} We shall here discuss limitations to size reduction, which ultimately is defined by the optical wavelength and the spatial requirements of the measuring system. Two miniaturised systems are described; one is based on a multiplexed holographic element, the other incorporates vertically emitting integrated lasers and detectors as a packaged unit as well as in-line diffractive elements. An outline of potential future developments incorporating the combination of waveguides and diffractive structures is given.

2. OPTICS

The optics serves to transmit and collect light in such a way that the velocity information is encoded as prescribed by the system definition and that the defined spatial constraints are fulfilled. Ultimately, the optical wavelength and the geometry of the system set a lower limit to the size of the optical configuration. Below we will briefly consider the limits.

Let the size of the measuring volume in the measuring direction be given by d_x . A resolution factor, N , may be defined by the ratio of d_x to the scale of the fine scale structure, d_t , in the field or intensity distribution in the measuring volume. (For an LDA the fringe spacing represents the *fine scale*; for an LTA the focal spot diameter gives the fine scale.) By simple diffraction considerations the transmitter aperture d_t in the measuring direction is given by

$$d_t \approx N \frac{\lambda L}{d_x}, \quad (1)$$

where λ is the optical wavelength and L is the distance from the transmitter optics to the measuring volume. Equation (1) gives a rough estimate of the transmitter size. The receiver will also require some area. However, it is often possible to share the same area between transmitter and receiver. For example: in the commonly used backscattering LDA configuration, light collection is done in the space between the (displaced) transmitted beams.

The overall length of the optics may be determined by the imaging that is normally necessary in the receiver part of the optics. To make the spatial filtering effective, the resolution has to be better than the image of the measuring volume. However, the fine scale need not be resolved. We may then claim that $f/1$ optics can be applied with an aperture d_r , but with a diffraction limited aperture that is only somewhat larger than d_r/N . Finally, assuming a circular cross section of the receiver aperture yields that the minimum volume of the optics is about d_r^3 . In addition to this volume come the laser, the detector(s), possibly a modulator (e.g. a Bragg cell) and auxiliary space because of problems with spatial multiplexing.

If we want to reduce the dimensions further, this can only be accomplished by applying guided wave optics as illustrated in Figure 1. The spatial filtering of the receiver is difficult to get as good as with conventional optics: with a receiver aperture larger than the cross section of the transmitted beams a multimode receiver *waveguide* is desirable; alternatively, collecting light in a single mode will only give a spatial resolution that essentially is defined by the intersection region of the two transmitted beams. A more detailed investigation shows that the problem is easier to resolve with a time-of-flight anemometer.

In Figure 1, in addition to waveguide optics we have also introduced *diffractive optics*. Diffractive optics has a number of actual and potential advantages relative to traditional refractive optics as illustrated in Table 1. Diffractive optics is preferable when it is possible to multiplex a number of optical functions into a single (or few) element(s) and when the chromatic aberration can compensate for wavelength changes (as encountered with unstabilised semiconductor lasers).

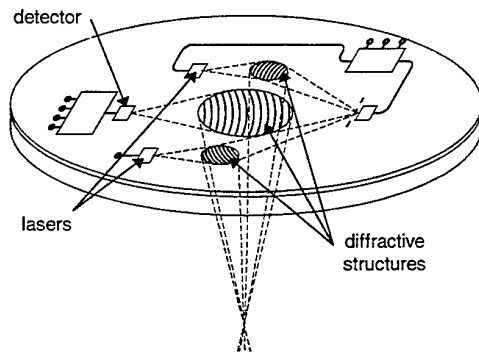


Figure 1. Conceptual layout of an LDA based on a combination of waveguides and diffractive optics. There are a number of nontrivial problems to be solved before such a system can be implemented. However, the configuration illustrates the fact that a drastic reduction in length of the set-up can be achieved by coupling light in and out of waveguides on a substrate.

Table 1. Comparing *diffractive* and *refractive* optics.

	<i>Diffractive</i>	<i>Refractive</i>
Cost	Single: high Many: low	Single: medium Many: medium
Multiplexing	Yes	No
Chromatic aberration	High - well defined	Low - not well defined
Systems	Integrated	Complex mechanical
Efficiency	Low - medium	High - medium

3. REDUCTION OF OPTICAL LENGTH - HOLOGRAPHIC SYSTEM

In order to reduce the overall length of the optics in an LTA system, one possible method is to replace the large number of separate components found in an LTA system with one custom element. In this section, a specialised holographic element has been realised in conjunction with semiconductor laser and photodiodes in order to produce a compact LTV measuring system. The holographic element performs all the transmitting and receiving optical functions for an LTV system. Although the described system has been directed towards applications requiring velocity measurements of moving surfaces, the extension of using holographic elements to anemometers follows a similar design process.

3.1. Holographic Elements in Laser Anemometry/Velocimetry

It is the generic properties of volume phase holograms that facilitate the holographic optical element (HOE) described in this paper. Although the properties of such holograms have been extensively treated in a number of

textbooks,⁷ the most salient features of these holograms pertinent to the present paper can be summarised as follows:

- Several optical functions can be incorporated in the same HOE due to the angular multiplexing capabilities of thick holograms.
- High diffraction efficiency and low scattering can be obtained if recording materials like dichromated gelatin (DCG) are used.
- The off-axis nature of HOEs prevents optical feedback from reflecting optical components into the laser.
- The diffractive nature of HOEs makes it possible to use unstabilised diode lasers (the diffractive effects may cancel the wavelength drift).
- Alignment of the optical system is predefined by the diffractive structure of the HOEs.

4. THE IMPLEMENTATION WITH AN HOE

The layout of a system implemented with an HOE is shown in Figure 2.⁸ Partly collimated light from a GaAs laser impinges on the HOE. The HOE deflects the light and focuses it into two separated elliptic spots on the target. Scattered light from the surface of the target is collected by another holographic structure in the HOE and is - by the mirror - directed to the double detector. The detector signals are inputs to a delay lock loop (DLL) that tracks the delay between the two signals. The output of the DLL is proportional to the surface velocity perpendicular to the beam axis in a direction given by the beam displacements.

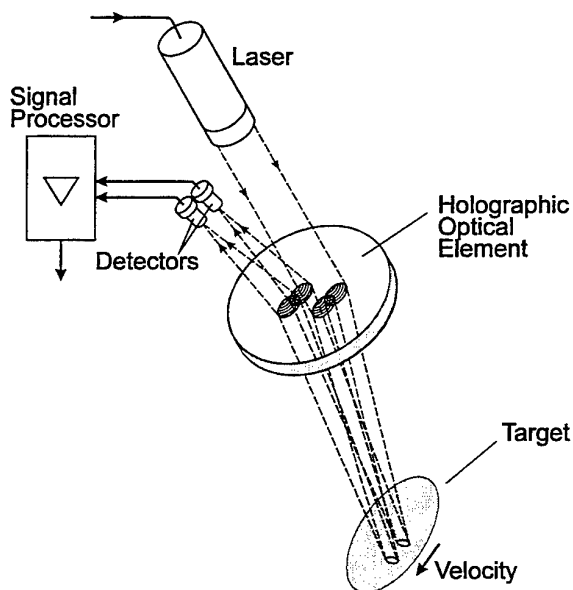


Figure 2. Layout of an LTV with a holographic optical element, a GaAs laser and a dual Si detector.

4.1. Design Considerations

The main issue in designing the HOE is the use of a volume phase hologram, a technique that makes it possible to store multiple gratings superimposed with negligible cross talk by angular multiplexing and, furthermore, it also facilitates the recording of diffractive optical elements with a diffraction efficiency approaching 100%. In the case of multiple recordings this requires a material with a sufficient dynamic range to accommodate for such exposure schemes; one material that meets this requirement is dichromated gelatin.⁹ Other materials like photopolymer and silver halide could be used instead. There are, however, a couple of problems associated with the use of these materials. In the case of photopolymer, a strong refractive index modulation is created during each exposure¹⁰ that causes strong self-diffraction in the case of multiple exposure schemes employed in most of the setups used in optical sensors. Such self-diffraction phenomena will produce spurious gratings that will seriously impede the performance of the HOE. The use of silver halide has been abandoned mainly because of the high scattering usually associated with bleached silverhalide materials.

By a judicious choice of the f-number and the spatial carrier frequency, aberrations caused by the shift in wavelength between the recording ($\lambda = 488$ nm) and replay geometry ($\lambda = 820$ nm) could be minimised. This alleviated the use of more sophisticated aberration correction schemes like computer-generated holograms.¹¹ The assumption was made on the basis of the theory elaborated by Latta.¹² The angle used in this embodiment represents the smallest permissible angle satisfying the volume hologram recording regime.

The layout of the processed hologram can be seen in Figure 3.

Table 2. The specifications of the HOE used in the LDV. Please note that all focal lengths and diffraction angles refer to a wavelength of 820 nm.

Transmitter		
Diameter of the aperture	7	mm
Distance between the two spots on the target	700	μ m
Diffraction angle of transmitter beam relative to the normal of the hologram	9°	
Focusing distance to object	117	mm
Spot size on target	70	μ m
Receiver		
Diameter of the aperture	7	mm
Diffraction angle of receiver beam relative to the normal of the hologram	5.5°	
Focusing distance from hologram to target	113	mm
Focusing distance from hologram to detector	115	mm
Focal length of the receiver	57	mm
Focal length of the receiver		

The fabrication procedure described above is just one example of how this element can be made. Other methods currently used in the production of diffractive optics comprise computer-generated holograms including kinoforms, E-beam writing, deep surface relief and micromachining. The specifications of the HOE for the surface velocity sensor are summarised in Table 2.

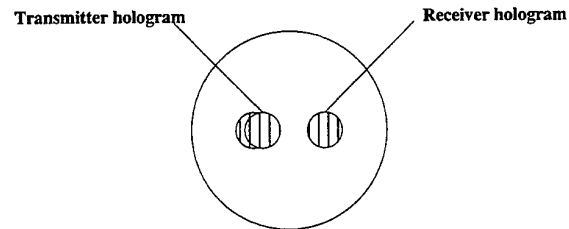


Figure 3. The layout of the holographic optical element. The diameter of the substrate is 30 mm.

5. MINIATURISATION OF AN LTA SYSTEM

Although the HOE system described in the previous section provided a neat microoptical solution, the holographic component requires an intensive fabrication process that does not lend itself to mass production. Even if there is the issue of attempting to design and realise an efficient anemometer/velocimeter, there is also the issue of trying to keep production costs low and the option of mass-producing the system.

Many different issues arise in miniaturising an LTV system. Not only do system requirements have to be satisfied, but these requirements need to be in tandem with constraints posed by the component devices. Unfortunately, more often than not, meeting system specifications using component devices is very difficult. This section deals with the strategy and problems involved in designing a micro-optical sensor.

An integrated sensor, such as a guided wave sensor, is a desirable concept, allowing the complete LTA system to be housed on one material platform. Figure 1 depicted the concept and is based on a planar waveguide technology. In essence, light is guided from the laser diode and diffracted out from the sensor to the moving flow by gratings. The scattered light is also collected by gratings and guided to the detectors. Two material technologies are suited to this task, namely silicon and III-V group semiconductor materials.

Silicon is an attractive platform, as tremendous microelectronic infrastructure exists in processing the material and waveguides (silicon dioxide) can easily be grown into or onto the silicon host. Silicon is a *passive* material; thus, an external light source is required. There are two possibilities for achieving this. Firstly, the external laser could be physically fixed accurately onto the end of the waveguide so that emitted light propagates into the waveguide (*butt-coupling*). Submicron alignment tolerances are required and in any case, as the laser diode is an active *channel* waveguide while the silicon dioxide waveguide is a planar waveguide, there is an intrinsic mode mismatch loss. Another method is the launching of light from the laser diode into the waveguide via a grating structure. Again, although it is relatively easier to manufacture gratings onto

silicon dioxide, coupling efficiency is now determined by fabrication accuracy of the grating and angular positioning of the laser diode. These problems are as difficult to overcome as for butt-coupling.

By choosing a III-V material, for example gallium arsenide (GaAs), it is possible to *grow* a laser on a wafer platform. By selectively doping areas on the wafer, lasers, waveguides and detectors can be manufactured in one step. This has the desirable property that all elements are automatically aligned. Although such devices have been demonstrated at the research level,¹³ *band-gap engineering* is still in its infancy. Due to problems in the efficiency of controlling the band-gap for each element, losses can occur, especially in the waveguide element. The problem lies in the fact that the material properties of a laser and detector are very different to that of a waveguide; consequently, trying to control the material properties of all three elements at once is very difficult. The result is that the waveguide suffers from high transmission losses.

Nevertheless, even if all problems were solved for the two material technologies, there is still the requirement to make the input-output gratings. The output gratings are responsible for outcoupling the light from the waveguide and focusing the light onto the moving surface. State-of-the-art research has shown that this is possible if *curved* gratings can be manufactured. A complete theoretical treatment for such a grating is a huge task and is still at the research level. Still, curved focusing gratings have been demonstrated¹⁴ with diffraction efficiencies of up to 40%, manufactured by electron-beam lithography. However, the beam quality at focus is not diffraction-limited. In the proposed velocity sensor system, an additional complexity of having two focused spots is required, which inevitably means that two curved gratings must overlap. This further reduces the diffraction efficiency of the elements and alters the quality of the focused spot.

These problems are not totally impossible to solve. However, what is apparent is that the solutions to such problems are still regarded as being state-of-the-art research. The goal of this project is to miniaturise a velocity sensor and lay the foundations for a (semi) mass-produced product. For these reasons, it was decided that a guided wave sensor strategy was not feasible in a short timescale. As a result, an alternative microoptical strategy was investigated.

Figure 4 shows the schematic outline for the micro-optical sensor. The sensor discussed here is for a miniaturised LTA/LTV sensor. There are evidently three component stages: (1) twin laser devices, (2) focusing transmission and receiver optics and (3) twin photodetectors.

A final consideration is the electronic processor. However, for brevity, we will limit the discussion to the optical measurement head. The advantage of this concept is that standard off-the-shelf optoelectronic components can be used. The important factors that affect the system performance are: ratio of focused probe spot size to probe spot separation, vertical change in probe spot size (bounce error), quality of the focused probe spots, degree of parallelism between the two transmission optical axes and detector cross talk.

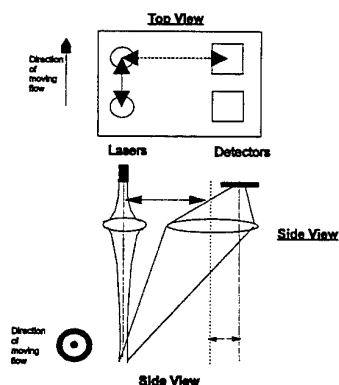


Figure 4. Schematic outline of miniaturised concept.

The choice of laser specifications is important when considering the probe spot size/separation ratio and the bounce error. The separation is dictated by the physical distance between the two adjacent devices, whereas the focused probe spot size and the bounce error are determined by the emitted single mode spot size at the laser source and the focusing optics.

Standard laser diodes, such as the devices found in CD players, are *edge emitting* devices, which inevitably means that the emitted spot is elliptical in profile. This is not such a disadvantage if the two elliptical spots have their long axes perpendicular to the direction of the moving flow. This essentially increases the acceptance angle of the velocity measurement, but does generate bias errors.¹⁵ It is desirable to have two laser sources to produce the two probe spots providing two parallel optical axes, thereby reducing the risk of decorrelation effects and bias errors. However, it is difficult to obtain a one-dimensional array of edge emitting lasers with the required spacing and emission area commercially. It would require custom-made lasers and could only be justified if a mass production of sensor devices is required.

A currently emerging technology in laser devices is the fabrication of *Vertical Cavity Surface Emitting Lasers* (VCSELs). Whereas an edge emitting laser has a rectangular waveguide structure with the optical axis running horizontally along the waveguide, a VCSEL is a vertical waveguide structure with a vertical optical axis. This is a more desirable device as it is now easier to fabricate such devices in one- or two-dimensional arrays with variable spacing. In fact, VCSELs are being exploited as devices in 2D parallel light data communication channels for optical fibre-to-copper cable signal conversion.¹⁶ For this application, it is essential that all VCSEL devices in the array have uniform characteristics in wavelength and in emitted power; this is exactly required for the velocity/anemometer sensor. The two major drawbacks are that the VCSEL devices do not emit at high powers (maximum 3mW single mode per device) and that they are available in a restricted commercial sense. However, one positive advantage is that the emitted beam profile is a single mode circular Gaussian, which simplifies tracing the behaviour of the light through an optical system. Certainly, these devices are preferred for the LTA/LTV sensor.

One requirement of the sensor is that it should be compact and should operate close to the moving flow. This indicates that the lenses should possess a short focal length. Short focal length refractive lenses are bulky and large, reducing the scope of miniaturisation for the sensor. Consequently, the possibility of using *diffractive* lenses has been explored. Diffractive lenses are surface relief thin elements with focusing properties and as VCSELs have a narrow bandwidth, chromatic aberrations are not a serious problem. Although refractive lenses have superior performance over diffractive lenses, diffraction efficiencies of 60-70% can be achieved with a near diffraction limited spot. Furthermore, mass production of the lenses via embossed replication is now becoming a standard technology.

Again, the design and the fabrication of the lenses have to be considered in tandem with the choice of the laser devices and the system specifications. Purely diffractive lenses can be manufactured and allow the possibility of larger than F/4 optics. However, the diffraction limited spot is not perfect. Improved performance can be obtained by having a combination of refractive/diffractive lenses, which relaxes the minimum feature sizes required for the lens as this is compensated by a change in depth.¹⁷ Furthermore, mass production of the lenses is relatively easy via embossing into a polymer material.

Standard silicon *p-i-n* diode detectors are adequate devices for the sensor. Twin devices are required in order to detect the two imaged scattered spots. Detectors are commercially available and are relatively inexpensive. The spacing of the detectors is obviously determined by the optical system and by availability, but this does not seem to be a limiting factor for many commercial suppliers. There may be an issue to detection of speed, i.e. silicon detectors can detect at rates of up to 1 GHz; however, this is more than sufficient for many applications. A further consideration is detector cross talk (i.e. light from one imaged spot falling onto the unmatched detector). As a result, the detectors may require apertures to avoid this situation.

5.1. Prototype Considerations

Figure 5 shows a possible method of realising the microoptical LTA/LTV. Commercially available VCSEL devices are mounted in a side-brazed housing. The VCSEL devices can be obtained as a one-dimensional, individually addressed array. A minimum of 1x2 lasers is required for the LTA/LTV, but as commercially available laser pitches are not usually the same as for system specifications, a larger array is utilised. This allows other spacings to be used by simply addressing the appropriate lasers.

The detectors are bonded in the housing cavity. Alignment of detector placement should be of the order of 10 micron. This can be achieved by laser scribing the housing floor with markers. A frame of reference can be calibrated by using the spacings of the laser emitting areas. Standard conductive adhesives and bonding can then be applied to place the detectors. The lens plate is located to cover the cavity area and will have to be actively aligned. The lenses are designed to have 60-70% diffraction efficiency and have been designed to theoretically diffract a

spot size of half that is required. This is to take into account any differences in the spot size due to aberrations. The receiver lens is also placed on the same plate, but only acts as an imaging lens. It has twice the diameter of the transmission lenses and the same focal length. The size of the lateral offset of the detectors does not warrant a carrier structure on the lens to provide off-axis focusing.

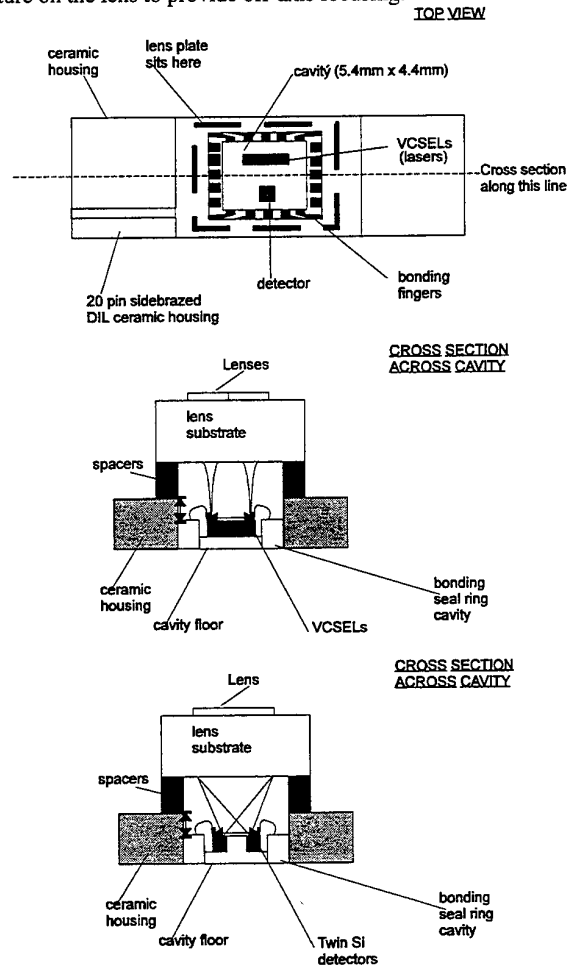


Figure 5. Prototype sensor.

This device has just been designed and will be constructed in the near future. The primary aim of the device is to test the component technologies and their integration to ascertain the feasibility of using such devices in an industrial environment. Once constructed, the prototype device will be subject to thorough testing to find the operational limits.

5.2. Mass Production Considerations

Although the prototype device is attractive as a miniaturised LTA/LTV, the feasibility of mass production is limited. Even though the lenses can be mass-produced by embossing and the side-brazed housing is standard, the placements of the laser chips, detectors and lenses require non-standard alignment techniques. In order to make mass

production a feasible option, it is beneficial to harness as many of the standard techniques as possible. Figure 6 shows such a concept, where a standard housing (TO-cap) is used to house all components. Standard packaging technologies can be employed to house the components as laser diodes with photodiodes and collimating optics are currently being sold as standard devices. The design and construction of this device is currently underway.

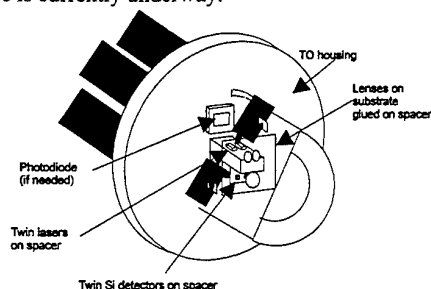


Figure 6. Mass production concept sensor.

6. FUTURE DEVELOPMENTS

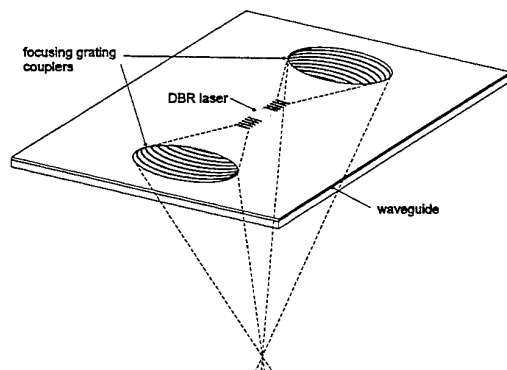


Figure 7. Transmitter part of a fully integrated LDA using one DBR laser, beam expansion in a slab waveguide, and focusing grating couplers. Recent work by Hagberg *et al.*¹⁸ has shown the feasibility of monolithically integrating grating outcouplers with a distributed Bragg reflector (DBR) laser. Thus, with a proper grating design it is possible to effectively outcouple the light. Due to symmetry, two grating output couplers are easily obtained, thereby making the device feasible for anemometer applications. D. Hofstetter *et al.*¹⁹ have presented a method of changing the bandgap outside the active region of the laser, whereby waveguide transparency has been achieved. Transition from the confined laser structure to the slab waveguide would inevitably introduce losses due to mode mismatch. However, this is not considered a viability problem for the proposed architecture. Only the transmitter part is shown. The receiver part could be monolithically integrated with the transmitter part as proposed in Fig. 1.

Although the possibility of realising a guided wave sensor is at a research rather than at a production level at present, it is expected that further technological breakthroughs will make these platforms feasible. Here we will discuss a III-V platform for LDA applications consisting of grating outcouplers monolithically integrated with a semiconductor laser. We have sketched the transmitter section of the considered system in Fig. 7.

The disadvantage of the proposed architecture is that III-V material is expensive. Let us consider an LDA design with a working distance of 10 cm, where we require a spot diameter between 0.1 mm and 1 mm and at least 20 fringes in the spot. For the smallest spot size this results in a minimum distance for the output grating couplers of about 3 cm. Further increases in working distance will increase the minimum distance between the grating couplers making a III-V platform expensive for these applications. However, these systems will still be comparatively much cheaper than bulk systems presently available and potentially more robust.

7. CONCLUSIONS

In order for anemometers to be utilised extensively in industry, it is imperative that both cost and size reductions are made in realising such devices. This paper has indicated that ultimate size reduction of an anemometer i.e. a one-dimensional planar geometry, is still at this stage very difficult to produce due to the technological hurdles that need to be overcome. However, the field of integrated optics is still in its infant stage and further progress in integration on planar waveguide technology is expected.

Nevertheless, it is still possible to reduce size and cost by using microoptical components, and two possible anemometer concepts have been described. These systems can be manufactured using current optoelectronics devices and technology combined with custom designed diffractive optics. However, a capability is required to be able to manufacture custom optoelectronic components in order to design a robust system. The emergence of VCSEL technology for telecommunications, for example, has also many desirable properties in the sensor industry and it has been shown how this relatively novel technology can be used effectively in a sensor design.

Many technological advances in integrated optics are being made in the telecommunications industry, where low cost, high efficiency and mass producibility are the important issues in device and system realisation. These technologies can be readily harnessed for sensor realisation and this paper has attempted to address the current feasibility. In a world where in-line automated process control for quality assurance is a key issue for industry, the ability to design and manufacture smart, low-cost measurement sensors will find a growing market.

REFERENCES

- ¹ Windeln, W., 1985, Entwicklung von Holografischen Optischen Elementen und Untersuchung ihrer Einsatzmöglichkeiten in der Laser-Doppler-Anemometrie, Dr. Ing. Dissertation, Technische Hochschule Aachen, Germany.
- ² Hanson, S.G., Lindvold, L.R. & Schmidt, G.H., 1987, Compact Sensor Head for Angular and Rotational Velocity Measurements Based on Holographic Optical Elements, Proceedings of the Second International Conference on Laser Anemometry - Advances and Applications, Glasgow, UK.
- ³ Jentink, H.W., Helsdingen, M.A., De Mul, F.F.M., Suichies, H.E., Aarnoudse, J.G. & Greve, J., 1989, On the Construction of a Small Differential Laser Doppler Velocimeters Using Diode Lasers, Int. J. Optoelectr., vol. 4, no. 5, pp. 405-414.
- ⁴ Belousov, P.Ya., Dubnistshev, Yu.N. & Meledin, V.G., 1990, Optical Velocimeters for Moving Surfaces Using Gas and Semiconductor Lasers, Opt. Las. Techn., vol. 22, pp. 335-339.
- ⁵ Schmidt, J., Völkel, R., Stork, W., Sheridan, J.T., Schwider, J., Streibl, N. & Durst, F., 1992, Diffractive Beamsplitter for Laser Doppler Velocimetry, Opt. Lett., vol. 17, pp. 1240-1242.
- ⁶ Dopheide, D., Strunck, V. & Pfeifer, H.J., 1990, Miniaturized Multi-component Laser Doppler Anemometers Using High-frequency Pulsed Diode Lasers and New Electronic Signal Acquisition Systems, Exp. in Fluids, vol. 9, pp. 309-316.
- ⁷ Syms, R.R.A., 1990, Practical Volume Holography, Clarendon Press, Oxford.
- ⁸ McCauley, D.G., Simpson, C.E. & Murbach, W.J., 1973, Holographic Optical Element for Visual Display Applications, Applied Optics, vol. 12, pp. 232-242.
- ⁹ The Dupont polymer exhibits the strongest self-diffraction, whereas the Polaroid DMP 128 is weaker.
- ¹⁰ Tedesco, J.M. & Fairchild, R.C., 1985, Design and Fabrication of Aspherical Holographic Optical Elements Using Computer-generated Holograms, Proc. SPIE, vol. 523, pp. 277-284.
- ¹¹ Latta, J.N., 1971, Computer-based Analysis of Hologram Imagery and Aberrations. II. Aberrations Induced by a Wavelength Shift, Appl. Opt., vol. 10, pp. 609-618.
- ¹² Hofstetter, D., Zappe, H.P., Riel, P., Epler, J.E. & Homan, O.J., 1995, III-V Based Integrated Optical Chip for Metrology: Device and Integration Technology, ECIO '95 Proceedings 7th European Conf. on Integrated Optics, pp. 109-112.
- ¹³ Nishihara, H., Haruna, M. & Suhara, T., 1989, Optical Integrated Circuits, McGraw-Hill Optical and Electro-optical Engineering Series 1989.
- ¹⁴ Rose, B., Imam, H., Lading, L. & Hanson, S.G., 1996, Time-of-flight Velocimetry: Bias and Robustness to be presented at Photon Correlation and Scattering Topical Meeting, 21-24 August 1996, Capri, Italy.
- ¹⁵ Strass, A., 1995, Surface-emitting Lasers Cut Data Transfer Costs, Opto & Laser Europe, April 1995, pp. 23-27.
- ¹⁶ Kunz, R.E. & Rossi, M., 1993, Phase-matched Fresnel Elements, Optics Communications, No. 97, March 1993, pp. 6-10.
- ¹⁷ Hagberg, M., Eriksson, N. & Larsson, A., 1995, High Efficiency Surface Emitting Lasers Using Blazed Grating Outcouplers, Appl. Phys. Lett., vol. 67, pp. 3685-3687.
- ¹⁸ Hofstetter, D., Zappe, H.P., Riel, P., Epler, J.E. & Homan, O.J., 1995, III-V Based Integrated Optical Chip for Metrology: Device and Integration Technology, ECIO '95 Proceedings 7th European Conf. on Integrated Optics, pp. 109-112.

EFFECTS OF PARTICLE SIZE ON REFERENCE LDA SCANNING PROBE FOR PROFILE MEASUREMENTS

V. Strunck, D. Dopheide

Laboratory for Fluid Flow Measuring Techniques
Physikalisch-Technische Bundesanstalt
Bundesallee 100
D-38116 Braunschweig

ABSTRACT

A new Laser Doppler technique to measure small velocity profiles with high spatial resolution and without traversing the measuring volume has been extended to measure particle size at the same instant. The particle sizing method is based on the direct determination of the distance between the centre of the particle and its scattering surface element. It uses a dual reference scatter set-up with an enlarged measuring volume compared to the standard beam cross-over probe. First test measurements to verify the basic operation are displayed.

1. INTRODUCTION

By combining the Laser Doppler method and the time of flight method the authors Strunck et al. (1993, 1994) have shown the ability to measure not only the velocity of a scatterer but also its trace through the measuring volume. The poor spatial resolution of a conventional LDA probe, limited in principle by the size of the probe volume, has been increased by the method proposed by an order of magnitude. Moreover, whole velocity profiles can be measured while leaving the sensor fixed.

This holds true for small scatterers with diameters below one fringe distance. For large scattering particles, the simple method to measure the time of flight from one fringe system to the second using Doppler signals and the cross correlation function leads to errors, because the scattering position on the surface of the scatterer is not the centre of the particle as already outlined by Strunck et al. (1994).

In this paper the profile probe is reviewed firstly to eliminate the dependency on particle size and secondly to give an answer on the type of scattering and on particle size. Only by changing the acquisition system the lateral velocity and particle size are now achievable simultaneously along the optical axis of the sensor without any moving apparatus. But also conventional LDAs can profit from the time of flight method and increase their spatial resolution inside the measuring volume. Depending on the application, Phase Doppler anemometers (PDA, see Tayali and Bates (1990)) do not need anymore to correct bias errors caused by the dependence of particle size on effective sampling space (slit effect), if the trajectory of the particle is measured with the method proposed.

The new technique is a mixture of conventional LDA, laser two focus (L2F), shadow imaging and PDA. In the following section the theory to combine all these methods will be outlined.

2. THEORY

The transmitting optics of the spatial sensor is a conventional cross beam LDA. Behind the measuring volume, in each centre of beams a photodiode forms a reference scatter (RS-) LDA measuring volume with the other beam as outlined in figure 1. It has to be noted that the length of the e^{-1} measuring volume is extended by a factor of five in our configuration compared to the beam cross-over region of a conventional e^{-2} beam cross-over measuring volume, because a small aperture of the photodiodes used opens a wide coherence cone, see Drain (1972). The length of the reference scatter measuring volume is about inversely proportional to the diameter of the active surface of the detector and can be adapted to the application needs.

The dual RS-LDA system offers twice the possibility of measuring the speed of a scatterer by using its Doppler signals, but the choral appearance of both RS-LDA signals is different. Their time difference is determined by the time of flight of a scatterer from one fringe system to the next. Assuming a one dimensional flow, the time lag of signals from both measuring volumes is proportional to their spatial separation and to the speed of the scatterer. By geometry, their separation is a function of the distance from the crosspoint of the two beams in the on-axis direction of the optical system.

With increasing particle size, the time of flight cannot be measured anymore using Doppler signals, equivalent to the position of the scattering element on the surface, because the scattering point on the surface of the particle is no more the centre of the particle. This biasing effect due to particle size causes similar difficulties in defining the sampling space in PDA applications, but in the spatial probe errors when determining the particle trajectory. Fortunately, in the RS-LDA set-up the extinction signals of the particle caused by the shadows on the detectors are available, too. This is processible when only one particle at a time crosses the measuring volume. Thus, the method to use extinction signals for the time of flight measurement eliminates the particle size influence and the trajectory based on the centre of the particle can be evaluated.

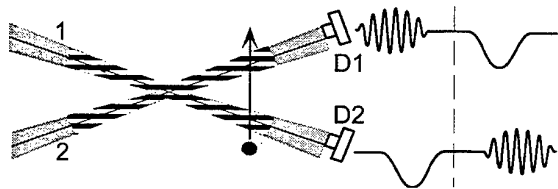


Fig. 1. Dual reference LDA and time of flight signals

In figure 1 there is a time lag between the Doppler signal at the photodiode D1 and the extinction signal at the photodiode D2 caused by their different detection processes of shadow signal and heterodyning signal generation. Unfortunately the maximum amplitude of the LDA signal is not correlated necessarily to a single point on the scattering surface of a particle due to reflective and refractive processes of scattering. Furthermore, in the beam cross-over region the particle itself hides parts of the reference beam as discussed later. To measure the displacement between particle centre and scattering surface based on phase differences, an asymmetry in the configuration resembling like that in Phase Doppler techniques (PDA) but with the reference beam method was examined. One photodiode was placed inside one beam with a large angle to the optical axis, the second photodiode with a small angle, indicated by a displacement of detectors in figure 1. To simplify the problem of a fine adjustment, we mirrored the symmetric situation at the optical axis and replaced one photodiode by a duo-photodiode D1 and D2 to obtain a defined difference angle of 0.05° of both virtual fringe systems for the test set-up shown in figure 2.

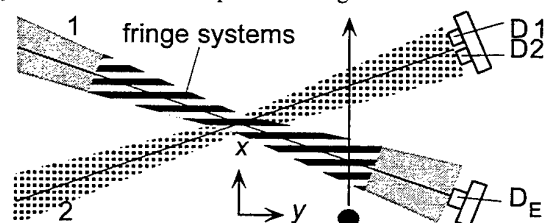


Fig. 2. Phase reference beam Doppler anemometer test set-up

Because the mono-photodiode D_E now only is to detect the extinction signal in the illuminating beam (1), the virtual fringe system as seen by D_E is not shown in figure 2. Therefore, the reference beam (2) to the duo-photodiode is coloured grey.

Two effects are essential to the duo-photodiode D1 and D2:

1. Slightly tilted virtual fringe systems by a half angle of 0.05° to the optical axis can be observed by photodiode D1 and D2. Because the fringe distances of both systems are different, moving a scatterer away from the beam cross-over midpoint will result in an increasing phase difference between both Doppler signals. The resulting phase difference is a function of the position of the scattering point on the particles's surface in the measuring volume.
2. Small 'standard' Phase Doppler effects (due to the small difference angle of 0.1°) by scattering from different points of the surface of the scatterer for both systems are present and have to be taken into consideration.

The position of the scattering element from the surface to the particle centre now mainly defines the phase difference of the Doppler signals at the duo-photodiode. Because of the displacement of both receiving elements in the duo-photodiode, the locations of scattering are also slightly displaced, exhibiting a small phase Doppler effect that reduces the above effect. But the advantage of the set-up is to know the location of the scattering element on the particle by measuring the phase difference of the Doppler signals of the duo-photodiode and to know the location of the centre of the particle by monitoring the extinction signals in both beams. If the phase difference of an infinitely small scatterer at the position of particle centre is compared with the position of the scattering point on the particle in test, the resulting phase difference is a measure of the distance between the particle's centre and its scattering surface element. In case of a signal from the reflecting part of a particle the difference of the two locations yields directly the radius of the scatterer. For mainly a refractive part the radius is evaluable when the refraction index is known or having a reflection and refraction part in the signal, sufficiently separated as in the case of large transparent scatterers, the refraction index can be measured, too. In the set-up proposed and the assumption of separated reflexion and refraction modes in the signals

- the trajectory of the centre of the particle using its shadow,
- the trace of the reflecting point on the surface of the particle and
- the trace of the refracting point on the surface of the particle

can be measured by using the proposed asymmetric dual reference scatter method.

3. EXPERIMENTS

No special adaption has been taken to the spatial probe to prepare it for particle sizing. Experiments have been performed with a copper wire, a glass fibre and several droplets of water and ink. The scatterers cross the laser beams in the lateral direction x at selected locations y on the optical axis of the set-up up to ± 2.5 mm away from the centre of the crossing beams in steps of about 0.25 mm.

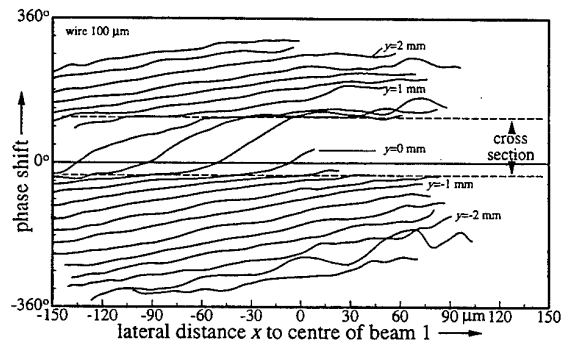


Fig. 3. Phase difference of Doppler signals at the duo-photodiode at discrete axial positions y of the scatterer

Figure 3 shows the phase difference of the signal of the duo-photodiode D1 and D2 in dependence of the local position of a 100 μm copper wire, thus only the reflexion mode is present. The exact position of the scatterer was measured from the extinction signals in both beams, whereas the phase difference was measured from the Doppler signals of the duo-photodiode. It has to be remarked that the beam cross-over section only has a length of 1 mm.

The overall increase of the phase from the left to the right in figure 3 shows the effect of slightly tilted fringe systems. In the middle part, marked by dashed lines, a strong phase shift of about 150° is the result of the extinction of the reference beam, when a particle traverses the cross section of the beams. It can be read at the axial distance parameter, that the cross section is extended to one mm in the axial direction (dashed line area). Whereas a dual scatter PDA only takes information from this region, the performance of the reference LDA set-up decreases with increasing particle size at the beam cross-over section.

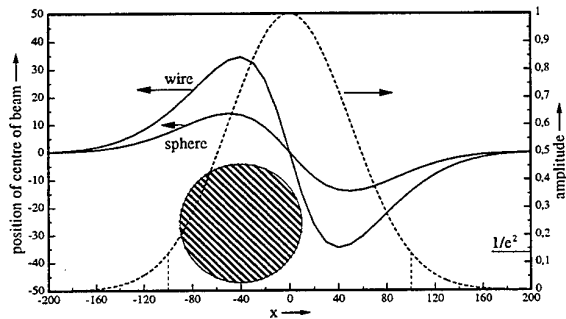


Fig. 4 Change of the centre position of the illuminating beam in the cross section produced by scatterers with diameter of 100 μm

However, the strong phase shift with the form of the differentiated beam profile is explicable. When a particle enters the reference beam (grey in figure 2), parts of the beam are hidden to the detector. In the far field at the photodetector the beam angle is changed, the virtual fringe system in the illuminating beam is tilted. Then a phase change is created in the Doppler signals during the passage of a scattering surface through the illuminating beam at the same time. This happens only to the cross section, and the effect is pronounced by the wire used. For spherical scatters the phase change produced by the beam deposition of a beam with a diameter of 200 μm is less remarkable as shown in figure 4. For comparison, the extent of a 100 μm particle also is exhibited by the filled circle.

For the whole measuring volume the phase difference obtained by the duo-photodiode signals for infinitely small scatterers has been calculated and subtracted from the results in figure 3. All phase curves now overlap in figure 5 at an angle of about 36° . Phase curves from the doubtful beam cross-over section are assigned by dashed lines.

The displacement of the centre of the particle to the scattering surface element in the lateral direction (x) mainly causes the phase difference of the Doppler signals. Calculating the attached 'standard' phase Doppler effect (phase difference by two distinct surface elements) yields an additional phase shift of only minus 7° as outlined in Fig. 6.

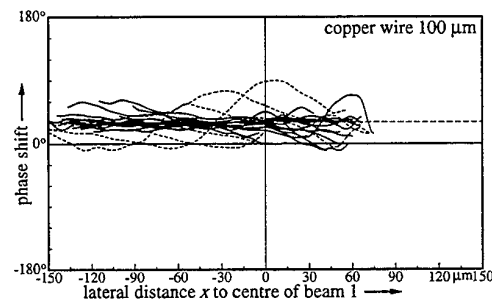


Fig. 5 Phase differences created by displacement between a copper wire and its scattering surface elements

The negative phase Doppler shift is produced by an axial displacement (y direction) of the two scattering surface elements as 'seen' by the duo-photodiode. Including both displacement effects the diameter of the scatterer is traceable, also when the uncertainty of the test measurement requires some efforts to improve the sensor.

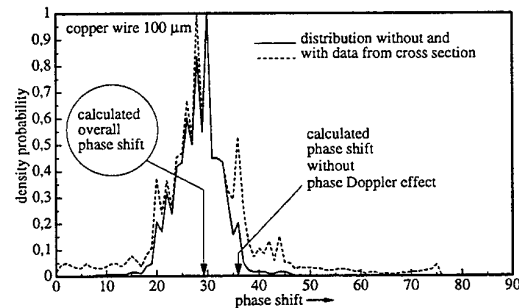


Fig. 6 Density probability distribution of measured phase shifts of a 100 μm copper wire

Similar measurements have been performed with a transparent fibre with a diameter of 125 μm and a core of 9 μm . Because the fibre moves in the plane of both beams, firstly the reflection mode and afterwards the refraction mode occurs in the signal. The phase difference curve now is more extended compared to a curve from solely reflective scatterers. Outside the measuring volume a phase change to lower values can be observed, when the refractive mode replaces the reflective mode in the middle of the figure. Inside the beam cross-over region the phase curve exhibits again the deposition of the illuminating beam (the effect was outlined in figure 4).

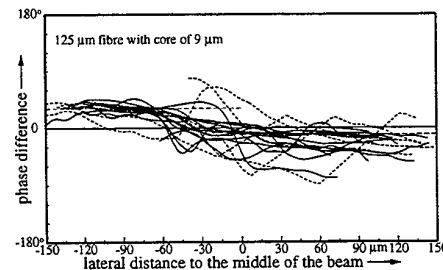


Fig. 7 Phase differences created by fibre and its scattering surface elements

In figure 7, again the positional dependence of the trajectory of the fibre in the phase differences has been eliminated. The phase difference curves nearly overlap and show the phase effect of the reflection mode, giving the radius of the scatterer. The refraction mode shows the displacement from the centre of the fibre to the emergency position of the light from the fibre. The measurement gives only a qualitative picture of the scatterer. The reflective mode allows to estimate the diameter of the fibre, the refractive mode only allows the statement, that the active refractive element is on the opposite side of the reflective element on the surface and between the centre of the particle. The phase differences in figure 7 show this by having negative phase values at positive axial positions. Because the probe was not designed for particle sizing, the situation of a fibre with a core is too ambitious to the test experiment. A second difficulty included was the size of the scatterer which has been similar to the size of the measuring volume.

A simple model in figure 8 repeats the main effects of the probe used for particle sizing:

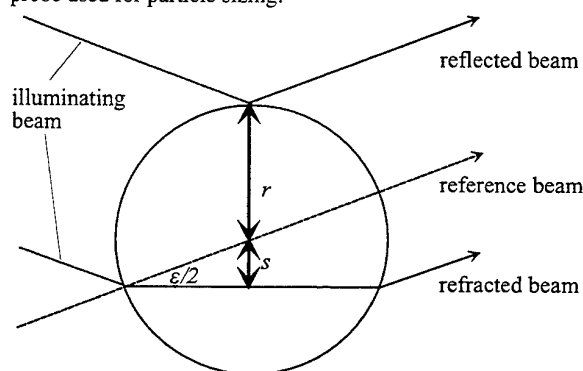


Fig. 8 Beam reflected and beam refracted giving the active scattering points on a fibre

The spatial probe is able to eliminate particle size effects, when the extinction signals in both beams are taken into account. The active scattering surface element position is determined by the phase difference of both Doppler signals. In the case of a reflective process, the radius r , and in a refractive process, the distance s to the centre of the particle can be calculated.

4. DISCUSSION

The results show that the spatial probe cannot compete with the high accuracy of PDA systems to acquire velocity and particle size at this date and this was not the aim of the experiments. To improve this type of sensor for particle sizing, the beam aperture has to be enlarged to obtain a greater angle between both detectors, say by 10, and the beam waist should be much larger than the particle size of interest. Using wires or fibres also include some unsteadiness in alignment when flying through the measuring volume, because they have been fixed on the shaft of a motor. But these preliminary results show the potential of attaining particle size with a new, alternative technique.

One profit of this method to LDA and PDA applications is to measure supplementarily the extinction inside the beams to

increase the spatial resolution and to eliminate the slit effect or to measure small flux profiles. The profit to the spatial probe is that particle size influence can be understood and corrected in special applications.

5. CONCLUSIONS

A new PDA-like method using the reference scatter method has been developed to measure velocity profiles, particle size profiles, and with some more efforts refractive index profiles on a span of about 5 mm while leaving the measuring apparatus fixed. Using a cross beam LDA, the time lag of extinction signals of both beams yields the on-axis distance from the centre of the probes independent of particle size. Involving a small asymmetry in the detector positions of the dual reference scatter LDA probe, particle sizing is possible by measuring the distance from the centre of the particle to its scattering surface element.

6. REFERENCES

- Drain, L.E. 1972, Coherent and Noncoherent methods in Doppler Optical Beat Velocity Measurement, *J. Phys. D: Appl. Phys.* 5, pp. 481
- Strunck, V., Grosche, G., Dopheide, D., 1994, Scanning Laser Doppler Probe for Profile Measurements, *7th. Int. Symp. on Appl. of Laser Techn. to Fluid Mechanics*, Vol. 1, 17.1
- Strunck, V., Grosche, G. & Dopheide, D., 1993, New Laser Doppler Sensors for Spatial Velocity Information, *Proc. of the 15th Int. Congress. on Instrumentation in Aerospace Simulation Facilities*, IEEE Pub. 93CH3199-7, 36, pp. 1-5
- Tayali, N.E. & Bates, C.J., 1990, Particle Sizing Techniques in Multiphase Flows: A Review, *Flow. Meas. Instrum.*, Vol. 1, pp. 7-105.

Development of fiber optic laser Doppler velocimeter sensor for measurement of local blood velocity

K.Ohba and K.Korenaga

Dept.of Mechanical & Systems Engrg.,Kansai University,
Suita, Osaka 564,Japan

ABSTRACT

In order to measure the local velocity field in opaque fluid flows like blood flow, a new laser Doppler velocimeter having a pickup consisting of a small distributed index lens attached at the tips of two fibers which are joined side by side in parallel has been newly developed. The distributed index lens is in the shape of a truncated cone. In order to examine adaptability of this sensor for real blood, the effect of blood density on the quality of the laser Doppler signal from this sensor has been examined by experiments. The penetration characteristics of He-Ne laser and laser diode (LD) for bovine blood have been measured. As a result, it has been shown that LD has a high penetration ratio for blood. Thus, LD has been used and the effect of blood density on the quality of the laser Doppler signal has been examined. As a result, it has been shown that it can measure the blood velocity at a little higher density as compared with the case of using He-Ne laser.

1.INTRODUCTION

Although knowledge of the detailed velocity field of local blood flow through bifurcation, curved vessel, tapered vessel and small vessel is very important, it is difficult to measure local velocity in such blood flows accurately and precisely due to lack of an appropriate measurement method. The ultrasound doppler velocimeter, which is widely used in the medical field, has a disadvantage of low spatial resolving power. Tanaka and Benedek¹ developed a fiber optic catheter for an *in vivo* measurement of blood velocity. Their catheter was, however, not capable of local measurement. This is because the pickup of their catheter consisted of a single fiber, and therefore a velocity signal originated from a stagnation region of the flow field around the fiber tip has a dominant contribution to the LDV signal because light intensity is strongest near the fiber tip and it becomes

weaker as the measuring volume becomes farther away from the fiber tip. A special technique for signal processing is required in order to obtain the correct velocity. Kilpatrick *et al.*² and Nishihara *et al.*³ developed modified types of the mono-fiber LDV probe. Their systems, however, suffered from the same disadvantage as the above-mentioned one. Whereas, a fringe mode fiber optic LDV developed by Knuhtsen *et al.*⁴ has a different disadvantage in that its large pickup inevitably disturbs flow.

Hence, one of the authors has been developing a dual-fiber optic laser Doppler velocimeter for blood flow measurements to overcome such disadvantages^{5,6}. However, it has a disadvantage of low signal-to-noise ratio. Hence, an improved fiber optic LDV to overcome this disadvantage has been developed. The new LDV has a pickup consisting of a small distributed index lens attached at the tips of two fibers which are joined side by side in parallel. It has been shown that this LDV sensor has a high signal-to-noise ratio for the mixture of white pigment and water⁷. In order to examine an adaptability of this sensor for real blood, the effect of blood density on the quality of the laser Doppler signal from this sensor combined He-Ne laser and LD has been examined.

2.PRINCIPLE AND PROCEDURE OF MEASUREMENT

According to Light absorption spectrum of living bodies, the light transmittancy is low due to absorption in water and pigment of the living body. However, the region of wavelength $\lambda=700\sim1200$ nm near the infrared is the spectrum window where the light absorption effect is low and light penetrates well through the living body⁸.

Therefore, improved penetration characteristics can be obtained by using laser diode (LD) whose wavelength is in the spectrum window.

A schematic of the present fiber optic LDV is shown in

Fig.1. The pickup consists of two graded index silicon optical fibers and a distributed index (D.I.) lens shaped like a truncated cone which is attached at the top of the two fibers. The two fibers are joined side by side in parallel, one of which is a transmitting fiber and the other is a receiving one. Laser light is emitted into fluid from the D.I. lens, and is converged at a focal point, which is considered to be the measuring (sampling) volume. The scattered light from scattering particles in fluid flow is collected by the receiving fiber via D.I. lens.

The Doppler frequency f_D is related to the flow velocity u by the following equation

$$f_D = 2 \frac{n}{\lambda_0} |u| \cos \theta$$

where θ is the angle between u and the axis of the laser beam emitted from the D.I. lens, n is the refractive index of fluid, and λ_0 is the wave length of laser light in vacuum.

A schematic diagram of the present LDV system is shown in Fig.2. The system works by the mode of reference beam. A part of the laser beam emitted from the transmitting fiber is reflected at the tip of the D.I. lens, which is used as a reference beam (local oscillator light). The D.I. lens used, consists of two distributed index lenses connected to each other in series, which are products of the Japan Sheet Glass Co.Ltd., having 2 mm in diameter and 0.23 in pitch. The focal length in water is 0.7 mm in the case He-Ne laser is used and 0.5 mm in the case LD is used. The optical fiber used is a multimode G.I. fiber of 80 μ m in core diameter and 125 μ m. The Doppler signal is processed by a commercial spectrum analyzer, HP Model 8553B/8552B.

In order to investigate the effect of the turbidity of fluid on the measurement by the fiber optic LDV, two types of experiments were made, i.e. an experiment on the extinction of He-Ne laser and LD light intensity in bovine blood and experiment on the change in the quality of Doppler signal with the increase in turbidity of blood. The experimental apparatus used in the former experiment is shown in Fig.3. The tips of two fibers face each other and the distance of them (penetration length z) is changed by making fine adjustment. This gap between the fibers is filled with bovine blood. Laser light is emitted from one of the fibers and received by a PIN photo diode through the other. And the light intensity I is obtained with a digital multimeter. In the latter experiment open channel was used. An annular channel

filled with bovine blood is put on the rotating disc which rotates at a constant speed. The LDV pickup was inserted into the fluid flow from the free surface at an inclination angle 130° .

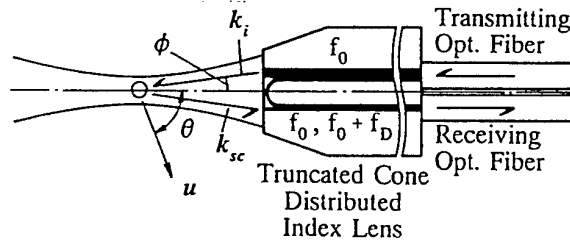


Fig.1 Schematic of the pickup of the present fiber optic laser Doppler velocimeter.

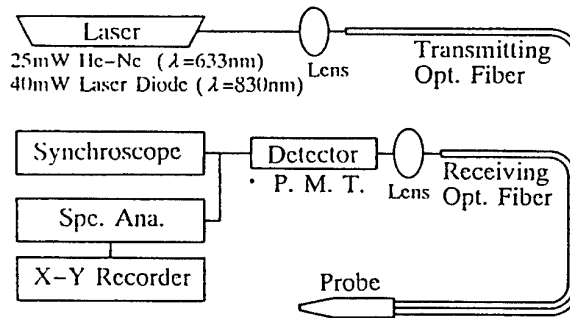


Fig.2 Schematic of the optical and signal processing system

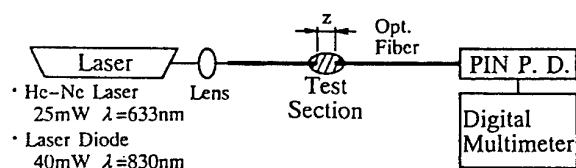


Fig.3 Schematic of the experimental apparatus for measurement of light penetration

3. EXPERIMENTAL RESULTS AND DISCUSSIONS

3.1 LIGHT PENETRATION CHARACTERISTICS

OF He-Ne LASER AND LD IN BOVINE BLOOD

The penetration curves, *i.e.* relationships between the dimensionless light intensity received I/I_0 and the penetration length of light z are shown in Fig.4. The light of LD is more penetrative than the light of He-Ne laser. At the point $z=0.5$ and 0.7 mm which are measuring points of the present LDV, the penetration ratio of the light of LD is about 10 times higher than that of He-Ne laser. And the I/I_0 versus z curves don't obey Lambert-Beer's law because greater part of the light is scattered by the blood.

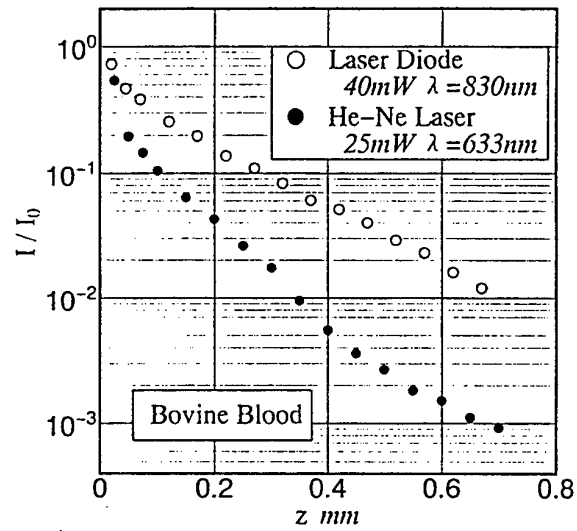


Fig.4 Penetration ratio of laser light in bovine blood

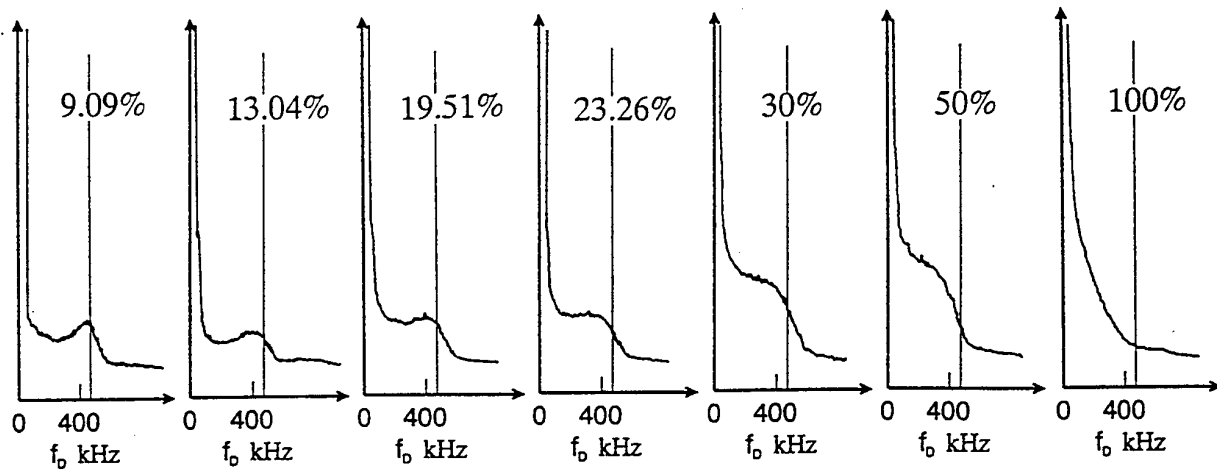


Fig.5 Effect of blood concentration on LDV signal in the case of He-Ne laser

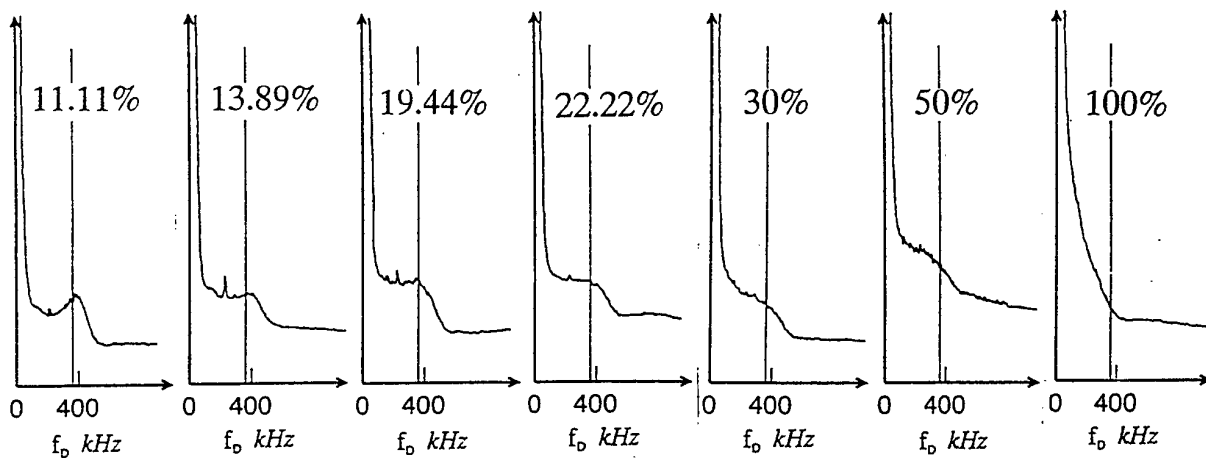


Fig.6 Effect of blood concentration on LDV signal in the case of LD

3.2 MEASUREMENT OF VELOCITY OF BOVINE BLOOD FLOW USING He-Ne LASER

In order to investigate the effect of turbidity of fluid on the quality of the Doppler signal, the change in the output signal from the spectrum analyzer which corresponds to a time-averaged Doppler signal was recorded by systematically changing the concentration of bovine blood. The open channel on the turn table was full of bovine blood. The sensor using He-Ne laser was inserted into the blood stream, an the angle between the fiber and the blood stream was 130° .

The results are shown in Fig.5. The horizontal axis shows a frequency, the vertical axis shows a P.D.F. The vertical lines of each graph show the frequency which corresponds to the real velocity obtained from the relation $v_\theta = \omega r$ calculation. In a low density condition, there is peak in a spectrum on the vertical line. But more than 20% of full blood, signals of low frequency increase and there isn't a peak. In full blood, there is little signal which the real velocity can be estimated.

3.3 MEASUREMENT OF VELOCITY OF BOVINE BLOOD FLOW USING LD

He-Ne laser of the experimental apparatus in the section of 3.2 was replaced by LD. The results are shown in Fig.6. As compared with the results using He-Ne laser, the shapes of spectra are similar to each other. But in the case of using LD, there are more signals around the signal which corresponds to the real velocity in high density conditions.

Next, insertion angle of probe θ was changed from 130° , and effect on the signals was investigated. In the past experiments using the mixture of white pigment and water, angle of 130° has been the best. But, as regards signal intensity, that is not always the best. The two cases, 11.11% and 22.22% were measured. The results are shown in Fig.7. Peaks of spectra are higher and clearer as insertion angle is small. However, in the case of 11.11%, the peak becomes small out of the correct value. But in the case of 22.22%, the peak for the small insertion angles indicates the correct value.

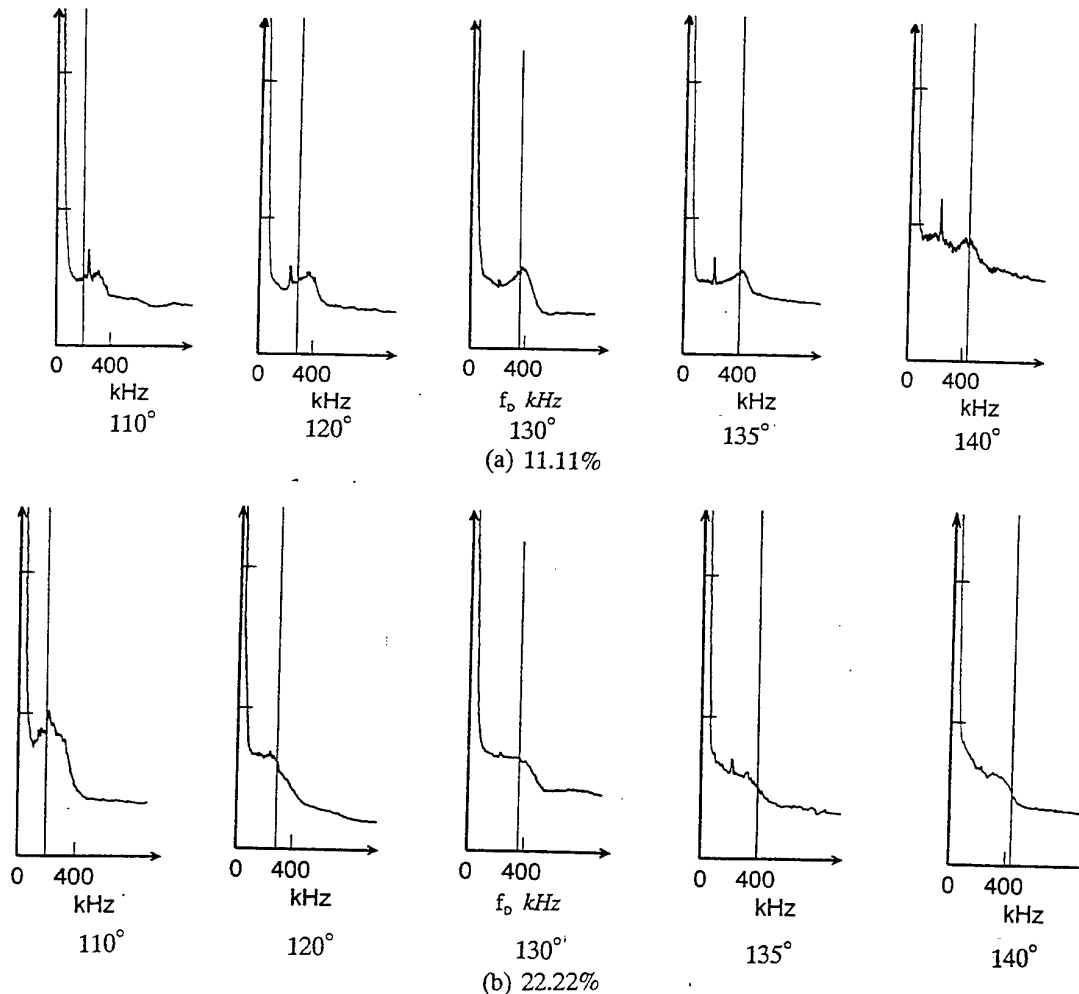


Fig.7 Change in the p.d.f.s of the Doppler signals with the change in the insertion angle

4. CONCLUDING REMARKS

The followings have been elucidated from the above-mentioned experiments and analyses;

- (1)The light of LD is more penetrative than the light of He-Ne laser in bovine blood.
- (2)The present LDV using He-Ne laser can measure bovine blood velocity whose concentration is 20%.
- (3)The present LDV using LD gave more signals correspond to the real velocity in high density conditions as compared with the results using He-Ne laser.

5. REFERENCES

1. Tanaka, T. and Benedek, G.B. 1975 Applied Optics **14** 189.
2. Kilpatrick, D. *et al*, 1982 IEEE Trans. **BME-29-2** 142.
3. Nishihara, H. *et al*, 1982 Applied Optics **21-10** 1785.
4. Knuhtsen, j. *et al*, 1982 J. Phys. E: Sci. Instrum. **15** 1188.
5. Ohba, K. and Matsuno, T. 1982 Engrg. Applicat. L. V., ASME 145.
6. Ohba, K. and Matsuno, T. 1983 Trans. JSME **49-447** 2380 [in Japanese].
7. Ohba, K. and Fujiwara, N. 1993 Laser Anemometry: Advances and Applications, SPIE 195-201
8. Shimizu, K. and Yamamoto, K. 1994 BME **8** 41

VELOCITY DISTRIBUTION MEASUREMENT USING A TRANSMISSION GRATING

Tsuyoshi NAKAJIMA and Yuji IKEDA

Department of Mechanical Engineering
Kobe University
Rokkodai, Nada, Kobe 657 JAPAN

ABSTRACT

This paper describes an experimental study of a new method for measuring flow velocity field. A spatial filtering velocimetry was used to measure velocity change of air jet almost simultaneously at eight measurement points. When an LDV processor was used as a signal processor, the data rate was about 250 Hz, i.e., 4 ms was consumed for one sequential scan of eight channels. Matching of optics and processor is also mentioned.

1. INTRODUCTION

There are two optical methods to measure flow velocity without giving any disturbance to the flow field, i.e. non-intrusive measurement: The one is time series velocity measurement at one point such as laser Doppler velocimetry or laser two-focus velocimetry. The other is whole field velocity measurement such as PIV or PTV, in which the data is obtained not continuously but at a certain long time interval. If we can develop a method of time series velocity field measurement which has both advantages of the above-mentioned methods, a great progress in flow field studies will be expected; for example, study on time-fluctuating coherent flow structure, study on flow field variation in an internal combustion engine and so on. We have already proposed an LDV optical system which can simultaneously form ten measurement volumes for two-dimensional velocity measurement (Ikeda, et al. (1989)).

In this study we have paid attention to a spatial filtering velocimetry or transmission grating velocimetry, and tried to apply for multipoint simultaneous velocity measurement in order to obtain velocity distribution with high temporal resolution. The principle of spatial filtering velocimetry is that,

when uniform light is illuminated to a moving object with different transmissivity at locations, spatial pattern of light intensity is obtained, and the velocity of the moving object is determined from the moving spatial pattern using a spatial filter by a certain transmissivity distribution. Ator has first showed that a signal with frequency proportional to flight velocity was obtained when the scenery of the earth was observed through a spatial grating filter from an airplane (Ator (1963)). Fluid velocity measurement using a transmission grating was first proposed by Gaster (Gaster (1964)). Ushizaka and Asakura measured flow velocity in small glass tubes using a transmission grating (Ushizaka & Asakura (1983)). We have applied this method for multipoint velocity measurement in similar idea to LDV, i.e. particle-image passing through grating pattern as if tracer particles pass through fringe pattern of LDV. This paper describes the measurement system developed and its application for velocity distribution measurement of air jet.

2. PRINCIPLE OF MEASUREMENT METHOD

Figure 1 shows the method for measuring flow velocity using a transmission grating schematically. A light sheet incident in the x-direction illuminates the fluid flowing in the z-direction and a photodetector with a spatial grating filter is placed in the y-direction. The light scattered from small particles in the fluid is collected by the lens and forms image of the flowing particles on the spatial filter plane. Since the spatial filter is a transmission grating, the intensity of the light passing through the grating varies periodically whenever the particle image passes through each grating fringe. The light intensity changes with a frequency, f , which is quite similar to that of laser Doppler signal, is measured by a photodetector mounted just behind the spatial filter. If the particles in the measurement volume have a velocity component, V , normal

to the grating fringe, the velocity component will be given by

$$V = f P / M,$$

where P is the grating fringe spacing and M is the magnification determined by the focal length and location of the lens. This method does not need any coherent light and any light sources are available if their light intensity is strong enough. Another feature is that its optical system is quite simple, cheap and easy to handle.

3. EXPERIMENTAL APPARATUS

In order to evaluate the method of velocity field measurement using a transmission grating, an experiment was carried out in the measurement of one-dimensional velocity distribution. An Ar-ion laser (SP:2017, 4W) was used as a light source. The light sheet of 0.3 mm in thickness was implemented in the measurement region of 8 mm in width using a cylindrical lens ($f=110$ mm).

Figure 2 shows a receiving optical system. The receiving lens is an achromat lens with aperture of 50 mm and focal length of 155 mm. As shown in Fig. 3, the optical receiving

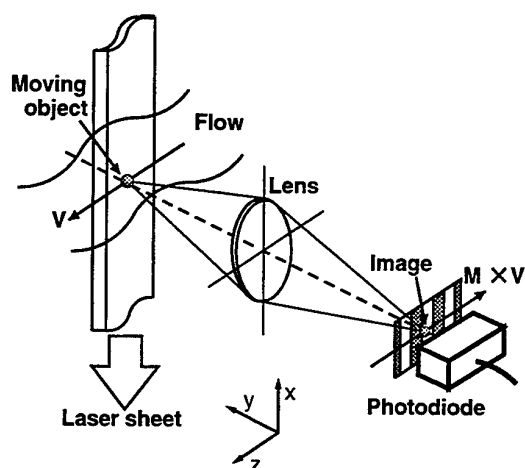


Fig. 1 Principle of flow velocity measurement

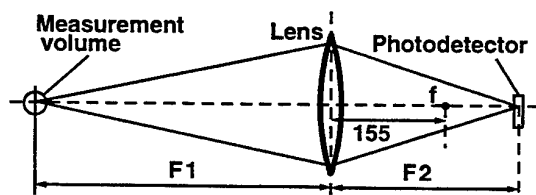


Fig. 2 Receiving optics configuration

element consists of the spatial filter and the photodiode array. A Ronchi grating with fringe spacing of 0.1 mm was used and although its effective area was 25 mm \times 25 mm, the grating fringe number was limited to 12 by using a mask. The reason will be mentioned later.

Figure 3 shows a silicon photodiode array (Hamamatsu Photonics S4113). Its receiving area consists of 35 photodiodes with receiving area of 4.4 mm \times 0.9 mm forming in a line at interval of 0.1 mm. In this experiment we used eight photodiodes near the center.

The signal processing system is shown in Fig. 4. The signals from the eight channels were amplified and one selected channel is connected to an LDV signal processor (Ono Sokki: BDC) using a multiplexer. In this experiment the channels were switched in turn after the valid signal was detected or not detected in a prescribed time.

Figure 5 shows the size and location of measurement region in the test section of air jet experiment. The flow velocity distribution was measured in the air flow out of the stainless steel pipe of 8 mm. Expancel (Japan Ferrite 091DE80) was used as scattering particle, which was hollow particle of about 20 μ m or 80 μ m in diameter and its bulk density was 0.02g/cm³.

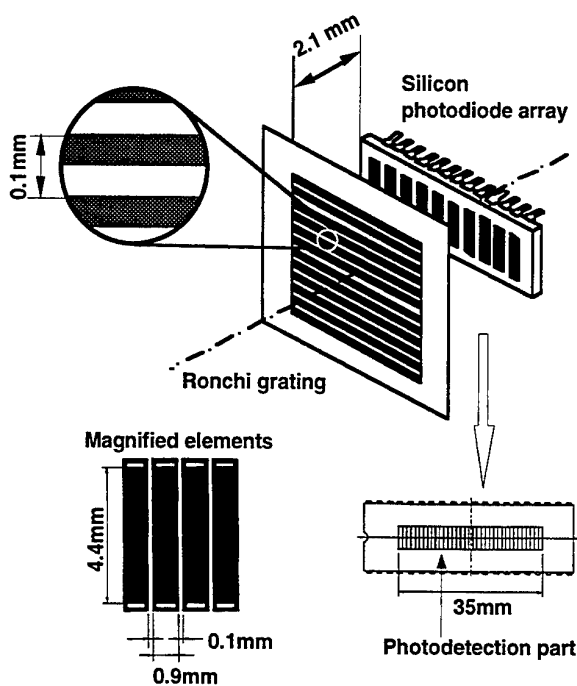


Fig. 3 Receiving optics

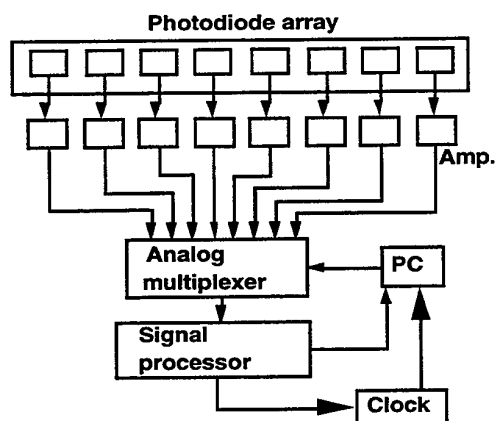


Fig. 4 Signal Processing system

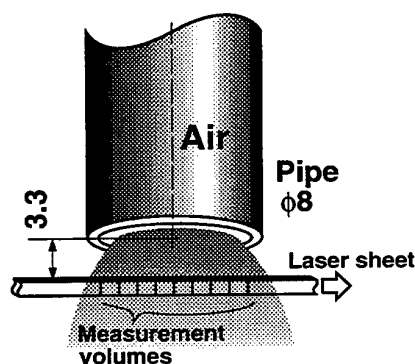


Fig. 5 Measurement points

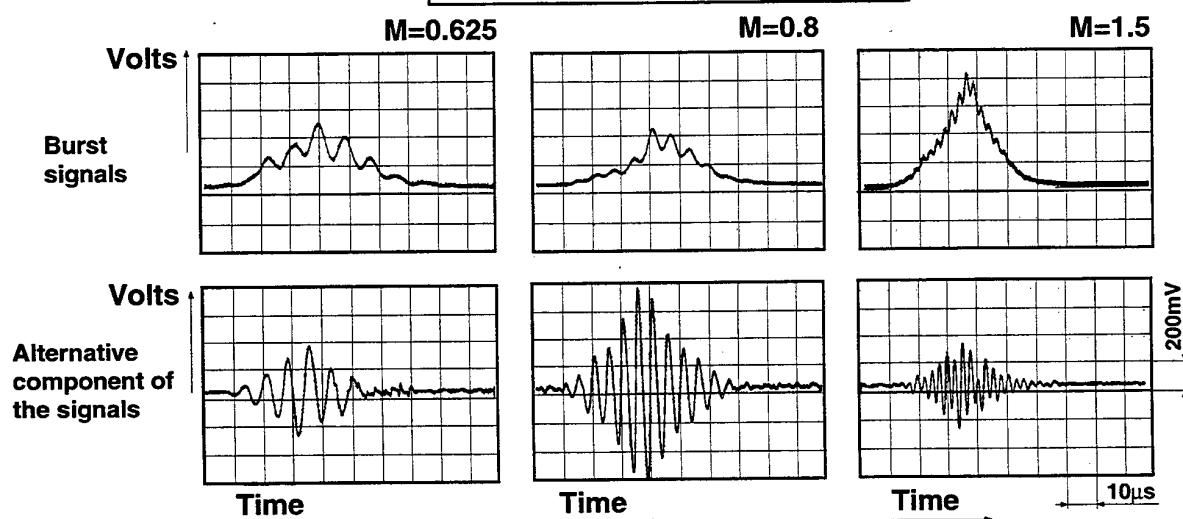
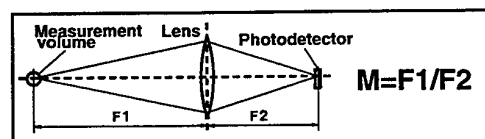


Fig. 6 Burst signal and alternative component of the signal

4. RESULTS

Figure 6 shows burst signals and alternative component of the signals for various image formation magnifications. Although the number of sinusoidal wave is small in comparison with that of LDV, we can verify a definite sinusoidal wave. For the case of small magnification, the number of sinusoidal wave is few, i.e., the frequency of the alternative component of the signal is low and approaches that of the pedestal component, while, for the case of large magnification, the number of sinusoidal wave is not so few, but its amplitude is small.

Figure 7 shows the effect of image formation magnification on the data rate and validity for the tracer particles of $80 \mu\text{m}$ and $20 \mu\text{m}$. The data rate and validity become highest when the magnification was 1.1 for two different particles. The magnification of 1.1 corresponds to $88 \mu\text{m}$ for the particle of $80 \mu\text{m}$ and $22 \mu\text{m}$ for the particle of $20 \mu\text{m}$. We thought that high alternative component of signal, i.e., good visibility of the signal would be expected, if the diameter of the particle image is equal to a half distance of the Ronchi grating spacing (i.e., $50 \mu\text{m}$ in this experiment). When we change the magnification, both the size of illuminating particle image on the grating and the corresponding grating fringe number which has the similar meaning to the fringe number for LDV change. Of course, the measurement volume and the signal frequency change also.

These relations are shown in Table 1. In the case of large magnification, the decreases of the width of measurement volume and the light intensity of the illuminating particle image cause decrease of data rate and validity. Measurable range of the processor used, i.e., BDC, was examined and it was found that the measurable range depended on the cut-off frequency of highpass filter, grating fringe number, signal frequency and sample clock of BDC. These facts show that the optical parameters above-mentioned and the processor affect data rate and validity, and the signal of low frequency and small grating fringe number may be missed. It is considered, therefore, that the data rate and validity are not only optical problem but also problem of processor.

The effect of grating fringe number on data rate and validity is shown in Fig. 8 for the magnification of 1.1. The grating fringe number over 12 was required for obtaining good data rate and validity. When we measure velocity profile using a spatial filtering velocimetry (SFV), its signal processor must analyze signal frequency of MV_{min}/P to MV_{max}/P , where V_{min} and V_{max} are minimum and maximum velocities for all measurement points, respectively. Since the velocity fluctuation in space is large and the grating fringe number is not large

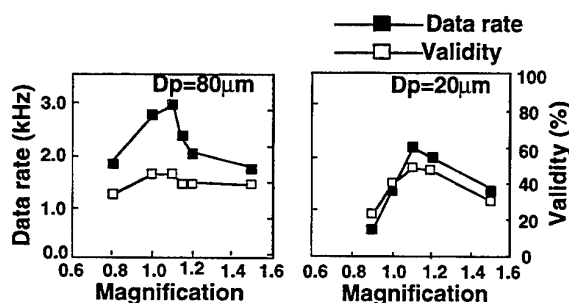


Fig. 7 Effect of image formation magnification

Table 1 Effect of magnification on measurement parameters

M	f_{cut} (kHz)	f-range (kHz)	W×H (mm)	fringe #
0.625	50	110-162	1.44×1.4	8
0.8	50	140-208	1.13×1.4	11
1.0	150	180-260	0.90×1.4	14
1.1	150	198-286	0.82×1.4	15
1.15	150	207-299	0.78×1.4	15
1.2	150	216-312	0.75×1.4	16
1.5	150	270-390	0.60×1.4	19

M : Magnification
 f : Cut-off frequency of highpass filter
 f-range : Frequency range to be measured
 W×H : Width × Height
 fringe # : Grating fringe number

enough to the fringe number of LDV, only one LDV signal processor is not enough to analyze SFV signals.

Figure 9 shows the effect of the deviation of image formation point from the receiving optics on the data rate and validity. There was not so much difference in data rate and validity in the range of the deviation less than 2 mm.

Figure 10 shows the time series data at eight measurement points obtained by scanning in regular order from the first position to the eighth position. Namely, the data at each channel were taken in turn whenever the signal was validated. When the valid signal was not detected at a certain position in a prescribed time, the measurement at this position was interrupted and the measurement point was moved to the next position.

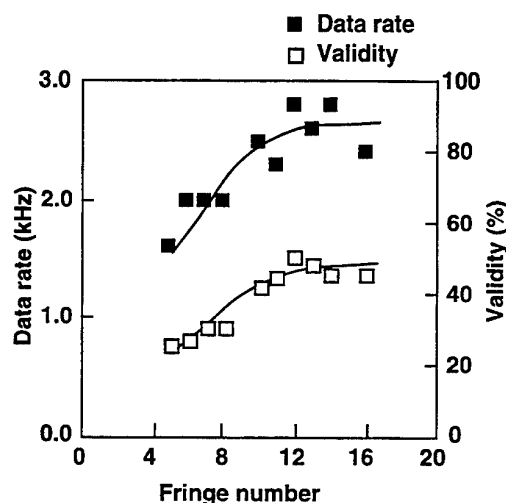


Fig. 8 Effect of grating fringe numbers

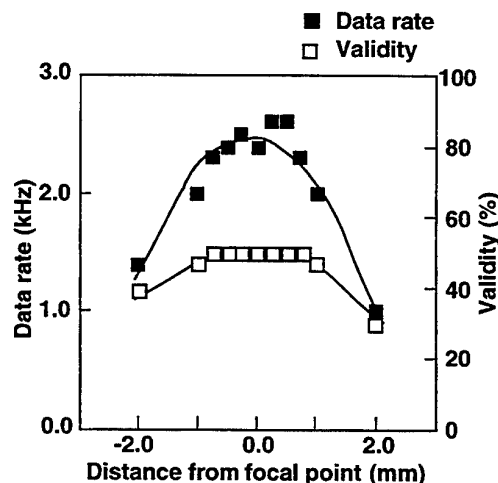


Fig. 9 Effect of deviation of image formation point

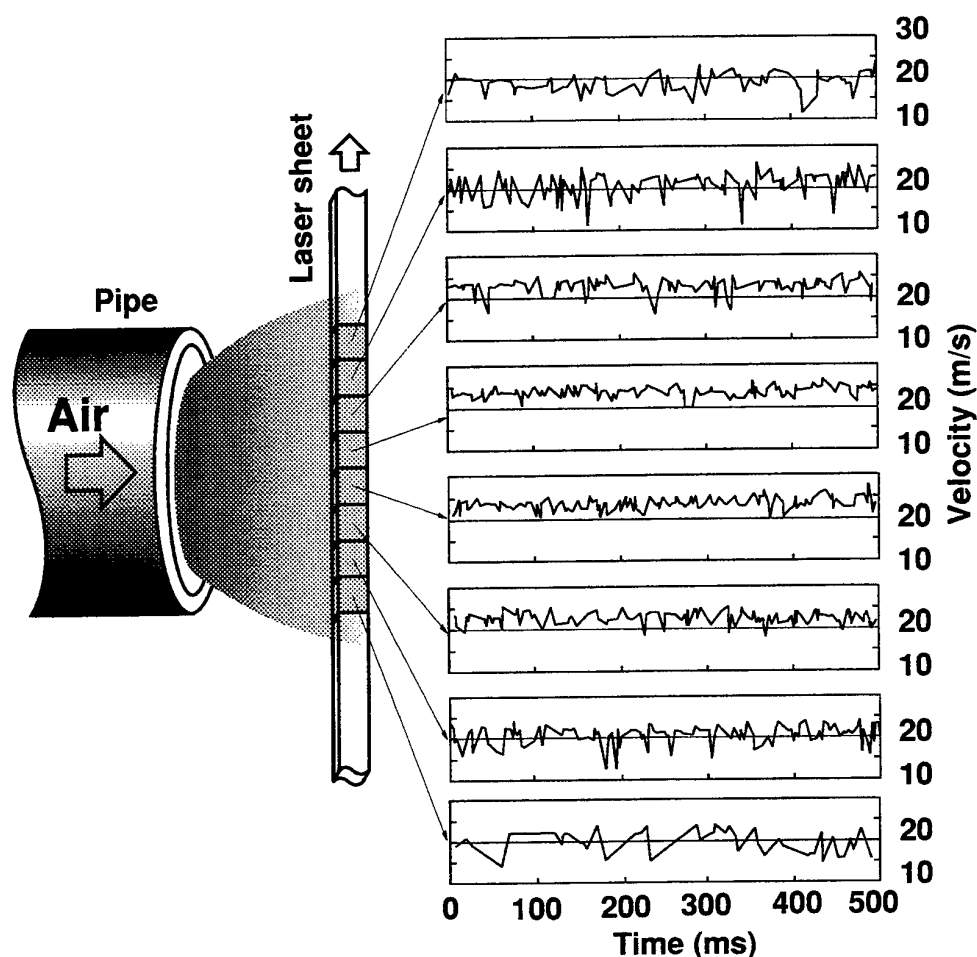


Fig. 10 Time-series velocity at the eight points

When the measurement point was fixed at one position, it was possible to obtain velocity data at the data rate of 2-3 kHz. If we have used eight LDV data processor, we could obtain velocity data at eight points at the data rate of 2 kHz and higher. In the present measurement, we used only one signal processor and measured data not at random but in sequential access. The scanning speed through eight channels, therefore, was limited to the value of the data rate for one channel (i.e. ~ 2 kHz in the present experiment) divided by the channel number, so that the data rate for each channel was about 250 Hz ($= 2 \text{ kHz} / 8$), i.e., 4 ms was consumed for one sequential scan of eight channels when the data rate was good. The low data rate at the measurement points on both ends might come from decrease of quantity of particles passing through the measurement points due to low velocity or limit of the signal processor used due to the signal

with wide frequency change.

In Fig. 11, the velocity distribution obtained from the eight channels near the center of the photodetector array of the spatial filtering velocimetry is compared to the theoretical values. The theoretical values were calculated by assuming that the flow near the nozzle exit had the same velocity distribution as that in the nozzle tube and followed 1/7-power law,

$$u = u_0 (x/R)^{1/7},$$

where u_0 is the velocity at the center of the tube, x is the distance from the inner tube wall, and R is the radius of the tube. The probability density functions of the axial velocity are also shown in Fig. 12, in comparison with LDV measurement. These results show that the present spatial filtering velocimetry has an ability to measure time series velocity fields with high accuracy.

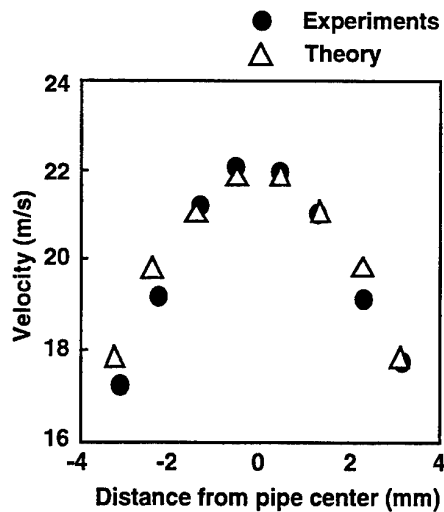


Fig. 11 Velocity distribution of jet

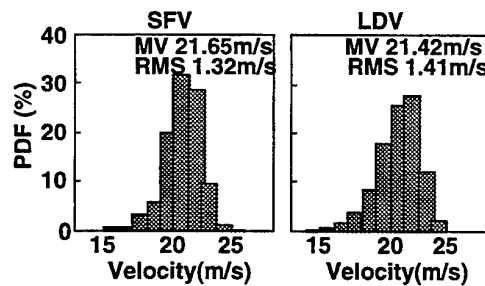


Fig. 12 Comparison of probability density functions of SFV and LDV

5. CONCLUSION

This paper describes an experimental study of a new method for measuring flow velocity distribution instantaneously. A transmission grating and a photodiode array were used for one-dimensional velocity distribution measurement.

The test results show that it is possible to obtain time series velocity at several points at almost simultaneously, though there are some improvements which should be done. For example,

- (1) It is required to detect flow direction
- (2) It is required to develop a new signal processor which can rapidly analyze multi-signal with small number of waves and large frequency change in time and space.

ACKNOWLEDGEMENTS

The participation of Mr. Kohara in the collection and analysis of the data is gratefully appreciated.

REFERENCES

- Ator, J.T., 1963, Image-Velocity Sensing with Parallel-Slit Reticles, *J. Opt. Soc. Am.* vol. 53, pp.1416.
- Ikeda, Y., et al., 1989, Multipoint Simultaneous LDV Optics, in *Application of Laser Anemometry to Fluid Mechanics*, eds. R.J. Adrian et al., pp.361, Springer-Verlag, Berlin Heidelberg.
- Gaster, M., 1964, A New Technique for the Measurement of Low Fluid Velocities, *J. Fluid Mech.*, vol.20, pp.183.
- Ushizaka, T., and Asakura, T., 1983, Measurements of Flow Velocity in a Microscopic Region Using a Transmission Grating, *Appl. Opt.*, vol. 22, pp.1870.

AUTHORS' INDEX

Abe, N., 33.2.1
 Achimastos, T.J., 38.5.1
 Adrian, R., 23.1.1, 17.1.1, 18.3.1
 Aftel, R., 20.5.1
 Akamatsu, F., 2.4.1
 Akoh, E., 37.2.1
 Anacleto, P., 19.2.1
 Anders, K., 9.2.1
 Anderson, D.J., 18.4.1
 Antonia, R.A., 17.2.1, 29.1.1
 Arcoumanis, C., 16.3.1, 25.1.1
 Aroussi, A., 37.3.1
 Astachow, G., 13.4.1
 Auger, P.L., 34.4.1
 Auriemma, M., 16.1.1
 Azizi, L., 6.2.1
 Azzopardi, B.J., 38.4.1

Bachalo, W.D., 2.3.1, 9.3.1
 Balabani, S., 33.3.1
 Baldwin, T., 33.5.1
 Barcouda, M., 37.1.1
 Barigozzi, G., 28.3.1
 Barrientos, A., 26.3.1
 Bearman, P.W., 18.5.1
 Bénard, J., 37.1.1
 Bencze F., 14.6.1
 Benech, P., 34.4.1
 Benedict, L.H., 36.1.1, 36.6.1
 Bergmann, V., 3.1.1
 Bernard, A., 26.5.1
 Berton, E., 14.1.1
 Beyer, W., 23.4.1
 Biage, M., 15.4.1
 Blümcke, E., 22.1.1
 Boesiger, P., 33.5.1
 Booi, R., 35.3.1
 Borrett, N.A., 8.5.1
 Botnar, R., 33.5.1
 Boulouchos, K., 13.2.1
 Bourguignon, E., 7.1.1
 Bousgarbiès, J.L., 26.5.1
 Boutier, A., 14.5.1
 Bräumer, G., 37.5.1
 Breeze, G., 14.4.1
 Brenn, G., 9.4.1
 Brücker, Ch., 4.2.1, 26.1.1
 Bruckner, R.J., 15.1.1
 Brun, M., 22.5.1
 Buresti, G., 30.3.1
 Bütetisch, K.A., 14.3.1

Cahen, C., 37.1.1
 Caldas, F., 7.3.1
 Campi, A., 12.4.1

Campos, V.A., 37.5.1
 Carosone, F., 21.2.1
 Cartellier, A., 34.4.1
 Castellini, P., 26.2.1
 Cenedese, A., 21.2.1, 27.3.1
 Chiné, B., 19.6.1
 Christofori, K., 12.1.1
 Coelho, P.M., 35.5.1
 Coghe, A., 25.6.1
 Cohn, R.K., 1.2.1
 Collicott, S.H., 15.2.1
 Collins, M.W., 17.3.1
 Concha, F., 19.6.1
 Cook, C., 20.5.1
 Corcione, F.E., 16.1.1
 Cossali, G.E., 25.6.1
 Cremers, C., 11.5.1
 Crompton, N., 14.4.1
 Cüppers, A., 19.4.1

Dabiri, D., 30.1.1
 Darabiha, N., 3.5.1
 Delgado, A., 8.1.1
 Denk, V., 8.1.1
 Derville, A., 4.1.1
 Dimopoulos, D.A., 38.5.1
 Dimopoulos, P., 13.2.1
 Djenidi, L., 17.2.1, 29.1.1
 Domann, R., 19.1.1
 Domnick, J., 20.4.1
 Dopheide, D., 6.6.1, 34.1.1, 40.3.1
 Draad, A.A., 29.3.1
 Dracos, T., 4.6.1
 Duarte, D., 7.3.1
 Dufour, C., 11.4.1
 Dufour, C., 31.2.1
 Dullenkopf, K., 20.1.1, 25.2.1, 25.3.1
 Dum, T., 32.2.1
 Durox, D., 20.3.1
 Durst, F., 6.3.1, 8.4.1, 16.4.1

Ebner, J., 25.2.1
 Egan, D., 28.2.1
 Egbers, C., 23.4.1
 Eisele, K., 33.5.1
 Ekmann, J.M., 10.3.1
 Elavarasan, R., 29.1.1
 Elder, R.L., 28.2.1
 Elsässer, A., 25.2.1, 25.3.1
 Escudier, M.P., 1.1.1
 Evenstad, J., 2.1.1
 Faram, M.G., 19.5.1
 Faure, M., 22.3.1
 Favier, D., 14.1.1
 Fentiman, N.J., 8.5.1
 Fernandes, E.C., 39.1.1

Ferrão, P., 7.3.1
Ferrara, G., 19.6.1
Fick, W., 10.4.1
Fiedler, O., 12.1.1
Fitzpatrick, J.A., 36.5.1
Ford, H.D., 11.3.1
Founti, M.A., 38.5.1
Frederiksen, J.P. 37.2.1
French, B., 16.3.1
Frohn, A., 9.2.1
Furuichi, N., 31.5.1

Gallagher, M.W., 38.2.1
Gan, C.L., 17.2.1
Gaspiretti, M., 12.4.1, 26.2.1
Gendrich, C.P., 1.2.1
Gharib, M., 30.1.1
Ghiglione, A., 28.3.1
Gjelstrup, P., 31.3.1
Glahn, A., 9.5.1
Gogineni, S., 18.2.1
Gökalp, I., 7.1.1
Goss, L., 18.2.1
Gottero, M., 35.1.1
Gouesbet, G., 6.5.1
Gougat, P., 38.3.1
Gould, R.D., 36.1.1, 36.6.1
Gouldson, I.W., 1.1.1
Gray, C., 7.4.1
Greated, C.A., 18.4.1
Gréhan, G., 6.5.1
Griffiths, A.J., 10.4.1
Grrem, R., 13.3.1
Gupta, A.K., 20.5.1

Hachiga, T., 31.5.1
Haile, E., 20.3.1
Hanratty, T.J., 17.1.1
Hanson, S.G., 40.2.1
Harden, J.M., 14.2.1
Harris, S.R., 15.3.1, 15.4.1
Hart, D.P. 21.1.1
Harvey, J.K., 18.5.1
Hassa, B., 26.6.1
Hassan, Y., 27.1.1
Heikal, M.R., 22.3.1
Heitor, M.V., 7.3.1, 19.2.1, 32.1.1, 39.1.1
Helbig, J., 26.6.1
Hensse, J., 13.4.1
Hermann, J., 39.2.1
Herve, P., 6.2.1
Herzog, P., 39.4.1
Hess, C.F., 6.1.1
Hicks, R.A., 10.1.1
Higashi, S., 33.2.1
Hirohata, T., 2.6.1, 10.5.1

Hirt, F., 33.5.1
Hishida, K., 29.4.1, 31.5.1, 35.2.1
Hishida, M., 2.5.1
Höfer, H., 28.1.1
Hoffmann, R., 32.1.1
Höfken, M., 8.4.1
Hofmann, D., 1.3.1
Hofmann, F., 37.1.1
Hönig, R., 7.6.1
Host-Madsen, A., 31.3.1
Houssaye, G., 31.2.1
Hsu, C.T., 12.6.1
Huber, L., 38.3.1
Hübner, W., 19.1.1
Hurst, D.W., 17.3.1

Ibrahim K.M., 2.3.1
Iizuka, K., 35.2.1
Ikeda, K., 24.2.1
Ikeda, Y., 2.6.1, 10.5.1, 13.6.1, 40.5.1
Ikeda, S., 37.6.1
Imam, H., 40.2.1
Imbach, J., 10.2.1
Ishima, T., 13.5.1, 22.2.1
Ito, A., 11.5.1
Iuso, G., 35.1.1

Jackson, D.A., 25.5.1
Jackson, N., 22.3.1
Jaffre, D., 7.4.1, 7.5.1
James, S.W., 28.2.1
Johari, H., 30.1.1
Jones, J.D.C., 18.4.1
Jud, E., 33.5.1

Kappler, G., 7.6.1
Karlsson, R.I., 35.6.1
Kato, F., 21.4.1, 24.2.1
Katsuki, M., 2.4.1
Katz, J., 4.3.1
Kawaguchi, Y., 29.4.1
Kawahara, N., 10.5.1
Kendrick, D.W., 7.5.1
Kepner, J., 33.5.1
Kettl, H., 7.6.1
Kijima, M., 33.2.1
Kimura, I., 24.6.1
Klasine, R., 32.2.1
Kleitz, A., 6.2.1
Kobayashi, K., 13.5.1
Koizumi, M., 27.1.1
Kompenhans, J., 4.1.1, 14.3.1, 18.1.1, 28.1.1
Köngeter, J., 19.4.1
Koochesfahani, M.M., 1.2.1

Kost, F., 28.1.1
Koyama, T., 13.5.1
Krüger, G., 13.4.1
Kruse, M., 29.2.1
Kumada, M., 31.5.1
Kumpart, J., 12.1.1
Kurihara, H., 34.5.1
Kurihara, N., 13.6.1

Labahn, N., 12.1.1
Lacas, F., 20.3.1
Lachner, R., 7.6.1
Lading, L., 40.2.1
Lai, W., 18.3.1
Larsen, P.S., 37.2.1
Lauren, T.S., 35.4.1
Lawes, M., 10.1.1
Le Roy, J.F., 11.4.1, 31.2.1
Lee, K.C., 8.5.1
Lefèvre, J., 14.5.1
Lehmann, B., 26.6.1
Leipertz, A., 1.3.1
Lempert, W.R., 15.3.1, 15.4.1
Lepicovsky, J., 15.1.1
Leporcq, B., 11.4.1, 31.2.1
Levy, Y., 39.3.1
Li, E.B., 25.4.1
Liard, V., 3.5.1
Lima, M.M.C.L., 30.4.1
Lindvold, L.R., 40.2.1
Liu, Z.-C., 17.1.1, 18.3.1
Lockey, R.A., 28.2.1
Logar, R.H., 32.2.1
Lowson, M.V., 14.2.1, 28.4.1
Lubarsky, E., 39.3.1
Lutz, M., 8.1.1

Macchioni, R., 16.1.1
Mackenzie, M.R., 25.4.1
Madarame, H., 27.1.1
Maeda, M., 2.5.1, 29.4.1, 35.2.1
Maeda, T., 2.5.1
Maekawa, M., 35.2.1
Mahmood, Z., 16.2.1
Marr, R., 38.1.1
Martel, C., 3.5.1
Martinez, R.E., 3.3.1
Mathur, M.P., 10.3.1
McCluskey, D.R., 35.4.1
McEwan, I.K., 38.2.1
Meier, U.E., 3.1.1
Meier, W., 3.1.1
Meinhart, C.D., 18.3.1
Melling A., 6.3.1
Menon, R., 2.1.1, 12.2.1
Merkel, G.J., 4.6.1

Meyers, J.F., 11.1.1
Micheli, F., 14.5.1
Michou, Y., 7.1.1
Miles, P.C., 40.1.1
Miles, R.B., 15.3.1
Mimatsu, J., 31.5.1
Miozzi, M., 27.3.1
Miyate T., 32.3.1
Mokaddem, K., 7.5.1
Mordacci, A., 30.3.1
Moreira, A.L.N., 19.2.1, 32.1.1
Morikita, H., 2.5.1
Moseley, R.P., 18.5.1
Most, J.M., 10.2.1
Müller, E., 36.2.1
Müller, H., 6.6.1, 34.1.1
Münch, K.-U., 1.3.1
Mundo, Chr., 20.1.1, 26.4.1
Mungal, M.G., 3.3.1
Muñiz, L., 3.3.1

Nakajima, T., 2.6.1, 10.5.1, 13.6.1, 40.5.1
Nakatani, N., 15.5.1
Naqwi, A., 2.1.1, 2.2.1
Narumi, A., 11.5.1
Nash, E.C., 28.4.1
Natrass, S.R., 25.5.1
Ng, K., 16.2.1
Nielsen, N.F., 37.2.1
Nijenboer, F.J., 31.4.1
Nimmo, G., 18.4.1
Nino, E., 3.4.1
Nobach, H., 36.2.1
Nocera D.G., 1.2.1
Nouri, J.M., 16.3.1
Nsi Mba, M., 14.1.1

O'Doherty, T., 10.4.1, 19.5.1
Obokata, T., 13.5.1
Ogino, F., 32.3.1
Ohba, K., 37.6.1
Ohta, Y., 22.2.1
Ohtake K., 32.3.1
Okamoto, K., 24.2.1, 27.1.1
Okamoto, S., 33.2.1
Oldenburg, M., 8.2.1
Onorato, M., 35.1.1
Onori, R., 12.4.1
Orglmeister, R., 8.6.1
Orthmann, A., 39.2.1
Oshio, T., 15.5.1
Ovalle, E., 26.3.1
Ozawa, M., 24.6.1

Palma, J.M.L.M., 30.4.1
 Panidis, Th., 12.5.1
 Paone, N., 3.4.1, 26.2.1
 Pap, E., 8.2.1
 Peng, J.Y., 25.4.1
 Pereira, J.C.F., 26.4.1
 Perrin, M., 7.4.1, 7.5.1
 Persson, N.J., 35.6.1
 Pestian, D., 18.2.1
 Peters, W.D., 23.5.1
 Piana, J., 3.5.1
 Pickering, S.J., 37.3.1
 Pinchemel, B., 11.4.1, 31.2.1
 Pinho, F.T., 8.3.1, 35.5.1
 Piqueiro, F.M., 8.3.1
 Podoleanu, A.Gh., 25.5.1
 Poireault, B., 10.2.1
 Poppe, C., 7.3.1
 Porporato, A., 36.3.1
 Potz, D., 13.4.1
 Prescher, K., 13.4.1
 Presser, C., 20.5.1
 Proença, M.F., 8.3.1

Qiu, H.H., 12.6.1

Raffel, M., 4.1.1, 14.3.1, 18.1.1, 28.1.1
 Raimann, J., 20.4.1
 Rambert, A., 38.3.1
 Ramos, J., 14.1.1
 Raposo, J., 26.4.1
 Rasmussen, J.J., 35.4.1
 Rath, H.J., 23.4.1
 Ren, K.F., 6.5.1
 Reuber, J., 22.1.1
 Revel, G.M., 3.4.1
 Richon, J.B., 7.4.1
 Rickards, J., 14.4.1
 Ridolfi, L., 36.3.1
 Riethmuller, M.L., 9.1.1
 Rist, D., 7.6.1
 Rivir, R., 18.2.1
 Robart, D.M., 9.3.1
 Rodrigues, A.H., 35.5.1
 Rolon, J.C., 7.5.1
 Romano, G.P., 27.3.1
 Ronneberger, O., 4.1.1
 Rose, B., 40.2.1
 Rossi, G.L., 12.4.1
 Roth, N., 9.2.1
 Rothlübbers, C., 8.6.1
 Rys, F.S., 4.6.1

Saito, K., 11.5.1
 Sakabe, T., 15.5.1
 Sakurai, A., 37.6.1
 Salyer, T.R., 15.2.1
 Samenfink, W., 25.2.1, 25.3.1
 Sankar, S.V., 9.3.1
 Santos, A.M., 8.3.1
 Sawa, K., 37.6.1
 Schäfer, M., 8.4.1
 Schanen Duport, I., 34.4.1
 Scheffler, T., 8.6.1
 Schmid, A., 7.6.1
 Schmid, H.-J., 37.4.1
 Schmisseeur, J.D., 15.2.1
 Schneider, S.P., 15.2.1
 Scholten, J., 36.5.1
 Scholten, J.W., 33.1.1
 Schöne, F., 20.1.1
 Schraml, S., 1.3.1
 Schulz, R., 17.4.1
 Seasholtz, R.G., 24.1.1
 Seccia, G., 16.1.1
 Seelhorst, C., 14.3.1
 Shen, X., 31.1.1
 Sheppard, C.G.W., 10.1.1
 Shibata, Y., 21.4.1
 Shimizu, I., 21.4.1, 24.2.1
 Shrimpton, J.S., 20.2.1
 Siekmann, H., 8.6.1
 Silva, N.A., 30.4.1
 Simmons, K., 37.3.1
 Simon, L., 36.5.1
 Smits, A.J., 15.4.1
 Socoliuc, M., 22.5.1
 Sommerfeld, M., 12.5.1
 Spork, V., 19.4.1
 Stasicki, B., 18.1.1
 Staude, W., 17.4.1
 Stenum, B., 35.4.1
 Stewart, J.N., 18.5.1
 Stieglmeier, M., 20.1.1
 Stricker, W., 3.1.1
 Strunck, V., 6.6.1, 40.3.1
 Susset, A., 7.4.1
 Swales, C., 14.4.1, 28.4.1
 Syred, N., 19.5.1

Takamoto, M., 34.5.1
 Takeda, C., 22.2.1
 Talamelli, A., 30.3.1
 Tanzini, G., 30.3.1
 Tao, B., 4.3.1
 Taplin, S.R., 25.5.1
 Tashtoush, G., 11.5.1
 Tatam, R.P., 11.3.1
 Tatam, R.T., 28.2.1
 Tawaraya, Y., 29.4.1

Tedeschi, G., 12.2.1
Teixeira, J.C.F., 37.5.1
Terry, N., 14.4.1
Theisen, D., 7.6.1
Tieu, A.K., 25.4.1
Többen, H., 34.1.1
Tokuhiro, A., 35.2.1
Tournois, G., 39.4.1
Tran, P.X., 10.3.1
Trimis, D., 16.4.1
Tropea, C., 9.4.1, 19.1.1, 20.1.1, 36.2.1
Troy, V., 23.1.1
Trump, D., 18.2.1
Tsunoda, K., 33.2.1
Tsushima, S., 2.4.1
Tukagoshi, M., 13.5.1
Tukker, J., 35.3.1
Tummers, M.J., 36.4.1

Ubaldi, M., 28.3.1
Uehara, K., 13.5.1
Ullum, U., 37.2.1
Umhauer, H., 37.4.1
Urabe, T., 37.6.1

Vad, J., 14.6.1
Valeau, V., 39.4.1
Valentino, G., 13.2.1, 16.1.1
Valière, J.C., 39.4.1
Van Beeck, J.P.A.J., 9.1.1
Van Maanen, H.R.E., 31.4.1, 36.4.1
Venart, J.E.S., 23.5.1
Veynante, D., 3.5.1, 20.3.1
Volkert, J., 19.1.1
Volkholz, P., 6.3.1
Vollmers, H., 14.3.1
Vortmeyer, D., 39.2.1
Vyrodov, A.O., 3.1.1

Wagner, S., 29.2.1
Wang, Q., 18.5.1
Watkins, A.P., 20.2.1
Webb, D.J., 25.5.1
Weclas, M., 16.4.1
Weigand, A., 30.1.1
Weiß, C., 38.1.1
Westerweel, J., 29.3.1
Whitelaw, D.S., 25.1.1
Whitelaw, J.H., 25.1.1
Wigley, G., 32.2.1, 38.1.1
Will, S., 1.3.1
Willert, C., 4.1.1, 14.3.1, 18.1.1, 28.1.1
Willmann, M., 9.5.1, 20.1.1
Wiseall, S., 18.4.1
Wittig, S., 9.5.1, 20.1.1, 25.2.1, 25.3.1

Witze, P.O., 13.3.1, 40.1.1
Wolf, G., 20.4.1
Wolley, R., 10.1.1

Xu, T.-H., 9.4.1

Yabe, A., 29.4.1
Yianneskis, M., 8.5.1, 16.2.1, 33.3.1
Yule, A.J., 20.2.1

Zaidi, S.H., 38.4.1
Zangl, P., 39.2.1
Zhang, H.L., 17.3.1
Zhang, J., 4.3.1
Zhang, X., 17.3.1
Zhang, Z., 33.5.1
Zhongming, M., 31.1.1
Zunino, P., 28.3.1